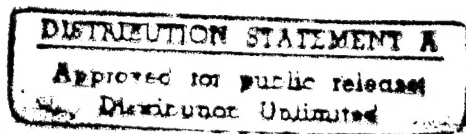
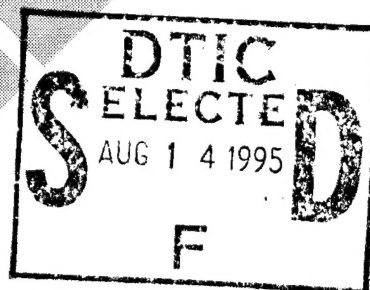


N92-23780



DTIC QUALITY INSPECTED 5

A Service of:



National Aeronautics and
Space Administration

Scientific and Technical
Information Office

19950807 025

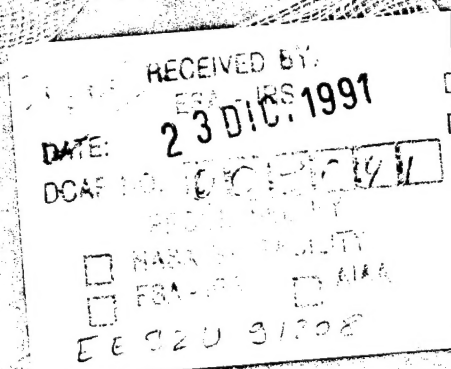
esa SP-321

(Volume 1)

(ESA-SP-321-Vol-1) SPACECRAFT STRUCTURES
AND MECHANICAL TESTING, VOLUME 1 (ESA)
487 p

N92-23780
--THRU--
N92-23850
Unclass
G6/18 0084692

Spacecraft structures and mechanical testing



Proceedings of the international symposium
organised by the European Space Agency
jointly sponsored by the Centre for Space Studies
d'Etudes Spatiales and the Forschungsinstitut für Luft- und Raumfahrt
e.V., and held at ESTEC, Noordwijk, The Netherlands,
on 24 - 26 April 1991

~~ACCESSIONING, REPRODUCTION AND DISTRIBUTION~~
BY OR FOR NASA PERMITTED



esa SP-321

October 1991

Spacecraft structures and mechanical testing

(Volume 1)

Proceedings of the international conference organised by the European Space Agency, jointly sponsored by the Centre National d'Etudes Spatiales and the Deutsche Forschungsanstalt für Luft- und Raumfahrt e.V., and held at ESTEC, Noordwijk, The Netherlands, on 24 - 26 April 1991

Accession For	
NTIS CRA&I	<input checked="" type="checkbox"/>
DTIC TAB	<input type="checkbox"/>
Unannounced	<input type="checkbox"/>
Justification	
By <i>Arg lti</i>	
Distribution	
Availability Codes	
Dist	Avail and/or Special
<i>A-1</i>	

european space agency / agence spatiale européenne

8-10, rue Mario-Nikis, 75738 PARIS CEDEX 15, France

~~ACCESSIONING, REPRODUCTION AND DISTRIBUTION~~
BY OR FOR NASA PERMITTED

PROGRAMME COMMITTEE

Co-Chairmen

C. Stavrinidis, ESA/ESTEC, Noordwijk, NL
 A. Mamode, CNES, Toulouse, France
 H. Bergmann, DLR, Braunschweig, FRG

Members

M. Bach, CNES, Toulouse, France
 G. Banino, Aeritalia, Turin, Italy
 H. Baier, Dornier, Friedrichshafen, FRG
 G. Bartelds, NLR, Emmeloord, The Netherlands,
 E. Breitbach, DLR, Göttingen, FRG
 P. Brinkmann, ESA/ESTEC, Noordwijk, NL

W.R. Burke, ESA/EPD, Noordwijk, NL
 J. Fougères, Aerospatiale, Les Mureaux, France
 B. Gerber, Matra, Toulouse, France
 E. Hornung, MBB/ERNO, Bremen, FRG
 J.F. Imbert, Intespace, Toulouse, France
 V.J.G. Molinero, CASA, Madrid, Spain
 K. Mühlbauer, IABG, Ottobrunn, FRG
 R. Ohayon, ONERA, Châtillon, France
 A. de Rouvray, ESI, Rungis, France
 D. Sach, MBB, Munich, FRG
 K. Spång, DNV Ingemansson, Göteborg, Sweden
 R.G. White, Univ. of Southampton, Highfield, UK

COLOPHON

<i>Serial number</i>	ESA SP-321 (2 vols.)
<i>Title</i>	Spacecraft structures and mechanical testing – Proceedings of an international conference held at ESTEC, Noordwijk, The Netherlands, on 24 – 26 April 1991
<i>Cover design</i>	C. Haakman/B. Haasnoot (Theme taken from paper by E. Haug et al., see p. 861)
<i>Proceedings published and distributed by</i>	ESA Publications Division ESTEC, Noordwijk, The Netherlands
<i>Compiled by</i>	W.R. Burke
<i>Printed in</i>	The Netherlands
<i>Price code</i>	E4
<i>International Standard Serial Number</i>	ISSN 0379 6566
<i>International Standard Book Number</i>	ISBN 92-9092-126-9
<i>Copyright</i>	©1991 by European Space Agency

CONTENTS

(volume 1)

Session 1.1.A: SPACE STATION I

Development of Japanese experimental module.....	3
<i>F. Otsuki, K. Kamesaki, K. Shiraki & K. Tasaki, National Space Development Agency of Japan, Tokyo, Japan</i>	
The Columbus free-flying laboratory.....	9
<i>J. Gülpen, ERNO, Bremen, FRG</i>	
Structural assessment of the Space Station Freedom's pressurised elements.....	19
<i>R.L. Grant, Boeing Defense & Space Group, Huntsville, AL, USA</i>	

Session 1.1.B: SPACE STATION II

Validation of hydrocodes for orbital debris impact simulation.....	29
<i>M. Lambert, ESTEC, Noordwijk, The Netherlands</i>	
<i>J. Frey, J. Rios, X. Garaud & J. Dubois, Engineering Systems International, Rungis, France</i>	
<i>E. Schneider, EMI-Fraunhofer-Institut f. Kurzezeitdynamik, Freiburg, FRG</i>	
Material considerations for habitable areas of manned spacecraft.....	37
<i>H. Babel, C. Jones, K. Simpson, B. Vickers & P. Ledoux, McDonnell Douglas Space Systems Co., Huntington Beach, CA, USA</i>	
Protection of spacecraft against meteoroid/orbital-debris impacts.....	43
<i>H. Reimerdes, MBB/ERNO, Bremen, FRG</i>	

Session 1.2.B: ANALYSIS I – DYNAMICS

Coupled load analysis: scatter related to model uncertainties.....	53
<i>P.W. Bousquet & F. Mercier, CNES, Toulouse, France</i>	
<i>M. Klein, ESTEC, Noordwijk, The Netherlands</i>	
The use of modal synthesis in conjunction with nonlinear transient dynamic analysis.....	59
<i>S.A. Challener & A.J. Vibert, Frazer-Nash Consultancy Ltd, Leatherhead, Surrey, UK</i>	
Improvements for interpretation of structural dynamics calculation using effective parameters for substructures.....	63
<i>T. Berthelon & A. Capitaine, MATRA, Toulouse, France</i>	

Session 1.3.B: VIBRO-ACOUSTICS I

Acoustic absorption due to specimen in test in a reverberant chamber.....	71
<i>A. Girard & C. Blanchard, Intespace, Toulouse, France</i>	
Maximal modal energy method: an overvaluing tool for low-frequency prediction of structure acoustic response.....	77
<i>S. de Zotti, P. Herman & B. Laviron, MATRA, Toulouse, France</i>	
Numerical and experimental study of noise generated by a vibrating plate.....	83
<i>O. von Estorff, IABG, Ottobrunn, FRG</i>	
<i>A. Homm & F. Bartels, Fraunhofer-Forschungsgruppe f. Hydroakustik, Ottobrunn, FRG</i>	

Session 1.4.B: MATERIALS I – FRACTURE/FATIGUE

Development of fatigue damage mechanics for application to the design of damage-tolerant composite components.....	91
<i>P.W.R. Beaumont, S.M. Spearing & M.T. Kortschot, Cambridge University, UK</i>	
Characterisation of interlaminar mode I and mode II fracture in CFRP laminates.....	97
<i>R. Prinz & M. Gaedke, DLR, Braunschweig, FRG</i>	
Fatigue analysis under random stresses.....	103
<i>A. Ricard, FRAMASOFT+CSI, Paris, France</i>	

Session 1.1.C: LAUNCHERS I – LOADS/OPTIMISATION

A review of space shuttle payload-bay lift-off flight data and analysis comparisons.....	111
<i>D.A. Hamilton, N.E. Tengler, NASA Johnson Space Center, Houston, TX, USA</i>	
<i>B.N. Nguyen & C.A. Lauritzen, Lockheed Corporation, Houston, TX, USA</i>	
Dynamic load cases on Ariane 5.....	117
<i>B. Chemoul & E. Louaas, CNES, Evry, France</i>	
Multi-parameter optimisation on Ariane 5.....	123
<i>G. Boullenger, Aerospatiale, Les Mureaux, France</i>	

Session 1.2.C: TESTING I – SYSTEMS

An advanced system for environmental sine testing.....	131
<i>J. Leuridan, F. Declercq, R. Mangelschots & G. Bossaert, LMS International, Leuven, Belgium</i>	
Noncontacting measurement of vibration.....	135
<i>A.J. Barker, Ometron Ltd, London, UK</i>	
On development of automated static loading system for spacecraft structures.....	139
<i>A.V. Patki & R. Samuel, ISRO, Bangalore, India</i>	

Session 1.3.C: ANALYSIS II – METHODS

Nonlinear finite-element analysis of sandwich shells.....	147
<i>O. Aamlid & P.G. Bergan, A.S. Veritas Research, Høvik, Norway</i>	
Influence of the substrate on the solar-cell interconnector: stress distribution and fatigue-life prediction.....	153
<i>S. Tizzi, M. Marchetti & S. La Terza, Università di Roma 'La Sapienza', Rome, Italy</i>	
Buckling of simply supported and clamped anisotropic plates under combined loads.....	161
<i>G. Romeo & G. Frulla, Politecnico di Torino, Turin, Italy</i>	

Session 1.4.C: MATERIALS II – CHARACTERISATION

Damping behaviour of unidirectional fibre-reinforced polymers.....	169
<i>H. Hanselka, DLR, Braunschweig, FRG</i>	
Computer simulation of moisture penetration in structures.....	175
<i>O. Wilmar, DNV Ingemannsø AB, Stockholm, Sweden</i>	
A new test facility for measuring the coefficient of moisture expansion of advanced composite materials.....	181
<i>G. Romeo, E. Miraldi, G. Ruscica, F. Bertoglio & G. Ruvinetti, Politecnico di Torino, Turin, Italy</i>	

Session 1.1.D: LAUNCHERS II – DEVELOPMENT

Ariane 5 structural definition of the upper composite.....	189
<i>A.L. González Blázquez, ESA, Paris, France</i>	
Advanced numerical analysis for the optimisation of the structural behaviour of the intersegment connection for the Ariane 5 booster case.....	197
<i>P. Agatonovic & D. Sygulla, MAN Technologie AG, München, FRG</i>	
Brief history of the development of the EPS-structure.....	203
<i>J. Martín, CASA, Madrid, Spain</i>	

Session 1.2.D: VIBRO-ACOUSTICS II – ENVIRONMENT

Ariane 4 internal acoustic environment: interpretation of flight data with a vibro-acoustic model of the upper part of the launcher.....	211
<i>B. Ritchie, CNES, Evry, France</i>	
<i>M. Beldi, STRACO U.T.C., Compiègne, France</i>	
Acoustic prediction on satellite structure.....	219
<i>C. Clerc, METRAVIB R.D.S., Ecully, France</i>	
<i>J.-N. Giraudbit, ALCATEL ESPACE, Toulouse, France</i>	
Acoustic cavity and fluid/structure interaction models: a methodological deterministic approach and problems encountered.....	223
<i>P.C. Marucchi-Chierro, Alenia Spazio, Turin, Italy</i>	

Session 1.3.D: ANALYSIS III – METHODS

Employment of Craig-Bampton models for nonlinear dynamic analysis.....	235
<i>M. Klein, ESTEC, Noordwijk, The Netherlands</i>	
<i>Ph. Deloo, Ikoss G.m.b.H., Stuttgart, FRG</i>	
Feasibility of payload sensitivity analyses for AR4 dynamic events.....	241
<i>F. Mercier, CNES, Toulouse, France</i>	
The response surface method: an efficient tool to determine the failure probability of large structural systems.....	247
<i>Prof. Schuëller, University of Innsbruck, Austria</i>	

Session 1.4.D: MATERIALS III – COMPOSITES

Aging of polymer matrix composites at elevated temperatures.....	255
<i>H. Twardy, DLR, Braunschweig, FRG</i>	
The torsional fatigue behaviour of the in-plane and out-of-plane shear moduli of composite materials.....	263
<i>D. van Hemelrijck, L. Schillemans, F. de Roey, I. Daerden, F. Boulpaep, J. De Visscher & A. Cardon, Free University of Brussels, Belgium</i>	
Experimental study of delamination growth in multidirectional CFRP laminates under fatigue loading.....	269
<i>H.C. Goetting, DLR, Braunschweig, FRG</i>	

Session 2.1.A: SPACE PLANE & RE-ENTRY I

Conceptional design to heat-resistant airframe of HOPE.....	277
<i>M. Yamamoto, National Space Development Agency, Japan</i>	
Large thin composite thermostructural parts.....	283
<i>D. Desnoyer, A. Lacombe & J.M. Rouges, SEP, St Médard-en-Jalles, France</i>	
Design challenges for the National Aero-Space Plane.....	293
<i>F.D. Boensch, National Aero-Space Plane Joint Program Office, NASA, OH, USA</i>	
The challenge of Hermès TPS shingles.....	299
<i>C. Pétau, Dassault Aviation, Toulouse, France</i>	

Session 2.2.A: MULTIBODY DYNAMICS I – MICROGRAVITY

Simulation of space station loads with active control systems.....	309
<i>P.A. Blelloch, SDRC Engineering Services Division, Inc., San Diego, CA, USA</i>	
<i>N.R. Beagley, SDRC Engineering Services, Hitchin, Herts, UK</i>	
<i>D.R. Ludwiczak & I. Yunis, NASA Lewis Research Centre, Cleveland, OH, USA</i>	
Influence of microvibrations on spacecraft performances.....	317
<i>N. Jourdon & V. Guillaud, MATRA Espace, Toulouse, France</i>	

Session 2.2.A: MULTIBODY DYNAMICS I – MICROGRAVITY (continued)

- On the modelling of a deployable telescope elastic beam-type element for on-orbit
multibody simulations..... 323
B. Kotzias, MBB/ERNO, Bremen, FRG

- Development and application of substructuring techniques for understanding and
controlling residual vibrations (microgravity aspects)..... 329
D. Francesconi, P.C. Marucchi-Chierro & R. Ullio, Alenia Spazio, Turin, Italy

Session 2.3.A: ANALYSIS IV – METHODS

- Minimisation of vibrations by broadband sensitivity approach..... 341
A. Girard, J. Chatelain & N. Roy, Intespace, Toulouse, France

- The continuous elements method..... 347
P.H. Kulla, TeWiSoft GmbH, Söchtenau, FRG

- Harmonic wave propagation in two-dimensional periodic large space structures..... 353
F. Bernelli-Zazzera & A. Ercoll-Finzi, Politecnico di Milano, Italy

- Nonlinear structural analysis of a thin-skin carbon-carbon rigid decelerator..... 359
Ch. Bonnet, J.P. Planas & M. Rigault, Dassault Aviation, France
D. Petersen, DLR, Braunschweig, FRG

Session 2.4.A: MATERIALS IV – CHARACTERISATION

- Dynamic characterisation of composite materials..... 365
I. Daerden, D. van Hemelrijck, L. Schillemans, F. de Roey, F. Boulpaep, J. De Visscher & A. Cardon, Free University of Brussels, Belgium

- Comportement mécanique des matériaux composites et assemblages collés aux basses températures..... 369
C. Laurent, Aerospatiale, Les Mureaux, France

- Mechanical testing on a composite flexible structure..... 375
F. Angrilli, P. Baglioni, G. Bianchini & G. Fanti, Università di Padova, Italy

- Buckling and failure of thin elliptical delaminations in composites..... 383
J. Heitzer, Dornier GmbH, Friedrichshafen, FRG

Session 2.1.B: SPACE PLANE AND RE-ENTRY II

- Stretched skin concept for the entry aerodynamic decelerator system of planetary probes..... 393
Ch. Bonnet, J.F. Puech & M. Rigault, Dassault Aviation, France

- Beryllium thermal protection technology..... 399
H. Leder, U. Lohse, W. Ohly, R. Rathjen, L. Schiwkosky, H. Weber & G. Wierheim, Interatom GmbH, Bergisch Gladbach, FRG

- CNSR-Rosetta - Earth return capsule..... 405
D. Desnoyer, J.M. Larrieu & C. Buck, SEP, St Médard-en-Jalles, France

Session 2.2.B: MATERIALS V – COMPOSITES

Notched strength of composite materials.....	415
<i>A.S. Herrmann, DLR, Braunschweig, FRG</i>	
Strength and deformation behaviour of Kevlar and carbon composite sandwich structures for space applications.....	421
<i>H. Bansemir & O. Haider, MBB, München, FRG</i>	
Modelling of honeycomb core for sandwich CTE prediction.....	427
<i>L. Scolamiero, Alenia Spazio, Italy</i>	
Investigations of the dynamic behaviour of compounds under preloading.....	431
<i>A. Geißler & W. Schmitt, Fraunhofer-Institut für Chemische Technologie, Pfaffzettel, FRG</i>	
<i>H. Weber, Universität Karlsruhe, FRG</i>	

Session 2.3.B: ANALYSIS V – FLUID/STRUCTURE INTERACTION

On the analysis of liquid-filled free-free tanks.....	437
<i>A. Kreis, Kreis Consultancies, Pragg-Jenaz, Switzerland</i>	
<i>M. Klein, ESTEC, Noordwijk, The Netherlands</i>	
Numerical investigation of fluid-structure-interaction problems with the finite- element method.....	443
<i>H.-P. Flicke & W. Mohr, IABG, Ottobrunn, FRG</i>	
Fluid/structure interaction problems: development of special processors.....	451
<i>M. Klein, ESTEC, Noordwijk, The Netherlands</i>	
<i>Y.M. Lefevre, MATRA Espace, Toulouse, France</i>	
A symmetric coupling between B.E.M. and F.E.M. for dynamical analysis of spacecraft.....	457
<i>A. Omrani & M.A. Hamdi, STRACO S.A., Compiègne, France</i>	

Session 2.4.B: DYNAMIC IDENTIFICATION I

Optimal exciter placement and force vector tuning required for experimental modal analysis.....	463
<i>N. Niedbal & E. Klusowski, DLR, FRG</i>	
Matching finite-element models to modal data.....	475
<i>S. Cogan & G. Lallement, CNRS, Besançon, France</i>	
Comparison of multipoint modal test methods.....	483
<i>K. Alexiou, CASA, Madrid, Spain</i>	
<i>J.R. Wright, University of Manchester, UK</i>	
Design parameter update of dynamic mathematical models in presence of test noise and mode pairing problems.....	491
<i>B. Caesar & L. Eckert, Dornier GmbH, Friedrichshafen, FRG</i>	
<i>A. Hoppe, University of Stuttgart, FRG</i>	

(volume 2)

Session 2.1.C: DYNAMIC IDENTIFICATION II

Updating and localising structural errors based on minimisation of equation errors.....	503
<i>M. Link & O. Flores, University of Kassel, FRG</i>	
The use of inverse frequency response functions for multi degree-of-freedom modal parameter identification with error bounds.....	511
<i>T.A. Brown, C.J. Kenchington & N.E. Kirk, Frazer-Nash Consultancy Ltd., Leatherhead, Surrey, UK</i>	
Modal identification of mechanical structures by means of tuned base-motion excitation	517
<i>K. Mühlbauer, S. Dillinger & J. Salzmann, IABG, Ottobrunn, FRG</i>	

Session 2.2.C: ANALYSIS VI – FLUID/STRUCTURE INTERACTION

Analysis of fluid/structure interaction of spacecraft's fluid tanks using combined boundary- element and finite-element methods.....	525
<i>S.M. Niku & R.A. Adey, Computational Mechanics (BEASY), Southampton, UK</i>	
<i>M. Klein, ESTEC, Noordwijk, The Netherlands</i>	
<i>W. Teichert, IKO Software Services, Stuttgart, FRG</i>	
<i>M. Kreis, Kreis Consultancies, Rudlingen, Switzerland</i>	
Some aspects for the application of a hierarchic family of Herrmann mixed compressible and incompressible finite elements.....	535
<i>F. Kiss, IKO Software Service GmbH, Stuttgart, FRG</i>	

Session 2.3.C: MATERIALS VI – FRACTURE

Spacecraft sustained load fracture control.....	543
<i>R.J.H. Wanhill, NLR, Amsterdam, The Netherlands</i>	
Crack initiation and growth in notched CFRE laminates: FEM analyses and tests.....	987
<i>M. Gädke, DLR, Braunschweig, FRG</i>	

Session 2.4.C: DESIGN & DEVELOPMENT I – MECHANICAL SYSTEMS

An analytical and experimental study on the design and verification of containment subjected to impact loading.....	553
<i>O. Fyrileiv & M.K. Nygård, A.S. Veritas Research, Høvik, Norway</i>	
<i>J.P. Tronskar & S. Wästberg, Veritec A/S, Høvik, Norway</i>	
Structural development of flight systems.....	559
<i>M.C.Lou, JPL, Pasadena, CA, USA</i>	
Sample container technology.....	567
<i>H. Grunditz, SAAB Space, Linköping, Sweden</i>	

Session 2.5.C: ANTENNA DESIGN I

Orbital manoeuvre effects on large flexible antennae.....	575
<i>W. Adam, A. Bramante & A. Meschini, Alenia Spazio, Italy</i>	
Adaptive structures for precision controlled large space systems.....	579
<i>J.A. Garba, B.K. Wada & J.L. Fanson, JPL, Pasadena, CA, USA</i>	
Trade-off and scale models of large deployable mesh reflectors for mobile communications satellite.....	589
<i>T. Sugimoto, A. Iso, S. Sato & T. Orikasa, Space Communications Research Corp., Tokyo, Japan</i>	

Session 2.1.D: DYNAMIC IDENTIFICATION III

Development of an interactive code for updating dynamic finite-element models:.....	597
<i>N.A. Roy, A. Girard, P.-E. Dupuis & L.-P. Bugeat, Intespace, Toulouse, France</i>	
Vibration characterisation for low-level disturbances induced in telecommunications spacecraft.....	603
<i>N.S. Ferguson, ISVR, University of Southampton, UK</i>	
<i>D.C.G. Eaton, ESTEC, Noordwijk, The Netherlands</i>	
Practical aspects of in-orbit modal identification using free-decay data.....	609
<i>A. Schenk, DLR, Göttingen, FRG</i>	
<i>R.S. Pappa, NASA Langley Research Center, Hampton, VA, USA</i>	
Excitation vector considerations in multiple sinusoidal testing.....	619
<i>D. Ote, J. Debillé, W. Bakkers & W. van der Auweraer, LMS International, Leuven, Belgium</i>	
A study of high-frequency vibrations due to pyrotechnic shocks in coupled systems.....	625
<i>D. Lednik & R.J. Pinnington, University of Southampton, Hants, UK</i>	

Session 2.2.D: CAD/CAE – METHODS & INTERFACES

CAD to FEM tool.....	633
<i>N. Jourdon & A. Mavrogenis, MATRA Espace, Toulouse, France</i>	
<i>M. Kleir, ESTEC, Noordwijk, The Netherlands</i>	
Simulation des configurations géométriques d'un satellite sur orbite.....	641
<i>T. Figeac & J.L. Le Gal, CNES, Toulouse, France</i>	
Integration of CAD tools in space vehicle design.....	647
<i>J.L. Le Gal, CNES, Toulouse, France</i>	

Session 2.3.D: MATERIALS VII – DAMAGE MECHANICS

Micromechanical concepts for the estimation of property evolution and remaining life.....	653
<i>K. Reifsnider, Zhanjun Gao & R. Swain, Virginia Polytechnic Institute & State University, Blacksburg, VA, USA</i>	

Session 2.3.D: MATERIALS VII – DAMAGE MECHANICS (continued)

Damage mechanics modelisation of composite structures: a physical approach of failure.....	659
<i>L. Perret, CNES, Toulouse, France</i>	
<i>E. Le Dantec & D. Engrand, Bertin, Plaisir, France</i>	
Damage mechanisms and constitutive relations for cracked UD layers in crossply laminates	665
<i>H. Eggers & H.C. Goetting, DLR, Braunschweig, FRG</i>	
Composite material damage and fracture models for numerical simulations in support of fracture control.....	671
<i>A. de Rouvray & E. Haug, ESI, Rungis, France</i>	
<i>C. Stavrinidis, ESTEC, Noordwijk, The Netherlands</i>	
Role of combined numerical and experimental investigations in the justification of the structural integrity and damage tolerance of space structures.....	679
<i>P. Agatonovic & M. Windisch, MAN Technologie AG, München, FRG</i>	

Session 2.4.D: DESIGN AND DEVELOPMENT II – MECHANICAL SYSTEMS

Isostatic mounting platform.....	689
<i>F. Arévalo, A. Ayuso & E. Ozores, CASA, Madrid, Spain</i>	
<i>A. Pradier, ESTEC, Noordwijk, The Netherlands</i>	
Inflatable, space-rigidised structures: progress in design, technology and verification.....	697
<i>M.C. Bernasconi, Oerlikon-Contraves, Zürich, Switzerland</i>	
Service module structure of the ISO spacecraft: testing and design qualification.....	703
<i>M. Caldentey, CASA, Madrid, Spain</i>	
Sunshade support structure (ISO Project): structure and testing.....	709
<i>M. Hager, ÖRS GmbH, Vienna, Austria</i>	
Polar Platform structure development programme.....	717
<i>J.G. San Martín & P. Luengo, CASA, Madrid, Spain</i>	

Session 2.5.D: ANTENNA DESIGN II

Acoustic test structural predictions.....	725
<i>C. Bruno & L. Scolamiero, Alenia Spazio, Italy</i>	
HISPASAT DBS reflector: mechanical analysis and environmental test correlation.....	731
<i>R. Jiménez, CASA, Madrid, Spain</i>	
Development, manufacturing and alignment of 2 m diameter mirror for PRONAOS.....	737
<i>F. Hofbauer, MAN Technologie AG, München, FRG</i>	
<i>M. Duran & Ph. Luquet, Matra, Toulouse, France</i>	
A systematic approach for the DRSS IOL APM design.....	743
<i>A. Meschini, Alenia Spazio, Italy</i>	

Session 3.1.A: MATERIALS VIII – METALLIC STRUCTURES

Damage tolerance checking on Ni/H ₂ battery cells.....	749
<i>J.L. Dodelin, Aerospatiale Aquitaine, Bordeaux, France</i>	
<i>B. Journet, Aerospatiale, Suresnes, France</i>	
<i>M. Kornmann, Battelle, Carouge-Genève, Switzerland</i>	
<i>L. Paugam, SAFT, Romainville, France</i>	
<i>L. Perret, CNES, Toulouse, France</i>	
Characterisation of Al 2219 material for the application of the spin forming process.....	755
<i>D. Müller-Wiesner, DASA/MBB-ERNO, Bremen, FRG</i>	
<i>E. Sieger, Zeppelin Metallwerke, Friedrichshafen, FRG</i>	
<i>K. Ernsberger, Fachhochschule Weingarten (TZW), FRG</i>	
Fatigue characterisation of Ni-base alloys.....	761
<i>G. Marci, DLR, Köln, FRG</i>	
Testing and characterisation of metallic materials for structural analysis of high-temperature components.....	769
<i>N. Taylor & P. Agatonovic, MAN Technologie, München, FRG</i>	
Residual stresses in welds and effect on crack growth prediction.....	775
<i>F. Bandini, Alenia Spazio, Torino, Italy</i>	

Session 3.2.A: ANTENNA DESIGN III

A high-precision sandwich reflector for 'FIRST': design and mechanical analysis of the sandwich core.....	783
<i>R. Sippel & G. Helwig, Dornier GmbH, Friedrichshafen, FRG</i>	
Analysis and test methods for the evaluation of deployment shock.....	231
<i>W. Adam, A. Bramante & A. Meschini, Alenia Spazio, Italy</i>	
Telecom 2 deployable reflectors.....	793
<i>A. Noir & J.D. Lefèvre, Aerospatiale, Les Mureaux, France</i>	
<i>D. Coquelet, Bertin et Cie., Plaisir, France</i>	

Session 3.3.A: VIBRO-ACOUSTICS III

Acoustically induced vibration of platform-mounted equipment containing printed-circuit boards.....	801
<i>J.N. Pinder, ISVR Consultancy Services, University of Southampton, UK</i>	
<i>D.C.G. Eaton, ESTEC, Noordwijk, The Netherlands</i>	
Generalised damping in fluid/structure interaction analyses using modal synthesis.....	807
<i>P. Göransson & J. Brandt, FFA, Bromma, Sweden</i>	
Experimental approach on the pyrotechnical shock reduction of Ariane-5 upper stage.....	813
<i>I. Uribarri & P. Tejero, CASA, Madrid, Spain</i>	
<i>B. Rivaillon & B. Laviron, MATRA, Toulouse, France</i>	
Power-flow finite-element analysis for beams and plates.....	819
<i>B. Klasén, DNV Ingemansson AB, Stockholm, Sweden</i>	

Session 3.4.A: TESTING II – METHODS

Development of a laser-based measurement system for modal testing of large space structures.....	827
<i>A.K. Mitchell & C.R. Hazell, Technical University of Nova Scotia, Halifax, NS, Canada</i>	
<i>Y. Soucy, Canadian Space Agency, Ottawa, ON, Canada</i>	
Development of a force-measurement device.....	833
<i>O. Wilmar, DNV Ingemansson AB, Stockholm, Sweden</i>	
On the dynamic qualification of large deployable antennas.....	839
<i>K. Alexiou & P. Luengo, CASA, Madrid, Spain</i>	

Session 3.1.B: MULTIBODY DYNAMICS II – DEPLOYMENT DYNAMICS

Deployment analysis and in-orbit control of large reflectors.....	849
<i>H. Baier, W. Charon & B. Specht, Dornier GmbH, Friedrichshafen, FRG</i>	
Dynamic deployment analysis of a mesh antenna reflector.....	855
<i>B. Gröger, MBB, München, FRG</i>	
The numerical simulation of the inflation process of space rigidised antenna structures.....	861
<i>E. Haug, J.B. Protard & G. Milcent, ESI, Rungis, France</i>	
Equations of motion of multibody systems in the ESA MIDAS software.....	871
<i>Duc Minh Tran, ONERA, Châtillon, France</i>	
Dynamics of large reflectors.....	877
<i>J.D. Lefebvre, C. Dauviau & P. Picard, Aerospatiale, Les Mureaux, France</i>	
<i>C. Garnier & C. Truchi, Aerospatiale, Cannes, France</i>	

Session 3.2.B: DESIGN & DEVELOPMENT III – STRUCTURES

CFRP integral end fitting for high-stability truss structures.....	887
<i>A. Cuadrado & A. Alonso, CASA, Madrid, Spain</i>	
Orpheus CFRP structure: high-stiffness/low-thermal-strain space telescope structure.....	893
<i>T. Schaeffler, MAN Technologie AG, München, FRG</i>	
Design of joints for damped structures.....	901
<i>P. Luengo, CASA, Madrid, Spain</i>	
Experiences with large CFRP radiotelescope reflectors.....	907
<i>D. Muser, MAN Technologie AG, München, FRG</i>	
Analytical dynamic model updating: the challenge for the nineties.....	913
<i>S. Ibrahim, Old Dominion University, Norfolk, VA, USA</i>	

Session 3.3.B: VIBRO-ACOUSTICS IV – METHODS

Structure-acoustic finite-element analyses for noise-reduction investigations of launcher payload-compartment structures made of CFRP sandwich material.....	925
<i>M. Faust, G. Schweickert & F. Strobel, Domier GmbH, Friedrichshafen, FRG</i>	
Fluid/structure interaction applied to the analysis of a test sandwich panel typical for space application.....	933
<i>D. Vaucher de la Croix, Metravib R.D.S., Ecully, France</i>	
<i>L. Perret, CNES, Toulouse, France</i>	
<i>J.M. Parot, IMDYS, Brioude, France</i>	
Mathematical modelling of pyrotechnic shock in the Ariane 5 VEB structure.....	939
<i>C. Huerta, SINEX, Madrid, Spain</i>	
<i>E. Alarcón & S. Gómez Lera, Politechnical University of Madrid, Spain</i>	
Effect of the payload on the surrounding internal acoustic environment at lift-off.....	945
<i>G. Borello, St Jean-l'Union, France</i>	

Session 3.4.B: TESTING III – FACILITIES

Recent developments in controlling a hydraulic multi-axis test facility.....	951
<i>G. Lachenmayr, IABG, Ottobrunn, FRG</i>	
Control of combined vibrations and multi-axis test.....	959
<i>G. Catteau & C. Hutin, ISTAR, Plaisir, France</i>	
Ground test validation for precision structures.....	963
<i>B.K. Wada, J.A. Garba & J.L. Fanson, JPL, Pasadena, CA, USA</i>	
The use of reverberant-room acoustic testing for spacecraft structures and their payloads.....	969
<i>D.C.G. Eaton, G. Boulked & G. Paindessous, ESTEC, Noordwijk, The Netherlands</i>	
Environmental tailoring: a major perspective for mechanical testing for future space projects.....	979
<i>J.F. Imbert, Intespace, Toulouse, France</i>	
<i>C. Lalanne, CEA-CESTA, Le Barp, France</i>	
Keyword index.....	995

PARTICIPANTS

Mr. M.K.L. BRUGHMANS
LMS Belgium BVBA
Interleuvenlaan 65
B-3001 Leuven
BELGIUM

Mr. J.I. BUENO
SENER
Av. Zugazarte 56
E-48930 Las Arenas
SPAIN

Mr. S. CAPITANIO
ESA/ESTEC/YMD
Postbus 299
NL-2200 AG Noordwijk (ZH)
THE NETHERLANDS

Mr O. BRUNNER
ESA/ESTEC/YMD
Postbus 299
NL-2200 AG Noordwijk (ZH)
THE NETHERLANDS

Mr. L.P. BUGEAT
Intespace
18 av E. Belin
B.P. 4356
F-31029 Toulouse Cédex
FRANCE

Mr M. CASTELLANET
Aerospatiale
100, Boulevard du Midi
F-06322 Cannes-la-Bocca Cédex
FRANCE

Mr C. BRUNO
Alenia Spazio
Via Saccomuro 24
I-00131 Rome
ITALY

Mr. W.R. BURKE
ESA/ESTEC/IP
Postbus 299
NL-2200 AG Noordwijk (ZH)
THE NETHERLANDS

Mr G.C CATTEAU
ISTAR
79, rue de la Gare
F-78370 Plaisir
FRANCE

Mr. A.S. BRUST
University of Wuppertal
Gaußstr. 20
D-5600 Wuppertal
FRG

Mr. N. CABLE
ESA/ESTEC/YMM
Postbus 299
NL-2200 AG Noordwijk (ZH)
THE NETHERLANDS

Miss A. CERESSETTI
Alenia Spazio
Corso Marche 41
I-10146 Torino
ITALY

Mr P.G. BUCHWALD
ESA/ESTEC/MAF
Postbus 299
NL-2200 AG Noordwijk (ZH)
THE NETHERLANDS

Mr. B. CAESAR
Dornier GmbH
Postfach 1420
D-7990 Friedrichshafen
FRG

Mr S.A. CHALLENGER
Frazer-Nash Consultancy Ltd.
Leatherhead
UK

Mr C. BUCK
SEP
BP 37
F-33165 Saint Médard-en-Jalles
FRANCE

Mr M. CALDENTY
CASA - Space Div.
Avda. Aragon 404
E-28022 Madrid
SPAIN

Mr J. CHANG
Aerospace Corp.
P.O. Box 92957
Los Angeles, CA 90009
USA

LIST OF PARTICIPANTS

Mrs. J. CHATELAIN
Intespace
18 ave. E. Belin
BP 4356
F-31029 Toulouse Cédex
FRANCE

MR. CONSTANTIN
Matra Espace
37, av. Louis Breguet
F-78146 Vélizy
FRANCE

Mr. T. DANGTRONG
Aerospatiale
BP no 2
F-78133 Les Mureaux
FRANCE

Mr B. CHEMAUL
CNES
18, Av. Edouard Belin
F-31055 Toulouse Cédex
FRANCE

Miss M.C. CONTINO
ESA/ESTEC/MAT
Postbus 299
NL-2200 AG Noordwijk (ZH)
THE NETHERLANDS

Mr E. DASCOTTE
Dynamic Engineering
Ambachtenlaan 21
B-3001 Heverlee
BELGIUM

Mr. B. CLEMENT
Aerospatiale
66, Route de Verneuil
F-78133 Les Mureaux
FRANCE

Mr D. COQUELET
Bertin & Cie.
59, rue Pierre Curie
B.P. 3
ZI des Gatines
F-78373 Plaisir Cédex
FRANCE

Mr C. Dauviau
Aerospatiale
BP No 2
F-78133 Les Mureaux
FRANCE

Mr. C. CLERC
Metrauib R.D.S.
BP 182
F-69132 Ecully Cédex
FRANCE

Mr P. CORDERO
ESA/ESTEC/FTB
Postbus 299
NL-2200 AG Noordwijk (ZH)
THE NETHERLANDS

Mr P.M.J. DE GRAEF
SABCA
Chaussée de Haccht 1470
B-1130 Brussel
BELGIUM

Mr. S. COGAN
Applied Mechanics Laboratory
VFRST
F-25030 Besançon Cédex
FRANCE

Mr. P. COSTE
ESA/ESTEC/YMM
Postbus 299
NL-2200 AG Noordwijk (ZH)
THE NETHERLANDS

Mr. K. DE LANGHE
KV Leuven PMA
Celestijnelaan 300b
B-3001 Heverlee
BELGIUM

Mr P. COLLINS
ESA/ESTEC/YME
Postbus 299
NL-2200 AG Noordwijk (ZH)
THE NETHERLANDS

Mr A. CUADRADO
CASA - Space Div.
Avenida Aragon 404
E-28022 Madrid
SPAIN

Mr. A. DE ROUVRAY
E.S.I.
20, rue Saarinen
Silic 270
F-94578 Rungis Cédex
FRANCE

M. COMBELLES
Matra Espace
31, Rue des Cosmonautes
Z.I. du Palays
F-31077 Toulouse
FRANCE

Mr I. DAERDEN
Free University Brussels
Peinlaan 2
B-1050 Brussel
BELGIUM

Mr S. DE ZOTTI
MATRA
31, Rue des Cosmonautes
Z.I. du Palays
Toulouse
FRANCE

LIST OF PARTICIPANTS

xvii

Mr. M. DEGENER
DLR/Institute of Aeroelasticity
Bunsenstrasse 10
D-3400 Göttingen
FRG

Mr. T. DOESBERG
SONACA S.A.
Route Nationale 5
B-6041 Gosselies
BELGIUM

Dr EGGERS
DLR/Institut f. Strukturmechanik
DLR Flughafen
D-3300 Braunschweig
FRG

Mr. P. DELOO
ESA/ESTEC/YMD
Postbus 299
NL-2200 AG Noordwijk (ZH)
THE NETHERLANDS

Mr L. DONATO
Spar Aerospace Ltd
21025 Trans-Canada Highway
Ste-Anne-de-Bellevue
H9X 3R2 Québec
CANADA

Mr M. EIDEN
ESA/ESTEC/YMM
Postbus 299
NL-2200 AG Noordwijk (ZH)
THE NETHERLANDS

Mr. W.A. DEN HAAK
Fokker Space & Systems
Postbus 12222
NL-1100 AE Amsterdam
THE NETHERLANDS

Mr K. DOVSTAN
KM Akustikbyrå AB
PO Box 3029
S-17203 Sundbyberg
SWEDEN

Mr D. EKENHORST
ESA/ESTEC/QMO
Postbus 299
NL-2200 AG Noordwijk (ZH)
THE NETHERLANDS

Mr R.D. DEPPE
DLR-GSOC
Münchnerstr.
D-8031 Wessling
FRG

Mr M. DRESCHER
ESA/ESTEC/YMD
Postbus 299
NL-2200 AG Noordwijk (ZH)
THE NETHERLANDS

Mr. ELLENBROEK
Fokker Space & Systems
Postbus 12222
NL-1100 AE Amsterdam
NETHERLANDS

Mr D. DESNOYER
SEP
BP 37
F-33165 Saint-Médard-en-Jalles
FRANCE

Mr. R. DRIMMELEN
Delft University of technology
Postbus 5058
NL-2600 GB Delft
NETHERLANDS

Mr E.E. ERBEN
MBB-ERNO
Hunefeldst. 1-5
D-2800 Bremen 1
FRG

Mr V.A. DIAZ MORALES
CASA - Space Div.
Ava. Aragon 404
E-28022 Madrid
SPAIN

Mr B.P. DUPUY
Metrarub R.D.S.
BP 182
F-69132 Ecully Cédex
FRANCE

Mr A. ERCOLI-FINZI
Politecnico di Milano
Dept. Ing. Aerospaziale
Via Golgi 40
I-20133 Milano
ITALY

Mr J-L DODELIN
Aerospatiale
B.P. 11
F-33165 Saint-Médard-en-Jalles
FRANCE

Mr D.C.G. EATON
ESA/ESTEC/YME
Postbus 299
NL-2200 AG Noordwijk (ZH)
THE NETHERLANDS

Dr W. ERICSSON
Bofors Aerotronics AB
S-18184 Lidingö
SWEDEN

Mr. L. FANCHI
ESA/ESTEC/YME
Postbus 299
NL-2200 AG Noordwijk (ZH)
THE NETHERLANDS

Mr E. FILIPPI
ETCA
BP 4097
B-6000 Charleroi
BELGIUM

Mr. R. FORMAN
NASA/Johnson Space Center
NASA Road N1
Houston, TX 77058
USA

Prof. G. FANTI
Dipartimento di Ingegneria
Meccanica
Università di Padova
Via Venezia 1
I-35131 Padova
ITALY

Mr. R. FIORANI
University of Rome 'La
Sapienza'
Via Evdossiana 16
I-00184 Rome
ITALY

Mr J. FOUGERAS
Aerospatiale
Centre Technique des Mureaux
B.P. 2
F-78133 Les Mureaux Cédex
FRANCE

Mr M. FAUST
Dornier GmbH
Postfach 1420
D-7990 Friedrichshafen
FRG

Mr L. FLAVIO CAMPANILE
DLR/Institute of Aeroelasticity
Bunsenstrasse 10
D-3400 Göttingen
FRG

Mr. D. FRANCESCONI
Alenia Spazio
Corso Marche 41
I-10146 Torino
ITALY

Mr D.E. FAUST
DLR/Institut f. Strukturmechanik
Linder Höhe, PT-D2
D-5000 Köln
FRG

Mr P.F. FLEMING
Alenia Spazio
Corso Marche 41
I-10146 Torino
ITALY

Mr G. FRULLA
Politecnico di Torino
Dept of Aerospace Eng.
Corso Duca degli Abruzzi 24
I-10129 Torino
ITALY

Mr. A. FENZ
ACT
Hochleistungskunststofftechnik
Hauptstraße 2
A-2630 Ternitz
AUSTRIA

Mr H.P. FLICKE
IABG mbH
Einstein str. 20
D-8012 Ottobrunn
FRG

Mr. U. FULLEKRUG
DLR/Institute of Aeroelasticity
Bunsenstrasse 10
D-3400 Göttingen
FRG

Dr N.S. FERGUSON
University of Southampton
ISVR Consultancy Services
The University
Southampton, SO9 5NH
UK

Mr. O. FLORES
University of Kassel
Monchebergstrasse 7
D-3500 Kassel
FRG

Mr O.F. FYRILEIV
Det Norske Veritas
P.O. Box 300
N-1322 Høvik
NORWAY

Mr T. FIGEAC
CNES
18 Av. Edouard Belin
F-31055 Toulouse Cédex
FRANCE

Mr S. FOCKERSBERGER
ESA/ESTEC/HA
Postbus 299
NL-2200 AG Noordwijk (ZH)
THE NETHERLANDS

Dr M. GÄDKE
DLR-Institut fuer
Strukturmechanik
DLR Flughafen
D-3300 Braunschweig
FRG

LIST OF PARTICIPANTS

xix

Mr G. GALIPIENSO
CASA - Space Div.
Avda. Aragon 404
E-28022 Madrid
SPAIN

Dr GEIER
DLR-Institut f. Strukturmechanik
DLR Flughafen
D-3300 Braunschweig
FRG

Mr PH. GINDRE
Eutelsat
Tour Maine Montparnasse,
47ème
33, av. du Maine
F-75755 Paris 15
FRANCE

Mr. J.A. GARBA
JPL
California Inst. of Technology
4800 Oak Grove Drive
Pasadena, CA 91109
USA

Mr A. GEISSLER
Fraunhofer Institut f. Chemische
Technologie
Postfach 1240
D-7507 Pfinztal 1
FRG

Mr P.G. GIORDANO
Alenia Spazio
Corso Marche 41
Torino
ITALY

Mr S. GARCIA DE PAREDES
CASA - Space Div.
Avda. Aragon 404
E-28022 Madrid
SPAIN

Mr. C. GENNARO
Alenia Spazio
Corso Marche 41
I-10146 Torino
ITALY

Mr. A. GIRARD
Intespace
18, av. E. Belin
BP 4356
F-31029 Toulouse Cédex
FRANCE

Mr R. GARCIA PRIETO
ESA/ESTEC/YME
Postbus 299
NL-2200 AG Noordwijk (ZH)
THE NETHERLANDS

Mr. M.M. GERADIN
University of Liège
LTAS Dynamique des
Constructions Mécaniques
21 rue E. Solvay
B-4000 Liège
BELGIUM

Mr. J.-N. GIRAUDBIT
Alcatel Espace
26, ave J.-F. Champolion
F-31037 Toulouse
FRANCE

Mr. C. GARCIA-
MARRIRODRIGA
ESA/ESTEC/YMM
Postbus 299
NL-2200 AG Noordwijk (ZH)
THE NETHERLANDS

Mr. B. GERBER
MATRA
31, Rue des Cosmonautes
Z.I. du Palays
F-31400 Toulouse
FRANCE

Mr J. GOMEZ-ELVIRA
I.N.T.A.
CRTRA Ajalvir KM 4300
Torrejon de Ardoz
E-28850 Madrid
SPAIN

Mr. C. GARNIER
Aerospatiale
100, bd du Midi
F-06322 Cannes-la-Bocca Cédex
FRANCE

Mr. P. GERREKENS
SAMTECH S.A.
Blv. Frère Orban 25
B-4000 Liège
BELGIUM

Mr A.L. GONZALEZ
BLAZQUEZ
ESA/DSTS
8-10, rue Mario-Nikis
F-75738 Paris Cédex 15
FRANCE

Mr. J. GAVIRA
ESA/ESTEC/YMM
Postbus 299
NL-2200 AG Noordwijk (ZH)
THE NETHERLANDS

Mr P. GILSON
IAL Space
Université de Liège
Avenue du Pré-Aily
B-4031 Angleur
BELGIUM

Mr L.E. GOOYER
Fokker Space & Systems
Postbus 12222
NL-1100 AE Amsterdam
THE NETHERLANDS

LIST OF PARTICIPANTS

Mr P. GÖRANSSON
Flygtekniska Försöks Anstalten
P.O. Box 11021
S-16111 Bromma
SWEDEN

Mr B. GROGER
Messerschmitt-Bolkow-Blohm
GmbH
Dept. KT 226
Postfach 80 11 69
D-8000 München 80
FRG

Mr P. HAHN
Austrian Research Centre
A-2444 Seibersdorf
AUSTRIA

DR GÖTTING
DLR/Institut f. Strukturmechanik
DLR Flughafen
D-3300 Braunschweig
FRG

Mr B. GROSSAUER
Österr. Raumfahrt- und
Systemtechnik GmbH
Operngasse 20b
A-1040 Wien
AUSTRIA

MR. HAIDER
MBB
Tegernseer Landstr. 19
D-8025 Unterhaching
FRG

Mr R. GRAHAM
Space Systems
British Aerospace Eng.Ltd.
Argyle Way
Stevenage Herts SG1 2AS
UK

Dr W. GRUEN
ESA/ESTEC/YTF
Postbus 299
NL-2200 AG Noordwijk (ZH)
THE NETHERLANDS

Mr. M. HALLE
Aerospatiale
66, Route de Verneuil
F-78133 Les Mureaux
FRANCE

Mr. GRANT
Boeing Aerospace & Electronics
Mailstop JA-63 / Bldg 48-19
P.O. Box 24002
Huntsville, AL 35824/6402
USA

Mr H.O. GRUNDITZ
SAAB Space AB
S-581 88 Linköping
SWEDEN

Mr M.A. HAMDI
STRACO
Compiègne
FRANCE

Mr J.A. Gratien
CNES
Rond Point de l'Espace
F-91023 Evry Cédex
FRANCE

MR GÜLPEN
MBB - Deutsche Aerospace
Postfach 801109
D-8000 München 80
FRG

Mr. D.A. HAMILTON
NASA/JSC
Mailcode ES4
NASA road 1
Houston, TX 11058
USA

Mr P.H.L. Groenenboom
The MacNeal-Schwendler
Company B.V.
Groningenweg 6
NL-2803 PV Gouda
THE NETHERLANDS

Mr. P. GWODZ
ESA/ESTEC/YMD
Postbus 299
NL-2200 AG Noordwijk (ZH)
THE NETHERLANDS

Mr R. HAMPTON
NASA Ames Research Center
Moffett Field
Los Angeles, CA 94035
USA

Mr P. GROEPPER
ESA/ESTEC/FSA
Postbus 299
NL-2200 AG Noordwijk (ZH)
THE NETHERLANDS

Mr M.H. HAGER
Österr. Raumfahrt- und
Systemtechnik GmbH
Operngasse 20B
A-1040 Wien
AUSTRIA

DR HANSELKA
DLR-Institut f. Strukturmechanik
DLR Flughafen
D-3300 Braunschweig
FRG

LIST OF PARTICIPANTS

xxi

Mr T. HASHIMOTO
The Institute of Space &
Astronautical Sciences
Sagamihara 229
Yoshinadai 3-1-1
JAPAN

Prof. A.S. HERRMANN
DLR-Institut f. Strukturmechanik
DLR Flughafen
D-3300 Braunschweig
FRG

Dr M.C. HUERTA
SINEX S.A
Modesto Lafuente 41, 2D
E-28003 Madrid
SPAIN

Mr. E. Haug
ESI
20, rue Saarinen
Silic 270
F-94578 Rungis Cédex
FRANCE

Mr W. HEYLEN
PMA- K.U. Leuven
Celestijnenlaan 300B
B-3001 Heverlee
BELGIUM

Prof. S.R. IBRAHIM
Dept. of Mechanical Eng. and
Mechanics
Old Dominion University
Norfolk, VA 23529-0247
USA

Mr R. Hazell
Technical University of Nova
Scotia
P.O. Box 1000
Halifax, Nova Scotia
CANADA

Mr Y. HISADA
NASDA
2-5-6 Shiba
Minato-ku
Tokyo 105
JAPAN

Mr. J.P. IMBERT
Intespace
Centre Spatial de Toulouse
18, av. Edouard Belin
F-31029 Toulouse
FRANCE

Mr. J. HEITZER
Dornier GmbH
Postfach 1420
D-7990 Friedrichshafen
FRG

Mr F. HOFBAUER
MAN-Technologie AG
Bauschingerstrasse 20
D-8000 München 50
FRG

Mr. D. JACOBS
ESA/ESTEC/YMD
Postbus 299
NL-2200 AG Noordwijk (ZH)
THE NETHERLANDS

Mr R. HELFRICH
INTES GmbH
Nobelstr. 15
D-7000 Stuttgart 80
FRG

Mr. R.H. HOHN
University of Wuppertal
Physics Dept.
Gauss-Straße 20
D-5600 Wuppertal 1
FRG

Mr. J.A. JIMENEZ
ESA/ESTEC/MTS
Postbus 299
NL-2200 AG Noordwijk (ZH)
THE NETHERLANDS

Mr. G. HELWIG
Dornier GmbH
Postfach 1420
D-7990 Friedrichshafen
FRG

Mr E. HORNUNG
MBB/ERNO
Postfach 105909
Hunefeldstrasse 1-5
D-2800 Bremen 1
FRG

Mr R. JIMENEZ
CASA - Space Div.
Avda. Aragon 404
28022 Madrid
SPAIN

Mr T. HENRIKSEN
ESA/ESTEC/YMD
Postbus 299
NL-2200 AG Noordwijk (ZH)
THE NETHERLANDS

Mr. P. HUBERT
CNES
Rd. Point de l'Espace
F-91023 Evry Cédex
FRANCE

Mr N. JOURDON
MATRA Espace
31, rue des Cosmonautes
ZI du Palays
Toulouse
FRANCE

Mr B. JOURNET
Aerospatiale
12, Rue Pasteur
BP 76
F-92152 Suresnes Cédex
FRANCE

Mr N.E. KIRK
Frazer-Nash Consultancy
Quay Head House
Colston Av.
Bristol BS1 1EB
UK

Mr A.S. KOTZIAS
MBB/ERNO Raumfahrttechnik
GmbH
Hunefeldstr. 1-5
D-2800 Bremen 1
FRG

Mr J. KAESE
MBB
Dept. KT 21
Postfach 801169
D-8000 München 80
FRG

Dr K. KISS
IKO Software Service GmbH
Postfach 800565
D-7000 Stuttgart 80
FRG

Mr. J. KRAESE
MBB
Postfach 801169
D-8000 München 80
FRG

Mr Y. KAJIO
NISSAN Motor Co.
Momoi, Suginami
Tokyo
JAPAN

Mr. A. KITAMURA
Ishikawajima-Harima Heavy Ind.
Co
1-6-2 Marunouchi
Chiyoda Ku
Tokyo
JAPAN

Mr A. Kreis
Kreis Consultancies
Iarella
CH-7231 Praag-Jenaz
SWITZERLAND

Mr. M. KELLE
MBB/ERNO
Hunefeldstrasse 1-5
Postfach 105909
D-2800 BREMEN
FRG

Mr B. KLASÉN
PNV Ingemansson
PO BOX 47321
S-10074 Stockholm
SWEDEN

Mr H. Krings
MAN-Technologie AG
Dachauerstr. 667
D-8000 München 50
FRG

Mr. M.A. KHOUDJA
Delft University of Technology
Postbus 5058
NL-2600 GB Delft
THE NETHERLANDS

Mr M. KLEIN
ESA/ESTEC/YMD
Postbus 299
NL-2200 AG Noordwijk (ZH)
THE NETHERLANDS

Mr. J. KROEKER
Dornier GmbH
Postfach 1420
D-7990 Friedrichshafen
FRG

Mr. H. KIKUKAWA
Fuji Heavy Industries Ltd.
1-1-11 Yonan ustunomiya
Tochigi, T320
JAPAN

Dr J. KLUG
MAN Technologie AG
Bauschingerstr. 20
D-8000 München 50
FRG

Prof. W. KROLL
DLR-Institut f. Strukturmechanik
DLR-Flughafen
D-3300 Braunschweig
FRG

Mr. N. KILL
SAMTECH S.A.
Bvd Frère Orban 25
B-4000 Liège
BELGIUM

Mr M. KORNMANN
Geneva Research Centres
7, route de Drize
CH-1227 Geneva
SWITZERLAND

Mr. C.L. KRUIMER
Delft University of Technology
Postbus 5058
NL-2600 GB Delft
THE NETHERLANDS

LIST OF PARTICIPANTS

xxiii

Mr P.H. KULLA
Tewisoft GmbH
Bahnhofstrasse 8
D-8201 Sochtenau
FRG

Mr M. LAMBERT
Aerospatiale
100 Boulevard du Midi
F-06322 Cannes
FRANCE

Mr. D. LEDNIK
University of Southampton
ISVR
Highfield, SO9 5NH
Southampton
UK

Mr. A.K. KUSUMO ADI
Delft University of Technology
Postbus 2600
NL-2600 GB Delft
THE NETHERLANDS

Mr. M.C.J.J. LAMBERT
ESA/ESTEC/YME
Postbus 299
NL-2200 AG Noordwijk (ZH)
THE NETHERLANDS

Mr J.D. LEFEVRE
Aerospatiale
66 route de Verneuil
F-78133 Les Mureaux Cédex
FRANCE

Mr. G. LABRUYERE
ESA/ESTEC/YMM
Postbus 299
NL-2200 AG Noordwijk (ZH)
THE NETHERLANDS

Dr S. LA TERZA
University of Rome 'La
Sapienza'
Via Eudossiana 18
Roma
ITALY

Mr. Y.M. LEFEVRE
Matra
Z.I. du Palays
31, Rue des Cosmonautes
Toulouse
FRANCE

Mr G. LACHENMAYR
IABG
Einstreinstrasse 20
D-8012 Ottobrunn
FRG

Miss C. LAURENT
Aerospatiale
66, Route de Verneuil
BP 2
F-78133 Les Mureaux Cédex
FRANCE

Mr J. LEURIDAN
LMS International
Interleuvenlaan 65
B-3001 Leuven
BELGIUM

Mr. B. LACOSTE
DSTS-ESA/HQ
8-10, rue Mario-Nikis
F-75738 PARIS Cédex 15
FRANCE

Mr. E. LE DANTEC
Bertin & Cie
BP 3
ZI des Gatines
F-78373 Plaisir Cédex
FRANCE

Mr M. LINK
University of Kassel
Monchebergstrasse 7
D-3500 Kassel
FRG

Mr. C. LALANNE
CEA/CESTA
D/AGCI/B. Junca
BP 2
F-33114 Le Barp
FRANCE

Mr J.L. Le Gal
CNES
18, av. Edouard Belin
F-31055 Toulouse Cédex
FRANCE

Mr M.C. LOU
JPL
Cal. Inst. of Technology
4800 Oak Grove Drive
Pasadena, CA 91109
USA

Mr. G. LALLEMENT
Applied Mechanics Laboratory
UFRST
F-25030 Besançon Cédex
FRANCE

Mr H. Leder
Interatom GmbH
Postfach 100351
D-5060 Bergisch-Gladbach
FRG

Mr E. LOUAS
CNES
18, Av. Edouard Belin
F-31055 Toulouse Cédex
FRANCE

LIST OF PARTICIPANTS

Mr P. LUENGO
CASA - Space Div.
Avda. Aragon 404
E-28022 Madrid
SPAIN

Dr G. MARCI
Institut für Werkstoff-Forschung
Postfach 906058
Linder Höhe
D-5000 Köln 90
FRG

Mr M. MENDOZA-
HAUPTMANN
ESA/ESTEC/YMD
Postbus 299
NL-2200 AG Noordwijk (ZH)
THE NETHERLANDS

Mr H.J. LUHMANN
ESA/ESTEC/YMM
Postbus 299
NL-2200 AG Noordwijk (ZH)
THE NETHERLANDS

Mr G. MARQUETTE
Bertin & Cie
B.P. 3
F-78373 Plaisir Cédex
FRANCE

Mr W. MENGES
ESA/ESTEC/YTM
Postbus 299
NL-2200 AG Noordwijk (ZH)
THE NETHERLANDS

Mr. S. MAEKAWA
Kawasaki Heavy Industry Co.
1, Kawasaki-chiyo
Kakamigahara-shi
Gifu
JAPAN

Mr J. MARTÍN
CASA - Space Div.
Acda Aragon 404
E-28022 Madrid
SPAIN

Mr MENRATH
Aerospatiale
BP 11
F-33165 Saint-Médard-en-Jalles
FRANCE

Mr J. MALPHETTES
ESA/ESTEC/XXA
Postbus 299
NL-2200 AG Noordwijk (ZH)
THE NETHERLANDS

Mr P.C. MARUCCHI-
CHIERRO
Alenia Spazio
Corso Marche 41
I-10146 Torino
ITALY

Mr F. MERCIER
CNES
18, Av. Edouard Belin
F-31055 Toulouse Cédex
FRANCE

Mr. A. MAMODE
CNES
18, av. Edouard Belin
F-31055 Toulouse Cédex
FRANCE

Mr. K. MATSUMOTO
Toshiba
1-Toshiba Komukai
Saiwa-Ku
Kawasaki City
Kanagawa 210
JAPAN

Mr A. MESCHINI
Alenia Spazio
Via Saccomuro 24
I-00131 Rome
ITALY

Mr J.L. MARCE
CNES
18, Av. Edouard Belin
F-31055 Toulouse Cédex
FRANCE

Mr D. MAYER
NASA Ames Research Center
Moffett Field
Los Angeles, CA 94035
USA

Mr E.I. MIRALDI
Politecnico di Torino
Dept. Fisica
Corso Duca Degli Abruzzi 24
I-10129 Torino
ITALY

Mr. P. MARCHESE
Alenia Spazio
Corso Marche 41
Torino
ITALY

MR A.H. MCGRATH
ESA/ESTEC/MES
Postbus 299
NL-2200 AG Noordwijk (ZH)
THE NETHERLANDS

Mr A.K. MITCHELL
Tech. University of Nova Scotia
P.O. Box 1000
Halifax, NS
CANADA

LIST OF PARTICIPANTS

xxv

Mr. V.J.G. MOLINERO
CASA - Space Div.
Avda. Aragon, 404
E-28022 Madrid
SPAIN

Mr R. MUSSALIAN
Eutelsat-Paris-Division 4
Tour Maine Montparnasse
33, av du Maine
F-75755 Paris 15
FRANCE

Mr. N. NIKOLAIZIG
ESA/ESTEC/YTF
Postbus 299
NL-2200 AG Noordwijk (ZH)
THE NETHERLANDS

Mr J.P. MORAND
CNES
18, av. Edouard Belin
F-31055 Toulouse Cédex
FRANCE

Mr F.H NABER
Fokker Space & Systems
Postbus 7600
NL-1117 ZJ Schiphol Oost
THE NETHERLANDS

Mr S.M. NIKU
Computational Mechanics
Ashurst Lodge, Ashurst
Southampton, SO4 2AA
UK

Mr J. MORANDI
SAFT
156 AV. de Metz
F-93230 Romainville
FRANCE

Mr S. NAGATA
Mitsubishi Heavy Ind. Ltd.
Nagoya Aerospace System
IO, Oye-Cho, Minatoku
Nagoya, 455
JAPAN

Mr. A. NOIR
Aerospatiale
Route de Verneuil
F-78130 Les Mureaux Cedex
FRANCE

Mr E. MOULAERT
Eutelsat
Tour Maine Montparnasse,
47eme E
33, av. du Maine
F-75755 Paris 15
FRANCE

Mr. W. NELLESSEN
ESA/ESTEC/MR
Postbus 299
NL-2200 AG Noordwijk (ZH)
THE NETHERLANDS

Mr. S. NOWAK
Space Research Center
W. Kopernika 11
51-622 Hroelan
POLAND

Mr. K. MUEHLBAUER
IABG
Einsteinstrasse 20
D-8012 Ottobrunn
FRG

Mr. A. NEWERLA
ESA/ESTEC/YMD
Postbus 299
NL-2200 AG Noordwijk (ZH)
THE NETHERLANDS

Mr. R. OHAYON
ONERA
29, Avenue de la Division
Leclerc
F-92 Châtillon-sous-Bagneux
FRANCE

Mr D. MULLER-WIESNER
MBB/ERNO
Hunefeldstr. 1-5
Postfach 10 59 09
D-2800 Bremen 1
FRG

Mr. N. NIEDBAL
DLR/Institute of Aeroelasticity
Bunsenstrasse 10
D-3400 Göttingen
FRG

Mr I. OLAZABAL
SENER
Avda. Zugazarte 56
E-48930 Las Arenas
SPAIN

Mr P. Muser
MAN-Technologie AG
Bauschingerstr. 20
D-8000 München 50
FRG

Mr. M.P. NIEUWENHUIZEN
Delft University of Technology
Ligusterlaan 24
NL-2015 LJ Haarlem
THE NETHERLANDS

Mr A. OMRANI
STRACO S.A.
Compiègne
FRANCE

LIST OF PARTICIPANTS

Mr A. ORDEN
Iberica del Espacio S.A.
Madrid
SPAIN

Mr J.L.P. PARQUET
ESA-ESTEC
Postbus 299
NL-2200 AG Noordwijk (ZH)
THE NETHERLANDS

Mr P. PICARD
Aerospatiale
Route de Verneuil
F-78130 Les Mureaux Cédex
FRANCE

Mr H. ORY
University of Aachen
Aachen
FRG

Mr P. PARRAUD
CISI Ingenierie
Parc d'activité Kennedy
BP 19
F-33702 Mérignay
FRANCE

Mr. L. PIERRE
SABCA
Ch. de Haecht 1470
Brussel
BELGIUM

Mr. P. OTSUKI
NASDA, SSG
2-5-6 Shiba, Minato-ku
Tokyo 105
JAPAN

Mr A.V. PATKI
ISRO
Bangalore
INDIA

Mr J.N. PINDER
University of Southampton
ISVR Consultancy Services
The University
Southampton, SO9 5NH
UK

Mr D.O. Otte
LMS Belgium BVBA
Interleuvenlaan 65
B-3001 Leuven
Belgium

Mr L. PERRET
CNES
18, av Edouard Belin
F-31055 Toulouse Cédex
FRANCE

Mr J-P. PLANAS
Dassault Aviation
78, Quai Marcel Dassault
F-92552 Saint-Cloud Cédex 300
FRANCE

Mr G. Paindessous
ESA/ESTEC/CSF
Postbus 299
NL-2200 AG Noordwijk (ZH)
THE NETHERLANDS

Mr M. PETERSSON
Ericsson Radar Electronics AB
Bergsfotsgatan 2
S-43184 Molndal
SWEDEN

Mr PLESCHER
FH Aachen, Space Dept.
Hohenstaufenallee 6
D-5100 Aachen
FRG

Mr. J. PANG
ESA/ESTEC/YMD
Postbus 299
NL-2200 AG Noordwijk (ZH)
THE NETHERLANDS

Mr C. PETIAU
DASSAULT AVIATION
78, quai Marcel Dassault
F-92214 Saint Cloud Cédex
FRANCE

Mr. W. PONGE-FERREIRA
DLR/Institute of Aeroelasticity
Bunsenstrasse 10
D-3400 Göttingen
FRG

Mr R.S. PAPPA
DLR/Institute of Aeroelasticity
Bunsenstrasse 10
D-3400 Göttingen
FRG

Mr W. PETRUSCHKE
Rheinisch-Westfälischer
Technischer Überwachungs
Verein
Kurfürstenstr. 58
D-4300 Essen
FRG

Mr S. PORTIGLIOTTI
Alenia Spazio
Corso Marche 41
Torino
ITALY

LIST OF PARTICIPANTS

xxvii

Mr. A. POUZET
CNES
18, av. Edouard Belin
F-31055 Toulouse Cédex
FRANCE

Mr K.L. REIFSNIDER
Virginia Polytechnic Institute
Materials Response Group
Blacksburg, VA 24061
USA

Mr. W. RITS
ESA/ESTEC/YME
Postbus 299
NL-2200 AG Noordwijk (ZH)
THE NETHERLANDS

Mr M. PRADIER
ESA/ESTEC/YME
Postbus 299
NL-2200 AG Noordwijk (ZH)
THE NETHERLANDS

Mr H.G. REIMERDES
MBB/ERNO Raumfahrttechnik
GmbH
Hunefeldstr. 1-5
D-2800 Bremen 1
FRG

Mr A.P. ROBBEN
ESA/ESTEC/XPG
Postbus 299
NL-2200 AG Noordwijk (ZH)
THE NETHERLANDS

Mr. A. PRAWIRANEGARA
Delft University of Technology
Postbus 5058
NL-2600 GB Delft
THE NETHERLANDS

Mr G. REKERS
Delft University of Technology
Postbus 5058
NL-2600 GB Delft
THE NETHERLANDS

Mr. A. ROBINSON
ESA/ESTEC/YMM
Postbus 299
NL-2200 AG Noordwijk (ZH)
THE NETHERLANDS

Mr Y. PREL
CNES
Rond-Point de l'Espace
F-91023 Evry Cédex
FRANCE

Mr O. REMONDIÈRE
Alcatel Espace
26, Av. J.F Champollion
F-31037 Toulouse
FRANCE

IAL P. ROCHUS
Parc Industriel de Recherches
Ave. du Pré Aily
B-4031 Angeleur
BELGIUM

Mr. G. RACCA
ESA/ESTEC/MRD
Postbus 299
NL-2200 AG Noordwijk (ZH)
THE NETHERLANDS

Mr A. RICARD
Framasoft TCSI
Tour Fiat
F-92084 Paris La Défense Cédex
16
FRANCE

Mr G. ROMEO
Politecnico di Torino
Dept. of Aerospace Eng.
Corso Duca degli Abruzzi 24
I-10129 Torino
ITALY

Mr P. RATHJEN
Interatom GmbH
Postfach 10035
D-5060 Berg. Gladbach 1
FRG

Mr S. RIDER
Space Systems
British Aerospace Eng.Ltd.
Earth Observation and Science
P.O. BOX 5
Filton, Bristol BS12 7QW
UK

Mr M. ROTH
MBB
Dept. KT 21
Postfach 801169
D-8000 München 80
FRG

Mr. G. REIBALDI
ESA/ESTEC/FTD
Postbus 299
NL-2200 AG Noordwijk (ZH)
THE NETHERLANDS

Mr B. RITCHIE
CNES
18, av Edouard Belin
F-31055 Toulouse Cedex
FRANCE

Mr PH. ROY
CNES
18, Av. Edouard Belin
F-31055 Toulouse Cédex
FRANCE

LIST OF PARTICIPANTS

Mr G. RUSCICA
Politecnico di Torino
Dept. Energetica
Corso Duca degli Abruzzi 24
I-10129 Torino
ITALY

Mr R. SCHERMANN
Österr. Raumfahrt- und
Systemtechnik GmbH
Operngasse 20b
A-1040 Wien
AUSTRIA

Mr L. SCOLAMIERO
Alenia Spazio
Via Saccomuro 24
I-00131 Rome
ITALY

Mr G. RUVINETTI
Politecnico di Torino
Dept. of Aerospace Eng.
Corso Duca Degli Abruzzi 24
I-10129 Torino
ITALY

Mr L. SCHILLEMANS
Free University Brussels
Peinlaan 2
B-1050 Brussel
BELGIUM

Mr. P. SEIBEL
ESA/ESTEC/YMD
Postbus 299
NL-2200 AG Noordwijk (ZH)
THE NETHERLANDS

Mr E.D. SACH
MBB
Postfach 801169
D-8000 München 80
FRG

Mr. D. SCHMITT
Fraunhofer Institut f. Chem.
Technologie
Postfach 1240
D-7507 Pfinztal
FRG

Mr T. Sgobba
ESA/ESTEC/QSS
Postbus 299
NL-2200 AG Noordwijk (ZH)
THE NETHERLANDS

Mr. J. SANTE
ESA/ESTEC/OS
Postbus 299
NL-2200 AG Noordwijk (ZH)
THE NETHERLANDS

MR SCHNEIDER
IKOSS
Waldburgstr. 21
D-7000 Stuttgart 80
FRG

Mr. E. SIEGER
Zeppelin-Metallwerke GmbH
Leutholdstrasse
Postfach 2540
D-7990 Friedrichshafen
FRG

Mr T. SCHAEFFLER
MAN-Technologie AG
Dachauer Strasse 667
Postfach 500426
D-8000 München 50
FRG

Prof. G.I. SCHUELLER
University of Innsbruck
Institut f. Mechanik
Technikerstr. 13
A-6020 Innsbruck
AUSTRIA

Mr M. SINAPIUS
DLR/Institute of Aeroelasticity
Bunsenstrasse 10
Göttingen
FRG

Mr. E. SCHEIDER
Ernst-Mach-Institut
Eckerstrasse 4
D-7800 Freiburg
FRG

Mr V. SCHULZE
Dornier GmbH
Postfach 1303
D-7990 Friedrichshafen
FRG

Mr. G. SINNEMA
Fokker Space & Systems
Postbus 12222
NL-1100 AE Amsterdam
THE NETHERLANDS

Mr A. SCHENK
DLR/Institute of Aeroelasticity
Bunsenstrasse 10
D-3400 Göttingen
FRG

Mr. G. SCHWEICKERT
Dornier GmbH
Postfach 1420
D-7990 Friedrichshafen
FRG

Mr R. SIPPEL
Dornier GmbH
Postfach 1420
D-7990 Friedrichshafen
FRG

LIST OF PARTICIPANTS

xxix

Mr. F.B.O. SJÖBERG
Swedish Space Corporation
P.O. Box 4207
S-17104 Solna
SWEDEN

Mr K. SPÅNG
DNV Ingemansson AB
Box 276
S-40124 Göteborg
SWEDEN

Mr. O.A.E. STORRER
LMS International
Interleuvenlaan 65
B-3001 LEUVEN
BELGIUM

Mr E. SLACHMUYLDERS
ESA/ESTEC/Y
Postbus 299
NL-2200 AG Noordwijk (ZH)
THE NETHERLANDS

Mr. A.R. STAM
Delft University of Technology
Postbus 5058
NL-2600 GB Delft
THE NETHERLANDS

Mr. T. SUGIMOTO
Space Com. Research Corp.
5F, Hayakawa Tonakai Bldg
2-12
Iwamoto-cho chiyoda-Ku
Tokyo 101
JAPAN

Mr. G.P. SLAGTER
Fokker Space & Systems
Schipholdijk 231
Postbus 7600
NL-1117 ZJ Schiphol Oost
THE NETHERLANDS

Mr H. STARK
ESA/ESTEC/YMD
Postbus 299
NL-2200 AG Noordwijk (ZH)
THE NETHERLANDS

Mr B. SULTAN
MBB/ERNO
Hunefeldstrasse 1 - 5
D-2800 Bremen
FRG

Mr J.E. SMIT
Delft University of Technology
Postbus 5058
Kluyverweg 1
NL-2600 GB Delft
THE NETHERLANDS

Mr. C. STAVRINIDIS
ESA/ESTEC/YMD
Keplerlaan 1
NL-2200 AG Noordwijk
THE NETHERLANDS

Mr. H.A. SUPERFINE
ESA/ESTEC/YM
Postbus 299
NL-2200 AG Noordwijk (ZH)
THE NETHERLANDS

Mr C. SNETHLAGE
PDA Engineering Int. B.V.
Agnieten straat 66-A
NL-2801 HZ Gouda
THE NETHERLANDS

Mr K-H. STECHER
MBB-ERNO
Hunefeldst. 1-5
D-2800 Bremen 1
FRG

Mr. P.B. SVEDHEM
Ericsson Radar Electronics
S-431 84 Molndal
SWEDEN

Mr J. SOLA
CASA - Space Div.
Avda. Aragon 404
E-28022 Madrid
SPAIN

Mr P. STIGELL
VTT/INS
SF-02151 Espoo 21
FINLAND

Mr A.J. TACK
ERA Technology Ltd
Cleeve Road
Leatherhead
Surrey KT22 7SA
UK

Mr. Y. SOUCY
Canadian Space Agency
P.O. Box 11490, Stn.H
Ottawa K2H 8S2 Ontario
CANADA

Mr R. STOLK
ESA/ESTEC/YTE
Postbus 299
NL-2200 AG Noordwijk (ZH)
THE NETHERLANDS

Dr N.G. TAYLOR
MAN-Technologie AG
Bauschingerstr. 20
D-8000 München 50
FRG

LIST OF PARTICIPANTS

Mr. N. TEKCHANDANI
ESA/ESTEC/YMD
Postbus 299
NL-2200 AG Noordwijk (ZH)
THE NETHERLANDS

Mr D.M. TRAN
ONERA
29, av. Division Leclerc
B.P. 72
F-92322 Châtillon Cédex
FRANCE

Mr E.P.M. VAN DEN
HEUVEL
Delft University of Technology
Korvezeestraat 233
NL-2628 DK Delft
THE NETHERLANDS

Mr G.R. TER HAAR
Fokker Space & Systems
Postbus 12222
NL-1100 AE Amsterdam
THE NETHERLANDS

Mr F. Tremblay
SPAR Aerospace Ltd
2125 Trans-Canada Highway
Ste-Anne-de-Bellevue
H9X 3R2 Québec
CANADA

Mr B. VAN DER DONK
Matra Datavision Benelux S.A.
Guimardstraat 15, Bus 4
B-1040 Brussel
BELGIUM

Mr M. TERLUNEN
ARGE DETECON/DLR
Scharnhorststr.4
D-5300 Bonn 2
FRG

Dr H. TWARDY
DLR-Institut f. Strukturmechanik
DLR Flughafen
D-3300 Braunschweig
FRG

Mr M.J. VAN DIJK
Delft University of Technology
Postbus 5058
NL-2600 GB Delft
THE NETHERLANDS

Mr M. THAIET
Association Goset
107.111 Ave. G. Clémenceau
Nanterre
FRANCE

Mr J.F. Tyrrell
Fokker space & Systems
Postbus 12222
NL-1100 AE Amsterdam
THE NETHERLANDS

Mr. D. VAN HEMELRIJCK
Free University Brussels
Peinlaan 2
B-1050 Brussel
BELGIUM

MR B. THEELEN
Delft University of Technology
Postbus 5058
NL-2600 GB Delft
THE NETHERLANDS

Mr I. URIBARRI
CASA - Space Div.
Avda. Aragon 404
E-28022 Madrid
SPAIN

Mr D.V.H. VANDEPITTE
Fokker Space & Systems
Postbus 12222
NL-1100 AE Amsterdam
THE NETHERLANDS

Dr S. TIZZI
University of Rome 'La
Sapienza'
Via Eudossiana 16
I-00184 Rome
ITALY

Mr R. VALLE
Aérospatiale
100 Bd. du Midi
F-06322 Cannes
FRANCE

Mr L. VASSEUR
Matra Datavision Benelux S.A.
Guimardstraat 15, Bus 4
B-1040 Brussel
BELGIUM

Mr. B. TOLENAAR
Delft University of Technology
Postbus 5058
NL-2600 GB Delft
THE NETHERLANDS

Mr. P.G. VAN BLADEL
Delft University of Technology
Postbus 5058
2600 GB Delft
THE NETHERLANDS

Mr D. VAUCHER DE LA
CROIX
Metrarub R.D.S.
64 Chemin des Mouilles
BP 182
F-69132 Ecully Cédex
FRANCE

LIST OF PARTICIPANTS

xxxi

Mr. M. VERAIR
ESA/ESTEC/YMM
Postbus 299
NL-2200 AG Noordwijk (ZH)
THE NETHERLANDS

Mr B.K. WADA
JPL
California Institute of
Technology
4800 Oak Grove Drive
Pasadena, CA 91109
USA

Mr G. WIERHEIM
Interatom GmbH
Postfach 100351
D-5060 Bergisch-Gladbach
FRG

Mr G.A.M. VERMIJ
Fokker Space & Systems
Postbus 12222
NL-1100 AE Amsterdam
THE NETHERLANDS

Mr. R.J.H. WANHILL
National Aerospace Laboratory
WLR
Postbus 153
NL-8300 AD Emmeloord
THE NETHERLANDS

Mr J.J. WIJKER
Fokker Space & Systems
Postbus 12222
NL-1100 AE Amsterdam
THE NETHERLANDS

Mr. N.W.M. VERSCHUREN
Ultra Centrifuge Nederland N.V.
Planhofsweg 77
NL-7601 PJ Almelo
THE NETHERLANDS

Mr S. WASTBERG
Det Norske Veritas
P.O. Box 300
N-1322 Høvik
NORWAY

Mr. TER WIJLEN
Ultra Centrifuge Nederland NV
Planhofsweg 77
NL-7601 PJ Almelo
THE NETHERLANDS

Mr C. VIDAL
Aerospatiale
100 boulevard du Midi
BP 99
F-06322 Cannes-la-Bocca Cédex
FRANCE

Mr. M. WEILAND
Universität Gesamthochschule,
Kassel
Monchebergstrasse 7
D-3500 Kassel
FRG

Mr O. WILMAR
DNV Ingemannsson AB
P.O. BOX 47321
S-10074 Stockholm
SWEDEN

Mr. M. VIDUSSONI
ESA/ESTEC/YMD
Postbus 299
NL-2200 AG Noordwijk (ZH)
THE NETHERLANDS

Mr D. WEINSTEIN
NASA HQ
955 l'Enfant Plaza
7800 Washington, DC 20024
USA

Mr M. WINDISCH
MAN-Technologie AG
Bauschingerstr. 20
D-8000 München 50
FRG

Mr P.A. VILLALAZ
Oerlikon-Contraves AG
Schaffhauser Str. 580
CH-8052 Zürich
SWITZERLAND

Mr J.J. WEISZ
SENER
Avda. Zugazarte 56
E-48930 Las Arenas
SPAIN

Mr R.J. WISE
TWI
Abington Hall
Abington, Cambridge CB1 6AL
UK

Mr O. VON ESTORFF
IABG
Einsteinstr. 20
D-8012 Ottobrunn
FRG

Prof. R.G. WHITE
University of Southampton
ISVR
Highfield
Southampton SO9 5NH
UK

Mr R. WOLLENDORFER
Osterr. Raumfahrt- und
Systemtechnik GmbH
Operngasse 20B
A-1040 Wien
AUSTRIA

Mr D. WRIGHT
Dornier GmbH
Postfach 1420
D-7990 Friedrichshafen
FRG

Mr H. WYNENDAELE
Numerical Integration
Technologies
Ambachtenlaan 29
B-3001 Leuven
BELGIUM

Mr M. YAMAMOTO
National Space Development
Corporation of Japan
2-1-1 Sengen
Tsukuba-shi
Ibaraki 305
JAPAN

Mr K.J. Zimmerman
AEO ita
Universitätstr. 87
Postfach 200
CH-8033 Zürich
Switzerland

OPENING ADDRESS

Marius Le Fèvre
Director of ESTEC
ESTEC, Noordwijk, The Netherlands

Fellow Directors, Chairmen, Ladies and Gentlemen!

Structures and mechanical testing are both disciplines with long histories. As far as spacecraft applications are concerned, however, significant and far-reaching advances have been witnessed in the last three decades, driven by the development of space systems with increasing complexity, dimensions and significantly increased service lifetimes.

Stringent project requirements, combined with the advances in new materials, in problem modelling and simulation, and in testing techniques for the flight/in-orbit environment, have contributed to the rapid pace in satellite development.

The concept of maintaining a space station as a permanent laboratory in space has raised many new issues, which include durability of the structure in aggressive environments, costs of repair and maintenance, the reliability of electromechanical and mechanical systems, and the need to design for long-term system support. In striving to meet such objectives, we need to encourage an ever-growing interaction among a range of disciplines, including applied mechanics, materials technology, dynamic-control technology, numerical analysis, software design, structural engineering, and advanced manufacturing and testing.

The international character of the Plenary Session, in which key papers based on the American, Japanese and European space segments will be presented, testifies to the cooperative spirit of Space Station Freedom. The technical challenges of two of the Agency's other pro-

grammes, Ariane-5 and Hermes, are also covered by key papers.

Many of the contributed papers cover the structural-engineering aspects of scientific, earth-observation and telecommunication satellites. Indeed, about two-thirds of the 148 papers are directly associated with space project applications, where hardware developments and experience will be reported by major space contractors. The other one-third will cover important technological advances in satellite structural design, development and verification.

Although recent advances in structure design and technology may be far reaching, the basic principle underlying all good structural design, namely that of establishing efficient load paths and providing material where it will be most effective, should not be overlooked by practising engineers.

There is a saying: 'God blessed many hands, but not many mouths'. Nevertheless, I hope that the next few days of presentations and ensuing discussions will show that this is unduly pessimistic in the case of space-oriented structural engineers and mechanical testers.

I am happy to welcome you all to this Spacecraft Structures and Mechanical Testing Conference, and I now formally declare the meeting open. I look forward to reading the proceedings of the conference and studying the recommendations that will result from your deliberations. The outcome of this gathering will certainly be taken into account when we come to establish directives for future Agency activities in this rapidly expanding and challenging area.

WELCOMING ADDRESS

Jean-Louis Marcé
Assistant Director for Technology
CNES, Toulouse, France

Ladies and Gentlemen!

On behalf of CNES, I am particularly happy to make a welcoming address for this international conference on spacecraft structures and mechanical testing.

Sixteen years ago, in 1975, the first conference of this kind took place at Frascati. It was followed by the second in Toulouse (1985) and the third in Noordwijk (1988). Now we are about to embark on the fourth, which comes very opportunely, just before the start of the development phase of the challenging European programmes: Hermès, Columbus and the Earth Observation Platforms.

During the last ten years, there have been very important changes in the field of structures; very briefly, they are the following:

- design tools have advanced enormously, with the general application of CAD technology, improvements in design software and standardisation of finite-element codes;
- integrated engineering systems based on a geometrical data base common to the various users, structural analyses, thermal analyses, radiation-dose computations and contamination assessments are becoming a reality;
- the participation of many industrial firms in each project leads to the need to standardise data exchange;
- attitude-control and structure specialists are tending increasingly to use common tools and languages, to a large extent because the increasing size of space vehicles is leading to lower structure frequencies;
- the fact that representative deployment tests on large structures cannot be performed on the ground has made it essential to improve modelling techniques in this field;
- the problem of microvibrations has become critical as a result of drastically increased pointing-stability requirements for payloads combined with a greater complexity of payload arrangements; this has made it necessary to improve modelling in this field, particularly as regards damping assessment;

— improvement of test methods has become imperative in two main areas:

- (a) on the one hand, representativity with regard to the real launch environment as a means of avoiding needless overstressing (Here, I once more take the opportunity to urge close co-operation between launcher and space vehicle designers; it is in all our interests to optimise design and reduce margins.);
- (b) on the other hand, partial testing (The general increase in the size of space vehicles means that it is no longer possible to test the fully integrated vehicle. Consequently, vehicles have to be tested element by element, entailing a need to improve qualification philosophy and dynamic-identification processes. We are facing the inevitability of qualification by analysis.);
- the increase in required lifetime (up to thirty years in the case of a space station) has made it necessary to improve our knowledge in the field of space debris, its impact on space vehicles and ways in which the latter can be protected;
- progress in the field of materials has been important, driven not only by the permanent requirement to reduce mass, but also by the increased stringency of payload-stability requirements and the space vehicle's need to survive re-entry into the earth's atmosphere.

This long but certainly not exhaustive list merely serves to emphasise the importance of the topics that are the subject of this conference. It makes very clear the need for the specialists of the various disciplines to exchange information and share experience.

I am happy to note the markedly international character of the list of participants and am especially glad to see many non-Europeans taking part. I have no doubt that the quality of the technical exchanges taking place in the next three days will be of a high order and that the space community in general will benefit. The large number of participants (more than 400 from about 20 countries) and

the many papers presented (about 140) are a further indication of the importance of the subject and the need that exists for conferences of this kind. In this connection, I am happy to announce that the next conference in the series will be hosted by CNES in Toulouse in 1994.

In conclusion, I should like to express my thanks to:

- ESA and DLR for their efficiency and co-operative efforts in organising and preparing for this conference;
- ESTEC management and staff for their hospitality;

- all those who have been involved in the preparation of the conference and who have in many cases had to put in a lot of overtime to make it a success;
- all those who are presenting papers;
- all those who are taking part and by their presence and active interest are helping to make sure that the conference is a worthwhile and stimulating event.

I wish the conference success and look forward to seeing you all in Toulouse in 1994.

Report on the Conference

(Reprinted from the ESA Journal, Vol. 15, No. 2)

The Conference attracted some 420 participants, emanating mainly from the ESA Member States but including a strong representation from the United States (15 delegates) and Japan (11 delegates).

The Conference was co-sponsored by the European Space Agency, CNES (F) and DLR (D). The opening addresses by ESTEC's Director, Mr M. Le Fèvre, and CNES's Technical Director, Mr J.L. Marcé, and a message from DLR's Director, Prof. W. Kröll, read in his absence, identified the importance attached to this area of activities by senior space management.

Two-thirds of the 149 papers presented were directly associated with space project applications of scientific, earth observation, and telecommunication satellites, reporting hardware design, development, and testing and related experiences of major space contractors. The other one-third covered important technological advances in satellite structural design, development and verification. As a result, the sessions were particularly useful to spacecraft mechanical engineers.

The papers were grouped into 40 sessions with the following themes:

- Space Station (2 sessions)
- Launchers (2 sessions): Loads/Optimisation, Development
- Space Plane and Re-entry (2 sessions)
- Design & Development (2 sessions): Mechanical Systems, Structures
- Analysis (6 sessions): Dynamics, Methods, Fluid/Structure Interaction
- Vibro-acoustics (4 sessions): Environment, Methods
- Materials (8 sessions): Characterisation, Fracture/Fatigue, Composites, Damage Mechanics, Metallic Structures
- Testing (3 sessions): Systems, Methods, Facilities
- Multibody Dynamics (2 sessions): Microgravity, Deployment Dynamics
- Dynamic Identification (3 sessions)
- Antenna Design (3 sessions)
- CAD/CAE (1 session): Methods & Interfaces
- Arianespace Plenary Session: Presentations on the Arianespace organisation, the Ariane family of launchers, and the dimensioning and testing of Ariane payloads.

The international make-up of the Plenary Session, in which key papers based on the American, Japanese, and European space segments were presented by the respective project managers, testified to the co-operative spirit of the Space Station. The concept of maintaining the Space Station as a permanent laboratory in space raises many new issues, which include durability of the structure in aggressive environments, costs of repair and maintenance, the reliability of electromechanical and mechanical systems, and the need to design for long-term system support. The technical challenges of two of the Agency's other major programmes, Ariane-5 and Hermes, were also covered by key papers. In striving to meet the programme objectives, an ever-growing interaction between a range of disciplines was presented, including applied mechanics, materials technology, dynamic control technology, numerical analysis, software design, structural dynamics, structural engineering, and advanced manufacturing and testing.

The most important points identified during the Conference are the need for a better understanding of launcher loads, qualification requirements imposed by launcher authorities to cover launch events, and particularly qualification requirements imposed by space projects and programmes to ensure mission success. It is generally considered that the latter is not treated adequately, and different practices are followed by the various space organisations, satellite developers, and within the various centres of the major space agencies. This problem has been experienced internationally, with in-orbit satellite functional failures occurring as a result. The establishment of a special panel to define policy and requirements in this area has been proposed by representatives of major space agencies and organisations.

The Conference attracted a high level of international specialists in spacecraft structures, and ESTEC was identified as a centre of knowledge in this area. During the Conference, visits were arranged to the ESTEC Test Facilities and the neighbouring Space Expo.

C. Siavrinidis, Conference Chairman

**SESSION
1.1.A**

**SPACE
STATION
I**

PRECEDING PAGE BLANK NOT FILMED

N92-23781

DEVELOPMENT OF JAPANESE EXPERIMENT MODULE

Fumio Otsuki, Kuniaki Shiraki,
Kazuhiko Kamesaki, Kazuyuki Tasaki

National Space Development Agency of Japan
2-5-6, Shiba, Minato-ku, Tokyo 105, Japan

Abstract

The National Space Development Agency of Japan (NASDA) started preliminary design of the JEM in January 1990 along with the component development test activities, and has a plan to conduct the Preliminary Design Review (PDR) in early 1992. NASDA's JEM Program faces many challenges as it strives to overcome the large number of technical obstacles associated with designing, developing and integrating the JEM.

This paper presents an overall picture of the JEM program structural development activities including design, testing and analysis activities. It focuses on some technical challenges which have been or must be surmounted in order to assure JEM structural safety. The paper introduces some approaches taken to implement these solutions.

1. Introduction

The JEM, shown in Fig.1 (*1), is a multi-purpose research and development laboratory which consists of five elements: a Pressurized Module (PM), an Exposed Facility (EF), a Remote Manipulator System (RMS) and a two-piece Experiment Logistics Module (ELM). (The ELM is composed of a pressurized Section (ELM-PS) and an Exposed Section (ELM-ES)).

These elements are assembled on orbit using the Space Station Manipulator System. The PM, attached to a Space Station Freedom (SSF) node, is a cylindrical laboratory where shirt sleeve clad crew members can conduct material processing and life science experiments in a micro-gravity environment.

The EF is an exposed platform attached to PM with a berthing mechanism. The EF provides attached payload accommodation for

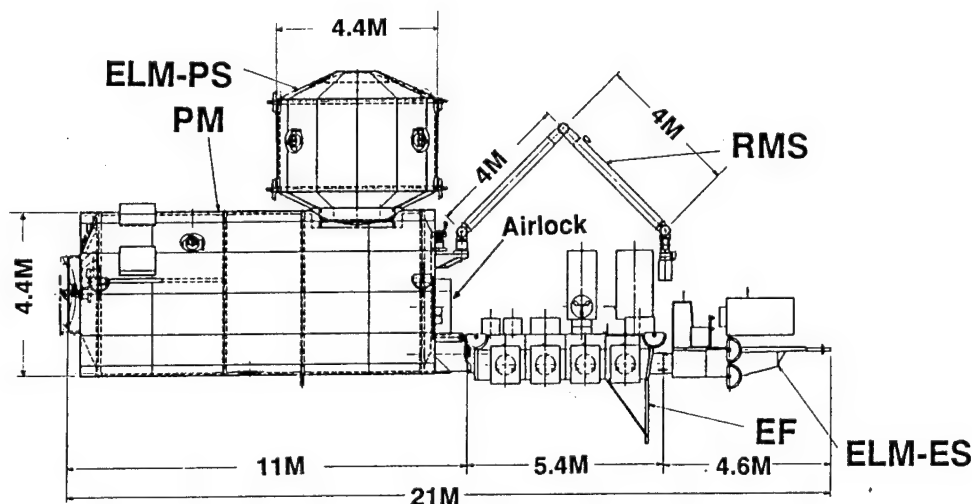


Fig.1 JEM CONFIGURATION

conducting material processing, earth observation, and technology development experiments in an environment exposed to space. The ELM-PS and ES are used as both carriers and for on-orbit stowage of pressurized and unpressurized items respectively. Such items include specimens and payload equipment as well as system equipment for on orbit exchange. The ELM-PS is normally located at the side port of PM, and ELM-ES, on the top of the EF. The RMS, attached at the aft end cone of the PM, will handle the ELM-PS and ELM-ES as well as user payloads. Payloads, specimens and equipment will be transferred between the interior of the PM and the EF through a scientific airlock on the aft end of the PM.

PM, ELM-PS, EF, ELM-ES and RMS are being integrated by four contractors, each of which will also design and manufacture the corresponding structure.

As the JEM is a complex facility with multiple functions, it is composed of a variety of structural elements each of which has a specific mission life requirement as shown in Table 1. This paper provides an overview of JEM structural development activities being conducted by NASDA.

2. JEM Structural Design Status

Although the JEM structural design approach is to use conventional technologies to assure product safety, some advanced technologies are being applied to achieve higher performance and to promote technology development for future space programs.

Table.1 MISSION LIFE REQUIREMENTS

JEM ELEMENT	MISSION LIFE REQUIREMENTS
PM	30 YEARS LIFE, CONSIDER RETRIEVAL
ELM-PS	15 YEARS LIFE, 10 CYCLE LAUNCH/LANDING
EF	10 YEARS LIFE, 2 CYCLE LAUNCH/LANDING
ELM-ES	10 YEARS LIFE, 10 CYCLE LAUNCH/LANDING
RMS	10 YEARS LIFE, CONSIDER RETRIEVAL

2.1 PM and ELM-PS Structure

The PM structure as shown in Fig.2 is a fusion welded pressure vessel, which consists of a cylinder section, a forward cone and an aft cone. The material is 2219 Aluminum alloy which has good weldability, strength and ductility.

The cylinder section, with internal diameter of 4.2m, is made of iso-grid-type integral stiffened panels and ring frames. At one end, there is a radial port where NASDA will locate a Space Station Common Berthing Mechanism (CBM) for attaching the ELM-PS. The forward cone has a 25 degree

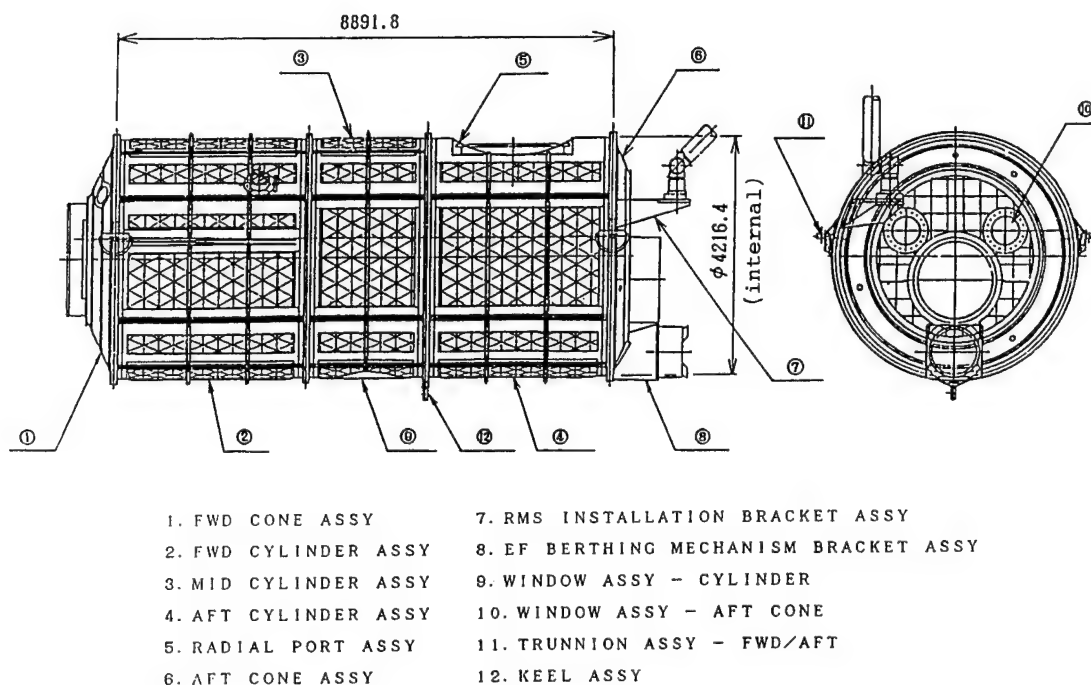


Fig.2 PM STRUCTURE

pitch and also uses an integrated welded construction. The endcone will house the Space Station CBM for attaching the JEM to the Space Station Node. The aft end panel has a large cut for the airlock, and attachment structure for the manipulator arm, and the RMS viewing windows. This structure is a machined integral panel which is made from a forged plate thereby providing high rigidity to sustain the RMS launch loads and internal pressure load, while minimizing structural deformation. The ELM-PS will utilize a common structural design with the PM, except the aft endcone is different.

The meteoroid and debris shield will use the multi-shield design approach. The current concept for implementing this approach is to cover the pressure shell with a double layer of aluminum alloy sheets.

The JEM PM and ELM-PS structure design and manufacture utilizes technology developed for manufacture of the Japanese H-II launch vehicle liquid H₂/O₂ pressure vessels.

The airlock structure consists of a cylinder with inner and outer hatches as shown in Fig.3. The airlock cylinder is an integrated pressure cylinder with stringers and frames for stiffness. The diameter of the cylinder varies between the inside and outside the PM. The airlock hatches are also integrated pressure plate stiffened with ribs. The airlock cylinder and hatches are made of 2219-T852 aluminum forgings, and the cylinder is manufactured by welding.

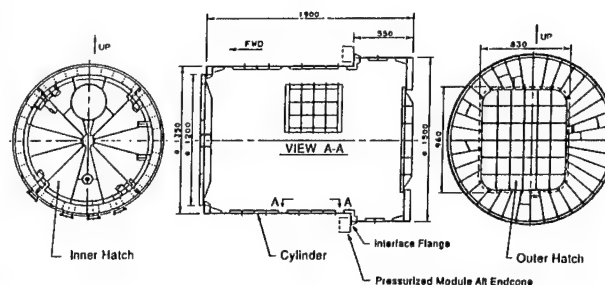


Fig.3 AIRLOCK STRUCTURE

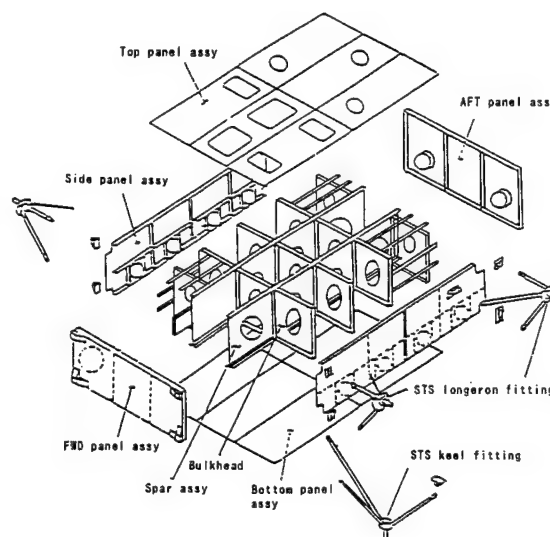


Fig.4 EF STRUCTURE

2.2 EF Structure

The EF shown in Fig.4 is composed of a box type main structure with a subordinate structure to support the Space Shuttle trunnions. The main structure is a formed semimonocoque structure assembled with panels and frames. The size is about 4.7m(L)x3.1m(W)x1.2m(H). As for the Shuttle trunnion support structure, there are two primary longeron fittings, two stabilizing longeron fittings and one keel fitting. The main structure and Shuttle trunnion support structure are made of 7075 Aluminum, and mechanically integrated constructions.

JEM EF Berthing Mechanism is attached on the forward panel.

2.3 ELM-ES Structure

The ELM-ES structure shown in Fig.5 consists of an upper part and a lower part.

The lower part is a pallet type structure which accommodates payloads on top of it. This pallet consists of two panels and frames which are placed between the two panels. The ELM-ES has 4 longeron trunnions and a keel trunnion. Two of the longeron trunnions are connected to the pallet structure with oblique frames. This feature is used to achieve wide payload mounting area as well as to enhance NSTS loading volume efficiency.

The upper part is made of rigidly connected frames covered with panels. This part accommodates bus equipment, grapple fixtures and a berthing mechanism.

Panels and frames are made of the Carbon Fiber Reinforced Plastics (CFRP), and joint parts are made of 7075 Aluminum alloy. Metal fasteners are used for their assembly.

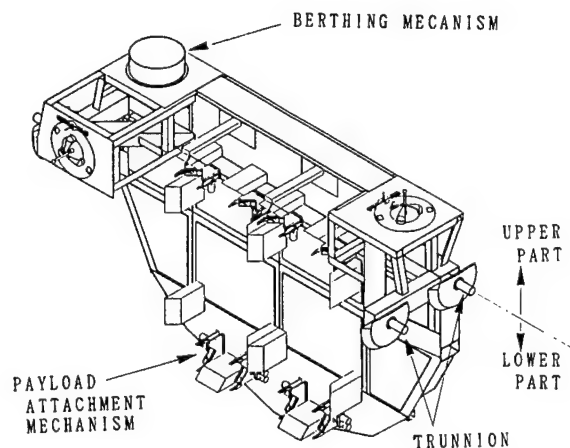


Fig.5 ELM-ES STRUCTURE

2.4 RMS Structure

RMS consists of a main arm, a small fine arm and a console. The Main arm is launched in a folded configuration attached at the aft endplate of the PM. It consists of a base mechanism, six joints, two booms and a Standard End Effector. The base mechanism uses a splined coupling to provide automatic alignment capability when replacing the arm on orbit. The joints have an inner and outer housing made of a titanium alloy in order to maintain the clearance between housings and bearings under thermal deformation.

The boom structure shown in Fig.6 consists of a CFRP tube with interface flanges made of aluminum alloy. Some internal rings made of CFRP are located in the tube to resist buckling by bending.

3. Development Plan

The JEM structural development plan consists of the development tests of components and full-scale structures, and the flight model acceptance tests, as well as analyses of dynamic load, stress and fracture.

3.1 Structural Components Development Test

The components development tests are conducted to obtain the structural elements characteristic data, design data, and to establish the work and assembly process as well as to qualify the major structural components.

Table 2 shows major structural components development activities and their purposes. These tests are being performed throughout the preliminary design to detail design phase and to finalize the component design and material selection.

3.2 Full Scale Testing

Structural testing of the full-scale structural model or engineering model which utilizes the flight equivalent structures will be conducted for each element. These include the static load and dynamic load tests. The purposes of the testing are (a) to verify the math model, (b) to measure the dynamic response, and (c) to qualify the structural strength.

Other dynamic environment exposure testing such as acoustics testing will be performed for those elements sensitive to the environment. The completion of this test activity will qualify the structural assembly.

For the flight structure, the proof tests will be conducted for the acceptance of fracture critical structures.

The major qualification tests planned for the PM structure are internal pressure of up to 2.0 times the maximum operating pressure, static loads, and modal tests.

A combined dynamic test of the JEM will not be done because of the complex configuration of JEM on the ground.

The verified math model for each element will be used to update each load analysis model and the synthesized overall JEM math model as well.

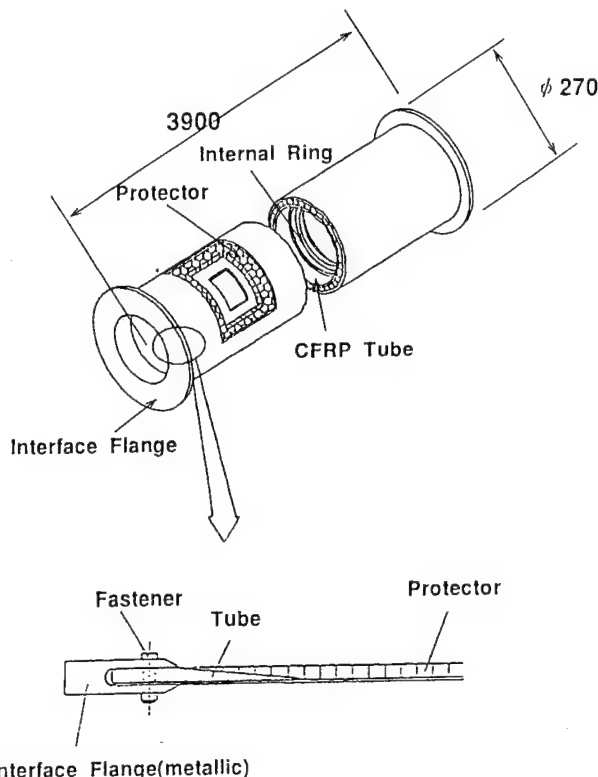


Fig.6 RMS BOOM STRUCTURE

Table.2 MAJOR STRUCTURAL COMPONENTS DEVELOPMENT

ELEMENT	DEVELOPMENT ACTIVITIES	PURPOSE
P.M	<ul style="list-style-type: none"> STRUCTURAL MATERIAL SELECTION METEOROID/DEBRI SHIELDING DEVELOPMENT BASED ON HYPER-VELOCITY IMPACT TEST MANUFACTURING TESTS 	<ul style="list-style-type: none"> EVALUATE TO SATISFY MAP REQUIREMENT OBTAIN DESIGN DATA ESTABLISH MANUFACTURING PROCESS ASSURE WELDING CAPABILITY
E.F	<ul style="list-style-type: none"> STRUCTURAL ELEMENT TESTS FOR PRIMARY STRUCTURE COMPONENT AND NTS SUPPORT STRUCTURE 	<ul style="list-style-type: none"> ASSURE STRESS ANALYSIS
ELM-ES	<ul style="list-style-type: none"> STRUCTURAL MATERIAL TEST STRUCTURAL COMPONENTS EVALUATION <ul style="list-style-type: none"> -JOINT -MAIN STRUCTURE BEAM -SUBASSEMBLY 	<ul style="list-style-type: none"> OBTAIN CHARACTERISTICS DATA OF CFRP TEST PIECES SUCH AS STRENGTH, STIFFNESS, FATIGUE, THERMAL EXPANSION, ETC. OBTAIN CHARACTERISTICS DATA OF ELM-ES STRUCTURAL COMPONENTS SUCH AS STRENGTH, FATIGUE, AND FAILURE TOLERANCE.
RMS	<ul style="list-style-type: none"> BOOM MATERIAL (CFRP) TEST BOOM COMPONENT TEST 	<ul style="list-style-type: none"> EVALUATE CFRP STRUCTURAL PROPERTIES BY TEST PIECES VERIFY SAFE LIFE OF BOOM JOINT BY FATIGUE TEST

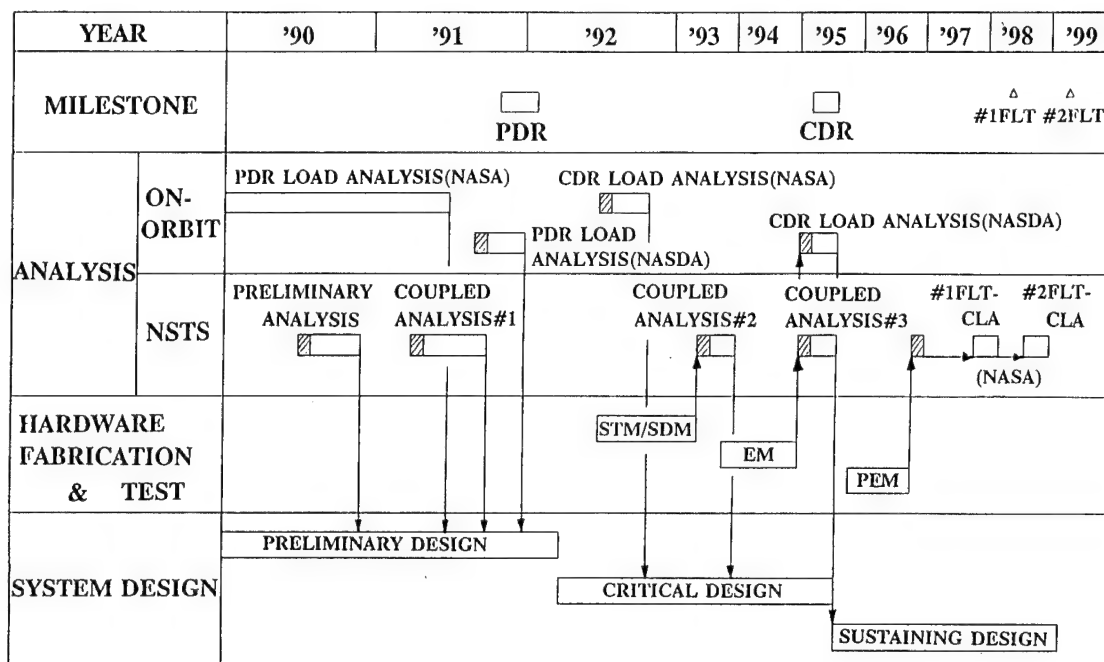


Fig.7 JEM LOAD ANALYSIS PLAN

 MODELING

3.3 Analyses

JEM is a combination of several elements, and those elements are launched by the Space Shuttle and assembled on-orbit. To define the critical operational loads, a large number of analyses are required for both Space Shuttle launch/landing and on-orbit configurations.

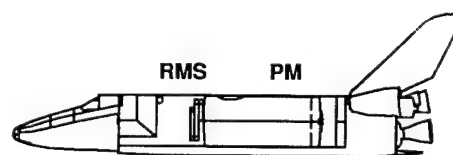
Fig.7 shows load analysis plans throughout the JEM development program synchronized with plans for design activities and hardware development.

The overall JEM on-orbit mathematical model is provided to NASA to be used for the overall space station on-orbit load analysis. This analysis will define the space station core to JEM interface loads and JEM major dynamic responses that is used for JEM on-orbit load definition.

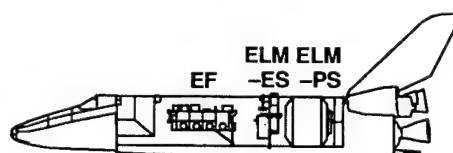
As JEM has overhanging structures, such as the RMS ARM and EF/ELM-ES, the micro-gravity environment is sensitive to external disturbances. Therefore, micro-gravity environment management and control are essential.

For defining the Space Shuttle launch loads, the current assembly flights are shown in Fig.8. Flight No.1 will contain the PM with attached RMS. Flight No.2 contains the EF, ELM-PS, and ELM-ES. As the ELM-PS and ES are used as carriers, to estimate the critical loads conditions, additional Space Shuttle combined analyses which consider launch and retrieval of these elements, manifested with other foreign cargos are required.

An example of the stress analysis by FEM (NASTRAN) is shown in Fig.9. This figure shows stress contour at the radial port of the PM under maximum operating pressure (1.05 kg/cm²).



JEM No.1 Flight



JEM No.2 Flight

Fig.8 JEM FLIGHT CONFIGURATIONS

4. Major Technical Challenges

Throughout the JEM development program, some technically challenging topics exist. Two of those topics are introduced below.

ANALYSIS LOAD: MAXIMUM OPERATING PRESSURE (MOP)
 LOAD = 1.0E+01
 TYPE OF ELEMENTS
 STRESS - MAX FROM MOP = 1.0E+01
 SHELL STRESS = 1.0E+01

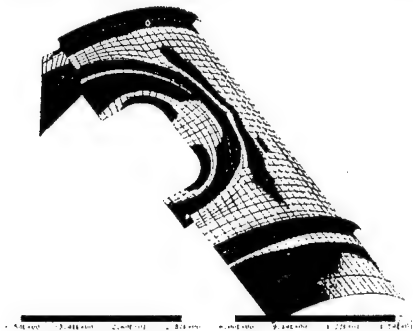


Fig.9 STRESS ANALYSIS EXAMPLE

4.1 Meteoroid/Debris Shield Development

NASDA has conducted several hypervelocity impact tests to observe the impact phenomena and to evaluate the shield design feasibility. (*2)

Debris with velocities from 2 to 16 km/s are considered to impact JEM with higher probability than meteoroids since the amount of debris has increased drastically in recent years.

The program design requirements require that the module structure protect the crew and system from meteoroids and debris.

NASDA utilizes a two-stage light gas gun, a shaped-charge launcher, and computational simulation as tools to implement the JEM shielding design.

Testing employing two-stage helium/hydrogen gas guns, capable of launching 1 gram weight aluminum up to 8km/s, have started for modeling hypervelocity impact phenomena and gathering data to define design parameters.

The current NASDA shield design approach employs a double-sheet metallic shield design which is considered to be more weight effective than a single-sheet.

The JEM shield will be designed based upon these test results, and considering the commonality with international partners to enhance the overall Space Station safety.

4.2 Fracture Control Implementation

As JEM is a long life manned system with an operational life time of 30 years, and carried by the Space Shuttle, assuring structural safety is essential.

On implementing the JEM structure fracture control program, the definition of environment, loads spectra history through complete mission life time, and obtaining mechanical and fracture properties of materials under all expected environments such as liftoff, ascent, on-orbit, and landing are key drivers.

The major fracture critical items are the welded metallic pressure shell of the PM, and the light weight composite/bonded structures of the ELM-ES and RMS. NASDA plans to gather mechanical and fracture property data of materials throughout the structural development phase to certify the safe life of the structure.

The other topics considered are the development of on-orbit inspection techniques, and estimating the safe life for the item to be retrieved after its service life, considering the material degradation and aging during on-orbit service.

5. Conclusion

This paper reviewed the whole spectrum of JEM structural development activities. The JEM program is very complex from the point of view of management and integration because five (5) different elements are involved, and due to the in-depth interfaces among JEM elements, NASA space station core and the Space Shuttle.

The structural development activities are quite varied ranging from manned system pressure shell design to development of light weight retrievable structures.

NASDA will manage and integrate the JEM stressing the product safety assurance.

6. Acknowledgements

The authors are indebted to Y.Tanoue of Mitsubishi Heavy Industries, LTD., Y.Hanada of Kawasaki Heavy Industries, LTD., A.Kitamura of Ishikawajima-Harima Heavy Industries Co.,Ltd., T.Konishi of Nissan Motor Co.,LTD., S.Motohashi of TOSHIBA Corporation, and M.Murakami of NASDA for preparation of the material.

7. References

(*1) Kazuo Matsumoto, Kuniaki Shiraki, et al 1990, Development of Japanese Experiment Module (JEM), 41st Congress of the International astronomical federation, Dresden, GDR, IAF-90-068

(*2) K.Shiraki, H.Hashimoto and K.Tasaki 1990, Shielding Considerations for the Japanese Experiment Module, AIAA/NASA/DOD orbital Debris Conference: Technical Issues and Future Directions, Baltimore, Maryland, U.S.A., AIAA-90-1335

N 92-23782

52-18
84297

THE COLUMBUS FREE FLYING LABORATORY
- MECHANICAL DESIGN ASPECTS -

Joachim Gülpén*

ERNO Raumfahrttechnik GmbH, Bremen (Germany)

Abstract

The COLUMBUS Free Flyer has a 30 year mission in low earth orbit with the primary objective to provide microgravity laboratory capabilities. The paper explains the particular mechanical requirements resulting from this mission, presents the relevant design features and outlines the verification approach envisaged in the development programme which shall lead to a launch of the laboratory in 2001.

1. Introduction

The objective of the COLUMBUS Free Flyer, which is presently being developed for the European Space Agency (ESA), is to serve as a permanent, man-tended laboratory in space: permanent has to be interpreted as continuously available for a life time of 30 years, based on a combination of design for the entire life time, and of repair and exchange of life limited items. Man-tended signifies that men have access to the facility in a shirt sleeve environment to inspect, install, retrieve payloads and to service and maintain the facility. The laboratory offers a set of resources and services to experimenters for research in various scientific fields centered around one of the outstanding environmental conditions offered by earth orbiting spacecraft, microgravity.

This objective results in a number of rather specific requirements in the mechanical design area, which are subject of the present paper.

2. Mission Description

A space laboratory for 30 years lifetime requires access not only for the users who wish to install and retrieve their experiments but also for regular servicing. The optimization of a mission scenario for this long period is a complex process which is driven to a large extent by the capabilities of the servicing vehicles.

Whereas it has been decided early in the programme that the Free Flyer shall be launched by Ariane 5 and shall draw support from HERMES and the Space Shuttle/Space Station Freedom (NSTS/SSF), key parameters such as:

Launcher performance
HERMES cargo capability versus orbit altitude
SSF orbit parameters
Propellant consumption
Life limited items
Solar activity variations
Microgravity requirements

have to be analyzed to find the optimum mission strategy.

The corner stones of this strategy have been determined in the past phases of the COLUMBUS program and are today:

- o A Free Flyer consisting of a Pressurized Module (PM) as permanent laboratory and a Resource Module (RM) which will be replaced after consumables have been used up.
- o Launch by Ariane 5
- o Servicing of the Pressurized Module by HERMES in one-year intervals
- o Exchange of the RM supported by NSTS every 5 years.

The life cycle (Fig. 1) starts by an Ariane 5 launch of the complete Free Flyer into a 28.5 degree inclined circular orbit of 470 km altitude, which offers the maximum payload mass taking into account the Ariane 5 capability and the Free Flyer propellant consumption. These mission characteristics generate two mechanical design cases:

- o The launch loads on a 17.8 ton spacecraft of 12.5 m length and 4.4 m diameter composed of two separable modules
- o The meteoroid and debris loads characteristic for this low earth orbit.

Whereas the first one is a classical case, though specific due to the combined effects of the parallel development of spacecraft and launcher and of the large dimensions of the spacecraft, the debris environment poses a number of problems to a man-tended long life spacecraft, which are new at least by European scales and represent very important design drivers.

Fig. 2 shows that the debris flux generated by past space activities is significantly higher than the natural meteoroid flux for particle sizes above a

*Dipl.-Ing., COLUMBUS Free Flyer Programme Manager

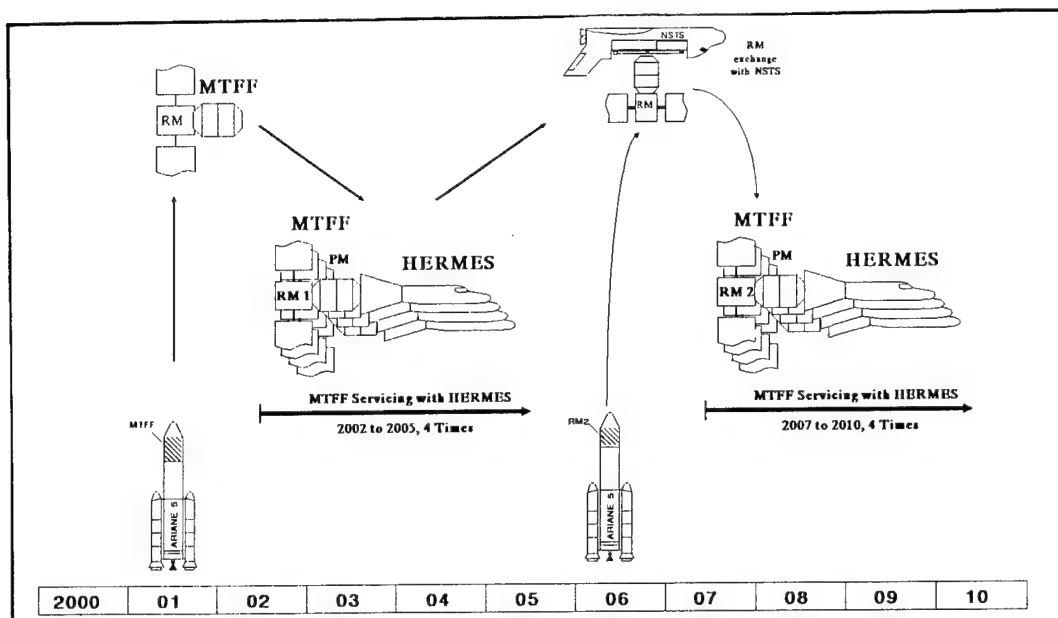


Fig. 1: Free Flyer Mission Scenario

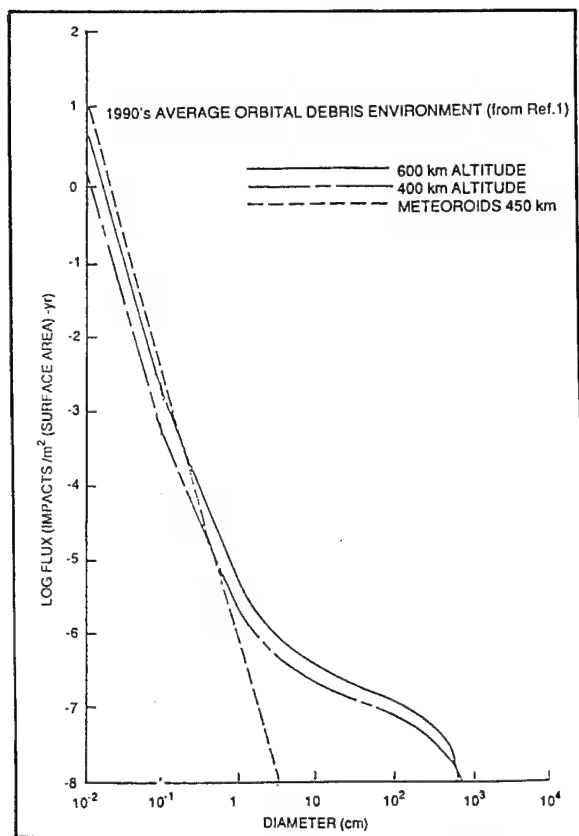


Fig. 2: Meteoroid and Debris Flux Distributions

few millimeter diameter. A set of requirements have been imposed on the Free Flyer (Fig. 3) which shall ensure survival in this environment.

They induce design requirements for inspection and repair of structures in orbit and for leakage and leak detection.

PROBABILITY	FAILURE CASE	INTERPRETATION
> 0.995	NO DANGER TO CREW SURVIVAL FOR INITIAL 10 YEARS IN ORBIT	- APPLIES TO MAN-TENDED PERIODS - CREW TO BE ABLE TO LEAVE MODULE PRIOR TO DEPRESSURIZATION
> 0.995	NO DANGER TO MODULE SURVIVABILITY FOR INITIAL 10 YEARS IN ORBIT	- PM TO SURVIVE UNTIL NEXT SERVICING VISIT - PM TO BE REPAIRABLE TO RESTORE NOMINAL OPERATION
> 0.995	NO PM LEAK OVER A ONE-YEAR PERIOD	- LIMITS FAILURES DUE TO NON-PENETRATING DAMAGE AND SUBSEQUENT CRACK GROWTH BETWEEN INSPECTION PERIODS
> 0.995	NO PENETRATION NOR BURST OF A PRESSURE VESSEL OR SEALED CONTAINERS (EXCEPT E.G. PM) DURING ONE YEAR	- LIMITS RISK FOR LOSS OF MISSION DUE TO PROPELLANT LEAK
> 0.995	NO MAJOR DEGRADATION OF FUNCTIONAL EQUIPMENT OVER A PERIOD OF ONE YEAR	

Figure 3: Meteoroid and Debris Protection Requirements

Microgravity is one of the important laboratory conditions offered by the Free Flyer. Its imperfections are caused by the natural environmental conditions, in particular the residual air drag, the effect of the earth gravity gradient field within the laboratory, the compensation of disturbance torques (air drag, gravity gradient, and other induced torques) by control torques (Magnetic Torquers, Reaction Wheels) and on the other hand by self-induced disturbances due to moving masses and noise generated in the laboratory. These disturbances have to be kept below the levels indicated in Fig. 4.

Whereas the control and limitation of the natural and low frequency microgravity disturbances is a task of the configuration design and the attitude control subsystem, the limitation of disturbances from on-board equipment like reaction wheels, pumps, valves fans etc. and the reduction of disturbance vibrations transmission from these sources to the sensitive payloads is a mechanical design task.

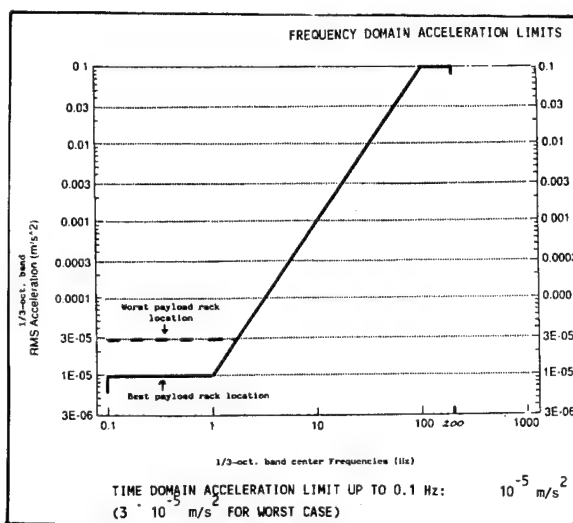


Fig. 4: Microgravity Environment Requirements

The servicing scenario contains two main elements: The European space plane HERMES will execute once every year a docking manoeuvre at the access port of the pressurized module and the NSTS will berth the Free Flyer in 5 years intervals by its manipulator arm to a fixation mechanism in order to then detach the old RM and replace it by a new one, using the manipulator arm. These manoeuvres represent yet another set of mechanical load cases: the repeated actuation of mechanisms and the docking/berthing and latching shocks. In addition the scenario requires the RM to be designed for two launch situations: as part of the Free Flyer and for an individual launch, in the latter case with much higher propellant masses.

In summary: In contrast to a standard satellite which has to be dimensioned mainly against the launch loads, the Free Flyer design is driven by a combination of

- Launch
- On-orbit manipulation
- Meteoroid and debris protection
- Microgravity disturbance suppression

requirements, which result in a significantly more intricate process of optimization towards the final mechanical objective of minimum mass.

3. Concept Description

The Free Flyer is composed out of two modules (Fig. 5) with rather different and specific functions: the shirt sleeve environment laboratory (PM) and the module which provides basic resources to the laboratory (RM). The module characteristics are

PM

- * Permanent (30 years) operation in space
- * Basic structure and equipment designed for 30 years life
- * Holds all life limited items (as far as admissible in a manned environment)
- * All internal equipment serviceable by HERMES
- * No external ORUs, i.e. no nominal external servicing.

RM

- * Supplies energy, heat rejection, communication links to the laboratory
- * Controls orbital attitude of the composite
- * Designed for replacement after 5 years lifetime
- * Holds all safety-critical equipment
- * No ORUs.

Seen from a mechanical point of view, the PM is a pressure vessel composed of a cylindrical shell and end cones which taper to a flange interfacing with

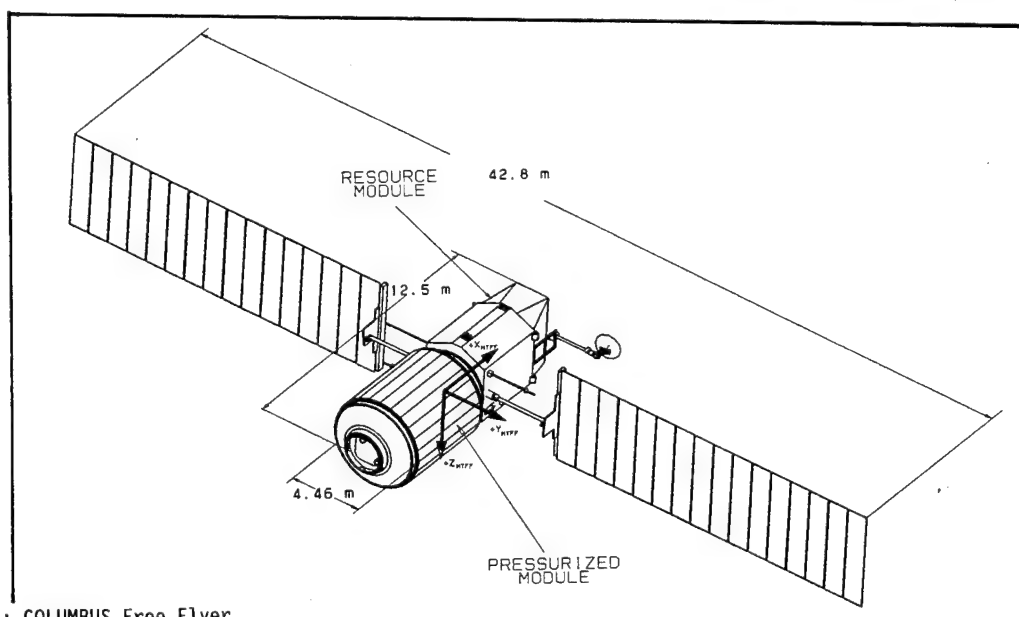


Fig. 5: COLUMBUS Free Flyer

the Docking/Berthing Mechanism and bulkhead respectively. The diameter of approx. 4.4 m is determined by similarity to the Attached Laboratory, i.e. by the NSTS interface. Fig. 6 shows the welded construction consisting of 3.2 mm thick waffle-reinforced cylinders, rings and cones in 2219 Al alloy. Bolted flanges with double seals, the inner one being maintainable, are used for 6 feedthrough plates and the DBM/bulkhead interface in the cone areas. This structure is dimensioned mainly by micrometeoroid and debris loads, leakage rate, eigenfrequency requirements, and load-carrying performance against buckling failure of the fully equipped Free Flyer in launch configuration.

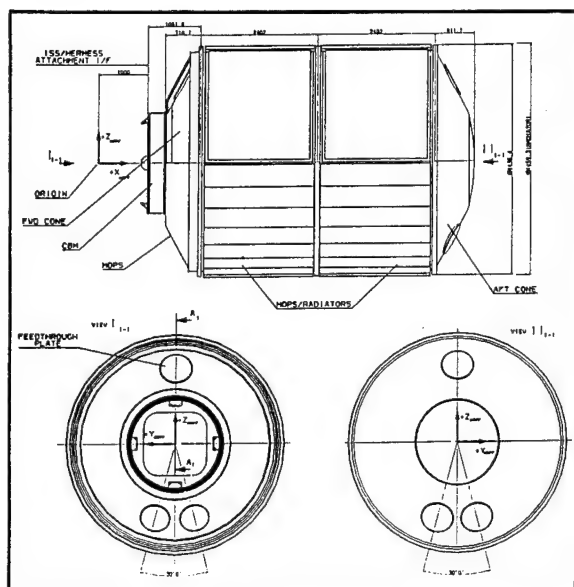


Fig. 6: Shell Assembly

The design of the internal (secondary) structure is driven by the requirement to accommodate exchangeable individual experiments and equipment as well as complete experiment racks. Stand-offs provide the load paths from the rack to the primary structure and house the utility distribution to the standardized racks which are mounted to form the four walls of the crew cabin (Fig. 7), the "floor" panels providing a vertical reference for the crew. All racks are hinged and can be tilted to provide access to their rear as well as to the shell for inspection.

The connection to the servicing vehicles is made by a docking/berthing mechanism (Fig. 8) which has to generate a leak tight interface against the space vacuum even after 30 operations over 30 years lifetime. For reliability reasons the active part of this mechanism is mounted on the servicing vehicle to allow maintenance and verification prior to use.

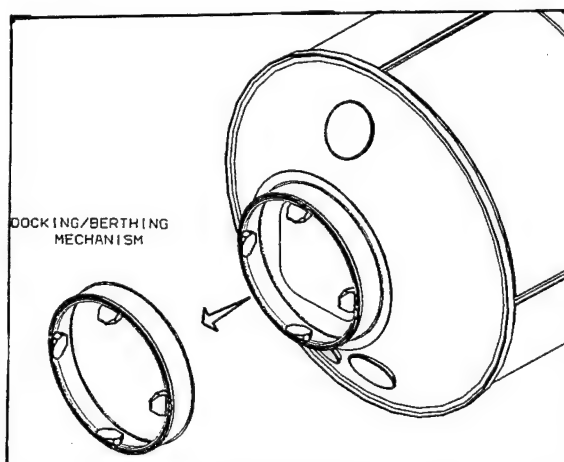


Fig. 8: Docking and Berthing Mechanism

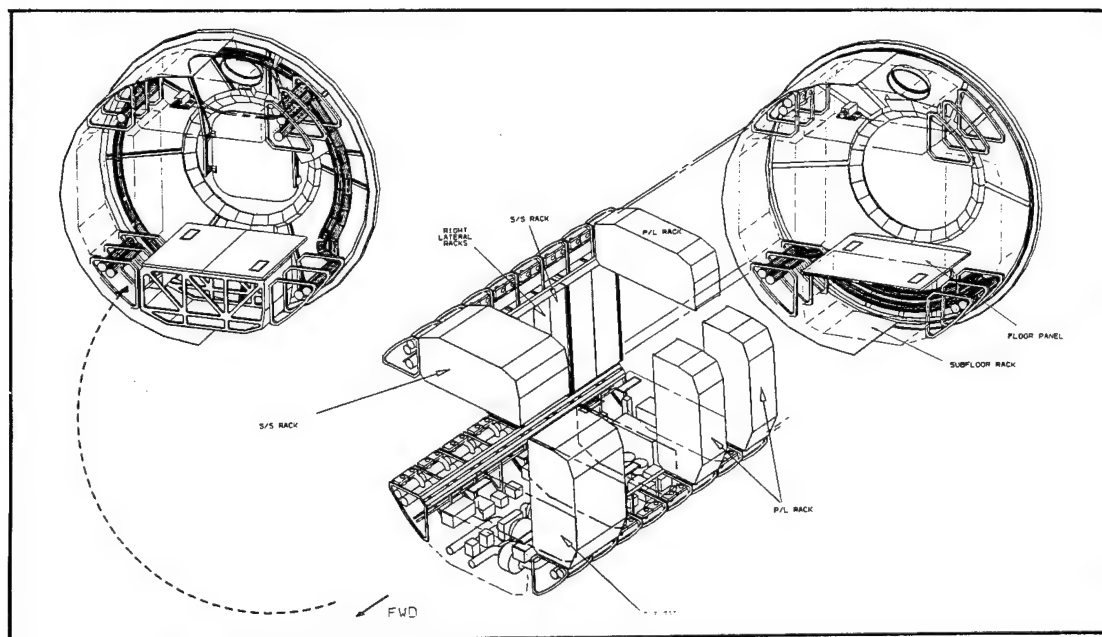


Fig. 7: PM Internal Layout

Meteoroid and debris protection is a very important and interesting mass optimization problem. By a clever geometrical configuration, by using assemblies whose primary purpose is a different one and by taking into account the failure mechanisms caused by MD impact one has to minimize the mass which is installed for the sole purpose of protection of sensitive items against MD. Generally, meteoroid and debris protection (MDP) is provided by a combination of protections shields and structure wall thickness (see Ref. 2 for details). A specific protection shield has to be built only for the forward cone. The cylindrical section is protected by thermal radiators, the facesheets of which are dimensioned for MDP and the aft cone is covered by the appropriately dimensioned RM/PM connection structure.

The RM is a non-pressurized element and has a classical satellite-type structure (Fig. 9) with a load carrying central tube, sandwich platforms and radiator walls which carry the equipment. A special combination of tasks is assigned to the RM/PM connection which has to carry the launch loads and must permit removal and berthing in orbit as well as transfer of utilities. This task is solved (Fig. 10) by:

- * A marman clamp connection for launch
- * 4 latches and 2 guidance stubs to provide the on-orbit structural connection, separable by the NSTS manipulator
- * 2 utility connector mechanisms to transfer power, N_2 , Freon and water.

As in the case of PM, the RM structure has to provide MDP to the equipment by an adequate configuration and wall thickness. For this reason, the propellant tanks which represent a "loss of

mission" single point failure in case of leak are located inside the central tube behind several structural protection layers.

A synopsis of all Free Flyer subsystem is given in Fig. 11. As this paper is oriented towards mechanical aspects, a description of these subsystems is beyond its scope (refer to [3]). As far as microgravity disturbance is concerned, however, most of these subsystems have to be critically reviewed because disturbances shall be reduced at the source, e.g. by higher balancing of reaction wheels, fans, or lower rotational speed, and by a reduction of the transmissibility from the source to the sensitive microgravity payload via source damping, e.g. anti-vibration mounts.

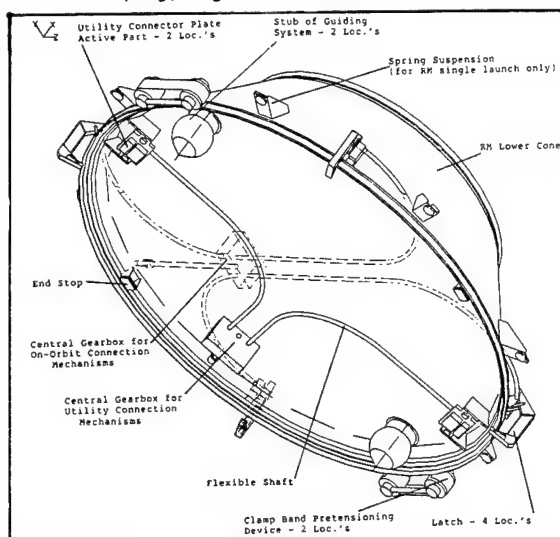


Fig. 10: RM/PM Berthing Mechanism

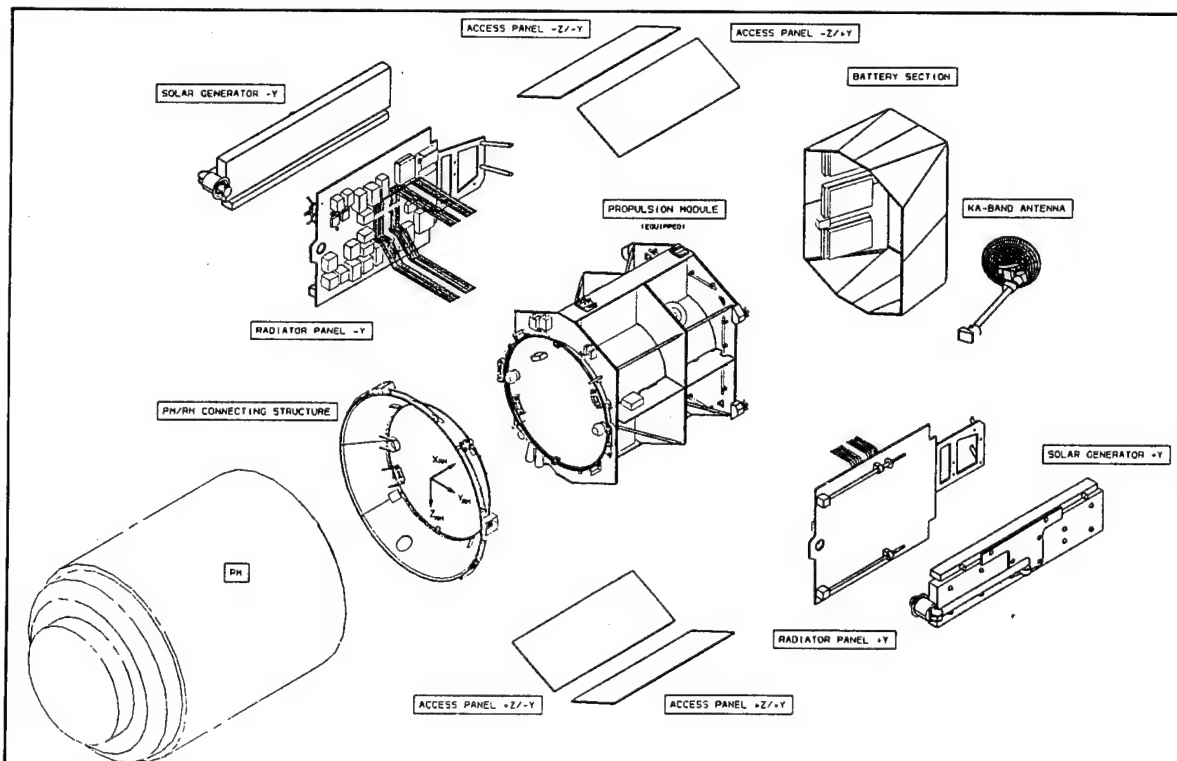


Fig. 9: RM Structure (exploded view)

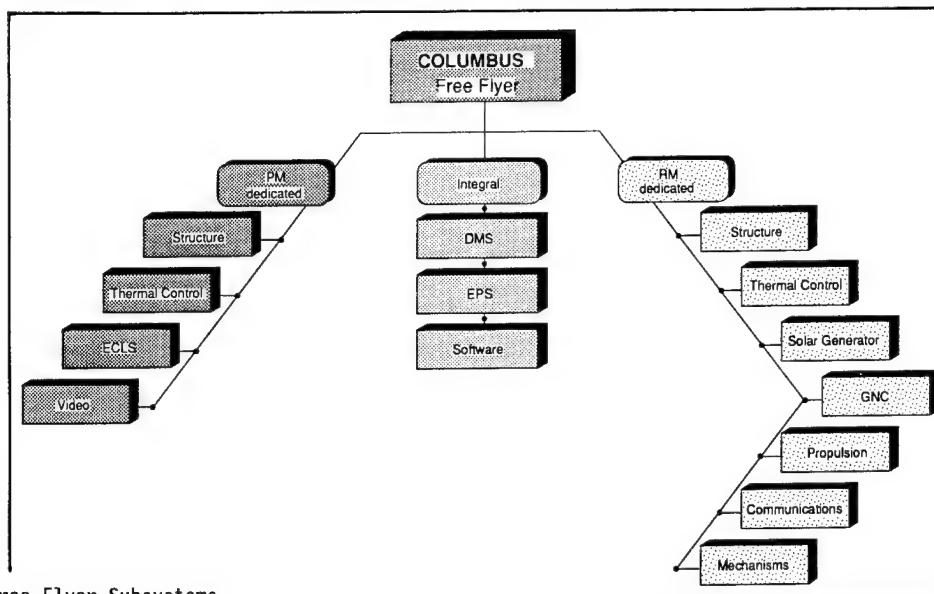


Fig. 11: Free Flyer Subsystems

Fig. 12 and Fig. 13 give an impression of the complexity of the task to determine the microgravity levels to be expected at the payloads and underlines the need for a strict microgravity control plan to be applied throughout the development program and at all levels from equipment up to system level.

the desires

to provide analytical proof prior to fabrication
to provide test evidence prior to launch
to avoid overtesting

the constraints of

budget
availability of facilities
limitations of facilities
limitations of analytical tools
schedule.

4. Verification Approach

The verification of requirements is always a compromise between partly conflicting constraints and desires:

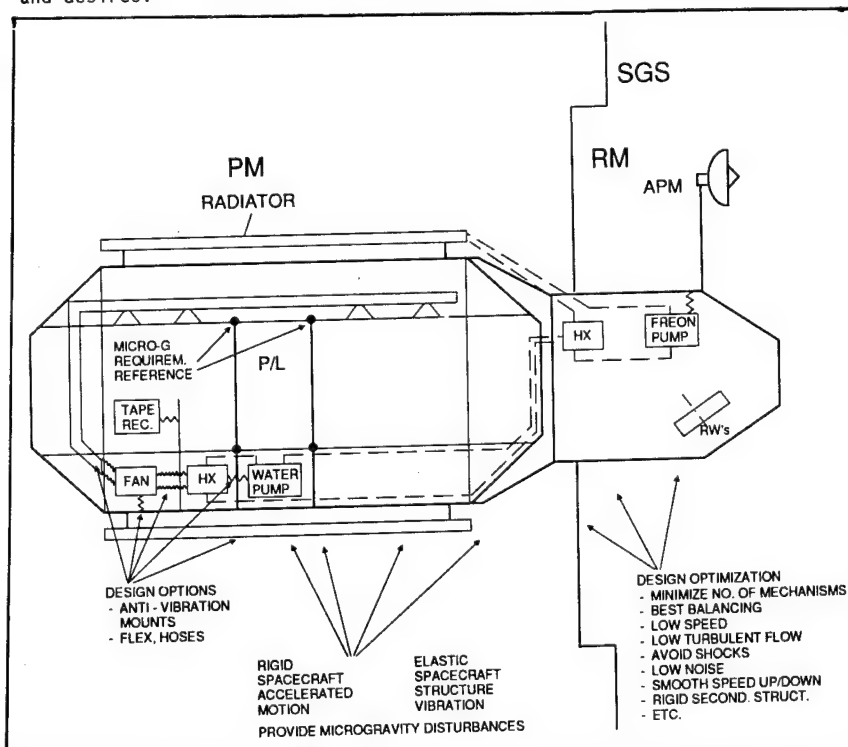


Fig. 12: Microgravity Environment, Subsystem/Equipment-Induced Disturbances

For each of the design drivers - launch loads, on-orbit manipulation, meteoroid and debris impact, microgravity disturbance - a specific verification approach has been elaborated.

As far as verification of the Free Flyer for launch requirements is concerned it is evident from the size and complexity of the end item that the routine structural test sequence-static load, sine vibration, and acoustic/random test on various models - is neither technically adequate nor programmatically feasible (budget and schedule constraints). Therefore, an incremental verification approach shown in Fig. 14 has been selected which is based on test and analytical verification.

Workmanship acceptance of the flight models will be performed by a proof pressure and leakage test of the pressurized module shell, by functional test of mechanisms and by inspection of all other structural assemblies.

S/S	EQUIPMENT	EFFECT
STRUCTURES	BOLTED JOINTS SHELL/ENDCONE RACKS, FLOORS	STICK/SKIP NOISE BY THERMAL STRESSES
DMS	HIGH-RATE DATA RECORDER WINCHESTER DISC (MM)	CR, MV CR, MV
Video	VIDEO RECORDER VIDEO MONITOR VIDEO CAMERA HIGH RESOLUTION PRINTER	CR, MV CR, MV CR, MV CR, MV
GNC	REACTION WHEELS GYROS	MV MV
KBS	ANTENNA POINTING MECH.	HV
OLS	ANTENNA TRANSFER SWITCH	MV
EPS	DC/DC CONVERTER DC/AC INVERTER MODULE LIGHTING UNIT BATTERY CHARGER PORTABLE LIGHT	MV MV MV MV MV
ECLS	FANS HEAT EXCHANGERS VALVES FILTERS DC/DC CONVERTERS DUCTS INLET MUFFLER DIFFUSORS	AD, CR, MV AD, CR, MV, FD AD, MV AD, CR, MV, LCA AD, CR, MV AD, CR, MV, LCA AD, CR, MV, LCA AD, CR, MV, LCA
TCS	PUMPS VALVES HEAT EXCHANGER PIPING RADIATORS COLD PLATES	CR, MV, FD CR, MV, FD CR, MV, FD MV, FC MV, FD, STICK/SKIP CR, MV, FD

Legend:
AD Aerodynamic
CR Casing Radiation Noise
FD Fluid Dynamic
LCA Leakage of Conducted Acoustics
MV Mechanical Vibration

Fig. 13: Mechanical Microgravity Disturbance Sources

The forces and shocks associated with the docking/berthing events on-orbit are generally encompassed by the launch loads. The immediately participating components and equipment, however, have to be verified for the repeated loading over the 30 years

life as well as for the design capability to capture and release the PM under worst-case dynamic misalignment conditions (see Fig. 15). Further dimensioning loads may result from these events for the solar generator and antenna booms, which have to sustain the shocks in deployed configuration.

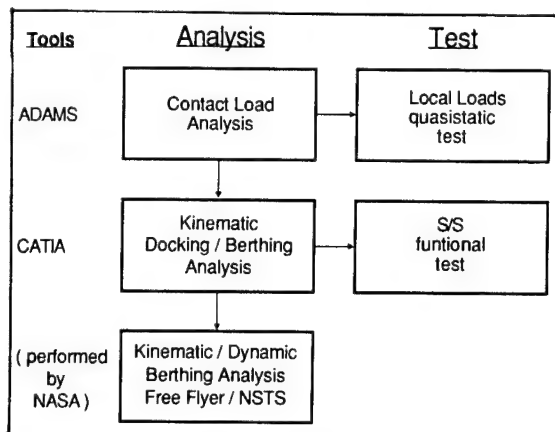


Fig. 15: Docking/Berthing Mechanical Verification

For these cases acceleration force spectra will be obtained through analysis of multibody dynamics and strength will be verified by quasi-static tests.

The protection against meteoroid and debris has to be verified for different damage modes (Fig. 16):

- o Sudden failure, in particular burst or leak of pressure vessels and destruction of electronics
- o Effect of impacts on material properties of pressure vessels, in particular with regard to fracture control
- o Effects of impact shock on electronics.

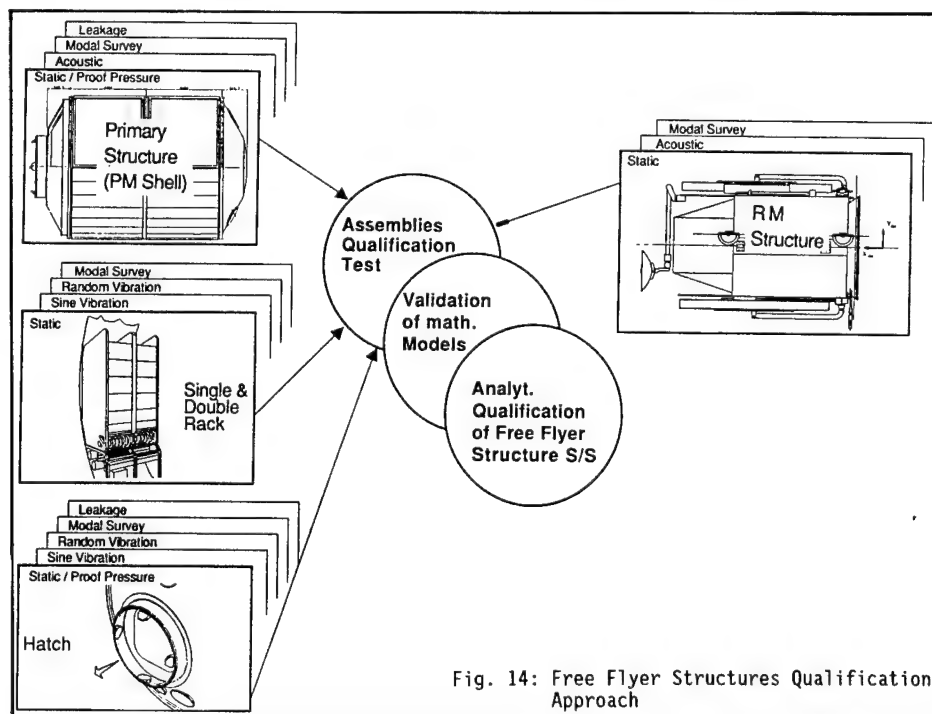


Fig. 14: Free Flyer Structures Qualification Approach

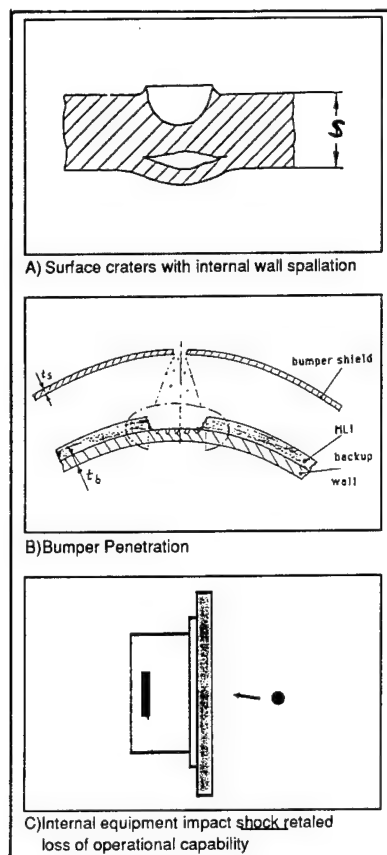


Fig. 16: MD Damage Modes

It is well known that the physical phenomena during hypervelocity impacts are very complex. The available results from theoretical investigations and tests are not sufficient to predict the shielding efficiency of all possible design configurations or to define in detail the damage results from different impacting particle/velocity combinations.

The dimensioning of MDPS will be based on semi-empirical damage laws found in the literature. They will be verified by tests performed on samples of actual Free Flyer hardware at various speeds and projectile sizes within the limits of available test facilities, i.e. up to 8 km/s (Fig. 17). At higher speeds, hydrocode analyses will be performed for selected cases. Fig. 18 outlines the logic of combination of tests and analytical methods for the MDPS verification.

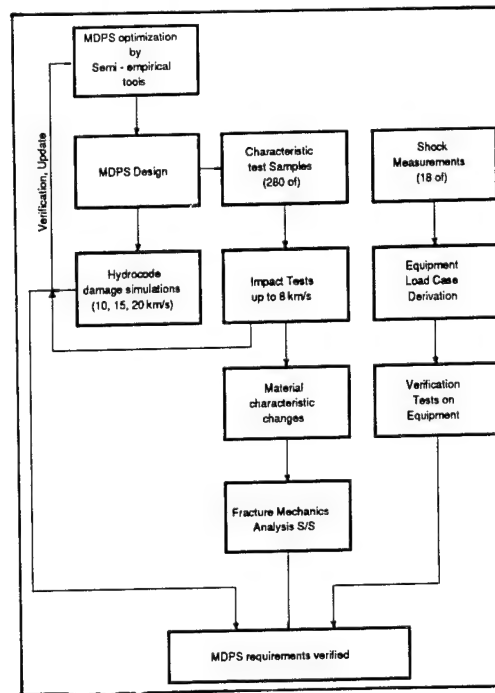


Fig. 18: MDPS Verification Logic

As microgravity disturbance is mainly a self produced effect, a "microgravity control plan" has been implemented, which shall ensure that

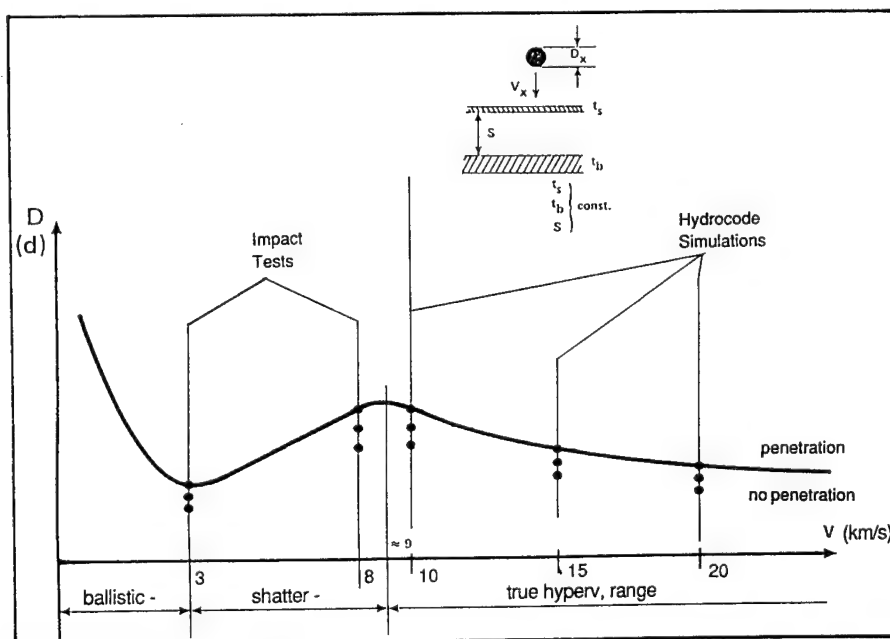


Fig. 17: Verification of MD Damage Laws

- o Designs at the lowest possible level avoid sources of disturbance
- o Disturbance sources are recognized early and protection measures are initiated (design alternatives, source damping, remote location) are implemented.

Fig. 19 outlines the verification logic which systematically encompasses all equipment and subsystems which participate in the generation and transmission of disturbances. Fig. 20 displays the test/analysis methodology.

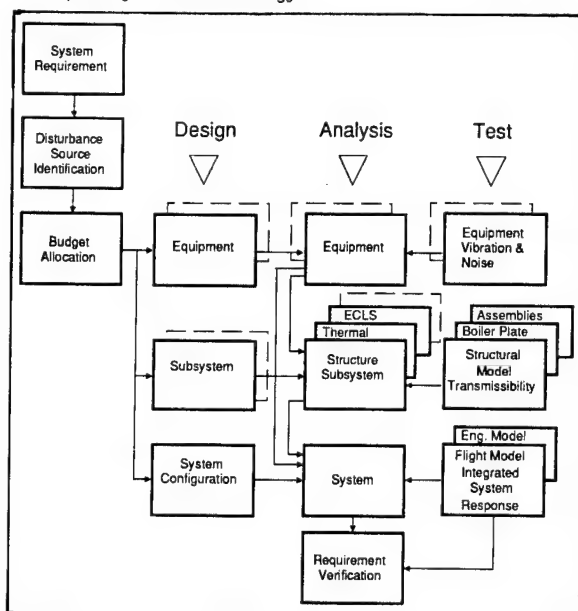


Fig. 19: Microgravity Environment Control Approach

5. Conclusion

The COLUMBUS Free Flyer as a permanent space laboratory has to sustain a variety of mechanical load cases over and above the usually predominant launch loads. Due to its size and complexity the verification of most of these requirements cannot be performed in representative tests at system level. Therefore, a verification approach has been conceived, which uses incremental test and analysis results to arrive at a conclusive analytical verification of the system performance.

Glossary

DBM	Docking & Berthing Mechanism
MD	Meteoroid & Debris
MDP	Meteoroid & Debris Protection
MDPS	Meteoroid & Debris Protection Shield
NSTS	National Space Transport System
ORU	Orbital Replaceable Unit
PM	Pressurized Module
RM	Resource Module
SSF	Space Station Freedom

References

- [1] Space Station Programme - Natural Environment Definition for Design, NASA, JSC 30425, 15.01.87, Sect. 3, Appendix "A".
- [2] H. Reimerdes: Protection of Spacecraft Against Meteoroid/Orbital Debris Impacts; International Conference on Spacecraft Structures and Mechanical Testing, ESTEC, Noordwijk, April 1991
- [3] J. Gülpén: COLUMBUS Free Flyer, Paper 44, Space Course 91, RWTH Technical University Aachen, March 1991.

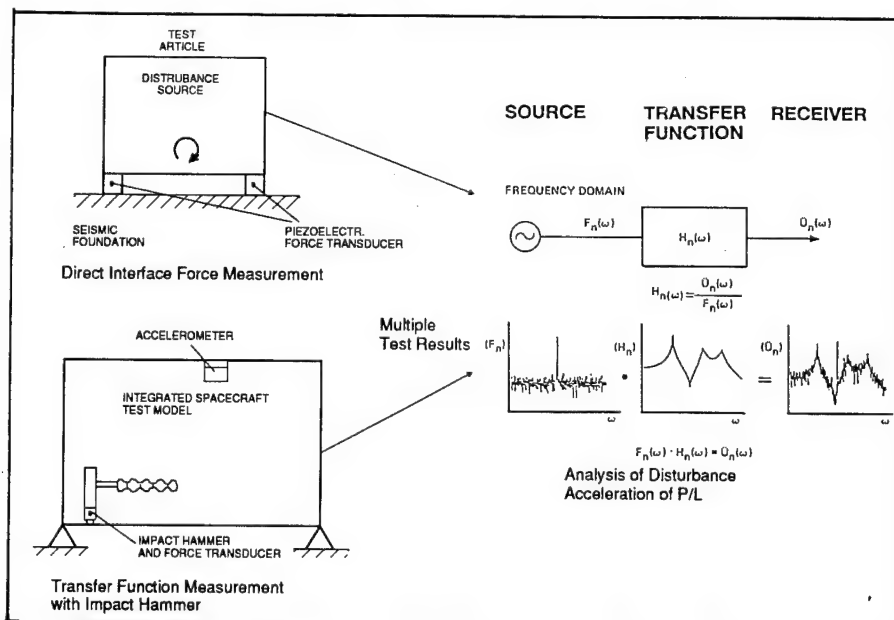


Fig. 20: Dynamic Disturbance Prediction Methodology

N92-23783

84695

STRUCTURAL ASSESSMENT OF THE SPACE STATION
FREEDOM PRESSURIZED ELEMENTS

R. L. Grant
Vice President, Space Station Freedom Program
Boeing Defense and Space Group
Aerospace & Electronics Division
Huntsville, Alabama

ABSTRACT

The design of the Space Station Freedom (SSF) pressurized element structure and the requirements that affect the structure and its associated mechanisms are unique and particularized to the unique set of load and functional environments. This paper describes the procedures used to develop the most significant structural requirements and presents typical results as they are known at the end of the preliminary design phase. Loads, acoustics, thermal environments, and the meteorite/orbital debris environments are discussed. A section of the paper discusses the materials chosen for SSF, as well as the rationale.

Finally, this paper describes the verification job. Detailed stress analyses, backed up with development tests, are used to ensure that the SSF pressurized element structure meets all imposed requirements. When the final design is complete, special flight-quality hardware is built and tested to prove that the hardware is qualified for flight. The structural qualification program planned for SSF is briefly described.

1. INTRODUCTION

An essential part of the SSF structure is the group of pressurized elements consisting of the U.S. Laboratory, the Habitation module, or living quarters, and the connecting resource nodes as shown in Figure 1. Boeing Defense and Space Group, Huntsville Division, under contract to Marshall Space Flight Center (MSFC) is responsible for the design and verification of the pressurized element structure, as well as the design, verification, and integration of all hardware and software into the U.S. Lab and Hab, and their integration into launch and on-orbit assembly sequences.

During the writing of this paper, the details of the pressurized element design are being reviewed with the intent of reducing the number of flights and the cost to assemble the full SSF on orbit. Although the details of the pressurized elements are changing (such as element length) the basic components (ring frames, trunnions, hatches, berthing mechanisms), as well as their requirements, are not expected to change. Therefore, the requirements processes and the typical results presented here are expected to apply to the configuration that results from these studies.

This paper concentrates on the task of ensuring that the structure of the pressurized elements will meet the requirements of the program and provide a habitat enclosure for up to 30 years.

© Copyright 1991, The Boeing Company, All Rights Reserved.

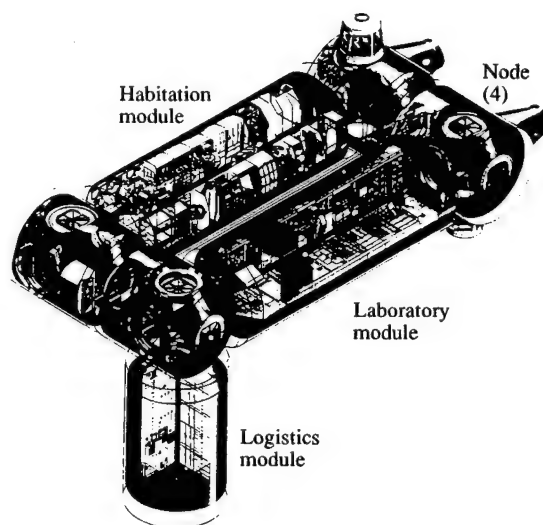


Figure 1. SSF pressurized elements

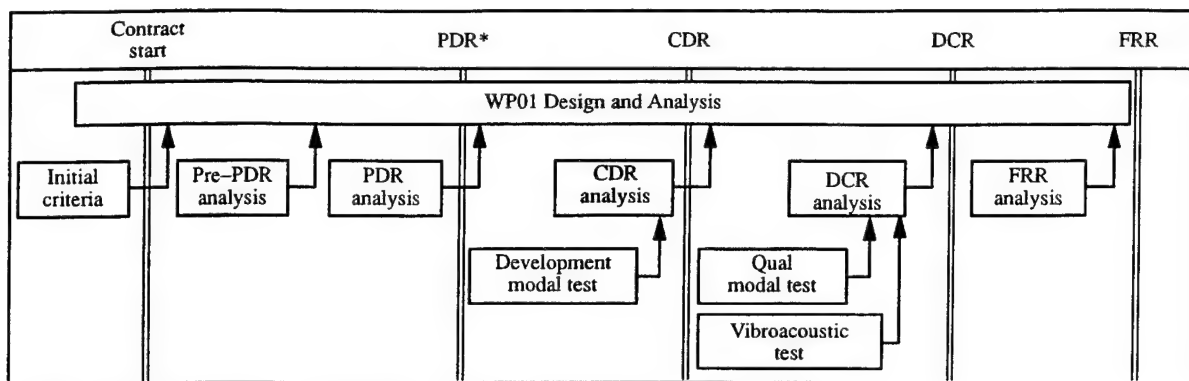
2. BASIC REQUIREMENTS

Before structural strength assessments, the applied environments must be converted to structural design criteria. Design criteria are derived that will envelop all events in the service life of the pressurized elements.

Figure 2 shows the loads development plan for the elements. The pre-preliminary design review (PDR) analysis derived some first-cut loads to help with initial sizing. The PDR analysis established the element design loads, while the critical design review (CDR) and design certification review (DCR) analyses will update these loads only if they are higher than the PDR results. The flight readiness review (FRR) analysis is the final analysis, performed by NASA National Space Transportation System (NSTS) engineers. Each design cycle uses the latest available models, test data, and forcing functions.

These events include pre- and postflight ground handling and transportation, Shuttle lift-off and ascent, on-orbit activities such as seen during space station assembly and operations, and Orbiter descent and landing. Combinations of these loads are considered as well.

Of all the events, the highest loads for the majority of structure are



* PDR analysis will establish the design loads. All other cycles will revise the loads if required

Figure 2. Loads development plan

Shuttle lift-off and Orbiter landing. These loads are derived from transient dynamic analyses using NASA-provided Shuttle and Orbiter dynamic math models and forcing functions. Figure 3 shows how the pressurized element models are combined with the Shuttle models for this analysis. Structural loads are derived from the model dynamic responses.

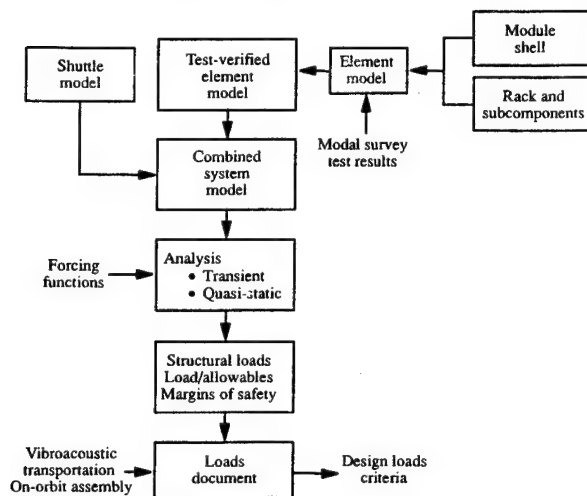


Figure 3. NSTS transient analysis

Figure 4 shows some typical loads results for the U.S. Laboratory lift-off analysis. The shear and moment data are used for cylinder skin design. Shuttle-to-element interface loads are used for element design and to compare with Shuttle allowable data. Load factors are derived for rack and other component design criteria.

On-orbit loads analyses, as in NSTS loads analyses, are based on space station response to time history forcing functions. The space station models are synthesized from element models provided by each partner. Forcing function time histories are derived from various sources and applied to the space station from which pertinent loads are backed out. Some of the on-orbit forcing functions are Orbiter docking, pressurized element berthing, EVA events, and Orbiter thruster plume impingement. Another forcing function being considered is Orbiter berthing. Figure 5 shows an alternative Orbiter berthing system and associated peak berthing impact forces.

Because the loads are dependent on the structural dynamic response to external forces, and these responses are calculated using math models, the math models of the pressurized elements must be test verified. This is done by performing fixed-base modal

surveys for NSTS flight events and free-free modal surveys for space station on-orbit events.

A second induced criterion affecting structure is the temperature variations caused by the natural thermal environment. As an example of the structural thermal analyses that are performed in accomplishing the overall structural development activity, thermal consideration of the common berthing mechanism is presented. The example is pertinent because the berthing mechanism section of the pressurized module will be the least protected during the berthing sequence.

Preliminary hot and cold temperature time history induced environments for the berthing mechanism alignment guide and associated structure were calculated using the steps provided pictorially by Figure 6. The analyses progressed from orbital natural thermal environment definition, to hardware material and optical property determination, to thermal analyses using available transient heat transfer programs, to component induced temperature environment definition, and finally to the berthing component functional and thermal tests in the Thermal Vacuum Test Facility.

Several orbital cases were studied. The element was assumed to be orbiting directly in line with the Sun ($\beta = 0$) and the element was oriented in each of three mutually perpendicular axes, one of them being with the berthing mechanism facing directly at the Sun. This gave temperature variations resulting in the hottest structure. The other cases studied included the element (in three separate axes) orbiting at a β angle of 52 deg, the largest β angle that SSF will see. This case, with the berthing mechanism facing space, provided the coldest structural temperatures.

The element initial temperature was assumed to be 70 deg, when it was separated from the Shuttle cargo bay. The debris shield and MLI surrounding the berthing ring were assumed to be removed. Results were calculated for a 6-hour orbital flight time following this initial orbital insertion time. Radiative heat transfer was simulated from the internal element mass to the element pressure shell with an emissivity = 0.8 for both surfaces. Analytical predicted hot and cold temperatures are provided for the alignment guides by Figures 7 and 8, respectively.

The berthing mechanism alignment guide calculated orbital cyclic temperature variation was used as an induced thermal environment definition to simulate during the berthing mechanism development test. Thermal analysis is required before the development test to ensure that the flight environments are simulated during the test. The data obtained from the development test will be used to verify the thermal flight hardware math model.

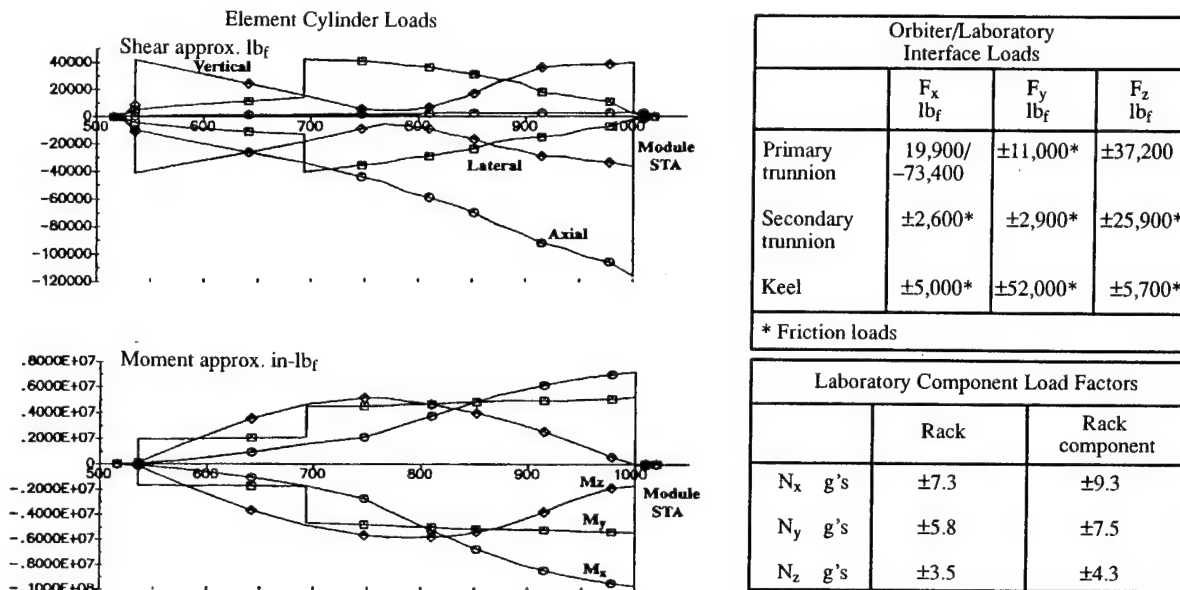


Figure 4. U.S. Laboratory typical transient lift-off loads

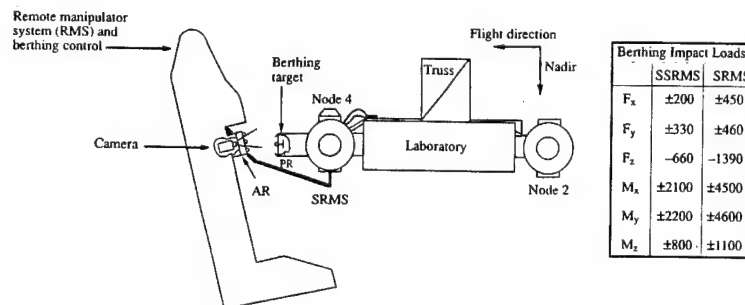


Figure 5. Alternative Orbiter berthing system design concept

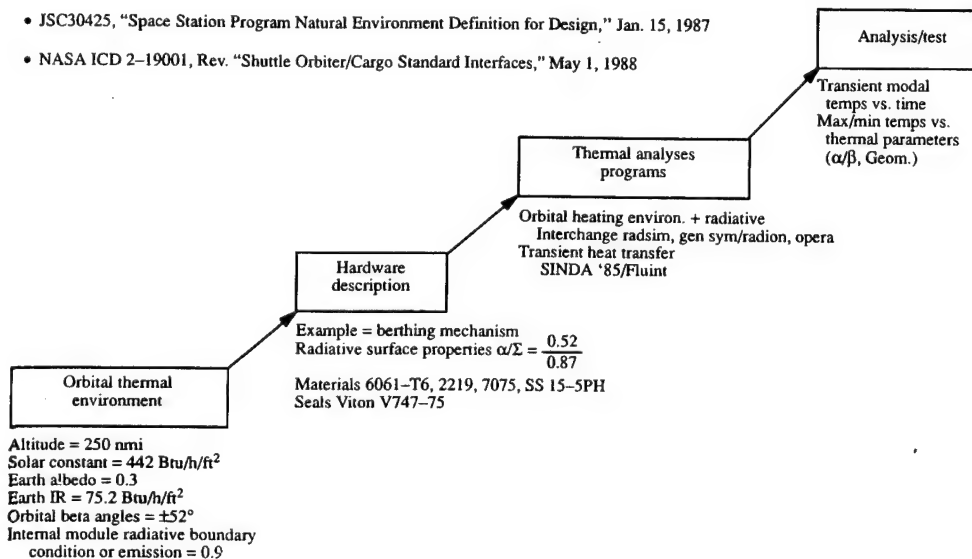


Figure 6. Thermal analysis/testing of structure

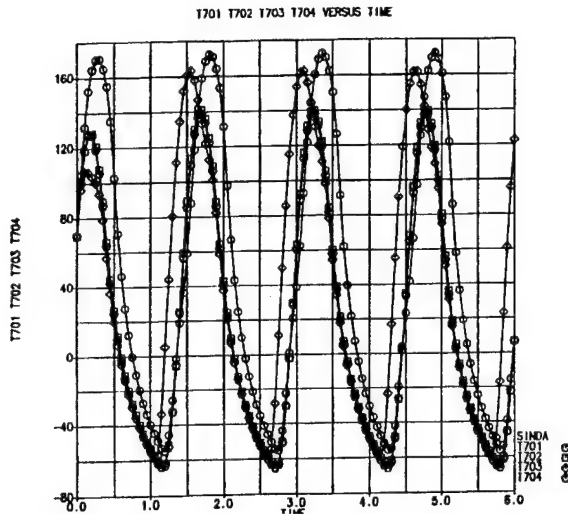


Figure 7. Alignment guide - hot case

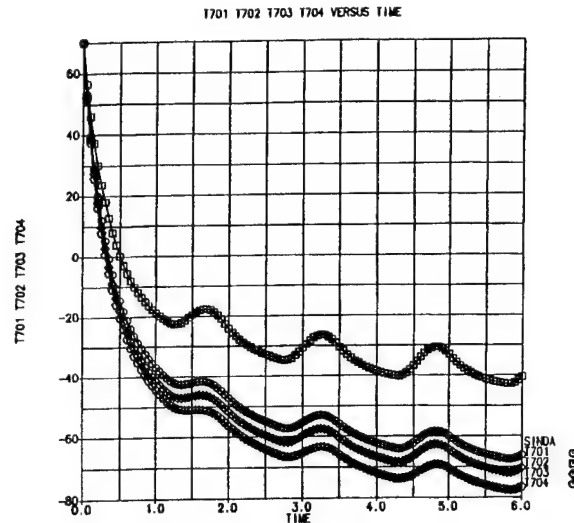


Figure 8. Alignment guide - cold case

1/3 Octave Band Center Frequency Hz	Sound Pressure Level dB Re 2×10^{-5} N/m ²	
	Lift-off	Aeronoise
31.5	122.0	112.0
40.0	124.0	114.5
50.0	125.5	116.0
633.0	127.0	118.0
80.0	128.0	120.0
100.0	128.5	121.0
125.0	129.0	122.5
160.0	129.0	123.5
200.0	128.5	124.5
250.0	127.0	125.0
315.0	126.0	125.0
400.0	125.0	124.0
500.0	123.0	121.5
630.0	121.5	119.5
1000.0	117.5	116.0
1250.0	116.0	114.0
1600.0	114.0	112.5
2000.0	112.0	110.5
2500.0	110.0	108.5
4000.0	106.0	104.5
5000.0	104.0	102.5
6300.0	101.5	100.0
8000.0	99.5	98.0
10000.0	97.0	95.5
Overall	138.5	133.5

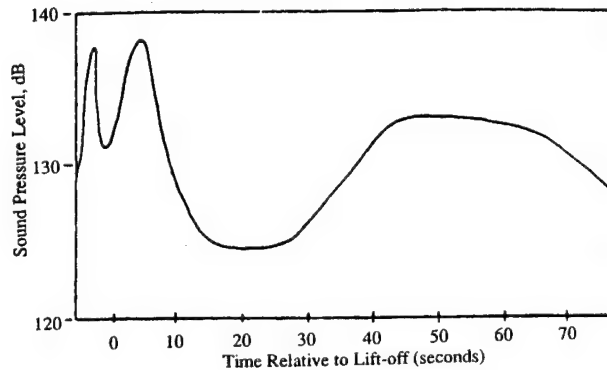


Figure 9. Acoustic excitation

A third environment affecting structural design, especially the lighter secondary structure, is the vibration induced by the engines and the aerodynamics during the atmospheric part of flight. The sound pressure level time history of a Shuttle flight and the enveloping levels for the maximum cases in the Orbiter bay are shown in Figure 9.

The sound pressure impinging on the element shell causes vibrations that must be considered as part of the structural loading, particularly for lightweight structure. During the preliminary phase of the element design, the vibration requirements for structure were derived from vibration data gathered on Spacelab. As the design matures, these requirements will be refined using mathematical techniques depicted in Figure 10.

The detailed structural parameters will be derived from drawings and resolved into a structural model using the finite element software NASTRAN. This model will be combined with the acoustic excitation data to form a statistical energy analysis (SEA) model. The SEA is then operated on by another software program,

VAPEPS (Vibroacoustic Payload Environment Prediction System) to derive vibration levels on the secondary hardware in the pressurized element as well as on the shell plates. These derived levels will be compared with the preliminary requirements, and the requirements will be adjusted as necessary for the final qualification of all SSF hardware.

A fourth environment that must be considered in the pressurized element design are meteoroids and space debris. A combination of testing and analyses are used to determine an effective design to minimize damage from these high-speed particles.

The role of testing in the shield validation is illustrated by Figure 11. Since the meteoroid and debris protection requirements are given as a probability of no penetration, the meteoroid and debris protection system must be verified by an analysis that demonstrates that the probability is met. The computer program BUMPER has been written to perform the analysis.

The inputs to BUMPER shown in Figure 11 are (1) the geometry of

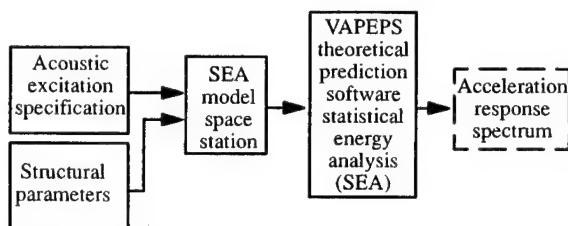


Figure 10. Techniques used to refine vibration requirements

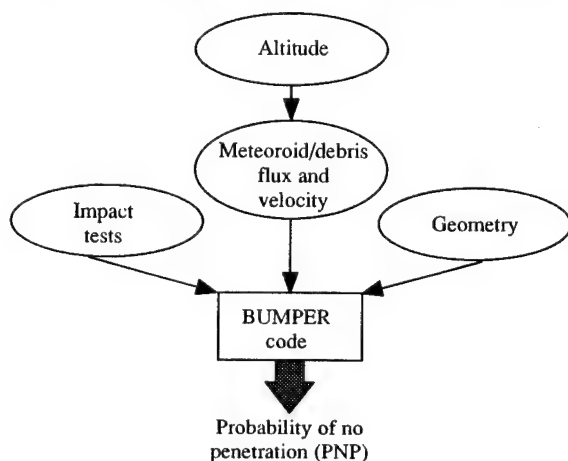


Figure 11. Shield validation procedure

the spacecraft for the calculation of self-shielding, (2) the altitude of the spacecraft, (3) the meteoroid and debris environment, and (4) the ballistic limit of the spacecraft shielding as determined by test.

The output of BUMPER is the calculated probability of no penetration (PNP) for the specified duration of exposure to the meteoroid and debris environment. BUMPER is also capable of calculating the probability of penetration per unit area as a function of position on the spacecraft. This feature is useful for identifying those portions of the spacecraft most likely to be penetrated.

The meteoroid/debris protection system requirements for SSF have necessitated a major adaptation of the impact test philosophy developed for previous manned spacecraft programs. Previously, the shield designs were qualification tested against a single "design particle." This came about because the distribution of meteoroid velocities is so sharply peaked at the average velocity of 20 km/s (66 kft/s). Hence, only impacts at 20 km/s (66 kft/s) were significant.

The meteoroid/debris development test was limited to the capability of present test techniques which can impact targets with particles up to 1 cm in diameter at velocities up to 8 km/s. Hence, each development test consisted of impacting a specimen at velocities of less than 8 km/s (26 kft/s) and by analysis calculating the PNP over the expected full range of velocities and particle sizes.

To illustrate the low-velocity effect some of the test data used as input for BUMPER are shown in Figure 12. These ballistic limit data were collected by varying the impact velocity while the projectile diameter was held constant. This procedure was repeated for a number of projectile diameters, mapping out the whole ballistic limit curve in the 3 to 8 km/s (10 to 26 kft/s) impact velocity range. The region below the ballistic limit curve

corresponds to the conditions leading to no penetration, and the region above the curve corresponds to the conditions leading to penetration. Note that a 3-mm (0.12 in) diameter debris particle could perforate the shielding at 2 km/s (6.6 kft/s) while a particle larger than 8 mm (0.32 in) would be required at 8 km/s (26 kft/s). Since the shielding has such a strong dependence on impact velocity, the full range of orbital debris sizes must be considered and not just a single "design particle."

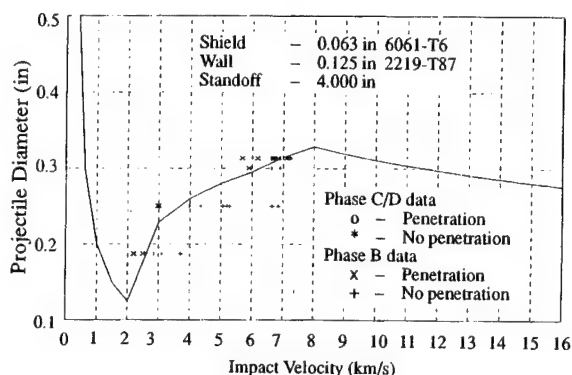


Figure 12. Ballistic limit test data

3. MATERIALS

The material for the SSF pressurized elements must be carefully selected to meet all the requirements of space with a goal of surviving 30 years in that space environment. The environments, as well as the program for selecting appropriate material, are shown in Figure 13.

In addition to surviving the environments, the materials must be reviewed from the standpoint of performance, risk, and cost. To optimize the proper materials, trade studies considering many materials were conducted early in the program. As a result of the trade studies, the materials shown in Figure 14 were selected for the major components.

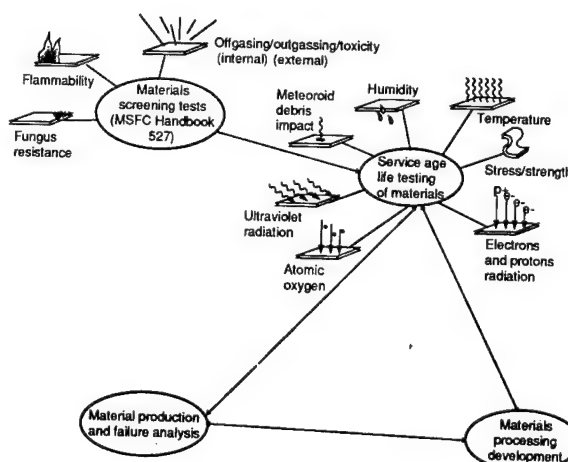


Figure 13. Materials and processing test evaluation and analysis

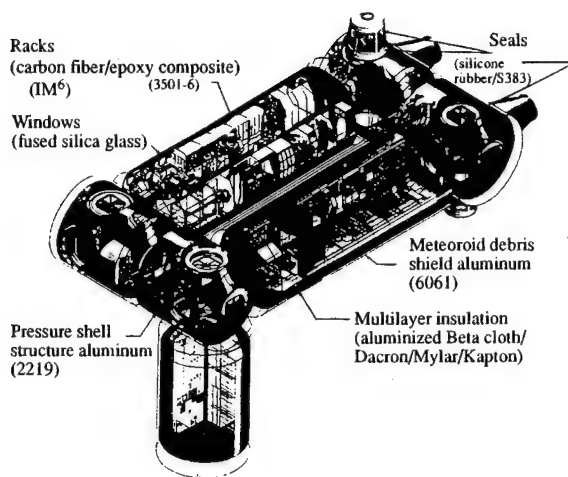


Figure 14. Space Station Freedom materials

4. ANALYSIS/TEST

With the requirements generally defined and the materials selected, the structural design then proceeds as an iteration between the designer and other affected organizations. The design must consider other factors such as manufacturing, inspection, safety, reliability, maintainability, and environmental.

Figure 15 shows the general flow from the requirements to the delivery of the hardware. The major analyses effort occurs between the preliminary requirements review (PRR) and the CDR. The first task of the designer and stress analyst is to develop a preliminary design that can be shown to meet the general requirements of the program. During this period, trade studies are conducted to select designs that optimize performance, risk, and cost and still meet requirements. Stress analyses are accomplished using traditional handbook analyses and finite element models. The process of developing a finite element model is shown in Figure 16.

Because the design is being generated on three-dimensional computer-aided design (CAD) equipment, it is possible to translate the configuration directly into a math model for stress analysis. Software translates the CAD geometry into one of two software programs, IDEAS or PATRAN, that construct finite

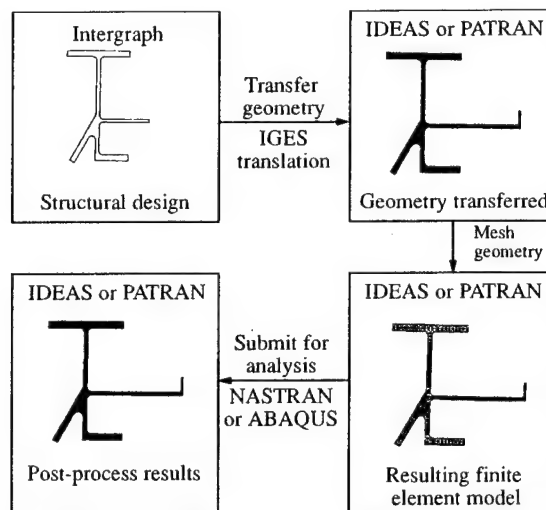


Figure 16. Finite element model development process

element models. Depending on the analysis required, the finite element model is submitted to one of these programs to develop the stress levels. NASTRAN, a NASA-developed program, provides good, quick linear results. ABAQUS, a privately developed program, has good nonlinear capability. Either is used depending on requirements of the analyst. The analysis results are fed back into IDEAS or PATRAN to post-process the results for all of its finite elements. These programs allow manipulation of the results into several formats. Figure 17 is a typical result of stress levels in the ring frame that joins the pressure element cylindrical skin to the endcone.

When a preliminary design is completed, a PDR is held with the customer to be sure they are satisfied with that design. When the preliminary design is satisfactory, the designer begins to add the details to finish the design, and the analyst refines his analyses to include all load conditions, fracture studies, and analyses of the details.

Also during this period, a series of development tests are planned and conducted to help the analyst determine that his methods and assumptions are correct. Several component tests, some including major sections of the pressurized elements, were planned and are

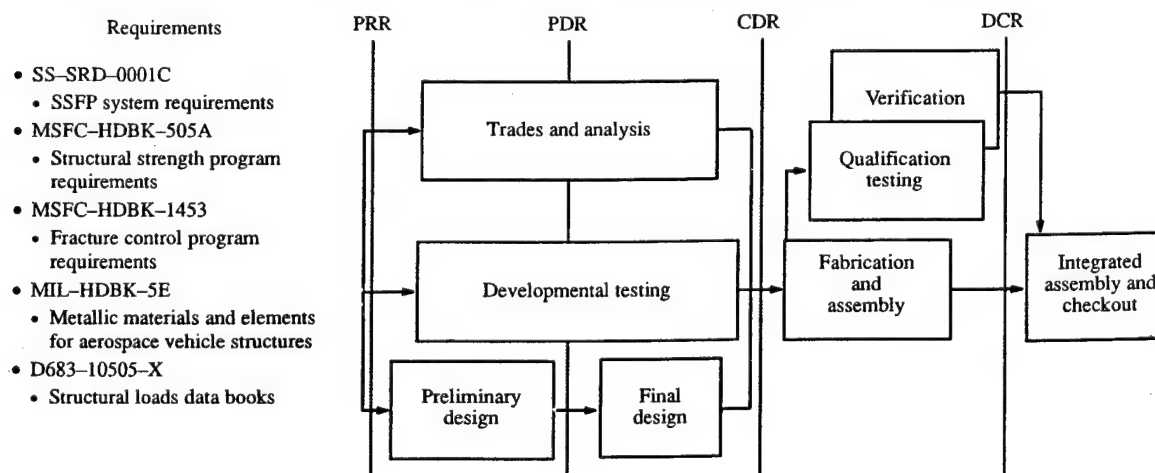


Figure 15. Flow of structural design from requirements to hardware delivery

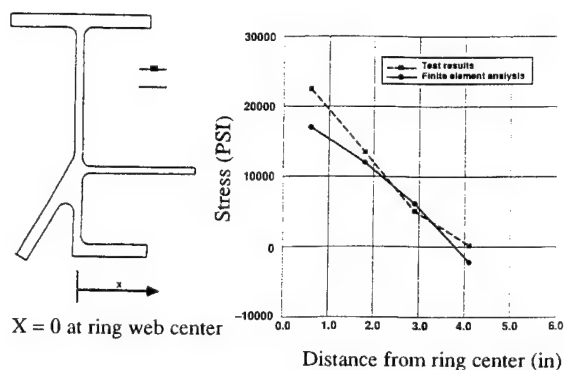


Figure 17. Typical result of stress levels in the bulkhead to cylinder ring frame

in work. The hardware and the type of tests planned are shown in Figure 18. The results of these tests will be used in the final analysis and design of the flight hardware.

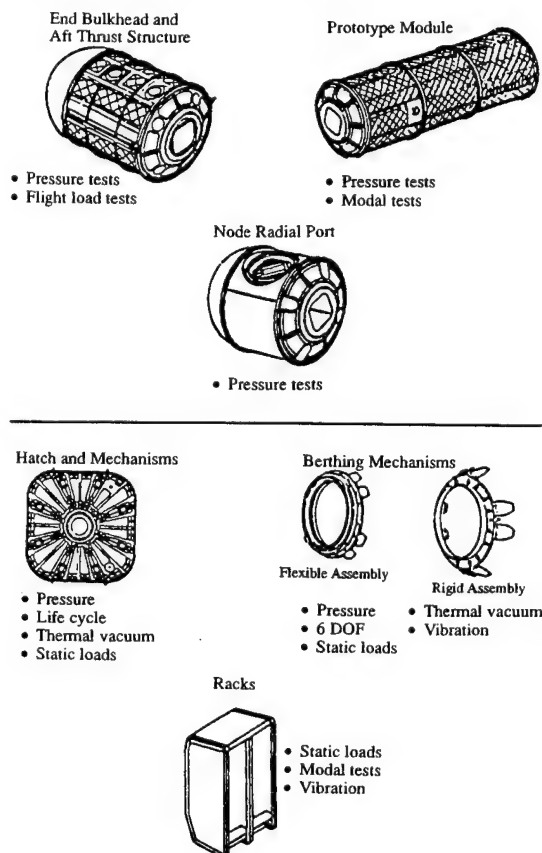


Figure 18. Hardware and development tests planned

5. VERIFICATION

The verification program planned for the pressurized elements consists of two types of tests and some analyses. The first tests are qualification tests designed to put flight identical hardware through tests simulating the full range of environments that could

occur in use. A final acceptance test is planned for actual flight articles to prove that the elements, as manufactured, will perform the intended mission.

The qualification test program is depicted in Figure 19. Structural test articles (STA) of each major pressurized element, and the unpressurized logistic elements, will be manufactured to exactly duplicate flight hardware. The tests planned on this hardware (shown in Figure 19) will prove that the hardware can withstand the extremes of the expected environments and meet the required FSs.

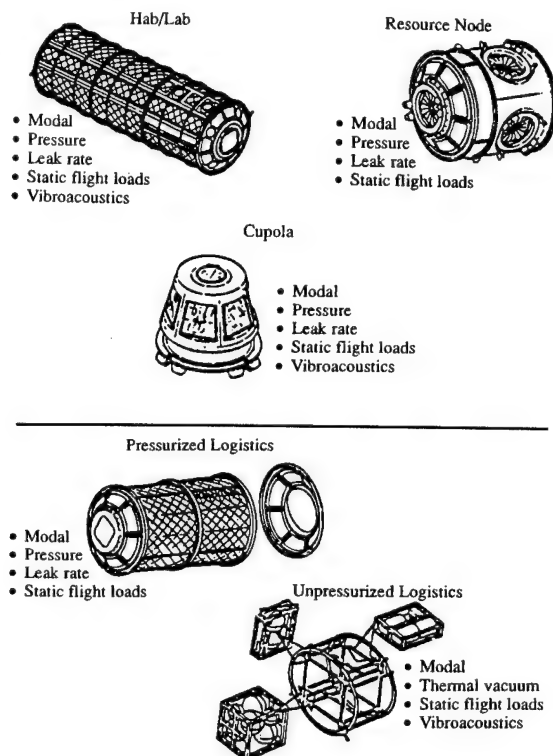


Figure 19. Qualification tests

In most cases, the tests are considered sufficient proof of compliance. However, since the tests can only simulate flight conditions, some analyses will be required to prove certain hardware meets the final requirements. For example, the modal tests only verify that the inputs to the loads models are correct. An analyses of the data is necessary to show that the models are indeed correct for the simulated conditions. In some cases, additional stress analyses, backed up with stresses measured on the qualified article, will be required to cover untested conditions.

Finally, when the flight hardware is fabricated, the pressurized elements will be tested to proof-test pressures to assure structural integrity and that the elements meet leakage requirements.

After the structural acceptance tests, the elements will be stuffed with their equipment and prepared for flight. The final tests are functional tests of all hardware and software.

As the final design nears completion, the CDR is held with the customer to gain his approval of that design. When all details are worked out, the fabrication of qualification hardware begins and a verification program is undertaken.

**SESSION
1.1.B**

**SPACE
STATION
II**

PRECEDING PAGE BLANK NOT FILMED

N92-23784

54-13

84696

THE VALIDATION OF HYDROCODES FOR ORBITAL DEBRIS IMPACT SIMULATION

M. Lambert, ESA - European Space Agency, Noordwijk, The Netherlands

J.D. Frey, J.F. Rios, X. Garaud, J. Dubois, Engineering Systems International,
Rungis, France

E. Schneider, EMI - Fraunhofer-Institut für Kurzzeiddynamik, Freiburg, Germany

ABSTRACT

Orbital debris poses a danger for spacecraft in orbit. Protection against this threat is obtained by shielding. One or more sheets placed at some distance from the structure to be protected can minimize the damage inflicted by projectiles at high velocity.

The range of velocity between 0 and 8 km/s is well covered by tests. Unfortunately, the average velocity of debris in low earth orbit is above 10 km/s with a maximum velocity around 15 km/s.

The methodology presented in this paper is aimed at validating the numerical approach. It will predict and extrapolate the behaviour of multishock shields in the velocity range between 8 and 15 km/s.

The formation of the debris cloud, after perforation of the shields on the one hand and the generation and propagation of damage in the backwall on the other hand, is a key factor.

It is examined, discussed and illustrated with correlation between numerical simulation, analytical formulae and test results.

Keywords : Hypervelocity, Impact, Orbital debris, Damage, Hydrocode.

1. INTRODUCTION

Orbital debris belongs to a man-made environment. It is generated by the destruction of payloads, upper stages or any hardware in orbit. The number and the size of debris is a function of the destruction mode : explosion or collision. The range of size is from tiny particles to huge chunks of satellites.

The debris size of interest is defined by the size of the spacecraft, the mission characteristics, and the associated systems requirements.

For manned craft, safety aspects of orbital debris are most relevant. Projectiles to be considered are generally of between 1 and 10 mm in diameter. The density of aluminium is up to now accepted as representative.

The most striking characteristic of debris is their potentially high relative velocity. Maximum relative velocity in low earth orbit is approximately 15 km/s with an average around 11 km/s.

For the considered projectiles, the velocity range between 0 and 8 km/s is well covered by testing. It follows thus that computer simulation is necessary for the investigation of the upper velocity range.

An acceptable level of confidence in the computer outputs has to be built up for the considered regime.

The following reports on the findings of ESA address this subject.

2. HYPERVELOCITY IMPACT PHYSICS

When solids collide at speeds of the order of several kilometers per second, the pressures generated reach megabar proportion (Table 1). Because these pressures exceed the strength of materials by many factors of ten, there is a regime where it is possible to neglect the effect of strength and to treat the solid as an inviscid compressible fluid. The pressures eventually decay and the material strength then becomes the dominant factor, determining the final configuration in which the material comes to rest.

If the target is thick enough, only cratering will occur. This complex process is driven by mechanical and metallurgical properties of the target as well as projectile characteristics.

In the beginning of the impact process a bright light flash occurs. It originates from a dense, hot plasma, ejected from the impact site. From the states of ionization within the plasma cloud, temperatures between 3000 K and 20000 K depending on the impact velocity, can be calculated (Ref 1)).

When a particle strikes a plate at high velocity, the compressive shock is attenuated as it travels through the plate and is generally reflected off the rear surface as a rarefaction wave.

If the plate is thin enough, the reflected wave will be so intense that a portion of the rear surface of the plate may be ejected with a momentum sufficient to damage other parts of the structure. This is spalling.

Shield material	Aluminium		
Projectile material	Aluminium		
Impact velocity (km/s)	3	6	10
Initial kinetic specific energy (kJ/g)	4.5	18	50
Max. pressure (Mbars)	.3	.76	1.64
Max. material density (g/cm ³)	3.3	4.	4.6
Max. temperature (°K)	689	2080	5455
Shock velocity (km/s)	7.4	9.4	12.1
Temperature after shock (°K)	480	922	1780
Material final state	solid	melted	liquid

Table 1 : Hypervelocity impact, state of material.

Perforation results from the combination of cratering and spalling. This mechanism shows that perforation can occur for plate thickness significantly greater than the expected depth of penetration when calculated as a semi-infinite target.

The rarefaction waves generated to satisfy boundary conditions can be looked upon as tension waves. Fracture in aluminium is created by void nucleation, growth and coalescence under tensile stress. In addition, rarefaction will be produced to satisfy boundary conditions at any nearfracture surfaces and these rarefactions can lead to further fractures.

The finite size of the projectile allows lateral shock waves to propagate back and forth. These waves generate uprange ejecta and are responsible for the dispersion of the debris cloud behind the plate.

The significance of a shield is that it can fragment the projectile, spread the fragments radially and significantly reduce the velocity of many of the fragments below the velocity of the original projectile (Fig 1).

If the conditions are adequate, released fragments are liquefied and fairly homogeneously distributed at the front of the debris cloud. It produces splashes of molten material as well as plastified droplets collapsing upon hitting the back-up structure (Fig 2). It allows a better distribution of the loading on the structure protected by the shield.

The debris cloud can thus induce in the structure three types of loading :

- cratering
- spalling
- impulse inducing gross deformations.

3. BACKGROUND WORK

This technological work has been undertaken to support the design of the COLUMBUS pressurized modules. Certain parameters like projectiles characteristics, shield spacing and material selections are driven by project requirements.

The baseline shielding is considered here (Fig 3).

Once the configuration is chosen, the basic need of the designer is to be able to predict if the pressurized wall will be perforated or not by a certain projectile. Projectiles to be considered according to project needs range from 1 to 10 mm aluminium spheres.

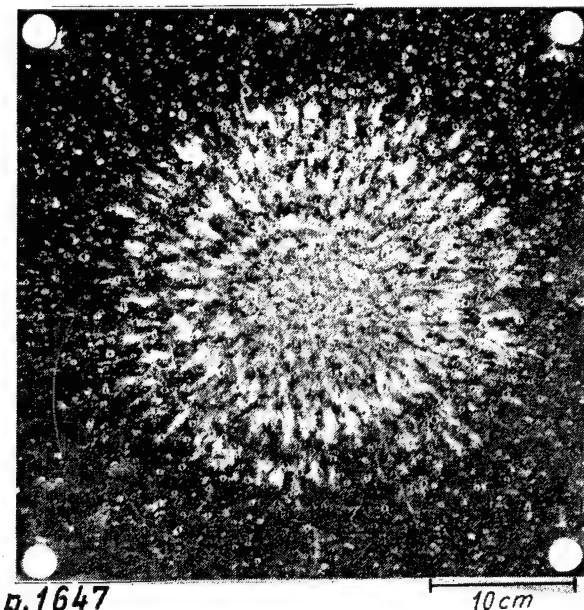


Figure 1. Backwall impact damage
4 mm diameter aluminium projectile, $V = 7$ km/s, normal impact.
2 mm aluminium bumper, 1.5 mm aluminium backwall, 200 mm spacing.

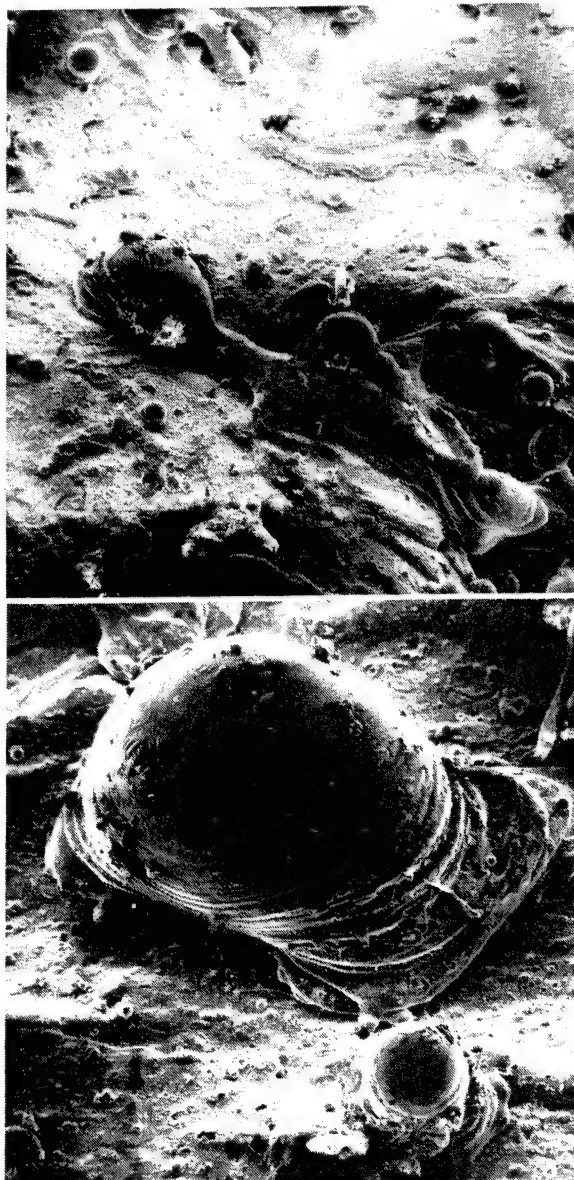


Figure 2. Examples of material splashes and plastified droplets after impact (Electron scanning microscope, magnification ~ 100, 200 x).

Illustrating the hypervelocity impact physics, the required backwall thickness shows (Fig 4) a first peak around 3 km/s, associated to a poor fragmentation of the projectile. The curve goes down from the peak to a minimum of around 8 km/s. It highlights the effects of the improved fragmentation with the velocity. The minimum corresponds roughly to the beginning of the liquid phase for the debris cloud. For higher velocities, the required thickness must increase again as the projectile momentum continues to grow.

Unfortunately, projectile accelerators are limited in performance. Technologies other than the commonly used light gas gun can be considered. They can only accelerate projectiles several orders of magnitude smaller than the one required for the electrostatic accelerators. Shaped charges are considered but the singleness of an adequate projectile is not yet demonstrated.

Experimental data are available in the velocity range defined by the accelerator performances (Fig 5). The exploration of the velocity range above 8 km/s is thus limited to computer simulation.

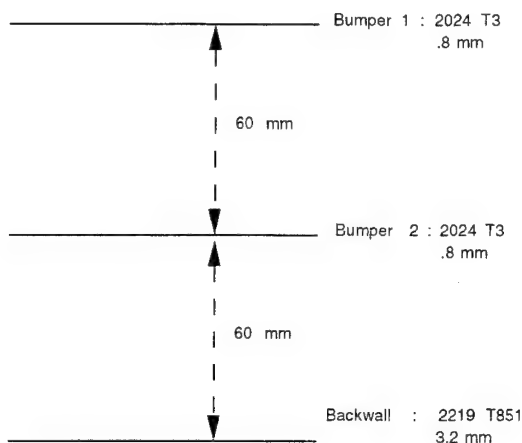


Figure 3. COLUMBUS attached pressurized module. Meteoroids and orbital debris protection configuration.

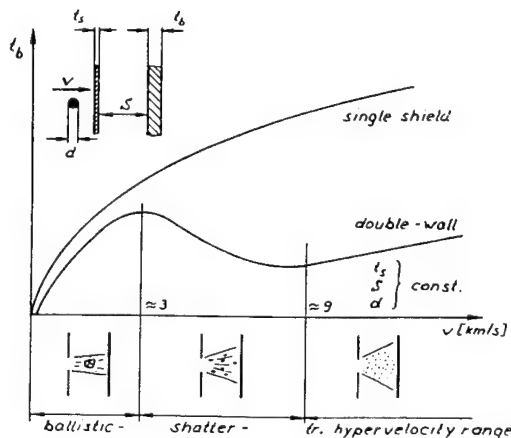


Figure 4. Ballistic limit curves of a single shield and a double wall meteoroids and orbital debris protection.

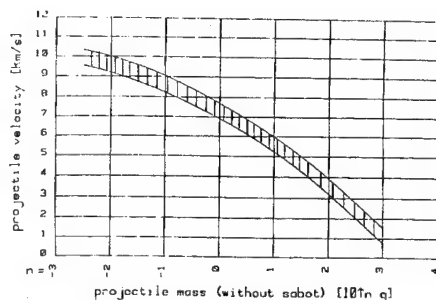


Figure 5. EMI light gas gun performances.

4. THE CODE

EFHYD-2/3D is a finite element Arbitrary Lagrange-Euler (ALE) Code for the elastoplastic and hydrodynamic analysis of multimaterial continua and structural systems. It builds upon the features of the original DYNA-3D code (J. Hallquist, Lawrence Livermore National Laboratory). The code handles in two and three dimensions solid and shell elements with impact sliding surfaces and various boundary conditions. Manual and automatic rezoning as well as complete remeshing coupled with ALE capabilities are available to perform simulations for the highly distorted shapes typical of hypervelocity impacts (Fig 6).

Key features of a hydrodynamic code are the materials descriptions (Ref 2) :

- equations of state (EOS) (High pressure and phase changes)
- constitutive modelling (strength)
- failure modelling (damage).

The velocity range (8 - 20 km/s) considered here covers all 3 states (solid, liquid, vapour) for Aluminium and the associated phase changes. A correct description of this transition is thus a must for the selection of the equation of states.

Many simple equations of state (Mie Gruneisen EOS or Tillotson EOS) do not cover all the pressure range encountered here.

More sophisticated EOS, like the ANEOS package (Sandia) or SESAME tables (Los Alamos) including several analytical models and experimental data enable the carrying out of operations for a large range of densities, temperatures and phase transitions.

The tabulated Sesame EOS is used here. It is well correlated with experiments and its accuracy is acceptable for most of the applications.

The constitutive model has to cope with the elastoplastic behaviour at high strain rates : Johnson Cook and Steinberg models in which the plastic flow depends on pressure, strain rates, temperature are incorporated in the code.

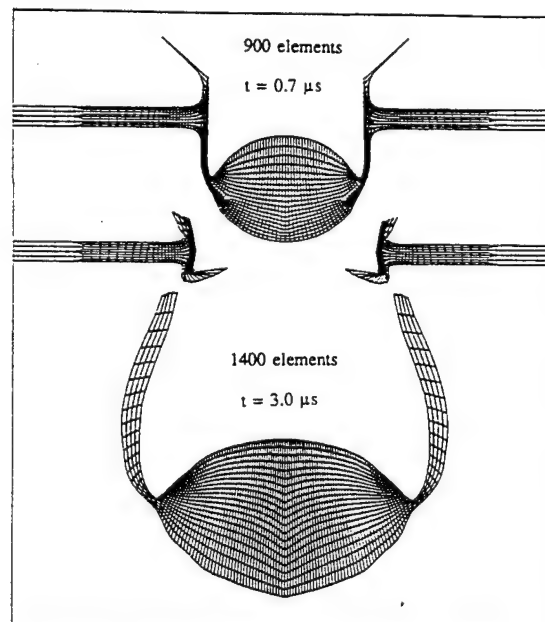


Figure 6. Typical remesh case for bumper impact (8 km/s).

Satisfactory ductile fracture models have to incorporate the contribution of 3 distinct mechanisms :

- . crack and void nucleation
- . crack growth and propagation
- . coalescence of cracks and voids.

A detailed description of these mechanisms, as in the SRI model, requires the determination of many material parameters. This approach is not practical from an engineering viewpoint. For this reason, the SRI model is not considered. The simpler Sandia Model (Grady and al.) based on energy balance and statistical considerations is incorporated in the code. It accounts for material degradation due to potential damage and includes a fragmentation model. The model has been used to describe dynamic fragmentation occurring in brittle and ductile solids with reasonable success (Ref. 3).

EFHYD has been extensively used and validated in a wide range of hydrodynamic applications for defence and space industries.

5. VALIDATION LOGIC

As no direct and full scale testing is possible with the current test capabilities, the validation beyond 8 km/s has to include the verification of two important features :

- each key physical phenomenon involved in the backwall loading has to be validated. For example for cloud density and spreading, cratering, spalling and gross deformation have to be checked versus cloud density and spreading angle (material validation cases) ;
- the trend observed with velocity increases have to be predicted by the code : it can be determined indirectly by assessing the pressure on the backwall (high velocity cases).

6. REFERENCE CASES

The purpose of this investigation is to confirm the ability of the code to predict, for the real geometry, the main features of the backwall with a projectile representative of those expected for COLUMBUS.

The velocity chosen must be compatible with the experimental device but fast enough to get the debris cloud in a liquid phase which is representative of the velocity range of concern. Parametric analysis has shown that apart from mass, velocity and spreading, the density of the debris cloud impinging on the backwall is a key element. For this purpose, bumper hole diameter, spray angle and backwall pressure have to be cross-checked with tests results.

In order to obtain an idea of the shock pressure levels induced in a back-up structure by fragment cloud loading, piezoresistive pressure pulse measurements have been mounted within back-up plates in a sandwich arrangement. In this way, a pressure time record measured in the center of a fragment cloud impact area or a back-up plate can be obtained (Fig 7). Pressure pulses of the order of some tens of kilobars have been detected.

Visualisation of fragment clouds has been achieved by means of flash X-ray techniques as well as image converter camera photo series. Both methods are appropriate to derive fragment cloud expansion velocities (Fig 8).

An additional case with different thicknesses for the second bumper is considered to explore the effect of the debris cloud variations on the backwall.

7. MATERIAL VALIDATION CASES

A relation has to be established between the shock wave amplitude and the debris cloud density on the one hand and the cratering and spalling on the other hand.

As some degree of shock wave uniformity is needed to correlate the test results with the calculations, the projectiles are made of circular flat plates impacting the target on a surface significantly larger than the measurement gauges.

Different projectile materials are used to explore the effects of the debris cloud density.

As spalling can be influenced by the time duration of the pulse, the projectile thickness allows a parametric investigation of this important impact characteristic.

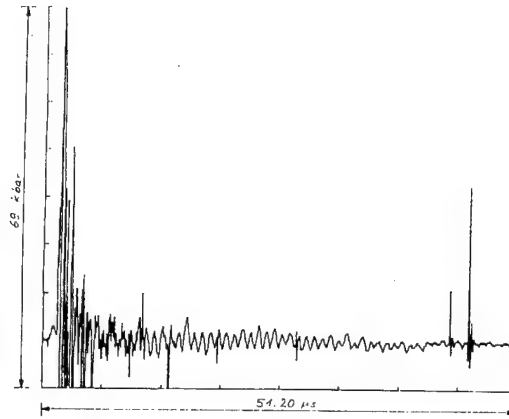


Figure 7. Hypervelocity impact pressure on the backwall measured with piezoresistive transducers.

ORIGINAL PAGE
BLACK AND WHITE PHOTOGRAPH

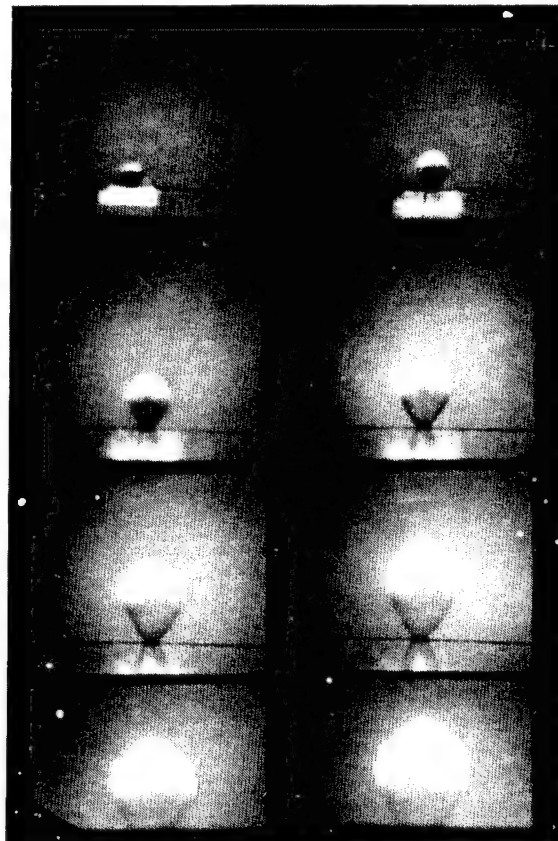


Figure 8. Kinematic of fragment cloud visualized by an image converter camera.
.5 mm Aluminium bumper, 2 mm diameter projectile, 8.1 km/s
Photos time step : 1 μ s
Fragment cloud velocity 7.1 km/s

8. HIGH VELOCITY CASES

The object of this investigation is to demonstrate the extrapolation capabilities of the code for very high velocities.

For this task, at least 2 conditions in the upper velocity range have to be investigated. As the accelerators have limited performances, a small projectile diameter is used to allow the covering conditions leading to liquid debris clouds. With small projectiles, a reasonable damage pattern on the backwall can only be obtained after scaling of the configuration.

The validity of geometrical scaling, at least for modest ratios, has been demonstrated (Ref. 4).

9. COMPARISON BETWEEN EXPERIMENTS AND NUMERICAL SIMULATIONS

9.1. Description of the methodology

Comparison with experiments are made on different parameters (kinematic parameters : residual velocities, hole diameters in the bumpers, spray angles and cloud parameters : the shape of the cloud with exploitation of x-ray pictures : pressure on the backwall indirect measurement) for the density of the cloud.

The 2D computations are performed for Whipple concept as well as for multishield concepts (3 plates). Due to the relative complexity of such calculations and the need of parametrical analyses to understand the physics, a simplified 1D methodology is also calibrated and used to predict the cloud state and the backwall behaviour. This mixed approach using 2D simulations, and a simplified 1D calculation has been already validated for typical cases and will be necessary to define the design curves of the studied configuration.

9.2. Description of a triple plate simulation

The numerical simulation of the triple plate configuration (Fig 9) involves the knowledge of several impact phenomena depending on the state of the projectile and the behaviour of the impacted target.

The simulation is divided into 5 steps as follows :

- Impact on the first bumper
- Flight and expansion of the debris cloud to the second bumper
- Impact on the second bumper
- Flight and expansion of the debris cloud to the backwall
- Impact on the backwall.

Using remeshing technique and AEL processor, it becomes possible to simulate these successive phenomena (Fig. 6).

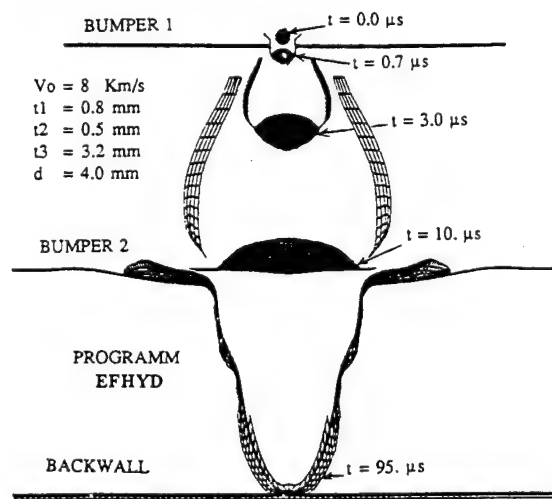


Figure 9. History of a high velocity projectile perforation of a triple plate.

a. Impact on the first bumper (B1)

The first impact simulation has been validated already (Ref 5). So it leads with high accuracy (less than a few percent with experiment) to the determination of the hole diameter and the residual velocity of the debris cloud (Table 2).

This phenomenon lasts about 2.5 microseconds (Fig 6) for the considered configuration.

b. Flight and expansion of the debris cloud to the second bumper (B2)

From this time to the impact on the second target (bumper in case of MS shield concept or backwall in case of a Whipple concept), which occurs at about 8 microseconds, one can observe a release and expansion of the cloud resulting in a heterogeneous distribution of mass (sharp gradient of density).

In particular, one can see in front of the cloud, a thin liquid zone of relatively high density. For this impact velocity (8 km/s) a density of about -0.56 g/cm^3 is found which is significantly greater than in the internal part of the cloud (Fig 10).

c. Impact on the second bumper

For a striking velocity of 8 km/s, physical phenomena involved in this second impact are quite different from those resulting from the first impact. A low density projectile made of vapour, liquid and fragments, impacts the second bumper with a velocity close to the initial velocity.

Physical phenomena are different (i.e. melting at the interface). Vaporisation during the compression of the impacting cloud occurs. This impact is not purely hydrodynamic.

The impacted bumper undergoes deformations under applied pressure and the use of an adapted failure law is necessary to obtain good results in terms of residual velocity or hole diameter. The simple EOS model alone is no more valid.

The correlation between the simulation and the experiment shows a good agreement concerning the residual velocity and the hole diameter in the bumper (Table 2).

For this case, the residual velocity is relatively low ($< 1 \text{ km/s}$).

d. Flight and expansion of the debris cloud to the backwall

The cloud continues to spread behind the second bumper. Only a little part of the total mass flying to the backwall seems to come from the initial debris cloud.

This kinematic phase is similar to the previous one between B1 and B2 at a lower velocity level.

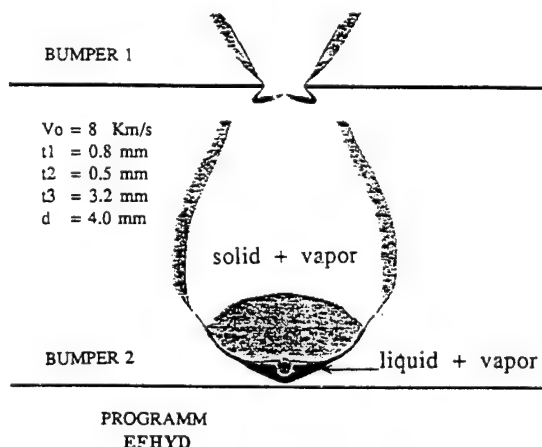


Figure 10. Debris cloud material state and density before second impact.

Table 2. Reference cases - comparison between experiments and computer simulations.

R1 $\phi = 4$ mm, $V = 8$ km/s, $t_1 = .8$ mm, $t_2 = .8$ mm, $t_3 = 3.2$ mm, $S_1 = S_2 = 60$ mm
 R2 $\phi = 4$ mm, $V = 8$ km/s, $t_1 = .8$ mm, $t_2 = .5$ mm, $t_3 = 3.2$ mm, $S_1 = S_2 = 60$ mm

Vb_1 debris cloud velocity after 1st bumper
 Vb_2 debris cloud velocity after 2d bumper
 ϕb_1 diameter of 1st bumper perforation hole
 ϕb_2 diameter of 2d bumper perforation hole
 $\gamma_{1/2}$ main and total spray angle behind 1st bumper
 $\gamma'_{1/2}$ main and total spray angle behind 2d bumper

	Vb_1 (km/s)	Vb_2 (km/s)	ϕb_1 (mm)	ϕb_2 (mm)	$\gamma_{1/2}$ (en°)	$\gamma'_{1/2}$ (en°)
R1						
Experiment	6.76	0.75	7.8	33	29/56	8/25
2D calculation	6.9	0.7	8	38	30/45	10/
1D calculation	5.85	5				
R2						
Experiment	6.76	0.975	7.8	70	30/56	14/37
2D calculation	6.9	0.9	8		30/45	
1D calculation	5.85	5.45				

e. Impact on the backwall

The last stage of the simulation is the impact of the resulting cloud on the backwall.

Measurements of the pressure were performed with a Manganin gauge.

Once again, the correlation between the calculation and the experiment is quite good (Table 2).

No significant damage appears on the backwall for this velocity.

9.3. Material validation cases

The early objectives of the material test cases were to reproduce the behaviour of the backup-plate impacted by a debris cloud generated by a very high velocity projectile (up to 20 km/s). Up to 10 km/s in the studied configuration, the average residual velocity after the second bumper appears to be less than 1 km/s. Such a velocity level is easy to reach with the current facility but experiments are now restricted by the low density and large radii inherent to an equivalent flat load.

An important requirement is to avoid the accelerated plate tumbling before it reaches the target. Moreover, materials with densities lower than .9 g/cm³ tend to collapse under acceleration imposed by a light gas gun. Considering these experimental limitations, it is difficult to reproduce at the same time, peak pressure and areal density representative of a typical debris cloud.

However, it is possible to observe the cratering and spalling processes in order to validate the material models implemented in the code. The selected configuration includes a flat projectile (Radius = 15 mm, thickness = 5 mm) impacting at 1 km/s an aluminium target 10 mm thick.

The material cases experiments as well as the related simulations are in progress.

9.4. High velocity cases

Numerical simulations give detailed information not directly measurable from tests like local density, temperature and state of the projectile, the bumper and the debris cloud (Fig 9). During the second impact, the rebound of the debris cloud (Fig 11) is typical of the rebound observed in the test.

The backwall impact damage is sensitive to projectile conditions and shielding configuration. At 7 km/s, craters generated by solid fragments are still present (Fig 1). At 8 km/s, for the triple plate configuration, no crater can be identified (Fig 12). Provided the projectile is completely shocked, the last example must be representative of what happens at high velocities.

According to the performance curves of the experimental facility, the maximum velocity case will be performed at approximately 9.5 km/s. This velocity is well inside the liquid phase regime for aluminium alloys.

The maximum pressure induced by the debris cloud on the backwall is correctly predicted by the code (Fig 13).

One calculation has been performed and validated on a Whipple concept at 8 km/s. After validation of an other calculation at a velocity as close as possible to 10 km/s, the validated tool will be used to extrapolate the behaviour of the structure up to 20 km/s.

The first correlation between experiments and calculations gives some confidence in the possibility of exploring higher velocities and other configurations.

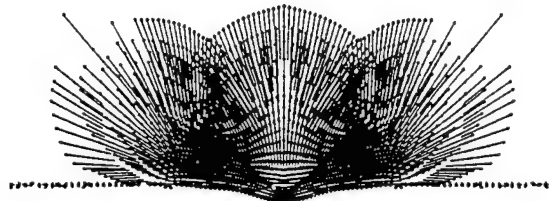


Figure 11. Velocity field after impact on second bumper.



Figure 12. Backwall impact damage.
4 mm diameter aluminium projectile, $V = 8$ km/s, normal impact.
.8 mm aluminium 1st bumper / .5 mm aluminium 2d bumper, 3.2 mm
aluminium backwall, 120 mm spacing.

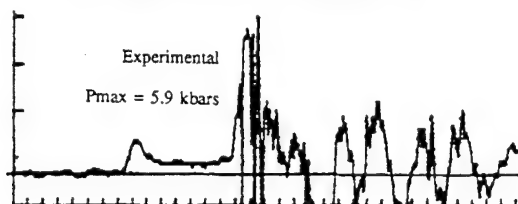
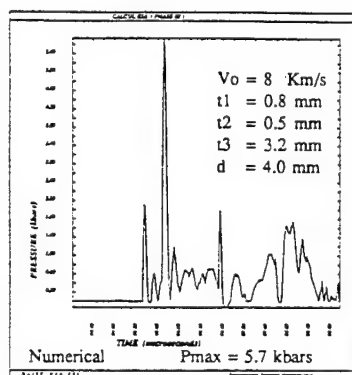


Figure 13. Comparison of numerical and experimental backwall pressure.

10. PLANNED WORK

Based on the present work, some problems to be solved can already be identified :

- the effects of oblique impact on the structure ;
- the damage induced at the backwall by poorly shocked projectile ;
- the strength of the backwall under gross deformations induced by the debris cloud impact.

11. CONCLUSIONS

The present correlation between the computer simulation and the performed experiments indicates that the code presents a reasonable accuracy in the velocity range above 8 km/s.

As soon as an experimental method is available to accelerate relevant projectiles to velocities in the range of 11 km/s, a final validation case will be performed.

12. REFERENCES

1. D. Smith & N.G. Adams 1973, Studies of Plasma Production at Hypervelocity microparticle impact. *J. Phys. D. Appl. Phys.*, vol 6.
2. Anderson Charles E, Jr 1987, An overview of the theory of hydrocodes, *International Journal of Impact Engineering*, vol 5.
3. T.C. Trucano, D.E. Grady, S.Mc Glaun 1989, Fragmentation statistics from hydrocodes calculations, *DNL nr 87185* - 5800.
4. Westine P & Mullin S 1986, 1987, Scale Modeling of Hypervelocity impact. *Proceedings of the Hypervelocity Impact Symposium, International Journal of Impact Engineering*, vol 5.
5. J. Dubois & al. 1988, Numerical simulation of micrometeoroids and debris hypervelocity impacts on COLUMBUS pressurised module. *ESA SP 289*.

N92-23785³⁷35-18
84697

MATERIAL CONSIDERATIONS FOR HABITABLE AREAS OF MANNED SPACECRAFT

Cherie Jones, Kaia Simpson, Brian Vickers, Paul Ledoux, and Hank Babel

McDonnell Douglas Space Systems Company

ABSTRACT

The purpose of this paper is to examine important material considerations relative to the design of habitable areas of manned spacecraft. The issues that are considered include flammability, toxic offgassing, particulate generation, fungus growth, odor, and general corrosion. Specific material applications such as hook and loop (Velcro™ type) fasteners and protective coatings for the interior of pressurized structures are also discussed relative to these issues. This paper shows that the greatest emphasis has appropriately been placed on characterizing materials for flammability and toxic offgassing, areas where life-threatening situations could occur if improper material selections are made. Less emphasis has been placed on the areas of particulate generation and fungus growth. Unresolved issues were identified in all areas.

Keywords: Materials, spacecraft, space station, manned, interior, particulates/fibers, flammability, offgassing, fungus, Velcro™, fasteners, paints.

1. INTRODUCTION

Material considerations for the Space Station Freedom (SSF) crew compartments are addressed, although the concepts are pertinent for any long-life spacecraft mission in low Earth orbit (LEO) or future manned lunar or Martian missions. This paper is an extension of the topics covered in Reference 1, which addresses the effect of LEO environments on materials, thermal control coatings, multilayer insulation (MLI), fluid/material compatibility, and lubrication issues. The material considerations include flammability, toxic offgassing, particulate generation, and fungus control. Odor and general corrosion are discussed briefly with respect to specific applications. In addition, hook and loop fasteners and long-life interior pressure wall finishes are discussed in terms of the design requirements for manned areas.

Material requirements for Space Station are specified in SSP 30233A, Space Station Requirements for Materials and Processes. NHB 8060.1B, Flammability, Odor and Offgassing Requirements and Test Procedures for Materials in Environments that Support Combustion, describes the tests used to evaluate candidate materials for spacecraft. Additional requirements related to flammability, toxicity, and particulates are contained in SSP 30213B, Space Station Program Design Criteria and Practices. The requirement for the number and size of airborne particles in the habitable areas of the SSF is specified in JSC 31013B, Medical Requirements of an In-Flight Crew Health Care System. There are no specific tests required for particulate generation or corrosion.

2. FLAMMABILITY

The oxygen concentration of the environment inside crew compartments of a spacecraft is important for two reasons (other than creating a breathable atmosphere): (1) it determines the amount of time that an astronaut must "prebreathe" in preparation for extravehicular activities (EVA) and (2) it is the key variable relative to the flammability risks associated with material usages. A higher concentration of oxygen in the crew compartment is desirable because it decreases the amount of time that an astronaut must prebreathe prior to an EVA. However, material flammability risks increase as the oxygen concentration increases and therefore a balance between these two competing requirements needs to be established.

Prebreathing prior to EVA is necessary to reduce the level of dissolved nitrogen in the bloodstream. Sudden decreases in pressure can cause nitrogen bubbles to form, resulting in a painful and potentially fatal condition referred to as the "bends." For example, the bends could occur if an astronaut whose body is accustomed to breathing space station air at a nominal 10,300 kg/m² (14.7 psia) and 21% oxygen is suddenly exposed to the low-pressure 3520 kg/m² (5 psia) environment of an EVA suit. The Space Station program has baselined a 7170 kg/m² (10.2 psia) atmosphere as the prebreathe environment prior to an EVA to minimize the time required for prebreathing. Medical personnel recommend that the oxygen concentration for a 7170 kg/m² environment should range between 28.9 and 31.8% (2070 and 2280 kg/m²) in order to meet the physiological needs of the astronauts.

Because of the strict flammability requirements imposed on NASA manned programs, candidate materials for the Space Station must be evaluated for flammability at the maximum oxygen concentration to which the crew environment will be exposed. All materials must pass NASA's Upward Propagation Test, as described in NHB 8060.1B, at the maximum oxygen concentration level that will be experienced. The number of materials tested by NASA at oxygen concentration levels ranging from 20.9 to 33% is shown in Table 1. At the 33% oxygen concentration level, material selection and design is restricted because of the limited number of acceptable materials that pass the flammability test. Flammability tests at 33%

Table 1. Flammability Test Results

Oxygen concentration (%)	Number of materials tested	Number of materials passed
20.9	1121	766
23.8	986	563
25.9	1504	658
30.0	1142	654
33.0	244	123

h7032: 11 04/17/91

oxygen were conducted on 244 materials used in the Orbiter. All had passed at 30% oxygen and only 123 passed at 33% oxygen. Materials that failed included polyimide foam insulation, silicone conformal coating used as a fire barrier, the fabric used for the crew uniforms, and the outer fabric of the EVA suits (Figure 1). Such high-use materials would be difficult and expensive to find substitutions for on Space Station. In addition, the rate at which a material burns increases with increased oxygen concentration and the minimum thickness at which a material passes the flammability test also increases. A 30% oxygen level has been recommended as the maximum oxygen concentration level for Space Station because of the significant reduction in the number of acceptable materials for oxygen levels above 30%.

Increasing the Oxygen Concentration —

- Reduces astronaut prebreathe time prior to an EVA
- Increases flammability risks
- Maximum allowable oxygen concentration should be 30%

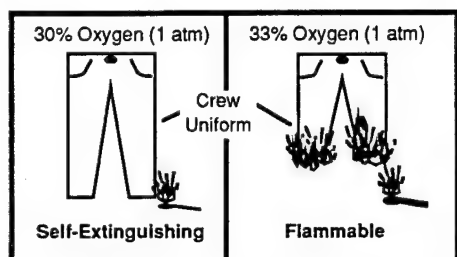


Figure 1. The effects of increasing oxygen concentration

2.1 Material Flammability Testing Requirements

The current NASA flammability test, described in NHB 8060.1B, Test No. 1, Upward Propagation Test, is a severe test for evaluating material flammability. Test 1 requires that a material be self-extinguishing when a vertical 30 cm length of the material is ignited at the bottom edge with a 1093°C flame. Most of the commercial tests use a top ignition or a 45-deg material incline and rarely ignite the sample at the edge. Many materials that are advertised as "self-extinguishing," "flame resistant," and "nonflammable" are based on horizontal propagation tests and will fail the NASA test.

A fire in space burns differently than it does on the Earth. In zero gravity a fire burns slowly, the flame front taking the shape of a slowly expanding sphere, which will be directed by forced airflow inside the Space Station. In normal gravity, a fire that starts at the bottom of a material rapidly rises upward as convection, due to gravity-induced buoyancy, ensures a continuous, fresh supply of oxygen. Therefore, NASA has taken a conservative approach to spacecraft material control by imposing the upward propagation test to evaluate flammability behavior.

2.2 Effect of Material Chemistry on Flammability Behavior

Manufacturers sometimes make small changes in their product to improve a material or to reduce production costs without changing the material's name or nomenclature and without notifying customers. Slight changes in chemistry do not usually create a flammability risk for aerospace materials.

One known case where a chemistry change has affected the flammability behavior of a NASA-qualified material involves electrical wire insulation. In the mid-1970s, the wire and insulation passed the NASA Upward Propagation Test. Later, in the mid-1980s, the same wire failed this test. The manufac-

turers claimed that they had only made a small change in their formulation, less than 1% of the weight of the insulation. The change had been made to satisfy NASA's special vacuum outgassing requirements for a particular application.

To eliminate this kind of problem, NASA had considered requiring batch testing of all materials used in NASA space programs. But because of the high costs involved, batch testing is currently imposed only on materials used in high-pressure oxygen fluid systems due to the hazardous nature of these systems. Batch testing costs arise primarily from the system required to track which batch of material is used on each component.

3. TOXIC OFFGASSING CONTROL

Two areas related to materials are controlled to ensure that unacceptable levels of toxic gases never exist in the habitable areas: selection of materials that meet the NASA toxicity requirements given in NHB 8060.1B and selecting materials to minimize those which release gases that can reduce the efficiency of (or "poison") the environmental control and life support system (ECLSS) by reacting with and reducing the efficiency of the catalytic oxidizer. Also, specific control procedures need to be established for cleaning the hardware during fabrication, test, and preflight checkout to avoid inadvertently having solvents absorbed into materials or trapped in faying surfaces.

3.1 Design Selection Considerations

The current NASA requirements to limit the total amount of a particular trace gas, spacecraft maximum allowable concentration (SMAC), have evolved as a result of several experiences. Early in the Apollo program, an ink that passed total organic compounds and carbon monoxide requirements caused a reaction in test panel members, indicating that the ink was toxic. Since then, NASA test facilities have identified and quantified all major offgassing components.

Most materials and/or components that are marginal or fail the offgassing test can be baked in a conventional air oven to make them acceptable. One incident in which the baking did not work was for a fabric-covered elastic shock (Bunge) cord. The manufacturer used a trichloroethylene cleaner that has an SMAC of 0.26 mg/m³. The elastic shock cords were baked for 4 days and they still exceeded the trichloroethylene limits. The hardware had to be remanufactured and cleaned with a less toxic substance. Organic materials may absorb cleaning solvents and should be controlled to prevent such occurrences.

Another incident occurred when a temperature-sensitive experiment was shipped to NASA's White Sands Test Facility (WSTF) packaged in a foam that contained a high concentration of acetonitrile, a highly toxic material. Acetonitrile was deposited on the experimental unit and was very difficult to bake out because of the temperature sensitivity of the unit. Further investigation indicated that the source of the toxic compound was the adhesive used to bond the packaging foam in the shipping container. To help avoid this kind of problem, an approved list of packaging materials is being created for WP-2.

Occasionally, the type and quantity of materials used in an off-the-shelf component are not known because obtaining a detailed materials list is not cost effective or the list may be protected as proprietary information. In these cases, the entire component is tested and the quantity of each trace gas is measured to ensure that no toxic gases are produced. Testing is also required to determine if toxic gases are produced from personal items such as shoe polish, shaving cream, deodorants, mascaras, etc.

The creation of toxic gases from small, limited fires or overheated components also needs to be addressed. Fluoro- and chloro-hydrocarbons have excellent flammability resistance but produce toxic compounds when ignited or exposed to high temperatures. Materials that produce the least toxic products of combustion are also highly flammable. These factors are considered during the design development activities. In the case of a fire, crews are trained to put on emergency oxygen masks, start venting the combustion gases, and extinguish the fire. During the many US space flights, only two very limited small fires are known to have occurred on American spacecraft in orbit, and they were handled without any adverse effects on the crew.

The low level of allowable trace gas contaminants requires control of experimental techniques to ensure comparable results between different laboratories. Several offgassing test programs were conducted comparing results from two NASA agencies and the Japanese Space Agency. Substantial differences were found between testing centers, and it was determined that results were highly dependent upon the types of gas chromatograph columns used to separate the components of the offgassing sample prior to identification with a mass spectrometer. Because capillary columns are viewed as more accurate than packed columns, NASA-JSC's WSTF began analyzing with capillary columns. Both Japan and NASA-JSC use capillary columns and have had satisfactory agreement in results. The types of columns used by the European Space Agency are not known. In addition, more sensitive mass spectrometers were installed at WSTF around 1985. It is recommended that borderline materials or materials that were tested more than 5 years ago be retested per NASA's standard test method at WSTF.

3.2 Material Selection to Prevent Poisoning of the ECLSS

The SSF program is considering the use of an activated charcoal adsorber and a catalytic oxidation system in combination with an adsorber/lithium hydroxide system such as used on the Orbiter. Figure 2 shows the proposed SSF trace contaminant control system. The activated charcoal adsorber removes most trace organic contaminants such as ammonia, methylene chloride, aldehydes, ketones, and alcohols as well as silicon and halogen compounds that could poison the catalytic oxidizer system. The catalytic oxidizer system is designed to oxidize methane and carbon monoxide as well as other organic compounds not adsorbed by the activated charcoal. Tests done for the Japanese Experimental Module (JEM) (Reference 2) indicate that if the catalytic oxidizer system were poisoned, large quantities of methane and carbon monoxide would be produced. These quantities could overwhelm the LiOH postsorbent system that is designed to remove any toxic gases and acids produced by the catalytic oxidizer.

There are a number of design considerations associated with the selection of materials to minimize the possibility of poisoning the catalytic bed. Silicon-containing products are commonly used inside spacecraft. Silicone rubber seals are the only kind of seal material currently being considered for windows because of their good low temperature properties and the unacceptable odors associated with polysulfides. Silicone potting compound in electrical connectors are also commonly used. Offgassing requirements are specified in NHB 8060.1B for only one silicone-containing compound, hexamethylcyclotrisiloxane. Most silicones pass the offgassing requirements, except acetic acid-curing RTVs which fail odor requirements. The available offgassing test data for silicones should be

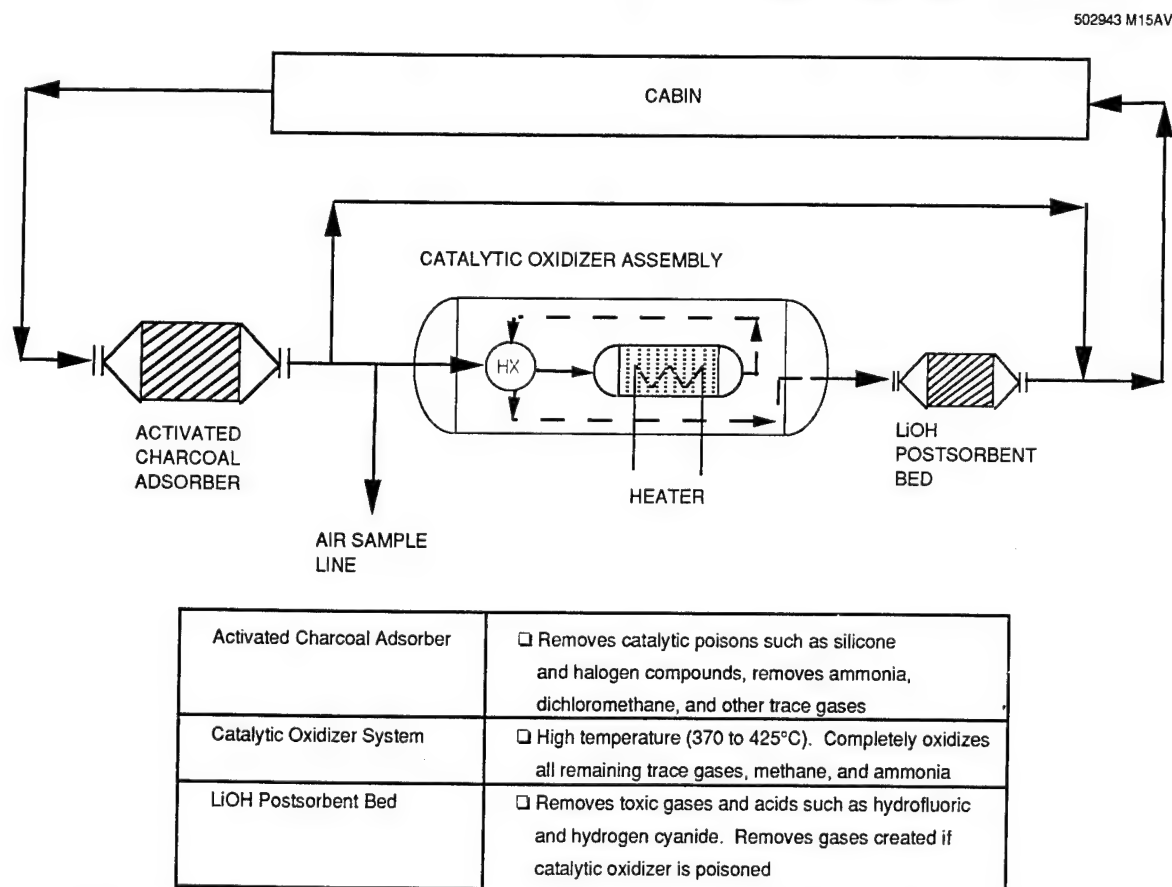


Figure 2. Proposed trace contaminant control system for Space Station

reviewed to ensure that the quantities emitted do not overwhelm the adsorption capacity of the activated charcoal and poison the catalytic bed. WP-2 requires that window seals be baked to reduce the outgassing to 1/10 of the requirement in NHB 8060.1 to prevent fogging of the windows. Although baking is believed to reduce offgassing, it needs to be confirmed experimentally. The approved material list for WP-2 only contains materials that meet NASA'S offgassing requirements and will also be used for the interior of the airlock and nodes.

In addition to control of materials used in design, the use of halogenated solvents must be controlled through all operations prior to launch. The systems-level offgassing test required in NHB 8060.1B of the completed module, airlock, and node is designed to identify any possible oversights. In the case of fire, the SSF has baselined CO₂ and N₂ fire extinguishers. This avoids the issues associated with halogenated fire extinguishers such as those using Halon 1301TM, which can quickly introduce large quantities of halogenated compounds into the air, even for relatively small fires, potentially overwhelming the activated charcoal adsorber and poisoning the catalytic oxidizer.

4. PARTICULATE/FIBER GENERATION

On manned spacecraft, particulates consisting of paint chips, metals, fibers, plastics, and miscellaneous debris floating in the cabin in space can create crew health and equipment problems. These are not considered critical or capable of causing a catastrophic failure on the SSF. JSC 31013 requires control of air particulate levels to less than 3,350,000 particles per cubic meter for particles greater than 0.5 μm . There is also a requirement in SSP 30213 that materials should be resistant to flaking. Efforts are under way to better control air quality by defining requirements for limits on particles greater than 0.5 μm and defining air filtration requirements.

The medical requirements for SSF were derived from experiences on Apollo, Spacelab, and the Shuttle. On Apollo, the primary source of particles was the woven fiberglass cloth made from the BetaTM fiber used for storage bags, insulation covers, clothing, and other applications. There were no requirements to control particulates. On the European Spacelab, there also were no particulate level requirements. On the Space Shuttle, astronauts complained about particles getting into their eyes and causing irritation. The initial inclination was to impose a class 100,000 clean room standard as defined in FED-STD-209, Clean Room and Work Station Requirements, for the Shuttle atmosphere. However, this was not deemed practical because of the normal shedding of human skin particles, dandruff, and hair and the normal expiration of particles and water droplets from human lungs. On orbit, particles do not settle to the floor as they do on Earth and would be very difficult to control in the atmosphere. Although no official requirements were placed on the Shuttle, a number of practices were adopted which helped reduce the particles encountered in space. One of these was for Velcro. Broken Velcro hooks had been a problem in the past but have been significantly improved by the practice of combing and vacuuming the Velcro after installation. The control exercised during ground operations is also very important.

Equipment problems due to particulates in the Shuttle were generally confined to filters becoming plugged on air cooled electronic boxes, causing the electronics to overheat and potentially malfunction. Filters were subsequently redesigned to be corrugated in order to maximize filter surface area within a minimum volume. This still has not entirely resolved the problem, as evidenced by a recent Shuttle flight on which the air filters for two computers on the Astro telescope experiment became plugged. The Astro manufacturer has admitted inadequate cleanliness controls during assembly, but particulates generated during the Shuttle flight also contributed to the problem.

In general 80 to 95% of the material in Shuttle filters are cotton fibers and lint that were shed from the crew's blue cotton

uniforms, towels, other cotton clothing, sleeping bags, and other miscellaneous cotton fabric supplies (Reference 3). Reduction in the use of cotton is continually being addressed. The use of chemically treated flame-resistant cotton fabric wearing apparel is primarily based on crew comfort. Other fabrics that would potentially meet the flammability requirements, such as a cotton blend with 50% polybenzimidol (PBI), are under consideration but have not been qualified for use in manned space programs or evaluated for crew comfort. Entirely synthetic fabrics, such as NomexTM and PBI, are generally unacceptable as underclothing because they do not ventilate well or readily absorb perspiration, thereby making them less comfortable for the crew to wear. NomexTM outer garments have been adopted to help reduce the amount of cotton lint produced. Another approach to help reduce total particulates in the atmosphere is to limit cotton fabrics not used in crew apparel or bedding to relatively lint-free fabrics, such as NomexTM or PBI. Candidate equipment are supply bags and privacy curtains. Where stiffer fabrics are required, a combination of a layer of ArmalonTM (TeflonTM-coated glass cloth) sandwiched between two layers of NomexTM is a candidate. This composite fabric is expected to meet flammability requirements and produce less lint than cotton fabrics.

Early in the program, consideration was given to quantify and rank particulate generating materials for habitable areas. This never became a requirement. There are no standard tests to measure the number and size of particles generated by a specific material. MDSSC has proposed that during all normal operations, habitable volumes should have an air filtration and circulation system that uses high-efficiency particle air (HEPA) filtration to filter a minimum of five cabin air volumes per hour. The 24-hr average mass of particles in the cabin atmosphere should be less than 0.2 mg/m³ for particles between 0.5 and 100 μm in diameter. In addition, MDSSC has proposed that equipment be designed to eliminate or contain the generation of loose particulate matter which may be detrimental to Space Station operation or crew safety. These requirements should mitigate some of the situations currently experienced on the Shuttle that could become problems on SSF during its 30 years on orbit.

5. FUNGUS

Certain forms of fungus create spores that can adversely affect some people, particularly those who have allergies or asthma. Fungus has not created any known problems in space except on the Soviet Salyut 4 mission. This vessel had a mahogany wood lining, a fungus nutrient per MIL-STD-810D, Method 508.3. The Salyut 4 had been left unattended, and when the cosmonauts returned they found mold on parts of the wall (Reference 4).

A potentially critical fungus problem for spacecraft would be fungus growth on the paint system, which could lead to corrosion, such as on a pressure bulkhead. Such corrosion could lead in the worst case to a weakening of the bulkhead and a subsequent need to reinforce the bulkhead wall. Paints used on spacecraft walls are polyurethane based, and some polyurethanes are known to be fungus nutrients. One candidate supplier of this type of paint declined to add an antifungal agent because of the extensive recertification required and the relatively small quantity of paint required for the Space Station. The candidate paint is similar to that used on the Shuttle program where no fungus has been reported on any of the vehicles. However, the extended time on orbit, 30 years for SSF as opposed to 7 days for the Orbiter, will provide greater opportunity for fungal growth. Areas of poor air circulation behind cabinet areas and water condensation on the walls are conducive to fungal growth.

A hardware design and system development goal on both the SSF and the Orbiter is to prevent water condensation on the wall. However, such condensation has occurred on previous Orbiter flights and it is likely that it will occur again.

Unfortunately designs that ensure good air circulation to help minimize the possibility of condensation may carry unacceptable weight and power requirements and cost penalties. Other design solutions may be available to reduce the degree of moisture condensation.

The requirements related to fungus are stated in SSP 30233A, which indicates that all materials will be submitted for fungus resistance testing and/or analysis. The cost of the testing specified in MIL-STD-810D for determining whether a material is a fungus nutrient is very expensive with cost estimates of \$2000 to \$3000 for one test. Service testimonials relative to fungus problems are lacking. Because fungus growth is a relatively long-term problem with some time being available to remedy the problem should it occur and it is noncatastrophic as a threat to human life, programs have met the specified fungus requirements by analysis based on the generic test results reported in MIL-STD-810D without conducting confirmational tests.

6. HOOK AND LOOP STYLE FASTENERS

Hook and loop (also called hook and pile) fasteners are frequently used in nonstructural fastening applications where easy assembly/disassembly is required. These fasteners are commonly known as Velcro, a trade name of Velcro USA, Inc. Hook and loop fasteners are generally available in NylonTM and NomexTM (Dupont trade names), polyesters, and 304 stainless steel. Peel strength, tensile strength, and cycle life vary greatly among the different materials.

Hook and loop style fasteners generally do not meet the flammability requirements when tested as a single material, but do meet the requirements when the configuration is controlled on assembly. Typically, maximum fastener size is 25 cm² and fasteners are separated from adjacent pieces by a minimum of 5 cm on all sides. These sizes and spacing were developed for the Shuttle program and are being used by WP-2 for the SSF. The 5-cm separation prevents fire propagation in the event of an ignition.

Hook and loop fasteners tend to create particles during cycling due to hook and loop filament breakage. These particles contributed to astronaut eye irritation on past Shuttle flights. There are no data on the rate of particle generation or the size distribution of the particles formed. Dual-LockTM (3M Corporation trademark) style fasteners, which consist of continuous plastic strips with mushroom-shaped stems, form fewer particles during cycling but are more difficult to close than hook and loop fasteners. Dual-LockTM fasteners require positive finger pressure and some manipulation to close securely. Figure 3 illustrates the closure mechanisms for hook and loop fasteners and Dual-Lock style fasteners. Whether or not Dual-LockTM fasteners would be acceptable to the astronaut corps has not been established.

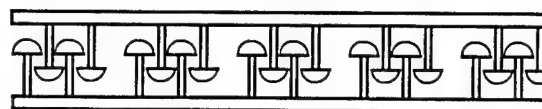
There are several attachment techniques for hook and loop fasteners, including adhesive bonding and mechanical fastening to a substrate by riveting, sewing, clipping and attachment using threaded inserts. The adhesives selected must also meet flammability, toxicity and fungal nutrient requirements as described in earlier sections of this paper.

7. INTERIOR PRESSURE WALL COATINGS

Paints were selected for the SSF in preference to anodic coatings and other finishing methods because they provide excellent corrosion protection for long periods of time. But paints do have some problems. Interior paints can be chipped during ground maintenance and on-orbit use, sometimes exposing bare aluminum. In space, this creates two potential problems, corrosion of the aluminum and floating paint chips. Tough paints resisting such chipping are of particular importance for interior pressure walls that can not be sent back to Earth for maintenance or repair. These structures include the

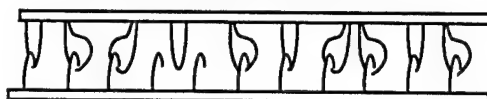
502936.1 M15AV

Dual-Lock Latching Schematic



- ☐ More difficult to close or open than VelcroTM-type hook and loop fasteners
- ☐ Fewer particles formed during cycling because fasteners are molded in one piece

Hook and Loop Latching Schematic



- ☐ Easier to close and open than Dual-LockTM-style fasteners
- ☐ Filaments are more easily broken during cycling, forming particles

Figure 3. Latching schematics for Dual-LockTM and standard hook and loop fasteners

nodes, airlock, crew transfer tunnel and modules, described in detail in Reference 5. Boeing (WP-1) will be selecting the coatings for the nodes and modules, while MDSSC (WP-2) will be coating the airlock and crew transfer tunnel. It is doubtful that paints will remain undamaged over the 30-year life of the Space Station. Since techniques have not been developed for on-orbit painting, repair methods for locally damaged areas will need to be established in order to ensure corrosion protection of the 2219-T6 and 2219-T851 aluminum pressure shells. This differentiates the Space Station from all previous US and European manned space programs, including Skylab, European Spacelab, and the Shuttle.

Coatings for interior pressure walls should provide corrosion protection, toughness, resistance to fungus growth, and they should meet NASA flammability and offgassing requirements. Interior surfaces of the Space Station airlock and crew transfer tunnel will be exposed to vacuum and need to pass vacuum outgassing requirements.

7.1 Design Considerations

The temperature of the interior of the Space Station will normally be held between 65°F and 80°F and the dew point will be held at around 60°F. The temperature may go below the dew point, causing condensation that may remain on the surface long enough to allow corrosion to develop in damaged areas, particularly those without ventilation sufficient to re-evaporate the water. Further, contaminants such as salt (from perspiration), grease, dust, and food particles can collect on surfaces, causing fungus problems and increasing corrosion risk.

Several design approaches are being considered for reducing the amount of condensation residing on these pressure walls. One approach is to install heaters to maintain the temperature of the structure surfaces above the dew point at all times, including during assembly. If condensation does occur, the heaters could be used to re-evaporate the condensation, thus minimizing the potential for corrosion and fungal growth. A second option is to minimize condensation behind close-out panels, racks, and hard-to-reach areas through increased ventilation. These options are not attractive because they increase weight and power requirements.

Less than 10% of the pressure wall area on the node and modules will be exposed to potential damage from astronauts during daily activities. The airlock and crew transfer tunnel will

have significantly more exposed pressure wall area. Expansion and contraction of structure surfaces must also be accounted for in the selection of a protective coating.

7.2 Coating Selection

Paint systems and anodic coatings were considered for use on the interior of the Space Station pressure walls. A summary of the evaluation of these materials is found in Table 2.

Anodic coatings can provide corrosion resistance in preferred exposure conditions, but they are known not to provide corrosion protection in habitable environments for long periods of time. Anodic coatings have good durability and scratch resistance, and they pass the NASA tests of toxicity, flammability, and outgassing. Practical considerations such as finding anodic baths of sufficient size limit the consideration of anodic coatings. For these reasons, anodic coatings were not pursued as finishes for interior pressure walls.

7.3 Polyurethane Paint System

A polyurethane paint system with compatible epoxy primer provides excellent durability and corrosion protection properties and has been selected for WP-2. The candidate primer is a chromated epoxy-amine primer, Desoto 515X349, selected for toughness, flexibility, and adhesion. Because the chromates leach into scratches, chromated primers provide some corrosion protection even in damaged areas. The candidate topcoat is a high-impact polyurethane, Desoto Desothane Series 1000, with 8 years of service on commercial aircraft wings and landing gear. It was selected for corrosion resistance, flexibility, and abrasion resistance. High-impact coatings are used to protect areas of commercial aircraft that are subject to damage from runway debris. To meet NASA's offgassing requirements, this paint system requires baking at approximately 110°C for 16 hr in an air oven. Corrosion protection prior to priming will be provided with either chromic acid anodize or a conversion coating, depending on the part size. Both of these coatings serve as excellent bases for application of primer.

No standard tests have been developed to rank paints coatings for space applications. Standard tests were used as a guide for evaluating the selected polyurethane paint. The tests conducted include a mandrel bend flexibility test (ASTM D522), an impact resistance test (ASTM D2794), an adhesion tape test (FED STD 141, method 6301.2), a chip resistance test (ASTM D3170), and the Taber abrasion test (ASTM D4060). Paint manufacturers commonly test their coatings for moisture

resistance, oxidation, color stability, adhesion, durability, and corrosion. Because the above tests do not fully predict performance of coatings, MDSSC weighted service experience as the most important consideration in selection of the paint system.

8. SUMMARY

Selection of materials for the habitable areas of manned spacecraft involves much more than mechanical properties and functionality. Crew safety mandates that materials be carefully evaluated and controlled for flammability and toxic offgassing. Other material characteristics such as particulate shedding and fungus resistance must also be evaluated to ensure crew health and hardware durability. NASA and its contractors have developed many test methods to evaluate materials for these properties. Through careful materials selection and control using a comprehensive material data base, safe and comfortable spacecraft interiors can be designed.

9. ACKNOWLEDGEMENTS

The authors would like to acknowledge the contribution of the following people for the technical information and assistance they provided in preparing this paper: Dr. Lubert Leger, Materials and Processes, NASA-JSC, Houston, TX; Jay Perry, NASA-MSFC, Huntsville, AL; Dr. Charles Smith, Chemist, MDSSC, Huntington Beach CA; Pam Philyaw, MDSSC, Huntsville, AL.

10. REFERENCES

1. Babel HW, Simpson KE, Jones CA, Material Considerations for Space Station Freedom, *41st Congress of the International Astronautical Federation*, Dresden, GDR, IAF-90-278., Oct. 1990.
2. Yoshimura Y, Manabe K, Kamishima N, Minemoto M, Hatano S, Etoh T, Lida H, Study of Trace Contaminant Control System for Space Station, *SAE Transactions on Aerospace*, Vol 97, Paper No. SAE-881117, 1988.
3. Coskren RJ and Kadikis A, *Analysis of Materials Collected from Various Shuttle Orbiter Vehicles by Mr. J. Goodman of JSC*, Case G82116, Albany International, 30 January 1985.
4. Oberg JE, *Red Star in Orbit*, Random House: New York, 1981.
5. Wensley DC, Vickers BD, and Gutkowski GP, Space Station Integrated Truss Structure and Assembly Techniques, *41st Congress of the International Astronautical Federation*, Dresden, GDR, October 6-12, 1990.

Table 2. Evaluation of Potential Interior Pressure Wall Coating Materials

Coating type	Corrosion resistance	Durability	Toxicity	Flammability	Vacuum outgassing	Repair concept
Sulfuric acid anodic coatings	Good	Good	Passes per NHB 8060.1	Passes per NHB 8060.1	Passes per SP-R-0022	Epoxy patches
Orbiter interior paint/primer system	Excellent	In test. Many service testimonials. Unexplained difficulties on Shuttle	Passes per NHB 8060.1 in configuration	Passes per NHB 8060.1	Passes per SP-R-0022 in configuration	Epoxy patches
Proposed WP-2 interior paint/primer system	Excellent	In test. Many service testimonials. Used on aircraft landing gear	Fails NHB 8060.1 without baking. Passes with 16-hr bake at 110°F	Passes NHB 8060.1 at 30% O ₂ , 10-mil aluminum substrate	Fails SP-R-0022 without baking. Passes with 16-hr bake at 110°F	Epoxy patches

h7032: 12 04/17/91

56-13
 56-13
 N92-23786

PROTECTION OF SPACECRAFT AGAINST METEOROID/ORBITAL DEBRIS IMPACTS

Hans-G. Reimerdes

MBB/ERNO-Raumfahrttechnik GmbH, Bremen, Germany

ABSTRACT

As a result of the space activities during the last three decades there are lots of artificial particles orbiting the earth, the so called orbital debris. These particles increase the probability that spacecraft will be hidden during mission considerably. Especially large spacecraft planned for long missions will be endangered and have to be protected against this new threat.

In this paper the present known techniques for protection of spacecraft are presented and compared. Semi-empirical formulae for calculation of dimensions of protection systems are given. Based on these formulae and on the directional distribution of the particles, three different approaches for reduction of the required mass of the protection system are presented.

Keywords: Orbital Debris, Meteoroids, Hypervelocity Impacts, Protection Systems

1. INTRODUCTION

Protection of spacecraft against impacts from meteoroids is considered to be needed since the first space activities. Intensive investigations were performed during the development of the APOLLO spacecraft. This is documented in a huge number of papers, published in the 60's (Refs. 1-5). The work was concentrated on impacts resulting from meteoroid particles having very high velocities and comparatively low masses. The preferred protection concept was the "Whipple" bumper shield already introduced in 1947 (Ref. 6). This concept is considered to be most effective at particle velocities above about 10 km/s. Design formulae were established based on test data and on analytical investigations. This work was followed by a period with no further activities related to meteoroid protection. This can be explained by the reduced number of manned space missions but also by the fact that one considered the problems as solved.

A new challenge were the Comet-Halley-missions. Here the spacecraft had to survive an environment with high concentrations of meteoroids (Refs. 7, 8). The success of GIOTTO is also based on a proper design of a meteoroid protection concept. These 1978 started investigations were followed by those related to the protection of the

international space station against impacts. There are mainly two reasons for this new work:

- o the long time of mission (30 years) and the large surface area of the space station increase the probability of impacts,
- o the space activities of the last three decades led to artificial particles orbiting the earth, which are more dangerous than meteoroids (Ref. 9).

Calculations show that in case of ten impacts with perforation about nine will result from orbital debris particles while only one will be produced by meteoroids.

To overcome this new problem NASA as well as ESA initiated technology studies to investigate the phenomena resulting especially from orbital debris impacts. In contrast to the work performed in the 60's, now higher particle masses have to be considered and the design formulae have to be extended to velocities below 10 km/s. The work is based on experimental and on numerical simulation of impacts. The main problem is the limitation of available test facilities with respect to the attainable velocity. The maximum velocity with particle masses of interest is about 8 - 9 km/s. Higher velocities can only be treated by analytical and numerical investigations.

2. ENVIRONMENT AND REQUIREMENTS

The presently considered environment models for the design of the COLUMBUS modules were defined by NASA (Refs. 10, 11). Fig. 1 shows the particle fluxes versus diameter for meteoroids and debris. The altitude is 500 km and the particles are assumed to be spheres. It can be seen that there are above about 2 mm diameter more debris fragments than meteoroids. Other properties of meteoroids and orbital debris shall be given briefly:

Velocities:

- o meteoroids:
 $9 \leq v \leq 72 \text{ km/s}$ average: $v_m = 20 \text{ km/s}$
- o orbital debris:
 $0 \leq v \leq 16 \text{ km/s}$ average: $v_d = 10 \text{ km/s}$

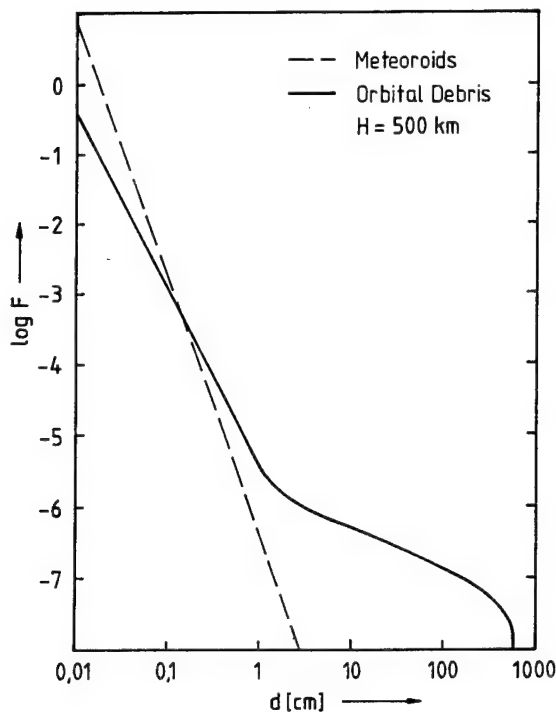


Fig. 1: Particle fluxes versus diameter

Average mass density:

- o meteoroids: $\rho_m = 0.5 \text{ g/cm}^3$
- o orbital debris: $\rho_d = 2.8 \text{ g/cm}^3$ ($d \leq 1 \text{ cm}$)

The meteoroids are considered to be omnidirectional with respect to the earth while orbital debris is assumed to fly parallel to the earth surface. The directional distribution of orbital debris relative to a spacecraft with 500 km altitude and 30° inclination is presented in Fig. 2.

Protection of spacecraft has to be designed such that certain requirements are fulfilled. One main requirement is a probability of no perforation. This probability is linked to the particle flux, the surface area and the mission duration as follows:

$$p_0 = e^{-FAT} \quad (1)$$

where; F - particle flux
A - surface area
T - exposure time.

If one knows which particle diameter will lead to perforation the flux for particles with that or with larger diameter can be determined which allows to compute the probability of no perforation. As the impact conditions are not constant over the surface area of a spacecraft Eq. 1 has to be modified accordingly:

$$p_0 = e^{-(\sum A_i F_i)T} \quad (2)$$

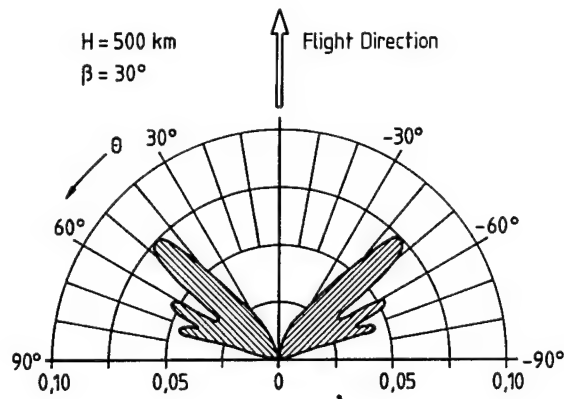


Fig. 2: Directional distribution of orbital debris

For the COLUMBUS modules it is required that the probability of no leak is 0.995 within one year. A first estimate shows that a module having a surface area of 200 m² has to be protected against about 5 mm debris particles in order to meet that requirement.

3. IMPACT BEHAVIOUR OF DIFFERENT WALL DESIGNS AND DESIGN FORMULAE

Within this paper the following wall designs will be described (Fig. 3):

- o single wall,
- o double wall,
- o triple wall.

The single wall represents the unprotected structure, the double wall is the classical concept for protection of spacecraft against meteoroid impacts, and the triple wall is selected for the COLUMBUS modules. As shown in Fig. 3 the complexity of the wall design increases with the number of walls. It should be mentioned that a full description of the three designs is not available. Fig. 4 gives a rough estimate of the percentage of understanding achieved for the different concepts. The lack of knowledge results mainly from:

- o limitation of test facilities in velocity (all concepts),
- o huge number of parameters to be investigated (double wall and especially triple wall).

3.1 Single Wall

In case of the single wall it is useful to distinguish into two problems:

- o Semi-infinite targets:
The target is much thicker than the crater depth produced by the impacting particle.
- o Thin target:
The target thickness is in the same order than the crater depth.

In case of the semi-infinite target the crater formation is not influenced by the rear side of the target. The crater depth and its shape depend on the mass, the shape and

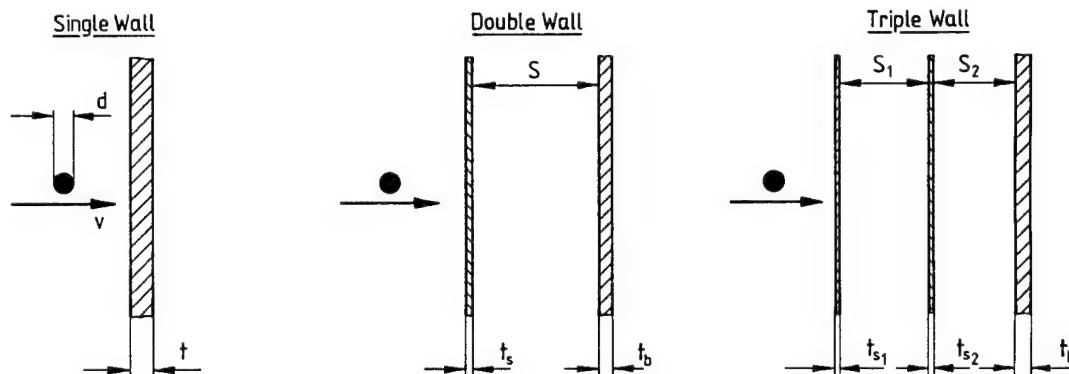


Fig. 3: Protection concepts

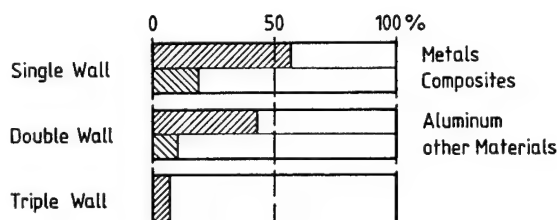


Fig. 4: Percentage of understanding achieved for the different concepts

the velocity of the particle as well as of the density, the hardness and the strength of the target. If the particle velocity is larger than about 3 km/s (aluminum projectile and target) and if the particle aspect ratio is near to one the crater is nearly hemispherical.

There exist a huge number of formulae to calculate for this case the crater depth. They rely mainly on test results. The following formula is commonly used for spacecraft design (Ref. 12):

$$p_{\infty} = K_{\infty} m_p^{0.352} \rho_p^{1/6} v^{2/3} \quad (3)$$

where: p_{∞} - crater depth [cm]
 m_p - particle mass [g]
 ρ_p - particle density [g/cm³]
 v - velocity [km/s]

K_{∞} is depending on on the target material. For aluminum alloy it is given to 0.42.

If the target is thin, a modification of Eq. 3 is suggested (Ref. 13). This is to consider that perforation can occur although the crater depth is smaller than the target

thickness. This results from plastic deformation and from spallation of material on the rear side as a consequence of tension waves exceeding the tensile strength of the material. The modified formula for the thin target thickness is:

$$t = k p_{\infty} \quad (4)$$

One can distinguish into 3 different cases as shown in Fig. 5:

- o $k > 3.0$: no spallation on the rear side,
- o $k > 2.2$: no detached spall on the rear side,
- o $k > 1.8$: no perforation of the thin target.

It has to be mentioned that Eqs. 3 and 4 are only valid in the velocity region up to 8 km/s where tests can be performed. A further limitation is the particle mass which should be smaller than about 1 gram. Extrapolation to higher velocities and masses might result in incorrect results. For higher velocities theoretical investigations were published by Bjork (Ref. 18) which should be taken into account.

3.2 Double Wall

The double wall concept is the classical design against meteoroid impacts. Its efficiency results from the fact that the incoming particle becomes destroyed upon impact with the first wall, the bumper shield. The fragments heat up and may melt or even vaporize. Between the two walls the produced cloud of particles, droplets or vapor expands and hits the second wall (back-up wall) over an enlarged area. This load can be defeated better without serious damage to the wall than an impacting solid

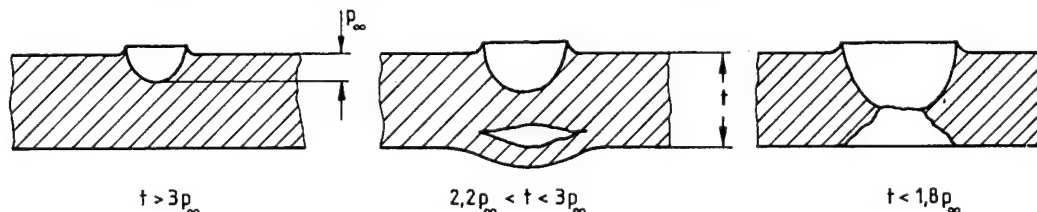


Fig. 5: Impact damages in thin sheets

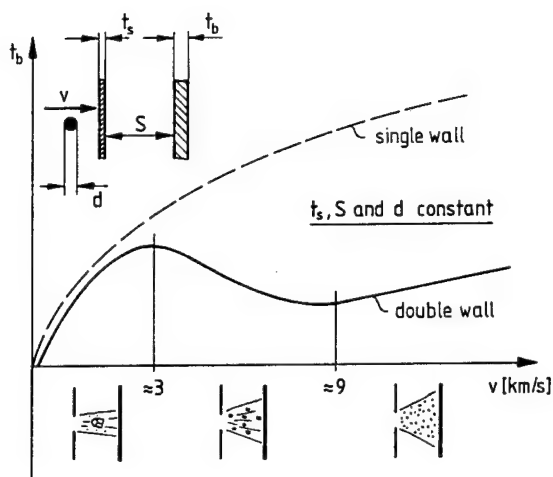


Fig. 6: Back-up wall thickness versus velocity

particle. Thus the total wall thickness of the double wall concept can be reduced down to about 20 % of that of a single wall design.

If the material is not changed the main parameters influencing the efficiency of the double wall design are:

- o particle velocity,
- o ratio: shield thickness/particle length.

Particle Velocity:

In order to destroy the particle a certain pressure is needed which occurs above a certain velocity. Below this velocity the shield is nearly ineffective. If the particle and the shield are out of aluminum this velocity is about 3 km/s. If the velocity is increased, the fragments become smaller begin to melt and to vaporize. At velocities above about 7 - 9 km/s the double wall concept is most efficient. Fig. 6 shows the back-up wall thickness needed to avoid perforation versus velocity.

Ratio: Shield Thickness/Particle Length:

The influence of the ratio: shield thickness/particle length on the impact behaviour of the double wall is shown in Fig. 7. Here the total wall thickness needed in order to avoid perforation of the second wall is plotted versus the shield thickness/particle diameter ratio. The particle velocity and the diameter as well as the distance between the walls are kept constant. The diagram shows a rapid decrease of efficiency if the shield becomes too thin. This is because a part of the particle remains solid if the shield is not thick enough. The optimum ratio depends on the material combination. Fig. 7 is representative if both particle and shield are out of aluminum.

Although many formulae exist for the double wall concept, there is no complete set available that describes the influence of all parameters over the total velocity regime. The following approach is presently used. The velocity is divided into three regions with different impact behaviour (Fig. 6):

- o ballistic region,
- o shatter region,
- o hypervelocity region.

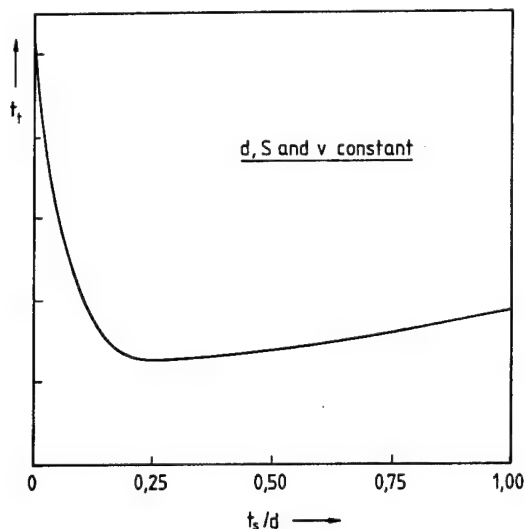


Fig. 7: Total wall thickness versus shield thickness/particle diameter (Ref. 3)

For typical spacecraft designs it is assumed that the ballistic region is between 0 to 3 km/s. The hypervelocity region begins above about 7 km/s. Based on results published in the literature the double wall is treated in the ballistic region similar to a single wall. In Ref. 16 it is shown that the crater depth in a protected semi-infinite target plus shield thickness is equal to the crater depth in a semi-infinite target alone (Fig. 8):

$$p_{\infty 1} = p_{\infty 2} + t_s \quad (5)$$

If one considers the relation between semi-infinite targets and thin plates (Eq. 4) one achieves the following expression for the back-up wall thickness:

$$t_b = p_{\infty 2} k = (p_{\infty 1} - t_s) k \quad (6)$$

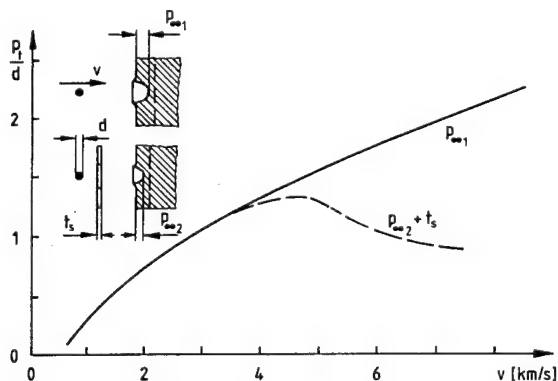


Fig. 8: Penetration in a bumper-protected target and in a semi-infinite target versus velocity (Ref. 16)

For velocities above 7 km/s a formula published by Cour-Palais (Ref. 8) is suggested. The original formula developed for small particles was modified according to suggestions made by Cour-Palais (Ref. 19) in order to apply it also to larger particles:

$$t_b = (0.045 + 0.084 d) (\rho_p \rho_s)^{1/6} m_p^{1/3} v \sqrt{\frac{482}{S \sigma_y}} \quad (7)$$

where: d - particle diameter [cm]
 ρ_s - shield density [g/cm³]
 σ_y - yield strength - back-up wall [N/mm²].

A further modification is suggested. In cases where the shield thickness/diameter ratio is below 0.2 the needed back-up wall thickness is larger than predicted by Eq. 7 (Fig. 7). In order to consider that Eq. 7 shall be multiplied by a factor F^* which is defined as follows:

$$F^* = 5 - 40 \left(\frac{t_s}{d} \right) + 100 \left(\frac{t_s}{d} \right)^2 ; \left(\frac{t_s}{d} \right) \leq 0.2 \quad (8)$$

For the shatter region there exists presently no design formula. Here a linear interpolation as shown in Fig. 9 is suggested. Fig. 9 shows also test results for 5 mm aluminum particles. It can be seen that the proposed approach is in that case somewhat conservative compared to the achieved test results.

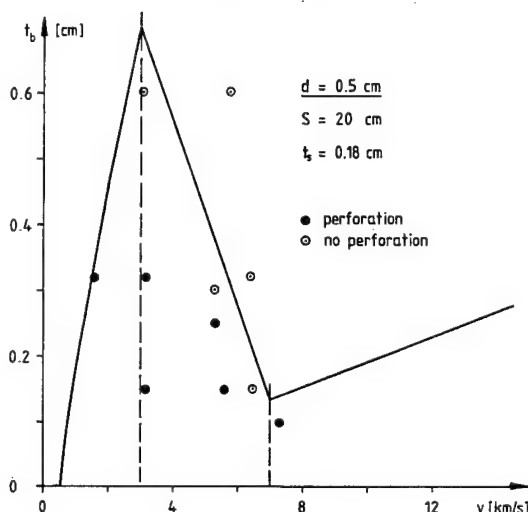


Fig. 9: Double wall: semi-empirical formulae compared to test results

3.3 Triple Wall

The triple wall concept showed in tests several advantages over the double wall design. These are:

- o the velocity of the debris cloud produced upon impact of the particle with the shields is reduced,
- o solid particles within the debris cloud resulting from the shields are small as the shields are thinner,
- o the limit between the ballistic and the shatter region might be shifted to lower velocities.

These advantages are all expected in the ballistic and in the shatter region. In the hypervelocity region which presently cannot be tested it is expected from theoretical considerations (Ref. 3) that the triple wall might be not as effective as the double wall. This is explained by the fact

that the expansion of the debris cloud is reduced by the intermediate shield. An other advantage of the triple wall is the fact that small particles can be already stopped by shielding alone which results in less damage to the back-up wall and e.g. to the thermal protection.

Presently there exist no formulae for the description of the impact behaviour of the triple wall design. To generate such formulae is quite complex as the number of parameters is very large and as the number of tests already performed is low. On the other hand to have formulae is very important in order to be able to find a mass optimum solution.

3.4 Oblique Impacts

The above given formulae are valid for normal impacts. In reality most of the impacts are oblique. Presently there are only few results available for oblique impacts. Based on theoretical considerations and on available test data one assumes that in case of oblique impacts the given formulae for computation of crater depth and of back-up wall thickness can be used if the normal component of the velocity vector is considered.

4. DESIGN OF PROTECTION SYSTEMS

Three different measures are thinkable to find a protection system with a minimum of additional mass. These are:

- o selection of a suitable protection concept,
- o optimization of the selected protection scheme,
- o consideration of threat directional distribution.

These measures will be explained using the surface area (200 m²) and the orbit of the attached pressurized modul (APM) of the COLUMBUS project. The modul is idealized as rectangular box (Fig. 10) in order to simplify the example calculations.

4.1 Selection of the Protection Concept

The selection of the protection concept is mainly driven by the following two considerations:

- o is the structure able to fulfill the requirements without additional shielding,
- o what is the expected particle velocity.

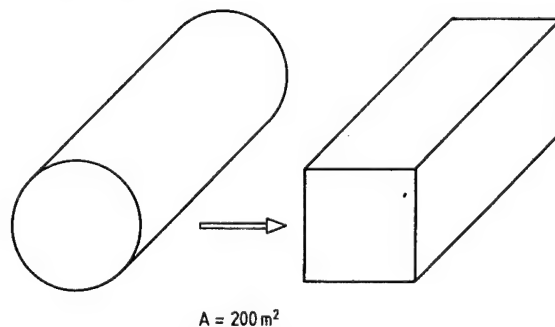


Fig. 10: Simplified modul structure

The conclusion from the answer to the first question is obvious and needs no further explanation. In case that shielding is needed the answer to the second question allows for example to decide if a double or a triple wall concept should be preferred. For orbital debris the average normal component of the velocity vector never exceeds 6.5 km/s. This indicates that the triple wall is from protection point of view the best selection as it is expected to be most effective at velocities below 7 km/s. It should be mentioned that there might be other design driving aspects for the selection of protection concepts as there are maintenance, repair, inspectability, stiffness, etc. which cannot be explained within this paper.

4.2 Optimization of the selected Protection Scheme

Protection concepts can be optimized if several parameters affect their efficiency. A further condition is that formulae are available that describe the influence of these parameters. This means an optimization of the triple wall design is presently not possible. Although for the double wall concept no complete set of formulae is available do the above presented formulae allow to perform a first optimization.

For the example calculation the distance between the shields was fixed to 12 cm. The probability of no perforation (no leak) was computed for constant total wall thicknesses while the ratio back-up wall/bumper shield thickness was varied. The results are presented in Fig. 11. It can be seen that there exists for each total wall thickness one thickness ratio leading to a maximum probability of no perforation. In case that the modul wall has to have a certain wall thickness not all thickness ratios can be realized. This is considered by the limit curves for the 0.24 cm and the 0.32 cm thick modul wall. If the modul has to be 0.24 cm thick a total wall thickness of 0.35 cm is needed in order to achieve a probability of no perforation of 0.995. This results in a mass of 1979 kg.

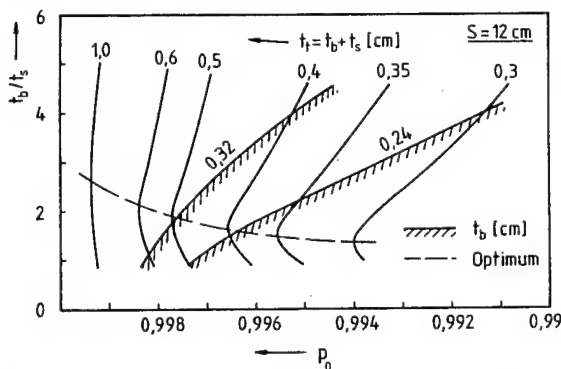


Fig. 11: Probability of no perforation for different wall thicknesses

4.3 Consideration of Threat Directional Distribution

There are two possibilities to consider the threat directional distribution for the optimization of the protection design:

- o vary the wall thickness at different locations to achieve a minimum mass,

- o vary the attitude of the spacecraft to reduce the expected number of impacts (Ref. 17).

Both strategies shall be explained for a single wall concept. This does not mean that the single wall is suggested for practical application but it is best suited to demonstrate the approaches.

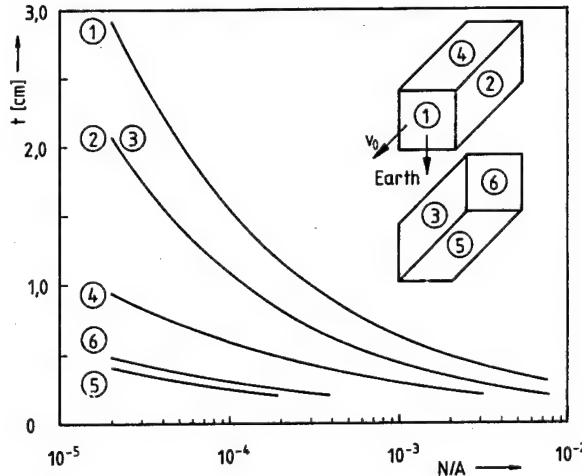


Fig. 12: Related number of impacts with perforation

Fig. 12 shows the number of impacts with perforation per surface area depending on the wall thickness (aluminum) for the six different surfaces of the box. If the wall thickness is equal for all faces it can be seen that the front face "1" will achieve the highest number of impacts which is a result of the velocity distribution and the relative velocity of the spacecraft. The surfaces "4", "5" and "6" will only be hidden by meteoroids and therefore they will have the lowest number of impacts.

If one designs the box such that the probability of no perforation is 0.995 per year by keeping the wall thickness constant for all surfaces this thickness has to be 1.59 cm which gives a mass of 8994 kg. If one varies the wall thicknesses such that the number of impacts per surface area is constant for all surfaces the following thicknesses are needed:

$$\begin{aligned} t_1 &= 2.66 \text{ cm} & t_2 &= 1.90 \text{ cm} \\ t_3 &= 1.90 \text{ cm} & t_4 &= 0.88 \text{ cm} & N/A &= 2.5 \cdot 10^{-5} \\ t_5 &= 0.38 \text{ cm} & t_6 &= 0.45 \text{ cm}. \end{aligned}$$

This results in a total mass of 7403 kg which means a 18 % reduction compared to the box with constant wall thickness.

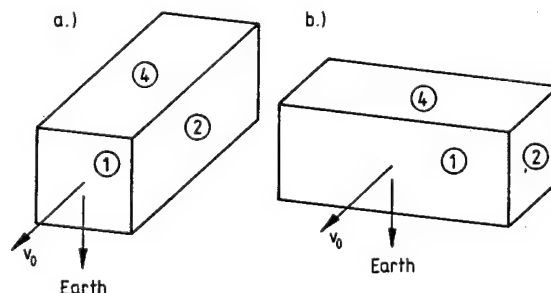


Fig. 13: Longitudinal and transversal orientation

If one changes the attitude of the box from longitudinal (Fig. 13a) to transversal orientation (Fig. 13b) a further mass decrease to 6868 kg is attainable. This can be explained by the fact that the surface area threatened by orbital debris is smaller in case of the transversal orientation.

The same strategies can also be applied to the double or the triple wall concept. It is obvious that this is not as easy as for the single wall concept. The same is valid for more realistic structures than rectangular boxes as there are for example cylindrical modules. A variation of the shield thickness over the surface area in order to equalize the related number of impacts is also suggested in that case.

5. CONCLUSIONS

Meteoroid and especially orbital debris impacts become a challenge for the design of future spacecraft. It was shown that presently not all problems are solved in order to allow an optimum design of protection concepts. The main reason is that extensive experimental and theoretical investigations are needed to understand all parameters influencing the impact behaviour. This is particularly valid for new up to now hardly considered concepts as for example the triple wall design planned for the COLUMBUS-APM. A main difficulty results from the limitation of available test facilities to velocities below 8 - 9 km/s.

The presented calculations have shown that careful design of protection measures will lead to considerable mass saving. The mass to be saved might be further increased if one develops other protection schemes like the multi-shock concept recently introduced by Cour-Palais (Ref. 20) or if one uses advanced materials in combination with advanced concepts as suggested by Christiansen (Ref. 21).

ACKNOWLEDGEMENTS

Part of the work described in this article was done under European Space Agency (ESA/ESTEC) contract with technical supervision by Mr. Lambert, which is gratefully acknowledged.

REFERENCES

1. Lundeberg J F & al 1965, Meteoroid Protection for Spacecraft Structures, NASA CR-54201.
2. Maiden C J & al 1965, Thin Sheet Impact, NASA CR-295.
3. Kinslow R (Ed.) 1970, High-Velocity Impact Phenomena, Academic Press, New York - London.
4. Humes D H 1965, Influence of the Bumper and Main Wall Material on the Effectiveness of Single Meteoroid Bumpers, NASA TN D-3104.
5. Nysmith C R 1968, Penetration Resistance of Double-Sheet Structures at Velocities to 8.8 km/s, NASA TN D-4568.
6. Wipple F L 1947, Meteorites and Space Travel, Astron. J., 52, 131.
7. Lainé R Felici F 1982, The Giotto Dust Protection System, ESA Bulletin, 32, 36-42.
8. Cour-Palais B G 1979, Space Vehicle Meteoroid Shielding Design, Proc Comet Halley Micrometeoroid Hazard Workshop, ESA SP-153, 85-92.
9. Space Debris, The Report of the ESA Space Debris Working Group, ESA SP-1109, 1989.
10. Cour-Palais B G 1969, Meteoroid Environment Model, NASA SP-8013.
11. Kessler D J 1984, Orbital Debris Environment Definition for Space Station, JSC 20001.
12. Frost V C 1970, Meteoroid Damage Assessment, NASA SP-8042.
13. DiBattista J D & al 1972, Multimaterial Lamination as a Means of Retarding Penetration and Spallation Failures in Plates, NASA TN-D-6989.
14. Cour-Palais B G 1985, Hypervelocity Impact Investigations and Meteoroid Shielding Experience related to APOLLO and SKYLAB, Orbital Debris - NASA Conference Publication 2360, 247-275.
15. Schonberg W P Taylor R A 1989, Oblique Hypervelocity Impact Response of Dual-Sheet Structures, NASA TM-100358.
16. Gehring J W & al 1965, Experimental Studies Concerning the Meteoroid Hazard to Aerospace Materials and Structures, J. Spacecraft, 2, 731-737.
17. Eichler P Rex D 1990, The Risk of Collision between Manned Space Vehicles and Orbital Debris - Analysis and Basic Conclusions, Z. Flugwiss. Weltraumforsch., 14, 145-154.
18. Bjork R L 1963, Review of Physical Processes in Hypervelocity Impact and Penetration, Proc 6th Symp on Hypervelocity Impact.
19. Anderson C E & al 1990, The Growing Challenge of Orbital Debris, SWRI-Short Course, San Antonio.
20. Cour-Palais B G & al 1990, A Multi-Shock Concept for Spacecraft Shielding, Int. J. Impact Engng, 10, 135-146.
21. Christiansen E L 1990, Advanced Meteoroid and Debris Shielding Concepts, AIAA/NASA/DOD Orbital Debris Conference: Technical Issues & Future Directions, Baltimore.

**SESSION
1.2.B**

**ANALYSIS
I**

DYNAMICS

PRECEDING PAGE BLANK NOT FILMED

N 9 2 - 2 3 7 8 7
84699

COUPLED LOAD ANALYSIS: SCATTER RELATED TO MODEL UNCERTAINTIES

P.W.Bousquet*, F.Mercier*, M.Klein**

*CNES, 18 AVENUE Edouard Belin, 31055 TOULOUSE CEDEX, FRANCE

**ESTEC, Postbus 299, NOORDWIJK 2200AG, THE NETHERLANDS

ABSTRACT

This work, carried out within the frame of a transient test feasibility study for ESTEC, is dedicated to the influence of spacecraft structural misrepresentation on Coupled Load Analysis (C.L.A.) results. The C.L.A.'s are performed using the equivalent force method and modal synthesis results. The study has a statistical approach in which regular Monte-Carlo procedures are applied to estimate C.L.A. scatter distribution.

Two main applications are presented ; both are limited to the launcher longitudinal axis, at one flight event (second stage burn-out), for an ARIANE 3 version. Firstly, we calculate an envelope for the shock spectra of any satellite compatible with the ARIANE user's manual in terms of modal characteristics. Results can be compared with ARIANE's first 15 flight measurements. Secondly, we simulate the influence of the uncertainties about the modal parameters (frequency and effective masses) of a given specimen. In this case, at certain frequencies, the greatest shock spectra can reach values twice as high as the nominal level.

KEYWORDS: Vibrations - Coupled Load Analysis - Statistical methods, Modal parameters, transient test.

1. INTRODUCTION

There is a tendency, in modern satellite manufacture, to reduce the margin between structural design loads and flight loads, at the start predicted by preliminary analyses. Moreover, C.L.A. again play a key role at the end of the development stage since test levels are expected to overtake their levels in all the frequency band. C.L.A. reliability is therefore essential; it depends on three sets of parameters:

- spacecraft structural representation,
- launch vehicle structural representation,
- excitation force estimation.

The study presented here is dedicated to the influence of the first set of parameters on C.L.A. accuracy. A statistical method is constructed that computes C.L.A. (characterized by shock spectra at launcher/spacecraft interface) scatter versus spacecraft modal parameter uncertainties. Such a method can be used to take into account various spacecraft misrepresentation origins such as:

- evolution during development,
- accuracy of the mathematical modelisation,
- variations between successive flight models.

This study was effected under a contract for ESA aimed at dimensionning on the basis of transient flight events and tests. However, its results could well be relevant for classical design methodologies.

2. TRANSIENT DESIGN AND TESTS

The option between transient tests or sinusoidal vibration tests is left open to the spacecraft authority in the ARIANE 4 user's manual, with respect to low frequency environment compatibility tests. However, the current practice is to use sinusoidal vibration tests, even though the true nature of the flight environment is transient.

Moreover, the transient loads computed from spacecraft/launcher coupled analysis tend to be taken into account earlier and earlier in spacecraft design, so that the sweep sine vibration tests performed during the validation phase need to be widely and deeply notched to avoid overtesting the spacecraft. This process does not always obtain the launcher authority agreement with ease.

Transient tests could represent an appropriate alternative to sine sweep vibration tests, since they are more representative of flight conditions. In order to evaluate their feasibility, an investigation was performed at CNES within the frame of an ESA contract started in 1985 for ARIANE class satellites (Ref. 1). The practical feasibility of transient testing was demonstrated using ARABSAT STM spacecraft, and a conventional electrodynamic shaker.

These investigations were extended to the dimensioning aspect at the end of 1989 under the form of a contract for ESA entitled "Dimensioning of spacecraft structures on the basis of transient flight events and tests". The final objective is to elaborate a complete methodology including design and appropriate testing. Both phases need reliable C.L.A. Moreover, the capacity to perform sensitivity analyses on C.L.A. to spacecraft representation is primordial:

- since the design is performed at an early stage with preliminary C.L.A., the uncertainty due to the evolution of the spacecraft during its development must be taken into account;
- if a qualification test is to be performed, the influence on C.L.A. of the variations between successive flight models has to be evaluated.

3. GENERAL HYPOTHESES

The aim of this study is to demonstrate the feasibility of a statistical treatment of the uncertainties associated to some input parameters in C.L.A., and to evaluate an order of magnitude of the scatter on the results. There is no need for the demonstration to be exhaustive and, therefore, this presentation is restricted to:

- one flight event: second stage burn-out (this event is generally the most demanding on spacecraft structure),
- one axis: longitudinal,
- one launcher: ARIANE 3,
- one launch configuration: double launch, upper position on Sylva.

Modal synthesis results are preferred to physical models for performance reasons. The C.L.A. are calculated with the equivalent force method (Ref. 2), using input data obtained during the previous study (Ref. 1). It is assumed that the launcher dynamic characteristics and the excitation forces are perfectly known. Therefore, $M_S(w)$ is the only member that will be scattered, in the left part of the equation below.

$$\chi(\omega) = \frac{F^*(\omega)}{M_1(\omega) + M_S(\omega)}$$

The acceleration at interface will be characterized here by its shock spectrum, but the strength at interface and the modal responses have also been investigated.

4. MONTE-CARLO SIMULATION (REF. 3, REF. 4)

This statistical method consists of building up many systems by computer calculation and evaluating the performance of such synthesized systems. This method is particularly efficient in evaluating the behaviour of a system modelised with a great number of input parameters (here the satellite modal characteristics) involved in a complex, non linear process. We assume that the input parameters follow independent identical probability distributions. The output parameter is chosen as the relative shock spectrum between 0 and 100 Hz of the acceleration at the launcher/satellite interface. This shock spectrum is sampled over 100 frequencies so that there are actually 100 output parameters. We concentrate the estimation procedure on the maximum value of the shock spectrum reached at each of the sampled frequencies.

Because the Monte-Carlo method involves random values, the results are subject to statistical fluctuations. Thus, any estimate will not be exact but will have an associated error band. In practice, the concept of confidence level can be used to represent the accuracy of the results. The larger the number of trials in the simulation, the higher the confidence.

In the general case, let x be a random variable with 2 possible outcomes A and \bar{A} ; we wish to estimate the probability P_A that the outcome of x is A .

We know that n_A outcomes out of a number of N trials were A . By using the binomial law, we can assume with a confidence level $(1 - C)$ that P_A lies between P_1 and P_2 , where:

$$P_1 \text{ is such that } \sum_{n=n_A}^N C_N^n P_1^n (1-P_1)^{N-n} = \frac{C}{2}$$

$$P_2 \text{ is such that } \sum_{n=0}^{n_A} C_N^n P_2^n (1-P_2)^{N-n} = \frac{C}{2}$$

In our case, at a given frequency, the random variable x is the value of the shock spectrum, the outcome A is "x higher than the maximum value reached during N trials", and n_A is therefore equal to 0. We are interested only in finding an upper boundary for P_A , so we can tell with a level of confidence $(1 - C)$ that $P_A < P_2$,

$$\text{where } \sum_{n=0}^0 C_N^n P_2^n (1-P_2)^{N-n} = C$$

$$\text{which becomes } (1-P_2)^N = C$$

Figure 1 shows the value of $1-P_2$ as a function of the sample size N for several values of $(1-C)$.

For practical reasons, we will limit N to 625 trials and the confidence level $1-C$ to 95 %, which give $P_2 = 0.48$ %. This means that at any frequency, for any satellite of the family, with a confidence level of 95 %, the probability that the value of the shock spectrum lies above the computed upper boundary is less than 0.5 %.

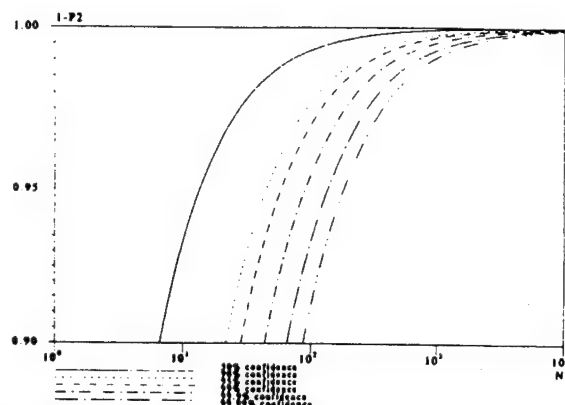


fig.1: Success probability as a function of the number of trials

5. RESULTS

5.1 General scatter of satellite characteristics

The main goal of this part is to build a global envelope for the shock spectra of all reasonable satellites that could be found in reality. This is a system study, in which synthetic satellites are generated and their responses analysed. During this process, the individual modes used have no relationship to a specific spacecraft mathematical model.

5.1.1 Definition of the satellite characteristics domain

In order to be consistent with the available launcher model (ARIANE 3, double launch upper position), the rigid mass of all satellites is kept equal to 1 000 kg. Each satellite has 10 dynamic modes.

Based on a set of existing satellites and considering design constraints, synthetic satellites are generated. This is done by varying the general modal properties (i.e. frequencies and modal masses) in a random way within bounds. The constraints which have to be respected by the repartition law chosen to draw the satellite modal characteristics are :

- to respect the Ariane 4 manual (all modes above 31 Hz),
 - to be realistic (in practice, a large amount of the longitudinal dynamic mass must be present below 60 Hz).
- Since the scope of this scatter analysis is not to be universal but rather, to cover reasonably a very wide range of cases, we defined the parameters as follows :
- the damping factors are all equal to 2.5 %,
 - the frequency of each of the 10 modes is chosen at random between 31 and 100Hz with a uniform repartition,
 - their effective masses are chosen at random between 0 and 1 000 kg with a uniform law, and are then multiplied by a coefficient C in order to guarantee a large amount of masses in the low frequency domain,

$$C(f_{\text{mode}}) = \left[0.6 + 0.4 \cos\left(\pi \frac{f_{\text{mode}} - 31}{69}\right) \right]^2$$

- the residual mass is chosen at random between 0 and 400 kg with a uniform law,
- a factor of scale is applied to the effective masses so that all rigid body masses stay equal to 1 000 Kg.

The cumulated effective mass diagrams of the 625 satellites randomly chosen with this method are shown in Figure 2. It can be seen that a large domain is covered.

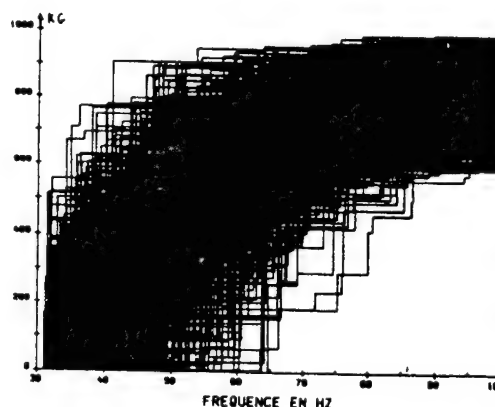


fig.2: general scatter, cumulated effective masses

5.1.2 Results

The transient responses and the absolute shock spectra corresponding to the acceleration at satellite/launcher interface obtained with each of the 625 drawn out satellites are computed. Figure 3 shows the envelope above and below these shock spectra, their average, and their standard deviation.

The damping factor of the oscillators taken into account in the calculation of the spectrums is 2.5 %.

It can be seen that apart from the zone around 50 Hz, the scatter of the results is very large. The level of the 2 peaks at 26 Hz and 34 Hz reaches values above 20 g's, which corresponds to an equivalent sine at interface above 1 g.

Above 35 Hz, the equivalent sine level always stays below 0.5 g apart from the zone between 65 Hz and 80 Hz. It is interesting to compare these results with the 15 ARIANE first flight measurements, where the equivalent sine was always below 0.5 g above 40 Hz (Ref. 5).

According to the developments detailed in 3.1, we can say with a confidence level of 95 % that 99.5 % of the shock spectrum of satellites within the domain we defined will be below the upper curve,

i.e. $P(\text{to exceed the upper curve}) = 0,5 \%$.

It seems, however, impractical to use this curve directly in a design process because the levels it reaches are relatively high. A specimen based approach in which reduced scatter is used is described in the next section.

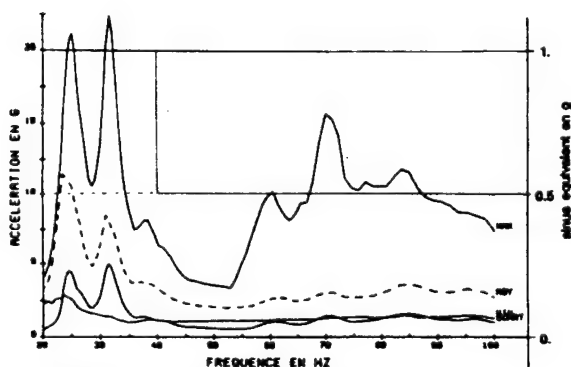


fig.3: general scatter, shock spectrum envelope

5.2 Specimen scatter of satellite characteristics

The objective of this part is to evaluate the scatter of C.L.A. results due to the uncertainties about the mathematical model of a specific satellite, called hereafter the "specimen". It is assumed here that the basic frequencies and effective modal masses result from that mathematical model.

The factors which are responsible for these uncertainties are beyond the scope of this study ; we assumed an arbitrary domain centered on the basis of the specimen's theoretical model and considered that the real model could be anywhere within this domain.

5.2.1 Definition of the satellite characteristics domain

The cumulated effective mass diagram of the specimen can be seen in figure 4, and its dynamic mass in figure 6. Its rigid mass is 1150 kg and its residual mass 184 kg. The damping factors of its modes are all equal to 2.5 % and will not be scattered.

In order to be realistic, we considered that the relative errors, in terms of modal frequency and effective mass, increase as the effective mass of the mode decreases.

More precisely, we assumed that a mode with characteristics (m_0, f_0) could be shifted with a uniform probability within the intervals:

$$[m_0(1-\Delta m_0), m_0(1+\Delta m_0)], [f_0(1-\Delta f_0), f_0(1+\Delta f_0)]$$

$$\Delta m_0 = m_0^{-0.482}$$

$$\text{where: } \Delta f_0 = \frac{1}{5} m_0^{-0.223}$$

These laws are indeed arbitrary though they do seem to give typical figures, since we get for example:

$$\begin{cases} \Delta m_0(500 \text{ Kg}) = 5 \% \\ \Delta f_0(500 \text{ Kg}) = 5 \% \end{cases} \quad \begin{cases} \Delta m_0(5 \text{ Kg}) = 46 \% \\ \Delta f_0(5 \text{ Kg}) = 14 \% \end{cases}$$

These variations have the same order of magnitude as variations found in practice (Ref. 5).

Figure 4 shows the cumulated effective masses diagram of the specimen and the boundaries of the cumulated effective masses of all the satellites chosen according to the laws specified above. The residual mass bar charts of these satellites stays between 120 kg and 240 kg.

Figure 5 shows the envelope of the dynamic masses of the chosen satellites, with the dynamic mass of the specimen in dotted lines.

Figure 6 shows the envelope of the dynamic mass of the specimen, the dynamic mass of the launcher and the dynamic mass of the composite which is the sum of the previous two. It is clear that the characteristics of the specimen are predominant above 40 Hz.

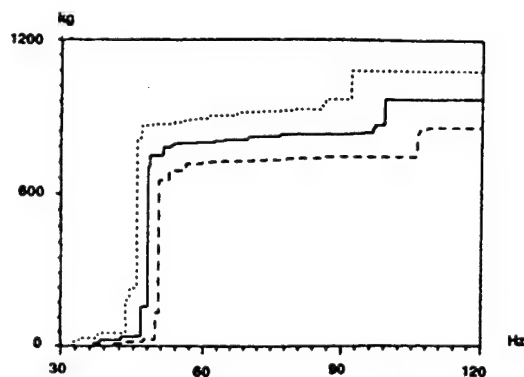


fig.4: specimen scatter, cumulated effective masses

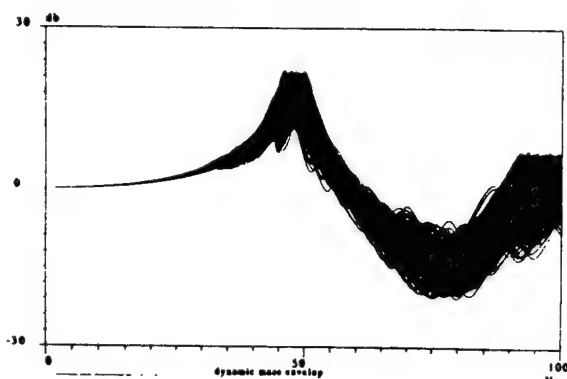


fig.5: specimen scatter, dynamic masses

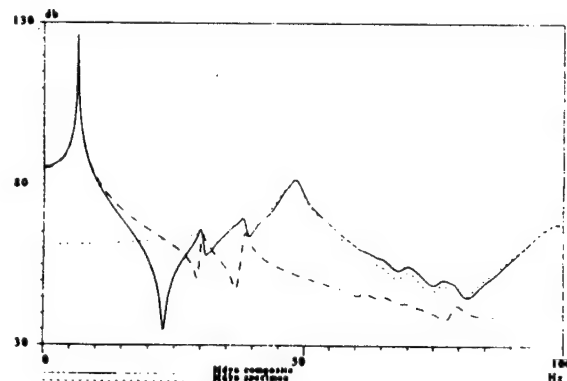


fig.6: launcher and specimen dynamic masses

5.2.2 Results

Figure 7 shows the envelope of the shock spectra obtained for each of the 625 satellites, their average, and the shock spectrum of the specimen. According to the Monte Carlo approach developed in chapter 3, the upper curve will be passed by less than 0.5 % of satellites in the defined domain, with a confidence level of 95 %.

It can be seen that the average curve stays close to the specimen curve, and that the scatter can be rather high, particularly around 70 Hz and 85 Hz. The peaceful zone between 45 Hz and 55 Hz is again present; the maximum value of the shock spectrum, above 35 Hz, stays below 10 g's, which corresponds to 0.5 g for the equivalent sine.

Figure 8 shows the envelope of the shock spectra obtained for the scatter around the specimen as line —, which stays within the envelope of the shock spectra obtained for the general scatter of paragraph 4.2., shown as line -----. It can be seen that both maximum curves present the same shape.

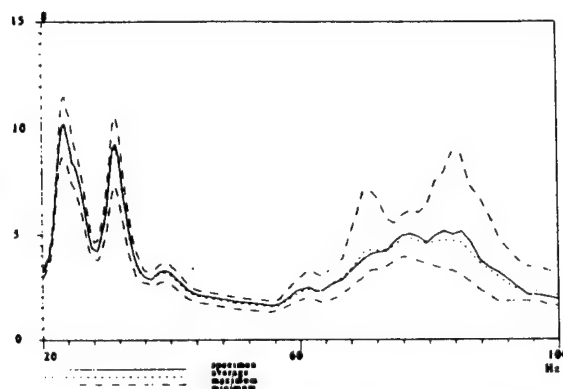


fig.7: specimen scatter, shock spectrum envelope

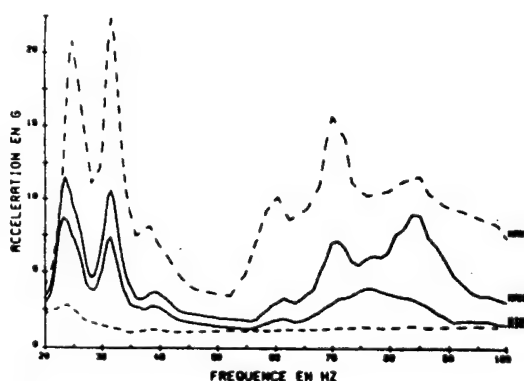


fig.8: specimen scatter and general scatter results

6. CONCLUSION

The primary achievement of this research is its demonstration of the feasibility of statistical treatment based on the Monte-Carlo method of Coupled Load Analyses over relatively large sample ranges (up to 625 samples) for the price of reasonable computer time (1 h C.P.U. on a CDC CYBER 180-992-31 for the largest simulations).

With the limitation of the hypotheses exposed in Chapter 2, and keeping in mind the arbitrary nature of the satellite characteristics scatter ranges, defined throughout Chapter 4 and 5, the main conclusions about shock spectrum scatter are :

- all simulations show little scatter for a zone of the shock spectrums around 50 Hz, which is in agreement with practical experience,
- for a moderate scatter range of effective masses and modal frequencies around the characteristics of a specimen, the scatter of the shock spectrum can be very large particularly above 70 Hz,
- great care has to be taken about the representativity of a model in the frequency bands with low effective mass density.

This statistical approach seems therefore, performant in determining influent spacecraft parameters on C.L.A. results. However, this worthy, qualitative performance cannot be extended to a true quantitative stage unless the probability densities concerning the spacecraft modal parameters scatter are known with reasonable accuracy. The scatter range assumed for the specimen study (Chap. 5.2) is consistent with the results of a study dedicated to this problem (Ref. 6), but the exact shape of the probability densities is difficult to evaluate with precision and will depend on the phenomena one wants to take into account (evolution during development, accuracy of mathematical modelisation, variation between successive flight models...). Moreover, depending on these phenomena, there might be some correlation between the parameter scatter of the versions mode.

This study hopes to stimulate a fuller exploitation of C.L.A. by spacecraft authorities. Such an approach would seem absolutely necessary when the sensitivity of C.L.A. to spacecraft, particularly in the upper frequency band, is born in mind. A next stage would be to extend it to the scatter of the internal stresses in the spacecraft.

7. REFERENCES

- REF. 1: Electrodynamic transient test - ESTEC Contract n° 6328/85/NL/PB, CNES, January 1988, final report.
- REF. 2: Interaction dynamique lanceur charge-utile - J.P. Morand, B. Chemoul et P.R. Bodagala, CNES Evry, ESA SP-238.
- REF. 3: Statistical models in Engineering - Hahn et Shapiers, John Wiley and Sons, New-York.
- REF. 4: Probabilité et statistiques en recherche scientifique A. Rosengard, Dunod.
- REF. 5: Résultat des vols du lanceur ARIANE et leurs effets sur le dimensionnement des structures satellites - M. Vedrenne, JP. Dulot, JL. Caneilles - ESA-SP-238.
- REF. 6: Dimensioning of satellite structures verified by transient test - ESTEC Contract n° 8221/89/NL/PH/SC - WP. 2.3, C. Vidal, AEROSPATIALE Cannes.

THE USE OF MODAL SYNTHESIS IN CONJUNCTION WITH NON-LINEAR TRANSIENT DYNAMIC ANALYSIS

N 92-23788

84700

S.A. Challener, A.J. Vibert

Frazer-Nash Consultancy
Leatherhead
England

ABSTRACT

Two methods by which modal synthesis can be used as part of a non-linear dynamic analysis are presented. The first method is based on the DYNA3D finite element code and describes the approach taken to incorporate a modal synthesis capability in the code. The second method is demonstrated for a missile rail launcher for which a particular computer code was developed based on the modal synthesis approach. Examples of both of the methods are presented.

Keywords: modal synthesis, DYNA3D, rail launcher.

under impact conditions. When considering the impact of a structure it can be expected that the part of the structure directly involved in the impact will undergo large strains and plastic deformation. Other parts of the structure away from the impact zone may remain linear and can therefore be modelled by modal properties. The implementation of modal synthesis in DYNA3D utilises the standard code features of discrete masses and spring elements to represent modal mass and stiffness but introduces a feature called multicoupling to enable the modal substructure to be connected to the main finite element model. The approach is summarised in Figure 1.

1. MODAL SYNTHESIS

Modal synthesis techniques are widely used in the aerospace industry to analyse a variety of dynamic response applications. They use the normal modes of vibration of a structure to describe its overall dynamic response. Each mode of the structure becomes a single degree of freedom in a numerical solution. This compares with the finite element approach where a system is described by a series of nodes each of which may have up to six degrees of freedom, corresponding to translation and rotation in the global axis system.

A major advantage of modal synthesis becomes apparent when one considers that the dynamic response of a structure is usually dominated by a relatively small number of modes. The structure can therefore be modelled by a few degrees of freedom instead of the hundreds or thousands of degrees of freedom required for a finite element model. Computation time can therefore be dramatically reduced.

The main limitation of modal synthesis is that it can only be used for structures that behave linearly. Frazer-Nash Consultancy has widened the scope of application by developing a method by which modal synthesis can be used in conjunction with non-linear analysis. Parts of a structure which behave linearly can be represented by modal properties and connected to other parts of the structure which exhibit non-linear behaviour. This approach has been implemented by Frazer-Nash Consultancy in the DYNA3D finite element code and has also been incorporated into a code for simulating the release of a rail launched missile.

2. MODAL SYNTHESIS IN DYNA3D

DYNA3D is a very powerful non-linear transient analysis code which is widely used for the analysis of structures

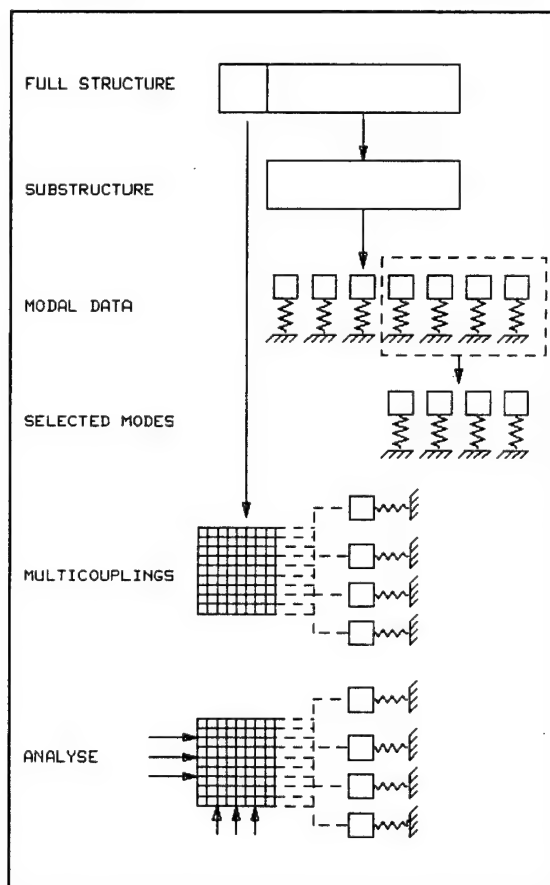


Figure 1: Modal Synthesis Approach

2.1 Cylinder Model

A validation case of an infinite cylinder under a half-cosine distributed pressure pulse has been analysed for the following:

- DYNA3D with 20 elements
- DYNA3D using modal synthesis

and compared with an analytical solution. The following modes were included in the model:

- rigid body translation
- five lowest frequency extensional modes
- five lowest frequency bending modes.

The results show that the modal synthesis results are in closer agreement with the analytical solution than the 20 element model. The comparative model run times were:

Case	Run Time
20 element model	312s
modal synthesis	203s

from which it can be seen that a run time saving of 35% has been achieved.

2.2 Bar Impact Model

The example of a copper bar impacting a rigid surface was chosen for a second example of the use of modal synthesis within DYNA3D. In this case the bar material is non-linear and a considerable amount of non-linear behaviour occurs as shown in Figure 2. However the results from the standard case show that the top half of the bar remains in the elastic region of material behaviour. It is thus possible to replace this part of the model with a modal representation.

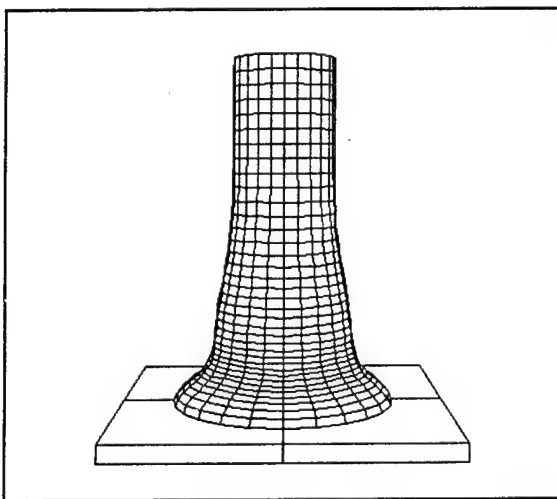


Figure 2: Bar Impact

One may intuitively suggest that the top half of the bar could be replaced by lumped masses attached to the bottom half as the main effect will be that of mass loading. This is of course a form of modal synthesis, in which only the rigid body modes are chosen.

In this case the top half of the bar was analysed using ABAQUS to obtain the first ten modes in terms of modal mass and stiffness and the modal displacement at each node on the end face. These modes were incorporated into a DYNA3D model with the lower half being modelled with brick elements. The modal masses were connected to the rest of the model using multicouplings.

The initial velocity loading was applied to the brick elements and also to the rigid body modal mass.

The results show good agreement with the results of the standard case.

This example shows that the modal synthesis approach can be used even where in parts of the structure large plastic deformation is occurring. Significant run time savings were obtained for this case, the time reducing from 23420 secs to 12410 secs showing a 47% reduction in run time.

2.3 Pipe Impact Model

The behaviour of a pipe under impact conditions is of interest in a wide range of engineering applications. An example of such a case has been analysed using a full finite element mesh and also making use of the modal synthesis capability in DYNA3D. A cylindrical bar travelling at 114 m/s strikes a pipe at the centre of an unsupported span as shown in Figure 3. The final deformed shape is shown in Figure 4. Making use of symmetry only one quarter of the pipe was modelled.

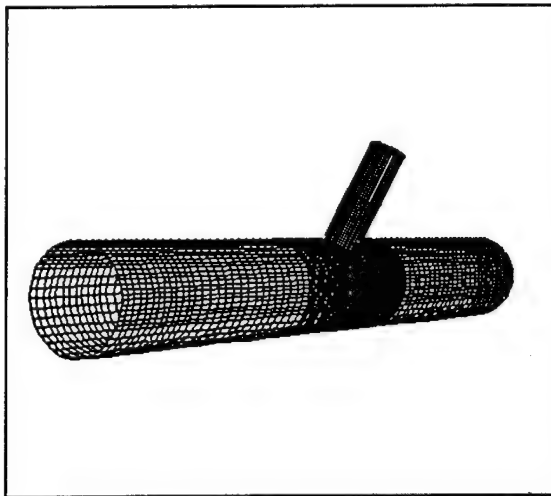


Figure 3: Pipe Impact Model

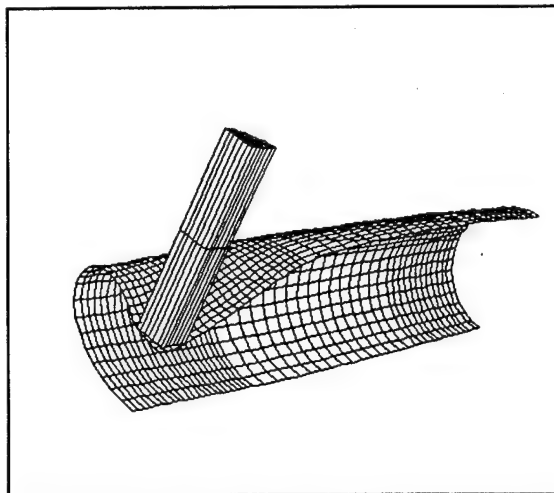


Figure 4: Deformed Shape

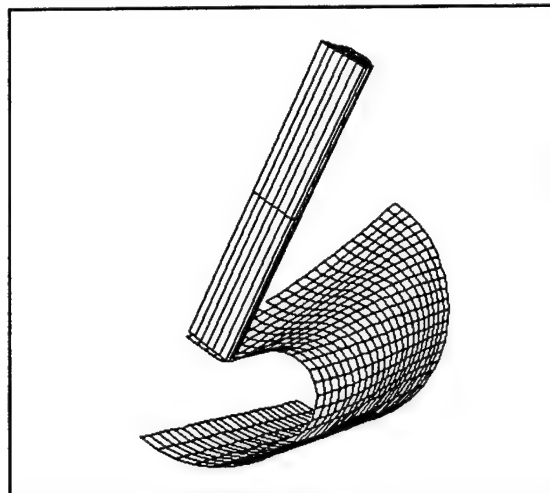


Figure 5: Modal Synthesis Model

Modal synthesis was then used to represent the part of the pipe away from the impact. Fourteen modes as given in Table 1 were used for the modal representation.

MODE NO	FREQUENCY (RAD/TIME)	GENERALIZED MASS
1	3802.	2.11495E-03
2	5157.	1.14899E-03
3	8968.	1.33526E-03
4	13909.	8.25524E-04
5	14618.	2.91635E-03
6	14987.	1.05952E-03
7	16931.	3.58730E-03
8	17496.	1.26719E-03
9	18241.	1.08620E-03
10	23564.	1.15058E-03
11	25747.	2.44305E-04
12	25974.	8.02551E-04
13	26350.	8.83247E-04
14	26954.	1.81780E-03

Table 1: Modal Parameters

The final deformed shape of the model is shown in Figure 5. Once again, symmetry conditions led to only one quarter of the pipe being modelled.

A computer run time saving of 47% was achieved for this model.

3. RAIL LAUNCHER MODEL

The application of modal synthesis techniques to the simulation of the launch event for a rail launched missile is quite novel. As discussed earlier, classical examples of

modal synthesis involve the analysis of systems where the structural response of the system is perfectly linear and coupling between modal substructures is at discrete points. The dynamic response of a rail launched system is geometrically highly non-linear since there are no fixed points of contact between the missile and the launcher. In fact the coupling between the two substructures varies continuously as the missile travels down the rail. Moreover, the number of coupling points reduces as each missile hook reaches the end of the rail.

The geometric non-linearities described would under most circumstances render a modal synthesis approach invalid. However, the use of an explicit integration scheme allows us to effectively uncouple the two substructures and handle interaction between the two components in terms of variable internal forces generated in the hooks. The internal forces are applied to the substructures in a similar way to the external aerodynamic and manoeuvre loads. The two substructures can now be considered to be geometrically linear systems which are subjected to a number of forces whose magnitudes vary during launch. These linear systems can then be analysed using modal synthesis techniques.

A typical rail launcher layout is shown in Figure 6, and two representations of it are presented in Figure 7. The finite element representation contains 216 degrees of freedom, whilst the modal model requires only 22 degrees of freedom to be representative up to a frequency of 2000 Hz. The analysis time for this model is significantly reduced over that of the finite element model.

As has already been indicated the novelty in the Frazer-Nash Consultancy rail launcher simulation program lies in its ability to handle the variable coupling between the modal substructures. This task is performed by special purpose hook elements. These elements perform two

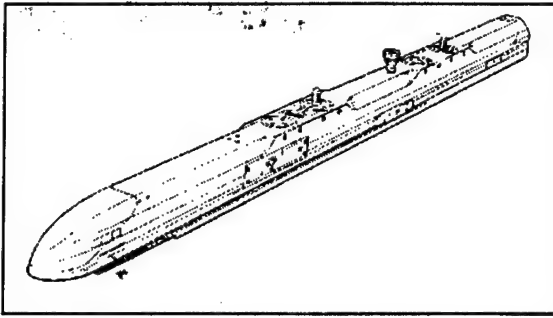


Figure 6: Typical Rail Launcher

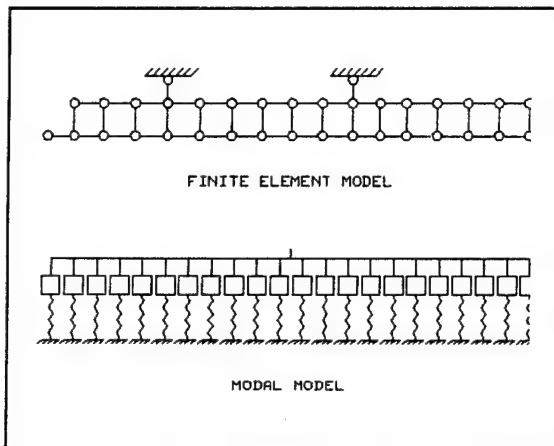


Figure 7: Rail Launcher Model

functions. Firstly they interpolate the mode shapes along the launcher rail in order to calculate the correct coupling coefficient depending on the exact location of each missile hook. Secondly each hook element behaves like a discrete spring, modelling the flexibility of the hook and the local flexibility of the rail, whilst calculating the interface forces between the two components. Before the hook forces can be calculated it is necessary to obtain the physical displacements at the two ends of the spring from the current modal amplitudes. The difference in the displacements of the two ends corresponds to the extension in the spring and hence the hook force can be calculated from its stiffness.

Once the interface forces and the correct coupling coefficients have been calculated the generalised forces for each mode can be calculated and the dynamic simulation continued by the explicit integration technique.

The dynamic simulation provides time histories for the modal amplitudes (displacements), modal velocities and accelerations. The physical displacements, velocities or accelerations at any particular point of interest can be obtained easily by post processing the modal results. The simulation also provides time histories of the interface forces. Typical hook force responses of a two hook

missile are presented in Figure 8. The discontinuities occur when the hooks detach from the rail.

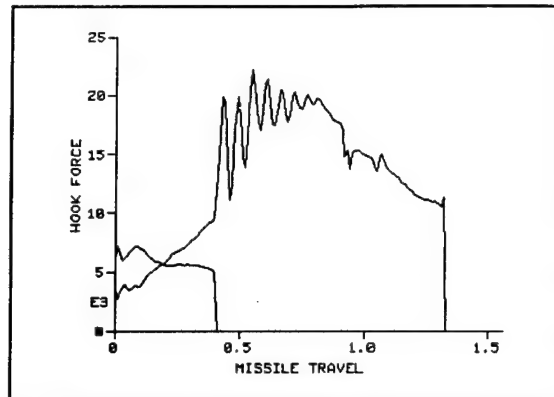


Figure 8: Typical Hook Force Responses

The simulation program tracks the response of the missile from the instant at which the total forward force on the missile exceeds the detent force up to the point where the rear of the missile passes the front of the launcher. Conceptually there is no reason why the simulation could not continue further into the free-flight regime. However, it must be emphasised that such an extension would require a full and accurate description of the inertial and aerodynamic forces acting on the missile.

The simulation also checks for boat tailing where the rear of the missile contacts and slides along the rail of the launcher. The program can also cater for the situation where one hook may detach prematurely if the effective rail lengths are different for the different hook positions.

4. CONCLUSIONS

Modal synthesis, which traditionally has been used only in completely linear analyses has been shown to be a viable technique in conjunction with non-linear analysis. A modal representation of linear parts of a structure can be connected by the use of special couplings to a non-linear finite element model where both material and geometric non-linearities may be present. This technique has been implemented for the well respected DYNA3D code.

The second approach to a non-linear application of modal synthesis uses special elements to provide non-linear coupling between modal models.

The methods can lead to significant reductions in model size and computer run times without compromising the accuracy of the results.

5. ACKNOWLEDGEMENTS

The development of a modal synthesis capability for DYNA3D was carried out under contract to Ministry of Defence, AWE, Aldermaston under the supervision of Mr. H.C. Kernthaler.

N92-23789

IMPROVEMENTS FOR INTERPRETATION OF STRUCTURAL DYNAMICS CALCULATION USING EFFECTIVE PARAMETERS FOR SUBSTRUCTURES

T. BERTHELON

A. CAPITAINÉ

MATRA Space Branch
Department of Mechanical Engineering
Toulouse (France)

ABSTRACT

In the past few years, with the extensive use of the finite element method, the concept of effective masses has been introduced to analyse the satellites structure. Up to now, the results used were applied to the whole system.

In this paper, we propose to transfer the use of effective parameters from the whole structure to all the subsystems, in order to define precisely which part of the spacecraft will tend to vibrate.

This note presents the theoretical study, the introduction of the new effective parameters and some example.

1. INTRODUCTION

The effective parameters characterize the different free-clamped eigenmodes of a structure, in order to estimate the response to an excitation at the base.

This concept, born in the seventies, is very useful for the satellites design. The principal parameter, the effective mass matrix, is necessary to determine the importance of the interface loads, between the launcher and the spacecraft, introduced by each mode. However, for a non global mode, it is impossible to determine the local importance and which part of the satellite creates these loads. For example, a local mode may be critical for an appendice, without giving high loads at the spacecraft/launcher interface.

Up to now, the solutions to solve these problems have been to "plot" the deformed shape, and to calculate the response at a base excitation in the three axes. This is a long procedure and the visualisations are not always very simple to analyse. That is the reason why we tried to develop new effective parameters in order to get information for every substructures.

This paper, after describing the existing theory, develops the new concept of effective parameters by subsystem.

Finally, we give some examples to illustrate the use of this new concept in mechanical analysis.

2. THEORY

2.1 Global effective parameters (recall of basic theory)

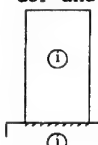
This theory uses the modal superposition method. It applies to slightly damped structures modeled by a viscous damping equivalent : the modal damping. The movement equations system for the finite element model can be written by this matricial equation :

$$M \ddot{q}(t) + C \dot{q}(t) + k q(t) = F(t) \quad (1)$$

Hypothesis 1

Consider a structure with n nodes M_i and support node R , whose degrees of freedom will be used to define rigid body displacements (3 translations and 3 rotations). This support realises an isostatic interface.

When we decompose the displacement vector in support doF and its complementary :



$$q = \begin{bmatrix} q_j \\ q_i \end{bmatrix} \quad \begin{array}{l} q_j : \text{support doF known} \\ q_i : \text{interior doF (unknown)} \end{array}$$

$$F = \begin{bmatrix} F_j \\ F_i \end{bmatrix} \quad \begin{array}{l} F_j : \text{reaction at the support} \\ F_i : \text{force known} \end{array}$$

The relation 1 becomes :

$$\begin{bmatrix} M_{jj} & M_{ji} \\ M_{ij} & M_{ii} \end{bmatrix} \begin{bmatrix} \ddot{q}_j \\ \ddot{q}_i \end{bmatrix} + \begin{bmatrix} C_{jj} & C_{ji} \\ C_{ij} & C_{ii} \end{bmatrix} \begin{bmatrix} \dot{q}_j \\ \dot{q}_i \end{bmatrix} + \begin{bmatrix} K_{jj} & K_{ji} \\ K_{ij} & K_{ii} \end{bmatrix} \begin{bmatrix} q_j \\ q_i \end{bmatrix} = \begin{bmatrix} F_j \\ F_i \end{bmatrix} \quad (2)$$

mass matrix damping matrix stiffness matrix

In the case of a base excitation, the displacement results in a rigid body movement and an elastic deformation :


$$q_i = \phi_{ij} q_j + \psi_{ik} \eta_k \quad (3)$$

Driving movement
due to the junction

Relatif movement
decomposed in a
eigenmode base

With :


- ϕ_{ij} : rigid body vectors which are solutions of $K\phi = 0$ and defined with a unit displacement of each support d.o.f. :

$$\begin{bmatrix} K_{ij} & K_{ji} \\ K_{ji} & K_{ij} \end{bmatrix} \begin{bmatrix} 1 \\ \phi_{ij} \end{bmatrix} = \begin{bmatrix} 0 \\ 0 \end{bmatrix} \Rightarrow \phi_{ij} = -K_{ii}^{-1} K_{ij} \quad (4)$$


- Φ_{ik} : eigen vector of the structure clamped at the base and solution of

$$(-\omega_k^2 M_{ii} + K_{ii}) \Phi_{ik} = 0 \quad (5)$$

ω_k eigenvalue



η_k are the generalized coordinates associated with the elastic eigen vectors.

When we apply the transformation $q = \Phi \begin{bmatrix} q_j \\ \eta_k \end{bmatrix}$ to the relation 2.

$$q = \begin{bmatrix} q_j \\ q_i \end{bmatrix} = \Phi \begin{bmatrix} q_j \\ \eta_k \end{bmatrix} = \begin{bmatrix} 1 & 0 \\ \phi_{ij} & \Phi_{ik} \end{bmatrix} \begin{bmatrix} q_j \\ \eta_k \end{bmatrix} \quad (6)$$

We obtain :

$$\begin{bmatrix} \bar{M}_{ij} & L_{jk} \\ L_{kj} & \bar{m}_{kk} \end{bmatrix} \begin{bmatrix} \dot{q}_j \\ \dot{\eta}_k \end{bmatrix} + \begin{bmatrix} 0 & 0 \\ 0 & \bar{c}_{kk} \end{bmatrix} \begin{bmatrix} \dot{q}_j \\ \dot{\eta}_k \end{bmatrix} + \begin{bmatrix} 0 & 0 \\ 0 & \bar{k}_{kk} \end{bmatrix} \begin{bmatrix} q_j \\ \eta_k \end{bmatrix} = \begin{bmatrix} F_j + \phi_{ji} F_i \\ \phi_{ki} F_i \end{bmatrix}$$

$$\begin{aligned} L_{kj} &= \Phi_{ki} (M_{ij} + M_{ji} \phi_j) && \text{modal participation matrix} \\ \bar{m}_{kk} &= \Phi_{ki} M_{ii} \Phi_{ik} && \text{generalized mass diagonal matrix} \\ \bar{k}_{kk} &= \Phi_{ki} K_{ii} \Phi_{ik} && \text{generalized stiffness diagonal matrix} \\ \bar{c}_{kk} &= 2 \xi_k K_{kk} \mu_k && \text{generalized damping diagonal matrix} \\ \bar{M}_{ij} &= \Phi^T M \Phi && \text{rigid body mass matrix} \end{aligned} \quad (7)$$

The second line of relation (7) gives an uncoupled equation allowing to write.

$$\eta_k = \frac{\left[\frac{H_k(\omega)}{K_k} \right] (\Phi_{ki} F_i + \omega^2 L_{kj} q_j)}{1 - (\omega/\omega_k)^2 + 2j \xi_k \omega/\omega_k} \quad (8)$$

For the excitation the solution of dynamic equation (7) is the transfer matrix following :

$$\begin{bmatrix} q_j \\ F_j \end{bmatrix} = \begin{bmatrix} \tilde{G}_{jj}(\omega) & \tilde{T}_{ij}(\omega) - M_{ii}^{-1} M_{ij} \\ -\tilde{T}_{ij}(\omega) + M_{ij} M_{ii}^{-1} & -\omega^2 \tilde{M}_{jj}(\omega) - \omega^2 (M_{ij} - M_{ji} M_{ii}^{-1} M_{ij}) \end{bmatrix} \begin{bmatrix} F_i \\ q_i \end{bmatrix}$$

$$\begin{aligned} T_k(\omega) &= 1 + (\omega/\omega_k)^2 H_k(\omega) \\ \tilde{G}_{jj}(\omega) &= \sum_k T_k(\omega) \Phi_{kj} \Phi_{kj} / m_k && \text{dynamic flexibility matrix} \\ \tilde{M}_{jj}(\omega) &= \sum_k T_k(\omega) L_{jk} L_{kj} / m_k && \text{dynamic mass matrix} \\ \tilde{T}_{ij}(\omega) &= \sum_k H_k(\omega) \Phi_{kj} L_{kj} / m_k && \text{dynamic transmissibility matrix} \end{aligned} \quad (9)$$

Hypothesis 2

We also consider that the internal forces F_i are null, so that the dynamic equation has explicit solutions for q_j and F_j .

$$q_i = (\tilde{T}_{ij}(\omega) - M_{ii}^{-1} M_{ij}) q_j \quad (10)$$

$$F_j = -\omega^2 \tilde{M}_{jj}(\omega) q_j - \omega^2 (M_{ij} - M_{ji} M_{ii}^{-1} M_{ij}) q_j \quad (11)$$

We are going to consider the forces F_j , which are the reactions at the base due to an acceleration of $-\omega^2 q_j$. We notice that the contribution of each mode is the product of an amplification coefficient $T_k(\omega)$ and a matrix $(L_{jk} L_{kj} / m_k)$ which depends only on the mode and which characterizes the importance of each mode for a dynamic response. This matrix is known as the effective mass matrix $\tilde{M}_{ij,k}$

$$\tilde{M}_{ij,k} = L_{jk} L_{kj} / m_k \quad (12)$$

The reactions at the base can be expressed by

$$F_j = \sum_k T_k(\omega) \tilde{M}_{ij,k} \ddot{q}_j + F_j' \quad (13)$$

$$\text{with } F_j' = (M_{ij} - M_{ji} M_{ii}^{-1} M_{ij}) \ddot{q}_i \quad (14)$$

We also introduce the effective transmissibility

$$\tilde{T}_{ij,k} = \Phi_{ik} L_{kj} / m_k \quad (15)$$

in order to simplify the expression of q_i :

$$q_i = \sum_k T_k(\omega) \tilde{T}_{ij,k} q_j + q_i' \quad (16)$$

$$\text{with } q_i' = M_{ii}^{-1} M_{ij} q_j \quad (17)$$

The amplification coefficient $T_k(\omega)$ is very significant when $\omega = \omega_k$, especially when the modes are uncoupled and the damping coefficients are small.

Remarks :

For $\omega = \omega_k$ the reactions can be estimated to be very close to :

$$F_j = \tilde{M}_{ij,k} / (2j \xi_k) \ddot{q}_j \quad (18)$$

All the equations above are relations between matrices, but we often use only the diagonal of the effective mass matrix. In fact, all the diagonal terms are positive and the others terms can be deduced (except the sign) from the diagonal terms.

$$\tilde{M}_{ij,k} = \tilde{M}_{ij,k} \tilde{M}_{jj,k} \quad (19)$$

The contribution of the effective mass of all the eigenmodes adds up to rigid mass matrix :

$$\sum_k \tilde{M}_{ij,k} = M_{\text{rigid}} - m_{\text{base}} \quad (20)$$

The effective mass can give us information about the modes which will create the greatest reactions at the base, therefore, permits us to characterize their relative importance. However, it is impossible to know which part of the structure is affected by this mode. The aim of the study is to determine some effective parameters for each substructure.

2.2 Application to subsystem

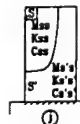
We want to determine the maximum forces at the interface of one subsystem with excitation at the base. The internal load F_i and the mass matrix of the support (M_{jj} an M_{ij}) are assumed to be null, in order to simplify the expressions : The relations (13) and (15) become

$$F_j = \sum_k T_k(\omega) \tilde{M}_{ij,k} \ddot{q}_j$$

$$q_i = \sum_k T_k(\omega) \tilde{T}_{ij,k} q_j$$

Let us consider the subsystem s and its complement s' (the rest of the structure), and express each matrix as the sum of two matrices for each part s and s' .

$$\begin{aligned} M &= M_s + M_{s'} \\ K &= K_s + K_{s'} \\ C &= C_s + C_{s'} \end{aligned} \quad (21)$$



Here, a subsystem is defined by elements and not grids.

The dynamic equation (1) can be written :

$$(K_s - \omega^2 M_s + j \omega C_s) q(\omega) = F(\omega) - (K_{s'} - \omega^2 M_{s'} + j \omega C_{s'}) q(\omega) \quad (22)$$

Let us take the force F_s :

$$F_s = (K_s - \omega^2 M_s + j \omega C_s) q(\omega) \quad (23)$$

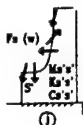
We note that only the non-zero components correspond to the interface nodes.

(Demonstration) : the left part of the above dynamic equation shows that the non-null components correspond to the degrees of freedom of s ; the right part shows that they also correspond to degrees of freedom of s' ; so, the non-null components are the degrees of freedom connected to both s and s').

Consider now the problem

$$M_s \ddot{q}_s + C_s \dot{q}_s + K_s q_s = F_s(t) \quad (24)$$

with F_s given



We know the solution of this problem. F_s can be considered as the equivalent load at the interface between s and s' , which gives the same response for the subsystem s as an excitation at the base. That is also the reaction at the interface for the excitation at the base. These are usually called quasi static loads.

2.3 Equivalent resultant of F_s - effective mass by subsystem

We can evaluate the force F_s :

$$F_s = (K_s - \omega^2 M_s + j \omega C_s) q(\omega) \quad (25)$$

$$\text{with } q_i = \sum_k T_k(\omega) T_{ij,k} q_j$$

In order to have the equivalent resultant T_s/j of these forces at the support, we project the relation in multiplying F_s by the transposed rigid vector. Assuming that the damping forces are not significant, the expression of can be written as follows :

$$T_{s/j} = \begin{bmatrix} 1 & \eta_j \end{bmatrix} \begin{bmatrix} K_{s,jj} - \omega^2 M_{s,jj} & K_{s,ji} - \omega^2 M_{s,ji} \\ K_{s,ij} - \omega^2 M_{s,ij} & K_{s,ii} - \omega^2 M_{s,ii} \end{bmatrix} \begin{bmatrix} 1 \\ \sum_k T_k(\omega) T_{jk,k} \end{bmatrix} q_j \quad (26)$$

A global rigid vector is also a local rigid vector (each subsystem is composed of elements and not grids) so that :

$$\begin{bmatrix} K_{s,jj} & K_{s,ji} \\ K_{s,ij} & K_{s,ii} \end{bmatrix} \begin{bmatrix} 1 \\ \phi_j \end{bmatrix} = \begin{bmatrix} 0 \\ 0 \end{bmatrix} \quad (27)$$

We can now easily transform the expression of $T_{s/j}$

$$T_{s/j} = (M_{s,jj} + M_{s,ii} \phi_j + \sum_k T_k(\omega) (M_{s,jj} + \eta_j M_{s,ii}) \phi_k L_{kj} / m_k) q_j \quad (28)$$

We note that the expression of this resultant is very similar to the expression of the reactions at the base for the whole structure.

Let us introduce new effective parameters for the subsystem s :

$$L_{s,kj} = \phi_k (M_{s,jj} + M_{s,ii} \phi_j) \quad (29)$$

modal participation matrix for the subsystem s

$$M_{s,jj,k} = L_{s,jk} L_{kj} / m_k \quad (30)$$

effective mass matrix for the subsystem s .

The resultant matrix can be written as follows :

$$T_{s/j} = (m_{s,base} + \sum_k T_k(\omega) M_{s,jj,k}) q_j \quad (31)$$

$$m_{s,base} = M_{s,jj} + M_{s,ii} \phi_j \quad \text{mass of } s \text{ at the base}$$

The effective mass matrix for the subsystem s is equivalent, for the resultant of the forces at the interface, to the global effective mass matrix for the reactions at the base.

Properties

- Sum over the subsystems

We can sum all the effective masses for all subsystems :

$$\sum_s \tilde{M}_{s,jj,k} = \tilde{M}_{jj,k} \quad (32)$$

So, we have decomposed the global effective mass matrix as the sum of matrices of the subsystems. This is to be expected because the sum of the reactions at the interface of each subsystem is, of course, the global reaction at the base.

- Sum over the frequencies

We can also sum the effective mass matrices for the subsystem s , and easily demonstrate, for a subsystem with no interface with the support, that :

$$\sum_k \tilde{M}_{s,jj,k} = M_{s,jj,rigid} \quad (33)$$

The contribution of the effective max of all the eigenmodes adds up to rigid mass matrix of the subsystems s .

- Sign of the diagonal

We have already mentioned that the most used components of the global effective mass matrix are the diagonal. This diagonal is obtained by squaring each component of the modal participation matrix (when m_k is normalized at 1), so all the terms are always positive.

For the effective mass of the subsystem, this rule is no longer true. The diagonal is the product of the corresponding terms of the global modal participation and the modal participation of the subsystem s . We have the equation :

$$\sum_s L_{s,kj} = L_{kj} \quad (34)$$

but the sign similarity of the two corresponding components is not known. A negative element in the diagonal of $M_{s,jj,k}$ indicates that this subsystem is globally opposed from the rest of the structure for this mode and this direction. Negative terms called "mass" could be surprising, however, the effective mass by subsystem is actually the decomposition of the global effective mass.

- Properties of the modal participation by subsystem $L_{s,jk}$

We decide to normalize $m_k = 1$. (However, if m_k was not equal to 1, the parameter independant of the normalization would be $L_{s,jk}/m_k$).

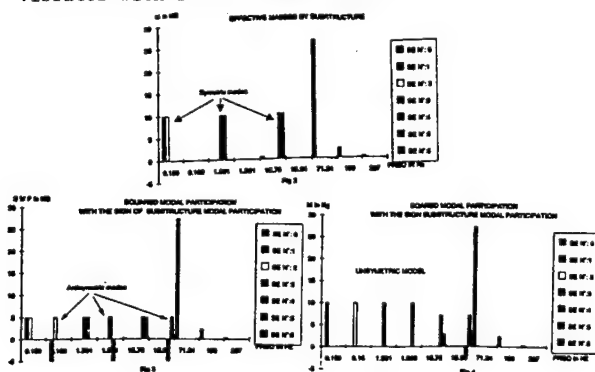
This parameter is very important to determine the modal deformation of the substructure, i.e. to give us information about ϕ_k for s .

If at each degree of freedom of the system we imposed the acceleration $(-\omega_k^2 \phi_k)$, the forces at the interface would be $(-\omega_k^2 L_{s,jk})$, and the resultant at the support would be $[(K_s - \omega_k^2 M_s) \phi_k]$. The modal participation gives us information about the direction and the importance of deformation of the subsystem s . However, it is difficult to have a comparative scale for this modal participation. A solution is to square all the terms of the modal

The effective mass decomposition enables us to find its origin. The results are in agreement with the theoretical calculations made for this very simple model. This decomposition is represented in the figure 2. However, in this example, it is very interesting to look at the squared modal participation, which we represent with the sign of the substructure modal participation.

This decomposition enables us to localize the modes which have null effective masses. As shown in figure 3, for the second frequency, the fact that the effective mass is null indicate only that this mode can not be excited by the base. It is therefore possible to know with the squared modal participation, the origin and the direction of this mode. This second mode is the antisymmetric mode for the subsystems 1 and 2.

Moreover, in the case of a change in the model, it is possible to get an estimation of the effective masses involved in the range of frequencies. In figure 4, all the subsystems frequencies are uncoupled, and we can see, that every subsystem vibrates with its own whole mass.

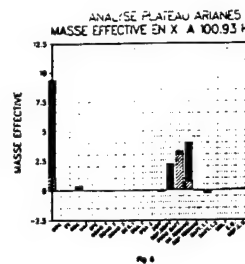
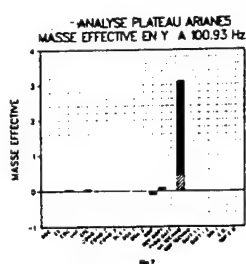
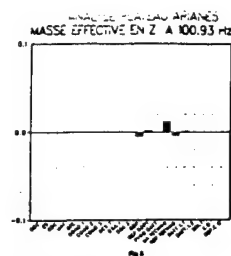
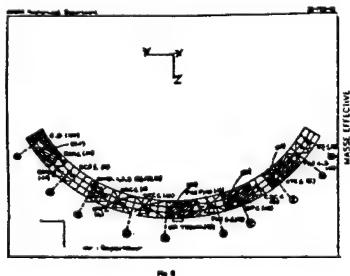


Moreover, in the case of a change in the model, it is possible to get an estimation of the effective masses involved in the range of frequencies. In figure 4, all the subsystems frequencies are uncoupled, and we can see, that every subsystem vibrates with its own whole mass.

3.2 Equipment platform

The aim of this study is to optimize the location of support points for the platform of Ariane 5 Vehicle Equipment Bay Structure. The first frequency must be higher than 100 Hz.

The subsystem decomposition results concerning the first frequency are displayed in figure 5 to 9 and the deformed shape in figure 10. The effective masses by subsystem are sufficient to know the origin and the direction of each mode.



3.3 Utilization of the effective masses by subsystems as representative of the interface loads

In the development of the telecommunications satellite LOCSTAR, it was necessary to identify the modifications of the dynamic behaviour of the satellite due to a different frequency specification for one appendice.

The satellite LOCSTAR is topped by a "tower", composed of a cylinder and a structure "FSS" (Feed Supporting Structure), on which two feed structures are fixed, called "S band feed" and "L band feed". All the following structure concerns the feed tower assembly clamped at its base.

These feed structure were initially specified not to have their first modal frequency below 130 Hz. The first development of these two subsystems showed that the L band feed has its first modal frequency around 228 Hz, whereas it was not possible to respect the specifications for the L band feed. The aim of the study was then to elaborate a new specification for the S band feed, but without interfering with the specification of the FSS and the L band feed.

In this structure, the main constraint is the interface load. The effective mass by subsystem gives us the importance of this load for each eigenmode. For the sensibility study, we consider 5 different frequential configurations of the S band feed and we want to know the impact on the effective masses of the FSS and the L band feed, which must not be larger than for the nominal case. The histograms on the following page give us the important effective masses for the first three eigenmodes. The substructures were :

- the cylinder,
- the FSS,
- the L band feed,
- the S band feed.

The nominal reference case is the first one. We see that the impact of the modifications is not significant at 52 and 54 Hz, but more important for the last frequency (80 Hz), where it appears that it is impossible to satisfy the constraint of having smaller effective masses.

participation. We obtain a new parameter, the squared modal participation by subsystem, whose unity is mass and which can be compared to the mass of the subsystem. We call this new parameter $\tilde{S}_{s,j,k}$.

$$\tilde{S}_{s,j,k} = L_{s,jk} L_{s,kj} / m_k \quad (35)$$

- The squared modal participation

The sum of $\tilde{S}_{s,j,k}$ above the frequencies can be estimated :

$$\sum_k \tilde{S}_{s,j,k} = \phi_{ji} M_{s,ii} M_{ii}^{-1} M_{s,ii} \phi_{ij} \quad (36)$$

This sum is often very close to the rigid mass of the subsystem. A comparison between the total mass and the squared modal participation gives the importance of the mode for the subsystem.

The study of this parameter is particularly interesting. When the effective mass matrix is null, because it gives the origin of this mode which cannot be excited at the base.

If the squared modal participations are important for some substructures, and the effective masses null, these subsystems have coupled and opposed modes, which could be uncoupled if we modified one of the substructures.

This notion introduced here could be very interesting for free-free studies, but has not been developed.

2.4 Energies

We can also calculate the effective energies of deformation in each subsystem :

$$E_{s,def} = 0.5 q^T K_s q \quad (37)$$

We have already calculated explicitly the value of q :

$$q_j \text{ is the acceleration imposed at the base} \\ q_j = \sum_k T_k(\omega) \tilde{T}_{ij,k} q_j \quad (38)$$

We can now estimate the energy. For $\omega = \omega_k$, we can approximate the energy by neglecting all the terms which do not have the expression $T_k(\omega_k)$, because $T_k(\omega_k) \ll T_k(\omega_k)$ for k different from k' . Hence,

$$\tilde{E}_{s,def}(\omega_k) = 0.5 T_k^2(\omega_k) q_j^T \tilde{T}_{ij,k} K_{s,ii} \tilde{T}_{ij,k} q_j \quad (39)$$

We can now consider the energy for a unit displacement q_j and calculate the effective energy $E_{s,def,j,k}$:

$$\tilde{E}_{s,def}(\omega_k) = 0.5 T_k^2(\omega_k) \tilde{E}_{s,def,j,k} \quad (40)$$

$$\tilde{E}_{s,def,j,k} = \tilde{T}_{ij,k} K_{s,ii} \tilde{T}_{ij,k} \quad (41)$$

We can also have the global effective strain energy :

$$\tilde{E}_{def,j,k} = \tilde{T}_{ij,k} K_{ii} \tilde{T}_{ij,k} \quad (42)$$

The interesting result is the fraction of strain energy in each subsystem, $\theta_{def,j,k}$. We can easily demonstrate that this fraction is directly obtained by using the eigenmodes, and that it is not necessary to calculate the transmissibility. We also note that this fraction is independent of the excitation axis.

$$\theta_{def,j,k} = (\phi_{ji} K_{ii} \phi_{jk}) / (\phi_{ji} K_{ii} \phi_{jk}) = (\phi_{ji} K_{ii} \phi_{jk}) / k_k \quad (43)$$

A similar calculation can give the fraction of kinetic energy :

$$\theta_{kin,j,k} = (\phi_{ji} M_{ii} \phi_{jk}) / (\phi_{ji} M_{ii} \phi_{jk}) = (\phi_{ji} M_{ii} \phi_{jk}) / m_k \quad (44)$$

The maximum subsystem deformation of translation can be obtained from the above parameters. A large fraction of strain energy and a small fraction of kinetic energy would show, for example, that only the interface is affected by the mode.

After having introduced the effective parameters :

- effective mass matrix by subsystem,
- modal participation by subsystem,
- squared modal participation by subsystem,
- fraction of strain energy,
- fraction of kinetic energy,

we are going to explain how we introduce these matrices in the NASTRAN solutions.

3. EXAMPLES

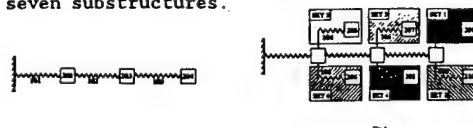
The interest of substructure effective mass concept is illustrated across some very simple examples. We underline the improvement given by those new parameters and we explain their physical interpretation.

The first application in an unidirectional mass spring model equivalent to a simplified satellite modelled by the structure with a few appendages.

The second application is based on the equipment platform of Ariane 5, from which we present the informations provided by the effective parameters for the modal analysis. And the third application shows the effective masses by subsystems as representative of the interface loads.

3.1 Mass & spring model

This model illustrated in figure 1 is made out of seven substructures.



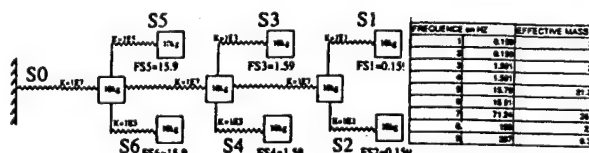
Set 0 : is represented by three frequencies using three spring and mass systems.

The effective mass study gives the results :

FREQUENCY in HZ	EFFECTIVE MASS
1	20.8
2	199
3	287

Set 1 : are six appendices, each one modelled by one frequency.

Those substructures are added in parallel to the principal structure.



FREQUENCY in HZ	EFFECTIVE MASS
1	0.139
2	1.801
3	1.801
4	18.76
5	18.76
6	71.34
7	188
8	287

SESSION
1.3.B

VIBRO-ACOUSTICS
I

PRECEDING PAGE BLANK NOT FILMED

PRECEDING PAGE BLANK NOT FILMED

N 92 - 23790

84702

ACOUSTIC ABSORPTION DUE TO SPECIMEN IN TEST
IN A REVERBERANT CHAMBER

A. Girard, C. Blanchard

INTESPACE, Toulouse

ABSTRACT

With the objective of determining an empiric law for the acoustic absorption of a specimen in test in a reverberant chamber, a methodology using commonly available test data is first presented. The approach is based on the determination of the reverberation times at test cut-off, leading to the acoustic absorption losses, then to the specimen acoustic absorption coefficients. This methodology is then applied to the acoustic test results of five satellite specimens already tested in the INTESPACE chamber. Finally, the empiric law is derived from these results by averaging, providing a quick estimation of acoustic absorption losses in any chamber with known characteristics and a check of the capability of acoustic generators to achieve specifications.

Keywords : acoustic simulation, test chamber, sound pressure, absorptivity, sound transmission, spacecraft.

1. INTRODUCTION

It is now a common practice to test satellites in a reverberant chamber to verify their ability to withstand the acoustic environment generated during launch. The walls are as reverberant as possible to obtain a diffuse pressure field with homogeneous and isotropic properties.

In order to achieve a given specified spectrum for the specimen in the chamber, the acoustic field is generated during a pre-test with a dummy specimen in the chamber, or with no specimen if the volume to be tested may be considered negligible with respect to the volume of the chamber, as is often the case for satellites.

The acoustic pressure spectrum is then analysed from measurements given by several microphones distributed in the chamber, generally by octave or 1/3-octave bands. The levels are then compared to the specifications and the test parameters are adjusted to obtain values within the tolerances. The values of all the test parameters are recorded in order to be reproduced during the test with the specimen.

However, when the specimen is in the chamber, the acoustic field is modified. There is an absorption of acoustic energy by the exposed surfaces of the specimen, giving mechanical motion in all its structural parts. Significant corrections on the test parameters must be performed to achieve the specifications.

As this absorption results from complex elasto-acoustic interactions between the specimen and the pressure field, it is very difficult to predict analytically the modifications. However for a given class of specimen, one can think that these modifications depend approximately on a very limited number of major parameters, such as the exposed areas. In this case, the estimation of the absorption of typical specimens from previous acoustic tests may lead to useful empiric laws.

This paper presents the study performed to derive an empiric law for the specimen acoustic absorption from the available test data concerning five specimens already tested in the INTESPACE acoustic chamber.

2. METHODOLOGY

2.1 Scope

The specimen acoustic absorption may be deduced from the acoustic absorption loss generated by the specimen in the chamber, which can be directly obtained from pressure measurements with and without specimen if all the test parameters remain the same between the two tests. However, as these test parameters are always adjusted during tests to achieve the specifications, this direct method is not applicable. It could be possible to estimate the variations of the test parameters to compensate for the acoustic absorption loss, but as these parameters are generally multiple and their impact on the acoustic loss are not obvious, it is difficult to obtain reliable results by this way.

A more convenient method is to use transient decay measurements, namely the reverberation times at the test cut-off from available microphone records, without any special device which would be anyway hardly compatible with project constraints, as summarized in figure 1.

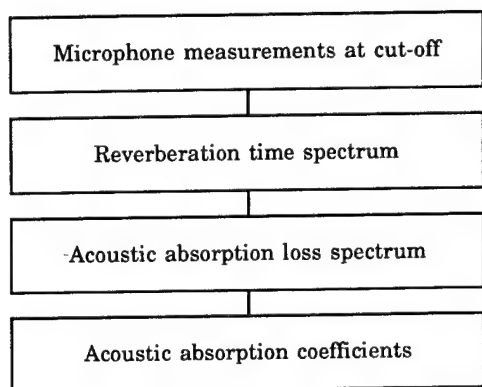


Fig. 1: Methodology

2.2 Formulation

For a specimen (s) in a chamber (c) with diffuse acoustic field, the determination of the reverberant time TR at test cut-off in each frequency band enables us to derive :

- acoustic absorption loss spectrum AL_s for each specimen from :

$$AL_s(\text{dB}) = 10 \log_{10} \frac{TR_c}{TR_{c+s}} \quad (1)$$

- acoustic absorption spectrum A_s of each specimen from Sabine's formula :

$$A_s = 0.16 V_c \left(\frac{1}{TR_{c+s}} - \frac{1}{TR_c} \right) \quad (2)$$

where V_c is the volume of the chamber and assuming that $V_s \ll V_c$,

- average acoustic absorption coefficient spectrum α_s of each specimen from :

$$\alpha_s = \frac{A_s}{S_s} \quad (3)$$

where S_s is the area of boundary surface.

For the last step, the delicate point is the estimation of the concerned areas S_s . Accurate determination from drawings is difficult and in fact not necessary because the empiric law will take advantage of simplicity. In this context the following strategy leads to satisfactory results :

- Decomposition of the specimen in simple "volumes" having a significant contribution to the exposed areas :
 - central part, generally cylindric or parallelepipedic (small appendages, such as sensor or thruster devices, neglected),
 - large appendages, mainly deployable solar arrays and large reflectors.

- Derivation of the corresponding areas, to be summed:

- area of the central volume,
- twice the areas (2 faces) of the large appendages assimilated to thick plates or shallow shells (total unfolded areas for solar arrays, even if folded during test, because all these surfaces are exposed to the sound pressure field)

3. EXPERIMENTAL RESULTS

3.1 Implementation

The reverberation times TR were estimated at test cut-off from the available microphone records. A comparison was made by a spectrum analyser (BK 2131 - 1/3 octave frequency bands) on two spectra corresponding to times separated by a few seconds, giving decreases generally between 10 and 30 dB. The reverberation times TR were derived by extrapolation to 60 dB.

Some problems were encountered, in particular :

- short time (inevitable) for acquisition of the second spectrum, leading to inaccuracies due to the limited number of averages, mainly at low frequencies (< 160 Hz),
- nitrogen exhaust after cut-off, which disturbs the acoustic decay at high frequencies (> 3 kHz),

leading to anomalies in some frequency bands. The corresponding results were not considered.

This technique was first applied to the INTESPACE chamber without specimen and compared to results obtained during the acceptance tests of the acoustic chamber.

An overview of the INTESPACE acoustic test facility is given in figure 2. The dimensions are approximately $10.3 \text{ m} \times 8.2 \text{ m} \times 13 \text{ m}$ (volume V_c about 1100 m^3 , area S_c about 650 m^2). The acoustic generators consist of 2 LING EPT 200 for high frequencies and 1 WYLE WAS 3000 for low frequencies.

The acoustic characterization of the chamber by reverberation time had been performed using 1 auxiliary source successively at 3 distinct locations and a large number of microphone measurements (96) giving reliable results, but at a very low level (103 dB) compared to usual levels for satellite testing. The average values obtained with the 3 sources in each 1/3-octave frequency band compared with the values obtained with the acoustic generators of the chamber at high level (150 dB) using the present approach are given in figure 3. The agreement is very good above 300 Hz. At lower frequencies, some discrepancies occur, the maximum differences being between 80 and 200 Hz. They are due partly to the low modal density and partly to the methods of determination. However, this comparison is globally quite satisfactory in the present context.

The same technique was applied with the test records available from five acoustic tests already performed at INTESPACE on specimens at qualification or acceptance levels (see figure 4): the reverberation times were determined in the same conditions as previously, in order to have the maximum reliability for the results. Several microphones were considered when possible.

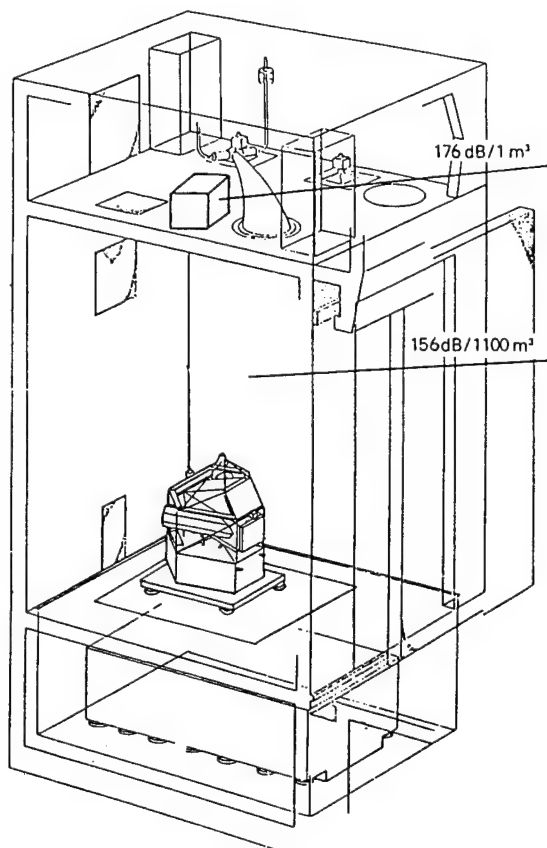


Fig. 2: INTESPACE reverberant chamber

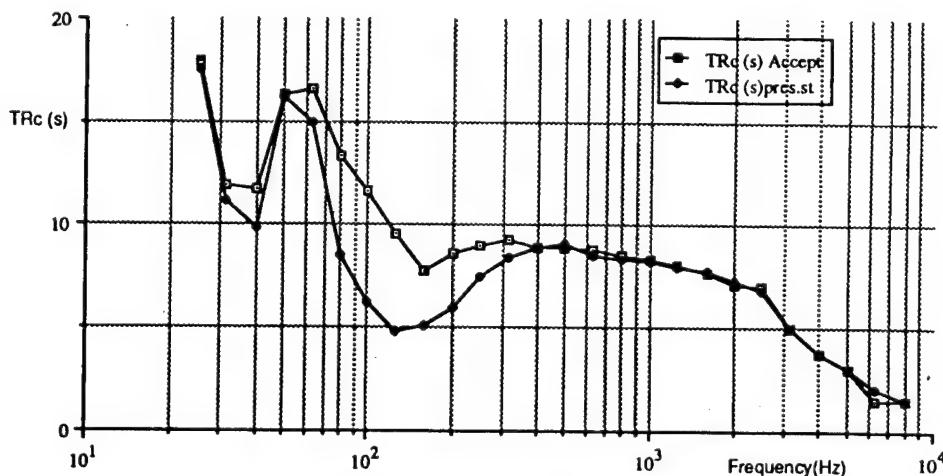


Fig. 3: Chamber without specimen - Reverberation times TR_c from acceptance test and present study

Specimen	OASPL	microphones	central volume + appendages
1. Observatory sat.	144.5 dB	6	$41 \text{ m}^2 + 0 \text{ m}^2$
2. Scientific sat.	146 dB	2	$14 \text{ m}^2 + 0 \text{ m}^2$
3. Hipparcos sat.	146 dB	1	$18 \text{ m}^2 + 13 \text{ m}^2$
4. ECS 4 sat.	143 dB	2	$15 \text{ m}^2 + 29 \text{ m}^2$
5. Telecom. sat.	143 dB	1	$17 \text{ m}^2 + 36 \text{ m}^2$

Fig. 4: Specimens

3.2 Main results

The acoustic absorption loss spectra AL_s of the five specimens are given in figure 5 (when several microphone results were available for a specimen, the average spectrum was used). Questionable values have been suppressed. Losses up to 2.5 dB may be noticed.

The acoustic absorption spectra A_s of the five specimens are given in figure 6. The influence of the exposed surface areas can be seen by higher absorption levels in all frequency bands for larger specimens (including appendages).

The estimation of the boundary surface areas S_s of the five specimens was made from the available project documentation. The results are given in figure 4.

The acoustic absorption coefficient spectra α_s of the five specimens are given in figure 7. These results show that the average acoustic absorption coefficient spectrum for the 5 specimens tested lies approximately between 0.2 and 0.3 between 250 and 2000 Hz. Below 300 Hz and above 2000 Hz, the values are rapidly decreasing, but difficult to assess due to test discrepancies.

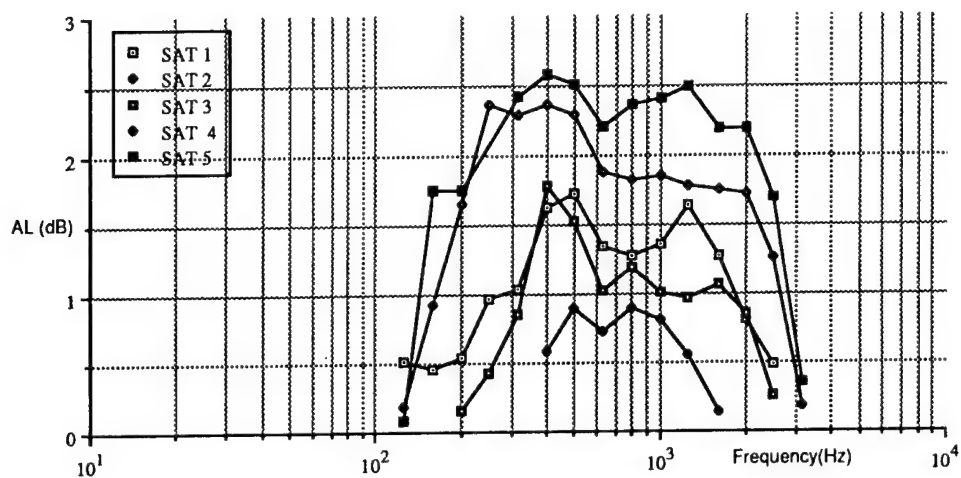


Fig. 5: Acoustic absorption losses AL_s (dB)

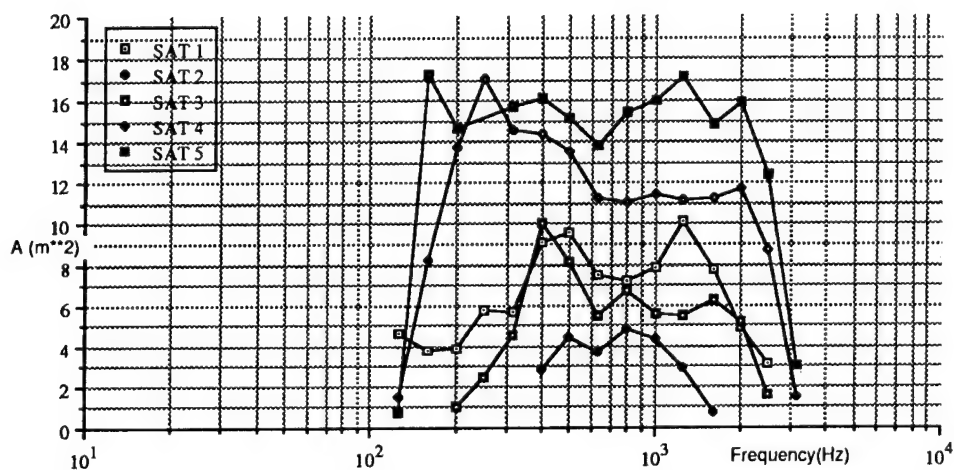


Fig. 6: Acoustic absorptions A_s (m^2)

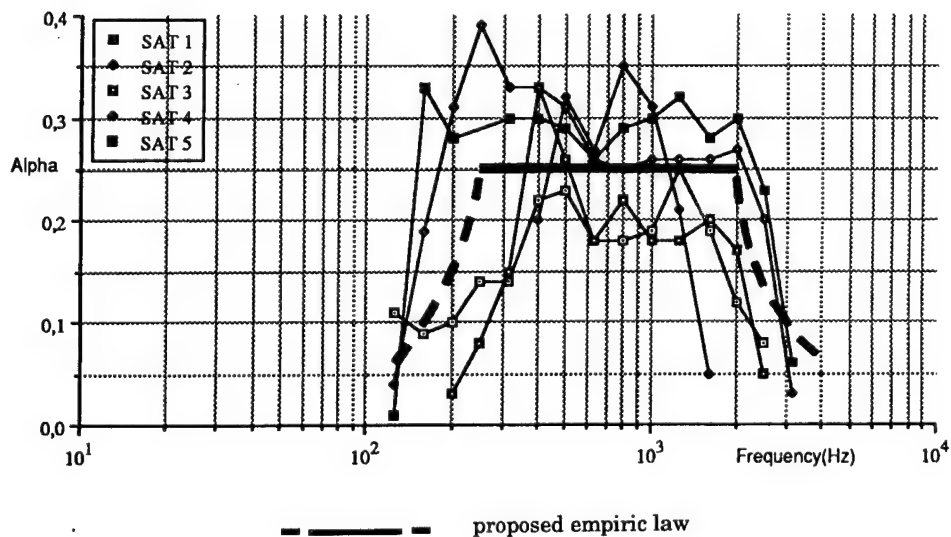


Fig. 7: Acoustic absorption coefficients α_s

3.2 Empiric law

From the previous results, a simple law may be proposed :

- up to 250 Hz : increasing value proportional to the square of the frequency,
- 250 - 2000 Hz : constant value of 0.25 (average, for nominal estimation) or 0.3 (max, for pessimistic estimation),
- above 2000 Hz : decreasing value inversely proportional to the square of the frequency.

with the following comments:

- 250 Hz is an average value, possibly varying with the specimen between 160 and 400 Hz),
- variation in f^2 and $1/f^2$ gives only an order of magnitude,
- the value of 0.25, which may be believed rather high with respect to current values, corresponds to a simplified estimation of the specimen exposed surface areas, as described in paragraph 2.2.

This empiric law is plotted in figure 7.

4. CONCLUSIONS

From the reverberation times measured in the chamber at test cut-off, coherent results concerning acoustic absorption of the five specimens considered have been obtained.

An empiric law has been derived giving a value of about 0.25 for the acoustic absorption coefficients up to 2000 Hz, which may be applied to any specimen provided that :

- its configuration is similar to that of a typical satellite structure tested in acoustic chamber (for example, a fairing would probably lead to different results)
- the associated exposed surface areas are estimated from : central part area + twice large appendage areas (small appendages and complex shape contribution neglected).

These results enable to estimate the acoustic loss in any reverberant chamber due to a given specimen, and therefore to verify the capability of the acoustic generators to achieve specifications.

ACKNOWLEDGEMENTS

The work described in this paper was performed under ESA contract 7821/88.

N92-23791

MAXIMAL MODAL ENERGY METHOD : AN OVERVALUING TOOL FOR LOW FREQUENCY
PREDICTION OF STRUCTURE ACOUSTIC RESPONSE

B. LAVIRON

P. HERMAN

S. DE ZOTTI

MATRA Space Branch
Department of Mechanical Engineering
Toulouse (France)

ABSTRACT

This paper demonstrates the development of a numerical tool for elasto-acoustics : MME Method.

Stress will be laid upon the advantages and limitations of the MME Method.

Moreover, comparisons will be drawn between this method, results of tests performed on space structures, and a classical modal superposition tool.

Keywords : acoustic, modal superposition.

2. THEORETICAL APPROACH

We start with an expression of the modal energy resulting from a modal superposition approach :

$$E_p = S_p(\omega_p) \frac{\pi C_o}{\rho_o \omega_p^2} \frac{\eta_{sa(p)}}{\eta_{sa(p)} + \eta_s} \quad (1)$$

Where :

E_p is the energy of the pth mode
 ω_p is the pulsation value of the pth mode
 $S_p(\omega_p)$ is the power spectral density calculated at ω_p
 C_o, ρ_o are respectively the celerity and the density of the surrounding fluid
 η_s is the structural damping coefficient
 $\eta_{sa(p)}$ is the average radiation damping coefficient of the pth mode.

The basic assumption in MME approach is to consider a strong structure/acoustic coupling. As a result, the structural damping coefficient η_s may be neglected in comparison with the modal damping added by acoustic radiation (η_{sa_p}).

Consequently, in the previous expression (1), the ratio $\frac{\eta_{sa(p)}}{\eta_{sa(p)} + \eta_s}$ is asymptotically equalled to 1.

A first expression of the maximal modal energy is :

$$E_{p_{max}} = S_p(\omega_p) \frac{\pi C_o}{\rho_o \omega_p^2} \quad (2)$$

Let's consider now the energy of pth mode as the sum of kinetic and potential energies of the same mode :

$$E_p = E_{cp} + E_{pp} \quad (3)$$

As energy can be assumed to be equally distributed between kinetic and potential effects, we set :

$$E_p = \frac{1}{2} V_p^T [M] V_p \quad (4)$$

V_p : velocity vector of the pth mode
 $[M]$: mass matrix of the structure.

1. INTRODUCTION

The development of powerful launchers such as the forthcoming Ariane 5, has given a large extent to the acoustic environment of the satellites : It is no longer possible to neglect the effect of noise on large and flexible satellite appendages such as solar arrays and reflector antennas.

As a result, the general trend is to obtain the most reliable predictions of acceleration and strain levels in these equipments when exposed to sound pressure.

At the present time, several softwares are available which can provide with these informations.

The major interest of the MME method relies on the fact that it gives with limited computation cost, maximum acceleration levels on every structure submitted to an acoustic field.

In concrete terms, the results obtained with the MME method can be very well applied to the dimensioning of satellite structures as they match the reality with a definite safety margin.

Now, there exists a proportionality relationship between displacement and modal shape :

$$q_p = \alpha \Phi_p = \frac{v_p}{i \omega_p}$$

If we substitute these relations in (4), we obtain :

$$E_p = \alpha^2 m_p \omega_p^2 \quad (5)$$

with $m_p = \int_V \rho [M] \Phi_p^2 dV$: generalized mass of mode p.

A very useful parameter, is the average acceleration level $\sqrt{\langle \ddot{q}_p^2 \rangle_t} = \bar{\gamma}_p$:

$$\bar{\gamma}_p = \frac{d^2 q_p}{dt^2} = -\omega_p^2 \alpha \Phi_p$$

$$\text{and } \bar{\gamma}_p^2 = \omega_p^2 \alpha^2 \langle \Phi_p^2 \rangle_t$$

As a result, E_p may be formulated in a 2nd way :

$$E_p = \frac{m_p \bar{\gamma}_p^2}{\omega_p^2 \langle \Phi_p^2 \rangle_t} \quad (6)$$

The comparison of the expressions (1) and (6) provides the following expression :

$$\bar{\gamma}_p^2 = S_p(\omega_p) \frac{\pi C_0}{\rho_0 m_p} \langle \Phi_p^2 \rangle_t \quad (7)$$

The total maximal acceleration is then obtained in adding up the contributions of all modes (at least, the most representative of the structure).

$$\bar{\gamma}_{\text{total max}} = \sqrt{\sum_{\text{modes } p} \bar{\gamma}_p^2}$$

(ie root-mean-square acceleration).

$$\bar{\gamma}_{\text{RMS max}} = \frac{\pi C_0}{\rho_0} \sqrt{\sum_{\text{modes } p} \frac{S_p(\omega_p)}{m_p} \langle \Phi_p^2 \rangle_t} \quad (9)$$

3. INPUTS/OUTPUTS OF MME PROGRAM

3.1 Inputs

The initial data can be subdivided into 2 main parts :

- Acoustic field :
 - . Basic properties of the surrounding fluid (celerity of sound, density),
 - . Definition of the excitation acoustic levels per band of frequency.
- Structure :
 - . Modal pulsations in vacuum,
 - . Modal displacements for each mode of the model and in the 3 directions.

These two last points result from a preliminary finite element computation.

3.2 Outputs

The final output of the MME computation method is a file which contains the modal maximal* accelerations in the three directions of a reference coordinate system.

* Note :

It is possible to improve the method by the use of modal radiation damping (at least, per band of frequency) determined from other sources (SEA for example), to the detriment of its overvaluing property.

4. RESULTS

4.1 Application to Locstar reflector antenna : comparison with a classical tool

MME Method has first been tested on a relatively simple structure.

The modal acceleration levels have been compared to those obtained by a classical modal superposition approach (the corresponding computation code, VIRUS, has been developed by Intespace).

More precisely, MME method's evaluation carries on two points :

- The "envelope" approach in terms of safety margin,
- The convergence of the two methods when the same modal radiation damping are used.

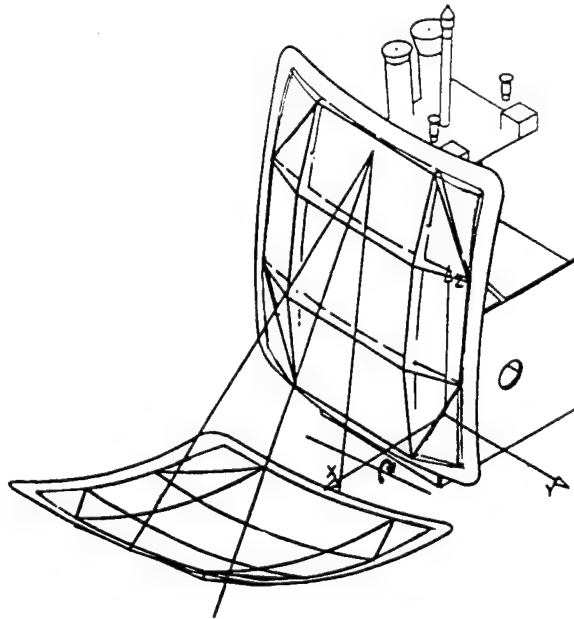


Figure 1 : Locstar reflector antenna

This first confrontation (figure 2) leads to the following conclusion :

- MME method, coupled to radiation damping introduction, and virus, give similar results (only a few % of difference) ;
- MME method, as a maximal approach, represents a very good envelope with regard to VIRUS's results (increase of 20 to 40 %, in average).

This last point may be explained by the fact that

the average ratio $\frac{\eta_{sa}}{\eta_s + \eta_{sa}}$ is not so far from 1 :

$$\text{From virus computation : } \frac{1}{\text{nb.modes}} \sum_{\text{modes up to 500}} \frac{\eta_{sa(p)}}{\eta_s + \eta_{sa(p)}} \approx 0,58.$$

4.2 Application to INMARSAT 2

The same study has been carried out on Inmarsat 2 solar array.

Nevertheless, MME method's evaluation has grown richer with the comparison with tests results.

4.2.1 Comparison with VIRUS

The comparison of the results obtained by VIRUS and MME program tends to confirm the previous conclusions for Locstar antenna :

The results obtained from the MME method with introduction of radiation damping are remarkably similar to those of VIRUS.

As for MME method, it represents a good over estimating tool compared with virus approach.

(Cf figure 4).

Note :

As the different modes are quite well coupled

(average radiation factor $\frac{\eta_{sa}}{\eta_s + \eta_{sa}} \approx 0,4$), the two previous methods can be reasonably compared.

We also have to lay stress upon a phenomenon that reveals the limitation of MME method :

The gap between the two approaches varies from 30 % up to 90 %.

1. The overestimation brought by MME approach is greater than in Locstar case, because of the decrease of the average radiation factor :

$$\text{Locstar} \rightarrow \left(\frac{\eta_{sa}}{\eta_s + \eta_{sa} \text{ average}} \right) = 0,58$$

$$\text{Inmarsat 2} \rightarrow \left(\frac{\eta_{sa}}{\eta_s + \eta_{sa} \text{ average}} \right) = 0,4.$$

2. The overestimation margin is slightly more extensive than in the previous case as the standard deviation increases from 0,2 (Locstar) to 0,233 (Inmarsat 2).

4.2.2 Comparison MME method/test results

Presentation of the test conditions

This acoustic test has been conducted in July 1988 by Fokker.

The aim was to set a figure to acceleration and stress levels in several points of the solar array submitted to a given acoustic field. Concerning the general conditions, the solar array was vertically hanged, and instrumented.

The figure 5 shows the margin between test and MME computation.

The striking point is that MME acceleration levels are in average twice as much as the test results.

The similarity of these two kinds of results seems to be influenced by the location of the accelerometers :

There are often relatively important differences when the measurement points are close to panel edges (example : accelerometers nb : 112, 109, 102, 303, 310, 312), whereas the location near a fixation point reduces the margin between test and computation (example : 100, 104, 200, 202, 204, 304).

Moreover, air effects on the intermediate panel were not taken into account when the modal analysis was performed.

As a result, acceleration levels are more overestimated on that part of the structure than on the outer panels.

However, this comparison may be led positively when maximal computation and test levels are compared :

Test maximum : 80 g

MME computation maximum : 150 g.

-> Ratio < 2.

Therefore, MME method can give an estimation of the maximal acceleration to be encountered during tests development with a safety margin of 2).

5. CONCLUSION

The comparison of MME method with the classical superposition approach and the test results has shown several advantages :

- The computation times are very short : 1 mn CPU to be compared with 7 to 10 hours for both Locstar and Inmarsat 2 models.
- Acceleration levels are obtained on every node of the model.
- These levels are definitively overestimated which tends to act in favour of safety.

On the other hand, some drawbacks have to be pointed out :

- The safety margin induced by MME method is not easy to control.

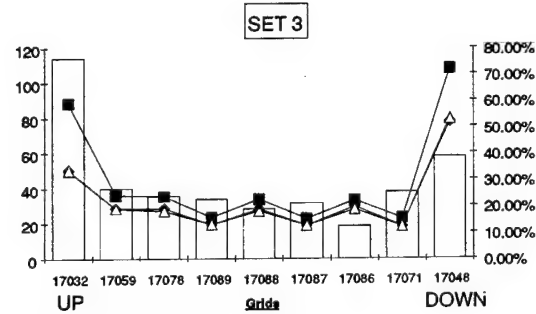
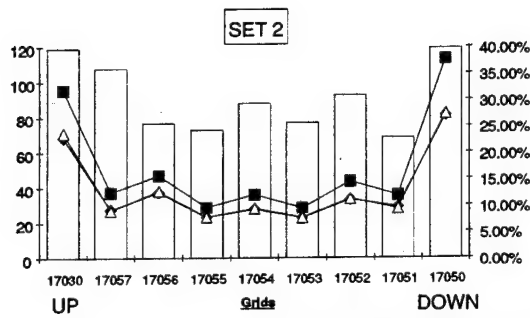
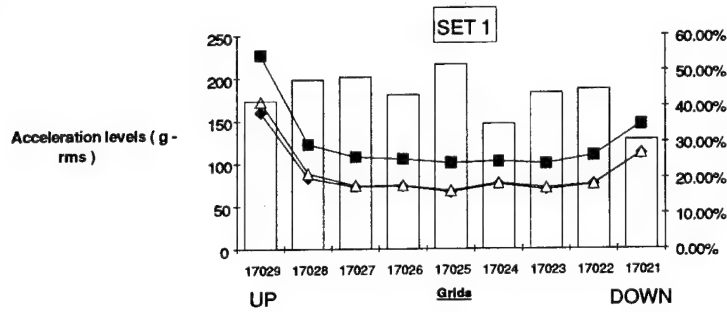
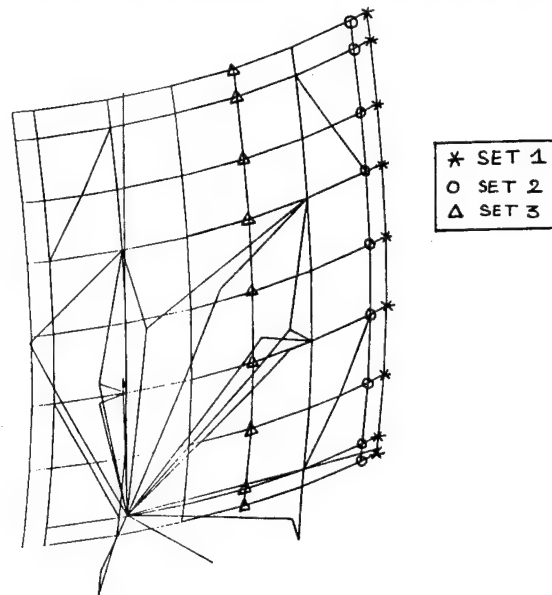
As a matter of fact, the knowledge of the modal radiation damping (at least an order of magnitude) is quite essential when the hypothesis of strong superstructure/acoustics coupling is not satisfied.

6. REFERENCES

1. C. Lesueur, Rayonnement acoustique des structures, Eyrolles
2. H. Defosse, VIRUS's user manual - Version 3.0, NT 88.091/EIA

Figure 2 :

COMPARISON MME METHOD / VIRUS ON LOCSTAR ANTENNA



◆ VIRUS ■ MME METHOD △ MME METHOD with radiation damping □ Difference between MME method and VIRUS

Figure 3 : Inmarsat 2 solar array

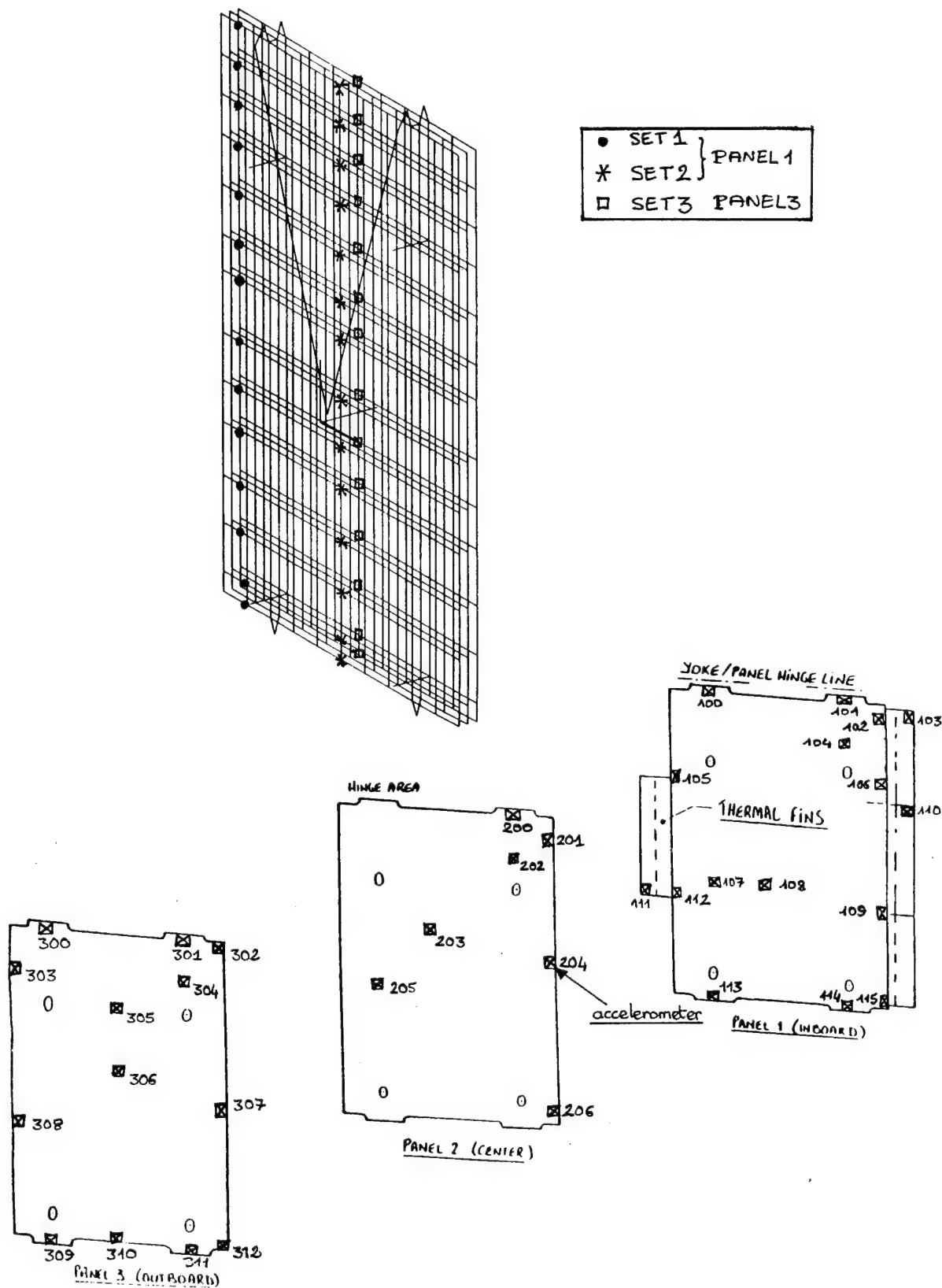


Figure 4 :

COMPARISON MME METHOD / VIRUS ON INMARSAT2 SOLAR ARRAY

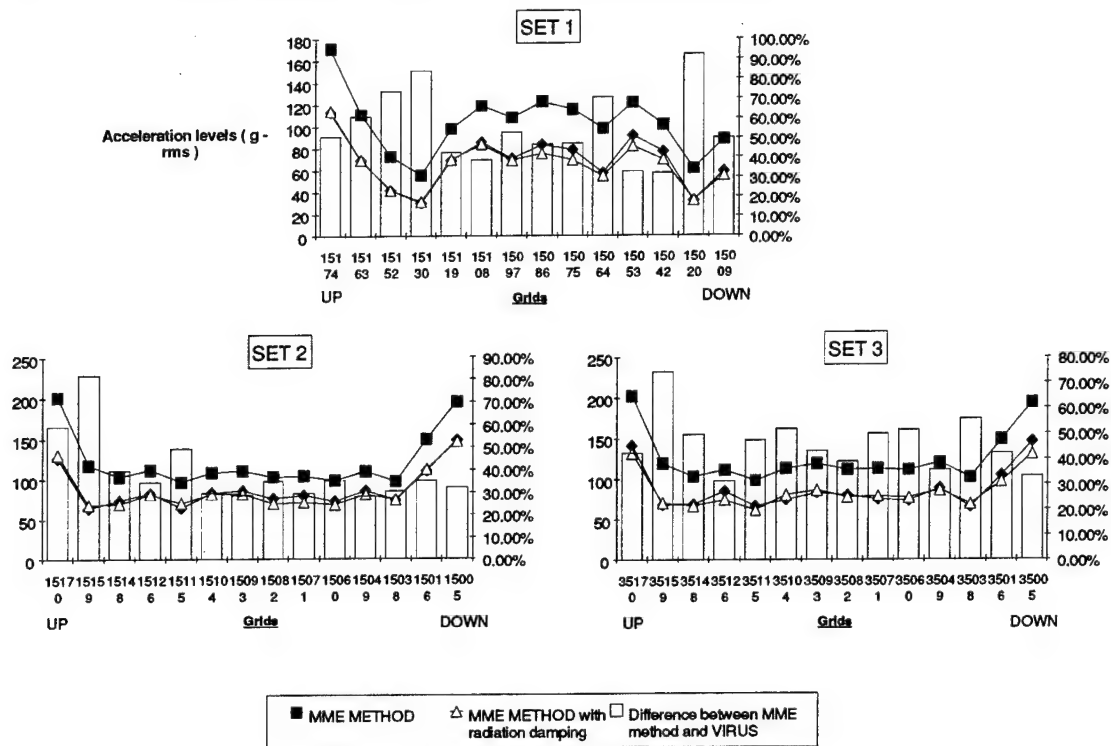
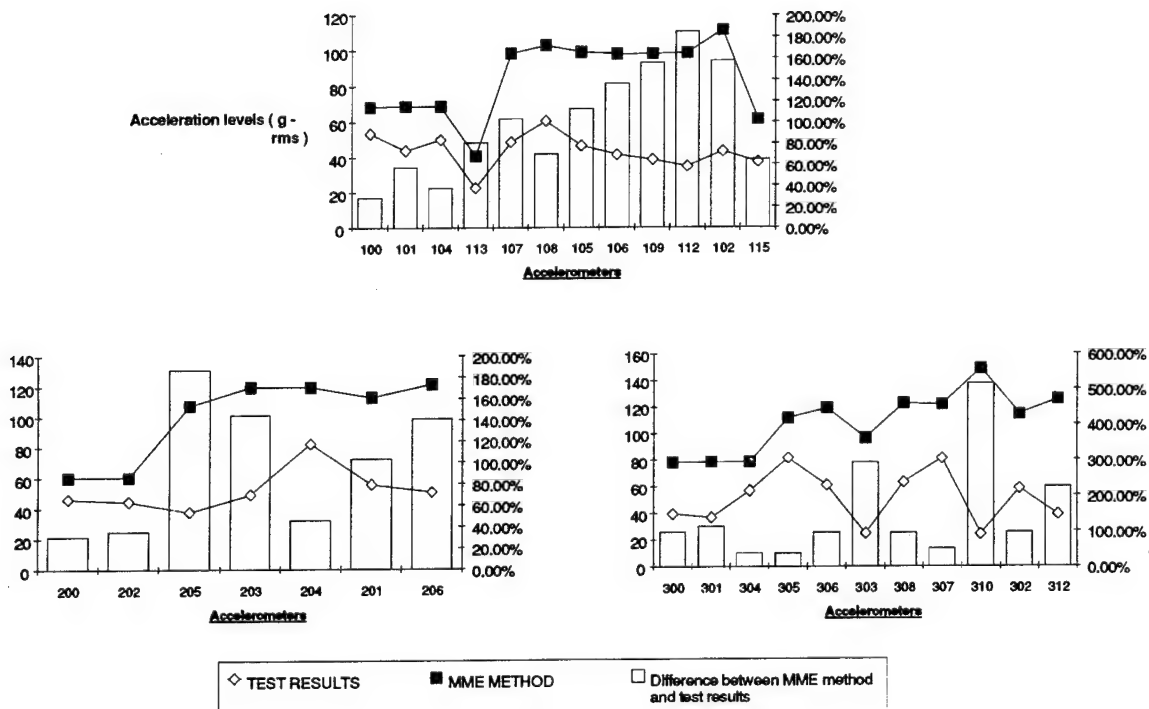


Figure 5 :

COMPARISON MME METHOD / TEST RESULTS ON INMARSAT2



N 92-23792

84704

NUMERICAL AND EXPERIMENTAL STUDY OF NOISE GENERATED BY A VIBRATING PLATE

O. von Estorff¹, A. Homm² and F. Bartels²¹ Industrieranlagen-Betriebsgesellschaft mbH, Einsteinstr. 20, D-8012 Ottobrunn, Germany² Fraunhofer-Forschungsgruppe für Hydroakustik, Waldparkstr. 41, D-8012 Ottobrunn, Germany

ABSTRACT/RESUME

Applying an indirect Boundary Element Method the sound radiation of a vibrating cantilever plate is investigated. The numerically obtained results are compared with measured data in order to show the accuracy and applicability of the numerical approach. The study clearly enhances the confidence in the computational solution of noise problems which are of particular importance in connection with the qualification of large spacecraft structures like HERMES.

Keywords: acoustic calculation, noise evaluation, sound radiation, Boundary Element Method, directivity pattern.

1. INTRODUCTION

With the advent of high-speed digital computers the development of numerical methods for acoustic analyses has been considerable during the last years. As a result, the design of many acoustic devices could be improved significantly.

Among the available techniques, the Finite Element Method (FEM) (Ref. 1) and the Boundary Element Method (BEM) (Refs. 2, 3), turned out to be the most suitable tools for acoustic calculations. Based on a volume discretization into 3-D finite elements, the FEM requires a large amount of data and considerable efforts to model this volume (acoustic fluid), but the method is very flexible and well known. The BEM, on the other hand, only requires a 2-D surface (boundary) discretization of the acoustic region which leads to a significant reduction of the total number of degrees of freedoms but also to fully populated coefficient matrices. Due to these aspects, the Boundary Element Method is best suited for exterior acoustic problems, such as the radiation of sound waves, while Finite Elements can be used more efficiently for interior problems, for instance, passenger compartments of an airplane.

While Raasch (Ref. 4), MacNeal, Citerley, Chargin (Ref. 5), Coyette and Guisset (Ref. 6), and von Estorff (Ref. 7) solved several interior problems using Finite Elements, Antes (Ref. 8), Amini and Wilton (Ref. 9), and Ciskowski and Brebbia (Ref. 10) discussed comprehensively the applicability of the Boundary Element technique to acoustic problems. Also Coyette, Dejeht, Guisset and Fyfe (Ref. 11), and Seybert and Cheng (Ref. 12) used the BEM, concentrating on harmonic problems, while Antes and von Estorff (Ref. 13), Mansur (Ref. 14), Antes and Meise (Ref. 15), and Groenenboom (Ref. 16) investigated transient problems by means of a BE-method working directly in the time domain.

Despite of the large number of numerical investigations, only very little work has been done in the field of validation of the acoustic models. The sound propagation in a passenger compartment of a car was investigated, e.g., by Burfeindt and Zimmer (Ref. 17) making use of the FE analogy described in (Ref. 5), and by Guy and Bhattacharya (Ref. 18) employing an analytical formulation. Ochmann and Wellner (Ref. 19), on the other hand, calculated the sound radiation of an L-shaped structure by Boundary Elements and compared their results with measured values. A fluid-structure interaction problem, namely a plate under water, was recently tested by Coyette and Fyfe (Ref. 20), but only the change of the resonance frequencies was considered.

Therefore, in the present paper the sound generated by a vibrating plate (exterior problem) is investigated numerically as well as experimentally. The comparison of the results is performed in two steps. First, several mode shapes of the cantilever plate (in air) are calculated using finite elements, and the results are compared with the tested configuration. Second, the acoustic field generated by the vibrating plate is considered. By means of an indirect boundary element approach, realized in the computer program SYSNOISE (Ref. 21), sound directivity patterns of the plate are analyzed and compared with the experimental results.

2. CALCULATION PROCEDURES

The numerical determination of the mode shapes of the plate was performed by a Finite Element analysis. Linear shell elements were used to model the plate, and the eigenvalue problem was solved by using the Subspace-Iteration-Method. Details of the FEM approach are extensively discussed in (Ref. 1).

For the calculation of the sound radiation, an indirect BEM was applied. Assuming time dependence with the circular frequency ω , the propagation of small-amplitude acoustic waves in a homogeneous acoustic medium Ω can be defined by a boundary integral equation of the form (Refs. 8, 11, 21)

$$p(X) = \int_{\Gamma} \left(\mu(Y) \frac{\partial G(X, Y)}{\partial n_Y} - \sigma(Y) G(X, Y) \right) d\Gamma(Y) \quad (1)$$

where p denotes the acoustic pressure and n the outward normal vector of the boundary Γ . The equation relates two singularities along Γ which are the jump of pressure, μ , and the jump of the pressure normal derivatives, σ .

The kernel $G(X,Y)$ is the fundamental solution of the Helmholtz equation for a point source, defined by

$$G(X,Y) = \frac{\exp(-ikR)}{4\pi R} \quad (2)$$

where R is the distance between a field point X and a point Y located on the surface Γ (boundary).

Defining appropriate boundary conditions for the singularities μ and σ , for instance,

$$\mu = 0 \quad \text{on } \Gamma_1 \quad (3)$$

$$\sigma = 0 \quad \text{on } \Gamma_2 \quad (4)$$

where $\Gamma = \Gamma_1 \cup \Gamma_2$, two integral equations can be derived which yield, in a first step, the unknown singularities μ and σ along the boundaries Γ_2 and Γ_1 , respectively. For details see (Refs. 8, 11, 21)

Once the singularities μ and σ are known, equation (1) can be used, in a second step, to determine the acoustic pressure p at any point X within the acoustic medium. (Note, that two steps are needed to compute the acoustic pressure. This is the reason why the presented BE-approach is called "indirect method".)

3. VIBRATION BEHAVIOR OF THE PLATE

3.1 Numerical Investigations

The considered system is shown in Figure 1. It consists of a horizontal aluminum plate of $a/b/t = 305/254/12.7$ mm which is held at one edge by a heavy circular steel disk to simulate a clamped end. The material data of the plate are YOUNG's modulus $E = 70000$ N/mm², Shear-Modulus $G = 27000$ N/mm², and density $\rho = 2660$ kg/m³. The plate was discretized by 320 finite shell elements and the Subspace-Iteration-Method (Ref. 1, 21) was used to determine the eigenfrequencies and mode shapes of the system. The result for the first 15 resonance frequencies is given in Table 1.

3.2 Experimental Studies and Comparison

The eigenfrequencies of the plate can be determined experimentally by measuring the shock response of the plate with accelerometers. A Fourier transformation of the transient accelerations yields the frequency response spectrum of the plate, where sharp peaks show the resonance frequencies of the system (see Fig. 2).

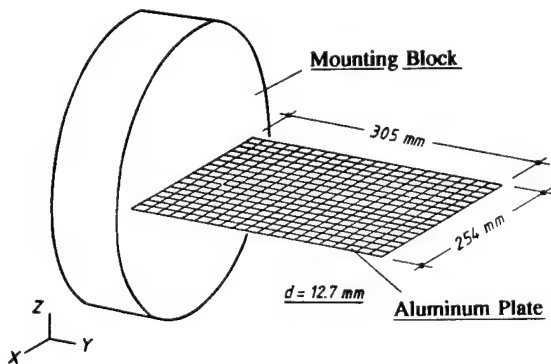


Fig. 1: FE-discretization of the plate.

Mode	f [Hz]	Mode	f [Hz]	Mode	f [Hz]
1	116.2	6	1788.7	11	3173.2
2	320.7	7	1982.4	12	3380.4
3	713.2	8	2089.2	13	3639.1
4	1109.8	9	2352.9	14	3919.0
5	1180.0	10	2379.5	15	4227.5

Table 1: Eigenfrequencies of the plate.

	7th Mode	8th Mode	11th Mode
Calculation (FEM)	1982 Hz	2089 Hz	3173 Hz
Experiment	1965 Hz	2130 Hz	3062 Hz

Table 2: Comparison of the eigenfrequencies.

With respect to the far field conditions (Ref. 23) for the acoustic evaluations (next section), three frequencies, namely 1965 Hz, 2130 Hz, and 3062 Hz were chosen from this spectrum. Table 2 shows that the measured and calculated values match remarkably well.

The structural modes of the plate can be visualized by the CHLADNI method (Ref. 22). For that purpose the horizontally adjusted plate has to be evenly covered with sand and one of its edges must be excited by an electromechanical shaker running with the plate resonance frequency of interest. The vibrations cause the sand to concentrate at the lines of zero vertical displacements, at the so-called nodal lines. Exemplary, a comparison of the computationally and experimentally obtained result for the 7th eigenmode can be seen in Figure 3, — both results agree very well. Although not shown here, the accuracy of the two other structural modes also was extremely good.

4. SOUND RADIATION OF THE PLATE

4.1 Numerical Investigations

After the calculated mode shapes were found to be in good agreement with the experiments, the plate and its mounting block were discretized with 946 boundary

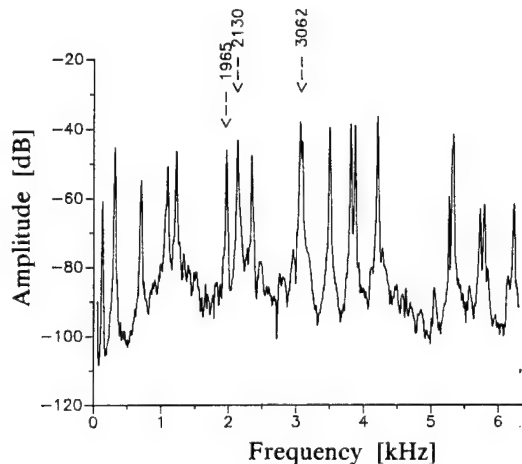


Fig. 2: Frequency spectrum of the plate (accelerations).

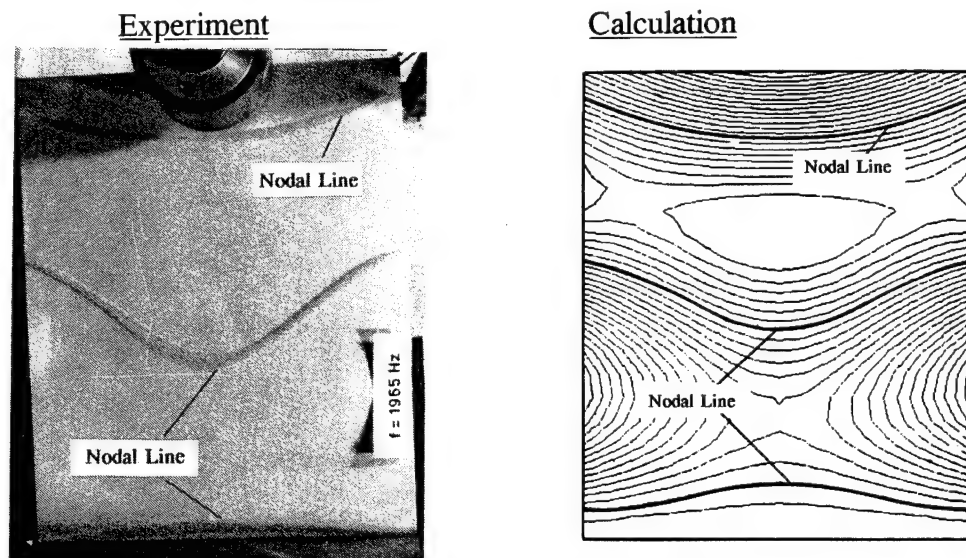


Fig. 3: Comparison of the 7th structural mode.

elements [Fig. 4]. At the elements modeling the surface of the plate the structural velocities, normal to the mid-plane of the plate, were prescribed. The mounting block, on the other hand, was assumed to be rigid, i.e. zero surface velocities were prescribed at the respective boundary elements. For the air surrounding the plate a density of $\rho^f = 1.189 \text{ kg/m}^3$ and a wave speed of $c = 343 \text{ m/s}$ were assumed.

First, applying the indirect BE-formulation provided in the program SYSNOISE, the unknown singularity distribution at the surface of the entire plate/block system was calculated for the three frequencies. Next, in a region of $1 \text{ m} \times 2 \text{ m}$, perpendicular to the mid-plane of the plate (see sketch in Fig. 5), 911 field points were defined. As an example, the acoustic pressure at these points, generated by the plate at a frequency of 1965 Hz, is plotted in Figure 5. The result clearly shows the typical sound characteristics (maximum/minimum) emitted by the vibrating surface of a structure.

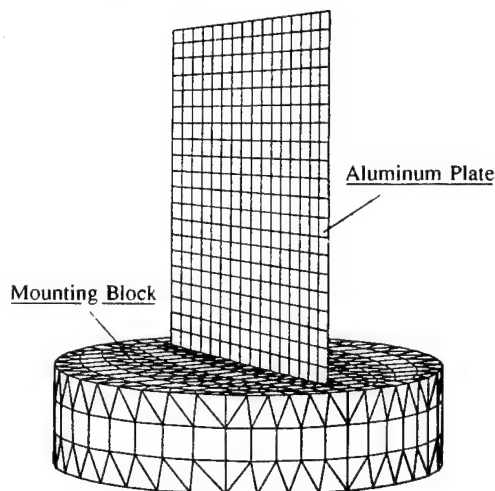


Fig. 4: BE-discretization of the plate and the mounting block.

System:

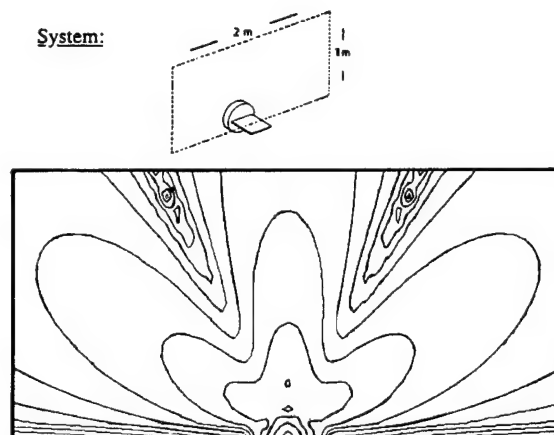


Fig. 5: Sound pressure in a plane perpendicular to the plate.

4.2 Experimental Studies

For the measurements of the acoustic field generated by the plate, an additional aspect has to be considered: it is difficult to excite the plate, e.g. with a shaker, and not to disturb the acoustic field. Therefore, a reciprocity approach is employed, where, instead of measuring the sound emitted by the vibrating plate directly (via a microphone), the plate is excited by a loudspeaker which is set up in place of the microphone. The method makes use of the fact that the vibration amplitude of the plate, measured by an accelerometer, is proportional to the radiated sound of the system.

The plate and its mounting block was installed in an anechoic chamber. Turning the complete system (on a horizontally revolving table) and keeping the loudspeaker at a distance of 0.95 m from the center of the plate (on a vertical, circular guide-rail), it was possible to scan a nearly complete sphere around the vibrating plate. Figure 6 depicts the spatial directivity pattern of the plate measured at a frequency of 1965 Hz.

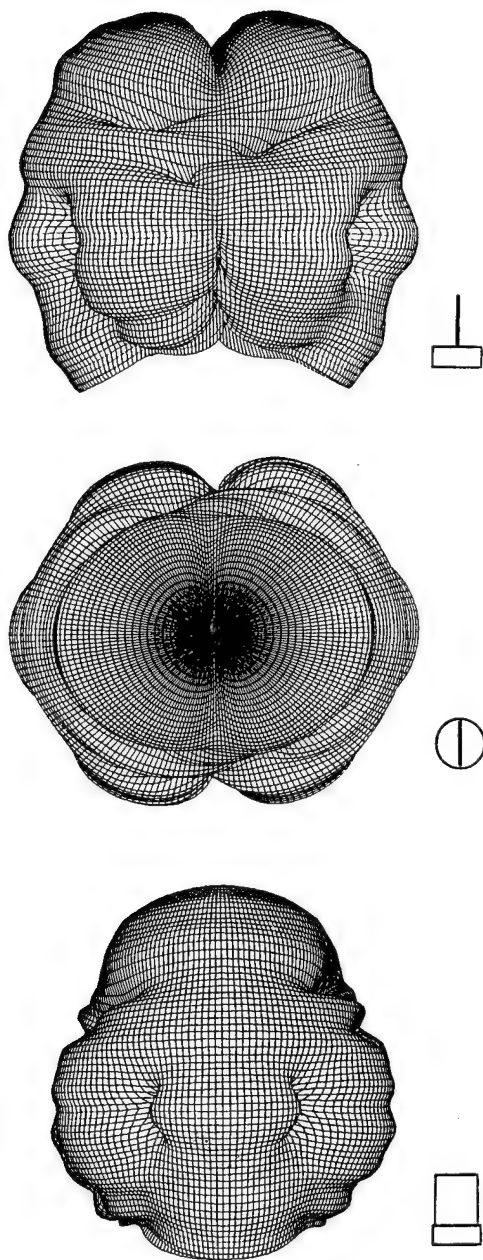


Fig. 6: Spatial directivity pattern: $f = 1965$ Hz.

4.3 Comparison of the Results

First, to compare calculated and measured values, 180 field points were defined on a circle of radius $r = 0.95$ m around the center of the plate (see Fig. 7, solid circle). For the selected frequency of 1965 Hz, the acoustic pressure at these points was calculated and plotted in Figure 8, together with the measured values, which are a part of the spatial directivity pattern shown in Fig. 6. The comparison of the patterns, particularly the locations of their minima and maxima as well as their general shape, shows excellent agreement between numerical and measured values.

Second, the acoustic pressure on a smaller, horizontal circle above the plate is considered. Its radius is 0.82 m around the vertical center line of the plate (see Fig. 7, dashed circle). Looking at Figure 9, it is obvious that also at this location the numerical and experimental data match quite well despite of some non-symmetric effects that can be observed in the case of the experiment.

At this point it should be mentioned that neither the FE solution of the eigenvalue problem, nor the performed experiments, yielded absolute results (e.g. absolute displacements). Therefore, the data had to be scaled to get equal maxima. The performed linear analysis, however, allows the scaling of the results with any factor, i.e. the consideration of the results presented here is sufficient to judge about the accuracy of the BE-model.

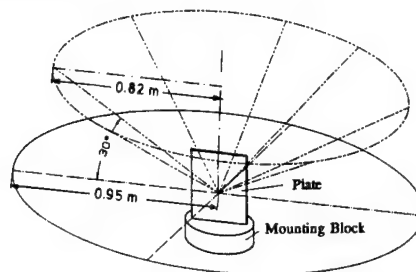


Fig. 7: Geometrical system: the pressure at the two horizontal circles was compared.

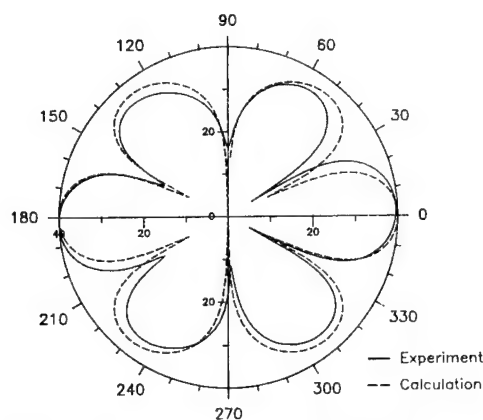


Fig. 8: Comparison of the directivity pattern:
 $f = 1965$ Hz, $r = 0.95$ m

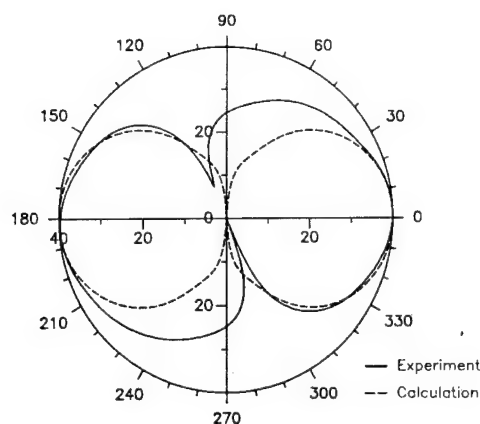


Fig. 9: Comparison of the directivity pattern:
 $f = 1965$ Hz, $r = 0.82$ m

5. CONCLUSIONS

The noise radiation of a cantilever aluminum plate has been investigated using an indirect Boundary Element Method. Comparing numerically and experimentally obtained results, it could be shown that not only the structural Finite Element calculation (mode shapes of the plate), but also the Boundary Element simulation of the sound radiated by the vibrating system yielded very accurate results.

In view of these facts, it can be stated that the currently available Boundary Element formulations are very well suited to handle noise radiation problems. In particular, during the development phase of acoustically sensitive systems, these methods will be very helpful and complete or even replace some costly series of experimental tests.

6. REFERENCES

1. Bathe K -J 1982, *Finite Element Procedures in Engineering Analysis*, Prentice-Hall, Englewood Cliffs, N.J.
2. Brebbia C A 1978, *The Boundary Element Method for Engineers*, Pentech Press, London.
3. Bausinger R, Kuhn G 1987, *The Boundary Element Method*, (in German), Expert-Verlag, Ehningen, FRG.
4. Raasch I 1981, Procedures to Solve Acoustic Problems with MSC/NASTRAN, *Proc. of the MSC/NASTRAN Users' Conf.*, Munich.
5. MacNeal R H, Citerley R, Chargin M 1980, *A New Method of Analyzing Fluid-Structure Interaction Using MSC/NASTRAN*, MacNeal-Schwendler Corporation, Los Angeles.
6. Coyette J P, Guisset P 1988, Finite Element Methods for Interior Acoustics, *Proc. of the 2nd Int. Conf. on Methodology and Innovations in Automotive Experimentations*, Florence.
7. von Estorff O 1991, Numerical Methods for Automotive Acoustics, *Proc. of the 3rd European Cars/Trucks Simulation Symposium*, Schliersee, FRG.
8. Antes H 1988, *Application of the Boundary Element Method in Elastodynamics and Fluidynamics*, (in German), Teubner-Verlag, Stuttgart.
9. Amini S, Wilton D T 1986, An Investigation of Boundary Element Methods for the Exterior Acoustic Problem, *Comp. Meth. in Appl. Mech. and Engng*, Vol. 54, pp. 59-65.
10. Ciskowski R, Brebbia C A (Ed.) 1991, *Advances in BEM in Acoustics*, Computational Mechanics Publications, Southampton.
11. Coyette J P, Dejehet E, Guisset P, Fyfe K 1989, Numerical Analysis of Acoustic and Elasto-Acoustic Problems Using Combined Finite Element and Boundary Element Methods, *Proc. of the 7th Int. Modal Analysis Conf.*, Las Vegas.
12. Seybert A F, Cheng C Y R 1987, Application of the Boundary Element Method to Acoustic Cavity Response and Muffler Analysis, *J. of Vibration, Acoustics, Stress and Reliability in Design*, Vol. 109, pp. 15-21.
13. Antes H, von Estorff O 1989, Radiation of Transient Acoustic Waves - Investigations Using a Time Domain BEM, (in German), *Ingenieur-Archiv*, Vol. 59, pp. 17-31.
14. Mansur W J 1983, *A Time-Stepping Technique to Solve Wave Propagation Problems Using the Boundary Element Method*, Ph.D. Thesis, Southampton University.
15. Antes H, Meise T 1989, Scalar Wave Propagation - Calculation Capabilities of a 3-D Time Domain Boundary Element Method, in *Advances in Boundary Elements*, (C.A. Brebbia and J.J. Connor, Eds), pp. 343-358 in Vol. 3, Stress Analysis, *Proc. 11th BEM Conf.*, Cambridge, USA, Springer Verlag, Berlin and New York.
16. Groenenboom P H L 1983, Wave Propagation Phenomena, Chapter 2 in *Progress in Boundary Element Methods* (Brebbia, C.A., Ed.), Vol. 2, Springer Verlag, Berlin and New York.
17. Burfeindt H, Zimmer H 1989, Calculating Sound Pressure in Car Interiors, *Proc. of the MSC/NASTRAN Users' Conf.*, London.
18. Guy R W, Bhattacharya M C 1973, The Transmission of Sound Through a Cavity-Backed Finite Plate, *J. of Sound and Vibration*, Vol. 27, pp. 207-223.
19. Ochmann M, Wellner F 1991, Analysis of the Noise Radiation of Three-Dimensional Vibrating Structures by a Boundary Element Multi Grid Method, (in German), *Acustica*, (in print).
20. Coyette J P, Fyfe K R 1989, *Solution of Elasto-Acoustic Problems Using a Variational Finite Element / Boundary Element Technique*, Dynamic Engineering, Heverlee, Belgium.
21. SYSNOISE 1988, *User's Manual*, Dynamic Engineering, Heverlee, Belgium.
22. Grinsted B 1952, Nodal Pattern Analysis, *Proceedings of the Institution of Mechanical Engineers (A)*, Vol. 166, pp. 309-326.
23. Junger M C, Feit D, 1986, *Sound, Structures, and Their Interaction*, MIT-Press, Cambridge, USA.
24. Meyer E, Neumann E G 1979, *Physical and Technical Acoustics*, (in German), Vieweg, Braunschweig.
25. Blöchl B, Gamser A 1989, *Experimental Determination of Acoustic Directivity Patterns of Two Propellers for Selected Resonance Frequencies*, (in German), Fraunhofer-Forschungsgruppe für Hydroakustik, FHAK Report 177/89, Ottobrunn, Germany.

**SESSION
1.4.B**

**MATERIALS
I**

FRACTURE/FATIGUE

PRECEDING PAGE BLANK NOT FILMED

N92-23793

73-37
84705

DEVELOPMENT OF FATIGUE DAMAGE MECHANICS FOR APPLICATION TO THE
DESIGN OF DAMAGE-TOLERANT COMPOSITE COMPONENTS

P.W.R. Beaumont, S.M. Spearing and M.T Kortschot

Cambridge University Engineering Department,
Trumpington St, Cambridge CB2 1PZ, U.K.

ABSTRACT

The basic principle that dominates is the recognition that the strength of a composite changes with accumulated damage and that the composite can retain adequate strength by creating a microstructure that permits regions of sub-critical damage growth.

This involves the development of computational models that describe changes in microstructure brought about by stress which simulate those in service. Application of practical damage mechanics analysis can be made to the prediction of residual strength and stiffness and fatigue-life of fibre composites. The extension of basic damage models of composite failure to design is a powerful tool in the development of design procedures for composite hardware.

KEYWORDS: Damage, notch strength, fatigue, failure modes, micro-mechanics

1. OBSERVATIONS OF DAMAGING MECHANISMS

1.1 Components of Damage

An X-ray image of a typical $(90/0)_s$ fatigue-damaged specimen is shown in Fig. 1. The dark images of the photograph indicate three forms of matrix crack emanating from the notch:

- 1) **splitting** in the 0° plies;
- 2) **delamination** zones at $90/0$ interfaces whose size is related to split length; and
- 3) **transverse ply cracking** in the 90° plies.

A concentration of fibre breaks occurs at the intersection of a split and a transverse ply crack.

In the example notch tip damage has grown in a self-similar manner, with a characteristic triangular-shaped delamination zone at the $(90/0)$ interface. At the tip of the split, the delamination angle, α , is constant at about 4° . Essentially, the damage pattern at the notch tip can be characterised by the average length, ℓ , of four splits. Fig. 2 shows a schematic view of the idealised damage pattern.

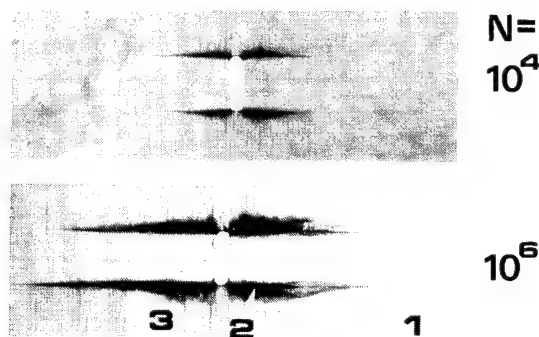


Fig. 1

X-ray images of a $(90/0)_s$ specimen subjected to a fatigue test. ($\sigma_{\max} = 300$ MPa, $R = 0.1$).

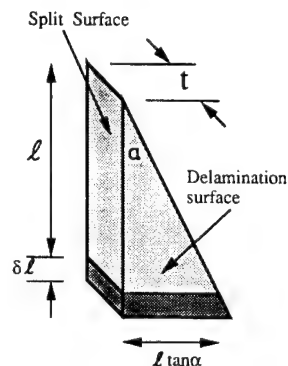
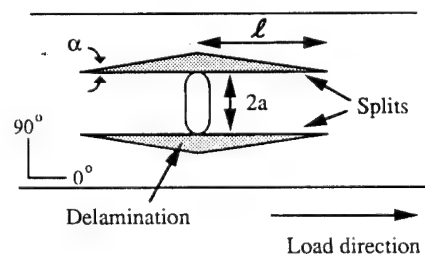


Fig. 2 Schematic of the notch-tip damage pattern

2. THE FATIGUE DAMAGE MODEL

Damage at notches in composite materials can be characterised by the split length ℓ , at the notch tip (Fig.2). The starting point of the model is the fatigue-crack growth law ("Paris" law) for isotropic materials [2]:

$$\frac{da}{dN} = \lambda_1 (\Delta K)^m \quad [1]$$

$\frac{da}{dN}$ is the crack growth rate;

ΔK is the stress intensity factor range; and λ_1 and m are empirical constants.

This can be recast in terms of the split growth rate, $d\ell/dN$, of the composite and energy release-rate, G (using $K^2 = YG$, where Y is an appropriate modulus):

$$\frac{d\ell}{dN} = \lambda_2 (\Delta G)^{m/2} \quad [2]$$

This, however, is inadequate when splits and delaminations grow in combination at the notch tip, as they do in carbon fibre-epoxy laminates. As the split length, ℓ , increases, the associated delamination area grows with a dependence on ℓ^2 , implying an increasing resistance to further crack advance. It is more appropriate, therefore, to normalise ΔG by the current toughness G_c (as measured in monotonic loading), giving:

$$\frac{d\ell}{dN} = \lambda_3 \left[\frac{\Delta G}{G_c} \right]^{m/2} \quad [3]$$

where λ_3 is a constant. In essence, the rate of damage growth is related to the ratio of the driving force, ΔG , to the current damage growth resistance G_c or toughness.

2.1 Damage Growth in Monotonic Loading

The growth of the damage zone in a notched tensile specimen is self-similar, i.e., the shape of the delamination front remains constant: it simply grows in scale (Fig. 1). For an increment of split growth, $\delta\ell$, the energy absorbed in forming new crack surfaces, δE_{ab} , is given by [1]:

$$\delta E_{ab} = G_s t \delta\ell + G_d (\ell \tan \alpha) \delta\ell \quad [4]$$

G_s is the energy absorbed per unit area of split;
 G_d is the energy absorbed per unit area of delamination;
 t is the thickness of a 0° ply; and
 α is the delamination angle at the split tip.

Some of the global energy of the system is dissipated when the split extends with a corresponding increase in specimen compliance (δC):

$$\delta E_r = \frac{1}{2} P^2 \delta C \quad [5]$$

where P is the applied load on one quadrant of the specimen given by:

$$P = \sigma_\omega (W/2) (2t) \quad [6]$$

σ_ω is the remote applied tensile stress on the specimen, W is specimen width and t is ply thickness.

For the damage zone to grow, $\delta E_r \geq \delta E_{ab}$:

$$\frac{1}{2} P^2 \delta C \geq G_s t \delta\ell + G_d \ell \delta\ell \tan \alpha \quad [7]$$

For the limiting case ($E_r = E_{ab}$):

$$\frac{1}{2} \frac{P^2}{t} \frac{\partial C}{\partial \ell} = G_s + G_d \frac{\ell \tan \alpha}{t} \quad [8]$$

$$(G = G_c)$$

This expression can be evaluated if $\partial C / \partial \ell$ is known. A finite element model can determine it numerically [1]. For a range of split length between $\ell/a = 0$ and $\ell/a = 6$ ($2a$ is notch length), $\frac{\partial C}{\partial \ell}$ was found to be constant, dependent only on the angle α and the lay-up [1].

Rearranging eqn. (8), the load for split initiation is given by:

$$P_i = \left[\frac{2G_s t}{\frac{\partial C}{\partial \ell}} \right]^{1/2} \quad [9]$$

For subsequent split growth under monotonic loading:

$$\ell = \frac{P^2 \frac{\partial C}{\partial \ell}}{2G_d \tan \alpha} - \frac{G_s}{G_d} \left[\frac{t}{\tan \alpha} \right] \quad [10]$$

Dividing both sides of eqn. (10) by notch length, a , and substituting for P (in terms of applied stress σ_ω , and $\frac{\partial C}{\partial \ell}$, (scaled from the finite element result $\frac{\partial C}{\partial \ell}|_{FE}$ this expression can be normalised as follows:

$$\frac{\ell}{a} = \frac{(\sigma_\omega)^2 (t) (W/2)_{FE} (2t)_{FE} \frac{\partial C}{\partial \ell}|_{FE}}{G_d \tan \alpha (2a/W)} - \frac{G_s}{G_d} \left[\frac{t}{a \tan \alpha} \right] \quad [11]$$

In practice, $G_s \ll G_d$, hence the second term of eqn. (11) is small, allowing the simplification:

$$\frac{\ell}{a} = \frac{(\sigma_\omega)^2 (t) (W/2)_{FE} (2t)_{FE} \frac{\partial C}{\partial \ell}|_{FE}}{G_d \tan \alpha (2a/W)} \quad [12]$$

Equation (12) indicates that for a given $2a/W$, the ratio ℓ/a is dependent only on applied stress, σ_ω .

The normalised split length versus applied stress curves for all $(90/0)_s$ specimens should be coincidental regardless of width. Figure 3 shows split growth data for three $(90/0)_s$ specimens ($W/2a = 3$) under monotonically increasing load. Equation (12) produces a good fit to the data using selected values of $G_d = 400 \text{ J/m}^2$ and $G_s = 158 \text{ J/m}^2$. Now we apply the model to fatigue damage.

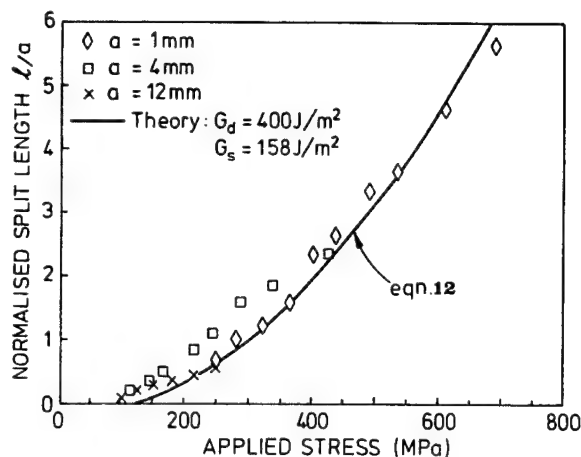


Fig. 3 Split growth in monotonic loading in carbon fibre-epoxy $(90/0)_s$.

2.2 Damage Growth in Cyclic Loading

We start with equation (3). Inserting the definition

$$\Delta G = \frac{1(\Delta P)^2}{2t} \frac{\partial C}{\partial \ell} \quad [13]$$

and combining with equation (8) gives:

$$\frac{d\ell}{dN} = \lambda \left[\frac{1/2(\Delta P)^2 \left(\frac{\partial C}{\partial \ell} \right)}{G_s t + G_d \ell \tan \alpha} \right]^{m/2} \quad [14]$$

For an initial split length, ℓ_0 , the split length after N cycles of constant load amplitude is given by the integrated form of eqn. (14):

$$\ell = \frac{1}{G_d \tan \alpha} \left[\lambda (\Delta G)^{m/2} \left[\frac{m+2}{2} \right] (G_d \tan \alpha) N + (G_s t + G_d \ell_0 \tan \alpha)^{(m+2)/2} \right]^{2/(m+2)} \quad [15]$$

where ΔG is given by equation (13). The split length in the first cycle, ℓ_0 can be determined using eqn. (12). It only remains to identify values for λ , m , and $(\partial C / \partial \ell)$.

3. APPLICATION OF THE FATIGUE DAMAGE MODEL

3.1 $(90/0)_s$ Laminates

Figure 4 shows split growth data for a $(90/0)_s$ laminate cycled at three different peak stresses. Assuming a delamination angle, α , of 3.5° , $\lambda = 8 \times 10^{-4}$, and $m = 14$, and a determined value of $(\partial C / \partial \ell) = 2.9 \times 10^{-7} \text{ N}^{-1}$, a good fit is obtained to the data [2].

For laminates containing 0° and 90° plies of varying thickness, the nature of damage is essentially the same. It is assumed that the damage pattern is similar in all plies and that the delamination shape is the same at all interfaces.

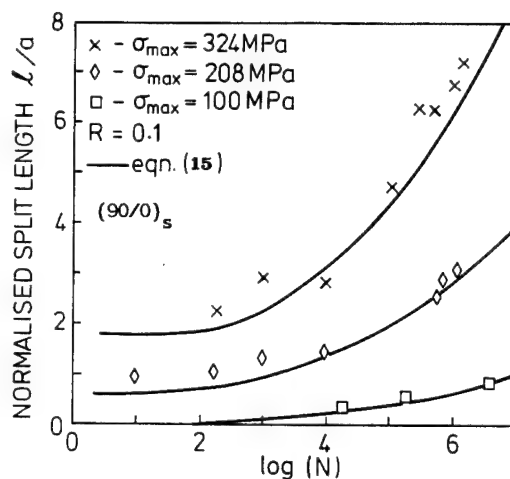


Fig. 4 Split growth in cyclic loading in carbon fibre-epoxy

The basic fatigue damage growth law (eqn. 3) has to be modified in order to cope with the different conditions controlling damage growth. For convenience, the growth laws are kept in differential form but used in integrated form.

3.2 $(90/0)_i$ Laminates

For this family, ΔG increases linearly with ply thickness; i.e. As for the $(90/0)_s$ case, there are only two interfaces at which delaminations can grow. If delamination growth is the dominant energy absorbing process (and it is since $G_d > G_s$, and delaminations have a greater surface area than splits), then the ratio $\Delta G / G_c$ increases as i increases. The fatigue law has the form:

$$\frac{d\ell}{dN} = \lambda \left[\frac{1/2(\Delta \sigma_w)^2 (W/2)(2it)(W/2) \left(\frac{\partial C}{\partial \ell} \right)_{FE}}{G_s it + G_d \ell \tan \alpha} \right]^{m/2} \quad [16]$$

Figure 5 illustrates the increasing rate of damage growth with increasing ply thickness. There is a good agreement between experimental data and the predicted split growth curves.

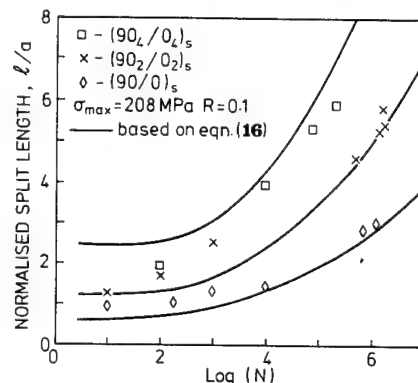


Fig. 5 Effect of ply thickness on split length data of $(90/0)_i$ laminates in cyclic loading.

3.3 $(90/0)_s$ Laminates

Laminates with 90° and 0° plies of unequal thickness can be modelled in a similar way. The relative ply thicknesses of the layers in the finite element meshes are adjusted, and the resulting values of $\left. \frac{\partial C}{\partial \ell} \right|_{FE}$ are scaled appropriately

[1, 2]. In this case, the fatigue law has the form:

$$\frac{d\ell}{dN} = \lambda \left[\frac{\frac{1}{2} (\Delta \sigma_\omega)^2 (W/2) ((i+j)t) (W/2)_{FE} (i+j)t_{FE} \left. \frac{\partial C}{\partial \ell} \right|_{FE}}{G_s i t + G_d (2n-1) \ell \tan \alpha} \right]^{m/2} \quad [17]$$

$\left. \frac{\partial C}{\partial \ell} \right|_{FE}$ does not have the same value as that for laminates with equal thicknesses of 0° and 90° plies. $\left. \frac{\partial C}{\partial \ell} \right|_{FE}$ increases with increasing thickness of the 0° plies; therefore laminates with $j > i$ will exhibit more rapid damage propagation than a $(90/0)_s$ laminate. The predicted split growth curves together with experimental data are shown in Fig. 6. Good agreement is achieved for the three laminates investigated.

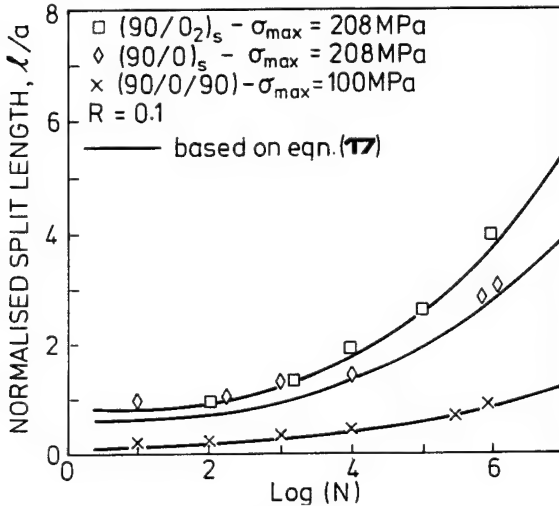


Fig. 6 Normalised split length as a function of load cycles for $(90/0)_{ns}$ laminates.

3.4 $(90/0)_{ns}$ Laminates

In this series, ply thickness is constant and equal for the 90° and 0° laminae, only the number of $90/0$ interfaces varies. Through half the laminate thickness, there are $2n-1$ interfaces at which delaminations can propagate. Since the surface area of a split is $n \times t \times \ell$, and $\left. \frac{\partial C}{\partial \ell} \right|_{FE}$ scales with the number of plies [1, 2], then eqn. (8) for split growth in monotonic loading becomes:

$$\frac{1}{2} \frac{p^2 (W/2)_{FE} (2t)_{FE} \left. \frac{\partial C}{\partial \ell} \right|_{FE}}{n t (W/2) (2n t) \left. \frac{\partial C}{\partial \ell} \right|_{FE}} = \frac{G_s + G_d (2n-1) \ell \tan \alpha}{n t} \quad (G) = (G_c) \quad [18]$$

The fatigue law is, therefore, modified to:

$$\frac{d\ell}{dN} = \lambda \left[\frac{\frac{1}{2} (\Delta \sigma_\omega)^2 (W/2) (2n t) (W/2)_{FE} (2t)_{FE} \left. \frac{\partial C}{\partial \ell} \right|_{FE}}{G_s n t + G_d (2n-1) \ell \tan \alpha} \right]^{m/2} \quad [19]$$

As the number of plies increases, the model predicts that the rate of damage propagation decreases slightly. In this instance, the model tends to underestimate damage growth (Fig. 7). This may be the result of unequal damage growth throughout the laminate thickness.

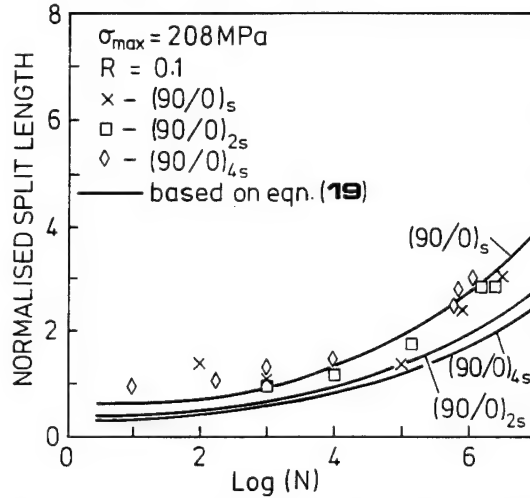


Fig. 7 Normalised split length as a function of load cycles for $(90/0)_{ns}$ laminates.

In summary, the model includes the important parameters and processes which govern fatigue damage behaviour. The ability to model fatigue damage growth in several laminates without altering the parameters which appear in the static and cyclic loading equations and between lay-ups is a significant advance on previous methods.

For damage growth in $(90/+45/-45/0)_s$ laminates, it is assumed that damage evolution is controlled by splitting in the 0° plies and by delamination at the interface between the 0° ply and the innermost -45° plies [2]. The shape of the delamination has been identified and the model developed in a logical way [2].

4. A DAMAGE-BASED POST-FATIGUE STRENGTH MODEL

4.1 Failure Criterion

Using a finite element representation of the damage at a notch tip, combined with the observed terminal damage-state and measured failure stress, Kortschot and Beaumont [1] showed that the maximum tensile stress in the principal load bearing (0°) ply was approximately constant at laminate failure, regardless of the extent of damage. This led them to propose a straightforward tensile stress failure criterion:

$$\sigma_{of} = \frac{\sigma_{of}}{K_t} \quad [20]$$

$\sigma_{\omega f}$ = failure stress of the notched laminate;
 σ_{Of} = the tensile strength of the (0°) ply; and
 K_t = the terminal notch tip stress concentration factor.

σ_{Of} is a material property which can be measured independently while K_t can be obtained from finite element modelling. For a centre-notched specimen K_t is found [1] to be:

$$K_t = \frac{6.3}{(1 - (2a/W)^2) (\ell/a)^{0.28}} = C_1 \left[\frac{\ell}{a} \right]^{-0.28} \quad [21]$$

Furthermore, the strength of a (0°) ply in the notch tip damage zone of a centre-notched tensile specimen depends on the size of that damaged zone [1]

$$\sigma_{Of} = \sigma_o \left[\frac{V_o}{KV_{CNT}} \right]^{1/\beta} \quad [22]$$

σ_o , V_o = a reference stress and reference volume (= 1.88 GPa and 7.4 mm^3 , respectively), for the 0° ply in an unnotched $(90/0)_s$ carbon fibre laminate.

KV_{CNT} = equivalent volume of the (0°) ply in a CNT specimen; and
 β = Weibull modulus (= 20).

The stress distribution at the notch tip varies with split length, ℓ , and the delamination angle, α , at the tip of the split [1]. For $\alpha = 3.5^\circ$, $K = 0.0014 + 0.0025 (\ell/a)$; hence

$$\sigma_{Of} = \sigma_o \left[\frac{V_o}{(0.0014 + 0.0025 (\ell/a)) 8 (a^2 t_0)} \right]^{1/\beta} \quad [23]$$

$$= C_2 \left[(0.0014 + 0.0025 (\ell/a)) a^2 \right]^{-1/\beta}$$

$V_{CNT} = 8 (a^2 t_0)$, where t_0 is the thickness of the (0°) ply.

4.2 Strength of a Damaged $(90/0)_s$ Laminate

The notch tip stress concentration factor K_t (eqn.(21)) and the (0°) ply strength, σ_{Of} , (eqn. (23)) both depend on split length, ℓ . Combining eqns. (20)–(23), we obtain an expression for the laminate failure stress in terms of the normalised split length ℓ/a (for $\alpha = 3.5^\circ$):

$$\sigma_{\omega f} = \left[\frac{(1 - (2a/W)^2) (\ell/a)^{0.28}}{6.3} \right] \sigma_o \left[\frac{V_o}{(0.0014 + 0.0025 (\ell/a)) 8 (a^2 t_0)} \right]^{1/\beta} \quad [24]$$

Experimental data of residual strength of fatigue-damaged $(90/0)_s$ specimens ($W = 24 \text{ mm}$, $a = 4 \text{ mm}$) are plotted against the measured

terminal split length (Fig. 8). These results are compared with the predicted strength eqn (24). The quasi-static failure strength is about 360 MPa, which corresponds to $\ell/a = 1.3$. If higher values of ℓ/a are obtained during load cycling, higher residual strengths result. A quasi-static strength of 360 MPa represents a lower limit for the residual strength after fatigue; hence, the predicted residual strength curves are truncated by a horizontal line at $\sigma_{\omega f} = 360 \text{ MPa}$, between $\ell/a = 0$ and $\ell/a = 1.3$.

Since the shape of the notch tip damage zone is similar for all notched cross-ply carbon fibre laminates [1,2], the model should apply successfully to other cross-ply laminates of equal thickness (0°) and (90°) plies. Equation (24) is, therefore, valid for all laminates of the general form $(90_i/0_i)_{ns}$.

RESIDUAL STRENGTH (MPa)

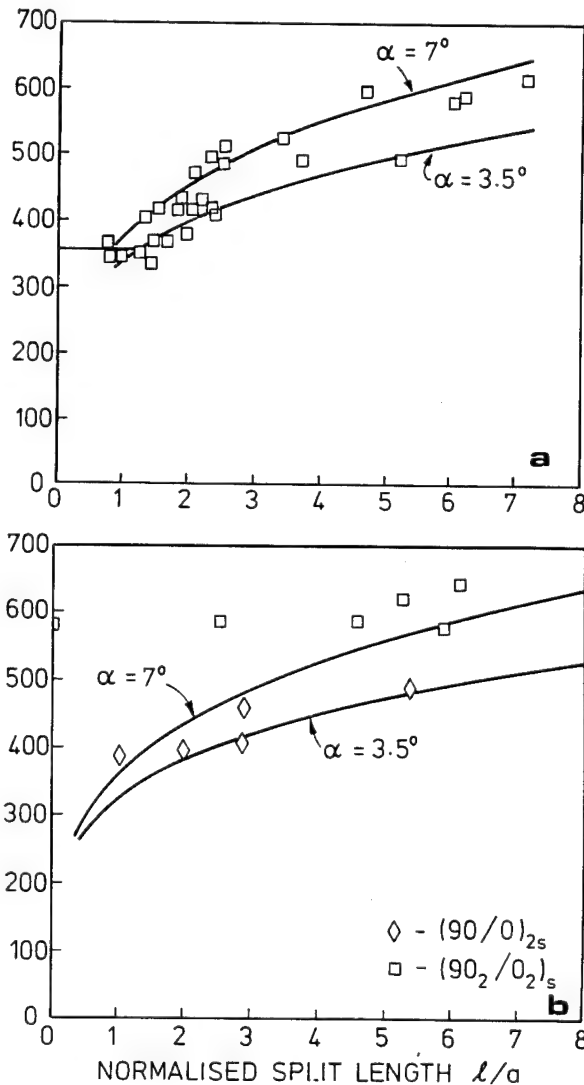


Fig. 8 Residual strength as a function of split length

(a) $(90/0)_s$ specimens.

(b) $(90_2/0_2)_s$ and $(90/0)_{2s}$ specimens.

4.3 Post-Fatigue Damage Strength

In many ways, a prediction of residual (damaged) notched strength is simpler than the prediction of notched strength in monotonic loading. We know that after fatigue loading there is no further damage growth during the residual strength test [2]. A successful strength prediction, therefore, depends on two distinct steps: (1) modelling damage growth; (2) equating strength to damage size at the end of a fatigue test using eqn. (20).

The split length for a notched $(90/0)_s$ laminate after N load cycles (after eqn. (15)) is given by:

$$\frac{\ell}{a} = \frac{1}{G_d a \tan \alpha} \left[\lambda (A G_t)^{m/2} \left[\frac{m+2}{2} \right] (G_d \tan \alpha)^N + (G_s t + G_d \ell_0 \tan \alpha)^{(m+2)/2} \right]^{2/(m+2)}$$

$$= C_3 [\Delta \sigma^m N + C_4]^{2/(m+2)} \quad [25]$$

Substituting into eqn. (24) for $\alpha = 3.5^\circ$:

$$\sigma_{\infty f} = C_5 [1 + C_6 (\Delta \sigma^m N + C_4)^{2/(m+2)} a^2]^{1/\beta}$$

$$\frac{[[\Delta \sigma^m N + C_4]^{2/(m+2)}]^{0.28}}{C_1} \quad [26]$$

where C_4 , C_5 and C_6 are combinations of material constants which can be derived from earlier expressions.

Equation (26) allows residual strength to be predicted as a function of the specimen dimensions and fatigue loading (Fig. 9). The level of effectiveness of the model is limited by the accuracy of both the damage growth prediction and the damage-based strength model. We find that the overall accuracy of the model is comparable to the scatter of the results due to inherent material variability.

5. CONCLUDING REMARKS

The development of a damage mechanics model is now complete. It allows the prediction of strength for notched cross-ply laminates in quasi-static and fatigue loading. Experimental observations show that fatigue damage has the same components as the damage which accumulates during a quasi-static load application. This observation allows the same parameters to be used to predict strength for both the quasi-static and fatigue cases. Their treatment by one model has not been achieved previously.

REFERENCES

1. Kortschot, M.T. and Beaumont, P.W.R., *Damage Mechanics of Composite Materials I-IV*, J. Composite Science and Technology 39 (1990) 289-326 and 40 (1990) 147-179.
2. Spearing, S.M. and Beaumont, P.W.R., *Fatigue Damage Mechanics of Composite Materials I-IV*, CUED/C-MATS/TR. 178, 179, 180, 181 (1990) submitted to Composite Science and Technology. (1990).

ACKNOWLEDGEMENTS

We would like to acknowledge the partial financial support of the European Space Agency. One of us (S.M.S.) was the recipient of a Science and Engineering Research Council research studentship. We would like to thank Professor M.F. Ashby for the many valuable discussions throughout this study.

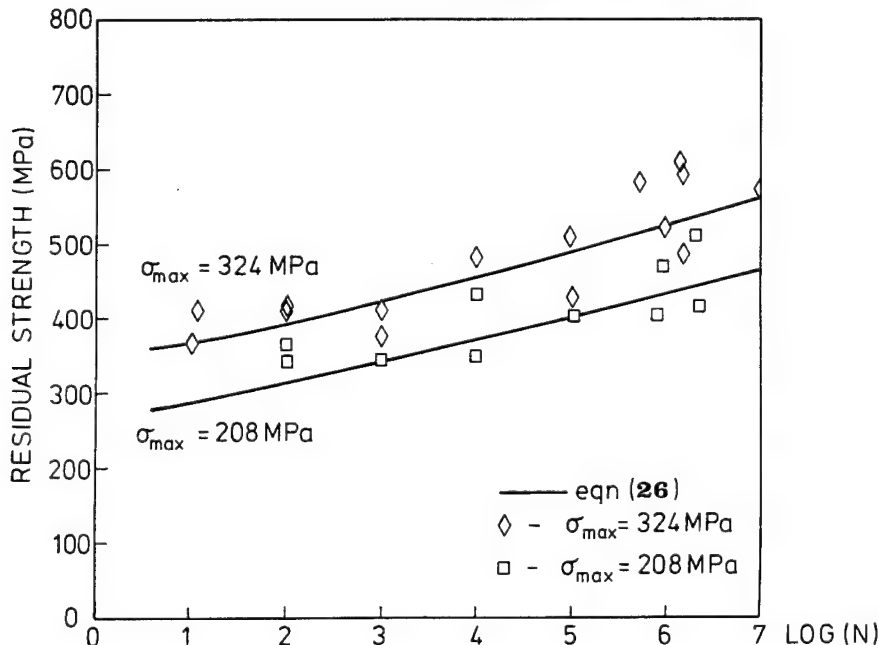


Fig. 9 Residual strength as a function of number of load cycles for $(90/0)_s$ specimens.

N92-23794

CHARACTERIZATION OF INTERLAMINAR MODE I AND MODE II FRACTURE IN CFRP LAMINATES.

Rudolf Prinz and Michael Gädke¹⁾

Deutsche Forschungsanstalt für Luft- und Raumfahrt e.V. (DLR)
Institut für Strukturmechanik
D-3300 Braunschweig / Germany

ABSTRACT

The interlaminar fracture toughness, in general, will be determined by using DCB- and ENF-tests for mode I and mode II fracture, respectively. New methods, the transverse crack tension-test (TCT) and the transverse crack tension compression-test (TCTC) for mode II fracture are presented, which utilized continuous graphite-fiber/epoxy laminates, whose central plies were separated at the specimen center prior to curing. In the course of cycling loading a lateral crack developed in the area of the separations from which two mode II delaminations initiated at each of the separated and the continuous ply interfaces. For the compliance and the energy release rate G_{II} simple equations were derived. The maximum cyclic energy release rate $G_{II\max}$ as a function of the delamination (crack front) propagation rate da/dN in correlation with the critical buckling state (CBS) of separated plies in transverse crack tension-compression test can be used for fatigue life estimations or of residual compressive strength calculations.

Keywords: Composite Materials, Tension-Compression Fatigue Test, Delamination, Crack Growth Rate, Strain Energy Release Rate.

1. INTRODUCTION

Continuous fiber composites are very attractive for a variety of applications because of their high strength and stiffness-to-weight ratios. However, the interlaminar strength or the fiber-matrix interface strength is often a limiting factor in the use of composites. The final failure of composite structures is mainly the result of delamination. Therefore, measurements of interlaminar strength or fracture toughness and predictions of residual compressive strength of laminates with separated plies after fatigue loading or impact are essential to a fail-safe design of composite structures.

Laminates, in general, are assemblies of unidirectional plies oriented under 0° , $\pm 45^\circ$ and 90° with respect to the main load path. The nature of final failure of the specimen depends on the kind of cyclic loading. At the stress ratio of $R = \sigma_l/\sigma_u$ (σ_l and σ_u lower and upper stress respectively) fatigue failure is usually due to an increasing number of lateral cracks in the 90° -plies (first ply failure,

FPF, and characteristic damage state, CDS, [1]) followed by interfacial delamination, 0° -fiber breaks in different locations and massive degradation by matrix cracks due to shear loading in the 0° -plies in longitudinal direction.

In contrast to that tension-compression fatigue tests with different stress ratios $R = \sigma_l/\sigma_u$ indicate that in graphite-fiber-reinforced resins fatigue damage manifests itself most severely at $R = -1$, [2], [3], [4]. The fatigue strength loss is due to delaminations which develop during the compression as well as the tension load phase at comparatively small stress amplitudes, [3]. After a period of stable delamination growth due to mode II and mode III loading, separated plies tend to buckle (figure 1), and the subsequent progression of the delaminations due to mode I, mode II and mode III (figure 2) will eventually lead to failure (instability), the residual life depending on the strength of the remaining intact cross-sections.

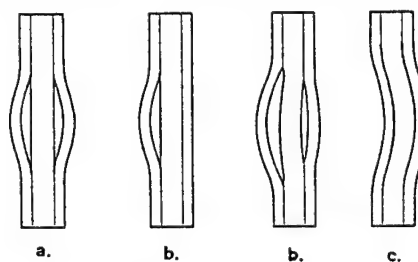


Figure 1. Different buckling shapes of delaminated laminates.

Based on these recognitions a model of delamination growth was developed with the aim of predicting the number of cycles at which buckling of delaminated plies is imminent [3], [4], [5]. The analysis method which has been applied in a number of cases is sound and is considered a valuable improvement of the qualitative and quantitative comprehension of the damage mechanisms in CFRP.

2. ENERGY RELEASE RATE

The formation and propagation of cracks in laminates is accompanied by energy releases which also cause a reduction of the laminate stiffness. By establishing a relationship between the extent of damage and the change of stiffness, the energy release rate G and the stress

¹⁾ Dedicated to Professor Dr.-Ing. H.W.Bergmann for his 65th birthday

intensity factors K can be determined. For the experimental determination of energy release rates different methods have been employed for mode I and mode II and for mode I/II loading [4]. See table 1. It is apparent that the majority of the methods utilize very simple test configurations like *double cantilever beam tests* (DCB) or *end notched flexure tests* (ENF) which do not accurately reflect the damage mechanisms occurring in realistic environments. Especially the cyclically changing conditions at the crack front of delaminations subjected to tension-compression loading and the unstable growth of delaminations due to buckling of delaminated plies are rarely taken into account. For that reason, new test configurations were developed which are denoted as *transverse crack tension test* (TCT) and *transverse crack tension compression test* (TCTC).

Mode	Sign	Designation	Test configuration
I	DCB	double cantilever beam	
II	TCT	transverse crack tension*	
II	TCTC	transverse crack tension-compression*	
II	SBS	short beam shear	
II	ENF	end-notched flexure	
I/II	CLS	crack lap shear	
I/II	EDT	edge delamination tension	
I/II	EDTC	edge delamination tension-compression*	
I/II	HDT	hole delamination tension	
I/II	HDTC	hole delamination tension-compression*	
I/II	ENT	edge notch tension	
I/II	ENTC	edge notch tension-compression*	

Table 1. Tests for experimentally determination of energy release rates for mode I, mode II and mode I/II. New test configurations are identified by asterisks.

From the experimental evaluation of the compliance $C = \delta/P$ and the delamination length a and on the assumption that the delaminations grow at constant force P , the energy release rate G can be formulated for constant width b as [6] and [7],

$$G = \frac{P^2}{2b} \cdot \frac{dC}{da} = \frac{\delta^2}{2bC^2} \cdot \frac{dC}{da} \quad (1)$$

The total energy release rate G for one delamination front in general, is composed of three contributions, see figure 2: G_I release rate due to tension perpendicular the delamination plane, G_{II} release rate due to shear in the delamination plane and G_{III} release rate due to shear transverse the delamination plane.

$$G = f(G_I + G_{II} + G_{III}) \quad (2)$$

For problems at hand (DCB-, ENF-, TCT- and TCTC-tests with unidirectional layered specimens), the latter is of no consequence. The corresponding stress intensity factors K can be obtained from the wellknown relationships for orthotropic materials [8].

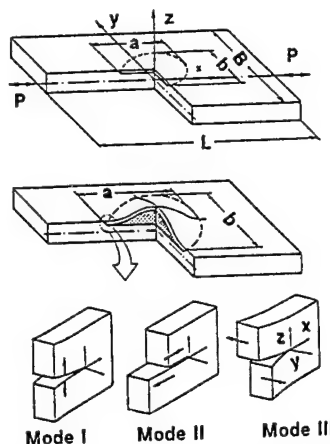


Figure 2. Kinematically admissible crack extension modes. Opening mode I, forward shear mode II and parallel shear mode III.

3. ANALYSIS

The following section introduces the expressions used to calculate the mode I and II energy release rate. Brief derivations are given and references are cited containing the full derivations.

3.1 Transverse Crack Tension-Compression Test

For the determination of mode II energy release rates unidirectional test specimens were used whose central plies, in accordance with figure 3, were separated prior to curing. Such laminates are referred to as $[0_n, \phi_m]_s$, the slash indicating the cut.

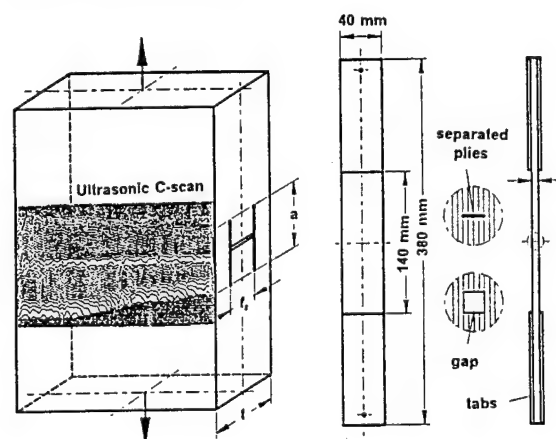


Figure 3. TCT-Test specimen with central separated plies and delaminations, emanating from the transverse crack tips, shown as ultrasonic-C-scan of a $[0_2, \phi_2]_s$ -laminate.

In the course of tension cyclic loading a lateral crack developed in the area of the separations from which two partial delaminations initiated at each of the interfaces of the separated and the continuous plies. To prevent contact between the separated plies during compression

phase of tension-compression tests, specimens with gap were used, see figure 3. Such laminates are referred to $[0_n, \phi_{mg}]_s$.

The two delaminations which were observed at specimen edges by a microscope, grew at approximate uniform growth rate, but the positions of the four delamination fronts are shifted by some mm. After predetermined cycle numbers extent of delaminations was recorded by C-scans (examples of which are given in figure 3), by X-ray examinations or by grid reflection method.

During cyclic loading load P and displacement δ were continually registered, so that a clear connection between the size of delamination, a , and the corresponding compliance C could be established in the form of

$$C = \frac{\delta}{P} = \frac{L}{E \cdot F} \left[1 + \frac{a}{L} \cdot \frac{t_c}{t_s} \right], \quad (3)$$

where P denotes the load, L the specimen reference length, E the initial stiffness of the test specimen separated plies and $F = b \cdot t$ the cross section. $t = t_s + 2t_c$ signifies the total thickness, t_s the thickness of separated and t_c the thickness of continuous plies.

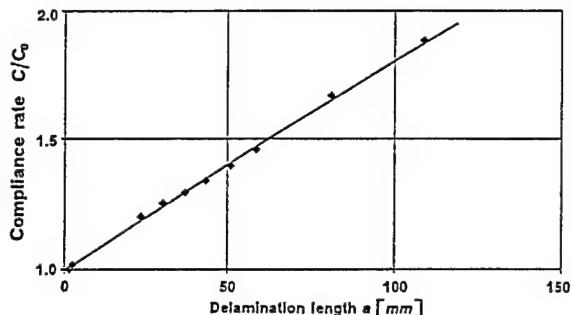


Figure 4. Specimen compliance C as a function of delamination crack length (equation 3).

Figure 4 shows strong relation of the specimen compliance C as a function of delamination length a . The initial compliance $C_0 = \delta/P = L/E \cdot F$ at $a = 0$ has to be measured during the first loading after formation of the transverse crack and prior to initiation of delaminations. Differentiating equation (3) with respect to delamination length a and introducing (1) the total energy release rate assumes the simple form

$$G = \frac{P^2}{4b} \cdot \frac{C_0}{L} \cdot \frac{t_s}{t_c}. \quad (4)$$

The individual contributions of G_I and G_{II} are not readily separable. A numerical approximation is possible by a finite element approach, which allows, by appropriate coupling of elements, the introduction of either a mode I or a mode II displacement and the simultaneous suppression of the other. Figure 5 shows, that energy release rate G_I is about 1% of G_{II} and therefore negligible. The energy release rate G_{II} calculated by finite elements compare very favorable with the result of equation (4). Therefore the maximum cyclic energy release rate for mode II in TCT- or TCTC-test yields

$$G_{II\max} = \frac{P_{\max}^2}{4b} \cdot \frac{C_0}{L} \cdot \frac{t_s}{t_c}. \quad (5)$$

In this equation the $G_{II\max}$ and P_{\max} can be replaced by G_{IIc} and P_c respectively for the critical value of static mode II delamination growth, above which the growth rate is unstable, or replaced by G_{IIth} and P_{th} for a mini-

mum threshold for cyclic loading, below which the delamination do not develop.

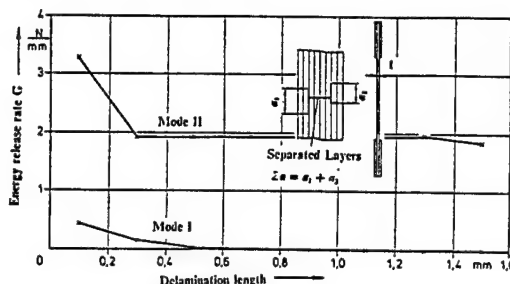


Figure 5. Results of finite element energy release rate calculations for G_I and G_{II} of TCT-test specimen.

3.2 End-Notched Flexure Test

An analysis similar to that for TCT was adopted for the ENF specimen, for which the compliance can be expressed as [10]

$$C = \frac{\delta}{P} = \alpha_1 \cdot a^3 + \alpha_2. \quad (6)$$

The constants α_1 and α_2 can be found by plotting experimental values of C versus a^3 . Classical beam theory gives values of $\alpha_1 = 1/(4EI)$ and $\alpha_2 = L^3/(6EI)$.

Differentiating equation (6) with respect to delamination length a and substituting into equation (1), yields the maximum energy release rate for ENF specimen as

$$G_{II\max} = \frac{3P_{\max}^2 \alpha_1 a^2}{2b} = \frac{3\delta_{\max}^2 \alpha_1 a^2}{2bC^2}. \quad (7)$$

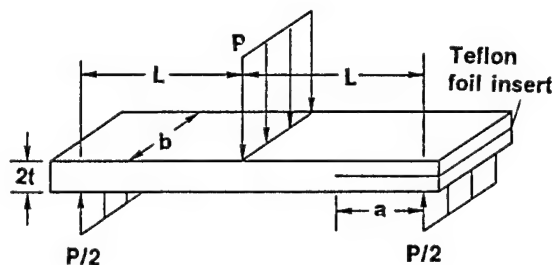


Figure 6. End-notched flexure test specimen.

3.3 Double Cantilever Beam Test

The compliance C of the DCB specimen can be shown [7] to be equal to a power law function of the delamination length a of the form

$$C = \frac{\delta}{P} = \beta_1 \cdot a^\beta, \quad (8)$$

where δ is the displacement of the specimen at the point of load application, P is the applied load, and β and β_1 are constants found by plotting experimental values of $\log C$ versus $\log a$. Classical beam theory expression would give values of $\beta = 3$ and $\beta_1 = 2/(3EI)$. However beam theory makes several assumptions that may not be true in experimental testing. Therefore the experimental and theoretical values of β and β_1 may differ. The values β and β_1 of static tests were used as an approximation to those determined in cyclic tests. It was assumed that any

variations in the values of β and β_1 between static and cyclic testing would be small.

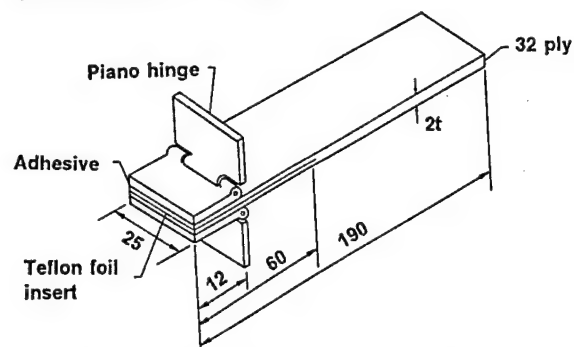


Figure 7. Double cantilever beam test specimen.

Differentiating equation (8) to a yields

$$\frac{dC}{da} = \beta \cdot \beta_1 \cdot a^{\beta-1} = \beta \cdot \frac{C}{a} \quad (9)$$

Substituting equations (9) and (8) into equation (1) yields the maximum cyclic energy release rate as

$$G_{I\max} = \frac{\beta \cdot P_{\max} \cdot \delta_{\max}}{2ba} \quad (10)$$

4. TESTS AND RESULTS

In order to determine the delamination growth rate da/dN constant displacement amplitude tests for ENF- and DCB-specimens and cyclic shedding or block load TCT- and TCTC-tests with increasing and decreasing amplitudes were conducted. The test specimens made of T300/914C and M40/Code69 material were preconditioned at environmental conditions of the laboratory with a temperature of 20°C and 40% relative humidity.

4.1 TCT- and TCTC-Tests

Tests run with a load amplitude frequency of 10 Hz and a stress ratio of $R = 0.1$ (or $R = -1$ for TCTC-tests). Test results of both materials are depicted in figure 8 for a stress ratio of $R = 0.1$.

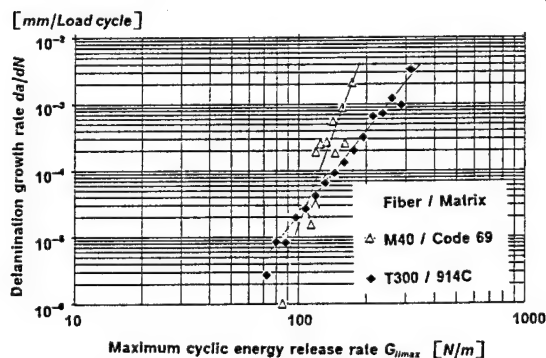


Figure 8. Delamination growth rate da/dN versus maximum energy release rate $G_{II\max}$ for TCT-Tests.

A logarithmic linear relationship between the delamination (crack front) growth rate da/dN and the energy release rate $G_{II\max}$ in the range of stable delamination growth was observed, see equ. (12)

$$\frac{da}{dN} = c \cdot G_{II\max}^n \quad (11)$$

A straight line was obtained by least squares fit of the data points between $da/dN = 2 \cdot 10^{-6}$ and $da/dN = 3 \cdot 10^{-3}$ mm / cycle. The comparison of results from block cyclic loading tests with $[0_2, \phi_2]_s$ -specimens and from load shedding fatigue tests with $[0_4, \phi_4]_s$ -specimens indicates that the delamination growth rate da/dN is not influenced by the specimen thickness and by increasing or decreasing load amplitudes.

The complete characterization of cyclic delamination of composites must include the threshold G_{IIth} below which the delamination does not develop, the delamination-growth rate and a critical value of G_{IIc} above which the growth rate is unstable. TCT-tests are relatively simple and should be considered for the characterization of toughness sensitivity of fiber-reinforced resin systems in general. The constants of the power law relationship of equation (11) are shown in table 2.

symbol	dim.	914C/T300	M40/Code69
c	1)	$3.774 \cdot 10^{-14}$	$5.050 \cdot 10^{-23}$
n	-	4.344	8.721
G_{IIth}	N / m	60	80
G_{IIc}	N / m	500	230

Table 2. Comparison of constants for mode II cyclic fracture toughness. Constant c and exponent n, equ. (11).
1) dimension of c: $[(m/N)^n \cdot mm/load\ cycle]$

In corresponding TCTC-tests with a stress ratio of $R = -1$ ultimate failure of the test specimens was caused by buckling of the delaminated sections during compression load cycle at critical buckling state (CBS). In a number of tests load cycling was terminated at various cycle numbers before failure and residual static compression strength was recorded. According to figure 9 linear relationship was found between the length of delamination a and the compressive strength (static or cyclic loading) of the test specimens. The solid lines in figure 9 represents the theoretically computed buckling strength (see equation (15)) of simply supported delaminated orthotropic plates [11]. The test results fit the experimental data quite well.

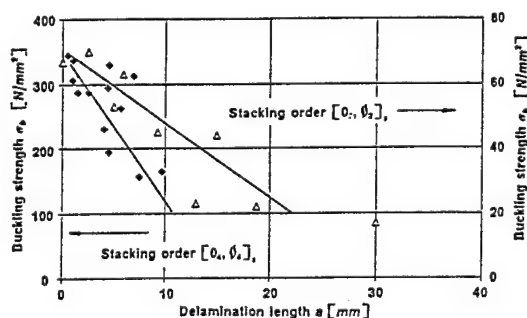


Figure 9. Residual compressive strength versus delamination length. Stacking order $[0_2, \phi_2]_s$ and $[0_4, \phi_4]_s$. Lines show the theoretical buckling strength of the simply supported plate.

4.2 ENF-Tests

The results for ENF-cyclic delamination growth at displacement ratio $R = 0.1$ are shown in figure 10 and compared with results of TCT-Tests. A straight line was obtained by least squares fit of the data points between $da/dN = 2 \cdot 10^{-6}$ and $da/dN = 2 \cdot 10^{-2}$ mm / cycle. The

constants of the power law relationship derived with equation (11) and the threshold and the critical energy release rate are listed in table 2. The scatter of results is very small and TCT-test results compare very well with conventional mode II ENF-tests as can be seen in figure 10.

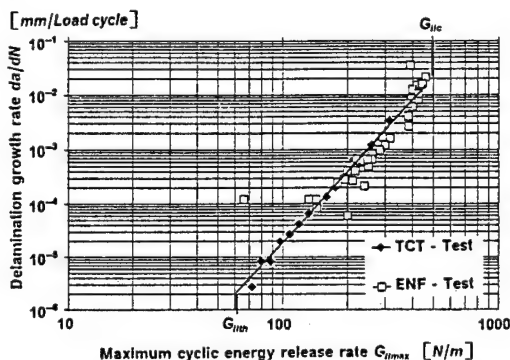


Figure 10. Delamination growth rate da/dN versus maximum cyclic energy release rate G_{Imax} for ENF- and TCT-tests.

4.3 DCB-Tests

The results of DCB mode I delamination growth at displacement ratio of $R=0.1$ are shown in figure 11. A straight line was obtained by least squares fit of the data points between $da/dN = 1 \cdot 10^{-6}$ and $da/dN = 2 \cdot 10^{-4}$ mm / cycle. The constants of the power law relationship of equation (11) are shown in table 3 for T300/914C and M40/Code 69.

symbol	dim.	914C/T300	M40/Code69
c	1)	$3.608 \cdot 10^{-26}$	$2.321 \cdot 10^{-50}$
n	-	10.610	28.037
G_{Ith}	N / m	68	36
G_{Ic}	N / m	140	48

Table 3. Comparison of constants for DCB mode I cyclic fracture toughness. Constant c and exponent n , equ. (11). 1) dimension of c : $[(m/N)^n \cdot mm/load\ cycle]$

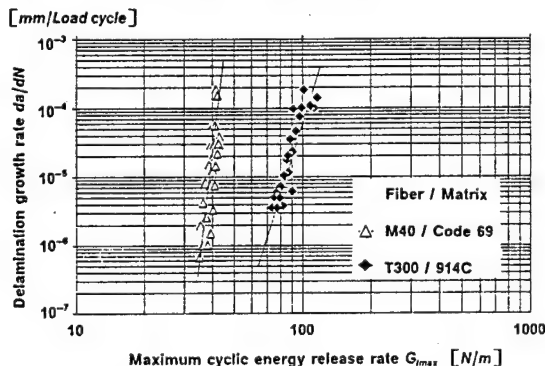


Figure 11. Delamination growth rate da/dN versus maximum energy release rate G_{Imax} for DCB-tests.

5. FATIGUE LIFE

The description of delamination growth in cyclically loaded *unidirectional* and *multidirectional* laminates may be based on formulations used in classical fracture

mechanics [12]. By distinguishing between the mean values of the growth components a_i and b_i in the x - and y -directions of the i^{th} -ply, the approximate size of the delaminated area $A_i = a_i \cdot b_i$ is governed by the equation, [4],

$$\frac{dA_i}{dN} = c \cdot f(G_{Imax})^n = \bar{c} \cdot \epsilon^n \cdot A_i^m, \quad (12)$$

where G_{Imax} is the amplitude of total energy release rate and ϵ the stress σ induced strain; c , \bar{c} , n and m are experimentally determined values. For delamination growth with $b_i = const$, the area A_i in the preceding equation can be replaced by $a \cdot b$. Upon integration and substitution of the limits for $N=0$ with $a=a_0$, a cycle number N_S for damage S and a cycle number N_B for *critical buckling state* (CBS) can be obtained, which corresponds to a delamination length a_S and a_B respectively, [4]:

$$N_S = \frac{a_S^{(1-m)} - a_0^{(1-m)}}{(1-m) \cdot c \cdot \sigma^n}, \quad (13)$$

$$N_B = \frac{a_B^{(1-m)} - a_0^{(1-m)}}{(1-m) \cdot c \cdot \sigma^n}. \quad (14)$$

Buckling of a delaminated section, or of the complete laminate, occurs when the delaminated area of the plies reaches a critical buckling dimension. Because of the complexity of the issue a precise assessment of the buckling load is not feasible, but the possibility of an approximation will be demonstrated by an example. Assuming an internal delamination of length a and width b the critical buckling load P_B , and therefor the critical delamination length a_B , is

$$P_B = K_B \frac{\pi^2 D_{11}}{b^2} = \sigma_B \cdot t_d, \quad (15)$$

$$a_B = \sqrt{2.69 \frac{\pi^2 D_{11}}{P_B}}.$$

$P_B = \sigma_B \cdot t_d$ is the load intensity per unit width, D_{11} the bending stiffness, and t_d the thickness of the delaminated section. K_B is the buckling factor, figure 12, which depends on the aspect ratio a/b , the boundary conditions and the stiffness properties of the delaminated sections. a_B follows on the minimum value of $K_B = 0.83$ for the aspect ratio of $a_B/b = 1.8$.

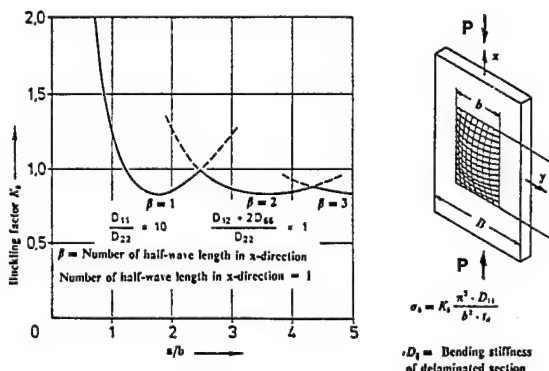


Figure 12. Critical buckling load of separated plies.

This model has been applied successfully for the estimation of residual strength and load cycles to failure of delaminated TCTC-specimens. To facilitate the comparison with residual strength tests results of *multidirectional*

laminates the following dimensionless formulation is introduced [4], for damage S

$$S = f \left(\frac{N_S}{N_B} \right) = \left[\frac{a_S}{a_B} \right]^n \quad (16)$$

and

$$S = \left[\frac{(\sigma_{c0}/\sigma_{cres})^{\frac{1-m}{2}} - 1}{(\sigma_{c0}/\sigma_l)^{\frac{1-m}{2}} - 1} \right]^n, \quad (17)$$

where σ_{c0} is the initial and σ_{cres} the residual compressive strength, respectively. σ_l is the lower compressive stress of cyclic loading. As the number of test results is as yet scant, $f \cdot (N_S/N_B) = (N_S/N_B)^n$ was introduced as a potential function. The associated scatter range and curves of equal survival probabilities $P_s = 90\%$, 50% and 10% for the damage state S are shown in figure 14.

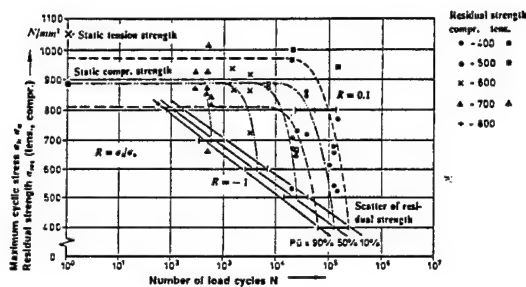


Figure 13. S - N - curve for fatigued graphite/epoxy specimens. T900/314C, $R = -1$, multidirectional stacking order of $[0_2, +45, 0_2, -45, 0, 90]_s$.

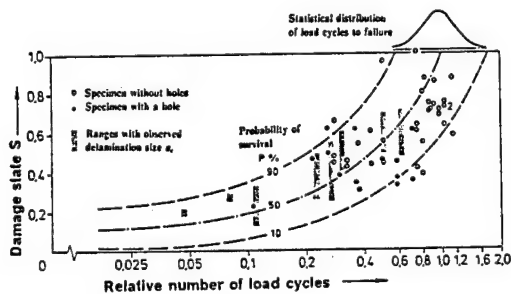


Figure 14. Damage state S of delaminated multidirectional laminates versus load cycle ratio N_S/N_B .

6. SUMMARY

Analytical and experimental investigations on unidirectional CFRP specimens with transverse separations of central plies (TCT- and TCTC-tests) for characterization of mode II delamination fracture in CFRP were reviewed. Cyclic double cantilever beam (DCB) and end notched flexure (ENF) tests were conducted. Delamination growth rates and corresponding cyclic energy release rates were measured.

A model for estimation of fatigue life based on mode II cyclic energy release rate was developed, which include buckling failure in cyclic tension-compression loading and which was used for approximate calculation of multidirectional laminates damage state and residual compressive strength.

7. BIBLIOGRAPHY

- [1] R.D.Jamison, K.Schulte, K.L.Reifsnider and W.W.Stinchcomb : *Characterization and Analysis of Damage Mechanisms in Tension-Tension Fatigue of Graphite/Epoxy Laminates*. Published in Wilkins,D.J.: *Effects of Defects in Composite Materials*. ASTM STP 836 (1982) pp. 21 - 55.
- [2] Prinz,R. : *Growth of Delamination under Fatigue Loading*. In Jube,G.: *Characterization, Analysis and Significance of Defects in Composite Materials*. AGARD Conference Proceedings No. 355 (1983) pp. 5.1 - 5.27
- [3] Prinz,R. : *CRP Damage Mechanics under Fatigue Loading*. European Space Agency ESA-TT-1093 (March 1987) 287 p., Translation of : *Schadensmechanik kohlenstoffaserverstärkter Kunststoffe bei Schwingbelastung*. DFLVR-Mitteilung 87-08, 1987, 246 p.
- [4] Bergmann, H.W. and R.Prinz : *Fatigue Life Estimation of Graphite/Epoxy Laminates under Consideration of Delamination Growth*. *Journal for Numerical Methods in Engineering* 27 (1989) pp. 323 - 341.
- [5] Prinz,R. : *Damage Rates for Interlaminar Failure of Fatigued CFRP Laminates*. In *Developments in the Science and Technology of Composite Materials*. Fourth European Conference on Composite Materials. ECCM4. Elsevier Applied Scienc: London and New York. 1990 pp. 189 - 194.
- [6] Irwin,G.R. : *Fracture*. In S.Flügge : *Handbuch der Physik*, Band VI, *Elastizität und Plastizität*. Springer Verlag, Berlin - Göttingen - Heidelberg, 1958, pp. 551 - 590, esp. p. 563.
- [7] Whitney, J.M., C.E.Browning and W.Hoogsteden : *A Double Cantilever Beam Test for Characterizing Mode I Delamination of Composite Materials*. *Journal of Reinforced Plastics and Composites*. Vol. 1 October 1982, pp. 297 - 313.
- [8] Sih,G.C.; P.C.Paris and G.R.Irwin : *On Cracks in Rectilinearly Anisotropic Bodies*. *International Journal of Fracture* 1(1965) pp. 189 - 203.
- [9] Russell,a.J. and K.N.Street : *Moisture and Temperature Effects on the Mixed Mode Delamination Fracture of Unidirectional Graphite/Epoxy*. Published in Johnson,W.S.: *Delamination and debonding of Materials*. ASTM STP 876 (1985) pp. 349 - 370.
- [10] Martin, R.H. and G.B. Murri : *Characterization of Mode I and Mode II Delamination Growth and Thresholds in AS4/PEEK Composites*. Published in Garbo,S.P.: *Composite Materials: Testing and Design (Ninth Volume)* ASTM STP 1059 (1990) pp. 251 - 270.
- [11] Shivakumar,K. and J.D.Withcomb : *Buckling of Sublaminates in a Quasi-Isotropic Composite Laminates*. *Journal of Composite Materials* 19(1985) pp. 2 -18.
- [12] Paris, P.C. and F.Erdogan : *A Critical Analysis of Crack Propagation Laws*. *Trans. ASME, Ser. D, Journal of Basic Eng.* 85 (1963) pp. 528 - 534.

N 92-23795

84707

FATIGUE ANALYSIS UNDER RANDOM STRESSES

A. RICARD

FRAMASOFT+CSI- Tour Fiat - Cedex 16
92084 PARIS LA DEFENSE

ABSTRACT

Fatigue is a primary risk of failure for metallic structural and mechanical components which respond dynamically to random loading, oscillatory stresses producing fatigue at "hot spots".

However an engineering description of fatigue behavior is complicated because the fatigue process consists in two phases (crack initiation and propagation), there is substantial variability in failure data even in well controlled experiments, and stress processes are often very complicated.

The goal of this study is to propose a classification of the high cycle fatigue design procedures for a structural component subjected to a stationary random stress process which in general can be wide band. We describe different methods to estimate the fatigue life time of structures including threshold and mean stress effects.

Such procedures could be useful in design of components for motor cars, aerospace vehicles, offshore platforms, ...

Keywords : Fatigue, Damage, Random Process.

1. INTRODUCTION

Fatigue can be defined as "the process of progressive localized permanent structural change and microcracks occurring in a material subjected to conditions which produce fluctuating stresses and strains at some points and which may culminate in crack after a sufficient number of fluctuations". It is a complex phenomenon depending upon many parameters such as mean stress, high temperature, multiaxial loading, environment, ...

The need to consider fatigue damage in the design of structural components arises when the in service loading conditions involve cyclic or fluctuating conditions. Typical examples are :

- . for nuclear power plants : flow induced vibrations, cyclic thermal stress internal, pressure variations in pipe line, earthquakes, ...
- . for off-shore structures : wind, ocean wave loading, ...
- . for automotive and flight vehicles : pressure variations, vibrations induced by turbulent flow, ...

Metal fatigue under such irregular loading is a principal risk of failure of components. Several methods of random fatigue analysis have been proposed in the literature, depending upon the domain of application, of the physical phenomena taken into account, of the input required, ...

The general goal of this study is to propose a classification of these methods with their assumptions and their domains

of applicability. We have performed, on typical examples, some of its and analysed the results.

2. DESCRIPTIONS OF THE PROBLEM AND GENERAL ASSUMPTIONS

2.1. Low and high cycle fatigue regimes

A fatigue resistance to total strain cycling is expressed as a function of its elastic and plastic resistance. The magnitude of the plastic strain in the high cycle fatigue life can be neglected. Transition fatigue life of metals is usually found to be in the vicinity of 10000 cycles. We consider in this study only high cycle fatigue where elastic strains dominate and control the life time of the component.

2.2. Parameters governing high cycle fatigue life.

High cycle fatigue life is mainly influenced by the following parameters :

Sequence : the sequence effect is described in fig.1. For the high-low sequence, a crack can be initiated by the high level and then failure occurs after a few cycles at the low level. For the low high sequence application of the large number of cycles at the low level does not significantly affect the number of cycles required for failure at the higher level. Therefore, the sequence has a significant effect on the crack initiation life.

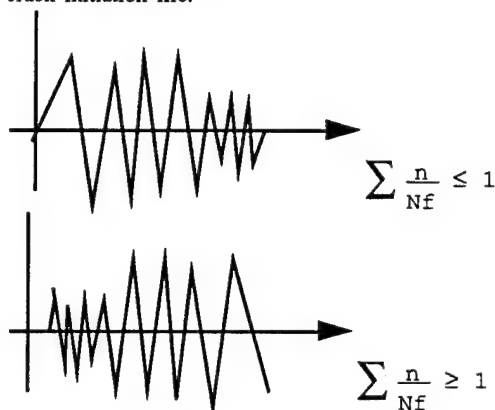


Fig.1 : Sequence effect

Mean stresses : for cyclic stress strain histories where mean stresses are large relative to the fluctuating stress, fatigue life cannot be adequately predicted without considering mean stress effects. Tensile mean stress shortens the fatigue life and a compressive mean stress prolongs it.

2.3. Formulation of fatigue damage laws

All the different fatigue laws in the literature can be included in the scope of the continuum damage mechanics developed by Lemaître Chaboche (ref 1 2).

A damage variable is defined by :

$$D = (S - \bar{S}) / S \quad (1)$$

S : overall section area of a volume element defined by the normal n

\bar{S} : effective resisting area

$D = 0$ corresponds to the undamaged element

$D = D_c$ corresponds to the rupture of the element

Assuming an isotropic behavior the damage is characterized by a scalar variable : D .

Using a thermodynamic potential theory, we can include in the same formalism many models of damage (brittle, ductile, plastic damage, creep, For each particular case of damage, a constitutive equation and its identification from experiments is given by (refs 1). An interaction effect between different kinds of damage can be formulated. For high cycle fatigue damage a general constitutive equation can be written :

$$\delta D = f(D, \sigma_M, \bar{\sigma}, ...) \delta N \quad (2)$$

where σ_M is the maximum tensile stress and $\bar{\sigma}$ the mean stress over one cycle.

The number of cycles to failure is obtained from integration

$$\begin{aligned} N=0 & \longrightarrow D=0 \\ N=N_r & \longrightarrow D=D_c \end{aligned}$$

If we assume that :

$$f(D, \sigma_M, \bar{\sigma}, ...) = f_1(D) * f_2(\sigma_M, \bar{\sigma}, ...) \quad (3)$$

We obtain the linear cumulative fatigue damage law as in the Palmgren Miner law.

2.4. Constitutive behavior law for high cycle fatigue

The fatigue behavior of the material can be described by the Whoelher's curve which is generally assumed to be of the piecewise form :

$$N_R (\Delta \sigma)^m = K \quad (4)$$

where $\Delta \sigma$ is the stress amplitude, N_R cycles to failure, m and K are empirical constants obtained from fatigue experiments. We assume the values of m and K are known. The scatter of the experimental data to determine these values is not taken into account in this study.

Mathematical models have been proposed to estimate the effect of mean stress $\bar{\sigma}$ on fatigue strength. For example, Goodman model is based on the following relationship :

$$\Delta \sigma(N) = [1 - \bar{\sigma}/\sigma_u] \Delta \sigma_{eq}(N) \quad (5)$$

σ_u is the ultimate tensile strength

$\Delta \sigma_{eq}$ is the equivalent stress range that would cause failure for a zero mean stress expressed as a function of cycles N .

If the mean stress varies significantly, the mean stress of each cycle must be conveniently determined.

Assuming linear cumulative law, we can write the constitutive behavior law for high cycle fatigue using (3) as :

$$\frac{\delta D}{\delta N} = \frac{\sigma_M - \sigma_1(\bar{\sigma})}{\sigma_u - \sigma_M} \left[\frac{\sigma_M - \bar{\sigma}}{B(\bar{\sigma})} \right]^\beta \quad \text{with } B(\bar{\sigma}) = B_0 (1 - b \bar{\sigma}) \quad (6)$$

where : $\alpha(\bar{\sigma}) = \bar{\sigma} + \sigma_{10} (1 - b \bar{\sigma})$

σ_1 is the fatigue limit

σ_M is the maximum stress over one cycle

The coefficients b , β , B_0 , σ_{10} can be identified using classical Woelher's curves.

2.5. Random stress process :

Assuming the Palmgren Miner hypothesis, the cumulative damage D is defined as :

$$D = \sum_i n_i / N_i \quad (7)$$

n_i : number of cycles of the process at stress amplitude $\Delta \sigma_i$

N_i : number of cycles at stress amplitude $\Delta \sigma_i$ to cause failure

According to this hypothesis, failure occurs when $D = 1$. We don't consider the statistical variability on the critical value of the cumulative damage at failure.

For continuous systems, D can be expressed by :

$$D = N \int_0^\infty \frac{f_s(S_i)}{N_i} dS_i \quad (8)$$

N_i : number of cycles at stress amplitude $\Delta \sigma_i$ to cause failure

$f_s(\Delta \sigma_i)$: probability density function of stress $\Delta \sigma_i$

For the purpose of fatigue prediction, it is assumed that a non stationnary random process $\sigma(t)$ can be described by a sequence of k stationnary processes. We consider below only stationnary processes which can be described by one of the following input :

- 1/ Power spectral density function associated with a zero mean process σ_u . The mean of the process μ_u can be given separately, but not the mean of each cycle.
- 2/ Probability distribution of peaks
- 3/ Probability distribution of stress ranges.

Using one of the input mentioned above, for computing a life time evaluation of the component, we must obtain previously a probability distribution of stress ranges. We describe below the approaches using a power spectral density.

3. RANDOM APPROACH USING A POWER SPECTRAL DENSITY FUNCTION OF A GAUSSIAN PROCESS

Knowing the power spectral density function of the process, we can compute easily (refs 3) :

- the k th moment of spectral density function : m_k

- the root mean square value : s
- the expected rate of zero crossings with positive slope : v_0^+
- the expected rate of peaks : v_m
- the irregularity factor : α
- the spectral width parameter : ϵ

3.1. Probability density function of peak stress

The probability density function of peaks is given by the following formula :

$$f(x) = \frac{\epsilon}{\sqrt{2\pi}s} \exp[-x^2/2 \epsilon^2 s^2] + \frac{\alpha x}{2s^2} [1 + \operatorname{erf}[x\alpha/\epsilon s\sqrt{2}]] \exp[-x^2/2s^2] \quad (9)$$

Where $\operatorname{erf}[x]$ is the Gaussian error function (refs 4).

Note that this function reduces to a Rayleigh density for a narrow band process with $\alpha = 1$ and to a Gaussian density for a broad band process with $\alpha = 0$.

3.2. Probability density function of stress range

A probability distribution for stress ranges of a broad banded stress can be obtained from the distribution of peaks if the following assumptions are made :

- . The stress process is assumed to be symmetric. The number of local maxima below the mean level are assumed equal to the number of local minima above the mean level.
- . All the stress peaks, both above and below the mean level are counted. A local maxima above the mean is paired with a local minima below the mean of approximately the same amplitude to form a stress cycle regardless of the position of these maxima and minima in the time history. This means that all cycle interaction effects are neglected.
- . Local maxima below the mean are also assumed to be equally damaging. Based on these assumptions, a probability density function for stress range can be obtained from the density function of the peaks by putting $x = \Delta\sigma/2$ where $\Delta\sigma$ is the stress range.

4. RANDOM VIBRATION APPROACH USING A POWER SPECTRAL DENSITY FUNCTION OF A NON GAUSSIAN PROCESS

When the stress histories follow other process than a stationary Gaussian process and/or we wish to take into account the effect of the mean stress of each cycle, the probability density function of peak stress cannot be easily derived. The use of a cycle counting method on cyclic strain/stress histories overcomes this problem. One of the disadvantages of using this method is that it requires an enormous amount of stress/strain history data to obtain a reliable high cycle fatigue life prediction. To overcome this problem, a typical stress/strain history data block is estimated, then this typical block is assumed to repeat itself to permit calculation of longer fatigue lives.

Using a power spectral density function of the process the two steps of this method are the following ones :

- 1 simulation of a time history $X(t)$

For a given spectral density function, a sample of $X(t)$ is simulated using :

$$X(t) = \sum_{i=1}^J \sqrt{2G(\omega_i)\Delta\omega_i} \cos(\omega_i t + \phi_i) \quad \omega_M = \sum_{i=1}^J \Delta\omega_i \quad (10)$$

$$0 < \omega_i < \omega_M$$

where ϕ_i is a random phase angle, uniformly distributed in $[0, 2\pi]$

- 2 cycle counting method.

The purpose of cycle counting method is to reduce time history to a counting of constant amplitude cycles. The most popular method is the rainflow method (refs 5) fig(2). We can obtain, for a given sample, a number of cycles associated to an amplitude and a mean value. Then, it is possible to group all the stress cycles of different stress range magnitudes into a discrete number of blocks and build a numerical approximation of the probability density function of peaks.

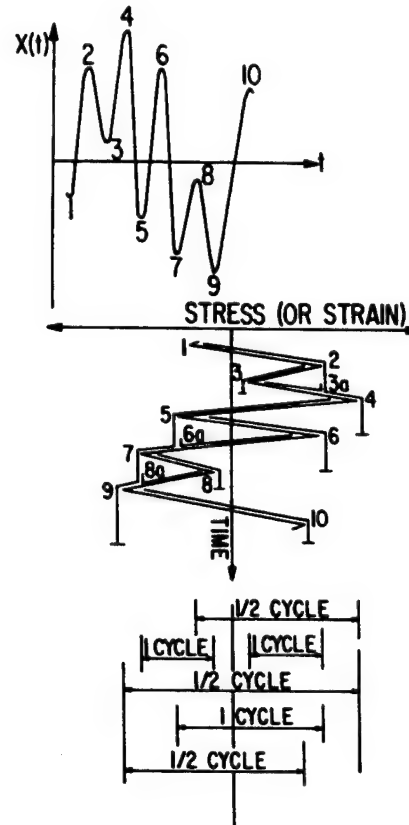


Fig. 2 : example of rainflow method

5. DETERMINATION OF THE LIFE TIME

Assuming Miner's rule and the basic fatigue curve is $N\Delta\sigma^m = K$, the fatigue damage becomes :

$$D = n \Delta\sigma^m / K \quad (11)$$

in which n is the total number of cycles

$\Delta\sigma^m$ is the mean value of $\Delta\sigma^m$

5.1. Gaussian process

For a narrow band process, fatigue cycles are easily identified and analytical solutions are available. The damage is given by :

$$D_{nb} = N \left(2 \sqrt{2} s \right)^m \Gamma(m/2 + 1) / K \quad (12)$$

where Γ is the Gamma function

For wide band process, we can define an equivalent number of cycles N_{eq} and an equivalent stress σ_{eq} which produce the same damage as the actual process :

$$D = N_{eq} \sigma_{eq}^m / K \quad (13)$$

A cycle is defined as the range between two peaks in the actual process and knowing the average frequency of peaks v_m , the equivalent number of cycles for a duration t is given by :

$$N_{eq} = v_m t \quad (14)$$

Using the stress range density function an equivalent stress range is given by :

$$\sigma_{eq}^m = E[\sigma^m] = \int_0^\infty \sigma^m f(\sigma) d\sigma \quad (15)$$

In general case numerical integration is need to estimate the equivalent stress range.

Some authors have proposed, in this case, approximate solutions to take into account the bandwidth of the process (refs 6 - 7).

The mean stress effect can be taken into account using Goodman model. If we wish to take into account a threshold effect as endurance limit we generalize (15) by :

$$\sigma_{eq}^m = E[s^m] = \int_{\sigma_0}^\infty \sigma^m f(\sigma) d\sigma \quad (16)$$

In the case of a narrow band process and for a Woehler curve as described in fig (3) the damage is given by :

$$D_{nb} = N (2\sqrt{2} s)^m \Gamma(1+m/2, \sigma_0^2/2 s^2) / K \quad (17)$$

where $\Gamma(x,y)$ is the incomplete gamma function. In the other case, numerical integration is need.

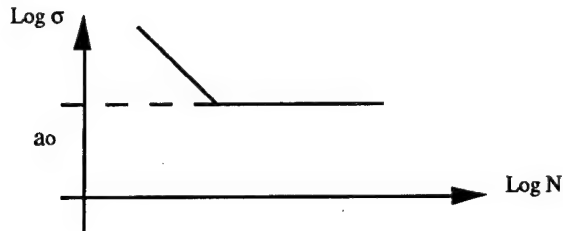


Fig. 3 : Woehler's curve with endurance limit

5.2. Block loading approach

For a particular stress time history, this approach consists in grouping all the stress cycles of different stress range magnitudes into a discrete number of blocks. The stress cycles in each block are all assumed to be of constant amplitude. Thus the actual variable amplitude loading is reduced to an equivalent block loading. Let be L blocks each of width Δt and constant amplitude stress range $\sigma_1, \sigma_2, \dots, \sigma_L$.

In the case of Gaussian process, using the probability density function of stress range, the probability p_l of a stress cycle of range σ_l and the number of stress cycles n_l in

the l th block out of a total of $N(t)$ cycles in the duration t can be obtained as :

$$p_l = f(\sigma_l) d\sigma$$

$$n_l = p_l N(t)$$

Then the expected cumulative loading due to all blocks is obtained as :

$$E\left[\sum_{l=1}^{N(t)} \sigma_l^m\right] = \sum_{l=1}^L p_l v_m t \sigma_l^m$$

In the other case we can compute the number of cycles at failure using equation (7).

The incorporation of threshold effects into the equivalent block loading approach is straight forward. Since each block of loading have stress cycles of constant amplitude, a block 1 cause a fatigue damage if the stress range is greater than the threshold value.

5.3. Non linear cumulative law

If we wish to use a nonlinear cumulative law and take into account sequence effect, we must simulate, by drawing lots, several samples of the process (Monte Carlo Simulation). Knowing the probability density function of peak stress, we generate a sample of the process by a random variable so as to define a sequence order of peaks. On each sample we use equation(2) with the appropriate behavior law to estimate damage of this sample. We repeat, for several samples, the same procedure, and provide an estimated value of the damage.

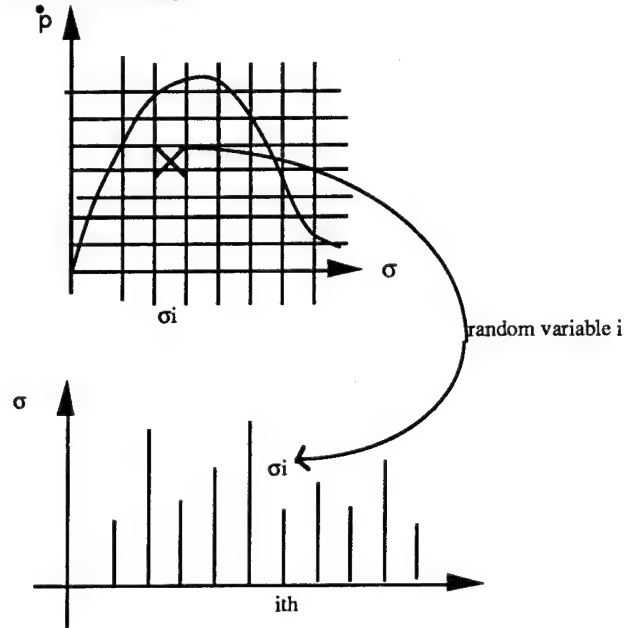


Fig.4 : Monte Carlo's simulation

6. CONCLUSIONS

We have described available methods for high cycle fatigue life estimation with its assumptions and validity domains. All these methods can be formulated using continuous damage formalism. A tentative classification can be obtained in respect to :

- available input data of the process
- probabilistic assumptions of the process
- fatigue behavior law taken into account.

We have summarized the main results below :

INPUT DATA	POWER SPECTRAL DENSITY		PROBABILITY DENSITY FUNCTION OF PEAKS	
Probabilistic Assumptions	Gaussian Process	Other	Gaussian	Other
Computation	Bandwidth	Simulation of $x(t)$ + Rainflow	Simulation of one Sample	
Fatigue law Linear cumulative law + Wohler's curve + endurance limit	Narrow Band	Wide Band	Block loading approach (one sample of the process)	
	Analytical	Equivalent Stress range approach semi-analytical formulation or numerical integration		
Non linear cumulative law Sequence effect Coupling with other mechanical phenomena			. Monte Carlo simulation of samples + Block loading approach for each samples + Expected value of damage	
Results (mean values)	Time life duration	Number of cycles at failure	Time life duration	Number of cycle at failure

7. REFERENCES

1. J. Lemaître - J.L. Chaboche - Mechanics of solid materials . Cambridge University, Press 1990.
2. J. Lemaître - How to use damage mechanics Nuclear Engineering And Design 80 (1984) pp 233-245.
3. S.H. Crandall - Random Vibration in Mechanical Systems Academic press 1973.
4. D.E. Cartwright M.S. Longuet-Higgins - The statistical distribution of the maxima of a random function. Proc. R.Soc. ser a 237 pp 212-232 - 1956
5. T. Endo - M. Matsuishi - Fatigue of metal subjected to varying stress - Jap. Soc. Of Mec. Eng. Fukuoka Japan March 1968.
6. G.K. Chaudhury - W.D. Dover Fatigue analysis of offshore platforms subject to sea wave loadings Int J. Fatigue 7 N° 1 pp.13-19 (1985).
7. N.K. Shetty - M.J. Baker - Fatigue reliability of tubular joints in offshore structures : Fatigue loadings 9th Int. Conf. on Offshore Mechanics and Arctic Engineering (OMAE 90) Houston Feb. 90.

ACKNOWLEDGEMENTS

The work described in this paper has been carried out in collaboration with the European Commission's BRITE Project n° P2381-5. The association with all the project partners is gratefully acknowledged.

SESSION
1.1.C

LAUNCHERS
I

LOADS/OPTIMISATION

PRECEDING PAGE BLANK NOT FILMED

A REVIEW OF SPACE SHUTTLE PAYLOAD-BAY LIFT-OFF FLIGHT DATA AND ANALYSIS COMPARISONS

NASA
N92-23796David A. Hamilton,¹ Nancy E. Tengler,²B. N. Nguyen,³ and Carl A. Lauritzen⁴516-16
84708¹ Chief, Loads and Structural Dynamics Branch, National Aeronautics and Space Administration, Lyndon B. Johnson Space Center, Houston, Texas² Chair, STS/Payload Structural/Mechanical Working Group, National Aeronautics and Space Administration, Lyndon B. Johnson Space Center, Houston, Texas^{3,4} Structural Dynamics and Loads Group, Lockheed Corporation, Houston, Texas

ABSTRACT

The design evolution of Space Shuttle payloads to be launched requires structural analyses and testing, based on Shuttle load environments, to ensure flight safety and mission success. The adequacy of predicted load environments is continually assessed against flight- and ground-measured data. The Space Shuttle Program has utilized extensive flight measurements to assess payload-bay environments. As part of the Orbital Flight Test Program on STS-1 through STS-5, the orbiter Columbia was equipped with a broad range of instrumentation, including accelerometers and microphones in the payload bay. The orbiter Challenger was equipped with payload-bay measurement systems on six of its flights, and the orbiter Discovery has been similarly instrumented beginning with STS-26. The payload-bay data, along with other measurements recorded on these flights, are compared to design load requirements for payloads, and updates are made as necessary.

payloads, require dynamic analysis to accurately define payload loads. Other mission events such as maximum acceleration (g), high-q, staging, gust loads, and pitch and yaw maneuvers result in small dynamic responses that are analyzed statically. Payloads that are deployed or otherwise change configuration in orbit may also be sensitive to dynamic excitations, including control systems, crew motion, and equipment operation. The effects of orbiter distortion caused by aerodynamic and thermal loads are also analyzed statically.

The Space Shuttle payload loads and analyses responsibilities are documented in the Payload Integration Plan (PIP). A Shuttle/payload-unique interface control document (ICD) documents and controls individual payload mechanical and environmental interfaces with the Shuttle. These unique Shuttle/payload ICDs generally refer to NSTS 07700, Volume XIV, Attachment 1, Shuttle Orbiter/Cargo Standard Interfaces, often referred to as the core ICD and to NSTS-21000-IDD-SML, Small Payload Accommodations. These document the payload dynamic envelope, attachment locations, preliminary design load factors, and interface allowable loads. Prior to flight, NASA provides a final Shuttle/payload dynamic and quasi-static verification loads analysis using test-verified payload dynamic math models.

1. THE SPACE TRANSPORTATION SYSTEM

The U. S. Space Transportation System (STS) is currently composed of the Space Shuttle, the European-developed Spacelab experiment and research laboratory, and upper stages. The Space Shuttle vehicle is capable of delivering payloads to low Earth orbit. Upper stages are designed to deliver spacecraft from low Earth orbit to geosynchronous orbit or to planetary flight. Space Shuttle facilities located at the NASA John F. Kennedy Space Center in Florida include orbiter and payload processing facilities, the vehicle assembly building, and two launch pads.

The Space Shuttle launch vehicle is composed of four principal structural elements (Fig. 1): two solid rocket boosters (SRB), the orbiter, and an external tank (ET) that provides liquid hydrogen and oxygen to the Space Shuttle main engines (SSME). The solid rocket boosters and the orbiter are reusable. The primary loading events in the Shuttle mission are lift-off, maximum dynamic pressure (high-q) boost, solid rocket booster staging at approximately 120 seconds into the mission, maximum acceleration, SSME end-burn and external-tank staging, orbit operations, entry, and landing.

The orbiter fleet consists of three orbiter vehicles (OV's), *Columbia* (OV-102), *Discovery* (OV-103), and *Atlantis* (OV-104), with *Endeavor* (OV-105) planned to be operational in 1992. The orbiter payload bay offers a 4.6- by 18.3-m cylindrical envelope to accommodate payloads.

2. PAYLOAD LOADS

For payload structural design, the Space Shuttle loading is characterized by dynamic and quasi-static load conditions. Lift-off and landing, which produce significant dynamic response of

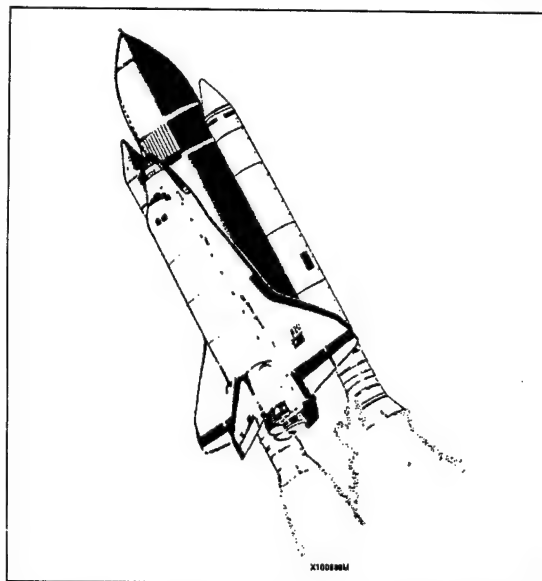


Figure 1: The Space Shuttle vehicle.

payload and Shuttle math models using component mode synthesis, and then converting the system model to a modal format. The Shuttle math models are generally developed in terms of free-free modes with residual flexibility for the payload interface or in terms of Craig-Bampton modes. The payload models are generally in the form of Craig-Bampton modes. In the response analysis, the Shuttle forcing functions are applied to the coupled model, and the responses of the coupled system are computed. The cargo element responses and loads are recovered from the coupled system responses.

3. DYNAMIC MATH MODELS

The orbiter dynamic math model is a condensed version of a large finite element model used to determine orbiter internal loads, deflections, and stresses. The model was reduced from over 30,000 degrees-of-freedom (DOF) to about 950 DOF, depending on payload manifest. The dynamic model of the ET has 159 DOF which are a mixture of physical and modal DOF. The liquid-oxygen tank of the ET, which represents most of the ET weight, is described with modal DOF. Each SRB dynamic model, which includes a representation of the SRB shell, is comprised of 141 DOF that are a mixture of modal and physical coordinates.

Extensive testing has been performed on the individual Shuttle elements and on the mated configuration. A modal test was conducted on the full-scale orbiter and on the full-scale, mated vehicle. Static test programs were conducted on the orbiter, ET, and SRB. In addition, a one-quarter scale model of the orbiter, ET, and SRB was used for modal tests of the individual elements and of the integrated vehicle. The integrated vehicle tests included various payload configurations. On the basis of the correlation of test data to math model data, the Shuttle element models and the mated model are considered to be test-verified.

Requirements for test verification of the payload models are contained in NSTS 14046B, Payload Verification Requirements. The payload developer is responsible for producing dynamic math models that adequately characterize the cargo element.

4. LIFT-OFF ANALYSIS

The Space Shuttle lift-off event commonly refers to the time period from SSME ignition through SRB ignition and several seconds beyond pad release. The lift-off is a highly transient load event that causes significant system dynamic responses. Therefore, payload responses and Shuttle/payload interface forces must be determined by coupled transient response analyses. The approach for the lift-off analysis includes two phases. In the first phase, the Shuttle vehicle model is attached to the mobile launch platform (MLP) model at the SRB holddown support posts. Cantilevered vehicle modes are used to calculate the restraining interface forces between the MLP and the SRBs up to the time of post release. These base interface forces and the applied loads, such as SRB and SSME thrust, overpressure, etc., constitute the lift-off forcing functions for payload specific lift-off analyses. In the second phase, these lift-off forcing functions are applied to the free-free, coupled Shuttle/payload model for calculation of payload responses. The standard payload lift-off analysis uses system modes that include frequencies up to 35 Hz. Payload analysis for frequencies above 35 Hz is generally performed using the Shuttle random vibration and acoustic environments. Additional information on Shuttle vehicle lift-off loads is provided in references 1 through 3.

4.1 Lift-off Forcing Functions.

The lift-off forcing functions for Shuttle payloads consist of the applied loads due to winds and gusts, SSME thrust, SRB thrust, SRB internal pressure buildup, vehicle control system responses,

SRB ignition overpressure, and the MLP reactions at the base of the SRBs. The parameters significant in developing the Shuttle lift-off forcing functions, in order of importance to payload loading, are SRB thrust buildup and thrust mismatch, SRB ignition overpressure, SSME thrust buildup, event timing, thrust misalignments, and ground winds.

The SRB and SSME thrust buildup values are the worst two-sigma ignition transients. Multiple combinations of SRB thrust buildup are used for payload analysis. The SRB thrust differentials are added to obtain the unsymmetrical thrust. An SSME thrust buildup representing a two-sigma probability of occurrence, two-sigma variance from the mean timing levels is used for payload lift-off conditions. The lift-off conditions include the vehicle control system responses that affect the SSME and SRB gimbal angles.

The SRB ignition overpressure forces are applied to DOFs representing external surface locations on the Shuttle. The SRB overpressure phenomenon occurs because the SRB exhaust interacts with the ambient air and exhaust ducts during the SRB ignition process. This results in an aerodynamic overpressure pulse that travels up the vehicle. The SRB ignition overpressure forces currently used for payload analysis is derived from flight data.

From STS-6 through STS-51L, the same set of analytical lift-off load cases was used for preflight payload loads analyses. These environments were designated the L0933 series and consisted of 10 cases which tended to maximize payload bay responses. These cases were a subset of more than 200 cases used for Shuttle design loads analyses and were selected to reduce the computational requirements for NASA, Rockwell, and payload developers. These forcing functions are discussed in reference 4.

In the post-STS-51L time period, a delta Design Certification Review (DCR) on the Shuttle system was conducted. This DCR activity involved reassessment and recertification of lift-off forcing functions and lift-off loads analyses. The Shuttle system was reverified to a revised set of 300 forcing functions. As in previous cycles, a subset of cases was selected for payload loads analyses. The revised set of 11 payload lift-off forcing function cases is referred to as the LR2000 series (Ref. 5). Two of the cases, 2165 and 2223, include supplemental forces which were added to encompass flight data at frequencies where underpredictions existed. These supplemental forces are applied to the orbiter and represent corrections for forcing function and modeling deficiencies.

5. FLIGHT DATA ASSESSMENT

The Shuttle Program has utilized extensive instrumentation on multiple vehicles to measure environments for the purpose of evaluating the adequacy of STS models and forcing functions used in loads analyses. The data assessment consists of the comparison of peak responses and shock spectra from flight to flight and between flight and analytical design case predictions. Appropriate analytical updates are made to the models and forcing functions as required. Significant instrumentation was used on the early Columbia flights, subsequently on the Challenger, and currently on the Discovery.

5.1 Columbia Payload-Bay Instrumentation.

The primary data used to assess low-frequency accelerations in the orbiter Columbia payload bay during the Orbital Flight Tests (OFT) Program (STS-1 through -5) were nine low-frequency accelerometers (table 1). These accelerometers had a frequency response from 0 to 14 Hz which was flat within ± 2 percent of full-scale output, 3 dB down at 20 Hz, and rolling off at 18 dB/octave above 20 Hz. Two accelerometers were located in the crew

Table 1: OV-102 low frequency accelerometers locations.

Description	DOF	Location		
		X	Y	Z
Crew Cabin	Y	513	-3	422
Crew Cabin	Z	513	-3	422
LHS Longeron	Z	823	-100	407
RHS Longeron	Z	973	100	407
LHS Longeron	Z	973	-100	407
near Keel Longeron	Y	979	+0	305
Aft Bulkhead	X	1294	+3	296
Aft Bulkhead	Y	1294	+3	300
Aft Bulkhead	Z	1294	+3	290

cabin, two on the left longeron, one on the right longeron, and one in the keel area. The aft three were located near the 1307 bulkhead below the payload-bay envelope. The output of these accelerometers was recorded at 100 samples per second.

The OFT environments were also measured with the Dynamic, Acoustic, and Thermal Environments (DATE) payload bay instrumentation package. This package included low-frequency accelerometers on both the orbiter longerons and keel area as well as on the development flight instrumentation (DFI) pallet and mission-unique payload structures. The DATE data are presented in more detail in publications from the NASA Goddard Space Flight Center.

5.2 OFT Lift-off Data Assessment.

The maximum lift-off responses of the nine low-frequency accelerometers for the first five Shuttle flights are given in table 2. The amplitudes for flights 2 through 5 were similar and well below the STS-1 levels because of the reduced overpressure. On STS-1, higher than expected orbiter responses occurred due to SRB ignition overpressure. The payload bay responses were high, as noted in table 2. To reduce this undesirable environment, launch pad modifications were made. A significant modification was the addition of fabric troughs filled with water that covered the open area around the SRB base and thus blocked the SRB-ignition shock wave. Also, the water purge flow rate into the SRB exhaust duct was increased. These modifications were very effective in attenuating the overpressure effect as seen by the reduced responses of subsequent flights. The maximum response levels computed for the pre-ST5 verification loads analyses using the LO933 forcing functions are also shown and are higher than flight levels. This difference between analyses and flight is due primarily to the nominal nature of flights 2 through 5 as opposed to the design-type environments used in analyses to predict maximum expected loads.

To illustrate flight-to-flight variability, shock spectra of the left longeron Z flight responses at station 973 for flights 1 through 5 are

Table 2: OV-102 Maximum accelerations for lift-off.

Direction	X ₀ Station	Oft Flight Data, G's					STS-5 Design Cases
		STS-1	STS-2	STS-3	STS-4	STS-5	
X	1294	2.10	1.79	1.91	1.82	1.87	2.37
Y	513	0.20	0.27	0.11	0.19	0.15	0.83
Y	979	0.40	0.16	0.16	0.14	0.15	0.30
Y	1294	0.25	0.13	0.19	0.08	0.13	0.33
Z	513	3.5	0.82	0.91	0.90	0.90	2.36
Z	823	2.8	0.74	0.72	0.84	0.77	1.37
Z	973	2.9	0.60	0.66	0.70	0.66	1.72
Z	973	2.9	0.52	0.58	0.72	0.66	1.84
Z	1294	1.25	0.25	0.25	0.35	0.32	1.06

compared in figure 2. Flight derived shock spectra were compared to analytical design cases for each flight. The STS-5 Z acceleration spectra at station 973 is shown in figure 3 and the Z acceleration spectra from the DATE package at station 1022 in figure 4. The

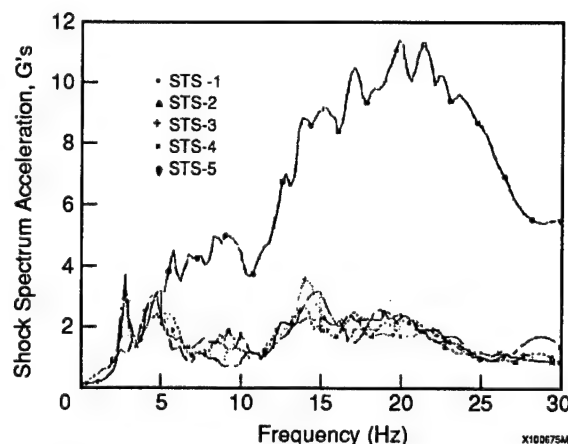


Figure 2: Lift-off shock spectra for Z acceleration at X = 973 for STS-1 through STS-5.

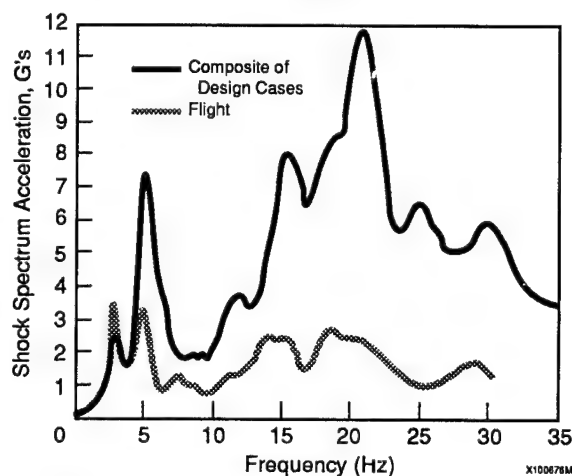


Figure 3: STS-5 lift-off shock spectra of right longeron Z acceleration at X = 973 for LO933 cases and flight.

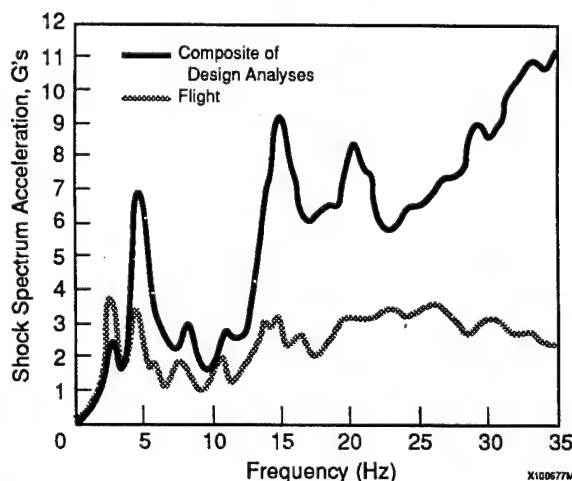


Figure 4: STS-5 lift-off shock spectra of Z acceleration at X = 1022 for LO933 cases and flight.

analytical shock spectra encompass the flight data at all frequencies except in the 3-Hz range. The 3-Hz responses are caused by low-amplitude oscillations, which begin about 1 second after SRB ignition. These oscillations do not significantly affect maximum longeron accelerations but can be a contributor to payload loading for payloads with frequencies in this range. The limitation of accelerometer frequency response did not adequately measure responses from 15 to 35 Hz. The DATE measurement shows more flight response above 20 Hz due to its higher frequency sensing capability. A more complete discussion of the Columbia data is presented in references 5 through 7 and for DATE data in references 8 and 9.

5.3 Challenger Payload-Bay Instrumentation.

The orbiter Challenger was instrumented with accelerometers and microphones to measure the payload-bay dynamic environment. The 10 low-frequency accelerometers had a frequency response that was flat from 0 to 35 Hz and 3 dB down at 50 Hz. These response characteristics represented a significant improvement in usefulness over the Columbia measurements for assessing payload bay load environments which are analytically predicted from zero to 35 Hz. As shown in table 3, the accelerometers were distributed along the payload bay with two left longeron X measurements, five left longeron Z, one mid-bay right longeron Z, one left longeron Y, and a keel Y. The output of these accelerometers was digitized at 500 samples per second. This Challenger instrumentation package flew on STS-41C, -41G, -51B, -51F, -61A, and -51L. As in the case of Columbia, the measured data from each flight were compared to the analytical design cases used in the payload verification loads cycles.

5.4 Challenger Data Assessment.

Maximum lift-off accelerations at each measurement location for each flight and shock spectra were used to assess the flight data. Results from the LO933 cases were used for design case comparison. To illustrate flight-to-flight repeatability, longeron X and Z acceleration shock spectra were derived from measured acceleration on each flight as shown in figures 5 and 6. Flight-to-analysis shock spectra of longeron accelerations comparisons generally demonstrated the adequate conservatism of LO933 lift-off forcing functions at frequencies from 0 to 35 Hz (Ref. 10). However, on STS-51B and again on STS-51L, the mid-bay responses exceeded the LO933 design cases in the 15- to 27-Hz ranges. These exceedances implied that the design load cases used for payload design and for flight readiness verification were deficient in this frequency range and could possibly underpredict payload flight loads. To correct this deficiency, a revised set of lift-off forcing functions was developed, as previously discussed. The maximum lift-off accelerations from flight and from the LR2000 design analyses are shown in table 4. Generally, the Z axis g-levels are about twice the flight data. The analytical responses shock spectra of STS-51B and -51L for the LO933 and LR2000 forcing functions are shown in figures 7 and 8. The revised forcing functions encompassed the flight data.

Table 3: OV-099 Low frequency accelerometer locations.

Description	DOF	Location		
		X	Y	Z
LHS, Longeron	X	878.	-102.5	407.
LHS, Longeron	Z	878.	-102.5	407.
LHS, Longeron	Z	976.	-102.5	407.
LHS, Longeron	Z	1057.	-97.5	407.
RHS, Longeron	Z	878.	102.5	407.
LHS, Longeron	Z	1200.	-97.5	407.
Keel	Y	880.	0.0	300.
LHS Longeron	X	698.	-102.5	407.
LHS Longeron	Y	698.	-102.5	407.
LHS Longeron	Z	698.	-102.5	407.

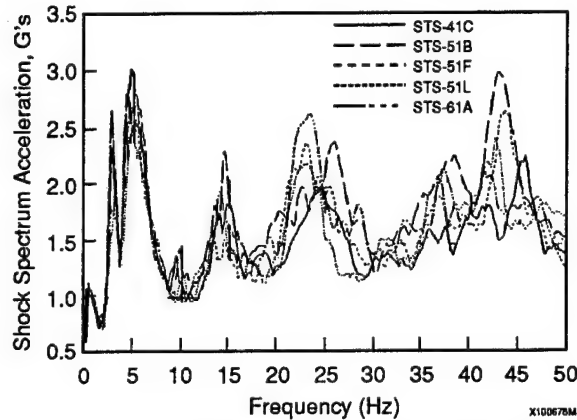


Figure 5: Lift-off shock spectra for X acceleration at 878 for 099 flights.

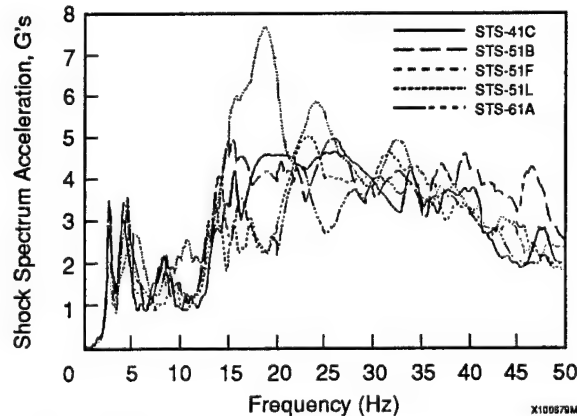


Figure 6: Lift-off shock spectra for Z acceleration at 976 for 099 flights.

Table 4: OV-099 Maximum accelerations for lift-off, flight and design analyses (G's).

Direction	Xo Station	41C		41G		51B		51F		61A		51L	
		Flt	Anal	Flt	Anal	Flt	Anal	Flt	Anal	Flt	Anal	Flt	Anal
X	698	1.90	2.54	2.00	2.85	2.03	2.61	1.96	2.55	2.01	2.65	1.96	2.59
X	878	1.89	2.53	—	2.59	2.02	2.53	1.99	2.54	2.12	2.59	1.91	2.60
Y	698	3.26	2.46	1.30	3.86	2.12	2.86	2.68	3.63	2.35	3.42	3.16	3.36
Z	698	0.82	1.54	0.84	2.09	0.89	2.17	0.96	1.79	0.87	2.07	0.92	2.46
Z	878	1.15	2.07	—	2.07	1.37	2.94	1.02	2.65	1.03	2.97	1.76	2.50
Z-R	878	1.15	2.09	—	2.15	1.37	2.41	1.38	2.55	1.02	2.32	1.71	2.59
Z	976	1.09	2.27	—	2.20	1.11	2.53	0.98	3.02	0.93	2.66	1.46	2.98
Z	1057	1.01	2.05	—	2.09	1.23	2.01	1.43	2.50	0.83	1.98	1.10	2.84
Z	1200	.61	1.84	—	1.65	1.07	1.81	1.27	2.28	0.91	1.73	0.77	2.48

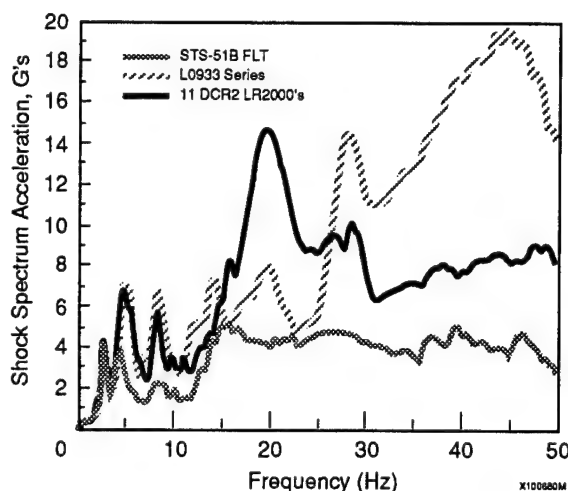


Figure 7: STS 51B lift-off shock spectra of Z acceleration at X = 976 for L0933 and LR2000 cases and flight.

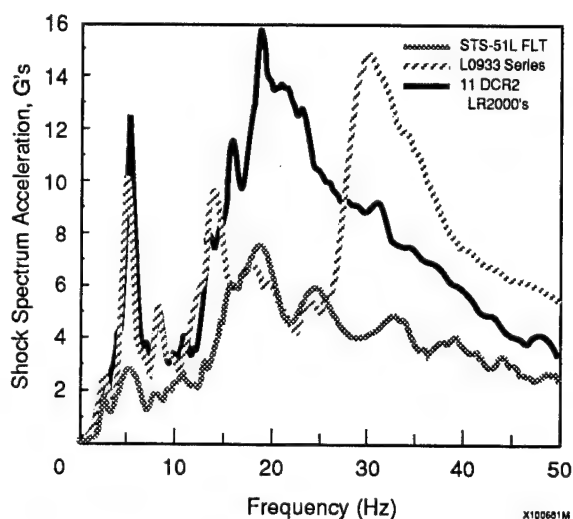


Figure 8: STS 51-L lift-off shock spectra of Z acceleration at X = 976 for L0933 and LR2000 cases and flight.

5.5 Discovery Payload-Bay Instrumentation.

Beginning with STS-26, the orbiter Discovery was instrumented with accelerometers and microphones to measure the payload-bay dynamic environment. The 13 low-frequency accelerometers have a frequency response which is flat to 35 Hz and 3 dB down at 50 Hz, similar in characteristics to those that were installed on Challenger. The location of the Discovery accelerometers is shown in table 5. Seven of the accelerometers are at similar locations to the Challenger measurements.

5.6 Discovery Data Assessment.

As in the case of previous flights, the measured data are compared to the analytical design cases used for verification loads cycles. Maximum accelerations from each flight are shown in table 6. The flight-to-flight variability of the Discovery data is illustrated by the shock spectra of Z responses at station 976 are shown in figure 9. Comparisons of the analytical response shock spectra and the LR2000 forcing functions have generally shown adequate, and at some frequencies, significant conservatism over flight data. The longeron shock spectra for Z axes accelerations at 976 on STS-41 show similar frequency domain trends in both flight data and analytical shock spectra (Fig. 10). On STS-31, there was a slight exceedance of analytical shock spectra by flight data at station 1029 (Fig. 11) in the 13-14 Hz frequency range. The Y and Z responses in the forward-bay area are quite conservative at most frequencies but are about equal to flight data at some frequencies, such as 15 Hz on some gages. The aft-bay responses are generally quite conservative, withstanding the responses in the 9-Hz range at some locations.

Table 5: OV-103 Low frequency accelerometer locations.

Description	DOF	Location		
		X	Y	Z
LHS, Longeron	Z	878.	-102.5	407.
LHS, Longeron	X	1029.	-102.5	407.
LHS, Longeron	Z	1029.	-102.5	407.
LHS, Longeron	Z	1207.	-97.5	407.
RHS, Longeron	X	878.	102.5	407.
RHS, Longeron	Z	878.	102.5	407.
LHS, Longeron	Z	976.	-102.5	407.
Keel	X	919.	0.	305.
RHS, Longeron	X	1029.	102.5	407.
LHS Longeron	X	878.	-102.5	407.
LHS Longeron	Y	701.	-102.5	407.
LHS Longeron	Z	701.	-102.5	407.
RHS, Longeron	Z	1029.	97.5	407.

Table 6: OV-103 Maximum accelerations for lift-off, flight and design analyses (G's).

Direction	X ₀ Station	STS-26		STS-29		STS-33		STS-31		STS-41	
		Flight	Analysis	Flight	Analysis	Flight	Analysis	Flight	Analysis	Flight	Analysis
Y	701	3.10	4.65	3.78	4.50	3.89	4.52	3.03	2.79	3.35	7.06
Z	701	1.22	2.98	0.95	2.73	1.04	2.63	1.08	2.63	1.14	2.80
X	878	1.99	2.89	2.16	2.78	1.97	2.61	1.94	2.70	1.97	3.30
X (Rhs)	878	1.98	—	—	—	1.91	2.73	1.98	2.79	1.92	3.31
Z	878	1.50	3.90	1.32	3.62	1.22	2.91	1.52	2.79	1.36	3.52
Z (Rhs)	878	1.26	3.92	1.16	3.56	—	2.97	—	2.72	—	3.31
X (Keel)	919	5.16	8.10	4.92	7.73	—	2.63	5.81	6.03	5.54	10.09
Z	976	1.46	3.88	1.20	3.86	1.14	3.03	1.26	2.52	1.02	3.86
X	1029	1.97	2.58	2.22	2.52	1.87	2.36	1.91	2.42	1.89	2.96
X (Rhs)	1029	1.96	2.69	2.08	2.65	1.93	2.54	2.01	2.58	1.91	2.87
Z	1029	1.18	3.13	1.14	2.84	1.09	2.89	1.14	1.66	1.01	3.15
Z (Rhs)	1029	1.19	3.93	1.28	3.63	1.28	2.89	1.05	2.34	1.01	3.14
Z	1207	0.85	2.50	0.83	2.43	0.64	2.76	0.72	2.14	0.74	2.97

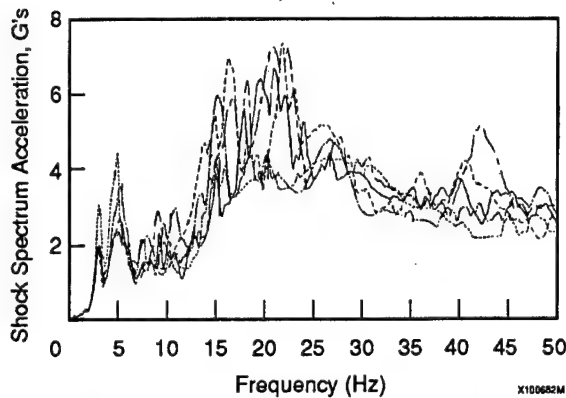


Figure 9: Lift-off shock spectra for Z acceleration at 976 for OV-103 flight.

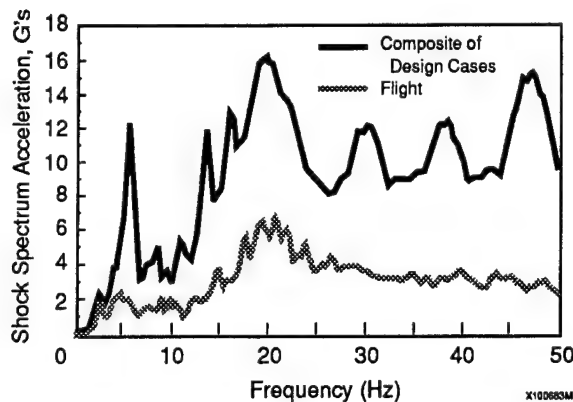


Figure 10: STS-41 lift-off shock spectra of Z acceleration at X = 976 for and LR2000 cases and flight.

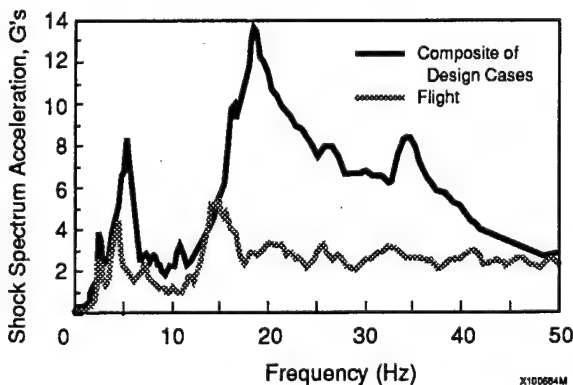


Figure 11: STS-31 lift-off shock spectra of Z acceleration at X = 1029 for LR2000 cases and flight.

SUMMARY

Flight data have been utilized since the first Shuttle launch to continually evaluate the adequacy of design load environments and to make revisions as required. Data from numerous flights of orbiter vehicles Columbia, Challenger, and Discovery have been assessed. Payload bay accelerations have been measured on these flights and compared to analytical design case predictions in both the time domain and the frequency domain.

Results have generally shown conservatism in the design cases compared to the nominal flights. On a few flights, flight-derived shock spectra exceeds design case by a small amount at certain locations and certain frequencies, but design load predictions for payloads are considered conservative. Flight-to-analysis shock spectra generally show significant margins between predictions and experience.

Additional effort to further assess math model effects on load predictions is in work. Testing of the one-quarter scale model of the Shuttle is being conducted at the Johnson Space Center Vibration and Acoustics Test Facility. The results will be used to assess potential model updates.

Additional instrumentation is being added to OV-102, which, coupled with OV-103, will provide data for continued dynamic environment evaluation.

REFERENCES

1. Frederick, D. H.; Haugen, E. A.; Hamilton, D. A., *Loads Environment for Payload/Cargo Integration*, AIAA 83-0328, January 1983.
2. Dagen, J. D., *Orbital Flight Test Lift-off Loads Evaluation*, NASA-JSC 18636, October 1982.
3. Kaminsky, J. A.; Ray, G. A., *A Monte Carlo Approach to Determining Lift-off Loads and Accelerations for the Space Shuttle and Its Payloads*, AIAA 83-2653, October 1983.
4. *Lift-off Forcing Functions (LR2000 Series) for Payload Loads Analyses*, Rockwell International document STS88-0609, April 1988.
5. Hamilton, D. A., *A Review of Shuttle Payload Bay Low Frequency Structural Response for STS-1 through STS-5*, AIAA 83-2579, October 1983.
6. Garba, J. A.; Trubert, M. R.; Wada, B. K.; Chen, J. C., *Summary of Payload Bay Loads Response Data Measured on STS-2 through STS-5*, JPL D-1337, September 1984.
7. O'Connell, M.; Garba, J. A.; Kern, D. A., *Shuttle Payload Bay Dynamic Environments, Summary and Conclusion Report for STS 1-5 and -9*, JPL 84-88, December 1984.
8. *Payload Bay Acoustic and Vibration Data from STS-1 (thru STS-5)*, DATE reports 002 through 006, Goddard Space Flight Center, June 1981, January 1982, June 1982, December 1982, May 1983.
9. Brodeur, S. J., *Comparison of Flight Data Versus Predictions for Low Frequency Loads on STS-3/OSS-1 Instruments*, JPL D-1347, January 1984.
10. Lauritzen, C. A.; Nguyen, B. N., *A Review of Shuttle Payload Bay Low Frequency Structural Response at Liftoff for OV-099 Flights*, Lockheed report LESC-27710, November 1989.

DYNAMIC LOAD CASES ON ARIANE 5

B. CHEMOUL - E. LOUAAS
Centre National d'Etudes Spatiales
91023 Evry - France

517-15
84709
N92-23797¹¹⁷

ABSTRACT

ARIANE 5 will be able to launch payloads weighting up to 20 tons. The environmental requirements for these various payloads must be given early in the launcher's development's program.

Nowadays, all the first launcher's instrumented tests have not yet begun, for this reason some load cases still remain unknown (e.g. engines thrust decay). To find those load cases, assumptions must be done using the experience of previous programs. If this experience doesn't exist and if the expected load cases are supposed to be critical, particular studies have to be carried out (e.g. blast wave).

The low frequency load cases considered on ARIANE 5 to establish the environmental requirements depend on the flight phases :

- Lift off :
 - blast wave
 - symmetrical and unsymmetrical ignition
- Aerodynamical flight (transonic or max dynamic pressure)
 - gust
- End of stage's thrust :
 - strap on boosters
 - VULCAIN
 - upper stage

Several cases will be presented and analysed. Applications with ASTRAL will be shown considering the dynamical coupling between ARIANE 5 and standard payloads.

1. INTRODUCTION

ARIANE 5, futur european launcher always in development is made of two solid rocket Boosters (230 T of Solid propellant) strapped on a main cryogenic stage (155 T of liquid propellant) above of which there is either the automatic upper part using a little stage and carrying 1 to 3 payloads or the HERMES Spaceplane.

The programm of this heavy launcher obviously targets to offer 5,9 T in geostationary transfer orbit (GTO) or 18 T in low earth orbit (LEO), but also to reach high level of reability and safety. Consequently, it was needed to know and to control, the earliest in the development, the dynamic environment which is one of the most important factors governing the launcher's design. Thus, dynamic models have been elaborated and dynamic studies have been carried out since the beginning of ARIANE 5's development. This process have also been motivated to give early the design datas to the satellite owing to flight on ARIANE 5 and to check these conditions remain sufficiently smooth.

As regard with the other ARIANE launcher, ARIANE 5 leads to cope with new dynamic case particularly at the lift-off when the strap-on boosters' pressure is building up or the blast waves are exciting the launcher. Even, for the classical cases of stage burn-out, the dynamic excitations are totally different of those occuring on ARIANE 4, due to the new propulsion system used.

The aim of this paper is to decribe the low frequency dynamic environment (below 100 Hz) induced on the ARIANE 5 payload. After, a brief description of each dynamic load case, the ARIANE 5 model developed by the CNES (launcher directorate) will be presented. Afterwards, some satellite dynamic responses will be shown.

2. DESCRIPTION OF THE LOAD CASES

2.1. Lift-off : blast wave

This phenomenon is due to the pressure buildup inside the booster's casing. The configuration of the launch pad has a high influence on the wave generation : we considere two waves (see fig. 1) :

- a) the overpressure coming from the entrance of the duct (Ignition Over Pressure).
- b) The overpressure coming from the exhaust side of the duct (Duct Over Pressure).

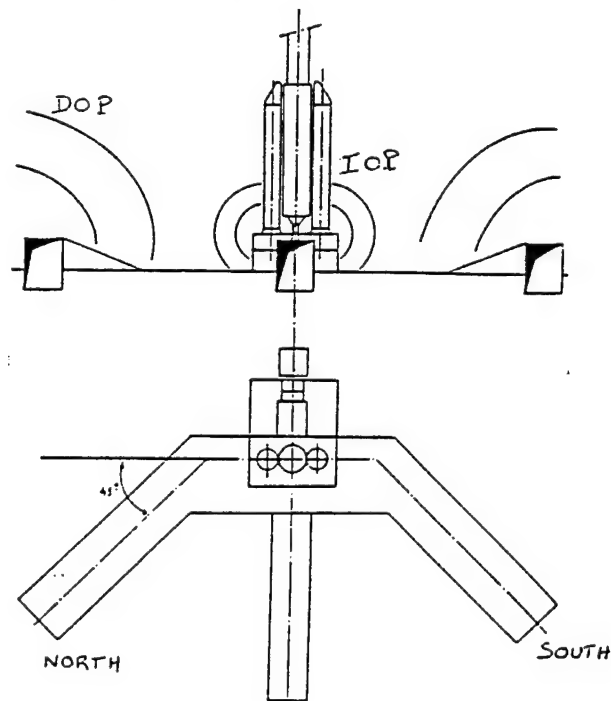


Figure 1 : global view of the launch pad with the ducts configuration

Studies has been performed by the Industrial Architect to idealize the phenomenon. The actual approach is based on a methodology developed by IKAWA and LASPESA for the Space Shuttle Solid Rocket Ignition [1].

This method needs to get precise informations such as the law of pressure evolution inside the chamber, the thermodynamic characteristics of the exhaust gas... It also needs test results informations to determine an empirical coefficient corresponding to the effect of the geometric configuration of the duct on the outside speed of the gas. Reduced scaled tests ($1/20^{\text{e}}$) at FAUGA validated this approach.

The result is briefly given in fig. 2 for the duct over pressure wave.

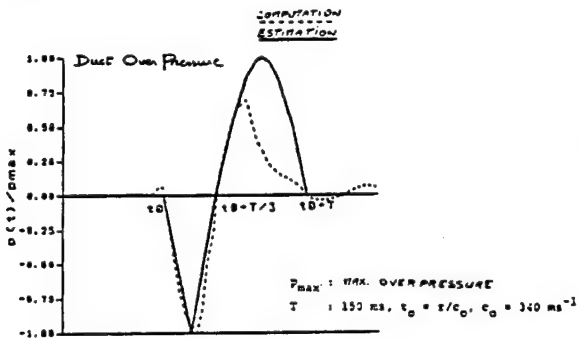


Figure 2 : evolution of the DUCT over pressure

The Ignition over pressure have mainly an influence on the dimensionning of the lower parts of the launcher. However, this wave doesn't excitate the launcher because it is a longitudinal one having a spectrum content very below the frequency of the first longitudinal eigenmode.

The Duct over pressure must be considered as an excitation of the lateral modes of the launcher with an effect on the payloads or on HERMES vehicle.

For the dynamic studies of this second wave, a delay between the two duct exhausting waves must be taken into account. Due to the high wavelength, the resultant force on the launcher is weak. The acceleration at the spacecraft base is also weak. The full scale test will completely validate the computation method and confirm the fact that it's not a dimensionning case.

2.2. Lift-off: Ignition

Before lift-off the launcher stands on the launch pad simply supported by the aft skirts of the strap-on boosters. The central body is then hung on the forward links. The chronological sequence implies the control of the VULCAIN good working order before the ignition of the solid rocket boosters.

The ignition of the VULCAIN engine as a negligible dynamic effect on the launcher.

At the ignition of the strap-on boosters, the dynamic levels are generated by an abrupt elongation of them, due to the pressure build-up, and the lift-off which occurs as soon as the launch vehicle weight is balanced by the total thrust (static load factor 1.5 g)

Figure 3 shows the launcher's configuration on the launch pad and typical evolution of the chamber's pressure inside a booster.

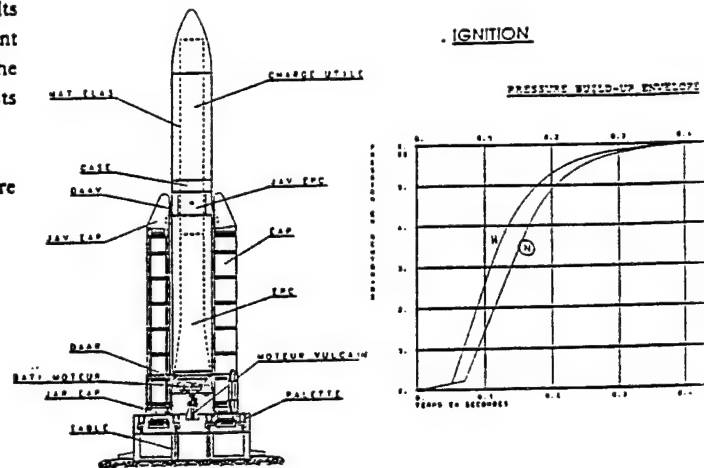


Figure 3 : launcher's configuration before lift-off.

A symmetrical ignition without delay between the two strap-on boosters induce longitudinal loads. A delay or an unsymmetrical ignition can excitate the lateral modes of the launcher. A complete dynamic approach needs to consider the change in boundary conditions occurring during the lift-off. A coupled load analysis made by CNES tend to show that the lift-off is one of the most important dimensionning load case on ARIANE 5.

2.3. Aerodynamic gust and wind

During the booster's flight, the launcher is submitted to loads coming from winds, lateral gusts and thrust orientation. The lateral gust is responsible of the high level of dynamic acceleration that can occur either at maximal dynamic pressure ($q_{\text{max}} \approx 40000 \text{ Pa}$) or at the transonic event when the aerodynamic factors are the most important. Figure 4 shows the lateral gust considered as a flight limit load.

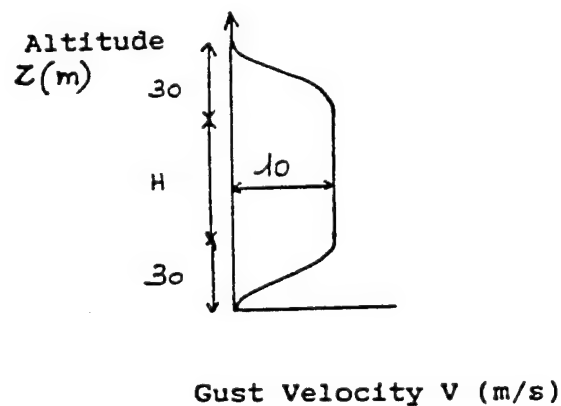


Figure 4 : lateral gust

This gust profile has been used on the last launchers. A characterisation of the optimum gust length (H) must be done for each dynamic analysis. The wind loads doesn't induce dynamic levels. The first computation showed that the maximum load factors were obtained for a lateral gust occurring at maximum dynamic pressure.

2.4. End of the booster's flight

The following figure shows the evolution of the booster's thrust during the flight. The thrust decay is so slow that this event is considered as minor for a symmetrical or unsymmetrical end of flight.

Therefore, this load case can be treated as a static case.

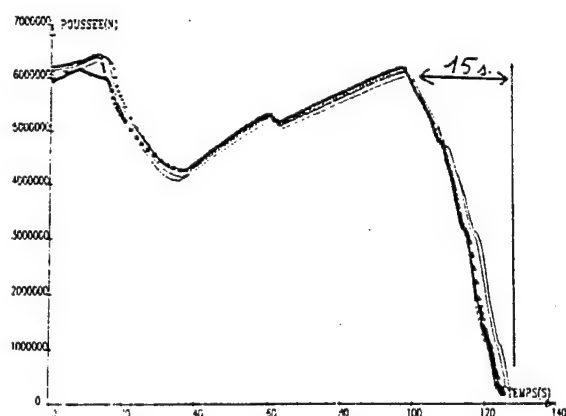


Figure 5 : EAP thrust evolution

2.5. Cryogenic Stage (EPC) end of flight

This event corresponding to the cut-off of the feeding valves, generate thrust fluctuations. This force fluctuation applied at the gimbal of the VULCAIN engine may excitate the longitudinal natural modes of the launcher during this phase.

Till now, the dynamic studies on ARIANE 5 were based on the use of the ARIANE 4 third stage end of flight exploitations : the HM7 was considered as a reference to establish the chugging of the VULCAIN.

Recent fonctionnal tests were conducted by SEP on the VULCAIN engine and permitted to give two characteristic frequencies of the pressure fluctuation : 17 Hz and 55 Hz. The complete signal shows a maximum peak to peak fluctuation corresponding to 5 % of the nominal thrust. These results are actually being analysed. The sequence of valves cut-off may have a great influence on the frequencies and levels.

Any way, for dynamic coupled analysis, one can considere this information as the most realistic load case for the moment.

2.6. Second Stage (EPS) end flight

For the EPS end of flight, there is no information at this day. This load case surely induce very weak vibrations considering the low thrust of that stage (27 kN).

3. CNES COUPLED LOAD ANALYSIS TOOLS

ASTRAL is an in-house software developed to analyse axisymmetrical structures filled with liquids.

The domain of use can be summarized as follow :

- Linear elasticity (small motions)
- Axisymmetric systems
- Fluid/structure interaction (MORAND/OHAYON) [2]

Fluids are assumed perfect, incompressible and irrotational. ASTRAL deals with hydroelasticity problem in flexible tank and sloshing problem in rigid tank.

The structure is made of thin conical shells with 4 degrees of freedom by node. The method is based on a finite elements approach. Uncompressible elements have also been developed to model the solid propellants. All these elements have been made by ONERA.

The evolution of ARIANE needed a new software. ASTRAL 3D was built on the base of ASTRAL 2D.

The constitution of the 3D-model is based upon the dynamic sub-structuring method as proposed by CRAIG and BAMPTON with the following way (fig. 6).

The procedure [3] can be detailed in the following steps :

- Every body composing the launcher (central body, strap-on-booster) is idealized in axisymmetric,
- We define on every one rigid sections called "interface",
- Every axisymmetric model is condensed on the eigenmodes with clamped interfaces and on the static modes corresponding to unitary motions of the interfaces,
- In order to constitute the 3D model of a axisymmetric body, the condensed longitudinal, lateral and torsionnal models are simply merged. The degrees of freedom are then the physical motions of interfaces (6 by interface) and the generalized coordinates of the "clamped" modes,
- The 3D model of launcher is got by merging of the 3D model of each body. The linking between each body is carried out by using stiffness matrices acting on the interfaces d.o.f. which simulate the link structures.

The size of a complet 3D model of ARIANE 5 is reduced to less then 300 dof. Figure 7 presentes modal shapes of ARIANE 5 with HERMES and with the triple launch configuration at lift-off.

In parallel, ASTRAL 3D include the possibility to use the concept of equivalent forces [3] in the transient response computation.

4. ARIANE 5 DYNAMIC RESPONSES

A) Lift-off

Figure 8 shows the impact of the lift-off case on the launcher and at the base of spacecraft (triple launch configuration). The change in boundary conditions (launcher simply standing on the table and launcher free) is modeled by introduction of non linear elements representing unilateral contact between launcher and launch table.

The given example corresponds to a symmetrical ignition.

The stretching of the strap-on boosters induce also at the beginning a momentary collapse of the table under the booster.

The load transmitted at the central body through the forward attachment oscillates at the suspension frequency of this body.

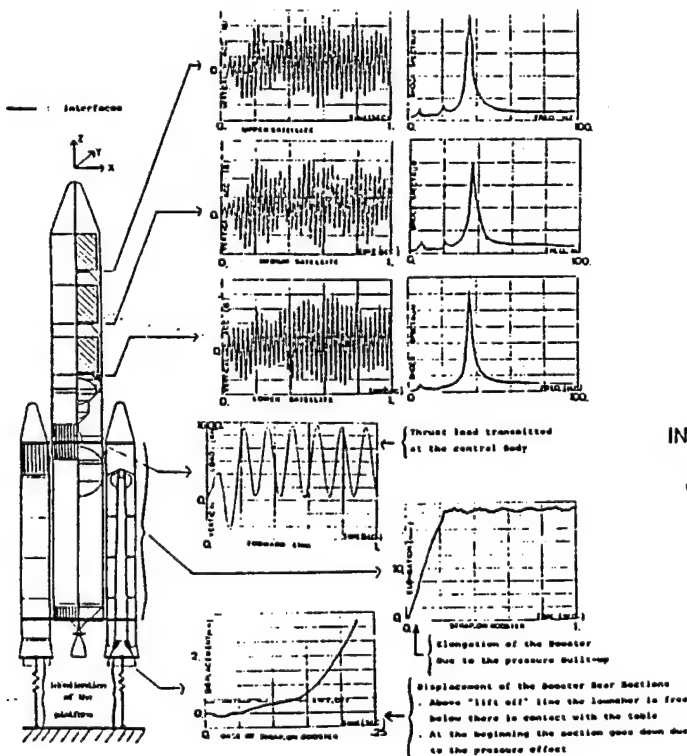


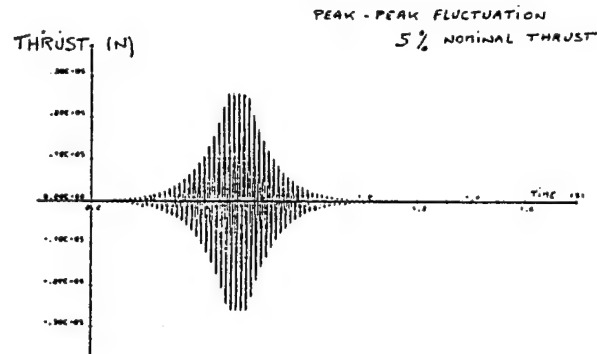
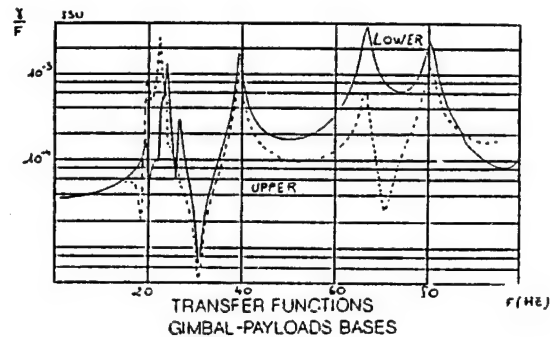
Figure 8 : transient responses results

Furthermore, during a symmetrical ignition, the excitations transmitted to the satellites are rather longitudinal but for an unsymmetrical one, the satellites could be submitted to significant dynamic accelerations both in longitudinal and in lateral, but of course not at the same frequency.

B) chugging of the VULCAIN engine

This load case can be studied with an axisymmetrical model. The transfer function between the gimbal joint and the payload interface (dual launch configuration) is shown in figure 9.

The natural mode at 67 Hz has a high excitability. The results for a simplified chugging at 55 Hz are also represented.



INTERFACES RESPONSES

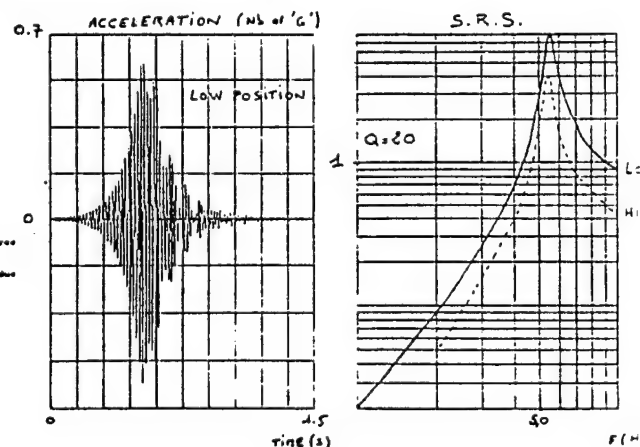


Figure 9

5. CONCLUDING REMARKS

ARIANE 5 is characterized by a low frequency dynamic behaviour quite different of the ARIANE 4 one, due to the new configuration of this launcher using new propulsion systems as the VULCAIN cryogenic engine on the central stage and the powerfull strap-on boosters.

Consequently, the satellites specifications have been fitted. Thus, the dynamic loads appearing in the ARIANE 5 user's manual are the results of a first dynamic studies process which have used elaborated three dimensionnal model permitting to accurately calculate the Dynamic behaviour anywhere in the launcher. This model is used for the ARIANE 5 coupled load analysis. It can cope with any satellite configuration. As a matter of fact, the satellite model doesn't need to be simplified in a longitudinal or lateral effective masses system, it can be very general provided that it has a rigid interface to allow the connection with the launcher model.

Obviously, during the ARIANE 5 development, it is foreseen to consolidate these specifications by studies and tests which, at the end, will allow also to settle reliable flight predictions. Thus, stage firing tests will have a dedicated instrumentation to accurately determine the forcing functions. Furthermore, the dynamic model of the launcher will be validated by modal survey tests carried out on full scale models of the central cryogenic stage, the strap-on booster and finally the upper part of the automatic version. The foreseen test configuration will allow to check the dynamic characteristic and to determine the modal damping for all the flight events.

REFERENCES

- [1] : H. IKAWA - F.S. LASPESA
Ignition/Duct overpressure induced by Space shuttle solid rocket motor ignition.
J. Spacecraft - Vol 22 - n° 4 (juillet - Août 85)
- [2] : H. J.P. MORAND - R. OHAYON
Substructure variational analysis for the vibrations of coupled fluid-Structure systems.
Finite element results - Int. J. Num. Meth. Ingng., 14/5/741.755
- [3] : B. CHEMOUL - H. J.P. MORAND
FOURIER type dynamic super-elements for the vibration analysis of the ARIANE launchers.
GIEN - 1991

Figure 6 : Model generation

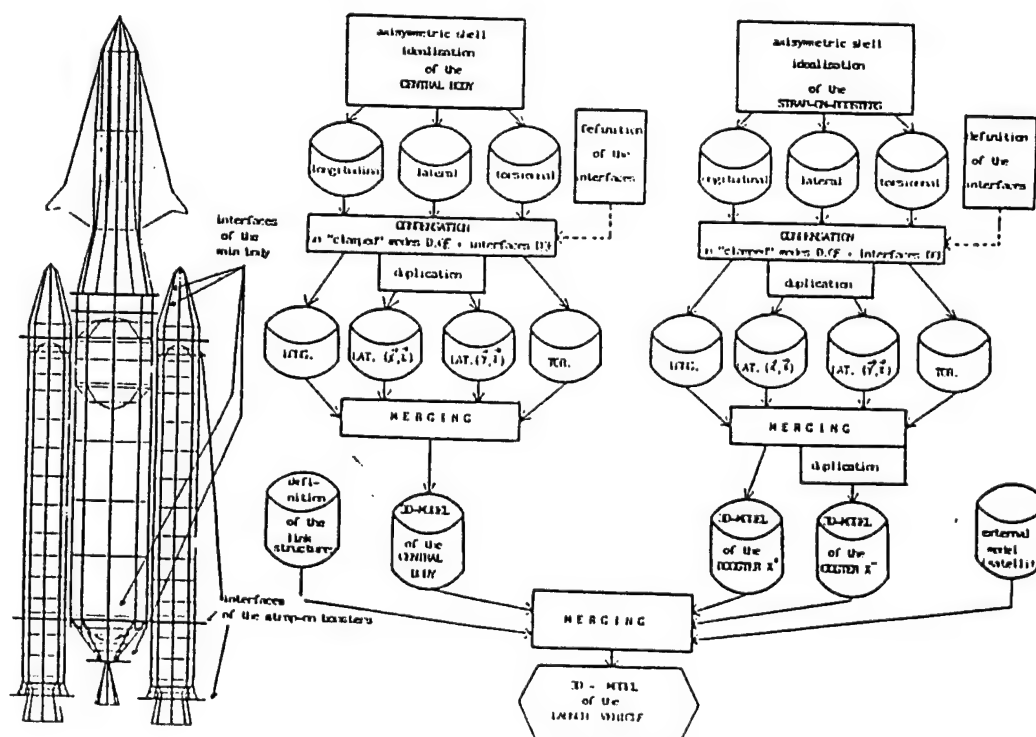
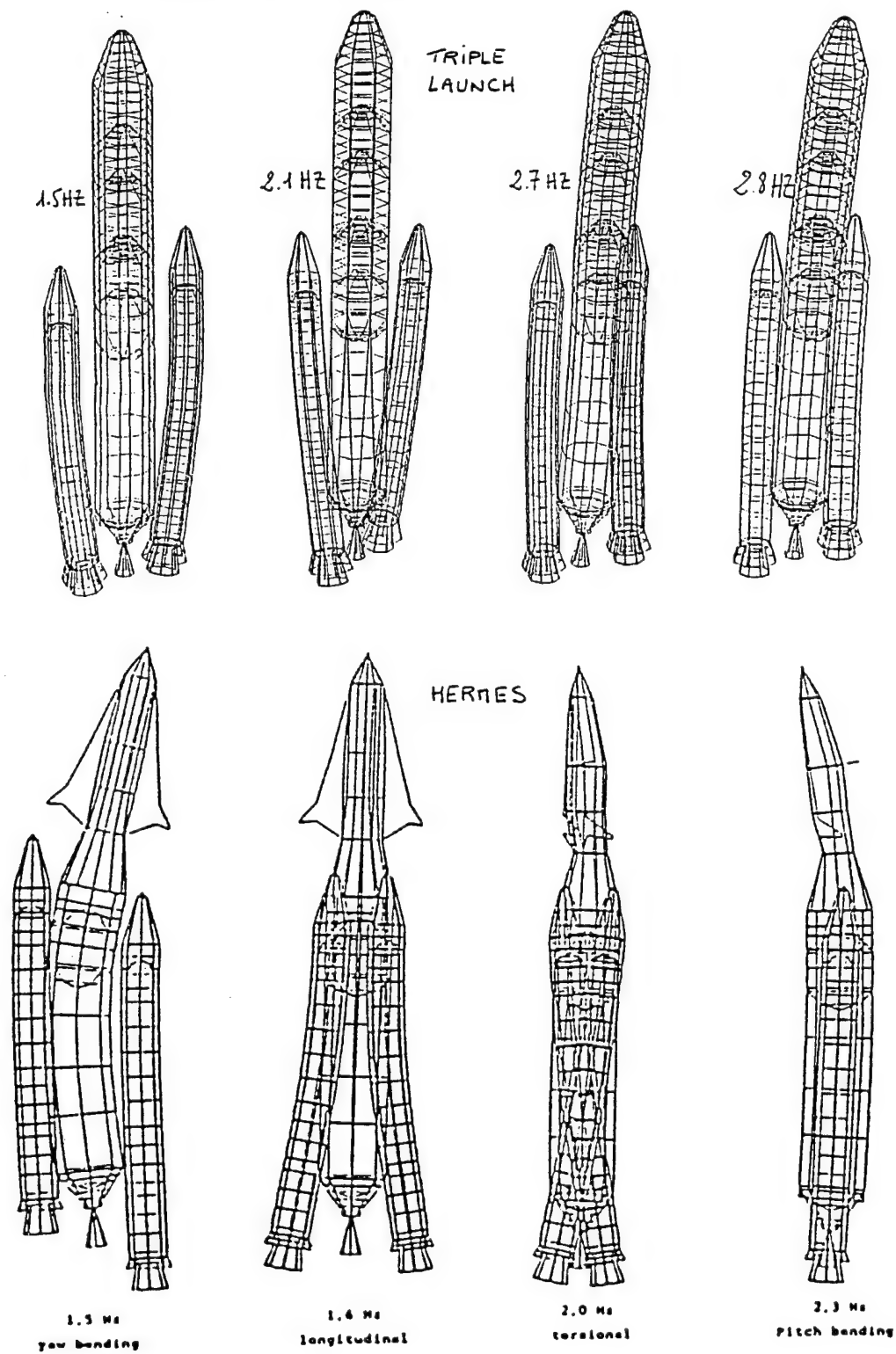


Figure 7 : Example of modal shapes



MULTI PARAMETER OPTIMIZATION ON ARIANE 5

G. Boullenger

AEROSPATIALE
Division des Systèmes Stratégiques et Spatiaux
Direction Technique
Centre Technique des Mureaux
Secteur Etudes Mécaniques et de Synthèse

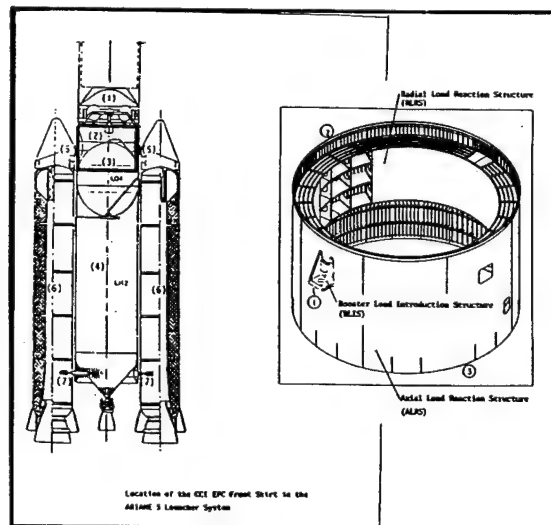
1. RESUME

Dans le cadre d'une campagne de réduction des masses sur l'Etage Principal Cryotechnique du lanceur européen ARIANE 5, AEROSPATIALE etagiste a effectué une étude d'optimisation de la Jupe Avant.

Pour ce faire, nous avons utilisé le module OPTI du logiciel SAMCEF, qui permet l'optimisation automatique d'une structure soumise à des spécifications multiples.

Les résultats obtenus ont permis pour un coût limité de recouper le dimensionnement effectué par le sous-contractant responsable de la structure MAN (Allemagne), puis d'évaluer l'influence de certaines spécifications sur le bilan masse du sous-ensemble, de manière à proposer à l'architecte du lanceur des modifications de celle-ci.

ensemble formant un caisson dont la rigidité répond aux spécifications de raideurs radiale et de diffusion des efforts.



2. La Jupe Avant :

Cette structure est conçue, fabriquée et testée par MAN (figure n° 1).

Au sommet de l'Etage Principal Cryotechnique, elle a deux fonctions mécaniques principales :

- transmettre la poussée des deux Etages d'Accélération au corps du lanceur : Composite Supérieur et Etage Principal Cryotechnique.
- Transmettre la poussée de l'Etage Principal Cryotechnique au composite supérieur, après séparation des boosters.

Ces fonctions sont assurées par trois sous-structures (figure n° 1) :

- Une structure de reprise de la poussée des boosters, comprenant la ferrure introduisant la poussée et les voiles usinées inclinées en assurant la diffusion dans la structure.
- Une structure de reprise de l'effort radial constituée par les cadres principaux, la peau interne en composite CFRP (Carbon Fiber Reinforced Plastic) et les voiles légers, cet

- Une structure de reprise de l'effort axial, constituée de la peau externe à raidissage intégré et des cadres légers.

A l'exception de la peau interne, l'ensemble de la Jupe Avant est réalisé en alliage léger 7075.

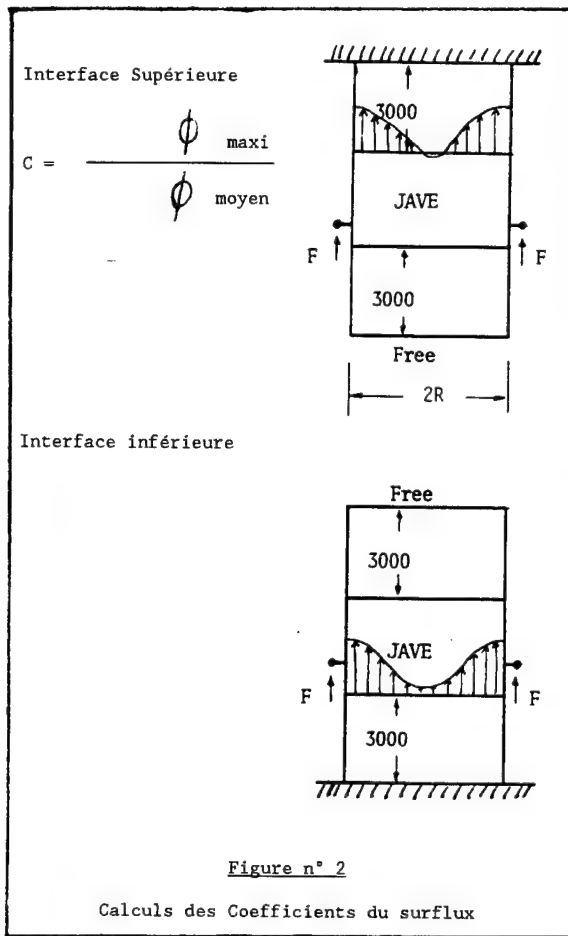
La structure doit répondre aux spécifications mécaniques suivantes :

- 1° Tenue aux efforts généraux et aux gradients thermiques.
- 2° Diffusion des surflux engendrés par la poussée des boosters. Les surflux aux interfaces sont évalués en disposant deux structures adjacentes de part et d'autre de la Jupe Avant et définis par :

Flux maxi

Flux moyen

pour chaque interface (figure n° 2).



3° Rigidités locales (efforts appliqués sur les ferrures d'accrochage des boosters) et globales (torseur d'effort appliqué aux interfaces).

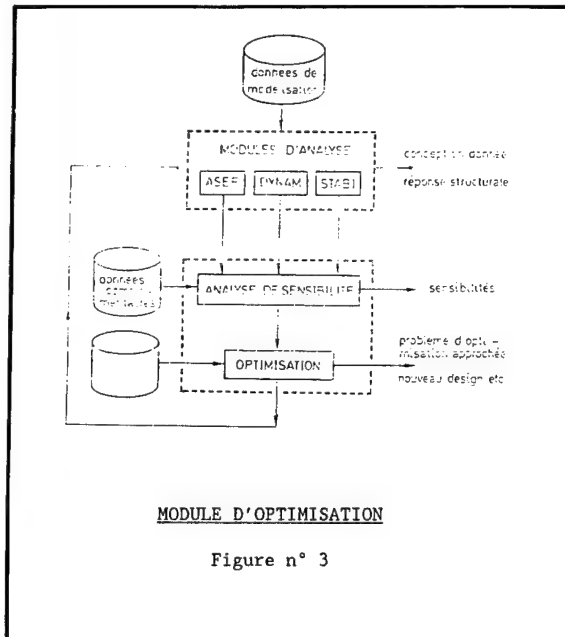
3. LE MODULE OPTI DU LOGICIEL SAMCEF

Le module d'optimisation est un post-processeur des modules d'analyse linéaire de SAMCEF. Il offre à son utilisateur une aide au dimensionnement sous la forme de sensibilités de la réponse structurale ou d'algorithmes d'optimisation automatique.

Ainsi, l'utilisateur définit la fonction objectif (en l'occurrence la masse) et les variables de dimensionnement (épaisseurs des coques), et le logiciel modifie ces dernières de manière à atteindre un extrémum de la première.

Les critères de défaillance et les contraintes technologiques de restrictions à la conception (contraintes maximales, épaisseurs minimales, ...).

Le logiciel conduit par itérations successives à un extrémum. Faisant alors varier les spécifications, l'ingénieur obtient une analyse précise de la sensibilité de la fonction objectif à ces spécifications (figure n° 3).



4. LE MODELE AUX ELEMENTS FINIS

Compte-tenu des conditions de symétrie, un quart de structure a été modélisé (figure n° 4), principalement en éléments de coque.

Compte-tenu des différentes conditions aux limites, neuf modèles (ayant chacun 7000 degrés de liberté) sont nécessaires pour calculer les différentes spécifications (figure n° 5).

Les épaisseurs de groupe d'éléments définissent les variables de conception.

La définition de celles-ci conditionnant fortement les résultats obtenus, un soin particulier y a été apporté. Certaines d'entre elles ont ainsi dû être modifiées au cours de l'étude pour ne pas contraindre artificiellement le processus.

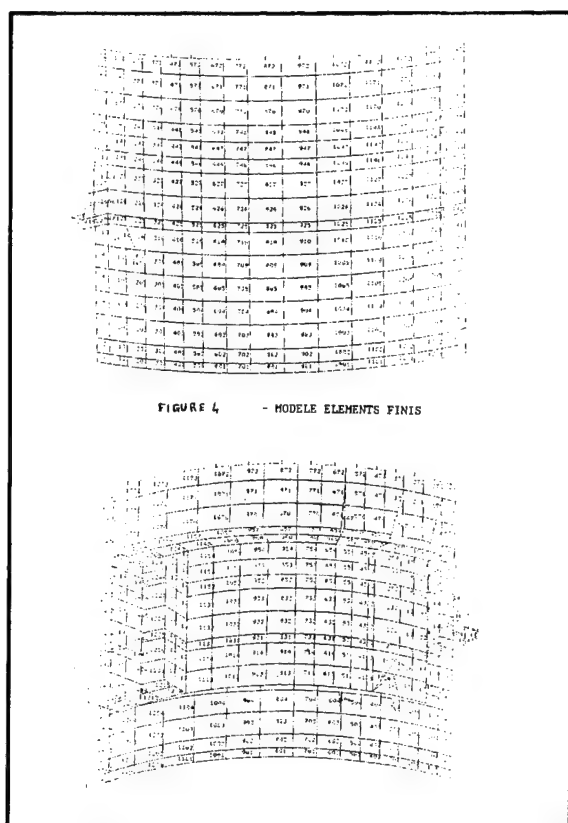
5. CRITERES DE DEFAILLANCE

Tenue aux efforts généraux

Les critères de rupture de la structure sont pris en compte par l'introduction d'une valeur maximale de la contrainte de Von Mises.

Par contre, les critères de flambage local des mailles (peau externe raidie intégralement) ne peuvent être introduits directement dans le logiciel. En conséquence, les raidisseurs et la peau externe ont été modélisés par des coques d'épaisseur équivalente et un dimensionnement en flambage local effectué manuellement entre chaque itération du calcul. Cette méthode ne permet pas d'atteindre une optimisation complète du revêtement (flambage local et diffusion des surflux) qui nécessiterait une optimisation séparée des raidisseurs et de la peau dans les zones travaillant en compression.

La stabilité générale de la structure, non critique, n'a pas été étudiée.



Rigidité

Les restrictions à la conception pour les spécifications de rigidité sont formulées en termes de déplacement maximal. Afin de tenir compte des souplesses apportées par les liaisons dans la structure réelle, une marge forfaitaire de 10 % est prise en compte.

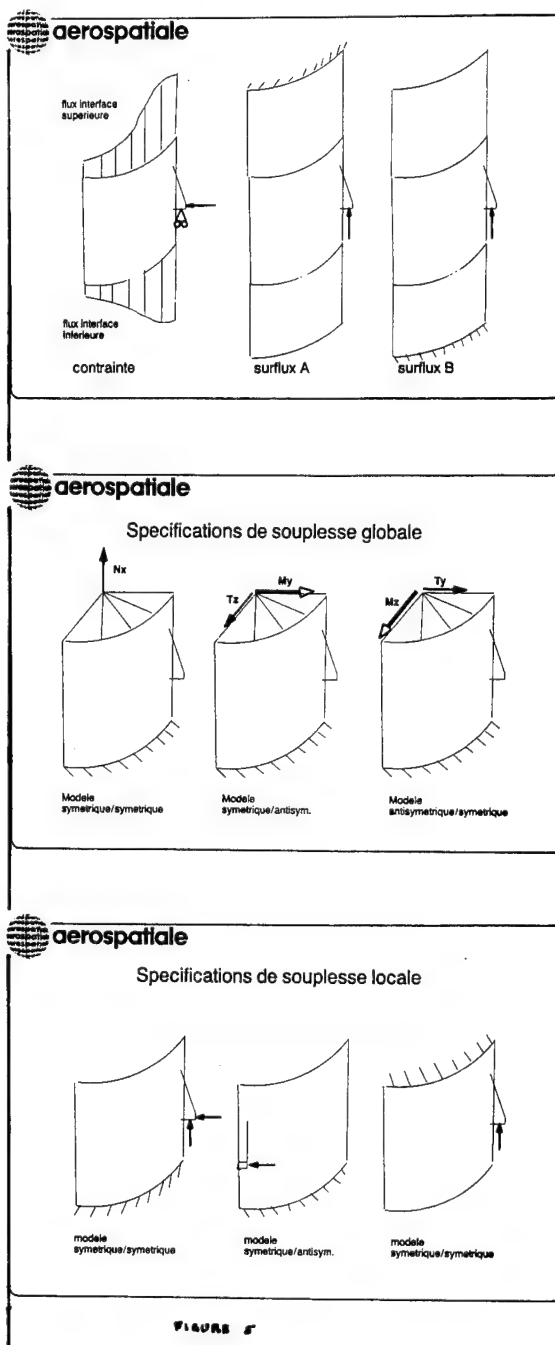
Surflux

Les coefficients de surflux sont évalués conformément aux spécifications (figure n° 2) sur les deux interfaces.

6. OPTIMISATION

La figure 6 présente l'organisation des calculs effectués. Après l'optimisation du modèle pour les spécifications nominales, nous avons pu déterminer les valeurs dimensionnantes et proposer deux types de modifications de celles-ci.

Le gain de masse envisageable a été évalué en introduisant ces deux variantes dans le processus d'optimisation.

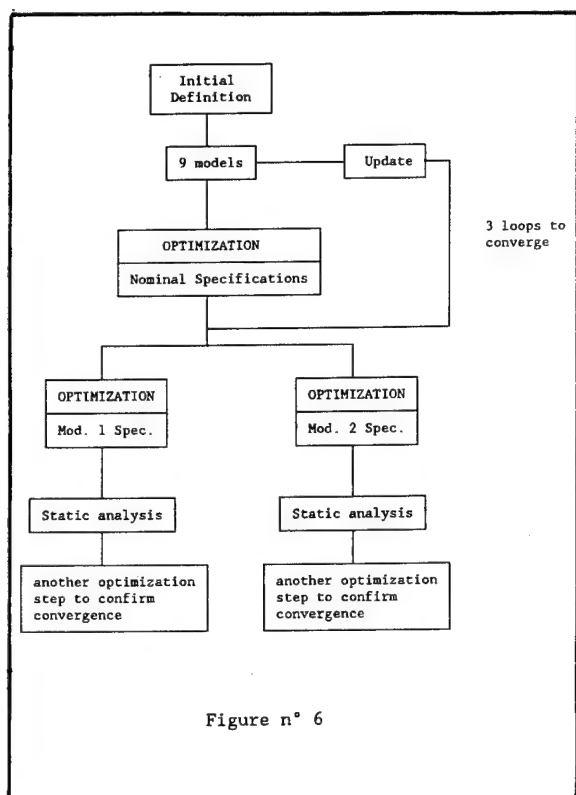


7. RESULTATS

La figure 7 compare la masse du modèle initial et celle des modèles optimisés pour les trois types de spécifications.

Notons que la conception initiale ne permettait pas d'assurer toutes les spécifications assignées à cette structure.

L'optimisation, définissant une nouvelle répartition des épaisseurs dans la peau externe et les cadres principaux permet, à masse équivalente, de tenir les spécifications.



Une optimisation conduite en parallèle par MAN a permis d'arriver à des conclusions proches, compte tenue des écarts de modélisation.

Par ailleurs, les modifications des spécifications proposées permettent d'envisager des gains de masse de 20 à 50 kgs sur la structure. Ces calculs ont ainsi permis de confirmer les résultats de MAN et de proposer des modifications de spécifications. La première a été acceptée et a ainsi permis d'améliorer les performances du lanceur ARIANE 5.

8. COUTS

Cette étude a été conduite sur le CRAY XMP 116 d'AEROSPATIALE sur le site des Mureaux.

L'analyse et l'optimisation de chacun des neuf modèles (7000 degrés de liberté chacun) nécessite en moyenne 250 secondes CPU, ceci à chaque itération.

Le coût informatique total de l'étude s'évalue autour de 3 heures sur ce type de machine.

9. LIMITATIONS

Actuellement, la limitation majeure des logiciels d'optimisation automatique des structures tient à la représentation par éléments finis de la structure. Ce type d'outil optimise le modèle et non la structure réelle. Il se pose donc le problème difficile du retour à la conception.

Les limitations technologiques et les critères de défaillance de la structure posent un délicat problème de formulation mathématique.

Dans l'étude présentée ici, le dimensionnement au flambage local n'a pu être pris en compte directement par le logiciel. Une analyse de stabilité aurait nécessité des modèles spécifiques très fins. Nous avons donc procédé manuellement en calculant à la main les critères classiques de flambage local et en les introduisant dans les modèles sous forme d'épaisseurs minimales.

Tout au long du processus, le concepteur et le calculateur doivent donc travailler en étroite collaboration afin de s'assurer entre chaque itération de la cohérence de la solution proposée par le logiciel.

Dans le cas d'une structure soumise simultanément à des spécifications de comportement statique et dynamique, il s'avère indispensable de pouvoir optimiser en parallèle

Kg	DAAN ⁽¹⁾	Voile Usiné	Peau Externe	Cadres Légers ⁽¹⁾	Voiles Légers	Goussets	Cadres Principaux	Total ⁽²⁾
<u>Modèle initial</u>	159	62.9	820.6	61.2	76.2	8.3	96.6	1 285
<u>Modèles optimisés :</u>								
Spécif. Nominales	159	37.1	830.6	61.2	95.2	5.9	96.2	1 285
Spécif. Modèle (1)	159	32.7	822.8	61.2	95.2	6.6	87.6	1 265
Spécif. Modèle (2)	159	39.1	763.4	61.2	95.2	5.8	93.9	1 218

NOTA -

(1) Ces éléments dimensionnés par des critères non pris en compte ici, n'ont pas été optimisés dans cette étude.

(2) La peau interne et les éléments non modélisés ne sont pas pris en compte ici.

FIGURE 7

ANALYSE DES MASSES DES MODELES

des modèles fort différents répondant aux besoins de ces deux types de d'analyse. On devra dans ce cas pouvoir définir des variables de dimensionnement communes aux deux modèles.

L'ensemble de ces considérations nous conduit à penser que la route est encore très longue avant le jour où l'on pourra optimiser les structures au cours d'un processus entièrement automatisé.

En l'état actuel, ce type de logiciel doit offrir à l'utilisateur toute latitude pour définir ses variables physiques de dimensionnement par rapport aux paramètres de modélisation, ses critères de défaillance par rapport aux résultats des calculs ainsi que ses limitations technologiques.

Dans le cas contraire, l'utilisateur sera obligé de simplifier, voire "d'oublier", certains de ces critères, ce qui, compte tenu de la finesse des résultats recherchés, mettra en cause la pertinence de l'étude.

**SESSION
1.2.C**

**TESTING
I**

SYSTEMS

PRECEDING PAGE BLANK NOT FILMED

N 92 - 23799

8471

AN ADVANCED SYSTEM FOR ENVIRONMENTAL SINE TESTING - BASIC PRINCIPLES REVISITED

J. Leuridan / R. Mangelschots / F. Declercq / G. Bossaert

LMS International
Interleuvenlaan 65
B-3000 Leuven, Belgium

ABSTRACT

The testing of ever more complex mechanical systems for more stringent environmental conditions has put increased requirements to the systems that are used for closed loop vibration control and data reduction from laboratory or fielded systems. For testing based on sine excitation, this implies increased capability for speed (sweep rates), while maintaining measurement accuracy and resolution even for structures that exhibit resonances with high Q factors, and from noisy data! The paper describes an implementation of a sine data reduction system using state-of-the-art hardware (computer workstation, modular multichannel front-end) and based on accepted principles for sine data processing.

1. INTRODUCTION

The testing of structures for the mechanical (vibration) environment is commonly done with shaker testing procedures using closed loop vibration control. During the shaker test, response data (acceleration, stress) are measured and recorded at many response locations. This enables a more detailed analysis of the structures dynamics, specifically important when during the test a problem or failure occurs. Therefore this response data is measured and preferably recorded as well as analyzed online, which creates the possibility of extended online protection of the device under test based on limit control of the response data. For tests based on swept sine excitation, this procedure is called sine data reduction.

Sine data reduction in principal aims at the characterization of swept sine response data. There are two components to this task: the determination of the instantaneous sine frequency, and the calculation of signal values of the data. With closed loop vibration control tests using sine excitation, the frequency extraction can proceed using the COLA (Constant Output Level Adaptor) signal, a clean, constant amplitude equivalent of the excitation signal that is used to drive the shaker. The signal values to be calculated are the fundamental component, harmonics, and subharmonics, either phase related to the COLA signal, to any other response signal, or eventually processed in transfer functions. Further important are the RMS and signal peak value.

The paper describes the implementation of a sine data reduction system on an engineering computer workstation and using a modular multichannel frontend. The algorithms developed for sine data processing are based on well established principles: data dependent identification of pulsation frequency based on AR (autoregressive) modelling, and the Least Squares identification of sine amplitude and phase of fundamental and related harmonics. The implemented technology enables to take full advantage of state-of-the-art data acquisition and digital signal processing systems, realizing exceptional performance in terms of speed and accuracy.

2. PRINCIPLES OF SINE DATA REDUCTION

A more traditional approach for processing sine data consists of sampling the data synchronous with a multiple of the fundamental frequency. This sampling frequency can be obtained from the COLA signal with analog circuitry (essentially a phase locked loop). A Fourier transform on the sampled data gives amplitude and phase information for the fundamental, the harmonics and subharmonics. The number of harmonics and subharmonics available is determined by the number of samples per fundamental period, and the number of periods in the time window over which the Fourier transform is applied. Clearly, to avoid aliasing, the data needs to be filtered as a function of the instantaneous sampling frequency, which implies the use of tracking filters. The success of this approach depends very much on the quality of the analog circuitry that is used to extract the fundamental frequency and on the quality of the tracking filters, making it less suitable for tests over broad frequency ranges, e.g. .5 Hz - 3000 Hz, at high sweep rates, e.g. 4 octaves/minute.

This paper looks into an approach for sine data reduction based on asynchronous sampling. This approach can be used with multichannel frontends such as the Hewlett Packard HP3565S, where every channel is sampled at a fixed high sample rate, and digitally filtered for a limited set of possible frequency spans. All expressions in the proceeding assume therefore a fixed sample rate.

The extraction of the fundamental frequency is based on the fact that a sampled sine wave, y_n , satisfies a second order recursion formula,

$$(1) \quad y_n + a_1 y_{n-1} + a_2 y_{n-2} = 0$$

This follows directly from,

$$(2) \quad y_n = e^{i\omega n \Delta t} (e^{j\omega \Delta t} - e^{-j\omega \Delta t}) / 2j$$

The coefficients a_1 and a_2 can be estimated from the samples using least squares linear regression,

$$(3) \quad \begin{bmatrix} r_{11} & r_{12} \\ r_{21} & r_{22} \end{bmatrix} \begin{Bmatrix} a_1 \\ a_2 \end{Bmatrix} = - \begin{Bmatrix} r_{01} \\ r_{02} \end{Bmatrix}$$

With the covariance coefficient r_{jk} defined by,

$$(4) \quad r_{jk} = \sum_n y_{n-j} y_{n-k}$$

The minimum number of required samples for a solution of equation (3) is 3. The frequency and damping of the sine wave follow then from,

$$(5) \quad z^2 + a_1 z + a_2 = 0$$

$$(6) \quad z = \left(-a_1 + \sqrt{a_1^2 - 4a_2} \right) / 2 = e^{\alpha \Delta t} \cdot e^{j\omega \Delta t}$$

When the sine wave is not damped, the above equations can further be simplified to [1],

$$(7) \quad y_n - 2 \cos(\omega \Delta t) y_{n-1} + y_{n-2} = 0$$

Which follows directly from,

$$(8) \quad y_n = (e^{j\omega n \Delta t} - e^{-j\omega n \Delta t}) / 2j$$

Equation (7) has just one unknown. The resulting frequency estimate was however found to be less accurate when distortions are present on the data samples.

The calculation of amplitude and phase of the fundamental component, possible harmonics and subharmonics can proceed from solving following expression in a least squares sense,

$$(9) \quad y_n = \sum_{k=1}^{2N} A_k e^{j\omega_k n \Delta t}$$

Remark that in this expression N components are implied, including the fundamental.

3. IMPLEMENTATION

The above approach for processing sine data is implemented as an option of the LMS CADA-X system [2], using the Hewlett Packard HP3565S. The principal characteristics of this modular multichannel data acquisition system are as follows,

- There is a fixed anti-alias filter per data acquisition channel : 12.8 kHz (HP35655A)
- The data is sampled at a constant sample rate for every channel : 32 kHz (HP35655A).
- Using digital filters, the data is decimated to a set of frequency spans (in octaves): 12.8 kHz, 6.4 kHz, 3.2 kHz, 1.6 kHz
- With every frequency span there is a corresponding sample rate that is 2.56 times higher.
- The blocksize is fixed between 8 and 8192 (powers of 2). The user can however define an absolute lower minimum value.

Consider the fundamental frequency to be f . The current frequency span should at least include the maximum specified harmonic, $maxharm$. Considering that the frequency span can be reset to the next or previous span once the maximum harmonic exceeds the maximum frequency of the current frequency span or becomes smaller than half of this frequency, then the required number of samples or blocksize, $blksz$, follows from,

$$(10) \quad blksz = 2 \cdot C_s \cdot maxharm \cdot P$$

Where P is the specified number of periods and C_s is the oversampling factor, for HP3565S equal to 2.56.

The setting of the asynchronous acquisition parameters as a function of the fundamental frequency, for specified maximum harmonic, minimum blocksize and required minimum number of periods, can be followed in Figure 1. Two examples are illustrated,

- Example 1 (solid line). Sweep range between 10 Hz and 1 kHz, maximum harmonic 4, minimum 2 periods. The required blocksize is 64.
- Example 2 (dashed line). Sweep range between 10 Hz and 1 kHz, maximum harmonic 1. Minimum 1 period between 10 Hz and 100 Hz, minimum 2 periods between 100 Hz and 1 kHz. The required blocksize is 16, but reset to a user defined minimum of 32.

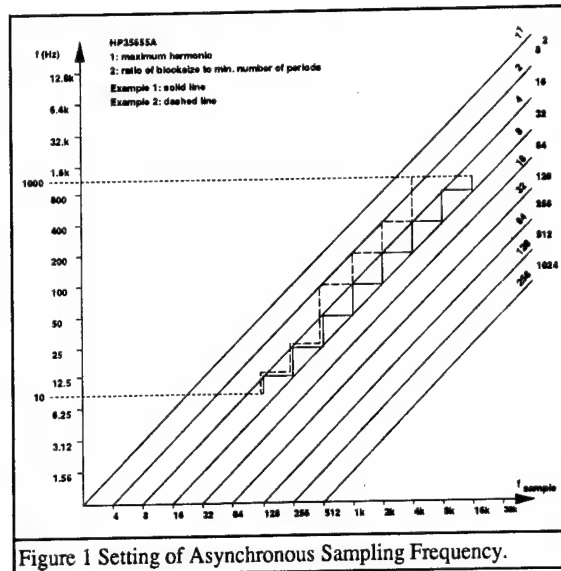


Figure 1 Setting of Asynchronous Sampling Frequency.

The setting of the acquisition parameters can further be optimized for maximum number of data points. Indeed, the acquisition time is determined by the sampling frequency; at lower frequency one has therefore interest in having the sampling frequency as high as possible, so as to synchronize with the data processing time. Once the data processing time exceeds the data acquisition time, it is advantageous to limit the number of frequency span switches. Considering this optimization for the number of data points for Example 2 in Figure 1 gives the switching strategy as illustrated in Figure 2.

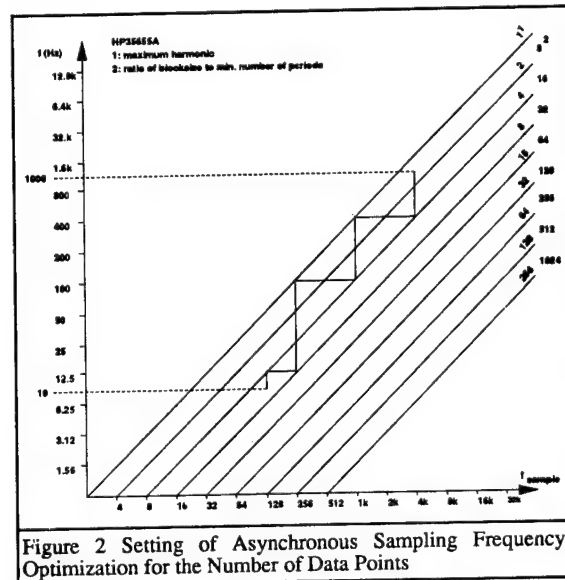


Figure 2 Setting of Asynchronous Sampling Frequency. Optimization for the Number of Data Points

To realise maximum precision, an autoranging procedure is implemented, enabling to reset the gain as a function of signal level during the sweep. The implementation should also be robust, for example to handle the case of a shutdown during the shaker test. This situation is handled by monitoring the amplitude of the COLA signal. The acquisition only starts or proceeds when the amplitude of the COLA signal is within user specified margins of a target value, and further when the frequency is between specified margins of the start frequency or the frequency where the amplitude of the COLA signal was last within margins.

Following functions can be calculated online : the fundamental, harmonics, subharmonics, either phase related to the COLA signal

or to any other response signal. Also calculated are the RMS and signal peak value. Transfer functions can be computed with these spectra. The frequency resolution for these functions can be specified as linear, in octaves, in decades, or by a user defined frequency resolution table.

As multiple sweeps can occur in one test, an averaging parameter (over sweeps) is further defined: stable, exponential, maximum, last or first occurrence. The values that are calculated online can be used for protection control on each of the measured response channels, possibly causing a shutdown of the shaker test. In parallel all sampled time data, or a subset, can be stored to disc; this data can be retrieved by time [range], sweep [range] or acquisition number [range], and postprocessed to any function that can be calculated online.

4. ILLUSTRATIONS

Illustrations

The measurement control display of the sine data reduction system is illustrated in Figure 3.

Remark that the operator can organise the display to show multiple data windows. Several status parameters are readily available, such as instantaneous frequency, amplitude of COLA signal, and current sweep direction. The actual measurement control is through softkeys, and/or through a dedicated multi function button box.

Figure 4 illustrates typical performance, based on an HP9000/375, an HP6000/335H hard disc and the HP3565S with HP35651B signal processor. The number of multiplexed acquisition/second including throughput of time data to disc, is plotted as a function of the number of simultaneous channels of data acquisition.

Finally, Figure 5 illustrates a typical measurement over a range from 100 Hz to 10 kHz, with a sweep rate of 4 octaves/minute. The measured fundamental on one channel is compared to the RMS and peak estimator.

REFERENCES

1. Vold, H., J. Crowley and J. Nessler, 1989, "Tracking Sine Waves in Systems with High Slew Rates", Proc. of the 6th Int. Modal Analysis Conf., Orlando FL, pp. 189-193
2. LMS CADA TEST/FOURIER MONITOR User Manual, CADA-X-1200-UM-024, 1990.

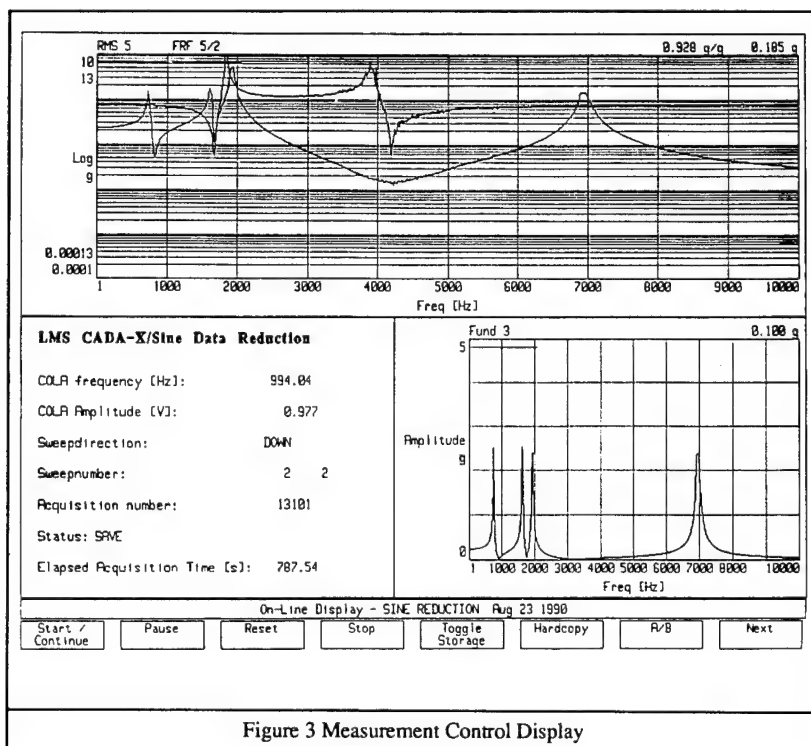
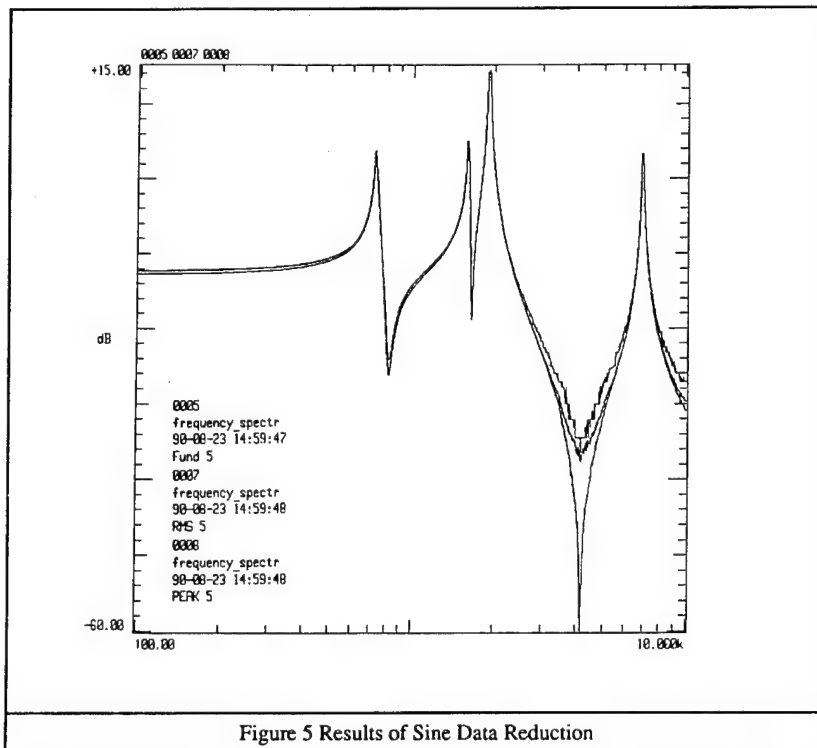
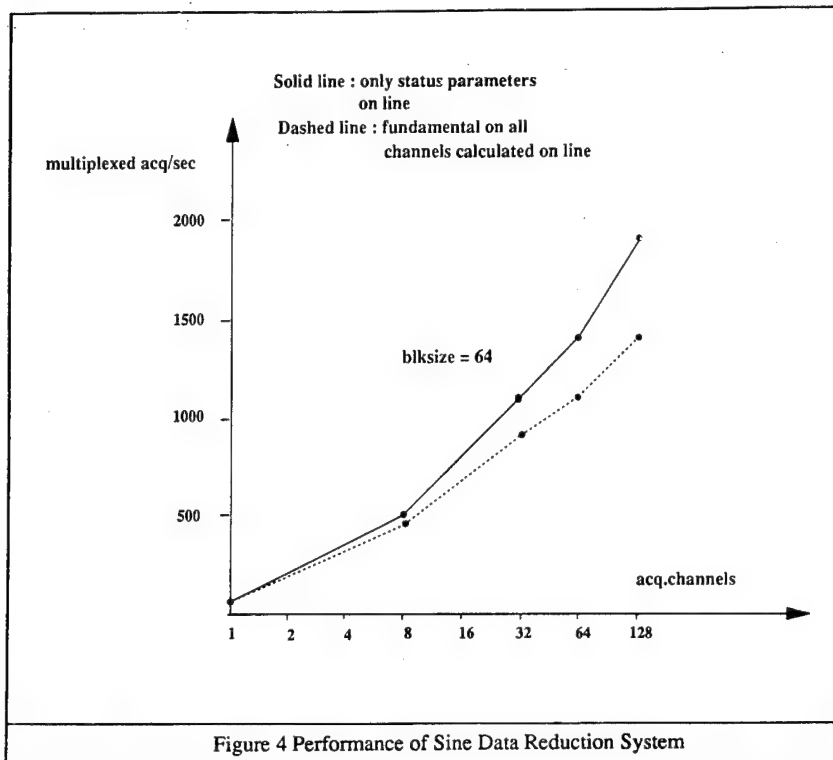


Figure 3 Measurement Control Display



N92-23800

50-39

84712

NON CONTACTING MEASUREMENT OF VIBRATION

A J Barker, Director

Ometron Ltd, Worsley Bridge Road, London SE26 5BX

ABSTRACT

Non-contacting methods of measurement have intrinsic advantages in many engineering applications. A new non-contacting laser Doppler sensor has been developed which enables conventional vibration measurements to be obtained at up to 200 m range with a 1 mW laser beam. The sensor is able to accommodate the examination of complex shapes without refocus by virtue of an exceptional working depth of field of several metres. Near real time mapping of full field vibration patterns has been achieved by combining the new sensor with special purpose electronic hardware controlled through an industry standard PC. The principle of operation of this new system is described and its broad capabilities in non-destructive testing and vibrational mode shape visualisation illustrated by application examples.

Keywords: Vibration, velocity, laser Doppler, non-contacting, full field.

INTRODUCTION

A laser Doppler vibration sensor can be used to measure the instantaneous velocity at a point on a vibrating structure without surface contact. Aiming a single laser beam onto the desired point of measurement results in direct instrumental output of test surface velocity as a calibrated analogue voltage. Provided that a line of sight can be established between the sensor head and the test surface, such a sensor can be employed as a movable, non-contacting velocity transducer, providing an analogue output directly comparable with that obtained from a conventional accelerometer/charge-amplifier combination. Full field vibration patterns can be measured by combining a laser Doppler vibration sensor and suitable beam scanning mechanisms together with signal processing and display systems all under central computer control.

VPI Sensor [Refs. 1, 2 and 3] is an industrially engineered laser Doppler interferometer with built in beam scanning capability optimised for maximum sensitivity and ease of use in mechanical vibration measurement. The advanced design concepts incorporated in the instrument result in a rugged unit of extremely high sensitivity, capable of measurement on natural surfaces over 20 m distant from the sensor head using a measuring beam power below 1 mW (Class II). This paper reports the introduction of a new generation of full field vibration mapping instrumentation in which the high performance capabilities of VPI Sensor are combined with the extreme speed of custom data processing hardware and the convenience of easy-to-use software running on an industry standard PC. The new system is capable of acquiring and displaying a full field vibration pattern in less than four seconds, setting new standards of performance and convenience for non-destructive testing and general vibration mode shape sensing.

BASIC PRINCIPLE OF LASER DOPPLER VIBRATION SENSING

In the same way that sound waves reflected from, or emitted by a moving object are subjected to a frequency change (the well-known Doppler effect heard on ambulance sirens etc.) a beam of light reflected from a moving surface is also changed in frequency. Although the fractional change in frequency of the light wave is very small (typically 1 part in 10^8 or less) it can be measured very accurately using optical interferometry in conjunction with electronic frequency measurement. The most practical optical configuration for vibration measurements on solid surfaces is the single beam backscatter arrangement in which the beam from a laser source is divided into an internal reference beam and an external measuring beam, the latter being directed onto the moving test surface. Light reflected back from the test surface is shifted in frequency by an amount $2v/\lambda$, where v is the velocity of the test surface and λ is the wavelength of the laser radiation. For a Helium-Neon laser at 633 nm, the frequency shift is 3.16 MHz per ms^{-1} velocity of the test surface.

Direct measurement of small shifts in frequency of an optical beam at 5×10^{14} Hz is impractical. However, by arranging for the frequency-shifted backscattered light to interfere with the internal reference beam, intensity modulation of the combined beams at the Doppler shift frequency may be sensed using an appropriate photodetector. An analogue voltage representing test surface velocity may then be derived from the detected modulation frequency using established frequency-to-voltage conversion techniques.

The great advantages of this approach to vibration measurement are:

1. The technique is non-contacting; there are no added mass effects associated with velocity measurements and data can be obtained from hot surfaces or in electrically noisy environments where the use of conventional contacting accelerometers would be extremely difficult.
2. The laser beam can be focused to a small spot, providing high spatial resolution even at long working distances.
3. Test surface velocity is related to the measured optical frequency shift by a fundamental physical constant.

The main technical challenge is the achievement of a robust system design capable of high optical sensitivity and long working depth of field for maximum ease of use over a wide range of vibration measurement tasks.

DESIGN CRITERIA FOR AN INDUSTRIAL SENSOR

In order to ensure successful application over a wide application base, an industrial laser Doppler vibration sensor should meet the following performance criteria:

1. Measuring beam power less than 1 mW (Class II laser product) for ease of use in an industrial laboratory with minimal safety precautions.
2. High optical detection sensitivity to permit measurements at long working distances or on surfaces of low reflectance (e.g. black rubber) without special surface preparation.
3. Simple "point and shoot" operation with no complicated procedures.
4. Maximum tolerance of the FM detection system to high levels of signal amplitude modulation caused by laser speckle effects.
5. Typical working depth of field of at least 1 m for ease of application to large, non-flat surfaces.
6. Built-in beam scanning facilities for ease of application to full field vibration pattern measurement.
7. Vibration frequency range at least 10 Hz - 10 kHz and velocity range at least $10 \mu\text{ms}^{-1}$ - 1 ms^{-1} .

VPI Sensor (figure 1) meets or exceeds all these criteria in a rugged, industrially designed package.

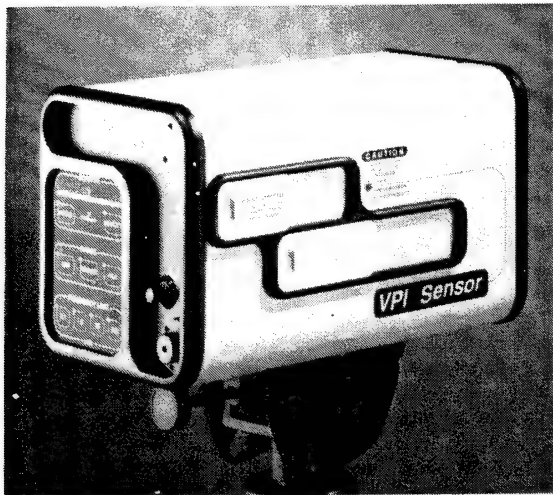


Figure 1 Scanning laser Doppler vibration sensor

The optical system (figure 2) is based on a Michelson interferometer with dual detection channels configured to provide a pair of analogue signals modulated at the same Doppler shift frequency but with a 90° mutual phase shift. The two Doppler signals are used in conjunction with electronic mixing techniques to derive a single, frequency-shifted Doppler signal from which an analogue voltage representing the instantaneous velocity of the test surface is derived using a frequency-to-voltage converter.

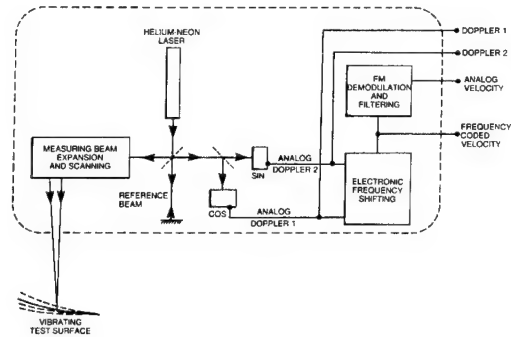


Figure 2 VPI Sensor system schematic

The high detection sensitivity of the optical system permits measurements on natural surfaces at working distances in excess of 20 m (200 m using retroreflective coatings) and provides a sufficient signal-to-noise ratio surplus under typical operating conditions to ensure minimal disruption of measurement performance by laser speckle effects. The combination of high detection sensitivity with a coaxial optical system, in which the outgoing and returning measuring beams follow a common path, results in a typical working depth of field of 3 m. Vibration frequencies from DC to 100 kHz can be accommodated, together with velocities from a few μms^{-1} to 1 ms^{-1} .

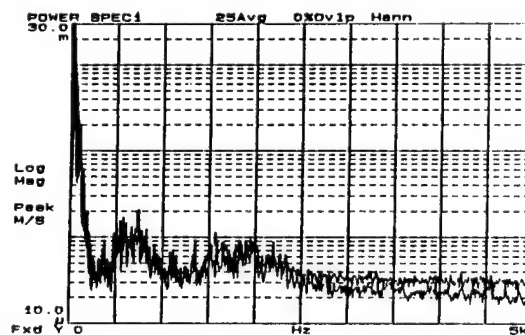


Figure 3 Comparative velocity measurements on a running engine

As a practical example of non-contacting vibration measurement under difficult operating conditions, figure 3 shows comparative velocity measurements made on the side of a running engine using both VPI Sensor and a contacting accelerometer. The accelerometer results are subject to severe drift as the engine block heats up under steady operating conditions; the VPI Sensor results remain steady.

RAPID FULL FIELD SCANNING USING A LASER DOPPLER VIBRATION SENSOR

Full field vibration pattern measurement using a scanning laser Doppler sensor is gaining popularity in vibration laboratories because of its versatility and the directly interpretable nature of the results obtained. To date, known full field systems have made measurements sequentially over a grid of discrete points accessed by computer-controlled beam positioning mirrors. Allowing sufficient time at each point for settlement of the deflection system and subsequent measurement of the desired velocity characteristic (e.g. RMS or phased amplitude) typically limits the measurement speed to approximately 50 points per second, corresponding with acquisition of a 64 x 64 point vibration pattern in 82 seconds, or a 256 x 256 pattern in 22 minutes. Although many orders of magnitude faster than the acquisition of equivalent data using discrete contacting accelerometers requiring individual bonding and calibration (an expensive and daunting task for 64 x 64 points, let alone 256 x 256) these scan times remain slow when compared with the primary data acquisition rate associated with the latest generation of holographic and electronic speckle pattern instrumentation.

VPI RapidScan is a new implementation of full field laser Doppler vibration sensing in which the enhanced capability of VPI Sensor to realise velocity measurements of good quality under non-ideal conditions has been exploited to achieve drastic cuts in previously achieved data acquisition times. By adopting a continuous scanning configuration and using novel analogue signal processing methods to extract either a modulus or phased amplitude characteristic from the time varying velocity signal, acquisition times for 64 x 64 and 256 x 256 patterns have been reduced to 3.8 and 15 seconds respectively. The measuring beam scans a square raster over the test piece and the measured vibration pattern is built up line-by-line in real time as a colour coded image on a display monitor. Since the system measures and displays velocity directly, no further digital analysis is required to interpret the pictorial display which can also be printed out as an annotated colour report sheet. The system is controlled through easy to use Windows software running on an industry standard PC (figure 4).

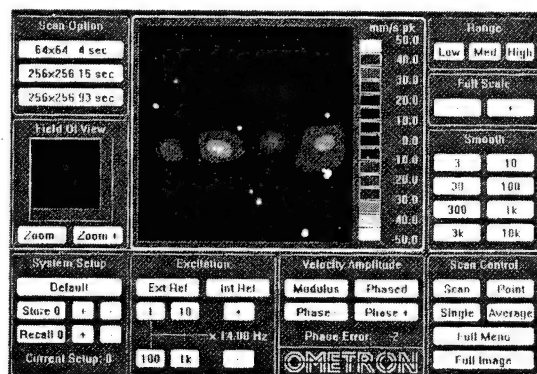


Figure 4 Operator interface for full field rapid scanning system

Non-destructive testing of specimens or structures is most conveniently performed using broad band vibrational excitation of the test piece and recording an RMS or modulus average velocity pattern. Localised weaknesses or defects in the structure resulting in localised abnormal vibrational motion may be identified clearly on the display images. Figure 5 shows bonding defects detected in the honeycomb composite surface of an aerial dish using VPI RapidScan in modulus average mode.

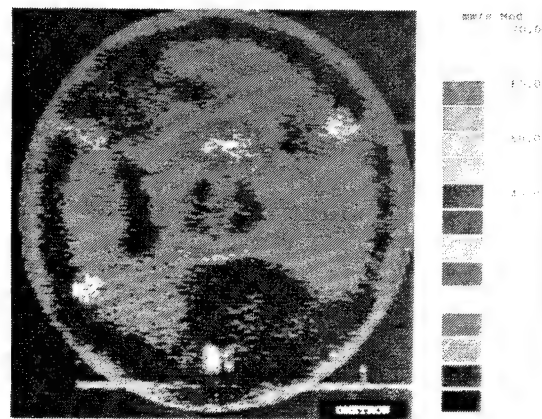


Figure 5 Visualisation of aerial dish bonding defects

The dominant modes of vibration of a structure are of relevance in engineering applications ranging from noise/vibration control in motor vehicles or domestic appliances to design optimisation of aerospace components. VPI RapidScan is ideally suited to modeshape visualisation at specific frequencies of interest. The sensor may be used initially as a non-contacting velocity transducer at one or more points to define key resonances of the test piece under broad band excitation in conjunction with an external signal analyser. The vibration pattern associated with each of the key resonances may then be measured under single frequency excitation. Figures 6, 7 and 8 show typical results obtained in this way. All measurements were made from a working distance of 2.5 m with no special preparation of the test surface, in this case the side panel of a domestic washing machine.

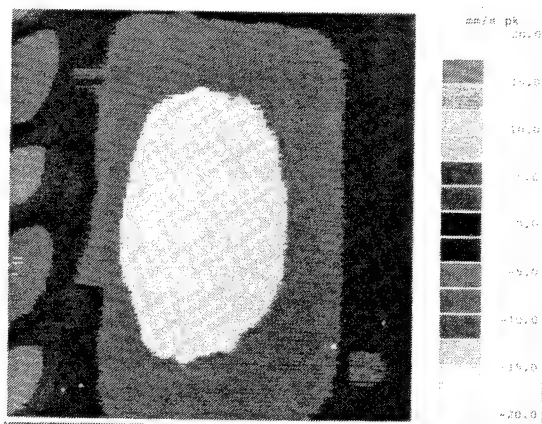


Figure 6 Side panel mode at 27.6 Hz

Figures 6, 7 and 8 show respectively the vibration mode shapes of the side panel at 27.6 Hz, 74.0 Hz and 364 Hz. The entire set of data was acquired in a few minutes using the phased amplitude mode in which the relative direction of motion in different regions of the vibration pattern is clearly depicted.

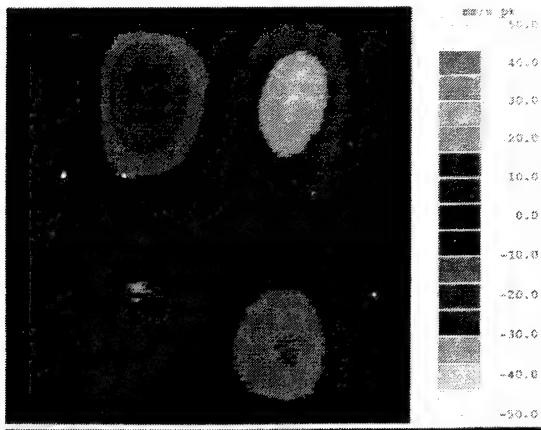


Figure 7 Side panel mode at 74.0 Hz

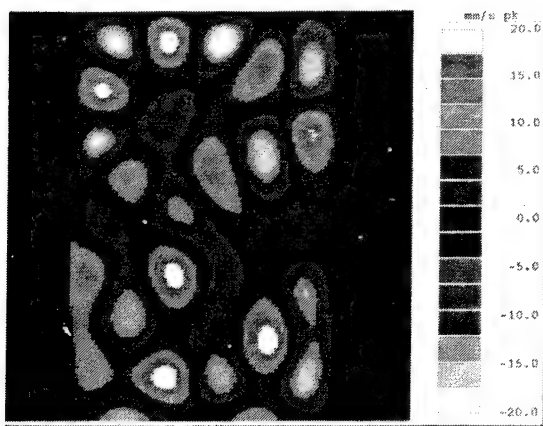


Figure 8 Side panel mode at 364 Hz

REFERENCES

1. Drain, L.E. "The Laser Doppler Technique", *John Wiley and Sons*, 1980.
2. Barnett, B. and Owens, R.H. "Advances in Laser Doppler Sensors for Modal Analysis", *15th Int. Seminar Modal Analysis, Leuven, Belgium*, 1990.
3. Oliver, D.E. and Jaeger, P. "A Unique Laser Doppler Vibrometer: Role in Design and Non-Destructive Testing", *37th Int. Instrumentation Symposium, San Diego*, 1991.

51-39
N92-23801

ON DEVELOPMENT OF AUTOMATED STATIC LOADING SYSTEM FOR SPACECRAFT STRUCTURES

A.V. Patki and R. Samuel

Mechanical Systems Group, ISRO Satellite Centre, Bangalore, INDIA 560 017

ABSTRACT

The quasi-static loads on large spacecraft structures experienced during launch are generally simulated by static loading. With optimized structure and the structural model being used as flight model spares, it is necessary that the static load tests are conducted in such a manner that overloading or catastrophic failure do not occur during such tests. With this objective an Automated Static Test System (ASTS) has been successfully developed, evaluated and used on a large communication satellite to demonstrate its utility in smooth conduct of the qualification tests.

Keywords: Automated test system, Static Load Tests, Spacecraft Structural Qualification.

1. INTRODUCTION

The static tests, specially on a large spacecraft structure, form an important part of the development and qualification of the optimized structures. The whiffle tree arrangement is generally used for simulating the structural loading encountered during the different phases of operation. Number of loading points needed on structure increase enormously if one has to restrict the percentage errors in simulation. The size and complexity of the structure make it obligatory to make use of multiple hydraulic actuators, specially to simulate biaxial loading. In the conventional set-up the actuators are not controlled together and the loading is manual. It is essential that these actuators operate gradually and simultaneously, in order to avoid unexpected overloads on structures during the tests. The phase difference in loading of two axial load simulating actuators can lead to large amount of torsional loads. Finally there is a need to release the loads immediately and simultaneously in case of a failure of a component of structure. Especially so,

since the failure causes loads to redistribute and can do further unintended damage to the hardware. The specimen being tested here, namely the spacecraft structure, is a very expensive item and needs significant time for repair before retests. Hence, aborting the loading quickly in case of a failure is essential to stop further perpetuation of the damage. These requirements lead to the development of Automated Static Test System [ASTS] (Ref.1) at Structures Division, ISRO Satellite Centre, Bangalore. A six channel automated loading system was conceived, designed and realised with these requirements in mind. It also has many other features incorporated. Data acquisition and reduction is essential for taking abortive action. Modularity has been kept in mind during the development. The development was then followed by the test and evaluation cycle. Finally the system was used successfully for conducting the tests on Structural Model of INSAT-2 spacecraft, being built indigenously at ISRO. This paper gives the salient details of the development of system. The additional features of the system includes automatic data reduction, some of which are to be used to generate internal abort based on preset limits. Different loading patterns can be achieved very easily giving different loading rates and dwell time. The system modularity is achieved using commercially available standard hardware. The efforts were focussed on developing necessary interface hardware and the control software. The basic requirements generated based on earlier experience and classical methods are given in the first part of the paper. The final system configuration that evolved is then given in the next part. It is followed by the performance details as per the evaluation exercise. In the end, the details of the actual application on the STM of the current satellite programmes are given.

2. SYSTEM REQUIREMENT

The static load tests are conducted on spacecraft structures using a whiffle tree system of loading (Ref.2) in which

in which many locations on the structure are combined, two loading point at a time, and a tree is constructed with the resultants till it is brought out to a single loading point and the loads are applied using linear hydraulic actuators. Six of such actuators were proposed for in-house qualification tests on INSAT-2 structural model. The loads have to be applied gradually, uniformly, simultaneously and with continuous monitoring of the response of the structure in terms of allowable displacements.

The system requirements can be summarised briefly as given below.

- * Generation of different pattern of loading specifications.
- * Static loading by 6 actuators with high degree of expandability
- * Continuous monitoring of 30 channels of loading system health parameters, displacement and strain data of structure
- * Smooth abort if the specified limits exceed or likely to exceed a specified value of a particular parameter.
- * Additional safety abort (hardware) on channels if the loading or response values exceed the preset values
- * External manual abort
- * 200 channel strain and displacement data acquisition and analysis (Real time analysis and display of 10 channels)
- * Report quality test results

3. SYSTEM CONFIGURATION

All the above requirements were taken into account in the configuration development and design stage. In addition importance was also given to modular concept and the need for versatility of the system to do multiple tasks such as dynamic and fatigue testing.

The ASTS system consists of two distinct subsystems (Figure.1). The first one relates to the automated loading system and the second to the data acquisition and analysis system. The former forms the heart of the ASTS. Among the feasible options this subsystem configuration was chosen for the following reasons viz.,

- * On the loading side the Servo Hydraulic Control System is accurate, flexible and can be used for future dynamic applications.
- * On the electronics side GP-IB Interface bus was used so that the computer accessories and many instruments can be interconnected by the users with a great degree of flexibility.

3.1 Automated Loading System

The system consists of HP 3497A data acquisition and Control system, HP 9836 computer with peripherals like plotter, printer and winchester disk drive, six channel load cell, signal conditioners, six channel servo controller, hydraulic powerpack, Servo actuators, Servo valves and Safety and abort Unit.

The HP3497A acquisition and Control

system has four plug-in modules namely

1. Dual channel Digital to Analog Converter.
2. Two Multiplexer Assembly for 40 channels of voltage measurement.
3. Relay Actuator Assembly
4. Two Strain gage card assembly with input from strain gages and displacement transducers for 10 channels.

Block diagram of Automated Hydraulic Servo control system is given in Fig.2. This data acquisition system HP 3497A can be programmed by HP 9836 Computer to load the structure in a desired fashion (Fig.3).

The flow chart of the control software is given in Fig.4. The Control software running on HP 9836 sets the control System into action as follows. The dual voltage DAC module generates loading ramp voltage which is fed to Control potentiometer to be divided into six variable slave voltages which serve as the command for six control loops. The command reaches the servo valves through the servo controller and load is applied to the structure. This load is measured by the load cells, conditioned and then fed to the servo controller for closed loop operation. The command and load cell feedback voltage of all the six loops are fed to the 3497A Control system and to the analog hardware safety and abort system. A comparison of command and feedback is made at both the systems and if the deviation exceeds preset limit, abort action is initiated by either software or hardware and hydraulic pump is tripped through the relay actuator assembly. In addition to this comparison, the critical response (maximum of 30 channels) data from the structure is monitored by the software and abort action is initiated if the conditions are abnormal.

3.2 Data Acquisition and Analysis System (DAAS)

The block diagram of DAAS (Fig.1) consists of a controller (HP1000E), Data Acquisition System (HP3497A) with extender, strain gauge plugin cards and high resolution voltmeter. The flow chart of Data Acquisition and analysis Software is given in Figure.5.

4. PERFORMANCE EVALUATION OF THE SYSTEM

This new facility was released for test purposes after a set of safety requirements as established by a team of experts was met. The evaluation included ascertaining the satisfactory performance of the system to meet the requirements already listed, stability of the control system, protection against overload of space hardware and safety of test personnel. All probable error conditions obtainable during the test were simulated and response of the system obtained. Some of the error conditions simulated were loss of load cell feedback, malfunctioning of feedback path signal conditioner, large flexibility of specimen as might be obtained during

yielding/failure of loading link etc., The reliability of the software was assured through the evaluation plan which was executed on a software -hardware integrated environment.

5. USE OF FACILITY FOR INSAT-2 SM STATIC LOAD TEST.

The inaugural use of the facility was for qualifying the structural model of INSAT-2 class of satellites. The qualification testing spanned 8 weeks of 10 hrs per day shifts. The test plan (Ref.3) included many low level load tests facilitating checking of linearity of structural response. In all about 18 test runs were planned to qualify the structure for longitudinal and lateral loads. 150 locations were selected for strain monitoring and 50 locations for displacement measurements (Ref.4). Safe release of loads was recorded on many occasions, the most common being the breakage of a link in the whiffle tree and the incorrect instrument settings. The improvements in terms of reduced testing time, reduced human attention, increased safety to the specimen against overload, elegant operational procedures were the high-lights of Automated loading system in comparison to the conventional system.

6. AUTOMATED LOADING SYSTEM SPECIFICATIONS (REF.5)

- 1 Number of Channels: Six (Expandable)
- 2 Max. load : 50 KN
- 3 Resolution : 0.1% full scale
- 4 Linearity : 0.5% full scale
- 5 Tolerance on Abort 1% F.S. (Nominal)

7. CONCLUSION

The experience gained during static tests of different spacecraft has helped

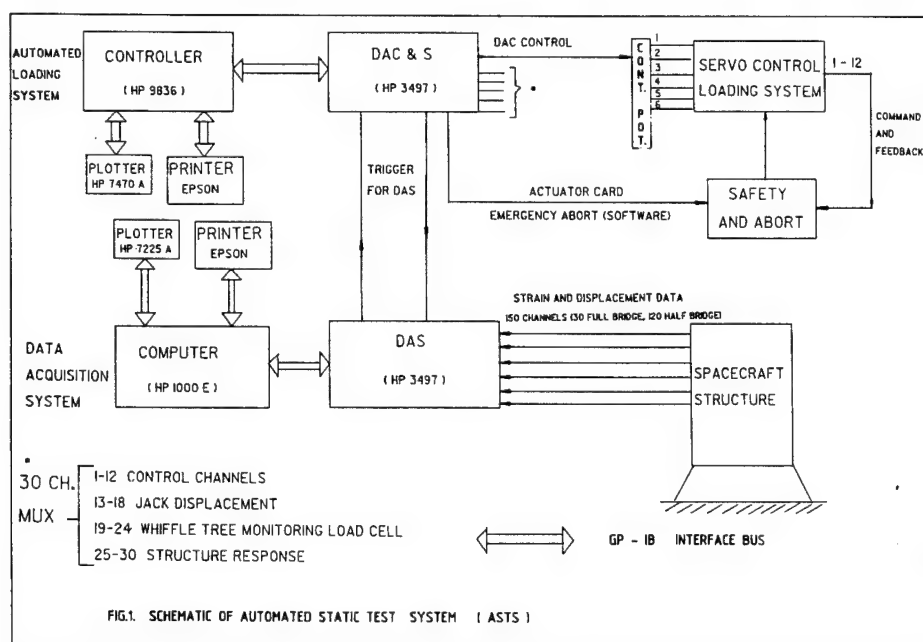
us in generating such requirements and develop a facility to conduct static load tests. The qualification tests conducted on INSAT-2 proved that with this improved technique, the testing becomes more systematic and accurate. The structure can be protected without much unexpected over loading. It is expected that this development will form very useful exercise for the fellow workers and also serve the authors as an important feed back.

8. ACKNOWLEDGEMENT

The authors acknowledge the efforts put by their colleagues towards this development. Special thanks are due to Dr.P.S.Nair, Deputy Project Director of INSAT-2 Project for using this development for testing the structural model. The authors wish to thank Mr.R.Krishnaswamy for Instrumentation support and Mr.T.S.Sriranga for compilation of data. Finally the authors thank Dr.K.Kasturi Rangan, Director, ISRO Satellite Centre for his permission to submit the paper.

9. REFERENCE

- 1 Samuel R 1985, Automated Static Test System (Honourable Mention Award in Hydraulics and Pneumatics Design Award Contest).
- 2 Kannan M V et al. 1990, Qualification of Spacecraft Structure for Quasistatic Loads, 'International Conference on Advances in Structural Testing, Analysis and Design'. Bangalore, India.
- 3 INSAT-2 Structure Static Test Plan. 1989 (Internal Report).
- 4 Report on Static Test Results of INSAT-2. 1989 (Internal Report).
- 5 Report on Automated Static Test System. 1986 (Internal Report).



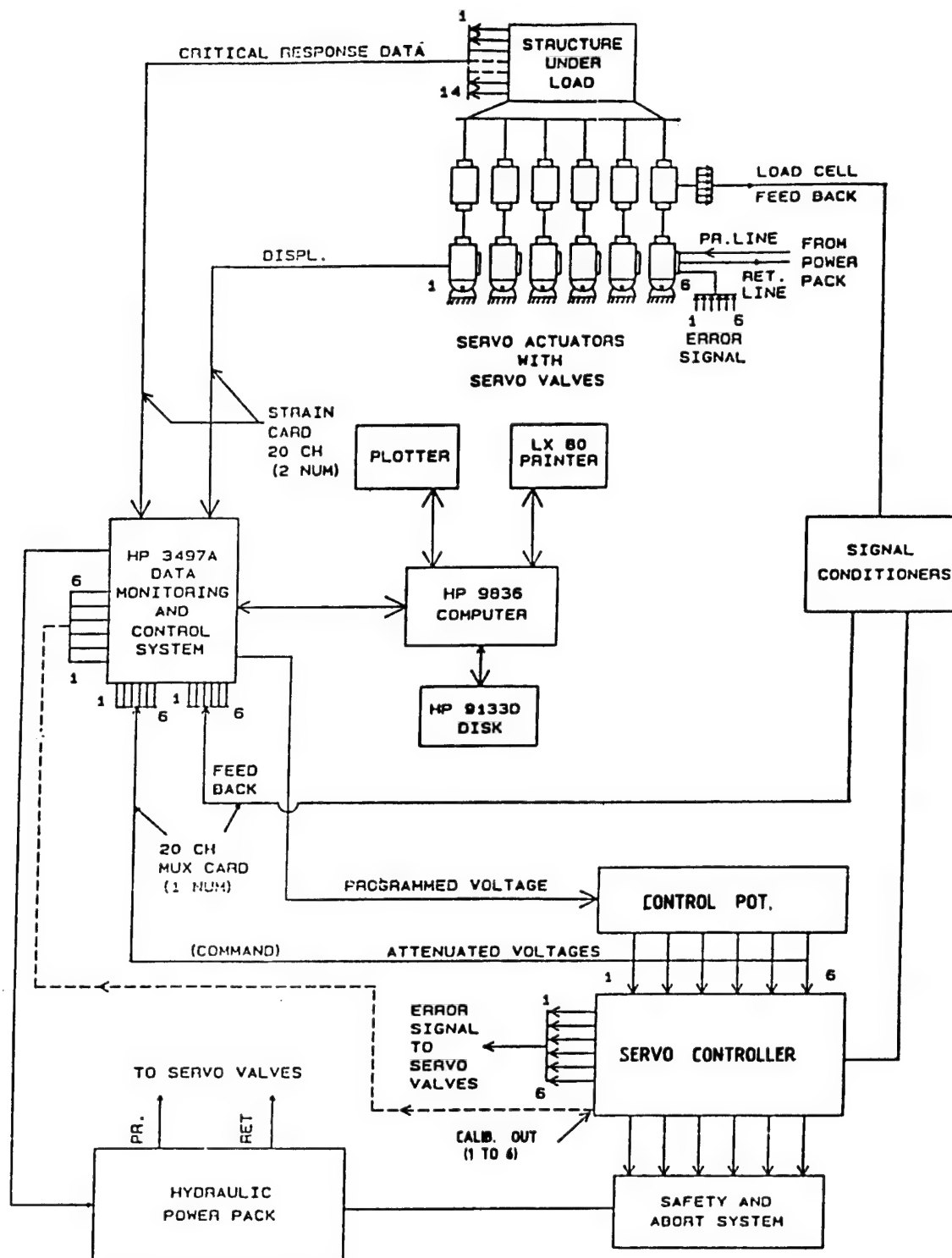


FIG.2 BLOCK DIAGRAM OF AUTOMATED LOADING SYSTEM

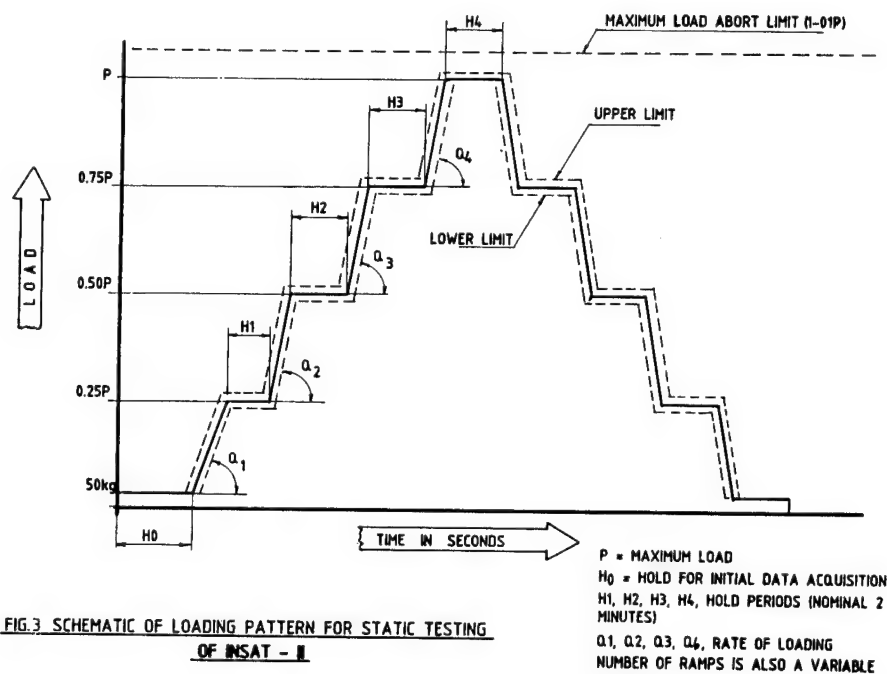


FIG. 3 SCHEMATIC OF LOADING PATTERN FOR STATIC TESTING
OF INSAT - II

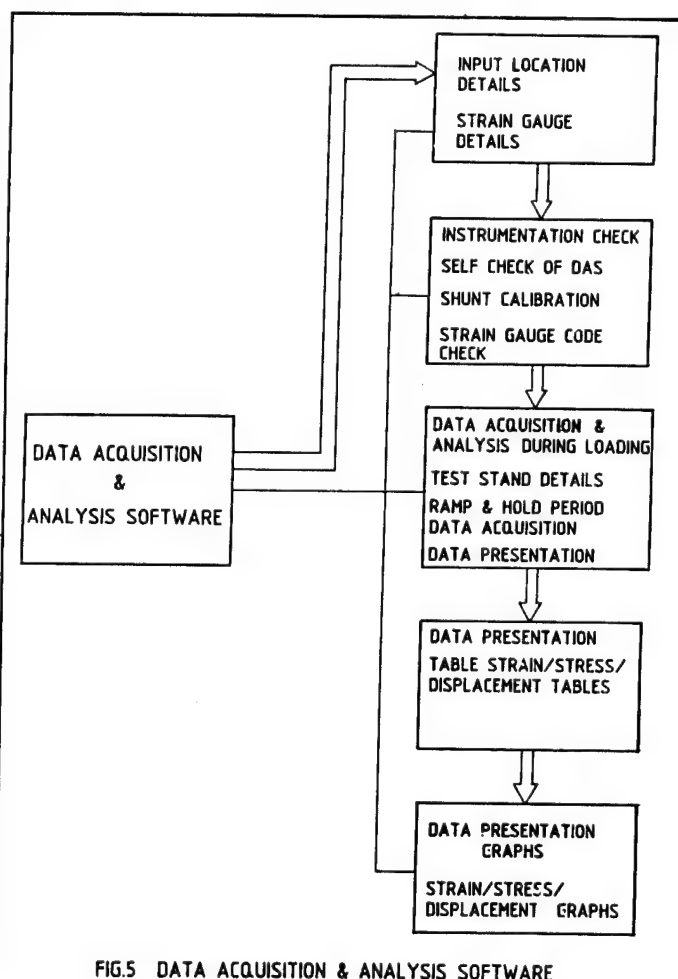


FIG. 5 DATA ACQUISITION & ANALYSIS SOFTWARE

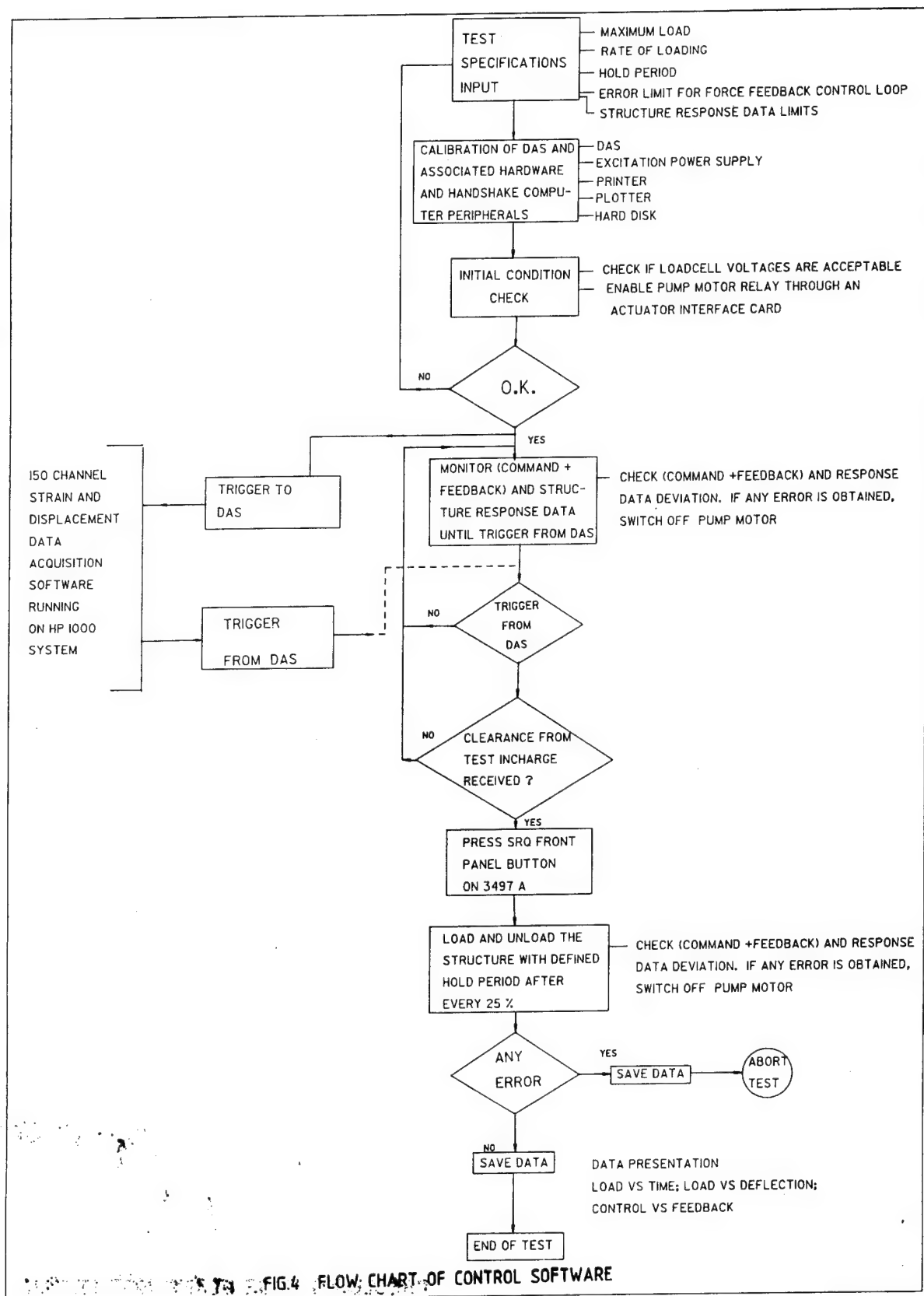


FIG. 4 FLOW CHART OF CONTROL SOFTWARE

**SESSION
1.3.C**

**ANALYSIS
II**

METHODS

PRECEDING PAGE BLANK NOT FILMED

PRECEDING PAGE BLANK NOT FILMED

N92-23802

22-39
84714

NONLINEAR FINITE ELEMENT ANALYSIS OF SANDWICH SHELLS

O. Amlid and P. G. Bergan

Veritas Research A.S., Høvik, Norway

ABSTRACT

Analysis of sandwich plates and shells poses a series of theoretical and practical problems to the design engineer. Local and global deformation modes and phenomena which are negligible when analyzing homogeneous members can turn out to be of significance when the member is layered and of sandwich type. In addition to this, a sandwich panel can exhibit failure modes which are unknown to homogeneous panels. Highly comprehensive, nonlinear finite element analysis capabilities are required to solve such problems accurately. This paper describes a new nonlinear sandwich element based on the free formulation theory. It has been implemented in a general purpose finite element program with capabilities for solving nonlinear static and dynamic problems (FENRIS).

Keywords: Sandwich structure, finite element method, free formulation theory, wrinkling.

1. THE FREE FORMULATION THEORY

The free formulation finite element theory, Refs.[1],[2] and [3] allows for use of nonconforming displacement functions at the same time as the method ensures that the patch test is implicitly satisfied. A displacement field \mathbf{u} within an element is expressed by a complete set of rigid body and constant straining fields (rc - modes) and a set of higher order fields (h - modes):

$$\mathbf{u} = \mathbf{N}_{rc}\mathbf{q}_{rc} + \mathbf{N}_{qh}\mathbf{q}_h. \quad [1]$$

The generalized displacement functions \mathbf{N}_{qh} must consist of a complete polynomial to the degree which corresponds to the number of rc - modes of the given type of problem, while \mathbf{q}_{rc} are the associated coefficients. \mathbf{N}_{qh} expresses a set of h - modes with \mathbf{q}_h as their associated coefficients. Total number of modes equals the number of degrees of freedoms of the element.

The kinematic relationship between the generalized modes and the nodal displacement vector is established by inserting the appropriate nodal coordinates into the displacement field defined by Eq.[1]:

$$\mathbf{v} = \mathbf{G}_{rc}\mathbf{q}_{rc} + \mathbf{G}_h\mathbf{q}_h. \quad [2]$$

It is necessary that all nodal values of the generalized pat-

terns are linearly independent such that Eq.[2] may be inverted:

$$\mathbf{q} = \begin{bmatrix} \mathbf{q}_{rc} \\ \mathbf{q}_h \end{bmatrix} = \begin{bmatrix} \mathbf{H}_{rc} \\ \mathbf{H}_h \end{bmatrix} \mathbf{v}. \quad [3]$$

A choice of functions that leads to linear dependency in \mathbf{G} does not necessarily imply that the 'problem' function has to be discarded. Such a case may be handled by augmenting the problem function with an additional function that restores the regularity of \mathbf{G} .

In order to satisfy the patch test, a special form of the strain-displacement matrix \mathbf{B}_u is applied, Ref.[3]:

$$\epsilon = \frac{1}{V}\mathbf{L}^T\mathbf{v} + \Delta\mathbf{N}_{qh}\mathbf{q}_h = \left(\frac{1}{V}\mathbf{L}^T + \mathbf{B}_{qh}\right)\mathbf{v} = \mathbf{B}_u\mathbf{v}, \quad [4]$$

where \mathbf{L} represents a weighting function which is calculated by evaluating the surface integral Ref.[3]:

$$\mathbf{L} = \int_A \mathbf{N}_u^T \bar{\mathbf{n}} dA. \quad [5]$$

\mathbf{N}_u interpolates the nodal displacements on the boundary and the $\bar{\mathbf{n}}$ matrix is constructed from the components of the outward unit surface normal, however the specific form of this matrix depends on the type of problem in question. By this procedure, the strain fields are separated such that the constant strain fields and thus the associated stresses are derived from continuous displacement fields, while the higher order strains and stresses are derived from the more versatile generalized displacement fields. This procedure allows for a great freedom in choosing displacement functions.

To ensure that the patch test is fulfilled, the higher order displacement functions contained in \mathbf{N}_{qh} should be modified such that they do not contribute to the mean level of the strain fields, i.e.:

$$\int_V \Delta\mathbf{N}_{qh} dV = \int_V \mathbf{B}_{qh} dV = 0. \quad [6]$$

If the requirement of Eq.[6] is fulfilled, the h - modes are said to be energy orthogonal to the rc - modes, Refs.[1] and [3]. It should be noted that this requirements does not put any restrictions on the choice of displacement modes. Nygård, Ref.[3], has proposed a scheme for how to modify an arbitrary displacement function such that this energy orthogonality requirement is satisfied.

Letting the constitutive matrix be denoted C , the stiffness matrix is easily established by use of the standard displacement formulation:

$$\mathbf{k} = \int_V \mathbf{B}_d^T \mathbf{C} \mathbf{B}_d dV$$

$$= \frac{1}{V} \mathbf{LCL}^T + \mathbf{H}_h^T \int_V \mathbf{B}_{qh}^T \mathbf{C} \mathbf{B}_{qh} dV \mathbf{H}_h \quad [7]$$

After solving the assembled system of equations with respect to the unknown nodal displacements, the stresses are retrieved by multiplying the strains of Eq.[4] by C . This formulation has been extended to apply to both material and geometric nonlinearities, Refs.[3] and [4]. However, it is considered outside the scope of this paper to discuss these parts of the theory.

2. TWENTY NODED SANDWICH ELEMENT

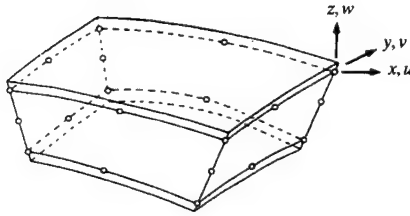


Figure 1. Sandwich element.

A uniform displacement formulation in the three directions requires a 20-term polynomial expansion. As for isoparametric elements the following set of functions may be used:

$$1, x, y, z, x^2, xy, y^2, yz, z^2, zx, x^2y, xy^2, y^2z, yz^2, z^2x, xz^2, xyz, x^2yz, xy^2z, xyz^2 \quad [8]$$

The four first terms represent N_{qrc} , while the rest of the polynomial terms make up N_{qth} .

As opposed to traditional shell theories and most thin and 'thick' shell elements, this solid formulation represents a higher order description of thickness effects, among which non-zero transverse stress and non-uniform shear are the most significant. Another aspect by these terms is that the same interpolation is used for the in-plane directions x and y as for the thickness direction z . The main consideration for the in-plane direction is that that the expansion should provide a good description of membrane and bending behavior while shear deformation is most important for the thickness direction.

For the speed of convergence, it would obviously be beneficial for a 20 noded solid element to include the modes x^3 , y^3 and z^3 , and thus describe a complete polynomial of third order. Unfortunately, this set of functions produces a singular G matrix and they can, for this reason, not be used directly. Having this in mind, an alternative expansion may be used, replacing the three last functions in Eq.[8] with the augmented polynomial terms

$$\epsilon x^2y + (1 - \epsilon)x^3, \epsilon xy^2 + (1 - \epsilon)y^3, \epsilon xyz + (1 - \epsilon)z^3 \quad [9]$$

where the weighing parameter ϵ is small compared to unity. Tests show that the formulation is insensitive to the choice of ϵ ; the value 0.01 has been used in the present study. The idea behind this modification of the displacement modes is that, for a small value of ϵ , the functions x^3 , y^3 and z^3 will dominate the solution while the small contributions from the fourth order terms will restore the regularity of the G matrix. The coordinates are made nondimensional such that the formulation retains objectivity. It is also important to note that the above terms allow for a near exact modeling of linearly varying bending moments.

Note that the outer nodes of the 20 node sandwich element shown in Figure 1 are located at the intersection between the core and the surface skins. This is done because of the convenience of having the nodes at this critical location when studying shearing forces and delamination. Full compatibility between surface skins of adjacent elements is still maintained. Note also that the volumes of the skins are parts of the total sandwich volume, and the numerical integration extends into the skins.

The total bending stiffness of one skin layer is the sum of the stiffness associated with bending about the neutral axis of the total sandwich and the stiffness associated with bending about the skins own neutral axis. For a skin section of unit width the total bending stiffness is given by:

$$D = E_f t d_1^2 + \frac{t^3}{12} \quad [10]$$

where E_f is Young's modulus of the skin material, t is the thickness of the skin layer and d_1 is the distance between the mid-plane of the skin layer and that of the total sandwich shell. Normally the first term in Eq.[10] will dominate, but the second term is not always negligible. Only one-point integration is used in the thickness direction of the skins, and a correct moment contribution from the skins is ensured by using an appropriate off-set from the skins mid-planes for the integration points. This off-set can be described by the parameter a which is given by the following relation:

$$E_f (a d_1)^2 t = E_f t d_1^2 + \frac{t^3}{12} \quad [11]$$

Solving for a gives:

$$a^2 = 1 + \frac{1}{12} \left(\frac{t}{d_1} \right)^2 \quad [12]$$

Normally three integration points are used through the core thickness and three by three integration points are used in the shell plane.

The present sandwich element has several advantages

- The midside nodes allows for modeling curved geometries and, hence, a wide range of shapes found in practical structural members, from simple flat plates with cut-outs to more complex cross-sections like air foils.
- The element is developed by separate consideration of each of the three layers, allowing for any arbitrary anisotropic, linear or nonlinear material property of each layer.
- Due to the three nodes through the thickness, the two skin layers are not required to undergo the same out-of-plane displacement and the element allows for warping of the shell cross-section.
- The high order displacement functions make this

sandwich element well suited for analysis of damaged parts and for representing special edge effects.

The initial stiffness matrices for each layer are calculated individually by way of Eq.[7]. The contributions from the two skins and the core are subsequently assembled to establish the total stiffness matrix for the sandwich element. The surface layers are normally much thinner than the core layer, and it is primarily the three in-plane stress components that contribute to the strain energy of these skins. These three strain components are extracted from the full six component strain tensor by applying the appropriate transformation matrix to the B_u - matrix. In the core layer, all six strain components are included in the expression for the strain energy.

In order to solve nonlinear problems, the linearized incremental form of the equilibrium equations and the nonlinear force balance equation are established. The tangential stiffness matrix is then established by using the nonlinear expressions for the Green strain tensor and their energy conjugate stresses represented by the second Piola-Kirchhoff stress tensor. The reader is referred to Ref.[4] for the derivation of the nonlinear tangential stiffness matrix and a detailed discussion of different aspects of applying the free formulation theory to nonlinear problems.

For calculation of the element mass matrix, a lumping technique proposed by Zienkiewicz, Ref.[8], is adopted: The diagonal terms of the consistent mass matrix are calculated and subsequently scaled by a factor which ensures that the sum of the diagonal terms equals the total mass of the element.

3. NUMERICAL EXAMPLES

3.1 Shear loaded cantilever beam

The simple case of a shear loaded cantilever beam is chosen to illustrate the sandwich element's ability to represent the basic modes of deflection and shear deformation of a beam or plate. This example is also used to clarify the effects of the augmented higher order displacement modes and the offset of integration points of the skin layers. The beam is modeled by a single element as shown in Figure 2.

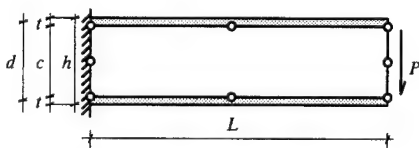


Figure 2. One element model of cantilevered sandwich beam

The beam has a fixed total height h , while the thickness t of the two surface skins vary from 0.1 to 45 per cent of the total height. This variation of skin thickness represents cases from extremely thin to unrealistically thick skins. The beam has a length to height ratio of 5, and a ratio of elastic modulus for skin and core materials equal to 100. The Poisson's ratio for both materials is taken equal to zero.

The finite element results are scaled by an analytical solution given in Ref.[5]:

$$w_{tip} = \frac{PL^3}{3D} + \frac{PL}{S} \quad [13]$$

The bending stiffness D and the shear stiffness S of the sandwich beam are:

$$D = E_f \frac{btd^2}{2} + E_f \frac{bt^3}{6} + E_c \frac{bc^3}{12} \quad [14]$$

$$S = G_c bc \left(1 + \frac{2t}{c} + \left(\frac{t}{c} \right)^2 \right) \quad [15]$$

E_c and G_c are Young's modulus and shear modulus of the core material, respectively. b is the width of the beam while d is the distance between the mid-planes of the two skins and c is the thickness of the core material.

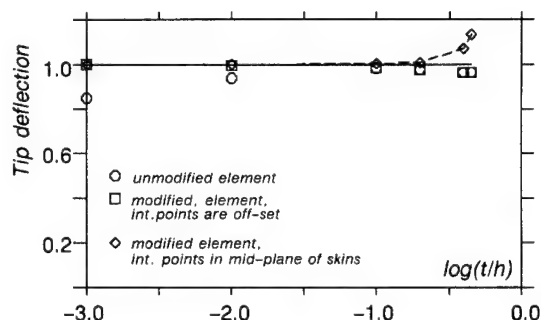


Figure 3. Tip deflection, cantilevered sandwich beam.

The results of the numerical study are given in Figure 3. The problem is designed to assess the performance of the element when subjected to deformation modes ranging from dominantly bending behavior on the left hand side of diagram where the bending contribution is about 97 percent to dominantly shearing deformation behavior on the right hand side of diagram where the bending contribution is at its lowest approximately 40 percent.

The so-called 'unmodified element' plotted in Figure 3 is based on the twenty polynomial terms of Eq.[8], while the 'modified element' uses the higher order functions of Eq.[9]. The plots of Figure 3 show that the unmodified element does not reproduce the deformation modes very well for thin skin cases, while the modified element gives excellent accuracy for the whole range of sandwich configurations. The improved performance is due to the inclusion of the corrective terms of Eq.[9] which enables the element to model a nearly exact linear variation of moment.

The diamond markers show the finite element solution when the integration points are situated in the mid-plane of the skins, while the dotted line represents the corresponding analytical solution, i.e. the second term in the expression for the beam's bending stiffness, Eq.[14], is omitted. It is clearly seen that the off-set of these integration points is indeed an appropriate remedy to this problem.

The axial and shear stress distributions over the height and along the beam axis are plotted in Figure 4 for the case of $t/h = 0.1$. The solid lines represent the analytical solution while the markers show the element stresses at the integration points. It is seen that one element is sufficient to reproduce to a high accuracy the stress distribution both over the cross section and along the length of the beam.

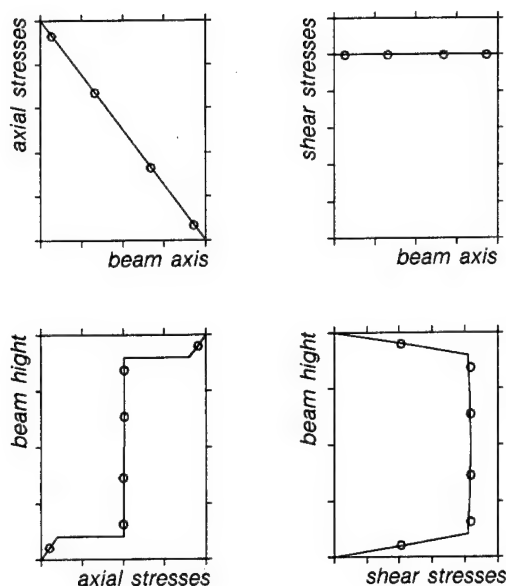


Figure 4. Scaled stress distribution, cantilever beam.

It should be noted that Allen, Ref.[5], has presented a more elaborate solution to this problem. A second order differential equation in terms of the shear force carried by the core is established and solved. For this solution one can specify as a boundary condition that the skin layers shall not rotate at the fixed end. As a consequence of this, the skins will sustain concentrated curvatures close to the fixed end, but the tip deflection will according to this theory differ significantly from the solution presented above only for very thick faces.

3.2 Instability of a sandwich column

The next example considers the problem of instability of sandwich beams. An axially loaded elastic column will buckle at a load level referred to as the Euler load if only overall bending deformation is included in the analysis. This Euler-type buckling mode is illustrated at the left hand side of Figure 5. In the case of a sandwich column, the core will allow for significant shear deformations. Such deformations reduce the overall stiffness and the critical load correspondingly becomes less than the Euler load. This reduction effect increases as the buckling wave length decreases, and an extremely short sandwich column will buckle in the mode shown in the middle of Figure 5 and sometimes denoted shear crimping. Note that shear deformations are not associated with transverse shear, but rather the core materials adoption to that the skins buckle as 'separate' columns. The skin layers buckle at a load level given by the sum of their individual Euler load, and shear deformations are dominant in the core layer. In addition to these failure modes, the compressed skins of a sandwich member may be subjected to a particular kind of instability. This type of skin buckling is usually described as wrinkling. The wavelength of the buckles is of the same order as the overall thickness of the beam, see right hand side of Figure 5. It should be noted that, according to the theoretical solution, the mid-plane of the core in this case remain flat. It is evident from this illustration that the out-of-plane stresses in the core layer are both significant and highly nonlinear when the panel undergoes such deformations.

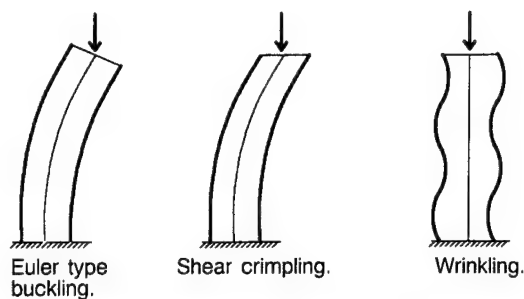


Figure 5. Buckling modes for a sandwich column.

Williams, Legget and Hopkins, Ref.[6], have presented an elaborate theory for wrinkling analysis which includes overall Euler-type instability and shear buckling as special cases. Both the outline of the theory and the resulting formula for the critical load is too lengthy to present here.

An axially compressed sandwich column is modeled by four elements in the axial direction and one element through the thickness as shown in Figure 6. The ratio between the skin thickness and the total height of the beam is 0.01, while the Young's modulus of the material used in the skins are 1000 times that of the core material. The column's critical load is computed via a linearized buckling algorithm which is implemented in the FENRIS program, Ref.[7].

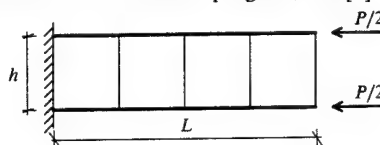


Figure 6. Column model, four elements.

Figure 7 shows the buckling load versus column length for the three types of buckling in a double logarithmic scale. The straight line to the right represents critical axial stress in the faces assuming that the member buckles in accordance with the Euler-type mode. The straight line to the left corresponds to pure shear buckling. The curved graph is obtained by evaluating the formula given in Ref.[6]. When the column is very long, overall bending deformations dominate. This is illustrated by the convergence of the curve representing the Euler load and the solution given in Ref.[6]. Shear deformations dominate when the column is very short. This is shown by the convergence between the curve according to the shear crimping mode and the solution which includes the wrinkling mode. If the column length is such that it falls within the wrinkling zone indicated in the figure, the column will, according to the theory, wrinkle at a lower load and in a shorter wave length, both given by the minimum point of the curve. The formula given by Williams, Legget and Hopkins therefore describes the complete buckling behavior of a sandwich column, including the case of wrinkling.

The computed critical stress versus the computed critical length is illustrated in Figure 7 by the markers. For long columns which will buckle according to Euler's theory, the results show good agreement with the analytical solution. Also the three models which are such that they fall within the wrinkling zone shows good agreement between critical stress and critical wave length. However two of these models are too coarse to correctly represent the short wrinkles predicted by the theory. In the case where the model is adjusted to cover two whole buckled wave lengths by four ele-

ments, the finite element solution is calculated to be within five percent of the analytical solution.

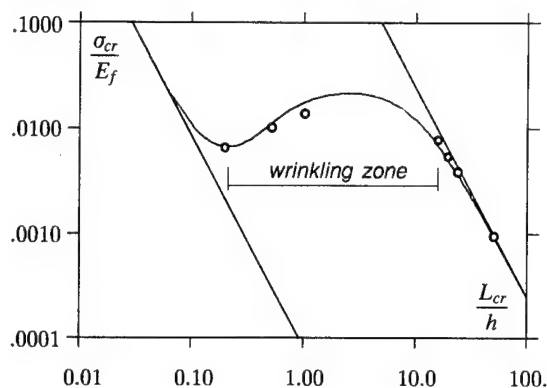


Figure 7. Critical stress versus wrinkling length for a sandwich column.

A lesson from this study is that there should be a sufficient number of elements to be able to represent a wrinkling mode and the corresponding wrinkling load. On the other hand, even a very coarse model is capable to predict the pure Euler load. In the case of wrinkling, it should be noted that the critical stress is not very sensitive to the assumed buckled wave length. This means that even if the finite element model is too coarse to correctly describe correctly the wrinkled waves, the computed critical stress itself will come out within a reasonable range of the analytically computed wrinkling stress. Typically for the sandwich configuration investigated in this example, the critical stress will increase by approximately ten percent if the assumed buckled wave length is twice the correct one.

Figure 8 shows the wrinkling mode for the finite element model in the case $L_{cr}/h = 0.2$, where the short waves are easily recognized. It is also seen that the mid-plane only sustains small deflections, which is in accordance with the wrinkling theory. The theoretical buckling half wave length is indicated in the figure and it is seen that the buckling mode of the finite element model corresponds well with this.

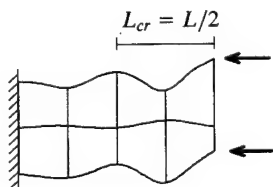


Figure 8. Computed wrinkling mode.

3.3 Nonlinear response

The nonlinear response of the element is investigated by studying the large displacement behavior of a long and slender sandwich beam which is pinned at both ends. The length to beam thickness ratio is 100, while the height of the beam is 100 times the thickness of each of the skins and the ratio between Young's modulus for the two materials is 50. The nonlinearity originates from overall axial tension due to the fact that both ends are restricted from moving horizontally.

As it is seen from Figure 9 the ends of the beam are pinned

in its mid-plane; that is in the soft core material. To avoid unwanted local distortion effects at these locations, vertical end stiffeners has been added to the model. As these do not affect the overall behavior of the beam they are not shown in the figure.

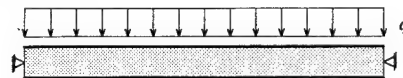


Figure 9. Pinned beam subjected to uniformly distributed load.

Timoshenko, Ref.[9], has presented an analytical solution to this problem. This solution has been evaluated at the mid point of the beam and compared to the numerical results plotted in Figure 10.

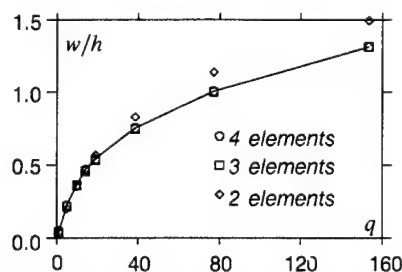


Figure 10. Mid-point deflection of sandwich beam.

At the maximum load level the mid-point deflection of the beam amounts to 131 per cent of the beam's height, and it is seen that the tangential stiffness has increased significantly compared to the initial stiffness. The model using two elements along the beam axis deviates from the analytical solution. However, by adding one more element to the model, the results are seen to be very good. At the first load increment the computed deflection of the three element model is 81.2 per cent of the analytical solution, while as for the last increment the deflection calculated with this model equals the analytical solution to the third significant digit. The initial stiffness for the four element model is 96.4 per cent of the analytical solution and the computed deflection for this model has after six load increments converged to the analytical solution within three significant digits.

3.4 Dynamic analysis

The dynamic behavior of the element is studied by calculating the three first eigenfrequencies for the simply supported beam of the previous example. Assuming that the n 'th eigenmode is described by n half sine-waves, the corresponding eigenfrequencies are given by:

$$\omega_n^2 = \left(\frac{n\pi}{l}\right)^4 \frac{D}{m} \quad [16]$$

where m is the beam's mass per unit length. The eigenfrequencies are calculated both by using the unmodified displacement functions of Eq.[8], $\epsilon = 1.0$, and by the use of augmented functions, Eq.[9], $\epsilon = 0.01$. Figure 11 shows graphically the convergence of the three first eigenfrequencies of this model. It is seen that the results are improved radically when the modified displacement modes are used.

These results also imply that the present free formulation element is substantially more accurate than the traditional 20 node isoparametric element.

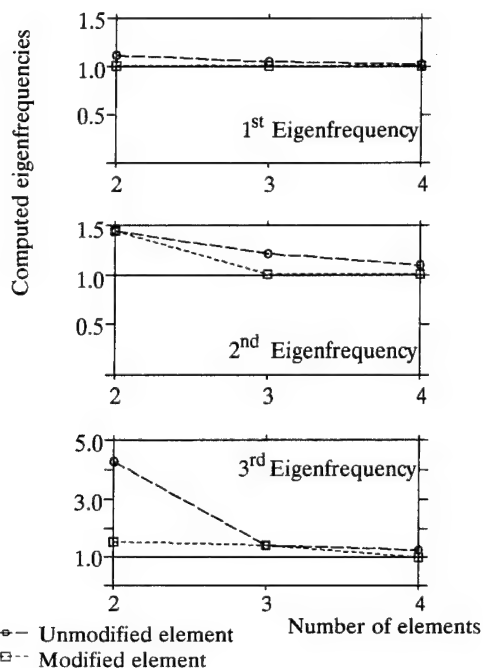


Figure 11. Eigenfrequencies of pinned sandwich beam.

Another important aspect with this and the previous examples is that they show that the chosen element formulation is not sensitive to high side aspect ratios.

4. CONCLUSION

It may be concluded from the present and supplementary test examples that the proposed sandwich element gives excellent results for displacements as well as stresses. In particular the use of the modified, nonconforming higher order modes improves the behavior significantly. In this context it is of decisive importance that the element is formulated in the context of the free formulation theory which ensures convergence even when nonconforming displacement functions are employed. It is also verified that the local bending stiffness of the skin layers can be included by an appropriate off-set of the integration points in these layers. The element seems also capable of representing very well the localized wrinkling mode and the corresponding critical load. The large displacement behavior and dynamic behavior have been confirmed to be very good.

5. REFERENCES

1. Bergan, P.G.: Finite Elements Based on Energy Orthogonal Function, *Int. J. for Numerical Methods in Engineering*, Vol. 15, pp. 1541-1555, (1980).
2. Bergan, P.G. and Nygård, M.K.: Finite Elements with Increased Freedom in Choosing Shape Function, *Int. J. for Numerical Methods in Engineering*, Vol. 20, pp: 643-664, (1984).
3. Nygård, M.K.: *The Free Formulation for Nonlinear Finite Elements with Application to Shells*, Dr. ing. thesis, Division of Structural Mechanics, The Norwegian Institute of Technology, Trondheim, (1986).
4. Bergan, P.G., and Nygård, M.K.: Nonlinear Shell Analysis Using Free Formulation Finite Elements, in P.G. Bergan, K.J. Bathe and W. Wunderlich (eds.), *Finite Element Methods for Nonlinear Problems*, Springer Verlag, (1985).
5. Allen, H.G.: *Analysis and Design of Structural Sandwich Panels*, Pergamon Press, Oxford, (1969).
6. Williams, D., Legget, D.M.A. and Hopkins, H.G.: *Flat Sandwich Panels under Compressive End Loads*, A.R.C., R & M 1987, (1941).
7. Bergan, P.G., Nygård, M.K. and Bjærum, R.O.: Nonlinear Collapse Simulation of Anisotropic and Corrugated Plates and Shells, *Spacecraft Structures and Mechanical Testing Conference*, ESA SP-289, ESTEC, (1988).
8. Zienkiewicz, O.C.: *The Finite Element Method*, 3rd edition, McGraw-Hill, (1977).
9. Timoshenko, S. and Woinowsky-Krieger, S.: *Theory of Plates and Shells*, International student edition, 2nd edition, McGraw-Hill, (1959).

N92-23803

INFLUENCE OF THE SUBSTRATE ON THE SOLAR CELLS INTERCONNECTOR: STRESS DISTRIBUTION AND FATIGUE LIFE PREDICTION

S. Tizzi, M. Marchetti, S. La Terza

Dipartimento Aerospaziale - Università di Roma "La Sapienza"

ABSTRACT

The purpose of this study is the analysis of the influence of the composite materials substrate on the stresses distribution in the solar array components: solar cell, adhesive, substrate and interconnector. At last a fatigue study for the life prediction of the interconnector, in low and geostationary orbits, and a further study on the substrate composite materials strength have been performed.

1. INTRODUCTION

The analysis has been conducted on the basis of theoretical mathematical models only.

Stress distribution in the components of the solar array arises mainly from their different thermoelastic properties in thermal variations environment during orbital missions.

A previous study (Ref. 1) of the substrate sandwich structure behaviour with the skins in Aluminium material has been already performed, while the same behaviour has been here analyzed in the case of ortotropic constituting material of the skins. The composite lamina of the skin is formed by carbon-fibres reinforced plastic (CFRP) and by a core in Aluminium honeycomb alloy.

A mathematical model concerning the substrate behaviour has been here introduced, taking into account the ortotropic feature of the composite constituting material; in this case it has been necessary to build and develop a bidimensional stress and strain numerical model. The interconnector constituting equations are reported in Ref. 1, with some variations which allow more accurate computations.

The other utilized materials are Molybdenum for the interconnector and Gallium Arsenide for the solar cells (Ref. 2-3-4).

2. THE CELL-SUBSTRATE CONSTITUTING EQUATIONS

The cell-substrate complex is reported in Fig. 1 with the main components:

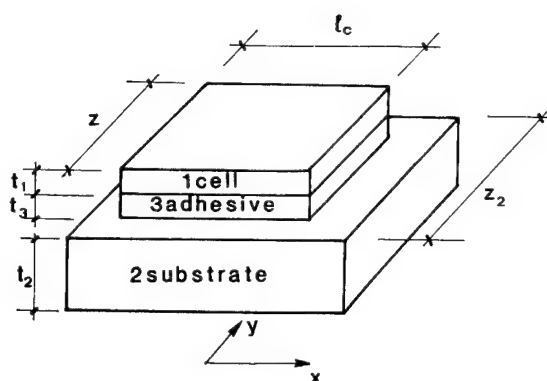


Figure 1. The main components of the cell-substrate whole structure.

By the composite laminates theory (Ref. 6) a study of the mechanical properties of the substrate has been performed. The laminate structure is such that its main mechanical properties are nearly similar to both symmetric and antisymmetric laminates, that is there is uncoupling between in-plane and out-of-plane behaviour and nearly orthotropy in the main axes plane.

The equilibrium equations for both the cell and the substrate along the x,y directions are respectively:

$$\left\{ \begin{array}{l} t_1 \frac{d\sigma_{1x}}{dx} + \tau_{xz} = 0, \\ t_1 \frac{d\sigma_{1y}}{dy} + \tau_{yz} = 0, \\ t_2 r_2 \frac{d\sigma_{2x}}{dx} - \tau_{xz} = 0, \\ t_2 r_2 \frac{d\sigma_{2y}}{dy} - \tau_{yz} = 0, \end{array} \right. \quad (1)$$

where $r_2 = z_2/z$. Considering a ΔT temperature variation it is possible to write the thermoelasticity relations:

$$\begin{cases} \frac{dv_{1x}}{dx} = \frac{\sigma_{1x}}{E_1} - v_1 \frac{\sigma_{1y}}{E_1} + \alpha_1 \Delta T, \\ \frac{dv_{1y}}{dy} = \frac{\sigma_{1y}}{E_1} - v_1 \frac{\sigma_{1x}}{E_1} + \alpha_1 \Delta T, \\ \frac{dv_{2x}}{dx} = \frac{\sigma_{2x}}{E_{2x}} - v_{2yx} \frac{\sigma_{2y}}{E_{2y}} + \alpha_{2x} \Delta T, \\ \frac{dv_{2y}}{dy} = \frac{\sigma_{2y}}{E_{2y}} - v_{2xy} \frac{\sigma_{2x}}{E_{2x}} + \alpha_{2y} \Delta T, \end{cases} \quad (2)$$

where E_{2x}, E_{2y} are the Young's moduli average values of the substrate; v_{2xy} and v_{2yx} are the mixed Poisson's moduli average values and α_{2x}, α_{2y} the average values of the thermal expansion coefficients. The adhesive equations are:

$$\begin{cases} \tau_{xz} = \frac{G}{t_3} (v_{2x} - v_{1x}) \\ \tau_{yz} = \frac{G}{t_3} (v_{2y} - v_{1y}) \end{cases} \quad (3)$$

By introducing the parameters:

$$\begin{aligned} A_x &= \frac{G}{t_1 t_3} \left(\frac{1}{E_{2x}} k - \frac{1}{E_1} \right) & A_{xy} &= \frac{G}{t_1 t_3} \left(\frac{v_1}{E_1} + \frac{v_{2yx}}{E_{2y}} k \right) \\ A_y &= \frac{G}{t_1 t_3} \left(\frac{1}{E_{2y}} k - \frac{1}{E_1} \right) & B_x &= \frac{G}{t_1 t_3} (\alpha_{2x} - \alpha_1) \Delta T \\ B_y &= \frac{G}{t_1 t_3} (\alpha_{2y} - \alpha_1) \Delta T \end{aligned}$$

and taking into account the system (1) it is possible to obtain:

$$\begin{cases} \frac{d^2 \sigma_{1x}}{dx^2} + A_x \sigma_{1x} + A_{xy} \sigma_{1y} + B_x = 0, \\ \frac{d^2 \sigma_{1y}}{dy^2} + A_y \sigma_{1y} + A_{xy} \sigma_{1x} + B_y = 0. \end{cases} \quad (4)$$

The general solution can be searched in the form (Ref. 5):

$$\begin{cases} \sigma_{1x} = R_x [1 - \cos h(\alpha x) \cos h(\beta y)] + S_x, \\ \sigma_{1y} = R_y [1 - \cos h(\alpha x) \cos h(\beta y)] + S_y. \end{cases} \quad (5)$$

The boundary conditions, taking into account the average value of the normal stress σ_{1x} and σ_{1y} , are:

$$\begin{cases} (\bar{\sigma}_{1x})_{x=l_c/2} = 0 \\ (\bar{\sigma}_{1y})_{y=l_c/2} = 0 \end{cases} \quad (6)$$

From the first of (2) integrated we obtain:

$$\begin{aligned} (\bar{v}_{1x})_{x=l_c/2} = -\alpha_{2x} \Delta T \frac{1}{2} - \alpha_1 \Delta T x_{11} - \frac{t_1 t_3}{G_3} R_x \alpha \bar{C}_x \sinh\left(\alpha \frac{l_c}{2}\right) + \\ - \frac{x_{11}}{E_1} [R_x + S_x - v_1 (R_y + S_y)] + \frac{\bar{C}_y}{E_1} \frac{R_x - v_1 R_y}{\alpha} \cdot \\ \cdot \left[\sinh\left(\alpha \frac{l_c}{2}\right) - \sinh\left(\alpha \frac{l_c}{2} - \alpha x_{11}\right) \right] \end{aligned} \quad (7)$$

where:

$$\begin{aligned} \bar{C}_x &= \frac{1}{l_c} \int_{-l_c/2}^{l_c/2} \cos h(\alpha x) dx, \\ \bar{C}_y &= \frac{1}{l_c} \int_{-l_c/2}^{l_c/2} \cos h(\beta y) dy. \end{aligned}$$

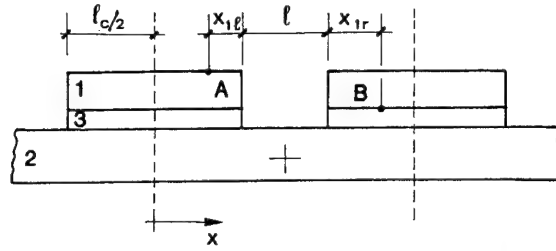


Figure 2. Contact elements between cell and interconnector.

From Fig. 2 it is possible to point out that the distance variation between the interconnector and cells welded contact points is equal to:

$$(\Delta v_{1x})_T = (v_{1x})_{x=l_c/2+x_{1r}} - (v_{1x})_{x=l_c/2-x_{1l}} \quad (8)$$

3. INFLUENCE OF THE INTERCONNECTOR ON THE CELLS DISPLACEMENT

The variation of the inter-cells gap depends also on the reaction of the interconnector at the welded contact points with the cells surface.

It means that there is another contribute to the distance between adjacent cells, which has to be calculated.

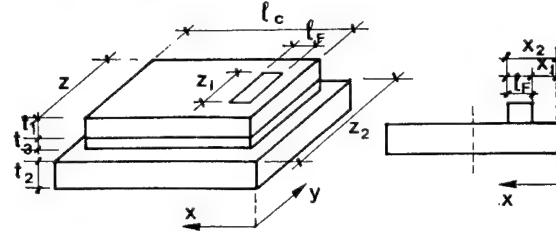


Figure 3. The contact zone between cells and interconnector.

The elasticity constitutive equations can be written in the form:

$$\begin{cases} \sigma_{1x} = \frac{E_1}{1-v_1^2} \frac{dv_{1x}}{dx} \\ \sigma_{2x} = \frac{E_2}{1-v_{2xy}v_{2yx}} \frac{dv_{2x}}{dx} \\ \tau_{xz} = \frac{G}{t_3} (v_{2x} - v_{1x}) \end{cases} \quad (9)$$

because the temperature variation effects have been already considered in the previous model, and furthermore the cross strain along the y axis can be neglected because of the narrowness of the welded contact zone, as in Fig. 3.

The equilibrium equations along the x axis can be then written:

$$\begin{cases} t_1 \frac{d\sigma_{1x}}{dx} + \tau_{xz} + \tau_F S_r r_1 r_2 = 0 \\ t_2 r_2 \frac{d\sigma_{2x}}{dx} - \tau_{xz} = 0 \end{cases} \quad (10)$$

where:

$$r_1 = \frac{z_1}{z} \quad r_2 = \frac{z_2}{z}$$

and S_n is a function which vanishes in every point but the interval $x_1 \leq x \leq x_2$ where its value is unitary.

The boundary conditions are:

$$\begin{cases} \sigma_{1x}(0) = 0 \\ \sigma_{2x}(0) = \frac{\tau_F l_F r_1}{t_2} \end{cases} \quad (11)$$

where $F = \tau_F l_F r_1$ is the resulting applied force at the contact zone between cell and interconnector.

In the interval $0 \leq x \leq x_1$, the expression of the $\sigma_1(x)$ stress can be found:

$$\sigma_1(x) = F \frac{k_2}{k_1} \sinh(2\beta x) - \frac{\tau_F l_F n r}{t_2 \left(1 + \frac{m n \rho}{r_2}\right)} [\cosh(2\beta x) - 1] \quad (12)$$

where:

$$m = t_1/t_2 \quad n = E_1/E_2 \quad \rho = (1 - v_{2xy} v_{2yx}) / (1 - v_1^2)$$

$$4\beta^2 = \frac{G}{t_1 t_2} \frac{1 - v_1^2}{E_1} \left(1 + \frac{m n \rho}{r_2}\right)$$

$$k_1 = \tan h(2\beta x_1) + \tan h(2\beta l_F)$$

$$k_2 = n \frac{1 + \tan h(2\beta x_1) \tan h(2\beta l_F)}{z_2 t_2 \left(1 + \frac{m n \rho}{r_2}\right)} + \frac{\tan h(2\beta l_F)}{2\beta t_1 z_1 \left(1 + \frac{m n \rho}{r_2}\right) \cosh(2\beta x_1)}$$

From the first of (9) we obtain:

$$v_{1x}(x_1) = K_3 F \quad (13)$$

where:

$$K_3 = \frac{(1 - v_{2xy} v_{2yx}) l}{2 t_2 z_2 E_2} + \frac{2 \beta t_1 t_3 k_2}{G k_1} + (1 - v_1) \frac{k_2 [\cosh(2\beta x_1) - 1]}{2 \beta E_1 k_1} + \frac{(1 - v_1^2) \sin h(2\beta x_1)}{2 \beta t_2 E_2 z_2 \left(1 + \frac{m n \rho}{r_2}\right)} + \frac{(1 - v_1^2) x_1}{t_2 E_2 z_2 \left(1 + \frac{m n \rho}{r_2}\right)}$$

There is a corresponding displacement of the right cell so that the distance variation between welded contact points of adjacent cells, due to the applied force F , is equal to

$$(\Delta v_{1x})_F = (K_{31} + K_{3r}) F \quad (14)$$

because both contributes of the cells, on the left and on the right (corresponding to K_{31} and K_{3r}), have to be taken into account and their effects must be added.

The displacement due to the temperature variation has been yet found as in (8), so that the total distance variation between welded points is equal to:

$$\Delta v_{1x} = (\Delta \bar{v}_{1x})_T + (K_{31} + K_{3r}) F \quad (15)$$

4. DETERMINATION OF THE STRESS DISTRIBUTION IN THE INTERCONNECTOR

In Fig. 4 the out-of-plane relief loop of the interconnector is shown:

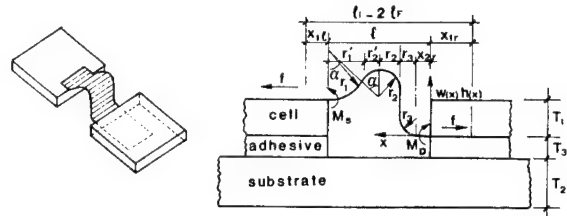


Figure 4. The out-of-plane interconnector relief loop.

The interconnector elasticity constitutive equations are:

$$\begin{cases} F t_1 = M_D - M_S \\ -F[h(x) + w(x)] + M_D = EI \frac{d^2 w}{dx^2} \left[1 + \left(\frac{dh}{dx}\right)^2\right]^{3/2} \end{cases} \quad (16)$$

with the boundary conditions:

$$\begin{cases} M_D = \left[EI \frac{d^2 w}{dx^2}\right]_{x=0} \\ M_S = \left[EI \frac{d^2 w}{dx^2}\right]_{x=l} \end{cases} \quad (17)$$

The $w(x)$ bending displacement can be expressed in the series expansion:

$$w(x) = \sum_n a_n \left(1 - \cos \frac{n\pi x}{l}\right) + a_F \sin \frac{\pi x}{l} \sin \frac{2\pi x}{l} \quad (18)$$

It is possible to obtain the distance variation between the two ends of the interconnector, which is equal to:

$$\Delta \bar{v}_{1x} = - \sum_n a_n U_n - a_F U_F + K_3'' F + \alpha_i \Delta T l_i \quad (19)$$

where α_i and l_i are the thermal expansion coefficient of the interconnector material and the distance between the welded contact points of adjacent cells respectively. The coefficients K_3'' and U_n , U_F expressions are:

$$\begin{aligned} K_3'' &= \frac{1}{EA} \int_0^l \frac{1}{\cos \alpha(x)} dx \\ U_n &= \frac{n\pi}{l} \int_0^l \tan \alpha(x) \sin \frac{n\pi x}{l} dx \\ U_F &= \int_0^l \tan \alpha(x) \sin \frac{\pi x}{l} \sin \frac{2\pi x}{l} dx \end{aligned} \quad (20)$$

By (15) and (19) it is possible to obtain:

$$F = - \frac{T_N - \sum_n a_n U_n - a_F U_F}{K_3} \quad (21)$$

where:

$$K_3 = K_3' + K_3'' \quad T_N = -(\Delta \bar{v}_{1x})_T + \alpha_i \Delta T l_i \quad T_N' = T_N - \sum_n a_n U_n - a_F U_F$$

Such expression of the interconnector stretching force F can be substituted into the IInd equation of (4), then the Galérkin method can be utilized to obtain:

$$\begin{cases} \sum_n a_n \left[U_n \frac{H_m}{K_3} + EI P_{nm} \right] + \frac{T_N}{K_3} \frac{1}{2} a_m + \\ + a_F \left[\frac{H_m}{K_3} U_F - \frac{T_N}{K_3} F_{*m} + EI P_{*m} \right] = T_N \frac{H_m}{K_3} \\ \sum_n a_n \left[U_n \frac{H_0}{K_3} + EI (P_{n0} - 1) - \frac{T_N}{K_3} 1 \right] + \\ + a_F \left[\frac{H_0}{K_3} U_F - \frac{T_N}{K_3} F_{*0} + EI (P_{*0} - 1) \right] = T_N \frac{H}{K_3} \\ \sum_n a_n U_n a_F \left[U_F - 2EI \left(\frac{2\pi}{l} \right)^2 \right] = T_N \end{cases} \quad (22)$$

where the first reported equation corresponds to $m/2$ equations with $m = 2, 4, 6, \dots$, the second corresponds to the $(m/2 + 1)^{th}$ equation with $m = 0$, the third to the $(m/2 + 2)^{th}$ equation obtained by the imposed boundary conditions (17). The system (22) is nonlinear and it can be solved by an iterations method.

The report coefficients are:

$$\begin{aligned} H_m &= \int_0^1 h(x) \cos \frac{m\pi x}{l} dx \\ F_{*m} &= \int_0^1 \sin \frac{px}{l} \sin \frac{2\pi x}{l} \cos \frac{m\pi x}{l} dx \\ P_{*m} &= \left(\frac{\pi}{l} \right)^2 \int_0^1 \frac{4 \cos \frac{\pi x}{l} \cos \frac{2\pi x}{l} - 5 \sin \frac{\pi x}{l} \sin \frac{2\pi x}{l}}{\left[1 + \left(\frac{dh}{dx} \right)^2 \right]^{3/2}} \cos \frac{m\pi x}{l} dx \\ P_{nm} &= \left(\frac{n\pi}{l} \right)^2 \int_0^1 \frac{\cos \frac{n\pi x}{l} \cos \frac{m\pi x}{l}}{\left[1 + \left(\frac{dh}{dx} \right)^2 \right]^{3/2}} dx \end{aligned}$$

The same equations system can be written in matricial form:

$$[K] [X] = [Z] \quad (23)$$

where:

$$[X] = \begin{bmatrix} a_2 \\ a_4 \\ a_6 \\ \vdots \\ a_n \\ a_F \end{bmatrix} \quad (24)$$

and $[K]$ is the equations coefficients matrix and $[Z]$ is the external stress column vector.

It is then possible to calculate the displacements and the bending moments in the interconnector and consequently the stress distribution. It must be observed that the total acting stress in each point of the interconnector is equal to the sum of normal and bending contribute:

$$\sigma_T = \frac{F}{A} \cos \alpha(x) + \frac{M_t y}{I} \quad (25)$$

where M_t is the bending moment, I is the flexural inertia moment and y is the distance from the neutral axis.

5. STUDY OF THE FATIGUE LIFE OF THE INTERCONNECTOR MATERIAL

For a study of the interconnector material life in the space environment of low and geostationary orbits, the Manson curve and the consequent constituting relations (Ref. 1-7) have been utilized. In the same papers a prospect of the analytical operations utilized procedure is shown, which has been here utilized.

6. APPLICATIONS

For a study of the ortotropic material influence on the interconnector stresses, three different composite laminates, an U.D. (0°), an angle-ply (±45°)_s and a cross-ply (0°/90°)_s respectively, have been supposed, whose thermomechanical properties are reported in Tab. I.

Table I: Mechanical Properties of the Substrate Material.

	E_{2x} (GPa)	E_{2y} (GPa)	α_{2x} (°C ⁻¹)·10 ⁶	α_{2y} (°C ⁻¹)·10 ⁶	ν_{2xy}	G_{xy} (Gpa)
U.D.	8.77	0.57	-0.30	28.10	0.30	0.27
±45°/s	0.97	0.97	1.88	1.88	0.80	2.26
90/0°/s	4.69	4.69	1.88	1.88	0.04	0.27

The mechanical properties of the materials utilized for the cell and interconnector are given in Tab. II.

Table II: Mechanical Properties of Cells and Interconnector Materials.

	E (GPa)	α (°C ⁻¹)·10 ⁶
Ga As	85.3	6.86
Mo	320.0	5.80
Ag	71.3	19.68

The adhesive material shear strain rigidity modulus versus the temperature is shown in Tab. III.

Table III: Shear Strain Rigidity Modulus of the Adhesive.

G (GPa)	T (°C)
0.34	+100
0.35	-60
3.7	-140
340	-180

In all the considered cases the temperature range -180 °C + +100 °C was supposed.

7. RESULTS ANALYSIS

In Fig. 5 and Fig. 6 the behaviours of the stress inside the solar cell and the adhesive versus the distance from the cell center

for the three considered composite laminate cases ($T = -180^\circ\text{C}$) are reported.

In Fig. 7 the interconnector bending displacement versus the distance from a cell edge is shown for the angle-ply ($\pm 45^\circ$) case, for both $T = +100^\circ\text{C}$ and $T = -180^\circ\text{C}$; in this figure the geometry of the interconnector versus the distance from a cell edge is also given. In Fig. 8 a comparison of the obtained bending displacements in all the three considered composite laminate cases at both foreseen temperatures is shown.

In Fig. 9 the stress behaviour inside the interconnector versus the distance from a cell edge is presented for the angle-ply ($\pm 45^\circ$) laminate case, and at the two temperatures $T = +100^\circ\text{C}$ and $T = -180^\circ\text{C}$, together with the interconnector geometry. In Fig. 10 a comparison of the obtained stress behaviour in all the three composite laminate cases at $T = +100^\circ\text{C}$ is presented and in Fig. 11 at $T = -180^\circ\text{C}$.

In Fig. 12 the maximum stress behaviour inside the interconnector versus the curvature radius r_2 (see Fig. 4) and for three different values of the radius r_1 is given for $T = +100^\circ\text{C}$, while in Fig. 13 the same stress behaviour when $T = -180^\circ\text{C}$ is reported.

In Fig. 14 the stress behaviour versus the distance from a cell edge is shown in the case of interconnector in Silver for the angle-ply ($\pm 45^\circ$) laminate case at $T = +100^\circ\text{C}$ and $T = -180^\circ\text{C}$.

Now the interconnector material life has to be considered together with the obtained results by Manson method (Ref. 7). Let's look at Tab. IV:

Table IV: Fatigue Life of Interconnector Material.

	$(\pm 45^\circ)_L$	$(0^\circ/90^\circ)_L$	U.D. (0°)	$(\pm 45^\circ)_L(\text{Ag})$
N=50000 σ [MPa]	$\sigma_A = 210$ ($\sigma_M = 2.5$)	$\sigma_A = 266$ ($\sigma_M = 3.2$)	$\sigma_A = 481$ ($\sigma_M = 5.7$)	$\sigma_A = 90$ ($\sigma_M = 1.1$)
	$\sigma_{\max} = 523$ ($N = 4.3 \cdot 10^6$)	$\sigma_{\max} = 520$ ($N = 10^6$)	$\sigma_{\max} = 512$ ($N = 70100$)	$\sigma_{\max} = 120$ ($N = 250000$)
	$\sigma_A = 223$ ($\sigma_M = 2.6$)	$\sigma_A = 308$ ($\sigma_M = 3.6$)	$\sigma_A = 599$ ($\sigma_M = 7.1$)	$\sigma_A = 110$ ($\sigma_M = 1.3$)
	$\sigma_{\max} = 865$ ($N = 39900$)	$\sigma_{\max} = 861$ ($N = 13500$)	$\sigma_{\max} = 852$ ($N = 3700$)	$\sigma_{\max} = 500$ ($N = 96000$)
N=3650 σ [MPa]				

The first two rows refer to low orbits while the last two refer to geostationary orbits ($N = 50000$ is the number of cycles in 10 years for low orbits, while the corresponding number for geostationary orbits is $N = 3650$). In the first and the third rows the cyclic stress amplitude σ_A and the average stress value σ_M are reported for the different composite laminate cases (the last column refers to the interconnector in Silver, while the others refer to the interconnector in Molybdenum). In the second and the fourth rows the maximum allowable cyclic stress amplitude for a 10 years life is reported in the various composite laminate cases. It can be emphasized that the effec-

tive stress amplitude is always smaller than the corresponding maximum allowable amplitude for such a life period. In the same rows also the life maximum cycles number corresponding to the effective cyclic stress amplitude is reported. It means, considering the cycles number corresponding to low or geostationary orbit in 10 years, that the effective life could be much bigger than the requested one. For example, considering the interconnector in Silver in the angle-ply laminate case, the effective life in low orbit is 5 times the requested one, that is 50 years.

A further study of the substrate strength utilizing both the "Maximum Strain Criterion" (M.S.C.) and the "Quadratic Failure Criterion" (Q.F.C.) has been performed (Ref. 6). Such a study refers both to the laminate on the whole and to the single lamina. The ratio between the maximum allowed stress and the effective stress in the whole laminate and the single lamina are reported in Tab. V and Tab. VI respectively.

Table V: Obtained Results for the Single Lamina.

	$(\pm 45^\circ)_L$		$(0^\circ/90^\circ)_L$		U.D. (0°)	
	M.S.C.	Q.F.C.	M.S.C.	Q.F.C.	M.S.C.	Q.F.C.
$T = +100^\circ\text{C}$	1790	2200	1790	2200	3260	4000
$T = -180^\circ\text{C}$	109	71.7	104	68.1	221	145

Table VI: Obtained Results for the Whole Laminate.

	$(\pm 45^\circ)_L$		$(0^\circ/90^\circ)_L$		U.D. (0°)	
	M.S.C.	Q.F.C.	M.S.C.	Q.F.C.	M.S.C.	Q.F.C.
$T = +100^\circ\text{C}$	3110	3360	3110	3360	5650	6120
$T = -180^\circ\text{C}$	56.5	52	53.7	49.4	114	105

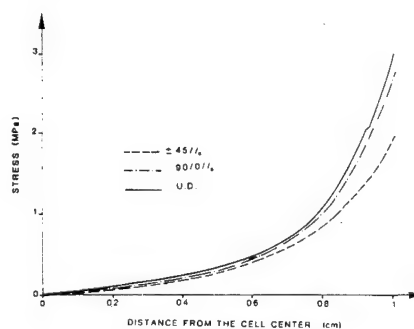


Fig. 5

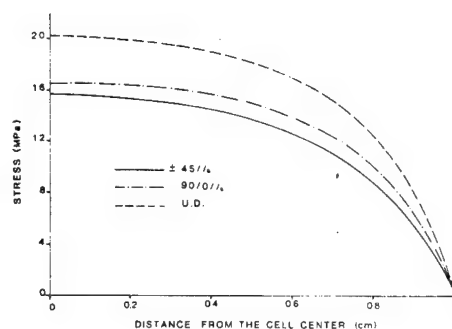


Fig. 6

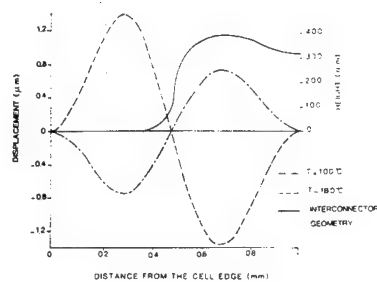


Fig. 7

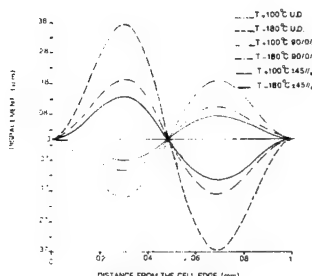


Fig. 8

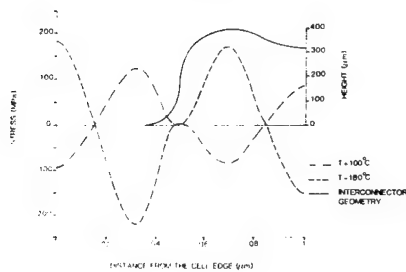


Fig. 9

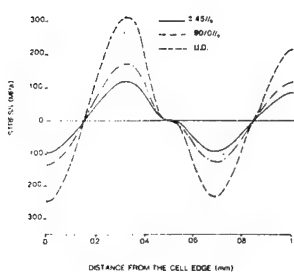


Fig. 10

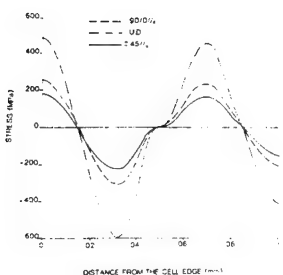


Fig. 11

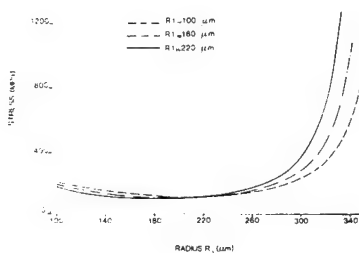


Fig. 12

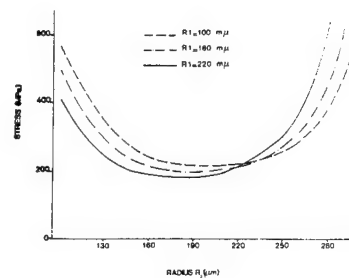


Fig. 13

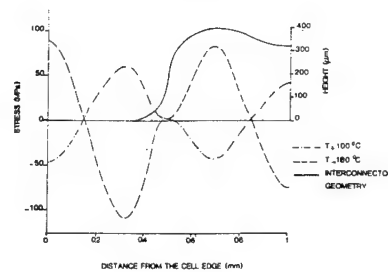


Fig. 14

8. CONCLUSIONS

From the obtained results the importance of the choice of the composite material constituting the substrate can be emphasized. The better substrate configuration is the angle-ply ($\pm 45^\circ$) laminate, because it allows to reduce the stress value inside the solar cell, the adhesive and the interconnector of about 6%, 29%, 26% respectively in the cross-laminate case ($0^\circ/90^\circ$), and of about 23%, 33%, 63% respectively in the U.D. (0°) laminate case.

Also the out-of-plane interconnector geometry becomes very important in the stress behaviour, and the best radii of curvature its loop configuration must be found for the interconnector project.

Thermal stresses, on the contrary, are not important for the substrate structure stability.

From the interconnector fatigue life obtained results it can be pointed out that the considered materials are very good for space missions in low and geostationary orbits.

REFERENCES

1. Capitanio R S, Marchetti M & Tizzi S 1989, Study of a Gallium Arsenide Solar Cell Interconnector, International Conference "Spacecraft Structures and Mechanical Testing", Noordwijk, The Netherlands - 24-26 April 1991 ESA SP-289, 351-357.
2. Crabb R L 1986, Approved NASA/ESA Atomic Oxygen Resistant Materials list, ESA, DOC.NO. LI-SA0003.
3. ESA, PSS-01-401 1985, Data for Selection of Space Materials, Product Assurance Division, Noordwijk, The Netherlands.
4. De Rooy A 1985, The degradation of Metal Surfaces by Atomic Oxygen, ESA-ESTEC, ESA SP-232, 99-108.
5. Santini P 1968, Matematica Applicata all'Ingegneria, ETAS COMPASS.
6. Stephen W Tsai 1980, Introduction to Composite Materials, TECHNOMIC Publishing Co., Inc - U.S.A.
7. Manson S S 1966, Fatigue a Complex Subject - Simple Approximation, NASA, Cleveland, Ohio.

ACKNOWLEDGEMENTS

Work carried in the frame of a FIAR (Milano) contract.

N92-23804

BUCKLING OF SIMPLY SUPPORTED AND CLAMPED ANISOTROPIC PLATES UNDER COMBINED LOADS

G. Romeo and G. Frulla

Politecnico di Torino, Dept. of Aerospace Eng., Turin, Italy

ABSTRACT

An analytical solution was developed for the buckling of laminated cylindrical plates under biaxial compression and shear loads. Linear equations for laminated cylindrical shells, Donnell-type equations, was used in conjunction with Galerkin's method to determine critical buckling loads. Several composite panels were tested under uniaxial compression or inplane shear load in order to verify the correlation between the above analysis and experimental results. Panels had several types of lay-up, balanced and symmetric as well as unbalanced and unsymmetric, and different boundary conditions. A good correlation between theoretical analysis and experimental results was obtained. A new test facility was built in order to apply contemporarily both biaxial compression and shear load.

Keywords: Composite, buckling, test facility.

2. BUCKLING ANALYSIS OF ANISOTROPIC PLATES

An analytical solution was developed for the buckling of anisotropic cylindrical plates under biaxial compression and shear loads. Linear equations for laminated cylindrical shells, Donnell-type equations, are used in conjunction with Galerkin's method to determine critical buckling loads. For many engineering applications of curved plates, the ratios of radius of curvature to plate thickness are often greater than 500; hence, Donnell's theory should provide sufficient accuracy. Furthermore, the ratio of inplane dimensions to thickness will be greater than 40; in such cases shear deformation will not be significant for practical laminate; thus, in a first stage, the shear deformation is not included in the buckling analysis. The plate thickness is denoted by h , the radius of curvature by R and the in plane dimensions by a and b ; the plate is composed of an arbitrary number of layers with arbitrary fibre orientation in each layer. Based on the Classical Lamination Theory, the following plate equations of equilibrium, in non-dimensional form, have been used:

$$L_{11}U + L_{12}V + L_{13}W = 0 \quad ; \quad L_{12}U + L_{22}V + L_{23}W = 0 \quad ; \quad (1)$$

$$L_{13}U + L_{23}V + L_{33}W = N_{\zeta}W_{,\zeta\zeta} + 2A N_{\zeta\eta}W_{,\zeta\eta} + A^2 N_{\eta\eta}W_{,\eta\eta}$$

where the linear operators L_{ij} are function of the extensional, coupling and bending stiffnesses of the laminate as well as of the geometric dimensions of the curved panels (Ref. 4-5); U , V and W are the displacements of the middle surface in the ζ , η and z directions; N_{ζ} , N_{η} and $N_{\zeta\eta}$ denote the pre buckled average axial, transverse and shear loads per unit width. Both the simply supported (BC-1) and fully clamped (BC-3) boundary conditions are taken into consideration; the following conditions are to be satisfied:

$$\text{BC-1 : at } \zeta=0,1 : N_{\zeta} = M_{\zeta} = V = W = 0; \\ \text{at } \eta=0,1 : N_{\eta} = M_{\eta} = U = W = 0 \quad (2)$$

$$\text{BC-3 : at } \zeta=0,1 : U = V = W = W_{,\zeta} = 0; \\ \text{at } \eta=0,1 : U = V = W = W_{,\eta} = 0$$

A solution of the problem was assumed to be in the well known form:

$$U = \sum_m \sum_n A_{mn} \phi_{mn}(\zeta, \eta); \quad V = \sum_m \sum_n B_{mn} X_{mn}(\zeta, \eta); \\ W = \sum_m \sum_n C_{mn} \psi_{mn}(\zeta, \eta). \quad (3)$$

1. INTRODUCTION

Analytical and experimental results on the structural efficiency of aerospace structures under compression and shear loads have demonstrated the mass saving potential of advanced composite panels to meet buckling requirements. Several experimental and analytical works are available in literature on buckling of composite panels under combined loads; in the most of the cases, the experimental results reported are relative to uniaxial compression or shear load only; herein too, as well as in Ref. 1-3, some results are reported on the buckling behaviour of advanced composite panels under uniaxial compression or shear load; in very few reports results are reported in which a combination of the two loads was applied. In the real condition, however, biaxial compression and shear load can be applied contemporarily on panel; theoretical analysis can predict the buckling load when combined loads are applied and several results are available in the literature or can be obtained by our computer program ALPATAR; experimental results, indeed, were not found. Starting from these considerations a new test facility was built at Turin University of Technology in order to apply contemporarily both biaxial compression and shear load.

The following functions were used for the two sets:

$$\text{BC-1)} \quad \phi_{mn} = \cos m\pi\zeta \sin n\pi\eta; \quad \chi_{mn} = \sin m\pi\zeta \cos n\pi\eta;$$

$$\psi_{mn} = \sin m\pi\zeta \sin n\pi\eta; \quad (4)$$

$$\text{BC-3)} \quad \phi_{mn} = \chi_{mn} = \sin m\pi\zeta \sin n\pi\eta; \quad \psi_{mn} = X_m(\zeta)Y_n(\eta)$$

$$\text{where: } X_m(\zeta) = \cosh \gamma_m \zeta - \cos \gamma_m \zeta - \alpha_m (\sinh \gamma_m \zeta - \sin \gamma_m \zeta)$$

$$Y_n(\eta) = \cosh \gamma_n \eta - \cos \gamma_n \eta - \alpha_n (\sinh \gamma_n \eta - \sin \gamma_n \eta)$$

are the beam characteristic shape corresponding to a beam clamped on each end. As derivation of the two sets BC-1 and BC-3, other two boundary conditions were obtained considering opposite ends clamped and sides simply supported (BC-2) and viceversa (BC-4). The plate equations of equilibrium, with the associated boundary conditions, were solved out by the Galerkin method. The computer program ALPATAR has been developed for working out the set of linear algebraic equations in the form of an eigenvalue problem:

$$[M_{ij}] - \lambda [K_{ij}] \{A_{mn}, B_{mn}, C_{mn}\}^T = \{0\} \quad (5)$$

Theoretical analysis and computer program have been developed for any unsymmetric and unbalanced laminate. Analytical results on the buckling of flat and cylindrical panels under inplane loads, obtained by the computer program ALPATAR, show the importance of anisotropic stiffnesses on the correct prediction of the critical loads. That means that is not possible, in the most of the case, to extend to a generic laminate the theoretical analysis of specially orthotropic plates for determining the buckling loads; significant non conservative errors (up to 50%) can occur in comparison with the anisotropic solution. In particular, the buckling load of panels under inplane shear is very much affected by the positive or negative direction of load application. Results obtained using this program showed (Ref. 5) how boundary conditions, aspect ratio, fiber orientation, stacking sequence, and curvature affect the buckling loads.

Furthermore, significant nonconservative errors can occur for the buckling prediction of thick plates (i.e. the ratio of inplane dimension to thickness less than 35) when the transverse shear deformation is not taken into account. A higher order shear deformation theory was performed on flat and cylindrical panels by assuming a parabolic distribution of transverse shear strain through the plate thickness (Ref. 5,6). By applying the principle of virtual work has been possible to obtain exact solutions of the governing equation of motion for a simple supported cross ply and antisymmetric angle ply. The first results obtained show as the shear effects on the buckling load are more pronounced as the ratio of the the principal moduli and the numbers of layers increase. For an angle ply laminate $(-45/45)_3$ with a length to thickness ratio of 10 and an E_1/E_2 ratio of 40 a buckling load reduction of 50% will occur in comparison with the CLT.

3. EXPERIMENTAL RESULTS FOR PANELS UNDER INPLANE SHEAR OR COMPRESSION LOAD

Several experimental tests were carried out on flat panels to verify the correlation between the preceding theoretical analysis and experimental results. Panels were manufactured by using graphite bismaleimide T800/5245C BASF (panels n.3, 8 and 9) or graphite epoxy material T300/5208 BASF (panels n.10, 11 and 12); all panels were vacuum bagged and autoclave cured. Panels n. 3 and 9 to 12 are unstiffened; panel n.8 has 3 blade stiffeners spaced 81mm and height of 20mm; lay-up and thicknesses are

reported in table 1:

Table 1: Lay-up and thickness of specimens.

Panel	Lay-up	Thickness (mm)
3	[45 ₂ /-45 ₂ /0 ₂ /90 ₂] _S	2.08
9	[45 ₂ /-45 ₂ /0 ₂ /90 ₂] _{2S}	4.25
10	[0 ₄ /30 ₃ /-30 ₃] _S	2.59
11	[0 ₄ /45 ₃ /-45 ₃] _S	2.55
12	[0 ₁₀ /45 ₁₀] _T	2.51
8	skin:[45/-45/0/90] _S	0.94
	stiff:[45/-45/0 ₂] _S	0.87

Panels n.3 and 8 were tested under shear load, both positive and negative; the overall dimensions resulted of 37 by 23.5 cm; the picture-frame test fixture used for shear tests is composed (Fig. 1) of two steel rails bolted to the edges of each specimen; the rails are connected with pins which do not extend through the test panels; a tension load, applied along one diagonal, was used to test the specimens; panels were assumed to be simply supported along all edges.

Panels n.9 to 12 were tested under compression load; the test fixture used for compression tests provided both clamped and simply supported boundary condition on loaded ends and unloaded sides of the panels (Fig. 3). The overall dimensions resulted of 42.2 by 25.3 cm for panel n.9 and of 41.8 by 28 cm (25.7cm when sides are clamped) for panels n.10 to 12. Panel n.10 and 11 were tested with two different boundary conditions.

Material properties used in the analysis were experimentally determined to be:

$$\text{T800/5245C: } E_1=142\text{GPa}; E_2=5.46\text{GPa}; G_{12}=2.86\text{GPa}; \nu_{12}=0.3$$

$$\text{T300/5208: } E_1=147\text{GPa}; E_2=9.65\text{GPa}; G_{12}=4.93\text{GPa}; \nu_{12}=0.3$$

Several strain gages, either linear or rosette, were back to back bonded to panels to measure in plane strains. Out-of-plane displacements were monitored by the shadow moiré method, and fringe patterns were recorded by a camera. The critical load at which a panel displayed buckling was defined by load-strain curves as the value at which strain reversal occur, together with moiré fringe patterns when clearly developed.

A summary of the results is reported in Table 2.

Table 2: Experimental results for panels under shear and compression load.

N.	Test Load	Boundary Condit	Theoret. Buckling Load (kN)		Experim. Buckling [kN]
			ALPATAR	ESA-CDH	
3	Shear +	BC-1	30.59(*)	26.50	30
3	Shear -	BC-1	19.91(*)	26.50	20
8	Shear -	BC-1	12.13(*)	18.60	11.5
8	Shear +	BC-1	18.69(*)	18.60	19.5
9	Compres	BC-2	75	none	75
10	Compres	BC-1	8.39	7.22	7.85
10	Compres	BC-2	17.32	none	16.68
11	Compres	BC-1	7.46	8.26	8.1
11	Compres	BC-3	23.81	none	19.62
11	Compres	BC-2	15.93	none	
12	Compres	BC-2	9.0	none	8.0

$$(*) \quad F_{buck} = N_{xy} \cdot b / \cos(57.58^\circ)$$

Theoretical analysis reported in paragraph 2 was used to determine the buckling load. The smeared

extensional and bending stiffnesses were considered in the case of stiffened panels. When possible theoretical results obtained by ESA - Composite Design Handbook (ESA-CDH) are reported.

Experimental results obtained for panels under shear tests are reported in Fig. 1 and 2. The applied load along the diagonal is reported as function of different back to back strain gages; strains obtained by rosettes were worked out to obtain principal strains; however, strains measured by the 45 degree gages, quasi perpendicular to applied load, are reported in the pictures, since they display the buckling load too. Results for panel 3 are reported in Fig. 1a and 1b; a positive shear was first applied up to 32.5 kN; then, after removing the load, a negative shear was applied up to the failure load; it is very clear, from the pictures, the great difference in buckling loads, as it was analytically predicted by ALPATAR computer program. Panel 3 carried

an high load in the postbuckling range and failure occurred at 77 kN by an explosive delamination having reached the maximum fibre compression strain.

Results for panel 8 are reported in Fig. 2a and 2b; a positive shear was first applied up to 22.5 kN; then, after removing the load, a negative shear was applied up to 30 kN; it is very clear, from the pictures, the great difference in buckling loads; as it was analytically predicted by ALPATAR computer program, buckling had to happen locally in the skin between stiffeners; overall buckling should have happened at a higher load.

These same panels, and others seven, were also impacted at different energy levels by the dropped mass test method; low velocity impact caused local delamination and intraply cracking of the laminate; with respect to the unimpacted panels, buckling loads reduction up to 30% was obtained for panels impacted up to 41 Joule (Ref. 7).

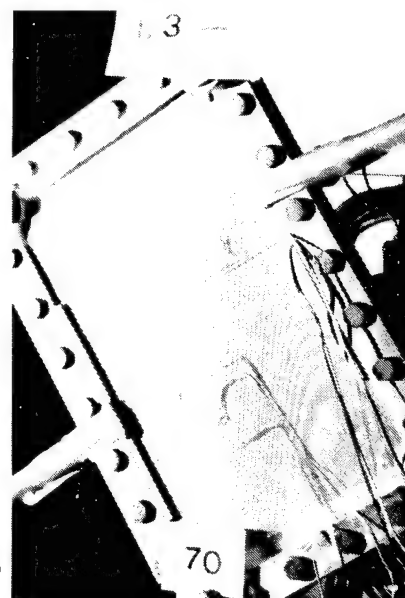
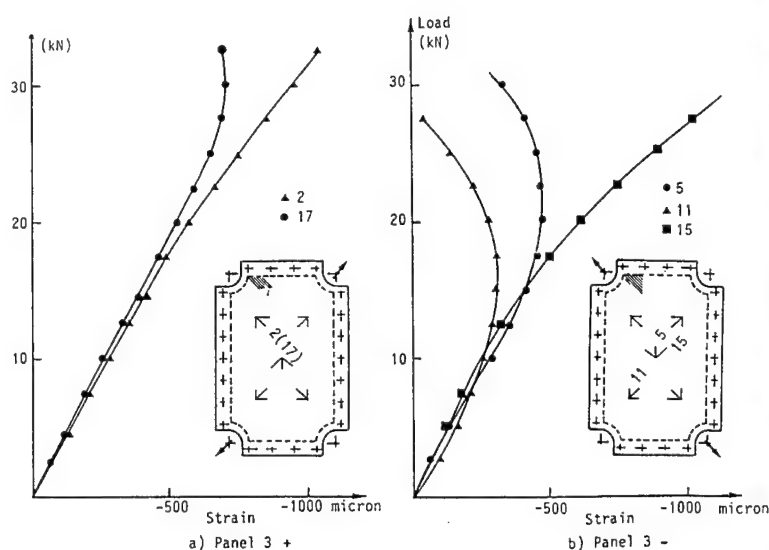


Figure 1. Experimental results for panel n.3 under positive(a) and negative(b) shear load.

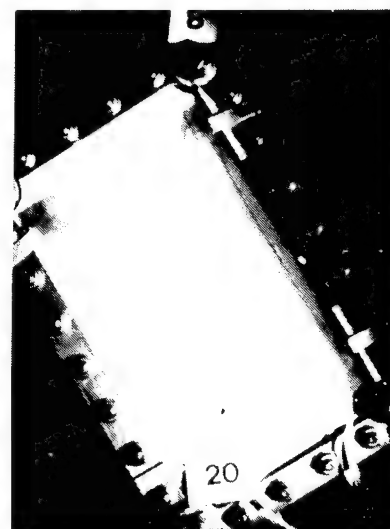
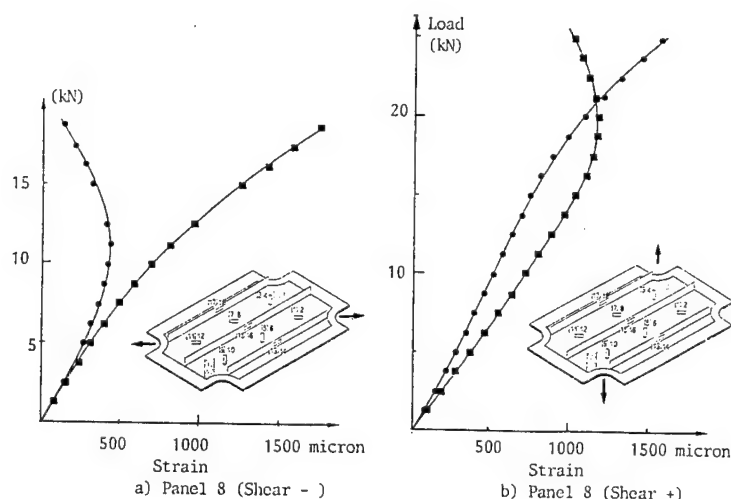


Figure 2. Experimental results for panel n.8 under negative(a) and positive(b) shear load.

Experimental results obtained for panels under uniaxial compression are reported in Fig. 3 to 6. The applied load is reported as function of different back to back strain gages disposed at half length. Fig. 3 represents the behaviour of panel n.9; strain results obtained by gages disposed at a quarter length are also reported; buckling occurred by two half-waves at a load of 75 kN corresponding exactly to the theoretical value obtained by ALPATAR computer program. Fig. 4a and 4b represent the behaviour of panel n.10 having boundary condition BC-1 and BC-2, respectively; average strains recorded at half length are reported; it is very clear, from the pictures, the great difference in buckling loads as

effect of the boundary conditions, as it was analytically predicted by ALPATAR computer program. Fig. 5a and 5b represent the behaviour of panel n.11 having boundary condition BC-1 and BC-3, respectively; average strains recorded at half length are reported; it is very clear, from the pictures, the great difference in buckling loads as effect of the boundary conditions; in this case, however, the experimental buckling load is 17% lower than one analytically predicted by ALPATAR computer program for BC-3 and 23% higher than one predicted for BC-2. In our opinion, the discrepancy is only due to the great difficulty in realising a really full clamp condition.

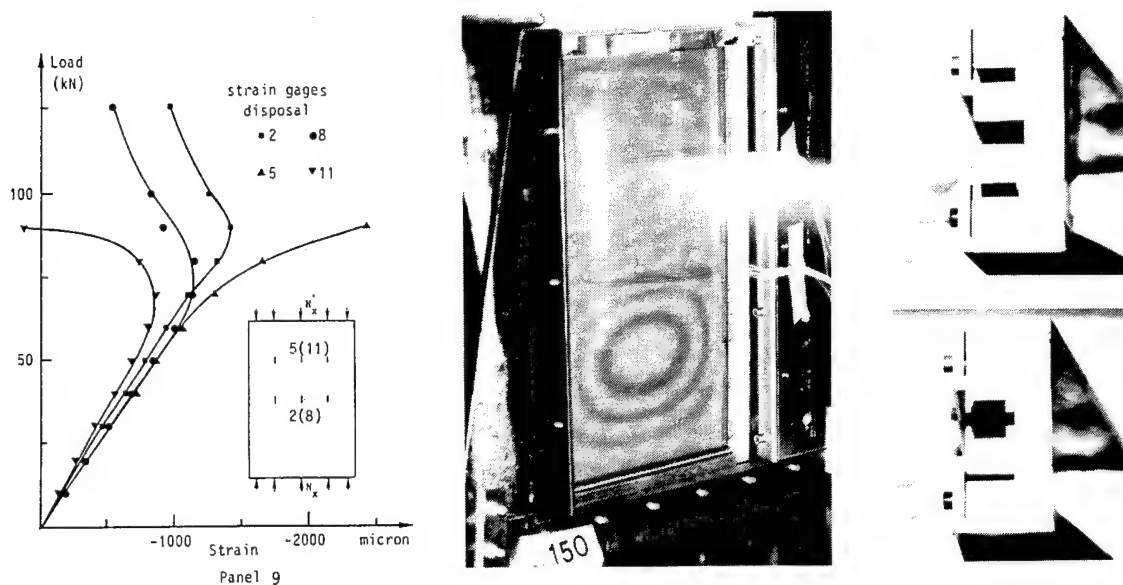


Figure 3. Experimental results for panel n.9 under uniaxial compression.

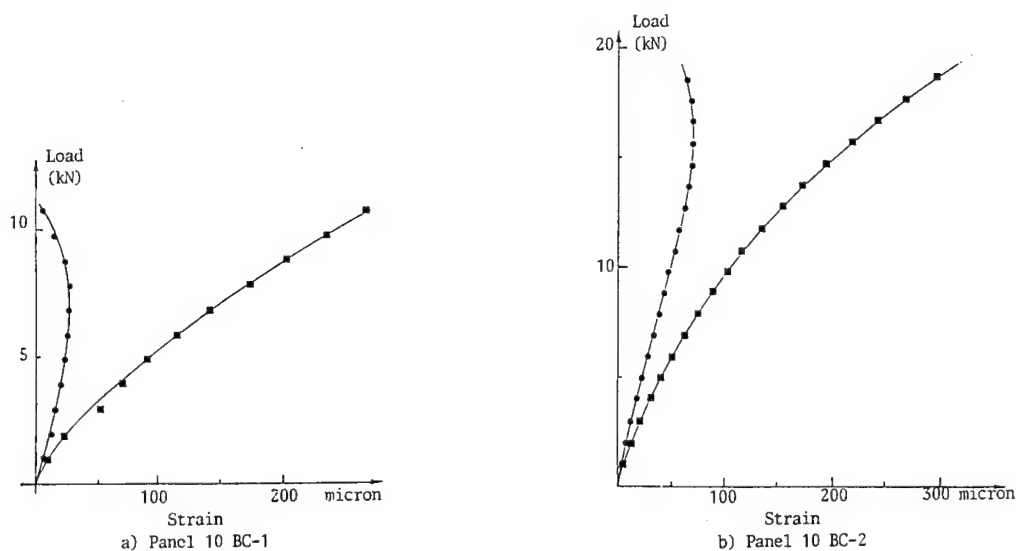


Figure 4. Experimental results for panel n.10 under uniaxial compression.

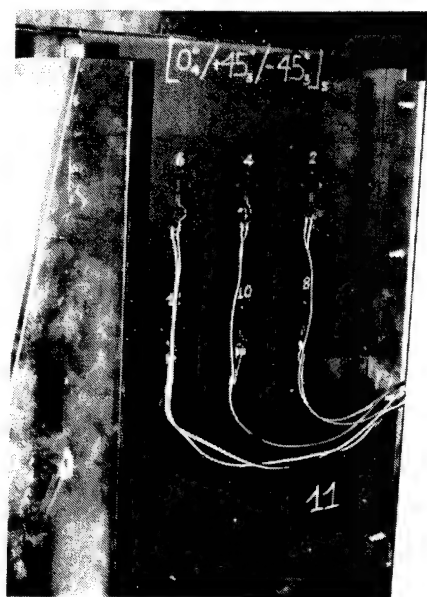
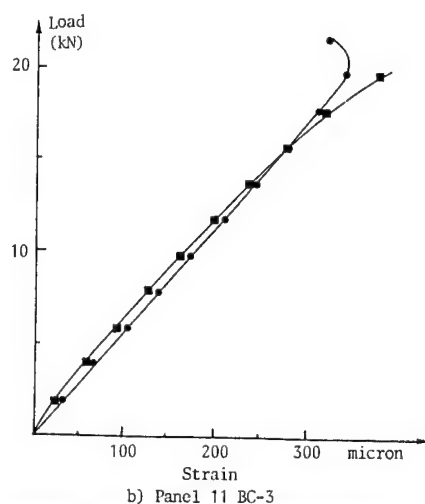
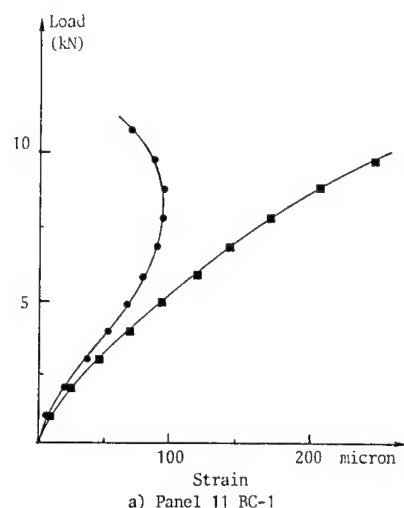


Figure 5. Experimental result for panel n.11 under uniaxial compression.

Fig. 6 represent the behaviour of the unbalanced and unsymmetric panel n.12 having boundary condition BC-2; due to its lay-up, panel was obtained, by the autoclave cycle, distorted and then forced to become "flat" into the compression fixture; indeed, some imperfections were noted before testing. In these case too, analytical prediction was in a good agreement with that one experimentally detected.

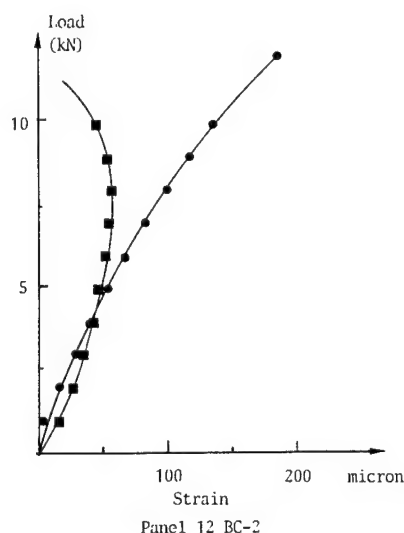


Figure 6. Experimental results for panel n.12 under uniaxial compression.

4. TESTING MACHINE FOR COMBINED BIAXIAL COMPRESSION AND SHEAR LOADS

In the real condition aerospace panels are mostly subjected to biaxial compression and shear load; theoretical analysis can predict the buckling load when combined loads are applied and several results are available in the literature or can be obtained by computer program ALPATAR; experimental results, indeed, were not found. Starting from these considerations a new testing machine was built in order to apply contemporarily both biaxial compression and shear load (Fig. 7). Actually, a maximum longitudinal compression load of 500 kN, a transverse compression or tension load of 200 kN and a positive or negative shear load of 200kN can be applied on panels having dimension lower than 1000 by 700 mm. The facility was predisposed to apply, in the future, tension load also in the longitudinal direction as well as fatigue load (in this case at half values of the above loads).

The load and supporting frames were manufactured by stell alloy and 2024 aluminium alloy. Longitudinal load is applied by two servo-actuators controlled separately to maintain the panel ends perfectly parallel one to each other; the angular rotation is controlled to zero within 0.001 degree. Transverse load is applied by two servo-actuators controlled separately to maintain the panel sides perfectly parallel one to each other; the system of transverse load application is floating in order to not interfere with the longitudinal and shear loads. Shear load is applied by one servo-actuator to the bottom end of the panel. The test rig is completely closed loop controlled via electronics moduls by 9 transducers. The test rig can apply other different load configurations than those above reported since the actuators can apply both tension and compression loads independently one to each other.

The facility has been already manufactured by Italian company AIP Studio; preliminary tests are being carried out on a thick aluminium panel to verify, by back to back linear and rosette strain gauges, the uniformity of the applied load in all the panel. First results obtained show a good control of the applied load, remaining perfectly steady as different loads are superimposed one to each other. Work is in progress and very soon should be possible to test advanced composite stiffened and unstiffened panels under combined loads.

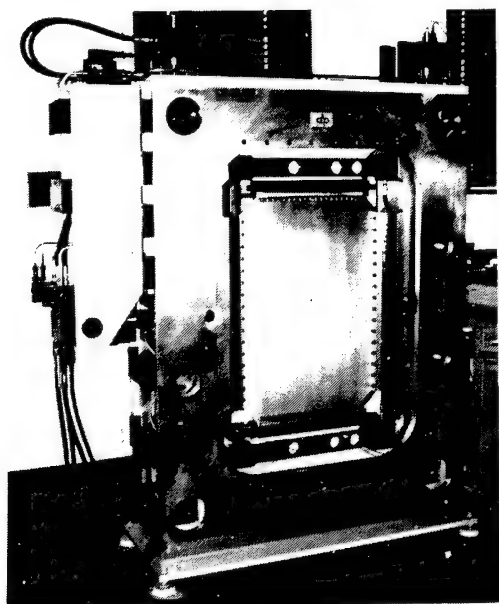
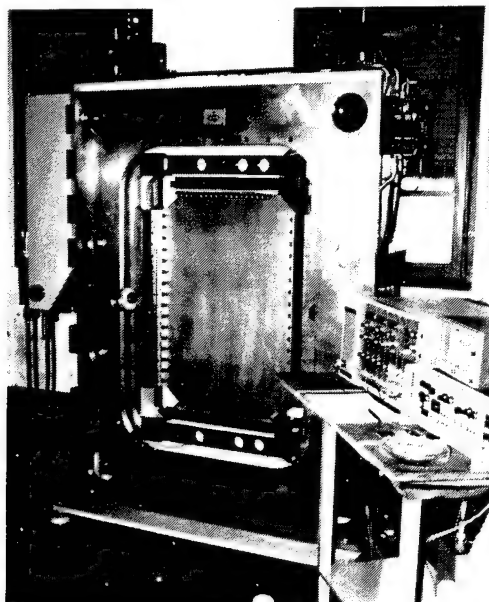


Figure 7. Testing machine for combined biaxial compression and shear load.

5. CONCLUSION

Test results for composite panels under shear or uniaxial compression load correlate well with theoretical results when anisotropic stiffnesses are adequately considered. In particular, shear buckling load is greatly affected by the load direction and unconservative errors can be obtained when the specially orthotropic solution is applied to anisotropic panels. By the new testing machine manufactured for applying contemporarily combined loads should be possible to verify in the next future the correlation with the theoretical analysis here in reported.

6. REFERENCES

1. Williams J.G. & al 1979, Recent developments in the design, testing and impact damage tolerance of stiffened composite panels, *Nasa TM 80077*.
2. Starnes J.H. & al 1984, Postbuckling behaviour of graphite-epoxy panels, *Proc. ACEE Composite Structures Technology*, Seattle, USA, NASA CP 2321, 137-159.
3. Romeo G. 1986, Experimental investigation on advanced composite stiffened structures under uniaxial compression and bending, *AIAA Journal*, 24, 11, 1823-1830.
4. Whitney J M 1984, Buckling of anisotropic laminated cylindrical plates, *AIAA Journal*, 22, 11, 1641-1645.
5. Romeo G & al 1990, Buckling of laminated cylindrical plates including effects of shear deformation, *Proc. Int. Symp. Space Application of Advanced Structural Materials*, ESA-ESTEC, Noordwijk, NL, ESA SP-303, 365-370.
6. Reddy J N & Liu C F 1985, A higher-order shear deformation theory of laminated elastic shells, *Int. J. Engng Sci*, 23, 3, 319-330.
7. Romeo G. et al 1990, Effect of low velocity impact damage on the buckling behaviour of composite panels, *Proc. 17th Congress of the Int. Council of the Aeronautical Sciences*, Stockholm, 1, 994-1004.

ACKNOWLEDGMENTS

The research was carried out by the financial sponsorship of the Ministry of University. Authors would like to acknowledge the efficacious cooperation of G. Ruvinetti and of: A. Bertolotti, L. Bisol, M. Pegolo and R. Pelazza, last year's undergraduates in aeronautical engineering.

**SESSION
1.4.C**

**MATERIALS
II**

CHARACTERISATION

PRECEDING PAGE BLANK NOT FILMED

N92-23805

55527

84717

DAMPING BEHAVIOUR OF UNIDIRECTIONAL FIBRE REINFORCED POLYMERS

Holger Hanselka¹⁾

German Aerospace Research Establishment (DLR)
Institute for Structural Mechanics
D-3300 Braunschweig, Germany

ABSTRACT

A method for the analytical description of damping for unidirectional fibre reinforced composites is shown. Generally the parameter damping can be described through the simple theory of a damped system with one degree of freedom or by the definition of complex modulus of elasticity.

To describe damping behaviour of composite materials, the complex modulus of elasticity is substituted into the orthotropic stress-strain relationship of unidirectional fibre reinforced laminates. With this modulus damping and stiffness can be described as a function of direction of fibre reinforcement. The analytical solution will be compared with experimental data. As an investigation method the thermal resonance vibration bending test is used.

At the end of this paper an optimization of dynamic behaviour of a simple structure, a single cantilever beam, will be carried out through variation of angle of fibre direction.

Keywords: Composites, Complex Modulus, Damping, Investigation Method.

1. INTRODUCTION

If static loaded spacecraft structures are to be designed, essentially by saving of weight, the advantage of using carbon fibre reinforced polymers is apparent when the fibres are put into direction of main stresses. Such fibre designed construction depicts excellent strength and stiffness behaviour at concurrently lower masses.

In most ranges of spacecraft applications stresses are of dynamical characteristic. Then, besides the stiffness and the mass of the structure the material damping has a significant influence on the vibrational behaviour of the structures. Where as the structure made of conventional materials like Aluminium can be damped by additional damping layers. The anisotropic fibre reinforced composites allow the variation of damping by changing the kind of fibre and matrix and orientation of the selected fibre in the laminate and by its volume, in a wide range. Thus by selecting appropriate parameters of a laminate, additional damping layers are dispensable.

Due to the viscoelastic behaviour of a polymeric matrix system and elastic behaviour of the reinforcement, the damping value increases with the increase in influence of the matrix, however with a reduction in stiffness and strenght. For problem tailored laminates an optimization between the contrary parameters like stiffness and damping, seems to be necessary.

In this paper, a contribution should be rendered to the damping behaviour of unidirectional fibre reinforced composites. In the first part, damping and its mathematical description are discussed. For velocity depending damping, the model of a damped system with one degree of freedom consisting of a spring, a viscous dashpot and a mass is used. If damping is independent of velocity, the use of hysteresis damping described through the complex modulus is advantageous. Fibre reinforced polymers show in a special frequency range a damping behaviour which is nearly independent of frequency. Because of that it will be shown, that the anisotropic law of elasticity of the unidirectional reinforced layer can be written in complex form to get transformation equations for damping. In the second part of this paper experimental investigative methods for the characterization of damping behaviour of composites are discussed and furthermore the analytical solution will be compared with experimental data. At the end of the paper an optimization of dynamic behaviour of a simple structure, a single cantilever beam, will be carried out with variation of the angle of fibre direction.

2. DESCRIPTION OF DAMPING BEHAVIOUR

Damping (Ref. 1) describes the change from mechanical energy in lower energy modes like thermal energy. That is an irreversible process related to an increase in entropy.

Kinds of damping can be loss of energy, which are depending on

- surrounding medium (e.g. air damping),
- effects of friction in joints and bearings,
- mechanical loss in materials (material damping).

Air damping can be represented through liquid elements with velocity depending damping, friction effects can be represented through path depending Coulomb

¹⁾ Dedicated to Professor Dr.-Ing. H.W. Bergmann for his 65th birthday.

friction force. Material damping can be explained physically through the motion of molecules. By that, mechanism of damping of polymers are different from that of metals. Therefore it is difficult to find models in order to describe material damping.

2.1 The damped single degree of freedom system

In order to describe the phenomenon of damping of an arbitrary structural element, it should be substituted by a single cantilever beam. This beam can be approximated by a system consisting of a spring, a dashpot and a mass. If stiffness, damping and resonance frequency of the beam are known, the simplification can be realized through a massless spring pole with a concentrated mass at the end as shown in figure 1.

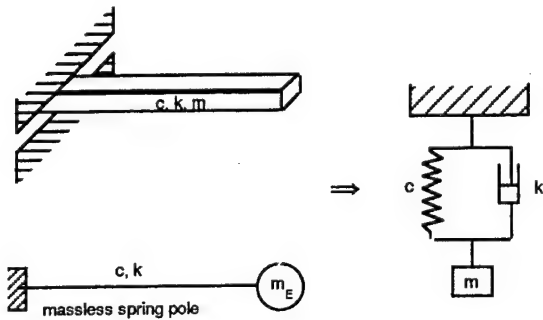


Figure 1: equivalent modelsystem

The equation of motion of this system is given in explicit form by

$$\ddot{x} + 2D\dot{x} + \omega_0^2 x = \left(\frac{F(t)}{m}\right) \quad (1)$$

with D : damping factor and ω_0 : resonance frequency.

In order to comprehend the measuring technique, the differential equation (D.E.) must be solved by considering the corresponding boundary conditions and damping must be derived from the solution.

The Lehr damping coefficient can be written as

$$\vartheta = \frac{D}{\omega_0} \quad (2)$$

Then from the D.E. through the initial conditions of free vibration test for damping factor follows

$$\vartheta = \frac{1}{2\pi} \ln \frac{x_1}{x_2} \quad (3)$$

The decay process of oscillation of a single cantilever damped beam is shown in figure 2.

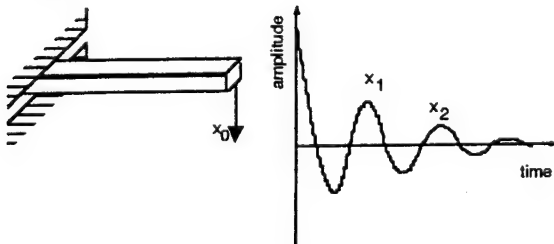


Figure 2: decay process

For free vibrations the effect of damping is shown by decreasing amplitude.

If the beam is excited with a signal which possesses all frequencies like a swept sinusoidal signal, the frequency spectrum will be like that as in figure 3.

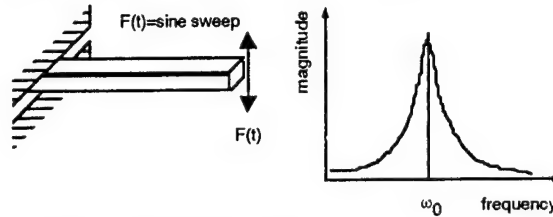


Figure 3: resonance behaviour

Damping can be derived by resonance curve through the method of half width to

$$\vartheta = \frac{\omega_2 - \omega_1}{2\omega_0} \quad (4)$$

The effect of damping in the case of resonance vibrations is a limitation of resonance amplitude.

For forced harmonic vibrations within sidebands of resonance frequency of the beam, the result of damping is a phase shift between the acting force and the resultant strain like that shown in figure 4.

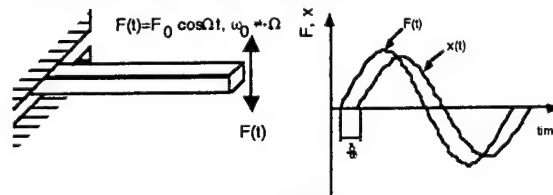


Figure 4: forced harmonic vibration

Through the model of a damped system with one degree of freedom the Lehr damping coefficient becomes to

$$\vartheta = \frac{\omega_0^2 - \Omega^2}{2\omega_0 \Omega} \tan \delta \quad (5)$$

The magnitude of phase shift is a measure to damping of material.

2.2 Complex modulus

Until now it was considered, that damping force was proportional to the velocity. But polymers (epoxy), especially at the interesting frequency range between 0 and 150 Hz show an independent damping behaviour (figure 5).

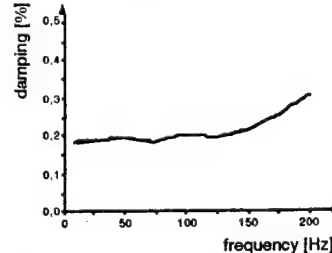


Figure 5: frequency dependence of damping

Therefore it is better to substitute velocity depending damping through hysteresis damping, which is depending on vibration amplitude (path depending).

At harmonic deformation of an arbitrary element of a volume (figure 6)

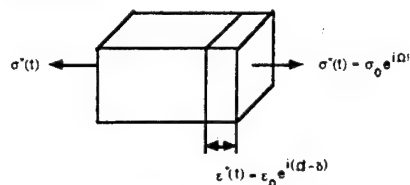


Figure 6: dynamic loaded element of a volume

of the beam there is a phase shift between stress and strain with the phase angle δ (figure 7).

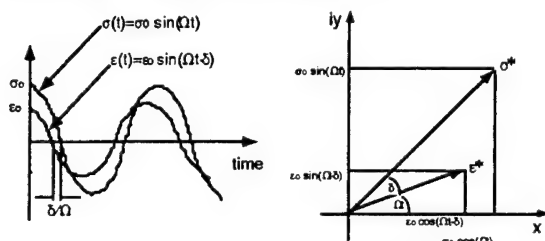


Figure 7: harmonic stress and strain (complex)

The stress-strain relationship is given by Hooke's law to

$$\sigma^* = E^* \epsilon^* \quad (6)$$

Because of the phase shift, that means because of the different angularity of the complex numbers $\epsilon^*(t)$ and $\sigma^*(t)$ in the complex domain, the modulus of elasticity E^* is a complex number too and can be written as

$$E^* = E' + iE'' \quad (7)$$

The real part E' means the storage modulus, the imaginary part E'' the loss modulus. The ratio of these numbers is defined as the loss factor d

$$d = \frac{E''}{E'} = \tan \delta \quad (8)$$

The loss factor characterises the material damping.

3. DETERMINATION OF ANISOTROPIC DAMPING

For the determination of fibre direction depending damping behaviour of an unidirectional reinforced laminate the knowledge of stress-strain relationship of an orthotropic material (Ref. 2) is necessary.

The general description of an element of a volume of an arbitrary material is shown in figure 8.

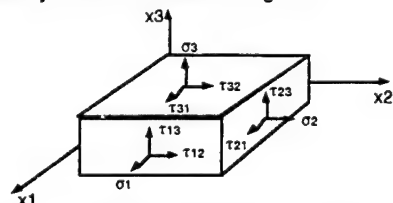


Figure 8: stresses at an element of a volume

Each of the 9 stress components secures 9 strain components and with proportionality between stress and strain, the relationship becomes to

$$\sigma_{ij} = C_{ijkl} \epsilon_{kl} \quad (i, j, k, l = 1, 2, 3), \quad (9)$$

where the stiffness C is a material tensor consisting of 81 coefficients.

In the classical theory of continuum mechanic it is considered, that stress and strain tensor are symmetrical. Then the reduced stress tensor can be written by

$$\sigma_1 = \sigma_{11}, \quad \sigma_2 = \sigma_{22}, \quad \sigma_3 = \sigma_{33}, \quad (10)$$

$$\sigma_4 = \sigma_{12}, \quad \sigma_5 = \sigma_{13}, \quad \sigma_6 = \sigma_{23},$$

and the strain tensor accordingly.

By that, the number of coefficients are reduced from 81 to 36. The generalized law of elasticity follows as

$$\sigma_i = C_{ik} \epsilon_k \quad (i, k = 1, 2, \dots, 6). \quad (11)$$

By the presence of an elastic potential \mathcal{Q} , that means a reversible isotherm or adiabatic process during the deflection, we can use the law of Maxwell-Betti

$$C_{ik} = C_{ki} \quad (i, k = 1, 2, \dots, 6). \quad (12)$$

Due to the symmetry to the main diagonal of material tensor the number of coefficients are reduced from 36 to 21 components, which are independent of each other and not equal to zero.

Mostly, technical laminates have three mutually perpendicular planes of elasticity. The number of independent elastic stiffness coefficients can be reduced then from 21 to 9.

Unidirectional fibre reinforced laminates are relative to one axis transversal isotropic. Then the number of elastic stiffness coefficients can be reduced from 9 to 5 components.

The Hooke's law for this case can be written as

$$\begin{pmatrix} \epsilon_1 \\ \epsilon_2 \\ \epsilon_3 \\ \gamma_{23} \\ \gamma_{13} \\ \gamma_{12} \end{pmatrix} = \begin{pmatrix} S_{11} & S_{12} & S_{12} & 0 & 0 & 0 \\ S_{12} & S_{22} & S_{23} & 0 & 0 & 0 \\ S_{12} & S_{23} & S_{22} & 0 & 0 & 0 \\ 0 & 0 & 0 & \frac{1}{2}(S_{11} - S_{12}) & 0 & 0 \\ 0 & 0 & 0 & 0 & S_{44} & 0 \\ 0 & 0 & 0 & 0 & 0 & S_{44} \end{pmatrix} \begin{pmatrix} \sigma_1 \\ \sigma_2 \\ \sigma_3 \\ \tau_{23} \\ \tau_{13} \\ \tau_{12} \end{pmatrix} \quad (13)$$

and S_{ij} is the compliance.

2) The specific deformation energy of volume can be written as

$$dW = \sigma_i d\epsilon_i = C_{ik} \epsilon_k d\epsilon_i$$

The derivation to ϵ_i and ϵ_k take

$$\frac{\partial^2 W}{\partial \epsilon_i \partial \epsilon_k} = C_{ik}$$

The sequence of derivation can be changed to a potential function:

$$\frac{\partial^2 W}{\partial \epsilon_i \partial \epsilon_k} = \frac{\partial^2 W}{\partial \epsilon_k \partial \epsilon_i} \Rightarrow C_{ik} = C_{ki}$$

These compliances can be expressed in terms of engineering constants, which are in direct relation to special load and deflection cases and can be measured through simple investigation methods.

In practical engineering problems one is often interested in a state of plane stress. For plane stress with respect to the x1-x2 plane, relationship (13) in terms of engineering constants becomes

$$\begin{pmatrix} \epsilon_1 \\ \epsilon_2 \\ \gamma_{12} \end{pmatrix} = \begin{bmatrix} \frac{1}{E_1} & -\frac{\nu_{12}}{E_1} & 0 \\ -\frac{\nu_{21}}{E_1} & \frac{1}{E_1} & 0 \\ 0 & 0 & \frac{1}{G_{12}} \end{bmatrix} \begin{pmatrix} \sigma_1 \\ \sigma_2 \\ \tau_{12} \end{pmatrix} \quad (14)$$

However, the principal directions of orthotropy often do not coincide with coordinate directions. A relationship is needed between stresses and strains in the principal material direction and those in the object coordinates (figure 9)

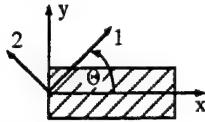


Figure 9: coordinate systems

With the transformation matrix

$$[T] = \begin{bmatrix} \cos^2(\theta) & \sin^2(\theta) & 2\sin(\theta)\cos(\theta) \\ \sin^2(\theta) & \cos^2(\theta) & -2\sin(\theta)\cos(\theta) \\ -\sin(\theta)\cos(\theta) & \sin(\theta)\cos(\theta) & \cos^2(\theta) - \sin^2(\theta) \end{bmatrix} \quad (15)$$

the stresses and strains in object coordinates becomes

$$\begin{pmatrix} \sigma_x \\ \sigma_y \\ \tau_{xy} \end{pmatrix} = [T]^{-1} \cdot \begin{pmatrix} \sigma_1 \\ \sigma_2 \\ \tau_{12} \end{pmatrix}, \quad \begin{pmatrix} \epsilon_x \\ \epsilon_y \\ \gamma_{xy} \end{pmatrix} = [T] \cdot \begin{pmatrix} \epsilon_1 \\ \epsilon_2 \\ \gamma_{12} \end{pmatrix} \quad (16)$$

and the stress-strain relationship in object coordinates can be written as

$$\begin{pmatrix} \epsilon_x \\ \epsilon_y \\ \gamma_{xy} \end{pmatrix} = \begin{bmatrix} \tilde{S}_{11} & \tilde{S}_{12} & \tilde{S}_{16} \\ \tilde{S}_{12} & \tilde{S}_{22} & \tilde{S}_{26} \\ \tilde{S}_{16} & \tilde{S}_{26} & \tilde{S}_{66} \end{bmatrix} \begin{pmatrix} \sigma_x \\ \sigma_y \\ \tau_{xy} \end{pmatrix} \quad (17)$$

The rotated compliance in x-direction can be calculated in terms of the original engineering constants by using the following transformation equation:

$$\frac{1}{E_x} = \frac{1}{E_1} \cos^4(\theta) + \left(\frac{1}{G_{12}} - \frac{2\nu_{12}}{E_1} \right) \sin^2(\theta) \cos^2(\theta) + \frac{1}{E_2} \sin^4(\theta) \quad (18)$$

To describe damping behaviour of a unidirectional fibre reinforced laminate, one has to remember the complex modulus. Through the corresponding principle the complex stiffness can be used analytically, like the absolute stiffness (Ref. 3). By that, the law of elasticity can be expressed in complex form and through the complex numbers

$$\begin{aligned} E_x &= E'_x + iE''_x = E'_x(1 + id_x), \\ E_{11} &= E'_{11} + iE''_{11} = E'_{11}(1 + id_{11}), \\ E_{22} &= E'_{22} + iE''_{22} = E'_{22}(1 + id_{22}), \\ G_{12} &= G'_{12} + iG''_{12} = G'_{12}(1 + id_{12}), \\ \nu_{12} &= \nu_{12}. \end{aligned} \quad (19)$$

the transformed complex modulus of elasticity in x-direction can be written as

$$\frac{1}{E_x(1 + id_x)} = \frac{1}{E'_{11}(1 + id_{11})} \cos^4(\theta) + \left(\frac{1}{G'_{12}(1 + id_{12})} - \frac{2\nu_{12}}{E'_{11}(1 + id_{11})} \right) \sin^2(\theta) \cos^2(\theta) + \frac{1}{E'_{22}(1 + id_{22})} \sin^4(\theta) \quad (20)$$

By separation of real and imaginary part follows an equation for the orientation depending storage modulus

$$E'_x = \frac{1}{\left(\frac{1}{E'_{11}(d_{11}^2 + 1)} \cos^4(\theta) + \left(\frac{1}{G'_{12}(d_{12}^2 + 1)} - \frac{2\nu_{12}}{E'_{11}(d_{11}^2 + 1)} \right) \sin^2(\theta) \cos^2(\theta) + \frac{1}{E'_{22}(d_{22}^2 + 1)} \sin^4(\theta) \right)} \quad (21)$$

and loss factor

$$E''_x = \frac{\frac{d_{11}}{E'_{11}(d_{11}^2 + 1)} \cos^4(\theta) + \left(\frac{d_{12}}{G'_{12}(d_{12}^2 + 1)} - \frac{2\nu_{12}}{E'_{11}(d_{11}^2 + 1)} \right) \sin^2(\theta) \cos^2(\theta) + \frac{d_{22}}{E'_{22}(d_{22}^2 + 1)} \sin^4(\theta)}{\left(\frac{1}{E'_{11}(d_{11}^2 + 1)} \cos^4(\theta) + \left(\frac{1}{G'_{12}(d_{12}^2 + 1)} - \frac{2\nu_{12}}{E'_{11}(d_{11}^2 + 1)} \right) \sin^2(\theta) \cos^2(\theta) + \frac{1}{E'_{22}(d_{22}^2 + 1)} \sin^4(\theta) \right)^2} \quad (22)$$

The loss factor, which describes damping of material, can be expressed by

$$d_x = \frac{E''_x}{E'_x} \quad (23)$$

to

$$d_x = \frac{\frac{d_{11}}{E'_{11}(d_{11}^2 + 1)} \cos^4(\theta) + \left(\frac{d_{12}}{G'_{12}(d_{12}^2 + 1)} - \frac{2\nu_{12}}{E'_{11}(d_{11}^2 + 1)} \right) \sin^2(\theta) \cos^2(\theta) + \frac{d_{22}}{E'_{22}(d_{22}^2 + 1)} \sin^4(\theta)}{\left(\frac{1}{E'_{11}(d_{11}^2 + 1)} \cos^4(\theta) + \left(\frac{1}{G'_{12}(d_{12}^2 + 1)} - \frac{2\nu_{12}}{E'_{11}(d_{11}^2 + 1)} \right) \sin^2(\theta) \cos^2(\theta) + \frac{1}{E'_{22}(d_{22}^2 + 1)} \sin^4(\theta) \right)} \quad (24)$$

The last equation represented the transformation equation of damping for the unidirectional fibre reinforced laminate.

For experimental investigation this means, that for a complete characterization of damping behaviour of a unidirectional layer, measurements at three different orientated laminates must be carried out:

- UD 0° for E'_{11} , d_{11} and ν_{12} ,
- UD 90° for E'_{22} and d_{22} ,
- UD 45° for E'_{45} and d_{45} .

The shear components can be solved through the results of the tests of UD 45° laminates to

$$G'_{\#} = \frac{E'_{\parallel} E'_{\perp} E'_{45}}{E'_{\parallel} (4E'_{\perp} - E'_{45}) + E'_{\perp} E'_{45} (2\nu_{\parallel\perp} - 1)} \quad (25)$$

$$d_{\#} = F(E'_{\parallel}, E'_{\perp}, G'_{\#}, \nu_{\parallel\perp}, d_{\parallel}, d_{\perp}, d_{45}) \quad (26)$$

4. METHOD OF TESTING

For the investigation of damping of unidirectional fibre reinforced laminates, two different kinds of testing equipments are used,

- the thermal resonance vibration bending test (DIN 53 440),
- the Dynamic-Mechanic-Thermal-Analyzer (DMTA).

In this paper only the first method should be presented.

For the thermal resonance vibration bending test, a long thin specimen (250 x 16 x 2 mm) is clamped at one end, the other end is free (figure 10).

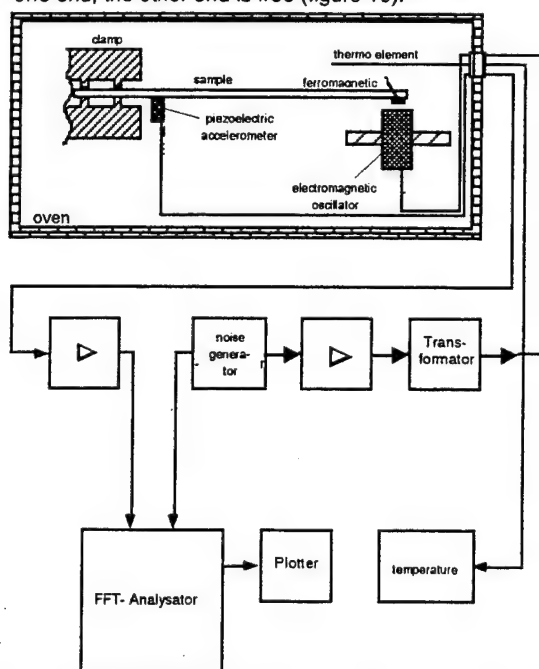


Figure 10: thermal resonance vibration bending test

At the free end an electromagnetic oscillator is attached, which receives a noise signal from an internal FFT-noise-generator. Near the clamp a piezoelectric accelerometer is fixed, which measures the real vibration of the beam. Both signals, the vibration excitation and the vibration answer are received from FFT-Analysator, which transforms the signal from time into frequency domain and builds the transfer function. The whole equipment is arranged in an oven, the temperature is measured through a thermoelement. As demonstrated before, the dynamic stiffness and damping can be calculated from transfer function. This method works very precisely, because the influence of damping to vibration behaviour is at resonance extreme.

5. CONFIRMITY BETWEEN THEORY AND EXPERIMENT

To compare the analytical results of the damping relation (24) with experimental data, specimens with fibre directions UD 0°, 5°, 15°, 30°, 45°, 60°, 75° and 90° were made from a large unidirectional reinforced plate. The specimens were tested using the thermal resonance vibration bending test at room temperature for their dynamic stiffness and their damping behaviour. For constant measurement frequency (30 Hz) the specimens were clamped at different free lengths. The experimental results are shown in table 1.

θ [degree]	E'_{θ} (stat.) [GPa]	d_{θ} (dyn.) [%]
0	106,5	0,1726
5	95,6	0,2954
15	53,3	0,5469
30	23,3	0,7783
45	13,7	0,7647
60	10,1	0,7219
75	8,6	0,6731
90	8,2	0,7158

Table 1: experimental data from bending test

The dependence of storage modulus and damping on the fibre angle can be shown most clearly by means of a polar diagram (figure 11).

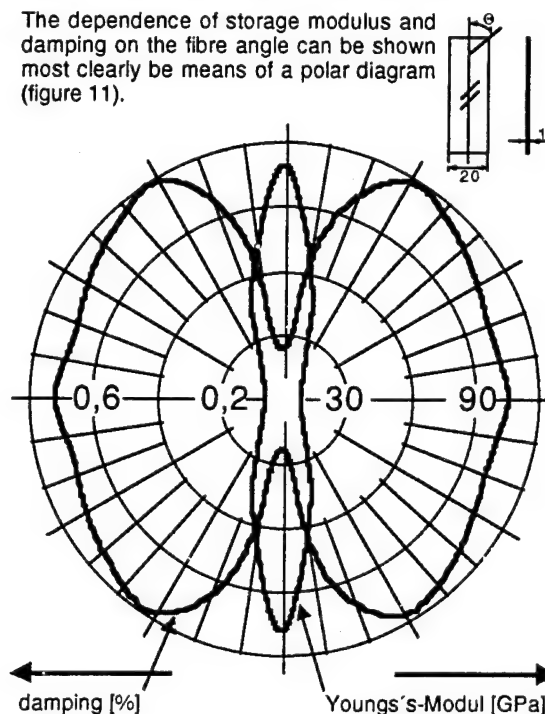


Figure 11: polar diagram of stiffness and damping

It can be seen, that the damping is particularly low where the storage modulus is a maximum, which occurs at an angle of 0° to the fibre direction. However, the maximum damping was found to occur not at 90° but at 30° to the fibre direction. Between 30° and 90° to the fibre direction damping decreases to a trifle while stiffness decreases extremely. The polar diagram shows, that for high vibration absorption and high stiffness, a fibre direction of 10° can be used.

The comparison of the experimental data with analyti-

cal results of the damping relation (24) solved with the technical constants of UD-layer

$$\begin{aligned} E'_{||} &= 106,5 \text{ GPa} & d_{||} &= 0,1726 [\%] \\ E'_{\perp} &= 8,2 \text{ GPa} & d_{\perp} &= 0,7158 [\%] \\ G'_{\#} &= 6,027 \text{ GPa} & d_{\#} &= 0,8176 [\%] \\ \nu_{||\perp} &= 0,216 \end{aligned}$$

is presented in table 2.

θ	d-experiment [%]	d-calculation [%]
0	0,1726	0,173
5	0,2954	0,223
15	0,5469	0,467
30	0,7783	0,698
45	0,7647	0,755
60	0,7219	0,747
75	0,6731	0,726
90	0,7158	0,716

Table 2: theoretical and experimental damping data

The conformity between the analytical result and experimental data is distinguished, like that shown in polar diagram (figure 12).

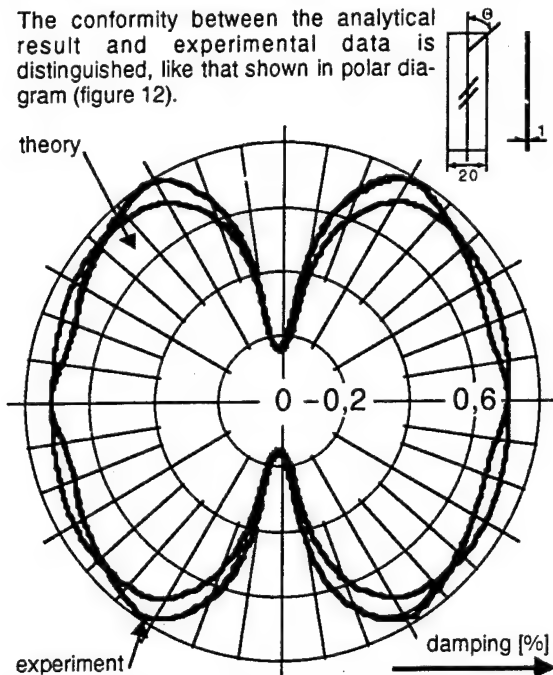


Figure 12: polar diagram of theoretical and experimental damping data

The maximum difference between theory and experiment is lower, than the limit of accuracy of the experimental method.

6. OPTIMIZATION OF DAMPING IN A STRUCTURE

Damping and stiffness of unidirectional fibre reinforced laminates are opposite parameters, so for a dynamic loaded structure the optimization between these parameters seems to be necessary. In substitution for an arbitrary structure this optimization should be shown with the help of a single cantilever beam (figure 4). Highest stiffness occurs at a fibre direction of 0° , but such a design shows lowest damping behaviour. A bi-

directional fibre reinforced laminate would have more damping and less flexural stiffness. For constant flexural stiffness the thickness of the laminate must be increased. The optimization results are shown in table 3.

laminate orientation	h [mm]	B_{11} [Nmm]	damping [%]
UD 0°	1,000	8910	0,173
BD $[\pm 10]^\circ$	1,017	8913	0,300
BD $[\pm 20]^\circ$	1,073	8913	0,420

Table 3: results of optimization

The optimization of the cantilever beam show, that by a suitable Off-Axis laminate construction, damping can be increased by multiple amount maintaining the stiffness value constant.

7. CONCLUSIONS

Damping shows determinative influence to the dynamic behaviour of structure. The employment of fibre reinforced polymers permits the variation of the parameter damping in a structure due to its anisotropic material behaviour. To use this effect, the analytical description of damping behaviour is necessary. A proposal to this problem was forwarded in this paper.

Viscoelastic material behaviour, that means damping, can be described with the introduction of complex modulus, which consists of an elastic storage component and a viscous loss component. With the corresponding principle in the law of elasticity, the complex stiffness can be used like an absolute stiffness, which means, that all known transformation equations for anisotropic materials can be used in complex form. Then it is easy to derive relationship for the transformed storage modulus and loss modulus. From this ratio a relationship for the transformed damping can be derived. The comparison of results of this analytical description with the thermal resonance vibration bending test experimental measured data, shows a distinguished conformity.

For design of dynamic loaded structures an optimization between the opposite parameters stiffness and damping is absolutely necessary. The shown polar diagrams are for this work an ingenious base. It is possible, to achieve threefold damping in a structure without a loss in stiffness with an appropriate selection of fibre direction and laminate thickness.

6. REFERENCES

1. Nashif A D & al 1985, *Vibration Damping*, John Wiley, New York
2. Jones R M 1975, *Mechanics of Composite Materials*, McGraw-Hill, Washington
3. Hashin Z 1970, *Complex Moduli of viscoelastic Composites - Part I and II*, Int J Solids Structures

536-24
N92-23806
84718

COMPUTER SIMULATION OF MOISTURE PENETRATION IN STRUCTURES

Otto Wilmar

DNV Ingemannsson AB, Box 47321, 10074 Stockholm, Sweden

ABSTRACT

A method for computer simulation of transient flow of moisture, heat and pressure in composite materials is described. The theoretical formulation is the LUIKOV coupled partial differential equations having the 3 mentioned potentials as variables. The solution is accomplished by finite elements in space and finite differences in time. Material property values are allowed to vary with the prevailing conditions at each step in time. Time dependant values of moisture, temperature and pressure may be applied to the boundaries of the computational model. At each step in time the distribution, content and flow of moisture in and through the structure are computed. The program has been applied to simulation of moisture distribution in polymers and air cavities. Some examples are presented.

Keywords: moisture penetration, computer simulation, environmental effects, finite element program.

1. INTRODUCTION

Moisture sorption in products containing porous materials occur during manufacturing, testing, transportation, storage and operational conditions. In polymers and sandwich- or fiber reinforced structures, moisture variations cause swelling and structural deformations, structural strength decrease, weight variations and variations in dielectrical properties. Such effects are of importance in spacecraft reflectors. Other aspects are corrosion and short circuits in encapsulated electronic components causing malfunctioning. Experimental verification of product environmental ruggedness may be carried out in climatic test chambers. Such testing is timeconsuming and expensive and often has to be compressed in time and limited to assumed "worst case" conditions.

The use of computer simulation of climatic effects opens new possibilities for product development and optimization before manufacture. The method may also be applied as an alternative or complement to final test verifications.

Moisture sorption in porous materials is a complicated and in most cases highly non-linear procedure. In order to obtain a meaningful solution to transient climatic variations the coupled influence of moisture and heat, and in some applications even pressure, must be considered. Transfer of inert gases, vapours and liquids may take place by different methods, by molecular means in the form of diffusion and capillary actions and by molar means by filtration motion due to overall pressure differences.

The equations formulated by A.V. Luikov (ref 1) show the interdependence of heat, moisture and pressure effects. For most materials moisture related material values are significantly non-linear.

Simulation of moisture flow and distribution under such conditions requires a step by step solution in time with an update of material parameters at each timestep.

By transforming the equations to a Finite Element (FEM) formulation a further advantage is obtained, in that the geometry of the component subject to the moisture may be accurately described and transformed to a computer model. The size and shape of the boundary surfaces subject to climatic changes may be accurately described.

2. THEORY

2.1 The LUIKOV equations

The Luikov (1) equations for moisture flow in porous materials due to the simultaneous combined influence of gradients of moisture, temperature and pressure are:

$$\begin{aligned} C_T \frac{\partial T}{\partial t} &= K_{11} \nabla^2 T + K_{12} \nabla^2 m + K_{13} \nabla^2 P \\ C_m \frac{\partial m}{\partial t} &= K_{21} \nabla^2 T + K_{22} \nabla^2 m + K_{23} \nabla^2 P \\ C_P \frac{\partial P}{\partial t} &= K_{31} \nabla^2 T + K_{32} \nabla^2 m + K_{33} \nabla^2 P \end{aligned} \quad \dots 1)$$

Here the transfer of vapour or liquid can

take place by molecular means in the form of diffusion as well as by molar means as filtration motion due to pressure differences. Chemical reactions and the influence of material dimensional changes due to swelling are assumed to be small and negligible in this formulation.

If the influence of external pressure variations may be neglected, as is most often the case, the equations reduce to

$$C_q \frac{\partial T}{\partial t} = \nabla \cdot [K_q \nabla T + K_e \nabla U] \quad \dots\dots\dots 2)$$

$$C_m \frac{\partial U}{\partial t} = \nabla \cdot [K_s \nabla T + K_m \nabla U]$$

for heat and mass flow respectively.

The coefficients above contain the following moisture related material properties:

$$\begin{array}{cccc} K_q & k_q + \epsilon \lambda \rho a_m \delta & K_m & a_m \\ K_e & \epsilon \lambda \rho a_m & C_m & 1 \quad \dots 3) \\ K_s & \delta a_m & C_q & \rho c_q \end{array}$$

T = temperature, P = pressure, U = moisture potential
 ρ = density of dry body, λ = latent heat of water
 k = thermal conductivity, k_m = moisture conductivity
 c_q = specific heat capacity, c_m = specific moisture capacity
 ϵ = thermogradient coefficient, a_m = moisture diffusivity
 δ = ratio vapour diffusion/total diffusion

2.2 Finite Element formulation

The basic principle of the Finite Element method is that the behaviour of a continuous body can be represented by a finite number of subregions, known as elements. Approximating functions are used to define the response of individual elements to applied loads, and adjoining elements are interconnected through a finite number of nodal points describing the geometry. It is the behaviour of a variable, such as temperature, moisture etc. at these nodal points that is the basic unknown of the problem.

By replacing the Luikov equations by the discretized form of finite elements as in a structural mechanics problem a computer model for moisture and heat flow is obtained.

The variation of temperature and moisture potential throughout the material is approximated in terms of the nodal values T_s and U_s

$$T \approx \sum_{s=1}^n N_s(x,y) T_s(t), \quad U \approx \sum_{s=1}^n N_s(x,y) \bar{U}_s(t) \quad \dots 4)$$

Using the well known Galerkin and Greens methods for operations on finite element equations, the result is summarized below as a single equation

$$K(\phi) \phi + C(\phi) \frac{\partial \phi}{\partial t} + J(\phi) = 0 \quad \dots\dots\dots 5)$$

The vector ϕ is the wanted unknown variables of temperature and moisture potential at each nodal point in the mesh and J is the boundary flow of heat or moisture.

2.3 Solution in time

For moisture flow problems the effect of the time variable is of importance. The time variation may be obtained by a finite difference recurrence formulation to be solved at each timestep. Here the numerical solution is achieved by using Lee's three level time stepping scheme:

$$\phi^{n+1} = - \left[\frac{K^n}{3} + \frac{C^n}{2 \Delta t} \right]^{-1} \left[\frac{K^n \phi^n}{3} + \frac{K^n \phi^{n-1}}{3} - \frac{C^n \phi^{n-1}}{2 \Delta t} + J^n \right] \quad 6)$$

The superscript n refers to the time level and Δt refers to the timestep. Here the solution for time level $n+1$ is achieved by evaluating the coefficient matrices at time level n .

In order to obtain a mathematically stable solution in time there are limits on the size of the timestep as the solution marches on.

The full set of simultaneous equations have to be solved at each step. This requires decomposition of the "stiffness" matrix and back substitution of the variables at each step.

The Luikov equations produce a nonsymmetric stiffness matrix. A symmetric formulation may be obtained by assuming that certain material properties do not vary significantly for the conditions simulated. This partly linear formulation requires less computer time and disc storage space.

2.4 Computer Program

A computer program **MOISTCOMP** for analysis of transient moisture flow through multi-material bodies according to LUIKOV's theory is described below.

2.4.1 Preprocessor capability:

- Interactive input of all data for problem description
- Moisture related material properties may vary with temperature and moisture content
- Easy change of parameters for time-stepping and restarts
- Plotting of nodes and elements in computer model
- Moisture related material values available from data base
- Special modelling feature for thin moisture barrier films
- Database for moisture related material properties

2.4.2 Main Program capability:

- 300 nodes, 100 elements, 5 materials
- Constant or time varying boundary conditions
- Assembly and solution of system equations
- Automatic timestepping scheme
- Computes moisture potential, temperature (and pressure) at nodal points at each timestep in two-dimensional or rotationally symmetric models
- Computed values written to port hole disc file for postprocessing or restart purposes

2.4.3 Postprocessor capability:

- Computes and presents colour diagrams of distributions of moisture potential, content or flow through the model.

The MOISTCOMP program is written in FORTRAN and may be run on a workstation or mainframe computer.

2.5 Modelling of barrier films:

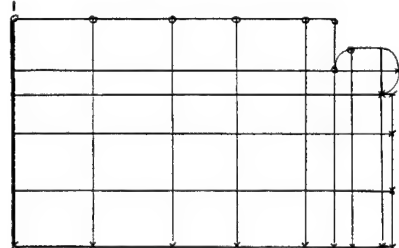
Moisture barrier films are often only parts of a mm thick. For numerical reasons such small elements are not easily introduced and solved in the FEM model. Films may therefore be modelled as a local moisture resistance between coincident nodes, thus avoiding numerical difficulties in the solution.

3. EXAMPLES

2 examples will demonstrate the use of the program. The first problem studied is moisture flow and distribution in a plate of polymer material with a nitril rubber seal. The second problem demonstrates moisture variations in the airfilled interior space of a cylindrical component. In these examples variations in ambient pressure are assumed small and the pressure term is therefore neglected.

Case 1. Moisture flow and distribution in polymer plate with rubber seal.

The geometry is shown in (fig 1) and the computational model in (fig 2). This is a constant temperature problem with one side of the plate being exposed to 100% humid air, the air on the other side being kept at 50% humidity. Initial conditions are 20°C and 50% humidity. The moisture flow through the plate is shown in (fig 3). After 20 hours the moisture front has progressed to the inside and throughflow begins. The flow increases rapidly until there is a steady state distribution across the plate. Thereafter there is a steady flow through the plate. The simulation is run up to and past the time of steady flow. This is 8.5×10^{-9} kg/h after 48 days (fig 3). The steady state moisture distribution through the plate is shown in (fig 4).



○ Boundary node with 100% Rh

× Boundary node with 50% Rh

Finite Element Mesh, rotational symmetry

FIG: 2

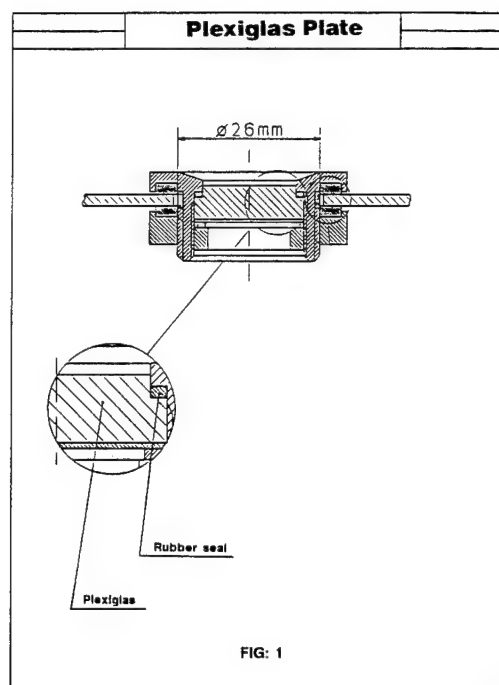


FIG: 1

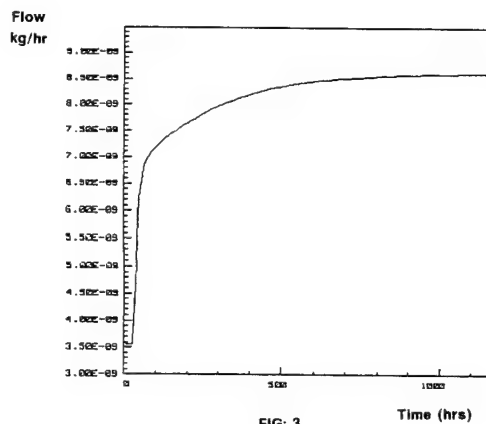
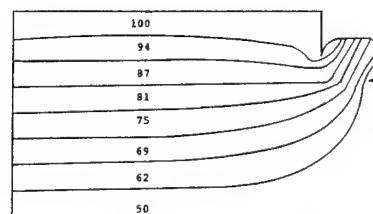


FIG: 3

Moisture flow through plexiglas



Moisture potential distribution through plate at t = 1000 hrs

FIG: 4

Case 2. Humidity variation in air inside container.

The example studied is a cylindrical shell of 100 mm height and 100 mm inside radius with a nitril rubber seal of rectangular cross-section between lid and cylinder (fig 5). The seal and contained air are initially at 30C and 85% relative humidity. The walls of the structure are assumed thermally insulated.

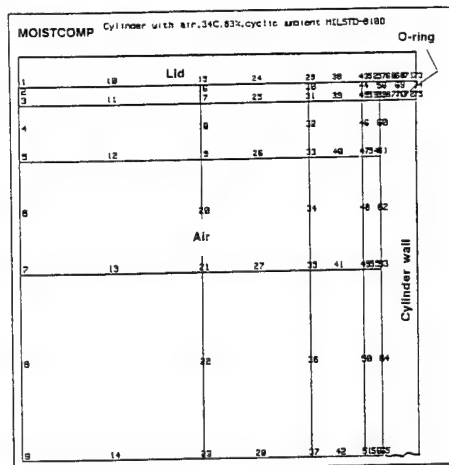


Fig 5
Finite Element model

Cyclic ambient conditions of temperature and humidity are applied at the seal surface as shown in (fig 6). This 24 hour test cycle is specified in MILSTD-810D for aggravated climatic conditions.

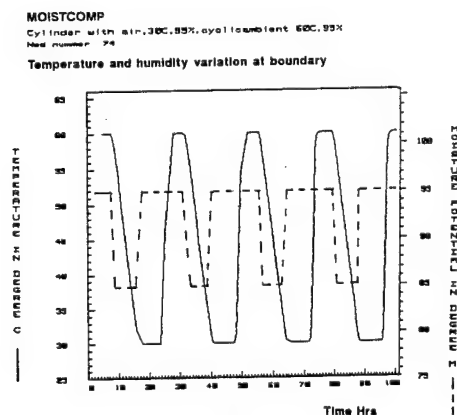


Fig 6

The moisture and heat flow through the seal into the enclosed air is computed. The computer simulation indicate that the ambient humidity variations are not sufficient to cause moisture ingress through the seal, the net moisture content in the contained air-filled space remains unchanged.

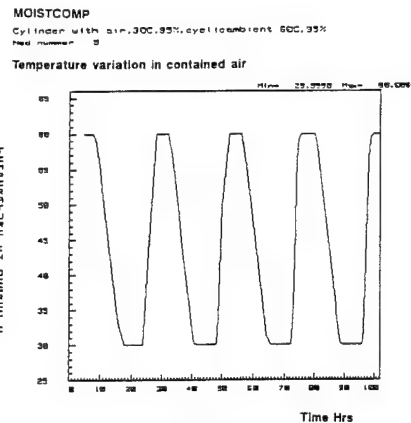


Fig 7

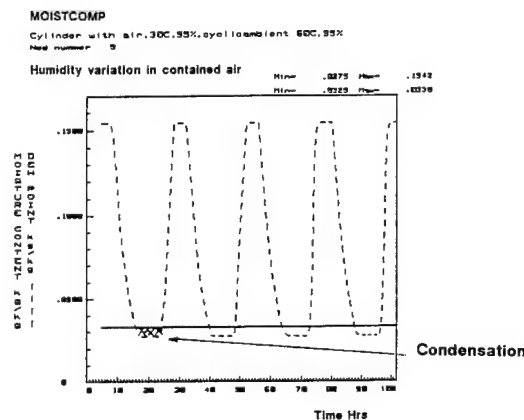


Fig 8

The ambient temperature variations penetrate rapidly into the cylinder (fig 7), and will cause condensation and water drops on the walls (fig 8) during the first cycle(s).

In the computations for the cases above the key moisture related material values used were:

Polymer plate: density: 1170 kg/m³, moisture capacity 0.4%, diffusivity 6.4x10⁻⁸ m²/hours (at 20 C)

Rubber seals: density: 1290 kg/m³, thermal conductivity 570 J/m h K, moisture sorption and diffusivity are allowed to vary with temperature and moisture content up to maximum values of 1.6% and 1.7x10⁻⁷ m²/hour (at 71 C)

Air: input material values vary with temperature as taken from a Mollier diagram at 1000 mBar atmospheric pressure.

4. CONCLUSIONS

The application of the finite element method to analysis of moisture flow and distribution has been demonstrated. The MOISTCOMP computer program described has been developed as a practical engineering tool for analysis of climatic effects in moisture sensitive products. The combined effects of time varying gradients of moisture, temperature and pressure may be included in the analysis.

Using this method complex multimaterial designs may be subjected to climatic variations in the way they would occur in real engineering problems, and the moisture ingress analyzed.

The computed results are reasonable, it is therefore concluded that the method may be used for parametric studies and comparisons of moisture penetration and distribution for different alternative designs. In order to fully utilize the capabilities of the program more detailed knowledge of moisture related material properties at different temperatures, to be used as input data, is required. The design and execution of such tests is a matter to be looked into.

A further development of the method would be implementation of linear or nonlinear elasticity theory, and subsequent computation of moisture related stresses and deformations. The present use of the finite element method for the moisture flow part of the solution facilitates such a development.

This development work has been subsidized by the Swedish Defence Material Administration.

5 REFERENCES

- 1) Heat and Mass Transfer, A.V.Luikov, MIR Publishers, Moscow, 1980.
- 2) A numerical solution of two-dimensional problems involving Heat and Mass Transfer R.W.Lewis et al, Int Journal of Heat and Mass Transfer, Vol 19, 1976.
- 3) MOISTCOMP Users Manual, Revision 2, Otto Wilmar, DNV Ingemansson AB, 1991.

N92-23807

A NEW TEST FACILITY FOR MEASURING THE COEFFICIENT OF MOISTURE EXPANSION OF ADVANCED COMPOSITE MATERIALS

G. Romeo¹, E. Miraldi², G. Ruscica³, F. Bertoglio³, G. Ruvinetti¹

Politecnico di Torino, Turin, Italy

¹Dept. of Aerospace Eng; ²Dept. of Physics; ³Dept. of Energetics

ABSTRACT

A new test facility is described; it has been designed in order to carefully measure CME in specimens made of advanced composite materials.

The facility is composed essentially by a thermostat contained in a vacuum chamber (10^{-3} Pa), in which five CFRP's samples with the displacement transducers are enclosed, and they can be contemporary measured and compared in the same environmental conditions between them and with an invar reference specimen. With a long term stability in the temperature of ± 0.1 K and a careful choice of displacement sensors (1×10^{-7} m is the typical accuracy) a maximum error of $\pm 5 \times 10^{-6}$ (m/m per $\Delta M/M$ %) in the CME has been confirmed.

A coefficient of moisture expansion of 3.85×10^{-5} and 3.098×10^{-3} was obtained along the fibre direction and normal to fibre direction, respectively.

Keywords: Composite, CME, Test facility.

1. INTRODUCTION

Structures with a high degree of dimensional stability are often required of many spacecraft components making especially attractive the use of advanced composite materials; since they are available with a wide range of mechanical and physical properties it is possible to tailor a structural component with a near zero coefficient of thermal expansion (CTE) by choosing the appropriate material and stacking sequence.

However, the dimensional stability of composites is highly affected by exposure to humidity environments causing swelling and plasticization of the resin system (Refs. 1,2).

In the space environment, the composite structure will have a moisture desorption and shrinkage modifying, for example, the initial calibration of optical instruments and in most cases it is necessary to evaluate accurately this dimensional variation, possibly in the quasi-real working condition.

Based on the Classical Lamination Theory (CLT), strains and curvatures of a laminate subjected to moisture load are evaluated by the coefficient of moisture expansion (CME) or swelling coefficient; the CME, or β , is defined by the ratio of length variation of specimen to the mass variation (%) due to moisture absorption or desorption:

$$\beta = (\Delta L/L)/(\Delta M/M)\%$$

Expected values of β_1 and β_2 for typical CFRP materials are 0.00002 and 0.005 for percent mass variation, respectively.

The swelling coefficient in the fibre direction is usually neglected in many handbooks, included the ESA Composite Design Handbook; however, since a length variations of few microns has to be evaluated, the measurements of the CME along the fibre direction (β_1) requires a very accurate test equipment. None standard procedure it was possible to find in the literature.

The several methods used for determining β are based on the measurement of dimensional variations of samples subjected to moisture absorption between a dry state and a stable saturated one; tests are made at atmospheric pressure at 293 K and 50% RH requiring, often, about one month for each specimen.

In Ref. 3 a dilatometer was used which incorporates a silica sample holder and a linear displacement sensor subjected, within a controlled enclosure, to 343 K and 95% RH; the dimensional variations were continuously measured while weight variations were discontinuously measured on similar sample suspended near the first; about five days are required for each specimen.

In the new test facility developed in our laboratory the measurement are made, indeed, in an opposite manner; specimens are first subjected in a climatic chamber to an accelerated absorption cycle at 348 K and 95% RH; after on, specimen are placed into a vacuum chamber, heated at a temperature of 333 K and exposed to a vacuum environment of about 10^{-3} Pa. Six specimens can be tested contemporary in four-seven days, reducing drastically time necessary to the characterisation of materials.

2. THE FACILITY

2.1 General Requisites

In this paper a new facility is described, now operating at Politecnico of Turin, that has been designed for making the test in the same experimental conditions on a representative number of the samples (5 + 6) cut from a single unidirectional or quasi-isotropic CFRP panel.

These simultaneous tests can give a very representative mean value of the measured quantity, since:

- a. The errors due to a non correct experimental set-up are minimized with respect to the "one at a time" proceeding.

- b. The errors due to the uncontrolled changes in the environmental conditions can be recorded if one of the specimens is made of invar or zerodur whose physical-chemical parameters are known.

2.2 Description of the Apparatus

The facility is composed of two main parts, namely:

- a. One thermostat enclosed in a vacuum chamber, in which are located the samples and the measuring systems.
- b. A temperature regulating system, realized with a circulating fluid network.

2.2.1 The Fluid Network (Fig.1). The fluid pipes feed the thermostat, item T, by a constant head supply, item A.

The liquid temperature is kept constant within ± 0.01 K by means of a heat rate controller, item B, connected with the superior tank, or by a chiller, item C, plugged in the inferior tank, item D.

The operating range of the fluid network is limited to $-30 \div 70$ °C for the tests described in this paper.

The fluid enters inside the vacuum chamber and feeds the thermostat with a constant flow rate, in order to improve the stability of the temperature in the apparatus.

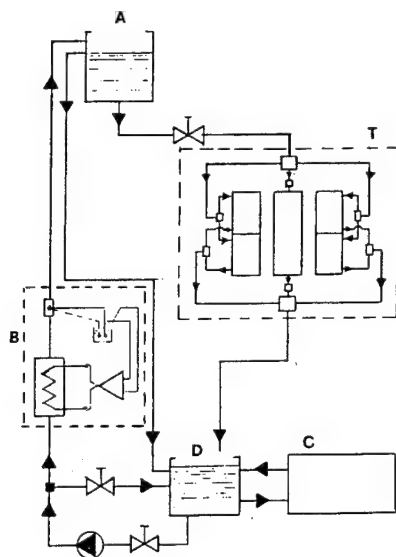


Figure 1. Fluid network

2.2.2 The Thermostat (Fig.2). The thermostat has been designed in order to test simultaneously six specimens with a maximum size of $200 \times 25 \times 4$ mm. The displacement sensors and the samples are supported and kept within six frames made of invar and mechanically disjointed from the inner and outer parts of the thermostat.

The heating of the CFRP specimens is effected by radiation. In order to improve the heat exchange the frames and the sensors are completely surrounded by isothermal surfaces that are coated with a black paint with a high radiation emissivity and a low outgassing.

The frames that inclose the samples are made of invar in order to have a minimal error in the moisture swelling coefficient measurements; namely a variation of 0.1 K produces a change in the frame length of $2 \cdot 10^{-8}$ m, since the typical invar CTE is of the order of magnitude of 10^{-6} K $^{-1}$.

The thermostat is made in aluminium to insure a good thermal conduction and temperature uniformity. It is composed of three main parts: a inner cylinder (item A) and two hemicylindrical hollow shells (items B₁ and B₂).

Great care has been taken in the design of the inner cylinder in order to avoid the temperature gradient in the specimens under test and in order to keep in an isothermal environment the displacement transducers, with their signal plugs and cables, and the electrical wires of the Pt 100 sensors connected with the invar frames.

Two pairs of shafts (items C₁, C₂ and D₁, D₂), allow to open the isothermal cavities in order to install the invar frames when they are ready for the measurement run.

With this device the three parts of the thermostat can be brought exactly in contact without mismatching the six invar frames yet inside.

The vacuum chamber, in which the thermostat is enclosed, is cylindrical with horizontal axis 2.5 m long and 1.5 m in diameter.

The final vacuum (about 10^{-3} Pa) is obtained with two rotative and one turbo-molecular pumps in cascade.

2.2.3 Displacement Transducers. A long set of preliminary tests has been made on the displacement sensors, in order to chose the transducers appropriate for this task and to match the suitable working conditions.

With the invar-frames described above, the spring loaded LVDT (Linear Variable Differential Transformers) have shown the best performance, namely:

- a. The output voltage is not affected by pressure change;
- b. with proper line-voltage stabilization the driving and measuring electronics shows an equivalent RMS noise bounded within $\pm 10^{-8}$ m;
- c. with the supporting structures properly sound-insulated, the transducers are not affected by a normal level of environmental noise;
- d. the surroundings of the LVDTs must be accurately isothermal since they show a variation in the output, due to a change only in temperature, that is equivalent to some tents of micrometer per degree;
- f. the operating range of the transducers can be chosen in the order of magnitude of 10^{-3} m since the total swelling deformation of composite samples is 10^{-4} m about. In the useful range the output ratio: voltage /displacement is found to be highly linear.

2.2.4 Experimental Procedure. The starting operations consist of: assembling each specimen in his frame, adjusting mechanically the transducer for a near zero output, putting the invar frames in their seats in the inner thermostat.

These preliminary procedures can be performed in very short time in a temperature not far from the operating one (60 °C typically), in the atmosphere.

The data acquisition starts as soon as the temperature of the monitored frames, and therefore the specimens, has reached the imposed one.

A first thermocouple probe is used to monitor the filling pressure up to 5 Pa and then a ionization-gauge can measure the operative pressure.

The temperatures of the fluid entering and leaving the thermostat and that of the invar frames are monitored with Pt 100 sensors, individually calibrated, while the external fluid circuit is controlled by means of T-type thermocouple.

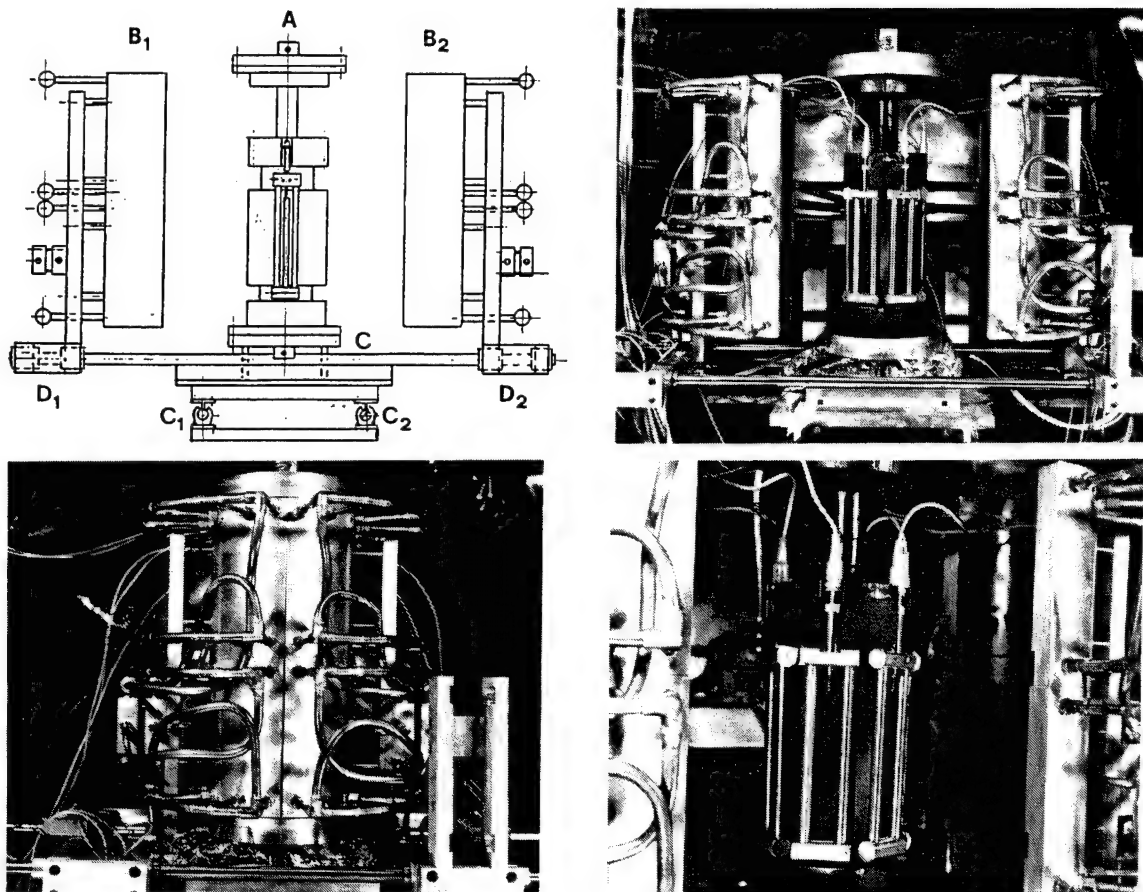


Figure 2. View of the thermostat including invar frames supporting CFRP samples

3. EXPERIMENTAL RESULTS

Several tests are in progress on CFRP materials, made from M40/914 prepreg, having different lay-up and thickness. Samples type A have 8 unidirectional layers and are 1 mm thick; type C have the lay-up $(0 \pm 60^\circ)_s$ and they are 0.76 mm thick. All samples were tested both in fibres direction (0) as in normal direction (90). Specimens were 140 ± 0.3 mm long. Specimens were for first subjected to the accelerated absorption cycle; the absorption kinetic curves for A-0, A-90 and C-0 samples are reported in Fig. 3; the abrupt loss in mass, measured after five days, is only due to an electrical black-out during Sunday. Samples A have an uniform absorption behaviour in the first part of the cycle; after on diverge one to each other of about 10% with respect to the average value. Samples C have a more uniform behaviour.

Each set of five specimens (four for samples A-90) was then placed into the vacuum chamber, heated at a temperature of about 333 K and exposed at a vacuum environment 10^{-3} Pa. As consequence of the moisture desorption, the specimens had a shrinkage; for each set, the length variation detected by LVDTs, as function of the time are reported in Figs. 4 ÷ 6; the overall look of curves seems to be good.

In each picture 6 curves are depicted; one is related to the invar sample, while the others to the CFRP ones; the desorption kinetic curves, as result from the length variation, seem to be almost similar to those one's of absorption.

Fig. 4 refers to samples type A-0; test was carried out at 337.4 K; specimens n.1 and 2 have recorded an higher length variation, as consequence of an higher desored moisture too. The length variation recorded for invar specimen (maximum value after 95 hours is 0.0001 mm) gives the error of the measurements; with respect to the average value recorded for 5 specimens (0.00414 mm) it represents the 2.4% only. The most important results obtained at the end of the test are reported in Table 1. A mean value of $\beta_1 = 3.851 \times 10^{-5}$ was obtained with a standard deviation of 5×10^{-6} .

Fig. 5 and Table 1 refer to samples type A-90; because of higher length variation expected, test was carried out at 320.5 K and limited to 77 hours; as effect of the temperature, a lower mass desorption was recorded in comparison with samples A-0; a mean value of $\beta_2 = 3.098 \times 10^{-3}$ was obtained with a standard deviation of 5×10^{-5} .

Fig. 6 and Table 2 refer to samples type C-0; test was carried out at 322.5 K and extended up to 136 hours; as effect of the temperature, about the same mass desorption, in higher time, was recorded in comparison to samples A-0. A mean value of $\beta_x = 13.476 \times 10^{-5}$ was obtained with a standard deviation of 6×10^{-6} . A maximum length variation of 0.0002 mm was recorded for invar specimen; with respect to the mean value recorded for 5 specimens (0.01486 mm) it represents the 1.4% only.

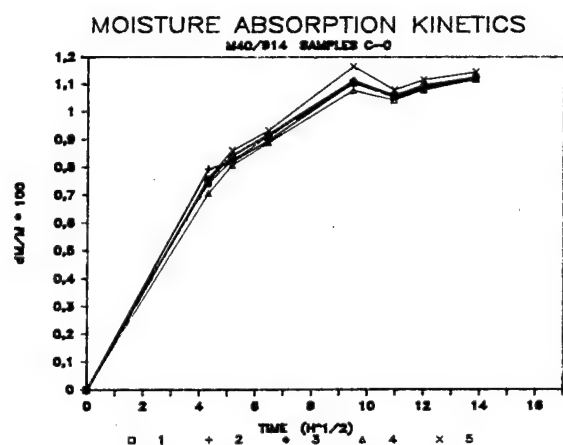
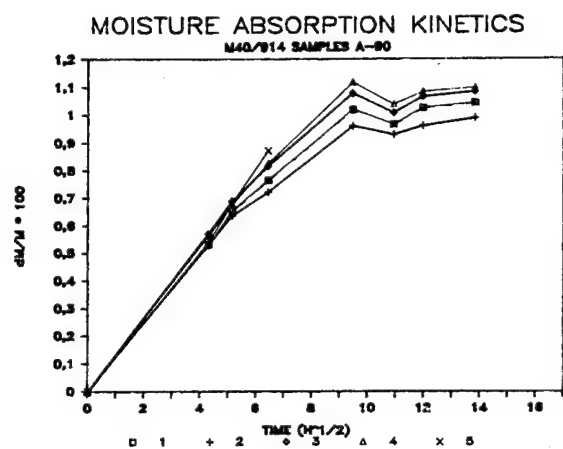
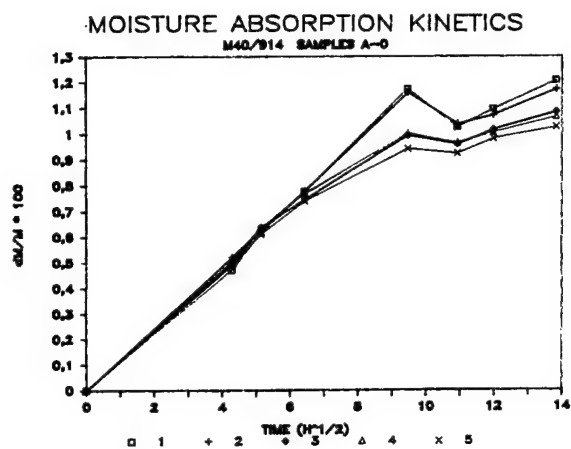


Figure 3. Moisture absorption Kinetics of CFRP M40/914 samples (A-0; A-90; C-0)

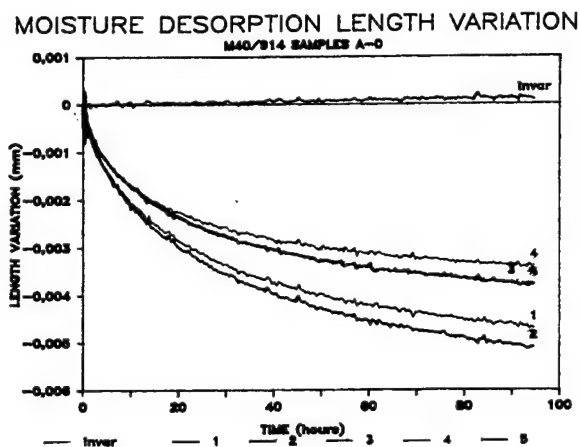


Figure 4. Desorption length variation of sample A along fibres direction

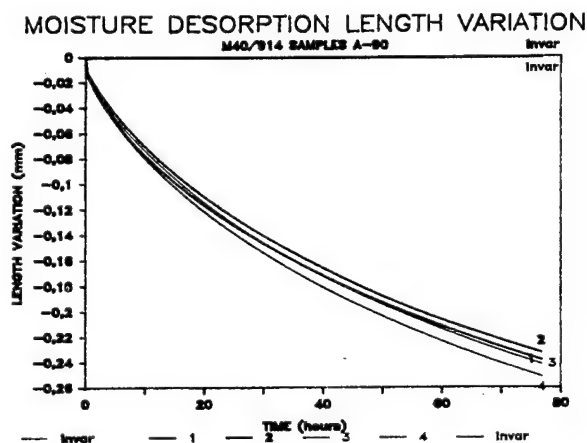


Figure 5. Desorption length variation of sample A normal fibres direction

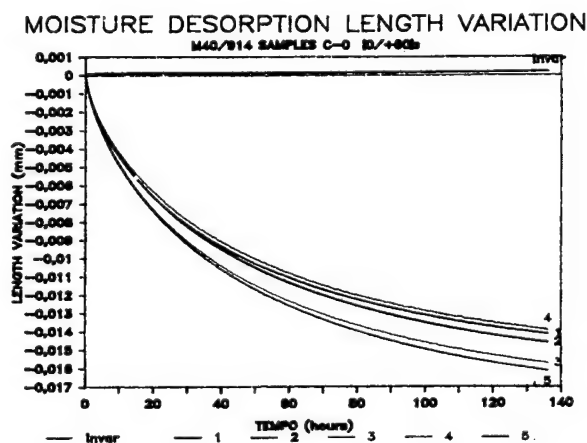


Figure 6. Desorption length variation for quasi-isotropic sample

Table 1: CME of graphite/epoxy (M40/914) material along fibre direction (A-0), normal to fibre (A-90)

N	ΔL [mm]	$\Delta M/M$ (%)	$\beta_1 \times 10^5$	ΔL [mm]	$\Delta M/M$ (%)	$\beta_2 \times 10^3$
1	-0.0046	-0.809	4.14	-0.2378	-0.554	3.06
2	-0.0051	-0.789	4.60	-0.2321	-0.525	3.15
3	-0.0038	-0.755	3.56	-0.2412	-0.568	3.03
4	-0.0034	-0.769	3.14	-0.2509	-0.567	3.15
5	-0.0038	-0.705	3.82	*	*	*

Table 2: CME of graphite/epoxy (M40/914) material for quasi-isotropic $[0/\pm 60]_S$ (C-0)

N	ΔL [mm]	$\Delta M/M$ (%)	$\beta_x \times 10^5$
1	-0.0141	-0.788	12.79
2	-0.0145	-0.766	13.53
3	-0.0157	-0.797	14.08
4	-0.0139	-0.776	12.81
5	-0.0161	-0.812	14.17

For specimen C-0, the β_x analytical value predicted by CLT (Ref. 1) is 14×10^{-5} . During tests, not all the moisture absorbed was fully desorbed.

In our opinion, the length variation recorded by invar sample is due to a thermal drift vs. the time of the measuring electronic instruments. An improvement is planned to eliminate this drift.

4. CONCLUSION

The experimental results show the facility to be adapt to perform measurements of swelling coefficient with very high accuracy. It is able simultaneously to measure the elongations of 6 specimens minimizing the experimental error due to different mechanical and thermal set-ups; at the same time it is possible to compare the measurements with a stable zero reference.

The same apparatus may be used for CTE measurements after CME ones without some change of the set-up.

With a reasonable approximation in the moisture absorption process the CFRP seems to follow a fickian diffusion (linear dependence $\Delta M/\sqrt{t}$); instead the desorption process shows a deviation from the above model that according to Springer (Ref.4) occurs at elevated temperatures.

Some improvements are planned to measure continuously the mass change of the specimens for studying the relation of $\Delta L/L$ and $\Delta M/M$, considered linear normally, to study accurately the temperature influence on desorption, and to eliminate the thermal electronic drift.

5. REFERENCES

1. Romeo G., Miraldi E., Gazzi M., 1988, Thermal and moisture expansion properties of advanced composite materials. Proc. Workshop on Advanced Structural Materials : Design for Space Applications, Noordwijk, NL, ESA WPP-004, 67-72.
2. Miraldi E., Romeo G., Ruvinetti G., 1990, Some results on the influence of the fibre orientation in the thermal expansion coefficient of advanced composite materials. 12th European Conf. on Thermophysical Properties, Vienna.
3. Baudinaud V et al, 1987, Thermal expansion and moisture expansion of carbon epoxy composite materials. High Temperatures-High Pressures, 19, 411-416.
4. G.S. Springer, 1988, Environmental effect. The composite design, ed. by Stephen W. Tsai, Sec. 16.6+16.18.

**SESSION
1.1.D**

**LAUNCHERS
II**

DEVELOPMENT

PRECEDING PAGE BLANK NOT FILMED

N92-23808

528-15

54720

ARIANE 5 STRUCTURAL DEFINITION OF THE UPPER COMPOSITE

A.L. GONZALEZ

EUROPEAN SPACE AGENCY

ABSTRACT/RESUME

This paper deals with the definition of the upper structural assembly of the Ariane 5 launcher. The philosophy of multiple payload launching is analysed and the different upper configurations presented. The general dimensioning requirements are then reviewed: payload factors and flight environment, particular requirements coming from the kinematics and dynamics of the payloads, and general launcher architecture. Special attention is given to the non-uniform load flow transmission and the pyrotechnic shocks induced in structure separation. The main structural tests of the upper structures are then outlined.

Ariane 5 launcher, structural dimensioning, flight environment, structural tests.

1. INTRODUCTION

The Ariane 5 launcher is designed to launch automatic payloads as well as the Hermes spacecraft. In both cases, the lower composite includes two solid boosters and a cryogenic stage. For launching satellites, the upper part comprises a propulsive stage, the launcher electronics, and the different support and protective satellite structures. The main characteristics of the launcher are given in Figure 1.

This paper deals with the upper structures definition. First, multiple launch philosophy is analysed and the structural configurations introduced. Next, the dimensioning requirements are reviewed. And in the last section, the structural tests foreseen are addressed.

2. UPPER COMPOSITE CONFIGURATIONS

2.1 Multiple Launch Philosophy

The philosophy of multiple launch was established in former Ariane vehicles. Ariane 1 was developed to launch a satellite of 1.7 tons in GTO (Geostationary Transfer Orbit). In Figure 2, flight L8 we see how a satellite fills up the fairing volume while achieving a maximum launch capacity of 1833 kg, in excess to that of the design performance. Having such capabilities in terms of mass and volume, to launch smaller satellites required to establish a multiple launch strategy. Initially the configurations were built as in flight L3 (Figure 2), however the constraints of the lower payloads are numerous, hence the flexibility of launcher accommodation low. Therefore, an internal structure, SYLDA 3900, was developed to perform double launch. In this manner, we can see the accommodation of two payloads in flight L6, one of approximately 1 ton on top of SYLDA and a small one of 130 kg inside the structure. The SYLDA 3900 mass was approximately 180 kg.

Ariane 2 and 3 were updated versions of the initial launcher, with performances of 2.1 tons and 2.6 tons (GTO) respectively. Both versions having the same new biconic fairing, Ariane 2 was used most often for single launch as in flight V20 (Figure 3), and Ariane 3 for double launch as in V21 (Figure 3) - both using SYLDA 4400 (updated version of SYLDA with a mass of approximately 190 kg).

Ariane 4 was conceived with the aim of achieving a more powerful version with a high degree of versatility. From the propulsion point of view, the addition of solid and liquid boosters allows the launcher to go from 2 tons (GTO) of performance in basic configuration (no boosters) to up to 4.2 tons with four liquid boosters. In the upper part structures, two fairing lengths were qualified as well as an external structure: SPELDA. The compatibility of SYLDA was maintained and in this way it was possible to obtain a smaller volume with low mass impact (190 kg). The use of SPELDA provides higher payload volume at a higher mass penalty (approximately 400 kg). The use of the different structures is illustrated in Figure 4.

2.2 Ariane 5 Configuration

A market survey on satellite trends showed an increase in mass and volume. Based on this tendency, Ariane 5 was conceived as a launcher to place two 3-ton satellites of the same volume (diameter 4.57m x 4.5m) in GTO. These initial requirements implied an external structure (SPELTRA) like the Ariane 4 SPELDA. In addition to this basic mission, Ariane 5 was to be capable of single launch with a high mass payload, or of triple launch to accommodate smaller satellites. For high mass payloads, a long fairing is foreseen. In the case of triple launch, two cases were considered: a) 1 long SPELTRA with a short SPELTRA, b) 1 long SPELTRA and a internal structure (SPILMA) on the SPELTRA and inside the fairing.

Option a) was initially retained because the frequency of triple launch foreseen was low, and the development cost also low. But after detailed analysis, it was discovered that this triple launch configuration was the dimensioning case for the aerodynamic loads and the large increase in payload volume was parallel with a large decrease in payload mass available. Therefore, SPILMA seemed to be a more suitable solution as the first problem disappeared, and with respect to payloads, performance mass decreases less with a decrease in volume offered. This is still sufficient for smaller payloads.

Ariane 5 upper part configurations are shown in Figure 5.

3. DIMENSIONING FACTORS

3.1 Payload Requirements

Ariane 5 performance for satellite launch is the following:

- Payload mass of up to 6800 kg in GTO including multi-satellite launch structures. This represents 5900 kg net of payload in double launch
- Payload mass of 18000 kg in LEO (Low Earth Orbit: 550 km x 28.5°) and 10000 kg in sunsynchronous orbit (800 km x 98.6°)

The volumes of the different configurations are shown in Figure 5.

The physical interface payload/support structure is of cylindrical flange type. The basic diameters have been established in accordance with the Ariane 4 launcher. Diameters 1920 and 2624 are common and dimensioned to carry up to 4500 kg, and a new diameter of 3936 is foreseen for the heaviest payloads. A diameter of 2624 is provided on top of L7 and SPELTRA frustra. A standard adaptor will be developed to pass from 2624 to 1920. Diameter 3936 is located at the VEB/L7 interface flange.

On the ground, access to the inside of the structures must be possible. Doors of 600 mm diameter are provided in different locations.

Payload ventilation during launch preparation implies the inlet duct mechanical interface and the exhaust holes, also used in flight for equalisation of the internal and external static pressure.

3.2 Induced Environment

The induced environment seen by the upper part comes mainly from the propulsion and aerodynamics. The most important events coming from these sources are outlined in the following sections.

3.2.1 Booster Propulsion

The boosters are a major source of mechanical loads: transient ignition loads, combustion oscillation, quasi-static acceleration, asymmetric thrust burn-out.

The curves in Figure 6 show the thrust build-up and the general profile. The thrust build-up is performed in a few tenths of a second. This will induce dynamic longitudinal loads in case of symmetric booster ignition, combined with lateral acceleration in case of asymmetric build-up. The global profile can be divided into three phases. In a first step of about 20 seconds, a high thrust is delivered by the boosters. The second phase starts with a lower thrust level, increasing steadily up to approximately 100 seconds, where the maximum longitudinal acceleration of about 4 g is reached. From that point until the end of booster flight, thrust decays slowly to avoid control problems in case of booster asymmetries.

Thrust oscillation can occur associated with the longitudinal acoustic resonances of the motor and the axial modes of the structure.

Finally, we will mention the ignition and duct overpressure coming from the gas ejected when going in and out of the ground exhaust ducts. This overpressurisation creates shock waves which can excite the launcher laterally.

3.2.2 Cryogenic Stage Propulsion

The HM60 engine propels the cryogenic stage. It is ignited on the launch pad before the boosters to verify proper functioning. The ignition time is longer than that of the boosters, the level of thrust much lower, and the dynamic loads induced by the HM60 are not as important as that of the boosters. Maximum acceleration at the end of stage flight is near that obtained during the booster phase.

A dynamic case to be considered corresponds to engine shutdown. Vibrations are induced that, in the case of Ariane 4, produce high acceleration at satellite levels (Figure 7).

During stage propulsion, POGO (structure propulsion coupling) appears. A damping device is foreseen in the oxygen line, but the low longitudinal frequency excitation must be taken into account.

3.2.3 Aerodynamic and Thermal Environment

During the atmospheric part of flight, aerodynamics play a major role in load generation. After take-off, the launcher trajectory is vertical for 5 seconds, and afterwards the vehicle engages a pitching manoeuvre with non-zero incidence. This becomes zero, and a zero incidence gravity turn is developed up until the end of booster flight. After booster separation, optimisation of the trajectory is performed, once again resulting in launcher incidence.

This quick overview of main trajectory events shows that nominal incidence is zero during the phase when maximum dynamic pressure appears. Nevertheless, launcher incidence exists due to lateral winds producing quasi-static loads. Lateral dynamics are also induced by wind gusts, which, for dimensioning purposes, are assumed to occur at the highest dynamic pressures.

Aerodynamic drag produces longitudinal quasi-static loads. The upper part specially concerned with this load is the fairing nose, supporting an important part of pressure drag.

The upper composite thermal environment during the atmospheric phase is created mainly by aerothermal flux. Again, the fairing forebody is deeply affected, and protection, as in the previous Ariane, is foreseen. This aerodynamic flux also dictates the instant for fairing jettison (flux < 1135 W/m²).

3.2.4 Summary of Quasi-Static Loads

The summary of the steady and low frequency dynamic loads as seen by the payloads is shown in Figure 8.

3.2.5 Acoustics

Three main periods usually considered are: take-off, transonic and maximum dynamic pressure. During take-off, acoustic loads are generated by the propulsion system. Blast waves already mentioned are of acoustic origin. While leaving the launch pad, acoustic waves reach the upper part directly, and, reflected by the pad and the mast, reinforce themselves to attain the highest level of sound pressure.

The source of the transonic and maximum dynamic pressure acoustics is aerodynamics. In the transonic case, shock buffeting generates the noise. In the latter case, the acoustic noise comes from the turbulent boundary-layer.

3.3 Other Launcher Requirements

3.3.1 Launcher Performance

The forebody shape of the fairing has great impact on launcher drag. This has been the reason for changing from the initial cylindric-conical fairing to the present "ogival" solution (Figure 9).

The masses of the upper part structures have a large impact on performance. Minimum mass is specified to gain more payload mass.

3.3.2 Launcher Dynamics

The upper structures in direct contact with satellites are the transmitting path for dynamic loads coming from the propulsive stages. Therefore stiffness requirements are imposed on the structures to avoid any dynamic coupling or amplification.

3.3.3 Separation Shocks

Wide-band frequency shocks originate during the various body separation. In order of occurrence we have:

- Booster separation from the central body
- Fairing jettison
- Upper composite separation (VEB level)
- Satellite + SPELTRA separation

3.3.4 Architecture

The architecture is based on two boosters transmitting thrust to the central body at two different points. High concentrated loads appear in the cryogenic stage upper skirt which cannot be transferred to the VEB with circumferential uniformity. There, the upper structures need to be optimised while considering non-uniform circumferential loads.

4. UPPER PART STRUCTURES

4.1 Structural Design

The upper part structures can be divided into external and internal parts. The external structures are of cylindrical shape with the fairing forebody of "ogival" form to reduce launcher aerodynamic drag. The diameter of 5405 mm provides a common neutral line to the different structures. The main internal structures are conical in shape to support the payloads. The L7 stage also contains a spherical shell to accommodate the tanks, engine and other equipment. And the VEB has two platforms to support the launcher electronic boxes.

The design is based on shells made of CFRP sandwiched with an aluminium core, except for the external cylinder of the VEB, made in reinforced aluminium, and the electronic box platform and L7 spherical shell sandwiched with aluminium skins. Frames are used in the interface planes between structures where the separation system is located. The table in Figure 10 shows the mass allocation to the panels, frames, and other structural elements. We can see that in the fairings and the SPELTRA the panels are the major contributors of total mass, while in the VEB and L7 stages the frames play a more important role.

4.2 Non-uniform load flow

This question arises from the launcher architecture and the structural design selected. As explained in para. 3.3.4, the boosters transmit the thrust at two points of the central body. The external upper part structures are cylindrical shells, therefore the problem of introduction of high concentrated loads in shells appears. Figure 11 shows two cases of axial load flow at the upper skirt/VEB interface and it can be the spikes in the boosters plane.

Another factor resulting in non-uniform load flow comes from the non-uniformity of the structures themselves: access doors, vertical separation system of the fairing. This last system includes two longitudinal stiff elements which were the subject of a detailed design to minimise the load concentration path.

4.3 Shock transmission

Shock loads present another problem for the upper part and specifically for the VEB. The VEB structure incorporates the system to separate the upper composite (without the fairing whose jettison is made before) from the cryogenic stage. This separation system consists of a pyrotechnic chord line cutting circumferentially the external VEB cylinder. As the electronic boxes are supported on the internal VEB cone, the transmission path between the source of the pyrotechnic shock and the boxes is very short. Special development work is being performed to properly define the damping materials to be included in the different joints encountered in the transmission path.

The other separation shocks will also be evaluated in the development and qualification programmes.

5. STRUCTURAL TESTS

The verification tests of the upper composite are divided into system tests and individual configuration assembly tests. The first ones affect more than one structural assembly while the latter ones regard the development and qualification process of each structure.

System tests deal mainly with the following:

- dynamic characterisation
- acoustics
- separation shock

For the dynamic characterisation of the launcher, three main tests are considered. The launcher can be considered built up of three bodies: the booster (two nearly identical units), the cryogenic stage and the upper composite. A test is foreseen to characterise each body.

The objectives of the acoustic tests are the verification of structural strength and validation of the vibro-acoustic models. A test is foreseen with the short fairing and another with an assembly including the cryogenic stage upper skirt, VEB, L7 stage, and SPELTRA.

Separation shock testing is a functional test programme aimed at the characterisation of the generated shock level, the transmission path, and the attenuation means. A test is planned with the structural assembly just described. This system test is coupled with the development and qualification shock programme of the VEB, due specifically to the problems explained in section 4.3.

The qualification programmes of each structure use static and sinusoidal tests on the one hand, and separation tests on the other. We specifically mention separation tests of the fairing which must be carried out under vacuum conditions.

6. CONCLUSIONS

The definition of the upper part configurations has been reviewed. Satellite requirements are the beginning constraints. The environment encountered and the launcher concept provide for other dimensioning factors. Objectives for the structural tests are mentioned.

The preliminary stages of the development programme are covered. Detailed definition and qualification tests are becoming more precise.

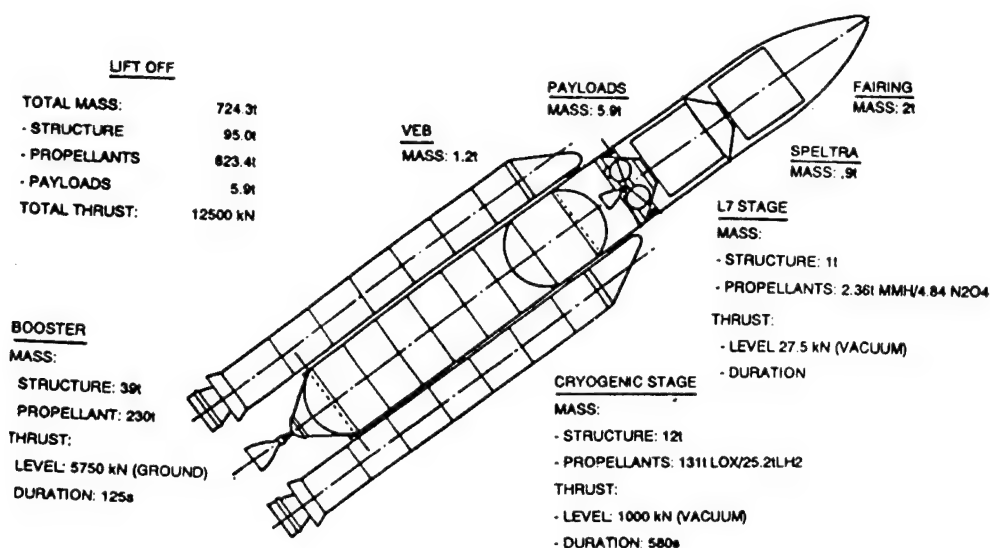


FIG.1 ARIANE 5. LAUNCHER MAIN CHARACTERISTICS

L8	L03	L6
AR1	AR1	AR1
INTELSAT V F8 (COMMUNICATIONS)	METEOSAT (METEOROLOGICAL) * APPLE COMMA & TECHNO * CAT (TECHNOLOGICAL)	ECS-1 (COMMUNICATIONS) * AMSAT PHILIP (RADIO AMATEURS)
1881	1678	1381

FIG.2 ARIANE 1 FLIGHTS

V20	V21
AR2	AR2
TV SAT 1 (T.V. BROADCASTING)	SPACENET IIIIR / GEOSTAR R01 (COMMUNICATIONS) * TELECOM 1C (COMMUNICATIONS)
2134	2632.8

FIG.3 ARIANE 2/3 FLIGHTS

OVERALL MASS
(kg)

V33	V34	V40	V41
AR4LP	AR4L	AR4SP	AR4L
TV SAT 2 (T.V. BROADCASTING) * HIPPARCOS (SCIENTIFIC)	INTELSAT VI F2 (COMMUNICATIONS)	SATCOM C1 (TELECOMMUNICATIONS) * QSTAR IV (TELECOMMUNICATIONS)	ITALSAT 1 (COMMUNICATIONS) * EUTELSAT II F2 (TELECOMMUNICATIONS)
3730	4888	8846.5	4888.7

FIG.4 ARIANE 4 FLIGHTS

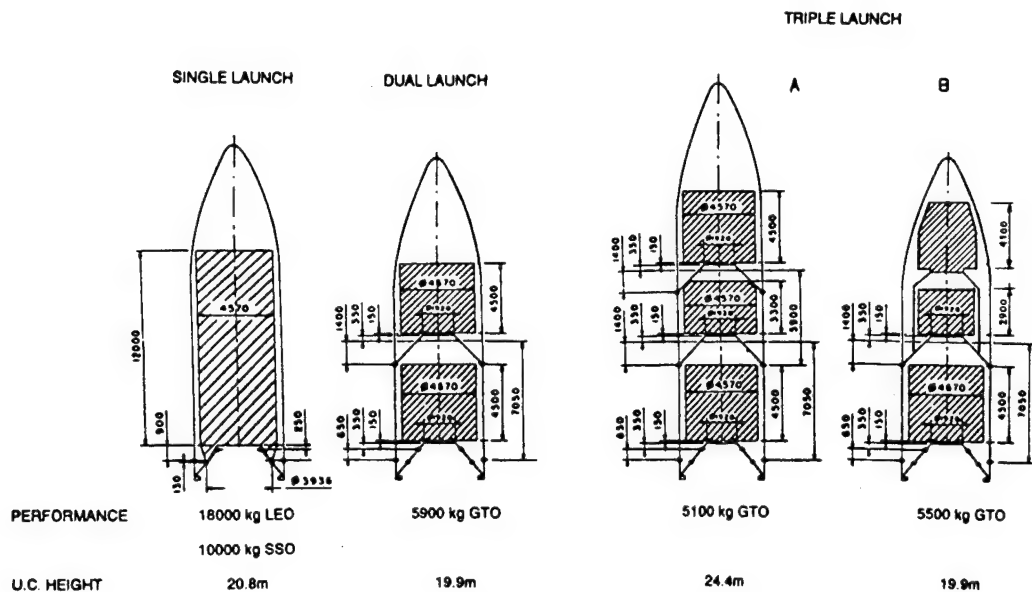


FIG.5 ARIANE 5. UPPER PART CONFIGURATIONS

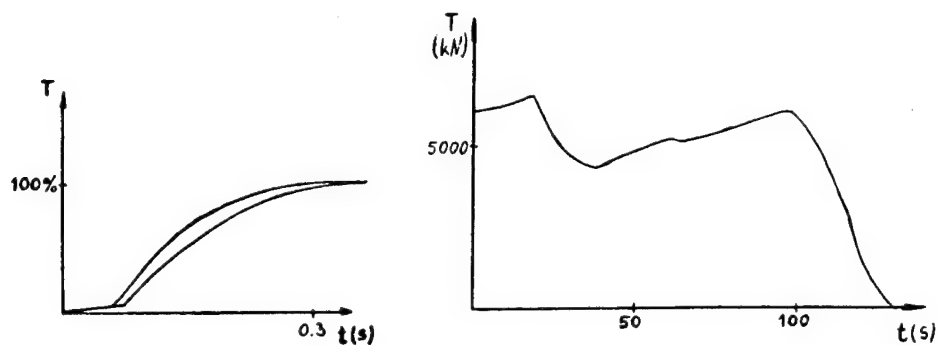


FIG.6 BOOSTER THRUST BUILD-UP & GLOBAL PROFILE

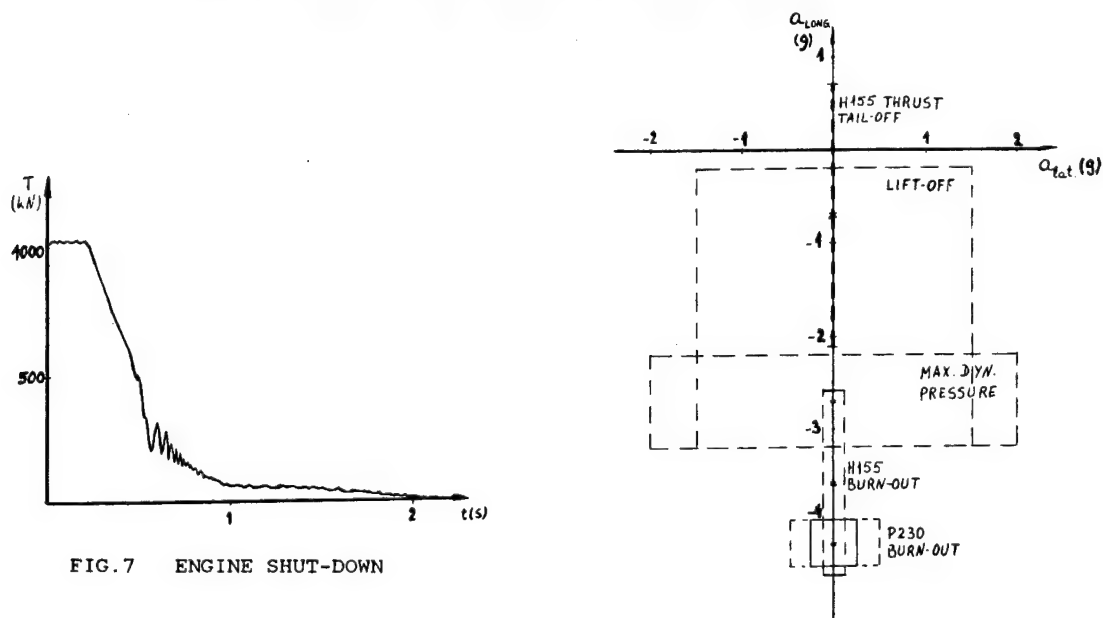


FIG.7 ENGINE SHUT-DOWN

FIG.8 QUASI-STATIC LOADS (PAYLOAD LEVEL)

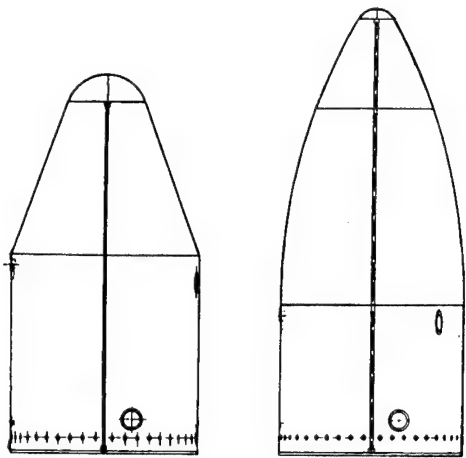


FIG.9 CONICAL AND OGIVAL FAIRING SHAPES

PERCENTAGE W.R.T. STRUCT. MASS	PANELS	FRAMES	OTHERS STRUCT.
SHORT FAIRING	66	19	15
LONG FAIRING	71	16	13
SPELTRA	73	22	5
VEB STRUCTURE	50	36	14
L7 STRUCTURE	40	33	27

FIG.10 STRUCTURES MASS BREAKDOWN

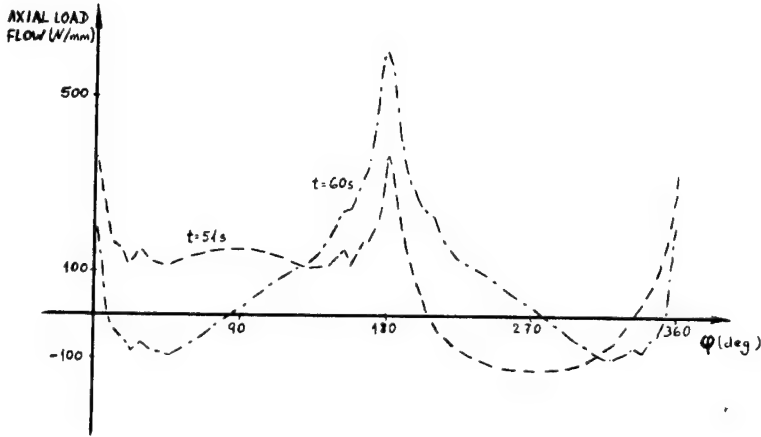


FIG.11 AXIAL LOAD FLOW AT VEB LOWER I/F

N 92 - 23809-20
SILVERADVANCED NUMERICAL ANALYSIS FOR THE OPTIMISATION OF THE STRUCTURAL
BEHAVIOUR OF THE INTERSEGMENT CONNECTION FOR THE ARIANE 5 BOOSTER CASE

P. Agatonovic and D. Sygulla

MAN Technologie AG, Munich, Germany

ABSTRACT

Presented is a short synthesis of the results of the structural analysis of the clevis-tang connection for the ARIANE 5 booster case carried out to establish a connection design which is optimally adopted to the general requirements of weight and cost saving, structural integrity and functional performance. The results of this synthesis have been used to develop the baseline solution for the connection geometry and to improve the necessary technological basis of the engineering approach in this area. By comparison of the results with experimental measurements, full verification of the basic procedure and the analysis model has been achieved.

Keywords: Clevis-tang connection, solid rocket booster ARIANE 5, structure analysis, connection rotation, gap analysis, optimisation.

1. INTRODUCTION

The booster rocket case for Ariane 5 consists of series of cylindrical segments which are assembled together using clevis-tang type joints. This kind of connection allows for completely weld-free case assembly. Each clevis-tang joint incorporates one or more O-ring seals to prevent leakage of the propellant during the firing of the booster at lift off. Failure of such a joint on the original Space Shuttle booster design was responsible for the accident which destroyed Challenger. It is clear that the design of the Ariane 5 clevis-tang connection must be made safe by optimising the design parameters of such a concept to exclude the possibility of any kind of failure.

This paper includes a short synthesis of the results of the work carried out on the structural analysis and development of the clevis-tang intersegment connection for Ariane 5 Booster case. The general strategy was based on the systematic consideration of different effects by numerical simulation of the connection behaviour for different boundary conditions generated by the design. The major effort centered on the optimisation of a conceptual design so as to minimize the danger of improper seal function or loss of structural integrity. For this purpose significant effects such as critical joint gap combinations, the kinematic mechanism of connection rotation which affects the gap change under operational conditions, the capture feature function, sensitivity analysis for pin load

etc. have been investigated and evaluated. In addition to the structural analysis work, to reduce the uncertainties associated with the different assumptions used in the analysis, data from appropriate experiments are necessary to verify the applied model and to support further analysis. Consequently to obtain relevant data about the component's operational behaviour, tests have been carefully planned to consider all the important features of the connection behaviour. The results of the tests carried out up to now have demonstrated the feasibility of the selected connection configuration and have provided proof that the analysis produced accurate results.

The requirements defining this work are based on the technical specifications prepared together with SEP as a main contractor and CNES. MAN Technologie AG is the subcontractor responsible for the conceptual design and the development of the booster case for the Ariane 5 Launcher.

We believe the results of this investigation have demonstrated the feasibility of the development of an improved clevis-tang connection, which attempts to eliminate all of the known problems present in some current designs of these connections.

2. REQUIREMENTS AND PRELIMINARY DESIGN
OF THE CONNECTION

The investigation of different previous designs at the beginning of the Ariane 5 development identified a couple of the weaknesses which could be relatively easily eliminated, for example by:

- control of the gaps between the components to limit rotation in the connection
- the use of some kind of the capture device to prevent unstable conditions and excessive rotation, and
- positioning other attachments on the case away from the joint not too close to prevent possible interaction of the effects.

Furthermore, different possibilities to improve the connection, which were considered in our design were established (see Fig. 1):

- Reducing the difference in thickness between the connection and cylinder wall will also reduce the difference in radial elongation and corresponding joint rotation. This results in higher bearing loads for pin connection and should be compensated by a larger pin diameter or an increased number of pins.

- If the transition in thickness is moved far away from the connection (through prolonged cones on both sides) the effect of wall ballooning, causing rotation and higher loads at the capture device, can be controlled. The transition at the tang side is more important in this respect.
- A capture device can control the gap opening. It can prevent any eccentric movement in the connection and helps in other less predictable situations as for example in the case of thermal and mechanical distortions.
- Increasing the length and reducing the height of the sealing branch causes higher bending effects induced by pressure loads, acting in the opposite direction to the joint rotation.
- Two sealing surfaces at the branch side make assembling the seal easier and more reliable. If, for example a surface scratch produces a seal damage, in the case of only one seal surface the possibility of damage to both rings is very high.
- Equal pin load distribution and reduced pin position eccentricity in the sealing branch will prevent gap opening due to the branch bending.

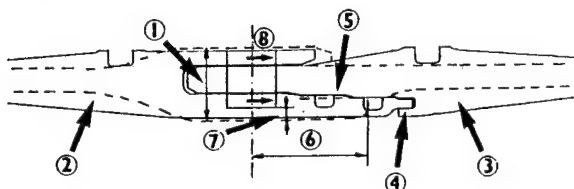


Fig. 1: Possibilities for improving the functional behaviour of the clevis-tang connection (1. Thickness ratio, 2. and 3. Transition to clevis and tang, 4. Capture device, 5. Two seal surfaces, 6. Length of seal branch, 7. and 8. Pin load eccentricity and distribution)

The clevis-tang connection at interface between two cylindrical segments has to ensure that under specified loading conditions an absolute tightness of the booster case to outside, and safe and homogeneous force transmission is achieved. The relevant failure modes for the structure, therefore, are excessive yielding or rupture in the critical section of the structure and leakage. In the case of a pin shear connection, however, additional specific failure modes determine the load carrying capacity of the overall structure:

- Shear failure of the pin
- Excessive yielding at the hole due to bearing pressure
- Shear failure of the plate, and
- Tensile failure (yielding or fracture) of the tang or clevis branch in the critical section between the pin holes.

The weakest of these will cause the connection to break, and is therefore assumed to define the design load capacity and the achieved safety margin of the connection itself. Additionally, these basic load capacities are influenced by the interaction with the geometry and by other loading modes. The shear properties of the pin, for example, can be lowered due to bending of the pin. The bearing capacity of the hole depends on the edge distance. By reducing the edge distance ratio below 1.5 the maximum stresses increase rapidly. Tensile failure of the plate, on the other hand, is influenced by the stress concentration in the critical section due to the pin hole. The maximum stress increases if the number of pins are reduced, so that the section cannot be effectively used. As in the case of bearing loads, the tensile capacity of the plate can be reduced due to an unequal stress distribution in the thickness direction. Due to uncertainties in evaluating all these parameters relating to the carrying capacity of the connection, an additional design safety margin is usually introduced in the specification. Consideration is given to safeguards and lessen the probability of any hazards due to the uneven load distribution between the pins, local stress concentrations in the hole area, joint rotation effects, friction etc.

If one considers all four carrying capacity limits, for some geometrical and material parameters a kind of relationship, as shown on Fig. 2, can be produced. The shaded area covers a possible combination of pin diameter and number. If the number of pins, for example have to be minimised for assembling conditions the best solution is at the lower boundary which, however, depends as shown on the edge distance. If the tang thickness is reduced the upper line moves down, but the lower limits then rise up. However it can also be necessary to hold the diameter of the pins constant and go upwards leaving the "optimal" lower line. In this way some compensation for unconsidered effects of the joint rotation, bending and stress distribution can be produced. Generally, this

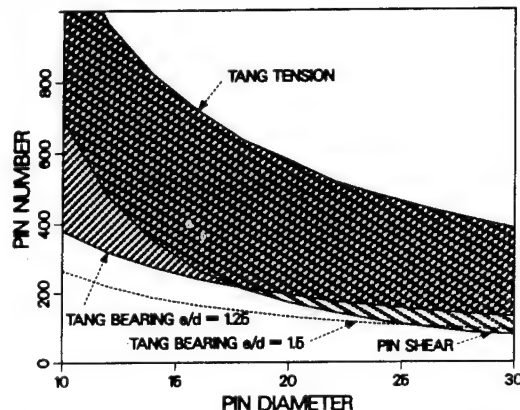


Fig. 2: Solution boundaries for connection parameter

method of concept screening is too simple and for this type of connection not sufficient. For example, the method does not consider the effect of joint rotation in any way. Nevertheless, a first estimate of pin diameter and number together with the plate thickness can be made using this diagram.

The tightness requirements impose the following specific design requirements for the components of the joint:

- Prevent, or reduce to negligible values, the gap opening under all operational conditions. The initial gap values at the sealing rings should remain nearly constant throughout the operational launching cycle. The maximum possible gap values should be in any case under the values required for normal functioning of the O-rings used for sealing purposes. Furthermore, the gap change should be insensitive to load variations and emergency conditions, such as a loss of the 1st ring sealing function, i.e. when sealing redundancy should be active.
- The sealing device should maintain a high standby performance during storage and after assembly before the start of launching to avoid a failure under critical operating conditions. The force transmission function is to provide a safe and homogeneous transition for all loads between the segments in a form which should also facilitate the fulfillment of the design requirements of the sealing devices. This requires a reliable joint system which will maintain mechanical integrity under all loads and resists additional influences during lifetime, as for example corrosion effects, transport loads etc..

The most severe constraint for the design of the Booster Case is the low weight of the overall design.

3. STRUCTURE ANALYSIS

For the purposes of detailed analysis and design optimisation more sophisticated structure analysis methods have to be used. This is especially true if the problem appears to be as critical, as is the case for the clevis-tang connection of a large booster. After Space Shuttle disaster it was recognised that the connections between the booster case segments are the

most critical mechanical parts of the booster case structure.

3.1 Requirements of the Analysis

The technical approach utilised in the structure analysis evolved from a consideration of the following basic requirements:

- Stress distribution on the clevis-tang connection components is strongly non-homogeneous, with local stress risers far above the material yield strength. Accurate analysis under these conditions can only be carried out using 3-D analysis methods.
- Behaviour of the connection is non-linear not only due to plasticity effects in the high stress areas, but also due to the non-linear effects at surfaces with different contact conditions and geometrical nonlinearities due to the large displacements and rotations in the structure. These nonlinearities produce significant differences in the behaviour of the structure compared to linear or simple elastic behaviour. Therefore, for the purposes of accurate numerical calculations these have to be included in the analysis method.

3.2 Selection of the Analysis Method

The applied method should, therefore, be capable of considering geometrical non-linearities and rotation, material inelastic behaviour, and gap or contact effects. On the other hand, for the purposes of the design optimisation and sensitivity analysis, it must be cheap and reliable to economically analyse different possible solutions and different combination of loads. To resolve these opposing requirements the analysis has been performed in two steps. The first optimisation step has largely been based on numerical analysis using simplified, but sophisticated finite element methods. Despite

- comparison of elastic, elasto-plastic and residual stresses and deformations.

The FE calculations were carried out with the non-linear finite element program MARC. A typical axisymmetric model is shown in Fig. 3. The model is based on use of 8-node isoparametric axisymmetric elements. The areas between the holes and the pin sections are simulated with plain elements without tangential stiffness. In all these simplified computations geometrical non-linearities and in some special cases material non-linearities were considered. The distributed pressure loads follows the geometrical contours also as the load increases. Unequal load and displacement distributions and any non-linearity of the material behaviour in circumferential direction were not considered, because of the inability of the axisymmetric elements to reproduce local inelastic deformations in the most critical areas, as for example at the pin-hole boundary. Special consideration was devoted to the simulation of the gaps. Different gap situations were simulated with open-close non-linear spring connections between the nodal points of the FE structure, which allowed the degrees of contact to be varied. In this way not only gap opening or closing were simulated, but also some non-linear transient conditions due to the uneven distribution of local contacts caused by the contour deviation due to the machining, out of roundness, set displacements, circumferential load distributions or similar random effects. To consider all of these different special numerical procedures (subroutines) were developed. Our non-linear method of structural analysis gives us the possibility of accurately evaluating different effects, especially at the interfaces between the parts of the connection and in the area of maximum loading.

The relevant dimensioning loading corresponds to the case of the limit value of the internal pressure and maximum axial flux due to the structural loads. For the analysis:

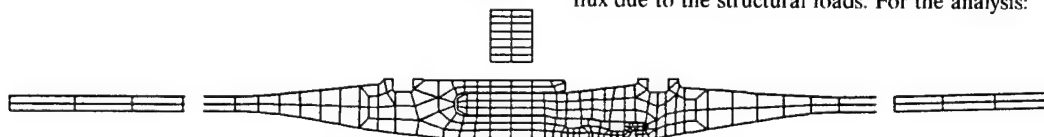


Fig. 3: A typical axisymmetric model for the analysis of clevis-tang connection

the uncertainties that sometimes can be produced by these methods, the results of the investigation were very useful in the development of an improved connection for the baseline solution on Ariane 5 design.

The verification of these initial results and the accurate evaluation of the safety margins of the selected basic design require, however, the use of complex finite element methods, which permit a more realistic simulation of the structure behaviour. The second step, therefore includes more expensive and time-consuming 3-D calculations. For this reason, these calculations cannot be used for a large number of different cases, as was done in the first step.

Clearly, in addition to this part of the design work different physical experiments will follow to support and verify the results, to reduce uncertainties associated with the different assumptions in the numerical analysis.

3.3 Preparation of the Analysis

The study approach was based on investigation of the design with respect to different nominal conditions concerning:

- load conditions, i.e. limit pressure and axial loads based on the dimensioning load conditions, proof test loading conditions, local pin overload and conditions after unloading,
- sensitivity of the structure to the gaps between the pins and holes and corresponding differences in local and overall load distribution,
- behaviour of the structure in case of failure of the first O-ring,

- the maximum axial flux loading was considered to act evenly over the circumference of the cylinder. This assumption produces conservative results. As the main portion of the axial load is produced by internal pressure, the variation of the axial flux around the circumference is in any case very low and the differences are negligible.
- both components of the load are applied proportionally to each other. Due to significantly larger complexity of the solution it was necessary to put the main effort of the analysis into the preparation and performance of the 3-D analysis. Different models using isoparametric full integration solid elements were used. In the case of the model based on the cyclic symmetry shown in Fig. 4, an angle sector corres-

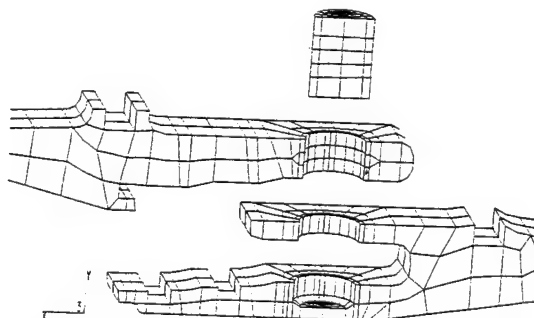


Fig. 4: A typical 3-D model for the analysis of clevis-tang connection

ponding to only one pin was modelled. To include more pins in the calculation a further extension of the model is achieved by mirroring. The contact conditions for 3-D calculation were simulated using both non-linear springs and so-called gap elements.

3.4 Analysis and Discussion of Results

Figure 5 shows a typical displacement plot of the connection under load. The penetration of the components into one another is artificial and is caused by the displacement scale. Nevertheless the typical rotation of the connection under load is clearly visible. Displacements in the connection generate a gap situation under load which is strongly influenced

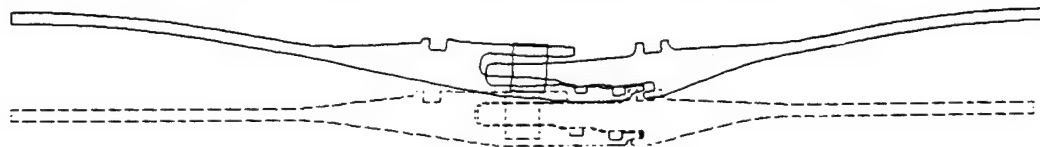


Fig. 5: The displaced clevis-tang connection under load

by the initial gap conditions. For this reason different possible initial gap combinations must be examined to find the most critical one. The results of the gap function analysis are shown in Table 1. The first block with four different gap combinations considers different extreme situations that can appear based on the combination of the dimensional tolerances necessary for the manufacture. The maximum rotation appears if the gap at the first position is at its maximum. The gap at the second position is not important and is always open. At the second redundant O-ring gap closing dominates. On the other hand, the first O-ring opens if the initial gap at this position has a minimum value and the gap at capture device is positive. The last row in Table 1 shows that for an initial value at the first position of over 0.8 mm the gap does not close at this place. Therefore if the gap values at position 1 are below this figure functional improvements in limiting the amount of the tang rotation can be achieved.

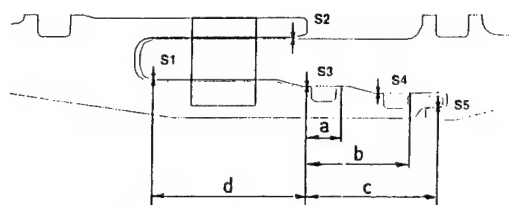
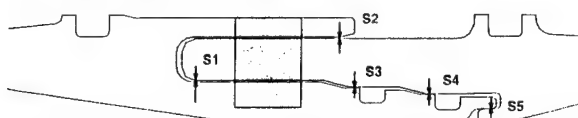


Fig. 6: Kinematic analysis of the gap changes

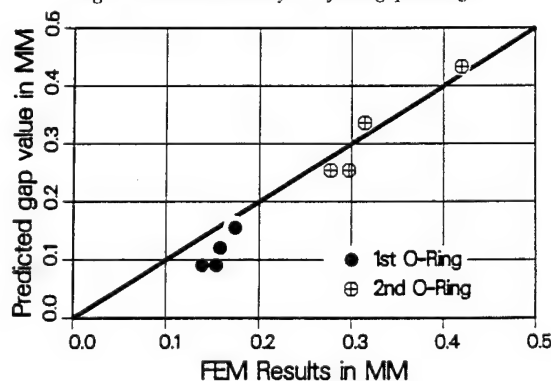


Fig. 7: Comparison of the FE results with the predicted gap values

rotation can be prevented by the friction between the pin and the bore. In this case the touch point for the above kinematic relationship will be not arrived and this relationship will be not effective. More can be said later about this problem based on the experimental results.

To determine the stress distribution the results of the axisymmetric calculation are insufficient. The axisymmetric models do not consider local pin loads and the stress concentration or uneven stress distribution in the circumferential direction. Because of this, only the results of the 3-D analysis can be used for these purposes. On the other hand, to validate the 2-D method and its results which were used for the investigation of the gap behaviour, comparison of the displacement results is necessary. These show (Fig. 8) very good agreement between the 2-D and 3-D elastic calculations.

A typical stress distribution based on the 3-D elastic calculation is presented in Fig. 9. The maximum von Mises equivalent stress, which is presumably based on the pin contact pressure effect, appears at the hole boundary of the tang, as presented in Fig. 9 in which the components are shown apart to make interesting details visible. The results also show that in the outer clevis arm the stresses are about 30 % lower.

	Gap Conditions [mm]														
	Initial Gap (0 bar)					Gap Opening					Total Gap (65 bar)				
Var.	S ₁	S ₂	S ₃	S ₄	S ₅	ΔS ₁	ΔS ₂	ΔS ₃	ΔS ₄	ΔS ₅	S ₁	S ₂	S ₃	S ₄	S ₅
1	0.7	0.2	0.13	0.13	0.20	-0.66	0.26	0.03	0.17	-0.18	-0	0.46	0.15	0.3	-0
2	0.7	0.2	0.33	0.33	0.00	-0.68	0.34	-0.19	-0.05	0.03	-0	0.54	0.14	0.28	-0
3	0.7	0.2	0.26	0.23	0.17	-0.68	0.32	-0.10	0.09	-0.14	-0	0.52	0.16	0.31	-0
4	0.7	0.2	0.26	0.26	0.30	-0.68	0.32	-0.09	0.16	-0.26	-0	0.52	0.17	0.42	-0
5	1.2	0.2	0.13	0.13	0.20	-0.80	0.29	0.05	0.21	-0.19	0.4	0.49	0.18	0.33	-0

In general the main part of the gap change is produced by the rotation. According to the displacement results from the FE analysis, the centre of rotation for the connection for all gap combinations is the touch point behind the second seal. The following relationships can be determined from Fig. 6:

$$S_3 = a/c \cdot (S_{30} + S_{50}) \quad S_4 = b/c \cdot (S_{30} + S_{50})$$

and for gap opening

$$\Delta S_5 = a/c \cdot S_{50} - (1 - a/c) \cdot S_{30}$$

$$\Delta S_4 = b/c \cdot S_{50} - (1 - b/c) \cdot S_{40} \quad (\text{for } S_3 = S_4).$$

Comparison of the FE results with the gap values predicted by above relationships shows (Fig. 7) that these are in good

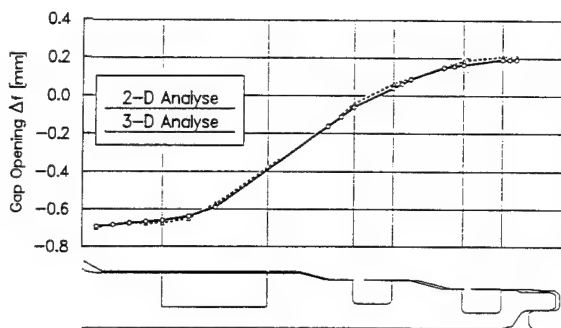


Fig. 8: Comparison of the FE displacement results of 2-D and 3-D analysis

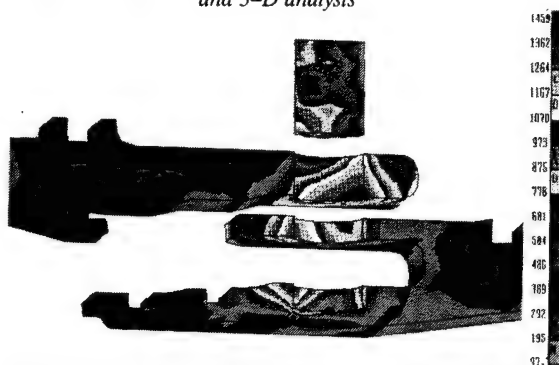


Fig. 9: A typical stress distribution for the pinned connection

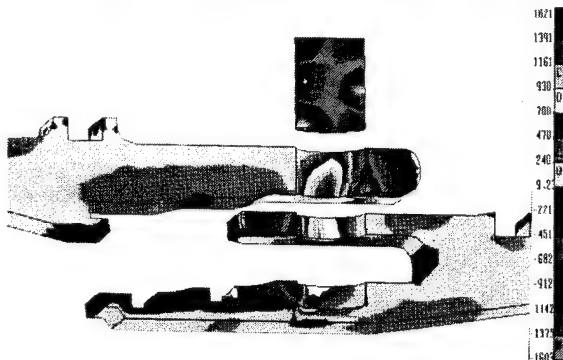


Fig. 10: The axial tensile stress distribution

More significant is the axial tensile stress distribution shown in Fig. 10. It produces the critical stress situation in the section between the holes (Fig. 11) responsible for the lowest calculated stress margin of the design. The peak elastic stress at the hole boundary caused by the stress concentration is far above the material yield strength. The corresponding yielding areas which are determined by the elasto-plastic calculation (Fig. 12) are, however limited to small local volumes near to the hole boundary. After yielding the maximum stress reduces below the material ultimate strength. The results show, based on the reduction of the bending portion of the stress, that the main part of the bending load in this section is displacement controlled. In spite of the high stress conditions the safety margin in the section is positive.

The stress state in the areas near to the hole is, however strongly influenced by the load transfer conditions between the pin and the hole. As Fig. 9 shows the load distribution at the hole boundary is very uneven. Based on the integration of the forces at the corresponding interfaces the global asymmetry of the load distribution between the clevis branches for ideal load conditions (without gaps between the pins and the holes) can be evaluated (Fig. 13). The figure shows that the

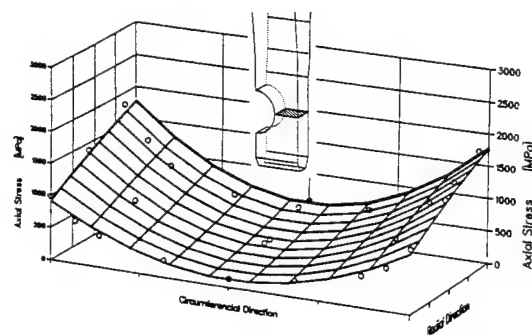


Fig. 11: The critical stress situation in the section between the pin holes

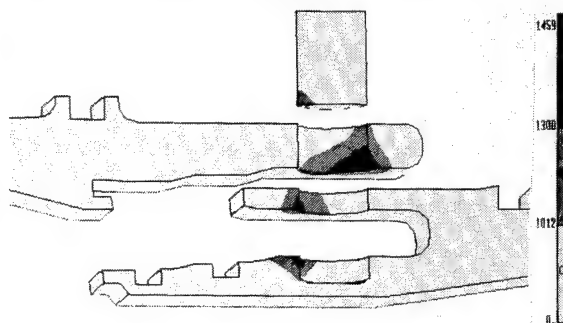


Fig. 12: Yielding areas determined by the elasto-plastic calculation

main influence in this respect is due to rotation or bending of the connection.

An additional calculation with different initial pin gap values (Fig. 14) shows that the effect of varying these is very small. The contact angle between the pin and the hole is reduced with the gap increase, but due to the reduced stiffness of the hole (plasticity) the variation of the stress in the critical section is negligible.

4. COMPARISON WITH THE DEVELOPMENT TEST RESULTS

A series of different experimental tests has been prepared to verify the design and calculation methods and the assumptions made during the numerical investigation.

For the initial validation of the FE analysis and eventually for further design improvements and selection of optimal configuration, flat plate clevis-tang tests are used. To simulate the rotation of the connection under the uniaxial loading conditions used for this test, lateral loading, calibrated on the calculation and the comparison of the test specimen with the real structure, are also introduced in addition to the axial loading. 10 different combinations of test specimens are planned selected to produce all relevant information for the optimal selection and design of clevis-tang connection.

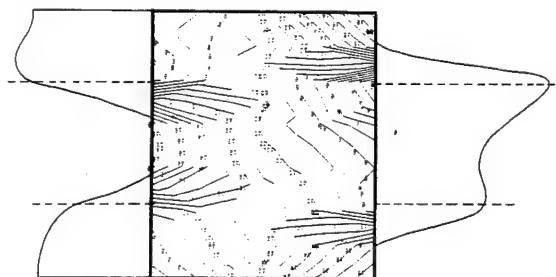


Fig. 13: Load distribution in the pinned connection

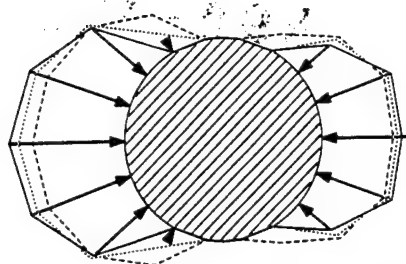


Fig. 14: Initial pin gap effect, continuous = 0.242 mm, dotted = 0.121 mm, dashed = 0.0 mm

The results of the first flat plate test, which was performed on the nominal connection, are shown in Fig. 15. Of chief interest for the validation of the analytical prediction was the gap behaviour and load transfer in the connection. Comparison with the FE prediction shows very good agreement. This confirms that all mechanisms of load transfer and general functional behaviour of the joint are accurately predicted by the models used in the calculation.

Figure 16 shows the results of a full scale test with a short cylinder segment and the so-called factory joint. This kind of

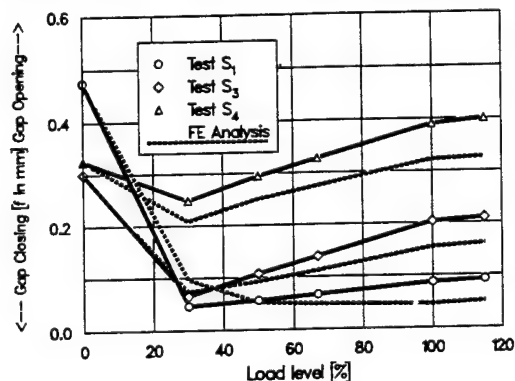


Fig. 15: Comparison of the flat plate test results with the calculated values

joint has only one O-ring. Again the comparison between the measurements and the FE calculation results shows very good agreement.

Further measurements which includes more than 500 displacement, strain and other gages performed during repeated loading cycles were also in full agreement with the predictions of the numerical analysis. The repeatability of all measurements was in all these cases excellent. All these results, however cannot be presented here.

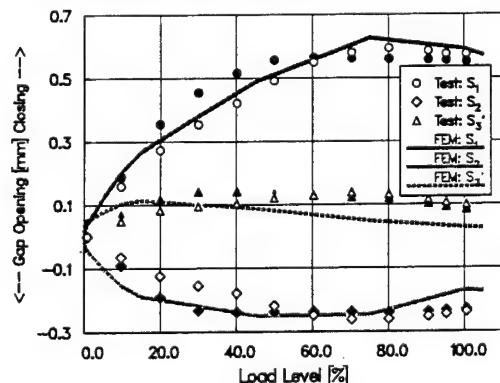


Fig. 16: Comparison of the factory joint test results with the calculated values

The final test which was performed on the full scale contour of the Field joint with the two O-rings shows similar agreement between the measured and predicted values. Although the test parts were manufactured with some geometrical differences compared to the calculated structure, the character of the all measurements agree with the expectations based on the FE calculation.

The results in Fig. 17 also show that the gap closing at the position of first touching and the corresponding pin movement in the hole are finished already during the first part (ca 20%) of loading. Therefore the effect of pin friction, although significantly reduced due to vibration under operational conditions, should not be very significant for the behaviour of the joint. Nevertheless good lubrication of the pins will ensure that the predicted behaviour can be achieved.

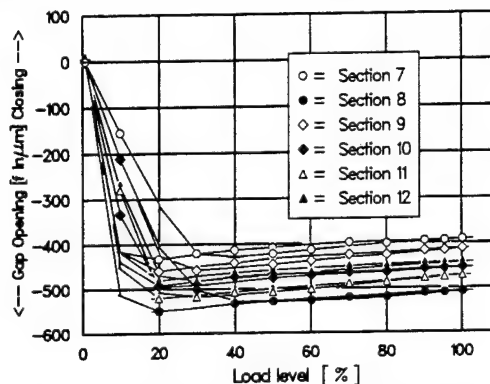


Fig. 17: The gap closing at the position of touching

5. CONCLUSIONS

The conclusions and the technical findings of this investigation can be summarised as follows:

1. The proposed design was selected based on numerical investigations which include, in addition to trade-off studies and stress and deformation behaviour analysis, systematic examination of the seal gap behaviour and comparison of different possible solutions. The results of the analysis and the models used were verified based on the test results.
2. Based on the evidence obtained the selected design of the clevis-tang joint provides the following advantages:
 - Nearly constant gap values at the seal rings throughout the operating cycle and their insensitivity to change of the operational loads.
 - Less tight fitting tolerances at the capture device, which makes the design less sensitive to malfunctions during assembly.
 - A simple design with only two seal rings and fully separate sealing and capture surfaces preventing any undesirable interaction.
 - Limited connection rotation, which produces a more equal load distribution between the pins and the holes and reduces stress concentrations in this area.
3. The gap effect can be used to improve the connection behaviour under operational conditions. For this purpose, the gap at the inside position between the clevis branch and the tang should be limited. Under this condition additional connection rotation and capture latch overloading can be prevented.
4. The investigation results confirm that for optimal seal functioning, the introduction of a capture device is necessary. For the effective prevention or reduction of the gap opening at the seals, the initial gap at the capture device must be significantly smaller than all other gaps, or even negative.

N92-23810

84722

BRIEF HISTORY OF THE DEVELOPMENT OF THE EPS-STRUCTURE

J. Martín

CASA División Espacio - Avda. Aragón, 404 - 28022 MADRID (SPAIN)

ABSTRACT

The EPS-Structure is a part of the Upper Stage of the ARIANE 5 launcher. The analysis of the functions and constraints requested to the structure led to its present design. The functions and a summary of the constraints will be presented, as well as a summary of the mechanical requirements. A brief description of the structure and several comments regarding the selection of the configuration of the different parts of the structure will be given.

The different analyses, performed during the development phase, have brought up interesting conclusions. Some of them will be presented.

Finally, some words regarding the present status of the structure will be included.

when similar needs are presented in other structures. In parallel with the development, the requirements have been evolving due to a better comprehension of the environment in which the structure has to perform its 'task'. For this reason, some of the information that is presented in this paper does not correspond to the present design but permits to draw some interesting conclusions.

The title of the paper might infer that all the aspects of the development of the EPS-Structure are going to be covered. Nevertheless, only the most relevant considerations about design and analysis are presented due to the impossibility of fully covering the development as a whole with the desired detail.

Keywords : ARIANE 5, Design, Analysis

ABBREVIATIONS

EAP : Etage Accélération à Poudre
EPC : Etage Principal Cryotechnique
EPS : Etage à Propelgols Stockables
GTO : Geosynchronous Transfer Orbit
LEO : Low Earth Orbit
MMH : Monomethyl Hydrazine
NTO : Dinitrogen Tetroxide (N_2O_4)
P/L : Payload
SSO : Sunynchronous Orbit
VEB : Vehicle Equipment Bay

1. INTRODUCTION

The development of the EPS-Structure started in January 1989 (under CASA responsibility, being MBB/ERNO in charge of the development of the stage). Since then, different studies were performed in order to obtain a concept of the structure presenting a good compromise between the different areas (design, manufacturing, cost, ...)

The retrospective analysis of these studies can help in getting a better understanding of the design, the reasons why the design looks the way it does, and the advantages of the selected design over other alternatives. This knowledge can be helpful in the future if a modification has to be implemented into the design, and can help to make design decisions

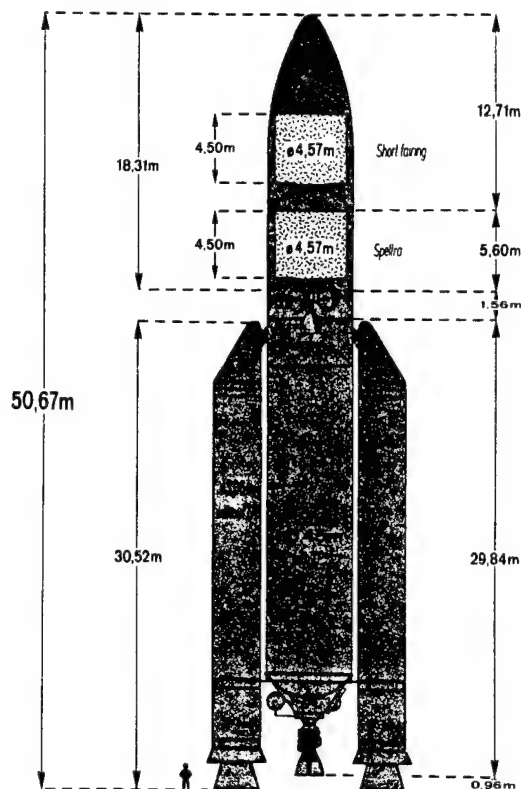


Figure 1. ARIANE 5 Launcher

2. STAGE DESCRIPTION

The EPS is located in the upper composite of the ARIANE 5 launcher; figure 2 shows a sketch to help visualize its location. It lies on the upper interface of the VEB inner cone and interfaces with the adapter for the lower payload in double launch configuration on its upper interface (configuration shown in figure 2) or with the Columbus adapter in single launch configuration on its lower interface. It supports the propellant tanks (containing up to 9.7 tons of propellant) and the engine of the upper stage.

The basic functions of the Upper Stage / EPS can be summarized as follows,

- Generation of Δv for payload insertion into GTO - LEO - SSO

GTO	300/36000 Km	5. - 12.°	6,000. Kg
LEO	550/550 Km	28.5°	18,000. Kg
SSO	800/800 Km	98.6°	12,000. Kg
- Trajectory Control
- Force Transmission
- Passivation/Deorbitation

The stage is composed of propellant tanks, engine, helium bottles, diverse equipment and structure. Figure 3 shows the different elements that compose the stage. The figure corresponds to an old concept of the EPS (containing 7.2 tons of propellant). The location and system to attach the Helium tanks to the structure (by means of a bipod and a tripod in the figure) is being reconsidered due to the propellant weight increase which reduces the available volume.

The engine can give a thrust of 27.5 kN and is fed by a NTO/MMH propellant system contained in the tanks. The engine is attached to the supporting structure via a gimbal that permits its pivoting in two perpendicular planes, in order to allow the thrust orientation. The orientation control is performed by two actuators. Four tanks are disposed, two for each one of the propellants. The two sets of tanks are different in shape due to the different volume they have to contain (the NTO tanks are bigger than the MMH ones); they are composed of a cylindrical portion closed by two spherical domes. The height of the cylindrical portion makes the difference between the tanks.

The structure provides the support for the other elements and gives continuity to the launcher

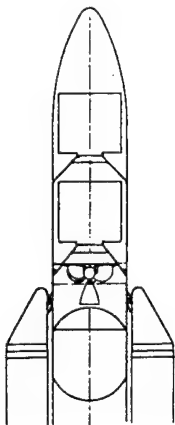


Figure 2. ARIANE 5 Upper Composite & Solid Boosters Attachment

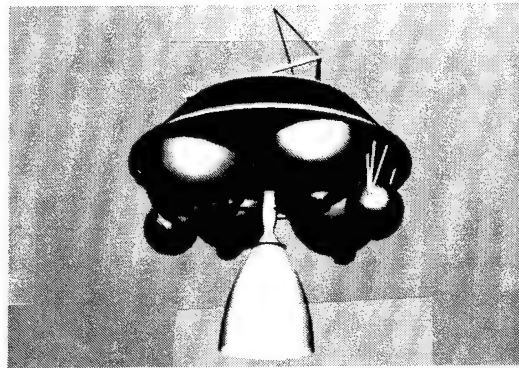


Figure 3. EPS Stage Elements

between two different interface planes. It is the 'skeleton' of the stage.

3. STRUCTURE REQUIREMENTS

The selection of the adequate design is performed bearing in mind the functions that must be satisfied by the structure and the constraints (requirements) under the ones these functions are to be fulfilled.

In the case of the EPS-Structure, the following functions and constraints are requested (the functions are described as stated in the Functional Specification of the structure),

- EPC and EAP loads transmission to the lowest payload
- EPS load transmission to the upper composite
- Support the four propellant tanks and the engine
- Support the rest of the stage elements
- Provide attachment for actuators for the EPS thrust orientation
- Provide proper attachment from EPS to the lowest payload
- Provide proper attachment from EPS to the VEB

A summarized compilation of the different constraints is presented next.

Several constraints are specified for the different interfaces (P/L adapter, VEB, propellant tanks, engine, ...) covering aspects as number of bolts required, flange thicknesses, and allocated volume. The inclined position of the tanks is included into this group of constraints.

In order to guarantee an adequate dynamic behavior of the engine/actuators when attached to the structure, the requirements regarding local stiffness (at the attachment of the actuators and at the engine support) are given.

A global frequency requirement is imposed at the stage level; this constraint is to be transformed into a stiffness requirement to allow for the structure qualification.

The above mentioned functions are to be achieved by keeping the mass of the structure to a minimum.

3.1 Summary of Requirements

- Mass $m < 235. \text{ Kg}$
- First Axial Frequency $15. \text{ Hz} < f_{ax} < 20. \text{ Hz}$
- Local Stiffness:
 - Engine Support $K > 3.5 \cdot 10^7 \text{ N/m}$
 - Actuator Attachment $K > 3.5 \cdot 10^7 \text{ N/m}$
- Interfaces 'Overflux'
 - P/L & VEB $\lambda < 1.3$
 - Propellant Tanks $\lambda < 1.7$
- Strength/Stability $MS > 0.$

The frequency requirement is to be fulfilled with the structure fully equipped, supporting the whole propellant mass and carrying a 4,500. Kg payload on its upper interface.

The interfaces 'overflux' requirement refers to the allowed alteration of the load distribution at the interfaces due to the presence of the structure. The non-axisymmetry of the structure produces this alteration, and is defined as the ratio between the 'real' line load (load per unit length) at the interface and the theoretical one. In the case of an uniform compressive load, the ratio between the maximum value and the mean value. Figure 4 shows, as an example to illustrate this point, the load distribution at the interface with the VEB structure inner cone when an uniform compressive load is applied at the upper interface. The graph represents the 'overflux' ratio versus the angle along the interface circumference (only one fourth is presented due to the existence of two planes of symmetry in the structure).

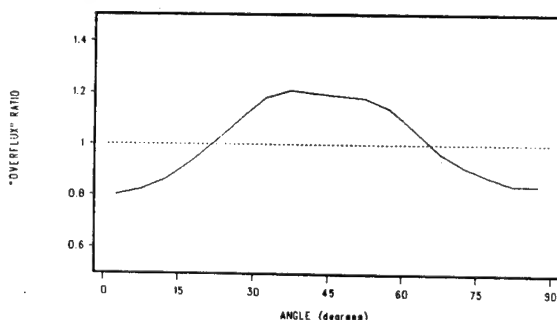


Figure 4. Interface 'Overflux'

3.2 Mechanical Environment

The strength/stability integrity of the structure has to be guaranteed for the structure subjected to the loads that can act on it during its mission multiplied by the appropriate factors of safety (1.1, yield factor; 1.25, ultimate factor).

Different ARIANE 5 program documents give the loads to be taken into account in the analysis. These loads fall into the following groups (only the ones influencing the global dimensioning),

- General Loads (Interface load and inertia acceleration)
- Dynamic Loads (acceleration on main masses)
- Differential Pressure (between compartments)

- Internal Loads : Tanks internal pressure
Engine Thrust

Figure 5 shows the line load at the lower interface for the load case corresponding to the non-symmetric extinction of the solid boosters (EAP). The graph represents the line load in N/mm versus the angle along the interface circumference. The full line gives the 'real' load distribution at the interface and the dashed line, the theoretical distribution based on the load resultant (axial and bending moment). The two peaks (0.° and 180.°) are due to the EAP load reacted at the upper attachment whose location can be seen in figure 2.

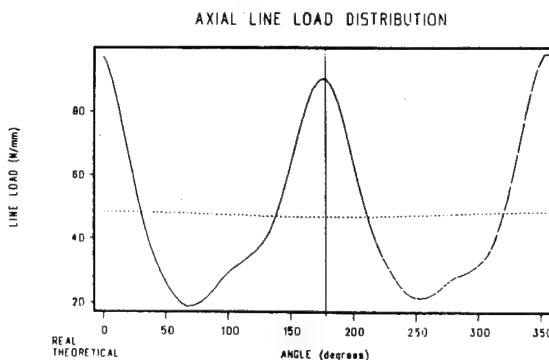


Figure 5. Interface Loading

4. STRUCTURE CONFIGURATION SELECTION

In the previous paragraph, a quick glance was given to the functions to be accomplished by the structure and the constraints that put limits in how this accomplishment is to be made.

When selecting the present configuration of the structure, different ways of performing the different functions were analyzed and, finally, the one with the best behavior accounting for all the constraints was retained.

4.1 External Structure

The need for connecting two interface planes of the launcher located 780. mm apart and with two different diameters (3936. mm and 2624. mm), by means of an airtight structure led to the selection of a truncated cone (see figure 5). In order to guarantee a good stability behavior, a sandwich shell construction was selected with the facings made out of CFRP in order to save mass.

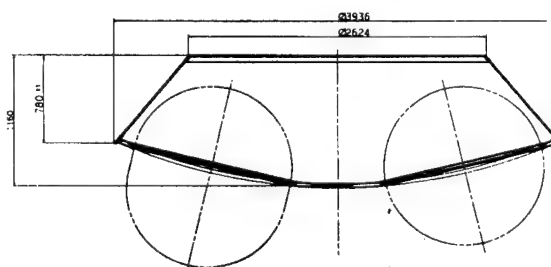


Figure 6. EPS-Structure Geometry

4.2 Support Platform

The selection of the structure to provide the support of the propellant tanks and the engine was not so simple. Three different geometries were studied: conical, pyramidal and spherical. In all the cases this supporting platform was considered to be lying on the 3936 mm diameter interface. The criterion leading to the selection of the spherical platform was its flat and circular interface with the truncated cone and the propellant tanks (due to their inclined position). The conical one had a circular and flat interface with the truncated cone, but the interface with the propellant tanks was not flat. The pyramidal one allowed a flat interface with the propellant tanks (pyramid faces normal to the tanks revolution axis), but not for the interface with the truncated cone. A sandwich construction was selected in order to provide some stiffness to the supporting function, selecting Aluminum Alloy facings because of cost reasons (manufacturing, material scraps, ...).

4.3 Reinforcing Structure

In order to attain the required stiffness, the addition of an internal reinforcing structure was found to be necessary. The high mass of the propellant (9.685 tons in its last version) caused a first axial frequency less than the one specified. To increase this frequency, several options were studied. The use of struts going from the midpoint between two tanks c.g. to the upper interface or panels forming a cross were the most promising. This last option was finally retained because it provided a best compromise with the other requirements to be fulfilled (local stiffness at engine attachment, ...). A sandwich construction was selected to improve its behavior towards buckling, with CFRP facings because of the mass saving involved. The panel was tailored (cut-outs, facings thickness, ...) in order to optimize from a mass point of view. Three zones were defined in the panel, and their thicknesses were used as design variables. The analysis showed that the thickness of the upper horizontal beam and slanted zone had to be reinforced (similar to the use of struts as reinforcing structure).

4.4 Interface Rings

The interfacing with the adjacent structures (propellant tanks, engine, VEB, payload adapter) is performed by means of metallic rings. The lower ring

is also used to connect the support platform to the cone. The shape and dimensions of the different rings respond to the different interface requirements, on the one hand, and to the guaranteeing of the structural integrity (load transmission, ...), on the other.

4.5 Connections between parts

The attachment of the internal panels between them and to the support platform and truncated cone is performed by means of special fittings. The selection of the present design was based on test results. The different candidates were subjected to tests in order to evaluate its capability to take ultimate flight loads. The test items were subjected to load combinations simulating the loads that would appear during the launch (obtained from a finite element analysis).

5. STRUCTURE DESCRIPTION

Figure 7 shows a blown-up sketch of the structure, allowing to identify the main parts of the structure. A brief description of these components will be given in this paragraph.

5.1 Conical Sandwich

The truncated cone is manufactured in four 90-degree sectors. The cocuring technique is used to manufacture each sector. Each curved panel is composed of an Aluminum Alloy honeycomb core and CFRP facings; the edges are reinforced by modifying the core and the facings thickness (adding plies). To connect the sectors, internal and external splices are used. These splices are bonded and riveted to the sectors, guaranteeing the structural continuity. The selected material for the facings is Vicotex 914/G829 for the basic plies and Vicotex 914/G803 for the reinforcing plies and splices. The material and the manufacturing process have been successfully used in previous ARIANE programs.

5.2 Spherical Sandwich (Support Platform)

The support platform, similarly to the truncated cone, is manufactured in four 90-degree sectors. The curvature is given to the panels by means of the stretching technique (the selected material, Aluminum Alloy 6061-T6 sheet, allows for it). A 30 mm thick Aluminum Alloy honeycomb is used as core of the sandwich; 1.6 mm thick facings provide the required in-plane and bending stiffness. The

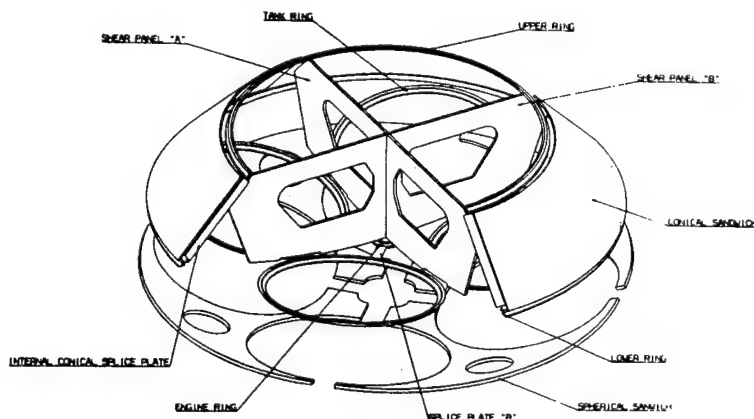


Figure 7. EPS-Structure Exploded View

connection between sectors is performed by means of internal and external splices to guarantee the structural integrity.

5.3 Reinforcing Panels

Three panels (one complete and two halves) are used to form the cross. The cocuring technique is used to manufacture the sandwich panels. In order to optimize the panel mass, three different zones are defined. Each one of these zones has a different thickness. To simplify the panel definition and manufacturing, a common base (lay-up) was defined for the complete panel and additional plies were added to each zone according to the required thickness ('playing' with three orientations, 0° , $+60^\circ$, and -60°). The same material system that is used for the cone, Vicotex 914/G829, was selected for the panels facings.

6. STRUCTURE ANALYSIS

After having performed a brief description of the EPS-Structure, we will focused in this paragraph on several aspects related to the analysis of the structure. Trying to summarize the different analyses performed since the beginning of the development program in a few paragraphs is almost impossible. The most relevant aspects will be presented.

6.1 Analysis Synthesis

Emphasis was given to the correct modeling of the different elements of the structure (§6.2.1). Figure 8 shows a view of the finite element model of the structure, split into its main components (truncated cone, support platform, reinforcing panels). This model was used to perform all the analyses: strength, stability, normal modes and local stiffness.

When selecting the dimensioning load cases to perform the strength/stability analyses, the 'classic' approach consists in a reduction of the number of load cases to study relying on 'engineering judgment' and applying conservative assumptions to combine the different loads. The special characteristics of the structure, the complex nature of the mechanical environment (§3.2), and the search for the 'optimum' structure made us follow a different approach. Several unit load cases were defined (their combination would allow to study

any load case), and analyzed (finite element method). The output from these analyses was processed accounting for the different loads in a time consistent basis and the critical load combination for every part of the structure was identified.

Since the beginning, the most important problems came from obtaining the required axial frequency. The propellant tanks dominated this frequency due to their large mass. The different mass of the tanks created additional problems. A considerable amount of work was invested in this topic. The selection of the panels (§4.3) was the result of a 'trade-off' study. An interesting conclusion from that study was the dependence on the requirement of the selection of the internal reinforcing structure configuration (struts or panels). An influence analysis was performed. The focus was centered on the first axial frequency, the other requirements were disregarded. Higher frequency values were obtained by reinforcing the internal structure (struts or panels), with the associated mass increase. If the design selection criterion is the mass, there is a frequency value that separates the ranges for which one alternative is 'better' than the other.

6.2 Analysis Particularities

During the analysis of the structure, several interesting points have appeared; some of them will be presented next. Most of the information will be related to the dynamic analysis since it was the driver during the first steps of the dimensioning of the structure.

6.2.1 Rings Modeling

A large impact of the way on which the interface rings are modeled was observed, specially the ring connecting the propellant tanks to the supporting platform. In a first approach the ring was modeled by means of BAR elements with the cross section properties and the plates modeling the support platform were assumed to continue up to the BAR centroid. A second approach was to model the ring by means of plate elements representing the flexibilities of the flanges. The properties of these plates were obtained by matching the behavior of a detailed model of the ring. This new way of modeling brought to light an excessive flexibility that obliged us to modify its design. Because of this result, the latter modeling approach was followed to model all the interface rings.

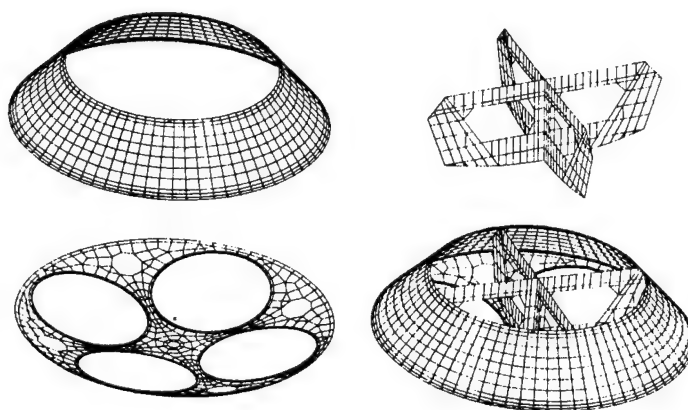


Figure 8. EPS-Structure Finite Element Model

6.2.2 Struts End-Fittings

When a set of struts was being used as internal reinforcing structure, the stiffness that was required was provided by the axial rigidity of the struts; being the first axial frequency very sensitive to this. For this reason, the drop in stiffness due to the end-fittings had to be carefully studied. For instance, an analysis of the end-fitting design that was foreseen in a first shot (turn-buckle system) showed an important reduction of the strut stiffness, so the struts ends had to be redesigned in order to get rid of this local flexibility.

6.2.3 Interface modeling impact in dynamic behavior

Normally, a stiffness is defined by the limits of the frequency that must be obtained when the structure supported in a given way has to carry different masses.

The way these masses are attached to the structure can have a considerable impact in the frequency value. The EPS-Structure has to carry the payload on top and the four propellant tanks; the frequency analysis was performed with the masses connected by means of rigid elements or by using adjacent structures.

Three different adjacent structures were taken into account,

- Propellant Tanks; according to the tanks definition drawings,
- P/L Adapter; according to the geometry of the 1920 Payload Adapter,
- VEB-Structure; a 200. mm high portion of the inner cone.

The lower interface of the model was clamped (VEB portion lower end or EPS lower end). When the propellant tanks were included in the model, the mass of tanks and propellant was lumped at its c.g. and connected to the interface by means of RBE3 MSC/NASTRAN elements; when the tanks were not included, rigid interface was assumed. The P/L mass was rigidly attached to the upper interface (payload adapter upper end or EPS upper end). Table 1 summarizes the value of the first axial frequency that was obtained (the symbol 'X' means that the adjacent structure was present in the analysis).

ADJACENT STRUCTURE			FREQUENCY (HZ)
VEB	TANKS	ADAPTER	
-	-	-	41.7
X	-	-	31.2
X	X	-	20.3
X	X	X	18.8

Table 1 - Adjacent structures impact on axial frequency

The last value in Table 1 (18.8 Hz) corresponds to the boundary conditions specified for the analysis.

6.3 Present Status

The EPS-Structure is going through a redimensioning phase due to two important facts; on the one hand, the increment of the amount of propellant to be carried ($\approx 35\%$ increase; from 7.2 to 9.7 tons) and, on the other hand, to the recent definition of the interface loading taking into account the influence of the ARIANE 5 solid boosters (\$4.2).

The main impact of these points is the change in the dimensioning philosophy; the axial frequency requirement was the driver in the past and the strength is turning to be the driver now.

7. CONCLUSIONS

The development of the EPS-Structure is still in progress; in fact a redimensioning is taking place. Nevertheless, the work performed in the past has revealed to be very useful in helping to perform the redimensioning and will be in the future for other programs.

Close attention should be paid to the way different local details of the structure are modeled, because, in spite of their small size, they could have a serious impact (ring flanges, fittings, ...). The way the boundary conditions are implemented (adjacent structures, clamped interfaces, ...) should be carefully studied.

**SESSION
1.2.D**

**VIBRO-ACOUSTICS
II**

ENVIRONMENT

PRECEDING PAGE BLANK NOT FILMED

N92-23811

ARIANE 4 INTERNAL ACOUSTIC ENVIRONMENT :
INTERPRETATION OF FLIGHT DATA WITH A VIBROACOUSTIC
MODEL OF THE UPPER PART OF THE LAUNCHER.

B. RITCHIE

CNES - Direction des Lanceurs
Rond point de l'Espace
91023 EVRY cedex

M. BELDI

STRACO
Rue des Fonds Pernant
60200 COMPIEGNE

Abstract/Resume

We present the theoretical and experimental approach used for the study of the vibroacoustic environment of ARIANE 4 payloads at lift-off.

We mainly deal with a comparison between predicted, by means of RAYON software -performed by STRACO - and measured flight acoustic levels under the fairing in the payload area, at low and medium frequencies.

The good agreement between the predicted and measured levels allows to use the model as a reliable interpretative tool of the flight data.

Keywords : ARIANE, ACOUSTIC, LAUNCHER, SPACECRAFT, ENVIRONMENT, NUMERICAL METHODS, VIBRATION, FLIGHT DATA.

INTRODUCTION

During the flight phase through the atmosphere a spacecraft launch vehicle is subjected to an intense aeroacoustic-based vibrational environment which may disrupt working equipments and damage the payloads [1,2].

During the take-off phase, the noise mainly comes from the gases ejected at high speed ($> \text{Mach } 3$) mixing with ambient air. The acoustic power produced is of the order of 0,1% of the mechanical power of the rocket engines, i.e. approximately 20 MW, that is to say 183 dB for Ariane 5. This noise is at its maximum in the region of the engine bay. It is reinforced, in the take-off phase, by the deflection of the jets by the deflectors which make the acoustic sources "visible" from the upper part, while during cruising flight they are "masked" as it were by the launch vehicle. This explains the high acoustic levels measured during the first 20 seconds of flight (which can exceed 145 dB on the external wall of the Ariane 4 fairing).

At transonic speeds the excitation of the launch vehicle structures is caused by the complex non-steady aerodynamic phenomena which accompany the appearance of shock waves (shock wave and boundary layer interaction, separation).

Finally, it is the boundary layer turbulence which explains the increase in vibration levels encountered when maximum dynamic pressure is reached.

These problems tend to be more acute for future launch vehicles for the following reasons:

- the increase in engine thrust and thus the global acoustic power produced
- the more and more frequent use of light carbon fiber-based composite materials which tends to make the structures more acoustically transparent
- the maintaining of launch vehicle competitiveness in the face of competitors for who control of the payload vibro-acoustic environment is a commercial challenge.

OBJECTIVES OF VIBROACOUSTIC STUDIES

In the 20-2000 Hz band it is a question of determining the vibration levels produced in the launch vehicle structures at the base of the equipment, as well as the acoustic levels in the different compartments, particularly the payloads ones. This data forms the basis for designing qualification test specifications for launch vehicle passengers (random vibration tests and reverberation chamber acoustic tests). Where the planned predicted vibration levels are judged to be excessive, corrective measures must be taken, for example to reduce the intensity of the noise sources (water injection, covering flame deflectors, jet deflectors), or to reduce the effects of these (acoustic protection designed to increase the noise reduction factor of the fairing, anti-vibration mounts for sensitive equipment).

The effect in terms of cost and time of such measures clearly illustrates the importance of having reliable vibroacoustic environment prediction.

The prediction amounts to solving by numerical means the stationary, three dimensional problems containing the following:

- for each altitude, an external acoustic sources model allowing the incident acoustic field to be reproduced satisfactorily - particularly at the level of the upper part of the launch vehicle.
- a vibration model of the elastic structures concerned
- an acoustic model of the cavities

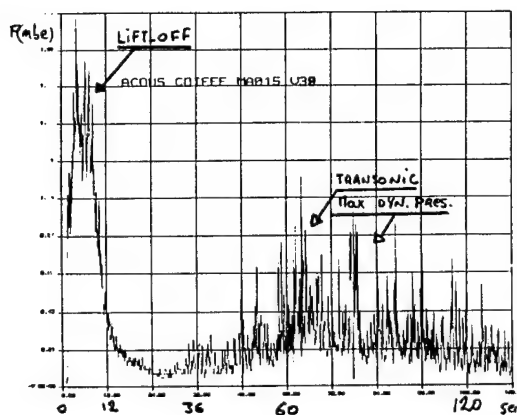


Figure 1: Noise under fairing: take-off and transonic

The numerical simulation then consists of solving the linear problem of external acoustic propagation - taking into account the presence of rigid obstacles such as the umbilical mast -, coupled with the internal vibroacoustic problem - taking into account the elastic structures, the acoustic cavities, and if necessary the payload vibroacoustic models-. In practice such numerical simulations cannot be carried out for the whole launch vehicle. For example, the predictions relative to the upper part of the launch vehicle use a structural model limited to the upper part which assure the validity of the conditions at the chosen limits.

APPLICATION TO ARIANE 4 PAYLOADS

The objective of the model presented hereafter is to provide the elements for interpreting flight measurements done inside the payload compartments i.e. the fairing and the SPELDA. The problem dealt with is, in this case, a complete vibroacoustic problem since it presents an infinite exterior environment coupled by an elastic structure to a resonant interior environment.

We are more specifically interested in the problem of low and medium frequencies. The limit is arbitrarily fixed at the top of the octave centered on 250 Hz.

At these frequencies the systems studied show low modal densities and a marked resonant characteristics. These two points have guided us in the choice of calculation methods.

The action taken consists of two steps:

- predict the acoustic levels opposite the flight microphones. The comparison with the measurements must validate the model.
- estimate the spatial averages in the acoustic cavities and thus define the corrections (field factors) to be applied to the local measurements.

This vibroacoustic analysis of the upper part of Ariane 4 was carried out by the STRACO company, using RAYON software. This activity is one application of recent developments on low frequency numerical methods applicable to launch vehicles, developments carried out, in particular, in the framework of R&T in vibroacoustics with the Université de Technologie de Compiègne [3,4,5].

In-flight measurements

Data on the acoustic environment during ARIANE 4 launches are gathered by means of measurements taken both on the launch pad and in the payload cavities. These measurements were taken during 8 of first 10 ARIANE 4 launches

External environment during the take-off phase

The external acoustic environment is determined during each launch by means of the microphones located close to the launch vehicle on the umbilical mast (figure 2).

We are more specifically interested here in the microphones located at fairing height during take-off.

The objective of these external measurements is not to physically describe the noise generated during take-off but rather to systematically provide data on each launch. They allow the different versions of the launch vehicle to be compared, the reproducibility of noise from one flight to another to be verified and the reduced scale tests carried out during the development phase to be validated and updated.

The curves of figure 3 show the external measurements obtained during 7 of the first 10 ARIANE 4 flights on the ELA2 launch pad.

After a stationary phase lasting a few seconds the measured level rises suddenly. This corresponds to the engine jets passing in front of the mikes.

A slight discrepancy can be seen from one flight to another, both at the global level and by frequency content per octave band or by 1/3 octave band (figure 4). The discrepancy for the OASPL remains less than 3 dB whatever the version of the ARIANE 4 vehicle used. It must also be noted that the frequency analysis is characteristic of broadband noise.

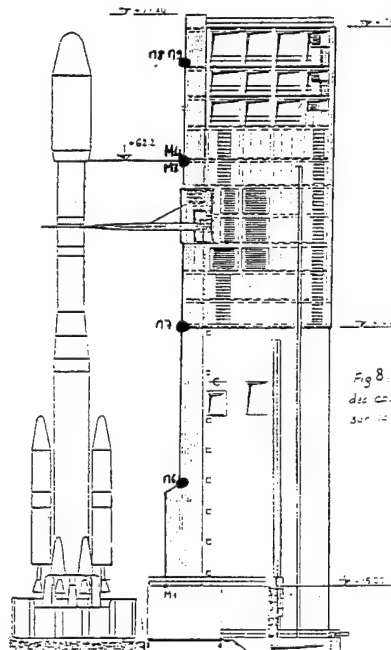


Figure 2: External microphones location

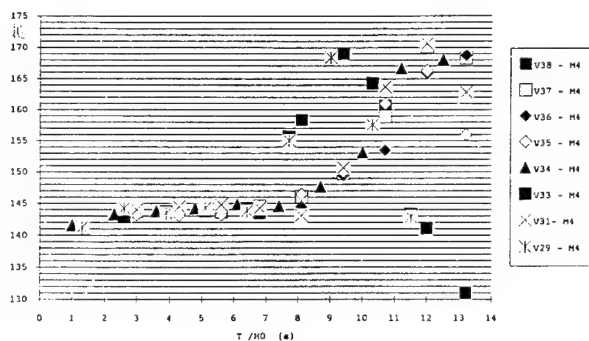


Figure 3: Global external acoustic level as a function of time (flight V29 to V38)

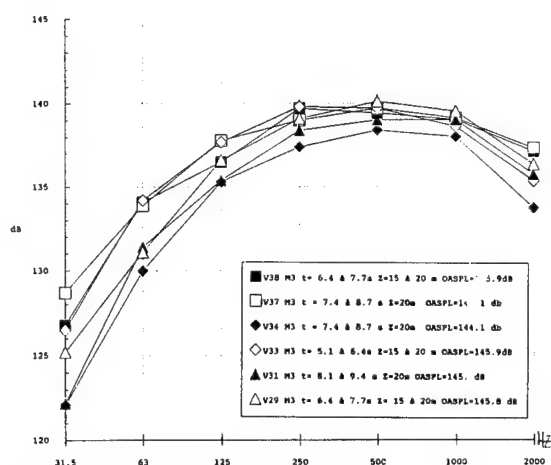


Figure 4: External acoustic levels by octave band (flights V29 to V38)

Internal acoustic environment

The objective of the internal flight measurements is first of all to prove the launch vehicle qualification, then, in the production phase to verify its normal behavior. We must particularly verify that the internal levels do not exceed the levels specified at the payloads for their qualification to the acoustic environment.

The Figure 5 gives an example of an internal measurement plan. It consists of 3 microphones under the fairing and 2 microphones under the Spelda. This corresponds to launch V33 (Ariane version 44LP with passengers TVSAT2 under the fairing and HIPPARCOS under the SPELDA). All the measurements are broadband ones (20-2000 Hz) and are processed on the ground in deferred mode.

The internal measurement plan is a compromise between the demonstration and verification requirements and the on-board processing capability. The limited number of microphones is due to the severe on-board weight restrictions.

Data may only be transmitted by radio. With this aim in mind an on-board control unit is used for acquisition, multiplexing of the different channels and signal transmission. This method, FM telemetry, has a weight limit and limits the number of measurement passband channels.

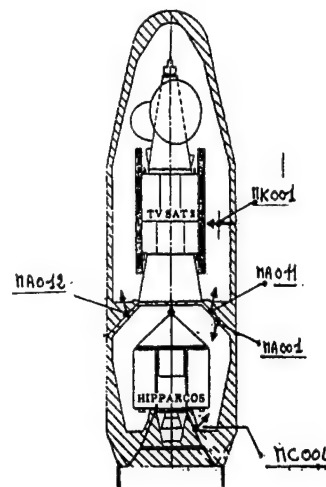


Figure 5: Microphone positions under the fairing and the Spelda (Flight V33)

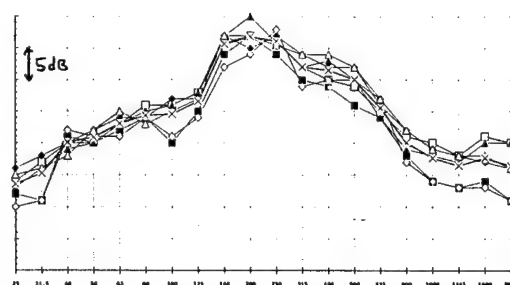


Figure 6: 1/3 octave comparison of the noise under fairing measured at the lower part of the fairing (flights V33 to V38)

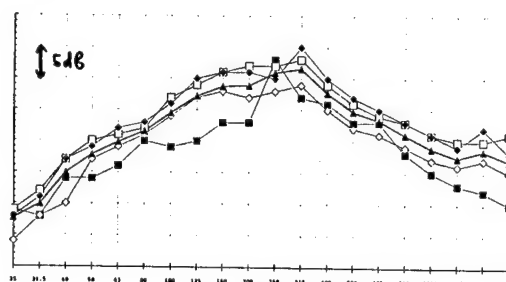


Figure 7: 1/3 octave comparison of the noise under the SPELDA (flights V33 to V38).

The measurements made during flights 405, 409, 410 and 411 under the Spelda and during flights 405, 409 and 410 under the fairing (2 symmetrical measurement points) show differences which rarely exceed 4 dB per 1/3 octave (figures 6 and 7).

We can conclude that there is a good spectral and level reproducibility of the local measurements. The spread is due in part to the uncertainties linked with each measurement.

At low frequency the narrow band analysis shows a spectrum characteristic of a modal response (figure 8).

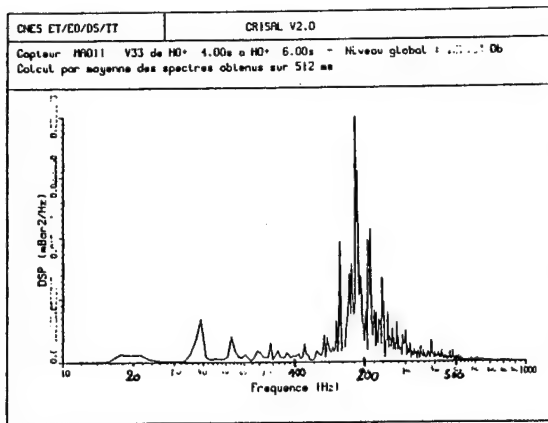


Figure 8: narrow band analysis of the noise at lift-off

The possibilities for interpreting these measurements remain limited:

- the number of measurement points is small given the size of the cavities. A correct spatial average cannot be deduced from them.
- their positions only give a partial indication of the average acoustic load on the satellite
- at low frequency there may be spatial level variations between the different measurement points. Thus, differences of more than 8 dB in 1/3 octave band have been noted from place to place during ground tests with fairing empty.

In conclusion, the measurement plans used do not allow a precise knowledge of the internal acoustic field.

Vibroacoustic model of the upper part of the launch vehicle

Calculation method and hypothesis

The theoretical bases of the RAYON software are given in references [3] [4] [5]. The model is based on the use of boundary finite elements for the internal and external fluid, coupled with the structure which is itself modelled using "classic" finite elements.

The response of systems coupled to the external acoustic pressure field is determined in the frequency domain, the broadband nature of the excitation imposes the requirement for a frequency sweep over the whole of the domain concerned.

The calculation hypotheses are the following:

the model is axisymmetrical, the vibration and acoustic fields are represented by their Fourier components. The internal cavities are delimited by the fairing or Spelda wall and by the external envelopes of the satellites. These are considered as being rigid axisymmetrical bodies representative in weight and in inertia.

The model is sufficiently accurate to cover response calculations up to 350 Herz.

Acoustic source model

At take-off, the noise sources are in the flame deflector and on the launch pad. American studies [6] and acoustic sources models built within the framework of CNES R&T programs with the CSTB [7] show that a reasonable description of the noise at take-off consists of a set of plane waves coming from the 2 flame deflectors and whose incidence varies from 5 to 45 degrees with regard to the launcher longitudinal axis (figure 9). Moreover, to simplify the calculation, the hypothesis that these plane waves are uncorrelated is made.

The definition of the acoustic power associated to each of the plane waves is deduced from the external flight measurements taken on the umbilical mast.

Figure 10 shows the geometrical configuration of the problem. The positions of the captors on the tower show that the measurements are certainly sensitive to the effects of diffraction of the assembly (launch vehicle + umbilical tower). For this reason a 2D diffraction model representative of this geometry is applied to the plane waves from the jets exhaust ducts. From this, we determine the correction to be applied to the tower measurements to define the free field level of the external sources.

Structural and acoustic model

The fairing and the Spelda are modelled by thin axisymmetrical shell elements with 4 degrees of freedom per node. Boundary Conditions are of the clamped or simply supported type for the satellite and supporting structure attachment points

The structural models have been validated by comparing the first vibration modes calculated with the results obtained during dynamic model system tests on the fairing and Spelda and with other models (CNES ASTRAL software)

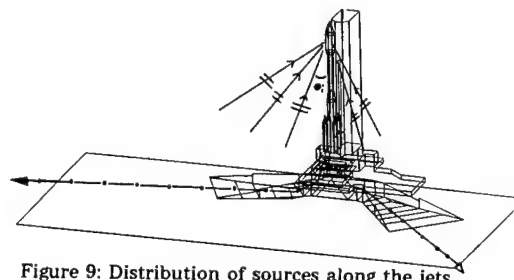


Figure 9: Distribution of sources along the jets

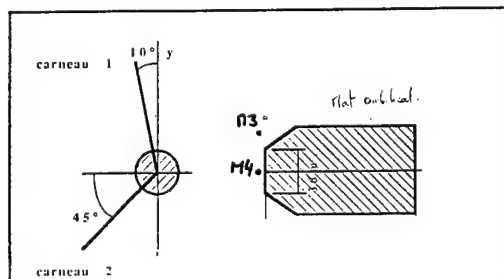


Figure 10: Launch vehicle/umbilical tower geometrical configuration

The acoustic grid pattern is defined on the wetted surfaces of the structure - elastic and rigid - by acoustic boundary finite elements with one DOF per node. Coupling is determined for all the nodes of the wet elastic structure.

In total, the vibroacoustic model is made of 168 nodes, 146 two-node elements and 428 degrees of freedom, i.e. a small model thanks to the use of boundary elements and of the axisymmetry of the problem (figure 11).

Modelling progress and results

The calculations are carried out from 20 to 350 Hertz with a frequency step of the order of 2 Hertz. The fine band results are then integrated on the 1/3 and full octave bands for comparison with the flights measurements.

The calculation is carried out in two steps:

- A basic response calculation is carried out for each plane wave and each Fourier index. The calculated pressure on the fluid domain boundaries are used to restore the pressure at a chosen number of calculation points inside each cavity. At this stage the calculation is purely axisymmetrical (figure 12).
- Using the external field definition the 3D pressure calculations are made by superimposing the responses on the different plane waves from the 2 flame deflectors, taking into account their respective angular positions (figure 10). These results are finally summed on the Fourier indices to get the physical solution.

It must be noted that this approach allows the resulting pressure calculations to be repeated at reduced cost in the case of a new external field definition.

We basically wish to determine three types of results:

- The "local" pressure at the calculation points corresponding to the locations of the in-flight measurements. Figure 13 gives an example of the fine band response obtained for microphone MA011 located at the lower part of the fairing.
- The average pressures in the two payload compartments as well as in different sub-regions of the cavities (around the antennas, in the annular volume, in the nose of the fairing...) (figure 14).
- The "field factors" which define the passage from local measurement to average pressure. We give, as an example, the average predicted pressure in the whole fairing cavity in the 1/3 octave band compared with a local pressure (figure 14). The result is directly the difference between the two curves shown in figure 14.

Comparison with flight data

We compare the 1/3 octave band results predicted with the model and the averages of the measurements obtained during flights at the same measuring positions.

We compare in particular (figure 15) the predicted level at the lower part of the fairing (MA011 and MA012, on average because of their symmetrical position with respect to the 2 flame deflectors) and the average of the measurements at the same points over three flights.

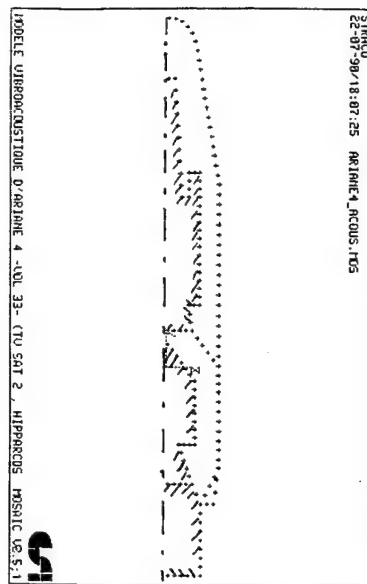


Figure 11: Structural and acoustic grid pattern

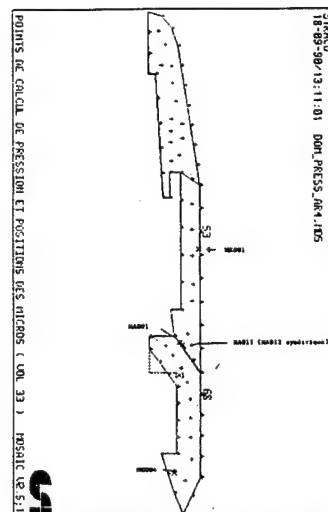


Figure 12: Internal pressure calculation points

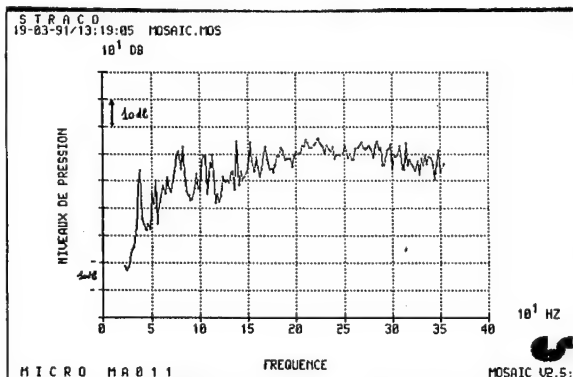


Figure 13: Predicted pressure opposite microphone Ma011

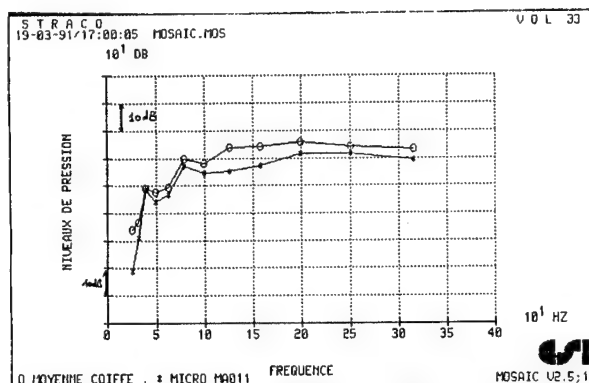


Figure 14: Average fairing pressure compared with Ma011 pressure in 1/3 octave band

We also compare the measurements and the predictions in the middle of the fairing (MK001, figure 16) and at the lower part of the SPELDA (MC004, figure 17).

We can conclude that there is a good agreement between the predicted values and the flight values except for the very low frequencies where quite large differences can be seen. The differences in levels in 1/3 octave band are almost always less than 3dB.

There are some elements which partly allow us to explain the differences noted at very low frequency:

- The signal processing conditions result in a poor frequency resolution (8 Hz) which give imprecise levels at the lowest frequencies (31.5 Hz octave band).
- Some recent investigations have shown that a systematic error has been committed at low frequencies on the external measurements during the flights, an error which results in an underestimation of the input levels used for our model.
- The SPELDA is the cavity the most sensitive to the boundary conditions used for modelling the structure.

All these points are still under investigations.

CONCLUSION

Concerning the results obtained with the model, one can see their very good agreement with the flights data. Therefore it seems possible to use the model as a reliable interpretative tool of the flight measurements. This leads to a better knowledge of the acoustic environment of ARIANE payloads.

Still, we are studying, at the present time, the main physical parameters at the origin of the uncertainties and the variations from the predictions :

- the sensitivity on the incidence, the position and the type of external acoustic sources
- the influence of the size and geometry of the payload.
- the influence of the hypothesis used to describe the payload: acoustic absorption, elasticity.

Finally, in order to improve our model and experimentally characterize the predicted spatial variations, some launch vehicles with an increased acoustic measurement plan for the upper part will be used in a next future.

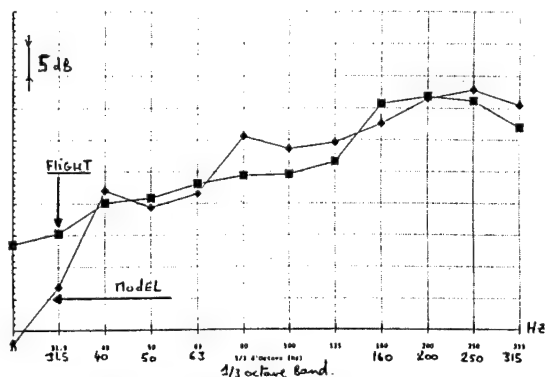


Figure 15: Flight and Model comparison, Average (Ma011, Ma012), lower part of the fairing.

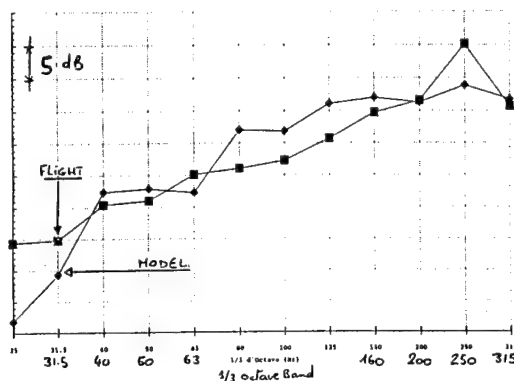


Figure 16: Flight and model comparison, Mk001, middle of the fairing

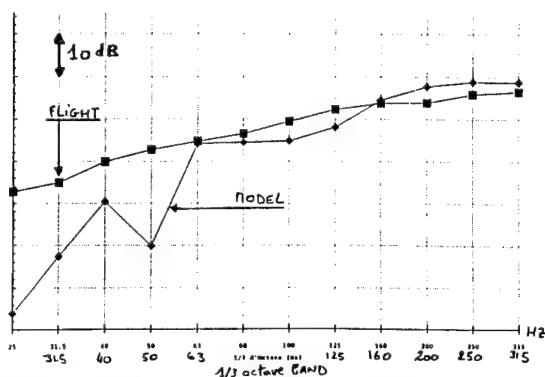


Figure 17: Flight and model comparison, MC004 Spelda

On a more general point of view, we wish to underline the research effort undertaken by the space community in the acoustic field.

The importance of the definition of the external acoustic environment has led CNES to start a research action plan coordinated by ONERA in this domain. It is mainly a question of understanding and modelling the jet interaction noise generation mechanisms. These studies must finally allow sources models to be defined which are adapted to vibroacoustic studies.

Also, the field of vibroacoustic studies must be extended to evaluating the influence of elastic three dimensional payloads on their surrounding acoustic field. This theme of study is taken into account by the European Space Research and Technology Center (ESTEC), in cooperation with CNES.

Finally, One must recognize that the methods currently used at low and medium frequencies are costly and difficult to implement. Consequently, these methods should be improved. As an illustration, the use of a modal representation of structures and acoustic cavities is an approach being implemented today within The CNES software ASTRAL [8]. Other approaches, based on a reduction of the initial modal model are currently under investigation.

These last objectives are taken into account in the vibro-acoustic pole set up jointly by Aérospatiale and CNES.

REFERENCES

- [1] Bec R., Borello G., Ariane ça fait du bruit... Document interne CNES 1980
- [2] Morand H.J-P., Problèmes vibroacoustiques des lanceurs spatiaux, 1er congrès français d'acoustique, Coll C2 Février 1990.
- [3] Hamdi M.A., C.R. académie des sciences de Paris, série II, Janvier 81, 292(17).
- [4] Hamdi M.A., Recent advances in vibroacoustic computation, Internoise 88.
- [5] Beldi M., Prévision de l'ambiance acoustique sous coiffe Ariane 4 au décollage, Note technique CNES A4-NT-0-468.
- [6] Eldred, Acoustic loads generated by the propulsion system, NASA SP 8072, JUIN 71.
- [7] Van Maercke, Roland, Etude du champ acoustique au voisinage de la coiffe d'Ariane 4 par une méthode d'acoustique géométrique. Rapport d'étude CNES CSTB.
- [8] Morand H.J-P., Modal methods for the analysis of the vibrations of structures coupled with fluids, Pressure vessels and piping ASME conf. July 1989.

N92-23812

S32-18

84-224

ACOUSTIC PREDICTION ON SATELLITE
STRUCTURE

Christian CLERC

Head of Fluid Structure Group

METRAVIB R.D.S

64, Chemin des Mouilles
69132 ECULLY Cedex
FRANCE

Jean-Noël GIRAUDBIT

Head of Mechanical and
Thermal Engineering Depart

ALCATEL ESPACE

26, Avenue J.F. Champollion
31037 TOULOUSE Cedex
FRANCE

During launching, satellites are submitted to a high level acoustic field. This field can generate high mechanical stresses on large light frames such as antenna reflectors or solar panels. Acoustic tests are performed on these structures, with specified acoustic incident field, in reverberant room. In order to simplify the tests, and because of the large size of the satellite body, the test structures are considered apart from satellite body in experimental configuration. Consequently, the geometrical environment is quite different in "Test configuration" compared to "Launch configuration". But these differences generate local over- or under-pressures on the specimen. In order to improve the test representativity, ALCATEL ESPACE and METRAVIB R.D.S. have developed a specific numerical method for comparison between "Test configuration" and "Launch configuration". The acoustic computations are performed with ASTRYD which is a general software for solving scattering and radiation problems. ASTRYD is based on space time scheme discretization ; at first, acoustic pressures are obtained in time domain, and then, they are obtained in frequency domain by classical FFT algorithms. The satellite structure, considered in this study, is TC2 satellite ; computations are performed on one antenna reflector in free space -Test configuration- or mounted on the satellite -Launch configuration-. For both configurations, main results are the acoustic field by octave and the acoustic pressure differential at the reflector's surface. Several over- or under-pressures are highlighted by computations specifically in the low frequency octave. Computations enable to screen the total frequency spectrum in which acoustic pressures are sensitive to the geometrical environment (frequency spectrum lies from 0 to 2000 Hz for a 2 m size specimen). Consequently, ASTRYD appears to be a powerful tool for the acoustic and structural engineer to predict acoustic loads on sensitive structures.

INTRODUCTION -

During launching, satellites are submitted to high level acoustic fields. The increased power of the launchers necessitates the knowledge of acoustic solicitations under the fairing, particularly on large light frames such as antenna reflectors. These ones are improved in reverberant room, with a specified acoustic level ; they have to pass the tests without any damage. In order to simplify the tests, and because of the large size of the satellite body, the test structures are considered apart from the satellite body. During the tests, the incident acoustic field is considered as diffuse. During launching, even if the acoustic field under the fairing is globally diffuse, there are some local under or over pressures, especially on the antenna reflector made by acoustic reverberations on the geometrical environment. These pressure gradients are more important if acoustic wave lengths are similar to distances between the reflector and its environment, the more often in medium and low frequencies ranges. Thus, the aim of this work is to evaluate the reflectors' environment effects on the acoustic pressure fields and to give a new point of view about the tests. In order to perform this objective, the main tool used is ASTRYD which is a software developed by METRAVIB R.D.S. ASTRYD is a general software for solving three dimensional acoustic problems. Some other specific numerical tools are also used for solving the problem and obtaining the results. Some applications samples show the software capabilities to highlight the partial containment phenomenon which generate local pressure gradients and acoustic pressure differences between both configurations. The tested structure is the k.u antenna reflector mounted on the TELECOM 2 satellite.

OBJECTIVE, HYPOTHESIS AND METHOD -

In order to obtain the differences between both configurations, computations are taken on the "Test configuration" and on the "Launch configuration". For the first one, the reflector is alone, with no structure around it. For the second one, the satellite body is also represented. We have to evaluate differences between the configurations ; we do not need to compute stresses (in the reflector) with a high accuracy ; consequently, the fluid structure coupling can be considered as negligible and the structures are considered as rigid bodies. Acoustic hypotheses are classical hypotheses of linear acoustics. The frequency band of computation lies from 0 to 2800 Hz (octaves 63 Hz to 2000 Hz are considered). When the upper frequency limit is reached (2800 Hz), the acoustic field becomes uniform and the configurations differential becomes very small. The incident acoustic field is simulated by a decorrelated plane waves serial. A computation is taken for each plane wave incidence. Then, a quadratic average of acoustic pressures at the structures surfaces is made. Scattering computations are performed by ASTRYD software (ref [1]). Pressures integration on the reflector surface allows to obtain a "strength resulting" which is a global criterion for the comparison of the different configurations.

COMPUTATIONS PERFORMING -

Acoustic computations : ASTRYD -

ASTRYD is a software program for solving scattering and radiation problems. It is based on space time discretization of the retarded potentials equation -or Kirchhoff's formulae- (ref [1], [2]). In the case of spherical wave scattering by a rigid body, the Kirchhoff's formulae can be written such as :

$$(4\pi - A) \cdot P(M_0, t_0) = [P(M, t_0 - d/c) \cdot \text{grad}(1/d) + 1/c \cdot d \cdot \dot{P}(M, t_0 - d/c) \cdot \text{grad}(d)] \cdot n_M \, d\Omega + 4\pi \cdot S(t_0 - r/c) / r \quad (1)$$

Where :

- $P(M_0, t_0)$ is the acoustic pressure level at point M_0 , at time t_0
- $\dot{P}(M_0, t_0)$ is the derivation of $P(M_0, t_0)$ in the time domain
- d is the distance from M_0 to M
- n_M is the normal outside vector to the surface Σ at the point M
- Σ is the surface which is bounding the structures,
- r is the distance from M_0 to monopoles
- S is a characterized monopole by its time evolution
- if $M \in \Sigma$ then $A = 2\pi$ else $A = 0$
- c is the sound's celerity in the fluid.

By using a noise source, with a large spectra, the results can be obtained for a broad band frequencies by a Fourier Transform of the time results. The bodies surface space discretization uses plane triangular meshes. The acoustic pressure is constant on each mesh and computed at its gravity center.

Thus, the first equation (1) becomes :

$$(4 \pi \cdot A) P_i(t_0) = \sum_{j=1}^{ne} A_{ij} \cdot P_j(t_0 - d_{ij}/c) + B_{ij} \cdot \dot{P}_j(t_0 - d_{ij}/c) + 4 \pi \cdot S(t_0 - r/c)/r \quad (2)$$

Where :
 A_{ij} and B_{ij} are space integration terms on the j^{th} element, computed for a semi-analytical method.
 ne is the elements number outcome from space discretization
 $P_j(t)$ is the acoustic pressure level, on the j^{th} element, at time t .
 $P_i(t_0)$ is the acoustic pressure level on the i^{th} element or at the i^{th} point in the fluid.
 $\dot{P}_j(t) = dP_j(t)/dt$

The time discretization is based on a finite semi-implicite differences method, with a constant time 'step' δt . Consequently, the surface acoustic pressure can be written as follows :

$$[A] \{P\}^k + [B] \{P\}^{k-n} = \{Pe\}^k \quad (3)$$

where :
 $\{P\}^k$ is the acoustic pressures vector at the k^{th} time 'step'
 $\{Pe\}^k$ is the right term, calculated explicitly as indicated by the equation (2)
 n is a stability parameter of the numerical scheme.

ASTRYD Software Validation -

ASTRYD was used for many different problems and the results were compared to either analytical results or acoustic measurements. Figure 2 shows a pulsating sphere directivity in a half-space media. The ASTRYD result is compared to the analytical result and to another numerical model result (ref [3]). The "schock wave on buildings" problem is illustrated in figures 3 and 4. The buildings meshing is shown in figure 3 and the acoustic pressure time evolution between both buildings is shown in figure 4. In both cases, a good comparison between ASTRYD results and the others is highlighted.

Satellite applications -

MOSAIC software (made by FRAMASOFT + CSI) was used for the meshing and the results presentation of results. We also used a specific numerical tool for automatic meshing of the reflector ; the inputs of this software are the parametric definition of the reflector and the characteristic size of a mesh (given by the user). The meshing must have six elements by wavelength at the higher octave medium frequency, for good computations accuracy. Some meshes, used for both configurations, are presented in figures 5 and 6.

Monopoles, which are far from the satellite (100 m), generate incident plane waves ; the frequency band bandwidth of its spectrum is sufficient to cover entirely the concerned frequencies band. The practical results are transfer functions which consist of ratio between computed pressure spectrum and the equivalent pressure spectrum under free field conditions (with the same monopole, at the same computation point).

Diffuse field simulation -

The scattering computations are taken for ns plane waves incidences and give ns transfer functions for each mesh element.

A quadratic average is taken ; thus, each incidence is decorrelated for each other and the incident acoustic field is considered as diffuse. The incidences choice is assited by some radiation computations in regard to the reciprocity principle. At that time, an octave average is taken and the resultant transfer function, for the fo octave and the i^{th} element, can be defined as follows :

$$T_i(f_0) = \sqrt{1/f_2 - f_1} \int_{f_1}^{f_2} \sum_{j=1}^{ns} w_j \cdot T_{ij}^2(f) df \quad (4)$$

where :
 $T_{ij}(f)$ is the transfer function from i to j , at the frequency f .
 w_j is the weight of incidence j
 f_1 and f_2 are respectively under limit and upper limit of octave
 f_0 ($f_1 = f_0/\sqrt{2}$; $f_2 = \sqrt{2} \cdot f_0$)

"Strength statistical resulting" on the antenna reflector -

$$F(f_0) = S(f_0) \int_{\Sigma} T(f_0) \cdot n_M d\sigma =$$

$$S(f_0) \cdot \sum_{i=1}^{ne} T_i(f_0) \cdot s_i \cdot n_i \quad (5)$$

where
 $S(f_0)$ is the incident pressure field level (in P_a unit)
 ne is the reflector 's elements number
 s_i is the i^{th} element's surface

This vector allows the comparison of both configurations and to check the computations coherence.

RESULTS-

The computations were realized for two antenna's reflector of the TELECOM 2 satellite. The following results concern the k.u antenna. One meshing is used in the "Test configuration", for the whole frequencies band (45-2800 Hz) ; it is shown in figure 5.

In "Launch configuration", the problem is more complex. At low frequencies, we have to take into account a large part of the satellite (earth plane in its whole, walls, sonar panels, lateral reflectors...etc.). At high frequencies, we must have a mesh size smaller than a sixtieth wavelength. Consequently, if we use the same meshing from 0 to 2800 Hz, we will have a great number of meshes and the computations will be too expensive.

Thus, we use three different meshings :

- one for the 2000 Hz octave,
- one for the 1000 Hz octave,
- one from the 63 Hz octave to the 500 Hz octave.

Note :

The majority of local reverberation problems are noticed in the low frequencies (less than 700 Hz) ; this means that the "Launch configuration" could be studied with one meshing.

The third mentionned meshing is shown in figure 6.

The computation 's results, obtained for the 250 Hz octave, are presented in figures 7 and 9. They concern the transfer function quadratic average computed with 24 plane waves incidences. The acoustic level is shown in relative decibel to the incident acoustic level.

The "Launch configuration" results can be seen in figure 7. The over-pressures are highlighted in the corner, but the reflector convexity also generates some over-pressures. The "Test configuration" results, shown in figure 8, confirm this phenomena ; the relative acoustic pressure lies from 0 dB, on the reflector edge, to 5 dB, at the reflector upper face 'center. Both configurations differentials are presented in figure 9. On this one, its average value is negative on the reflector upper face ; this means that the acoustic level is higher with "Test configuration". This result can be applied to the other octaves as shown on the table A. These results mean that the acoustic level is higher in "Test configuration". However, the differences are very small and both configurations can be considered the same.

Octave (configuration)	Average value	Minimal value	Maximal value
63 (A/D)	- 0.12	- 4.19	2.9
125 (A/D)	- 2.58	- 7.	1.5
250 (A/D)	- 2.46	- 8.1	.77
500 (A/D)	- 0.77	- 4.03	1.86
1000 (B/D)	- 2.09	- 4.92	- 0.03
2000 (C/D)	- 3.3	- 8.3	- 0.67

Indicated values :

Pressure differences on the reflector between "Launch configuration" and "Test configuration". A positive value means that the pressure is higher in "Launch configuration". The average difference (in dB) is shown in the first column, the smallest difference in the second and, the largest difference in the third.

Table A : Comparison between "Test configuration" and "Launch configuration".

CONCLUSION -

The ASTRYD application to the prediction of the acoustic loading on satellite reflectors is very interesting. It gives a new point of view on the tests analysis and allows to check that the "Test configuration" was good. The software originality, which is the time domain computation, allows to compute on a large frequencies band, with a high upper limit, with a small frequency step and with a small computation cost. In the satellite applications, computations are taken from 0 to 2800 Hz, for a 2 meters long structure. Specific numerical tools give results easy to analyze such as differential pressures map. The objective was the comparison of acoustic response between two configurations ; therefore the fluid structure coupling effects were negligible. But, if we should obtain some exact numerical values, such as stresses in the reflector, we ought to take into account the air's interaction with the mechanical behaviour of the structure. For doing this, we shall need to use the ASTRYD-coupling software. "ASTRYD-coupling" is also based on the same time domain computations method which refers to the Kirchhoff's formulae and the structure behaviour is taken into account by its modal characteristics in vacuo. "ASTRYD-coupling" has already been used for spatial applications. The results, which have been compared with experimental results, proved the software capabilities.

ACKNOWLEDGMENTS -

This study has been realized within the framework of a Research Contract for the account of ALCATEL ESPACE, whom we thank for their collaboration.

REFERENCES

- [1] Dimensional acoustics of rigid or moving surfaces : integral formulation, explicit time scheme and subsequent frequency analysis.
J.M.PAROT, D.VAUCHER DELACROIX
S.GRIOTIER-P.VERPEAUX*(C.E.A.-DEMT)
UNIVERSITY COLLEGE OF SWANSEA
NUMETA-87- - Proceedings of the international Conference on : "Numerical methods in engineering : theory and applications" - SWANSEA (U.K.)
6-10 Juillet 1987
- [2] Farfield and radiation calculations by means of a time domain integral equation formulation.-
D.VAUCHER de la CROIX, J.M. PAROT-
INTER-NOISE 88 - AVIGNON
30Août-1 Sept.88-
- [3] Radiation and scattering of acoustic waves from bodies of arbitrary shape in three-dimensional half space
A.F. SEYBERT - B.SOENARKO
Transact° of ASME-Vol110-Janvier1988

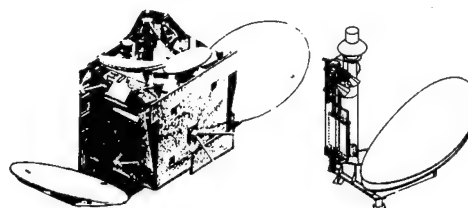


Figure 1 : TELECOM2 Satellite and k.u antenna

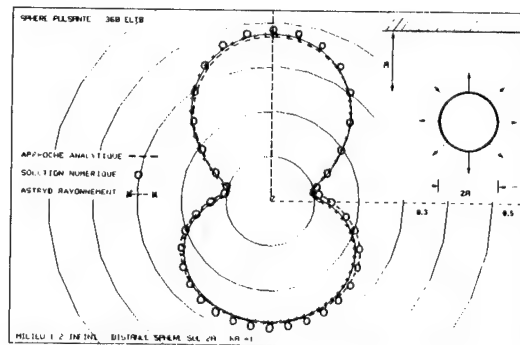


Figure 2 : Pulsating sphere directivity in half-space medium

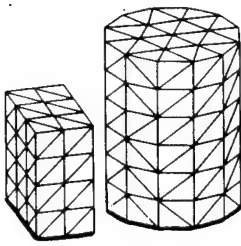


Figure 3 : Schock wave : Buildings meshing

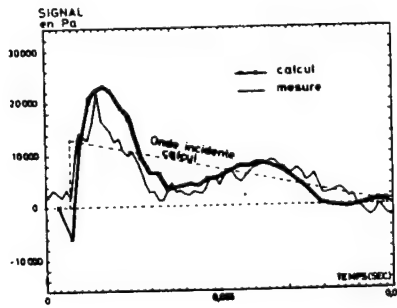


Figure 4 : Schock wave : Acoustic pressure between both buildings

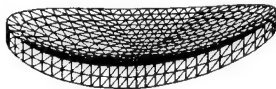


Figure 5 : k.u reflector meshing

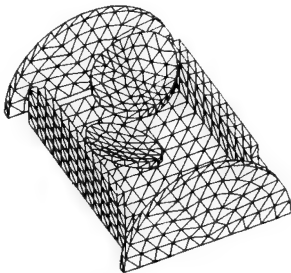


Figure 6 : Meshing of TELECOM2 upper part

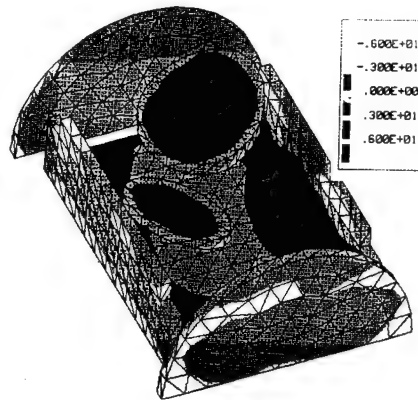


Figure 7 : Acoustic pressure field on TELECOM2 ; octave 250 Hz

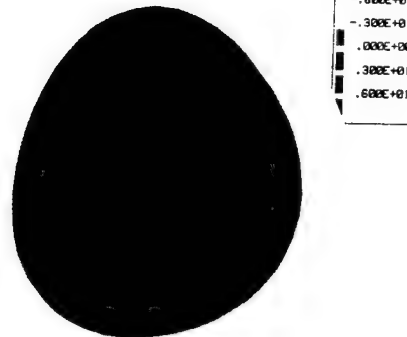


Figure 8 : Acoustic pressure field on k.u reflector ; octave 250 Hz

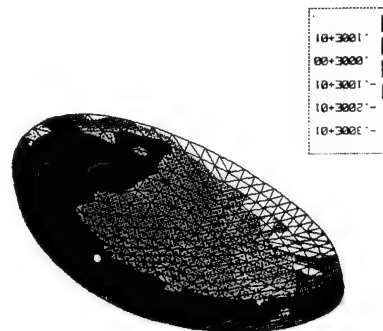


Figure 9 : Acoustic pressure differential on k.u reflector ; octave 250Hz.

N 92-23818

ACOUSTIC CAVITY AND FLUID/STRUCTURE INTERACTION MODELS A METHODOLOGICAL DETERMINISTIC APPROACH AND PROBLEMS ENCOUNTERED.

Pietro Carlo MARUCCHI-CHIERRO

Alenia Spazio S.p.A. (*)

533-37
84725

ABSTRACT

The aim of this paper is to demonstrate the feasibility and reliability of the mathematical model based on the acoustic-structural analogy and its numerical simulation, only in the presence of low modal density, using F.E.M. technique.

To develop the methodology, the study was carried out on simple cases where it is also possible to control the numerical results by analytical approach. In this manner, it has been possible to highlight numerical imprecisions when we study 2D and 3D acoustic cavities.

Moreover, a method is shown that is able to transmit both the complex mode shapes and the complex modal model of the coupled fluid/structure system to the SDRC/SUPERTAB and SDRC/SYSTAN postprocessors.

Keywords: Acoustic Cavity. Fluid/Structure Interaction. Audible Noise.

1. INTRODUCTION

The audible noise levels in a manned space project depend on the structural and acoustic transmission paths between disturbance sources (structural, acoustic and fluidodynamic ones) and receivers (inside the acoustic cavity) and from the fluid/structure interaction between the acoustic cavity and its structural boundaries.

For this aspect, the designers must ensure an acceptable (vs. requirements) environment up to high frequency (16 KHz).

The aim of this paper is to demonstrate the feasibility and reliability of the mathematical model based on the acoustic structural analogy and its numerical simulation, only in the presence of low modal density, using F.E.M. technique.

To develop the methodology, the study was carried out on simple cases where it is also possible to control, by analytical approach, the numerical results.

In this manner, it was possible to highlight numerical problems where we study 2D and 3D acoustic cavities or 2D structural box with geometrical symmetries (i.e. 2D acoustic square area, 2D structural cubic box, 3D acoustic cubic cavity...).

In these cases the eigensolution presents single and multiply roots.

The presence of multiply roots causes serious imprecisions for the F.E.M. algorithm not only for the mode shapes computation but also for the computation of the frequency responses (see transfer function or forced frequency function).

To highlight this problem and improve the numerical solution, two acoustic models of a cubic cavity were studied, one with wrong numerical modal coefficients resulting from a standard acoustic F.E.M. model (Ref. 1) of the cubic cavity and the other with improved numerical modal coefficients resulting from a corrected acoustic F.E.M. model of the same cavity.

Before computing and comparing frequency responses, the modal acoustic viscous damping ratio ($C/C_{cr} = 0.0005$) were added for each considered real eigenvectors of both modal models.

Moreover, in order to avoid the modal approach, frequency responses related to the two above mentioned acoustic F.E.M. models were computed using direct approach of MSC/NASTRAN code.

The comparison of the frequency responses show that it is possible to have slight, significant and unacceptable differences between the two acoustic models of the cavity.

So, by means of this study it was demonstrated that this numerical imprecision present at multiple roots may be a serious problem for a structure or acoustic cavity with geometrical symmetries.

(*) Alenia Spazio SpA is a Company of ALENIA SpA, the new Company belonging to the IRI-FINMECCANICA Group, resulting from the merger of Aeritalia and Selenia, taking over full responsibility for their functions, responsibilities and activities.

Lastly, a method is described to transmit complex mode shapes and complex modal models of the coupled fluid/structure system to the postprocessor SDRC/SUPERTAB in order to study coupled mode shapes, and to the postprocessor and solver SDRC/SYSTAN in order to study complex systems of acoustic cavities.

2. DEFINITION OF ANALYTICAL APPROACH FOR THE FLUID/STRUCTURE INTERACTION

In this approach, we use the acoustic-structural analogy (Refs. 2, 3) for the fluid/structure interaction where the structural equations become waves equations. So, we assume that:

- * we consider only one physical d.o.f. (x for example) volume forces ($\dot{f}_x = 0$)

These two conditions represent the characteristics of the acoustic field.

While the acoustic/structural analogy imposes the following conditions:

$$\frac{\theta + 2\mu}{\mu} = 1$$

$$\frac{\rho_s}{\mu} = \frac{1}{c^2}$$

where:

μ, θ	LAME constants
ρ_s	structural density
c	sound speed
u	displacement
p	pressure of the fluid

So, with the above hypothesis we obtain:

$$\frac{\theta + 2\mu}{\mu} \frac{\delta^2 u}{\delta x^2} + \frac{\delta^2 u}{\delta y^2} + \frac{\delta^2 u}{\delta z^2} + \left(\frac{\theta + \mu}{\mu} \right) \left(\frac{\delta^2 v}{\delta x \delta y} + \frac{\delta^2 w}{\delta x \delta z} \right) + \frac{1}{\mu} (f_x) = \frac{\rho_s \delta^2 u}{\mu \delta t^2}$$

(NAVIER equation ==> structural field)

$$\frac{\delta^2 p}{\delta x^2} + \frac{\delta^2 p}{\delta y^2} + \frac{\delta^2 p}{\delta z^2} = \frac{1}{c^2} \frac{\delta^2 p}{\delta t^2}$$

(Acoustic field)

This wave equation must be solved with F.E.M. technique for computing the acoustic field enclosed into a cavity with rigid walls.

When we consider a cavity with flexible walls, we must simulate these two boundary conditions:

$$\frac{\delta p}{\delta n} = -\rho \ddot{u}_n \quad \text{structural effect on the fluid}$$

$$F = P A \quad \text{fluid effect on the structure}$$

Where:

\ddot{u}_n	normal acceleration on the walls of the cavity
A	area of the cavity's walls

and imposing the acoustic/structural analogy, we obtain:

for the structural effect on the fluid

$$F = -GA \rho_A \ddot{u}_n$$

for the fluid effect on the structure

$$F = P A$$

Moreover, the formulation for the coupled system fluid/structure is done considering:

- * the structural dynamic described by:

$$[M_s] \{\ddot{u}\} + [K_s] \{u\} = \{F_s\}$$

- * the fluid dynamic described by:

$$[M_a] \{\ddot{p}\} + [K_a] \{p\} = \{F_a\}$$

- * the boundary conditions:

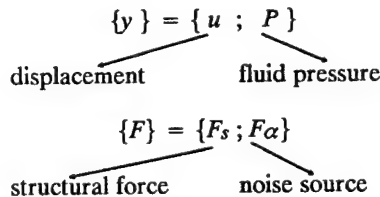
$$F = GA \rho_A \ddot{u}_n \quad (\text{structural effect})$$

$$F = -P A \quad (\text{fluid effect})$$

Finally, the coupled system (fluid/structure) is described by:

$$\begin{bmatrix} M_s & O \\ M_{AS} & M_A \end{bmatrix} \{\ddot{y}\} + \begin{bmatrix} K_s & K_{SA} \\ O & K_A \end{bmatrix} \{y\} = \{F\}$$

Where: M_{AS} is the structural effect
 K_{SA} is the fluid effect



We have chosen two different formulations for M_{AS} and K_{SA} for our applications:

- * The non-symmetric formulation ($P = x$)

$$\begin{bmatrix} M_s & O \\ M_{AS} & M_A \end{bmatrix} \{\ddot{y}\} + \begin{bmatrix} K_s & K_{SA} \\ O & K_A \end{bmatrix} \{y\} = \{F\}$$

- * The symmetric formulation ($p = \Phi$) (Ref. 4)

$$\begin{bmatrix} M_s & O \\ O & M_A \end{bmatrix} \begin{Bmatrix} \ddot{x} \\ \ddot{\Phi} \end{Bmatrix} + \begin{bmatrix} O & A \\ A^T & O \end{bmatrix} \begin{Bmatrix} \dot{x} \\ \dot{\Phi} \end{Bmatrix} + \begin{bmatrix} K_s & O \\ O & K_A \end{bmatrix} \begin{Bmatrix} x \\ \Phi \end{Bmatrix} = \begin{Bmatrix} F_s \\ F_A \end{Bmatrix}$$

3. TRANSLATION OF THESE TWO FORMULATIONS FOR THE COUPLED SYSTEM TO MSC/NASTRAN F.E.M. TECHNIQUE

The translation of the two mentioned analytical formulations into a numerical method using the MSC/NASTRAN F.E.M. technique is done by means of the following methodology:

- * both for the non-symmetric and symmetric formulations, we choose the modal analysis approach so we can study the coupled mode-shapes of the coupled system (fluid/structure)
- * the effect of fluid on the wall of the cavity is computed, for both formulations, using sol 24, with which we compute the matrix [A]
- * the matrix of the fluid/structure interaction is built by means of a dedicated software (MATINTER) written by Alenia Spazio this matrix contains the contributions of the interaction associated at each fluid/structure coincident nodes
- * the symmetric formulation does not need ALTER to compute the fluid/structure interaction represented by the following matrix:

$$\begin{bmatrix} 0 & A \\ A^T & 0 \end{bmatrix}$$

- * while the non-symmetric formulation needs a specific ALTER to compute the matrix:

$$-\rho A^T$$

- * the coupled modal analysis is done by performing SOL 29 with a specific alter (written by Alenia Spazio) to generate the output (.out2) readable by the postprocessor SDRC/SUPERTAB
- * for a modal frequency and random response, we can perform:
 - SOL 30 without a specific ALTER to compute the responses.
 - SOL 29 with a specific ALTER (written by Alenia Spazio) to generate the outputs (.UT1;.UT2) readable by the dynamic postprocessor SDRC/SYSTAN.

The advantages of this method are:

- we can study, with only one NASTRAN run, the coupled mode-shapes and the forced responses.

- SYSTAN permits:

to excite the analytical coupled modal model by means of analytical and/or experimental inputs (forces,...)

to study the dynamic behaviour of the acoustic and mechanical systems under specific constraints, in order to assemble other systems treated as subsystems and evaluate the dynamics of the resultant system.

Note:

It is not suitable to use the direct frequency and random response approach, rather than the modal one, for the higher C.P.U. time consumption.

Example: to compute a forced response (acoustic pressure) due a single local source inside a cubic box with flexible walls, we need the C.P.U. time:

6.34 hours for SOL 30 (Modal Approach)

72.23 hours for SOL 26 (Direct Approach)

4. CHECKING AND RELIABILITY OF APPROACHES STUDYING TYPICAL TEST CASES FOR ACOUSTIC CAVITY F.E.M. MODEL

4.1 F.E.M. approach using MSC/NASTRAN.

To check this approach, we have studied simple dedicated 2D and 3D acoustic models. The results of all these numerical models were compared with the analytical ones (Refs. 5, 6).

The 2D acoustic models studied are:

- * square enclosure (1000mm x 1000mm)
- * circular enclosure (R=914.4 mm)

The problems encountered in this application on VAX computer (32 bits) are:

numerical instability at multiply roots (see Table 1 for the comparison between the theoretical and numerical mode shapes, while Fig. 1 (*) shows the comparison between theoretical mode shapes (1,2); (2,1) and numerical ones for a square section)

2D ACOUSTIC CAVITY

(square section : 1 m x 1 m)

Type of mode (*)	Frequency (Hz)		% difference (**)
	Theoretical	Numerical	
(0, 0)	0.0	0.0	/
(1, 0)	170.1	168.9	0.7
(0, 1)	170.1	168.9	0.7
(1, 1)	240.6	235.0	2.3
(0, 2)	340.2	331.3	2.6
(2, 0)	340.2	331.3	2.6
(2, 1)	380.4	362.4	4.7
(1, 2)	380.4	362.4	4.7
(2, 2)	481.1	439.0	8.7

Legend :

(*) mode (j,k)

j = number of nodal lines along X-axis

k = number of nodal lines along Y-axis

(**) referred to theoretical frequency

Table 1 - Comparison between theoretical and numerical mode shapes

(*) see Figures at the end of the paper

2D ACOUSTIC CAVITY

(square section: 1 m × 1 m)

Type of mode [**]	MODAL COEFFICIENTS [**]			% difference [**]	
	Theoretical	Numerical acoustic model		Standard FEM: acoustic model	Improved FEM: acoustic model
		Standard FEM	Improved FEM		
(0, 0)	+ 1.0	+ 1.0	+ 1.0	/	/
(1, 0)	- 1.0	- 0.729	- 1.0	27.1	/
(0, 1)	- 1.0	- 1.0	- 1.0	/	/
(1, 1)	+ 1.0	+ 1.0	+ 1.0	/	/
(0, 2)	+ 1.0	- 0.559	- 1.0	44.1	/
(2, 0)	+ 1.0	+ 1.0	+ 1.0	/	/
(2, 1)	- 1.0	- 1.0	- 1.0	/	/
(1, 2)	- 1.0	+ 0.563	- 1.0	43.7	/
(2, 2)	+ 1.0	+ 1.0	+ 1.0	/	/

Legend : [*] calculated on grid point 729 (+ 1.0, + 1.0, + 1.0)

[**] mode (j,k)
j = number of nodal lines along X-axis
k = number of nodal lines along Y-axis

[***] referred to theoretical value

Table 2 - Comparison between theoretical and numerical modal coefficients

To correct these numerical imprecisions, the values E, G and ν have been tuned inside MAT1 card. These values are computer dependent (*).

Now for VAX computer (32 bits), this numerical instability is completely controlled (see Table 2 for the comparison between imprecise modal coefficients and right ones, and Fig. 1 for the comparison between the wrong and right mode shapes for a quadratic section).

This method is also reliable for any section (see Table 3 for the comparison between theoretical and numerical mode shapes and Fig. 2 for the comparison between theoretical and numerical mode shapes [2,0] for a circular section).

(*) For example, the 2D acoustic models were also studied on I.B.M. 3090 (32 bits) and CDC/CYBER 180/930 (64 bits) computers. Only CDC/CYBER computer does not have the numerical instability for this application.

2D ACOUSTIC CAVITY

(circular section: R = 0.9144 m)

Type of mode [**]	Frequency (Hz)		% difference [**]
	Theoretical	Numerical	
(0, 0)	0.0	0.0	/
(1, 0)	109.0	109.0	/
(2, 0)	180.7	179.9	0.4
(0, 1)	226.7	225.7	0.4
(3, 0)	248.6	245.5	1.2
(4, 0)	314.7	307.5	2.3
(1, 1)	315.5	312.6	0.9

Legend : [*] mode (j,k)
j = number of nodal diameters
k = number of nodal circles

[**] referred to theoretical frequency

Table 3 - Comparison between theoretical and numerical mode shapes

The 3D acoustic models studied are:

- * cubic cavity (1000mm x 1000mm x 1000mm)
- * cylindrical cavity (R = 2108mm ; L = 5600mm)

The problems encountered in this application on VAX computer (32 bits) are:

- * numerical instability at multiple roots (see Table 4) for the comparison between theoretical and numerical mode shapes and Figure 3 for the comparison between theoretical and numerical mode shapes [1,2,0];[1,0,2] for a cubic cavity

For this test case also, the E, G and ν values were tuned inside MAT1 NASTRAN card in order to correct the numerical imprecisions.

These values are machine dependent also for the 3D acoustic cavity model.

3D ACOUSTIC CAVITY

(cubic volume: 1 m × 1 m × 1 m)

Type of mode [**]	Frequency (Hz)		% difference [**]
	Theoretical	Numerical	
(0, 0, 0)	/	/	/
(0, 0, 1)	170.0	169.0	0.6
(0, 1, 0)	170.0	169.0	0.6
(1, 0, 0)	170.0	169.0	0.6
(0, 1, 1)	240.4	236.0	1.8
(1, 0, 1)	240.4	236.0	1.8
(1, 1, 0)	240.4	236.0	1.8
(1, 1, 1)	294.4	285.3	3.1
(2, 0, 0)	340.0	331.5	2.5
(0, 2, 0)	340.0	331.5	2.5
(0, 0, 2)	340.0	331.5	2.5

Legend : [*] mode (i,j,k)
i = number of nodal lines along X-axis
j = number of nodal lines along Y-axis
k = number of nodal lines along Z-axis

[**] referred to theoretical frequency

Table 4 - Comparison between theoretical and numerical mode shapes

3D ACOUSTIC CAVITY

(cubic volume: 1 m * 1 m * 1 m)

Type of mode [*]	MODAL COEFFICIENTS [*]				% difference [**]	
	Theoretical	Numerical acoustic model		Standard FEM acoustic model	Improved FEM acoustic model	
		Standard FEM	Improved FEM			
(0 , 0 , 0)	+ 1.0	+ 1.0	+ 1.0	/	/	
(0 , 0 , 1)	- 1.0	- 0.656	+ 1.0	34.4	/	
(0 , 1 , 0)	- 1.0	+ 0.487	- 0.934	51.3	6.6	
(1 , 0 , 0)	- 1.0	+ 0.790	+ 1.0	21.0	/	
(0 , 1 , 1)	+ 1.0	- 0.804	+ 1.0	19.6	/	
(1 , 0 , 1)	+ 1.0	- 0.398	+ 0.527	60.2	47.5	
(1 , 1 , 0)	+ 1.0	- 0.632	- 1.0	36.8	/	
(1 , 1 , 1)	- 1.0	+ 1.0	+ 1.0	/	/	
(2 , 0 , 0)	+ 1.0	- 0.868	+ 1.0	13.2	/	
(0 , 2 , 0)	+ 1.0	+ 0.978	+ 1.0	2.2	/	
(0 , 0 , 2)	+ 1.0	+ 0.319	+ 0.660	68.1	34.0	

Legend : [*] calculated on grid point 729 (+ 1.0, + 1.0, + 1.0)

[**] mode (i,j,k)
i = number of nodal lines along X-axis
j = number of nodal lines along Y-axis
k = number of nodal lines along Z-axis

[***] referred to theoretical value

Table 5 - Comparison between theoretical and numerical modal coefficients

In fact, the 3D acoustic cavity models were studied on CDC/CYBER 180/930 computer (64 bits) and also on this machine we impact with the numerical instability.

Now for VAX computer (32bits), this numerical instability is quite completely controlled (see Table 5 for the comparison between imprecise modal coefficients and "quite controlled ones", and Fig. 3 for the comparison between the wrong and "quite" right mode shapes for a cubic cavity)

This method is quite reliable for any cavity (see Table 6 for the comparison between theoretical and numerical mode shapes, and Fig. 4 for the comparison between theoretical and numerical mode shapes [0,2,0] for cylindrical cavity. The near future investigations are oriented to study the complete control of the numerical instability present at the 3D symmetric acoustic cavity models.

3D ACOUSTIC CAVITY

(cylindrical volume: R = 2.108 m, L = 5.6 m)

Type of mode [*]	Frequency [Hz]		% difference [**]
	Theoretical	Numerical	
(0 , 0 , 0)	0.0	/	/
(1 , 0 , 0)	30.3	30.3	/
(0 , 1 , 0)	47.3	47.2	0.2
(1 , 1 , 0)	56.2	55.5	1.2
(2 , 0 , 0)	60.7	60.4	0.5
(2 , 1 , 0)	76.9	74.9	2.6
(0 , 2 , 0)	78.4	73.8	5.9
(1 , 2 , 0)	84.1	78.5	6.6
(3 , 0 , 0)	91.0	90.2	0.9
(2 , 2 , 0)	99.1	90.8	8.3

Legend : [*] mode (i,j,k)
i = number of nodal line along cylindrical axis
j = number of nodal diameters
k = number of nodal circles

[**] referred to theoretical frequency

Table 6 - Comparison between theoretical and numerical mode shapes

5. EFFECTS OF THIS NUMERICAL INSTABILITY ON THE 2D AND 3D ACOUSTIC CAVITY MODELS

5.1 Case of the acoustic model of a cubic cavity

The numerical instability present for both 2D and 3D acoustic cavity models, with multiple roots, causes serious imprecisions not only for the mode-shapes computation (as we have seen in the previous Chapter) but also when we compute the frequency responses (see transfer function or forced frequency function).

To highlight this problem, a numerical instable model and a "quite stable" model have been studied for 2D and 3D acoustic models. For both test cases, these assumptions were chosen:

- * rigid walls for the structure
- * acoustic viscous damping ratio $c/ccrit. = .0005$.

The approaches used for this study are the modal and the direct ones.

The following analyses were performed for the modal approach:

- * normal mode analysis for the 2D and 3D F.E.M. acoustic cavity models (NASTRAN SOL 3) and successive computation of the frequency response functions from the F.E.A. modal models using the sw SDRC/SYSTAN (see Figures 5-6 for a cubic cavity)
- * or directly by performing SOL 30 of the F.E.M. acoustic cavity models (see Fig. 7)

From the comparison of these results, we see that it is possible to have slight, significant and not acceptable differences between the unstable and stable acoustic models as shown respectively in Figures 5 - 7 using the modal approach.

While for the direct approach, the following analysis was performed:

- * direct frequency and random response (NASTRAN SOL 26) of the F.E.M. acoustic cavity models without acoustic modal damping (see Figure 8).

The comparison of these results shows that the numerical imprecisions are not dependent on the modal approach; on the other hand, these imprecisions are not dependent on the computation of the modal coefficient both for single and multiple roots. But this numerical instability depends only on the numerical conditioning derived by the values E , G and ν for acoustic cavity F.E.M. models using structural algorithms and imposing on it the acoustic-structural analogy.

6. CHECKING AND RELIABILITY OF APPROACHES STUDYING A TEST CASE FOR FLUID/STRUCTURE INTERACTION F.E.M. MODELS

It was checked:

the effect of fluid on the walls of the cavity

This effect was studied on:

- * square enclosure (2D) (1000mm x 1000mm)
- * cubic box (3D) (1000mm x 1000mm x 1000mm)

No problems were encountered for this application on VAX computer (32bits). The theoretical results are the same as the numerical ones (see Table 7 for a cubic box). To simulate this effect, a constant pressure (10-3N/mm²) was applied on the normal direction of each wall of the cubic box (see Figure 9).

2D STRUCTURAL BOX
(cubic box : 1 m * 1 m * 1 m)

Effect of the fluid on the walls of a cubic box			
Node	Theoretical (mmN)	Numerical (mmN)	% difference
1001, X	+ 3.90625	+ 3.90625	/
1001, Y	+ 3.90625	+ 3.90625	/
1001, Z	+ 3.90625	+ 3.90625	/
1002, X	0.0	0.0	/
1002, Y	- 7.81250	- 7.81250	/
1002, Z	- 7.81250	- 7.81250	/
1011, X	0.0	0.0	/
1011, Y	- 15.625	- 15.625	/
1011, Z	0.0	0.0	/

Legend : [*] effect of the fluid: $P_{el} \cdot (A_{el}/4)$
where: P_{el} = pressure on the element
 A_{el} = area of element

[**] referred to theoretical value

Table 7 - Comparison between theoretical and numerical values of the effect of the fluid on the structure

In this manner, all the matrix elements a_{ij} of the matrix [A], which represents the area matrix, are constructed.

numerical simulation of the fluid/structure interaction

This fluid/structure interaction was studied on:

- * square enclosure (1D structural model) containing a thin layer of air (2D acoustic model, see Fig. 10)
- * cubic box (2D structural model) containing a volume of air (3D acoustic model, see Fig. 11).

To perform this fluid/structure interaction, the non-symmetric formulation using the dedicated NASTRAN alter/2/ was used in order to perform the computation of the matrix - ρA^T . Both approaches (modal and direct) was tested for the fluid/structure interaction of a cubic box containing 1m³ of air. The comparison (see Figure 12) of the results coming from NASTRAN SOL 30 (modal approach) and from NASTRAN SOL 26 (direct approach) shows that the methodology is reliable.

7. POST-PROCESSING OF THE DATA OF THE COUPLED SYSTEM FLUID/STRUCTURE

In order to study the coupled fluid/structure mode shapes, and consequently to improve both the dynamic behaviour of the structural system and optimize the distribution of the acoustic pressure inside the cavities, two routes to post-process the data coming from MSC/NASTRAN were chosen:

- 1 visualization and study of the coupled mode-shapes. This goal is pursued by means of the SDRC/SUPERTAB tool.
- 2 dynamic analysis and acoustic optimization of the coupled system (fluid/structure) by means of the SDRC/SYSTAN tool.

Now the methodology of the transmission for the complex coupled mode-shapes from NASTRAN SOL29 on VAX mainframe to the SDRC/SUPERTAB on HP workstations is reliable.

Figure 13 shows the flowchart for the transmission of the complex modal data and complex modal models. But to permit the transmission between NASTRAN and SUPERTAB, it was written:

- * a dedicated alter for SOL 29 to extract and store in a binary file the informations coming from a standard modal complex eigenvalue analysis.
- * a dedicated sw (TRASFORM) that allows:

- 1 - the transformation from the binary format to an ASCII readable by SDRC sw (Ref. 7).
- 2 - to perform a real mode approximation on the complex mode-shape (Ref. 8).

The real mode approximation is determined by taking the amplitude of the complex mode-shape coefficient.

The sign of that amplitude value is determined by the sign of the imaginary part of the original complex value for displacement data (=acoustic pressure when we use the non-symmetric formulation), or by the sign of the real part of the original complex value for velocity data (=acoustic pressure when we use the symmetric formulation).

Figure 14 shows some coupled mode-shapes of the fluid/structure interaction model, read by SUPERTAB sw.

8. CONCLUSIONS AND FUTURE DEVELOPMENTS

The numerical simulation of the fluid/structure interaction considering the acoustic-structural analogy seems to be reliable, even if the numerical instability for the 3D acoustic cavity models with geometrical symmetries remains. Investigations for the near future are mainly oriented to testing and tuning the symmetric formulation using NASTRAN SOL29 for modal complex eigenvalue analysis and NASTRAN SOL30 for modal frequency and random response. Moreover, specific ALTERS are under study to permit the transmission of the complex modal model of the coupled fluid/structure system. Lastly, passive and active noise control model will also be studied. For the passive intervention (i.e. soundproofing materials,...), two different analytical formulations will be considered:

- * the field formulation
- * the boundary condition

while the active intervention could be done by means of two principal methods:

- * loudspeakers and microphones system
- * active control of vibrational behaviour of the structure via piezo-electric materials.

For the particular characteristics of this kind of active control, studies are oriented to improving the analytical and numerical models of the piezo-electric material. Finally, other types of algorithm using F.E.M. acoustic element or B.E.M. method will be studied and checked in order to improve the acoustic cavity model and the fluid/structure interaction model.

9. REFERENCES

1. D.S. Nefske, J.A. Wolf jr., J. Howell - *Structural-acoustic finite element analysis of the automobile passenger compartment: a review of current practice*, Journal of Sound and Vibration, 1982, 8012, 247-266.
2. F. Grosveld, B.M. Sullivan, F. Marulo - *Aircraft interior noise prediction using a structural-acoustic analogy in NASTRAN modal synthesis*.
3. S.H. Sung, D.J. Nefske - *A coupled structural-acoustic finite element model for vehicle interior noise analysis*, ASME 1983 .
4. R.H. Mcneal, R. Citerley, M. Charging - *A symmetric modal formulation of fluid/structure interaction, including a static approximation to higher order fluid modes*.
5. L.L. Beranek - *Acoustics*, American Institute of Physics 1986.
6. R.D. Blevins - *Formulas for natural frequency and mode shape*, Van Nostrand Reinold Company 1979 .
7. I-DEAS level 4 , Users Guide vol.1, SDRC 1988.
8. *Modal-plus 8.0*, Reference Manual, SDRC 1983.

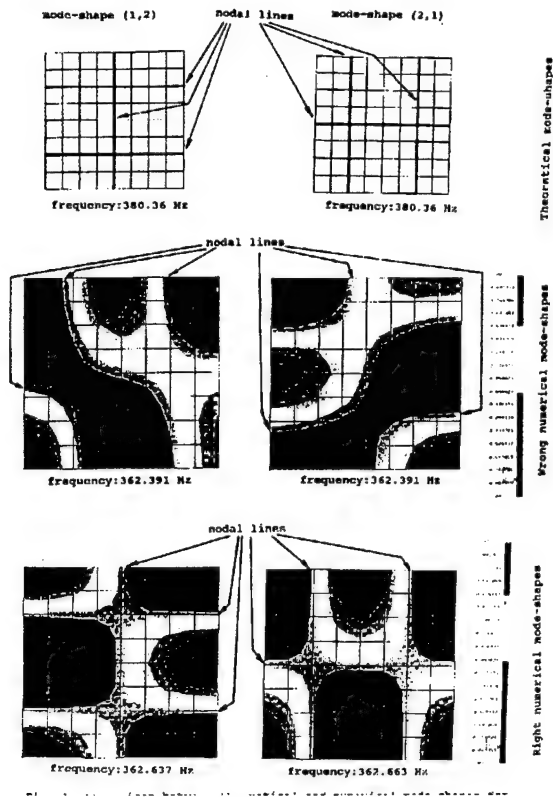


Fig. 1 - Comparison between theoretical and numerical mode-shapes for a square section

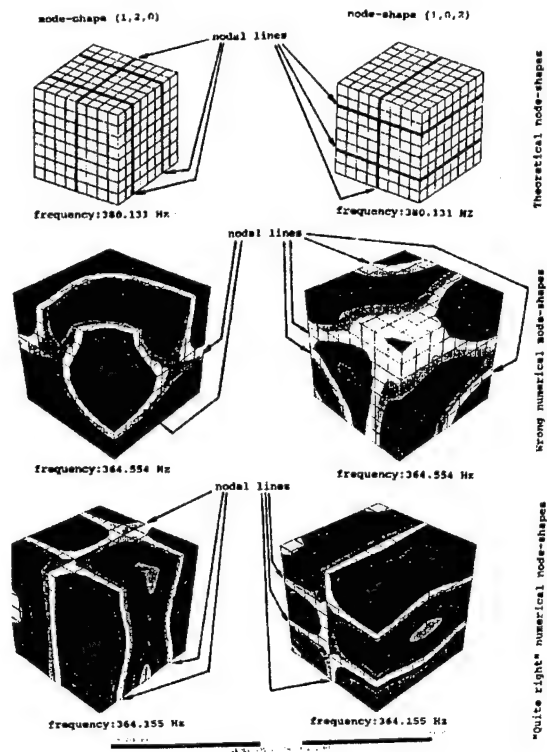


Fig. 3 - Comparison between theoretical and numerical mode-shapes

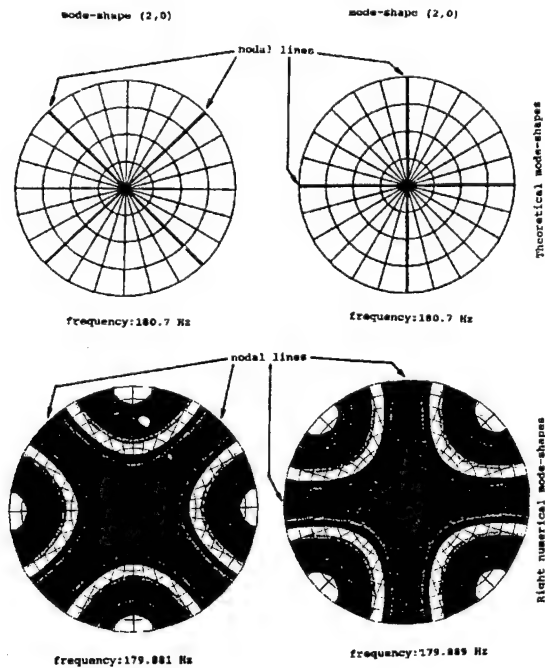


Fig. 2 - Comparison between theoretical and numerical mode-shapes for a circular section

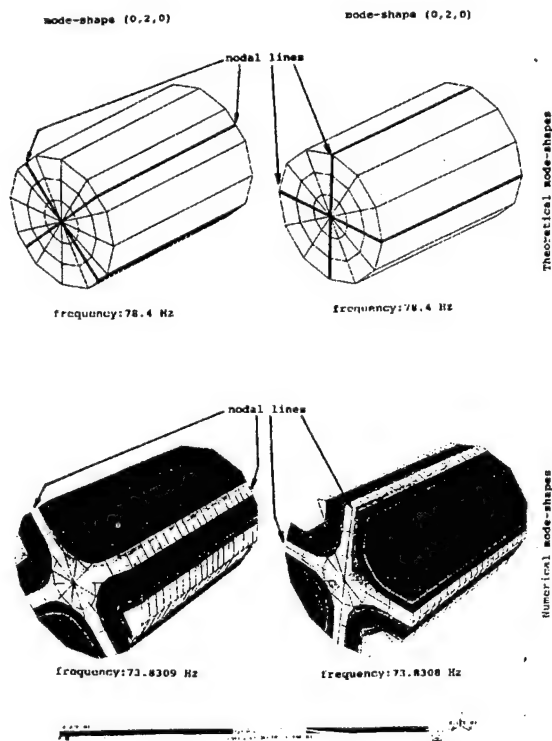


Fig. 4 - Comparison between theoretical and numerical mode-shapes

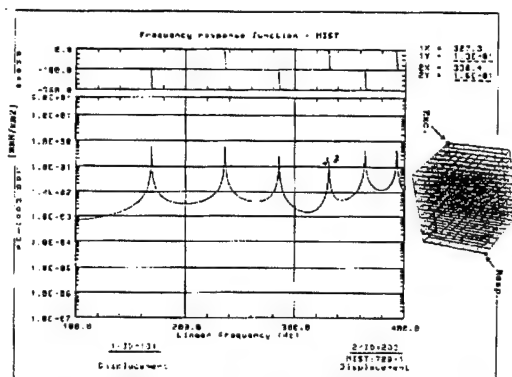


Fig. 5 - Comparison of the fluid pressure between an instable and stable acoustic cavity 3D F.E.M. model

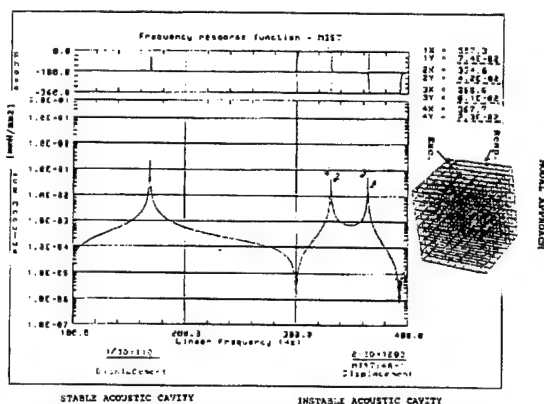


Fig. 6 - Comparison of the fluid pressure between an instable and stable acoustic cavity 3D F.E.M. model

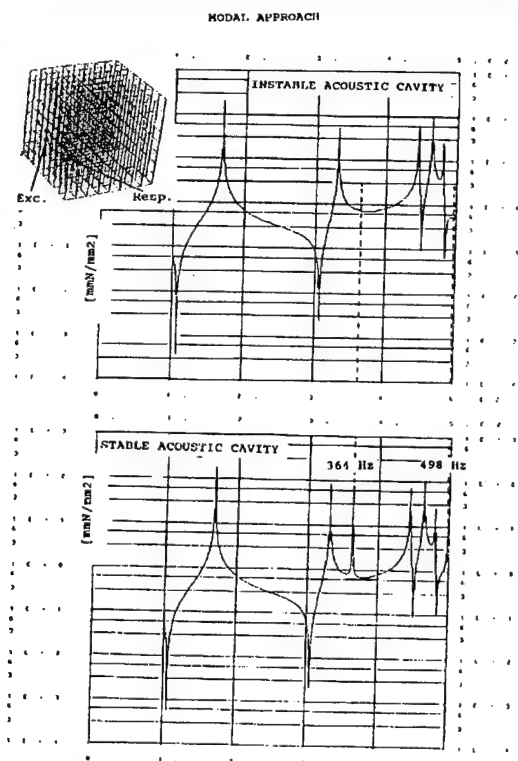


Fig. 7 - Comparison of the fluid pressure between an instable and stable acoustic cavity 3D F.E.M. model

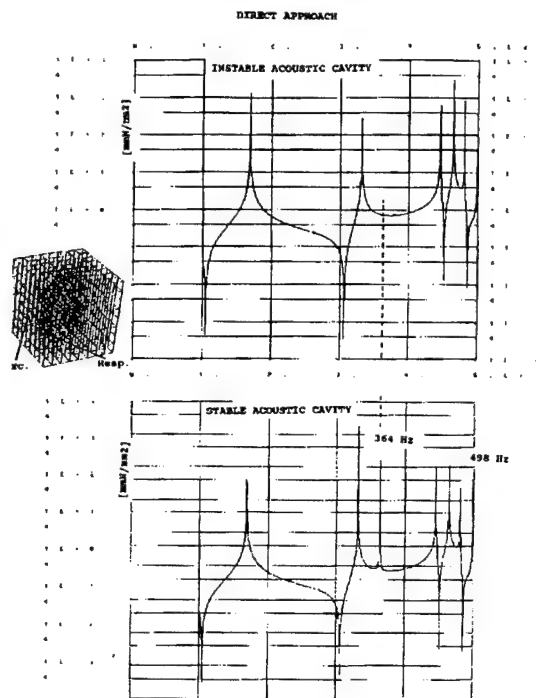


Fig. 8 - Comparison of the fluid pressure spectra between an instable and stable acoustic cavity 3D F.E.M. model

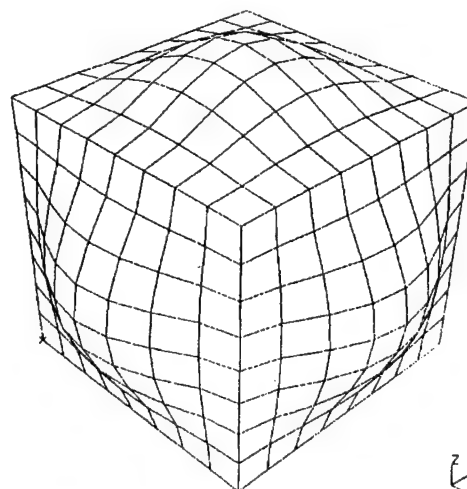


Fig. 9 - Effect of the fluid on the walls of a cubic box

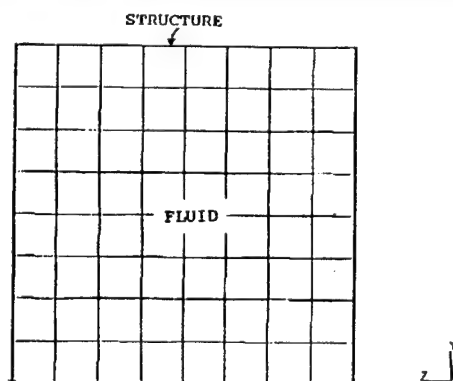


Fig. 10 - Fluid / Structure Interaction F.E.M. model (2D/1D)

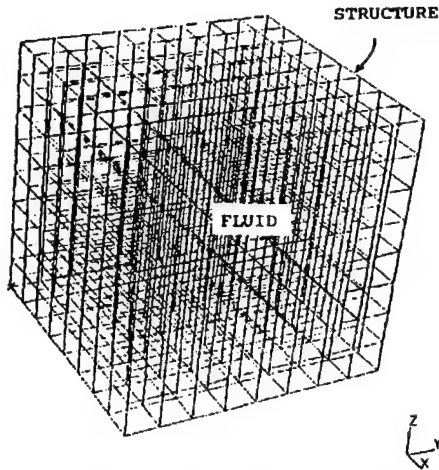


Fig. 11 - Fluid / Structure Interaction F.E.M. model (3D/2D)

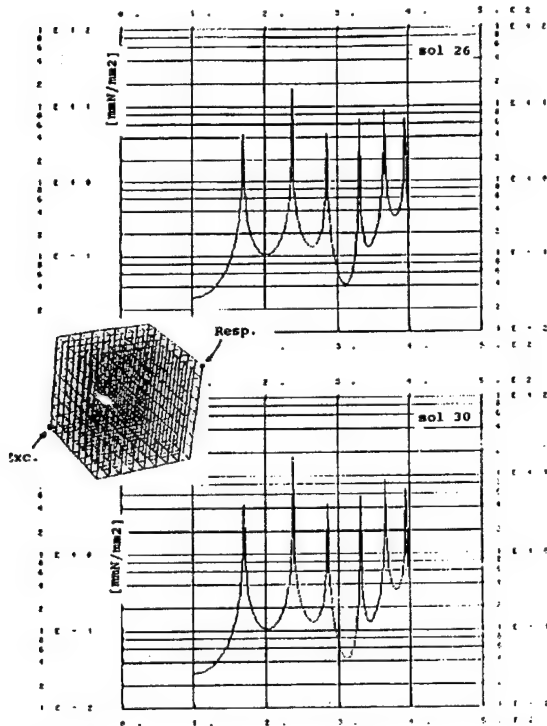


Fig. 12 - Forced frequency responses: fluid pressure comparison between sol 26 (direct approach) and sol 30 (modal approach)

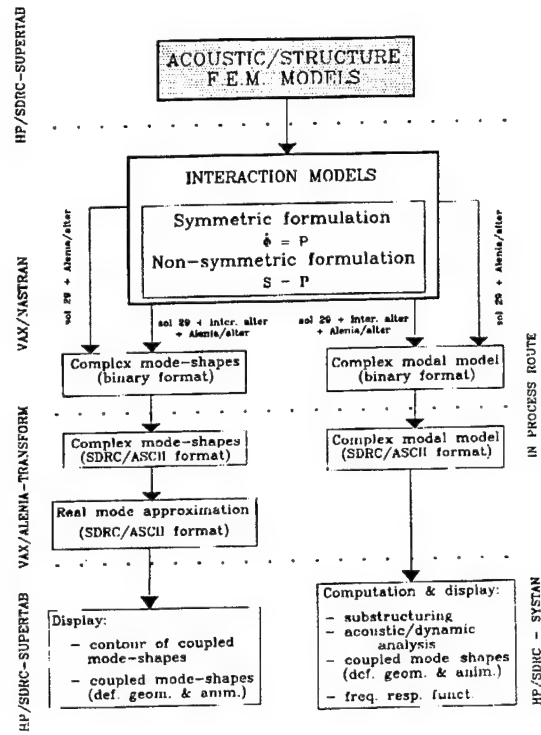


Fig. 13 - Flow-chart for the transmission of the complex modal informations and complex modal model

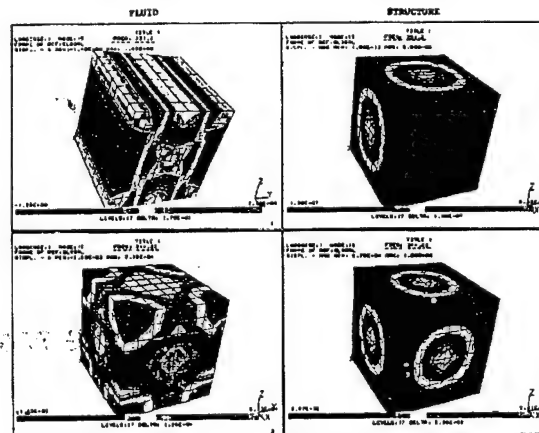


Fig. 14 - Coupled mode-shapes of the fluid / structure interaction model

SESSION
1.3.D

ANALYSIS
III

METHODS

PRECEDING PAGE BLANK NOT FILMED

N 92-23814

534.39

534.39

Employment of C.B. models for non-linear dynamic analysis

Ph. Deloo¹ M.R.M. Klein²¹ Consultant, Ikoss GmbH, Waldburgstrasse 21 D-7000-Stuttgart 80, FRG² European Space Agency / European Space and Technology Center ESA/ESTEC
Postbus 299, 2200AG Noordwijk, The Netherlands.

Abstract:

The non-linear dynamic analysis of large structures is always very time, effort and CPU consuming. Whenever possible the reduction of the size of the mathematical model involved is of main importance to speed up the computational procedures. Such reduction can be performed for the part of the structure which perform linearly. Most of the time, the classical Guyan reduction process is used. For non-linear dynamic process where the non-linearity is present at interfaces between different structures, Craig-Bampton models can provide a very rich information, and allow easy selection of the relevant modes with respect to the phenomenon driving the non-linearity.

The paper presents the employment of Craig-Bampton models combined with Newmark direct integration for solving non-linear friction problems appearing at the interface between the Hubble Space Telescope and its Solar Arrays during in-orbit manoeuvres. Theory, implementation in the FEM code ASKA and practical results are shown.

1. Craig-Bampton models background

The general equation of motion of a structure can be written as

$$M \ddot{q} + C \dot{q} + K q = F(t) \quad (1)$$

Considering the interface of the structure with other structures, we can split the dof's in internal dof's i and interface dof's j and write :

$$\begin{bmatrix} M_{ii} & M_{ij} \\ M_{ji} & M_{jj} \end{bmatrix} \begin{pmatrix} \ddot{q}_i \\ \ddot{q}_j \end{pmatrix} + \begin{bmatrix} K_{ii} & K_{ij} \\ K_{ji} & K_{jj} \end{bmatrix} \begin{pmatrix} q_i \\ q_j \end{pmatrix} = \begin{pmatrix} 0 \\ F_j(t) \end{pmatrix} \quad (2)$$

where without loss of generality we have assumed that only interface loads are applied and neglected the damping matrix. The Craig-Bampton approach consists of developing the displacements q on the basis of the static interface modes Φ , and the elastic modes φ_p of the structure clamped at the interface j :

$$q = \Phi_j q_j + \varphi_p \eta_p = \Psi X \quad (3)$$

where

$$\Psi = (\Phi_j \varphi_p) \quad \text{and} \quad X = \begin{pmatrix} q_j \\ \eta_p \end{pmatrix} \quad (4)$$

$$\Phi_j = \begin{pmatrix} \Phi_{ij} \\ I_{jj} \end{pmatrix} \quad \text{where} \quad K \Phi_j = \begin{pmatrix} 0 \\ R_j \end{pmatrix} \quad (5)$$

$$\varphi_p = \begin{pmatrix} \varphi_{ip} \\ 0 \end{pmatrix} \quad \text{where} \quad (K_{ii} - \omega^2 M_{ii}) \varphi_{ip} = 0 \quad (6)$$

As a consequence of such transformation, the initial equations of motion get transformed to

$$\begin{bmatrix} \bar{M}_{jj} & \bar{M}_{jp} \\ \bar{M}_{pj} & m_{pp} \end{bmatrix} \begin{pmatrix} \ddot{q}_j \\ \ddot{\eta}_p \end{pmatrix} + \begin{bmatrix} \bar{K}_{jj} & 0 \\ 0 & k_{pp} \end{bmatrix} \begin{pmatrix} q_j \\ \eta_p \end{pmatrix} = \begin{pmatrix} F_j(t) \\ 0 \end{pmatrix} \quad (7)$$

where :

\bar{K}_{jj} is the stiffness matrix statically reduced to the j interface.
 \bar{M}_{jj} is the mass matrix reduced at the interface according to the Guyan reduction concept.

k_{pp} and m_{pp} the generalized stiffness and mass matrices.

$\bar{M}_{jp} = \Phi_{ij}^T M_{ii} \varphi_{ip} + M_{ji} \varphi_{ip}$ is the modal participation factor matrix.

It must be noticed that both the physical and CB representation of the structure are mathematically equivalent, and both sets of matrices represent the free-free structure.

Modal selection can be performed based on the well known "Effective Modal Mass" concept with respect to the j interface. However, modes with low interface force contribution but describing internal spacecraft dynamics which is of interest have to be kept in addition to the modes dominating the interface response. This selection reduces significantly the size of the CB models, which is one of their advantages.

Furthermore, CB models avoid the usual stiffness and low frequency mass truncation problems, since the interface stiffness is included in the \bar{K}_{jj} matrix and the total mass in the \bar{M}_{jj} matrix.

In the same way FEM models are assembled. Craig-Bampton models can also be assembled, the connection always taking place using the physical dofs. The reduced size of all individual CB models reduces the size of the system CB model to a minimum set of modes which produces the most efficient representation of the spacecraft. Currently 3000 to 10000 dof FEM models can be efficiently reduced to 30 to 1000 Craig-Bampton freedoms.

The final assembled system model can if necessary be analyzed in free-free conditions. In this case, to ensure simplest correct recovery of interface forces and of stresses, most of the spacecraft free-free modes have to be used. Using Craig-Bampton models reduces this set to the most significant modes for the problem.

Another advantage of those models is their relationship with the clamped modes identified during testing, which provides a good engineering approach.

2. Handling non-linearities

Craig-Bampton models intrinsically address linear phenomenon, since constant material properties and usual FEM small deformation and displacement theory is used. However, there is room for non-linearity at the interface freedoms. This can occur as variable stiffness, connected/disconnected status of some freedoms and variable loads function of some interface freedom responses.

These limited cases are, however, representative of many practical interface effects, like gapping, non-linear tension-compression contact, torque limiter effects, etc..

These processes introduce time dependent perturbations in the equations of motion, limited to the interface freedoms for the CB mass and stiffness matrices, which shall be accounted for in the time integration process. They lead to a modification of the clamped condition of the interface freedoms as considered in the clamped modes. However, there is no contradiction in releasing CB interface dof's since we have seen that the CB model actually represents the complete free-free structure.

Since non-linearities are present in the behaviour of the final assembled system, standard time integrations methods as modal superposition cannot be applied anymore. A direct integration scheme has to be selected. This can be performed without problems since the CB model is just another representation of the physical FEM model. Integrating equations in a modal space by direct integration, although being unusual, is not contradictory. It must be noticed that the reduction of number of equations to integrate, usually resulting from the modal superposition approach, has actually now been performed at the Craig-Bampton model level. Thus this approach is not penalizing in terms of size reduction.

One of the most problematic aspects of usual direct integration approach (i.e. with physical dof matrices) is the damping aspect. Indeed, although modal damping values can be inferred from engineering experience or derived from testing, the implementation of these (in form of Raleigh series matrices) is quite cumbersome and seldom performed. Using the CB approach on the other hand, these values appear naturally in the equations of motion.

Indeed, the physical damping matrix C transforms into the CB space as ...

$$\Psi^T C \Psi = \begin{bmatrix} \Phi_j^T C \Phi_j & \Phi_j^T C \varphi_p \\ \varphi_p^T C \Phi_j & \varphi_p^T C \varphi_p \end{bmatrix} \quad (8)$$

In case of static determinate interface, Φ_j are the rigid body modes which are assumed not damped, hence $C \Phi_j = 0$ and $\Psi^T C \Psi$ bolts down to

$$\Psi^T C \Psi = \begin{bmatrix} 0 & 0 \\ 0 & [2m\xi\omega] \end{bmatrix} \quad (8)$$

where $[2m\xi\omega]$ is a diagonal matrix and the ξ are the percentages of critical viscous damping ratios of the clamped interface modes. Correctness of this assumption can easily be verified by considering the global CB system equations and clamping the system at the interfaces. The modal response equations as derived directly from the physical matrices are identical to those derived from the CB model equations.

In case of non static-determinate interfaces, the 3 other terms of the damping matrix can be either ignored, or handled in the usual way, i.e. using proportional damping $C = \alpha K + \beta M$. Raleigh series or discrete dampers. The direct integration algorithm will have no problem handling damping-coupled equations.

3. Implementation in ASKA

The methodology described has been implemented in the general purpose FEM package ASKA distributed by IKOSS. Considering the application planned (torque limitation and slippage induced by a friction brake on a shaft) only static determinate interface was implemented in a first step.

The standard Newmark integration scheme has been used, together with matrix manipulation and partition/merge tools to handle the interface condition charges.

The freedoms for which non-linearities will occur are attached to 2 nodes. These freedoms are either disjoint but subject to self equilibrating loads simulating friction, or connected. In this last case, the combined equation of motion are merged into one unique dof and constrain relations are applied to the other dof, thus maintaining constant the dof pattern of the dynamic system.

Equilibrium iterations are performed at each time step, and variable time step is used (bisection method) to ensure a proper convergence to the change of state of the non-linear freedoms (i.e. slippage/no-slippage). This change of state is defined considering the system state vector using user-written Fortran routines which can be naturally interfaced with ASKA. The considered change conditions are :

No slippage until maximal torque is reached in shaft:

Once slippage occurred :

- constant maximal balanced torque applied to both disconnected parts of the shaft;
- slippage until relative velocity of 2 shaft parts comes back to zero.

4. Application to HST

The procedure including all features described above has been applied in the frame of the Hubble Space Telescope project, where the European Space Agency (ESA) is responsible for the Faint Object Camera and the Solar Arrays. Whatever sky region the HST is looking at, the SA is designed to be oriented toward the sun to get the maximal power. When the optimal position is obtained, a brake is released to prevent any modification of the SA position.

The deployment of the SA in orbit occurs when the HST is held on the Space Shuttle remote manipulator system (RMS). After deployment of the SA, the HST is still on the remote manipulator system for a few hours before release. During that period the Shuttle performs manoeuvres to hold attitude, firing thrusters. This induces loads on the SA. Since the HST-SA interface is basically a 6 dof's joint, the interaction can be described by the interface accelerations. A CB model of the SA has been developed by ESA to assess the in orbit load level when subject to such manoeuvres

Figure 1 shows the complete 3000 dofs FEM model and some of the clamped interface modes. The location of the brake between HST and SA is sketch-wise explained in Figure 1a.

The main modes of the SA in clamped interface conditions are identified in Table 1 in terms of modal masses (percentage of rigid body mass corresponding terms); those 21 modes were used to build the SA CB model. Figure 2 shows free-free modes computed with this model. Notice that although blanket aspects are completely accounted for, only boom motions are visualised since those are used later on to compute boom bending moments. These booms are indeed the most delicate mechanical parts of the deployed SA.

The brake slippage procedure has been tested using the angular acceleration around the SA Y axis shown in Figure 3 applied at the HST / SA interface. The torque actually seen by the SA on the other side of the brake is shown in Figure 4, and the related SA angular acceleration is in Figure 5. The inspection of the response of the system shows that the change of configuration/loading procedure is working fine. The interactive torque never exceeds 0.5 Nm which is the specified maximum brake torque in this test. The change of configuration/loading is smooth, however it is interesting to note that a shock is induced in the system (see Figure 5) when the brake starts slipping. The SA oscillates about its axis at a frequency close to 1 Hz. The mode which is excited is equivalent to the free-free mode 13 of the SA model presented in Figure 6. It shows a large rotation of the drum while the boom tip hardly moves.

Regarding in-orbit actual manoeuvres, classical rigidly connected linear CB analysis using modal superposition method applied to the free-free modes has shown that for some types of manoeuvres the interface torque overshoot largely the torque the brake could withstand without slippage. In addition loads in the SA booms were exceeding boom bending moment allowables. Thus the analysis had to be refined. In order to account for this effect, transient analyses have been performed using the procedure described above. This allowed changes of the brake connection from rigid state to slippage state and vice-versa as many times as requested during each computer simulation. A more realistic behaviour could be simulated, slippage of the SA evaluated and subsequent reduction of loads in the booms demonstrated.

Figure 6 shows results related to in-orbit event PO4 for the +V2 wing. As can be seen, the interface torque does not

overshoot the maximum brake-through torque (0.87 Nm) and slippage occurs after this limit is reached. Table 2 shows a summary of 17 worst load cases which were analysed. Substantial load reduction occurs for the solar array booms, with relative low array rotation which does not affect significantly the SA power performances. The computing time per run was quite reasonable (20 minutes on VAX 8650 for a response of 40 sec) considering the highly non-linear aspects of the brake conditions, and allowed a satisfactory computation of all cases; it must be kept in mind that these results reflect the information related to a 3000 dofs model, which itself could never be used for such complex analyses.

5. Conclusions

Craig-Bampton dynamic models enable a very rich information to be condensed in a very compact format. In combination with direct integration they are able to handle non-linearities related to interface freedoms. Moreover, they can use in a straightforward way the usual modal damping. As such, they build a very efficient tool to analyse certain class of non-linear problem with minimum computer resources.

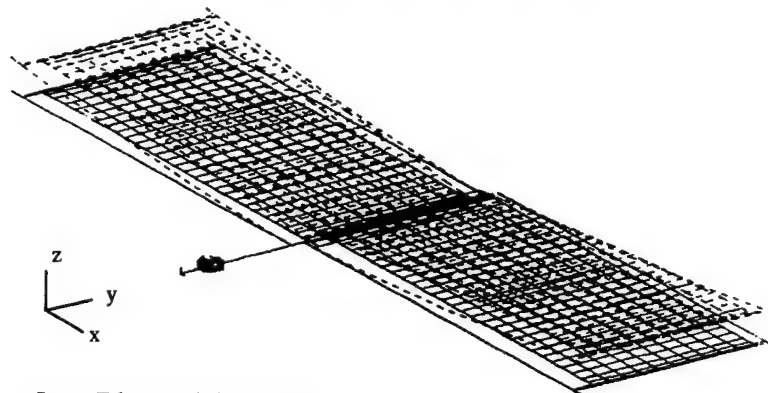
The application to the HST deployment manoeuvre scenario was very successful; it showed substantial SA boom load reduction and allowed to estimate the SA rotation.

This promising procedure is now in development for application to more general cases involving non static-determinate interfaces.

References

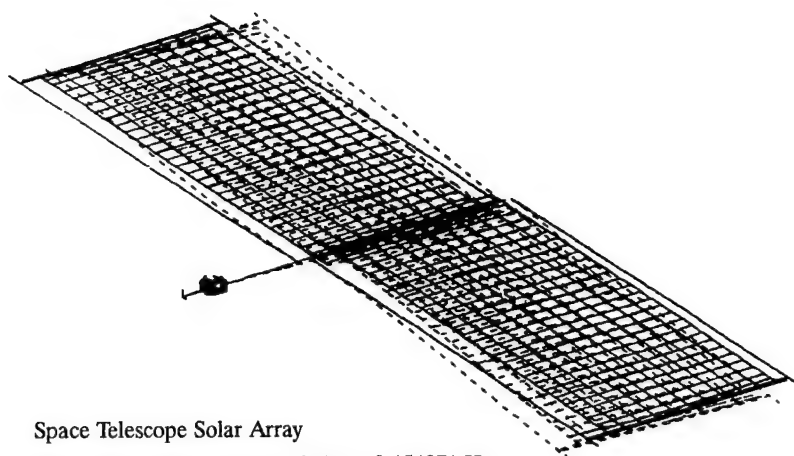
1. P. Deloo, J. Reynolds, M. Klein : "STSA Deployed Finite Element Model E1", TN-SA-0011 Vol.1 Model description, Vol.2 Modal properties and Reduced Model, Vol.3 Boom Force Recovery Methodology. ESA-ESTEC 1990
2. P. Deloo, M. Klein : "Procedure to perform a non-linear integration of a Craig-Bampton model in ASKA", TN-SA-0018 ESA-ESTEC Dec.1990.

Figure 1: FEM model and some related main modes.



Space Telescope Solar Array

Modal deformation Mode 2 Freq. 0.086614 Hz



Space Telescope Solar Array

Modal deformation Mode 13 Freq. 0.454871 Hz

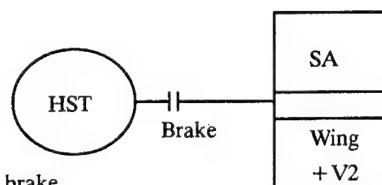


Figure 1a : location of the brake

EIG. FREQ.	NO	MX(%)	MY(%)	NZ(%)	IX(%)	IY(%)	IZ(%)
0.085713	1	0.000000	0.000000	0.001612	0.001868	99.100212	0.000001
0.086614	2	0.001069	0.000000	27.330700	31.494280	0.205601	0.000917
0.226470	3	0.000003	0.000000	0.029525	1.816183	0.000000	0.000076
0.315740	7	0.000281	0.000001	3.737133	3.941284	0.000141	0.000415
0.454871	13	25.777058	0.000170	0.000002	0.010451	0.002712	94.543091
0.541241	16	0.000193	0.000004	1.564985	2.401618	0.000002	0.000630
0.703183	27	0.463858	0.000001	0.000092	0.000048	0.000030	1.021423
0.763398	33	0.000063	0.000008	0.905543	1.022478	0.000017	0.000065
0.940869	43	0.000359	0.000039	0.775949	2.121378	0.000086	0.000125
0.983912	45	0.001190	0.000131	2.521466	5.759458	0.000284	0.000377
1.032549	49	0.000291	0.000035	0.692529	1.280281	0.000074	0.000084
1.058607	51	0.000444	0.000053	1.153723	1.805675	0.000107	0.000124
1.092661	53	0.014043	0.001497	15.655893	39.598808	0.003226	0.003325
2.684306	156	39.684685	0.000099	0.003183	0.001318	0.000882	3.694604
4.178203	251	0.000007	0.000044	3.512241	1.282615	0.000041	0.000000
4.194105	253	0.000006	0.000030	1.898331	0.696061	0.000030	0.000000
4.199246	255	0.000010	0.000048	2.741392	1.005311	0.000050	0.000000
4.227032	257	0.000008	0.000039	2.118525	0.789823	0.000041	0.000000
5.386452	320	0.000288	14.689480	0.000000	0.000000	0.000001	0.000000
5.466548	327	2.170738	0.004099	0.001671	0.000341	0.003833	0.068066
5.867115	349	0.000139	8.441351	0.000000	0.000000	0.000000	0.000022

Table 1 : Main modes of the FEM model, in terms of rigid mass percentages.

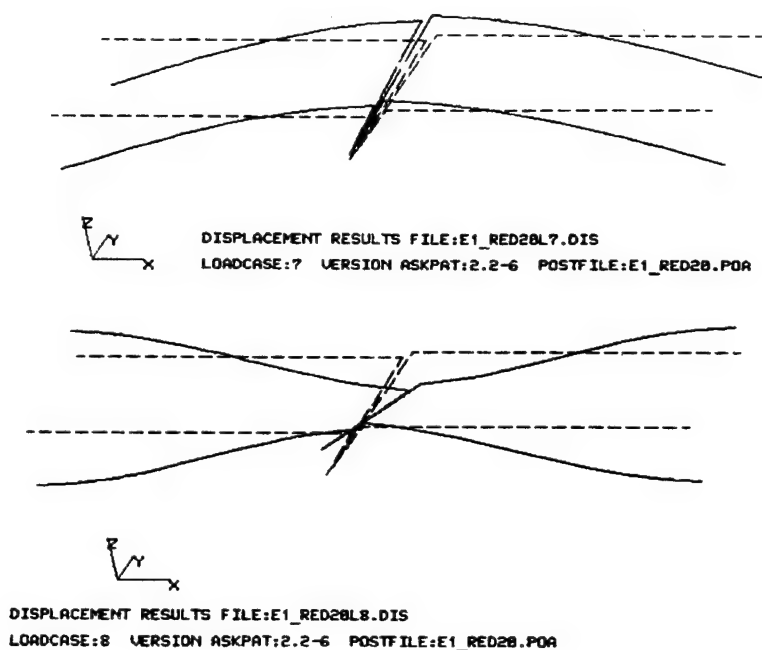


Figure 2: Free-free modes computed with the Craig-Bampton model.

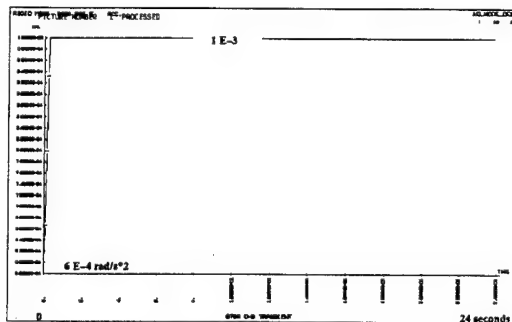


Figure 3: angular acceleration about Y axis at the HST interface (HST side of the brake)

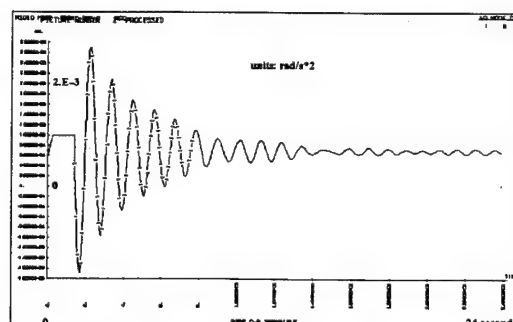


Figure 5: angular acceleration of the SA side of the brake

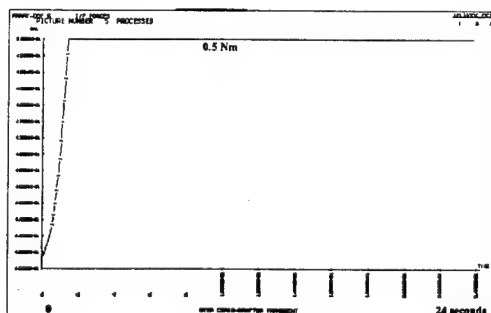


Figure 4: Interface torque about the Y axis (SA side of brake)

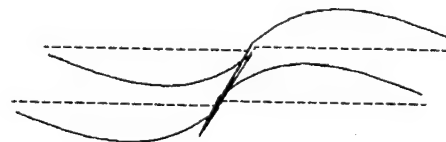


Figure 6: Free-free mode 13 of Craig-Bampton reduced model

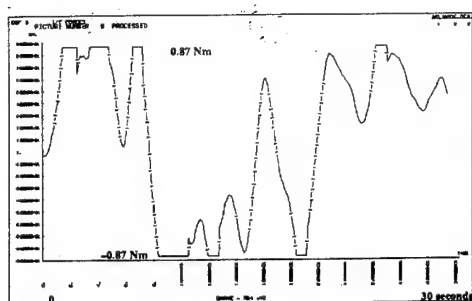


Figure 7: interface torque about Y, SA side of brake event PO4 wing +V2

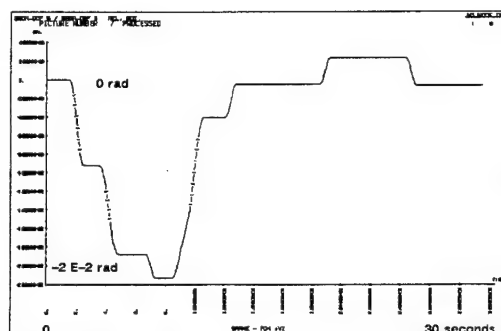


Figure 8: relative rotation around Y of both brake sides

	Infinitely Rigid Brake				Brake allowing slippage (Negative Margins in Bold)			
CASE	Manoeuvre Type		Bending Moments (Nm)	Margin	Bending Moments (Nm)	Margin	Max. Slip-page of the array * (deg)	Percent-age of BM re-duction
AD11 +V2	RMS Run-away		5.8	-0.10	4.9	0.07	1	16
R12 +V2	RMS Run-away		7.5	-0.30	5.9	-0.11	1	21
EP4 +V2	RMS Run-away		6.8	-0.23	3.4	0.54	5	50
EP4 -V2	RMS Run-away		6.1	-0.14	2.6	1.01	3	57
EP6 +V2	RMS Run-away		11.4	-0.54	9.1	-0.42	2	20
EP6 -V2	RMS Run-away		10.4	-0.50	8.0	-0.35	1	23
PO2 +V2	PRCS Auto hold	Low Z	5.8	-0.10	4.7	0.11	3	19
PO3 +V2	PRCS Auto hold	Low Z	6.1	-0.14	4.0	0.31	1	34
PO4 +V2	PRCS Auto hold	Low Z	8.3	-0.37	5.8	-0.10	2	30
PO4 -V2	PRCS Auto hold	Low Z	7.5	-0.30	5.2	0.01	2	31
EP1 +V2	PRCS Auto hold	Nom Z	5.5	-0.05	3.5	0.49	2	36
EP2 +V2	PRCS Auto hold	Nom Z	5.7	-0.08	4.6	0.14	3	19
EP4 +V2	PRCS Auto hold	Nom Z	5.8	-0.10	5.4	-0.03	2	7
EP4 -V2	PRCS Auto hold	Nom Z	5.5	-0.05	5.0	0.05	2	9
EP5 +V2	PRCS Auto hold	Nom Z	6.8	-0.23	6.2	-0.16	1	9
EP5 -V2	PRCS Auto hold	Nom Z	5.9	-0.12	5.4	-0.03	1	8

* Maximum angle obtained during simulation period, 60 seconds.

Table 2: Maximum bending moments in the Solar Array booms.

Note: An modal critical viscous damping ratio of 0.5% for all modes was used for the HST analyses. This value derives from ground test data (ESA-BAe) and agrees with results of in-flight experiment of large solar arrays (Nasa SAFE in-orbit experiment).

N92-23815
35-39
54127

FEASIBILITY OF PAYLOAD SENSITIVITY ANALYSES FOR AR4 DYNAMIC EVENTS

F. Mercier

C.N.E.S. Toulouse

ABSTRACT

The coupled load analysis is a very important stage for the mechanical design and testing of spacecrafts. The effects of the spacecraft model precision are usually not considered. These effects are now very important to study because the spacecrafts need deeper notches for the sine tests.

A method is proposed here to perform these analyses with the data coming from a standard coupled load analysis for uniaxial events, taking into account the corrections for the truncation effects. Examples are presented for different spacecrafts.

Keywords: Coupled load analysis, Scatter, Sensitivity, Modal truncation, Coupling of dynamic systems.

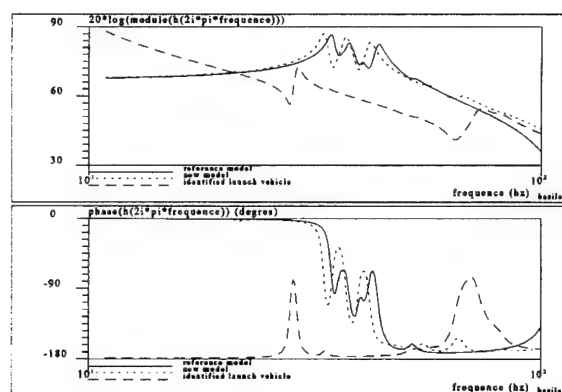


Figure 1.1

Spacecraft and launch vehicle dynamic characteristics

1. INTRODUCTION

The coupled load analysis is a very important stage for the mechanical design and testing of spacecrafts. This step becomes more and more important due to the increasing size of the payloads and due to the general work to become a better evaluation of the flight loads.

But due to the fact that the spacecraft dynamic models do not represent accurately the reality, some analyses are needed to increase the confidence in the levels. The spacecraft dynamic behaviour may also change during its development due to the design evolution. Finally, for a given platform family, it may be useful to have coupled load analyses for various spacecraft dynamic configurations.

All these considerations show the need of a fast loop for the coupled load analysis. Many formulations are available but usually the given data are not well suited to the problem of the spacecraft dynamic behaviour sensitivity analysis.

This paper shows how it is possible to perform these analyses on AR4 longitudinal events using a minimum set of coupled load analysis output data.

Figure 1.1. shows an example of the dynamic mass of a spacecraft model compared with the launch vehicle dynamic mass.

It is obvious that the spacecraft interface dynamic characteristics are of great importance in the upper part of the frequency spectrum.

2. CONTEXT

Figure 2.1. shows the coupled load analysis process for the longitudinal events (Ref. 1):

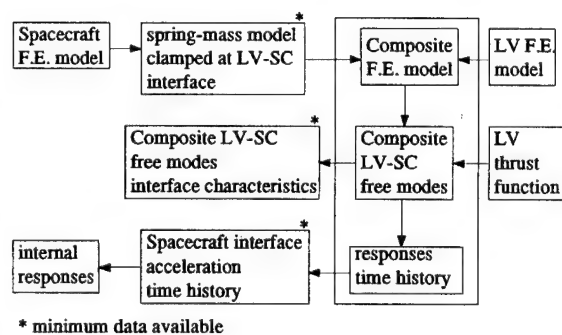


Figure 2.1

End of flight event coupled load analysis

The main output for the spacecraft is the interface acceleration. Usually, the spacecraft internal responses are computed using the spacecraft clamped model and the interface acceleration. An other solution is to make a restitution of the spacecraft internal stresses or responses directly on the composite free modes responses using correct transformation matrices. The damping laws used for the different computations are not the same. Modal damping coefficients proportional to the modal frequency are used for the computation of the composite responses. These damping coefficients are not changed if the damping law of the spacecraft model is changed.

The output data from a coupled load analysis which are supposed available are shown on figure 2.1.

3. FORMULATION

3.1 General formulation

The problem is expressed in terms of transfer functions. The "equivalent force" methodology (Ref. 2) will be used for some equations. It corresponds to a dynamic substructuring using a Craig-Bampton formulation. The different models and transfer functions used are shown in figure 3.1.

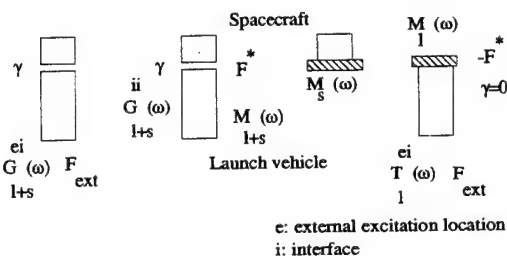


Figure 3.1

The different functions are defined by the following relations:

interface acceleration:

$$\gamma(\omega) = -\omega^2 G_{l+s}^{ii}(\omega) F^*(\omega) = -\omega^2 G_{l+s}^{ei}(\omega) F_{ext}(\omega)$$

equivalent force:

$$F^*(\omega) = M_{l+s}(\omega) \gamma(\omega) \quad F^*(\omega) = T_l^{ei}(\omega) F_{ext}(\omega)$$

G_{l+s}^{ii} composite dynamic flexibility between external force and interface

G_{l+s}^{ii} composite dynamic flexibility at interface

T_l^{ei} launch vehicle dynamic transmissibility

M_{l+s} composite dynamic mass at interface $M_{l+s} = M_l + M_s$

M_l launch vehicle dynamic mass at interface

M_s spacecraft dynamic mass at interface

The problem of the computation of γ is thus to use models which reflect a correct computation of these functions.

At this stage, it shall be outlined that these different functions are usually computed using different configurations of finite element models (free modes for the flexibilities and clamped modes for the masses). Some terms depend only on the spacecraft or on the launch vehicle:

M_s spacecraft
 T_l^{ei} , M_l , F^* launch vehicle.

3.2 Spacecraft model changes

The spacecraft model changes will be considered here in terms of dynamic mass. The interface acceleration variations are expressed using the equations of paragraph 3.2:

Spacecraft 0: M_{s0} γ_0

Spacecraft 1: M_{s1} γ_1

$$\gamma_1 = \gamma_0 \frac{M_l + M_{s0}}{M_l + M_{s1}}$$

$$\gamma_1 = \gamma_0 \frac{1}{1 + (-\omega^2 G_{l+s_0}^{ii})(M_{s1} - M_{s0})}$$

These well known expressions are correct for transfer functions computed with coherent models. Some truncation effects (due to the fact that only the lower modes of a model are used for some parts of the computations) may lead to erroneous results for the ratio γ_1 / γ_0 .

3.3 Evaluation of the transfer functions

The different functions of paragraph 3.2 may be computed using clamped or free modes of the structures. Here, the complete models will be supposed of total size $N + 1$. The interface moves only in the axial direction:

$$M(\omega) = M_r - \sum_{p=1}^N \frac{-\omega^2}{-\omega^2 + 2i\xi_p\omega_p\omega + \omega_p^2} M_p$$

M_r rigid body mass

f_p frequency of a clamped mode $\omega_p = 2\pi f_p$

ξ_p damping coefficient of the mode

M_p effective mass of the mode

$$G(\omega) = \sum_{q=1}^N \frac{1}{-\omega^2 + 2i\xi_q\omega_q\omega + \omega_q^2} G_q$$

$$G_q = \frac{\phi_q^2}{m_q}$$

ϕ_q modal deformation at location i

f_q frequency of a free mode $\omega_q = 2\pi f_q$

ξ_q damping coefficient of the mode

m_q generalized mass of the mode.

An important property of these two functions is that, for conservative models ($\xi_p=0$, $\xi_q=0$), $M(\omega_p)=0$ and $G(\omega_p)=0$. The values of M_p (resp. G_q) can also be expressed using the derivatives of $G(\omega)$ at ω_p (resp. $M(\omega)$ at ω_q).

3.4 Truncation effects on the conservative models

In paragraph 3.3 the expressions are exact because all the modes are used. But, if the computations are performed on the models using only the $n+1$ modes of lowest frequency, the expressions become for conservative models:

$$M(\omega) = M_r - \sum_{p=1}^N \frac{-\omega^2}{-\omega^2 + \omega_p^2} M_p + m(\omega) \quad m(\omega) = O(\omega^2)$$

$$G(\omega) = \sum_{q=1}^N \frac{1}{-\omega^2 + \omega_q^2} G_q + g(\omega) \quad g(\omega) = g_0 + O(\omega^2)$$

These two expressions correspond exactly to the finite element model modal truncation by setting $m(\omega)$ and $g(\omega)$ to 0. Thus the use of truncated models will not be consistent with the formulas of paragraph 3.2. Specially for the obtention of the second expression, it

is necessary to write that $-\omega^2 G_{l+s} M_{l+s} = 1$.

If the poles of M and G are not coherent this relation is not valid: this means that the zeros of M_{l+s} will not cancel the poles of $-\omega^2 G_{l+s}$.

and small shifts in frequency will give high errors in the results due to the important variations of the levels near the resonances.

The expressions of paragraph 3.2 will thus be valid for a maximal frequency which may be very small with respect to the highest computed mode frequency. Strictly speaking they are now exact only for $\omega = 0$.

The effects due to the damping will be treated in paragraph 3.6. The present approach corresponds to the current procedure where conservative models are assembled and solved. After the obtention of the eigen modes, the damping law is added.

3.5 Methodology for the truncation correction

Now it is necessary to deal with the data presented in chapter 2:

Spacecraft: M_r , M_p , ω_p , complete model used in the CLA analysis (no truncation effect for the contribution in the CLA). n_s clamped modes.

Composite: G_q , ω_q , truncated free model used in the CLA analysis. n_c+1 modes with rigid body mode.

From these data, it is obvious that the raw data are not sufficient for a computation using directly the formulas of paragraph 3.2. But these data are not independant because $G_{l+s}^{ii}(\omega_p) = 0$.

So it is possible, with a given form of the correction function $g(\omega)$ of paragraph 3.4, to identify this function to have a correct representation of the spacecraft in the composite interface flexibility. By an adequate choice of the form of this function, the resulting transfer function is correct for the direct representation (free modes of the composite) and also for the inverse representation (clamped modes of the composite). The choice of $g(\omega) = a/(b-\omega^2)$ allows these properties. The coefficients a and b are easily determined by a minimisation of $1/g(\omega_p) - 1/G(\omega_p)$ which is a linear identification problem. A second

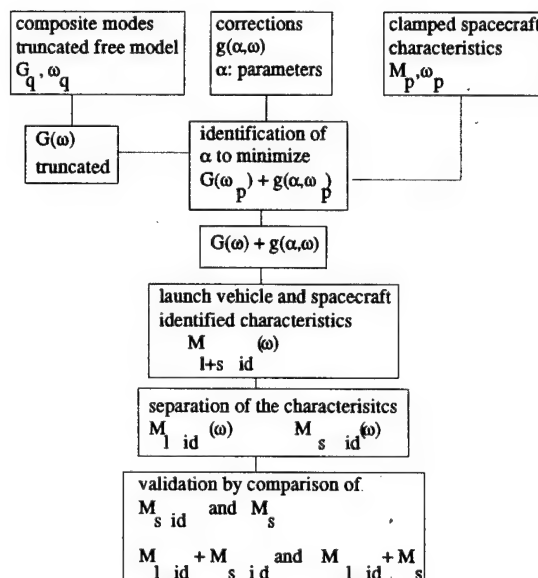


Figure 3.2

General correction process conservative model

result is that the launch vehicle dynamic mass is also identified by eliminating the spacecraft dynamic mass from the inverse of the composite identified flexibility (Figure 3.2).

Then, the expressions of paragraph 3.2 are used for the evaluation of γ_1 using the spacecraft data and the identified launch vehicle dynamic mass. The present demonstration doesn't take into account the damping laws and is valid for the conservative models. Due to errors resulting from the expansion of the flexibility term, there are still discrepancies between the clamped models real characteristics and the identified ones. But now they are small enough to be smoothed by the damping effects.

3.6 Modelisation of the dissipations

The next question is: which damping modelisation must be used for the application of the correction expressions?

The use of damping coefficients proportional to frequency at composite level is of great interest because the proportionality coefficient is then independent of the configuration of the model. Due to the fact that the expressions of paragraph 3.2 deal with the behaviour of the composite launch vehicle and spacecraft, the law is the composite one. In this case, the exact form of the expressions of $M(\omega)$ and $G^{ii}(\omega)$ for dissipative models is obtained by using modal damping coefficient terms computed in a unique manner:

$$\xi_p \text{ and } \xi_q \text{ for clamped or free modes with } \xi_p = \xi_0 \frac{\omega_p}{\omega_0} \text{ and } \xi_q = \xi_0 \frac{\omega_q}{\omega_0}$$

4. APPLICATIONS

The formulation has been applied on different cases. To have a complete validation, the first case presented here was performed on a problem where the launch vehicle was modelised with an equivalent model to see how the model was recovered after a free mode resolution with truncation. The second case is an application on an AR4 case with results coming directly from a coupled load analysis.

4.1 ARIANE 2 payload (equivalent LV model Ref. 2)

The whole process correspond to the Figure 3.2. The composite truncated free model is obtained using the spacecraft clamped modes and the launch vehicle clamped modes at interface. All the free modes are computed and the modes after 100 Hz are eliminated.

Figure 4.1 shows the discrepancies obtained between the clamped characteristics of the truncated model and the spacecraft reference.

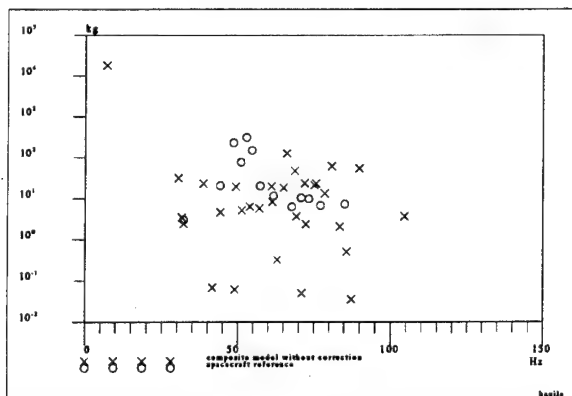


Figure 4.1

Figure 4.2 shows the values of $G_i(\omega_p)$ (truncated model) and the identified function $g(\omega)$ for ω_p pulsations of the reference spacecraft.

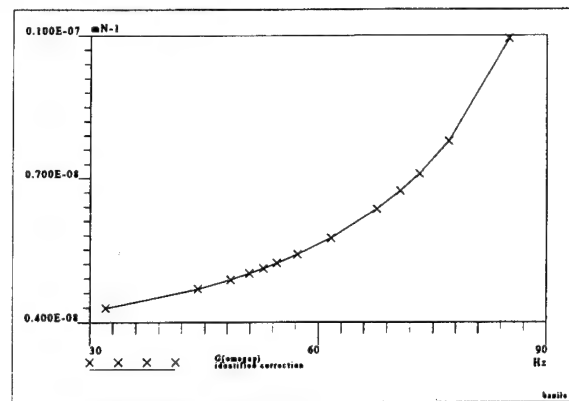


Figure 4.2

The characteristics after correction are plotted on figure 4.3.

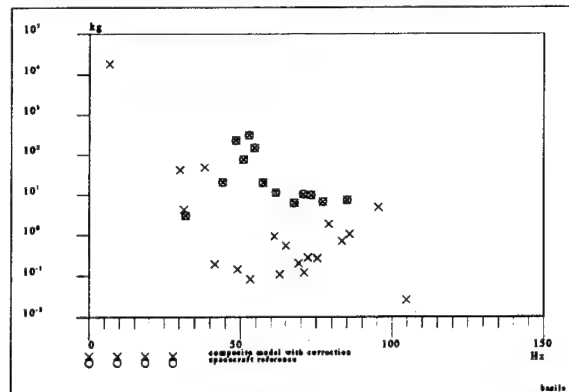


Figure 4.3

Figure 4.4 shows the effect of the correction on the composite dynamic mass at the interface. The correction is very efficient (the identified dynamic mass is identical to the reference dynamic mass). This shows that a correction term is necessary to become a correct evaluation of the interface acceleration, and that the methodology is very efficient.

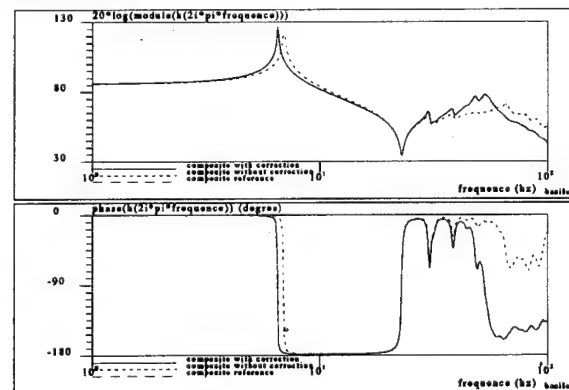


Figure 4.4

C-4

4.2 ARIANE 4 payload

The process is applied for an ARIANE 4 payload for the second stage end of flight event. The difference with the precedent case is that now, the composite free modes coming from the coupled load analysis are directly used to identify the clamped characteristics of the composite. Figures 4.5 and 4.6 show the clamped characteristics before an after correction. The small discrepancies in the identified spacecraft characteristics are due to round off errors in the data (only four digits for the frequencies).

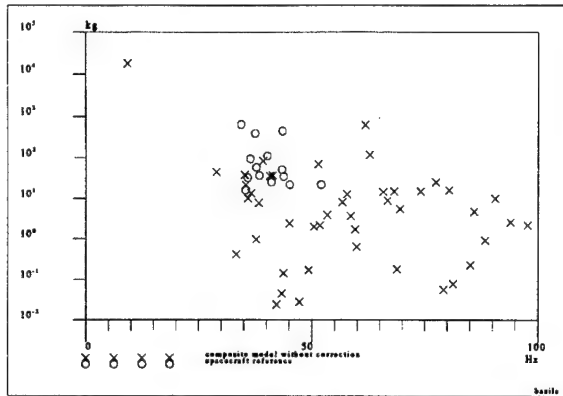


Figure 4.5

Composite clamped at interface ($g(\omega)$ set to 0)

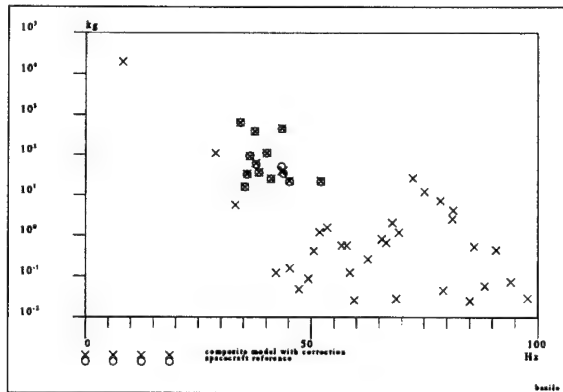


Figure 4.6

Composite clamped at interface (identified $g(\omega)$)

Figure 4.7 shows the different transfer functions obtained. There is an important difference between the composite dynamic mass without correction and with correction.

Figure 4.8 shows the effects of variations of the main modes of the spacecraft on the interface acceleration ratio $\gamma_1(\omega)/\gamma_0(\omega)$. The spacecraft models are presented in Figure 1.1. The formulation using the composite flexibility without correction leads to erroneous results which will have important effects in the frequency band where the levels are high (around 80 Hz). Figure 4.8 shows also an estimation of the performance of the correction term by evaluation of the effects of the identified and the reference spacecraft model ($M_1 + M_s$ reference / $M_1 + M_s$ identified which must be equal to 1 if the identification process is perfect).

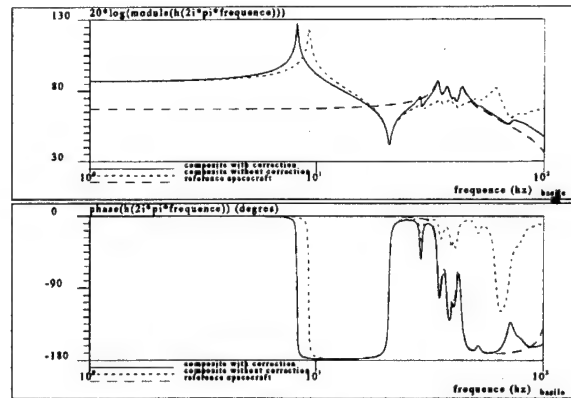


Figure 4.7

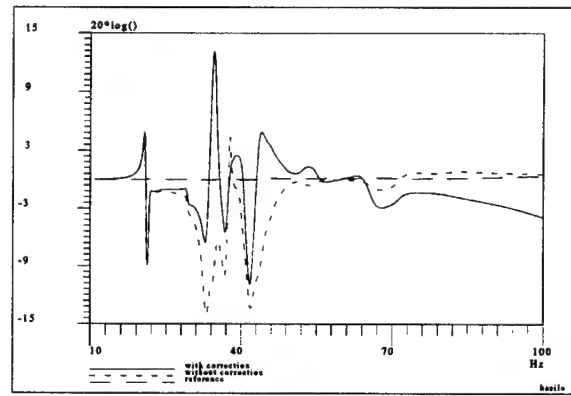


Figure 4.8

acceleration ratios

Figure 4.9 shows the corresponding interface acceleration shock spectra. The differences in the upper part of the frequency spectrum are important (about 20% variation coming only from these spacecraft model variations). The effect of the correction is important and leads to more realistic results: an increase of the spacecraft dynamic mass induces usually a decrease of the interface acceleration levels.

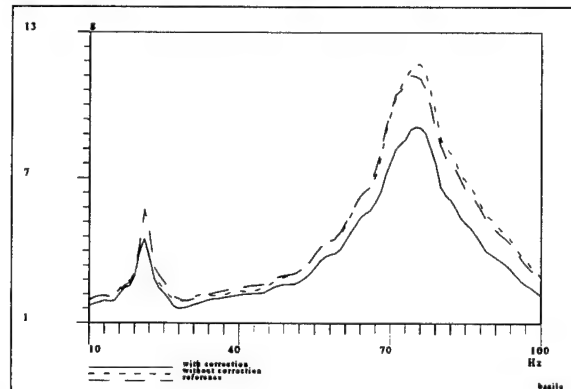


Figure 4.9

interface accelerations shock spectra

5. CONCLUSION

The proposed method allows an estimation of the effects of the spacecraft model changes on the interface acceleration levels coming from a reference coupled load analysis. It has been applied for ARIANE 4 coupled load analysis results for the second stage end of flight. The data needed for such an analysis are obtained from the coupled load analysis results without any special resolution on the launch vehicle model. The use of correct data (specially by minimizing the round off errors) will give better results for the correction term.

The sensitivity of the coupled load analysis results with respect to the spacecraft data must be performed to have a more reliable philosophy of design and tests (ref 3). This may be applied to the preliminary design where relatively important changes of the dynamic mass are expected due to the spacecraft evolutions. This will be also useful for the sine tests provisions to define the notchings taking into account the precision of the coupled load analysis spacecraft model. Finally the use of direct measurements of the spacecraft dynamic mass (Ref. 2) is allowed by this approach.

Further studies will be necessary to extend this approach to multiaxial junctions because the relations used will then be based on the study of the singularity of dynamic mass or flexibility matrices.

6. REFERENCES

1. Arianespace Workshop, dimensioning and testing 1991, MIT Boston, USA.
2. Morand H J P & al 1986, Interaction dynamique lanceur-charge utile, Spacecraft structures, Toulouse, France, ESA SP-238.

Electrodynamic transient testing, Phase 1 report, ESTEC contract 6328/85/NL/PB.
3. Dimensioning of spacecraft structures on the basis of transient flight events and tests, ESTEC contract 8221/89/NL/PH (SC)

THE RESPONSE SURFACE METHOD - AN EFFICIENT TOOL TO DETERMINE THE FAILURE PROBABILITY OF LARGE STRUCTURAL SYSTEMS

G.I. Schuëller, C.G. Bucher and H.J. Pradlwarter

Institute of Engineering Mechanics, University of Innsbruck
Austria

ABSTRACT

An efficient computational procedure for the analysis and design of structures under random loading - by considering the statistical variations of the structural resistance - is introduced. The interrelation between flexible mechanical modeling (e.g. Finite Element procedures) and efficient stochastic analysis (e.g. by accurate variance reduction simulation techniques) allows the treatment of complex systems without excessive computational effort. Hence, the practising engineer is provided with a tool which enables him to design structures according to particular target reliabilities, and which, moreover meets the requirements of the state-of-the-art for both the structural mechanical and the probabilistic procedures respectively. Finally, the procedure is applied to sample structures.

1. INTRODUCTION

It is a well known fact that by utilizing deterministic procedures for analysing and designing structures and mechanical components, "representative" (mean, maximum, minimum, etc.) values are selected to describe the parameters involved. By applying stochastic methods, however, the *entire* information, i.e. the whole spectrum of data available on the parameters is utilized. Since the degree of sophistication of the mechanical modeling has to be maintained when compared with deterministic procedures, this type of information processing requires the development of efficient computational procedures. This increase in computational effort results then in a *quantification* of the safety and reliability of structures. It is often overlooked, that deterministic procedures do not provide such a valuable information. Stochastic procedures allow optimization as well as sensitivity analyses with respect to costs, quality control requirements, reliability, etc.. Moreover, different types of structures may be designed for a particular target reliability which implies a more uniform safety level of these structures.

In the past stochastic procedures did not get the attention by the practising engineers as they deserved. This was mainly due to two reasons. On one hand traditional education of civil-, mechanical- as well as aeronautical engineers does not provide sufficient knowledge on probability and statistics, but on the other hand, and this is quite important, probabilistic procedures by and large do not yet contain the state-of-the-art of mechanical modeling and hence are prone to non acceptance by analysts and designers. Although this is admittedly an argument, it should not be discussed here whether or not this is a good reason for not applying the procedures altogether.

The present paper should be considered as a contribution to overcome this shortcoming and show the way how the state-of-the-art for both mechanical as well as probabilistic procedures may be utilized and hence provide credible

methods for the quantification for the risk of structural failure. In this context reference is made to some earlier work by the authors [1-5].

Before discussing the theoretical developments and computational procedures, a reflection of the respective requirements by the engineering practice is in order:

- (1) since in modern structural analysis procedures all structural system parameters are discretized, it is quite natural that the load parameters should be discretized as well. This implies that complex finite element models should also be suitable for stochastic structural analysis.
- (2) the design criteria, such as serviceability, collapse, fatigue, brittle fracture, etc., as used in deterministic analysis and design procedures should also apply when using probabilistic methods.
- (3) stochastic procedures have to meet standard requirements for practical application with respect to *efficiency* and *accuracy*. In other words the computational effort must not exceed acceptable limits while providing the required accuracy.

2. METHOD OF ANALYSIS

For cases where only two parameters are involved, e.g. the load S and the resistance R of a structure or a structural member, its probability of failure may be defined by

$$p_f = P(R - S \leq 0) \quad (1)$$

where $P(\cdot)$ is the probability that the resistance R exceeds the loading S . For the more general case where R and S consist of several variables, X_1, X_2, \dots, X_n , themselves, in other words where the system parameters may be represented by a random vector X , the design criterion can be described by a so called limit state function $g(X)$ of the randomly distributed parameters:

$$\begin{aligned} g(X, T) > 0 & \quad \text{no failure} \\ g(X, T) \leq 0 & \quad \text{failure} \end{aligned} \quad (2)$$

where T is the time range of observation, e.g. the design life of a particular structure. Note that eq(2) allows for taking into account the time varying properties of the structural resistance, e.g. due to crack propagation, embrittlement, corrosion, etc..

To determine the effect of the various randomly distributed input parameters - e.g. load and systems parameters respectively - on the structural response, a sensitivity analysis is in order. For this purpose, a so called response surface method is most instrumental. In particular the procedure which is used here allows the simultaneous determination of

the response surface. In other words the limit state function as defined by eq(2) will be approximated by interpolation and hence by a function $\bar{g}(X)$. When treating practical problems, where generally a large number of variables is involved, a procedure for reducing the variables to those which significantly contribute to the failure probability was developed [1]. This was done by comparing the size of so called critical values. The effect of the remaining variables on the system behavior is investigated by a pairwise combination. The response surface may be characterized most conveniently by the following expression [1]:

$$\bar{g}(X) = a + \sum_{i=1}^r b_i x_i + \sum_{i=1}^r \sum_{j=1}^r c_{ij} x_i x_j \quad (3)$$

where r is the number of variables involved and a, b, c are coefficients to be determined by structural analysis. It is important to note that within the further analysis the actual limit state function $g(X)$ is represented by the response surface $\bar{g}(X)$. The latter only approximates the region where transition from the safe to the unsafe state respectively takes place. For a procedure to estimate the error of approximation it is referred to [1, 3].

Finally, following the discretization of the load and system variables respectively (a detailed procedure to discretize the load variables is shown in the APPENDIX) for any required design criterion the failure probability can be calculated by

$$P_f(T) = \frac{\int_{g(X,T) \leq 0} f_X(x) dx}{g(X,T) \leq 0} \quad (4)$$

where $f_X(x)$ represents the joint probability density of the randomly distributed parameters X and $g(X,T)$ characterizes the time variant failure domain as defined by eq(2). For evaluating eq(4) most advantageously both efficient and accurate methods, such as advanced simulation procedures (see e.g. [6-8]) are utilized. Quite obviously, the replacement of the actual limit state surface $g(X)$ by the response surface $\bar{g}(X)$ results in a significant reduction of the required computational effort.

3. NUMERICAL EXAMPLES

3.1 General

The procedure as outlined above is now applied to two examples. In the first case a larger frame structure under static loading for the total collapse failure condition is analyzed, while in the second example a plate structure under dynamic loading is treated.

3.2 Frame Structure

A two-bay two-storey frame as shown in Fig. 1, under both vertical and horizontal loading is considered. The structure is modelled according to perfectly rigid-plastic behavior with possible formation of plastic hinges. Seven important failure modes are taken into account. The loading L_i and the plastic moment R_i are assumed to be Gaussian distributed with statistical properties as listed in Tab. 1.

The response surface includes all mixed terms which results in a highly accurate estimate of the failure probability $\bar{P}_f = 4.3 \cdot 10^{-2}$ as compared to the exact value of $P_f = 3.9 \cdot 10^{-2}$ obtained from adaptive sampling using 8000 samples.

Tab. 1: Statistical Data for Frame Structure

	Mean Value	Standard Deviation
L_1	124.5	37.4
L_2	71.2	19.9
L_3	93.4	26.2
L_4	31.1	7.8
R_1	94.7	14.2
R_2	203.3	30.7
R_3	94.7	14.2
R_4	121.9	18.2
R_5	162.8	24.5

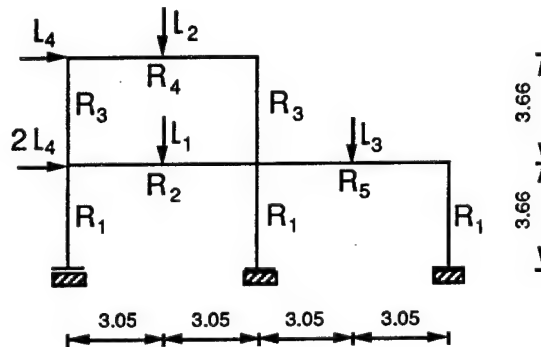


Fig. 1: Two-Bay Two-Storey Frame (units in [m])

3.3 Plate Structure

A plate modelled by Finite Elements is considered, as shown in Fig. 2. It consists of 94 triangular TUBA-3 elements and has 348 DOF. The plate is subjected to stationary random loading caused by turbulence and is defined by the Dryden Spectrum [9].

$$S_{ff}(\omega) = \frac{1+3c^2\omega^2}{(1+c^2\omega^2)^2} \quad (5)$$

where c represents the ratio U/L in which U denotes the forward velocity and L the scale of turbulence. The values $U=60\text{m/sec}$ and $L=150\text{m}$ are used. The pressure $p(y)$ is assumed to be proportional to y^3 and fully correlated along the y -direction. The spatial correlation along the x -direction is modelled by triangular shape functions $h_k(x)$ as indicated in Fig. 2. Hence, the loading is represented by

$$p(x, y, t) = \sum_{k=1}^5 h_k(x) p(y) f_k(t) \quad (6)$$

where the correlation between different f_k can be selected freely.

The damping ratio D is considered to be uncertain, i.e. as a random variable. Its value is regarded as lognormally distributed with a mean and standard deviation of 0.010 and 0.003 respectively. For the evaluation of the failure probabilities, the covariance function of linear stochastic response conditioned on three damping ratios $D_i = 0.005$,

0.010 and 0.015 are determined in a first step. The detailed FE-model is reduced to 34 DOF with full stiffness and mass matrices by static condensation. The spectrum of the forcing function $S_{ff}(\omega)$ is realized by utilizing a linear second order filter driven by white noise. The stochastic response is determined by applying the state vector approach and complex modal decomposition leading to the covariance matrix of the state vector. In Fig.3 the autocovariance function of the critical bending moment (as indicated in Fig.2)

is shown for the damping ratio $D_i = 0.005$.

In the next step the failure probabilities, i.e. exceedance probabilities over a certain threshold level ξ conditional on D_i for the critical bending moment is evaluated by means of Monte Carlo Simulation. Finally, the uncertainty of the damping ratio is taken into account by applying the response surface technique for interpolation. The final failure probabilities for different correlation of the loads are shown in Fig.4.

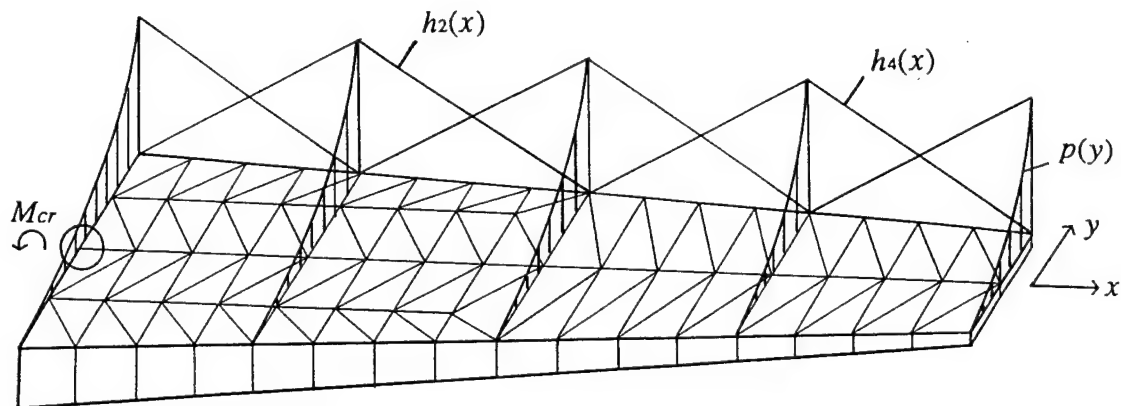


Fig. 2: FE-Model of the Plate and Its Loadings

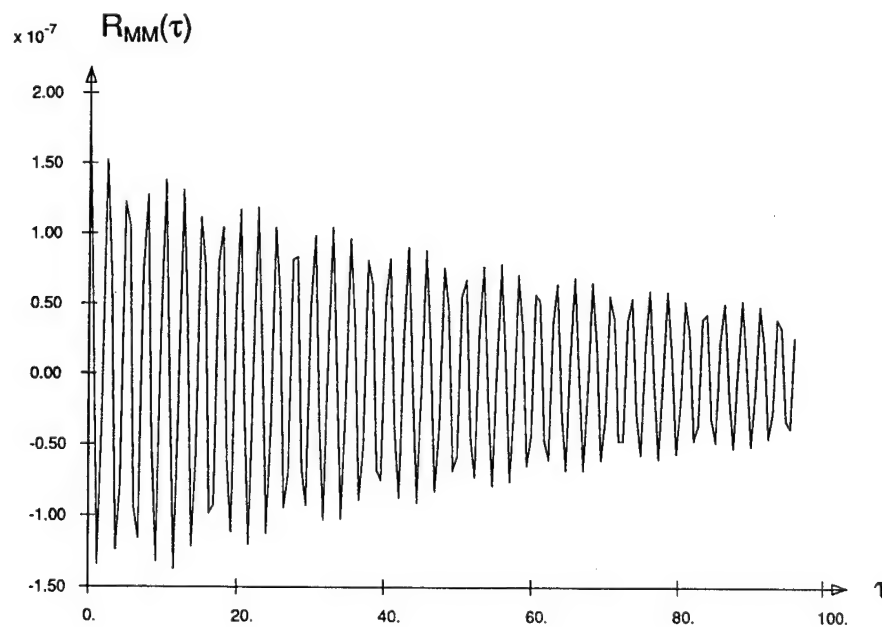


Fig. 3: Autocovariance Function of the Critical Bending Moments

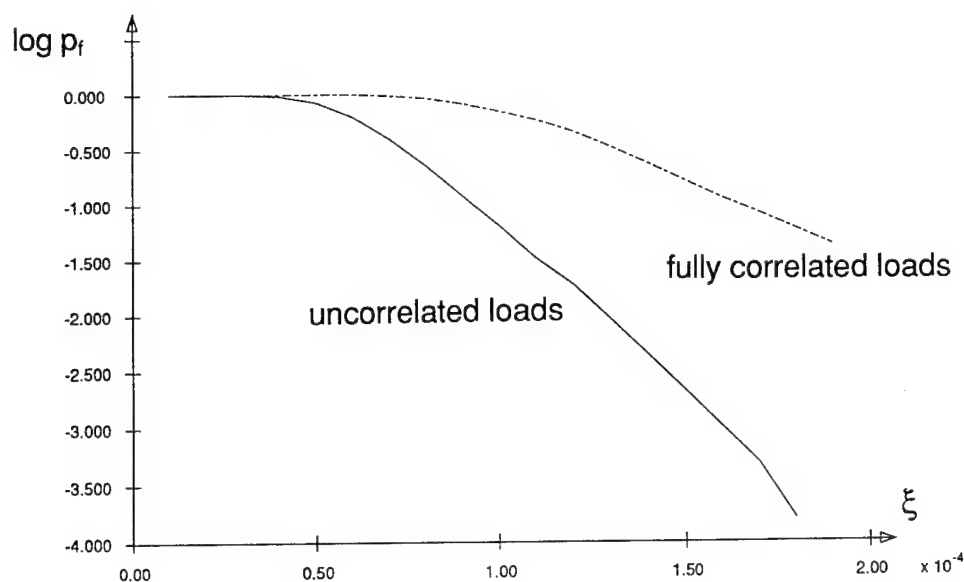


Fig. 4: Failure Probabilities with Uncertain Damping

4. CONCLUSIONS

The procedure to determine failure probabilities of structures under static as well as dynamic loading - as described in this paper - proved to be both efficient and versatile. Its main advantage is the fact, that the state-of-the-art with respect to structural mechanical and load modeling as well as numerical methods can be utilized. In general there are also no restrictions with respect to the utilization of material laws, structural analysis procedures, types of probability distributions of the input parameters, etc.. The approximation of the actual limit state surfaces by response surfaces of second order polynomial type proved to be applicable. For practical use it is of particular advantage that any desired design criterion can be included directly in the analysis. This allows the design for a particular target reliability and hence a probability based optimization of structural systems. The procedure along with the available software is designed for a direct application by the practising engineer.

ACKNOWLEDGEMENT

This research is partially supported by the Austrian Industrial Research Promotion Fund (FFF) under contract no. 6/546 which is gratefully acknowledged by the authors. C.E. Brenner's help with numerical computations is acknowledged.

REFERENCES

- [1] BUCHER, C.G., PRADLWARTER, H.J., SCHUËLLER, G.I.: "COSSAN - Ein Beitrag zur Software-Entwicklung für die Zuverlässigkeitsbewertung von Strukturen", VDI-Bericht Nr. 771, 1989, pp.271-281 (in German).
- [2] BUCHER, C.G., PRADLWARTER, H.J., SCHUËLLER, G.I.: "Computational Stochastic Structural Analysis (COSSAN) - A Contribution to the Software Development for the Reliability Assessment of Structures under Dynamic Loading" in: "Structural Dynamics - Recent Advances", G.I. Schuëller (Ed.), Springer Verlag, Heidelberg, New York, 1991 (Ch. 4.2), pp.301-315.
- [3] SCHUËLLER, G.I., BUCHER, C.G., PRADLWARTER, H.J.: "Computational Methods in Stochastic Structural Dynamics", In: "Structural Dynamics", Vol.2, W.B. Krätzig et al. (Eds.), A.A. Balkema, Rotterdam/Brookfield, 1991, pp.599-606.
- [4] SCHUËLLER, G.I., BUCHER C.G.: "Computational Stochastic Structural Analysis - A Contribution to the Software Development for the Reliability Assessment of Structures under Dynamic Loading", *J. Probabilistic Engineering Mechanics*, 1991, to appear
- [5] SCHUËLLER, G.I., PRADLWARTER, H.J., BUCHER, C.G.: "Efficient Computational Procedures for Reliability Estimates of MDOF Systems", *J. Nonlinear Mechanics*, 1991, to appear
- [6] SCHUËLLER G.I., STIX, R.: "A Critical Appraisal of Methods to Determine Failure Probabilities", *Structural Safety*, Vol. 4, 1987, pp.293-309.
- [7] BUCHER, C.G., NIENSTEDT, J., OUYPNORPRASERT, W.: "Adaptive Strategies in ISPUD V3.0 - A User's Manual", Report No. 25-89, Institute of Engineering Mechanics, University of Innsbruck, Innsbruck, 1989.
- [8] BUCHER, C.G.: "Adaptive Sampling - An Iterative Fast Monte - Carlo Procedure", *Structural Safety*, Vol. 5, No. 2, June 1988, pp.119-126.
- [9] HOWELL, L.J. and LIN, Y.K.: "Response of Flight Vehicles to Nonstationary Atmospheric Turbulence", *AIAA JOURNAL*, Vol. 9, No. 11, November 1971, pp. 2201-2207.

APPENDIX

Load Modeling

Numerical analyses require a discrete representation of the load. While this is a priori the case for static loading, the loading history has to be discretized for random dynamic loading. In other words, a continuous process $a(t)$ is described by discrete values a_k , $k=1 \dots, N$.

This corresponds to the generally applied procedure in structural dynamics.

For a given covariance function,

$$R_a(t,s) = E[a(t)a(s)] \quad (A1)$$

(assume zero mean for $a(t)$) of a continuous process the covariance matrix of a discrete process is defined by

$$C_{km} = E[a_k a_m] = E[a(t_k)a(t_m)] \quad (A2)$$

Hence, the loading process is now defined by N correlated random variables a_k . With respect to simulation it is advantageous to diagonalize the matrix C , i.e.

$$\Phi^T C \Phi = \text{diag } \lambda_m \quad (A3)$$

where Φ represents the orthogonal transformation matrix (eigenvectors).

By denoting

$$\underline{a} = \Phi \underline{y} \quad (A4)$$

the load process $a(t)$ is represented by a linear combination of *uncorrelated* variables y_m with a variance of λ_m . For realistic cases the values of λ_m show a strongly decreasing tendency, i.e. in general significantly less than N random variables are required to describe $a(t)$ sufficiently well.

**SESSION
1.4.D**

**MATERIALS
III**

COMPOSITES

PRECEDING PAGE BLANK NOT FILMED

N92-23817

84729

AGING OF POLYMER MATRIX COMPOSITES AT ELEVATED TEMPERATURES

H. Twardy

DLR, Institute for Structural Mechanics
Braunschweig, West-Germany

ABSTRACT

Experimental studies were performed to examine the influence of thermal aging on strength and stiffness of CFRP. Exposure times up to 3300 hours were conducted, however, interest was focused on elevated temperatures with the consequence of low exposure durations. Materials selected for tests were four bismaleimide composites (among these 5250-2/T800) and the polyimide composites PMR-15/T300 and LARC 160/T800. Isothermal aging was conducted at temperatures in the range of 200 °C to 340 °C. Comparative studies were performed in nitrogen and oxidizing air environment. Results of mass loss measurement were compared with mechanical properties changes.

Mass losses were permanent measured during the isothermal aging process as a possibly indicator for material degradation. A question was, if the degree of mass loss is an appropriate measure for the extent of mechanical degradation. However, it was observed, that exposure temperature and time are furthermore needed as parameters.

Mechanical tests of virgin and aged laminate specimens were conducted under tensile load. The environmental effects of air were studied at samples aged in an air flow at ambient pressure and for comparison at samples from nitrogen atmosphere. These tests were performed under tensile and compressive loads.

2. MATERIALS

For the program six carbon fiber reinforced composites were selected, which partly were considered as representative materials for Hermes, see table 1.

1. INTRODUCTION

Among orbital and terrestrial effects on polymer materials, heat has a dominant role for many applications. The behaviour of CFRP when exposed to heat is of decisive importance for the availability of this material group for space applications and future earth-to-orbit transport vehicles. Interest is focused on the behaviour of matrix composites under long-term conditions (Refs. 1, 2) as well as short-time overheating near the glass transition temperature and in oxidizing atmosphere (Ref. 3). Exposure to continuous temperature can affect the matrix which results in reduced mechanical properties of the composite (Refs. 4, 5).

This section reports on a study of temperature aging of four graphite/bismaleimide composites and two high temperature resistant graphite/polyimide composites in a temperature range of 200 °C to 300 °C and at 340 °C respectively. The maximum exposure duration has been up to 3300 hours, however short duration exposures at elevated temperatures have been emphasized. This is important for two reasons: Firstly, material behaviour as consequence of overheating is of direct relevance to high temperature application. Secondly, temperature elevation is a means of accelerated aging for prediction of allowable exposure durations at low temperatures.

MATERIAL	MANUFACTURER, CONTRACTOR	CHEMICAL CLASSIFICATION	TG (°C) DRY STATE
5250-2 / T800	Narmco, BASF	Bismaleimide	329
Vicotex 5564 / T800 (former SX 5564)	Brochier, Ciba	Bismaleimide	312
Compimide 896 / T800	Technochemie, Shell	Bismaleimide	260
CPI 2278 / T800	Ferro	Bismaleimide (modif.)	264
CPI 2237 / T300 (PMR 15)	Ferro	Polyimide	398
CPI 2274 / T800 (LARC 160)	Ferro	Polyimide	399

Table 1. Material systems with glass transition temperature.

The reinforcement used were Torayca carbon fibers T800 and T300 for the polyimide PMR 15. The laminates were fabricated in an autoclave process from commercial prepreps with the exception of Compimide 896/T800. In this case prepreps were prepared in house by conventional solvent impregnation of T800 fibers during drum winding.

The two polyimide matrix resins are similar thermosetting polyimides, differing primarily in the aromatic diamines used. The maximum autoclave temperature were 310 °C for PMR 15/T300 and 300 °C for LARC 160/T800. Initially fabrication problems with LARC 160/T800 we got over using an autoclave cycle recommended by the Sonaca company. However, the bismaleimide matrix resins were advantageous according to laminate fabrication.

3. EXPERIMENTAL

Thermal aging tests were done in three steps:

- Thermoanalytical tests were conducted to get a survey of the appropriate temperature range for aging. To this the glass transition temperatures of the unaged laminate materials were determined by the DMA method. A further suitable help is Differential Scanning Calorimetry, which indicates temperature ranges, where oxidation or decomposition of the matrix occurs.
- Isothermal aging of specimens in an air or inert nitrogen environment at different temperatures (see below). The aging process was observed by mass loss measurement at separate specimens (4 for each material), which were not mechanically tested.
- Mechanical tests in tension and compression (5 specimens for each measuring point) were carried out at virgin and aged specimens. Due to the fact, that aging is time consuming at low temperatures the aging process of these specimens was stopped, when 4 % mass loss was reached. Specimens were mechanically tested at room temperature.

Mechanical tests were focused on aging behaviour due to the following effects:

1. Environmental effect of air in comparison to inert nitrogen.
2. Effect of temperatures, partly elevated near or above the glass transition temperatures.
3. Effect of material.

For limiting the experimental effort, appropriate materials, aging temperatures and test methods were selected according to the order of the above listed effects:

1. Test methods: Tension and compression
Aging temperatures: 230 °C, 260 °C, 300 °C
Gas flow: Air, Nitrogen, 6 l/min at ambient pressure.
Materials: Laminates 5250-2/T800, Vicotex 5564/T800
2. Test method: Tension
Aging temperatures: 200 °C, 230 °C, 260 °C, (300 °C) for BMI-Laminates; 300 °C, 340 °C for the polyimides.
Materials: Laminates 5250-2/T800, Vicotex 5564/T800, CPI 2278/T800, and polyimides LARC 160/T800, PMR 15/T300.
3. Test method: Tension
Aging temperature: 260 °C
Materials: All laminates (s. table 1).

Expecting that aging of laminates would manifest itself in matrix-controlled layups, tensile and compressive tests were conducted with +/- 45° crossplied specimens. The dimension were:

Tensile samples: 15 mm x 200 mm x 1 mm
Compressive samples: 12 mm x 135 mm x 2 mm

4. RESULTS

4.1 Outgassing of laminates

The laminate specimens, which were heated at constant temperatures, suffered mass losses during the thermal aging process of many hundreds of hours. The mass loss of each material was measured in a time stepping mode at four separate specimens, which were not mechanically tested lateron. These specimens were taken from the oven during weighing only, so there was nearly no temperature disturbance for the other mechanical specimens.

Figures 1 and 2 display results of mass losses of five materials at 260 °C with an air flow environment and of the laminate 5250/T800 at 300 °C respectively. From the plots displayed here it can be seen, that to loose equal mass (in percent) considerable differences of time are needed for aging depending on material. For a mass loss of 10 % for example the necessary time ranges from 440 to 1060 hours. Secondly it was observed, that mass loss may increase severely after an initial period of a slight increase, as the Compimide 896 laminate demonstrates at about 225 hours. This might be caused by breakage of the chemical structure of the resin after exposure to the hot environment for many hours.

Mass loss measurement was done with the aim, to compare these results with results of mechanical degradation. The question is, if the degree of mass loss is an appropriate measure for the extent of mechanical degradation. Since thermal aging is a time consuming process, mass loss of the specimens for mechanical tests was limited to four percent. Aging time to reach this mass loss for instance at 300 °C is shown in table 2.

The influence of the environment, i.e. oxidizing or inert, was measured at laminate 5250/T800, figure 2. At 300 °C the mass loss in air flow environment is nearly twice as high as in nitrogen atmosphere, after 200 hours.

4.2 Mechanical Properties

Thermal aging of polymer laminates affects mechanical properties dependent on duration of exposure. Aging time is therefore an appropriate basis parameter for comparative studies. The comparison of the material properties is made clear by plotting the percent ratios of residual and initial properties. All properties were measured at room temperature.

4.2.1 Environmental Effects

Tension

The environmental effect of air at temperatures of 230, 260 and 300 °C was tested at the laminates 5250/T800 and Vicotex 5564/T800. For comparison, the tests were carried out in an inert atmosphere of nitrogen, figures 3 and 4. Differences of residual tensile strengths in air and nitrogen environment are small so that they still are within the scatter of the results. The difference data are in maximum 3 % for laminate 5250/T800 and 6 % for Vicotex 5564/T800. At 230 °C aging temperature tensile strength in air environment of laminate 5250/T800

is worse than in nitrogen environment. This coincides with the trend of higher mass loss in air. However, this cannot be observed at 300 °C for both the laminates.

The relative tensile strengths after 100 hours aging at 300 °C are:

Laminate 5250/T800:	71 % (N ₂)
	74 % (Air)
Vicotex 5564/T800:	74 % (N ₂)
	80 % (Air)

Typical aging effect on stiffness is displayed in figures 5 and 6. At constant temperatures stiffness increased slight or even remained constant during the aging process. Degradation of stiffness was observed only for air aging at 260 and 300 °C of laminate 5250/T800. There is an obvious effect of air aging in comparison to nitrogen. The stiffness data were lower when specimens were exposed to air flow.

The relative stiffness properties after 100 hours aging at a temperature of 300 °C were:

Laminate 5250/T800:	99 % (N ₂)
	92 % (Air)
Vicotex 5564/T800:	113 % (N ₂)
	107 % (Air)

Compression

Compressive strength degradation is displayed in figures 7 and 8 for the laminates 5250/T800 and Vicotex/T800 respectively. The aging study of these laminates was performed using +/- 45° crossplied specimens as used for tensile studies, too. This kind of fiber orientation is sensitive to matrix degradation which plays the dominant role in laminate aging. A compressive strength degradation due to air aging and nitrogen aging was observed for all exposures. At an aging temperature of 230 °C for the laminate 5250/T800 a visible difference between air and nitrogen aging was detected when aging time 100 hours exceeded. However, after 900 hours the difference was only about 4 % with increasing tendency when the aging time was raised.

At 300 °C aging temperature a clear difference between air aging and nitrogen aging was observed for both laminate types. Air aging had a stronger effect on compressive strength degradation than nitrogen aging. The relative residual compression strength data after 100 hours at an aging temperature of 300 °C were:

Laminate 5250/T800:	78 % (N ₂)
	70 % (Air)
Vicotex 5564/T800:	86 % (N ₂)
	82 % (Air)

Stiffness data are shown in figures 9 and 10 for the laminates 5250/T800 and Vicotex/T800 respectively. Again air aging led to lower compressive data in comparison to nitrogen aging with one exception. This is the laminate 5250/T800 at 230 °C with stiffness data of air aging higher than in a nitrogen environment.

A clear tendency of stiffness properties during the aging process was not detected for both materials and different aging temperature commonly. A typical result was that stiffness increased in the initial phase of the aging process and decreased later on. The relative stiffness data alterations observed were between 111 % and 92 %.

The relative stiffness properties after 100 hours aging at a temperature of 300 °C were:

Laminate 5250/T800:	104 % (N ₂)
	96 % (Air)
Vicotex 5564/T800:	106 % (N ₂)
	99 % (Air)

4.2.2 Effect of temperature on strength and stiffness

Temperature effects in many cases cannot be described separately because they are coupled with specific material behaviour. The effect of air aging at different temperatures on tensile strength is displayed in figures 3, 11, 12 for bismaleimide laminates and in figure 13 for the polyimide laminates. Aging was carried out at constant temperatures in the range of 200 °C to 300 °C for the bismaleimides, at 300 °C and 340 °C for the high temperature resistant polyimides. Two effects of thermal aging were obvious for all materials used in the tests. Firstly, tensile strength decreased clearly at constant temperature when the aging time increased. Secondly, when the temperature was raised, a reduced time at which the tensile strength decreases was observed. This coincides with increase of mass loss when the temperature was raised.

When comparing strength degradation of the five materials at 300 °C aging temperature significant differences of the decreasing characteristic versus aging time were observed. The laminates 5250/T800, Vicotex/T800 and 2278/T800 in the initial phase severely degraded, followed then by slight degradation. This might be due to matrix embrittlement at the beginning of the aging process. The laminates PMR 15/T300 and LARC 160/T800 continuously degraded during the whole aging process. Severe tensile strength loss was evident for these laminates at 340 °C aging temperature, though these polyimides are predestinated for high temperature operation at temperature like this. The reason possibly might be an insufficient production process, which may have led to laminates not free of voids.

For the two laminates 5250/T800 and Vicotex/T800 the tensile degradation data at 4 % mass loss - that is the end point of each plot - were close together for all temperatures (5250/T800 in the range of 79 % to 73 %, Vicotex/T800: 80 % to 74 %). However, this cannot be generalized, as can be seen from the laminate 2278/T800 and especially from the polyimides LARC 160/T800 and PMR 15/T300. Retention data for equal mass loss are quite different as is shown in table 2 for a mass loss of 4 % at 300 °C. Generally it can be said at equal exposure time, however, tensile strengths decreased when the aging temperatures were raised.

In figure 14 residual tensile strength is summarized at 80 % of the initial properties depending on aging time and aging temperature. These are so called Arrhenius-plots, which in an ideal case would be straight lines as consequence

of exponential functions. The temperature-time relation gives an impression, how aging time decreases when the aging temperature is raised. The laminate 2278/T800 for instance can suffer about one hour exposure time at 300 °C only until 80 % retention is reached. This might be due to the fact that aging at 300 °C has been done above the glass transition point of 264 °C here. However, one must know, that this time-temperature display gives no complete impression for a comparison of materials. This display is created for the relative residual strength. Besides the absolute property data of each material must be kept in mind, table 3.

The effect of air aging at different temperatures on stiffness was presented in figure 5 for 5250/T800 and the polyimides LARC 160/T800 and PMR 15/T300 in figure 15. These plots are representative for temperature behaviour during the isothermal aging process of other laminates, too. Two characteristics have been observed during exposure:

- Slight increase of stiffness or stronger increase followed by decrease in course of time. The upper limit data do not exceed 110 % in some cases 118 % of the virgin stiffness data. There was no clear tendency according to temperature raising.

- Slight decrease of stiffness. Decrease became stronger when the temperature was raised.

4.2.3 Effect of Materials

The effect of different materials on the relative tensile strength and stiffness degradation due to thermal aging is shown in figures 16 and 17 respectively. Those are results of measurement with the bismaleimide laminates which were aged in an air flow at constant temperature of 260 °C. The polyimide laminates were not enclosed here, because they were provided for operation at temperatures in the range beginning with 300 °C. So we could not compare them altogether with the BMI's.

Strength degradation after 4 % mass loss (i.e. end point of each material plot) was measured in a range of 91 % to 75 % depending upon the materials type. The lowest value was reached by the laminates 2278/T800 and Vicotex/T800. However, aging time for both the laminates was quite different with 100 hours and 532 hours respectively. As a consequence from this observations it can be said:

- Equal mass loss of materials can lead to quite different relative strength degradations (see table 2)

- Aging time cannot indicate alone how severe degradation is.

At some materials compared with one another it was observed, that the more time was required to reach equal mass loss the lower residual strength was (see laminates Compimide 896, 5250 and Vicotex 5564). However, this cannot be valid generally as seen from this display too, for instance at the laminates 2278/T800 or SX 5564.

Figure 17 indicates, how stiffnesses change during the thermal aging process. Various characteristics have been observed for the five materials. The stiffness spread out from increase (laminate 2278/T800) to striking degradation (laminate SX 5564/T800). After 100 hours aging the relative

stiffnesses varied between 104 % and 86 % depending on the material, whereas at the same time the relative strength varied between 93 % and 75 %.

Comparing different materials on basis of relative property ratios alone, will give on insufficient survey. For a complete overview the absolute property data of each material must be considered.

A comparison of the selected materials is shown in figure 18. Residual tensile strength and elastic moduli data are displayed for 100 hours aging at 260 °C and 300 °C respectively. Briefly it can be said:

- Laminate 5250 obtained the highest tensile strength according to highest strength of the unaged laminates.

- The order of the materials basing on strength after aging remained as in the virgin state with the exception of laminate 2278, which obtained worst tensile strength.

- Stiffness of laminate 2278 was highest in virgin and aged state.

5. SUMMARY

Summarizing the projected results which were observed at thermal aging process it can be said:

- Laminates suffer mass losses and change of mechanical properties during exposure to hot environment. However, mass losses are no direct measure for property changes.

- The effect of air and nitrogen environment was studied with 5250/T800 and Vicotex 5564/T800 laminates at three temperatures. In most cases strengths and stiffnesses at tensile and compressive load were worse when aged in air (exceptions: tensile strengths at 300 °C, compressive stiffness of 5250/T800 at 230 °C).

- Temperature effects were studied by tensile tests. At constant temperature strengths decreased during exposure time, whereas stiffnesses in most cases initially increased (max. 18 %). When temperature was raised, strengths and stiffnesses at equal exposure time decreased.

REFERENCES

1. J.F. Haskins, Thermal Aging, Sampe Journal, Vol. 25, No. 2, March/April 1989, p. 29-33
2. J.B. Nelson, Long-Term Thermal Aging of Two Graphite/ Polyimide Composite Materials NASA TP 2369 (Nov. 1984)
3. K.J. Bowles, G. Nowack, Thermo-Oxidative Stability Studies of Celion 6000/PMR-15 Unidirectional Composites, PMR-15 and Celion 6000 Fiber, Journal of Composite Materials, Vol. 22, (Oct. 1988), p. 966-985
4. R.D. Vannucci, PMR Polyimide Compositions for Improved Performance at 371 °C, NASA TM 88942 (1987)
5. H. Twardy, Alterung von CFK bei Heißluftlagerung im Langzeitversuch, DFVLR-FB 88-05 (1988)

MATERIAL	AGING TIME (hr)	RETENTION RATIO TENSILE STRENGTH	RETENTION RATIO YOUNG'S MODULUS
Ferro CPI 2278 / T800	2.75	0.677	1.01
Compimide 896 / T800	23	0.848	1.09
5250-2 / T800	123	0.731	0.91
Vicotex 5564 / T800	149	0.795	1.09
Ferro CPI 2237 / T300 (PMR 15)	336	0.539	1.05
Ferro CPI 2274 / T800 (LARC 160)	424	0.750	1.04

Table 2. Tensile strength and Young's modulus changes of laminates at a mass loss of 4 % and 300 °C air aging.

MATERIAL [± 45°] 2S	TENSILE STRENGTH MPa	STAND. DEVIATION MPa	TENSILE MODULUS GPa	STAND. DEVIATION GPa
5250-2 / T800	208	4.06	23.8	0.823
Compimide 896 / T800	132	6.76	16.8	0.853
Vicotex 5564 / T800	176	2.30	19.3	0.688
Ferro CPI 2278 / T800	138	4.56	23.4	2.17
Ferro CPI 2274 / T800 (LARC 160)	148	6.45	20.1	1.18
Ferro CPI 2237 / T300 (PMR 15)	148	5.97	18.6	0.555

Table 3. Tensile test results of virgin material with stacking sequence [± 45°] 2S.

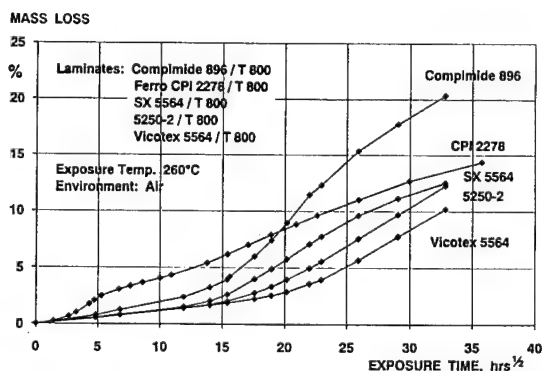


Fig.1 Mass losses of bismaleimide laminates vs. exposure time in air environment at 260 °C.

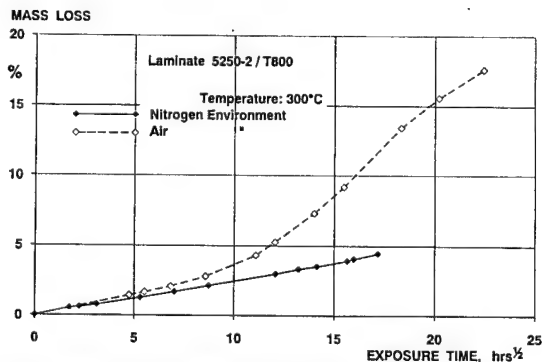


Fig.2 Mass loss of laminate 5250-2 / T800 in an air and nitrogen environment

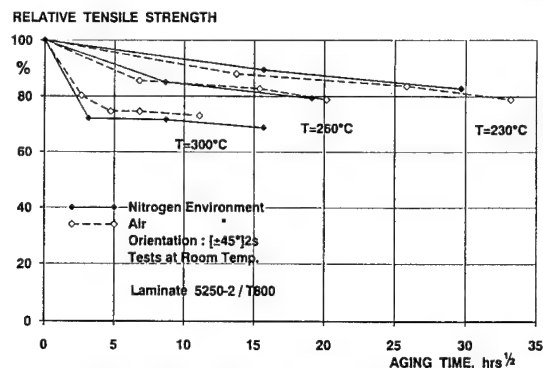


Fig.3 Residual tensile strength of 5250-2 / T800 after exposure in air and nitrogen environment.

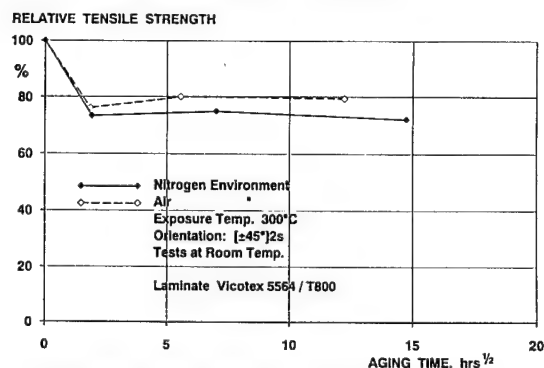


Fig.4 Residual tensile strength of Vicotex 5564 / T800 after exposure in air and nitrogen environment.

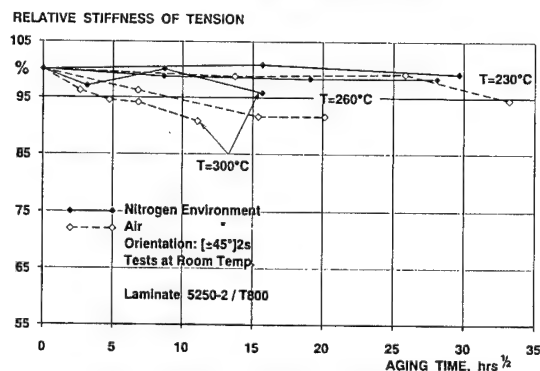


Fig.5 Change of stiffness in tension of 5250-2 / T800 due to exposure in air and nitrogen environment.

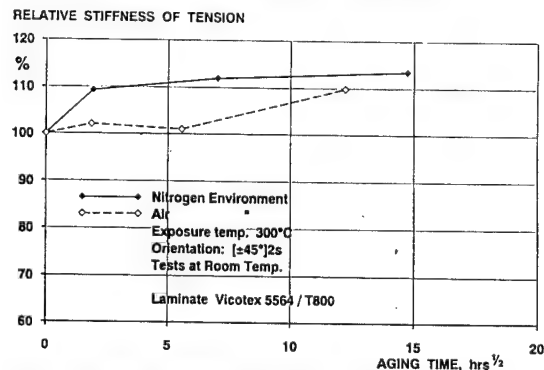


Fig.6 Change of stiffness in tension of Vicotex 5564 / T800 due to exposure in air and nitrogen environment.

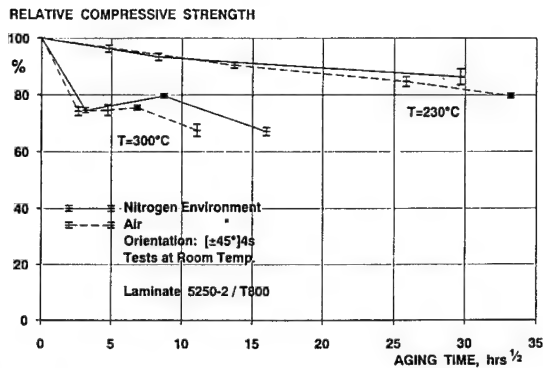


Fig.7 Residual compressive strength of 5250-2 / T800 after exposure in air and nitrogen environment.

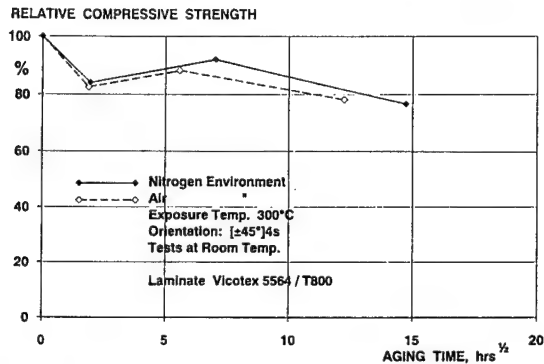


Fig.8 Residual compressive strength of Vicotex 5564 / T800 after exposure in air and nitrogen environment.

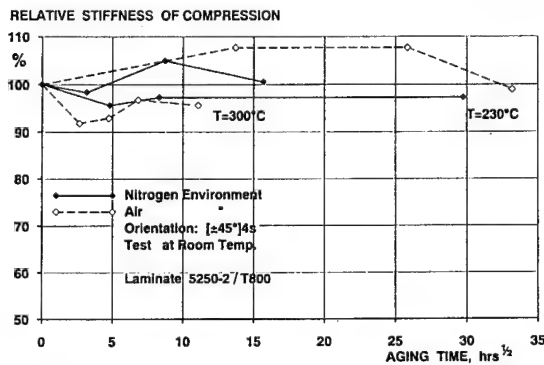


Fig.9 Change of stiffness in compression of 5250-2 / T800 after exposure in air and nitrogen environment.

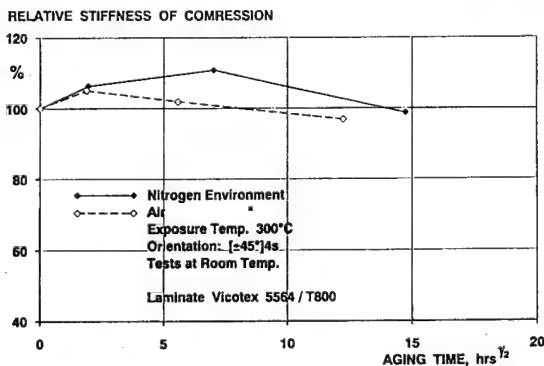


Fig.10 Change of stiffness in compression of Vicotex 5564 / T800 after exposure in air and nitrogen environment.

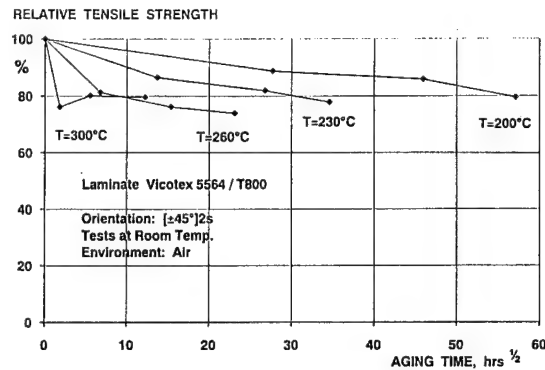


Fig.11 Residual tensile strength of Vicotex 5564 / T800 due to thermal aging at different temperatures.

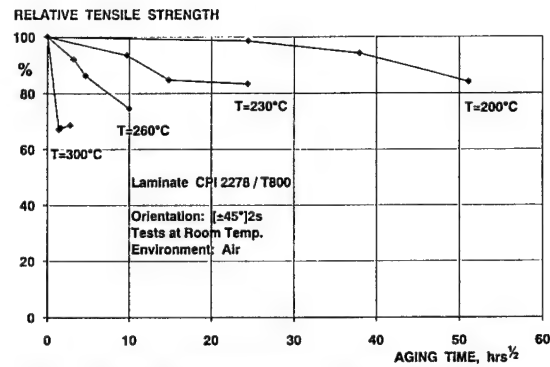


Fig.12 Residual tensile strength of CPI 2278 / T800 due to thermal aging at different temperatures.

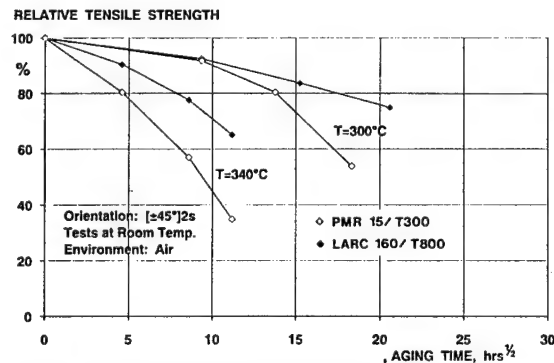


Fig.13 Residual tensile strengths of polyimide laminates due to thermal aging at 300°C and 340°C.

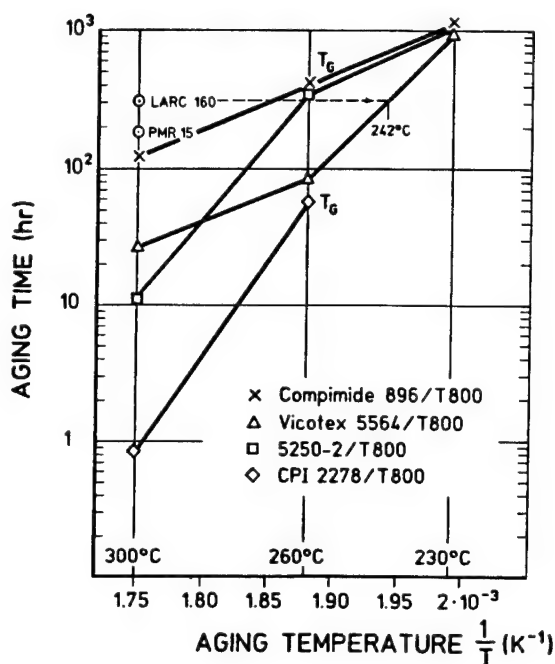


Fig. 14 Aging time for retention of tensile failure strength to 80%.

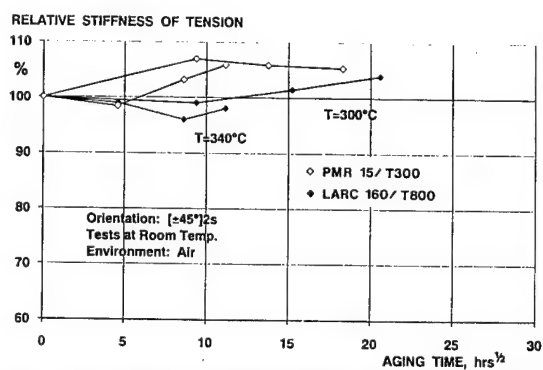


Fig. 15 Stiffnesses of polyimide laminates due to thermal aging at $300^\circ C$ and $340^\circ C$.

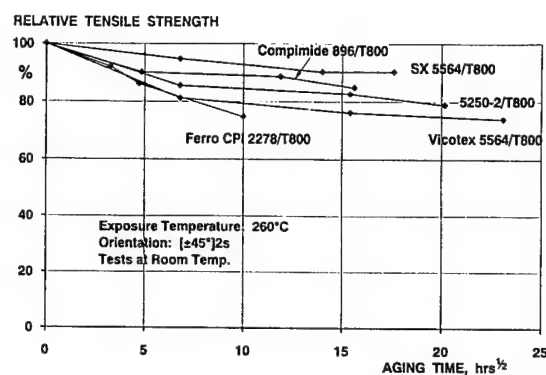


Fig. 16 Strengths of bismaleimide laminates after exposure to $260^\circ C$ air environment.

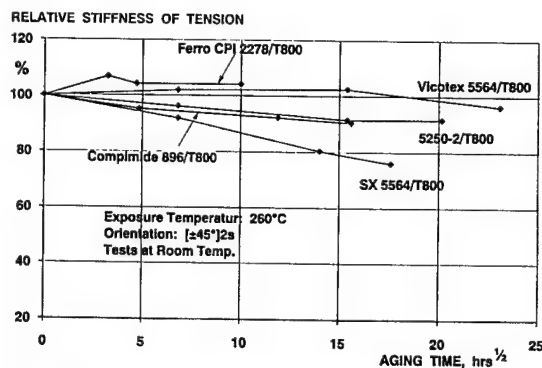


Fig. 17 Change of stiffnesses of bismaleimide laminates after exposure to $260^\circ C$ air environment.

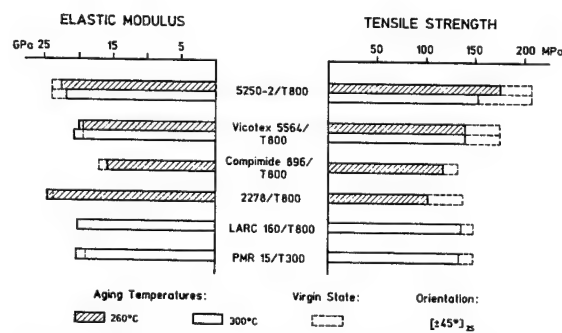


Fig. 18 Elastic moduli and tensile strength data after 100 hours aging and of virgin laminate materials.

N92-23818

84730

THE TORSIONAL FATIGUE BEHAVIOUR OF THE IN-PLANE AND OUT-OF-PLANE SHEAR MODULI OF COMPOSITE MATERIALS

D. Van Hemelrijck, L. Schillemans, F. De Roey, I. Daerden, F. Boulpaep,
J. De Visscher, A. Cardon.

Composite Systems and Research Group (COSARGUB)
Free University of Brussels
VUB - TW-Kb - Pleinlaan 2 - B1050 Brussels - BELGIUM

ABSTRACT

An automated torsion test is proposed for the determination of the in-plane and out-of-plane shear modulus. The obtained results show that for some composite systems the out-of-plane shear modulus is much different from the in-plane shear modulus, certainly sufficiently to be considered in some design application. The results of the inplane shearmodulus are in good agreement with the results obtained with the RESONALYSER, which is a method base on the vibration behaviour of a testplate. Fatigue data for the studied composite systems is also given.

axial displacement. It was found that this parameter was a more sensitive parameter to describe fatigue then the reduction of the shear-moduli.

THEORY

The definition of the dimensions used in the following formulas are according to the designation in figure 1.

INTRODUCTION

The development of new fibers like boron, carbon and improved glasses has considerably intensified interest in composite materials. The application of these new anisotropic materials in structural engineering requires the production of laminates which have to be designed for a general state of stress and strain in the three dimensions. Unfortunately, to allow such careful and accurate stress and deformation analysis the coefficients of the general hooke's law have to be identified. The determination of the longitudinal and transverse stiffness moduli is quite straightforward. But in the case of composite materials the shear moduli G_{ij} cannot be computed and have to be determined by use of specific shear tests. Conventional shear test methods [1], such as the $\pm 45^\circ$ coupon, the rail-shear, the 10 degrees off-axis test are used to obtain the in-plane shear modulus. The system developed at the Free University Brussel is a mixed numerical/experimental technique for the characterisation of polymer matrix composite laminates [5], [6], it is a fast method for the determination of the four complex engineering constants of orthotropic sheet materials: E_1^* , E_2^* , ν_{12}^* , G_{12}^* . Following the specifications of Chiao and al. [2] an ideal shear test has to provide all shear properties. Sumsion and Rajapakse [3] described a method to obtain by use of a torsion setup the out-of-plane as well as the in-plane shear modulus. Another interesting point is the increasing concern of the degradation and durability of composite systems. It is our objective to determine the in situ properties of damaged laminates and so to study the torsional fatigue behaviour. The reduction of the shear moduli was monitored together with the evolution of the

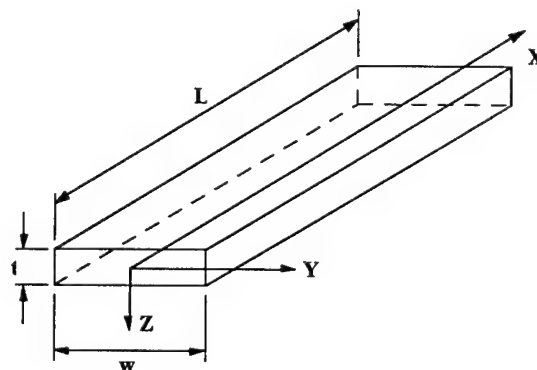


Figure 1. Designation of axis system

For an orthotropic rectangular bar the relation between torque and torsion angle is:

$$M_T = G_{12} \beta(c) w t^3 \frac{\theta}{L} \quad (3)$$

$$\text{where } \beta(c) = \frac{32 c^2}{\pi^4} \sum_{n=1,3,5}^{\infty} \frac{1}{n^4} \left(1 - \frac{2c}{n\pi} \tanh \frac{n\pi}{2c} \right)$$

and
$$c = \frac{w}{t} \sqrt{\frac{G_{13}}{G_{12}}}$$

with G_{12} being the in-plane shearmodulus and G_{13} the out-of-plane shearmodulus.

Due to the coupling between the inplane and the out-of-plane shearmodulus we need at least two torsiontests on specimens with different cross sectional dimensions in order to compute the in-plane, as well as the out-of-plane shear modulus:

TEST 1: $w_1, t_1, L_1 \Rightarrow$

$$M_T^1 = G_{12} \beta(c_1) w_1 (t_1)^3 \frac{\theta^1}{L_1}$$

linear regression \Rightarrow

$$M_T^1 = a_1 \frac{\theta^1}{L_1} \Rightarrow a_1 \quad (4)$$

TEST 2: $w_2, t_2, L_2 \Rightarrow$

$$M_T^2 = G_{12} \beta(c_2) w_2 (t_2)^3 \frac{\theta^2}{L_2}$$

linear regression \Rightarrow

$$M_T^2 = a_2 \frac{\theta^2}{L_2} \Rightarrow a_2 \quad (5)$$

combining (4) and (5) results in

$$\frac{a_1}{a_2} = \frac{G_{12} \beta(c_1) w_1 (t_1)^3}{G_{12} \beta(c_2) w_2 (t_2)^3} \quad (6)$$

when defining
$$\alpha = \frac{c_2}{c_1} = \frac{w_2/t_2}{w_1/t_1} = \frac{w_2 t_1}{w_1 t_2}$$

we have
$$\frac{w_2 (t_2)^3}{w_1 (t_1)^3} a_1 \beta(\alpha c_1) - a_2 \beta(c_1) = 0$$

we can now solve this equation for c_1 and use

$$G_{12} = \frac{a_1}{\beta(c_1) w_1 (t_1)^3}$$

to obtain the in-plane shear modulus G_{12}

and
$$c = \frac{w}{t} \sqrt{\frac{G_{13}}{G_{12}}}$$

to calculate the out-of-plane shear modulus G_{13}

To be able to combine more than two different width's, a Smith least square fit of the function (7) was programmed.

$$\frac{a_i}{w t^3} = G_{12} \beta\left(\frac{w}{t} \sqrt{\frac{G_{13}}{G_{12}}}\right) \quad (7)$$

where a_i is the first order coefficient of the linear regression relating torque and torsion angle of each experiment.

EXPERIMENTAL SETUP

The torsion setup, as constructed and used at the Free University of Brussel, is given in figure 2.

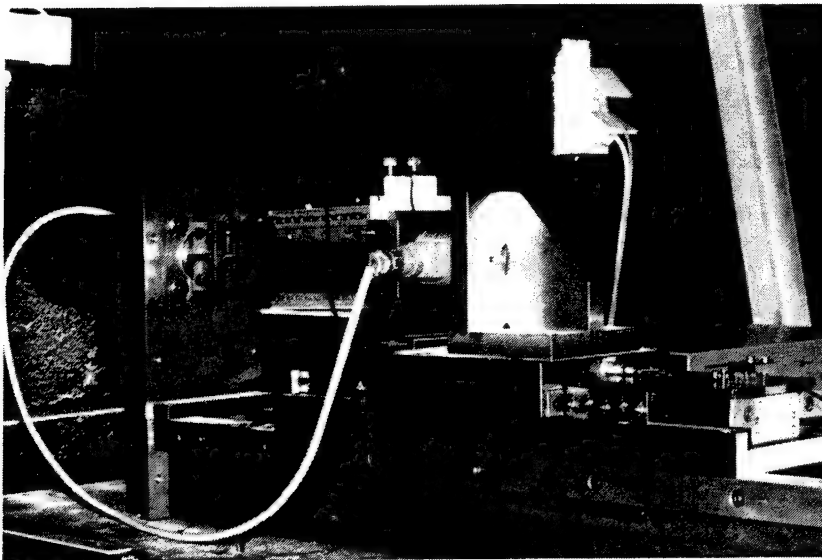


Figure 2. experimental setup

It consists of a steppingmotor with a planetary gearbox so that for one step an angular rotation of 0.036 degrees is obtained. The maximum torque which can be applied is 25 Nm. A torque-cell measures the applied torque up to 26 Nm with a minimum resolution of 4 Nmm. The construction is such that one end is completely free to move so that no tensile forces can be introduced. An LVDT with a range of 1.5 mm was added to monitor the axial displacement during testing. A personal computer equipped with an analog-to-digital convertor board is used to control every device and to perform the data-acquisition and processing. The software is written in C and is completely menu-driven.

EXPERIMENTAL RESULTS

STATIC TESTS

Flat aluminium bars were used as testspecimens for the proposed procedure. The results from standard straining measurements and torsion tests were compared and showed good agreement. The in-plane shear modulus deviated only 1%, the out-of-plane shear modulus 5%. Other materials tested were glassfiber polyester (0°/90°)8 and carbon epoxy

(fibredux 914). Results of the tests are summarized in table I. The first column gives the material system and the fiber orientation of the test specimen. The second column lists for each tested specimen the width over thickness ratio. The next column gives the shear modulus calculated with the "isotropic" formula. The third and fourth column give the in-plane and out-of-plane shear modulus calculated by using the Smith's least squares fit to equation (7) which is valid for orthotropic materials. The last column list the result obtained by use of the resonalyser.

The results on aluminium show that there is no increase in shear modulus with increasing w/t ratio. Instead, for cross-ply material there is a consistent increase. The in-plane shear moduli for the +/- 45° composite system is significantly greater than those for the uniaxial composites, the ratio is approximately 6 to 1. The out-of-plane shear modulus (G₁₃), which is generally considered to be the same as the in-plane shear modulus (G₁₂) is in fact slightly lower for the unidirectional laminates and about 12% lower for the (0°/90°) laminates. For the +/- 45° material the difference between the in-plane and the out-of-plane shear modulus is much greater.

	w/t	G ₁₂ isotropic	G ₁₂ orthotropic	G ₁₃ orthotropic	G ₁₂ Resonalyser
		GPa	GPa	GPa	GPa
Al	2.3	26.8	27.0	25.9	25.46
	3.3	26.9			
	4.3	26.9			
	5.3	27.1			
	6.6	27.0			
	7.7	26.9			
GFRP (0°/90°)8	3.0	2.7	2.8	2.1	
	5.2	2.7			
	8.2	2.8			
Fibredux 914 (0°)16	4.8	3.7	3.8	3.6	3.25
	7.5	3.8			
	9.2	3.9			
	11.5	3.8			
Fibredux 914 (0,90)16	4.7	3.5	4.1	3.6	4.77
	7.1	3.5			
	10	3.7			
	12	4.1			
	14.6	4.1			
Fibredux 914 (±45°)16	5.6	22.5	28.7	4.1	
	7.4	24.2			
	9.6	25.6			
	12.2	26.2			
	14.3	26.2			

Table I: Shear moduli for different material systems.

EXPERIMENTAL RESULTS FATIGUE TESTS

The results of the static torsion tests up to failure appear in table II.

MATERIAL	τ_{xyf} [N/mm ²]	ψ_f [°/m]	G_{12} [N/mm ²]
Aluminum	150	200	27000
[0] ₁₆	245	550	5810
[0 ₃ ,90 ₄ ,0] _s	265	720	4270
[90 ₃ ,0 ₄ ,90] _s	255	760	4202
[0,90,0,...] _{s16}	350	700	5614
[+45,-45,...] _{s16}	380	370	27656

Table II: Failure stresses for different material systems.

τ_{xyf} = failure shear stress

ψ_f = specific rotation at failure

G_{12} = in-plane modulus

Fatigue values for the unidirectional specimen are given in figure 3. The in-plane shearmodulus is scaled and the stress-level is 40% and 50% respectively of the failure stress. We observe a substantial reduction of the modulus within the very first cycles. After 10^4 cycles the modulus was reduced to 75 % of its initial value.

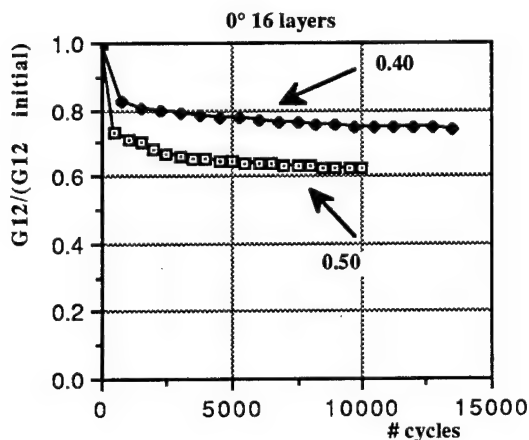


Fig. 3 Torsional fatigue curve for unidirectional specimens.

Figure 4 gives the results for $\pm 45^\circ$ specimens, in this case the reduction starts for the same stress level after 1500 cycles. After the same number of cycles there was a loss of torsional stiffness of nearly 50%.

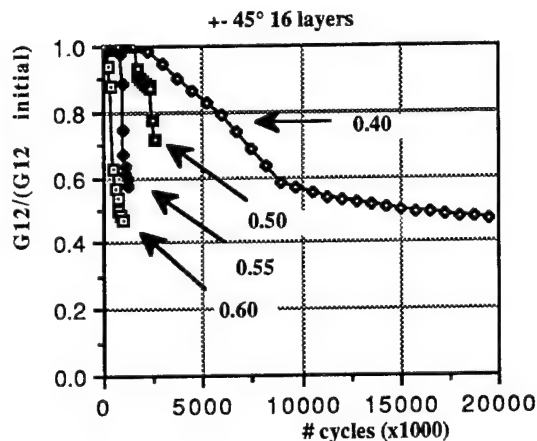


Fig. 4 Torsional fatigue curve for $\pm 45^\circ$ specimens.

The evolution of the out-of-plane shearmodulus for the same composite system is shown in figure 5.

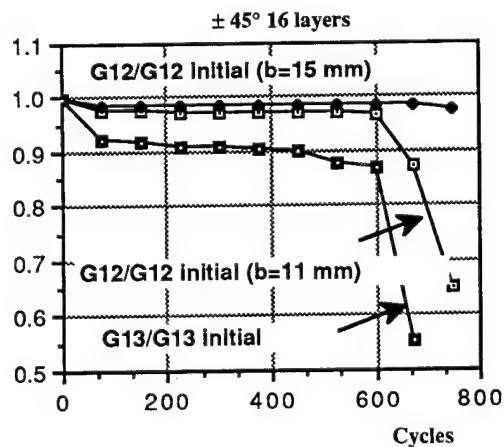


Fig. 5 Torsional fatigue curve for $\pm 45^\circ$ specimens.

Figure 6 shows the fatigue behaviour of two composite systems. Although the failure stress for these systems is nearly the same, we observe a fatigue behaviour which is very different.

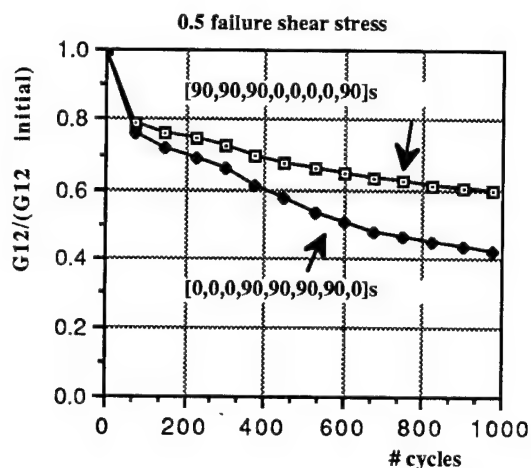


Fig. 6 Fatigue curves for $(90^\circ_3, 0^\circ_4, 90^\circ)_s$ and $(0^\circ_3, 90^\circ_4, 0^\circ)_s$ specimens.

By use of a LVDT the axial displacement was monitored. The results shown in figure 7 indicate that this parameter is more sensitive to fatigue damage than the reduction of the torsional stiffness.

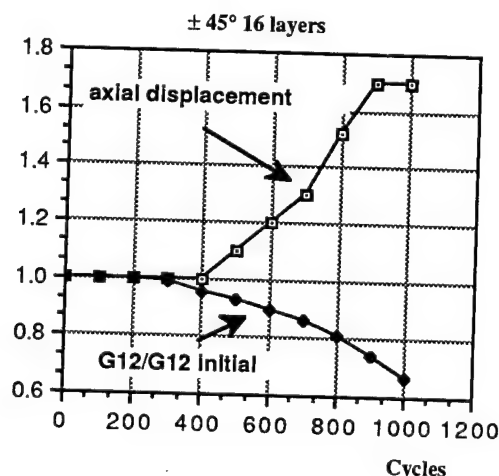


Fig. 7 Axial displacement during fatigue life.

Conclusions

The determination of both the in-plane and the out-of-plane shearmodulus is possible with this torsion setup. The results show for some composite systems serious differences between both moduli. The fatigue behaviour of all composite systems show a large reduction of torsional stiffness. This reduction is highly dependent on fibre orientation in the specimens. Based on the experimental data obtained the axial displacement (mm/m) seems to be a more sensitive parameter to describe fatigue life than is the reduction of the stiffness.

REFERENCES

1. Van Hemelrijck D., 'Materiaalkarakterisatie van vezelversterkte composietmaterialen' Thesis, 1984.
2. Chiao C.C., Moore R.L., 'Measurement of shear properties of fibre composites', Composites, Vol. 8, No 3, pp 161-169.
3. Sumsion H., Rajapakse Y., 'Simple torsion test for shear moduli determination', Proc. ICCM2, 1978, pp 994-1002.
4. Ferent B., Vautrin A., 'Computer aided torsion test', Proc. CADCOMP 90, 1990, pp 325-337.
5. Sol H., 'Identification of anisotropic plate rigidities using free vibration data', Doctoral thesis, okt 1986.
6. De Visscher J., Sol H., Vantomme J., 'Mixed numerical/experimental techniques for the characterisation of polymer matrix composite laminates', Proc DURABILITY 26-31 aug. 1990, pp 514-523.

N92-23819

EXPERIMENTAL STUDY OF DELAMINATION GROWTH IN MULTI-DIRECTIONAL CFRP-LAMINATES UNDER FATIGUE LOADING

H.C. Goetting

DLR Institute for Structural Mechanics, Braunschweig, Germany

ABSTRACT

An experimental study on damage mechanisms and failure mechanisms of multidirectional CFRP-laminates was conducted with special reference to delamination onset and growth under compression-compression and tension-compression fatigue loading. Different laminate stacking sequences of unnotched test specimens as well as of laminates containing holes, notches and artificial delaminations, were investigated. Besides the well-known NDT-techniques for the evaluation of damage states new optical on-line measurement methods were applied. The basic damage mechanisms like cracks in off-axis plies and their influence on delamination development were studied with respect to the final fatigue damage state, e.g., the transition from stable to unstable delamination growth caused by buckling of sublaminae. Characteristic delamination states were found for different notch sizes and notch shapes which affect the redistribution of strains or stresses, respectively, during cycling.

Keywords: Composite Fatigue, Damage Mechanics, Delamination Growth, Failure Mechanisms

1. INTRODUCTION

Damage mechanics investigations of the last ten years showed that, for laminated composites the delamination is a major damage mode with respect to failure under quasi-static as well as under fatigue loading conditions. Many researchers have studied the problem of delamination onset and growth, especially for simple and idealized conditions as unidirectional test specimens, DCB- and ENF-tests, and quasi-static or monotonic tensile fatigue loading. Idealized conditions enable the analytical description and modelling of delamination growth based on linear-elastic fracture mechanics and energy release rate concepts (Ref. 1,2,3,4).

However, of more practical interest are damage development, critical damage states and failure modes of multidirectional laminates under loading conditions similar to service load spectra. This field is of high complexity because the development of damage is not limited to single cracks and delaminations but is an accumulation of many small cracks and delaminations with a three-dimensional distribution leading to more massive matrix cracks, fiber-bundle breaks, interface failures and buckling of sublaminae under compressive loads. The various damage and failure modes influence one another and produce a very complex damage progression.

It was the aim of this experimental study to get more insight into the delamination development and progression of differ-

ent multidirectional laminates, and to give a phenomenological description of typical damage mechanisms and their interactions leading to the decrease of stiffness and strength and to the final laminate failure. Because the fatigue life of laminated

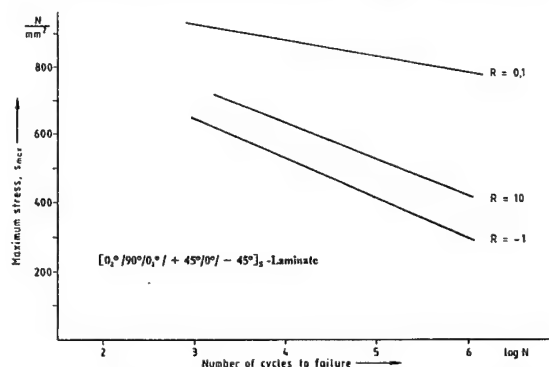


Figure 1. Influence of stress ratio R on fatigue strength of multidirectional laminates

composites is considerably reduced under compression-compression and more under tension-compression loading compared with the tension load regime, see Fig. 1, most of the tests were performed at a stress ratio of $R = -1$, fully reversed cycling, which is of more interest with respect to practical applications.

2. EXPERIMENTAL PROCEDURE

Different laminate stacking sequences with 0° , $\pm 45^\circ$ and 90° -ply orientations were fabricated from T300/914C prepreps. Cure procedures were made in a computer-controlled autoclave according to the standard recommended by the manufacturer. For the clamping reinforcement, the 380×380 mm panels were bonded with glass-fiber tapes of 1 mm thickness. The following laminate stacking sequences were investigated:

- Type 1: $[0_2, +45, 0_2, -45, 0, 90]_s$
- Type 2: $[0_2, 90, 0_2, +45, 0, -45]_s$
- Type 3: $[0_2, +45_2, -45_2, 90_2]_s$
- Type 4: $[(0, +45, -45, 90)_2]_s$

Laminates of type 1 and type 2 were selected as "fiber-dominated" laminates, whereas type 3 and type 4 represent quasi-isotropic laminates. With exception of type 3 all of the test specimens were cut to a width of 40 mm. The width of type 3-laminates was varied with 20, 40, 80 and 160 mm. These test specimens were prepared with central holes and sharp notches

¹⁾ Dedicated to Prof. Dr. H.W. Bergmann for his 65th Birthday

of different sizes in order to study characteristic damage development and possible size effects.

The fatigue tests were conducted in servohydraulic test facilities with computer controlled loading and data acquisition.

By monitoring of actual load and strain this system evaluates on-line the decrease of tension and compression stiffnesses as functions of the number of cycles. Also, the load cycling can be stopped automatically upon reaching a prescribed residual stiffness level in order to subsequently study the state of damage by ultrasonic scanning or X-ray techniques. A special program in the micro-computer system serves to detect the significant strain increase during the last load cycles, and to unload the test specimen at the same instant preventing total destruction of the test specimens. This rapid strain increase caused by instable delamination growth was observed with most of the laminates under tension-compression loading. Fig. 2 shows the recorded strain response during this event for a laminate of type 1:

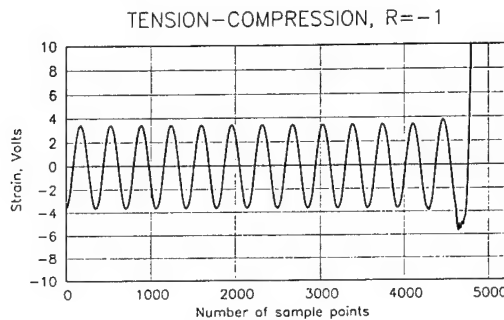


Figure 2. Increase of compression strain prior to failure, laminate type 1

This final fatigue damage state was examined by ultrasonic B- and C-scans and penetrant enhanced X-ray radiography. The onset and growth of delaminations was observed by means of optical on-line methods. The grid reflection method (Ref. 5) was applied to observe and record during the test the onset and growth of delaminations located between the outer plies. The principle of this method is the observation of the distortion of reflected grid lines due to out-of-plane deformations of the mirror-like specimen surface.

A self-developed optical strain measurement facility based on light diffraction enabled the fast and contactless registration of local strains and strain distributions especially in the vicinity of holes and notches (Ref. 6). This method requires the preparation of a reflecting diffraction grating (400 l/mm) onto the test specimen surface. Illuminated by a laser beam n orders of diffraction can be observed at discrete angles α_n :

$$n \cdot \lambda = p \cdot \sin \alpha_n$$

with the wave-length λ and the grating constant p . A change of p due to tensile or compressive strains leads to changes of the diffraction angles which can be measured by opto-electronic devices. By means of this method the strain redistribution due to damage development under fatigue loading can be observed and evaluated.

3. TEST RESULTS

3.1. Un-notched Laminates:

Former investigations on un-notched multidirectional laminates (Ref. 7) in the tensile load regime showed that delamination onset and growth occurred always at the free edges of the test specimens. The difference of the transverse contraction

for different ply orientation generates peeling stresses σ_{33} at the free edges and initiates the delamination onset in interfaces between on-axis and cracked off-axis plies. This delamination process is strongly dependent on the laminate stacking sequence and the applied stress. With tension-compression loading the formation of transverse cracks and edge delaminations is clearly reduced compared with that under tension-tension loading because the maximum stress must be reduced as indicated in Fig. 1. Fig. 3 shows a typical X-ray radiography of the delamination state of a type 1 laminate after 1,000,000 load cycles under tension-compression loading at $\sigma = \pm 350 \text{ N/mm}^2$.

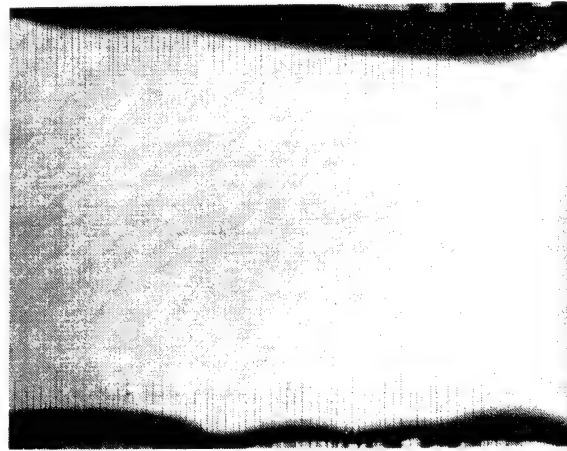


Figure 3. Damage state after 1,000,000 l.c. at $R = -1$, $\sigma = \pm 350 \text{ N/mm}^2$, laminate type 1

The edge delaminations are located in the 0/90- and 90/0-interfaces with relatively short matrix cracks in the 90°-plies. The central area seems to be free of cracks, but there are also short cracks which are visible only after cutting and repeated penetrating as demonstrated in Fig. 4 for a type 4 quasi-isotropic laminate:

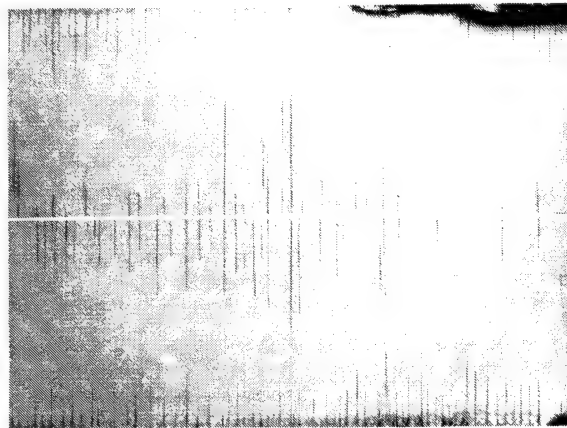


Figure 4. Damage state after 250,000 l.c. at $R = -1$, $\sigma = \pm 200 \text{ N/mm}^2$, laminate type 4

This development of short matrix cracks the density and average length of which increased with higher numbers of cycles was observed with all of the types of laminates. In type 1 and type 3 laminates first the cracks in the 90°-plies were initiated, in type 2 and type 4 laminates more in 45°-plies. Crack density and onset of crack development depend both on the number and on the position or stacking sequence of the off-axis plies. Fig. 5 displays as an example the crack density versus number of cycles of a type 4 laminate:

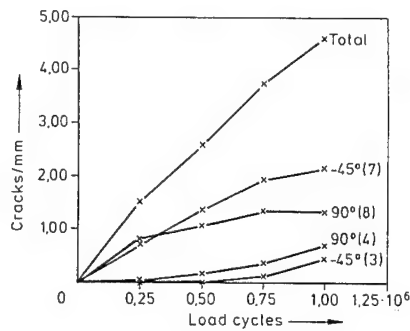


Figure 5. Crack density in individual plies versus number of load cycles, $R = -1$, $\sigma = \pm 200 \text{ N/mm}^2$, laminate type 4

The development and stable growth of matrix cracks and edge delaminations is represented by the decrease of stiffness measured as secant modulus versus number of cycles. For most of investigated laminates in the literature (Ref. 8) this curve shows three stages. But the existence of stage III depends on the laminate stacking sequence (fiber-dominated or matrix-dominated) and on the damage mechanisms leading to the laminate failure. For such fiber-dominated laminates as type I and type 2 never such a stage III could be observed as depicted in Fig. 6:

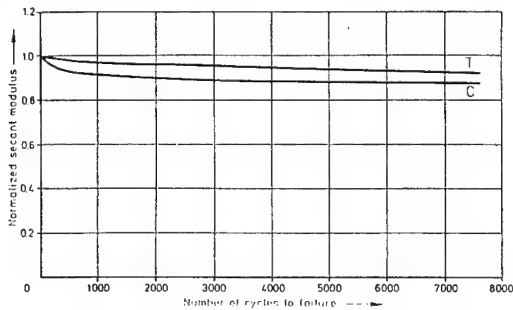


Figure 6. Tension and compression stiffness decrease during cycling, $R = -1$, $\sigma = \pm 450 \text{ N/mm}^2$, laminate type 2

This characteristic stiffness response exhibits that the initiation of the final fatigue failure occurs as a very fast process as shown in Fig. 2 by the strain response during the last cycles prior to failure. By means of the method described in chapter 2 it was possible to examine extensively the final damage state leading to failure.

Fig. 7 shows the X-ray records exhibiting the characteristic damage of a type 3 laminate after about 60 % of the mean lifetime (upper picture) and at the final state one cycle prior to failure (lower picture). At 60 % a characteristic damage state is developed with strong transverse cracks in the central four 90°-plies, only a few 45°-cracks and relatively small edge delaminations. The final state shows obviously more 90°-cracks, much more 45°-cracks, extension of the edge delaminations and a massive central delamination the buckling of which is indicated by the longitudinal cracks in the 0°-plies. The rapid increase of this delamination occurred in a time below 10 milliseconds, and would lead to a catastrophic compressive failure during the next cycle. The higher crack density observed in the left side of this record seems to be the reason for the occurrence of the rapid delamination process in this area. This is established more quantitatively by the C-scan of the same test specimen, recorded by through-transmission, as depicted in Fig. 8. The areas of matrix cracks are represented by areas of different grey-tones according with the measure of acoustic attenuation whereas the delaminated areas are black. B-scans showed that not only the 0/45-interface was delaminated but also the +45/-45- and the -45/90-interface, e.g. the

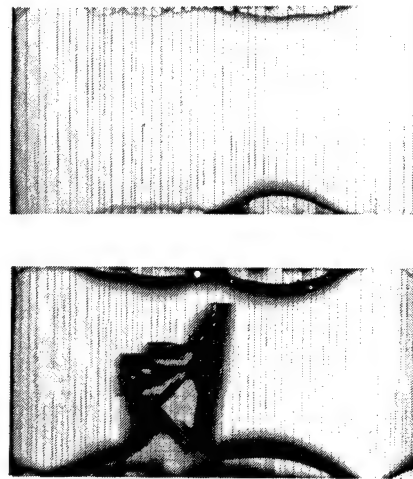


Figure 7. Damage state after ca. 60 % and at 100 % of fatigue life, $R = -1$, $\sigma = \pm 200 \text{ N/mm}^2$, laminate type 3

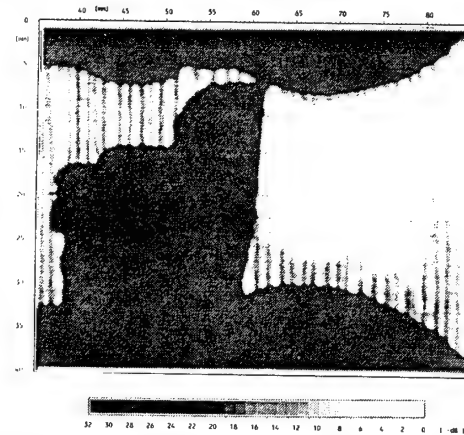


Figure 8. C-scan of the same specimen of Fig. 7 with areas of acoustic attenuation caused by matrix cracks

black areas display the envelope of overlapping delaminations in these interfaces.

The extensive crack formation in 90°- and $\pm 45^\circ$ -plies apparently leads to a damage state which causes the transition from stable delamination growth to subsequent unstable growth and buckling of the sublaminate. Micrographic investigations after cutting of the test specimens showed at the end of single cracks at the interface small interlaminar cracks, so called "micro-delaminations":



Figure 9. SEM-micrograph of a "micro-delamination" at the 0/90-interface, type 1 laminate

At higher crack densities in the off-axis plies interfaces with such micro-delaminations get up to a critical state with respect to unstable delamination growth and buckling. With tests under tension-compression loading on specimens of laminate type 1 containing artificially introduced central delaminations in some cases the final fatigue failure was initiated by instable growth of a "natural" edge delamination whereas the artificial circular delamination up to diameters of 15 mm showed no growth as displayed by the X-ray record in Fig. 10:

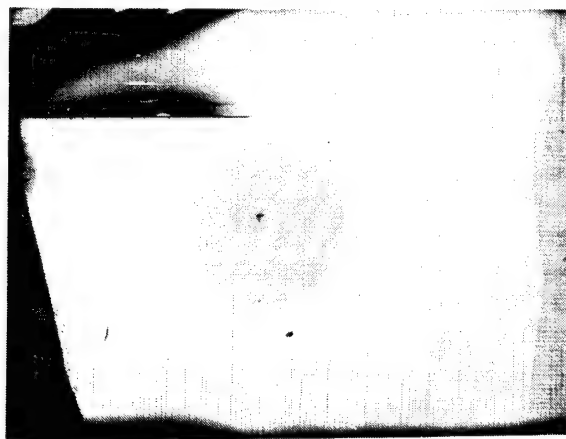


Figure 10. X-ray record of the final fatigue damage state of type 1 laminate containing an artificial delamination in the -45/0-interface

The crack formation in the 90°-plies precipitates the rapid increase of the edge delamination because only a few cracks developed in the -45°-ply of the -45/0-interface of the artificial delamination.

3.2. Notched Laminates:

As mentioned in chapter 2 a comprehensive test program was performed on notched quasi-isotropic laminates of type 3 with variations of the specimen width, notch size and notch shape in order to study possible size effects in dependence on damage initiation and damage growth under tension-compression fatigue. The following table gives an overview of the test matrix with respect to notch size ($2a$) and specimen width (w):

w [mm]	20	40	80	160
a [mm]				
1.25		0.0625		
2.50	0.25	0.125	0.0625	
5.00	0.5	0.25	0.125	0.0625
10.00		0.5	0.25	0.125
20.00			0.5	

Two different notch shapes were used in this program: Circular open holes and sharp notches, both located in the center of the test specimens. Delamination onset and growth was studied by means of the grid reflection method and in selected cases by the optical strain field measurement, the final fatigue damage state by X-ray- and ultrasonic investigation. Because the test program is not yet completed, in this presentation only a selected part will be reported and discussed.

The onset of delamination development occurred in all of the tested specimen configurations relatively early depending on the stress level. The delamination emanates always from the edge of the open hole, or from the notch tip, respectively. The delamination area increases with increasing number of load

cycles in a stable manner. Rapid steps in the delamination growth can be observed during incidence of strong longitudinal cracks in the 0°- plies. As an example the grid reflection pictures of a specimen of 80 mm width containing a hole of 20 mm diameter are displayed in the next Figure:

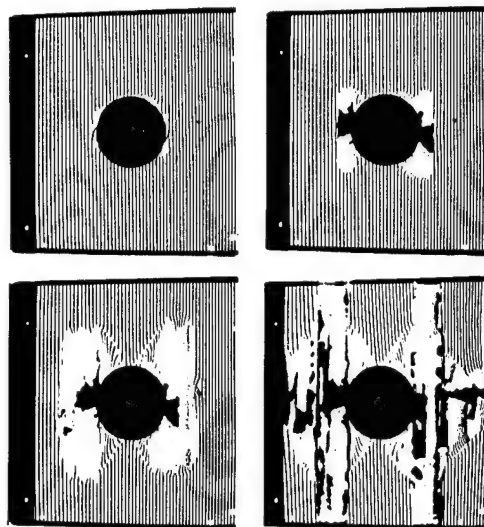


Figure 11. Grid reflection pictures of delamination growth at 1000, 10000, 80000, and 93610 cycles, $2a/w = 0.25$, $w = 80$ mm, $\sigma = \pm 180 \text{ N/mm}^2$

The delamination starts after ca. 100 l.c., at 10000 l.c. longitudinal cracks at the edges and parallel generate delamination strips of ca. 5 mm width the buckling of which can be observed under each compression cycle. After 80000 l.c. is increased in longitudinal direction corresponding to the cracks and also extended in transverse direction. This damage state leads to the final failure after 93610 l.c. caused by instable growth in both directions.

Another damage growth characteristic can be seen in Fig. 12 where the grid reflection pictures of a specimen of 40 mm width with a hole of 2.5 mm diameter are depicted:

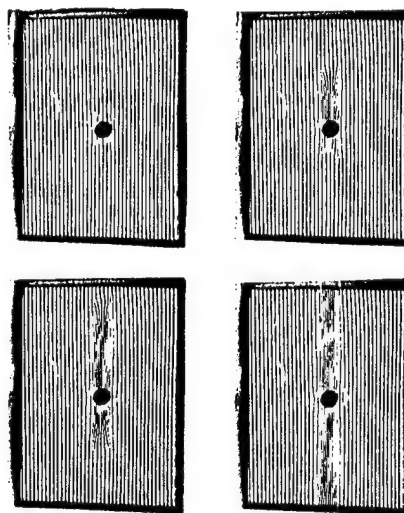


Figure 12. Grid reflection pictures of delamination growth at 500, 2000, 4000, and 8000 cycles, $2a/w = 0.0625$, $w = 40$ mm, $\sigma = \pm 240 \text{ N/mm}^2$

The delamination area is restricted to the width of the hole diameter because strong longitudinal cracks started to grow after ca. 1000 l.c. the length of which corresponds with the delamination length. A small delamination development in transverse direction first could be observed after 40000 l.c. (not displayed here). With specimens containing holes of 5 mm diameter the delamination extent is also more oriented to the longitudinal direction, but small strips of a width of a few millimeters developed besides the hole edges. This can be seen in Fig. 13, where X-ray records of the final fatigue damage state are displayed for holes of 5 mm, 10 mm and 20 mm diameter:

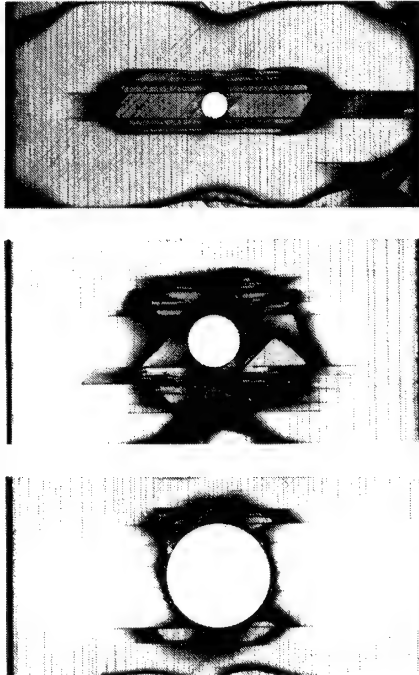
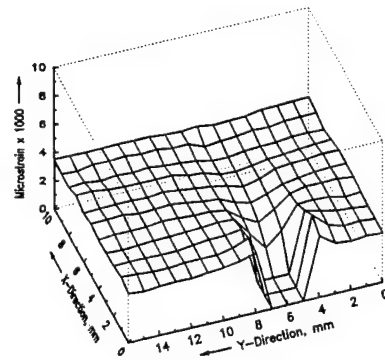


Figure 13. X-ray records of the final fatigue damage state for different hole diameters of a 40 mm wide test specimen, $\sigma = \pm 240 \text{ N/mm}^2$

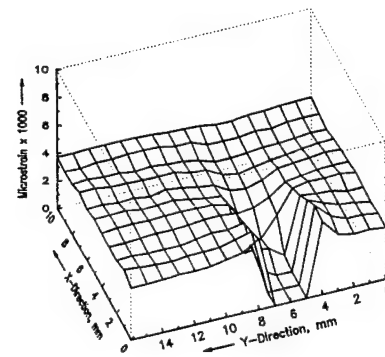
With $2a/w$ - ratios higher than 0.25 the delamination growth into the longitudinal direction is more restricted, parallel longitudinal cracks generate parallel delamination strips additional to edge delaminations emanating from the free edges of the hole into transverse direction. This pronounced damage of the residual load-carrying cross-section explains the significant decrease of the fatigue strength of those laminate configurations. The crack formation in the 45°- and 90°-plies is more concentrated to the residual cross-section and increases at higher numbers of cycles the risk of early unstable delamination growth and buckling in this area.

The redistribution of strains or stresses, respectively, by damage development like matrix cracks and delaminations can be studied by means of the optical strain measurement facility briefly described in chapter 2. The strain distribution of the longitudinal strains ϵ_{11} was measured by scanning a field of $16 \times 10 \text{ mm}$ in steps of 1 mm in a few seconds. After certain intervals of cycling the scans were repeated. An example is shown in Fig. 14: The measured strain distributions of a 40 mm wide specimen containing a hole of 2.5 mm diameter are displayed by three-dimensional plots. The bottom line of the scan field is laid through the center of the hole, the x-direction (10 mm) represents the load axis. The first plot exhibits only a slight elevation of strain besides the hole edges of 0.43 % compared with the average strain at the top line of 0.35 % under quasistatic loading of $\sigma = + 200 \text{ N/mm}^2$ before the cycling.

QUASISOTROP, 2.5 MM HOLE, 0000 CL.



QUASISOTROP, 2.5 MM HOLE, 5000 CL.



QUASISOTROP, 2.5 MM HOLE, 20000 CL.

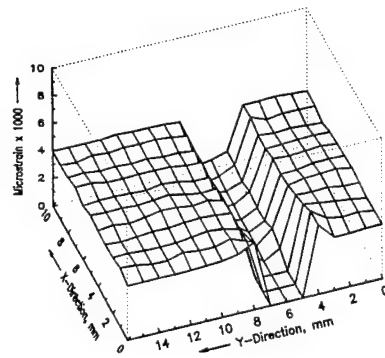


Figure 14. Plots of the measured strain distributions of a 40 mm wide test specimen with a hole of 2.5 mm after 5000 l.c. and 20000 l.c.

After 5000 l.c. of tension-compression loading with $\pm 200 \text{ N/mm}^2$ the strain peak is higher (0.52 %) due to the edge delamination growing in transverse direction, a longitudinal strip delamination has developed, and the average strain is slightly increased to 0.37 %. After 20000 l.c. only the strip delamination was enlarged (actual length evaluated from X-ray was 20 mm), whereas the small edge delamination showed no extent. The average strain is now nearly constant with a level of about 0.4 %.

The measurement of such strain distributions facilitates the evaluation of damage patterns observed by X-ray records.

QUASIISOTROP, 5 MM HOLE, 60000 CL.

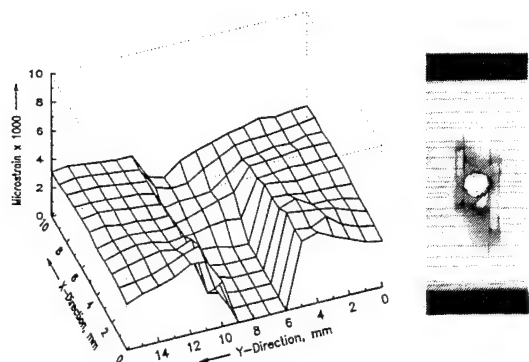


Figure 15. Plot of the strain distribution of a 20 mm wide test specimen with a hole of 5 mm after 60000 l.c. compared with X-ray damage pattern

This is demonstrated in Fig. 15 for a 20 mm wide specimen containing a 5 mm hole, after 60000 l.c. with tension-compression loading under $\pm 220\text{N/mm}^2$. The strain distribution exhibits the different load-carrying capabilities of different delaminated areas given by the X-ray record. So this method enables the evaluation of stress redistributions due to the development of damage under fatigue loading.

4. CONCLUSIONS

For different laminate lay-ups of multidirectional laminates under loading containing compressive cycles the fatigue performance depends on the fiber orientation and the stacking sequence of the individual plies. But the fundamental damage mechanisms like initiation and growth of matrix cracks in off-axis plies and delamination development seem to be the same:

Under tension-compression fatigue loading first transverse cracks occur in the 90°-plies which can reach after a certain number of cycles a nearly constant mean distance, the well known characteristic damage state (CDS). At higher numbers of cycles matrix cracks also develop in $\pm 45^\circ$ -plies. Emanating from the free edges delaminations are initiated preferably at interfaces between 0° and 90°-plies. The density and the average length of the cracks grow, as well as the edge delaminations, with increasing number of cycles. At the tips of transverse cracks small interlaminar cracks can be observed, so-called micro-delaminations. So the interfaces become "delamination-critical", e.g., the stable growth of the edge delamination changes to rapid instable growth and local buckling leading to catastrophic failure of the laminate. Concurrent investigations of the growth of artificially introduced delaminations established that the "natural" delaminations caused by matrix-cracking of off-axis plies may be more dangerous with respect to fatigue failure than the artificial delaminations if they don't exceed certain sizes.

The investigation of notched quasi-isotropic laminates showed that the stable delamination growth started always from the edges of holes or notches. The transition of stable delamination growth to rapid unstable growth and buckling leads to the final compressive laminate failure. For different hole or notch sizes characteristic delamination growth and damage patterns could be observed. Measured strain distributions in the vicinity of holes indicated the influence of stress concentrations and redistributions on delamination development and subsequent laminate failure.

5. REFERENCES

1. Reifsnider, K.L. and Talug, A.: *Analysis of Fatigue Damage in Composite Laminates*. Int. J. Fatigue, Jan. 1980, pp.3-11.
2. O'Brien, T.K.: *Characterization of Delamination Onset and Growth in a Composite Laminate*. In: *Damage in Composite Materials*, ASTM STP 775, pp. 140-167 (1982).
3. Highsmith, A.L., Stinchcomb, W.W. and Reifsnider, K.L.: *Effect of Fatigue-Induced Defects on the Residual Response of Composite Laminates*. ASTM STP 836, pp. 194-216 (1984).
4. Bergmann, H.W. and Prinz, R.: *Fatigue Life Estimation of Graphite/Epoxy Laminates under Consideration of Delamination Growth*. Internat. Journal for Numerical Methods in Engineering, Vol. 27, pp.323-341, 1989.
5. Schütze, R. and Goetting, H.C.: *On-Line Measurement of Onset and Growth of Edge-Delaminations in CFRP-Laminates by an Optical Grating Reflection Method*. Z. Werkstofftechnik 16, 9(1985), pp.306-310.
6. Goetting, H.C. and Schütze, R.: *An Optical Strain Measurement Facility for Damage Mechanics Investigations on Composites*. Mat.-wiss. u. Werkstofftechn. 20, pp.344-350, 1989.
7. Goetting, H.C.: *Einfluß verschiedener Parameter auf die Schadensentwicklung*. In: *Schadensmechanik kohlenstoffaserverstärkter Kunststoffe bei Schwingbelastung*. DfVLR-Mitt. 87-08, S. 29-61, Juli 1987.
8. Schulte, K. and Stinchcomb, W.W.: *Damage Development Near the Edges of a Composite Specimen During Quasi-static and Fatigue Loading*. Composites Technology Review, Vol. 6, No.1, Spring 1984, pp. 3-9.

**SESSION
2.1.A**

**SPACE PLANE
&
RE-ENTRY
I**

PRECEDING PAGE BLANK NOT FILMED

N92-23820

84732

CONCEPTIONAL DESIGN TO HEAT-RESISTANT AIRFRAME OF HOPE

Masataka YAMAMOTO

National Space Development Agency of Japan

ABSTRACT

We recognize that HOPE airframe meets with severe thermal and mechanical environment through the operation phases such as launch, reentry and landing. Conceptional design model is studied using the results to R&D of heat resistant materials and to heat resistant structural design. Structural configuration to heat resistant is to fit the thermal protection panels out of frame structure, in addition to mount the inboard thermal insulation material. Primary structural materials are carbon fiber reinforced polyimide (up to 300°C) and carbon-carbon (up to 1700 °C), thermal protection materials are ceramic tile, titanium alloy panel and carbon-carbon panel.

Keyword: heat-resistant airframe structure, aerodynamic heating, structural configurations, primary structural materials, carbon fiber reinforced polyimide(C/Pi), carbon/carbon(C/C), thermal protection system (TPS)

1. INTRODUCTION

R&D of HOPE started in 1986, and has carried out the latter half of conceptional design. There are three technical difficulties on the development, (1) Determine to aerodynamic shape of orbiter, (2) Navigation, control and landing on an unpiloted airplane, (3) Development of heat-resistant materials and heat-resistant structural design to protect aerodynamic heating [1].

HOPE vehicle will be exposed to severe aerodynamic heating and loading conditions at launching, on-orbiting and re-entry phase. Also we are required to keep all the more payload weight by means of lightweight structural design and fabrications. To satisfy of these requirement, we develop the advance materials which are excellent heat-resistant properties and high specific strength/rigidity. And so we study heat-resistant airframe studies using those advance materials, and fabrication technique of airframe components.

This paper introduce current status of conceptional design of HOPE heat-resistant structure.

2. STRUCTURAL DESIGN REQUIREMENTS AND STRUCTURAL MATERIALS

On the study of structural configuration of airframe, we set out the mechanical and thermal environment conditions during the flight.

(1) Scale of the Vehicle

On the first step, we studied total weight 10ton vehicle to be able launch by H-II rocket. But 10ton vehicle could keep only 500~1000kg payload weight.

Table 1: Baseline configuration of 20 ton HOPE

Gross Weight	20ton at Launch 15ton at Return
Payload Weight	3ton at Launch 5ton at Return
Dry Weight	10ton
Wing Area	60m ²

Table 2: Applied mechanical load conditions to airframe in flight

Overall Load	Dynamic Pressure	$q_{max} = 5.4 \text{ ton/m}^2$ $M \approx 70 \text{ ton-m}$ $S \approx 17 \text{ ton}$
Overall Rigidity	Longitudinal Lateral	30Hz 10Hz
Acceration (Static)	Longitudinal Lateral	5G 0.7G
Acoustic		155dB (Overall)

Therefore, now more big vehicle (total weight 20ton) has been studying. We can keep about 3000kg payload weight to use the 20ton HOPE. Table.1 shows main demensions of 20ton HOPE vehicle.

(2) Load Conditions in Flight

The applied loads on orbiter are invesigated each phase of handling, launch, on orbit, re-entry and landng. As the result, launching load is the biggest on each phase. Table 2 shows load conditions of launch and landing.

(3) Thermal Environmental Conditions

Thermal environmental conditions were evaluated launching, on orbit and re-entry, and surface temperature of orbiter were calculated to determine the employment temperature of primary structural materials(C/Pi,C/C) and thermal protection panels(C/C, ceramic tile, Ti multi wall). Fig.1 shows typical expected maximum surface temperature of orbiter at altitude = 75km, mach = 27 in a nominal trajectory. Table 3 shows employment temperature of C/Pi, C/C primary structural materials. Those temperature are an objective on the development of materials and structural design.

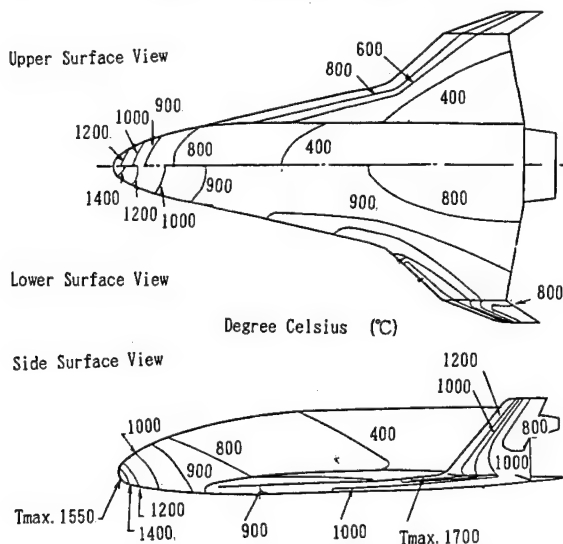


Fig.1: Distribution of Surface temperature

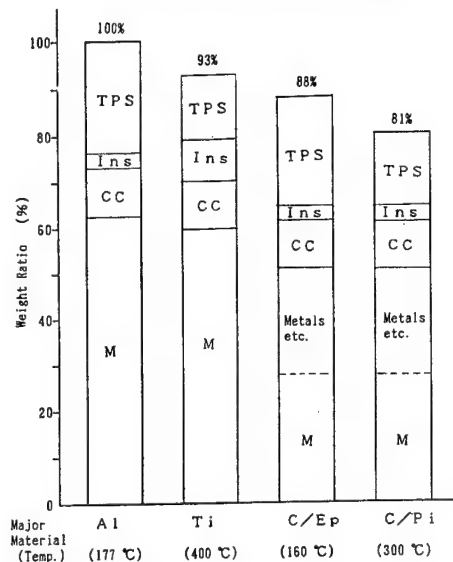
Table 3: Employed temperature of C/Pi, C/C

Mat.	Event	Temperature °C
C/Pi	Ascent	Max. 130(For.Fuselage) Min. No Critical
	On Orbit	Max. 89(For.Fuselage) Min. -80(For.Fuselage)
	Reentry/Landing	Max. 300(Overall) Min. No Critical
C/C	Ascent	Max. 317(Nose Cone) Min. No Critical
	On Orbit	Max. 51(Nose Cone) Min. -51(Nose Cone)
	Reentry/Landing	Max. 1700(Leading Edge) Min. No Critical

(4) Structural Materials and Airframe Weight

Candidated materials consistient of warm structure were aluminum alloy, titanium alloy, carbon fibre reinforced epoxy and carbon fibre reinforced polyimide. Hot structural such as nose cone, leading edge, tip fin will be employed C/C material with deoxidization coating of SiC, SiO₂. Table 4 shows airframe weight of 20ton HOPE for those candidated materials. C/Pi material will be able to lightweight about 20% compare with aluminum alloy. Fig.2 shows employment materials of each component on airframe.

Table 4: Comparison with structural weight for candidated materials



M: Major Material } Primary Structure
 CC: Carbon-Carbon }
 Ins: Inboard Insulator
 Ceramic Tile assumed to TPS for each case

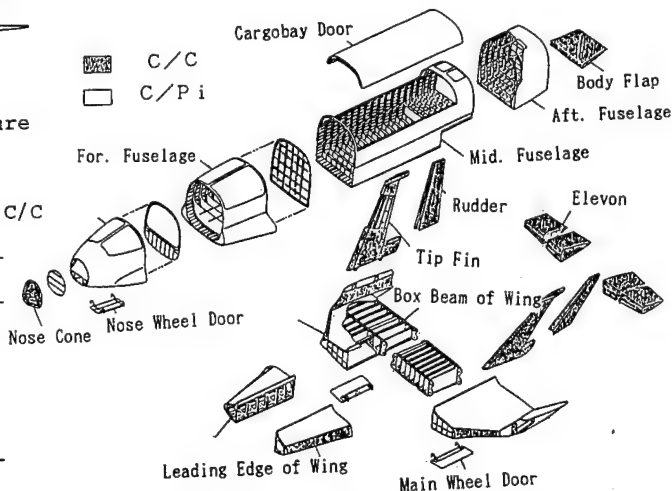


Fig.2: Employed materials of each component

3. STRUCTURAL CONFIGURATION

Structural configuration was investigated in consideration of orbiter size, H-II rocket interface, structural material properties and thermo-mechanical conditions. Structural concept and candidate structural materials are shown in fig.3(a)

(1) Heat-resistant Structural Configuration

To protect the airframe from severe aerodynamic heating as shown in fig.1, heat-resistant structure was made up of outer thermal protection panels, primary structure (C/Pi) and inner insulator at the warm structure (up to 1300°C), and also hot structure above 1300°C was made up of C/C primary structure and inner insulator. Fig.3(b) shows cross section of forward fuselage to be installed electronic equipments.

(2) Structural Configuration of Fuselage
Fuselage is semi-monocoque structure which are used widespread on airplane.

Middle fuselage has a big notched structure for cargo bay doors, so we must attend that wingload does not apply directly to middle fuselage.

(3) Structural Configurations of wings and Tipfins

Wings and tipfins are box beam structure consist of several spars, upper and lower plates. These structure resists to loads of shear, bending and torsion.

(4) Substructure, Connection of Components

Wings and fuselage were connected by carry through, so lift occurred on the wings were transferred to fuselage. Because it appeared about 1000°C temperature difference between hot structure (C/C) and warm structure (C/Pi), we must considered the connection method which had functions of thermal insulation and thermal stress relaxation. Fig.3(c), (d), (e) show warm structure connections with hot structure nose cone, leading edge, tip fin respectively.

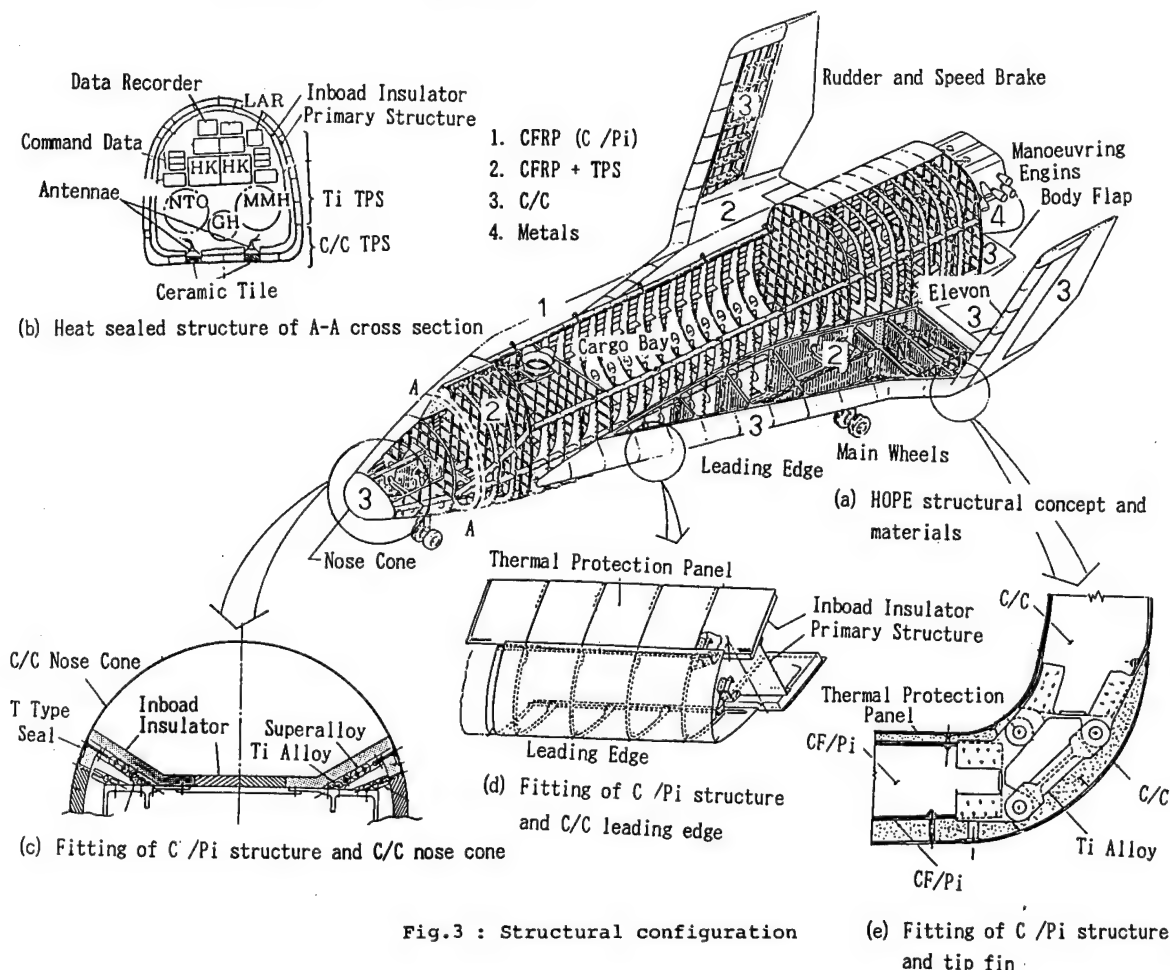


Fig.3 : Structural configuration

4. HEAT-RESISTANT MATERIALS

4.1 Primary Structural Materials

(1) Warm Structural Materials

Primary structural materials were required the properties of high specific strength and high specific rigidity on high temperature. Categorized materials for warm structure are aluminum alloy, titanium alloy, C/Ep, C/Pi. We performed trade off study for those materials with regard to structural weight, thermal-mechanical properties, fabrication of components, cost.

As the result, although C/Pi must be investigated fabrication process and accumulation of thermal-mechanical properties, it is excellent material to make up lightweight airframe [2],[3]. Fig.4 shows trial produced C/Pi skin-stringer component. Fig.5 shows typical mechanical properties of C/Pi.

(2) Hot Structural Material

Hot structure heated up to 1700°C by aerodynamic heating was employed C/C material with excellent heat-resistant, high strength and high rigidity. Fig.6 shows trial produced C/C skin-stringer component.

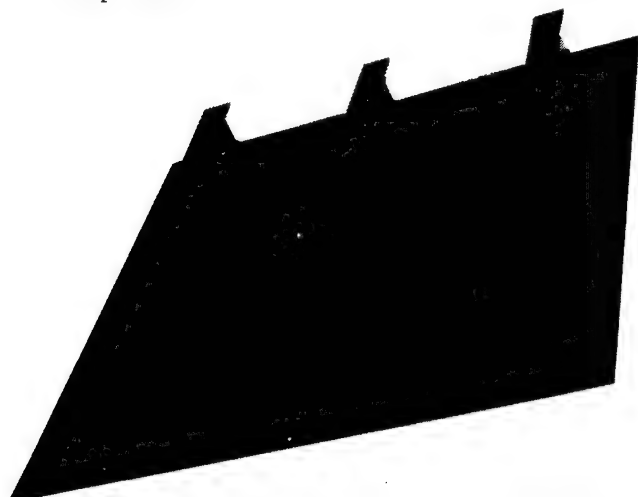


Fig.4: Trial fabrication of C/Pi component

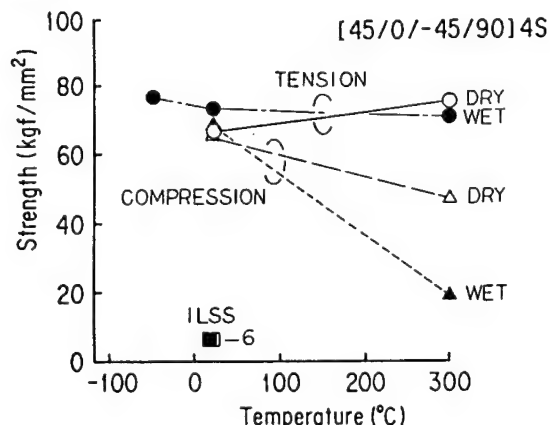


Fig.5: Mechanical properties of C/Pi

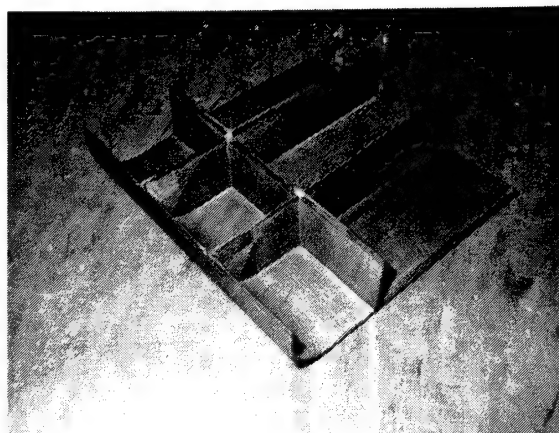


Fig.6: Trial fabrication of C/C component

4.2 Thermal Protection Panels

Thermal protection panels are required properties of reusable, lightweight, maintenance, attaching to primary structure.

(1) Ti Alloy TPS

Ti alloy TPS is employed up to 550°C . Heat shield concept of TPS is shown in fig.7, thin flat sheet and dimple sheet are laminated alternately and soldered. Trial product was lightweight and excellent insulator.

(2) Ceramic Tile

Ceramic tile was fabricated to constituents of Al_2O_3 , SiC fibre and binder. These constituents are mixed and sintered in the furnace. After that ceramic tile was coated to get high heat-resistant property to SiO_2 , B_2O_3 , SiC. Thermal, mechanical, electrical properties of ceramic tile are shown in table 5.

(3) C/C TPS

C/C TPS consisted of three elements, C/C panel with heat-resistant coating, fasteners and thermal insulator. C/C panel was attached to the primary structure by post, and insulator was placed between C/C panel and structure. Fig.8 shows concept of C/C TPS. Fig.9 shows photograph of C/C panel.

When structural designer select to those TPS, structural weight is one of the important factor. Fig.10 shows relation of weight and employed temperature of TPS. The example of TPS arrangement is shown in Fig.11. The area over 1300°C are hot structure to be used C/C primary structural material.

5. STRUCTURAL AND HEAT TRANSFER ANALYSIS

Feasibility of conceptional design model were investigated by structural and heat transfer analysis using above result.

5.1 Structural Analysis

Eigen frequency of airframe was calculated finite element model consist of 23 beam elements and 59 mass. Fig.12 shows main

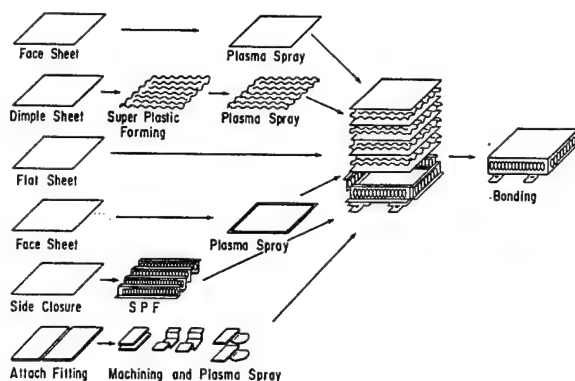


Fig.7: Fabrication process of Ti TPS

Table 5: Composition, mechanical, thermal and electrical properties of ceramic tile

Composition	Al_2O_3 , SiC, Binder
Coating	SiC, B_2O_3 - SiO_2 CVD
Density	0.12 g/cm^3
Specific Heat	$0.25 \text{ cal/g}^\circ\text{C}$
Thermal Expansivity	$3.23 \times 10^{-6} \text{ 1/}^\circ\text{C}$
Bending Strength	8.7 kgf/cm^3
Dielectric Constant	1.15
Dielectric Loss	0.00016

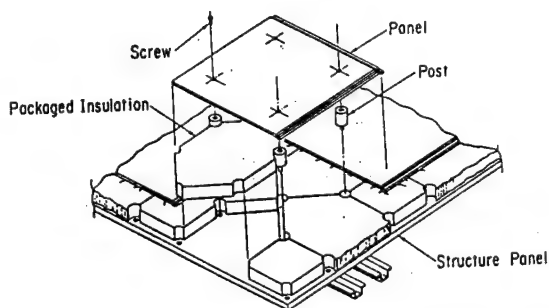


Fig.8: Concept of C/C TPS

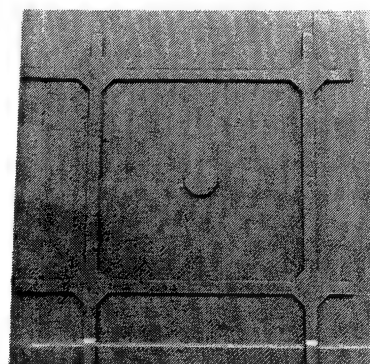


Fig.9: C/C panel of C/C TPS

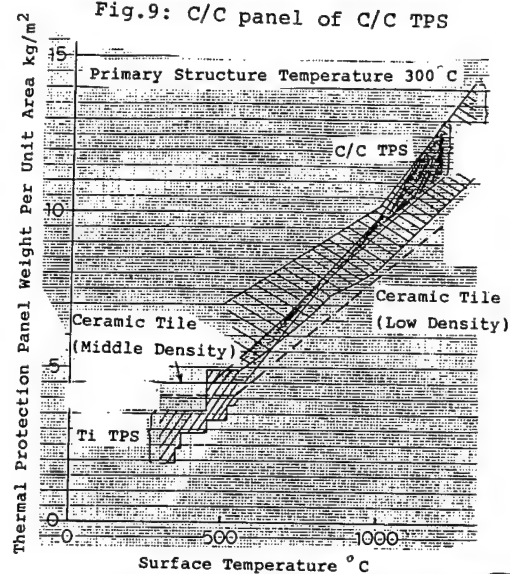


Fig.10: Comparison with TPS weight for candidated TPS

UPPER SURFACE

LOWER SURFACE

- C/C Hot Structure ($1300\sim1700^\circ\text{C}$)
- C/C Stand-off TPS ($550\sim1300^\circ\text{C}$)
- Titanium Multiwall TPS ($300\sim550^\circ\text{C}$)
- Ceramic Tile TPS (Antenna area $\sim1200^\circ\text{C}$)

SIDE SURFACE

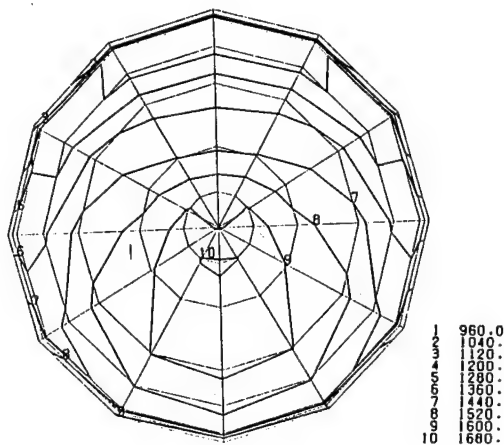


Fig.11: Distribution of TPS

mode and eigen frequencies of airframe. These frequencies are not satisfied to requirement of H-II rocket, so requirement will be reset to satisfy for orbitor with lower frequency.

5.2 Heat Transfer Analysis

Heat transfer analysis were performed to nose cone and a part of leading edge to be heated severe by aerodynamic. Finite element modeling were used to configuration as shown in fig.3(c) and fig.3(d). Heat transfer was calculated through inner structure of nose cone and leading edge using time history of heating rate. Fig.13 shows temperature distributions of nose cone after 1000 sec from re-entry.



1000 sec after reentry, °C

Fig.12: Eigen frequency and mode of airframe

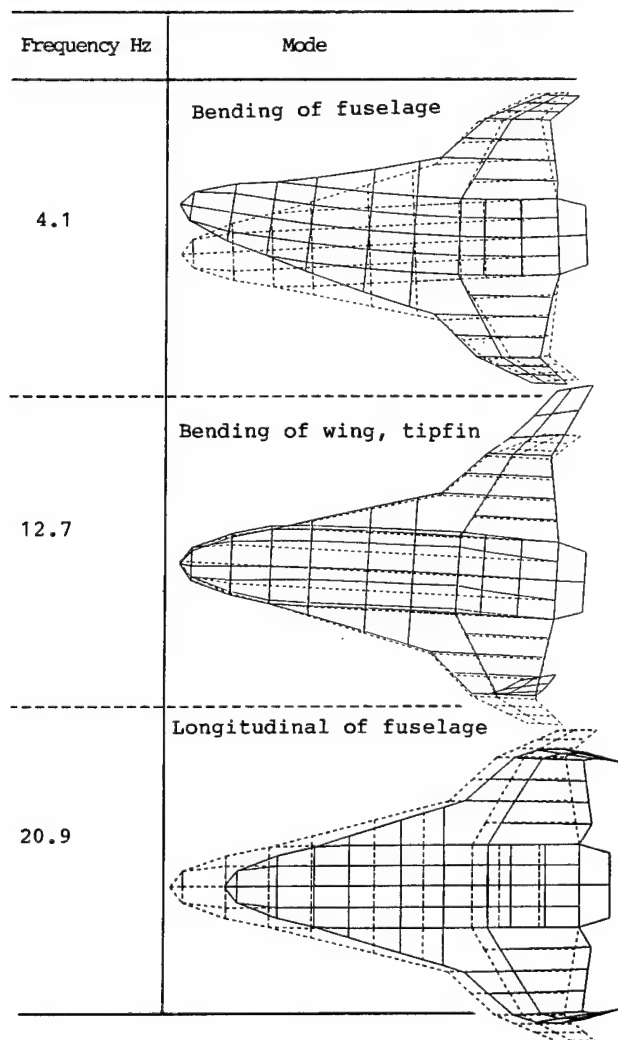


Fig.13: Temperature distribution of nose cone by aerodynamic heating

6. CONCLUSION

Structural design of HOPE must be considered to thermal and mechanical conditions. Therefore we started to develop the high quality heat-resistant structural materials such as C/Pi, C/C, ceramic tile, titanium alloy TPS. Now we have acquired the accumulation of thermal, mechanical datum those advanced materials, and fabrication process of components. Conceptual structural design has been performed using load and temperature conditions, material properties. We can forecast the material properties of conceptual structural model.

REFERENCE

- [1] Ito, T., Akimoto, T., HOPE-Japan's First Step for Spaceplane, Proc. First Int. Conf. on Hypersonic Flight in the 21 Century, Sep. 1988, PP.134-142.
- [2] Kobayashi, T., Matsushita, T., Yamamoto, M., et al., Study on the Primary Structural Members and Thermal Protection System for HOPE, Proc. First Int. Conf. on Hypersonic Flight in the 21st Century, Sep. 1988, PP.199-208.
- [3] Tamura, H., Mitsuma, H., Kobayashi, T., Atsumi, M., Fabrication Test and Evaluation of Graphite/PMR-15 for HOPE Primary Structure, 17th ISTS, May 1990, PP.483-488.

LARGE THIN COMPOSITE THERMOSTRUCTURAL PARTS

N 92 - 23821

D. DESNOYER, A. LACOMBE, J.M. ROUGES

SEP

B.P. 37

33165 ST MEDARD EN JALLES

ABSTRACT

The new space transportation projects (Sanger, Hotol, STAR-H, STS 2000, NASP, HERMES) have a challenge with their system mass performance.

The traditional technologies lead to no feasible missions and improvements have to be performed in most of the domains. But, a very challenging area is the field of materials for high temperatures which are encountered in the engines (intakes, nozzles and combustion chambers) and in the airframe (nose, leading edges, flaps, rudders, ailerons).

Due to the overall size of these systems, large surface high temperature parts are mandatory in order to increase the system reliability in decreasing the junction number (seals, fasteners) and to decrease the overall mass. To be mass efficient, these large parts should be thin. The rigidity is provided by integrated stiffeners.

Depending of the reentry atmosphere, two main types of environment constraints should be considered :

- oxidizing environment
- non oxidizing environment.

For the oxidizing environment, SiC matrix have been selected and large parts (about 2 m²) have been manufactured under ESA-CNES contract demonstrating the availability and validity of the technologies.

Material tests performed under plasma arc jet have shown the oxidizing resistance of the material.

For non oxidizing environment (i.e. Planetary Reentry) carbon-carbon can be selected. SEP has studied and manufactured a conic shaped panel (about 0.35 m²) with integrated stiffeners. The skin thickness is 0.5 mm with no delaminable preform.

In parallel, advanced facilities have been implemented under ESA-CNES contract to meet new manufacturing requirements, such as :

- special processes which have been developed
- large part size
- reproducibility and reliability.

1. INTRODUCTION

The new space transportation projects which are dedicated to hypersonic vehicle have enlightened the need of technology improvement in many fields. Among all these, the problem of thermal protection against large heat fluxes induced by high enthalpy gas is very challenging.

Due to geometry constraints imposed by the aerodynamics, the thermal protection concept is no longer valid and should be replaced by the thermostuctural concept in which both functions, thermal and structural, are taken in charge by the same material.

The size of the new space transportation vehicle is between 50 m and 80 m long as far as they are defined today.

This shows the requirement of large parts or assembly of small parts.

In the past, as it has been demonstrated by the US orbiter experience, the trend was a decrease of the number of parts. (Apparition of chin panel in place of window tiles, decrease of tile number on the forward part.)

The main advantages are a design simplification, a decrease of junction number (seals, ...) and then a reliability increase.

For control surfaces US orbiter has adopted a solution with cold structure protected by silica tiles. This system was possible thanks to the heat fluxes level and requested aerodynamic performances. For space plane, the aerodynamic drag is a challenge which will lead to thinner control surface in which it will not be possible (in relation with the heat flux) to design a similar system. But the junction analysis shows that the need of a cold structure is linked to the no availability of suitable material at the time of shuttle design. A thermal structure acting at high temperature as a structure will meet the functional system requirements.

In order to be compatible with the mass budget, the material should have mechanical properties, and be available in low thickness.

The design of such a part will be comparable to current At aeronautic structures (ribbed and stiffened skin) but adapted

to the process. A design to process is necessary in order to compromise and then optimize the parts.

The skin thickness is an important driver to meet the mass budget requirements and the technology has to place skin as thin as possible at the disposal of the designer. It is the reason why SEP has developed thin preforms for thermostructural parts.

Another driver to select material is the environment to which it will be exposed.

In most of case, the environment is an oxidizing environment by direct presence of oxygen as on Earth, or by indirect presence of oxygen (after gas dissociation) as on Mars. Then no oxidation sensitive material is required.

SEP has selected Ceramic matrix composite to withstand oxidation environment and specifically Silicon Carbide matrix. Indeed, a carbon-carbon material coated with non oxidizing surface treatment (SiC or other) has to withstand mechanical loads with the carbon-carbon core, and need an extra thickness for the coating. This coating thickness is depending of the environment mission requirement and not depending of the mechanical loads. Then, if that extra mass does not jeopardize the mass budget for thick parts, it can more than double the efficient mass of thin shell (for instance .5 mm coating on each side for a C-C core of .5 mm).

2. PRODUCTION OF CARBON-CARBON OR SILICON CARBIDE COMPOSITES

The production of carbon-carbon or silicon carbide matrix composites is made up of three basic stages (Fig. 1)

At the first stage, a textile preform is created. This preform is obtained in the traditional manner by preparing a stack of carbon woven fabric layers.

To improve mechanical performance of composites the fiber ratio by volume of the preform is increased by compaction of the stack in a special tool.

To be compatible with the procedure of gaseous processing of the silicon carbide of carbon matrix the fiber ratio by volume is generally 45%.

With carbon fiber, three directional textures are also achieved :

- Novoltex ® texture with average mechanical characteristic is well suited to great thickness. It is used mainly for C-C brakes, nozzles, heat shields and fasteners. This preform is used to transfer 3D mechanical loads.
- Skinex ® texture with high mechanical performance is specifically designed to meet the requirement of thermal mechanical structures made up of thin stiffened skins. (e.g. spaceplane hot structure).

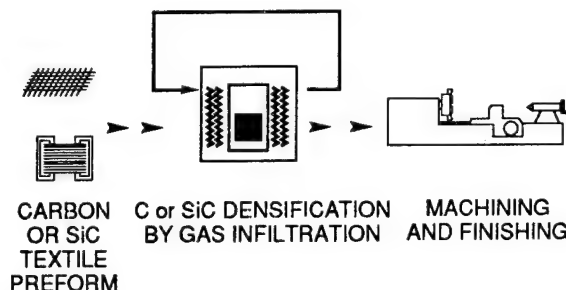


Fig 1 : CARBON-CARBON OR SILICON CARBIDE MATRIX COMPOSITES MANUFACTURING PROCESS

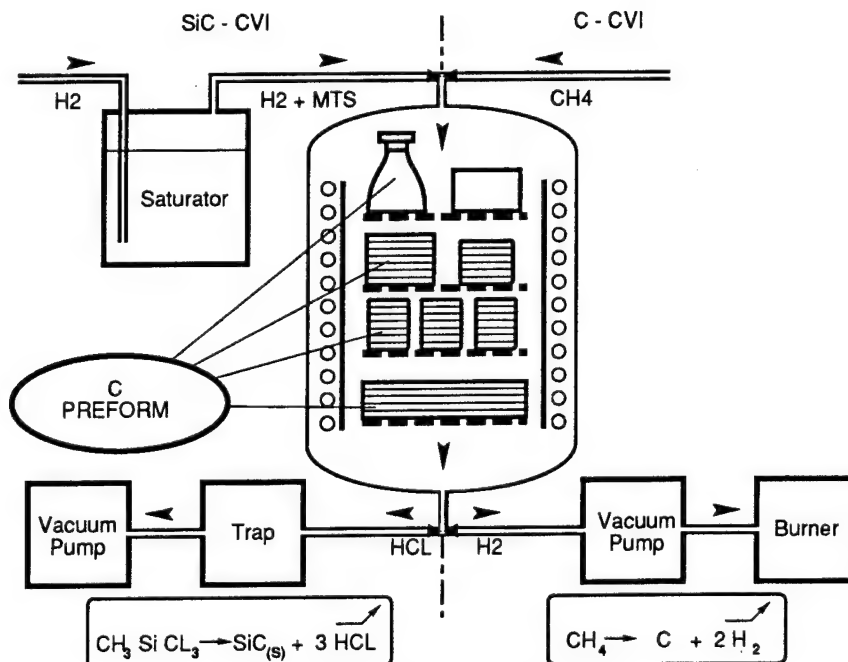


Fig 2 - DENSIFICATION PROCESS

the second stage, the carbon or silicon carbide matrix is positioned in the preform. The carbon or silicon carbide is obtained by the cracking of gas circulating through the carbon preform which is maintained at high temperature in a specific infiltration furnace (Fig. 2). Several infiltration cycles are repeated until the optimum densification of the preform is obtained, corresponding to the SEPCARB R C-C density of 1,750 kg/m³ or SEPCARBINOX R C-SiC density of 2,100 kg/m³.

The residual open porosity of the densified blanks is generally in the region of 10% by volume.

At the third stage, the blanks are machined and undergo various finishing operations. In particular surface treatments are performed in order to improve the resistance of the C-SiC to oxidation and especially to provide effective protection of the carbon fiber-based reinforcement for the whole range of potential operating temperatures.

3. CHARACTERISTICS OF CARBON-CARBON AND CARBON-SILICON CARBIDE MATERIALS

Carbon fiber reinforced carbon matrix is a very large family of materials which are characterized by :

- high thermal shock resistance
- mechanical strength maintained up to 2,500°C
- very high sensitivity to oxidation effects thus limiting life time under air environment above 400°C unless protected by a coating system.

Carbon fiber reinforced silicon carbide matrix materials provide remarkable mechanical characteristics in comparison with standard materials. The main characteristics can be summarized as follows :

- high specific mechanical strength which is

maintained at temperatures above 1,700°C

- high oxidation resistance due to matrix composition
- high level of toughness ensuring an excellent resistance to thermoshock and impact plus providing a non-catastrophic failure mode.

These properties are the result of carbon fibrous reinforcements, especially with respect to crack growth which is related to the absorption of energy resulting from the stress applied (Fig. 3).

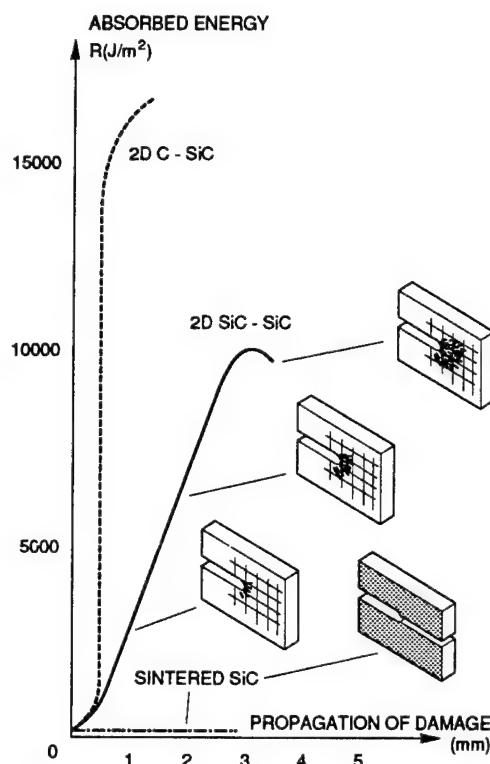


Fig 3 - CRACK TOUGHNESS TEST

PROPERTY	UNITS	TEMPERATURE			
		73°F (23°C)	1832°F (1000°C)	2552°F (1400°C)	
Fiber Content	%	45	45	45	
Specific Gravity		2.1	2.1	2.1	
Porosity	%	10	10	10	
Tensile Strength	KSI (MPa)	51 (350)	51 (350)	46 (330)	
Elongation (Tensile)	%	0.9	0.9	NA	
Young's Modulus (Tensile)	MSI (GPa)	13 (90)	15 (100)	15 (100)	
Poisson's Ratio					
V12	—	0	NA	NA	
V13	—	0.5	NA	NA	
Flexural Strength	KSI (MPa)	73 (500)	.102 (700)	.102 (700)	
Compressive Strength					
In Plane	KSI (MPa)	84 (580)	87 (600)	102 (700)	
Thru the Thickness	KSI (MPa)	61 (420)	65 (450)	73 (500)	
Shear Strength (Interlaminar)	KSI (MPa)	5.0 (35)	5.0 (35)	5.0 (35)	
Thermal Diffusivity					
In Plane	10 ⁻⁶ FT ² /S (10 ⁻⁶ M ² S ⁻¹)	118 (11)	75 (7)	86 (8)	
Thru the Thickness	10 ⁻⁶ FT ² /S (10 ⁻⁶ M ² S ⁻¹)	54 (5)	20 (2)	20 (2)	
Coefficient of Thermal Expansion					
In Plane	10 ⁻⁶ /°F (10 ⁻⁶ /°K)	1.7 (3)	1.7 (3)	NA	
Thru the Thickness	10 ⁻⁶ /°F (10 ⁻⁶ /°K)	2.8 (5)	2.8 (5)	NA	
Specific Heat	BTU/lbm °F (J/KG ⁻¹ /°K)	.15 (620)	.33 (1400)	NA	
Total Emissivity		0.8	0.8	0.8	

Table 1 - 2D C-SiC CHARACTERISTICS

Indeed, unlike unreinforced monolithic ceramics, the fibrous component inhibits crack growth in the silicon carbide matrix.

The main mechanical and thermal characteristics of 2D C-SiC are specified in Table 1.

C-C properties particularly ACC ones well known and described in several references.

C-SiC is characterized by low density, high rupture strengths associated with good elongation, high shear strength and low coefficients of expansion, both at ambient and at high temperature. In comparison with conventional carbon-carbon material, the C-SiC higher elongation capacity facilitates part and assembly designs.

Figures 4 to 11 show some typical characteristics of C-SiC. Figure 4 shows the behavior under tensile stress at ambient temperature. A nonlinear behavior of the material is noted from the origin. This is explained by the multiple cracking of the matrix during manufacture of the material due to differential expansions between the carbon fiber and the silicon carbide matrix. We can also note a permanent set the amplitude of which increases with the level of stress applied, the modulus at the origin remaining practically constant.

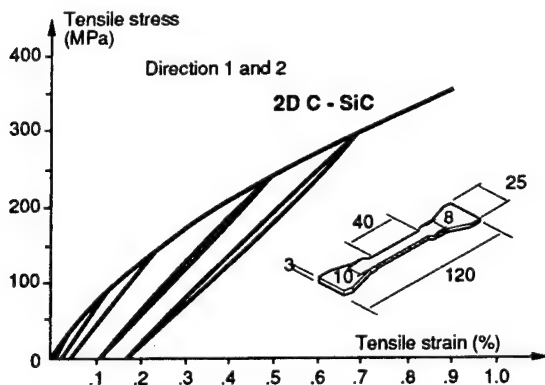


Fig 4 - LOAD/UNLOAD STATIC BEHAVIOR AT AMBIENT TEMPERATURE

C-SiC coated with a specific treatment improves its oxidation resistance life time as showed in the Table 2.

Figure 5 shows the behavior of the C-SiC under tensile stress at high temperature up to 1,500°C. The tests were performed under a neutral atmosphere and also under air atmosphere. The behavior of C-SiC remains practically unchanged up to 1,500°C.

Figure 6 shows the excellent behavior under mechanical fatigue at ambient temperature. After 10^6 cycles at 100 Hz, tensile/compression loads from -150 MPa to 150 MPa (i.e. 40% of the tensile rupture strength), residual properties identical to those initially measured can be noted (rupture strength of 370 MPa, elongation = 0.9%).

TEST PARAMETERS	RESIDUAL/ ULTIMATE TENSILE STRENGTH(%)
Cycle definition Plateau temperature : 1,550°C Plateau time exposure : 20 minutes 80 cycles (≈ 27 hours)	80
Tensile prestressing : 150 MPa (40% of ultimate strength) Temperature : 1,550°C Time exposure : 9 hours Permanent tensile stress : 150 MPa	93
Temperature : 1,550°C Time exposure : 6 hours	88
Stress : .0 to 150 MPa .0.1 hertz Temperature : 1,450°C Time exposure : 3 hours	93

TABLE 2 - RESIDUAL STRENGTH AFTER AGEING IN OXIDIZING ATMOSPHERE

Numerous fatigue tests were conducted at room temperature under various frequencies from 20 Hz to 100 Hz, tensile/tensile loads up to 80% of strength or, tensile/compression loads up to 75% of tensile strength. After 10^6 cycles the material has essentially the same properties.

Fatigue tests under tensile/tensile loads were implemented under a neutral atmosphere at temperatures up to 1100°C. The main results are shown in Figures 7-8-9. After 10^5 cycles, residual tensile strengths are identical to those initially measured at any fatigue stress level up to 75% of the initial tensile rupture level.

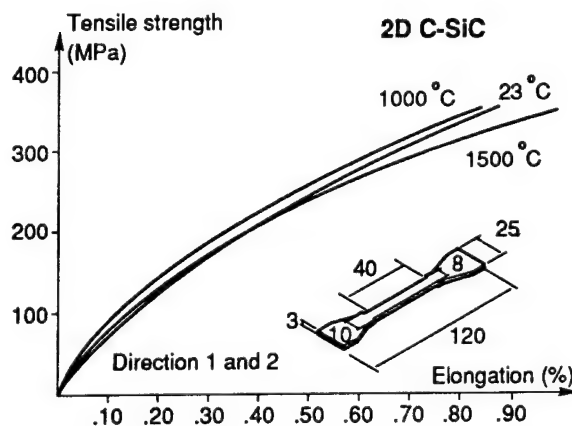


Fig 5 - TENSILE TESTS AT HIGH TEMPERATURE UNDER INERT ATMOSPHERE AND UNDER AIR

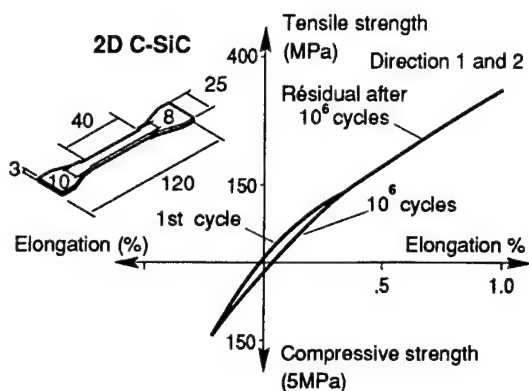


Fig 6 - T/C FATIGUE TEST AT AMBIENT TEMPERATURE

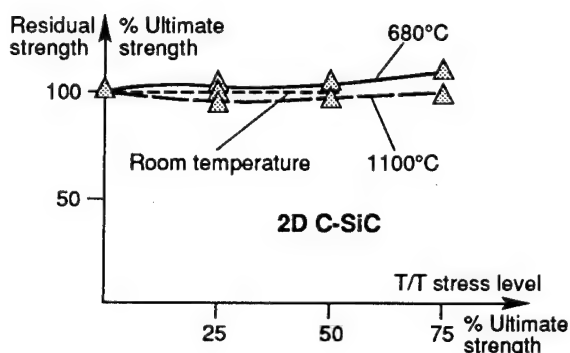
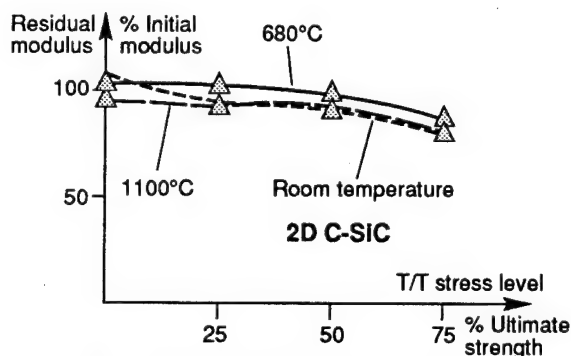
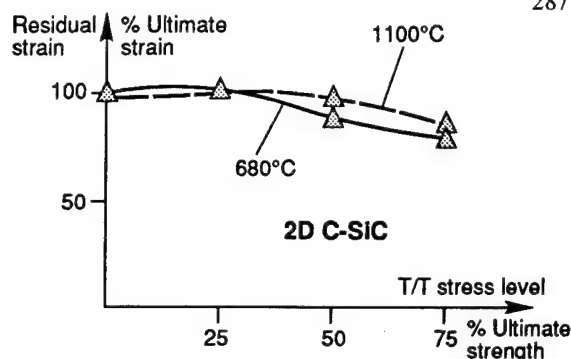
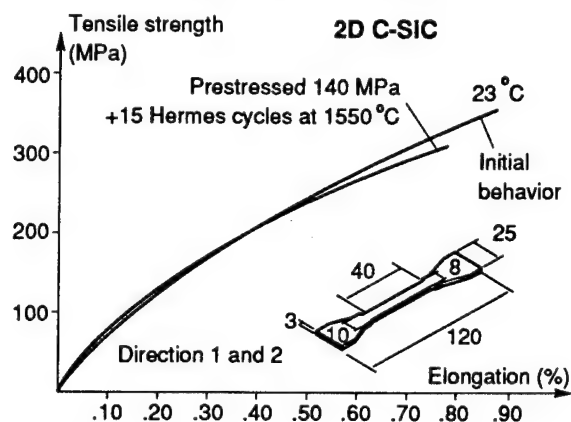
Fig 7 - T/T FATIGUE TESTS AT VARIOUS TEMPERATURES. - RESIDUAL STRENGTH (10⁵ CYCLES)Fig 8 - T/T FATIGUE TESTS AT VARIOUS TEMPERATURES. - RESIDUAL MODULUS (10⁵ CYCLES)Fig 9 - T/C FATIGUE TESTS AT VARIOUS TEMPERATURES. - RESIDUAL STRAIN (10⁵ CYCLES)

Fig 10 - TEST AT AMBIENT TEMPERATURE AFTER OXIDATION IN AIR

Figure 10 shows the mechanical behavior of C-SiC after tensile prestressing and thermal ageing simulating the stresses planned for these materials in their application to Hermes thermal structures.

After 15 cycles at 1,550°C, representing an accumulated exposure time of 5 hours, the mass loss is lower than 1.2% and the mechanical behavior remains good.

The oxidation tests are performed on 3 mm thickness tensile test samples in air at normal atmospheric pressure.

Based on SKINEX ® 3 directional carbon fiber textile preforms, quasi in-plane isotropic C-C and C-SiC materials are produced.

CHARACTERISTICS AT ROOM TEMPERATURE	RUPTURE STRENGTH (MPa)	RUPTURE STRAIN (%)	MODULUS (GPa)		
			AT ORIGIN	AT 0.3%	AT 0.3%
Tensile	220	0.9	50	25	20
Compression	350	-0.45	50	70	
In-plane shear	2300	>1	20	20	20
Interlaminar shear	<30				
MATERIAL THICKNESS : 2 mm to 10 mm					
MATERIAL TEST DIRECTIONS : 0° - 45° - 90°					

TABLE 3 - SKINEX R C-SiC CHARACTERISTICS

They are characterized in particular by high shear strengths. Main C-SiC characteristics are given in Table 3.

These values remain unchanged for any in-plane material directions (0° 45° 90°) and for thicknesses up to 10 mm.

On the basis of these thermal mechanical characteristics associated with high chemical stability, C-SiC composites can be considered to be materials with exceptional performance, suitable to replace traditional materials, refractory alloys and ceramics, and also heralding the development of highly advanced new thermal protection systems.

4. APPLICATIONS TO THERMAL STRUCTURES AND PROTECTION

Two examples of applications under development are given here after : the European space plane Hermes and the Cassini mission probe Huygens.

Hermes will be used for space transportation to earth orbit and will meet an oxidizing environment during reentry to earth. Thus, the improved oxidation protection of C-SiC is better suited to meet thermal protection and structures requirements.

The Huygens probe will explore the moon Titan during the Cassini mission to Saturn. Since the Titan atmosphere is non oxidizing, C-C thermal structures and protection have been selected for this application. A panel demonstrative of a potential aerobraking system has been designed, manufactured and tested.

4.1 HERMES

SEP is developing thermal protection and structural parts for the Hermes space plane in cooperation with Dassault Aviation, under contract to CNES and on behalf of ESA (Fig. 11).

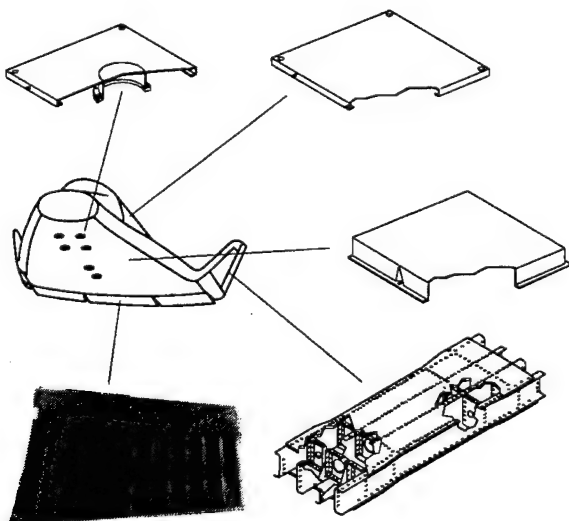


Figure 11 - THERMAL STRUCTURE OF HERMES IN C-SiC

4.1.2 Thermal structures

Two types of thermal structures are included on Hermes :

- Aerodynamic stagnation point parts which are locally very hot with high surface thermal gradients. These are the wing and vertical stabilizer leading edges and the nose. Complex shaped parts are made up of skin and stiffeners forming box structure cooled by heat reradiation.
- The vertical stabilizer and control surface parts in which the concept of thermal protection around a cold structure cannot be used due to the low thicknesses available (<300 mm).

The large-sized parts with dimensions of more than 2 m are subjected to great mechanical loads (bending, twisting, etc...) at high temperatures (>1,300°C and up to 1,700°C locally).

They are made up of skins and stiffeners integrated during manufacturing or prepared separately and assembled after manufacturing.

An example of an integrated skin-stiffener part is a prototype Hermes wing leading edge panel made of C-SiC. This panel is made from skin and stiffeners linked by SiC CVI process at an intermediate level of SiC matrix densification.

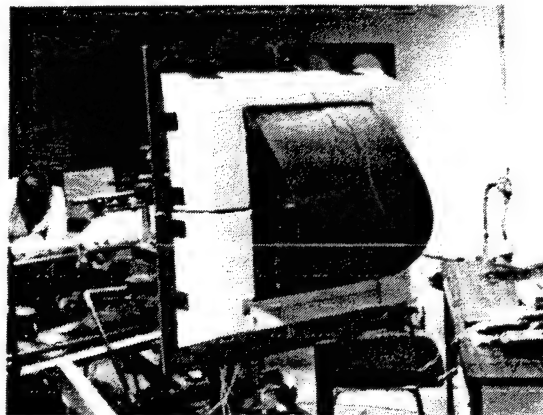


Fig 12 - C-SiC LEADING EDGE PANEL ON TEST

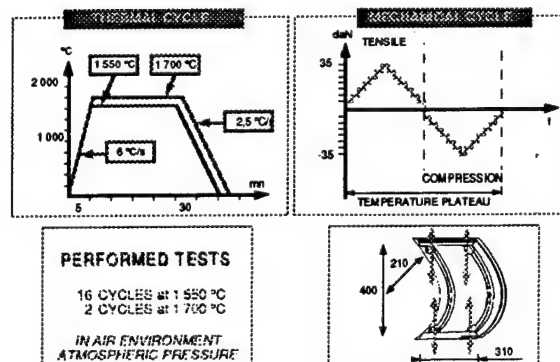


Fig 13 - TEST CONDUCTED ON A C-SiC LEADING EDGE

This leading edge panel was tested under combined thermal and structural loads in a solar facility in Spain (Fig. 12). Figure 13 provides the thermal and structural test conditions. Post test analysis indicated approximately 1.8% mass loss and high residual mechanical properties.

This result is in very close correlation with oxidation resistance characterization tests performed on laboratory coupons made of the same oxidation protection materials.

The second manufacturing technique used, consisting of mechanical fastener assembly, is illustrated by a thermostructural test article representing the Hermes winglet structure (Fig. 14).

This test article was used to demonstrate technologies developed in materials and processes, assembly techniques and high temperature fasteners.

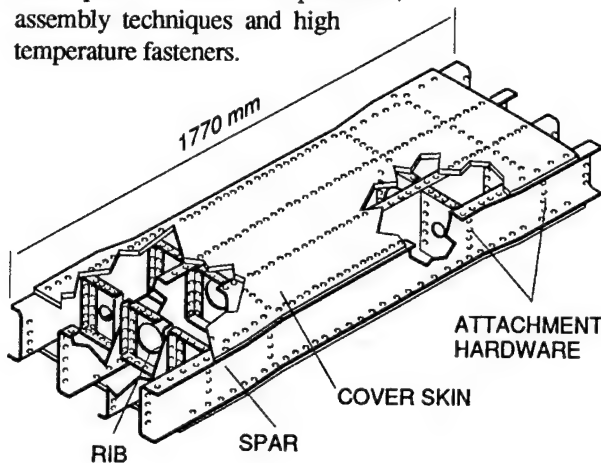


Fig 14 - C-SiC BOX FOR THERMAL STRUCTURE

For that purpose we used Skinex R, a 3D carbon fiber texture developed by SEP to produce a strong thin-skinned optimum weight part (Fig. 15).

Special manufacturing technologies, densification adjustments and new tooling design were developed to produce C-SiC large parts and to control distortions or geometrical variations.

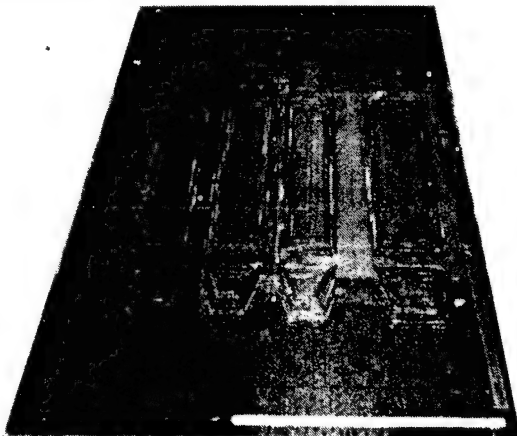


Fig 15 - TEXTILE PREFORM OF WING BOX OUTER SKIN



Fig 16 - SKINEX® C-SiC OUTER SKIN



Fig 17 - SKINEX® C-SiC SPAR BAR

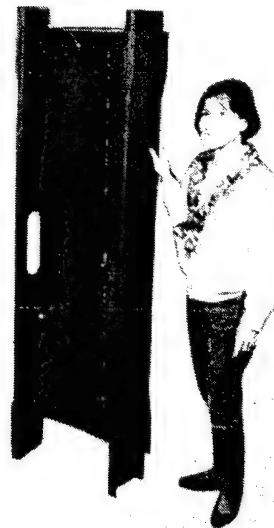


Fig 18 - WING BOX PART BEFORE FINAL ASSEMBLY

Outer skins (Fig. 16) and spar bars (Fig. 17) were manufactured with success and delivered in mid 1990 to Dassault Aviation for assembly and testing.

The outer skin is 1.6 m long and 0.6 m wide, with thicknesses varying from 1.9 mm to 9.9 mm in spar assembly zones. It weighs about 12 kg.

The spar bars are 1.8 m long and about 0.2 m wide with a constant thickness of 3.5 mm. The mass of one spar is less than 3.5 kg.

The C-SiC parts will be secured by very high temperature resistance metallic fasteners ($<1,300^{\circ}\text{C}$) currently developed in Europe.

However, such an assembly (Fig. 18) will not withstand very high heat fluxes and induces a limitation of the C-SiC part thermal capabilities.

In addition, due to the specific gravity of the used metal (over 8), the mass budget is considerably increased. An alternative is constituted by ceramic fasteners.

Development of advanced ceramic composite fasteners engaged at SEP will continue in order to utilize the high temperature characteristics of C-SiC structures when assembled mechanically.

Prototype C-SiC screws, hinges and attachments systems have been fabricated and are in evaluation (Fig. 19).

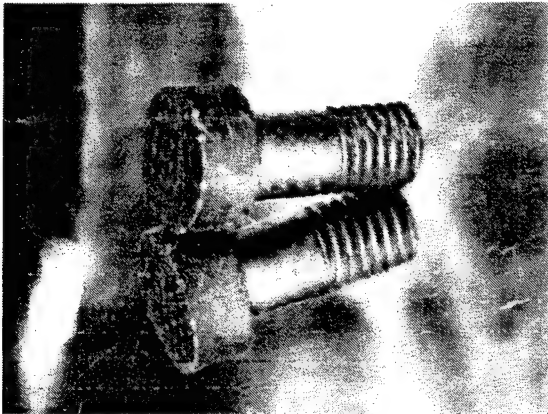


Fig 19 - C-SiC FASTENERS

New manufacturing techniques are now in progress at SEP in order to perform integrated skin stiffened C-SiC monolithic parts.

Some advantages for advanced large C-SiC thermostructures are :

- reduced number of detail parts
 - improved shear strength and reliability of skin stiffener assembly
 - improved design of complex architectures by eliminating mechanical assembly
 - increased thermal/life performance by eliminating fastener restrictions
 - lower weight by reducing local overthickness needed for mechanical fasteners.

These technologies have been already used by the past to achieve complex shapes, such as a nose cap.

It may be concluded, then, that with the development of thin quasi 3D carbon reinforcement combined with a silicon carbide matrix CVI process and an on line production facility which can produce full scale structural parts, the capability currently exists for the design and fabrication of advanced thermal mechanical structures for hypersonic space plane vehicles.

4.2 Huygens aerobraking device demonstrating panel

The Cassini spacecraft mission to Saturn is a joint NASA/ESA project and includes a secondary probe, Huygens, which will explore the atmosphere and possibly the surface of Titan, the greatest moon of Saturn.

SEP has been selected to design the thermal protection and aerobraking device of the Huygens probe during the Phase A study (Fig. 20).

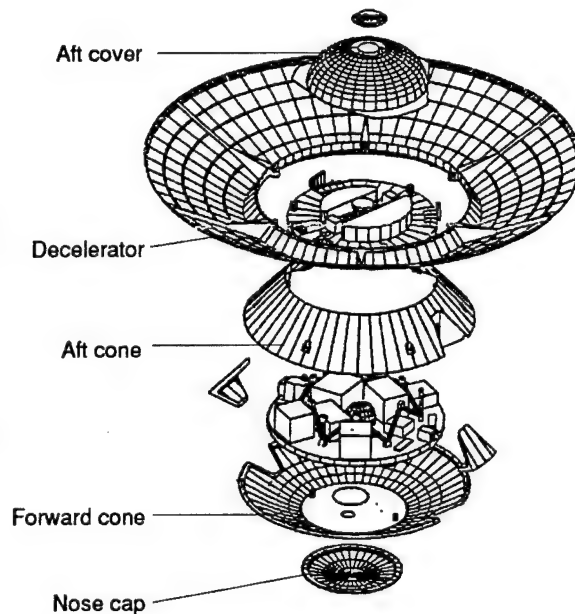


Fig 20 - HUYGENS PROBE

SEP is priming a Technology and Research Program under ESA contract during which a demonstrative aerobraking device panel has been studied, manufactured and tested. As the Titan atmosphere is non oxidizing C-C material can be used.

In the Huygens project, this aerobraking device, named decelerator, is made of six C-C panels linked together by a fish-plate and fastener system. The C-C skin is .5 mm thick, reinforced by stringers and stiffeners. Its outer diameter is 3.1 m and inner diameter is 1.65 m.

During the TRP, a conic shape panel (60° angle, 550 x 680 mm) has been developed and manufactured (Fig. 21).

Its .5 mm thick skin is made of non delaminable preform as

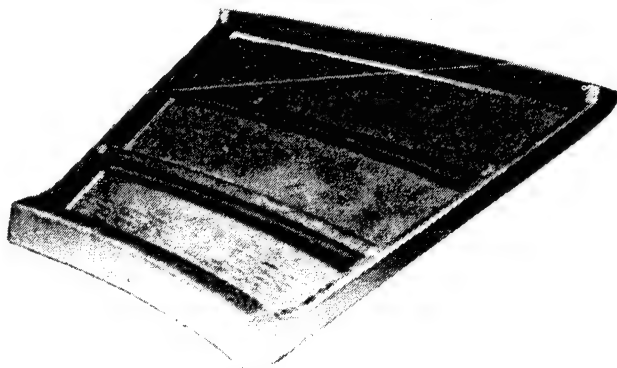


Fig 21 - HUYGENS PANEL

well as the stiffeners and stringers (2 mm thick). The thermostructural welding technic is used to joint skin and beams. 3D Novoltex R carbon-carbon is also used in the link area in order to insure 3D load transfer.

Mechanical, thermal, dynamic analyses including large displacement analysis have been performed. Tests will be made to correlate with analysis results.

5. CONCLUSION

SEP has developed a family of C-C and Ceramic Matrix Composite materials with high thermal mechanical performance that are available for the design and production of parts subjected to high mechanical stress and operating at very high temperatures.

Testing to date and the developments in progress confirm the enormous potential of these materials, especially C-SiC for use in oxidizing environments.

Considerable industrial facilities have been provided to meet the requirement of the manufacture of complex and large-sized parts. Several silicon carbide infiltration furnaces of significant capacity are currently available at SEP.

SEPCARBRC-C and SEPCARBINOXRC-SiC material families thus appear to be well suited and ready to meet the thermal protection and thermal structural needs of advanced space plane, spacecraft and planetary probes.

6. BIBLIOGRAPHY

- (1) KLEIN, A.J. - «Carbon-Carbon composites» - Advanced materials and processes Pg 64, NOV. 1986
- (2) HUNN, D.L., BELARDINELLI, R., HUCKNALL, A. - «The design and fabrication of complex carbon/carbon structure» - 32nd International SAMPE, APRIL 6-9, 1987
- (3) LACOMBE, A. - «Ceramic matrix composites materials for aerospace plane thermal structures» - Workshop on advanced structural materials for space applications, ESA 23 to 25 MARCH 1988
- (4) FURNISS, S.G. WALTERS, I.M. - «Performance integration of a reusable launch vehicle with hydrid airbreathing rocket propulsion» - 2nd ESA conference on progress in space transportation, MAY 22-24, 1989
- (5) BERGMANN, H.W., BUNK, W., GRUNINGER, G. - «New materials and structural concepts for space transportation systems» - 2nd ESA conference on progress in space transportation, MAY 22-24, 1989
- (6) LACOMBE, A. - «Ceramic matrix composites perform technological breakthrough» - Matériaux et Techniques - Revue N° 6 - JUNE 1989
- (7) BURKLAND, C.V., YANG, J.M. - «Chemical vapor infiltration of fiber reinforced SiC matrix composites» - SAMPE journal - Vol. 25 N° 5, SEPT./OCT. 1989
- (8) LACOMBE, A., ROUGES, J.M., TAVEAU, P. - «Development of C-SiC large parts technology for aerospace plane thermal structures» - Symposium on space applications of advanced structural materials, ESA, 21 to 23 MARCH 1990
- (9) JOUIN, J.M. - «Matériaux composites pour applications à hautes températures» - Journées AMAC CODEMAC, 29 to 30 MARCH 1990
- (10) LACOMBE, A., ROUGES, J.M. - «Ceramic Matrix Composites» - AIAA 90 - 3837 - SEPT 25-27, 1990

N92-23822
542-05
8424DESIGN CHALLENGES FOR THE
NATIONAL AERO-SPACE PLANE

by Mr Frank D. Boensch*
Director of Interagency Programs
National Aero-Space Plane Joint Program Office
Wright-Patterson Air Force Base, Ohio 45433-6503

Abstract

The National Aero-Space Plane is a program conceived in 1986 by the United States' Defense Advanced Research Projects Agency, to develop and demonstrate in flight, the technologies necessary for hypersonic flight including single-stage-to-orbit (SSTO) and cruise at sustained mach numbers. In order to do this, a number of technologies, propulsion, structures, aerodynamics, computational fluid dynamics (CFD), and materials must be matured to the point that hypersonic flight is practical. This paper will show the progress that has been made in the critical areas of materials and structures. It will highlight advances in propulsion, computational fluid dynamics made possible by high materials such as titanium aluminides and carbon-carbon. Finally, the paper will conclude with an examination of the utility of hypersonic flight both in terms of a single-stage-to-orbit mission, and the commercial potential for hypersonic flight.

Introduction

The National Aero-Space Plane is a program which will, for the first time, develop all of the necessary technologies to achieve single-stage-to-orbit (SSTO) flight. This program was conceived in the early 1980s by a group of dedicated individuals in the Defense Advanced Research Projects Agency (DARPA). That activity began by asking the question, "Is there any reason why one cannot fly a vehicle single-stage-to-orbit?" Finding none, the program was launched.

The formal announcement of the National Aero-Space Plane was given by President Reagan in his 1986 State of the Union Address, when he committed the United States to building an airplane which he called the Orient Express, and which had the capability of flying from Washington to Tokyo in two hours. With this as the national challenge, the National Aero-Space Plane Program was born.

In order to realize Mr. Reagan's vision, it became apparent that we would, as a nation, develop many critical technologies. All of them necessary for single-stage-to-orbit. It is those technologies for SSTO that are currently driving the program. However, before a commitment to any production system, all the technologies would be demonstrated in flight on the X-30 experimental airplane.

By applying the stringent requirements of single-stage-to-orbit, we began the process of developing the materials and structural concepts necessary for the aircraft to survive in an extremely hostile environment. We also began the development of the air breathing propulsion necessary to power such a vehicle. The requirements on the aerodynamics community are tremendous in that there are no wind tunnels which

will give the necessary run times, which in turn will produce the type of data necessary for such a vehicle. This establishes the requirement for the new generation of super computers to perform the aerodynamic calculations and predictions necessary for such a vehicle. Finally, there is the development of the techniques necessary to manage the flow of liquid hydrogen throughout the vehicle so that we may recover the heat otherwise lost. Heating the hydrogen fuel prior to injection into the engine enhances the engine performance.

The Environment

The National Aero-Space Plane (X-30) is truly an airplane. As seen in Figure 1, we are dealing with an airplane. We must develop the design criteria and loads which are typical of an airplane. These design loads will encompass everything from the usual flight loads to high temperature effects, and will include the ground handling loads. All are necessary in order to have an adequate aircraft design. In addition, one will note the need to have some means of fueling this very large liquid hydrogen container. As is obvious from Figure 2, the National Aero-Space Plane will fly a significantly different trajectory than that of the Space Shuttle.

Since the Space Shuttle is not an air breathing system, the shuttle must exit the atmosphere as rapidly as possible. It operates in an area of relatively low dynamic pressure and has no need to process oxygen. The National Aero-Space Plane on the other hand, must fly in a sensible atmosphere for a relatively long time, up to 30 minutes, in order to burn the liquid hydrogen on board, and accelerate to near orbital velocities. The flight profile is set by the propulsion system need for oxygen at dynamic pressures up to 2,000 lbs./sq. ft., temperatures on the structures are typically limited to 2200°F. It is at this temperature limit that the X-30 begins to pull up, using a small rocket to not only circularize the orbit, but to push out of the atmosphere.

The internal environment must accommodate the liquid hydrogen fuel. The structures or tankage must accommodate the thermal stresses associated with the cool down to -427°F. On the other hand, actively cooled engine panels will see temperatures in excess of 1500°F. These engine panels must also survive sound pressure levels of over 160 decibels. Because of the embrittling nature of hydrogen, the designer's choices are severely restricted.

Finally, data to date has indicated that there are significant increases in local heating where shock waves coalesce and then strike the structure.

Heating rate multipliers of 50 or more can cause severe local heating on such things as cowl and wing leading edges (See Figure 3).

Configuration

As with most complex questions there are a variety of solutions. The National Aero-Space Plane has looked at a minimum of four different configurations as shown in Figure 4. The original Government base line put forth by duPont Aerospace basically had a cylindrical fuel tank sitting atop the wing. This configuration does have merit in that it allows the forebody to provide the compression necessary for a supersonic combustion ramjet (scramjet) engine.

The blended body configuration also has the engine on the lower surface, using the lower surface to compress the air. The difference between the blended body and the cylindrical body is in the structural arrangement. The cylindrical body tends to be long and requires extreme stiffness, whereas the blended body has inherent stiffness. The cone, or the non-lifting fuselage, maximizes the amount of engine inlet area to the vehicle. In that particular configuration, however, changes in angle of attack make marked changes in the way each individual engine processes air, and thus the thrust of this vehicle is continually changing. This in turn, leads to an extremely complex engine/flight control system. Finally, the contained flow field approach is an excellent configuration for a point design. The X-30 must fly at all mach numbers between 0 and 24 as opposed to being optimized for a single mach number such as the Concord. Thus, the wing body and the blended body configurations appear to be more suited to the X-30.

In Figure 5, one begins to get an appreciation of the need to blend the engine and the airframe into a single entity. This also adds to the structures and materials challenge of the X-30. The shape of the inlet and forebody are dictated by the engine and the performance desired from the engine. The aft body is also key to engine performance. It is the shaping of these and the use of potentially actively cooled structures which begin to shape the materials and structures needs of the airplane.

Computational Fluid Dynamics (CFD)

As a nation, we had modest computational capabilities in 1986. The first of the super computers were coming on line, and we could calculate with great accuracy the flow fields around subsonic and supersonic aircraft. We had the ability to go from wind tunnel predictions and flight predictions to correlations of data. With the advent of the X-30, a new level of complexity was introduced. The problems associated with the viscous effects of the air and as we performed calculations in the engine, the chemistry effects as the oxygen combines with the hydrogen fuel. As can be seen in Figure 6, we have used the CRAY computer system to perform calculations on a typical X-30 inlet. We are getting good agreement between wind tunnel data and CFD predictions.

Materials and Structures Augmentation Program (MASAP)

Early in the program it became apparent that all of the Industry participants were using the same general classes of materials, carbon-carbon, titanium matrix composites, titanium aluminides and high conductivity materials such as graphite copper and beryllium. The joint program office (JPO) also recognized that to continue in a form of competition would be counterproductive. Thus the NASP MASAP was born in March 1988 (See Figure 7).

It was determined that each of the competitors, General Dynamics, McDonnell Douglas, Pratt & Whitney, Rocketdyne, and Rockwell, would be responsible for the development of particular materials systems. Thus, the objectives of the program were to develop and characterize those specific materials which met the requirements established by the group. In the case of titanium aluminides, for example, Rockwell, General Dynamics and McDonnell Douglas would each develop the requirements for titanium aluminide materials. It would then be up to Rockwell to develop and characterize the materials and the processes necessary to meet their own requirements as well as those of their airframe competitors. Each company would develop the processes for their particular material. These processes would, of necessity, be repeatable and provide the sort of material necessary to meet the requirements. Structural components would be built and tested, and finally, the program would have sheets of materials produced in sizes up to 4 ft. x 12 ft.

The underlying principle of the program would be team participation. For example, even though a company was responsible for developing high conductivity composites, they would oversee and integrate high conductivity composite activities going on at Pratt & Whitney, General Dynamics, Rockwell, and McDonnell Douglas. By having one company concentrating on a material, they had the leadership role. The others would share in the results as well as make a contribution towards making the materials work. The individual contractors had associate contractor agreements which were necessary so that they could not only share the results of this funded activity, but they could also share their independent research and development activities.

The program itself is managed by the joint program office, and technical management is done by the Wright Research Development Center Materials and Flight Dynamics Laboratories. A Joint Management Team is made up of individuals from Industry representing each of the companies, which in turn reports to an Executive Steering Committee made up of the program managers from each of the five companies. This is a three year program worth approximately \$136M. The basic philosophy and flow is shown Figure 8. It begins with a Master Planning and Control Document (MCD) which takes the entire program, lays out a schedule, and then becomes the management tool for the program. Next, we define the requirements. These are the requirements for the X-30. They deal with strength, stiffness, durability, fracture toughness, hydrogen compatibility, etc. This set

of requirements provides the guidance to the material developers. If a material does not meet a requirement, it is dropped. The materials and process and development activity sets out to look at material constituents which will yield those materials which will meet the requirements. Small lots of the material are made and processed, and then are characterized in task four. It is this material characterization that is used to develop the design allowable which is used to design the X-30. In fabrication development, we are attempting to make small structural details joint, extrusions, Ts, angles, the sorts of things that are necessary to gather structural data. In addition, we learn how to weld, drill and form the materials which has come from Task 3. Once we are satisfied that we can manufacture parts from the particular material, we then scale-up and make large components utilizing the 4 ft. x 12 ft. sheets of material. It is that detailed parts fabrication and the big test articles which then lead to the major component tests in the X-30 program.

The X-30 has been able to manufacture large parts. These have included titanium aluminide components. Panels up to 30 in. x 8 ft. long have been manufactured (Figure 9). Thus, we have demonstrated the capability to superplastically form and diffusion bond these materials into large panels. This was done by the North American Rockwell Corporation in their facility at El Segundo, California. McDonnell Douglas has successfully manufactured several large titanium aluminide/silicon carbide reinforced parts. These large panels, again on the order of 4 ft. x 8 ft. (Figure 10), were successfully done on company IR&D and funding from the National Aero-Space Plane. General Dynamics and its subcontractors, Super-Temp and Rohr, have made large structural panels. In Figure 11 is a 4 ft. x 10 ft. long integrally stiffened panel made by B.F. Goodrich Super-Temp. That panel has not been coated because the United States does not have a facility large enough to coat a ten foot long panel. However, the U.S. is in the process of rectifying that situation. In the high conductivity composite area, the program has examined graphite reinforced copper which has extremely good thermal characteristics and strength for engine type applications. Beryllium is also a high conductivity material, and is being examined. Both the copper and beryllium exhibit excellent hydrogen resistant characteristics. These materials are necessary in order to deal with the high heating rates associated with the engine and the nozzle. Last but not least, Pratt & Whitney is attempting to develop materials which can

survive the high temperature high stress environment of the engine without exhibiting unwanted creep which could potentially lead to the degradation of engine performance or the outright rupture of the parts. It is this challenge which has forced the abandonment of gamma titanium aluminide material as the material of choice in the engine for high pressure applications.

Status

The X-30 (Figure 12) is currently in the process of developing a single configuration. Up to now, there have been three competing airframe companies and two competing engine companies. For a variety of reasons, not the least of which is funding, we have chosen to develop a single configuration. This configuration is being generated by a national team made up of the five participants already named. Once that configuration is solidified, we will begin working to scale-up the processes previously developed in the Materials and Structures Augmentation Program. This will allow the routine manufacture of these materials by companies within the United States. This materials and process scale-up program, which will begin in March 1991, will lead to the routine production of materials of very high strength, very high temperature capability and minimum weight, which will serve the needs of the X-30.

Conclusion

This paper has discussed the origins of the X-30 and the fact that the X-30 is a demonstration vehicle. A truly experimental airplane following in the footsteps of the X-15. Unlike the X-15 however, we see the demonstration of critical hypersonic technologies leading to things like a Space Shuttle replacement and perhaps Mr. Reagan's dream of an Orient Express. We see, however, the prime function of these technologies is in the earth to orbit vehicles supporting America's thrust into space with Space Station Freedom. The second greatest challenge (propulsion being the first), to making the X-30 a viable airplane, is the materials development program. It is through the innovative thinking and management expertise of dedicated people in both Government and Industry that will make the materials and structural concepts for the X-30 a reality.

Acknowledgment

The author wishes to gratefully acknowledge the role of Mrs. Maria T. Ford in providing the secretarial support for this paper.

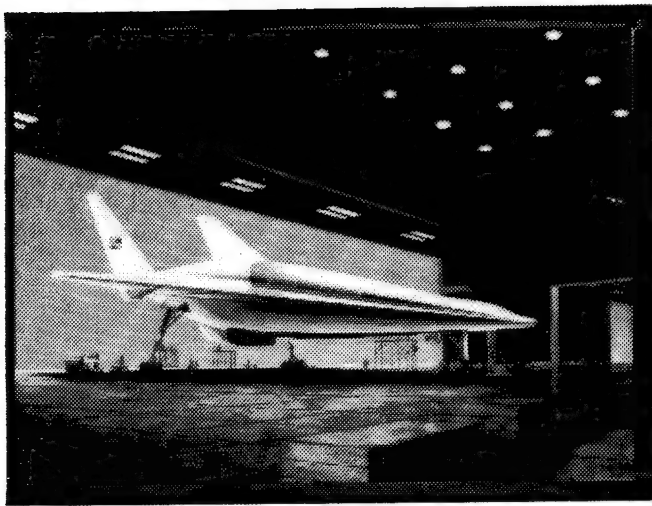


Fig. 1 Rocketdyne Picture of Airplane in Hangar

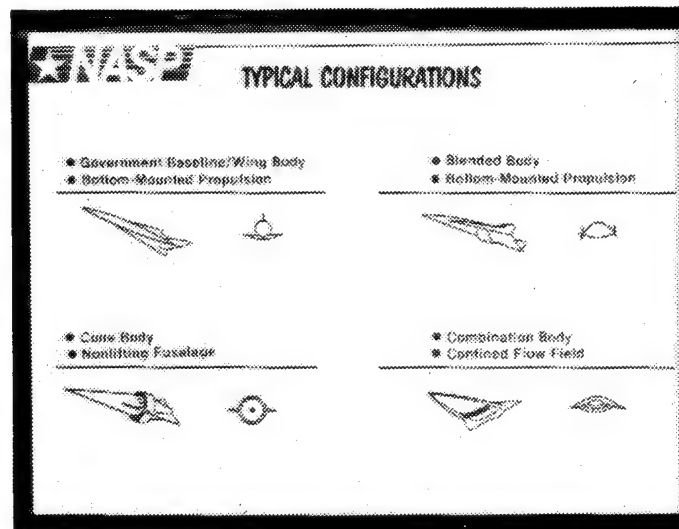


Fig. 4 Typical Configurations

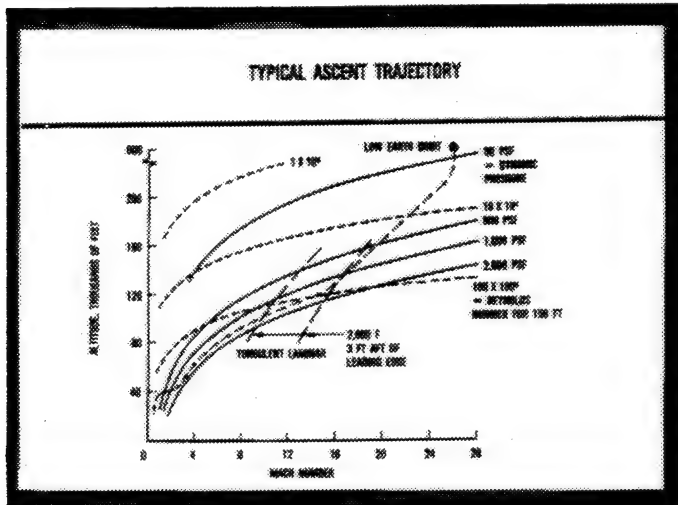


Fig. 2 Ascent Trajectory

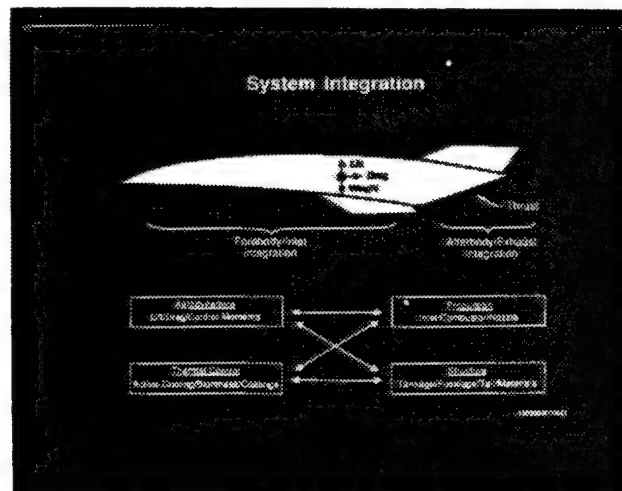


Fig. 5 System Integration Chart

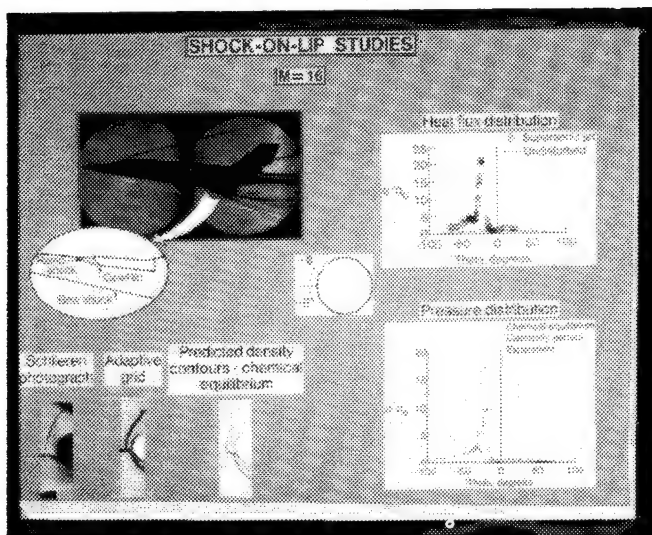


Fig. 3 Cowl and Wing Leading Edges

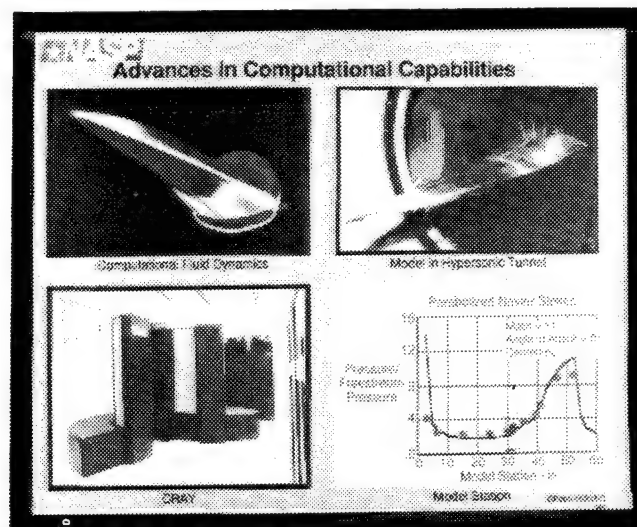


Fig. 6 CRAY Computer

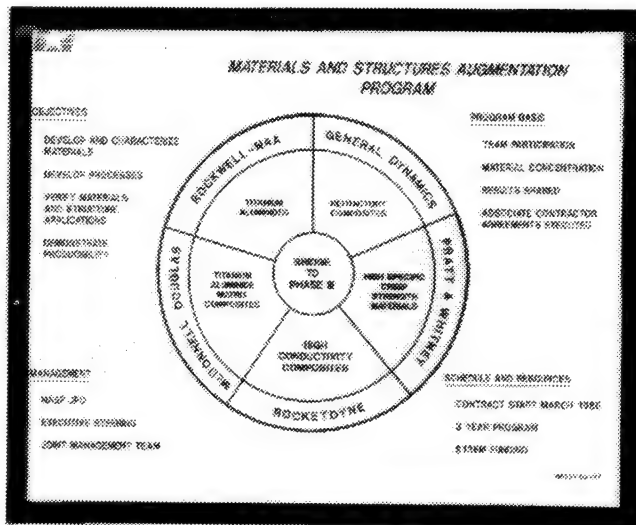


Fig. 7 NASP MASAP

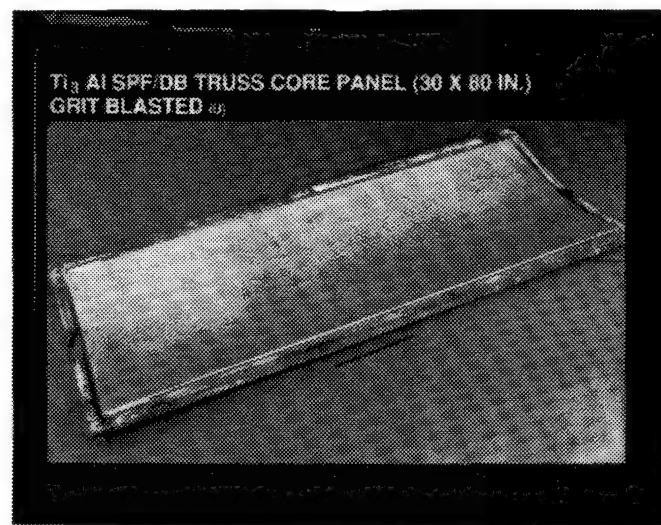


Fig. 10 Large Titanium Aluminide Panel

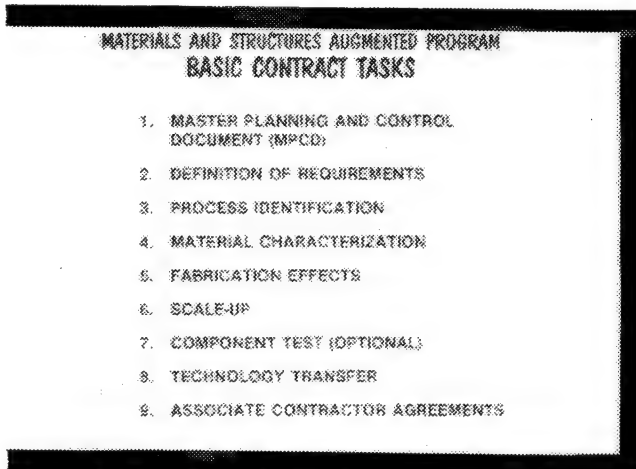


Fig. 8 Basic Philosophy and Flow

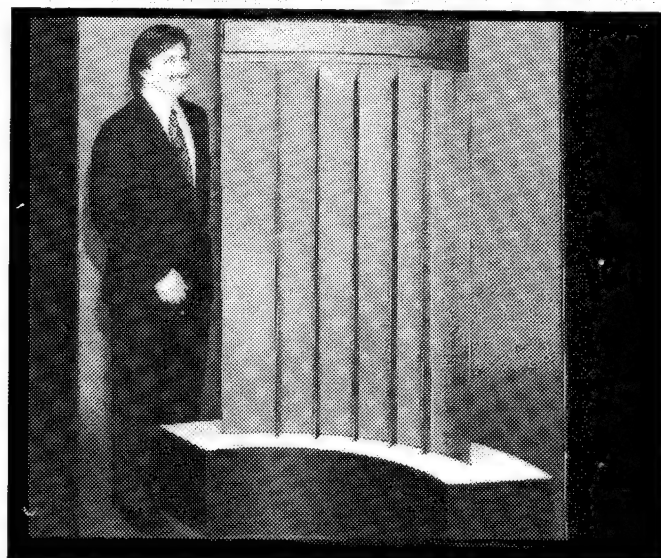


Fig. 11 Super-Temp Panel by B.F. Goodrich

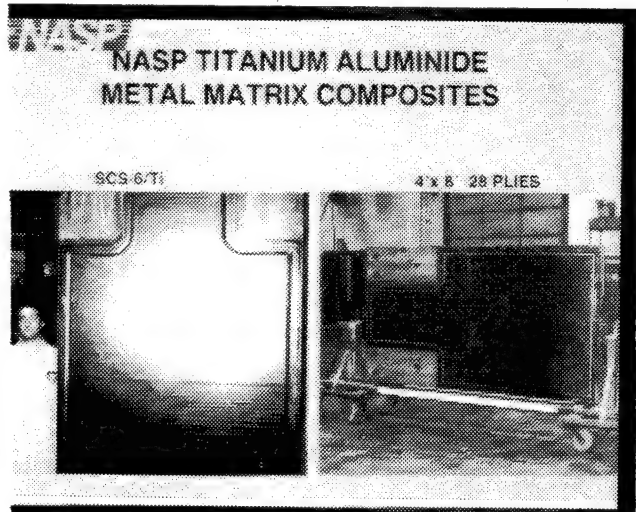


Fig. 9 Titanium Aluminide Panel

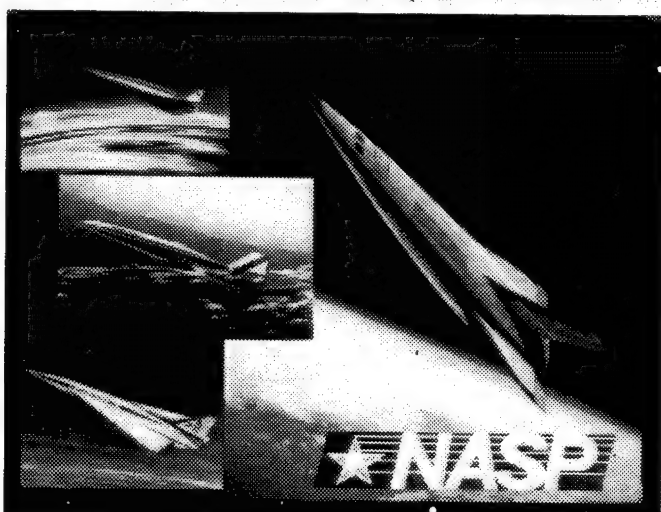


Fig. 12 X-30

N92-23823

THE CHALLENGE OF THE HERMES TPS SHINGLES

Christian PETIAU

DASSAULT AVIATION

Centre Spatial Dassault - Toulouse - Blagnac (France)

343-16
84735

ABSTRACT

After a brief presentation of the general principles of the Thermal Protection and "Hot Structure" design for the space shuttle HERMES, the "Shingle-type thermal protection, made of thin C-SiC ceramic composite panels protecting a very light multi-screen insulation, is explained in greater detail.

A description is provided of the technical requirements, as well as of the particularly complex numerical simulations and tests that have to be conducted for analysis of all phenomena (thermoelastic, acoustic, aeroelastic, internal venting, oxidation, etc.) that have to be sustained by the shingles.

Finally is presented the generalized CAD-CAM tool that is needed for automated designing and analysis, and for the production of the hundreds of shingles which, although all being quite similar, show some distinctive features.

1. INTRODUCTION :

GENERAL DESIGN OF THE HERMES SHUTTLE THERMOSTRUCTURES AND THERMAL PROTECTIONS

The Hermes space shuttle has to sustain, during reentry, considerable kinetic-origin heat fluxes (see Fig. 1), which lead to temperatures ranging from 900°C to 1300°C on the lower surface and reaching 1600°C on the nose and 1500°C on the control surfaces ; the hot phase during reentry lasts roughly 20 minutes.

The following solutions have been developed for the space shuttle to withstand this environment :

- an external thermal protection, for areas in which the purpose is to maintain the internal structure, and what is contained in it, at a low temperature level (i.e. < 175°C)
This thermal protection itself includes two types of hardware :
 - "Shingles" (termed REI), for areas where the wall temperatures range from 650°C to 1300°C ; these shingles are made of rigid, ceramic composite, panels which protect an ultra-light insulant made of reflective screens. The shingles are suitable for the whole of the lower surface of fuselage and wing and for the upper surface of the forward fuselage (see Fig. 1)
 - insulants (termed FEI) : "flexible blankets" made of Silica fiber-base fabric and felts, for the least hot areas (< 650°C) on the upper surface.

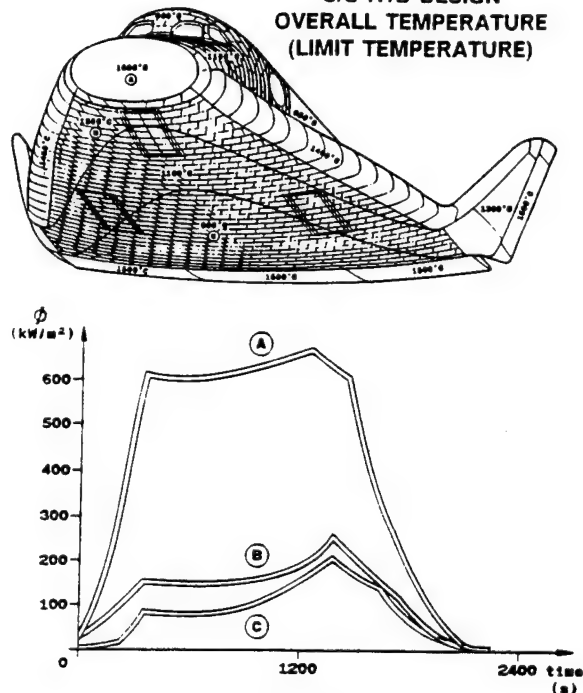
S/S H1B DESIGN
OVERALL TEMPERATURE
(LIMIT TEMPERATURE)

FIGURE 1

- hot structures, which directly carry the mechanical loads under high temperatures (up to 1600°C) and without any internal insulation ; they include :

- the nose
- the leading edges
- the wing tip fins (winglet)
- the control surfaces (body flap, elevons, rudders)

The above only became envisageable solutions with the use of ceramic matrix composite materials (the SEP-manufactured C-SiC and the doped matrix C-C, made by AS-AQ), being capable of withstanding very high temperatures (beyond 1600°C for C-C) and relatively oxidation-resistant, and offering appreciable mechanical strength (from 200 MPa to 350 MPa for C-SiC).

DASSAULT Aviation is responsible for the overall design of the Subsystem Thermal Protection and Hot Structures on Hermes ; the work on design, manufacture and qualification of the shingles is conducted in cooperation with the associated partner industries, SEP and MAN-Technologie.

2. TECHNICAL REQUIREMENTS FOR THE SHINGLES

The technical requirements, apart from those relative to reusability for the specified life (15 years or 30 flights) are as follows :

- to maintain the external spaceplane shape, with a surface condition that must prevent premature boundary layer transition (risk of considerable overheating)
- to provide high emissivity on the external wall (ϵ 0.85) so as to reduce its temperature through maximum thermal radiation
- to use non-catalytic coatings to prevent exothermic recombination of the dissociated chemical species in the aerodynamic flow at the wall
- to fulfil the function of thermal insulation for the areas requiring protection during reentry ; the cold structure temperature must be maintained below 175°C, whereas the temperatures on the external wall will reach 1300°C for more than 20 minutes (see Fig. 2).
- to withstand both the natural and the induced environment, i.e. essentially :
 - high temperatures in oxidizing environments,
 - the mechanical loads in cold condition during the launch phase, and in hot condition during reentry,
 - the vibrational environment, notably the acoustic excitations on the launch pad (155 db) and the aeroacoustic excitations during the transsonic and the supersonic phases of launch (up to 165 db on certain parts)
 - damage tolerance and repairability : more specifically, the hot structures and thermal protection will be sized to withstand any damage liable to occur until such damage is detected and repaired.

3. DESCRIPTION OF THE SHINGLES

The Hermes cold structure, made of Aluminium, will be protected by 836 shingles covering the whole of the lower surface and the forward portion of the fuselage on the upper surface.

The shingles are of a trapezoidal shape with 300mm long sides ; they are distributed in a staggered arrangement (see Fig. 2 & 3) ; the overall thickness is 80 to 100mm on the lower surface and 50mm on the upper surface.

Each shingle is made of 4 types of components (see Fig. 3) :

- One monolithic, 1 mm thick, C-SiC matrix panel with a 50 to 60mm high flange on all four sides.
- Four metallic supports onto which the panel is mechanically attached with fasteners (see Fig. 4).
- Two blocks of ultra-light, thermal insulant made up of reflective screens, being a ceramic fabric coated with metal (platinum, gold), which are separated by Silica or Alumina-fiber spacer felts
- A seal system

The function of the C-SiC panel is to maintain the external aerodynamic shape and to withstand the aerodynamic loads.

The function of the metallic supports is to provide the panel, as regards deflections, with some degree of independence from the cold structure but, at the same time, to limit any occurrence of thermal leaks liable to be caused by the shingle attachment. The temperature of the support and the attaching fastener does not exceed 700°C, and therefore admits the use of standard stainless steel fasteners. The panel's position can be adjusted by means of shims. The space between the shingles is sufficiently large to allow the passage of a screw driver.

HERMES TPS AND HOT STRUCTURE DESIGN

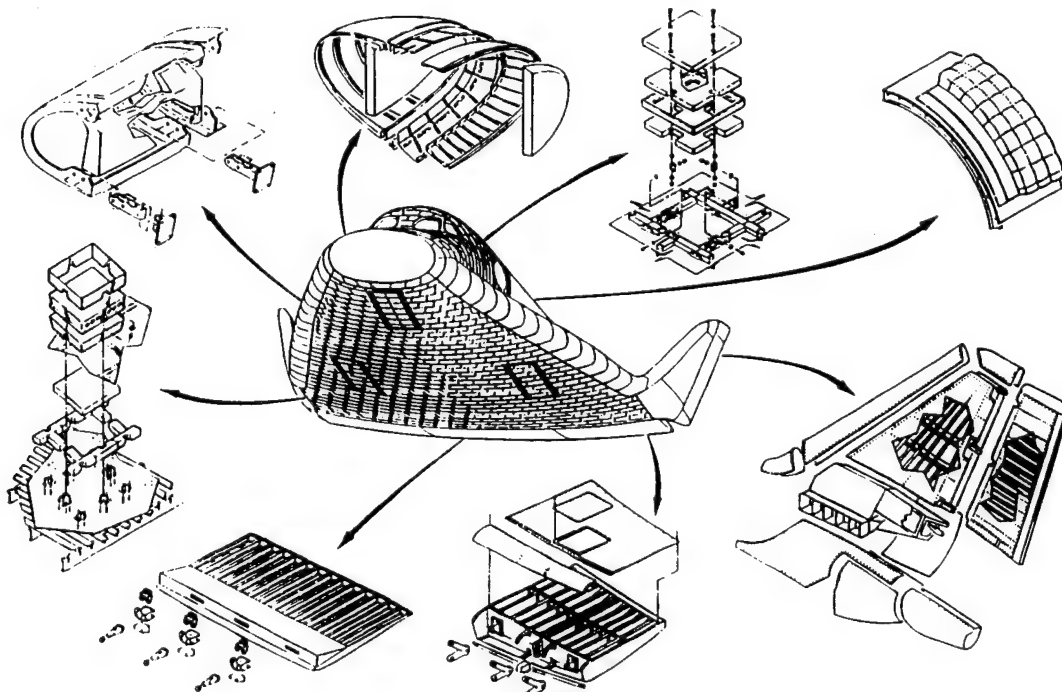


FIGURE 2

FLANGED SHINGLE DESIGN

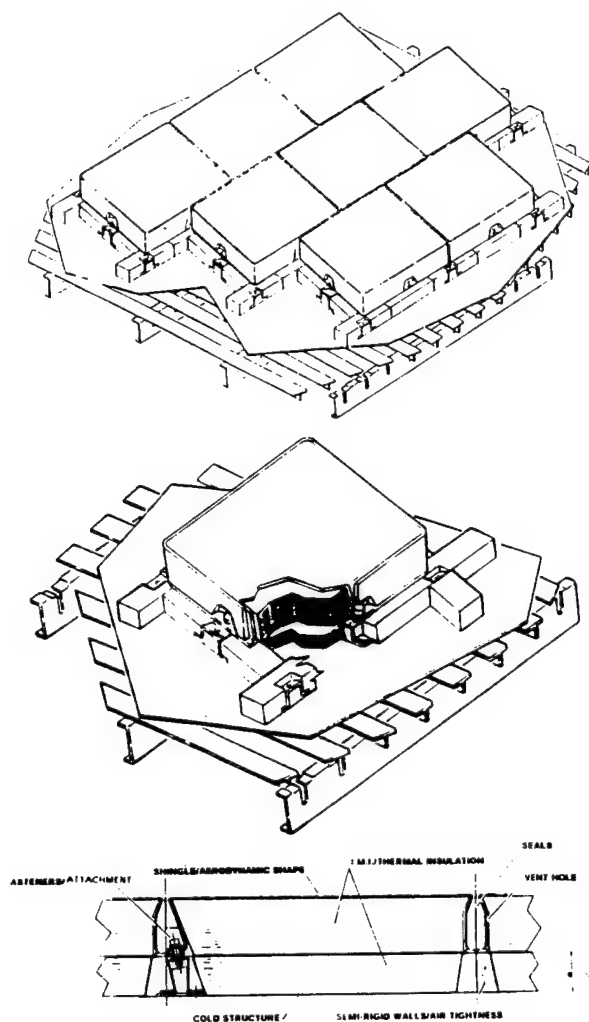


FIGURE 3

The shingle system is a fail-safe concept ; it is so designed as to accommodate the rupture of one fastener or the rupture of one of the supports.

The seal system includes :

- An external seal, edging the shingles, the function of which is to maintain aerodynamic surface continuity and to prevent any significant aerothermal convection in the gaps between the shingles. The external seals are nevertheless sufficiently porous to accommodate the depressurization and repressurization flow rate and that of the air contained in the shingle cavities, which is evacuated via dedicated vent holes on the rear flange of the shingles. The external seals will be re-waterproofed after each flight to prevent water penetrating under the shingles.

- A semi-rigid seal, ensuring the partitioning between the cavities under each shingle ; these seals prevent hot air circulation under the flanges. The seals are bonded to the cold structure and maintained in compressed condition by the panels' flanges.

SHINGLE SUPPORT CROSS-SECTION

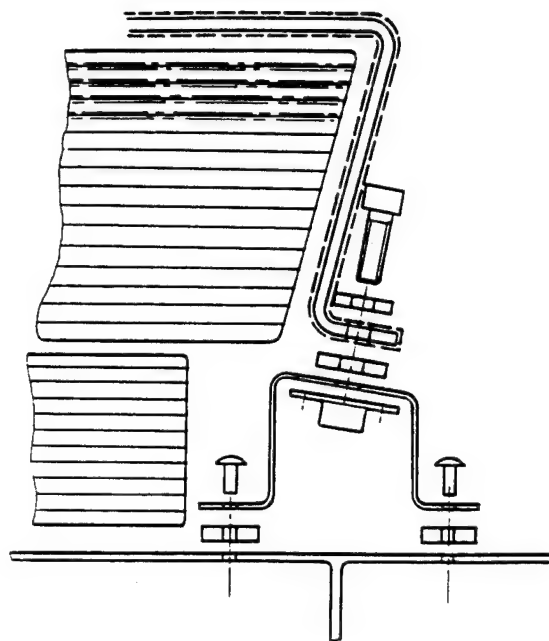


FIGURE 4

The shingles on the upper surface, which have to withstand temperatures that are markedly less high (650°C to 900°C) than those on the lower surface, have a different attachment system using flush-fitted fasteners and thus allow the use of less thick shingles (see Fig. 5).

CABIN SHINGLE DESIGN

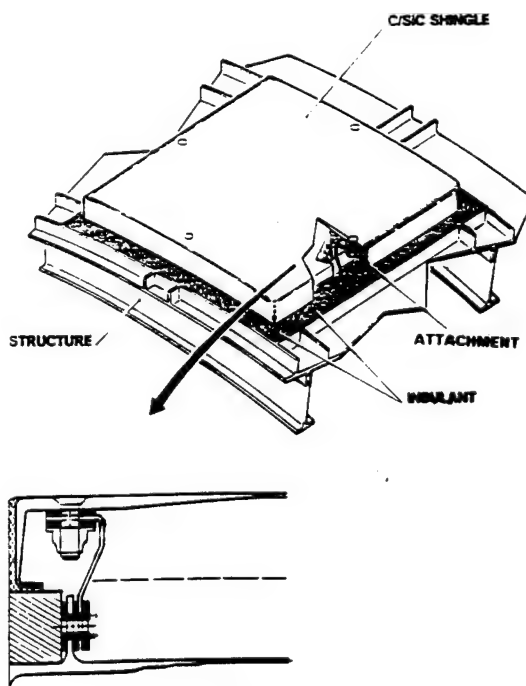


FIGURE 5

4. COMPARISON WITH THE US ORBITER TILES

The Hermes shingle principle significantly differs from that used for the US Orbiter tiles and for the Russian shuttle Buran (see Fig. 6)

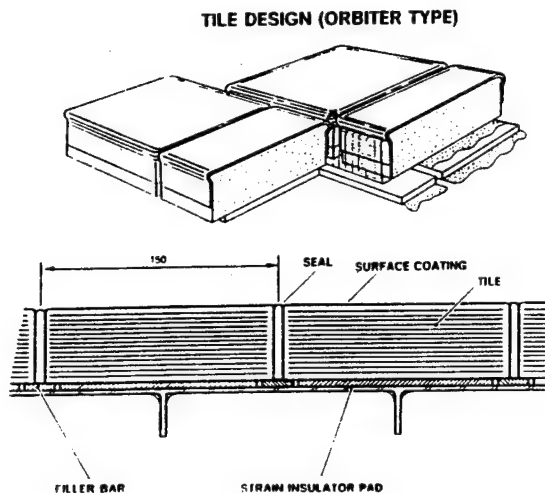


FIGURE 6

The latter had adopted solutions involving a massive, rigid tile made of short, compacted silica fibres. The tile is bonded to the structure via a strain isolator pad.

It is worth noting that the shingles and the tiles, despite the differing solutions, have to satisfy the same functional requirements (thermal insulation, mechanical resistance to local loads, aerodynamic sealing, venting, water tightness, compatibility with substructure deflections).

The fundamental difference, compared to our solution, is that in the tile solution, the functions Mechanical Resistance and Thermal Insulation are confounded, whereas in our system, they have been separated.

Besides a slightly more favourable mass budget, the main advantages identified for the shingles are :

- lesser fragility
- fail-operational attachment system using fasteners, which is more reliable than the bonding system for the tile,
- no surface condition constraint, and no deflection constraint for the cold substructure (local buckling of the cold structure panel can be admitted without any fear of damage)
- the insulation function can potentially be strengthened simply by adaptation of the insulant's density, and there is a sizeable reserve available as regards the allowable temperature (the C-SiC panel currently withstands temperatures higher than 1300°C)

This is an all the more appreciable potential as Hermes is thermally significantly more constrained than the US Orbiter (wall temperature higher by a magnitude of 100 to 200°C, markedly lower cold structure thermal inertia, this essentially on account of the scale effect).

5. PARTICULARITIES OF THE ANALYSIS AND TESTS ON THE SHINGLES

The shingle system's particularity is that it requires analysis methods which are at the limits of the currently available techniques and test means, many of which are totally specific or were non-existing in Western Europe at the beginning of the Project.

• THERMAL ANALYSES

Their purpose is to establish thermal maps for the temperatures prevailing within the shingle system and the adjacent cold structure, and to optimize the required quantities and types of IMI insulants.

Two types of calculations are conducted :

1. 3D finite-element thermal calculations (performed with the CATIA-ELFINI software package), which produce an evaluation of the temperature fields as a function of time. Typical results are shown on Fig. 7.

The finite-element meshes include more than 12000 nodes. For these calculations, some of the not so well assessed conductivity characteristics (notably, for the insulant and the assembly) have been derived from Thermal Transfer tests using mathematical identification techniques.

The presented models have been validated by Thermal Shock tests performed on the solar platform at Almeria (Spain) ; further, more detailed, validations will shortly be conducted at IABG (Germany), using low-pressure infrared test means.

2. General optimization of the insulation thickness over the entire vehicle surface, in relation to trajectories that have to be sustained and to the cold structure's local heat sink capabilities, is conducted with a much simpler technique, which uses a quasi-1D modelization that has been calibrated by the identification technique on the above-mentioned 3D models. The iterations are automatically controlled by a mathematical optimization monitor, and thus is finally obtained the optimal insulation thickness that satisfies the cold structure's maximum temperature requirement.

FE THERMAL ANALYSIS

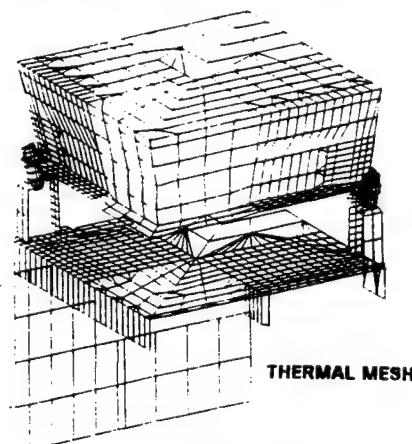
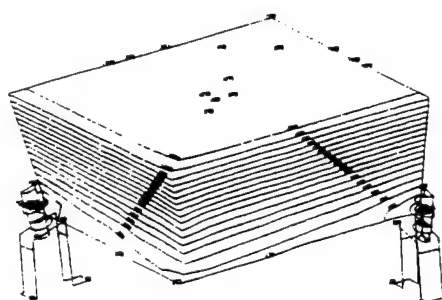


FIGURE 7

FE THERMAL ANALYSIS CONT'D



ISOTHERMS (°C)

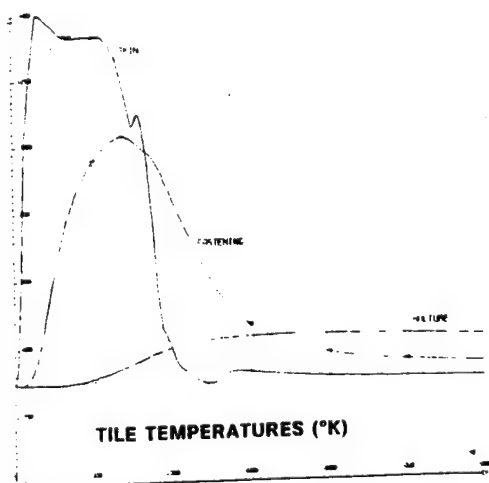
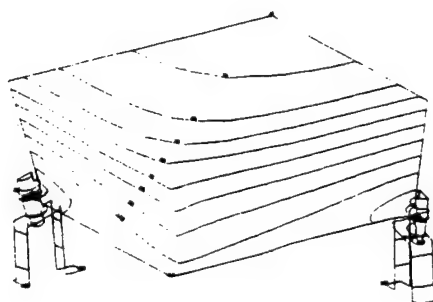


FIGURE 7

MECHANICAL AND THERMOMECHANICAL ANALYSIS

The shingle behaviour is governed by the following effects :

- The remarkable mechanical properties of the used 2D C-SiC material (tensile strength greater than 200 MPa, and interlaminar shear strength greater than 25 MPa, with low notch-effect and fatigue sensitivity. What complicates modelizations, on the other hand, is its highly non-linear rheological behaviour (see Fig. 8)

TYPICAL STRESS/STRAIN BEHAVIOUR OF CMC MATERIAL

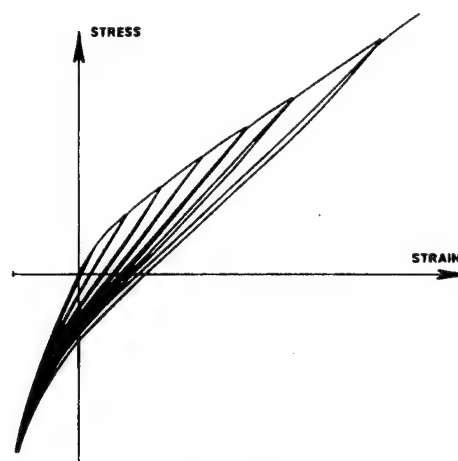


FIGURE 8

- The very marked non-linearity of the shingle panel, which globally operates as a membrane.
- Significant coupling with the surrounding fluids :
 - acoustic coupling on the launch pad with the external air (being a major element for dissipation of the vibration energy) ;
 - coupling with the internal air which, despite the presence of vent holes, constitutes a non-negligible "pneumatic" stiffness complement ;
 - aeroelastic coupling in flight, being very significant during the transsonic and supersonic flight phases (dynamic pressure in the order of 400 mb). From this coupling results a potential risk of flutter. This type of aeroelastic coupling has a direct effect on the response to the "aeroacoustic" excitation generated by the detached flow conditions and the movement of shock wave in the transsonic regime ;
 - interaction with the seals and insulants, which provide additional damping and stiffness ;
 - thermoelastic stresses, induced by the temperature gradients of the thermal shock during early reentry (above all, for abort reentries)
- (thermal or mechanical origin) deflection incompatibilities between the panel and the cold structure, which result in additional loads in the attachment areas around the supports.

For all these points, shingle designing has been supported by calculations performed with the CATIA-ELFINI software package ; validation tests have been performed (static pressure, acoustic fatigue tests in the progressive wave tube, transonic flutter and buffeting tests in wind tunnels, thermal shock tests on the solar platform). A special fixture that will allow simultaneous pressure loading and thermal shocks is currently being built at the IABG.

In the following figures will be presented some significant results of the mechanical analysis :

Fig. 9 : Calculation vs. Test Comparison of the evolution of the stresses in the panel, in a static pressure case ; this case illustrates the highly non-linear membrane behaviour.

COMPARISON TEST/COMPUTATION

DEFLECTION EVOLUTION (PANEL CENTER)

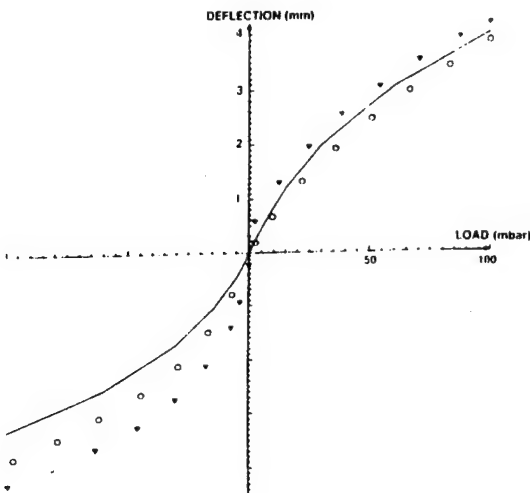


FIGURE 9

Fig. 10 : Shingle Eigenmode Calculation, being the input for the linearized, dynamic response, calculation

NATURAL MODE ANALYSIS

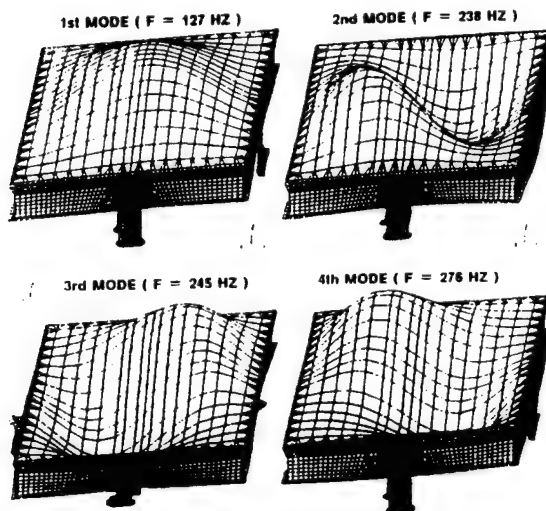


FIGURE 10

Fig. 11 : Flutter Curves (evolution of frequencies and damping as a function of velocity) calculated at Mach 0.9 and Mach 1.2. They distinctly show a tendency towards static divergence of the very first bending mode under subsonic conditions, and standard-type flutter under supersonic conditions, due to coupling of the first two modes.

FLUTTER CURVES

Alu specimen th. = 1.0mm

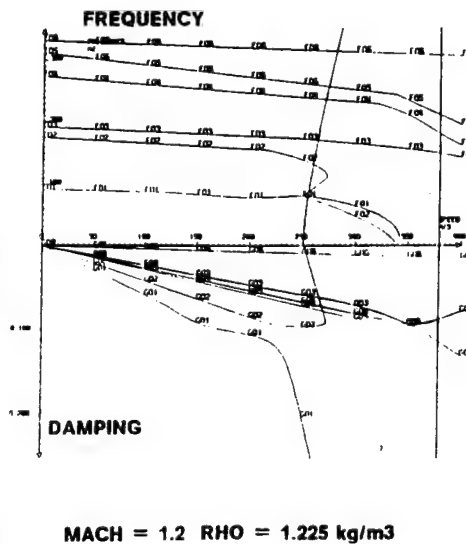
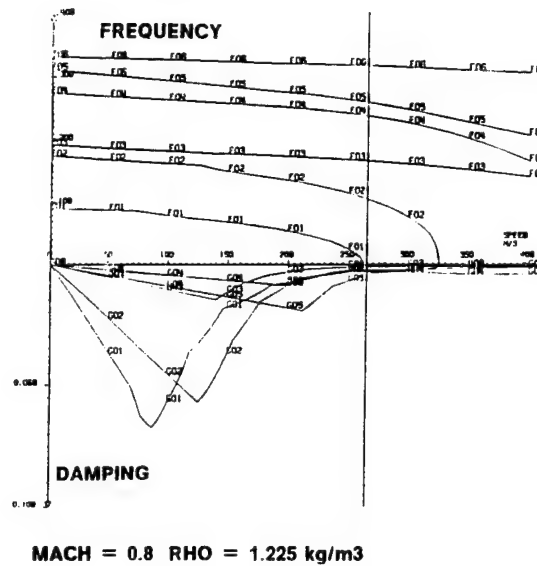


FIGURE 11

Fig. 12 shows the comparison between calculations and wind tunnel flutter tests (conducted on shingles with thicknesses reduced to $th. = 0.7mm$); these tests highlight the flutter sensitivity to the internal pressure conditions. (The modes were established in the vicinity of static equilibrium positions, by non-linearized calculations.)

FLUTTER : COMPARISON TEST/COMPUTATION

Alu specimen $th. = 0.7mm$

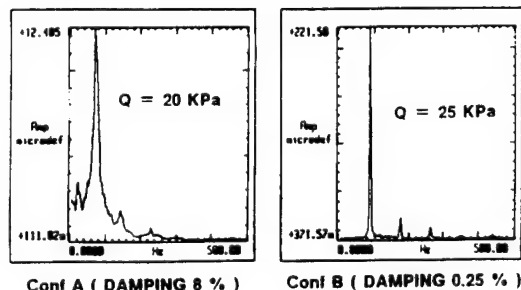
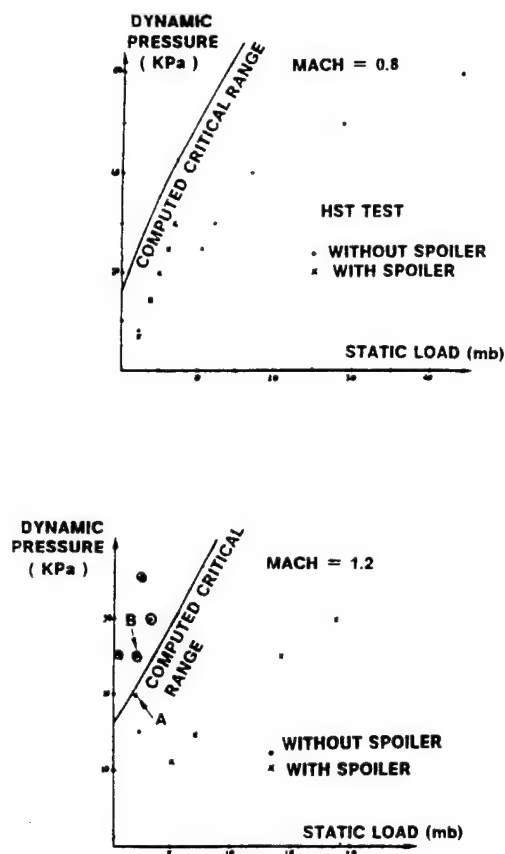


FIGURE 12

In Fig. 13 are shown the results of the non-linear dynamic response calculations on a shingle panel, with aeroelastic coupling; one can see that limit cycles appear when the flutter speeds are exceeded.

NON LINEAR FLUTTER ANALYSIS - TIME RESPONSE

Alu specimen $th. = 1.0mm$

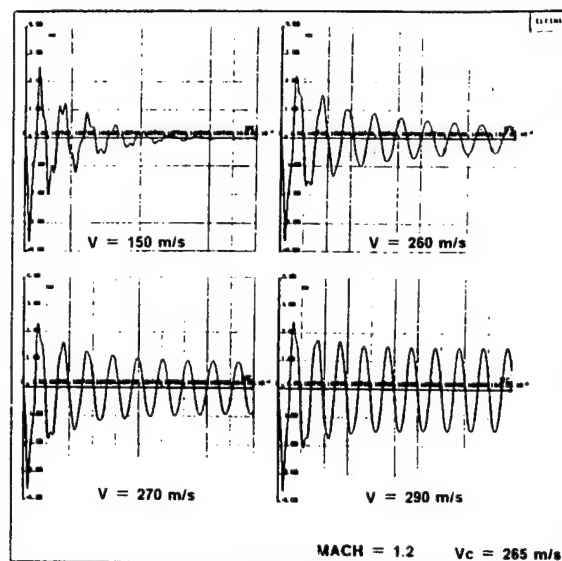


FIGURE 13

• OXIDATION AND LOCAL AEROTHERMICS

The behaviour of the C-SiC material and of its protective coating has been tested in different oxidation simulation means, amongst which the Plasma Arc Jet facilities, being the more important ones (University of Stuttgart, "Simoun" Plasma Arc Jet Facility of Aérospatiale Aquitaine)

More complex tests will be performed (Simoun, Ames of NASA, Scirocco of CIRA) to analyze the aerothermal effects in the gaps, the behaviour of the seals and various cases of damage tolerance.

These tests will be supported by aerothermal calculations that will provide for extrapolation from the test cases to the flight configuration.

• PRESSURIZATION AND DEPRESSURIZATION

As it has been said, these phenomena are amongst the "Design Drivers" for the shingle system. They are analyzed with the models for diffusion of air in porous media, the physical constraints of which have been identified via loss of pressure load tests.

Global verification will have to be conducted through tests on groups of shingles subjected to cold-condition and hot-condition pressure variations.

This verification list is not exhaustive ; many other points need to be verified, as, for example :

- the behaviour in rain and humidity
- the discharge of electric charges and of lightning
- the behaviour in orbital environment
- the effect of impacts during the service life, notably those of micrometeoroids and orbital debris
- damage tolerance and the effect of all envisageable failure modes
- the effects of ageing (oxidation, mechanic fatigue).

6. INDUSTRIAL PRODUCTION OF SHINGLES

Manufacture and qualification of all of the 836 shingles at reasonable costs and within reasonable timescales poses a problem on account of the fact that the shingles, per family, are similar in terms of morphology, although almost all of them are different in terms of geometry.

We therefore got our industrial partners (SEP and MAN-Technologie) to envisage the development of a "generalized" CAD/CAM system so as to provide the highest possible degree of automation in design and manufacture using, as inputs, the baseline design and the process sheets for "generic" shingles, together with those for the external skin shapes and those for the cold structure.

Such a system must be capable of generating :

- the parts design
- the verification computations : it must, in particular, allow automatic elaboration of finite-element meshes and computations
- the design and machining of the manufacturing tools
- the lay-up and cutting-to-size of the fabric strata
- the shingle manufacturing process
- the manufacturing inspection
- the integration onto the spaceplane, and the manufacture of the associated tooling

The use of such a tool, in our opinion, appears as an indispensable warrant for quality and reliability.

7. CONCLUSION

Production of the shingles for the Hermes shuttle is a technological challenge in practically all respects :

- In respect of materials, industrial development is required for :
 - the C-SiC ceramic composite,
 - the ultra-light thermal insulation
- The numerical simulations or mathematical models to be used are of rare complexity, involving :
 - large-scale finite-element thermal computations, in conjunction with systematic use of model reduction and mathematical identification techniques ;
 - static and dynamic non-linear elastic and thermoclastic analysis ;
 - elastoacoustic and aeroelastoacoustic analysis of highly non-linear structure ;
 - modelization of the sneak flow diffusion in porous media
 - Navier-Stokes aerothermal computations, in which the external flow is coupled with the sneak flows.
- In the area of tests, practically all experiments are novel, and a good deal of the test means were not available in Western Europe at the beginning of the Hermes project (e.g. thermomechanical test means, plasma arc jet facilities). The basic techniques used for these means were only poorly assessed (e.g. high-temperature metrology, heating techniques for low-pressure and oxidizing atmosphere conditions)
- The qualification philosophy itself poses a problem since the experiments that can be conducted on ground are only remotely representative of the conditions in flight, and since even progressive extension of the flight envelope, as this is done for aircraft, is not possible.

Qualification will be achieved via a succession of computations and partial tests that will mutually validate each other, in a process for which it will have to be demonstrated that it is conservative.

- At industrial level, manufacture of the 836 shingles per shuttle also is a challenge, if it is to be conducted to satisfy cost and quality ; automation of the production of these items, which are only "almost" identical, requires the creation of a specific CAD/CAM tool.

**SESSION
2.2.A**

**MULTI-BODY
DYNAMICS
I**

MICROGRAVITY

PRECEDING PAGE BLANK NOT FILMED

N 92-238245

82736

SIMULATION OF SPACE STATION LOADS WITH ACTIVE CONTROL SYSTEMS

P. A. Blelloch¹, N. R. Beagley², D. R. Ludwiczak³ and I. Yunis³¹SDRC Engineering Services Division, Inc., 11995 El Camino Real, San Diego, CA 92130, USA.²SDRC Engineering Services, York House, Stevenage Road, Hitchin, Herts. SG4 9DY, UK.³NASA Lewis Research Center, 21000 Brookpark Rd., Cleveland, OH 44135, USA. ✓

ABSTRACT

A methodology for calculating dynamic loads for the Space Station *Freedom* is presented. The methodology minimizes the repeated calculation of duplicate structural elements, while analyzing a large number of different Space Station configurations with different alpha and beta joint angles. We will pay particular attention to the issue of model reduction using a combination of component mode synthesis (superelements) and component mode selection to generate accurate system level models with a minimum number of modal degrees of freedom. We will also discuss the modeling of the control systems during simulation of the structural response.

Keywords: Space Station, loads, superelements, control systems

1. INTRODUCTION

The Space Station *Freedom* is expected to provide a platform for space-based research and exploration well into the next century. Because of the requirements for reliable performance and durability while minimizing weight, it is essential to accurately predict dynamic structural loads early in the design phase. There are a number of challenges associated with this prediction. Some of these are summarized below:

- The Space Station actually consists of a large number of different structures as it is constructed and as it continues to evolve during its lifetime.
- For each configuration of the Space Station, loads are a function of the orientation of alpha and beta joints used to point the photovoltaic arrays. An infinite number of different alpha and beta joint orientation angles are possible. Even if a small selection is chosen (e.g., twelve combinations per configuration), this multiplies the number of models that are analyzed significantly.
- Each Space Station model consists of a number of complex components whose models are delivered by a number of different contractors from around the world in various different formats.
- The large number of very flexible components results in such high modal density at low frequency ranges that it is infeasible

to calculate modes without some form of initial model reduction.

- Control systems at the alpha joints, used to point the photovoltaic arrays, have a significant effect on the loads outboard of the alpha joints and cannot be neglected.
- The Space Station design changes so quickly that it is essential for any methodology to allow the analyst to repeat calculations with a minimal turnaround time.

The methodology presented here uses MSC/NASTRAN¹ superelements with a number of modifications to generate system models of the various Space Station structures. Before calculating normal modes for the system models, "important" component modes are selected for the superelements in order to reduce the size of the problem. The system modal data including data recovery matrices is transferred to the CO-ST-IN program (Ref. 1) which defines active control systems, simulates the response, and writes data recovery outputs for postprocessing.

2. PROBLEM STATEMENT

The Space Station is sequentially constructed in orbit during a number of shuttle flights, implying that a number of different but related structures must be analyzed to ensure integrity. As examples of the various structures to be analyzed, Figure 1 illustrates the Manned Base Two (MB2) configuration, Figure 2 the Permanently Manned Capability configuration (PMC), and Figure 3 the Assembly Complete configuration (AC) (Ref. 2). Each of these structures is very different, though they share a number of common characteristics. In every case electric power is supplied by photovoltaic (PV) arrays (two arrays for MB2, four for PMC, and eight for AC). The PV array surfaces are oriented towards the sun using two rotational joints. The alpha joint is located in the truss and rotates about the truss (y) axis once per orbit. The MB2 configuration has a single alpha joint, while the PMC and AC configurations have two alpha joints each. The beta joint is located at the base of each PV array and rotates about the axis of the PV array mast to correct for inclination of the orbit plane with respect to the solar ecliptic plane.

The rotations of the alpha and beta joints add two complications to a loads analysis. The first is that the loads transmitted to the PV array are a function of the alpha and beta angles, so it is not suffi-

¹MSC/NASTRAN Version 65 was used for the analyses presented in this paper.

cient to analyze the structure for one choice of alpha and beta angles. The second is that the loads transferred across the joints are functions of the joint dynamics, including control systems which are continuously controlling the rotation of the joint. If the control system is very soft (low gain), the joint will act like a rotational bearing and no torque will be transmitted. If, on the other hand, the control system is very stiff (high gain), the joint will act as if it is locked and the torque will be transmitted with no attenuation. The actual control system behavior lies somewhere between these two extremes. The beta joint control systems affect only torsion in the PV arrays, which is currently not a design driver, so we have assumed that these are locked. The alpha joint control systems, on the other hand, have a significant effect on bending moments in the PV array masts. We have shown that representing the alpha joints as either fixed or free fails to accurately predict loads. Including a torsional spring to represent proportional control gain is an improvement but can underpredict some important loads. The result of these analyses is that in order to predict accurate loads in the PV arrays, it is essential to include a model of the alpha joint control systems in the simulation.

Further complications in the analysis of Space Station *Freedom* loads arise from the number of low frequency modes and the high modal density. Each PV array has first bending and torsion modes near 0.1 Hz. The truss has first bending modes near 0.2 Hz. Other components with low frequency modes include Active Thermal Control Systems (ATCS) and the assembly work platform (AWP). Forcing functions—including docking, Reaction Control System (RCS) jet firing, and astronaut pushoff—on the other hand, are not limited to low frequencies. While an upper frequency limit of 5 Hz is relatively standard in the Space Station loads community, we have seen situations where modes up to 20 Hz are required to predict accurate loads. In a later section we show that without some form of component level model reduction, later Space Station configurations such as AC will have thousands of modes below 20 Hz.

One final complication arises from the fact that no one contractor is responsible for the entire Space Station *Freedom*. The Electric Power System (EPS) including PV arrays is assigned to one contractor, the truss structure to another, and the modules to others (including international partners). Each of the contractors develops a model of its portion of the structure. These models must then be combined in order to calculate dynamic loads.

In summary, the Space Station *Freedom* consists of a series of complex structures associated with various configurations. Each configuration is a continuously varying structure because of the rotation of alpha and beta joints in order to point PV arrays. The control systems used to point the PV arrays have a significant effect on structural loads in the arrays. Finally, each structure contains a large number of modes from a first flexible frequency near 0.1 Hz to an upper range of about 20 Hz. The combination of these factors dictates a careful loads methodology that generates accurate load predictions with a minimum of time and effort.

3. METHODOLOGY

The methodology presented here to calculate Space Station *Freedom* loads can be divided into four parts. The first of these is the development of an alternative superelement representation in MSC/NASTRAN to represent repeated substructures such as PV arrays. The second is the selection of component modes before generation of a system model in order to significantly reduce the number of system modes. The third is the representation of alpha joint control systems, and simulation of the Space Station response with these control systems. The fourth and final part is

the data reduction process. While no one of these parts represents a unique capability, they are state-of-the-art methods that are applied in combination to tackle an extremely complex structural dynamics problem.

3.1 Use of Superelements

A superelement in MSC/NASTRAN is simply a component of a larger structure. The mathematical model of each component is reduced to a smaller number of degrees of freedom, and these "exterior" degrees of freedom are then coupled to form the system model. For dynamics, each component is represented by a small set of physical degrees of freedom as well as a set of "component" modes. This is often referred to as a Craig-Bampton component. The reduced representations are then coupled into a model of the overall structure, usually called the "system" model.

There are a number of reasons for using superelements. A few that are particularly applicable to the Space Station are listed below:

- By solving the problem in a number of small steps rather than one large step, the overall solution time can be reduced significantly.
- Repeated elements such as solar arrays need only be solved once.
- Component models can be coupled in different orientations minimizing the time required to solve for different alpha and beta joint angle combinations.
- Unimportant component modes can be eliminated from the problem to further reduce the size of the system model.
- Different components can be modeled by different organizations. Only the reduced order component model is needed to construct the system model.

MSC/NASTRAN offers a number of standard superelements. These can be divided into primary superelements and secondary superelements. A primary superelement is represented by finite element input data (grids, elements, etc.) Primary superelements allow the user to break a large problem into a number of smaller problems while retaining all the capabilities available when the structure is not broken into superelements.

Secondary superelements are divided into two types: image superelements and external superelements. An image superelement is a component which is identical to (image of) a primary superelement. An image superelement can be translated, rotated, or reflected with respect to the primary superelement. Image superelements allow the analyst to take advantage of repeated substructures.

An external superelement is represented by the reduced order mass and stiffness matrices only. The options for graphically representing and recovering data for external superelements are limited. External superelements are typically used when models of the structural components are developed by different organizations. In this case, the model of each component is solved independently and delivered to an integration contractor who couples the various component models into a system model.

In the case of Space Station *Freedom* PV arrays, none of the three standard superelement types proved to be convenient. A primary superelement would not allow us to take advantage of the fact that this is a repeated structure (up to eight copies). An image superelement would at a minimum require a primary superelement whose grid and element numbering did not conflict with the rest of the model. Plotting system mode shapes for standard image superelements is also difficult. An external superelement would

not allow us take advantage of the fact that we have finite element input data available, limiting our ability to plot the coupled structure and to recover data.

Because of these limitations, we developed the concept of an "external-image" superelement, retaining many of the properties of both external and image superelements. The superelement is external to the extent that it is solved independently of the rest of the model. There is no requirement that grid numbers, element numbers, coordinate systems, etc. be unique with respect to the rest of the model. The superelement is an image superelement to the extent that multiple copies are generated from a single solution by equivalencing datablocks. This not only eliminates the necessity to recalculate component modes for the copies, but also results in a database representing any number of "images" which is no larger than the size of the database representing a single copy. For the PV arrays, this database is generated once and then used for all subsequent Space Station models.

The external-image superelements are coupled to the rest of the structure by assigning a coordinate system to the external physical grids. This coordinate system is then translated and rotated to locate and align each superelement with respect to the rest of the structure. In order to plot system modes MSC/NASTRAN ALTERS were used to generate unique grid numbers for each superelement and to transform the mode shapes back to the system level basic coordinate system using the coordinate systems associated with each superelement. Modifications were also made to the inertia relief solution required for mode acceleration data recovery so that MSC/NASTRAN would treat these superelements correctly.

The external-image superelement offers the advantage of an external superelement to the extent that the component is solved independently of the rest of the structure with no requirements on unique numbering schemes. It offers the advantage of an image superelement to the extent that multiple copies are generated from a single solution. Finally it offers the advantage of a standard primary superelement to the extent that system modes can be plotted for the combined structure and that all data recovery capabilities are directly available.

The number of superelements used to represent a given Space Station configuration is large. As an example, a superelement "map" for the permanently manned configuration (PMC) includes 27 different superelements, illustrated in Figure 4. The main truss (superelement 300) includes all structure inboard of the two alpha joints. This includes nine standard external superelements to represent the cluster and five standard primary superelements to represent the assembly work platform (AWP) and utility distribution module (UDM), a mobile transporter (MT), the module-to-truss structure (MTS), and two active thermal control systems (ATCS), as well as the truss structure itself. These elements are coupled into a collector superelement. There are two other collector superelements representing the structure outboard of each alpha joint (superelements 200 and 250). Each of these includes two PV arrays, two beta joints, and an integrated equipment module and radiator (IEA/RAD). Superelements 200 and 250 are not images of each other because of slight asymmetries in the structure. The PV array, beta joint, and IEA/RAD components are all represented by external-image superelements. The final step in the superelement procedure is to couple the three collector superelements into a "residual" structure. As the station continues to expand, the complexity of the model increases further. The assembly complete (AC) configuration, for example, includes 41 superelements.

Since the alpha joints rotate 360° during each orbit and the beta joints rotate $\pm 26^\circ$ over a longer time period, and since the loads in the structure are a function of these rotations, it is not sufficient to analyze each Space Station configuration for only one choice of alpha and beta joint angles. We chose to consider four different alpha angles (0° , 45° , 90° , and 135°) and three different beta angles (-26° , 0° , and 26°) for a total of twelve alpha/beta angle combinations for each Space Station configuration. This is a situation where the superelement representation of the structure can be used to great advantage. For instance, the main truss collector superelement remains unchanged among all alpha and beta angles. The collector superelements outboard of the alpha joints need to be solved for each beta angle, but remain unchanged among all alpha angles. For each Space Station configuration, therefore, we need calculate only one main truss component and three copies of each outboard component. These are then combined into twelve different system models. Further savings in time and effort can be realized by recognizing that many components do not change from configuration to configuration. For instance, the structure outboard of the alpha joints remains unchanged from the second to the thirteenth flights and then again from the fourteenth to the twenty-ninth flights. Components such as PV arrays, once they are deployed, remain unchanged throughout the development of the Space Station.

One of the most dangerous sources for error in this process is the definition of accurate alpha and beta angles. These are represented in MSC/NASTRAN by coordinate system rotations, but it is easy to make an error in specifying a rotation. In order to minimize the potential for such an error, we use display models of each Space Station configuration in SDRC I-DEAS. These provide a simple means for rotating coordinate systems as well as graphical feedback. The rotated coordinate systems are then written to the NASTRAN model using the I-DEAS NASTRAN file translator. Once the system modes are calculated, the rigid body modes (including all upstream superelements) are combined and displayed using the display model. This procedure will clearly identify any errors associated with incorrect or inconsistent coordinate system rotations.

In summary, the superelement procedure used to construct Space Station *Freedom* models is designed to minimize the time and effort involved, while ensuring consistently accurate results.

3.2 Selection of Component Modes

While the procedure outlined in the previous section greatly facilitates the assembly and solution of Space Station *Freedom* models, it does not adequately address the issue of model reduction. An accurate methodology for reducing the size of component models for the Space Station is essential due to the large number of components and the high modal density at very low frequencies.

As an example consider the PV arrays. Each PV array is reduced to a Craig-Bampton component model by calculating modes of the array with a fixed base. These component models are then coupled with other components to generate a system model. The reason for this method is that the number of component modes in the frequency range of interest is typically much smaller than the number of physical degrees-of-freedom in the model. The PV array models used in this analysis, however, have 481 modes, each below 20 Hz. Even if we reduce the upper frequency limit to 5 Hz with the potential for inaccurate loads, over 200 modes remain. The AC configuration includes eight PV arrays, corresponding to nearly 2,000 component modes below 20 Hz. Using

a similar level of detail for other components would result in close to 5,000 modes below 20 Hz. While modern computer algorithms and hardware can handle much larger problems than were feasible just a few years ago, a model with 5,000 modes is still impractical.

In order to address this problem we developed a procedure for selecting only those modes of a component that contribute significantly to the desired response of the structure. The method is based on well known procedures for selecting "important" system modes (Ref. 3). These procedures are based on examining mathematical norms on the transfer function from system inputs to system outputs and determining which modes contribute most strongly to these norms. Conversely those modes that do not contribute significantly to the norms are unobservable or uncontrollable and can be eliminated from the problem without any loss in accuracy.

Unfortunately these procedures are not directly applicable to component modes since component modes are fixed at the input point. However, they are applicable if the component is treated as a system whose input is an enforced base acceleration (Ref. 4). One simple way to represent the base acceleration is to place the component on a large mass and solve for the system modes. If the mass is large enough, these system modes will be identical to the component modes but can be selected using the procedures outlined in (Ref. 3). Each component, therefore, is treated as a system excited by an enforced acceleration at its base. Modes which contribute significantly to transfer functions from this input to a selection of outputs on the component (typically physical displacements, accelerations, or element forces at critical points) are retained, while those that do not are eliminated from the component model. Since we select the same outputs that we will be recovering from the system model, we are ensured that our results will be accurate.

This method provides a significant advantage over global measures of modal importance such as strain energy, kinetic energy or "effective mass." This is because it is tailored for specific outputs and will select the minimum number of modes required to generate accurate results at these outputs. To obtain this advantage, the locations of the critical structural responses must be known in advance. Note also that the components are solved only once and modes are selected only once since the procedure does not depend on the manner in which the component is coupled to the structure.

For the PV arrays used in the Space Station model the inputs were six enforced accelerations at the base. The outputs included 26 physical displacements, 24 physical accelerations, and 72 element forces. Based on these we were able to reduce the number of component modes required to represent the PV array from 481 to 33. A further advantage of the method is that it provides a measure of which modes contribute to which outputs, increasing the analyst's physical understanding of the model. For instance, while 33 modes are required to accurately represent all the PV array outputs, only four modes are required to represent bending moments at the base of the mast.

The modal selection procedure was also applied to the IEA/RAD model, though in this case the number of modes was only reduced from 34 to 26. Other components were either reduced in size by the associated contractor or were included in the model without any further reduction. The number of system modes below 20 Hz ranged from about a hundred for early configurations to about a thousand for the assembly complete configuration. While this is still a large number, it represents a great reduction from the number of physical degrees of freedom and the

number of modes which would have resulted without the component mode selection. The problem was feasible on the Cray supercomputer at the NASA Lewis Research Center. If it had been essential to further reduce the size of the model, the component mode selection scheme could have been applied to other components with high modal density.

3.3 Control Systems

The effect of active control systems on structural loads is often neglected. In the case of the Space Station *Freedom*, however, most of the forcing functions (docking, berthing, reaction control system firing, etc.) are applied inboard of the alpha joints, while important structural components such as the PV arrays are located outboard of the alpha joints. The manner in which loads are transferred across the alpha joints is a function of the alpha joint dynamics which are in turn a function of the alpha joint control systems. A very stiff (high gain) control system, for instance, will tend to transfer torsional moments across the alpha joints, with very little attenuation, while a very soft (low gain) control system will tend to attenuate torsion loads significantly. We have seen cases in which fixing the rotation of the alpha joints over-predicted bending moments at the base of the PV arrays due to docking of the shuttle by more than an order of magnitude. For other loading cases, such as astronaut pushoff outboard of the alpha joint, treating the alpha joint as fixed underpredicted loads. Even representing the alpha joint control system stiffness with a torsional spring did not accurately predict loads when compared to a more detailed representation of the control systems.

Because these results indicated that an accurate representation of the alpha joint control systems was essential to predict loads in the PV arrays, we chose to include the control system model in the simulation using CO-ST-IN (Ref. 5). CO-ST-IN (Control-Structure-Interaction) is a program that provides a number of tools designed to facilitate the analysis of controlled structures. These include the ability to simulate the response of a structure coupled with one or more control systems and recover the output response using a mode acceleration method for increased accuracy (Ref. 6).

A block diagram of the Space Station alpha joint control system is included in Figure 5. Since the control system is attempting to point the structure outboard of the alpha joint with respect to an inertial reference frame, it uses both a measurement of the rotation of the structure inboard of the alpha joint with respect to the inertial reference frame as well as a measurement of the rotation of the alpha joint. The inertial measurement is low-pass filtered and delayed and then combined with the alpha joint rotation and rotational velocity measurements in a PID control law. This is still a simplified model of the control system since it assumes perfect sensors and actuators and neglects friction, but it is sufficiently accurate for the calculation of structural loads.

In order to minimize the computational time required to simulate the coupled system, CO-ST-IN treats the structural model as a set of uncoupled modes to which a closed-form solution algorithm is applied. At each time step CO-ST-IN calculates the response of a discretized version of the controller and applies this until the next time step. The discrete time controller approaches the continuous time controller as the length of the time step is decreased. Since the final alpha joint control system design is likely to be discretized in any case, this is a valid approach to simulating the coupled system.

3.4 Processing of Results

The methods presented in the previous three sections are used to generate Space Station models and simulate response in an efficient and accurate manner for a large number of complex models. For the analyses described here we are recovering 122 outputs for each PV array, 132 outputs for each IEA/Radiator, and 36 outputs for each beta joint. This translates to 448 outputs for early configurations (MB1 - MB5), 896 outputs for intermediate configurations (MB6 - PMC), and 1,792 outputs for later configurations (MB11 - AC). The number of forcing functions for each configuration includes two docking loads, astronaut pushoff, and firing of reaction control system (RCS) jets. Taking into account the 12 alpha and beta joint combinations, this results in up to 86,016 time histories for each Space Station configuration. Besides threatening the world's forests, it is unclear that any benefit could be gained from generating all this data in printed form.

The first step in reducing the amount of data is to store only minimum and maximum values for the outputs, reducing the data to 172,032 numbers rather than 86,016 plots. These values are stored in a RIM database using STUMP (STructural-analysis-Utilities-and-Management-Program). The values are then sorted over all forcing functions and alpha/beta joint combinations to determine the worst case peak response value for each output. At this point the amount of data is reduced to at most 1,792 numbers for each Space Station configuration. Further reduction could be realized by forming groups of outputs (such as bending moments in PV array masts) and sorting over these groups to generate the worst case response within this group, though this has not yet been implemented. A final reduction of data would then sort over all Space Station configurations to find the worst case response of each group of outputs, though this also was not applied in this case.

4. SUMMARY AND CONCLUSIONS

As in many structural dynamics problems, the problems associated with calculating Space Station loads are not associated with fundamental technology issues so much as with the size of the problem involved. With the Space Station the issue of size refers not only to the number of physical degrees of freedom in the model, but also to the number of models that need to be solved, to the number of system modes associated with each model, and to the amount of data that is generated.

The methods presented here reduce the problem to a practical size. Superelements not only break the model into feasible pieces but eliminate unnecessary repetitious solution of model components. The selection of component modes further reduces the size of component models and the number of modes in the corresponding system models. Control systems are added without appreciably adding to the complexity of the analysis or the time involved. Finally a database is used to store and sort the large amount of output data.

These methods have been applied to a number of Space Station *Freedom* configurations from MB2 to MB11. As the Space Station design continues to evolve, further loads analyses can be performed at a minimal incremental effort.

REFERENCES

1. "CO-ST-IN User's Manual, Version 1.50," SDRC Report 1.60, September 25, 1990.
2. Space Station Freedom Stage Summary Data Book, Dec. 15, 1989.
3. Blueloch, P.A., Carney, K.S., "Modal Selection in Structural Dynamics," Proceedings of the 7th IMAC, Las Vegas, Nevada, Jan. 30 - Feb. 2, 1989.
4. Blueloch, P.A., Carney, K.S., "Selection of Component Modes," Proceedings of the AIAA Dynamics Specialists Conference, Long Beach, California, Apr. 5-6, 1990.
5. Blueloch, P.A., Beagley, N.R., "Tools for Analysis of Control-Structure Interaction," *Computer-Aided Engineering Journal*, Aug. 1990, pp. 107-112.
6. Blueloch P.A., "Calculation of Structural Dynamic Forces and Stresses Using Mode Acceleration," *AIAA J. of Guidance, Control and Dynamics*, Vol. 12, No. 5, Sep.-Oct., 1989, pp. 760-762.

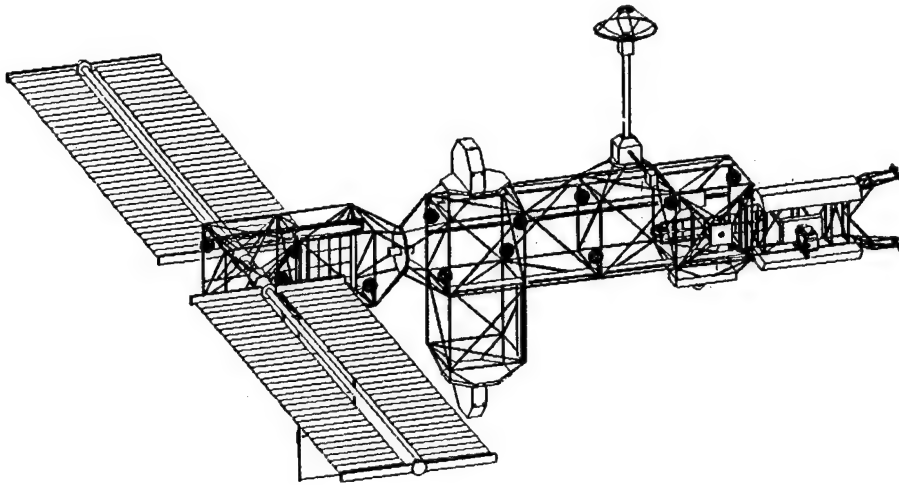


Figure 1. Space Station *Freedom* MB2 Configuration

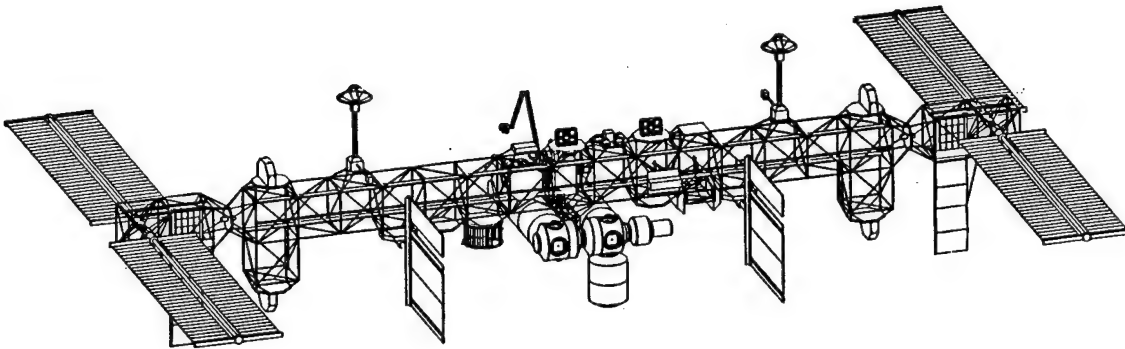


Figure 2. Space Station *Freedom* PMC Configuration

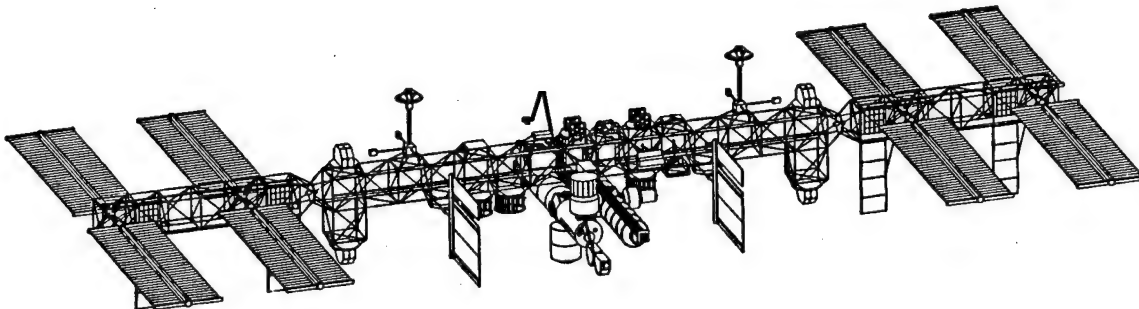


Figure 3. Space Station *Freedom* AC Configuration

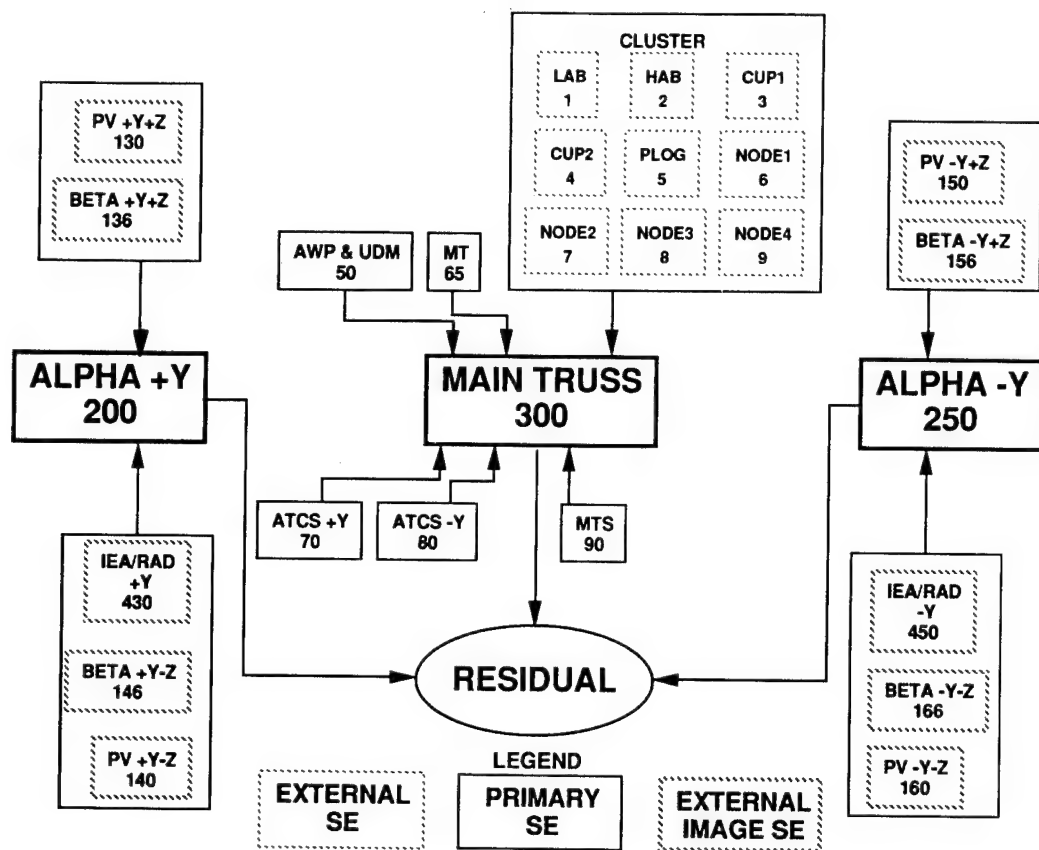


Figure 4. Superelement Map for PMC Configuration Model

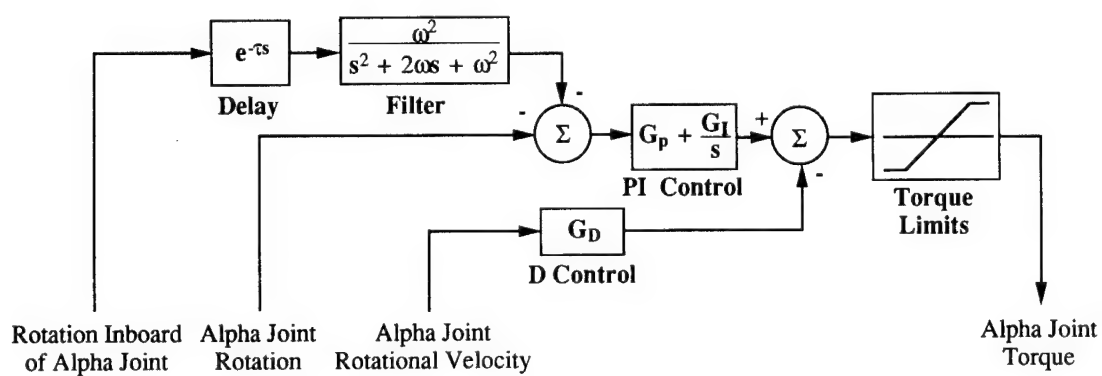


Figure 5. Block Diagram of Alpha Joint Control System Model

PRECEDING PAGE BLANK NOT FILMED

N92-23825

INFLUENCE OF MICROVIBRATIONS ON SPACECRAFT PERFORMANCES

N. JOURDON
MATRA SPACE

V. GUILLAUD
MATRA SPACE

ABSTRACT

Along with technology advances in the field of optical and laser payload, spacecraft pointing accuracy requirements become more and more severe, especially for scientific and earth observation satellites. Attitude and orbit control equipments and payload moving parts generate in-orbit microvibrations which are critical to instruments line-of-sight pointing performance.

In the past few years, MATRA SPACE has undertaken a number of activities that aim at characterizing (the in-orbit microvibrations endured by spacecraft payloads under its responsibility : SPOT 4, SILEX, SOHO.

This paper focuses on a ground-test campaign performed on SPOT flight model 3. Primary objectives were to measure the structural damping coefficient.

The test led to the conclusion that damping coefficients of 0.5 % can be anticipated in-orbit. It also demonstrated a relatively good representativeness of finite element models used for performance predictions.

1. INTRODUCTION

Technology advances allow the development of more performant optical and microwave instruments. In turn, the advanced instruments are more sensitive to dynamic disturbances from the spacecraft body, and pointing and stability requirements become more and more severe. This is especially true for scientific and Earth observation spacecrafts such as SPOT, SOHO, FIRST.

Dynamic disturbances are primarily generated by attitude and orbit control equipments (momentum or reaction wheels, reaction control thrusters, solar array drive mechanisms, gyroscopes,...) but to a larger extent by all moving parts of the spacecraft including the payload itself (magnetic tape recorders, mirrors, antennae,...). Although the induced perturbations are often below the milling level, they are critical to payload pointing performance : operation of optical instruments is very sensitive to line-of-sight jitter, both in the spatial and frequency domains.

A problem with which spacecraft manufacturers are faced in the prediction of in-orbit performance rests in the lack of knowledge of the behaviour of a spacecraft structure in a vacuum environment and under a low level of excitation. To deal with this problem, MATRA SPACE has undertaken in the past few years, a number of activities that aim at characterizing the in-orbit microvibrations so as to be in the position to propose, whenever necessary, passive or active isolation systems allowing proper operation of spacecraft and payload under its responsibility. These activities include extensive analytical and software analyses supported by a comprehension program of on-ground and in-orbit tests.

This paper focusses on a ground test campaign on SPOT 3 in december 1990. The test was performed in cooperation with CNES in the assembly facility of MATRA SPACE Toulouse Center. The primary test objective was to measure the structural damping of the satellite in a free-free configuration and under low level excitation. Other objectives were to validate the representativeness of Finite Element Models used in the prediction of in-orbit performance and to characterize, end-to-end, the disturbances induced by the reaction wheels, the magnetic tape recorders and the mirrors of the optical instrument on the line-of-sight of the other optical instruments.

Analysis of internal perturbations is still going on at the time of this paper, so the discussion will focuss on the identification of spacecraft eigen structural modes and their associated damping coefficients.

After a presentation of the test configuration, the problem of ground tests representativeness will be addressed, since air and gravity effects are potential limitations to the applicability of ground measurements extrapolated data to in-orbit performance predictions.

2. TEST CONFIGURATION

The satellite was mounted on a trolley of mass 2015 kg which was uncoupled by four "air-cushions" which assured the free-free configuration of the system (satellite + trolley) above 10 Hz.

The satellite was not equipped with solar array or super isolation and its tanks were empty.

As the measured excitation levels were very low, the smaller acoustic exterior perturbations could degrade the measurement quality. The test was therefore performed at night and the air conditioning system was switched off.

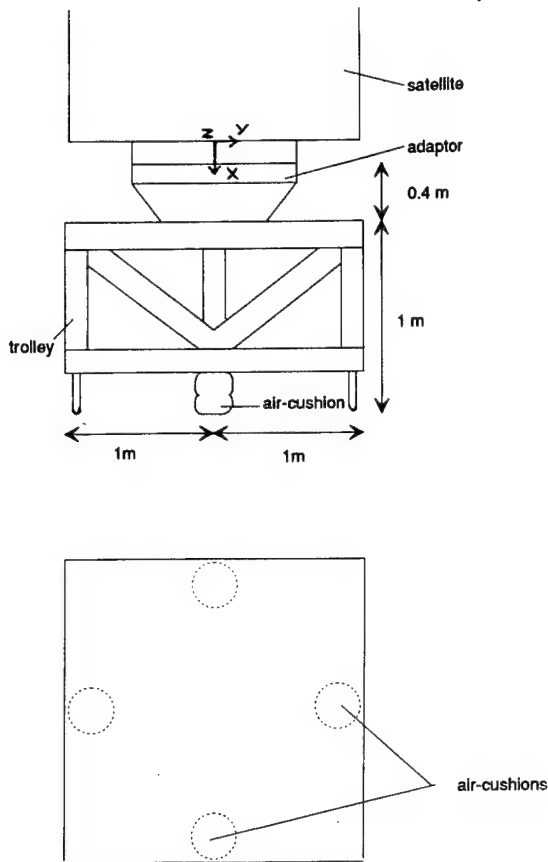


Figure 1 : Test configuration

3. TEST PREPARATION

Research and analysis were led in order to prepare the test and evaluate its eventual limits in terms of representativeness. The principal subjects of study were centered on the impacts of the ground equipment (trolley) and of the acoustic effects on the measured damping values.

3.1 Air effects

Calculations have been performed in order to evaluate the acoustic impact on the test measurements carried out in ambient conditions.

These calculations are based on the following hypothesis :

- structure immersed in a far and diffuse field,
- baffled configuration,
- eigen modes separated in frequency, generalized damping matrix diagonal.

Taking into account these hypothesis we can write for the p^{th} mode of the considered structure, in the basis of eigenvectors.

$$(1) \quad m_p (-\omega^2 + \omega \cdot 2i \xi_p \omega_p + \omega_p^2) \eta_p = - [p_{bl}(M_i, t) + p_{rad}(M_i, t)] \phi_p(M_i) dS_i$$

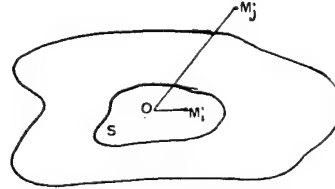
where : η_p : p^{th} component of the modal coordinates vectors
 ϕ_p : p^{th} component of the modes matrix
 m_p : generalized mass
 ξ_p : critical damping coefficient
 p_{bl} : pressure field due to acoustic excitation
 p_{rad} : pressure generated by the structure motion (mode radiation).

$$p_{rad}(M_i, t) = \rho \omega^2 \int_{\Sigma} \frac{e^{ikr}}{4\pi r} q(M_j) dS_j$$

k = wave vector

$$q(M_j) = \sum_q \Phi_q(M_j) \eta_q$$

$$r = \|OM_j - OM_i\|$$



From the equation (1) we obtain :

$$(2) \quad (-\omega^2 (m_p + M_{pp}(\omega) + i\omega (2\xi_p \omega_p m_p + R_{pp}(\omega)) + m_p \omega_p^2) \eta_p(\omega) + \sum_{q \neq p} (-\omega^2 M_{pq}(\omega) - i\omega R_{pq}(\omega)) \eta_q(\omega) = - p_{bl}(M_i, t) \phi_p(M_i) dS_i$$

where :

$$M_{pq}(\omega) = \rho / 2\pi \iint_S \frac{\cos kr}{r} \phi_p(M_i) \phi_q(M_j) q(M_j) dS_i dS_j$$

(3)

$$R_{pq}(\omega) = \rho \omega / 2\pi \iint_S \frac{\sin kr}{r} \phi_p(M_i) \phi_q(M_j) q(M_j) dS_i dS_j$$

If we neglect the cross terms M_{pq} and R_{pq} of air-structure interaction we obtain :

$$(4) \quad (-\omega^2 (m_p + M_{pp}(\omega) + i\omega (2\xi_p \omega_p m_p + R_{pp}(\omega)) + m_p \omega_p^2) \eta_p(\omega) = - p_{bl}(M_i, t) \phi_p(M_i) dS_i$$

The terms M_{pp} and R_{pp} are called respectively the added mass and added damping or radiation damping. For direct comparisons with the critical damping coefficient ξ_p , the term $\xi_{padd} = R_{pp} / (2 m_p \omega_p)$ is currently used.

From this formulation it has been shown that the coefficient ξ_{padd} related to the modes of a baffled plate representative of a satellite panel of SPOT 3 can reach 1 %. This value is not negligible with respect to the foreseen values of structural damping (about 0.5 %).

On the other hand, the pass coefficient related to the first global modes of a structure representative of SPOT 3 is about 0.05 % and, consequently, is entirely negligible compared to the estimated structural damping (about 0.5 %).

The air effects will then have no influence on the modal damping coefficients associated to principal modes measured in test. The test is therefore limited to the characterization of the global modes only.

3.2 Air cushions effects

During the test, "hand" excitations on the trolley have permitted to perform transient measurements at low frequencies in order to characterize the air-cushions frequencies. The analysis of data have led to the identification of three types of modes :

Transversal modes (Y, Z) : 0.4 Hz
Longitudinal mode(X) : 2.2 Hz
Turn-over/transversal modes (Y, Z) : 1.7 Hz.

The average damping associated to the transversal and longitudinal modes (calculated from the 3 dB length of band at peaks) are respectively 4 % and 0.5 %.

Finite Elements (FE) calculations have been performed in order to evaluate the influence of these air bags on the principal modes of the satellite (located about 30 Hz) taking account the above characteristics.

These analyses have shown that the location of these modes in the frequency domain was not affected at all. The modal damping coefficients are increased by air cushions damping characteristics in a no consequent way.

3.3 Trolley behaviour

Finite Element Analysis have predicted a coupling between the trolley and the first modes of the satellite (see further chapter).

This will consequently decrease the value of damping seen in test with respect to the real satellite damping, in proportion to the structural damping of the trolley and its participation in strain energy.

As the trolley is a completely welded structure made of steel, its structural damping is small (order of 0.1 %) compared to the expected satellite structural damping (order of 0,5 %).

Therefore its contribution to the value of damping of the complete system satellite + trolley is negligible.

3.4 Dynamical analysis

A NASTRAN Finite Element Model representative of the test configuration has been elaborated. This model was used to determine the location of the excitation and measurement points so that the first eigen modes of the satellite could be excited and easily identified.

The second purpose of this model was to compare the test measurements with the model predictions in order to update the model and progress in the modelization activities.

The results of the modal analysis are given hereafter :

MODE	FREQUENCY	IDENTIFICATION	TROLLEY BEHAVIOUR*
1	31.6 Hz	Lateral Y	33 %
2	32.1 Hz	Lateral Z	8 %
3	33.1 Hz	HRV mode	
4	35.2 Hz	Lateral Y	18 %

* Ratio of strain energy with respect to the total strain energy.

Table 1 : Modal analysis by NASTRAN

4. TEST EQUIPMENT

4.1 Measure of accelerations

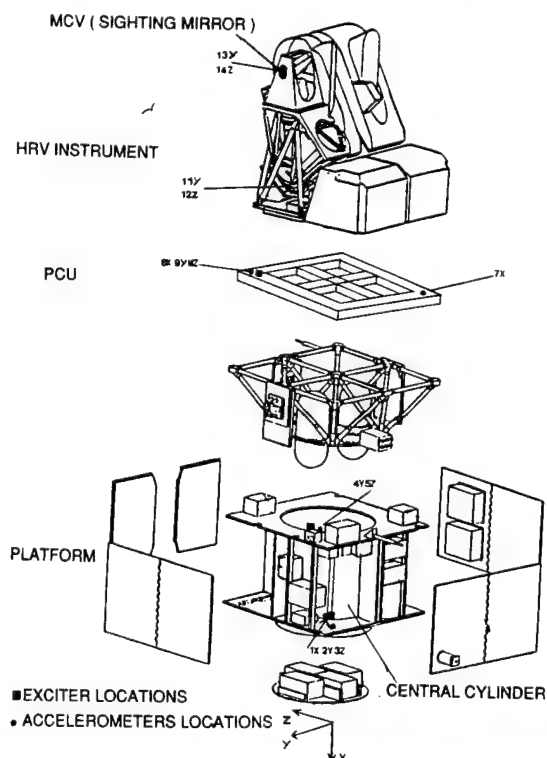
The satellite was instrumented with 14 linear accelerometers of very low sensitivity, 2 angular displacement sensors (Systron-Donner 8301) and 1 angular accelerometer (Systron-Donner 4591). The characteristics of the linear accelerometers are given below.

TYPE OF ACCELEROMETERS	CURRENT SENSITIVITY
Endevco 7707 - 1000 (7)	1000 pC/g
Septa A889 (3)	1,2 à 1,8 mA/g
Sundstrand QA 1400 (2)	1,3 mA/g
JAE (2)	1,3 mA/g

Table 2 : Accelerometers characteristics

The accelerometers were displaced during the test in order to have the maximum of workable data.

Some of them were placed on the trolley during a specific test step in order to identify its behaviour and confirm its eventual participation to the principal satellite modes to identify.



4.2 Excitation

The force excitation was delivered by an electro-dynamic exciter Brüel & Kjaer 4810. A piezo-electric force transducer was located between it and the excited structure (B & K8201). The excitation was generated by the moving slung mass reaction. The nominal level of excitation was 1 N.

Consecutive sweep sine tests for several excitation points and along each principal axis of the satellite were performed. The exciter was placed on the center cylinder in order to correctly excite the eigen modes.

These tests were accomplished with different excitation levels (1N ; 0.1N ; 0.01N) to verify the linearity of the structure.

Furthermore a specific test with the exciter placed on a measurement point permitted to verify the structure reciprocity.

5. TEST RESULTS

5.1 Structure linearity

. Reciprocity

For a linear and reciprocal structure the following equality must be respected :

$$(5) \quad \frac{\gamma_i}{F_i} = \frac{\gamma_j}{F_j}$$

where : γ_k : acceleration at degree of freedom (d.o.f.)k
 F_k : input force at degree of freedom k.

Comparison between the two transfer functions represented hereafter allows to verify the above equality. Table 3 compares the levels at peaks.

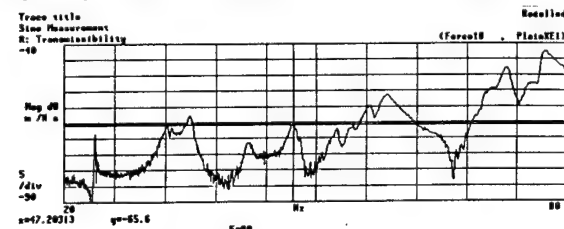


Figure 2 : Transfer function at point 9Y
Excitation X at point 1

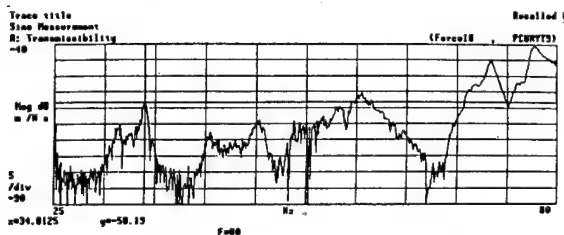


Figure 3 : Transfer function at point 1X
Excitation Y at point 9

TRANSFER FUNCTION	32,5 Hz	34,8 Hz	58,5 Hz	72,8 Hz
$\frac{\gamma_9}{F_1} (m/s^2 N)$	$5,6 \cdot 10^{-4}$	$1,3 \cdot 10^{-3}$	$1,6 \cdot 10^{-3}$	$5,6 \cdot 10^{-3}$
$\frac{\gamma_1}{F_9} (m/s^2 N)$	$5,6 \cdot 10^{-4}$	$7,5 \cdot 10^{-4}$	$1,6 \cdot 10^{-3}$	$4,2 \cdot 10^{-3}$

Table 3 : Reciprocity verification

The curves $\frac{\gamma_i}{F_j}$ have the same shape. The comparison between levels at peaks leads to a mitigated conclusion concerning the structure reciprocity.

. Excitation level effect

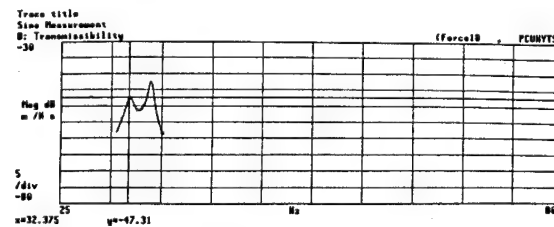
The transfer functions acceleration/input force at each measurement point obtained for two different excitation levels at the same point, respectively 1N and 0.1N are similar.

The comparison in terms of acceleration levels at peaks is given hereafter for an Y excitation direction.

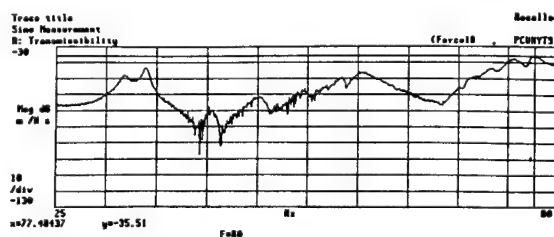
FREQUENCY	EXCITATION FORCE	32,5 Hz	34,8 Hz	58 Hz	76 Hz
$\frac{\gamma_{2Y}^*}{F} (m/s^2 N)$	1 N	$2,8 \cdot 10^{-3}$	$1,0 \cdot 10^{-3}$	$3,2 \cdot 10^{-3}$	$7,2 \cdot 10^{-3}$
	0,1 N	$2,9 \cdot 10^{-3}$	$1,1 \cdot 10^{-3}$	$3,2 \cdot 10^{-3}$	$7,4 \cdot 10^{-3}$
$\frac{\gamma_{4Y}^*}{F} (m/s^2 N)$	1 N	$4,0 \cdot 10^{-3}$	$1,6 \cdot 10^{-3}$	$1,3 \cdot 10^{-3}$	$7,4 \cdot 10^{-3}$
	0,1 N	$4,0 \cdot 10^{-3}$	$1,7 \cdot 10^{-3}$	$1,6 \cdot 10^{-3}$	$7,4 \cdot 10^{-3}$
$\frac{\gamma_{5Z}^*}{F} (m/s^2 N)$	1 N	$2,8 \cdot 10^{-3}$	$1,0 \cdot 10^{-3}$	$1,7 \cdot 10^{-3}$	$5,4 \cdot 10^{-3}$
	0,1 N	$2,7 \cdot 10^{-3}$	$1,0 \cdot 10^{-3}$	$1,9 \cdot 10^{-3}$	$5,4 \cdot 10^{-3}$

* γ_i : acceleration level at dof i.

Table 4 : Structure linearity



Input force : 1 N



Input force : 0,1 N

Figure 4 : Excitation level effect
Excitation Y at point 1

5.2 Principal modes identification

. Modal test

A modal analysis was performed from the measured transfer function $\frac{Y}{F}$ acceleration/input force recorded during the test. It was performed on the basis of the enforced motion of a system with dissipation

$$(6) \quad M \ddot{q}(t) + B \dot{q}(t) + K q(t) = F(t)$$

For an harmonic load $F(t) = F e^{j\omega t}$ the solutions of this system are:

$$(7) \quad q(t) = \left[\sum_p \frac{q_p^T q_p}{s - s_p} + \sum \frac{\bar{q}_p^T \bar{q}_p}{s - \bar{s}_p} \right] F(t)$$

where q_p : complex eigenvectors
 s_p : complex pulsation, $s_p = a_p + i\omega_p$
 q/F : measured transfer function.

. Modal test results

Three eigen modes of the satellite were identified in the 30-40 Hz frequency range. Their form and associated modal damping coefficients are given hereafter :

MODE	FREQUENCY	IDENTIFICATION	DAMPING ξ	TROLLEY DEFORMATION
1	32,4 Hz	Lateral Z	0,7 %	Yes
2	32,7 Hz	Lateral Y	2,2 %	Yes
3	34,8 Hz		0,7 %	

Table 6 : Principal modes measured

The analysis of the modal deformations of the trolley shows, as foreseen by FE calculations, that it contributes to the deformation of the global system. Its exact movement can not be accurately identified because of the low number of sensors available.

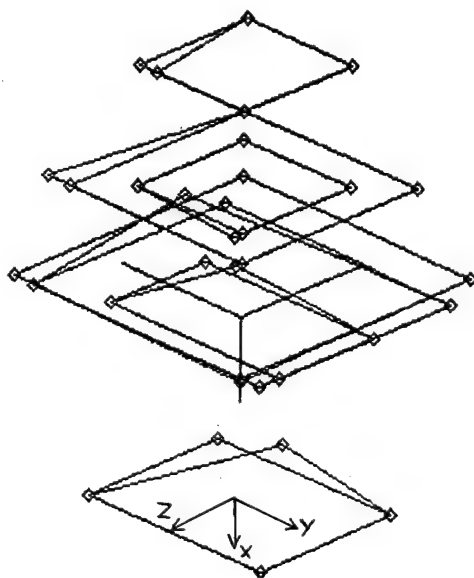


Figure 5 : 1st lateral Y mode - Modal deformation

5.3 Calculations - Test correlation

The predicted (calculated) frequencies were similar to those measured as shown in the following table.

CALCULATIONS		MEASURE	
FREQUENCY	IDENTIFICATION	FREQUENCY	IDENTIFICATION
32,1 Hz	Lateral Z	32,4 Hz	Lateral Z
31,6 Hz	Lateral Y	32,7 Hz	Lateral Y
35,2 Hz	Lateral Y	34,8 Hz	

Table 7 : Calculations - Measurements comparison

Test simulations were accomplished by enforced motion calculations on the basis of a modal damping coefficient of 0,5 % on the frequency range 30-40 Hz.

The transfer functions $\frac{Y}{F}$ obtained at each measurement point were directly compared with the actual measurements results.

This step has confirmed the first mode (32.4 Hz) as a lateral Z mode. The ratio between predicted transfer functions related to the second mode (32,1 Hz) and measured transfer functions related to the first mode (32,4 Hz) is constant with respect to the measurement points within ± 30 % accuracy.

The identification of the two other eigen modes is more difficult since they are very close in magnitude.

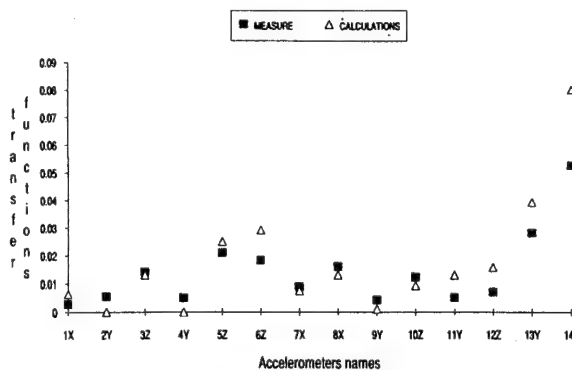


Figure 6 : Correlation measurement - Calculation for the 1st lateral Z mode

Based on these comparisons, the trolley behaviour was correctly predicted since similar deformations are observed both in calculated and measured data on the principal modes.

6. CONCLUSION

The microvibration test performed on SPOT 3 was satisfactory. The measurements were of good quality without any noise contaminations and reproducible, that led to a relatively easy data analysis.

This test has shown the ability to excite a satellite structure with a very low level of excitation, and ensuring that the behaviour of the structure remains linear.

On the other hand F.E. calculation test comparisons in terms of frequencies and acceleration levels have shown a relatively good prediction ability by F.E. calculations at low frequencies.

The modal damping coefficients associated with the global satellite modes are varying between 0.7 % and 2.2 %.

The minimum value of 0.7 % has to be compensated by air-cushion effects, trolley flexibility effects, scatter of damping coefficient according to the different materials of the structure, and accuracy of modal deformations identification.

These compensations lead to a minimum structural coefficient of 0.5 %. This result justifies the current assumption used for performance predictions.

In order to reduce the predicted perturbations on the pointing performances of satellites, studies are continuing on the use of suspension-damping systems at the pointing instrument/structure interface as well as at the exciter/structure interface.

N 92-23826
5773 B

ON THE MODELLING OF A DEPLOYABLE TELESCOPE ELASTIC BEAM-TYPE ELEMENT
FOR ON-ORBIT MULTIBODY SIMULATIONS

Bernhard Kotzias

ORIGINAL PAGE
BLACK AND WHITE PHOTOGRAPH

MBB/ERNO, Hünefeldstr. 1-5, 2800 Bremen 1., GERMANY

ABSTRACT

The theory of a continuous deployable beam type element for telescope applications is presented. The inertia tensor of this element is described by 3rd order theory for large deformations. Stress stiffening from gyroscopic and external forces is included. In order to save numerical operations, continuous base functions, dedicated to the actual length of deployment, are used. These satisfy Dirichlet boundary conditions on the moving telescope joint. They are selected as polynomials, representing transversal, torsional and longitudinal motion in a cartesian deformation base. Precalculation of stiffening and nonlinear inertia terms is done in advance. The numerical extensive part is thereby separated from time integration.

Keywords: deployable telescope element, beam, continuous element, stress stiffening

An adequate beam model to handle those effects is given subsequently.

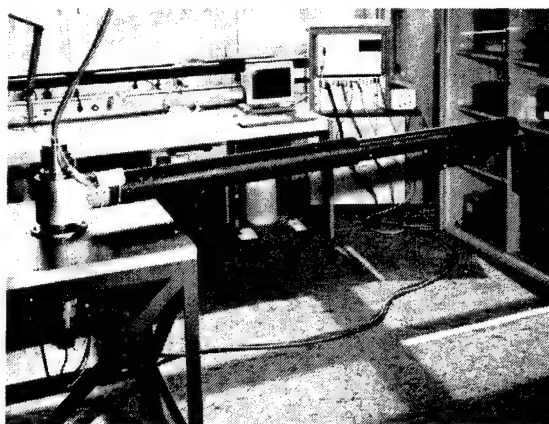


Fig.1: Prototyp Manipulator Telescope

Advanced concepts of structures for space applications have been developed in view of future tasks. Typically, beam type structures apply, because of advantageous mass, volume and modularization properties. Issues of those structures are shown below. Fig. 1 is a telescope type roboter, designed for on-orbit maintenance and servicing tasks. Fig. 2 is an example of a future space power plant, built up by a spoke stiffened wheel. These structures undergo high precision tasks on alignment and guidance. This requires ambitious dynamic modelling of the following effects for simulation:

- Stiffening by gyroscopic and external forces. Therefrom shifting system eigenfrequencies appear. Mode shapes are effected significantly.
- Early beam deformation - in the order of beam diameter - can change some eigenfrequencies dramatically.
- Deployable system dynamic can force oscillation during the retrieval or deployment phase and changes system eigenfrequencies as well.

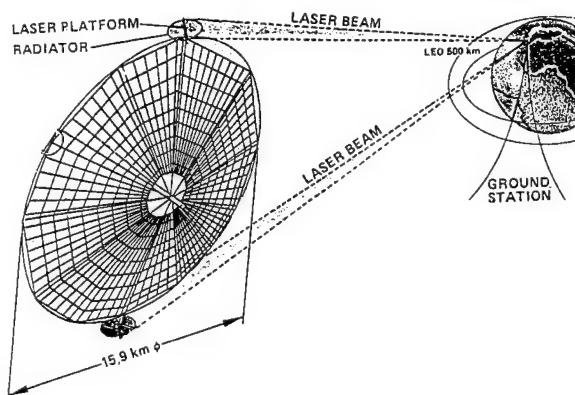


Fig.2: Orbital Solar Energy Platform built up by Telescope Type Elements, used as wheel spokes.

2. Theoretical Approach

2.1 General Inertia and Elastomechanical Description

The time evolution of the actual path of the beam shall be solved in configuration

space (q, \dot{q}) . Therefore, generalized co-ordinates q are divided into 6 co-ordinates $\bar{x}_i, \bar{\theta}_i$ ($i=1,2,3$), describing the orientation of the body reference system in space, and n_f co-ordinates q_{fi} ($i=6+1, n_f+6$) for the presentation of the deformations \bar{u} (Fig. 3). Corresponding, we get 6 rigid body velocities $\dot{\bar{x}}_i, \dot{\bar{\theta}}_i$ and n_f elastic speed variables \dot{q}_{fi} . This separation into a rigid body part and an elastic part is convenient for the description of relatively stiff elastic bodies, since it decomposes the dynamic into two subproblems - the formulation of the large but bounded elastic motion given in the body reference frame, and the unbounded gross motion of this reference frame with respect to the inertia system. The body reference frame is accelerated and depends itself on the rigid body configuration space variables $(\bar{x}, \bar{\theta})$. The following section shows that rigid body motion and large deformation is represented by this way without the use of trigonometric functions. Once the mass matrix M for the undeformed body $M(q)$ is derived, the exact (3rd order) inertia properties for the large deformed body can be reconstructed with suitable numerical effort. This method has been reported by Likins /1/ and Bodley /2/. It is the formulation on which elastic body inertias in the Multi Body Algorithm DISCOS are formulated.

A variational principle, based on Lagrangian density can be used to describe the beam dynamic. The Lagrangian density is given by

$$\mathcal{L} = \mathcal{T} - \mathcal{V} \quad (1)$$

where \mathcal{T} is the kinetic energy density and \mathcal{V} the elastic potential density. The variation of Lagrangian density is given in physical or generalized coordinates by

$$\delta \mathcal{L} = \frac{d}{dt} \frac{\partial \mathcal{L}}{\partial \dot{v}} \delta v + \frac{\partial \mathcal{L}}{\partial v} \delta v = - \frac{d}{dt} \frac{\partial \mathcal{L}}{\partial \dot{q}} \delta q + \frac{\partial \mathcal{L}}{\partial q} \delta q = 0 \quad (2)$$

where q and v are related by the mapping

$$\vec{v} = \eta \vec{q} \quad \vec{v}^T = (\vec{x}, \vec{\theta}, \vec{u})^T \quad (3)$$

Note that η is a matrix, containing mode functions that depend for the deployable beam part on x_e (Fig. 4). Rigid body motion $\bar{x}, \bar{\theta}$ and elastic deformations \bar{u} are identified as subsets in the q configuration space.

2.1.1 Inertia Description

The inertia properties are derived from the kinetic energy by the canonical formula for the momentum

$$\vec{p} = \frac{\partial \mathcal{L}}{\partial \dot{q}} = \frac{\partial \mathcal{T}}{\partial \dot{q}} \quad (4)$$

Usually the linear part of \vec{p} in \vec{q} is called mass matrix M , and is transformed to the body reference frame by $\vec{\beta}(x, \theta)$ /1/, /2/.

Starting with the positional description of a deformed volume element of an elastic body, we get from Fig. 3

$$\vec{R} = \vec{r}_0 + A (\vec{r} + \vec{u}) \quad (5)$$

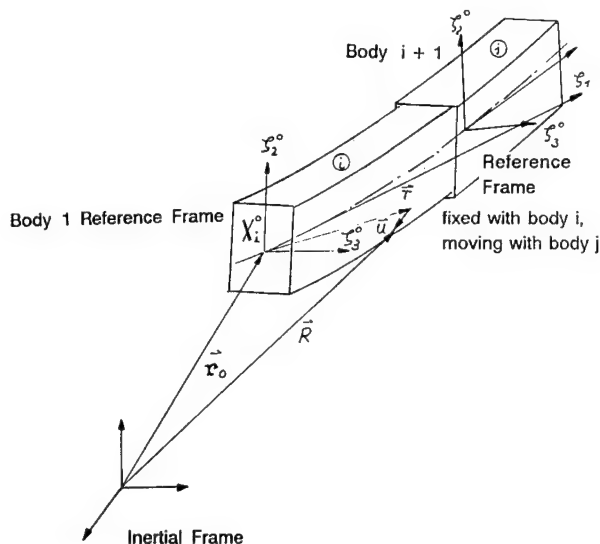


Fig. 3: Co-ordinate Frames and References

where A is the rotation matrix from the body fixed reference frame to the inertia reference frame. Differentiating R with respect to time and transforming also the body reference system translational velocity $\dot{\vec{r}}_0$ to the body reference system base, we get

$$\dot{\vec{R}} = A(\dot{\vec{x}}_0 + \dot{\vec{u}}) + \dot{A}(\vec{r} + \vec{u}) \quad (6)$$

Using the unitary properties of A

$$A A^T = 1 \quad (7)$$

$$\text{and} \quad A^T \dot{A} = \epsilon \dot{\theta} \quad (8)$$

where ϵ is the Levi Civita Tensor and $\dot{\theta}$ the reference frame angular velocity, the kinetic energy of an elastic body is written in the non-inertial body reference frame X^0 by the variables $\bar{x}, \bar{\theta}, \bar{u}$ as

$$T = \frac{1}{2} \int_V dm \rho \dot{\vec{R}}^T \dot{\vec{R}} \quad (9)$$

$$= \frac{1}{2} \int_V dm \rho \{ (\dot{\vec{x}}_0 + \epsilon \dot{\theta} + \dot{\vec{u}})^2 + (\epsilon \dot{\theta})^T (\dot{\vec{x}}_0 + \dot{\vec{u}}) + (\dot{\vec{x}}_0 + \dot{\vec{u}})^T (\epsilon \dot{\theta}) + (\epsilon \dot{\theta})^2 \}$$

Easily, deformation independent and dependent terms can be identified. Latter are linear and of second order in the deformation \bar{u} . They are responsible for a changing rigid body inertia tensor, if deformation becomes large. Especially, beam elements (Fig. 4) changes their inertia moment I_{xx} very rapidly under transversal deformation. It is therefore of importance to retain second order terms in \bar{u} for the inertia properties of the beam. Equations (3), (9) and $\dot{\vec{p}}$, derived from (4), are used to identify the mass matrix M (10) and gyroscopic forces G (see /1/, /2/). M and G are given in configuration space q by

$$M(q) = M + q^T M_{\Delta} + q^T M_{\Delta\Delta} q \quad (10)$$

$G = \Omega M \dot{q} + \dot{q} M_{,k} \dot{q} - \dot{M} \dot{q}$ (11)
where $M_{,k}$ is the derivation of M with respect to k the elastic co-ordinates q_k and

$$\Omega = - \begin{bmatrix} \epsilon \dot{\bar{\theta}} & 0 & 0 \\ \epsilon \dot{\bar{x}}_0 & \epsilon \dot{\bar{\theta}} & 0 \\ 0 & 0 & 0 \end{bmatrix}$$

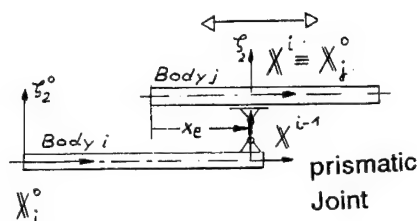


Fig. 4: Schematic of Telescope Beams; Body j is modelled as deployable Euler Bernoulli Beam. Body i is a specialized version of Body j with a fixed reference frame on its left end.

2.1.2 Elastomechanical Description

Elastic properties are obtained from the elastic potential density of the beam

$$\mathcal{V} = \int \frac{1}{2} (E \gamma_{xx}^2 + \mu (\gamma_{xz}^2 + \gamma_{zx}^2)) dv \quad \epsilon = 2, 3 \quad (12)$$

where E , μ is Young's and shear modulus.

γ_{ij} are strain displacement relations for extensional strain and shear strain. The latter is responsible for torsional elasticity: Introducing 1st and 2nd order strain displacements quantities $\gamma_{xx} = \epsilon_{,x} x^1 x^2 x^3$, $\gamma_{xz} = \epsilon_{,x} x^1 x^2$ for extensional and bending strain, respectively, $\delta \mathcal{V}$ is written as

$$\delta \mathcal{V} = \delta q \int_0^1 d\zeta_1 \frac{\delta \phi}{\delta q}$$

$$\delta \phi = \{ (ES \bar{v}_{1,1} \delta \bar{v}_{1,1} + \mu I^1 \varphi_1 \delta \varphi_1 + EI^2 \bar{v}_{2,1} \delta \bar{v}_{2,1} + EI^3 \bar{v}_{3,1} \delta \bar{v}_{3,1}) \} \quad (13a)$$

$$+ ES \mathcal{E}(\zeta_1) (v_{1,1} \delta v_{1,1} + v_{2,1} \delta v_{2,1} + v_{3,1} \delta v_{3,1}) \quad (13b)$$

$$ES ((v_{1,1}(v_{1,1} \delta v_{1,1}) + v_{2,1}(v_{2,1} \delta v_{1,1}) + v_{3,1}(v_{3,1} \delta v_{1,1}))) \quad (13c)$$

Using Saint Venant principle, deformations are expressed by simple quantities related to the beam center line

$$v_1 = \bar{v}_1(\zeta_1) \quad (14a)$$

$$v_2 = -\varphi \zeta_3(\zeta_1) + \bar{v}_2(\zeta_1) \quad (14b)$$

$$v_3 = \varphi \zeta_2(\zeta_1) + \bar{v}_1(\zeta_1) \quad (14c)$$

where v_1, v_2, v_3 are the local displacement in ζ_1, ζ_2 and ζ_3 direction, $\bar{v}_1, \bar{v}_2, \bar{v}_3$ are related quantities on the center line. These are introduced into the strain displacement relations for subsequent variation of the elastic potential (equation 13). The stiffness matrix is therefore obtained by the variation of the elastic potential.

$$K_q = \int d\zeta_1 \frac{\delta \phi}{\delta q} \quad (15)$$

$$K_q = \int_0^1 d\zeta_1 \eta^T (K_{u,u}^{op} + K_c^{op} + K_r^{op}) \eta \quad (16)$$

K_q is divided into a linear part

$$K_{lin} = \int_0^1 d\zeta_1 \eta(\zeta, x_e(t)) \begin{bmatrix} ES \bar{\partial}_1 \bar{\partial}_1 & 0 & 0 & 0 \\ 0 & EI^2 \bar{\partial}_1 \bar{\partial}_1 & 0 & 0 \\ 0 & 0 & EI^3 \bar{\partial}_1 \bar{\partial}_1 & 0 \\ 0 & 0 & 0 & I \bar{\partial}_1 \bar{\partial}_1 \end{bmatrix} \eta^T(\zeta, x_e(t)) \quad (17a)$$

and a nonlinear parts, proportional to axial strain ϵ

$$K_C = \int_0^1 d\zeta_1 \epsilon(\zeta) \eta(\zeta, x_e(t)) \begin{bmatrix} ES \bar{\partial}_1 \bar{\partial}_1 & 0 & 0 & 0 \\ 0 & ES \bar{\partial}_1 \bar{\partial}_1 & 0 & 0 \\ 0 & 0 & ES \bar{\partial}_1 \bar{\partial}_1 & 0 \\ 0 & 0 & 0 & EI \bar{\partial}_1 \bar{\partial}_1 \end{bmatrix} \eta^T(\zeta, x_e(t)) \quad (17b)$$

and to retraction forces.

$$K_r = \int_0^1 d\zeta_1 \frac{ES}{2} \begin{bmatrix} \eta_1(v_{1,1} \bar{\partial}_1 \bar{\partial}_1 | v_{2,1} \bar{\partial}_1 \bar{\partial}_1 | v_{3,1} \bar{\partial}_1 \bar{\partial}_1 | 0 \\ 0 \\ 0 \\ 0 \end{bmatrix} \quad (17c)$$

(17b) is responsible for stress stiffening effects while (17c) are forces, generated under transversal displacement and acting in axial direction. Those cause a shortening of the beam element under large deformations. Geometry compatible deformations are therefrom obtained.

In the above matrices, S denotes the area of beam cross section and I^1, I^2, I^3 the one polar and the two axial moments of inertia. The above used operators $\bar{\partial}_1, \bar{\partial}_2, \bar{\partial}_3$ are given by the partial derivation $\frac{\partial}{\partial \zeta_i}$. Through that, K_{lin}, K_C become its operator matrices, acting on the right

displacement $\eta^T(x_e(t))$ and on the left virtual displacement function base $\eta(x_e(t))$. The displacements function base is thereby partitioned into 1 longitudinal, 2 transversal and 1 torsional set (18), corresponding to torsions $\bar{v}_1, \bar{v}_2, \bar{v}_3$ and φ (see equation (14)).

$$\eta(\zeta, x_e(t)) = \begin{bmatrix} \eta_1 \bar{e}_1 \\ \eta_2 \bar{e}_2 \\ \eta_3 \bar{e}_3 \\ \eta_r \bar{e}_r \end{bmatrix} (\zeta, x_e(t)) \quad (18)$$

2.2 Continuous Base Function Description

It is a general procedure for multi-body dynamics to model elements like a beam by a set of continuous base functions. Therefore, physical displacements \bar{v} and velocities $\dot{\bar{v}}$ are expressed in generalized co-ordinates and velocities by the mapping

$$\bar{v} = \eta(\bar{q}(t)) \bar{q}(t) \quad (19)$$

is a functional matrix, depending implicitly on time by $x_e(t)$ and on $q(t)$. Its dependency on x_e is used for the deployable beam in order to satisfy following boundary condition at the body input coordinate frame location:

$$\eta = \begin{cases} \eta_0 & \text{rigid} \\ \eta_{el} & \text{elastic} \end{cases} \quad (20)$$

$$\eta_{el}(x_e) = 0; \quad \eta_{el, \dots}(x_e) = 0$$

where $x_e(t)$ is the length of the undeformed beam part. These conditions save numerical operations, when implementing the element into a multi body simulation algorithm, because v_1, v_2 lie directly in the null space of the joint constraints. No further projection method is therefore needed to satisfy the joint constraints. Mass matrix and stiffness matrix built up by the functions $\eta_{el}(x_e)$ become itself dependent on time:

$$M = \int \rho \eta(x_e(t)) \eta^T(x_e(t)) dx_e \quad (21)$$

$$K_i = \int \eta(x_e(t)) K_i^{\text{op}} \eta^T(x_e(t))$$

ρ is the mass density and K_i^{op} the stiffness operator, identified in equation (17).

It is now of interest to find a proper set of base functions $\eta(x_e, q)$, where two directions may be followed. Otter /3/, Johanny /4/, Likins /5/ and Kane /6/ proposed non-linear base functions $\eta(q)$ in order to obtain geometrical deformations. Stress stiffening contribution appear therewith directly in the mass matrix by additional terms. Those are obtained by differentiation of (19) with respect to time and substitution into the formula for the canonical momentum (4). The resulting mass matrix is of high order in q and is usually cut at powers of 4 or 5.

The approach, followed here, is to use the linear mapping (3) of physical displacements v . The inertia description is therefore of 4th order in q (equations 10,11). Cutting in higher order term of q can therefore be avoided. The theory remains exact at large deformations.

The linear mapping is done by a set of polynomials - the base functions. Selecting only base function for \bar{v}_2, \bar{v}_3 and \bar{v} results in almost correct linear system eigenfrequencies.

In order to account for stress stiffening effects, the base function set is supplemented by polynomials η_i for v_1 . The function $\xi(\xi_i)$ for extensional strain (see equation 17b) is calculated from this by

$$\xi(\xi_i) = (v_{1,1} + \frac{1}{2}(v_{1,1}^2 + v_{2,1}^2 + v_{3,1}^2)) \quad (22)$$

$$\text{where } v_{i,1} = \sum_{j=1}^n q_j^i \eta_{i,1}^j \quad (23)$$

v_1 displacements are calculated by the balance of external and mass forces by internal beam forces. Either a static equilibrium between external and gyroscopic with internal forces or a fully dynamic solution, which takes the v_1 degrees of freedoms (longitudinal motion) within the multibody simulation, can be used. A convenient set of base functions for v_1 can be found. External joint forces induce a constant extensional strain ξ . Corresponding base functions η_1^j are found by the Integration of the linear part $v_{1,1}$ in equation (23).

The same procedure is used to account for base functions η_1^{L3} , corresponding to mass/gyroscopic forces. Those are of the type $m\ddot{r}$ and $m\omega \times \omega \times r$. Corresponding strain

and displacement fields v_1 , which appear upon the projection of the mass forces on the ξ_i -axis are shown in Fig.5. It is evident that polynomials up to order 3 in ξ_i are sufficient.

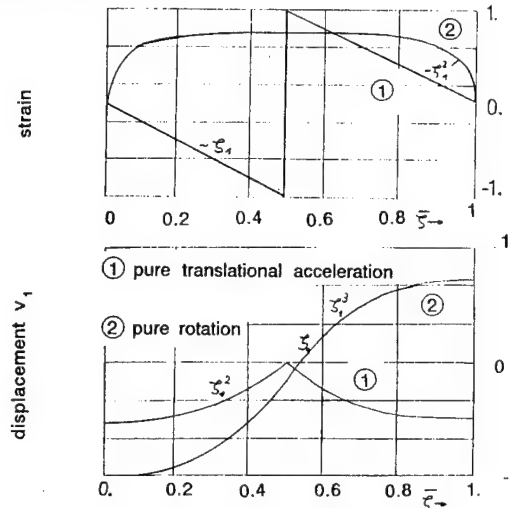


Fig.5: Extensional Strain and Displacement Fields, generated by Pure Translational and pure Rotational Acceleration

In order to account for non-linear mass forces in equations (10) and (11), it is recommended to use a deformation shape preprocessing to obtain geometry modes. That means, the deformation must be compatible with a real deformed beam geometry, implying an axially backward motion under transversal displacements of all beam elements. Only those deformations will generate meaningful contributions of the above mentioned nonlinear mass forces.

A corresponding backward motion mode can be assessed by equation (2) and given base functions for v_2 and v_3 . A zero strain mode in v_1 is therefrom given by

$$\xi = 0$$

$$v_1 = -\frac{1}{N} \int_{x_e}^x (v_{2,1}^2 + v_{3,1}^2) d\xi_i$$

where N is a suitable normation, that prevent the mass matrix to become singular, when v_2, v_3 approaches zero.

3. Results

For first test purposes, base functions for v_2, v_3 and \bar{v} are selected as polynomials. No preprocessing is used. The first cantilevered eigenfrequency accuracy, obtained with two base functions $(\xi - x_e)^2 \bar{e}^2$ and $(\xi - x_e)^3 \bar{e}^2$, is better than 1%. A typical eigenvalue shift, during deployment is shown in Fig. 6. For transient analysis, the test configuration in Fig. 7 is used. The deployable telescope part undergoes a constraint reference frame motion, given by the velocity $\dot{x}_e(t)$:

$$\dot{x}_e(t) = \ddot{x}_0 * (t - 1.6 \sin(2\pi t / 10 \text{sec}))$$

where \dot{x}_e is the deployment velocity and t the time. A simultaneous eccentric constraint rotation is forces at the static

telescope part.

It is given by

$$\dot{\theta}(t) = 0.2 \frac{\text{rad}}{\text{sec}^2} \left(t \cdot \frac{15 \text{ sec}}{2\pi} \sin(2\pi t/15 \text{ sec}) \right)$$

Corresponding transient response of the telescope tip is given in Fig. 8a. Curve 1 and 2 are calculated with stress stiffening for two deployment accelerations ($\ddot{x}_0 = 0.01 \frac{\text{m}}{\text{sec}^2}$ and $x = 0.1 \frac{\text{m}}{\text{sec}^2}$)

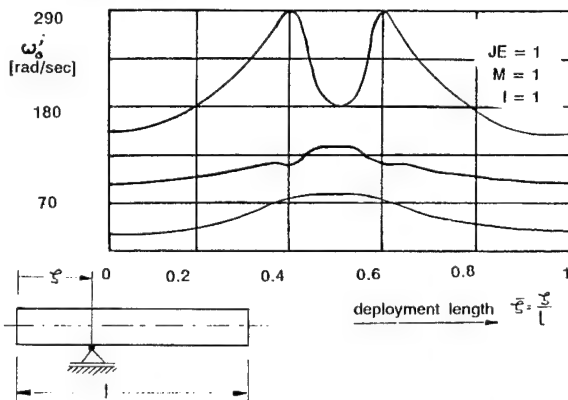


Fig. 6: Eigenvalue Shift during Deployment (3 elastic Modes)

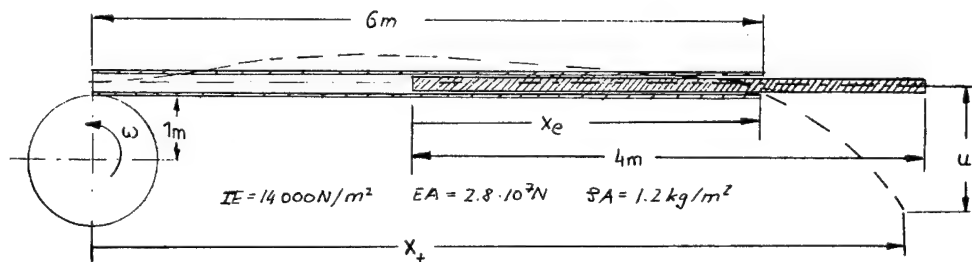


Fig. 7: Telescope Test Configuration

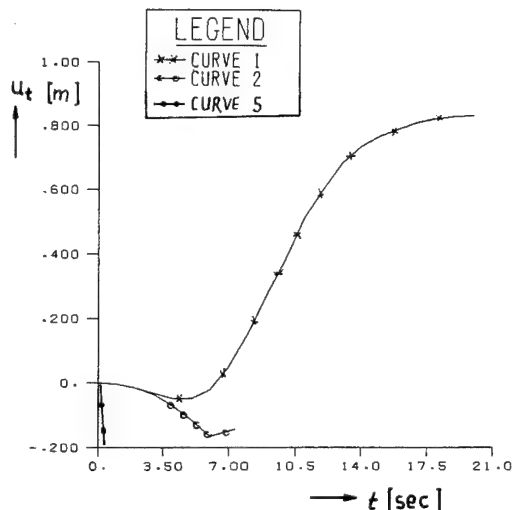


Fig. 8a: Telescope Tip displacement (transversal)
Simulation Test Bed: SIMPACK

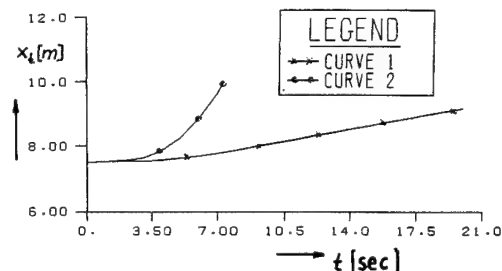


Fig. 8b: Telescope Tip displacement (ξ_1 -direction)

Calculations without stress stiffening are not possible for the given example, since the simulation is unstable at the very beginning (Curve 5). Curve 2 is calculated up to 7.3 sec. This is the time on which the telescope is fully deployed for $\ddot{x}_0 = 0.1 \frac{\text{m}}{\text{sec}^2}$. Curve 1 is calculated for a low deployment acceleration of $\ddot{x}_0 = 0.01 \frac{\text{m}}{\text{sec}^2}$. Therefore the total time evolution from the drive up, determined by acceleration forces, up to the equilibrium, determined by centrifugal forces is shown. The different behaviour in Curve 2 is due to the fact that the telescope length is higher at the same time. Therefore, the rotational acceleration forces becomes higher and the telescope loses stiffness, resulting

in higher displacements. Only for a short time, above 5 sec, the centrifugal forces grow rapidly and compensate the inertia motion which are induced by the rotational acceleration. Fig. 8b shows the corresponding tip location in ξ_1 direction.

This motion is merely due to the kinematical constraints of the two body problem and not a result of the introduced elastic restraint motion. The non-linear mass forces do also not contribute to this figures, since the linear accelerations become low at high displacements.

4. Concluding Remarks

The need for a simulation software for telescopes was the motivation for deriving the preceding dynamic nonlinear equations, dedicated to deployable motion. A continuous model approach was selected in order to avoid the problems, which arise within simulations of moving elastic bodies, if discrete degrees of freedoms are used. The equations can be easily modified for related tasks. With fixed deployable length

x_e , they are identical to the general beam equations, which might be also used for result comparison. The presented results, however, are dedicated to the response under deployable motion. The underlying test example can be extended to more complicated simulations. Another important simulation would be the solution during orbital maneuvers, where the accelerated spacecraft reference system effects the tip displacement as well. This on-orbit standard application for a telescope type roboter is one of the major task for further investigations.

5. Literatur

- /1/ Likins, P.W., "Analytical Dynamics and Nonrigid Spacecraft Simulation", Technical Report 32-1593, Jet Propulsion Laboratory, Pasadena, California, July 1974
- /2/ Bodley, C.S., Devers, A.D., Park, A.C. and Frisch, H.P., "A Digital Computer Program for the Dynamic Interaction Simulation of Controls and Structures (DISCOS)", Vols. I & II, NASA TP-1219, May 1978
- /3/ Otter, M., "Modellierung eines Industrieroboters als starr-elastisches Mehrkörpersystem und Entwurf einer einfachen Regelung, Thesis TU-Munich Lst.B
- /4/ Johanny, R., "Automatisches Aufstellen der Bewegungsgleichungen von baumstrukturierten Mehrkörpersystemen mit elastischen Körpern, Thesis TU-Munich Lst.B
- /5/ Likins, P.W., "Geometric Stiffness Characteristics of a Rotating Elastic Appendage", International Journal of Solids and Structures, Vol. 10, No. 2, 1974, pp. 161-167
- /6/ Kane, T.R., Ryan, R.R., and Banerjee, A.K., "Dynamics of a Cantilever Beam Attached to a Moving Base", Journal of Guidance, Control and Dynamics, Vol. 10, March-April 1987, pp. 139-151
- /7/ Man, G. and Laskin, R. (ed.), "Proceedings of the Workshop on Multibody Simulation", NASA Jet Propulsion Laboratory, California Institute of Technology, Pasadena, April 15, 1988
- /8/ Banerjee, A.K. and Kane, T.R., "Dynamics of a Plate in Large Overall Motion", to be published in the Journal of Applied Mechanics
- /9/ Bisplinghoff, R.L., Ashley, H. and Halfman, R.L., "Aerelasticity", Addison-Wesley, 1955, pp. 95-97
- /10/ Meirovitch, L., "Analytical Methods in Vibrations", MacMillan, pp. 443-445
- /11/ Levinson, D.A. and Kane, T.R., "Spin Stability of a Satellite Equipped with Four Booms", Journal of Spacecraft and Rockets, Vol. 13, April 1976, pp. 208-213
- /12/ Turcic, D.A. and Midha, A., "Generalized Equations of Motion for the Dynamic Analysis of Elastic Mechanism Systems", ASME Journal of Dynamic Systems, Measurement and Control, Vol. 106, December 1984, pp. 243-248
- /13/ Turcic, D.A., Midha, A. and Bosnik, J.R., "Dynamic Analysis of Elastic Mechanism Systems. Parts I & II, ASME Journal of Dynamic Systems, Measurement and Control, Vol. 106, December 1984, pp. 249-260
- /14/ Simo, J.C. and Vu-Quoc, L., "On the Dynamics of Flexible Bodies Under Large Overall Motions - The Plane Case: Parts I & II", Journal of Applied Mechanics, Vol. 53, December 1986, pp. 849-863
- /15/ Vu-Quoc, L. and Simo, J.C., "Dynamics of Earth-Orbiting Satellites with Multibody Components", Journal of Guidance, Control and Dynamics, Vol. 10, November-December 1987, pp. 549-558
- /16/ Housner, J., McGowan, P.E., Abrahamson, L.A. and Powell, M.G., "LATDYN User's Manual", NASA Technical Memorandum 87635, January 1986
- /17/ Wu, S.-C. and Haug, E.J., "Geometric Nonlinear Substructuring for Dynamics of Flexible Mechanical Systems", to appear in the International Journal for Numerical Methods in Engineering
- /18/ Hopkins, A.S. and Likins, P., "Analysis of Structures with Rotating, Flexible Substructures", Proceedings of the AIAA/ASME/ASCE/AHS 28th Structures, Structural Dynamics and Materials Conference, 1987, pp. 944-954
- /19/ Modi, V.J. and Ibrahim, A.M., "On the Dynamics of Flexible Orbiting Structures", Large Space Structures: Dynamics and Control, S.N. Atluri and A.K. Amos (Eds), Springer Verlag, 1988, pp. 93-114
- /20/ Zeiler, T. and Buttrill, C., "Dynamic Analysis of an Unrestrained Rotating Structure Through Nonlinear Simulation", AIAA 29th Structures, Structural Dynamics and Materials Conference, Williamsburg, Virginia, Paper No. 88-2232, April 18-20, 1988
- /21/ Amirouche, F.M.L. and Ider, S.K., "The Influence of Geometric Nonlinearities in the Dynamics of Flexible Tree-Like Structures", to appear in the Journal of Guidance, Control and Dynamics
- /22/ Singh, R.P., van der Voort, R.J. and Likins, P.W., "Dynamics of Flexible Bodies in Tree Topology - A Computer Oriented Approach", Journal of Guidance, Control and Dynamics, Vol. 8, September-October 1985, pp. 584-590
- /23/ Cook, R.D., "Concepts and Applications of Finite Element Analysis", McGraw-Hill, 1985, pp. 331-341

N 92 - 23827

84739

DEVELOPMENT AND APPLICATION OF SUBSTRUCTURING TECHNIQUES FOR UNDERSTANDING AND CONTROLLING RESIDUAL VIBRATIONS (MICROGRAVITY ASPECTS)

Daniele FRANCESCONI, Pietro Carlo MARUCCHI-CHIERRO, Roberto ULLIO

Alenia Spazio S.p.A. (*)

ABSTRACT

New computation and experimental methods are required to meet the targets of microgravity requirements in modern space system projects.

For example, in the Columbus project accurate analysis needs detailed monitoring of the system dynamics behaviour in terms of acceleration levels up to 1000 Hz for microgravity aspects.

While Statistical Energy Analysis (S.E.A.) will have to be introduced in order to analyse high modal density ranges, a classical computation method such as F.E.M. has to be updated in order to increase its capabilities for the monitoring of the low modal density structural dynamics: **Component Mode Synthesis (C.M.S.)**, linking substructuring approach to efficient dynamics oriented reduction algorithms, permits a strong subsystem zooming which implies an accurate monitoring of the dynamics of the system.

This paper illustrates the main features of a particular CMS technique and the capabilities of the method are shown in simple but meaningful examples.

Keywords: Microgravity. Substructuring. Component mode synthesis. Modal analysis.

1. SUBSTRUCTURING

In structural analysis, substructuring is the approach which considers a complex structure (system) as a set of functional parts (components). This technique has been conceived as a tool able to give the engineer useful hints in the design phase. Indeed, in case overall performances of the system have to be solved, the study of the interactions among each component (subsystem) allows a better comprehension of the involved phenomena.

Furthermore, the entire design development phase is strongly rationalised: in case of application to great projects, the analysis of the system obtained by

assembling the models of each component let the analyst follow and eventually suggest modifications either on the component, or on the interface configuration (geometry and physical characteristics) during the development of the job, in order to force the design, right from the beginning, to be a function of the performances to be achieved (i.e. a certain dynamical behaviour in operating conditions).

The alternative approach to such a procedure consists of evaluating the requirements of the product when the project has reached a terminal status, with models or tests performed on the complete system: the development of the design is less efficient and it could be very difficult to try corrective actions without wasting a great deal of sources.

2. REDUCTION

The adoption of a substructuring technique in dynamic analysis to develop a certain project does not exclude, in principle, the use of component models with a high number of degrees of freedom, particularly for those parts of the structure most difficult to model, such as joints, or when the range of analysis has to be increased towards high frequencies; indeed, structural mass and stiffness matrices produced by a relatively dense mesh (i.e. those used in static analysis) can also be used.

However, the assembly of structural models (sub-structures) with a high number of DOF's (many thousands) can induce the following criticalities:

- * time and cost associated to the complete structure analysis
- * data evaluation and management
- * hardware and software computation limits

All the preceding considerations justify the need for efficient reduction methods for complex systems.

(*) Alenia Spazio SpA is a Company of ALENIA SpA, the new Company belonging to the IRI-FINMECCANICA Group, resulting from the merger of Aeritalia and Selenia, taking over full responsibility for their functions, responsibilities and activities.

3. SUBSTRUCTURING TECHNIQUES IN DYNAMIC ANALYSIS

3.1 Component mode synthesis approach

In the analysis of a complex system, Rayleigh/Ritz transformation algorithms can be associated with substructuring and the following procedure applied:

- * analyse each component and create a simplified mathematical model which represents in a satisfactory way the dynamic behaviour of **low modal density range** (component reduction).
- * assemble the simplified models of each component in order to study the global structure dynamic behaviour.

This technique is named **Component Mode Synthesis (CMS)** (Refs. 1, 2).

Generally, the dynamic behaviour of the reduced component is described with a Ritz vectors basis including normal modes obtained in free-free, or free-constrained, or constrained-constrained conditions.

One of these Ritz reduction methods (Mac Neal) uses a set of normal modes obtained in a free-free analysis corrected by the effect of the residual flexibility of the structure at the connection points in order to take into account the effect of the interactions between components. It has to be underlined that such a data base (except for rotational DOF's) could also be obtained from an experimental modal analysis; rotational DOF's can then be added by means of interpolation techniques (Refs. 3, 4).

3.2 Component mode synthesis-Mac Neal method (Ref. 4)

The general equation of motion of a given supposed undamped subsystem is:

$$M \ddot{x} + Kx = F \quad (1)$$

\ddot{x} , x represent respectively acceleration and physical displacement vectors; M , K are respectively n DOF's mass and stiffness matrices; μ_i is the i^{th} eigenvalue; we can furthermore partition x and f vectors as follows:

x_b represent the degrees of freedom of interface to adjacent substructures;

x_o are the internal physical DOF's;

f_b are the interaction forces;

N_k represents the matrix of first normal modes of the substructure (kept modes):

$$N_k = [\Phi_1, \Phi_2, \dots, \Phi_k].$$

The truncated residual flexibility matrix is defined as (2):

$$Z_b = \sum_{i=k+1}^N \frac{\Phi_i^t \Phi_i}{\mu_i} \quad (2)$$

We suppose now that the displacement vector of the subsystem is given by the **Ritz transformation** illustrated in (3):

$$\begin{bmatrix} x_o \\ x_b \end{bmatrix} = \begin{bmatrix} N_{ko} & Z_{ob} \\ N_{kb} & Z_{bb} \end{bmatrix} \begin{bmatrix} q_k \\ q_b \end{bmatrix} = \beta_1 q \quad (3)$$

where

$$q = \begin{bmatrix} q_k \\ q_b \end{bmatrix}$$

is a vector of generalised coordinates and N_k , Z matrices have been partitioned at the internal and interface DOF's.

Applying the transformation (3) to the equation (1) we obtain the equation of the reduced subsystem which is clearly a consistent Ritz reduction:

$$M_1^r \ddot{q} + K_1^r q = F^r \quad (4)$$

with:

$$K_1^r \cong \beta_1^t K \beta_1$$

$$M_1^r \cong \beta_1^t M \beta_1$$

$$F_1^r \cong \beta_1^t F$$

The equation (4) can be further transformed in order to permit easy coupling between subsystems.

From equation (3), it can be obtained:

$$q_b = -Z_{bb}^{-1} N_{kb} q_k + Z_{bb}^{-1} x_b$$

and hence:

$$q = \begin{bmatrix} I & O \\ -Z_{bb}^{-1} N_{kb} & Z_{bb}^{-1} \end{bmatrix} \begin{bmatrix} q_k \\ x_b \end{bmatrix} = \beta_2 \begin{bmatrix} q_k \\ x_b \end{bmatrix} \quad (5)$$

Applying the transformation (5) to the equation (4), it can be written:

$$\underline{M} \ddot{\underline{q}}^* + \underline{K} \underline{q}^* = \underline{F} \quad (6)$$

where:

$$\underline{M} = \beta_2' M_1' \beta_2 = \beta_2' \beta_1' M \beta_1 \beta_2 = \beta' M \beta$$

$$\underline{K} = \beta_2' K_1' \beta_2 = \beta_2' \beta_1' K \beta_1 \beta_2 = \beta' K \beta$$

$$\underline{F} = \beta_2 F_1' = \beta_2' \beta_1' F = \beta' F$$

being

$$\beta = \beta_1 \beta_2$$

and

$$\underline{q}^* = \begin{bmatrix} q_k \\ x_b \end{bmatrix}$$

With the last Ritz transformation, the interface physical degrees of freedom have been included in the vector \underline{q}^* of generalised coordinates.

Craig [Ref. 1, pag. 471] clearly shows coupling of two dynamically reduced subsystems in a free-free case by means of application of Lagrange equations with constraints at interface physical degrees of freedom. The Ritz reduced equations for two components (1 and 2) are :

$$\underline{M}^1 \ddot{\underline{q}}^{*1} + \underline{K}^1 \underline{q}^{*1} = \underline{F}^1$$

$$\underline{M}^2 \ddot{\underline{q}}^{*2} + \underline{K}^2 \underline{q}^{*2} = \underline{F}^2$$

(\underline{F}^1 and \underline{F}^2 are reactions at the common interface) imposing $\underline{F}^1 + \underline{F}^2 = 0$ and $x_b^1 = x_b^2 = x$

the equation of the assembled system becomes of the form:

$$\underline{M}^s \ddot{\underline{q}}^{*s} + \underline{K}^s \underline{q}^{*s} = 0 \quad (7)$$

with

$$\underline{q}^{*s} = \begin{bmatrix} q^1 \\ x_b \\ q^2 \end{bmatrix}$$

3.3 Simplified Mac Neal transformation (Ref. 6)

If we suppose to neglect the residual effect in the mass matrix, it can be shown that:

$$M_1' = \begin{bmatrix} N_k' M N_k & O \\ O & O \end{bmatrix} = \beta_3' M \beta_3$$

In this case, a transformation β_3 less accurate than β_1 has been used to reduce M :

$$x = N_k q_k = \begin{bmatrix} N_k & O \end{bmatrix} \begin{bmatrix} q_k \\ q_b \end{bmatrix} = \beta_3 q_k \quad (8)$$

the equation (4) becomes:

$$-11 \begin{bmatrix} N_k' M N_k & O \\ O & O \end{bmatrix} \begin{bmatrix} q_k \\ q_b \end{bmatrix} + \begin{bmatrix} N_k' K N_k & O \\ O & Z_{bb} \end{bmatrix} \begin{bmatrix} q_k \\ q_b \end{bmatrix} = \begin{bmatrix} N_k' \\ Z_{bb} \end{bmatrix} f_b$$

in this case, it can be verified that:

$$q_b = f_b, \text{ and} \quad (9)$$

$$x = N_{kb} q_k + Z_{bb} f_b$$

The layout of the assembly of two simplified Mac Neal components is represented in Fig. 1 (*). It has been shown that the components of the coupled system have been obtained by means of a Ritz reduction performed on FEM structural mass and stiffness matrices.

It can be stated generally that the eigenvalues r_1 of the system obtained by coupling the synthesised components with certain constraint equations represent the upper limit of the correspondent eigenvalues μ_i of a system obtained applying the same constraint equations on the unreduced components. The error ($r_1 - \mu_i$) depends on the Ritz vector basis used in the component transformation but it is not possible to state any rule about the exact error value estimation.

Anyway it is clear that the component bases of Ritz vectors necessary to obtain a good approximation of the model must be such that a linear combination of these vectors can constitute a good approximation of the requested eigenvectors.

(*) See Figures at the end of the paper

Mode type (i,j,k) :
 i : nodal lines along x axis (fig. 2)
 j : nodal lines along y axis
 k : nodal lines along z axis

REFERENCE STRUCTURE		COMPONENT A (28 MODES + RESIDUALS) COMPONENT B (28 MODES + RESIDUALS)		
FREQUENCY	MODE TYPE	FREQUENCY	MODE TYPE	VARIATION
6.56E+01	(2,0)	6.56E+01	(2,0)	-
1.20E+02	(1,1)	1.20E+02	(1,1)	-
1.83E+02	(3,0)	1.83E+02	(3,0)	-
2.54E+02	(2,1)	2.54E+02	(2,1)	-
3.63E+02	(4,0)	3.63E+02	(4,0)	-
4.15E+02	(3,1)	4.15E+02	(3,1)	-
5.99E+02	(5,0)	5.99E+02	(5,0)	-
6.16E+02	(4,1)	6.17E+02	(4,1)	0.16%
6.25E+02	(0,2)	6.25E+02	(0,2)	-
6.84E+02	(1,2)	6.84E+02	(1,2)	-
8.01E+02	(2,2)	8.01E+02	(2,2)	-
8.70E+02	(5,1)	8.70E+02	(5,1)	-
9.35E+02	(6,0)	9.36E+02	(6,0)	0.1%
1.01E+03	(3,2)	1.01E+03	(3,2)	-
1.18E+03	(6,1)	1.19E+03	(6,1)	0.8%
1.26E+03	(4,2)	1.26E+03	(4,2)	-
1.32E+03	(7,0)	1.32E+03	(7,0)	-
1.51E+03	(0,0,2)	1.56E+03	(0,0,2)	3.3%
1.56E+03	(5,2)	1.56E+03	(5,2)	-
1.57E+03	(7,1)	1.57E+03	(7,1)	-
1.79E+03	(8,0)	1.79E+03	(8,0)	-
1.83E+03	(0,3)	1.83E+03	(0,3)	-

Table 1 - List of modal characteristics of the assembled system compared with the reference structure

4. CASE TEST N.1

4.1 Test description

We describe an application of a CMS - Mc Neal technique for two panels that we supposed to connect uniformly (ideally elastic, isothropic, homogeneous welding). In practice, we performed the following steps:

- generation of the FEM mathematical model of the structure shown in Fig.2 (Reference Structure)
- analysis of the Reference Structure (Reference Analysis)
- division in half of the reference structure, that is generation of two equal FEM models (components A, B in Fig. 3)
- MacNeal synthesis of each component starting from their FEM structural matrices
- constraint equations imposition in order to generate the mathematical model of the synthesised system (Fig. 4).

Tests have also been performed to understand the reliability of bare truncated modal bases as component mathematical models: the mathematical model of the component A is still a fixed Mac Neal synthesis, while the component B is represented by a

bare truncated modal basis the number of modes of which has been varied in order to evaluate their influence on the response of the system.

4.2 Analysis of the results

Frequencies and modes of the solved system and percent variations relative to the reference structure have been listed in the annexed tables.

In Table 1, second column, data refer to a system obtained by assembling two substructures both represented by a truncated modal basis (30 modes) and by a residual flexibility matrix.

A very good correlation can be deduced between the approximated system and the reference structure (Table 1).

Two of these correlated modes in Fig. 5 and in Fig. 6. Therefore, to obtain the convergence to the first 22 elastic modes of the reference structure, we solved an eigenvalue problem in which the matrices have order 56*56. The original structural matrices have order 875*875 (Fig. 2).

An analysis of results obtained using a truncated modal basis (28 modes) without the correction effect given by the residual flexibility matrix (component B) and a truncated modal basis with correction effect (component A) gives the results shown in Table 2 (see page 5).

REFERENCE STRUCTURE		COMPONENT A (28 MODES + RESIDUALS) COMPONENT B (28 MODES)			COMPONENT A (28 MODES + RESIDUALS) COMPONENT B (24 MODES)		
FREQUENCY	MODE TYPE	FREQUENCY	MODE TYPE	VARIATION	FREQUENCY	MODE TYPE	VARIATION
6.56E+01	(2,0)	6.80E+01	(2,0)	3.6%	6.86E+01	(2,0)	4.5%
1.20E+02	(1,1)	1.21E+02	(1,1)	0.8%	1.21E+02	(1,1)	0.8%
1.83E+02	(3,0)	1.83E+02	(3,0)	-	1.83E+02	(3,0)	-
2.54E+02	(2,1)	2.56E+02	(2,1)	0.8%	2.56E+02	(2,1)	0.8%
3.63E+02	(4,0)	3.74E+02	(4,0)	3.0%	3.78E+02	(4,0)	4.1%
4.15E+02	(3,1)	4.18E+02	(3,1)	0.7%	4.18E+02	(3,1)	0.7%
5.99E+02	(5,0)	5.99E+02	(5,0)	-	6.00E+02	(5,0)	0.2%
6.16E+02	(4,1)	6.26E+02	(4,1)	1.6%	6.26E+03	(0,2)	1.6%
6.25E+02	(0,2)	6.29E+02	(0,2)	0.6%	6.29E+03	(4,1)	0.6%
6.84E+02	(1,2)	6.85E+02	(1,2)	0.1%	6.86E+02	(1,2)	0.3%
8.01E+02	(2,2)	8.07E+02	(2,2)	0.7%	8.09E+02	(2,2)	1.0%
8.70E+02	(5,1)	8.75E+02	(5,1)	0.6%	8.75E+02	(5,1)	0.6%
9.35E+02	(6,0)	9.66E+02	(6,0)	3.3%	9.76E+02	(6,0)	3.3%
1.01E+03	(3,2)	1.01E+03	(3,2)	-	1.02E+03	(3,2)	1.0%
1.18E+03	(6,1)	1.22E+03	(5,1)	3.4%	1.22E+03	(6,1)	3.4%
1.26E+03	(4,2)	1.27E+02	(4,2)	0.8%	1.28E+03	(4,2)	1.6%
1.32E+03	(7,0)	1.32E+03	(7,0)	-	1.33E+03	(7,0)	0.7%
1.51E+03	(0,0,2)	1.58E+03	(5,2)	1.2%	1.58E+03	(7,1)	1.2%
1.56E+03	(5,2)	1.58E+03	(7,1)	0.6%	1.59E+03	(5,2)	1.9%
1.57E+03	(7,1)	1.84E+03	(0,3)	0.5%	1.84E+03	(0,3)	0.5%
1.79E+03	(8,0)	1.86E+03	(8,0)	3.9%	1.88E+03	(1,3)	*
1.83E+03	(0,3)	1.88E+03	(1,3)	*	1.89E+03	(8,0)	5.0%

Table 2 - List of modal characteristics of the assembled system compared with the reference structure

Obviously, increasing/decreasing the number of modes contained in the truncated basis gives better/worse results (Fig. 7, Table 2, 3).

Consider now the system mode (0,0,2): the mode (0,0,2) is not included in the basis of the component modes and therefore the system mode (0,0,2) cannot be well synthesised.

The residual flexibility matrix 'replaces' the lack of the component mode (0,0,2): the system mode (0,0,2) is still correlated to the reference mode (0,0,2) (Fig. 8, Table 1).

Indeed, including the residual flexibility matrix is equivalent to adding a set of mode shapes obtained

taking into account the interface configuration to the truncated normal modes basis.

Particular attention has to be paid to the frequency response functions. It is shown in Fig. 9 that there is a very good correlation between the levels of the synthesised system and the reference, when the residual flexibility matrix is taken into account. This aspect of the analysis has to be strongly underlined when the vibration control of structural dynamic behaviour has to be made on levels (for example RMS acceleration in microgravity).

COMPONENT A (28 MODES + RESIDUALS) COMPONENT B (28 MODES)			COMPONENT A (28 MODES + RESIDUALS) COMPONENT B (16 MODES)			COMPONENT A (28 MODES + RESIDUALS) COMPONENT B (13 MODES)		
FREQUENCY	MODE TYPE	VARIATION	FREQUENCY	MODE TYPE	VARIATION	FREQUENCY	MODE TYPE	VARIATION
6.96E+01	(2,0)	6.1%	6.96E+01	(2,0)	6.1%	7.14E+01	(2,0)	8.8%
1.22E+02	(1,1)	1.6%	1.24E+02	(1,1)	3.3%	1.25E+02	(1,1)	4.1%
1.84E+02	(3,0)	0.5%	1.84E+02	(3,0)	0.5%	1.84E+02	(3,0)	0.5%
2.57E+02	(2,1)	1.2%	2.57E+02	(2,1)	1.2%	2.60E+02	(2,1)	2.4%
3.83E+02	(4,0)	5.5%	3.83E+02	(4,0)	5.5%	3.93E+02	(4,0)	8.2%
4.19E+02	(3,1)	1.0%	4.25E+02	(3,1)	2.4%	4.31E+02	(3,1)	3.8%
6.01E+02	(5,0)	0.3%	6.01E+02	(5,0)	0.3%	6.06E+02	(5,0)	1.2%
6.26E+02	(0,2)	0.2%	6.26E+02	(0,2)	0.2%	6.26E+02	(0,2)	0.2%
6.33E+02	(4,1)	2.7%	6.36E+02	(4,1)	3.2%	6.60E+02	(4,1)	7.1%
6.87E+02	(1,2)	0.4%	6.89E+02	(1,2)	0.7%	6.94E+02	(1,2)	1.5%
8.11E+02	(2,2)	1.2%	8.12E+02	(2,2)	1.3%	8.15E+02	(2,2)	1.7%
8.79E+02	(5,1)	1.0%	8.91E+02	(5,1)	2.4%	1.03E+03	(6,0)	10.1%
9.94E+02	(6,0)	6.3%	9.94E+02	(6,0)	6.3%	1.16E+03	*	*
1.02E+03	(3,2)	1.0%	1.04E+03	(3,2)	3.0%	1.17E+03	*	*
1.24E+03	(6,1)	5.1%	1.25E+03	(6,1)	5.9%	1.74E+03	*	*
1.28E+03	(4,2)	1.6%	1.29E+03	(4,2)	2.3%	1.84E+03	*	*
1.34E+03	(7,0)	1.5%	1.34E+03	(7,0)	1.5%	1.85E+03	*	*
1.59E+03	(7,1)	1.2%	1.66E+03	(7,1)	5.7%	1.97E+03	*	*
1.61E+03	(5,2)	3.2%	1.83E+03	(5,2)	17.3%	2.18E+03	(1,0,0)	44.3%
1.84E+03	(0,3)	0.5%	1.87E+03	*	*	2.23E+03	*	*
1.88E+03	(1,3)	*	1.97E+03	(8,0)	10.0%	2.60E+03	*	*
1.95E+03	(8,0)	8.9%	2.18E+03	(0,0,2)	44.3%	2.88E+03	*	*

Table 3 - List of modal characteristics of the assembled system compared with the reference structure

	REFERENCE PANEL (Analytical)	REFERENCE PANEL (MSC/Nastran)	Panel A	Panel B	Panel C
Units	S.I.	S.I.	S.I.	S.I.	S.I.
Length of plate (m)	1.0	1.0	0.6	0.4	0.6
Width of plate (m)	1.0	1.0	0.6	1.0	0.4
Side ratio a/b	1.0	1.0	1.0	0.4	1.5
Thickness of plate (m)	0.01	0.01	0.01	0.01	0.01
Young's modulus (N/m ²)	2.68 E+11	2.68 E+11	2.68 E+11	2.68 E+11	2.68 E+11
Poisson's ratio	0.3	0.3	0.3	0.3	0.3
Density (Kg/m ³)	7820.0	7820.0	7820.0	7820.0	7820.0

Table 4 - Physical parameters of the components and the reference models

5. CASE TEST N. 2

5.1 Test description

We describe a second application of a C.M.S. technique for three panels uniformly connected (named A, B, C) using a Mac Neal reduction algorithm (Refs 5, 7).

On the I-DEAS Systan module, it is possible to analyse the dynamics of a system composed of analytical and/or experimental modal components (coming from MSC/NASTRAN F.E.A. and/or testing), oriented and subsequently connected together using the MSC/NASTRAN superelement analysis.

In this case, we test the I-DEAS substructuring technique using the constraint equations defined on Systan module.

The substructures are assembled into a system using the displacement relationship (called constraint equation, see Fig. 10) between a dependent dof related to a node on one component and an independent dof related to a node on another component (Fig. 11).

In a general form, the constraint equation is a homogeneous equation with constant coefficients defined by:

$$a_0 \cdot X_0 + a_1 \cdot X_1 + a_2 \cdot X_2 + \dots + a_n \cdot X_n = 0$$

where:

$$\begin{aligned} X_0 &= \text{dependent dof} \\ X_1, \dots, X_n &= \text{independent dof} \\ a_0, \dots, a_n &= \text{constant coefficients} \end{aligned}$$

In this case, we use a constraint equation defined in the form:

$$a_i \cdot X_i + a_j \cdot X_j = 0$$

where:

$$\begin{aligned} a_i &= +1.0 \\ a_j &= -1.0 \\ X_i &= \text{dependent dof of component } i \\ X_j &= \text{independent dof of component } j \end{aligned}$$

We know that physical dof's, in I-DEAS systan module, are treated as independent dof's only if these are associated with residual flexibility effects and so we must include also the effects of residual flexibility in the MSC/NASTRAN analysis results.

If these dof's are not part of a connection, their associated residual flexibility is ignored and these dof's are automatically defined as dependent dof's through mode shape matrix.

5.2 Analysis of the results

For the verification of the results referred to the assembled system, we defined these two complete reference models simulating the coupled structure:

1. analytical free-free square plate
2. MSC/NASTRAN finite element analysis (frequencies, modal mass, modal stiffness)

For these reference models and for the corresponding substructures (panels A, B, C), Table 4 describes the physical parameters, Table 5 (see page 7) the type of F.E.A. and Table 6 (see page 7) describes the relative modal matrices.

From the point of view of the modal characteristics, we see that the substructuring technique using constraint equation is correct compared to MSC/NASTRAN reference model and quite correct compared to analytical model.

In fact, Table 7 (see page 8) shows the percent variations between the frequencies of the reference models (analytical and MSC/Nastran) and the frequencies referred to the assembled system.

For the computation of the transfer functions, we have added a structural damping ratio ($C/C_r = 0.02$) for all considered mode shapes.

The analysis of mode shapes shows that the extracted mode shapes, with single eigenvalue, have a very good correlation as regards the corresponding mode shapes of the two reference models (see Fig. 12).

	COMPONENTS				SYSTEM
	REFERENCE	PANEL A	PANEL B	PANEL C	PANEL A+B+C
	PANEL				RESIDUAL FLEXIBILITY
SOFTWARE	Mac/Nastran	Mac/Nastran	Mac/Nastran	Mac/Nastran	I-DEAS Syster
TYPE OF ANALYSIS	Normal mode	Normal mode	Normal mode	Normal mode	Normal mode
TYPE OF SOLVER	No reduction	No reduction	No reduction	No reduction	Transformation method
EIGENSOLUTION TECHNIQUE	MGIV	MGIV	MGIV	MGIV	Householder QR
CONNECTIONS (total number)	none	none	none	none	95 (*)
PHYSICAL DOFS					
independent	0	239	269	169	9
total number	726	95	61	61	834
dependent	0	0	0	0	0
master	0	0	0	0	0
restrained	0	0	0	0	0
free	0	0	0	0	0
MODAL DOFS					
independent	12	12	12	12	12
total number	0	0	0	0	36

Legend :
 (*) only in I-DEAS Syster module
 (**) relate to constraint equations

Table 5 - Type of F.E.A. for the components and the systems (reference and assembled)

Whereas the extracted mode shapes with double eigenvalues have a bad correlation as regards the corresponding MSC/NASTRAN reference model and also with respect to the analytical reference model. These last differences are only due to the mode shape extraction algorithm in presence of eigenvalues with multiple roots.

In fact, if we evaluate the responses of the system we note that the transfer functions of the assembled system and the MSC/NASTRAN reference panel are the same (see Fig. 13).

5.3 Observations

Moreover, on I-DEAS Syster module, it is possible to assemble substructures into a system using the connector elements.

The connector is a F.E.M. element composed of two different, but coincident, nodes each having up to six dof's (Fig. 14), which is used to define the connections between a node on one component and the coincident node on another one (Fig. 15).

When we create it, we define separate matrices for mass, stiffness and damping (viscous and hysteretic) where each matrix represents all relationships between the dof of both nodes.

Also, with this assembling technique, it is necessary to include, in the modal model of the substructures, the effects of residual flexibility if we want to obtain the right results.

Moreover, the reliability of the results referred to a system assembled using the connectors depend on the real difficulty of knowing the actual values of the stiffness for the connector elements (Ref. 8).

For this reason, it is not suggested to simulate continuous connection (welding) by means of a general scalar connector element, while it seems useful to use this kind of element to simulate the dynamic behaviour of simple mounts and springs.

6. CONCLUSIONS

The case tests performed here show that there is a very good correlation in terms of modal characteristics/forced responses between systems synthesised using the Mac Neal algorithm and the reference structures.

It can therefore be stated that Component Mode Synthesis techniques, optimising computation sources towards results accuracy, represent a powerful tool for the dynamics analysis of space structures at low modal density as regards microgravity aspects.

		COMPONENTS								SYSTEM	
		MSC/NASTRAN		PANEL A		PANEL B		PANEL C		PANEL A+B+C	
		Rows	Columns	Rows	Columns	Rows	Columns	Rows	Columns	Rows	Columns
MODAL MATRICES	Shape	726	12	294	12	330	12	210	12	870	12
	Mass	12	1	12	1	12	1	12	1	12	1
	Stiffness	12	1	12	1	12	1	12	1	12	1
	Damping	12	1	0	0	0	0	0	0	12	1
	Residual flexibility	0	0	239	239	269	269	169	169	0	0

Legend : (*) on I-DEAS Syster module

Table 6 - Modal matrices for the components and the systems (reference and assembled)

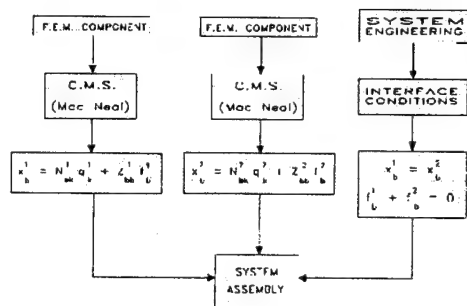
		SYSTEM							
		REFERENCE PANEL (analytical)		REFERENCE PANEL (MSC/Nastran)		PANELS A, B, C WITH RESIDUAL FLEXIBILITY			
		Mode shape	Value	Mode shape	Value	Mode shape	Value	Variation % (*)	Variation % (**)
NATURAL FREQUENCIES (Hz)	Mode number 7	(2, 2)	38.63511929	(2, 2)	37.270	(2, 2)	37.473	1.478	- 0.545
	Mode number 8	(1, 3)	55.79739932	(1, 3)	52.411	(1, 3)	54.064	3.142	- 1.105
	Mode number 9	(3, 1)	68.88050143	(3, 1)	66.518	(3, 1)	67.429	2.107	- 1.217
	Mode number 10	(3, 2)	88.73905691	(3, 2)	94.177	(3, 2)	94.502	4.291	- 0.365
	Mode number 11	(2, 3)	98.73905691	(2, 3)	94.177	(2, 3)	96.406	2.362	- 0.357
	Mode number 12	(4, 1)	173.4841283	(4, 1)	163.88	(4, 1)	164.36	5.259	- 0.255

Legend: (*) referred to analytical reference panel
 (**) referred to MSC/Nastran reference panel

Table 7 - Comparison of the frequencies between the reference systems and the assembled system

7. REFERENCES

- 1] Craig, Jr., R.R. - *Structural Dynamics*, John Wiley & Sons, New York
- 2] Bathe - *Finite Element Procedures in Engineering Analysis*, Prentice Hall.
- 3] Hermanski, Ostholt, H. - *Linking finite element with experimental modal analysis*, Journal of Modal Analysis, July 1987, pp.144-147.
- 4] Haisty, M., Springer, W.T. - *A simplified method for extracting rotational degree-of-freedom information from modal-test data*, IJMA, July 1986, pp.35-39.
- 5] Mc Neal, R.H. - *A Hybrid Method of Component Mode Synthesis*, Computer and Structures, Volume 1, 1971, pp.581-601.
- 6] Martinez, D.R., Gregory, D.L. - *A Comparison of Free Component Mode Synthesis Techniques Using MSC/NASTRAN*, SAND 83-0025, 1984.
- 7] Blevins - *Formulas for Natural Frequency and Mode Shape*, Van Nostran Reinhold, New York, 1977.
- 8] Ullio R. - *Sviluppo ed applicazione delle tecniche di sottostrutturazione in campo dinamico per problemi di microgravita' con il codice di controllo MSC-NASTRAN*, CL-TN-AI-607, ISSUE 01, December 1990.



\mathbf{N}_b^i : truncated mode basis of the component i at the interface degrees of freedom
 \mathbf{q}_b^i : first k modal coordinates of the component i
 \mathbf{f}_b^i : interface physical DOF's of the component i
 \mathbf{Z}_b^i : residual flexibility matrix of the component i partitioned at the physical correction DOF's

Fig. 1 - System assembly flow-chart

reference plate dimensions = $0.01 \times 0.90 \times 0.30$ [m³]
 $E = 21 \times 10^9$ N/m²
 $\rho = 7860$ Kg/m³
 $\nu = 0.3$

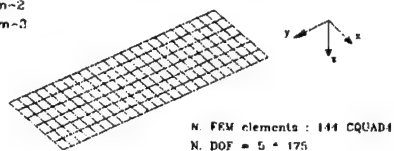


Fig. 2 - Reference structure

plates dimensions = $0.01 \times 0.45 \times 0.30$ [m³]
 $E = 21 \times 10^9$ N/m²
 $\rho = 7860$ Kg/m³
 $\nu = 0.3$

component A

component B

N. FEM elements = 72 CQUAD4
 N. DOF = 450

Fig. 3 - Components: F.E.M. models

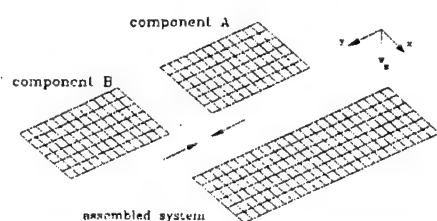


Fig. 4 - Assembled system configuration

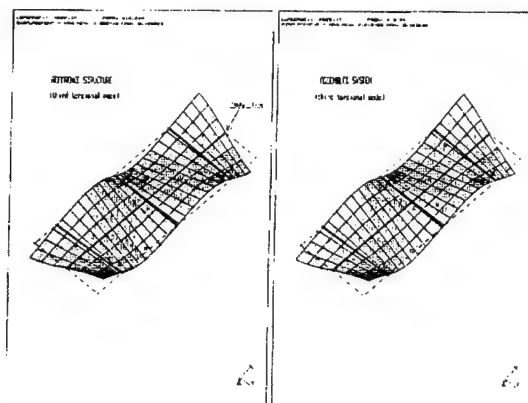


Fig. 5 - Comparison of third torsional modes

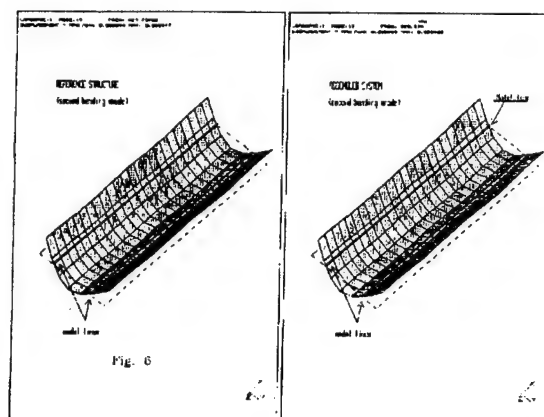
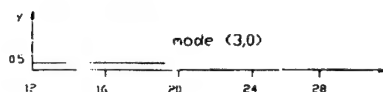
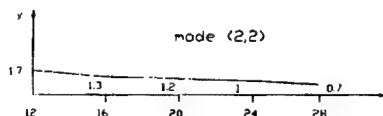
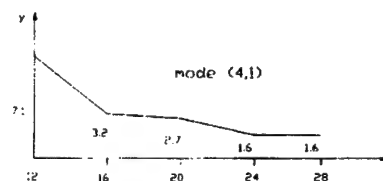
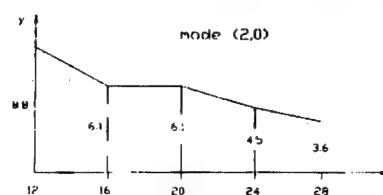


Fig. 6 - Comparison of second bending modes



x = number of nodes in the truncated basis of component B
 y = percent variation from the eigenfrequency of the reference structure

Fig. 7 - Effect of number of modes included in a truncated component modal basis on the response of the assembled system

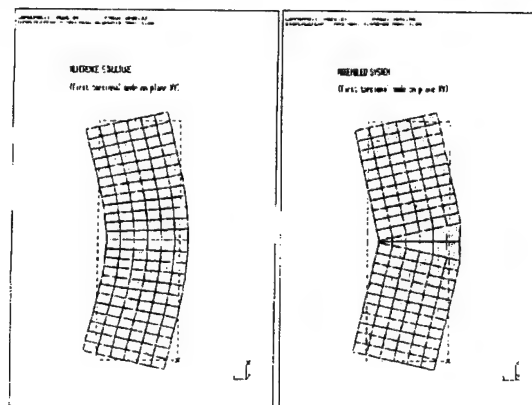


Fig. 8 - Comparison of modes (0,0,2)

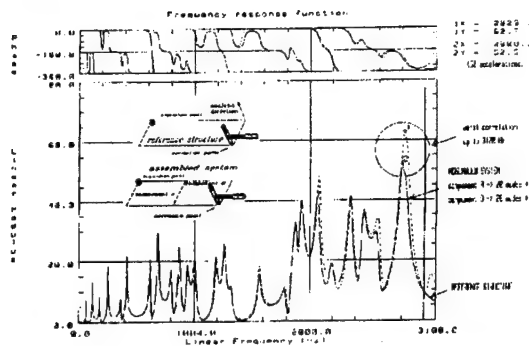
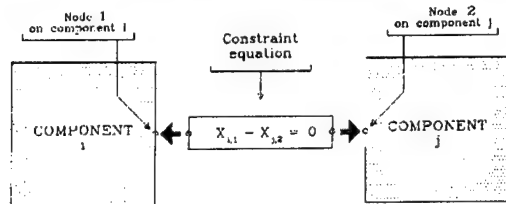


Fig. 9 - Comparison between the forced responses obtained from the reference structure and the assembled system (component A and B contain 28 modes and residual flexibility matrix)



$X_{1,1}$ = dependent dof
(Component 1, Node 1, Direction X)

$X_{2,2}$ = independent dof
(Component 2, Node 2, Direction X)

Fig. 10 - Example of the connection between two generic components using the systan constraint equations

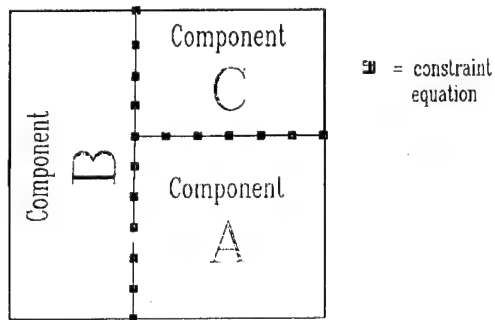


Fig. 11 - Description of the substructuring technique with constraint equations

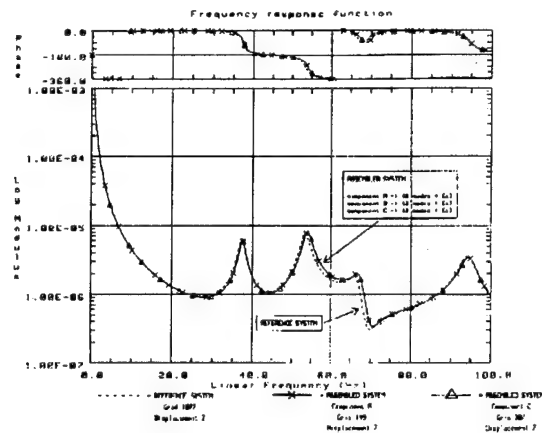
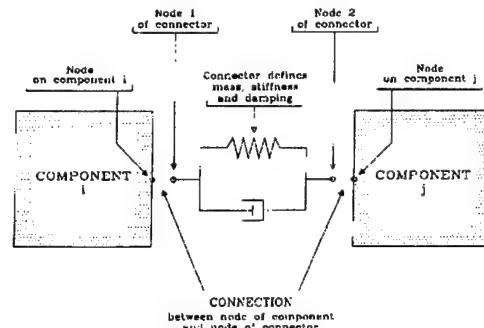


Fig. 13 - Comparison between the transfer functions of the assembled system and the MSC/NASTRAN reference system



ALL FOUR NODES AT THE CONNECTION ARE COINCIDENT

Fig. 14 - Example of the connection between two generic components using the systan general scalar connector elements

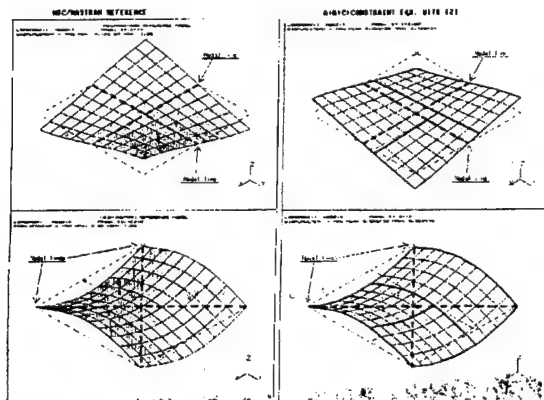


Fig. 12 - Mode shapes of the reference and assembled system

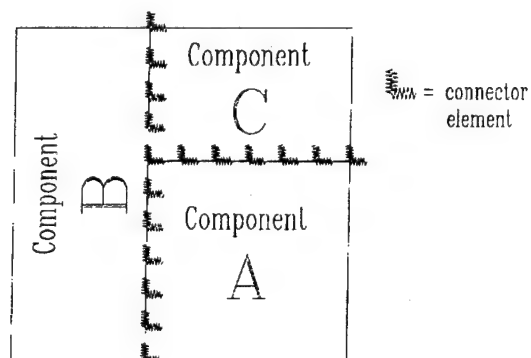


Fig. 15 - Description of the substructuring technique with connector elements

**SESSION
2.3.A**

**ANALYSIS
IV**

METHODS

PRECEDING PAGE BLANK NOT FILMED

N92-23828

548-39

84740

MINIMIZATION OF VIBRATIONS BY BROADBAND SENSITIVITY APPROACH

A. GIRARD, J. CHATELAIN, N. ROY

INTESPACE
18 Avenue Edouard Belin
Toulouse, FRANCE

ABSTRACT

The transmissibility of vibrations due to mechanical sources through complex structures may be reduced by adequate modification of structural parameters. In order to globally account for uncertainties in the frequency content of the real environment, a sensitivity analysis on frequency responses due to broadband excitation is performed. Simplifying assumptions on the relationship between the physical parameters and the element matrices lead to an efficient computation of modal parameter derivatives expressed in the modal basis. Localization of sensitive zones, followed by estimations of the modified structure's responses give the way to obtain a minimal vibration level. This paper presents first a theoretical description, then an application to a beam truss in order to illustrate the minimization of dynamic transmissibilities between excitation and reaction forces.

Keywords : Dynamic Structural Analysis, Optimization, Frequency Dynamic Response

1 INTRODUCTION

A mechanical source of vibration transmits excitation to the entire structure through its support ; the level of vibration transmitted may be reduced by acting on the support physical properties. This may be obtained through a sensitivity analysis on modal parameters and frequency response functions with respect to the physical design parameters. After localization of sensitive zones, a first order estimation may then be performed on the modified structure's responses.

The first work performed at INTESPACE on this subject concerned responses due to sinusoidal excitation ¹, where attention was focused on responses at a given frequency.

However, the excitation source for a structure may be well known but random in nature, being described by a particular power spectral density (PSD) function. Other times, the excitation may be sinusoidal in nature but with uncertainties existing either in the frequency content of excitation or in the natural frequencies of the finite element model. This second case leads us again to consider a random type excitation where the excitation PSD can be considered

as a weighting function ². For these reasons attention was focused on responses within a frequency range. In this paper, the same approach is used and adapted to deal with peaks in the frequency range of interest.

After a presentation of broadband analysis, the method is applied to a medium size beam truss in order to minimize dynamic transmissibilities between excitation and reaction forces.

2 FORMULATION

2.1 Response evaluation

In the frequency domain, the response $y(\omega)$ of a structure is related to the excitation $x(\omega)$ by the frequency response function (FRF) $X(\omega)$:

$$y(\omega) = X(\omega) x(\omega) \quad (1)$$

The general form of basic FRF (flexibility $G(\omega)$, transmissibility $T(\omega)$, or dynamic mass $M(\omega)$) of a structure, expressed in a basis of constraint modes and fixed junction normal modes ³ is given by :

$$X(\omega) \approx \sum_{k=1}^m A_k(\omega) \tilde{X}_k + \tilde{X}_{res} \quad (2)$$

where

$$\tilde{X}_{res} = \tilde{X}_{stat} - \sum_{k=1}^m \tilde{X}_k \quad (3)$$

with

$A_k(\omega)$ = dynamic amplification for mode k , complex dimensionless, depending on natural frequency $\omega_k = 2\pi f_k$ and damping coefficient η_k (structural) or ξ_k (viscous), giving a maximum amplification $Q_k = 1/\eta_k$ or $1/2\xi_k$

\tilde{X}_k = modal effective parameter (real, independent of ω)

\tilde{X}_{res} = residual term
(in the presence of modal truncation)

\tilde{X}_{stat} = static term

In case of a random excitation described by the PSD $W_x(\omega)$ over the frequency range (f_{min}, f_{max}) , the PSD response $W_y(\omega)$ is given by :

$$W_y(\omega) = |X(\omega)|^2 W_x(\omega) \quad (4)$$

leading to the mean square value :

$$\Psi_y^2 = \int_{f_{min}}^{f_{max}} |X(f)|^2 W_x(f) df \quad (5)$$

If $W_x(\omega)$ is slowly varying in the vicinity of the natural frequencies, and if the modes are relatively well separated, for the FRF defined in Eq (2), the mean square value can be discretized by the following sum over the modes within the frequency range :

$$\Psi_y^2 = \sum_k \frac{\pi}{2} f_k Q_k \tilde{X}_k^2 W_x(f_k) + \tilde{X}_{res}^2 \Psi_x^2 \quad (6)$$

So, for sinusoidal or random excitations, the response in a given frequency band depends essentially on three fundamental modal parameters (natural frequency, damping coefficient and effective parameter) completed by a residual term. If attention is focused on one mode k , the dominant mode for example, the maximum response can be approximated by :

$$|y(f_k)| = Q_k |\tilde{X}_k| |x(f_k)| \quad (7)$$

$$W_y(f_k) = (Q_k \tilde{X}_k)^2 W_x(f_k) \quad (8)$$

2.2 Sensitivity analysis

Let us consider a structure composed of structural parts p which are related to structural parameters x_p . By assuming that the physical parameter x_p is entirely and uniquely associated with the structural part p and in no way alters the geometry of the structural nodes, along with the assumption that mass, damping and stiffness element matrices are proportional to a power n of x_p , the derivatives of the element matrices can be expressed as :

$$(M_p \text{ or } C_p \text{ or } K_p)_{x_p} = \frac{n}{x_p} (M_p \text{ or } C_p \text{ or } K_p) \quad (9)$$

The contribution of each part p to a given mode can be described by introducing real valued energy-type contribution factor, t_p , which satisfy the summation rule. Among the many factors identified in reference ¹, two of the most useful are those corresponding to the part's contribution to the modal kinetic $t_p(m_k)$ and strain energies $t_p(k_k)$ where m_k and k_k are respectively generalized mass and stiffness for mode k .

These contribution factors play a double role of identifying the important parts for a given mode, as well as entering directly into the equations of the

derivatives of the modal parameters ; for example the derivative of the natural frequency is given by :

$$\frac{\partial \omega_k^2}{\partial x_p} = \frac{\omega_k^2}{x_p} [n_{K_p} t_p(k_k) - n_{M_p} t_p(m_k)] \quad (10)$$

The mode shape derivatives expressed in the base of normal modes lead to similar equations (1, 4, 5). Finally the derivative of modal effective parameters and residual terms can be established ².

Notice that, due to two simplifying assumptions concerning the dependence of element matrices with respect to x_p^n , and the projection of the derivatives in a truncated modal basis, this first order development is very efficient. In practice a judicious choice of n and an adequate truncation limit the errors.

2.3 Minimization of vibrations

The minimization process requires first the choice of a cost function to minimize. If the objective is to globally reduce the response level in the frequency range of interest, considering for example the mean square value of the response, Eq.(6) should be used. If the objective is to reduce the value of the most important peak in the range, Eq. (7) or Eq. (8) should be used.

Then a sensitivity analysis may be performed on the concerned modal parameters and the appropriate physical parameters are then selected from the magnitude and signs of derivatives.

After establishing variations of the best physical parameters, a first order estimation of the modified value of modal parameters is computed by :

$$\hat{u} = u + \frac{\partial u}{\partial x_p} \frac{\Delta x_p}{x_p} \quad (11)$$

with $u = f_k, \tilde{X}_k, Q_k, W_x(f_k)$ or \tilde{X}_{res}

The new value of the cost function can be obtained by substituting the modified values of the modal parameters directly into the cost function. Once a satisfactory estimation has been found, the modifications are introduced in the finite element model, and a new calculation of the modified structure is performed. The number of iterations will be related to the step size. Notice that the cost function may change during the process, for example if the predominant mode changes.

3 APPLICATION TO A PLANE TRUSS

3.1 Definition and objectives

The approach presented above is illustrated by considering the plane truss of Fig. 1. The structure is composed of beams with circular sections. The support beam with a radius of 160 mm (non modifiable) is assumed massless. Its ends are rigidly bounded to the clamped point A. The truss to optimize is composed of a reference structure (solid lines in Fig. 1) and of possible struts (dotted lines). Symmetry of the structure results in five independent radii as

physical parameters. The radius of the beams of the reference structure is 12 mm and 0 for the struts.

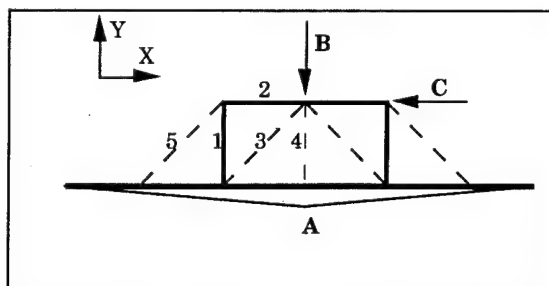


Fig. 1 : Plane truss

Structural damping is assumed constant with a value of $\eta = 0.02$. The structure is submitted to independent excitations in the Y direction at the top middle edge (B) and in the X direction at the top right corner (C).

The responses considered here are the vertical reaction $(F_Y)_A$ and the moment reaction $(M_Z)_A$ about the Z axis at A. In addition the total mass must not increase more than 50% and radius of the initial beams must not decrease more than 50%.

The minimization concerns the maximum value of transmissibilities given by :

$$T_{AB} = (F_Y)_A / (F_Y)_B \quad \text{and} \quad T_{AC} = (M_Z)_A / (F_X)_C \quad (12)$$

Two objectives have been examined :

- minimization without limitation of the frequency range,
- minimization within a frequency range limited to a given frequency f_{\max} .

3.2 Preliminary analysis

Due to symmetry, effects of the two excitations are uncoupled : the vertical force excites only symmetric behaviour, whereas the horizontal force excites antisymmetric behaviour of the truss with slight symmetric coupling due to the excitation location on beam BC.

A preliminary analysis was performed with artificial massless springs in the X and Y directions connecting point B and the middle of the support beam, in order to identify the tendencies and determine initial values for the sensitivity analysis.

Results are presented in Fig. 2 which gives the variation of natural frequencies and effective transmissibilities with respect to the ratio (spring stiffness / initial static stiffness). The results are given for ratios equal to 10^n ($n = -1 \dots 4$) completed by intermediate values coming from a sensitivity analysis.

The effective transmissibility curves (Fig. 2.b) have intersections at values about 0.5. This situation corresponds to 2 dominant modes contributing to half the static transmissibility 1. So if no limitation is assumed on the frequency content of the excitation, the FRF will have peaks about $Q_k/2$ for the frequency f_k . On the contrary, if an upper bound f_{\max} is assumed, it may be possible to shift the dominant modes beyond this frequency to decrease more significantly the levels. In order to be coherent with the constraints on the total mass, the frequency $f_{\max} = 400$ Hz has been considered here.

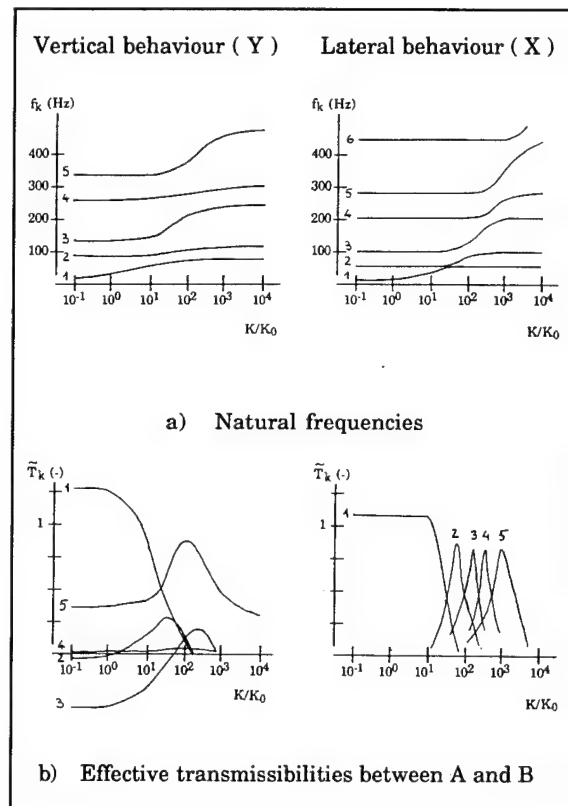


Fig. 2 : Modal parameters versus spring stiffness ratio

3.3 Minimization without frequency limitation

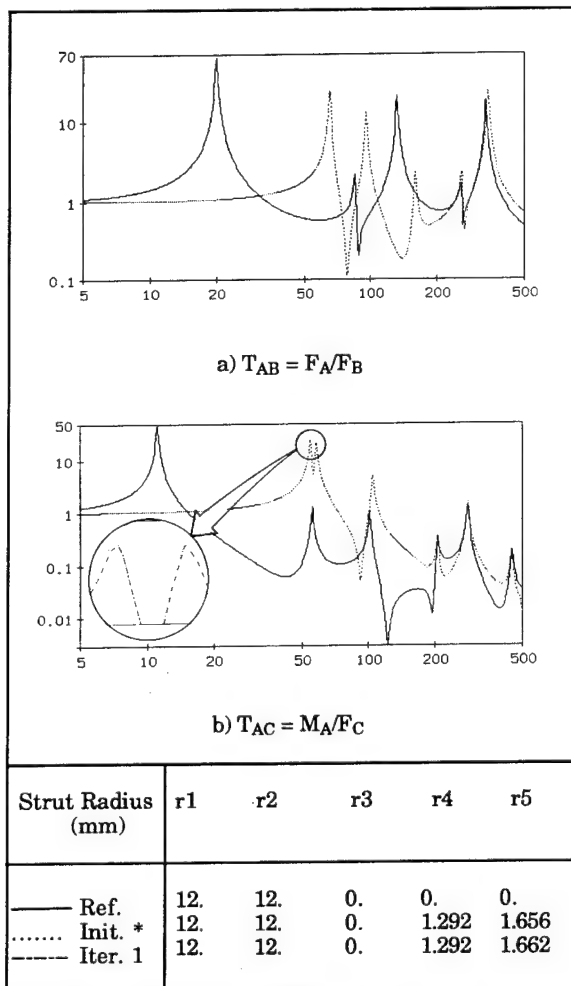
The previous results give a good initial configuration for a minimization of FRF by using real struts instead of the massless springs. The attention was focused on the first intersections found in the preliminary analysis. Equivalent struts with small radii have been chosen in order to get the spring stiffnesses. As little mass is added to the structure, little change is expected.

The calculation was performed according to the following steps :

- select adequate struts, for example 4 and 5, and calculate the equivalent radii,

- perform a dynamic analysis to obtain natural frequencies and mode shapes, then calculate T_{AB} and T_{AC} ,
- perform a sensitivity analysis on the two dominant modes in each direction in order to find identical effective transmissibilities,
- perform a dynamic analysis on the modified structure for verification.

The FRF are plotted in Fig. 3 where equality of the two peaks can be noted for the two directions. The initial configuration was close to the optimum, thus only one iteration was performed to reach it. The maximum level is now about 25 and 22 for Y and X directions respectively instead of 63 and 48 for the reference model.



* identical to iteration 1 for Fig. 3a

Fig. 3 : Optimization without frequency limitation

3.4 Optimization with frequency limitation

The optimization was performed according to the following iterative process :

- Select the most efficient struts and beams to reach the objective with a minimum of physical parameters. Give an initial value to the associated radii and calculate mode shapes and FRF.
- Perform a sensitivity analysis on all modes lying in the range and on the dominant modes beyond f_{max} . Compute derivatives of natural frequencies and effective parameters as in Eq. (10).
- The choice of the power n in Eq. (9) was derived from considerations on the ratio of membrane to bending energy : kinetic energy for the mass and strain energy for the stiffness. This leads to $n = 2$ for mass and $2 \leq n \leq 4$ for stiffness.
- Perform a dynamic analysis on the modified structure in order to verify the estimations and iterate if necessary.

Three cases of increasing complexity have been considered :

- optimize the FRF T_{AB} only,
- optimize the FRF T_{AC} only,
- optimize the FRF T_{AB} and T_{AC} with the same truss.

For T_{AB} , the vertical strut 4 is the best candidate, leading to three physical parameters (with the two radii of the reference truss) to be optimized. The results are plotted in Fig. 4, the initial configuration gives a maximum value for T_{AB} at $f_{max} = 400$ Hz. This level is reduced with iteration 1 but two significant peaks appear in the frequency range. This problem is solved with the third iteration.

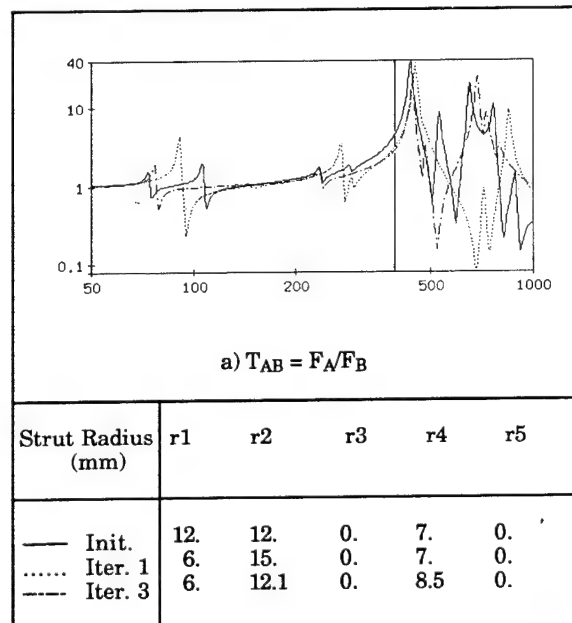


Fig. 4 : Optimization of T_{AB} with frequency limitation

For T_{AC} , the diagonal struts 3 and 5 have been selected, leading to four physical parameters to be optimized. The results are plotted in Fig. 5, the initial configuration gives a maximum level for T_{AC} at 400 Hz. After one iteration, this level is reduced and is equal to an increasing peak which appears just before 400 Hz.

For the last case, the same truss must satisfy the objective for the $(F_Y)_B$ and $(F_X)_C$ excitations considered separately. The struts 3, 4 and 5 have been selected leading to five physical parameters to be optimized. The results are plotted in Fig. 6.

3.5 Summary

The transmissibility levels found in each case are summarized in Table 1.

Configurations	Range (Hz)	F_A/F_B	M_A/F_C
Reference Truss	0 - ∞	63.	48.
Elements 1, 2, 4, 5	0 - ∞	25.	22.
Elements 1, 2, 4	0 - 400	3.2	*
Elements 1, 2, 3, 5	0 - 400	*	2.0
Elements 1, 2, 3, 4, 5	0 - 400	4.5	4.5

* : not considered

Table 1 : Optimum level summary

The results show the reduction levels which can be obtained for various configurations. This reduction, depending on the frequency contents of the excitation, may be very large.

4 CONCLUSION

The broadband sensitivity method, which can be adapted to various objectives, has been successfully applied to configurations of increasing complexity, leading to substantial level reductions with a limited number of iterations.

Future developments are planned to improve the efficiency of the analysis by a better accuracy of the response estimations and automation of the whole process. This approach is being incorporated into the general structural dynamic analysis software developed at INTESPACE⁶, in order to solve vibration level reduction problems in various areas, including space activities.

ACKNOWLEDGEMENTS

This research was supported by the Centre d'Etudes et de Recherche sur la Discrétion Acoustique des Navires (Toulon/Etudes).

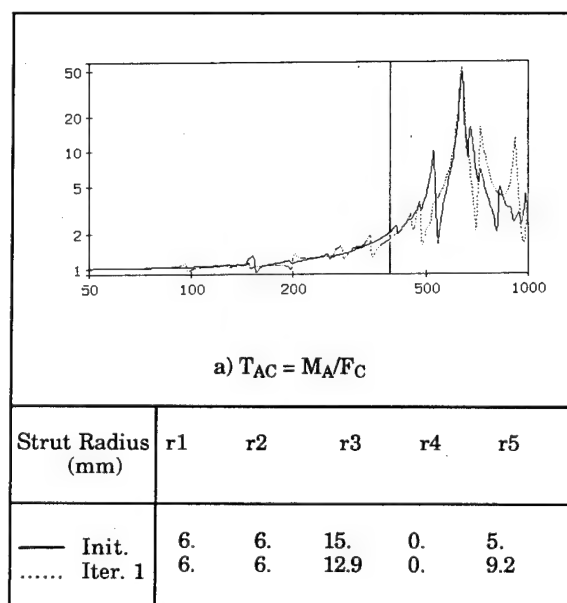


Fig. 5 : Optimization of T_{AC} with frequency limitation

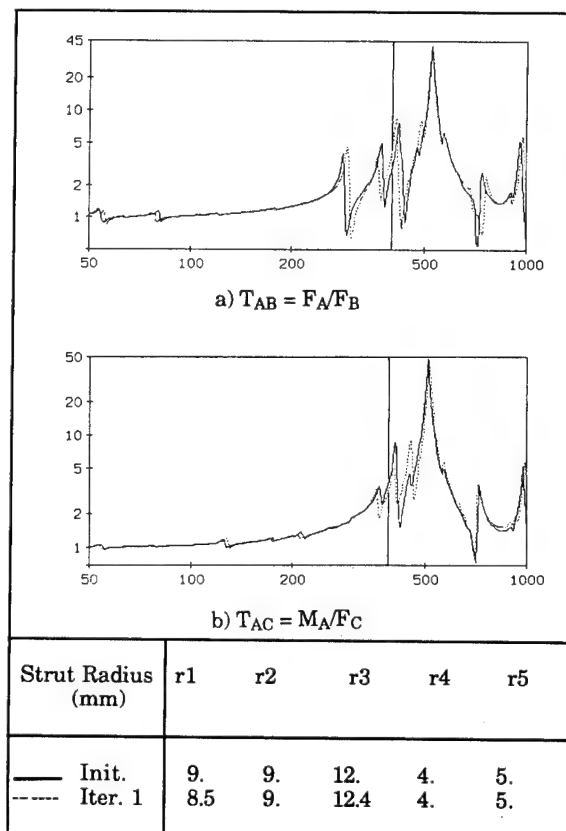


Fig. 6 : Optimization of T_{AB} and T_{AC} with frequency limitation

REFERENCES

- 1 Roy N.A., Girard A., Bugeat L.P., **Sensitivity Analysis of Structural Frequency Response Functions**, Proceedings, 7th Int. Modal Analysis Conference, pp 765-771, Las Vegas, 1989.
- 2 Roy N.A., Girard A., Bugeat L.P., **Sensitivity Analysis of Structural Random Frequency Functions**, Proceedings, 8th Int. Modal Analysis Conference, pp 954-960, Kissimmee, 1990.
- 3 Girard A., Imbert J.F., **Modal Effective Parameters and Truncation Effects in Structural Dynamics**, Proceedings, 5th Int. Modal Analysis Conference, pp 820-826, London, 1987.
- 4 Nelson R.B., **Simplified Calculation of Eigenvector Derivatives**, AIAA Journal, Vol. 14, No. 9, Sept. 1976.
- 5 Mills-Curran W.C., **Calculation of Eigenvector Derivatives for Structures with Repeated Eigenvalues**, AIAA Paper 89-1333-CP, 1989.
- 6 Bugeat L.P., Roy N.A., Imbert J.F., Girard A., **Integration of Analytical and Experimental Tools for Optimal Structural Design Under Dynamic Loads**, Proceedings, Int. Conference on Spacecraft Structures and Mechanical Testing, Noordwijk, The Netherlands, Oct. 1988.

N 92 - 23829

THE CONTINUOUS ELEMENTS METHOD

Peter H. Kulla

TeWiSoft GmbH
D-8201 Söchtenau

1 Abstract

The term Continuous Elements stands for a technique that avoids the discretization error inherent in Finite Elements. This is achieved by describing the dynamic stiffness matrix of an element of the structure in terms of the complete analytical solution of the underlying differential equations. The matrix elements are transcendental functions of the frequency and the matrix can not be split up into a mass and a stiffness matrix. Recently the method has been generalized by the author to include also two-dimensional Continuous Elements, what clearly broadens the scope of its applicability. In fact, it is this generalization which makes it a general purpose tool for Structural Dynamics. In the paper an outline of the Continuous Elements Method is given, the generalization to two-dimensional Continuous Elements is highlighted and the method is used to find the first eigensolutions of an L-shaped cantilever plate.

Keywords: Continuous Elements, Plates

2 Introduction

Mechanical systems are continuous in three spatial coordinates. For the purpose of analysis the actual system is replaced by a theoretical model. The complexity chosen for this model depends on the accuracy desired for the results and on the resources available for the investigation. The spectrum reaches from three-dimensional continuous models to simple lumped parameter approximations.

The choice of the mechanical model also implies a choice of the mathematical formulation of the problem and hence on the effort to solve the problem. After transformation to the frequency domain, continuous models are described by partial differential equations (PDEs) plus boundary conditions, whereas discrete models are described by sets of algebraic equations. To avoid the solution of PDEs, discrete models (e.g. Finite Elements) are in general preferred. The direct treatment of continuous systems, though historically older, has never reached the degree of popularity of the FE method. In the last years, however, direct continuous methods have gained some popularity. It is the main intention of this paper to draw the attention of a broader public to the availability of direct continuous methods in the form of Continuous Elements, to their advantages as compared to Finite Elements and also to their drawbacks.

The most prominent feature of Continuous Elements is that they, basically, avoid discretization and hence also discretization errors. The behaviour of a system is described by a dynamic stiffness matrix, that relates a displacement vector to its adjoined force vector. In contrast to discrete methods, the elements of this dynamic stiffness matrix are transcendental functions of the frequency. A splitup of the matrix into (frequency independent) mass and stiffness matrices is not possible and the toolbox developed for the solution of discrete systems is in large parts not adequate. New procedures are under development now to handle transcendental problems in an efficient and reliable way [7, 2]. On the other hand, the lack of a discretization error not only may give more accurate numerical results but also lead to a broader understanding of the theory of (structural) dynamic systems.

A serious restriction of the Continuous Elements Method has been the fact, that only one-dimensional Continuous Elements (typically beams and strings) have been available [6]. In certain cases (e.g. prismatic plate arrays or solar blankets [12, 11]), two-dimensional structural elements can be treated as one-dimensional elements if one direction can be eliminated.

General Two-dimensional Continuous Elements have been developed by the author since 1983 and are in use there since 1985 for the analysis of plate systems under static loads. The method was first published in 1989 [8]. It is obvious that the availability of two-dimensional Continuous Elements drastically broadens the scope of applicability of the method. This generalization, however, also includes one marked drawback: Two-dimensional Continuous Elements are based on a Fourier decomposition of the continuous boundary functions. (Note that for one-dimensional elements the boundary conditions are discrete and finite *a priori*.) The Fourier development has to be truncated somewhere and consequently the element matrix is not exact in the sense it was for one-dimensional elements. On the other hand, this drawback is not too serious from a practical point of view, since the truncation point can easily be controlled by the user and the effect of the truncation on the result is readily evaluated without reelementation of the structure.

The generalization of the Continuous Elements Method to include two-dimensional (plate) elements is based on a technique that was earlier used to investigate the natural frequencies and the related eigenforms of free rectangular plates [3, 4]. In these early works, the specific boundary conditions of the

plates to be analyzed were included at an early stage of the analysis. In contrast, the method to be outlined here formulates a plate element that is independent of specific boundary conditions. This allows for an assembly of plate elements to a more complex structure, where the specific boundary conditions of this structure are entered only after the assembly process. So all conceivable cases of boundary conditions are covered by only one element type.

The term "accurate" used in this context needs some clarification, however. Here it means, that only numerical (and no methodical) errors should be present in the result. In other words, the error should only be due to the finite word length of the compiler in use. Note however, that poor conditioning still may turn the result completely useless.

The term "continuous" in the title of this paper is another potential source of misunderstanding since it has different meaning to different people. When calling the approach "Continuous Elements Method", it was born in mind to make clear already in the name that no *a priori* spatial discretization was introduced. "Distributed Elements" is another common term that emphasizes this aspect. In contrast to the use outlined above, the word "continuous" is also used in the literature to distinguish methods that imply continuity of deformations and/or stresses across element boundaries from methods that do not imply this property. In the Continuous Elements Method continuity of deformations across element boundaries is explicitly used during the assembly of elements to a more complex structure and continuity of stresses follows implicitly from the solution of the differential equations.

The method to be demonstrated, though not new, has never been automated and cast into program modules, that would allow an average user to profit from it without going into the details of the approach. Rather, it was generally used for the individual solution of special problems by specialized people. Well, "never" is not quite true, since for a couple of years there are ongoing efforts to give a broader public access to the merits of the method. For a few classes of problems the method has been furnished with more or less user friendly surfaces and is in practical use with a few institutions.

SFVIBAT (Space Frame Vibration Analysis Tool) is one of the earlier products in this series. It was written at Chalmers University of Technology, Gothenburg, Sweden [1]. At the European Space Technology Centre (ESTEC), two program packages using Distributed Elements have been developed and are in use now: DISTEL (Distributed Elements) [11] can be used to investigate the dynamic behaviour of three axis stabilized spacecraft and VAMP-G (Vibration Analysis Modular Package) [5] is specialized to the analysis of spinning spacecraft. IDA (Interactive Dynamic Analysis) was written at RESSULT/TeWiSoft for the analysis of three-dimensional frames including damping. PLATTE was written at TeWiSoft for the analysis of plate systems under static loads. Certainly more program packages based on Continuous Elements exist, but the community supporting the method is just starting to organize regular channels for the exchange of ideas. The Availability of two-dimensional Continuous Elements can be expected to add strongly to the momentum of the idea.

The precision of the method is one of its strongest points. As a consequence, arbitrarily large elements can be used without loss of accuracy. The elementation of the method is determined by its geometric properties rather than by a certain *a priori* knowledge of the result to be obtained. Geometrically simple structures need not be cut down to pieces in order to get reasonable precision. Precision is a topic that has traditionally been treated in a somewhat casual way. ("Oh, better

than three percent!") Without going into details it is stated here, that certain fields of structural analysis like spectral decomposition, parameter reconstitution from spectral data and structural modification (model updating) virtually depend on a base of precise results, in specific precise eigensolutions. The usual test on natural frequencies alone may highly overestimate the precision of the results. This is the more true if arbitrary damping and gyroscopic effects are included.

3 One-Dimensional Continuous Elements

A typical one-dimensional continuous substructure is a beam. A beam is described by a set of Partial Differential equations (PDEs) with two independent variables, one being a parameter running along the beam axis and the other being the time. In this paper we restrict ourselves to linear systems with time constant parameters. Note that this restriction does not exclude tapered and twisted beams, for example. Also, beams with arbitrary prebending and/or prestress are included, if small disturbances of this nominal state are considered. This class of PDEs can always be transformed into the frequency domain without loss of generality. This eliminates the time at the cost of introducing the additional frequency parameter s . The general solution of the resulting Ordinary Differential Equations (ODEs) is given by the complete set of base solutions. If an ODE has constant parameters (with respect to the space coordinate), the base solutions are available in analytical form. Else, they can always be obtained by numerical integration of the ODE with n linearly independent initial conditions, where n is the order of the ODE. The difference to the analytical solution is only the runtime.

The deformations and forces at the two boundaries of the beam are then expressed in terms of the base solutions:

$$\mathbf{D}\mathbf{b} = \mathbf{d} \quad (1)$$

$$\mathbf{F}\mathbf{b} = \mathbf{f} \quad (2)$$

The vectors \mathbf{d} and \mathbf{f} contain the displacements and forces at the boundaries, the vector \mathbf{b} contains the base solutions and the matrices \mathbf{D} and \mathbf{F} relate the displacements and forces to the base solutions. The elements of \mathbf{f} and \mathbf{d} are adjoined in such a way that $\mathbf{d}^T \mathbf{f}$ is the "dynamic potential" of the element.

Premultiplying (1) with \mathbf{D}^{-1} and inserting \mathbf{b} into (2) gives

$$\mathbf{F}\mathbf{D}^{-1}\mathbf{d} = \mathbf{f} \quad (3)$$

$\mathbf{F}\mathbf{D}^{-1}$ is the dynamic stiffness matrix of the beam element. The eigensolutions of (3) with zero right hand side represent the natural frequencies and eigenforms of the free element. Since no discretization has been used, (3) contains an infinity of eigensolutions.

The assembly of the elements to a complete structure is essentially identical for all methods of structural analysis based on stiffness matrices. In contrast to standard methods, however, the system matrix obtained with the Continuous Elements method is exact and can therefore *not* be split up into frequency-independent mass and a stiffness matrices in general. After solution of the system equations the complete state of the system can be determined for every point of every element by back substitution of the solution of the system equations into the ODEs of the beam elements.

4 Two-Dimensional Continuous Elements

The most prominent example of a two-dimensional continuum is probably the plate. Here we restrict ourselves to Kirchhoff plates. The related PDE for transversal displacement w is given in non dimensional form:

$$\Delta \Delta w + \ddot{w} = p \quad (4)$$

where w is the plate's deflection, and p is the surface load. Dots stand for partial derivation w.r.t. time τ and the Laplace operator is defined in the coordinates ξ and η as

$$\Delta(\cdot) = (\cdot)_{,\xi\xi} + \frac{1}{\Phi^2}(\cdot)_{,\eta\eta} \quad (5)$$

with

$$\Phi = \frac{b}{a} \quad (6)$$

where a and b are the half plate lengths in ξ and η directions, i.e. $-1 \leq \xi \leq 1$ and $-1 \leq \eta \leq 1$. The inclinations of the plate's surface and the forces in the plate are defined in dimensionless form as

$$\Psi_\xi = -w_{,\xi} \quad (7)$$

$$\Psi_\eta = -\frac{w_{,\eta}}{\Phi} \quad (8)$$

$$m_\xi = -(w_{,\xi\xi} + \frac{\nu}{\Phi^2} w_{,\eta\eta}) \quad (9)$$

$$m_{\xi\eta} = -\frac{1-\nu}{\Phi} w_{,\xi\eta} \quad (10)$$

$$m_\eta = -(\frac{1}{\Phi^2} w_{,\eta\eta} + \nu w_{,\xi\xi}) \quad (11)$$

$$v_\xi = -(w_{,\xi\xi} + (2-\nu)\frac{w_{,\eta\eta}}{\Phi^2})_{,\xi} \quad (12)$$

$$v_\eta = -(\frac{w_{,\eta\eta}}{\Phi^2} + (2-\nu)w_{,\xi\xi})_{,\eta} \frac{1}{\Phi} \quad (13)$$

The Ψ are the inclinations of the plate surface, m are the bending moments in the plate, v are the effective vertical forces and with respect to τ it describes an initial value problem. The solution of (4) is composed of the solutions of the homogeneous and the inhomogeneous problems. It is tried to find a solution of the homogeneous problem under the following form:

$$w(\xi, \eta, \tau) = w_0 e^{\alpha\xi + \beta\eta + s\tau} \quad (14)$$

Inserting (14) into (4) with the right hand side of (4) equal to zero and dividing by (14) we get the characteristic equation of the plate:

$$(\alpha^2 + \frac{\beta^2}{\Phi^2})^2 + s^2 = 0 \quad (15)$$

Since the parameters contained in (15) are all squares, the values for the parameters are grouped in real or imaginary pairs with opposite sign. A positive value for a square parameter corresponds to hyperbolic sine and cosine functions in the respective independent variable (ξ, η or τ), whereas a negative value corresponds to standard (circular) sine and cosine functions.

The characteristic equation (15) can be fulfilled by tuning three parameters, α, β and s . The latter parameter defines the solution with respect to the variable time. We choose a harmonic motion with circular frequency ω :

$$s^2 = (j\omega)^2 = -\omega^2 \quad (16)$$

In addition to s one of the parameters α and β can be chosen freely and the other one follows from (15). Every combination of α, β and s that fulfills (15) represents an exact solution to the PDE (4) with zero right hand side. This gives us a host of solutions for the PDE (4).

5 Continuous Boundary Conditions

In contrast to the beam case treated earlier, the plate is a two dimensional domain with its boundary being one dimensional. The fact that the boundary conditions must be fulfilled on an infinity of points is a major obstacle to an exact solution of the problem. Only in rare cases exact solutions can be given. In general, however, the boundary conditions on the one dimensional continuous boundary are approximated by n discrete conditions.

The discretization introduces an error and it is mainly the technique of discretization which makes up for the differences between various methods of solution. A straight forward method of discretization would be to cut the boundary into n sections and to define the boundary conditions as constant within one section. This procedure can be improved in different ways, e.g. by allowing for higher order polynomials in the sections. The boundary element techniques proceed along these lines. In contrast, we discretize the boundary conditions by development into Fourier series. The pros and cons of the methods will not be discussed here. We rather interrupt the discussion on the topic by stating, that both methods are approximations and approach the true result if the number of terms used in the discretization goes towards infinity.

The rectangular plate has two symmetry lines which, for our concerns, coincide with the axes of the coordinate system. A general deformation of the plate can be split up into four different symmetry cases.

$$w = w_{SS} + w_{SA} + w_{AS} + w_{AA} \quad (17)$$

The four symmetry cases are decoupled and therefore treated separately. The further development holds for the double symmetric case (SS), the other cases follow by replacing cosines by sines and vice versa in the formula work. Also, only two edges ($\xi, 1$) and ($1, \eta$) of the plate need be considered, the two opposite edges are taken care of by the symmetry case.

An infinity of base functions is now generated by choosing for the parameter α in (15) the series

$$\alpha_m = m\pi j, \quad m = 0, 1, 2, \dots \quad (18)$$

For every individual α_m follow four β_m from (15).

$$\beta_m = \pm \sqrt{(m\pi)^2 \pm \omega} \quad (19)$$

These four values cover two symmetry cases with respect to the ξ axis as symmetry axis. Sorting out the antisymmetric case, two integration constants are free for every m , which fits with the fact that two boundary conditions have to be met on the boundary ($\xi, 1$) for every m .

To satisfy also the boundary conditions on the other edge (1, η), an additional series of base functions is generated by choosing

$$\beta_m = m\pi j, \quad m = 0, 1, 2, \dots \quad (20)$$

The introduction of the series (18) and (20) for the ξ and η directions is a restriction of generality of the available base functions. As far as the PDE is concerned, any real number can be chosen for α^2 or β^2 .

Depending on the sign of the radicand in (19), the character of the base function in the η direction may be hyperbolic or circular. Only the hyperbolic case is presented here. The circular case is treated in an analog way and looks very similar.

For the hyperbolic case ($\beta_m^2 > 0$) the deformation of the plate can be given as

$$w_m = \cosh(\beta_m \eta) \cos(m\pi \xi) \quad (21)$$

The second series of base functions, which follows from (20), is given by

$$w_m = \cosh(\alpha_m \xi) \cos(m\pi \eta) \quad (22)$$

This second series is very similar to (21), in fact it follows from (21) by interchanging ξ and η . The further development is therefore only shown for the series (21).

(21) is inserted into the expressions for the inclinations and the forces and moments of the plate, (7) through (13). For this purpose (21) must also be partially derivated with respect to ξ and η as required by the expressions. Omitting intermediate steps the following expressions are obtained for the deformations and forces:

$$\Psi_{\xi m} = m\pi \cosh(\beta_m \eta) \sin(m\pi \xi) \quad (23)$$

$$\Psi_{\eta m} = -\frac{\beta_m}{\Phi} \sinh(\beta_m \eta) \cos(m\pi \xi) \quad (24)$$

$$m_{\xi m} = -(-m\pi)^2 + \nu \frac{\beta_m^2}{\Phi^2} \cosh(\beta_m \eta) \cos(m\pi \xi) \quad (25)$$

$$m_{\xi \eta m} = (1 - \nu) \frac{\beta_m}{\Phi} m\pi \sinh(\beta_m \eta) \sin(m\pi \xi) \quad (26)$$

$$m_{\eta m} = -(\frac{\beta_m^2}{\Phi^2} - \nu(m\pi)^2) \cosh(\beta_m \eta) \cos(m\pi \xi) \quad (27)$$

$$v_{\xi m} = -((m\pi)^3 - (2 - \nu) \frac{\beta_m^2}{\Phi^2} m\pi) \cosh(\beta_m \eta) \sin(m\pi \xi) \quad (28)$$

$$v_{\eta m} = -(\frac{\beta_m^3}{\Phi^3} - (2 - \nu) \frac{\beta_m}{\Phi} (m\pi)^2) \sinh(\beta_m \eta) \cos(m\pi \xi) \quad (29)$$

The deformations and forces at the boundaries can now be developed into Fourier Series. For the edge ($\xi, 1$) the quantities w , Ψ_η , m_η and v_η are developed into harmonics in ξ , for the edge (1, η) the quantities w , Ψ_ξ , m_ξ and v_ξ are developed into harmonics in η .

The deflection on the boundary $\eta = 1$ is

$$w_m = \cosh(\beta_m) \cos(m\pi \xi) \quad (30)$$

Developing (30) into a Fourier series of the form

$$w_m = \sum_{n=0}^{\infty} a_{mn} \cos(n\pi \xi), \quad n = 0, 1, 2, \dots \quad (31)$$

the coefficients a_{mn} are determined by

$$a_{mn} = \cosh(\beta_m) \int_{-1}^1 \cos(m\pi \xi) \cos(n\pi \xi) d\xi \quad (32)$$

Carrying out the integration one gets

$$a_{mn} = \cosh(\beta_m) \quad (33)$$

for $n = m$ and

$$a_{mn} = 0 \quad (34)$$

for $n \neq m$.

The other quantities on the boundary $\eta = 1$ to be developed also contain $\cos(m\pi \xi)$ as a factor and consequently their series development is covered above as well.

The deflection on the boundary $\xi = 1$ is

$$w_m = \cosh(\beta_m \eta) \cos(m\pi) \quad (35)$$

or

$$w_m = (-1)^m \cosh(\beta_m \eta) \quad (36)$$

Developing (36) into a Fourier series of the form

$$w_m = \sum_{n=0}^{\infty} a_{mn} \cos(n\pi \eta) \quad (37)$$

the coefficients a_{mn} are determined by

$$a_{mn} = (-1)^m \int_{-1}^1 \cosh(\beta_m \eta) \cos(n\pi \eta) d\eta \quad (38)$$

Carrying out the integration one gets

$$a_{mn} = (-1)^{m+n} \frac{\beta_m}{\beta_m^2 + (n\pi)^2} \sinh(\beta_m) \quad (39)$$

The other quantities on the boundary (1, η) to be developed also contain $\cosh(\beta_m \eta)$ as a factor and consequently their series development is covered above as well.

Having developed the deformations and forces of the base functions at the boundaries into Fourier series, the problem is reduced to the form of the one-dimensional case, i.e. to the form of (1) through (3). In contrast to the one-dimensional case, however, the length of the vectors \mathbf{d} , \mathbf{f} and \mathbf{b} is not only determined by the order of the differential equation but also by the point of truncation of the series development, i.e. by the desired accuracy. The rest of the procedure is identical to the procedure applied in the one-dimensional case.

6 Results and Conclusions

The method of analysis outlined above was applied to the analysis of a simple plate system. The first few natural frequencies and the related eigenforms of an L-shaped cantilever plate were investigated. The geometry of the system is given in Fig.1, the Poisson ratio was chosen as $\nu = .3$.

The L-shaped plate is modeled as an assembly of 3 identical square plates. The dynamic stiffness matrix of the complete system is obtained by assembling the stiffness matrices of the plate elements. The eigensolutions are obtained by scanning the system matrix for singularities.

The first 6 eigenforms are plotted in Fig.4 - Fig.9. Positive and negative deflection values are distinguished by solid and dotted lines, the zero line was chosen to be solid.

To give an impression of the accuracy of the results, the first and sixth natural frequency are plotted in Fig.2 and Fig.3 over the number of terms used in the Fourier decomposition. The highest accuracy cases shown here resulted in system matrices of about 100 DOFs, the runtime was a few minutes per eigensolution on an AT.

To test the performance of the Continuous Elements Method, a simple but not trivial system has been chosen above as a test case. So the results can easily be verified with other methods, while the convergence of the eigensolutions over the Fourier terms gives an idea of the performance of the method presented here. More complex examples (not shown here) have confirmed the numerical stability of the approach.

The results indicate, that plate systems can effectively be treated using continuous plate elements. Once the method is tested, it may readily be used to generate Two Dimensional Continuous Elements for other structural elements, e.g. plates including in-plane and/or shear deformations. The next logical step will be to develop a library of standard Continuous Elements and software routines to assemble the elements to complex structures. This may result in a tool, that allows for easy and independent verification of findings obtained with other methods.

References

- [1] Akesson, B.A.: PFVIBAT - A Computer Program for Plane Frame Vibration Analysis by an Exact Method, *Int. J. Num. Meth. in Eng.*, Vol 10, No 6, (1976)
- [2] Derksen, F.: On the Transcendental Eigenvalue Problem, *ESA Workshop on Continuum Methods*, June 15-16, 1989, ESTEC, Noordwijk, The Netherlands
- [3] Gorman, D.J.: Free Vibration Analysis of the Completely Free Rectangular Plate by the Method of Superposition, *J. Sound and Vib.* 57 (1978), pp.437-447
- [4] Iguchi, S.: Die Eigenschwingungen und Klangfiguren der vierseitig freien rechteckigen Platte, *Ingenieur Archiv* 21 (1953) pp. 303-323
- [5] Janssens, F.; Crellin, E.: Analytical Modal Analysis of Flexible Spacecraft, Paper presented at the 8th Seminar on Modal Analysis, K.U. Leuven, Belgium, September 1983
- [6] Kolouček, V.: *Dynamics in Engineering Structures*, Butterworths, London
- [7] Kulla, P.H.: Analytical Finite Elements, *Sec. Int. Symp. on Aeroelasticity and Struct. Dyn. in Aachen, FRG*, Apr. 1-3, 1985, DGLR Bericht 85-02.
- [8] Kulla, P.H.: Two-Dimensional Continuous Elements, *European Forum on Aeroelastic and Structural Dynamics*, Aachen, April 17-19, 1989, DGLR-Bericht 89-01
- [9] Kulla, P.H.: Continuous Elements, Some Practical Examples, *Proc. ESA/ESTEC Workshop on Modal Representation of Flexible Structures by Continuum Methods*, 15-16 June 1989, ESTEC, Noordwijk, The Netherlands, esa WPP-09
- [10] Kulla, P.H.: Two-Dimensional Continuous Elements, *Proc. 1. Int. Conf. on Dynamics of Flexible Structures in Space*, Cranfield, UK, 15-18 May 1990; *Comp. Mech. Pub & Springer*
- [11] Poelaert, D.: DISTEL, a Distributed Element Program for Dynamic Modelling and Response Analysis of Flexible Structures, *Proc. 4th VPI & SU/AIAA Symposium on Dynamics and Control of Large Space Structures*, Blacksburg Va., 1983
- [12] Williams, F.W.: Computation of Natural Frequencies and Initial Buckling Stresses of Prismatic Plate Assemblies, *J. Sound & Vibr.*, Vol. 21, No. 1, March 1972.

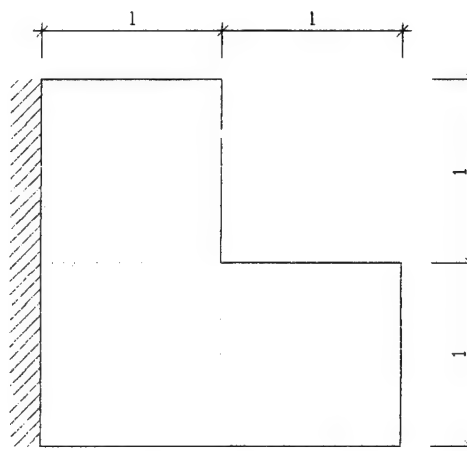


Fig.1: L-Shaped Cantilever Plate

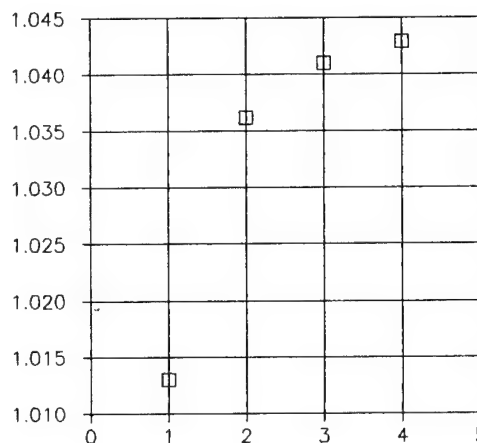


Fig.2: 1.Natural Frequency over Fourier Terms

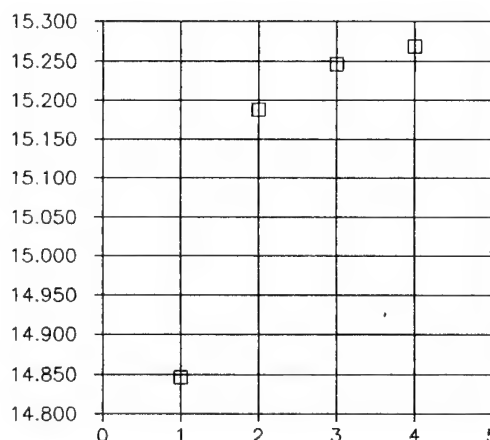


Fig.3: 6.Natural Frequency over Fourier Terms

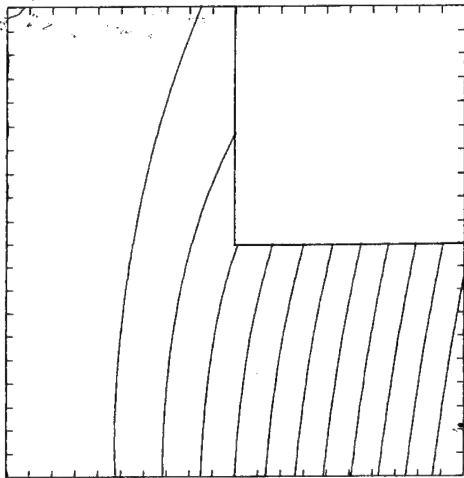


Fig.4: 1.Mode $\omega = 1.043$

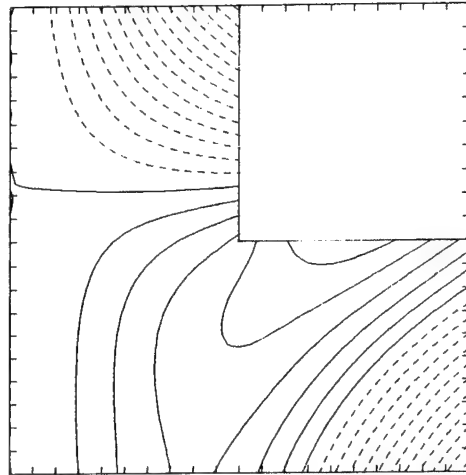


Fig.7: 4.Mode $\omega = 6.803$

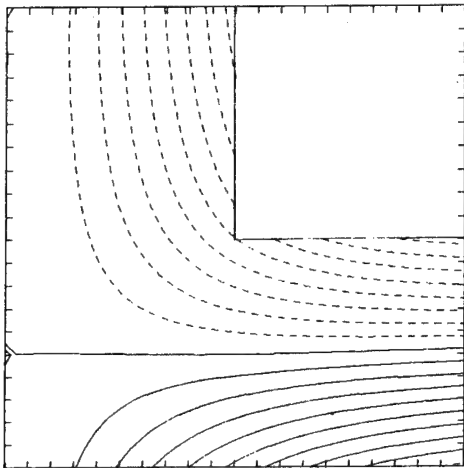


Fig.5: 2.Mode $\omega = 3.802$

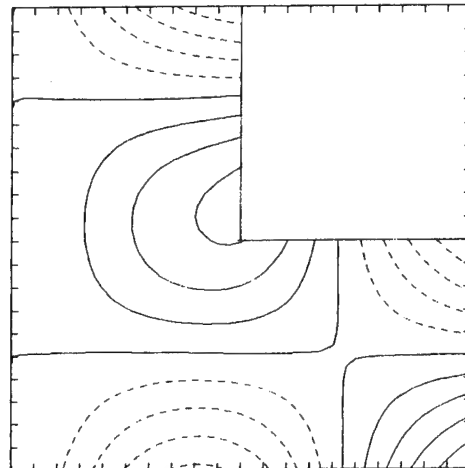


Fig.8: 5.Mode $\omega = 12.165$

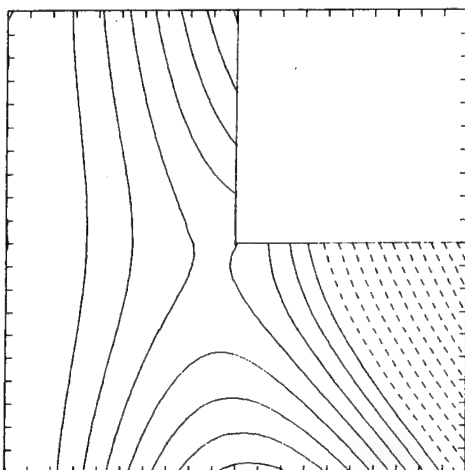


Fig.6: 3.Mode $\omega = 5.005$

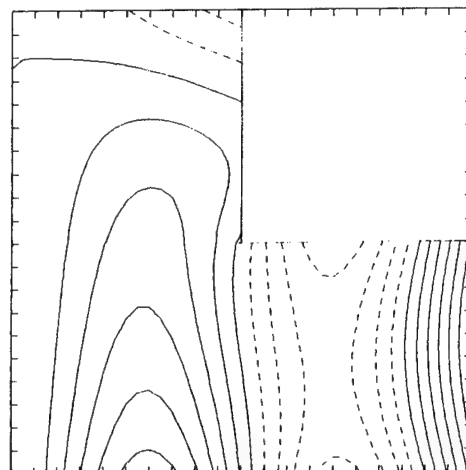


Fig.9: 6.Mode $\omega = 15.268$

N92-23830

HARMONIC WAVE PROPAGATION IN TWO-DIMENSIONAL
PERIODIC LARGE SPACE STRUCTURES

F. Bernelli-Zazzera, A. Ercoli-Finzi

Dipartimento di Ingegneria Aerospaziale
Politecnico di Milano
Via Golgi 40 - 20133 Milano - ITALY

ABSTRACT

The work aims at the development of a suitable method for the analysis of harmonic wave propagation in large two-dimensional periodic space structures. The dynamic behavior of modular structures is synthesized by the propagation coefficients of the repetitive element. The finite element method is used to compute the dynamic stiffness matrix of the periodic element; the application of the repetitive boundary equilibrium and compatibility conditions and the use of Floquet's theory on periodic differential equations leads to a nonlinear system of equations, whose solution gives the propagation coefficients for rectilinear wave fronts propagating along a generic direction. It is demonstrated that in some very special cases the solution of the nonlinear system is equivalent to an eigenvalue problem.

Keywords: Modular Structures, Large Space Structures, Structural Dynamics.

1. INTRODUCTION

All the proposed configurations of the permanent space stations show a series of "operational areas" (crew modules, laboratories, solar panels, antennas, ...) interconnected by slender truss structures. Due to their orbital dimensions it is obvious that all the elements have to be assembled directly in space; for this reason, and in order to minimize the overall weight without sacrificing the structural strength, modular structures represent the ideal candidates for the interconnecting elements (mono dimensional structures) and also for large panels or reflectors (two-dimensional structures). It is also well known that the very low operational loads are relevant only from the dynamic point of view, due to the strict shape and pointing performances required by Large Space Structures (LSS) coupled with their extreme flexibility. A consistent stiffening of the structure or active control systems may therefore be required for vibration suppression and shape control, and in this context the investigation of the propagation properties of structural members becomes of primary interest.

The peculiar topology of modular LSS, a high number of identical substructures, small compared to the dimensions of the whole structure, and large distances between junctions, allows their comparison to solid crystals and to suspect the presence of the same wave propagation

characteristics, such as dispersion and filtering. The dispersion effect occurs due to a frequency dependent wave propagation velocity, while filtering is caused by wave reflection in some frequency ranges.

Many different approaches to the dynamic analysis of mono dimensional periodic structures have been proposed (Refs. 1-5), all leading to the conclusion that elastic waves are not allowed to propagate in some frequency bands. The dependence of the propagation characteristics on the frequency is known as dispersion relation; it is a complex valued function, in general nonlinear, whose real part represents the attenuation in space of the propagating waves while the imaginary part represents the phase difference between incoming and outgoing waves within a single element.

The analysis of two-dimensional periodic structures has been up to now object of limited studies, all dealing with particular cases (Refs. 1,6-8) due to the complexity of the problem.

In this context the present work aims at the development of a general method for the analysis of the dispersive behavior of a two-dimensional periodic structure.

The proposed approach to the analysis of two-dimensional periodic structures represents an extension of the concepts adopted for mono dimensional periodic structures (Ref. 5). The dynamic characteristics of the repetitive element are determined with the finite element method and the application of boundary equilibrium and compatibility conditions in the two directions defining the periodicity, together with the Floquet's theory on partial differential equations, leads to a nonlinear system of equations governing the propagation in any direction of rectilinear wave fronts. It is demonstrated that for some particular wave front orientation the solution is more conveniently expressed as an eigenvalue problem.

Examples are given for two different structural topologies, and the results are compared to the propagation characteristics of the equivalent mono dimensional structures.

2. TWO-DIMENSIONAL PERIODIC STRUCTURES

A periodic two-dimensional structure can be intuitively represented by identical elements physically connected at some points along their boundaries in two directions (Fig. 1). The boundary connections can be divided into left, right, top and bottom connections (l,r,b,t), with the left connections equaling the right ones and the top

equaling the bottom ones.

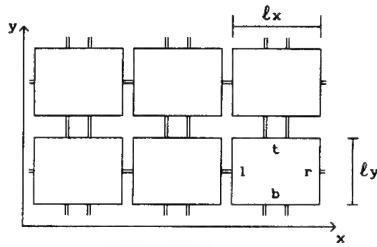


Figure 1: two-dimensional periodic structure

This approach, first proposed by Mead (Ref. 1), is however limiting in the sense that not all the topologies can be modelled in this way: a hexagonal honeycomb (Fig. 2) for instance has connections which can not be simply represented as left, right, top, bottom, since each vertex is connected to elements laying at least on two different sides (e.g. top and right).

Therefore a different modeling technique is proposed, in which the repetitive element is ideally contained in a rectangle and connected to the adjacent elements by 4 equal interfaces (Fig. 2), identified by the letters a, b, c, d. In a cartesian plane we will denote by l_x and l_y the characteristic lengths of the rectangle in the two directions x and y , and with the indexes k and j the positions of the generic element along the x and y directions. We will also identify the "a" interface as the bottom-left one, the others following in the clockwise sense (Fig. 2).

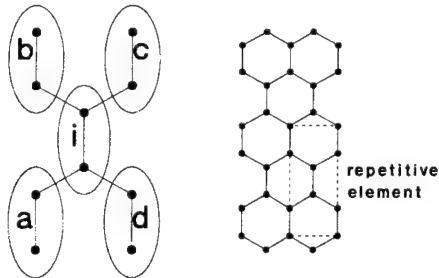


Figure 2: schematic representation of a hexagonal honeycomb

The dynamics of the repetitive module can be represented by computing the stiffness, mass and damping matrices via the finite element method (Ref. 9), leading to

$$[K - \omega^2 M + j\omega C] \begin{Bmatrix} u_a \\ u_b \\ u_c \\ u_d \\ u_i \end{Bmatrix} = \begin{Bmatrix} P_a \\ P_b \\ P_c \\ P_d \\ P_i \end{Bmatrix} \quad (1)$$

where $\{u_i\}$, $\{P_i\}$ are internal coordinates and loads, i.e., not connected to adjacent elements, $[K]$, $[M]$, $[C]$ are the stiffness, mass and damping matrices and $\{u_a\}$, $\{u_b\}$, $\{u_c\}$, $\{u_d\}$, $\{P_a\}$, $\{P_b\}$, $\{P_c\}$, $\{P_d\}$ are the boundary coordinates and loads, each of order n .

The use of the finite element method is recommended in order to handle arbitrary complex structures while maintaining the same computational scheme.

Eq. 1 can be written in a partitioned and more concise form by introducing the dynamic stiffness matrix

$$[A] = [K - \omega^2 M + j\omega C] \quad (2a)$$

$$\begin{bmatrix} A_{aa} & A_{ab} & A_{ac} & A_{ad} & A_{ai} \\ A_{ba} & A_{bb} & A_{bc} & A_{bd} & A_{bi} \\ A_{ca} & A_{cb} & A_{cc} & A_{cd} & A_{ci} \\ A_{da} & A_{db} & A_{dc} & A_{dd} & A_{di} \\ A_{ia} & A_{ib} & A_{ic} & A_{id} & A_{ii} \end{bmatrix} \begin{Bmatrix} u_a \\ u_b \\ u_c \\ u_d \\ u_i \end{Bmatrix} = \begin{Bmatrix} P_a \\ P_b \\ P_c \\ P_d \\ P_i \end{Bmatrix} \quad (2b)$$

If we suppose the structure loaded only at the boundaries of the modules, the internal loads $\{P_i\}$ will be zero, so that the last equation of the system (2b) can be solved for the internal displacements and, by substitution into the remaining equations, the system is reduced to

$$\begin{bmatrix} A_{aa} & A_{ab} & A_{ac} & A_{ad} \\ A_{ba} & A_{bb} & A_{bc} & A_{bd} \\ A_{ca} & A_{cb} & A_{cc} & A_{cd} \\ A_{da} & A_{db} & A_{dc} & A_{dd} \end{bmatrix} \begin{Bmatrix} u_a \\ u_b \\ u_c \\ u_d \end{Bmatrix} = \begin{Bmatrix} P_a \\ P_b \\ P_c \\ P_d \end{Bmatrix} \quad (3)$$

where

$$[A_{hl}] = [A_{hl} - A_{hi}(A_{ii})^{-1}A_{il}] \quad (h, l = a, b, c, d) \quad (4)$$

The boundary compatibility constraints on element k, j and the equilibrium conditions at the "c" interface of the element k, j are, referring to Fig. 3,

$$\begin{cases} \{q_b\}_{k,j} = \{q_a\}_{k,j+1} \\ \{q_c\}_{k,j} = \{q_a\}_{k+1,j+1} \\ \{q_d\}_{k,j} = \{q_a\}_{k+1,j} \end{cases} \quad (5)$$

$$\{P_c\}_{k,j} + \{P_b\}_{k+1,j} + \{P_d\}_{k,j+1} + \{P_a\}_{k+1,j+1} = 0 \quad (6)$$

For conciseness the "a" subscript will be omitted in the sequel, being intended that all coordinates and loads not specified are evaluated at the "a" interface.

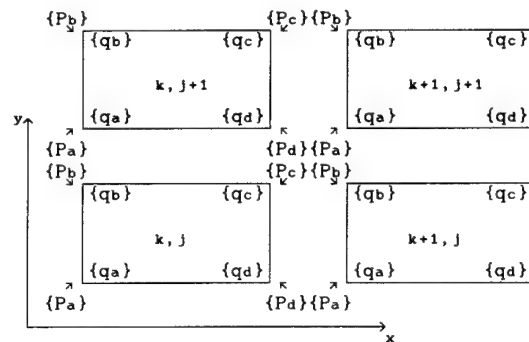


Figure 3: boundary equilibrium and compatibility conditions

The substitution of Eq. 3 and Eq. 5 into Eq. 6 leads to the equation

$$\begin{aligned} & [A_{ca}]\{q\}_{k,j} + [A_{cd} + A_{ba}]\{q\}_{k+1,j} + [A_{bd}]\{q\}_{k+2,j} + \\ & [A_{cb} + A_{da}]\{q\}_{k,j+1} + [A_{aa} + A_{bb} + A_{cc} + A_{dd}]\{q\}_{k+1,j+1} + \\ & [A_{bc} + A_{ad}]\{q\}_{k+2,j+1} + [A_{db}]\{q\}_{k,j+2} + \\ & [A_{dc} + A_{ab}]\{q\}_{k+1,j+2} + [A_{ac}]\{q\}_{k+2,j+2} = 0 \end{aligned} \quad (7)$$

which represents the dynamics of the element k, j in terms of only "a" nodal displacements, i.e. with force variables eliminated. Repeating the procedure for all the elements, the dynamics of the complete two-dimensional structure will be represented by a set of differential equations with spatially periodic coefficients; the Floquet theory (Ref. 10) can therefore be applied to infer the wave propagation characteristics.

3. WAVE PROPAGATION WITH RECTILINEAR WAVE FRONT

3.1 The general case

In order to solve Eq. 7 and compute the dispersion relation, the conditions typical of the propagating wave front must be introduced. It is here briefly recalled that the wave front is the line on which all displacements are equal in both amplitude and phase. The present work deals with rectilinear wave fronts, which can be generated by a continuous distribution of forces along a straight line on the repetitive structure. Referring to Fig. 4, in accordance with (Ref. 1), two propagation coefficients for the two orthogonal directions x and y are considered

$$\begin{cases} \mu_x = \alpha + i k_x \\ \mu_y = \alpha + i k_y \end{cases} \quad (8)$$

where α is the attenuation coefficient (space attenuation of the propagating wave) and k is the wave number (phase difference between incoming and outgoing waves within a single element).

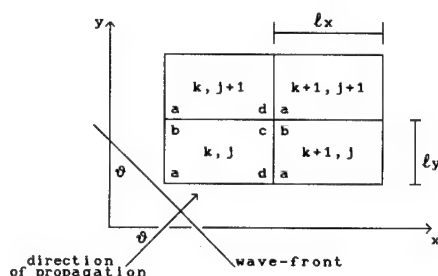


Figure 4: propagating wave front

Let

$$\begin{cases} m = e^{\mu_x} \\ \rho = e^{\mu_y} \end{cases} \quad (9)$$

the Floquet's relations become

$$\begin{cases} \{q\}_{k+1,j} = m \{q\}_{k,j} \\ \{q\}_{k,j+1} = \rho \{q\}_{k,j} \\ \{P\}_{k+1,j} = m \{P\}_{k,j} \\ \{P\}_{k,j+1} = \rho \{P\}_{k,j} \end{cases} \quad (10)$$

If the wave front is propagating in a direction θ with respect to the positive x direction, calling $t = \tan \theta \cdot (l_y/l_x)$, the following relations hold (Ref. 1), if $\pi/2 < \theta < \pi/2$

$$\begin{cases} \mu_y = \mu_x t \\ \rho = m^t \end{cases} \quad (11)$$

Inserting Eqs. 10-11 into Eq. 7 leads to the following nonlinear system of equations

$$\begin{aligned} & [Aca + m^t(Acb+Ada) + m^{2t}(Adb) + m(Acd+Aba) + \\ & m^{t+1}(Aaa+Abb+Acc+Add) + m^{2t+1}(Adc+Aab) + \\ & m^2(Abd) + m^{t+2}(Abc+Aad) + m^{2t+2}(Aac)]\{q\} = 0 \end{aligned} \quad (12a)$$

$$\{q\}^T \{q\} = 1 \quad (12b)$$

completely defining the propagation of rectilinear wave fronts in any arbitrary direction.

This procedure becomes singular if the wave front is parallel to the x axis ($\theta = \pm \pi/2$), in which case the dual relations $t = \cot \theta \cdot (l_x/l_y)$ and $\mu_x = \mu_y \cdot t$ should be used to determine the resolving

nonlinear system. However this will not be done since, as demonstrated in the next sections, an even more practical solution is feasible when the wave front is parallel to any coordinate axis.

The normalization of the propagation modes, Eq. 12b, is added in order to have a unique solution in terms of m and $\{q\}$ of Eq. 12a, which can be carried out by an iterative Newton-Raphson method, provided an approximate knowledge of at least the coefficients m . In fact Eq. 12a is actually linear in terms of $\{q\}$ and the nonlinearities concern only the propagation coefficients m , so that the Newton-Raphson iterative procedure should easily converge once m is approximately known. It is usually quite simple to obtain the approximate values for m and $\{q\}$, since the dispersion curves are usually searched in a range from zero to a defined maximum frequency, and at $\omega=0$ the propagation coefficients are real numbers (wave number equal to 0 or π); therefore the first guess solution at any frequency can be the final solution at the previous frequency value, whereas a couple of trials may be required in order to trim the propagation coefficients at $\omega=0$.

The only problem arising in the solution of Eq. 12 is that, due to the nonlinearity of the system, the number of propagation coefficients is not known a priori and can vary with the propagation angle; an extra computational effort is then required, still at $\omega=0$, to determine the number of independent propagation coefficients, but it is remarked that this has to be done only once for each propagation angle. This reflects the fact that the wave propagation is expressed in terms of a single group of boundary coordinates, which has a different periodicity along each direction (i.e., the number of elements crossed by the wave front before the boundary coordinates of the first element fall on the same coordinates of another element). This will be evident in the sequel of the paper, where it will be demonstrated that an even more comfortable solution is possible for three particular propagation directions, corresponding to $\theta=0$ (vertical wave front), $\theta=\pi/2$ (horizontal wave front), $\theta=\arctg(l_x/l_y)$ (wave front along the diagonals of the repetitive element). In fact for these particular cases the nonlinear system of Eq. 12 can be reformulated as an eigenvalue problem.

3.2 Vertical wave front

Referring to Fig. 4, a vertical wave front is defined by the equality constraints

$$\begin{aligned} \{q\}_{k,j} &= \{q\}_{k,j+1} = \{q\}_{k,j+2} \\ \theta &= 0 ; \quad \mu_y = 0 ; \quad \rho = 1 \end{aligned} \quad (13)$$

so that Eq. 7 can be rewritten in the simplified form

$$\begin{aligned} & [Aca + Acb + Ada + Adb]\{q\}_{k,j} + \\ & [Acd + Aba + Aaa + Abb + Acc + Add + Adc + Aab]\{q\}_{k+1,j} + \\ & [Abd + Abc + Aad + Aac]\{q\}_{k+2,j} = 0 \end{aligned} \quad (14)$$

Introducing the state vector

$$\{v\}_{k,j} = \begin{Bmatrix} q_{k,j} \\ q_{k+1,j} \end{Bmatrix} \quad (15)$$

Eq. 14 is recast as a standard eigenvalue problem in the form

$$\begin{aligned} & \begin{bmatrix} 0 & I \\ -\Phi^{-1}\Gamma & -\Phi^{-1}\Sigma \end{bmatrix} \{v\} - m [I] \{v\} = 0 \\ & [\Phi] = [Abd + Abc + Aad + Aac] \\ & [\Gamma] = [Aca + Acb + Ada + Adb] \\ & [\Sigma] = [Acd + Aba + Aaa + Abb + Acc + Add + Adc + Aab] \end{aligned} \quad (16)$$

the solutions of which are directly the $2n$ propagation coefficients and modes, n left going and n right going waves, where n is the number of degrees of freedom at any of the a,b,c,d interfaces.

3.3 Horizontal wave front

The conditions defining a horizontal wave front are, still referring to Fig. 4,

$$\{q\}_{k,j} = \{q\}_{k+1,j} = \{q\}_{k+2,j} \quad (17)$$

$$\theta = \pm \pi/2 \quad ; \quad \mu_x = 0 \quad ; \quad m=1$$

which, when inserted in Eq. 7 and with the introduction of the state vector

$$\{v\}_{k,j} = \begin{Bmatrix} q_{k,j} \\ q_{k,j+1} \end{Bmatrix} \quad (18)$$

lead to the eigenvalue problem

$$\begin{bmatrix} \emptyset & I \\ -\Phi^{-1}\Gamma & -\Phi^{-1}\Sigma \end{bmatrix} \{v\} - \rho [I] \{v\} = \emptyset \quad (19)$$

$$[\Phi] = [Adb+Adc+Aab+Aac]$$

$$[\Gamma] = [Aca+Acd+Aba+Abd]$$

$$[\Sigma] = [Acb+Ada+Aaa+Abb+Acc+Add+Abc+Aad]$$

still presenting $2n$ solutions, n up going and n down going waves.

3.4 Wave front along the diagonals

The conditions defining a wave front directed as a diagonal of the repetitive element are obviously dependent on which diagonal is considered. In the present analysis only the diagonal at $\theta = \arctg(l_x/l_y)$ will be considered (positive x and y directions), being the extension to the second diagonal trivial.

The wave front conditions are

$$\begin{cases} q_{k,j+1} = q_{k+1,j} \\ q_{k,j+2} = q_{k+2,j} \\ q_{k+1,j+1} = q_{k+2,j} \\ q_{k+1,j+2} = q_{k+3,j} \\ q_{k+2,j+1} = q_{k+3,j} \\ q_{k+2,j+2} = q_{k+4,j} \end{cases} \quad (20)$$

and the augmented state vector to be introduced is

$$\{v\} = \begin{Bmatrix} q_{k,j} \\ q_{k+1,j} \\ q_{k+2,j} \\ q_{k+3,j} \end{Bmatrix} \quad (21)$$

so that the following eigenvalue problem determines the propagation coefficients

$$\begin{bmatrix} \Psi & \Phi & \Gamma & \Sigma \\ \emptyset & I & \emptyset & \emptyset \\ \emptyset & \emptyset & I & \emptyset \\ \emptyset & \emptyset & \emptyset & I \end{bmatrix} \begin{Bmatrix} q_{k,j} \\ q_{k+1,j} \\ q_{k+2,j} \\ q_{k+3,j} \end{Bmatrix} + \begin{bmatrix} \emptyset & \emptyset & \emptyset & \Omega \\ -I & \emptyset & \emptyset & \emptyset \\ \emptyset & -I & \emptyset & \emptyset \\ \emptyset & \emptyset & -I & \emptyset \end{bmatrix} \begin{Bmatrix} q_{k+1,j} \\ q_{k+2,j} \\ q_{k+3,j} \\ q_{k+4,j} \end{Bmatrix} = \begin{Bmatrix} \emptyset \\ \emptyset \\ \emptyset \\ \emptyset \end{Bmatrix} \quad (22)$$

with

$$\begin{aligned} [\Phi] &= [Acb+Ada+Acd+Aba] \\ [\Gamma] &= [Adb+Abd+Aaa+Abb+Acc+Add] \\ [\Sigma] &= [Aab+Adc+Abc+Aad] \\ [\Omega] &= [Aac] \\ [\Psi] &= [Aca] \end{aligned} \quad (23)$$

In this case the number of solutions is double than for the horizontal and vertical wave fronts, due to the fact that in the direction of propagation the wave front will be in the identical conditions at the "a" interfaces of the elements k,j and $k+1,j+1$, thus after 2 elements (one to the left and one to the top).

It is to be remarked that, according to Eq. 11, in this case $\mu_x = \mu_y$, and moreover the eigenvalue problem can be solved only if $[Aac]$ is nonsingular; if this does not hold, the general formulation has to be applied and the nonlinear system (Eq. 12) needs to be solved.

4. NUMERICAL EXAMPLES

The method of analysis proposed has been extensively tested on various structural configurations. Results not shown here demonstrate that indeed, when applicable, the eigenvalue problem of Eqs. 16,19,22 leads to the same solution of the nonlinear Eq. 12 with much less computational effort. Moreover, for those topologies which can be represented with no doubt also in the form of Fig. 1, suggested by Mead (Ref. 1), the dispersive behavior for rectilinear wave fronts directed along the x and y axes matches the results of Eqs. 16,19.

The reported results concern two slightly different topologies and show (Fig. 5,6) the dispersion curves for three directions of propagation on a two-dimensional structure and the dispersive behavior of the equivalent mono dimensional structure. Table 1 reports the natural frequencies and summarizes the dimensions, section and material properties of the repetitive element, supposed to be pin-jointed at all the connections. Since only "in plane" waves are considered, the finite element representation of the module has one node and two degrees of freedom at each interface.

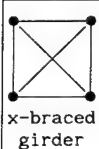
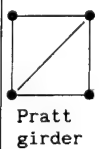
Topology	Natural Frequencies (rad/sec)	Dispersion relation	Element Dimensions, Beam Section and Material Properties
 x-braced girder	2.56 104.15 134.83 139.25 147.20 183.58	Fig. 5	l_x 1600 mm l_y 800 mm Area 300 mm ² J_{xx} 14324 mm ⁴ J_{yy} 10129 mm ⁴
 Pratt girder	2.75 96.18 137.59 163.04 194.47 200.72	Fig. 6	J_{zz} 10129 mm ⁴ ρ 2768 Kg/m ³ E 71700 N/mm ² G 26900 N/mm ²

Table 1: list of structural topologies analyzed

The natural frequencies are reported since it is known that for mono dimensional structures (Refs. 4,5) they represent boundaries of passing and stopping bands, as clear from the relative plots of Figs. 5-6, and an analogous relation is searched also for two-dimensional periodic

structures.

As expected due to the minor topological differences between the repetitive elements, the analysis of the dispersion curves points out the similar dispersive behavior of the two configurations studied; this similarity is particularly enhanced in the case of a diagonal directed wave front, when the opposite diagonal of the x-braced girder adds no extra stiffness with respect to the Pratt girder and therefore induces almost no different filtering characteristics. It is evident that also two-dimensional periodic structures, as the mono dimensional ones, exhibit a neat dispersive behavior, with wave distortion (frequency dependant group velocity $c = \partial\omega/\partial k$), filtered disturbances (wave number k equal to 0 or π) or attenuation in space of propagating waves (nonzero attenuation coefficient α).

Unfortunately no connections are evident between the filtering behavior of two-dimensional periodic structures and the natural frequencies of the constituting elements, and also between the mono and two-dimensional dispersion curves: apparently the mono dimensional structure shows a much more complicated behavior, comparable at first sight with the behavior of a diagonal-directed wave front. It is remarked, however, that restricting assumptions were made in imposing the wave front orientation, since the displacements at two boundary interfaces are supposed equal. This is not required in the analysis of mono dimensional structures, in which the wave front is not supposed orthogonal to the direction of propagation (Ref. 5), so that the "a" and "b" interface nodes, treated as a unique boundary, can vibrate out of phase. The translation of this extra freedom on each module of the two-dimensional structure is unfeasible, being equivalent to a mono dimensional representation with a representative element

indefinitely long (at least very long) in the second direction; the interconnecting degrees of freedom would become too many to allow a significant interpretation of the results, which would indeed include those presented for rectilinear wave fronts.

5. CONCLUSIONS

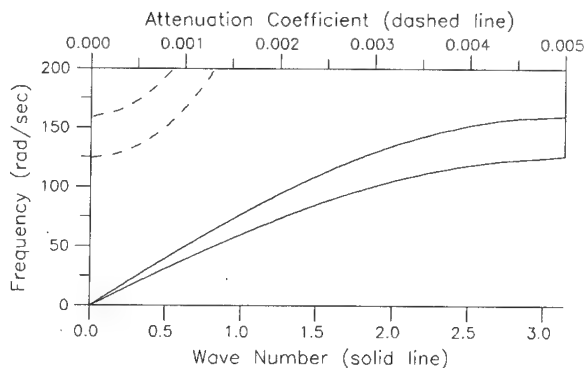
The method proposed for the analysis of harmonic wave propagation in two-dimensional periodic structures can be considered an extension of the one used for mono dimensional structures: anyway the more general case can not be solved as an eigenvalue problem, due to the higher complexity of the system which involves a different periodicity, and therefore a different number of solutions, depending on the direction of the propagation.

Nevertheless the theoretical developments are still synthetic, due to the application of the Floquet's theory on the particular representation of the periodic module which allows to formulate the problem in terms of only one of the boundary interfaces. Moreover in some particular conditions the solution has been reformulated as an eigenvalue problem.

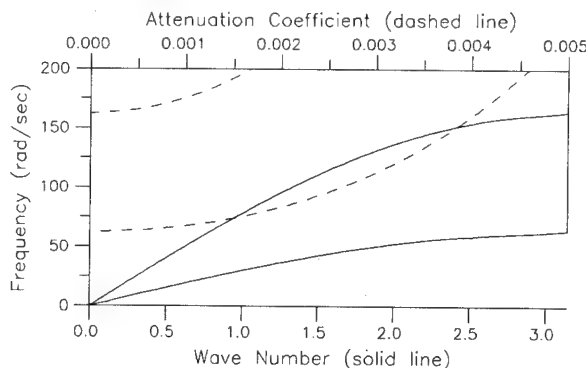
The results obtained on different structures have demonstrated the practical applicability of the method and have pointed out, as expected, the typical dispersive and filtering behavior of periodic structures.

It is in the opinion of the authors that the method would require minor improvements in order to handle either finite-dimensional two-dimensional structures or propagating waves with non-rectilinear wave fronts, as for instance those produced by a single point excitation.

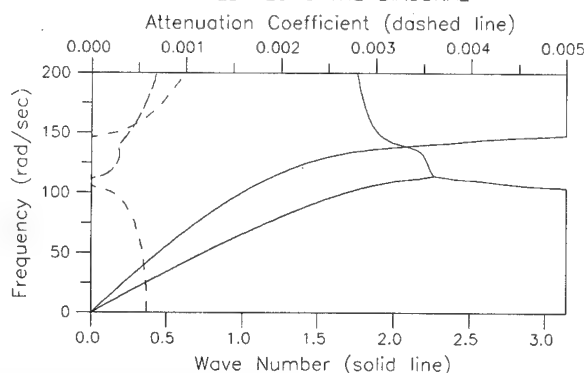
VERTICAL WAVE FRONT



HORIZONTAL WAVE FRONT



WAVE FRONT DIRECTED ALONG THE DIAGONAL



MONO DIMENSIONAL STRUCTURE

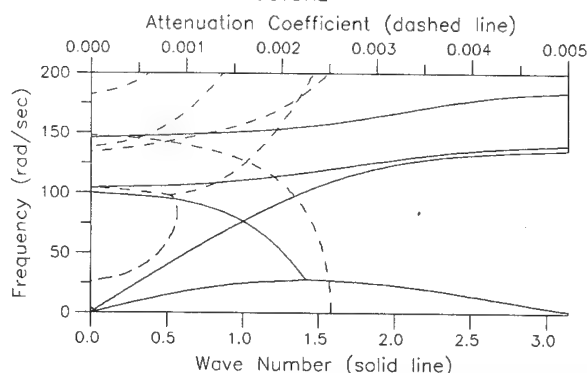
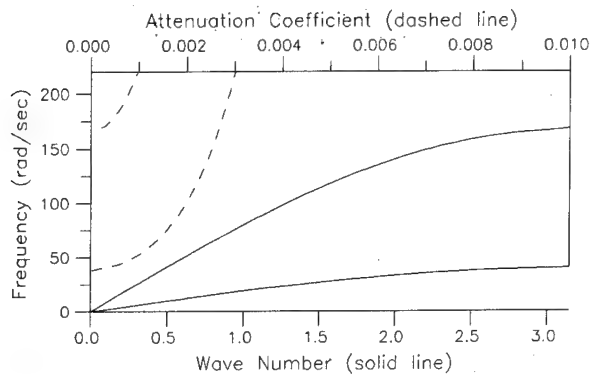
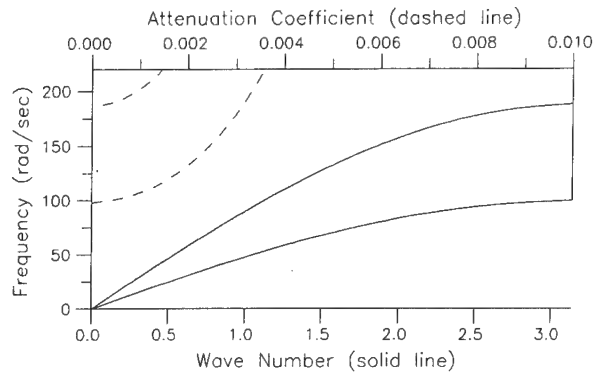


Figure 5: dispersion relations for a x-braced girder

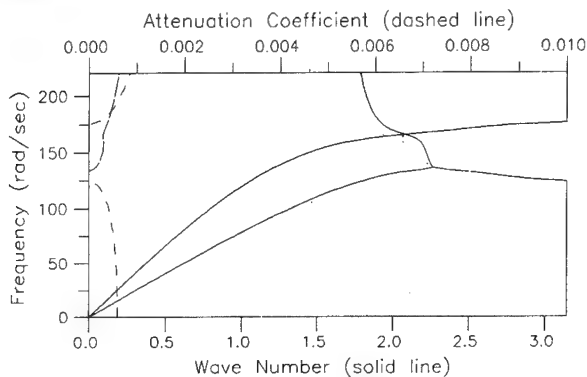
VERTICAL WAVE FRONT



HORIZONTAL WAVE FRONT



WAVE FRONT DIRECTED ALONG THE DIAGONAL



MONO DIMENSIONAL STRUCTURE

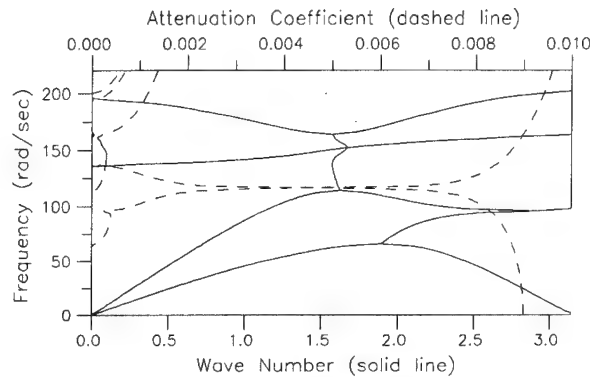


Figure 6: dispersion relations for a Pratt girder

6. ACKNOWLEDGMENTS

This research was sponsored by Fondazione Ing. Paolo Foresio.

7. REFERENCES

1. Mead D J 1973, A General Theory of Harmonic Wave Propagation in Linear Periodic Systems with Multiple Coupling, Journal of Sound and Vibration, 27, 2, 235-260;
2. Denke P H & al 1975, Matrix Difference Equation Analysis of Vibrating Periodic Structures, AIAA Journal, 13, 2, 160-166;
3. Von Flotow A H 1986, Disturbance Propagation in Structural Networks, Journal of Sound and Vibration, 106, 3, 433-450;
4. Sgubini S & al 1989, Evaluation of Dispersive Behaviour in Periodic Structures by Discrete Fourier Transform, Proc. Int. Conf. on Spacecraft Structures and Mechanical Testing, Noordwijk, The Netherlands, ESA SP-289, 207-212;
5. Bernelli-Zazzera F & al 1989, Modular Large Space Structures Dynamics, Journal of the Astronautical Sciences, 37, 2, 195-210;
6. Sun C T & al 1973, A Continuum Approach Toward Dynamics of Gridworks, Journal of Applied Mechanics, 40, , 186-192;
7. Park S K & al 1981, Elastic Wave Propagation in Hexagonal Honeycombs: 1. Method of Analysis and Low Frequency Characteristics, 2. High Frequency Characteristics, Journal of the Acoustical Society of America, 70, , 1445-1462;
8. Kim K S & al 1986, Harmonic Wave Propagation in Materials with Periodic Beam-Structures, Journal of Sound and Vibration, 107, 1, 59-70;
9. Przemieniecki J S 1968, Theory of Matrix Structural Analysis, McGraw-Hill, New York, N.Y.;
10. Eastham M S P 1973, The Spectral Theory of Periodic Differential Equations, Scottish Academic Press, Edinburgh.

N92-23831

84743

Non linear structural analysis of a thin skin carbon-carbon rigid decelerator

by

Ch. BONNET, J.P. PLANAS, M. RIGAULT

Dassault Aviation

ABSTRACT

Aerodynamic braking decelerator systems will play a major role in the scenarios of future European Space missions where entry in the atmosphere of various planets is required.

In the frame of an ESA contract, Planetary Entry System study, Dassault Aviation has performed structural linear analysis on the phase A carbon-carbon decelerator concept for the Huygens probe. The study has shown that the validation of such thin skin structure design requires precise instability phenomena analysis. The buckling, locally or general is likely to be size determining. Dassault Aviation has performed non linear buckling and post buckling analysis of the carbon-carbon Huygens decelerator on internal funding, using an in-house developed software taking into account the combined thermomechanical and mechanical loading. This paper presents the results of this non linear structural analysis.

Today, experience on such an ultra thin and ultra light carbon-carbon structure is not available. The only way to give the necessary credibility to the concept definition is to rely on sophisticated structural analysis including non linearity in the equations under both mechanical and thermal loading.

1. INTRODUCTION

Most typical entry devices consist of a thermal protection shield surrounding a given geometry of descent module, the drag area being limited mainly to the descent module diameter. Planetary exploration missions require longer descent phase into the planetary atmosphere and therefore rely on much lower ballistic coefficient to meet the entry trajectory specifications. A large diameter entry decelerator is therefore required to meet the scientific requirements.

As mass is a very stringent parameter for space application, severe mass constraints are imposed although large surfaces are required to achieve strong enough deceleration during the entry phase. The Cassini mission, ref. 1, provided preliminary studies on such ultra light weight decelerator concept. They led to a conical (frustum-shaped) design using very thin carbon-carbon skin (0.5mm) stiffened by a network of radial and circular carbon-carbon stiffeners. Figure 1 shows a general view of the decelerator.

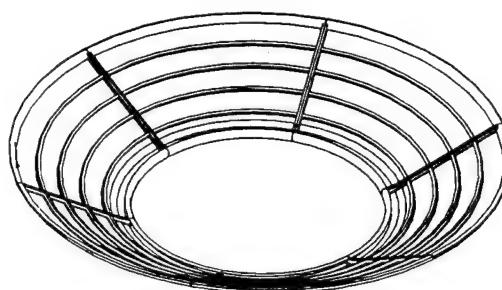


Figure 1. CASSINI phase A baseline decelerator : 6 panels

Dassault Aviation performed preliminary structural analysis on the proposed design, in the frame of the ESA-Planetary Entry System study and concluded that the design of hot atmospheric reentry structures using exotic materials is hindered by several difficulties :

- General engineering rules are hardly applied because they are at the border of their application range.
- Classical computer codes using linear only computations under purely mechanical loads are not well suited for such thin thicknesses (0.5mm) under hot environment.
- There is no facility available to simulate the extreme external conditions sustained by these structures, therefore, it is difficult to test structural elements or even samples under the actual thermal heat fluxes and mechanical loads.

This is why, for such special use, more sophisticated computer codes are to be put into action even at the very early stage of the design. Typically, those studies must cover stability assessment as well as Non-linear thermomechanical analysis of the structures.

2. SHORT DESCRIPTION OF THE CATIA-ELFINI TOOL

ELFINI Finite Element software has been in use for Dassault Aviation's airplane design since the mid 1970s, and for Hermes spaceplane since 1984. CATIA-ELFINI links around a central core of finite element and various branches of analysis for aircraft/spacecraft structures, figure 2. It includes :

- the well-known CAD tool CATIA, which gives geometry and mesh generation
- static finite element analysis for linear and Non-linear problems
- static aeroelasticity, calculation and management of loads
- linear dynamics : calculation of eigenmodes, harmonic and transient responses
- nonlinear dynamics : impact and crash analysis, landing system and vehicle interaction
- unsteady aeroelasticity, flutter and coupling with flight control system
- fatigue and crack propagation analyses
- heat transfer and thermo-elastic coupling
- acoustic and elastoacoustic coupling

STRUCTURAL ANALYSIS & OPTIMIZATION

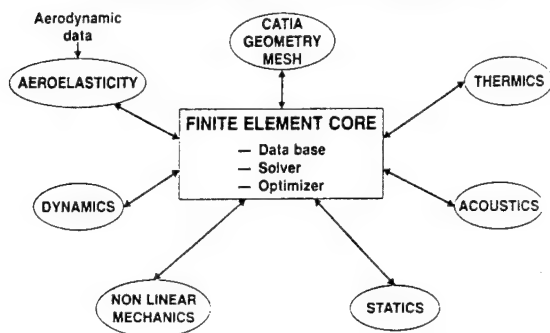


Figure 2. CATIA-ELFINI functional diagram

The system works on request in either an interactive or a batch mode, and uses a common data base managed automatically. Some of the main common characteristics of branches are :

- a topological dialogue for mesh and all data generation which leads to very clean meshes for all types of structure from the whole aircraft meshes to tridimensional analyses of fitting details.
- a great range of possibilities for visualization of inputs and outputs.

The solution of linear problems is run by a very powerful variant of the Frontal Gauss method, which minimizes the computer time for classical linear problems (about 1 min of CPU on IBM 3090-VF for a complete aircraft calculation. For large three-dimensional problems, the use of the conjugate gradient technique enables the same level of performance to be maintained, taking into account the contact non-linearities. For geometric non-linear problems (membrane effects, post-buckling, snap through, etc) an original algorithm called preconditioned BFGS with exact line search has been developed. This algorithm benefits directly from the biquadratic character of total potential. It can handle the most severe snap-through conditions, ref. 3 and 4.

We must underline the strong practical interest of the post-buckling analysis, which enables the design of thin composite skin, which buckles before ultimate loading.

3. CALCULATIONS CONDITIONS

In the scope of the Cassini mission, the Huygens probe will survey the Titan atmosphere and perform scientific experiments during its entry and descend. Several trajectories are available. The chosen trajectory provides the worst conditions regarding to dynamic pressures as well as maximum heat transfer rates. this trajectory lead to a 25g peak deceleration corresponding to a 6000 Pa equivalent static pressure. This baseline represents the most stringent nominal case of ref. 5, (Entry velocity = 7.2 km/s, Entry flight path angle = -90°, colder Titan atmosphere).

4. GENERAL STABILITY ASSESSMENT

A special Finite Element model of the phase A concept decelerator was set up in order to perform general buckling computations. The skins are modeled by shear-only elements, the stiffeners webs by plate elements, and the flanges by beams of equivalent inertia. The working section of skins in the circumferential direction was represented by bars. The full skin section was considered working in the radial direction. This section was thus idealized by bars.

The model represents the whole decelerator (360 deg) in order to be freed from symmetrical modes. We therefore dispose of a simplified model, totally isolated from the multiple local buckling modes in the skins.

The material was considered as homogeneous and isotropic with a young modulus of 80000 Mpa (same in traction and compression). This represents a generic material integrating potential improvements. These characteristics were used in order to be consistent with former studies performed in the frame of the ESA PES contract. Maximal nominal external pressure of 6000 Pa was applied.

Linear buckling calculations were performed under the nominal mechanical loads. these computations are based on the addition of a geometrical operator to the stiffness matrix. They led to a general safety coefficient of 2.17. Non-linear buckling calculations were performed under the nominal mechanical loads and led to a general buckling safety coefficient of 2.2. The model consists in 8508 DOF, 1485 nodes, 2406 elements and 35 mn are necessary for a full computation on an IBM 3090. Such calculations are impossible to perform with an analytical method. As shown in figure 3, Linear and Non-linear general buckling analysis present different buckling modes as well as deformation shapes. Linear and Non-linear bulges are symmetrical with regard to a XOX' axis. Non-linear bulges are smoother than linear ones. Both linear and Non-linear deformation modes are linked to the uppest circumferential stiffener instability.

It is to be assessed if a safety coefficient of 2.2 with regards to general buckling is enough, considering the stiffening hypothesis used for the idealization such as total continuity of the stiffeners network, although the decelerator is constituted of 6 independant panels connected together by a device to be determined, or' the optimistic value for the material young modulus.

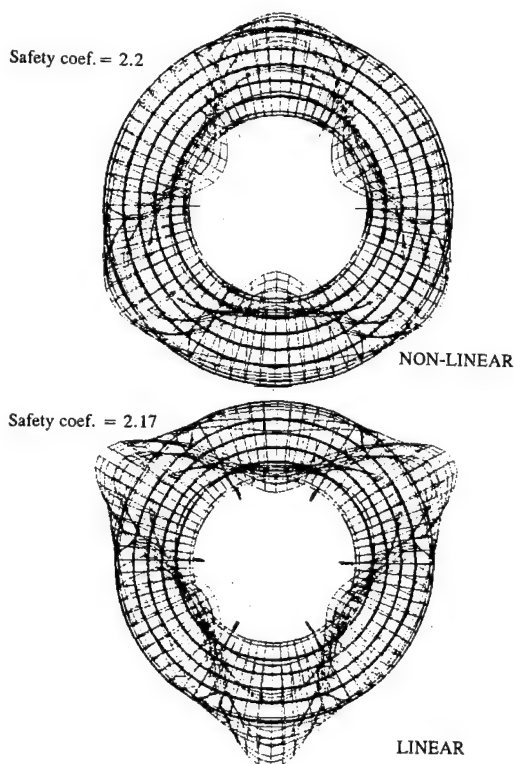


Figure 3. Deformation of the first buckling modes from linear and non-linear analysis

5. LOCAL STABILITY ASSESSMENT

Local buckling under mechanical loads

Simple analytic calculations showed that the thin skin panels were likely to buckle. Of course, shapes and amplitudes of the buckling modes were impossible to predict. Therefore Non-linear static computations were to be performed on a refined model in order to generate a realistic displacement case. Thus a very refined model was set up. This model is entirely constituted of plate elements and only 1/4 of the decelerator was represented, including the use of 2 symmetry planes, figure 4. The material characteristics are the same as in the general buckling problem.

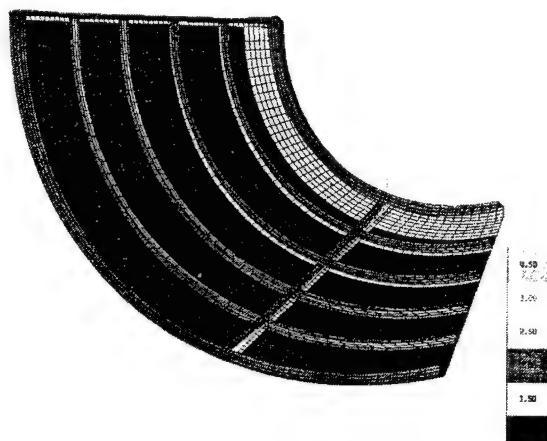


Figure 4. Decelerator refined modelization for post-buckling analysis

These Non-linear computations led to a multibuckled strain field, specially on the outer panels, with deformation values of more than 2.5mm. These deformations can hinder ballistic coefficient or generate local overfluxes. Their influence should be assessed through further specific studies. The strain field is of course conditioned by the buckling behaviour of the panels.

The Linear and Non-linear deformation modes are totally different as well as the stress maps, figure 5. The Linear deformation mode shows a very regular inflation of the different panels. On the contrary, the Non-linear strains show a network of several bulges in the panels. Up to 8 bulges can be counted in the outer panel which is the most loaded. This number of bulges depends on the accuracy (number of nodes) of the model, and can be held as definite only if the convergence of the finite element model is established. This is not quite the case in the present study but nevertheless the model accuracy is satisfying for such early phase.

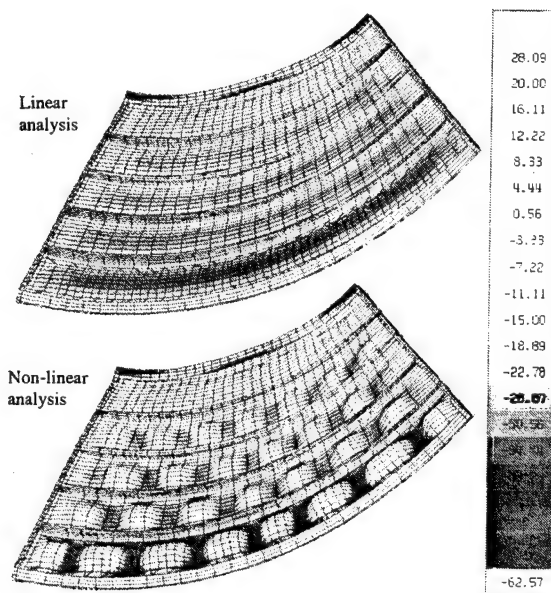


Figure 5. Lower principal stress distribution over a deformed model under pure mechanical load

The stress map follows the strain canvas, and Linear calculations provide a fairly regular repartition with light compression in the panels. The outer panel shows a more sustained regular compression. Non-linear computations provide much heavier compression between the bulges and traction on top of the latter (upper side stresses presented).

Obviously, Linear-only computations would not provide the designer with accurate enough strain and stress maps. The model consists in 26636 DOF and 4531 nodes. It requires about 90 mn CPU on an IBM 3090.

Local buckling under combined thermal and mechanical loads

Thermal transient calculations were realized on a thermal model along a typical trajectory. They take into account the conduction, radiation with enclosures between stiffeners and internal side of skins as well as the incident heat flux. No contact resistance is idealized between skin and stiffeners. An initial temperature of 108 K was imposed. The maximum temperature of about 1600 K is reached around 100 seconds after the beginning of reentry. This computation needs about 20 mn CPU (IBM 3090).

The same structural modelization is used for the thermomechanical and mechanical calculations. The computation needs 270 mn computer time (IBM 3090). As for the mechanical-only study, thermomechanical analysis shows a highly Non-linear behaviour of the decelerator. Therefore, local stability problems in the skins are of major importance. Figure 6 shows significant discrepancies between Linear and Non-linear thermomechanical computations. Stress and strain maps are on a totally different scheme. As for the mechanical-only study, Linear thermomechanical and mechanical calculations show regular panels inflation. Non-linear computations depict multi-bulged networks with as many as 6 bulges per panel according to the Finite Element density used for the thermo-elastic model as the convergence is not entirely reached.

The linear computations show regular compression stresses everywhere on the panels. Non-linear calculations show heavier compressive stresses between the bulges and stiffeners roots. Light traction appears on top of the bulges (upper side stresses presented).

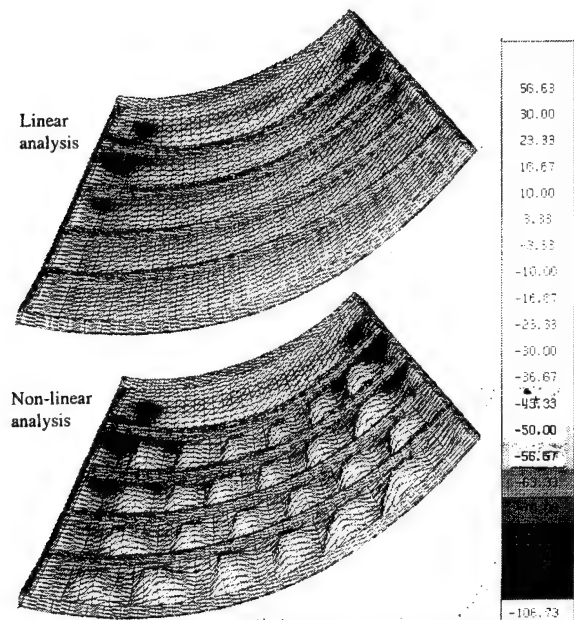


Figure 6. Lower principal stress distribution under combined mechanical and thermoelastic loads

6. CONCLUSION

Such thin skin clearly has a very Non-linear behaviour and only Non-linear analysis can lead to realistic strain and stresses. These Non-linear analysis must obviously cover combined thermo-elastic and mechanical loadings. Very thin margin is drawn from stability computations. Considering that the material behaviour is not well characterized as well as not widely used in space applications, such a margin cannot be considered as satisfying.

All the above calculations have been performed with the hypothesis that the constitutive material is homogeneous and isotropic. Being in fact composite, one cannot know if this material and structure will withstand post-buckling behaviour. Specially the quality of the skin stiffeners connection will be of utmost importance with regards to skin bulges propagation from a panel to another and general structural integrity.

Reference list

- (1) ESA-Cassini report on the phase A study
ESA ref. SCI (88) 5, October 1988
- (2) G. Lecina & C. Petiau, Optimization of aircraft structure - In Foundations of Structure Optimization Approach, ed. A.J. Morris, John Wiley, Chichester 1982, pp 4-8
- (3) C. Petiau & C. Cornuault, Efficient algorithms for post-buckling computation - Computing Methods in Applied Science and Engineering. ed. R. Glowinski & J.L. Lions, INRIA, Paris France 1983, p. 2
- (4) C. Petiau & C. Cornuault, Algorithmes efficaces pour le calcul des équilibres en post-flambement - 3ème Colloque - Tendances Actuelles en Calcul des Structures, ed. J.P. Grellier & J.M. Campel, Editions Pluralis Paris 1984, p. 2.
- (5) A. Smith, Cassini Titan Atmosphere Probe. Phase A2 - Entry Trajectories - CR 68/88
Fluid Gravity - MSS/19023/7355q/006, 1988

**SESSION
2.4.A**

**MATERIALS
IV**

CHARACTERISATION

PRECEDING PAGE BLANK NOT FILMED

N 9 2 - 2 3 8 3 2

DYNAMIC CHARACTERIZATION OF COMPOSITE MATERIALS

I. Daerden, D. Van Hemelrijck, L. Schillemans, F. De Roey, F. Boulpaep, J. De Visscher, A. Cardon.
Composite Systems and Adhesion Research Group of the Free University of Brussels
COSARGUB - VUB - TW - Kb - Pleinlaan 2 - 1050 Brussels - Belgium

ABSTRACT

This paper deals with the determination of axial and torsional damping ratios by use of a dynamic testbench. The results will be compared with those obtained by a mixed numerical/experimental technique, called resonalyser. During pure axial and torsional fatigue-testing of carbon- and glassfibre reinforced polymers, the evolution of phase-shift between load and displacement, which is a measure for the damping, is observed.

1. INTRODUCTION

The resonalyser (Ref. 1) is a non-destructive method for the determination of the four complex engineering constants of orthotropic sheet materials: the two Young's moduli E_1^* and E_2^* , Poisson's ratio ν_{12}^* and the shear modulus G_{12}^* . The method is developed at the department of structural analysis of the Free University of Brussels and it is based on the measurement of the vibrational response of a rectangular test plate, submitted to a controlled excitation.

Another way to characterize specimens dynamically is by submitting them to a forced vibration in a dynamic testbench. Two different calculation methods are applied on the captured load- and displacement signals.

2. CALCULATION METHODS

The first calculation method is based on the following. When a linear viscoelastic material is subjected to a sinusoidal axial displacement, a phase-shift δ exists between the applied stress σ and the strain response ϵ of the same frequency (fig. 1). When plotting stress and strain against each other, an hysteresis loop is obtained (fig. 2).

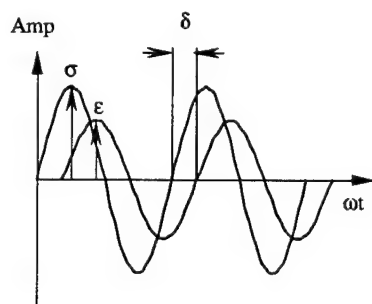


Figure 1.

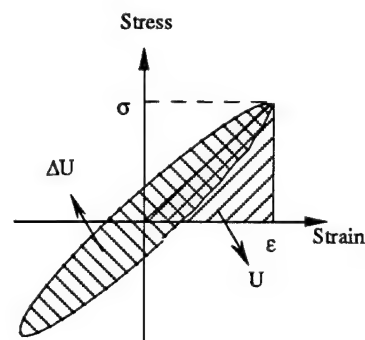


Figure 2.

The specific damping capacity is defined as

$$\psi = \frac{\Delta U}{U} \quad (1)$$

where ΔU = energy dissipated per cycle
= area surrounded by the hysteresis loop
 U = maximum strain energy stored per unit volume

and the loss-factor is written as

$$\eta = \tan \delta \quad (2)$$

where δ = phase shift.

Both parameters are related to each other as

$$\frac{\Delta U}{U} = 2\pi \eta \quad (3)$$

so δ can be found by calculating the area within the hysteresis loop and determining maximum stress and maximum strain:

$$\delta = \arctan \eta = \arctan \frac{\Delta U}{2\pi U} = \arctan \frac{\Delta U}{\pi \sigma \epsilon} \quad (4)$$

The same formula can be applied when replacing stress and strain by force and displacement or, when subjecting the specimen to a dynamic torsional load, by torque and angle.

But, when the material behaves linear, the strainresponse to a sinusoidal stress is a sinusoid and the hysteresisloop is a perfect ellipse from which the area can be calculated exactly :

$$\text{with } \sigma(t) = \sigma \sin(\omega t) \quad (5)$$

$$\varepsilon(t) = \varepsilon \sin(\omega t + \delta) \quad (6)$$

$$\text{and } \Delta U = \int y \, dx$$

the integral becomes

$$\begin{aligned} & \int_{t=0}^{t=2\pi/\omega} \varepsilon \sin(\omega t + \delta) \omega \sigma \cos(\omega t) \, dt \\ &= \omega \sigma \varepsilon \int_{t=0}^{t=2\pi/\omega} \sin(\omega t + \delta) \cos(\omega t) \, dt \\ &= \pi \sigma \varepsilon \sin(\delta) \end{aligned}$$

and we obtain

$$\delta = \arcsin \frac{\Delta U}{\pi \sigma \varepsilon} \quad (7)$$

The explanation of the difference between Eq. 4 and Eq. 7 is as follows. The stress σ and strain ε are maximum at different moments of time, determined by the phase-shift. So, the presentation in figure 2 as if the maxima of σ and ε would coincide is at least ambiguous. Figure 3 is a more realistic approach of the reality.

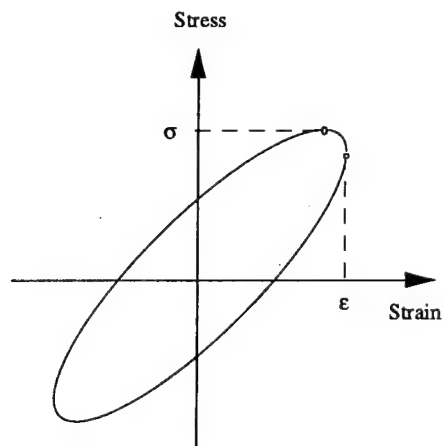


Figure 3.

When the calculation is based on the maxima of σ and ε , Eq. 7 is valid. Eq. 4 is correct when σ and ε are taken at the same moment of time and when this moment is either when σ or ε reaches a maximum.

For example, when $\omega t = \frac{\pi}{2}$, the stress reaches a maximum and Eq. 5 becomes

$$\sigma\left(\frac{\pi}{2\omega}\right) = \sigma$$

and the strainresponse is then given by Eq. 6

$$\varepsilon\left(\frac{\pi}{2\omega}\right) = \varepsilon \cos \delta$$

Eq. 4 becomes

$$\delta = \arctg \frac{\Delta U}{\pi \sigma \varepsilon \cos \delta}$$

so,

$$\delta = \arcsin \frac{\Delta U}{\pi \sigma \varepsilon}$$

which is equal to Eq. 7.

Eq. 4 and 7 give the same results for small values of δ - which is true in most of the cases - but the error becomes considerable for higher values:

$$\begin{aligned} \delta = 5^\circ & \quad \text{then error} = 0.34 \% \\ \delta = 20^\circ & \quad \text{then error} = 6.40 \% \end{aligned}$$

Compared to measuring δ directly at the zero-crossing points, this calculationmethod has some advantages. Firstly, much more datapoints are used for a greater accuracy. Secondly, when the material behaves non-linear, the strainresponse to an applied sinusoidal stress is a distorted sinusoid. In that case, it makes no sense to speak about a phaseshift, because it is varying throughout the cycle, giving a distorted hysteresisloop and a dampingratio determined from a single measurement of the phaseshift would be incorrect.

But by calculating the area of the loop, the obtained lossfactor is correct and can be used to derive the apparent phase angle which represents the equivalent energy within the true elliptic shaped hysteresisloop for a linear material.

To obtain phase-shift values, also a Fast Fourier Transform was applied on both stress and strain signals. But unfortunately, this calculationmethod only considers the fundamental frequency and does not take into account other harmonic components. Thus, when non-linear behaviour is exhibited, the obtained result is incorrect.

3. HARD AND SOFTWARE

The data-acquisition and -calculation is performed on a Apple Macintosh II computer with 5 Mbyte memory, equipped with a 4 channel sample and hold analog to digital conversionboard, with a maximum samplefrequency of 1 MHz.

The program is written in a fourth generation programming language, called Labview (Ref. 2).

4. TEST SYSTEMS

The dynamic tests were performed on a MTS servo-hydraulic testbench with two degrees of freedom. The maximum force in tension-compression is 100 kN and maximum torque is 1 kNm. The frequency is limited up to 20 Hz.

When loading axially, the displacement could be measured by using the signal returned by the MTS (which is measured by an internal LVDT). By doing this, the damping in the end-tabs is also considered. Using strain gauges during fatigue-tests had to be stopped, because they did not sustain at high strains for a long time. Finally we clamped an extensometer on the specimen which gave results with an estimated error of about $\pm 0.1^\circ$.

When loading in torsion, we had to deal with a big problem. The failure torque of thin test specimens (16 layers), even with fiber orientation of $\pm 45^\circ$ was smaller than 15 Nm. Using this machine is like killing a mouse with an elephant gun and the returned torque-signal was very noisy.

Nevertheless, when the torque-signal is high enough, a maximum error of $\pm 0.1^\circ$ is possible.

Besides, The electronic system of the MTS introduces an initial phase-shift between torque and angle signals, which is also frequency dependent (fig. 4).

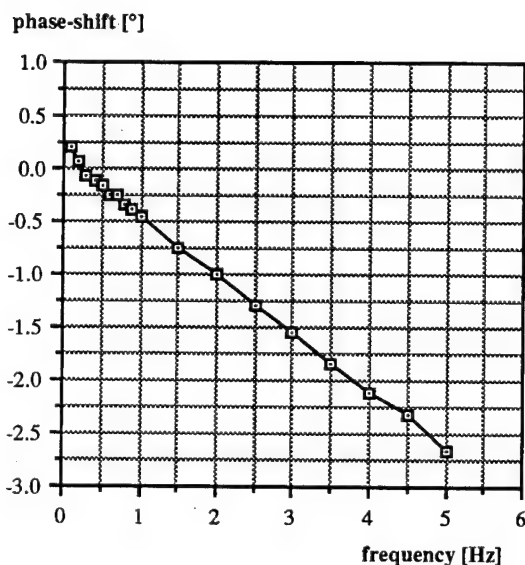


Figure 4. Initial phase-shift introduced by MTS.

This curve is obtained by testing a specimen of a material with very low damping behaviour, for example steel.

So, for testing thin specimens in torsion, we used a self-developed torsion testbench (Ref. 3) which consists of a steppingmotor with planetary gearbox. The maximum torque applied is 25 Nm and the minimum resolution of the torque-cell is 4Nmm. The estimated error on obtained phase-shifts is again $\pm 0.1^\circ$.

5. EXPERIMENTAL RESULTS

Table 1 lists axial and torsional phase-shift values obtained by the different test methods. For unidirectional and cross-ply specimens axial damping values are too low to determine accurately by use of the testbenches. The error on the values determined by use of the resonalyser are not mentioned because these depend on the number of homogeneities in and the variation of the thickness of the tested plate. The results obtained by the different methods agree quite good.

Layup	Testsystem	Phase E ₁ [°]	Phase G ₁₂ [°]
[0] ₁₆	MTS/torsionbench	0.01±0.1	1.3±0.1
	Resonalyser	0.07	1.34
[0,90] _{s16}	MTS/torsionbench	0.04±0.1	1.2±0.1
	Resonalyser	0.07	0.90
[±45] _{s16}	MTS / MTS	0.57±0.1	0.23±0.1
	Resonalyser	0.49	-

Table 1. Axial and torsional phase-shift results.

Carbonfibre/epoxy and glassfiber/polyester specimens were subjected to a sinusoidal varying load applied in tension with a frequency of 5 Hz. The R ratio was 0.1. The carbon specimen was made of 16 plies of Fibredux 914 prepreg. The glassfiber specimen consisted of 8 plies of bidirectional woven fabric of 300g/mm². Both lay-ups were $\pm 45^\circ$ oriented in order to get a considerable amount of friction between fiber and matrix.

Figure 5 monitors evolution of phase-shift with number of cycles. During the fatigue-test, stress-levels were increased in order to accelerate the damage process. Just before failure (at 77.000 cycles), phase-shift is increasing very pronounced. At every moment of the fatigue-process, difference exists between the phase-shift obtained by calculating the area of the hysteresisloop and by applying a Fast Fourier Transform, which assumes non-linear behaviour of the specimen. This difference increases with number of cycles.

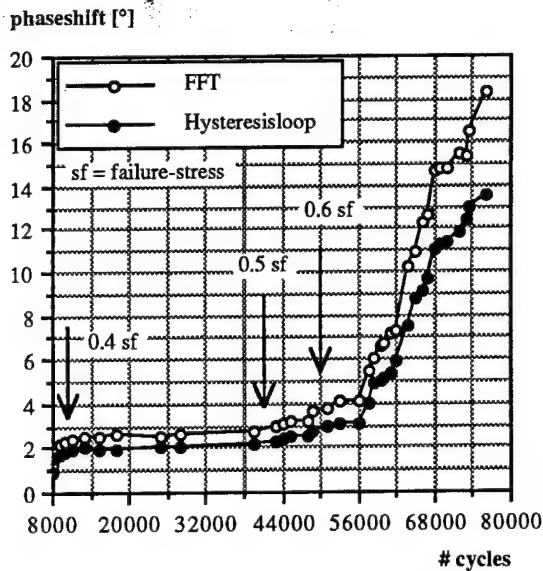


Figure 5. Glassfiber/polyester specimen ($\pm 45^\circ$).

Figure 6 demonstrates the strong dependency of the stress-level. At $0.4 \sigma_f$, phase-shift varies little, no matter what the number of cycles is.

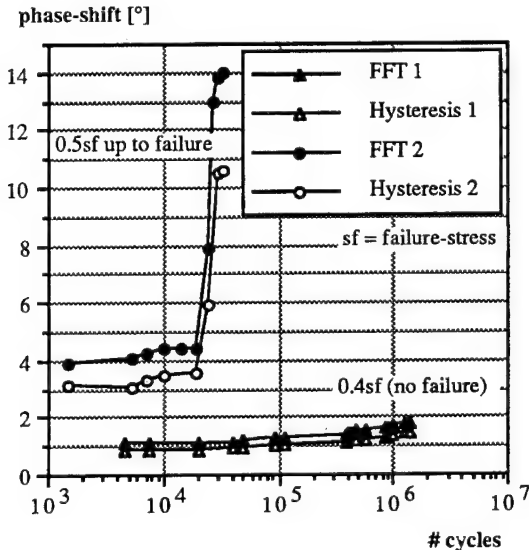


Figure 6. Carbonfiber/epoxy specimen ($\pm 45^\circ$).

A carbonfiber specimen with fiberorientation of $\pm 45^\circ$ was dynamically loaded in torsion. Figure 7 shows the evolution of torsional damping in function of number of cycles for different levels of maximum in-plane shearstress. Also the corresponding degradation of the in-plane shearmodulus is plotted. The used formulas to calculate the maximum in-plane shearstress and the in-plane shearmodulus can be found in reference 3. Increasing

of energydissipation due to damage starts simultaneously with decreasing of the in-plane shearmodulus.

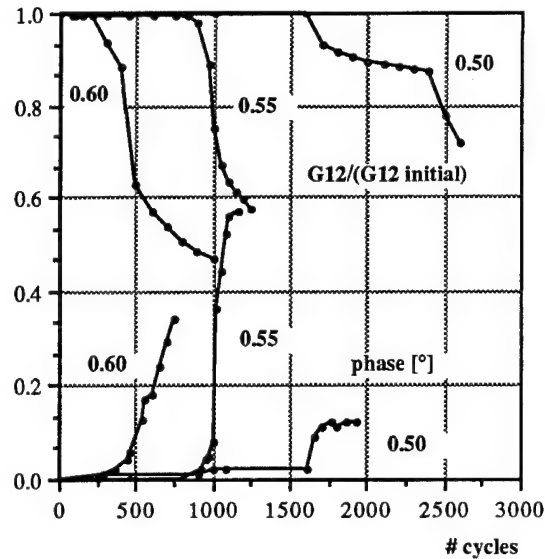


Figure 7. Evolution of in-plane shearmodulus and torsional phase-shift at 0.6, 0.55 and 0.5 times the max in-plane shearstress.

6. CONCLUSIONS

Damping measurements must be carefully made : the apparatus must be purged of extraneous losses by calibrating it with some metal of very low damping properties.

When the signals are "clean", the error on phase-shift determined by use of dynamic testbenches does not exceed $\pm 0.1^\circ$ and agreement exists with the results of the resonalyser. Dampingratio's are sensitive for damage initiation and propagation.

7. REFERENCES

1. Sol H., De Visscher J., Vantomme J., Mixed numerical/experimental techniques for the characterisation of polymer matrix composite laminates, *Proc. Durability of polymer based composite systems for structural applications*, Brussels, Belgium, aug. 1990 p 514-523.
2. Daerden I., Van Hemelrijck D., Schillemans L., De Roey F., Boulpaep F., Cardon A., Static and dynamic characterization of composites, using a fourth generation programming language on a Macintosh, *Proc. Euromech 269*, Saint-Etienne, France, dec. 1990.
3. Van Hemelrijck D., Schillemans L., Daerden I., De Roey F., Boulpaep F., De Visscher J., Cardon A., The torsional fatigue-behaviour of the in-plane and out-of-plane shear moduli of composite materials, *Proc. International Symposium on Spacecraft Structures and Mechanical Testing*, ESTEC, Noordwijk, The Netherlands, 24th-26th April 1991.

N92-23833

53-27
84-45

COMPOTEMENT MECANIQUE DES MATERIAUX COMPOSITES ET ASSEMBLAGES COLLES AUX BASSES TEMPERATURES

C. Laurent

Aérospatiale, Les Mureaux, France

RESUME

Que ce soit dans le domaine des structures de satellites (90K), ou dans celui des réservoirs cryotechniques, (4K), la connaissance des comportements des matériaux composites, fibres de carbone-matrice organique, aux basses températures devient indispensable si on envisage de les utiliser pour de telles applications.

La bibliographie à ce sujet est relativement muette et pourtant, ces matériaux présentent à froid un comportement fragile et sont par conséquent très sensibles aux contraintes internes, prenant naissance au refroidissement.

Aujourd'hui, les travaux réalisés ont permis d'évaluer les performances mécaniques à froid (jusqu'à 90K) d'un certain nombre de matériaux, fibres de carbone-résine et d'assemblages collés, d'un point de vue :

- température de polymérisation des résines ou des adhésifs

- nature des fibres

et de dégager des tendances en mettant l'accent sur les aspects sensibles et méconnus.

Les résultats montrent, contrairement à certaines idées reçues, que les résines (ou les adhésifs dans le cas des assemblages collés) qui polymérisent à plus haute température et qui présentent la meilleure tenue à chaud, ont bien souvent le meilleur comportement à froid malgré le plus haut niveau de contraintes thermiques.

Mots clés : basses températures, essais mécaniques, composites, assemblages collés.

1. INTRODUCTION

Les véhicules spatiaux, que ce soient les structures satellites, dont certaines sont soumises à des cycles thermiques compris entre -180°C et +150°C (réflecteurs) ou les lanceurs, dont les réservoirs d'ergols peuvent atteindre des températures de 4K, font de plus en plus appel aux matériaux composites et plus spécifiquement aux fibres de carbone associées à une matrice organique.

Les structures réalisées avec ces matériaux pour de telles applications sont le siège de fortes contraintes internes en raison des grandes variations de températures.

La fatigue, due au cycle thermique à laquelle peuvent s'ajouter des sollicitations statiques ou dynamiques, peut affecter la fiabilité de ces structures dans le temps si on ne maîtrise pas le mécanisme de dégradation et si on n'en pallie pas leurs effets.

L'expérience acquise au cours de simulations au sol (cycle thermique et vibrations) sur des structures complètes fait souvent apparaître des ruptures par délaminage du composite au niveau des liaisons collées.

Ce phénomène a été confirmé avec de petits éléments structuraux, soumis aux mêmes types de sollicitations, montrant que les propriétés mécaniques des liaisons pouvaient être réduites de 50% sans pour autant remettre en cause la qualité du collage ou son principe.

La bibliographie portant sur le comportement mécanique des matériaux composites en subambiant est peu fournie, ce qui nous a incité dans un premier temps à mettre en évidence quelques paramètres influents et surtout leurs effets tels que le mode d'élaboration des matériaux (température de polymérisation des résines et des adhésifs), la nature des fibres (adhérence fibre-matrice, module, résistance); les résultats de ces travaux embryonnaires font l'objet de notre présentation.

La prise de conscience de ces comportements doit nous inciter à développer des outils de calcul et à les intégrer dès le stade avancé de la conception.

L'objectif final sera évidemment de comprendre le mécanisme de ruine des matériaux composites aux basses températures et de le modéliser pour en prévenir les effets nocifs.

2. ORIGINES DES CONTRAINTES INTERNES

Nous recensons trois causes principales aux contraintes internes dans les matériaux composites :

- les contraintes résiduelles de cuisson, induites, au refroidissement, par la disparité des coefficients de dilatation thermique et des modules (fibres et matrice). En effet, entre la température de fageage du polymère (généralement, température de cuisson et contraintes nulles) et la température ambiante, la résine tend à se contracter* et la fibre à s'allonger*.

- les contraintes dues au retrait chimique au cours d'une sollicitation thermique (isotherme ou cyclique) résultant d'un accroissement du taux de réticulation et par conséquent d'un retrait dimensionnel.

- les contraintes dues à la température d'essai: si cette dernière est supérieure à la température ambiante, les contraintes seront moindres, si par contre elle est inférieure, les contraintes internes s'ajouteront aux contraintes résiduelles de cuisson.

Or le module d'Young de la fibre étant très supérieur à celui de la résine, cette dernière verra son allongement

* ($\alpha_{résine}=30$ à $60.10^{-6}/^{\circ}C$, $\alpha_{fibre}=0.5.10^{-6}/^{\circ}C$ pour une fibre de carbone haute résistance)

imposé par celui de la fibre. La résine sera alors soumise à des contraintes de traction et de cisaillement à l'interface :

$$\sigma_{th} = f(\Delta T, \Delta \alpha, E) \quad \text{avec } E = g(T)$$

Si le matériau est unidirectionnel et que son allongement le permet, la déformation étant libre dans le sens transversal, ces contraintes se dissiperont normalement; par contre si les couches sont croisées, les déformations seront bloquées dans les deux directions et l'allongement en sera fortement réduit.

A ces contraintes, s'ajoutent normalement les contraintes mécaniques et le niveau de rupture globale dépendra de :

- de l'adhérence fibre-résine,
- de l'allongement à rupture de la résine, sens transversal (résine époxy: 0,5%, résine polyimide: 0,6%, résines tenace et thermoplastique: >1%),
- de l'orientation des plis par rapport à l'axe d'effort,
- de l'épaisseur des couches,
- de la séquence d'empilement.

Les mêmes phénomènes se retrouvent globalement dans les assemblages collés, plus ou moins pondérés avec la nature de l'adhésif (nature chimique, charges, support).

Les travaux qui sont présentés ici tentent de mettre en évidence l'effet de ces contraintes internes sur la tenue mécanique à froid de matériaux composites et assemblages collés.

3. DOMAINES EXPLORÉS

Composites

Afin de dégager des tendances et d'examiner l'influence de différents paramètres sur le comportement aux basses températures des matériaux composites, tels que le mode d'élaboration des matériaux (température de polymérisation), l'adhérence fibre-matrice, nous avons choisi d'étudier les matériaux suivants:

- 3 types de fibres de carbone de caractéristiques différentes d'un point de vue module d'Young, résistance, adhérence et coefficient de dilatation,
- 2 types de résines polymérisant à des températures différentes

L'association des différents types de fibres et de résines conduit aux combinaisons suivantes (tableau 1) :

Tableau 1 : Matériaux composites

	RESINE EPOXY (Polym.175°C)	RESINE POLYIMIDE (Polym.300°C)
FIBRE HAUTE RESISTANCE	T300/914	T300/LaRC160
FIBRE HAUTE MODULE	HM35/914	HM35/LaRC160
FIBRE TRES HAUT MODULE	GY70/914	-

Assemblages collés

Afin d'examiner l'influence de différents paramètres, tels que la température de polymérisation des adhésifs, leur nature, mais également la nature du substrat, nous avons choisi d'étudier les matériaux suivants:

- 3 adhésifs époxy (HYSOL EA 9321, polymérisant à température ambiante et à 105°C, REDUX 312L, polymérisant à 120°C, REDUX 319L, polymérisant à 180°C).
- 3 types de substrats : aluminium, composite carbone-époxy, composite carbone-polyimide.

L'association des différents matériaux conduit aux combinaisons suivantes (tableau 2) :

Tableau 2 : Assemblages collés

	Polym. temp. amb.	Polym. à 105°C	Polym. à 120°C	Polym. à 180°C
Substrat ALUMINIUM	EA 9321 2024	EA 9321 2024	R 312 L 2024	R 319 L 2024
Substrat CARBONE* EPOXY	EA 9321 T300/914	EA 9321 T300/914	R 312 L T300/914	R 319 L T300/914
Substrat CARBONE* POLYIMIDE	-	-	R 312 L T300/LaRC160	R 319 L T300/LaRC160

Méthodologies d'essais

Sur composites, des essais de cisaillement interlaminaire et de flexion 3 points ont été réalisés respectivement sur drapage unidirectionnel et quasi-isotrope 16 plis.

Les schémas des éprouvettes sont donnés figures 1 et 2.

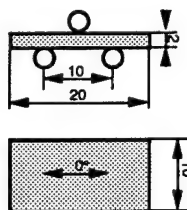


Figure 1 : Epreuve de cisaillement interlaminaire

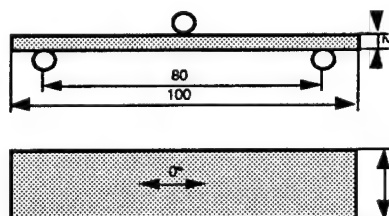


Figure 2 : Epreuve de flexion 3 points

* drapage : (0, 0, 0, +45, 90, -45, 0, 0) sym

Le schéma des éprouvettes de cisaillement adhésif est donné figure 3.

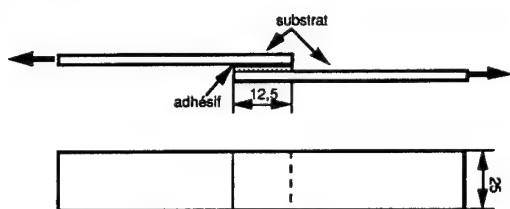


Figure 3 : Eprouvette de cisaillement adhésif

Domaine de température

Les essais ont été réalisés :

- sur composites carbone-époxy : entre -150°C et $+150^{\circ}\text{C}$,
- sur composites carbone-polyimide : entre -150°C et $+280^{\circ}\text{C}$,
- sur assemblages collés : entre -180°C et $+150^{\circ}\text{C}$.

4. RESULTATS

Cisaillement interlaminaire

Les courbes de la figure 4 donnent l'évolution de la contrainte à rupture en cisaillement interlaminaire, en fonction de la température, de matériaux composites unidirectionnels renforcés de fibres de carbone haute résistance, haut module et très haut module.

Bien que l'influence des contraintes thermiques ne soit pas prépondérante dans le cas de matériaux unidirectionnels, on observe néanmoins un effet des basses températures sur l'adhérence fibre-matrice : plus les fibres ont un module élevé, plus la chute de caractéristiques est prématurée et plus le domaine de rupture par délaminage est étendu.

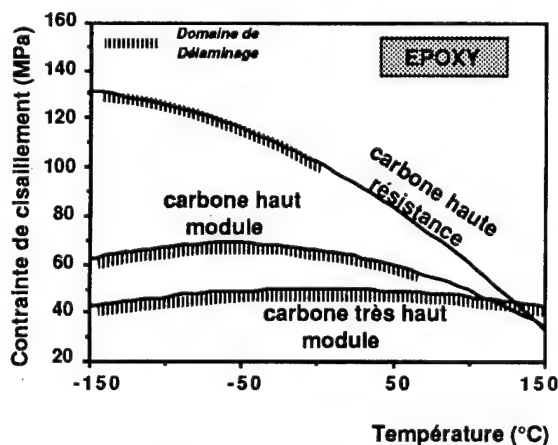


Figure 4 : Essais de cisaillement interlaminaire
Composite unidirectionnel

Flexion

Les courbes de la figure 5 représentent l'évolution de la contrainte à rupture en flexion, en fonction de la température, pour des matériaux composites à couches croisées renforcés de fibres de carbone haute résistance et haut module, imprégnés de résine époxy et polyimide.

On observe, sur les matériaux à base de résine époxy, que plus les fibres ont un module élevé et un coefficient de dilatation thermique faible, plus la chute de caractéristiques est accentuée aux basses températures; de plus, le domaine de rupture par délaminage est plus étendu que sur les matériaux à base de résine polyimide.

Malgré les contraintes thermiques plus importantes sur les composites polyimides, ces derniers se révèlent supérieurs aux composites époxy, en deçà de -100°C , pour les fibres haut module et probablement en deçà de -200°C , pour les fibres haute résistance. Ceci constitue un résultat inattendu et fort appréciable dans le domaine aérospatial qui appelle généralement à la fois les très basses températures et la haute rigidité.

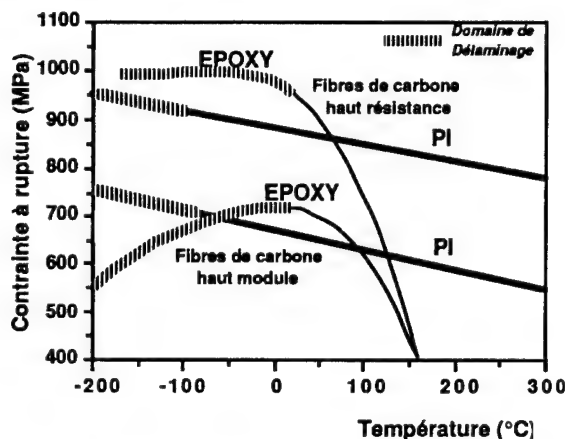


Figure 5 : Essais de flexion 3 points
Composite quasi-isotrope

Assemblages collés

Influence de la température de polymérisation

Les courbes des figures 6 et 7 montrent qu'un adhésif durcissant à température ambiante, mais non totalement polymérisé à cette température, peut voir ses propriétés améliorées à froid sur aluminium, par une polymérisation complémentaire ce qui a pour effet d'améliorer l'adhérence; par contre, sur substrat carbone, une température de polymérisation élevée conduit à accroître les contraintes thermiques dans la liaison (contraintes résiduelles de cuisson, retrait chimique et température d'essai) et donc à diminuer sa tenue à froid avec des ruptures en délaminage dans le composite.

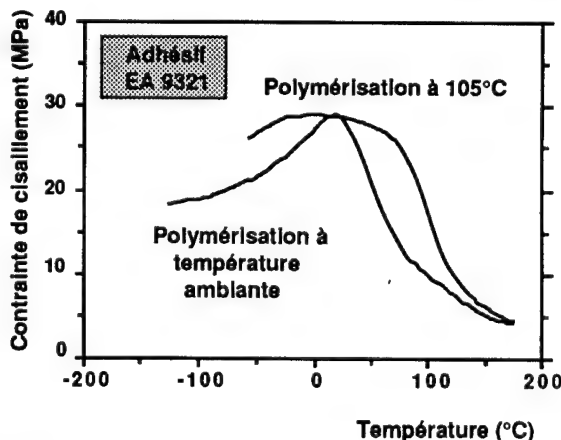


Figure 6 : Essais de cisaillement adhésif
Adhésif EA 9321. Substrat aluminium

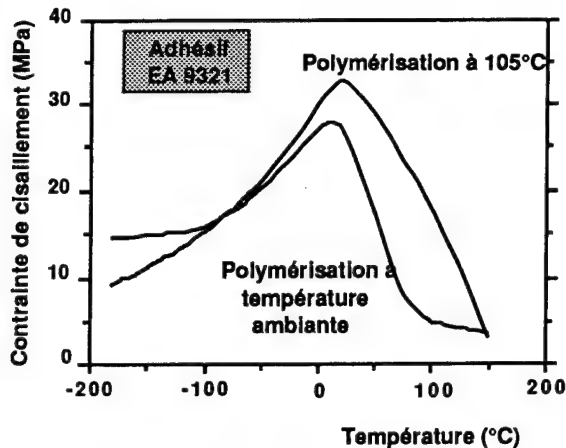


Figure 7 : Essais de cisaillement adhésif
Adhésif EA 9321. Substrat Carbone-époxy

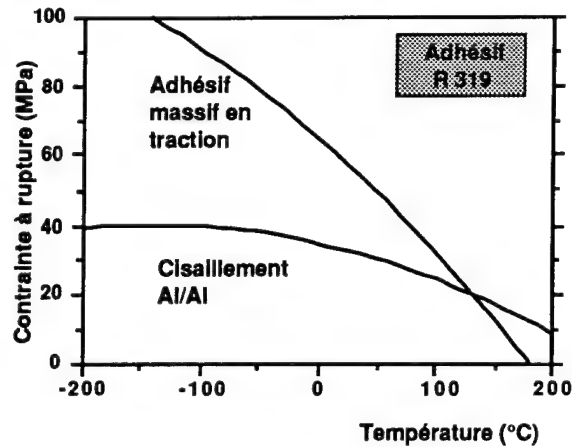


Figure 9 : Comportement comparé d'un adhésif en masse et d'un assemblage collé. Adhésif R 319L

Influence de la nature de l'adhésif

Les courbes de la figure 8 montrent que, sur substrat aluminium, les caractéristiques en sub-ambient des adhésifs Rédux 312L et Rédux 319L sont nettement plus élevées que celles de l'adhésif EA 9321, malgré une polymérisation à plus haute température.

Les contraintes thermiques existent néanmoins sur collage aluminium et limitent les caractéristiques de la liaison par rapport à l'adhésif en masse (figure 9).

Malgré une polymérisation à plus basse température que la Rédux 319L, les caractéristiques de la Rédux 312L chutent prématurément en subambient associées, dans les deux cas, à des ruptures en délaminage dans le composite (figure 10). Ce résultat peut être rapproché par les courbes de la figure 11 qui montrent que les écarts de coefficients de dilatation entre le substrat carbone et l'adhésif sont plus importants dans le cas de la Rédux 312L que dans celui de la Rédux 319L et peut donc traduire une différence d'état de contrainte. La même remarque pourrait probablement être faite en ce qui concerne les modules élastiques, bien que les mesures n'aient pas été réalisées.

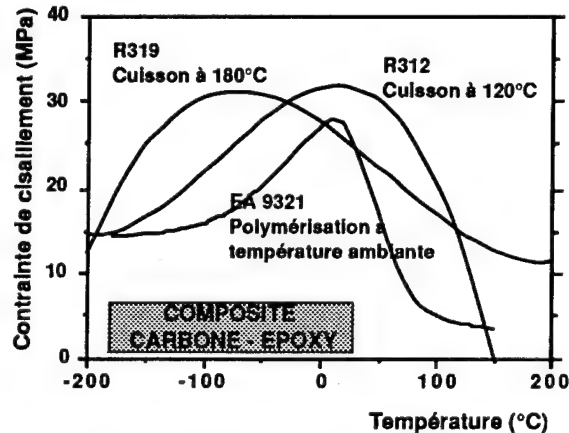


Figure 10 : Essais de cisaillement adhésif
Substrat Carbone-époxy

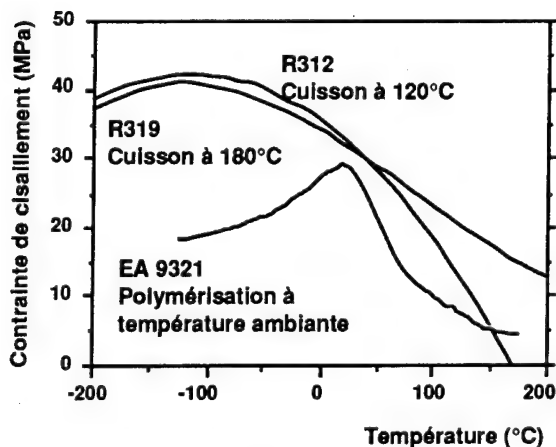


Figure 8 : Essais de cisaillement adhésif
Substrat aluminium

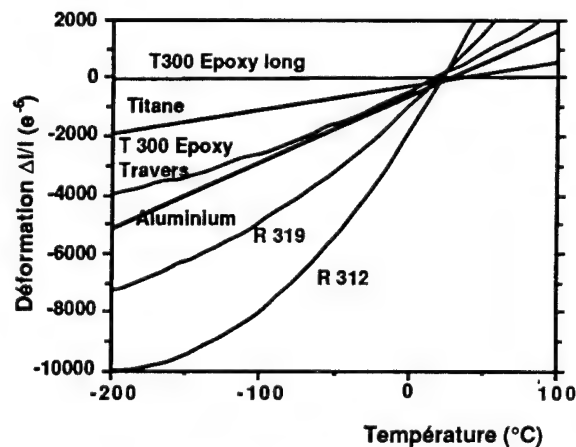


Figure 11 : Coefficients de dilatation thermique.
Comparaison adhésif/substrat

Influence du type de substrat

Les courbes de la figure 12 montrent que la nature du substrat joue un rôle important sur la tenue aux basses températures des assemblages collés. En effet, dans le cas de l'adhésif Rédux 319L, alors que sur substrat époxy, à basses températures, les chutes de caractéristiques de l'assemblage sont associées à des ruptures en délaminage, sur substrat polyimide, les ruptures se produisent par perte d'adhérence, expliquant ainsi les dispersions observées.

Le délaminage n'étant plus une limitation, une optimisation du traitement de surface des PI permettrait de réduire la dispersion et accroître les caractéristiques à froid de l'assemblage pour tendre vers celles obtenues sur aluminium.

Conformément à ce qui avait été observé avec un substrat époxy (figure 10), la figure 13 montre que, sur substrat polyimide la nature de l'adhésif a, ici encore, une influence prépondérante sur la tenue à froid des liaisons collées. On observe, bien que la résistance de l'assemblage ne soit pas limitée par le délaminage du composite, que l'adhésif R 312L se révèle toujours en dessous de l'adhésif R 319L. Il aurait été intéressant d'examiner (et ceci fera l'objet d'une étude ultérieure plus exhaustive), avec un traitement de surface et une polymérisation plus optimisés, si les liaisons PI-R 312L ne se rapprocheraient pas de celles des assemblages sur aluminium (figure 8).

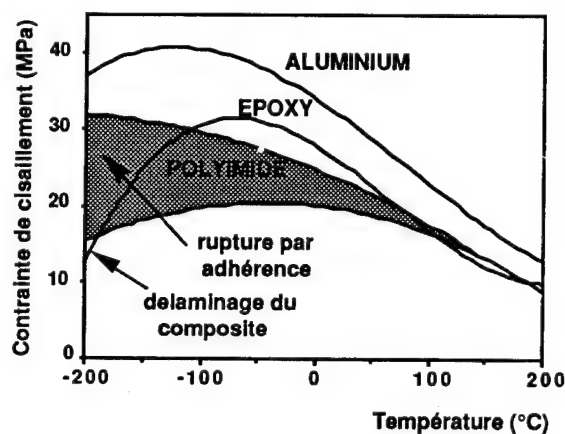


Figure 12 : Essais de cisaillement adhésif
Adhésif REDUX 319L

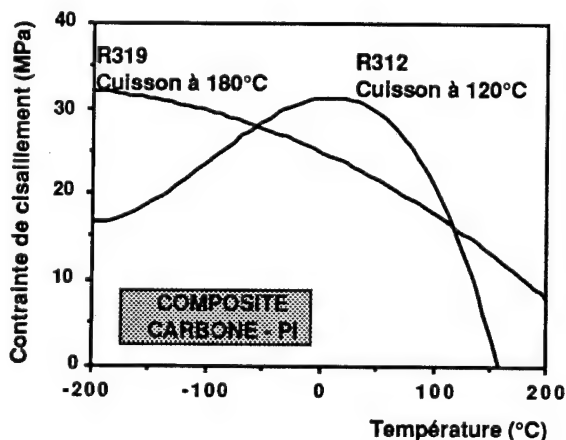


Figure 13 : Essais de cisaillement adhésif
Substrat Carbone-polyimide

5. CONCLUSIONS

En résumé, du point de vue des propriétés mécaniques des composites carbone-résine époxy, la tenue aux basses températures est d'autant plus faible et la sensibilité au délaminage croissante que la rigidité des fibres est élevée (ces deux paramètres étant intimement liés).

En ce qui concerne les assemblages collés, leur comportement à froid dépend :

- du degré de polymérisation des adhésifs,
- des modules d'élasticité et des coefficients de dilatation thermique de l'adhésif et des substrats,
- de la résistance mécanique de l'adhésif et des substrats,
- des écarts de température entre la polymérisation et la température de service,
- de l'état de surface du substrat.

Contrairement aux idées reçues, les résines polyimides se révèlent supérieures aux résines époxy, comme l'atteste leur bon comportement mécanique en sub-ambient, malgré l'existence de contraintes thermiques plus élevées (hautes températures de polymérisation):

sur composites

- leur résistance au délaminage est supérieure et ce quelle que soit la nature de la fibre,
- leurs caractéristiques mécaniques sont supérieures vers les basses températures (selon le type de fibres) comme vers les hautes températures.

sur assemblages collés

- leur résistance au délaminage est supérieure mais du fait de leur plus grande cohésion, la sensibilité au traitement de surface paraît plus grande. Des efforts technologiques devront porter sur l'optimisation du traitement de surface.

La prise de conscience de ces comportements doit nous inciter à développer des outils de calcul et à les intégrer dès le stade avancé de la conception, l'objectif final étant de comprendre le mécanisme de ruine des matériaux composites aux basses températures et de le modéliser pour en prévenir les effets nocifs.

Pour ce faire et afin d'apporter les éléments qui permettront de sélectionner les constituants des matériaux composites, susceptibles d'être utilisés aux basses températures, il est nécessaire de s'intéresser non seulement aux propriétés des matériaux, mais également à celles des constituants élémentaires tout en examinant les possibilités d'assemblage de ces matériaux.

Afin de dégager des règles de choix pour répondre aux besoins relatifs à la conception et au calcul de structures composites aux basses températures, l'approche doit être expérimentale (obtention de l'ensemble des caractéristiques relatives aux matériaux et à leurs constituants) et théorique (pour pouvoir modéliser les phénomènes et utiliser au mieux dans les calculs les caractéristiques obtenues expérimentalement : caractéristiques élastiques, modèles d'endommagement, influence de l'environnement et du vieillissement ...).

N92-23834

504-37

847-5

MECHANICAL TESTING ON A COMPOSITE FLEXIBLE STRUCTURE

G.Fanti, F. Angrilli, P. Baglioni, G. Bianchini

Dipartimento di Ingegneria Meccanica, Università di Padova,
Via Venezia 1, 35131, Padova, Italy (Fax 39/49/8070071)

1. ABSTRACT

A measuring method for the evaluation of the mechanical parameters of very flexible structures like long, multilayered ropes, such as that used in Tethered Subsatellite System TSS-1, is presented here.

Stiffness, longitudinal propagation velocity, loss factor and hysteresis are determined in tether samples with different lengths (3+25 m) and submitted to different environmental conditions such as temperature, pressure and humidity.

Two stick-slip mechanisms among adjacent layers of the rope have been detected: the first one, that we call "macro-slidings", comes out in tethers about 25 m long at room temperature, and in tethers about 7 m long at low temperature (about -100° C); the second mechanism, "micro-slidings", is always present with a loading cycle. As a consequence of these slidings, a tension transfer among the layers occurs. To explain this behavior, a "beads model" of the tether has been considered.

A finite element model of a three-layer rope was also developed in order to clarify the behavior of the composite tether.

Keywords: mechanical parameters, rope, TSS-1, stick-slip.

2. INTRODUCTION

This study analyzes the mechanical behavior of some samples of the 20 km long composite tether that will be used to connect the TSS-1 (Tethered Subsatellite System) subsatellite to the Space Shuttle, see figure 1.

During the TSS-1 Mission sudden variations of the temperature due to sun/dark transition of the whole system are expected (the temperature range should be about -120 + -20°C).

Previous works, to which readers are referred for an exhaustive discussion, investigated the mechanical properties of a sample of TSS-1 tether about 3 m long at room temperature (1) and the mechanical properties of samples of TSS-1 tether about 4 m long, at different temperatures (from -100°C to +80°C) (2).

In the present work both the effects due to scale and the environmental conditions on the mechanical properties of the rope have been investigated.

Tests were done at room temperature on a 25 m tether sample and in the range of temperature -120°C + +30°C on 6.90 m samples. Both vacuum and humidity effects have been analyzed on this latter.

The behavior of the layers in the composite rope is then discussed and explained.

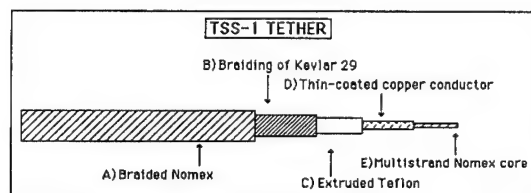


Figure 1: The TSS-1 tether is made of 5 different layers. There is multistrand Nomex core around which a thin-coated copper conductor is wound; the conductor is insulated with a coating of extruded Teflon; a braiding of Kevlar 29 around the conductor might function as a strength member and, lastly an outer jacket of braided Nomex is used for protection against mono-atomic oxygen.

In the previous paper (2) it was found that:

- "the mechanical parameters depend to a considerable extent not only on applied prestress but also on the state of internal layer so that both stress and load histories are very meaningful": this statement is still confirmed;

- "higher stress on the tether cancel previous load history": this statement is also confirmed;

- "the virgin tether shows high non elasticity due to easy tether layer sliding"; regarding this statement, the relevant braiding effect in the layers, must be added; each fibre, in a stressed braided layer (such as external Nomex and Kevlar) changes its orientation angle causing both fibres sliding, and a compression of the inner layers, see figure 2.

- "when temperature decreases (to about -100°C) Kevlar elongates but Nomex contracts and a percentage of stress is consequently transferred to the Nomex compressing the layers"; this mainly happens during the early thermal cycles and so the external Nomex get packed; after this transitory phase, elastic stress moves among the layers and stick/slip mechanisms occur. Furthermore, when the tether is tensioned, it must be considered that also the inner Copper and Nomex layers react with the external Nomex and Kevlar layers.

The study of the scale effect is very important to understand the behavior of a 20 km long tether. It is not possible to measure directly the mechanical parameters in a so long structure.

The scale effect has been studied in samples of different lengths up to 25 m.

It seems that these lengths are big enough (with respect to the rope diameter), to measure some mechanical parameters of the composite structure such as stiffness or loss factor, but not sufficient for a complete evaluation of the "packing effects".

It is planned to make some tests on tether samples up to 100 m long in the near future.

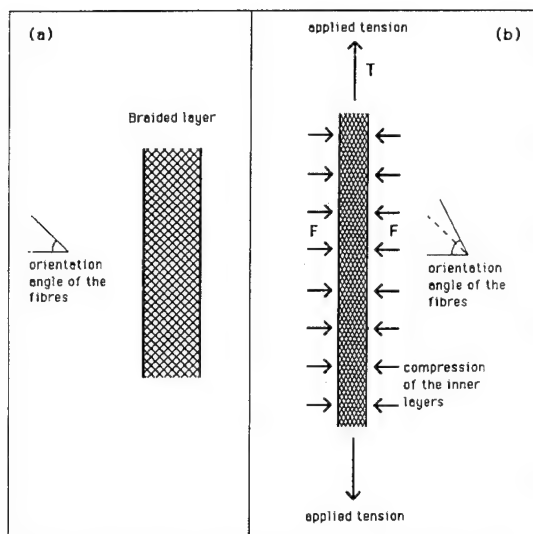


Figure 2: In the composite tether, a braided layer (a) changes its orientation angle when tensioned (b). A partially irreversible process, called "packing", caused by the applied tension T , induces the compression F of the inner layers.

3. EXPERIMENTAL APPARATUS

The basic experimental apparatus consists on thermal and vacuum pipes containing the tether (see figure 3) equipped with the following devices:

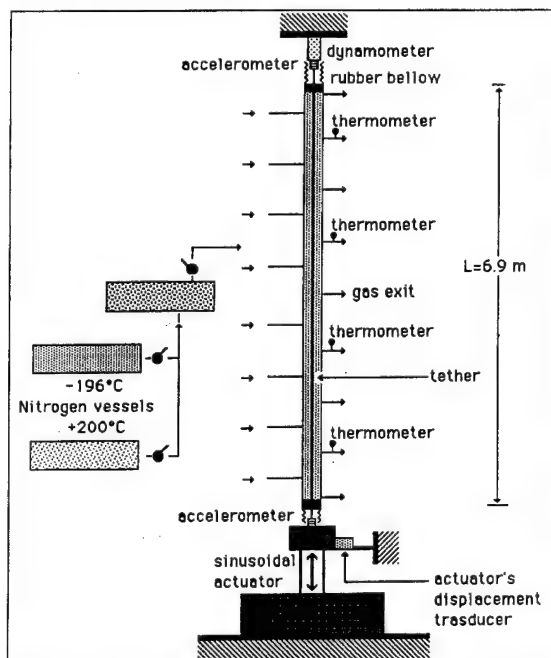


Figure 3: Experimental apparatus used for testing samples of tethers 6.90 m long, at different temperatures; it consists of a thermal pipe containing the tether, one dynamometer placed at the upper end of the tether, two motion transducers located at each end, a sinusoidal motion actuator with variable amplitude and frequency and a data acquisition and recording system. The thermal pipe consists of an inner Comflex layer ($\varnothing 100$ mm) stiffened externally by a PVC pipe, 2 mm thick.

- two accelerometers located one at each end of the tether;
- one dynamometer placed at the upper end of the tether;
- a sinusoidal motion actuator with variable amplitude (0.1 ± 200 mm) and frequency (0.002 ± 2 Hz);
- a data acquisition and recording system.

The thermal pipe is made by an inner Comflex layer ($\varnothing 100$ mm) stiffened externally with a PVC pipe, 2 mm thick. The desired temperature is obtained by mixing flows of gaseous nitrogen coming from two vessels, one at $+200^\circ\text{C}$ and the other one at -196°C . Temperature was monitored along the pipe by four digital thermometers.

With such a thermal pipe it was possible to attain a uniform variation of the temperature along the rope, in few tens of seconds from about 20°C to -120° (such condition will arise in orbit during a sun/dark transition).

Three different experimental set-up have been made.

The **first** one, has been used for testing samples of tethers 3.30 and 6.90 m long, at different temperatures.

The **second**, similar to the first, has been used for testing samples of tethers 3.30 and 6.90 m long, at different environmental pressures. All the sensors were contained with the tether in a Plexiglass pipe connected to a vacuum pump.

The **third** one has been used for testing samples of tethers up to 25.00 m long, at room temperature. It is similar to the first, but it is not equipped with the thermal pipe.

Particular care was taken in clamping both rope ends in order to prevent sliding, either among the layers or in the clamp. The clamping system is shown in figure 4; each tether end was previously stuck by a cianoacrylic glue penetrating in the layers. Then the tether end was stuck to a PVC bar by means of epossidic glue; the bar was finally clamped in a mandrel.

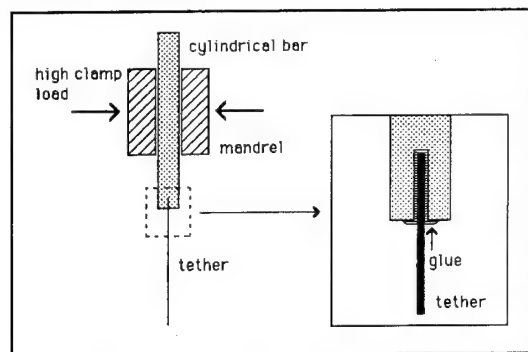


Figure 4: Clamping system of the tether end.

4. TEST RESULTS AND COMMENTS

Before each new set of tests, each tether sample was prestressed with ten load cycles at an average tension of $300 \text{ N} \pm 200 \text{ N}$. This was done, on the basis of the previous results (2), in order to eliminate the dependance of the mechanical properties on the load history.

Actually mechanical parameters of the tether depend both on applied prestress and on internal layer status.

The following aspects were considered and analyzed:

- 4.1 Elastic non-linearity and stiffness at different temperatures;
- 4.2 Possible presence of macro-slidings during a load cycle;
- 4.3 Scale effect on loss factor;
- 4.4 Frequency effect on hysteresis and loss factor;
- 4.5 Longitudinal propagation velocity at different temperatures;
- 4.6 Vacuum and humidity effects on mechanical properties.

4.1 Elastic non-linearity and stiffness at different temperatures

Some parameters related to the mechanical behavior of the composite tether may be derived from hysteresis loops. In particular from an hysteresis cycle it is possible to measure the local stiffness of the tether and then the non-linearity of the Young modulus E .

The EA product can be measured as:

$$EA = (dT/dL) L$$

being A the cross section of the tether, dT the increment of tension and dL the increment of tether length L .

In figure 5a many load cycles at various tether temperatures are superimposed. The tether is preloaded with a mean tension of 34.5 N. Then a sinusoidal displacement of 9.4 mm corresponding to a tension variation of ± 25 N, is applied.

The temperature ranges from 20° to -110° C but the behavior at low temperature is evidenced.

In figure 5b many load cycles are superimposed. The tension variation is 35 ± 25.5 N while the temperature ranges from -110° to -12° C. The behavior at high temperature is evidenced.

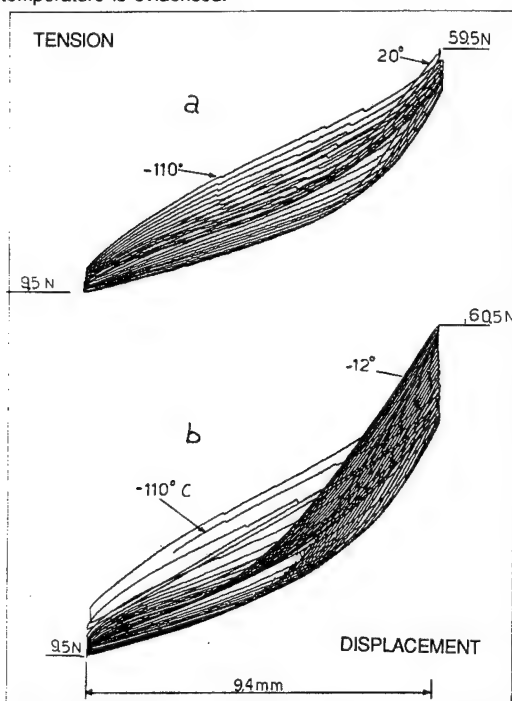


Figure 5: In this figures many load cycles at various tether temperatures, with sinusoidal imposed displacement are superimposed (sample 6.90 m long). The temperature ranges from 20° to -110°. The behavior at low temperature is evidenced in figure 5a and the behavior at high temperatures is evidenced in figure 5b.

In figure 6 many hysteresis cycles, recorded at different temperatures, with a average tension of 45 N and an imposed sinusoidal displacement of 9.9 mm, are plotted. Each plot results from the superimposition of 2÷6 hysteresis cycles at about the same temperature ($\pm 4^\circ\text{C}$).

In figure 6a, obtained at room temperature, the larger tether stiffness due principally to Kevlar is evidenced. The corresponding average EA factor is 42000 N.

In figure 6h, obtained at -60° C, the changing in stiffness is evidenced. At low tension a great percentage of the total load is supported by the Nomex and the copper layers because Kevlar elongates. With high tension, on the contrary, the Nomex and the copper must elastically elongate

more than the thermal elongation of the Kevlar so that a great percentage of the tether tension is again supported by the Kevlar.

In figure 6o, obtained at -110° C, a low tether stiffness due only to Nomex and copper is shown. In this plot the presence of one macro-sliding per cycle is also shown. Each macro-sliding has a magnitude of about 1 N (about 0.1 mm in the tether).

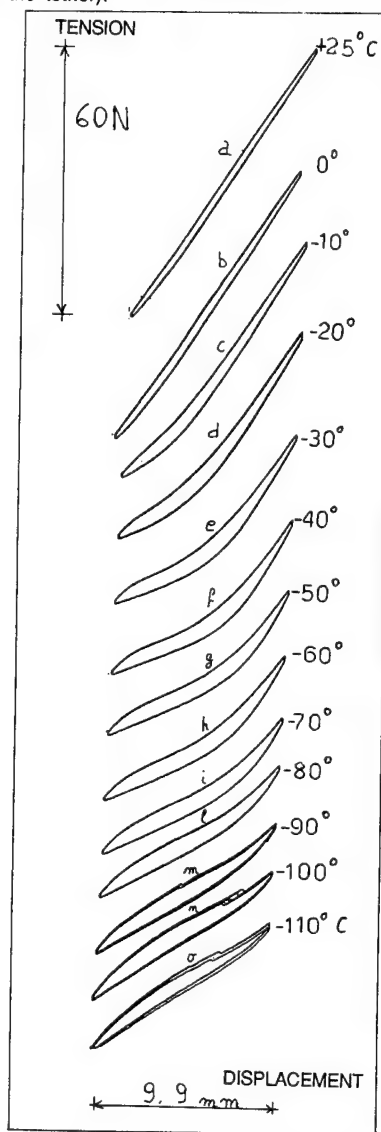


Figure 6: Many hysteresis cycles, recorded at different temperatures, with a average tension of 45 N and an imposed sinusoidal displacement of 9.9 mm, are plotted here (sample 6.90 m long).

4.2 Possible presence of macro-slidings during a load cycle:

The study of possible presence of slidings among the layers during each load cycle is important for the evaluation of the effects on the subsatellite dynamics (3), for example during sudden variations of the temperature due to sun/dark transition.

For the different tether samples considered, the following results have been obtained, during load cycles with average tension equal to 45 N:

1) length = 3.30 m: the experimental apparatus does not detected slidings. A step-like behavior perhaps due to slidings among layers has been nevertheless pointed out

during sudden temperature variation from 30° to -120°C.

2) length = 6.90 m: macro-slidings has been detected only at low temperatures (about -100° C). The first load cycle at -100° C (with a period of 80 s), revealed the presence of some slidings, see figure 7. They principally come out when the tension increases and when the tether stiffness rises because of the Kevlar contribution.

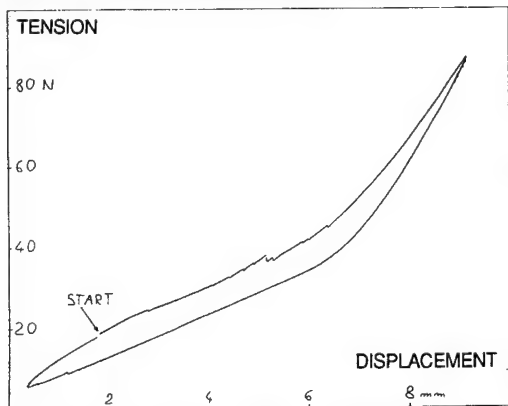


Figure 7: First load cycle for a sample 6.90 m long, at -100° C, with a period of 80 s. The plot reveals the presence of some slidings among the layers.

Three typical load cycles, with a period of 10 s and a temperature of -100°C, are superimposed in figure 8. Note the presence, in each cycle, of only one sliding. The repeatability of the macro-sliding both in position and in size is clearly shown in this figure.

Since the sliding mechanisms are repeatable, the internal status of the layers does not changes after a load cycle. The plot shows that the macro-sliding comes out only with increasing tension. With decreasing tension there should be a lot of micro-slidings, necessary to restore the internal status of the layers.

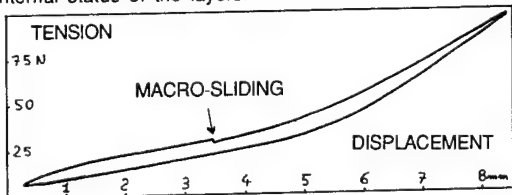


Figure 8: Three typical load cycles, for a sample 6.90 m long, with a period of 10 s and a temperature of -100°C, are superimposed. The repeatability of the macro-sliding both in position and in size is clearly shown in this figure.

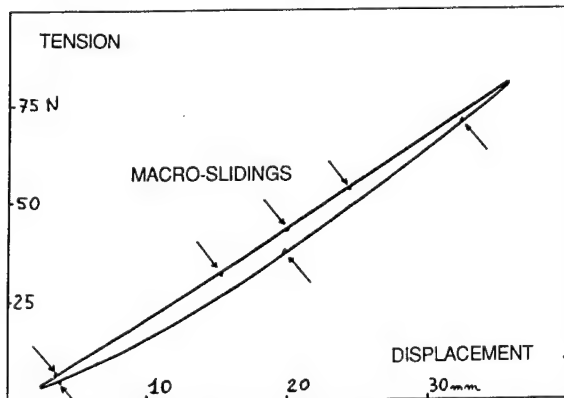


Figure 9: Three typical load cycles for a sample 25.0 m long, with a period of 10 s and a temperature of 25°C, are superimposed.

3) tether sample length = 25.00 m: macro-slidings has been detected during load cycles with average load equal to 45 N at room temperatures.

In figure 9 three typical load cycles are superimposed at 25° C. The repeatability of the macro-sliding in this case is only in size but not in position.

These results suggest the following remarks for the model of the composite tether after having verified that both tether ends are clamped so that no slidings among the layers occur.

- At room temperature macro-slidings arise if the tether length is about 25 m. As discussed in the following numerical model, there are some discontinuities along the layers, the length of each of them may be of the order of 5 m; the sliding probably comes out between the Kevlar and the Teflon layers because the relative Coulomb friction is low.

- If sudden big temperature variations take place, the Kevlar fibers elongates and the length of the discontinuity decreases (about 1+3 m).

- Between the Nomex jacket and the braided Kevlar the Coulomb friction is high. Moreover because of the braided structure only micro-slidings can happen. Further tests done only on these two layers showed that it is very difficult to unpack them and make them slide each other even if the length is only 0.02 m.

4.3 Scale effect on loss factor

The lower end of the tether samples, was stressed with a sinusoidal motion as shown in figure 3. Tests were done imposing an average tension of 45 N equal for all samples; sinusoidal tension range was chosen equal to 9 N and to 63 N, therefore the ratios (tension range/average tension) were 0.2 and 1.4 respectively.

The loss factor(4), is defined as the ratio:

$$\eta = D / (2\pi U)$$

where D and U are respectively dissipated and stored energy during one cycle.

In figure 10 the results of these tests are plotted as function of tether length. It is clear that the loss factor increases with the tether length when the tension range is low. This behavior may be interpreted as the greater possibility for long tethers of manifest slidings. On the contrary the loss factor is almost constant with the tether length when the tension range is high; perhaps this is due to the different internal status of the layers and the greater Coulomb friction among them.

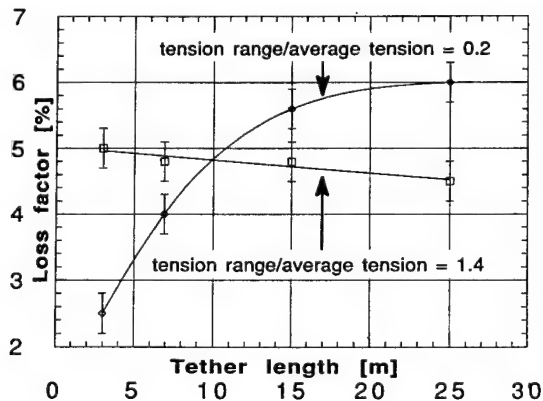


Figure 10: The measured loss factor is plotted as function of tether length. Each curve refers to a particular tension range in the loading cycle.

4.4 Frequency effect on hysteresis and loss factor

The signals recorded by the displacement transducer and the dynamometer are shown in figure 11a,b. The hysteresis cycles of a tether sample 6.90 m long at temperature of 25° C and -100° C are respectively shown. In each plot, two hysteresis cycles with a period of 2s and 120 s are superimposed.

Contrarily to the tests previously done (1,2) on tether samples about 3 m long, here is evidenced a little influence of the frequency on the shape of the hysteresis cycles. In particular at high frequency the tether is about 5% stiffer. This behavior may be partially due to creep effects.

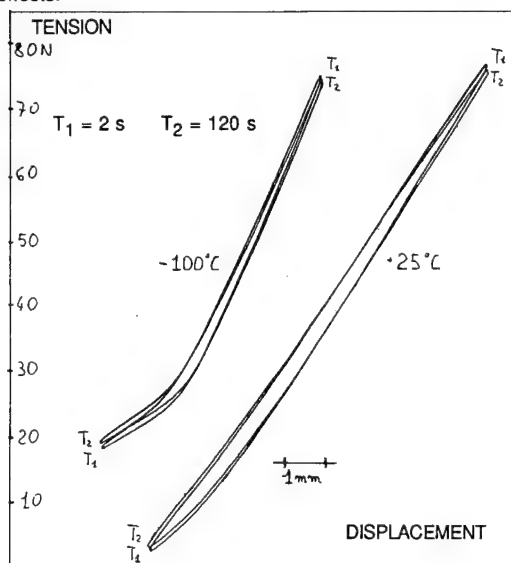


Figure 11: The hysteresis cycles of a tether sample 6.90 m long at temperature of 25° C and -100° C are respectively shown. In each plot, an hysteresis cycle with a period of 2s (frequency = 0.5 Hz) is superimposed to a second one of 120 s period (0.0083 Hz).

4.5 Longitudinal propagation velocity

The EA product may be also evaluated with the formula:

$$EA = \mu c^2$$

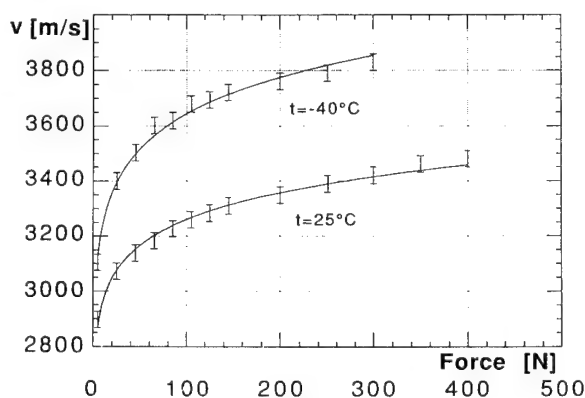


Figure 12: The longitudinal propagation velocity of a 6.90 m long tether is plotted as function of tension at temperature of 25° C and -40° C.

being the linear mass density $\mu = 0.0082$ kg/m and c the longitudinal propagation velocity in the tether. EA product was measured evaluating the time delay between the signal coming from two piezo-accelerometers located one at the end of the tether, after having applied a shock at one end. Tether samples of various lengths, gave similar results.

In figure 12 the longitudinal propagation velocity of a 6.90 m long tether has been plotted as a function of tension at temperature of 25° C and -40° C.

According to the results of §4.1, the velocity c and so the EA product are higher with lower temperatures. This confirms that the tether stiffness increases at low temperatures.

The quasi-logarithmic increase of EA product with tension is plotted in figure 13.

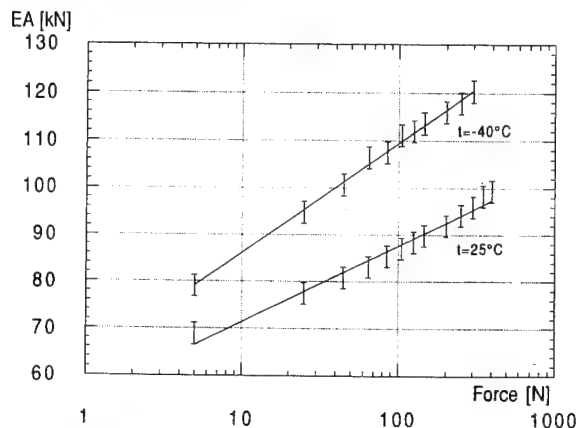


Figure 13: From the results of figure 12, the quasi-logarithmic increase of EA product is shown.

4.6 Vacuum and humidity effects on mechanical properties

Tests previously discussed were repeated in a vacuum pipe, at room temperature, in the case of 3.30 and 6.90 m tether samples. The same tests were also repeated, with temperatures ranging from 20° to -100° C with a relative humidity, measured in the environment around the tether, ranging from 10% to 90%.

Since all the tests gave similar results it seems that both vacuum and humidity do not influence appreciably the mechanical parameters here considered.

5. NUMERICAL MODEL

A two layers model (2) of the TSS-1 rope, see figure 1, is not able to represent completely the mechanisms that take place in the multilayered tether. A preliminary model can be made using a three layers schematization.

The first layer (see fig.1) represents the outer jacket of braided Nomex used for protection against mono-atomic oxygen (A).

The second layer (B) represents the braiding of Kevlar 29 that has been designed to function as a strength member, but at low temperatures (about -100° C) it lengthens too much to react to the total tensions.

The third layer itself is a composite rope: a thin-coated copper conductor is wound around a multistrand Nomex core while a coat of extruded Teflon insulates the conductor. As a first approximation, this third layer can be imagined as homogeneous if assumed that the helicoidal copper wires, drowned in the Teflon, elongate with the Nomex fibres without sliding each other (this is confirmed by proper test).

Coulomb friction is relevant between the first and the second braided layer, but it is small between the second and the third layer because of the smooth Teflon surface.

A finite element program (MARC) was used to study the model of a sample of tether. The mesh, see figure 14, consists on three series of beam elements (MARC n°5) with three degrees of freedom (d.o.f.) per node. Each line consists on 100 elements; the total number of d.o.f. is 197.

Each node can only translate in the horizontal direction. The boundary conditions are: tether clamped at the left end and free at the right end.

The packing effect caused by the braided layers is simulated by normal forces FN1 and FN2, proportional to the tension, acting in each node.

The "friction and gap elements" (MARC n°12), capable to simulate the Coulomb friction and the temperature gradients, connect the nodes of each layer.

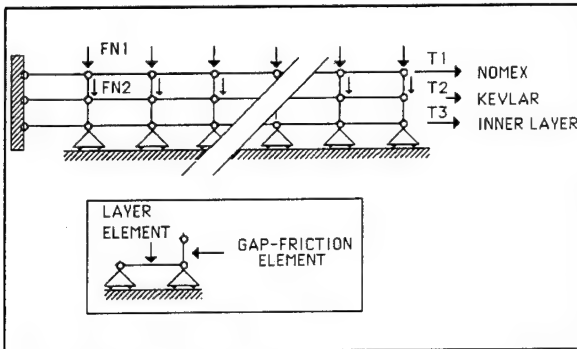


Figure 14: Finite element mesh used to study the model of a sample of tether. It consists on three series of beam elements (MARC n°5). The friction and gap elements (MARC n°12) connect the nodes of each layer.

In order to understand the behavior of the three layers, different numerical models have been set up: in the first one, at the right end of the tether no slidings between the layers were allowed, but the EA product (E =Young modulus, A = cross section) of each layer was supposed to vary in a sinusoidal way to simulate the non-linearity due to packing effects.

Another model is capable of simulating elongations due to temperature of each layer with two gap elements at the right end.

In a different model, three forces are applied at the free end; the intensity of each force is proportional to the measured stiffness of each layer.

Some parameters, such as the normal forces FN1 and FN2 representing the packing effects, are difficult to measure directly. These numerical models are therefore able to evaluate the influence of such parameters on the overall

effects and, from the comparison of the numerical results with the experimental one, to provide reliable values. The numerical models evidenced the great influence of the Coulomb friction among the layers.

The models, according to the experimental tests, show two different kinds of mechanisms, about layers sliding. The first mechanism, consist on a lot of "micro-slidings" along all the tether length. The second one consists on few "macro-slidings" that take place when the temperature decreases and the Kevlar fibers elongates or in tether samples 25 m long.

Let us consider for example only the first two layers (A) and (B) of the numerical model (the external Nomex jacket and the braided Kevlar) see Figure 15a. The tether is tensioned with a constant load at room temperature. If the temperature decreases, a fraction of the total tension moves to the layer (A) because the Kevlar elongates and the Nomex contracts. This tension transfer occurs by means of the friction between the layers.

If the Coulomb friction between the layers is low, the strains are almost uniformly distributed along the tether, so there are a lot of micro-slidings, see Figure 15b.

If the friction is high, the strain of layer (B) is prevented by the friction force until a limit value is reached. Then a macro-sliding occurs and it interests a "characteristic length" of the tether along which the stress redistribution occurs.

The experimental tests confirm the presence of these "characteristic lengths".

Along these lengths the braided Kevlar layer is not uniformly tensioned. The tether in such a model, behaves as a "beads", see Figure 15c; there are some regions very packed with high tension and other regions low tensioned.

From the numerical models above described, the loss factor can be evaluated, if a load cycle is introduced. It can vary from 10^{-5} to 0.1 as a function of the Coulomb friction among the layers. Imposing a loss factor similar to that found in the tests (about 0.04), it was possible to evaluate in a numerical way the friction among the layer as:

- Coulomb friction between the Kevlar and the Nomex: about 0.8;
- Coulomb friction between the Kevlar and the Teflon: about 0.1.

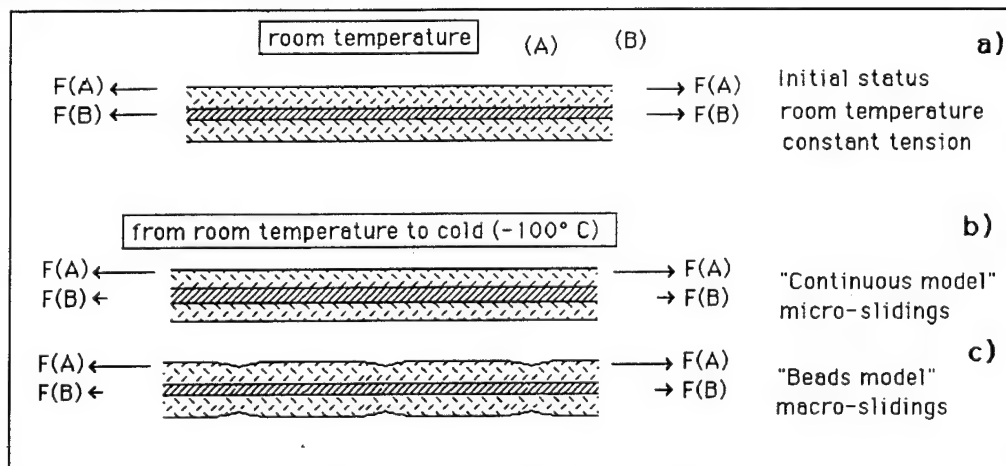


Figure 15: Two possible mechanisms of sliding between the external layer (A) and the internal layer (B), when the temperature of the composite rope decreases.

6. CONCLUSIONS

The experimental investigation on thermal, vacuum and humidity effects on mechanical parameters of composite tethers leads to the following main results:

- two mechanisms of sliding among tether layers have been evidenced: the first, called macro-sliding, comes out at room temperature in tethers about 25 m long, and at low temperatures (-100°C) in tethers about 7 m long. The second mechanism, called micro-sliding, is always present in any loading cycle.

- as a consequence of the macro-slidings, there is a tension transfer among the layers that is not uniform along the tether. A braided layer is then more packed in a region and less in the surroundings. Therefore it may be represented as a "beads model"; the length of each "beads" has been evaluated as a function of the temperature in a range from 1 to 10 m;

- in the range of the tether length considered (3+25 m) loss factor increases with the tether length when the tension is low; with higher tension the loss factor versus length is almost constant (or slightly decreases): this effect can be due to higher compression among layers that inhibits the slidings;

- creep effect reduces tether stiffness of about 5% in hysteresis cycles at higher frequency (0.5 Hz);

- at low temperatures (-10°C to -80°C) two-values tether stiffness have been found: a great percentage of the total load is supported by the Nomex and copper layers if the tension is less than the average load (40 N), and a great percentage of the total load is supported by the Kevlar layer if the tension is greater;

- both vacuum and humidity do not influence appreciably the measured mechanical parameters.

A finite element model of a three-layer tether was also developed. The layers are coupled by means of friction and gap elements representing Coulomb friction and temperature gradients. The numerical model is able to represent the sliding mechanisms among the layers and so it can partially explain the mechanical behavior of the composite tether.

These results prove that any linear model of the tether is unrealistic. Therefore it is necessary to take into account these non-linearities for more accurate models to predict the subsatellite dynamics.

7. ACKNOWLEDGEMENTS

This work was performed under a ASI grant. The TSS-1 tether samples, manufactured by Cortland Cable Company, have been kindly supplied by Martin Marietta and NASA Marshall Space Flight Center. Nitrogen was furnished at reduced cost by SIO/ALPHAGAZ, Vicenza, Italy.

8. REFERENCES

- 1) F. Angrilli, G. Bianchini, M. Da Lio, G. Fanti: MODELLING THE MECHANICAL PROPERTIES OF TETHERS FOR THE TSS-1 AND TSS-2 MISSIONS, ESA Journal 1988, vol.12.
- 2) F. Angrilli, G. Bianchini, D. Da Lio, G. Fanti: MECHANICAL AND THERMIC PROPERTIES FOR EVALUATION OF TSS-1 TETHER DYNAMIC BEHAVIOR, 3rd Int. Conference on Tethers...., San Francisco U.S.A. May 17-19 1989.
- 3) Paul A. Penzo, Paul W. Ammann: TETHERS IN SPACE HANDBOOK- SECOND EDITION-, NASA 1989.
- 4) A. D. Nashif, D. I. G. Jones, J. P. Henderson: VIBRATION DAMPING, John Wiley & Sons, N.Y., 1985.
- 5) Book of abstracts of the Second International Conference of Tethers in Space, Venice, Oct. 1987.
- 6) G. E. Gullahorn: Investigation of dynamic noise affecting geodynamic information in a tethered subsatellite, NASA Grant, NAG-325, May, 1984.
- 7) A. K. Misra, D. M. Xu, V. J. Modi: On vibration of orbiting tethers, Acta Astronautica, vol.13, pg. 587-597, 1986.
- 8) F. Graziani, S. Sgubini, A. Agneni: Disturbance propagation in orbiting tethers, First International Conference of Tethers in Space, Arlington, Virginia, Sept. 1986.
- 9) X. He, G. D. Powell: Tether damping in space, Second International Conference of Tethers in Space, Venice, Oct. 1987.
- 10) G. E. Gullahorn, R.G. Hohlfeld : Tether as a dynamic transmission line, Second International Conference of Tethers in Space, Venice, Oct. 1987.
- 11) E. Lorenzini: The investigation of tethered satellite system dynamics interim report/ executive summary, Smithsonian Institution Astrophysical Observatory Cambridge, Massachusetts, Nov. 1986.

N92-238354

84747

BUCKLING AND FAILURE OF THIN ELLIPTICAL DELAMINATIONS IN COMPOSITES

J. Heitzer

Dornier GmbH, Technology and Mechanics Development Division

ABSTRACT

The Raleigh-Ritz method is used to analyze the buckling of elliptical delaminations in the linear and nonlinear regime. The delaminated region is separating a thick isotropic base laminate from a thin, anisotropic sublaminate. The delamination is oriented arbitrarily with respect to the loading axis. The base laminate enters the calculation only by its Poisson ratio so that the problem can be reduced to the calculation of the buckling behaviour of an elliptical plate under suitable boundary conditions and loading. In contrast to previous approaches all couplings (full A-B-D matrix) are considered. Buckling strains are calculated by formulating the stability condition in terms of the derivative of the total energy and solving the corresponding eigenvalue problem. Solutions are checked with FE-results for various aspect ratios and lay-ups.

Keywords: Delamination buckling, postbuckling, energy release rate

1. INTRODUCTION

The buckling- and post buckling behaviour of elliptical anisotropic plates had attracted the interest of a large number of authors during the past few years. This is due to the observation that the ultimate failure of layered composite structures which had been subjected to a low velocity impact while being under compression seems to be governed by the instable growing of an elliptically shaped thin delaminated area. It is therefore highly desirable to appraise the influence of such defects on the compressive strength of laminates used in aerospace-structures which are, for example, subjected to launch loads.

Shivakumar and Whitcomb /1/ presented an analysis of the buckling loads of special orthotropic elliptical sublaminate using the Raleigh-Ritz method cross checked with FE-results. They observed good coincidence between both methods for moderate anisotropy. Their solution was not extended to the nonlinear regime. A Raleigh-Ritz solution for the postbuckling behaviour had been obtained by Chai and Babcock /2/. Their solution also is restricted to specially orthotropic ellipses with a semiaxis parallel to the loading direction. Using a simple energy balance criterion, the authors were able to analyze the fracture problem that arises, when the buckled delamination is extending. A finite element analysis of postbuckled rectangular delaminations using a crack closure technique for plate elements was carried out by Shivakumar and Whitcomb /3/. A mode

separation was carried out by Whitcomb in ref. /4/ using a three-dimensional, geometrically nonlinear FE-analysis. This analysis predicted a pronounced mixed-mode behaviour along the crack front with large gradients in G_I and G_{II} and a negligible G_{III} component.

In addition to the work addressed so far, the simplified problem of a through-width delamination had been dealt with. Chang and Kutlu /5/ developed a finite element code capable of computing the post-buckling behaviour of composite plates and cylindrical shells containing multiple delaminations. Calculating the energy release rates they found out, that delamination growth is dominated by mode I fracture in flat plates and by mode II fracture in cylindrical panels. Whitcomb in ref. /6/ treats the post-buckled through-width delamination as a column. Additional finite element analysis was needed to determine all the parameters necessary to calculate the deflection and the energy release rate G_I . Chai, Babcock and Knauss /7/ analyzed the postbuckling behaviour of an isotropic homogeneous beam column for the most general case, when the supporting base laminate buckles globally so that the zero-slope boundary condition for the thin sublaminate becomes invalid. Deflections and the total energy release rate are calculated for this case. A similar approach was used by Kardomateas who extended the solution to include orthotropic materials /8/. The most general work on one-dimensional delaminations stems from Sheinman, Bass and Ishai /9/. They solved the differential equations of a composite delaminated beam under arbitrary loading and boundary conditions with a finite-difference method. Bending-stretching coupling was taken into account and turned out to significantly influence the buckling loads.

2. SCOPE OF THE WORK AND STATEMENT OF THE PROBLEM

The aim of the work is the calculation of the compressive strength of a thin laminate which contains an elliptical delamination. The thin sublaminate is assumed to be bonded to an infinitely thick homogeneous base laminate, as for example a sandwich core. First, the linear buckling problem is solved. Then the von-Karman relations are introduced and the solution is extended to the nonlinear regime. The postbuckling deflection and the total energy are compared to FE-results. The configuration is depicted in Fig. 1:

The local coordinate system x, y is rotated at an angle θ with respect to the global coordinate system x', y' . The major and the minor axis shall be

denoted a and b , respectively. The angle between the fibre direction in the K^{th} layer and the global x' -axis shall be denoted ϕ_K . The sublamine consists of plies of equal thickness.

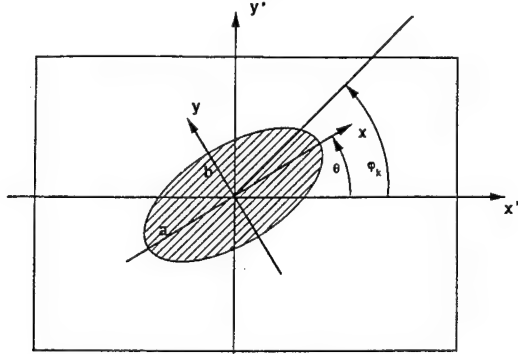


Fig.1 : Coordinate systems and orientation of the elliptical delamination

3. THE RALEIGH-RITZ METHOD

3.1 Load and Boundary Conditions

The infinitely thick base laminate experiences a uniform strain ϵ_0 which acts in the direction of x' . Due to the Poisson contraction ν_{lam} a strain of the value $-\nu_{lam}\epsilon_0$ acts in y' direction. Suitable boundary conditions for the ellipse must be formulated in terms of displacements in the x - y system. Obeying the transformation law for the tensor component ϵ_0 one arrives at the following equations which are applicable in the x - y system:

$$\begin{aligned} u &= \epsilon_0 [(\cos^2\theta - \nu_{lam}\sin^2\theta)x - (\sin\theta\cos\theta(1+\nu_{lam})y)] \\ v &= \epsilon_0 [(\sin^2\theta - \nu_{lam}\cos^2\theta)y - (\sin\theta\cos\theta(1+\nu_{lam})x)] \end{aligned} \quad (1)$$

The boundary conditions for the z -displacement read:

$$w(x,y) = w(x,y)_{,x} = w(x,y)_{,y} = 0 \quad (2)$$

The zero-slope conditions reflect the assumption of a thick foundation which cannot bend. The Raleigh-Ritz method requires an expansion of the displacement fields in terms of the Raleigh-Ritz coefficients which are determined from the requirement of stationary potential energy. A power series expansion of the following, most general form is appropriate:

$$\begin{aligned} u &= \epsilon_x \cdot x + \frac{1}{2} \epsilon_{xy} \cdot y + (\epsilon_x + \frac{1}{2} \epsilon_{xy}) \\ &\quad (1 - \frac{x^2}{a^2} - \frac{y^2}{b^2}) \sum_{m,n=0}^{\infty} a_{m,n} x^m y^n \\ v &= \epsilon_y \cdot y + \frac{1}{2} \epsilon_{xy} \cdot x + (\epsilon_y + \frac{1}{2} \epsilon_{xy}) \\ &\quad (1 - \frac{x^2}{a^2} - \frac{y^2}{b^2}) \sum_{m,n=0}^{\infty} b_{m,n} x^m y^n \\ w &= (1 - \frac{x^2}{a^2} - \frac{y^2}{b^2})^2 \sum_{m,n=0}^{\infty} c_{m,n} x^m y^n \end{aligned} \quad (3)$$

with $\epsilon_x, \epsilon_y, \epsilon_{xy}$ derived from the transformed ϵ_0 .

3.2 Linear Theory

For the linear theory, the expansions of eq. 3 are truncated to:

$$\begin{aligned} u &= \epsilon_x \cdot x + \frac{1}{2} \epsilon_{xy} \cdot y + (\epsilon_x + \frac{1}{2} \epsilon_{xy}) \\ &\quad (1 - \frac{x^2}{a^2} - \frac{y^2}{b^2}) (c_1 + c_2 \frac{x}{a} + c_3 \frac{y}{b}) \\ v &= \epsilon_y \cdot y + \frac{1}{2} \epsilon_{xy} \cdot x + (\epsilon_y + \frac{1}{2} \epsilon_{xy}) \\ &\quad (1 - \frac{x^2}{a^2} - \frac{y^2}{b^2}) (c_4 + c_5 \frac{x}{a} + c_6 \frac{y}{b}) \\ w &= (1 - \frac{x^2}{a^2} - \frac{y^2}{b^2})^2 (c_7 + c_8 \frac{x}{a} + c_9 \frac{y}{b} + c_{10} \frac{x^2}{a^2} + c_{11} \frac{y^2}{b^2} + \\ &\quad c_{12} \frac{xy}{ab} + c_{13} \frac{x^3}{a^3} + c_{14} \frac{x^2 y}{a^2 b} + c_{15} \frac{xy^2}{ab^2} + c_{16} \frac{y^3}{b^3} + \\ &\quad + c_{17} \frac{x^4}{a^4} + c_{18} \frac{x^3 y}{a^3 b} + c_{19} \frac{x^2 y^2}{a^2 b^2} + c_{20} \frac{xy^3}{ab^3} + c_{21} \frac{y^4}{b^4}) \end{aligned} \quad (4)$$

Odd and even powers in x and y are admitted up to fourth order. Odd powers permit asymmetry in the z -displacements and thus prevents certain coupling terms from vanishing. The total potential energy which must be evaluated consists of two parts:

$$\begin{aligned} \Pi_{lin} &= \frac{1}{2} \int_{-a}^a \int_{-b}^b dx dy (N_x w_{,x}^2 + N_y w_{,y}^2 + 2N_{xy} w_{,x} w_{,y}) + \\ &\quad \frac{1}{2} \int_{-a}^a \int_{-b}^b dx dy (A_{11} u_{,x}^2 + 2A_{12} u_{,x} v_{,y} + A_{22} v_{,y}^2 + \\ &\quad 2A_{16} (u_{,x} u_{,y} + u_{,x} v_{,x}) + 2A_{26} (v_{,y} u_{,y} + v_{,y} v_{,x}) + A_{66} (u_{,y} + v_{,x})^2 - 2B_{11} u_{,x} w_{,xx} \\ &\quad - 2B_{12} (v_{,y} w_{,xx} + u_{,x} w_{,yy}) - 2B_{22} v_{,y} w_{,yy} - 2B_{16} (u_{,y} w_{,xx} + v_{,x} w_{,xx} + 2u_{,x} w_{,xy}) \\ &\quad - 2B_{26} (u_{,y} w_{,yy} + v_{,x} w_{,yy} + 2v_{,y} w_{,xy}) - 4B_{66} (u_{,y} w_{,xy} + v_{,x} w_{,xy}) + D_{11} w_{,xx}^2 \\ &\quad + 2D_{12} w_{,xx} w_{,yy} + D_{22} w_{,yy}^2 + 4D_{16} w_{,xx} w_{,xy} + 4D_{26} w_{,yy} w_{,xy} + 4D_{66} w_{,xy}^2) \end{aligned} \quad (5)$$

The above expressions can be evaluated most conveniently in polar coordinates. Inserting eq. (4) into (5) leads to an expression of more than 20000 terms. This problem was handled using the software package Mathematica capable of symbolic mathematics /11/. The program delivers Fortran statements which were copied into the corresponding program so that no transcription errors could occur. After integration, the total energy can be written in the form:

$$\Pi_{lin} = \Pi_{ij} C_i C_j + \text{const}(i,j = 1 \dots 21) \quad (6)$$

Requiring an extremum of the energy leads to

$$\frac{\partial \Pi_{lin}}{\partial C_m} = 0 = \Pi_{im} C_i \quad (7)$$

and furthermore to the condition

$$\det [\Pi_{im}] = 0 \quad (8)$$

for a nontrivial solution.

The Fortran program LBUCKLING was written to solve eq. (8). The program allows an arbitrary number of the 21 Ritz-constants to be used for the calculation of the buckling strains so that the convergence behaviour of the solution as a function of the number of Ritz-constants could be examined.

3.3 Nonlinear Theory

If large displacements in w should be taken into account, the strain-displacement relations known from ordinary plate theory must be modified. This is usually done by introducing the von-Karman relations as the most simple nonlinear extension. They read:

$$\epsilon_x = u_{,x} - zw_{,xx} + \frac{1}{2}w_{,x}^2 \quad (9)$$

$$\epsilon_y = v_{,y} - zw_{,yy} + \frac{1}{2}w_{,y}^2$$

$$\epsilon_{xy} = u_{,y} + v_{,x} - 2w_{,xy} + w_{,x}w_{,y}$$

Those relations are inserted into the energy expression for a laminated plate which can be taken for example from ref. /10/. Integrating over the thickness gives an expression in terms of the ABD-matrix and displacement derivatives. The expansion of the displacement fields was chosen according to eq. (4) with w only including the terms up to C_{12} . Despite this restriction, the energy still consists of more than 50 000 terms before integration. If the total energy is rearranged accordingly it can be brought into the form of a polynomial of fourth order in the C_i 's. The postbuckled configuration represents a minimum of the total energy which can be found by imposing eq. 7. This leads to a system of nonlinear equations in C_i which is of the form:

$$K_{ji} C_j + L_{mji} C_m C_j + M_{nmji} C_n C_m C_j = 0 \quad (10)$$

(i, j, m, n = 1 ... 12)

The above equation contains the strain ϵ_0 as a variable whereas the C_i still remain unknown. The strain ϵ_0 is not a buckling strain to be determined but an external load which itself determines the shape of the postbuckled configuration.

The absence of an inhomogeneous term indicates the absence of transversal forces which naturally would lead to a half-wave type of displacement /12/. With the system being nonlinear and homogeneous it is no longer possible to find a nontrivial solution in a straightforward manner. Instead, the choice of the first guesses for the C_i 's as well as the value of load ϵ_0 influences the solution. Eq. 10 was solved with the fortran program NBUCKLING which uses a subroutine from the NAG-library /13/. In contrast to LBUCKLING, the number of Ritz-constants is not optional any more so that always the full expansion up to C_{12} according to eq. 4 is used. Although intended for postbuckling, the program allows the calculation of the critical buckling strain by using an interval halving method to look for the transition between trivial and nontrivial solutions. It is decisive to use a reasonable starting vector if the subroutine should iterate the desired buckling mode: The first mode corresponds to a halfwave with its maximum at the origin. Clearly the coefficients $C_1, C_{10}, C_{11}, C_{12}$ in w must be unequal to zero with the same sign.

4. COMPARISON WITH FE-RESULTS

4.1 Influence of Material and Ellipse Orientation

An ellipse with $a = 3$ mm and $b = 1$ mm which was oriented at $0^\circ, 45^\circ$ and 90° with respect to the loading axis having a total thickness of 0.01 mm was examined. The material was arranged to produce a special orthotropic material ([0,0] laminate), an orthotropic material ([45,45] laminate) introducing the tension-shear coupling terms, and an unsymmetric laminate ([0,90] laminate) introducing tension-twist couplings. In this and all the following calculations the material data indicated in Tab. 1 was used.

Tab. 1 contains all possible combinations of materials and geometry. The R.-R. method was used in three different ways: program LBUCKLING with all 21 constants and only 12 constants and program NBUCKLING with 12 constants. The error between the FE-result and LBUCKLING with 21 constants is indicated. Comparing the results from the linear program using 21 and 12 constants, respectively it is evident, that using the full expansion yields a buckling strain which is always a little lower than that of the truncated expansion. This is a common feature of the R.-R. method: using a larger expansion results in a softer structural response. The differences in solution that occur using the three methods are negligible. It can thus be concluded, that the first mode has converged sufficiently with an expansion that uses 12 constants. The results of NBUCKLING compare favourably with those of the linear program.

An oblique orientation seems to have a detrimental effect as the largest errors occur at $\theta = 45^\circ$. The errors grow, if stretching-twisting effects are introduced. A strange effect was observed with the $\theta = 0^\circ$ ellipse: All three R.-R. calculations found a tension buckling solution whereas the FE-solution is compressive. It had been confirmed, that all the solutions describe one half-wave. Nevertheless an asymmetry must not necessarily lead to large errors as can be seen from the $\theta = 45^\circ$ and $\theta = 90^\circ$ ellipse.

4.2 Postbuckling Analysis

A geometrically nonlinear analysis was performed for the [0,90] and a [45,90] laminate both with $\theta = 90^\circ$, using the FE-program ABAQUS. In order to enforce the right buckling path, the displacements of the first mode, multiplied by $5 \cdot 10^{-4}$, were used as nodal coordinates. The strain range extended to a value just below the second buckling mode which has the value of $4.76 \cdot 10^{-5}$ for the [0,90] laminate and $1.36 \cdot 10^{-4}$ for the [45,90] laminate. The intervals were divided into equal loading steps in each of which the total energy and the centre displacement $w(0,0)$ were calculated. These values are compared to the corresponding values derived with the R.-R. method with the centre displacement being equal to the constant C_1 . The total energy is calculated by inserting the constants found by solving eq. 10 into the energy expression from which eq. 10 had been derived. Figs. 2, 3, 4, 5 show a good agreement in displacements and energies. The deviations in the displacements at the onset of loading must be attributed to the predeformation of the FE-mesh which causes a smooth postbuckling. The energies calculated by the stiffer R.-R. method are higher whereas the displacements are lower than the corresponding FE-values.

θ	[0,0]		[45,45]		[0,90]	
0°	$-3.12 \cdot 10^{-6}$	$-3.21 \cdot 10^{-6}$	$-1.64 \cdot 10^{-4}$	$-1.68 \cdot 10^{-4}$	$1.94 \cdot 10^{-4}$	$1.94 \cdot 10^{-4}$
	$-3.07 \cdot 10^{-6}$	$-3.21 \cdot 10^{-6}$	$-1.65 \cdot 10^{-4}$	$-1.66 \cdot 10^{-4}$	$-5.80 \cdot 10^{-5}$	$1.93 \cdot 10^{-4}$
	1.6 %		0.7 %		434 % !	
45°	$-5.45 \cdot 10^{-6}$	$-5.51 \cdot 10^{-6}$	$-7.21 \cdot 10^{-5}$	$-7.32 \cdot 10^{-5}$	$-5.96 \cdot 10^{-5}$	$-5.97 \cdot 10^{-5}$
	$-5.55 \cdot 10^{-6}$	$-5.45 \cdot 10^{-6}$	$-7.38 \cdot 10^{-5}$	$-7.00 \cdot 10^{-5}$	$-5.59 \cdot 10^{-5}$	$-5.53 \cdot 10^{-5}$
	-1.8 %		2.3 %		6.6 %	
90°	$-8.65 \cdot 10^{-6}$	$-8.85 \cdot 10^{-6}$	$-1.31 \cdot 10^{-4}$	$-1.32 \cdot 10^{-4}$	$-3.50 \cdot 10^{-5}$	$-3.50 \cdot 10^{-5}$
	$-8.7 \cdot 10^{-6}$	$-8.85 \cdot 10^{-6}$	$-1.33 \cdot 10^{-4}$	$-1.33 \cdot 10^{-4}$	$-3.40 \cdot 10^{-5}$	$-3.49 \cdot 10^{-5}$
	-0.6 %		1.5 %		2.9 %	

LBUCKLING with 21 constants	LBUCKLING with 12 constants
FEM	NBUCKLING with 12 constants
ERROR	

$E_x = 230000 \text{ MPa}$
 $E_y = 7000 \text{ MPa}$
 $G_{xy} = 5000 \text{ MPa}$
 $\nu_{xy} = 0.35$
 $\nu_{lam} = 0.30$

Tab. 1: Buckling strains for different material orientations and ellipses

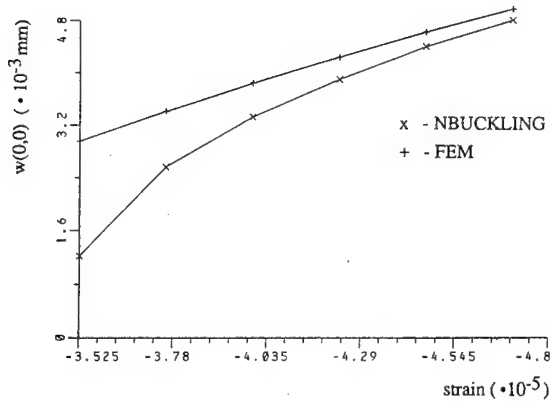


Fig.2 : Displacement $w(0,0)$ for [0,90] laminate

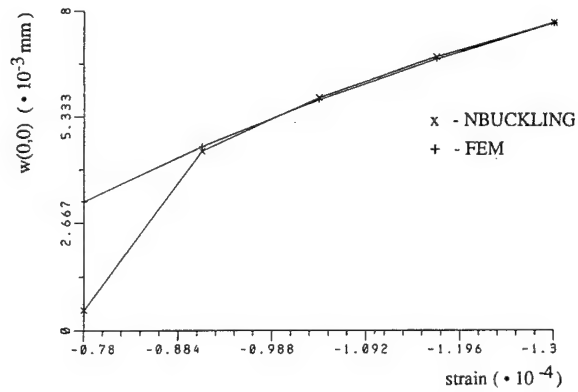


Fig.3 : Displacement $w(0,0)$ for [45,90] laminate

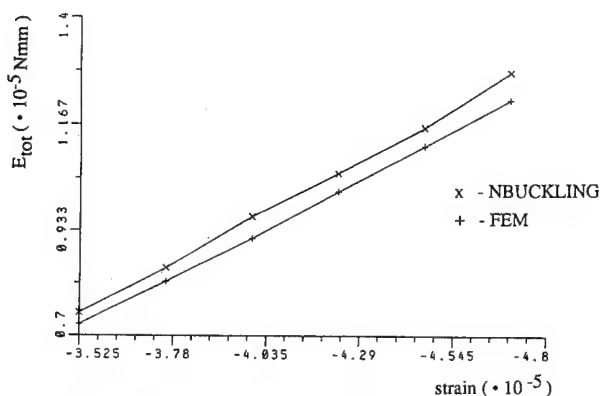


Fig. 4 : Total energy for the [0,90] laminate

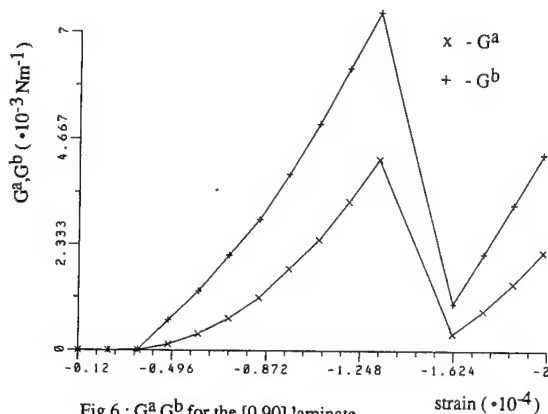
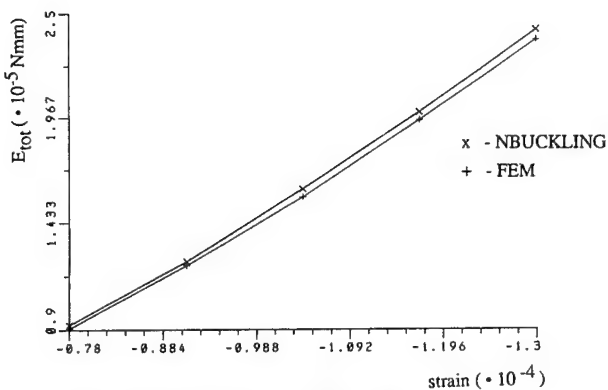
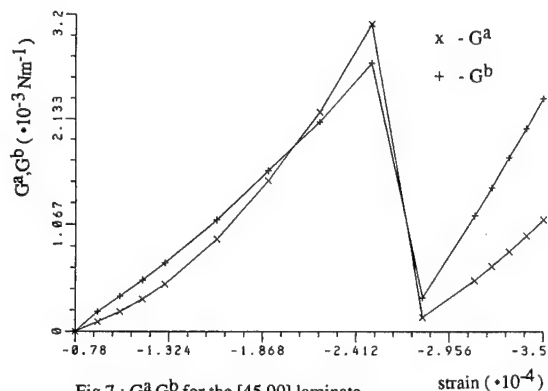
Fig. 6 : G^a, G^b for the [0,90] laminate

Fig. 5 : Total energy for the [45,90] laminate

Fig. 7 : G^a, G^b for the [45,90] laminate

5. A PRACTICAL APPLICATION

5.1 Calculation of the Energy Release Rates

The energy released by a crack per unit of newly created surface is a convenient measure to assess its criticality. A profound treatment concerning the assumptions, prerequisites and limitations of a fracture mechanics treatment of interlaminar crack growth driven by buckled layers can be found in ref. /2/. Here, a brief summary will be given: For a given ellipse with the semiaxis a and b , a second configuration is defined with the infinitesimally larger semiaxis denoted $a + \Delta a$ and $b + \Delta b$, respectively. Crack growth then occurs, when the energy released by the crack exceeds a certain characteristic value when it switches to the second configuration. It had been asserted by Chai and Babcock /2/ that the total energy in early stages of post-buckling consists mainly of G_I so that the knowledge of the critical energy release rate G_I^C for mode I would suffice for a complete characterization of the onset of fracture. The method outlined so far does not permit a mode separation, but bearing in mind that G_I is much lower than G_{II} and G_{III} , one is on the safe side if the energy release rate is compared to G_I^C solely.

The energy available for crack growth consists of the energy stored in the postbuckled configuration $\Pi(a, b)$ plus the membrane energy of the elliptical ring of widths a and Δb minus the energy of the spreaded delamination $\Pi(a + \Delta a, b + \Delta b)$. In terms of energy release rates this reads:

$$G = \frac{\Pi(a, b) - \Pi(a + \Delta a, b + \Delta b)}{dA} + G_0 \quad (11)$$

with

$$d\Pi = \frac{\partial \Pi}{\partial a} da + \frac{\partial \Pi}{\partial b} db \quad (12)$$

it follows that

$$G \left(\frac{db}{da} \right) = \frac{G^a + G^b \cdot \frac{a}{b} \frac{db}{da}}{1 + \frac{a}{b} \frac{db}{da}} + G_0 \quad (13)$$

with G_0 as the energy in the ring per unit area and

$$G^a = -\frac{1}{\pi b} \frac{\partial \Pi}{\partial a} + G_0$$

$$G^b = -\frac{1}{\pi a} \frac{\partial \Pi}{\partial b} + G_0$$

A close inspection of eq. 13 reveals that for $G^a > G^b$ the energy becomes a maximum for $db/da = 0$ thus implying crack growth along the axis a. If, on the other hand, $G^b > G^a$ then G is maximized for $db/da = \infty$ and the crack growth is along the axis b. For $G^a = G^b$ the crack grows in a more complicated manner along both axes.

The calculation of G^a and G^b is performed by numerical differentiation of Π according to eq. 11. Figs. 6, 7 depict the development of G^a and G^b for the [0, 90] and the [45, 90] laminate with increasing strain: The values rise monotonically until the second mode is reached and then fall off. Then they rise again when the third mode is approached. This behaviour can be explained considering that it is just the difference in bending energy between two adjacent states that makes up the right side of eq. 11: As the amplitude of the postbuckled configuration increases, the bending energy increases, and so does the difference between two configurations.

5.2 Evaluation of a Fabrication Defect

The two programs were used in the analysis of a compressively loaded sandwich that showed a reduced compression strength. Facesheets were tested together with the core as part of the quality control program for the manufacturing of a large satellite carrier. The facesheet had the stacking sequence $[-55, 0_2, 55]_s$ with the UD-data indicated before. Compression tests repeatedly yielded global failure at a strain of $\epsilon_0 = 3.8 \cdot 10^{-3}$. Surprisingly, several test samples failed at $\epsilon_0 = 3.0 \cdot 10^{-3}$. Subsequent X-raying revealed bright lines that were oriented in fibre direction. Occasionally, these lines clustered together to form an irregularly shaped bright area. (Fig. 8).

The puzzle was unravelled by cutting the facesheet into pieces. Figs. 9, 10 show edge-on views of the bright lines which turned out to be nothing but large voids. Conglomerates of these voids thus can form large delaminated areas which can buckle.

The void clusters were treated as two-dimensional delaminations. The cluster from Fig. 8, for example, was replaced by an ellipse of the semiaxes $a = 8$ mm, $b = 4$ mm with an angle of $\theta = -55^\circ$. In a first step, the buckling strains for the first two modes were derived. The value for v_{lam} was set to $v_{lam} = 0.42$ being the Poisson contraction of the whole sandwich.

As the location of the delamination in the layup was unknown, the delamination was placed between increasingly more layers until the strain for the first mode exceeded the value of $3 \cdot 10^{-3}$ measured for the damaged panels (Tab. 2). From this first analysis it could be inferred, that a delamination of the aforementioned size could not be situated below the fourth ply if it should have any effect on the strength at all. Then the total energy release rate for this ellipse was calculated assuming the strain of $3 \cdot 10^{-3}$. It was found that only a delamination between the second and third or between the third and fourth ply yields a value large enough for crack growth as compared to $G_c = 50 \text{ Jm}^{-2}$. This result is in complete agreement with the microscopic observations: Voids were only found either between layers two and three or three and four. The observed pin-like voids treated as a slender ellipse with $a = 50$ mm and $b = 0.5$ mm (Fig. 8) turned out to be insensitive to buckling under the critical load: The lowest buckling strain that could be found for a void beneath the first ply ($\theta = -55^\circ$) was as high as $\epsilon_0 = -6.2 \cdot 10^{-2}$.

Circularly shaped delaminations often occur after low velocity impact. They are also used as references to evaluate the criticality of defects found during non-destructive inspection. A circular defect with a radius larger than 6 mm beneath the first ply can buckle, but does not release enough energy to grow. Between the second and the third ply the energy release rate becomes large enough ($G^a = 1.8 \text{ Jm}^{-2}$, $G^b = 48 \text{ Jm}^{-2}$) for a radius of 6 mm. The same radius produces energy release rates of $G^a = 38 \text{ Jm}^{-2}$, $G^b = 47 \text{ Jm}^{-2}$ if the void is situated between layer three and four. The equivalent defect radius in the upper half of the facesheet can therefore be fixed at 6 mm.

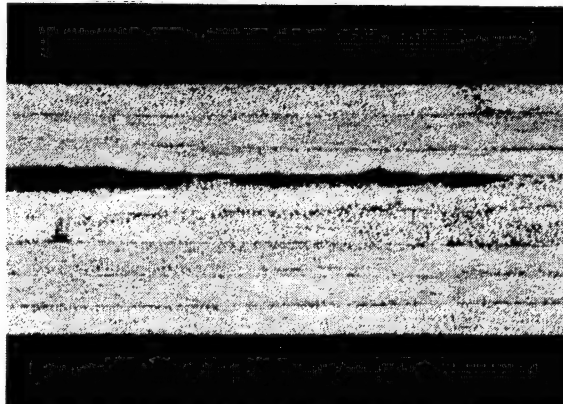


Fig. 9: Edge - on view of defective facesheet

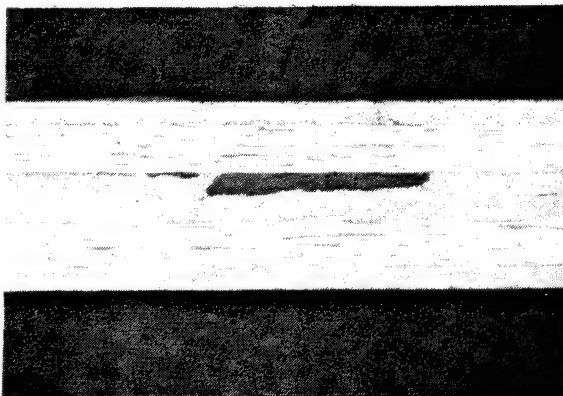


Fig. 10: Edge - on view of defective facesheet

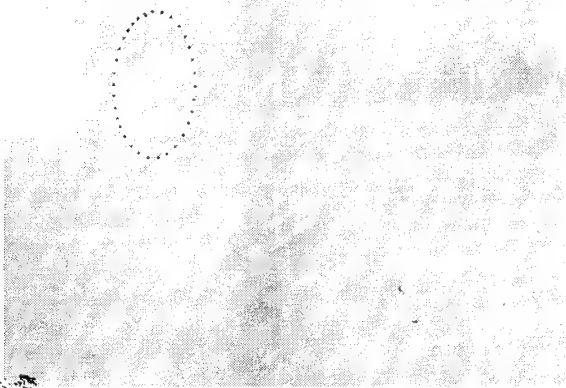


Fig. 8: X - ray picture of defective facesheet

6. SUMMARY

The Raleigh-Ritz method together with the theorem of stationary potential energy was used to calculate the buckling strains and the postbuckling behaviour of anisotropic laminates. The solutions were compared to FE-results and show an excellent agreement in buckling strains, energies and displacements. The energy release rates along both semiaxes were calculated for two unsymmetrical laminates and showed a monotonous rise with increasing load. The method was then used to analyse a defective sandwich panel. The linear buckling analysis correctly predicted the location of the defects. A subsequent calculation of the energy release rates as compared to measured values for this material confirmed the location of the defects in accordance with photographic findings.

The following limitations of the Raleigh-Ritz method could be identified:

- i) The method shows too stiff a behaviour in the higher modes, especially for unsymmetric laminates. This results in buckling strains which are too large so that a postbuckling analysis between mode one and mode two could become invalid by exceeding the "true" mode two buckling strain.
- ii) The linear buckling solutions show a strange convergency behaviour for a [0,90] laminate with a certain geometry. It can be assumed, that the relation $B_{11} = -B_{22}$ for the only non-vanishing B-matrix terms results in an ill-conditioned matrix.
- iii) The contact between base laminate and sublaminate which could occur in higher modes has not been accounted for.

Acknowledgement

The author thanks Mr. M. Feucht, University of Stuttgart, for his programming assistance in Fortran and MATHEMATICA.

References

- /1/ K.N. Shivakumar, J.D. Whitcomb, "Buckling of a Sublaminate in a Quasi-Isotropic Composite Laminate", Journal of Composite Materials, 19, pp. 2-18, 1985
- 2/ H.Chai, C.D. Babcock, "Two-Dimensional Modelling of Compressive Failure in Delaminated Laminates", Journal of Composite Materials, 19, pp. 67-98, 1985
- /3/ J.D. Whitcomb, K.N. Shivakumar, "Strain-Energy Release Rate Analysis of a Laminate with a Postbuckled Delamination", in "Numerical Methods in Fracture Mechanics", Pineridge Press, UK, pp. 581-605, 1987
- /4/ J.D. Whitcomb, "Three-Dimensional Analysis of a Postbuckled Embedded Delamination", Journal of Composite Materials, 23, pp. 862-889, 1989
- /5/ F.K. Chang, Z. Kutlu, "Collapse Analysis of Composite Panels with Multiple Delaminations", Proceedings of AIAA/ASME/ASCE/AHS 30th Structures, Structural Dynamics, Materials Conf., Mobile, Alabama, Apr. 3-4, pp. 989-999, 1989
- /6/ J.D. Whitcomb, "Approximate Analysis of Postbuckled Through Width Delaminations", Composites Technology Review, 4, pp. 71-77, 1982
- /7/ H. Chai, C.D. Babcock, W.G. Knauss, "One-Dimensional Modelling of Failure in Laminated Plates by Delamination Buckling", Int. J. Solids and Structures, 17, pp. 1069-1083, 1981
- /8/ G.A. Kardomateas, "Large Deformation Effects in the Postbuckling Behaviour of Composites with Thin Film Delaminations", Proc. of AIAA/ASME/ASCE/AHS 29th Structures, Structural Dynamics, and Materials Conf., Williamsburg VA, pp. 382-389, Apr. 1988
- /9/ I. Sheinman, U. Bass, O. Ishai, "Effect of Delamination on Stability of Laminated Composite Strip", Composite Structures, 11, pp. 227-242, 1989
- /10/ J.E. Ashton, J.M. Whitney, "Theory of Laminated Plates", Technomic Publishing Co. Inc., 1970
- /11/ S. Wolfram, "Mathematica", User's Manual Addison Wesley Publ.
- /12/ N.A. Weil, N.M. Newmark, "Large Deflection of Elliptical Plates", J. of Applied Mechanics, 23, pp. 21-26, 1956
- /13/ The NAG Fortran Library, Numerical Algorithms Group Limited, 1988

	Mode 1	Mode 2	G^a [Jm ⁻²]	G^b [Jm ⁻²]
[-55]	$-1.74 \cdot 10^{-3}$	$-2.07 \cdot 10^{-3}$	0.65	0.2
[-55,0]	$-8.77 \cdot 10^{-4}$	$-3.44 \cdot 10^{-3}$	44.3	46.9
[-55,0 ₂]	$-2.33 \cdot 10^{-3}$	$-6.04 \cdot 10^{-3}$	12.7	46.8
[-55,0 ₂ ,55]	$-5.01 \cdot 10^{-3}$	$-1.09 \cdot 10^{-2}$	-	-

Tab. 2: Buckling analysis of the void cluster of Fig. 8

**SESSION
2.1.B**

**SPACE PLANE
&
RE-ENTRY
II**

PRECEDING PAGE BLANK NOT FILMED

N92-23836

356-18

84748

Stretched skin concept for the entry aerodynamic decelerator system
of planetary probes

by

Ch. BONNET, J.F. PUECH, M. RIGAUDT
Dassault Aviation

ABSTRACT

The joint NASA/ESA Cassini/Huygens mission is one of the forthcoming planetary exploration missions making use of high drag decelerator. Also the requirements of this mission have been used to support studies at Dassault Aviation on new concepts for entry devices.

Preliminary linear analysis performed within PES study for ESA on a very light weight concept decelerator, based on ultra thin C/C skin have shown that buckling is a driver during the entry phase. To avoid the consequence on stability of these stresses in the skin, the idea of using only a carbon fiber fabric without carbon impregnation was suggested. This was the first step towards the stretched skin concept. The second step has been to design a proper structure to stretch the fabric. This paper describes this new concept composed of a high temperature annular fabric, stretched onto a rigid medium temperature armature and connected to the cold descent module structure.

A performance analysis is globally performed and the predicted mass of the stretched skin concept is competitive. The technical feasibility is outlined.

Keywords : Aerodynamic braking device, Hypersonic decelerator, Planetary entry device.

vehicle should satisfy different specifications, and the chosen technologies for both these applications are not necessarily the best solutions for that kind of mission.

Cassini phase A study led to a C/C concept for the decelerator, based on current Hermes development technology, ref. 4. As regards the decelerator static equilibrium, the aerodynamic pressure on the conical shaped decelerator generates two kinds of stresses :

- a useful radial stress transmitted through the lower ring of the decelerator to the descent module links,
- an unwanted and perverse induced circumferential stress whose main impact is to generate compressive stresses and instability phenomena.

To avoid the consequence on stability of these stresses in the skin, the idea of only using a carbon fiber fabric without carbon impregnation was put forward. The radial fibers are loaded by tensile stresses between two rigid rings and circumferential fibers are only required to control the porosity parameter and to stretch the whole fabric on the nominal shape. This solution presents the advantage of avoiding instability phenomena and therefore deformations are predictable all along the entry phase, either under mechanical or combined mechanical/thermomechanical loading.

1. INTRODUCTION

The joint NASA/ESA Cassini/Huygens mission is one of the forthcoming planetary exploration missions. Also the requirements of this mission have been used to support studies on new concept for entry devices. The first concept was a deployable structure, ref. 1 and ref. 2 and this paper now describes a stretched skin concept for aerobraking devices, protected by patents, ref. 3.

The entry phase in the atmosphere of TITAN offers very peculiar points compared to what has been studied up to now. It cannot be compared to purely ballistic reentry of strategic weapons because of its very much lower heating flux level and in spite of a comparable heating flux, it cannot be comparable to Hermes reentry either, because of its very much shorter entry time, 3 mn for Huygens against 20 mn for Hermes. The thermal protection system of both ballistic weapons and guided Hermes

2. ENTRY AND DESCENT SCENARIO

In order to simplify the separation sequence defined during the Cassini phase A and describe in ref. 5, the separation scenario has been limited to 2 separation sequences, figure 1 :

- an aft separation, where the decelerator including the aft cover are separated from the descent module
- a front separation, where the forward cone is separated from the descent module, avoiding the jettison of multiple elements as nose cap and several viewing-port covers.

This scenario offers the advantage of keeping the descent module inside a kind of protection envelope, wholly jettisoned before the scientific phase of the descent. The requirement of non pollution of the scientific experiments is in this way more easily fulfilled.

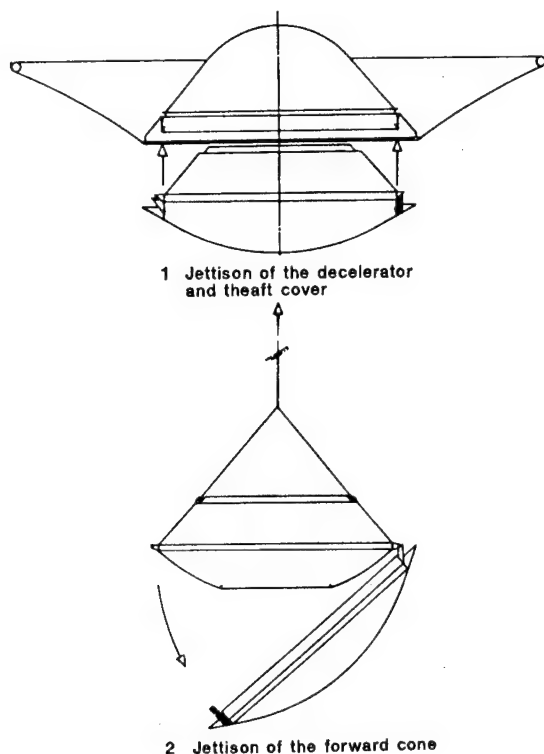


Figure 1. The separation sequence scenario

3. STRETCHED SKIN CONCEPT DECELERATOR DESCRIPTION

The decelerator is composed of a high temperature annular fabric, stretched onto a rigid medium temperature armature and connected to the cold descent module structure, figure 2.

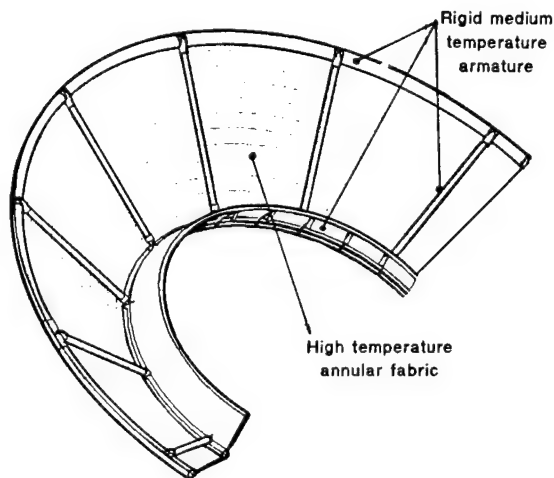


Figure 2. The stretched carbon skin decelerator

The fabric has an axisymmetric concave shape and is made of a very smooth texture of closely woven thin carbon fibers (satin) to reduce the porosity. The decelerator fabric is edged with bolt-rope or luff-wire to allow strong anchoring in the rigid armature. This annular fabric is stretched onto the radial direction between two rings of the armature through bolt-rope anchoring devices.

The concavity of the skin is characterized by a deflection compared to the real frustum of a cone. Because of this concavity, the uni-axial radial tensile strain induces a bi-axial (radial and circumferential) tensile strain in the skin. In fact, the radial strain has a tendency to reduce the deflection and then to lengthen the circumferential fibers so creating a circumferential strain.

The deflection has been fixed at 22 mm and has a direct influence on the strength equilibrium. The larger it is, the lower the tensile stress in the skin and the stresses in the structure will be. Furthermore the concave shape has a favourable effect on aerodynamics (higher drag coefficient and static stability). An optimization of the skin deflection should result, between aerodynamic and aerothermodynamic estimated effects and stress reduction in the decelerator structure, which means weight saving.

The structure is based on a heat soak thermal protection system, so that the heat absorbed by the outer layer in contact with the hot carbon fabric is distributed and stored in the heat soak material. The very short entry time gives a moderate total heat load, compatible with medium range temperature materials. As the entry is characterised by the superposition of the peak heat flux and the peak deceleration load, the candidate materials should therefore keep good mechanical characteristics up to medium temperatures (500°-600°C). Beryllium which has a very low density ($d = 1.85$) is the metallic material with the best specific characteristics (specific modulus, specific heat) and has been selected as the best candidate material for the design of the decelerator structure armature, to fulfill the very tight mass budget.

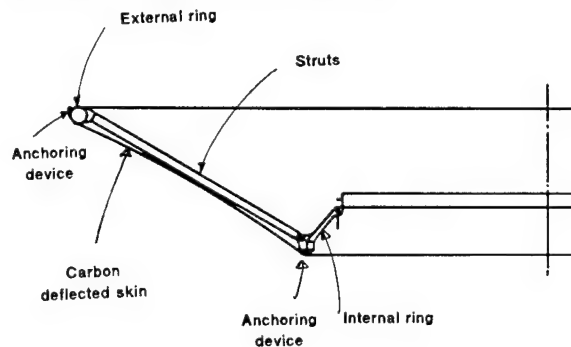


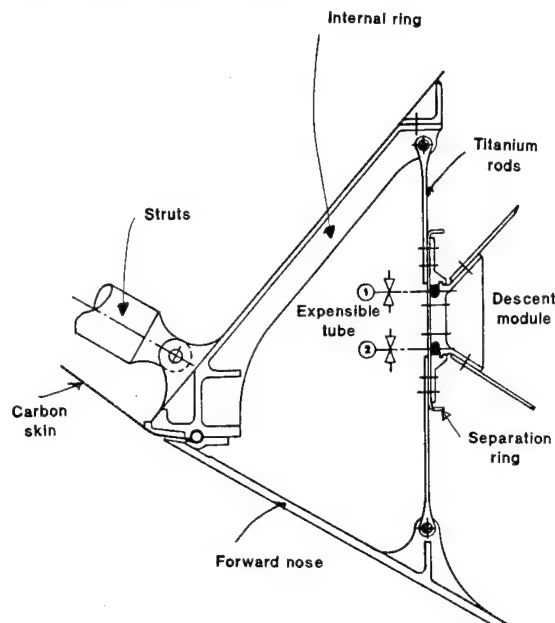
Figure 3. Cross-section of the decelerator

The rigid decelerator structure is composed of two rings (external and internal) connected by 12 equidistant struts. The two rings are designed to hold the aerodynamic annular carbon fabric anchoring devices and to collect the tensile stresses induced by the deceleration load. The struts are designed to steady the shape and to provide the required stiffness. They balance the internal tensile stresses of the annular aerodynamic surface without ever being in contact with it, figure 3.

4. MECHANICAL INTERFACE AND SEPARATION DEVICE DESCRIPTION

The decelerator is connected to the cold descent module structure by small intermediate rods, linked to a coupling ring and integrating an expandable tube for the jettison of the decelerator. The rods are clamped on the coupling ring side and jointed on the internal ring side. The mechanical interface has

been designed to present great enough stiffness (to satisfy the dynamic requirements of the launch phase), to allow thermal expansion, to reduce thermal transfer conduction and to be compatible with the jettison of the decelerator.



- ① Jettisoning of the decelerator
- ② Jettisoning of the forward nose

Figure 4. Mechanical interface and separation device (cross-section)

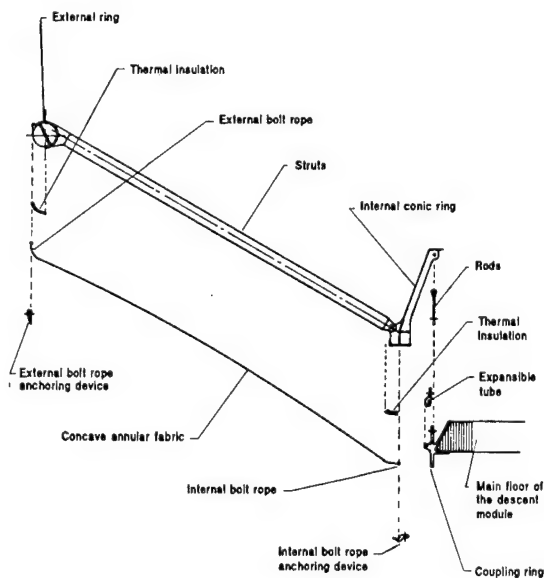


Figure 5. Exploded view of the stretched carbon skin decelerator

A symmetrical interface could be used for the jettison of the forward cone, figure 4. Figure 5 shows an exploded view of the stretched carbon skin decelerator. In the "breathing" of the whole system, the differential dilatation is absorbed by flexion

of the rods, but axial dynamic acceleration in the X (or Y) direction are held by the stiffness of the rods in the XZ (or YZ) plane. Because of the circular shape of the mechanical interface, the stiffness is identical in all directions in the XY plane, figure 6.

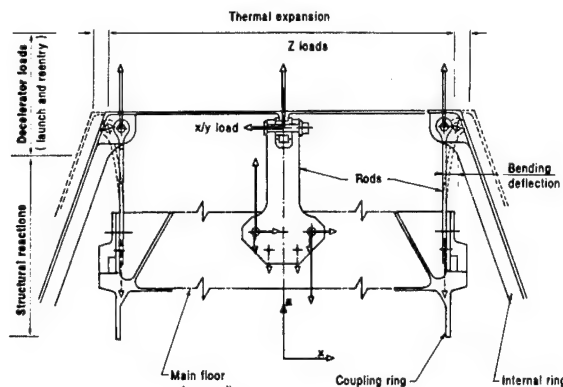


Figure 6. Mechanical interface and strength equilibrium

5. PERFORMANCE ANALYSIS

In a preliminary structural analysis the external and internal rings are linked to circular section curved rods. The stresses encountered are a scheme of flexion and torsion combined in the general tensile stress in the internal ring. The struts collect a scheme of flexion and compression and obviously only tensile stress appears in the carbon skin.

To allow comparison with the previous phase A C/C decelerator used in PES study, the mechanical interface between the decelerator and the descent module has been chosen identical to phase A, i.e. 6 explosive bolts, for the structural analysis, figure 7. The loading hypotheses are based on the worst trajectory case of ref. 6 (Entry Velocity = 7.2 km/s, Entry flight path angle = - 90°, colder Titan atmosphere), which means a maximum aerodynamic pressure of 6000 Pa (i.e. 25 g).

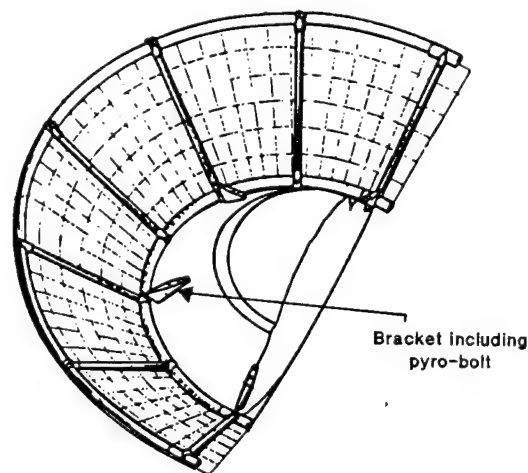


Figure 7. Stretched carbon skin with phase A mechanical interface type for structural analysis and comparison

To take into account the influence of thermal load, the mechanical characteristics of the material are taken in the 500° to 600°C temperature range. The Beryllium characteristics are therefore :

- tensile strength = 180 mPa
- shear strength = 90 mPa
- young modulus = 240000 mPa

The first analysis was an optimization of the struts number to minimize the mass. The compression and the torsion in the struts are mainly dependent on the skin tension and the skin deflection. The induced flexion in the external and internal rings is directly dependent on the sector size between two struts.

To reduce the deflection of the rings and therefore the section area, the sector size between two struts should be reduced. The balance is obtained between the weight saved in the cross area of the rings and the weight lost in the additional struts. The optimum, under the described hypothesis, is a structure composed of 12 struts dividing the decelerator into 30° sectors.

5.1. Mechanical requirement

The preliminary mechanical analysis gives the following results :

Parts			Cross section	Max.stress
External ring	Max.bending moment	500 000 mmN	diam. = 50 mm t = 2 mm	144 mPa
	Max.twisting moment	50 000 mmN		
Internal ring	Max.bending moment	700 000 mmN	diam. = 50 mm t = 2.5 mm	165 mPa
	Max.twisting moment	60 000 mmN		
Struts	Max.bending moment	180 000 mmN	diam. = 30 mm t = 2 mm	Critical compressive load = 33 000 N
	Max. compressive strength	5 000 N		
Skin	Max. tensile flow	20 N/mm	The thickness is not required for mechanical reason. t = 0.4 mm	

The internal ring is more loaded than the external one because of concentrated loads generated by the 6 brackets phase A mechanical interface. A larger number of flexible attachments will allow to reduce the stress level of the internal ring to the same level of the external ones.

The margin will therefore be about 50 % relative to the ultimate strength.

5.2. Thermal requirement

To check that the maximum temperature reached in the Beryllium parts is within the capability of the material, a preliminary thermal analysis has been performed. The most critical part is the external ring in contact with the hot carbon skin.

In the framework of the ESA technical study "Planetary Entry System", Dassault Aviation has performed boundary layer calculations showing no transition to turbulent flow for 4 to 5 mm rearward facing step, at the junction with the decelerator, ref. 7 and ref. 8. The Reynolds number is so low, that the boundary layer will most probably remain laminar throughout the entry phase. The factor of 2 on the laminar distribution from the decelerator junction to the decelerator edge, taken in the phase

A study, to take into account transition phenomena, could be discussed, and both fluxes have been considered for this preliminary thermal analysis, figure 8.

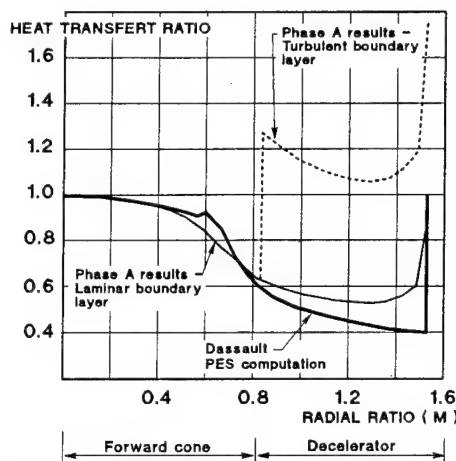


Figure 8. Flux repartition along the probe profile with transition and no transition assumption at the junction forward cone/decelerator

The identified thermal insulation material is SiO₂, under development for the Hermes programme. A layer of 2 mm thick has been taken as contingency in the mass budget. View factors have been considered and the results are listed below :

	Direct contact between Be & C-skin	Thermal insul. between Be & C-skin
No transition hypothesis	T max = 350° C <u>Case A</u>	T max = 260° C
Full transition hypothesis factor=2	T max = 750°C	T max = 470° C <u>Case B</u>

The temperature distributions along the external ring diameter are shown in figure 9 for the cases A and B.

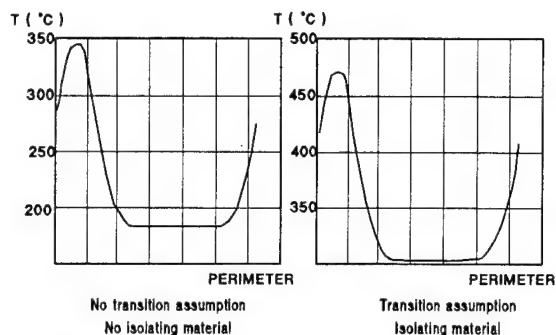


Figure 9. Temperature distribution along the external ring diameter for case A and B

5.3. Stiffness requirement

In PES study, dynamic analyses have shown the great sensitivity of the decelerator links on the first eigen mode frequency. The mechanical interface composed of rods clamped on the coupling ring side, gives a great stiffness in the 3 directions.

5.4. Mass budget

Based on the aforesaid analysis, reinforcements have been considered in order to remain below the yield strength, leading to a 50 % margin relative to the ultimate strength.

The corresponding mass budget is presented below :

Parts	Nb	Mass kg
Internal ring	1	7.4
External ring	1	3.9
Bolt rope	2	4.3
anchoring devices		
Struts	12	3.2
Mechanical links	24	1.6
Bolts	60	0.9
Skin	1	2.7
Insulation material	1	1
Total		25

At this stage of the study, the stretched skin concept has a similar mass budget, compared to the C/C phase A concept decelerator.

6. FEASIBILITY

The stretched decelerator concept is based on two technologies currently used : the carbon fiber weaving and the Beryllium application technologies.

The carbon fiber weaving technology is widely used for composite materials either with epoxy, carbon or ceramic matrix. Great improvements have appeared in the weaving process which are fully developed today and fulfill the requirements.

Beryllium has been used for 30 years in space applications in the United States and it is considered at NASA today as a standard material. During the last years there have been many spacecrafts carrying Beryllium hardware : Voyager, Magellan, Superbird, INSAT, Galileo and the US Shuttle. The applications are many :

- US Shuttle window frames,
- radiators,
- support structures, struts, primary central cylinders,
- domes for radio isotopic thermo-electric generators.

In conclusion, the necessary technologies for manufacturing the stretched skin decelerator concept are available today.

Reference list

- (1) C. BONNET, J. PUECH, M. RIGAULT
Deployable structure for the entry aerodynamic braking decelerator system of planetary probes.
IAF-90-271 October 6-12, 1990/Dresden, GDR.
- (2) Brevet 90 04998
Dispositif deployable, notamment destiné au freinage des corps de rentrée planétaire.
- (3) Brevet 90 04807
Dispositif de freinage aérodynamique.
- (4) P. FURNESS and al.
Cassini Saturn survey Huygens Titan probe.
Phase A study - Final report
Marconi Space System BLS 6744 ISS D November 1989.
- (5) G. SCOON, G. WHITCOMB, M. EIDEN, A. SMITH
Cassini/Huygens entry and descent technologies
ESA journal 1989, vol 13.
- (6) A. SMITH
Cassini Titan atmosphere probe - Phase A2
Entry trajectories - CR 68/88
Fluid Gravity - MSS/19023/7355/006, 1988.
- (7) S. POTHIER, P. DELATTRE
Aerodynamic and aerothermodynamic performances analysis deployable Cassini Decelerator
Planetary Entry System study
Dassault Aviation - DGT 39868, October 1989.
- (8) V. MAUDET, S. WAITER
Cassini deployable aerothermodynamic analysis
Planetary Entry System study
Dassault Aviation - DGT 44300, November 1990.

BERYLLIUM-THERMAL PROTECTION TECHNOLOGY

N92-23837

H. Leder, U. Lohse, W. Ohly, P. Rathjen, L. Schiwkosky,
H. Weber, G. WierheimInteratom GmbH
P.O. Box 10 03 51
D-5060 Bergisch Gladbach 1

ABSTRACT

Beryllium known as the most light weight metallic heat sink structural material has been considered for realisation of a thermal protection system (TPS) to be employed for entry bodies in future space missions. In the frame of a feasibility study for realisation of a probe TPS manufactured out of beryllium design considerations have been carried out by considering the Huygens Titan Probe as an example. Especially technological aspects related to material characteristics, manufacturing, design and analysis are addressed.

Key words: reentry technology, beryllium, thermal protection.

1. INTRODUCTION

Future space missions employing aerodynamic braking in planetary atmospheres (Earth, Titan, Mars) will require TPS's on the outer surface of entry vehicles for insulation of the inner compartment from the entry heating and to provide the aerodynamic shape of the entry body. Beryllium is considered as the most light weight metallic heat sink structural material.

Typical applications for beryllium can therefore be envisaged in the frame of future missions. In previous studies concerning the TPS of Huygens Titan Probe (Ref. 1) e.g. beryllium has been identified as the baseline solution for the forward heat shield and the rear part of the entry probe (Fig. 1). This is due to the excellent performance characteristics of beryllium: lower weight to stiffness ratio than for any other metal, high thermal conductivity, very high specific heat at normal and elevated temperatures, very high modulus of elasticity, very low specific density, low electrical resistivity, and high melting point.

This paper describes design considerations performed in the frame of a feasibility study (Ref. 2) for realisation of a Probe TPS manufactured out of beryllium by considering as an example the Huygens Titan Probe. Especially technological aspects related to material characteristics, manufacturing, design and analysis will be addressed.

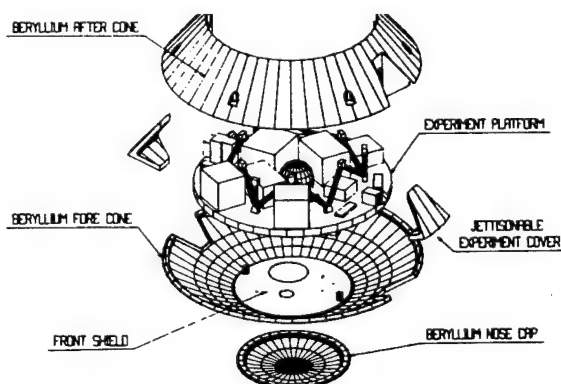


Fig. 1: Cassini Huygens-Exploded View

2. DESIGN REQUIREMENTS (Ref. 5)

2.1 Geometrical Requirements

The geometrical data taken as a basis for the probe TPS are those given in Fig. 5.

2.2 Stiffness Requirements

The design goal frequency of the total probe shall be 24 Hz as a minimum. Taking into account that the design is at an early stage, the analytically predicted first frequency shall include a design margin of about 10 %.

2.3 Strength Requirements

- Launch loads, 13.8 g in z-direction
- Loads from reentry

The maximum deceleration of the probe is -25 g, corresponding to an aerodynamic pressure (quasi static pressure load) of 0.08 bar acting on the nose cap/ fore cone and 5000 N for each of the 6 fixing points of the decelerator cone.

2.4 Thermal Requirements

The TPS must withstand the heat fluxes given by Ref. 6, 7. The baseline case chosen for the thermal calculations is the UR2 case. This case gives the maximum heat transfer rate at the stagnation point: $q_{dot} = 46.07 \text{ W/cm}^2$. During the design life of the TPS the structure is operating in the temperature range of -120 °C (cruise) to about 770 °C (reentry condition).

2.5 Mass Requirements

The design must minimize the mass. The goal to be reached for the TPS-structure inclusive the thermal insulation is 41.2 kg as given in (Ref. 9) for a carbon/carbon solution.

2.6 Apertures

The following dimensions of apertures are required:

- jettisonable nose cap 650 mm in diameter
- 2 opposite apertures 200 mm x 200 mm in the region with the external diameter of the fore cone.

3 MATERIAL CHARACTERISTICS OF BERYLLIUM

3.1 Material Selection

Beryllium is considered as the ideal structural material for space applications because of its unique stiffness-to-weight properties, and the excellent combination of thermal conductivity and specific heat. A great number of successful applications in various spacecraft structures has been reported. Beryllium was found to be a suitable material for heat-shield application because of the high specific heat which increases with increasing temperature. Consequently the first Mercury and Gemini missions were covered with beryllium shingles as thermal protection. Beryllium has also been used as rocket nose (e.g. Polaris, Poseidon, Agena, Minuteman missiles), to absorb the aerodynamic heating during launch and reentry phases (Ref. 3, 4).

The most usual form of beryllium is vacuum hot pressed block. By variation of chemical composition, controlling the impurity concentration, powder-particle-size and temperature different beryllium grades can be produced. The structural grades - S65 and S200*) - with high ductility are standard materials for several spacecraft components.

Vacuum hot pressed block is also the input material for hot rolled sheet which is available in thickness from 0.5 to 6 mm.

Beryllium is not hazardous in the bulk form, but fine particles, powder or vapour may produce health hazards. Therefore adequate safety precautions should be imposed at every stage of manufacture. National and international safety regulations have been established to prevent any risks.

3.2 Properties of Beryllium

Beryllium is one of the lightest structural metals and has a unique combination of properties. The density is 1.84 g/cm³ and the Young's modulus is about 300,000 MPa, giving a modulus/density ratio at RT which is 6 times better than other materials. Physical properties of interest are given in Table 1 compared to other light metals. From Fig. 2 one can see why beryllium is unique as a heat sink material: beryllium can e.g. absorb 100 percent more energy than aluminium.

		Be	Mg	Al	Ti
Density	g/cm ³	1.84	1.74	2.7	4.5
Young's Modulus	10 ⁵ MPa	3.0	0.451	0.70	105
Conductivity	cal/cm s °C	0.38	0.38	0.57	0.039
Specific Heat	cal/g °C	0.48	0.24	0.21	0.125
Thermal Expansion	10 ⁻⁶ /°C	11.5	24.5	23.5	9.4
Melting Point	°C	1280	650	660	1668

Table 1: Physical Properties of Beryllium and other Materials

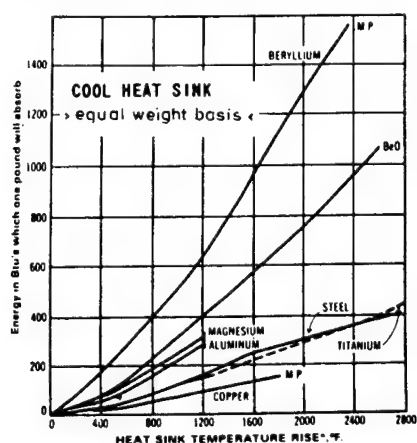


Fig. 2: Beryllium as a heat sink material

The mechanical properties of beryllium vary significantly from grade-to-grade and are dependent upon fabrication history. Fig. 3 shows tensile data for grade S-200F. Note that the ductility increases as a function of temperature to a maximum at about 350 - 400 °C. When beryllium is used at temperatures above ~550 °C thermal creep must be considered. Material properties are well established between -200 and about 600 °C, some creep-rupture tests up to 750 °C are available.

*) Brush-Wellman, Ohio, USA

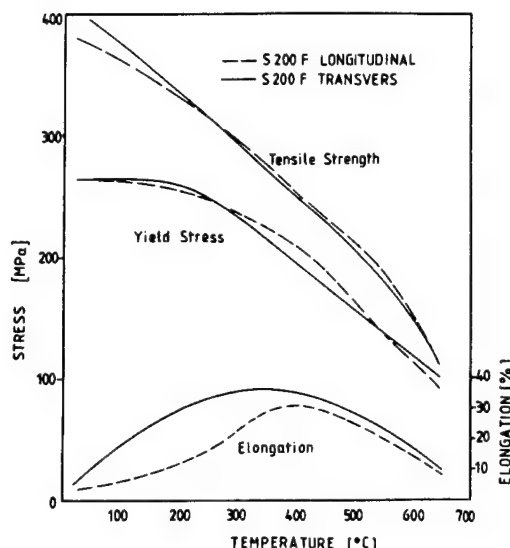


Fig. 3: Tensile properties of Beryllium grade S-200F

3.3 Machining Procedures

Most beryllium parts produced today are machined from block material, all conventional machining operations can be used (saw cutting, electric discharge machining, turning, milling, drilling).

Following to any material removal operation beryllium surfaces must be chemically etched to remove the surface damage. Mechanical machining operations produce compressive stresses in the surface to a depth of about 0.1 mm. This damage is in the form of twins and possibly, microcracks at intersecting twins; it can be limited by controlling the machining procedures, particularly the depth of cut. Because no practical non-destructive-test method for detecting machining damage is specified, all machined surfaces must be etched (see Fig. 4).

3.4 Joining Techniques for Beryllium

Mechanical fastening (rivets, bolts), brazing and adhesive bonding are joining procedures that can be regarded as production processes. Diffusion bonding and resistant welding have been used on a limited scale. Fusion welding is not recommended due to weld cracking and the poor mechanical properties of the welds.

A combination of riveting and adhesive bonding was used in many structural applications where the operating temperatures exceeded the maximum service temperature of the adhesive.

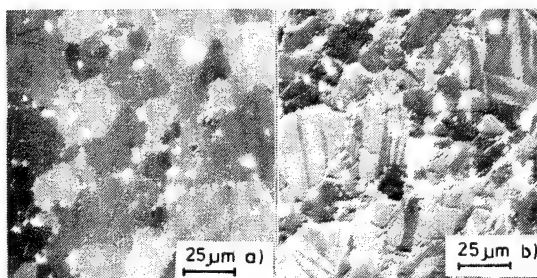


Fig. 4: Microstructure of Hot Pressed Beryllium Block
a) Damage free surface
b) Deformation twins in machined surface
Unetched, polarized light

4. GENERAL LAYOUT OF TPS PROBE COMPONENTS

With respect to the large temperature differences during the flight mission between the forward heat-shield (nose cap, fore cone) and the primary structure of the probe, the selected TPS design solution is of a self carrying type (without a supporting back-structure) and contains measures which allow for stress free thermal expansion.

The general layout of the design solution of the probe TPS is given in Fig. 5. Taking into consideration deliverable sizes of Be semifinished product forms and suitable manufacturing processes the definition of the structural configuration is as follows:

- nose cap manufactured out of one piece
- fore cone assembled out of 6 pieces, joining of the 6 segments by brazing and bolting (bolting as a redundancy during high temperature period of reentry)
- reinforcement of fore cone by radial and circumferential ribs at locations of inner/external diameter and the 2 external apertures
- hinge connection of fore cone/after cone to allow stress free thermal expansion
- after cone consisting of
 - 6 beams clamped to the antenna platform from carbon fiber composite (CFC), primary structure
 - 6 skin panels from Be fixed by screws to the CFC-beams, secondary structure.

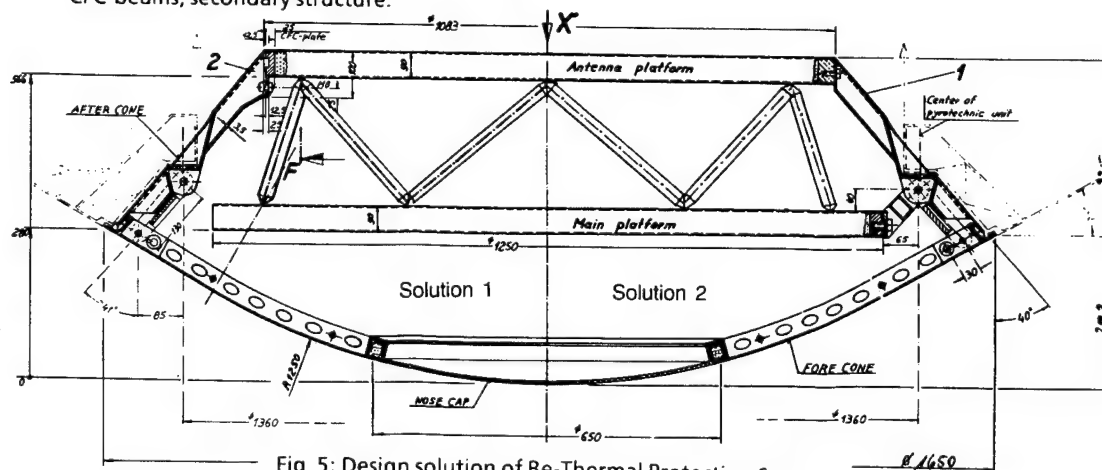


Fig. 5: Design solution of Be-Thermal Protection System

5. ANALYSIS OF TPS PROBE COMPONENTS

5.1 Loading to be used for Sizing Calculations

Strength requirements have been specified for the launch case and the reentry case. Since the aerodynamic pressure loading during the period of reentry is acting on a hot forward Be-structure, the determining load case to be considered for the sizing calculations is the condition of entry into the atmosphere (combination of pressure loading and structure temperature). The aerodynamic pressure loading during reentry is of a transient type with a characteristic time duration of ≤ 60 s. The maximum Be-structure temperatures given as an envelope (Ref. 6) are:

- T_{\max} nose cap $\leq 530^\circ\text{C}$ (6 mm wall thickness)
- T_{\max} fore cone $\leq 770^\circ\text{C}$ (3 mm wall thickness)

5.2 Definition of Design Criteria for Be-Components

Structural beryllium grades have limited ductility when comparing with other structural material but the minimum elongation (determined in a tensile test) at room temperature is $> 2\%$ and this value is increasing significantly when operating in the elevated temperature region.

Taking this material behaviour into account the definition of the design stress intensity values S_m and S_t and the determination of the Primary and Secondary Stress Limits follow the concept used for ductile structural materials in the various structural design codes.

S_m is the time independent design stress intensity value and is determined from the conventional yield strength and the ultimate strength using appropriate design factors.

S_t is the time dependent design stress intensity value and is determined from the creep rupture strength and the stress which produces 1% total strain using appropriate design factors.

The definition of S_m and S_t is given in Table 2.

Concerning the Primary Stress Limits two design levels are defined

- Design level A which applies to the total design life of the probe except the time period of reentry
- Design level B which applies to the time period of reentry

and a distinction between membrane and membrane + bending stress will be made. The given Table 2 contains the values of primary stress limits which are a function of the design level, type of stress and temperature.

The temperature dependent primary stress limits of Be structural grade are given in Fig. 6. Allowable max. temperatures are determined by Be creep strength data. Assuming two characteristic stress levels/time durations the max. allowable temperatures are given below

max. allowable temperature		time duration
$S_t = 20 \text{ MPa}$	$S_t = 30 \text{ MPa}$	-
775 °C	735 °C	60 s
740 °C	710 °C	180 s

Definition of the allowable design stresses S_m and S_t

$$S_m = \min \left\{ \begin{array}{l} S_y / 1.5 \\ S_u / 2.0 \end{array} \right. \quad \begin{array}{l} S_y = \text{Yield strength} \\ S_u = \text{Ultimate strength} \end{array}$$

$$S_t = \min \left\{ \begin{array}{l} S_r / 1.5 \\ S_{1\%} \end{array} \right. \quad \begin{array}{l} S_r = \text{creep rupture strength} \\ S_{1\%} = \text{stress which produces} \\ \quad \quad \quad 1\% \text{ total strain} \end{array}$$

Primary stress limits (MPa)

Design level	Stress	Temperature range	
		below $T = 550^\circ\text{C}$	above $T = 550^\circ\text{C}$
A	Membrane	$\leq S_m$	---
	Membrane + Bending	$\leq 1.5 S_m$	---
B	Membrane	$\leq 1.2 S_m$	$\leq S_t$
	Membrane + Bending	$\leq 1.8 S_m$	$\leq 1.2 S_t$

Design level A : total design life of the probe except time period of re-entry

Design level B : time period of re-entry

Table 2 : Definition of design criteria for Be - components

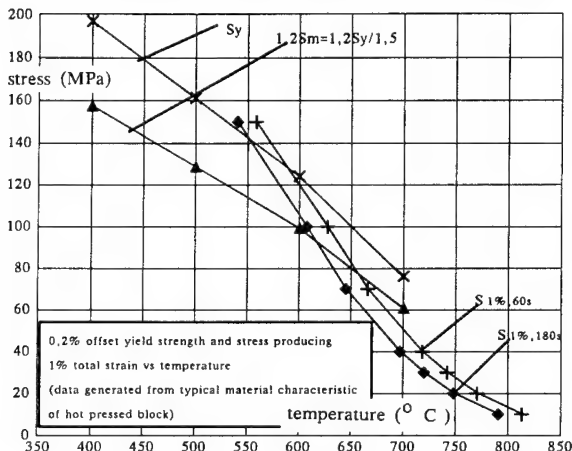


Fig. 6: Short- and long time strength behaviour of Beryllium

Significant thermal stresses are expected during the time period of reentry only where a rapid temperature increase will take place but the material ductility will increase simultaneously. Due to this, concerning the Secondary Stress Limits no limitation of thermal stresses during the time period of reentry is considered necessary, but strain limits have to be respected:

- elastic-plastic membrane strain $\leq 1\%$
- elastic-plastic membrane + bending strain $\leq 2\%$

5.3 Thermal Analysis

Thermal calculations have been carried out to study the influence of Be-mass heat sink on max. temperature of the after cone and the fore cone taking into account the radial ribs of the fore cone. The thermal model definition used and the heat transfer rates taken for the period of reentry were in accordance with the data used in (Ref. 6).

A one dimensional model has been used in the case of the after cone. With an assumed Be-sheet thickness of 0.8 mm the calculated max. temperature is of about 260°C and thus far below any critical value of Be-material. Furthermore max. values of temperatures can be controlled by local thickening of the Be-sheet material where ever it is considered necessary (e. g. bolted joint of skin panel/CFC-beam).

A two dimensional model has been used in the case of the fore cone taking into account the radial ribs. Different wall thicknesses of the radial ribs have been investigated concerning their influences on max. temperature of the ribs. As a result skin temperatures at the locations of the ribs as a function of Be-rib thickness are given in Fig. 7.

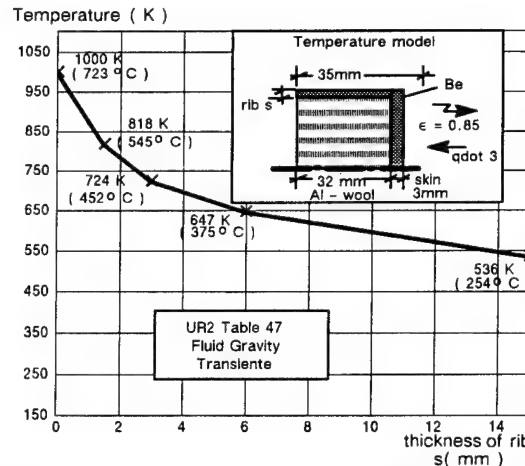


Fig. 7 : Fore cone temperature at the location of the rib as a function of Be rib thickness

A strong influence of the heat sink of Be-mass of the rib on the max. temperature is identified. With a 3 mm rib thickness chosen the drop of the max. temperature of the rib in relation to the unaffected 3 mm skin of the fore cone is of about 270°K corresponding to a max. rib temperature below 500°C .

5.4 Mechanical and Thermomechanical Analysis

Finite element calculations (2d and 3d structure models) have been performed for the analysis of deformation and stresses of the TPS-components taking into account the pressure and temperature loading associated with the reentry load case.

A two-dimensional model (Fig. 8) of the TPS-structure using 2d axisymmetric and plane stress elements of the ADINA code (Ref. 10) was used for the investigation of the overall behaviour of the TPS-assembly in form of a parametric study. From the results obtained it was concluded that the connection between fore cone and after cone requires a joint solution which allows for stress free radial thermal expansion.

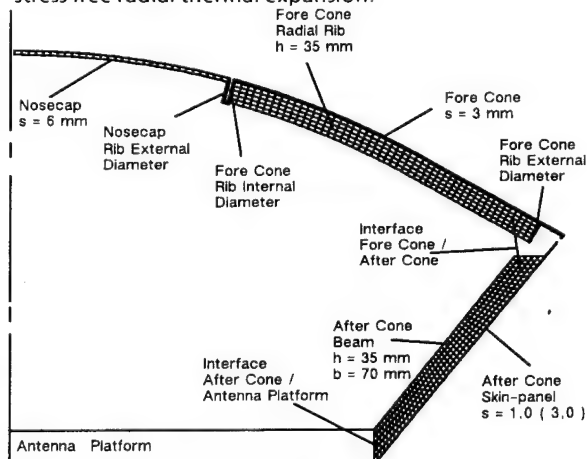


Fig. 8 : 2D - model of TPS structure

A three-dimensional model of a 90° symmetry section of nose cap, fore cone and after cone was used for the verification of all TPS-components with respect to deformations and stresses. The finite element model (8 node shell elements of the ADINA code) which contains the nose cap, the fore cone with radial and circumferential ribs, the hinge connection between fore cone and after cone, the after cone beams and the after cone skin panels is given in Fig. 9. Special attention was taken in the modelling of structure cut out for the external apertures. The structure was supported by a clamped condition at the upper end of the after cone beams (common interface of the TPS to the primary probe structure). Two load cases (pressure loading and temperature loading) were analyzed.

A summary of the stress results obtained is given in Table 3. On this basis of the given design data all stresses from the mechanical loading are within design allowable stress values.

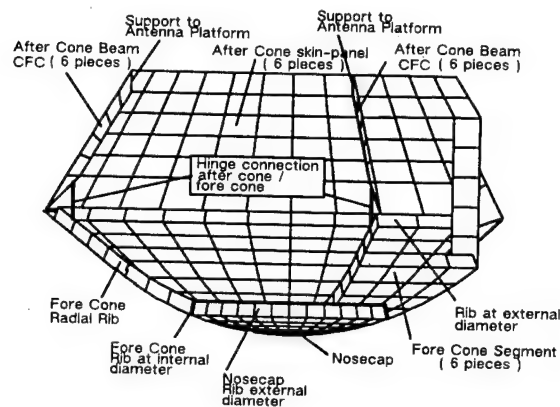


Fig. 9 : 3D - model of TPS structure

Location	mech. model		therm. model	
	Stress	(MPa)	Stress	(MPa)
	calculated	admissible	calculated	admissible
Nosecap (Be)				
membrane	< 5,0	20	—	1.0 %
membrane + bending	5,0	24	—	2.0 %
Fore cone (Be)				
membrane	< 15,0	20	—	1.0 %
membrane + bending	56,0	150	—	2.0 %
After cone beam (CFC)				
membrane	10	400	—	
membrane + bending	330	400	—	
After cone skin panel (Be)				
membrane	—	—	455 = < 0.5 % strain	1.0 % strain

Beryllium design allowable stress :

- Temperature $T = 775^{\circ}\text{C}$, Time = 60 s
- Allowable membrane stress : $\sigma_t = 20 \text{ MPa}$
- Allowable membrane + bending stress : $\sigma_t = 1,2 \cdot 20,0 = 24,0 \text{ MPa}$
- Temperature $T = 500^{\circ}\text{C}$
- Allowable membrane stress : $1,2 \sigma_m = 100 \text{ MPa}$
- Allowable membrane + bending stress : $1,8 \sigma_m = 150 \text{ MPa}$

CFC design allowable stress :

- (for example Gy - 70 / Epoxy according CDH ESA PSS-03-1101, Dec. 1986)
- Allowable membrane + bending stress : $\sigma = 400 \text{ MPa}$

Table 3 : Summary of stress results of TPS structure

First estimates concerning the temperature input of $T = 770^{\circ}\text{C}$ (nose cap and fore cone), $T = 210^{\circ}\text{C}$ (skin panel of after cone) and $T = 20^{\circ}\text{C}$ (after cone beam) have been used for the appraisal of thermally induced deformations and stresses. Since the supporting concept of the fore cone chosen allows for stress free thermal expansion, thermal stresses are occurring in the skin panel of the after cone only. The calculated max. value of thermal stress is 455 MPa assuming linear elastic material behaviour. This result of course is strongly affected by the assumptions of temperature loading input (20°C for the beams and 210°C for the skin panels). Thickening of the skin panels along their edges (e.g. 2.3 mm instead of 0.8 mm as indicated before) will lower the max. skin panel temperature significantly. Thus the above max. stress value of 455 MPa represents an upper bound of the thermal stresses of the after cone skin panels. When assuming a plastic correction factor of about 2 in the correlation between the elastically calculated thermal stress and the associated elastic plastic strain the calculated stress of 455 MPa is equivalent to about 0.5 % strain which is below 1.0 % (allowable value).

The selected suitable joining method for assembling the six Be-pieces to the fore cone (for providing strength and tightness) is brazing using a silver brazing alloy and bolting (bolting as a redundancy for the loading condition during the period of reentry).

The melting temperature of silver brazing alloy is of about 730°C while the different methods of brazing require temperatures in the range of 650°C to 820°C .

Based on the results of the thermal calculations performed the structure temperature of the brazed joints during the period of reentry is below 500°C . Sufficient strength of the brazed joint under this temperature condition is expected in order to fulfil the strength requirements with respect to the mechanical loading associated with the period of reentry. Nevertheless, bolting as a redundant joining method is incorporated in the design solution. Below 500°C titanium can be used as screw material while above 500°C service temperature the screws have to be manufactured from steel.

Thermal stresses as a result of an inhomogeneous Be heat sink (e.g. mass concentration of radial ribs) have to be considered in future design calculations.

5.5 Vibration Analysis

To validate the overall design of the Be-TPS and its interface structure vibration analyses for the total probe structure have been carried out.

Concerning the support concept of the after cone beams two design solutions are considered (Fig. 5):

- after cone beams acting as cantilevers without an additional support to the primary probe structure (solution 1)
- an integrated design solution obtained by the incorporation of an additional connection between the beams and the main platform (solution 2).

In both design solutions the forward heat shield of the TPS is acting as a hot structure without an additional supporting back structure. The intention for the development of solution 2 was the expected improvement of the probe vibration behaviour with respect to mass saving.

The structure model used for the vibration analysis is a 180° symmetry model of the total probe structure using the ADINA code (Fig. 10).

The model incorporates all relevant structural components of the total probe. Stiffness data and mass data of the primary probe structure are chosen in accordance to (Ref. 8, 9).

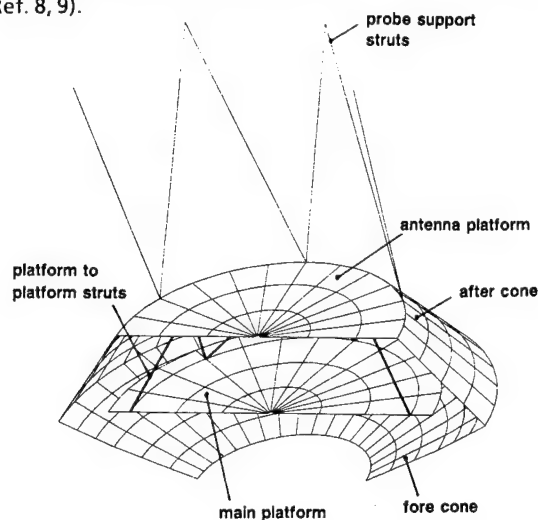


Fig. 10: Vibration model of the probe

The total probe is supported at the upper end of the probe support struts and the connections fore cone/after cone beam, after cone beam/antenna platform, after cone beam/main platform (solution 2 only) are placed at the circumferential angles of 30°, 90° and 150° respectively.

A summary of calculated frequencies is given in Table 4 while the deformed shape of mode 1 (solution 1) is given in Fig. 11.

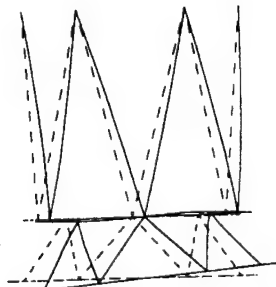


Fig. 11: Mode shape of vibration mode 1, solution 1

Solution 1 of the TPS support concept fulfils very well the stiffness requirement of the total probe (36.6 Hz > 24 Hz) while the improvement of the TPS-structure to platform structure stiffness (solution 2) was found of little effect on the global vibration mode of the total probe (36.6 Hz to 37.5 Hz). This behaviour seems to be logical due to the fact that the 1st mode of the total probe is determined by the stiffness of the probe support struts.

5.6 Determination of the Mass Budget

The estimation of the mass of the TPS-components is 21.75 kg for nose cap/fore cone, 9.3 kg for the after cone and 8.7 kg for the thermal insulation. Total mass of the TPS (without fastening devices, pyrotechnics, springs etc.) is 39.75 kg. This is close to the 41.2 kg given in (Ref. 9) for a carbon/carbon solution.

Summary of calculated frequencies

solution	frequency (cycles / s)			remark concerning mode 1
	mode 1	mode 2	mode 3	
heat shield only	64,9	90,2	92,4	Shell vibration mode of skin panel
1	36,6	50,3	61,3	Global bending mode of probe support struts
2	37,5	50,3	61,3	Global bending mode of probesupport struts

Design requirement of the probe $f \geq 24$ Hz

Table 4 : Summary of calculated frequencies, TPS and total probe

6 CONCLUSION

As a result of the investigations carried out it can be stated that the realisation of a TPS manufactured from Be is assessed feasible. The performance of a Be-TPS solution concerning heat sink, mass budget, strength and stiffness fulfils the specified requirements.

To secure the design solution further more detailed investigations for validation of the Be strength data in the material creep range and of the chosen joining methods (brazing, bolting) are recommended.

7 REFERENCES

- [1] G. Scoon, G. Whitcomb, M. Eiden, A. Smith
Cassini/Huygens Entry and Descent Technologies,
ESA Journal, Vol. 13, Pages 175 - 190, 1989
- [2] ESA Contract on Beryllium Thermal Protection
Technology (Theme 1)
ESTEC No. 8824/90/NL/PP
- [3] Proceedings of the Beryllium Conference
Nat. Res. Council; Nat. Mater. Adv. Board (1970)
- [4] Beryllium 1977
Proc. 4th Conference on Beryllium
Metal Society (1977)
- [5] Cassini Titan Atmospheric Probe
Phase A2 - Technical Note
Heatshield Design
S.E.P. ECN° 845836-BB/CS, Issue A
Bordeaux, September 88
- [6] Cassini Titan Atmospheric Probe
Phase A2 - Technical Note
Heatshield Thermal Calculations
S.E.P. ECN° 845837, Issue A
Bordeaux, September 88
- [7] Cassini Titan Probe, Phase A2
Entry Trajectories, Heating and Dynamics Assessment
MSS/19023/7355/006
Fluid Gravity Engineering Ltd.
August 1988
- [8] Cassini Titan Probe, A2 Phase
Descent Module Structure
SENER CT-TN-006, 26.05.88
- [9] Huygens/Titan Probe
Phase A Study
Executive Summary Report
BLS6850 ISSF November 1989
- [10] ADINA Finite Element Code, Release 5.6

N92-23838
 3878
 84750

CNSR ROSETTA - EARTH RETURN CAPSULE

D. DESNOYER, J.M. LARRIEU, C. BUCK

SEP

B.P. 37

33165 ST MEDARD EN JALLES - FRANCE

ABSTRACT

CNSR Rosetta mission will bring back to Earth comet nucleus samples. The mission will consist in landing on a comet after, collecting samples and return them to Earth stowed in a capsule performing a direct reentry.

During the system definition study, the preliminary design of the Earth Return Capsule Thermal Protection Subsystem has been performed. Due to high heat flux level, a high density ablative material was chosen for the heatshield. This design lead to a mass that did not meet the requirements.

The SEPCORE ® concept was proposed in order reduce the heatshield thickness. This concept requires the introduction of a thermal resistant structure. The material with high specific characteristics proposed for the aeroshell is a Ceramic Matrix Composite, and the insulation function is ensured by an lightweight internal multilayer material.

The application of SEPCORE ® concept on the CNSR Rosetta Earth Return Capsule allows a mass saving of 50 % at Thermal Protection Subsystem level and of 20 % at capsule system level. The mass budgets established with this design met the requirements.

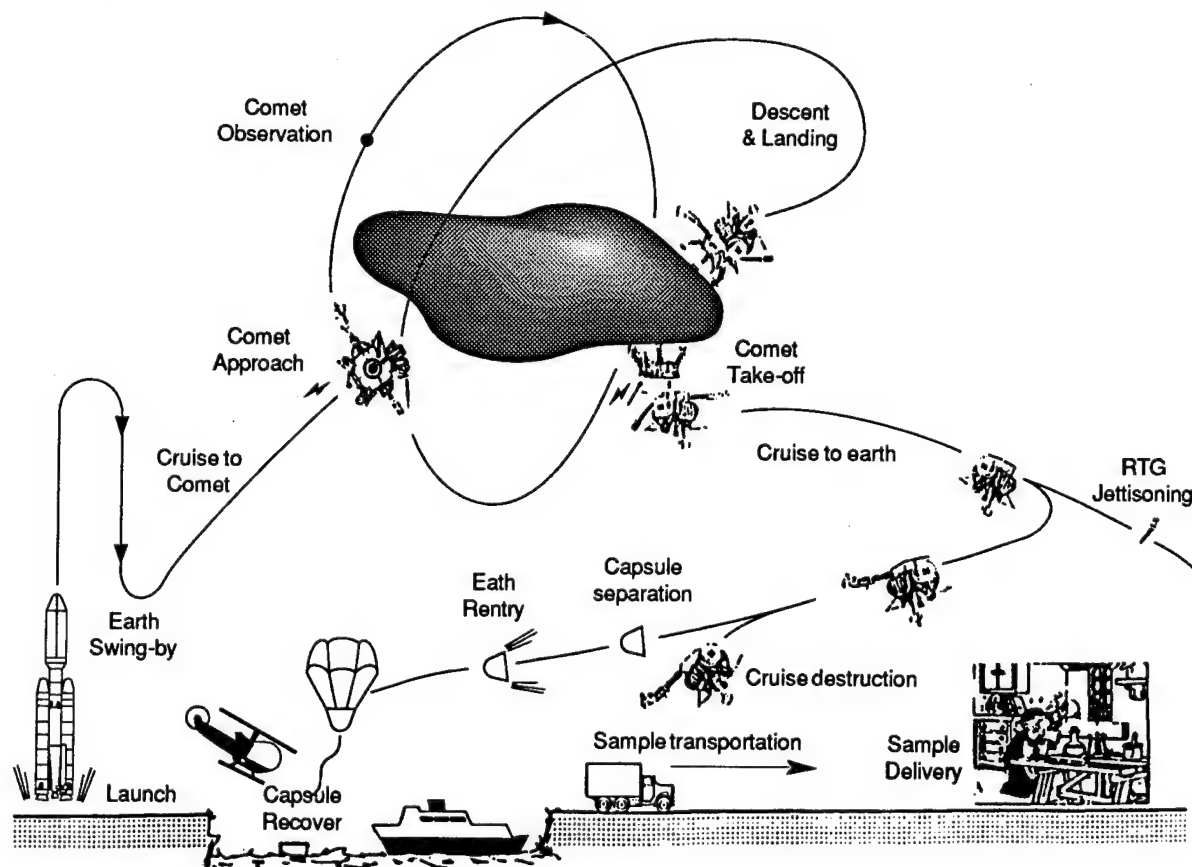


FIGURE 1 - SYNTHETIZED OPERATIONS

1. INTRODUCTION.

The aim of the Comet Nucleus Sample Return (CNSR) mission is to bring back to Earth samples of the core of a comet. The mission phases will consist in a flyby of a comet, landing on its nucleus, collecting material samples and return them to Earth with the help of a direct reentry. The trade-offs performed during the mission definition study (ref. 1), raised the need of three modules for the different mission phases : a Lander, a Cruiser and an Earth Return Capsule (ERC). Synthesized operations of the mission are presented in figure 1.

The configuration of the different components of the mission on the comet is presented in figure 2.

In the frame of the system definition study led by Matra under ESA contract, the design of the ERC at subsystem level has been performed (ref. 2). An iteration in the design of the Earth Return Capsule Thermal Protection Subsystem has led to introduce the SEPCORE ® concept.

In this paper, the new thermal protection concept is presented and its application to the CNSR Earth Return Capsule described.

2. THERMAL PROTECTION FUNCTIONS.

The functional analysis of a thermal protection subsystem requires the gathering of an important amount of technical informations. A preliminary functional analysis has been performed on the CNSR Earth Return Capsule thermal protection based on the experience of design of thermal protections for Huygens Titan entry probe (which is part of the Cassini mission) and the european spaceplane Hermes.

The Thermal Protection Subsystem of the capsule should ensure the following function :

- decelerate the capsule during the entry in Earth atmosphere in order to allow samples recovery (this technique is known under the generic name of aerobraking),

Several constraint functions are induced as well by the environmental conditions during the whole mission than the different hardware operating during the mission.

Those are :

- adaptation to launcher envelope and launch environmental conditions,
- integrity when submitted to space travel environmental conditions,

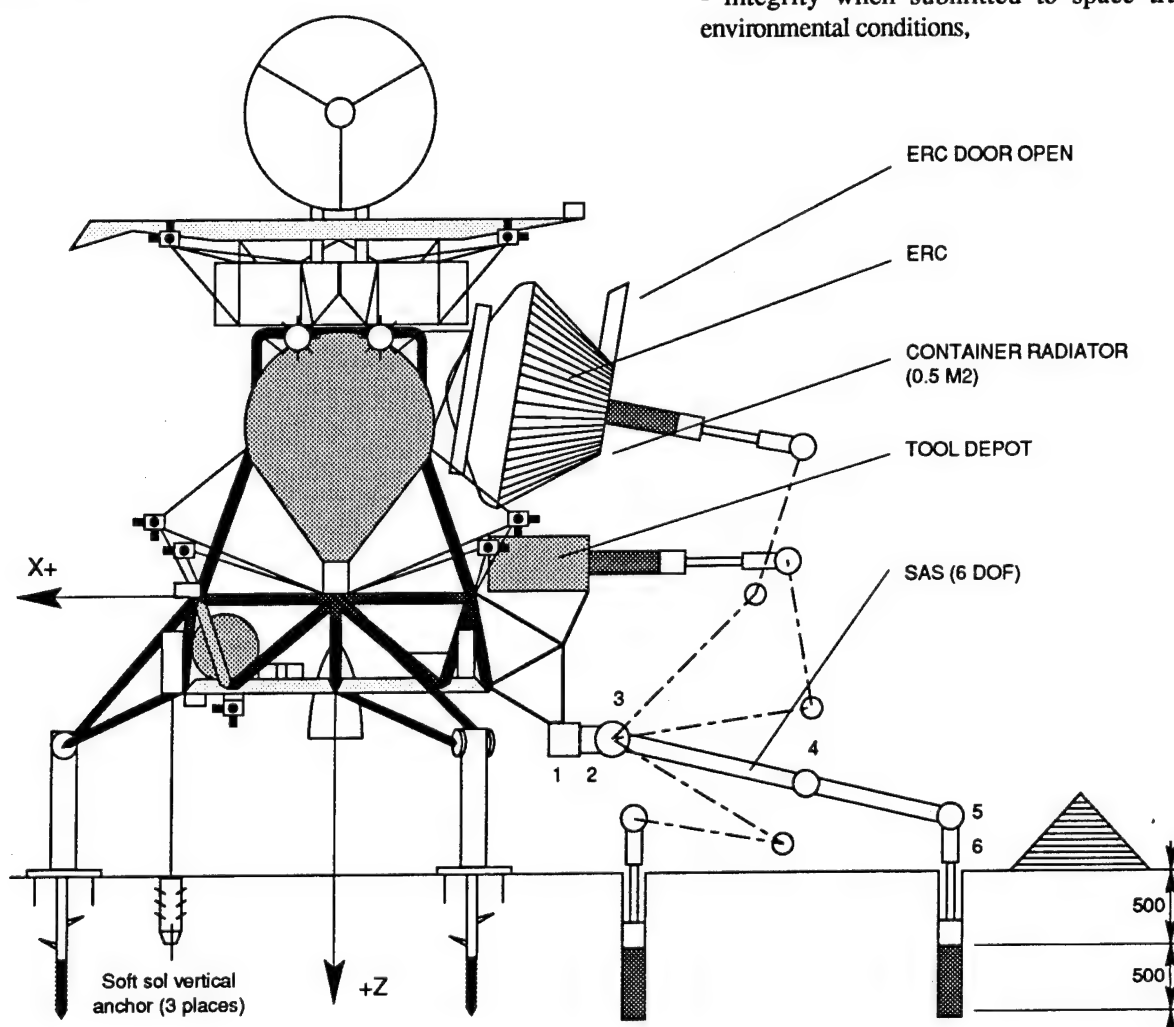


FIGURE 2 - SYSTEM CONFIGURATION

- adaptation to comet environment,
- adaptation to the capsule structure,
- compatibility with the capsule different components,
- adaptation to the Earth reentry and post-reentry environmental conditions,
- compatibility with the cruiser system.

Several technical solutions can ensure the hereabove functions. Among them, two are presented hereafter.

3. ERC - TPS PRELIMINARY STUDY.

The objective of the TPS preliminary study was to establish a first mass budget for this subsystem on the basis of a conservative baseline design.

The Earth entry, descent and immersion in the sea are the phases of the operational life of the ERC retained for the design of the TPS.

Preliminary trade-offs led to define a baseline Thermal Protection Subsystem linked to the capsule until sample recovery. It is not jettisoned after reentry as in the case of Viking or Galileo missions.

The Earth Return Capsule characteristics are a total mass objective of 320 kg, an external diameter of 1.63 m, a 60 degrees cone forward shape with a nose radius of 1 m. The capsule configuration is presented in figure 3.

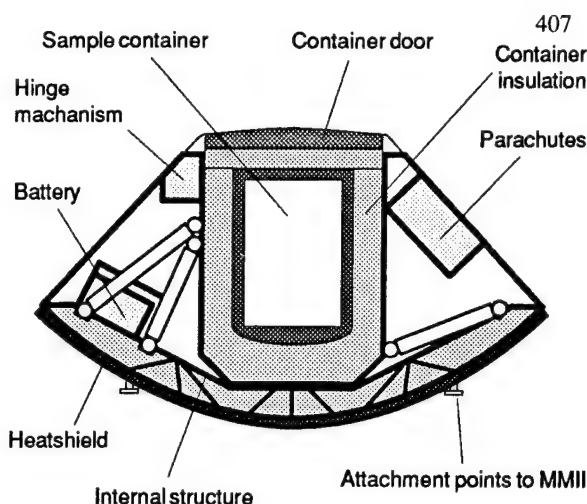


FIGURE : 3 - AEROCAPSULE CONFIGURATION

The reentry conditions are defined for a ballistic trajectory with an initial velocity of 15 km/s and an entry angle of 11 degrees. Trajectory analysis for these conditions led to a peak deceleration of 55 g and a peak heatflux at stagnation point of 10 MW/m² (ref. 3).

The peak heatflux level requires the use of a dense charring ablative material in order to limit external aerodynamic shape changes due to recession. Carbon Phenolic composite developed for this range of heatfluxes for solid rocket motors exit cones is therefore appropriate. The conservative design of the thermal protection subsystem with this material is a heatshield bonded on a metallic structure. This sandwich like internal structure indicated in figure 3 is made of two sheets of Titanium linked with struts.

With the help of an inverse parametric thermal analysis the heatshield thickness required in order to limit the bondline temperature to 420 K is established. This analysis was performed over the three phases indicated in figure 4 with the associated thermal boundary conditions.

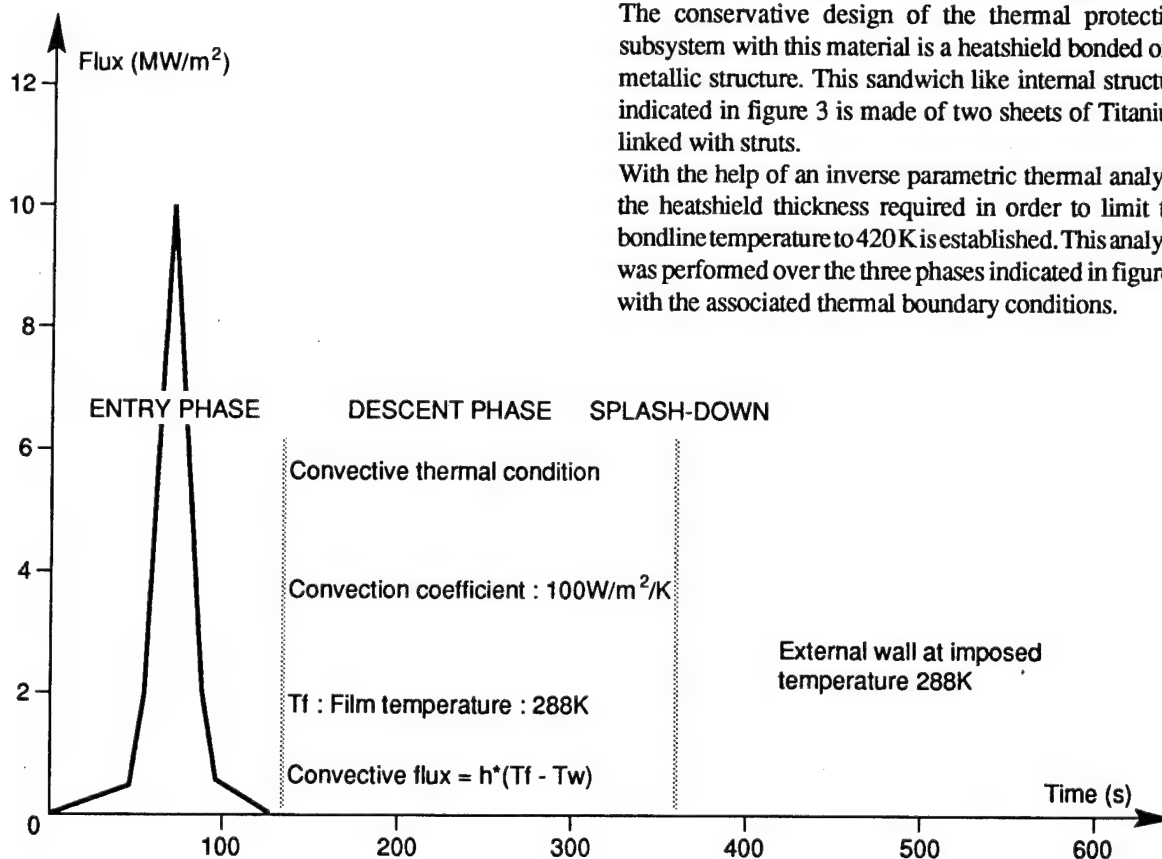


FIGURE : 4 - THERMAL BOUNDARY CONDITIONS AT STAGNATION POINT

The thermal characteristics of the carbon phenolic material are :

- Emissivity : 0.85,
- Density : 1480 kg/m³,
- Specific heat at 100 K : 846 J/kg/K,
- Specific heat at 2500 K : 2778 J/kg/K,
- Conductivity at 100 K : 0.965 W/m/K,
- Conductivity at 2500 K : 7.59 W/m/K.

The heatshield thickness required at the stagnation point is 40 mm in order to respect the bondline maximum allowed temperature. The energy stored in the heatshield during the entry phase is propagated by conduction to the bondline through the heatshield during the descent and immersion phases. The external thermal conditions resulting from the air convection during the descent phase and the water imposed temperature during immersion after splash-down are too weak thermal effects in order to cool down the heatshield.

The resulting heatshield thickness induces an important time-shift between :

- the peak heatflux occurring 75 seconds after the beginning of the modeled phases,
- and the bondline maximum temperature observed 770 seconds after the beginning of the reentry.

The mass budget without margins resulting from this analysis is 140 kg for the forward heatshield.

This result does meet the mass objective at Earth Return Capsule system level.

4. SEPCORE® CONCEPT PRESENTATION.

For the specific needs of the Rosetta ERC mission, the preliminary study performed with a conservative thermal protection concept indicates that its thickness at the end of the entry phase is divided in the following parts :

- 2 mm recession,
- 5 mm of charred material,
- 13 mm of pyrolysed material,
- 20 mm of virgin material working as insulator.

The major relative part of the heatshield is acting as an insulator. An allowed temperature at the rear side of the heatshield higher than the bondline design one, will allow an external insulation thickness reduction.

This suggestion requires the introduction of a structural part made of a material with a maximum allowed temperature higher than the titanium of the existing structure. On the other side, the insulation function with regards to the subsystems at the rearside of the structure will be ensured by a lightweight insulator ensuring radiative decoupling.

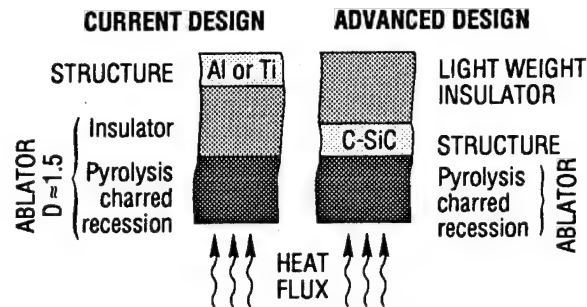


FIGURE : 5 - FUNCTIONAL ANALYSIS

The two concepts are presented in figure 5.

In order to take benefit of the developments performed in the frame of the HERMES european spaceplane program, the material proposed for the structure is a Ceramic Matrix Composite named SEPCARBINOX®. This material will be used for the manufacturing of the Thermal Structures of this spaceplane : winglets, elevons and body-flap.

From a conceptual point of view, the SEPCORE® concept can be considered as an evolution of the radiative thermal protection and structural parts of Hermes. As the heatfluxes level seen during the entry of Rosetta Earth Return Capsule can not be endured by a radiative thermal protection, an external ablative material heatshield covers the thermal resistant structure.

5. SEPCORE® APPLICATION TO ERC.

The application of the SEPCORE® concept to the design of the Rosetta Earth Return Capsule induces the following tasks :

- capsule conceptual general configuration,
- carbon phenolic heatshield thermal design,
- lightweight insulator thermal design,
- thermal resistant structure static preliminary design.

This different tasks are described in reference 4.

5.1. CAPSULE CONFIGURATION.

The introduction of a Ceramic Matrix Composite primary structure suggests to suppress the internal structure shown in figure 4. The generic requirements of the interfaces between the thermal structure and the capsule structure are :

- radial flexibility in order to allow the aeroshell thermal expansion,
- axial rigidity in order to transmit the deceleration efforts during entry,
- low conductivity at the mechanical interfaces ensuring the two hereabove functions.

The thermal expansion of the primary structure occurring during the entry phase induces that the mechanical interfaces should be managed as near as possible to the capsule axis.

5.2. HEATSHIELD.

The analysis of the the forward heatshield has been conducted with the same hypotheses than those presented in paragraph 3. The introduction of the SEPCORE ® concept leads to an evolution of the thermal design criterion : the temperature at the rear side of the heatshield is not determined by the bondline material but by the structure material. The ultimate use temperature of the Ceramic Matrix Composite is depending on thermodynamic conditions : temperature and surrounding gas composition, and exposure duration. In order to establish a reference point for the heatshield mass and given the uncertainties of the environment composition the retained value of temperature is : 1270 K.

For this iteration on the design of the thermal protection subsystem, due to configuration changes at system level, the capsule overall diameter increased from 1.63 m to 1.79 m. This new configuration did not induce changes in the environmental entry conditions.

The result of the inverse parametric thermal analysis is that a carbon phenolic heatshield of 15 mm thickness at stagnation point is required in order to respect the structure allowed temperature. The thermal inertia of the reduced thickness heatshield is lowered as the maximum structure temperature occurs 145 seconds after the peak heatflux solicitation.

This analysis leads to a heatshield mass of 70 kg.

5.3. REAR SIDE INSULATOR.

The insulator proposed for the rear side of the structure is an internal multilayer insulation material developed in the frame of the Hermes spaceplane Reusable External Insulation. Its principle consists in a multiscreen arrangement that constitute a chain of thermal radiative resistances.

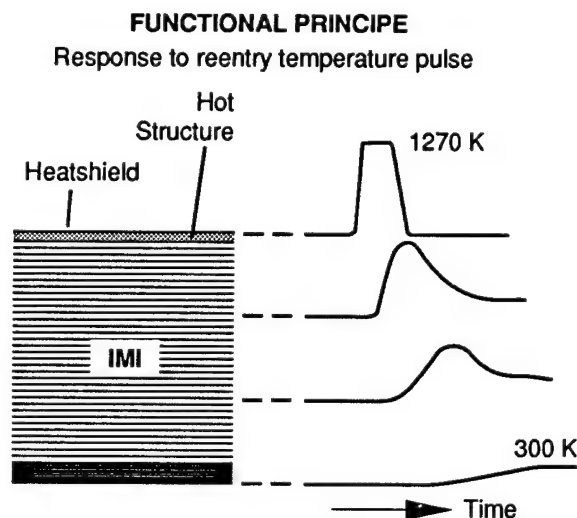


FIGURE : 6 - INTERNAL MULTILAYER INSULATION (IMI)

The response to a reentry temperature pulse is indicated in figure 6.

The material characteristics retained for the thermal design of this part are :

- density : 60 kg/m³,
- Specific heat at 300 K : 869 J/kg/K,
- Specific heat at 1300 K : 1183 J/kg/K,
- Conductivity at 300 K : 0.023 W/m/K,
- Conductivity at 1300 K : 0.138 W/m/K.

The thermal boundary condition on the link between the structure and the internal multilayer insulation is the structure temperature resulting from the analysis described in paragraph 5.2.

The design criterion is a rear side temperature limited to 300 K in order to limit the radiative thermal exchange between this part and the other capsule subsystems.

The thermal analysis performed with analytical rules leads to a required thickness of 70 mm. The maximum temperature at the backside of this thickness is obtained 20 minutes after the moment the entry peak heatflux occurs.

This thickness leads to a mass of 10 kg.

5.4. THERMOSTRUCTURAL PART.

A preliminary design of the thermal resistant structure made of Ceramic Matrix Composite has been performed in order to establish its mass.

This design takes into account the experience gained during the design of the Hermes Thermal Structures. Nowadays state of the art of design of this type of structures allows the use shell structures which is an intermediate type in the range of lightweight structures located between the beam and sandwich structures. Associated manufacturing technologies are developed in the frame of the Hermes Thermal Structures program.

The entry peak deceleration (55 g) quasi-static load case has been retained for the design of this part. The associated stagnation pressure applied on the external side of the shell is 50 kPa.

Given the external diameter of the sample container (see figure 4) aerodynamic loads will be transmit from the primary structure to the payload at this location through a ring allowing punctual attachments.

The Ceramic Matrix Composite used for this design is composed of a carbon fiber reinforcement associated to a silicon carbide matrix. The type of reinforcement is named Skinex ®. This name is based on a manufacturing technique of the reinforcement at textile preform level which allows the establishment of links between the ply during their build up. This technique is particularly adapted to skin stiffened structures. The different application of this material are presented in paper in reference 5.

The material mechanical characteristics retained for this

analysis are constant in the use temperature range of the structure : 100 K to 1300 K. The behaviour is modeled as an orthotropic composite material adapted to shell type structures :

- density : 2100 kg/m³,
- Young's modulus (in plane) : 40 GPa,
- Young's modulus (perpendicular to plane) : 30 GPa,
- shear modulus : 10 GPa,
- tensile strength : 200 MPa,
- compressive strength : 300 MPa,
- shear strength : 30 MPa.

Analytical rules were used in order to establish the shell thickness, the rings and stringers distribution and their sections and inertia. The resulting design is presented in figures 7 and 8.

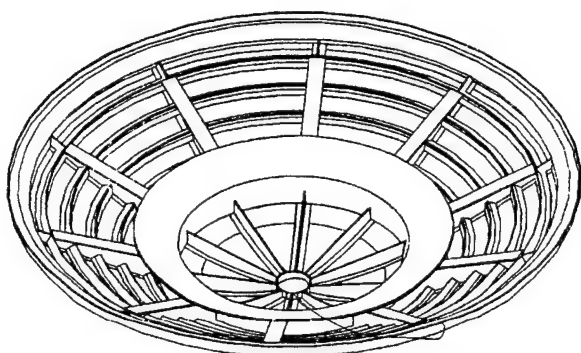


Figure : 7 - THERMAL STRUCTURE

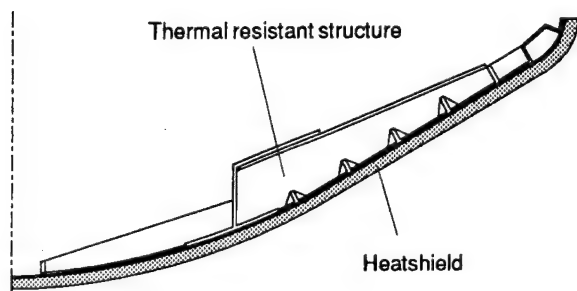


Figure : 8 - T.P.S. SECTION

This design has been verified by Finite Element Method code as described in paper in reference 4. The results of this analysis are :

- displacements on the outer diameter of the structure are equal to 1.6 mm which will induce low changes in the external shape of the heatshield.
- calculated stresses levels present a safety coefficient equal to 3 which is satisfactory for the preliminary design of a part.

The resulting mass of the structure is equal to 39 kg.

6. CONCEPTS COMPARISON.

In order to compare properly the designs presented in paragraphs 3 and 5, mass budgets of the capsule subsystems consisting in the heatshield and the part of the internal structure located behind the heatshield transmitting the deceleration efforts to the whole system are to be established.

For the concept presented in paragraph 3, the metallic structure working behind the heatshield as an aeroshell is estimated to 20 kg. And the mass of the heatshield when calculated for the diameter of the capsule retained during the study of SEPCORE ® applicability is equal to 188 kg.

The comparison of mass budgets is given in the following table :

CAPSULE CONCEPT		COLD STRUCTURE	SEPCORE ®
Aerodynamic Structure	(kg)	20	39
External Heatshield	(kg)	168	70
Internal Insulation	(kg)	0	10
Total mass	(kg)	188	119

This mass comparison indicates a clear mass saving on the heatshield with the introduction of SEPCORE ® concept. At Thermal Protection Subsystem level relative mass saving is 50% of the mass of the first proposed design. At capsule system level, this mass saving represents 20% of first configuration.

The introduction of SEPCORE ® concept allows the respect of the mass objectives.

On the other side the mass loss noticed for the structural part is due to the fact the metallic structure is a sandwich type one and the SEPCORE ® one is a shell type one. The design experience of parts with metallic material is much greater than with new thermostructural material, which explains the conservative design approach used for the new design.

7. CONCLUSION.

The introduction of the SEPCORE ® concept on the Earth Return Capsule for the CNSR Rosetta mission induces an important mass saving : 20% of the capsule mass.

The SEPCORE ® concept is a novative concept of thermal protection able to stand high heatfluxes environments. It is based on known technologies :

- Carbon phenolic ablative heatshield,
- Skinex-SiC material structure.

Its introduction requires detailed trade-offs at system level as changes occur in the design at thermal protection subsystem level and structural subsystem level.

Its adaption on future planetary exploration missions is possible, especially with the development of aerobraking techniques in space transportation area.

REFERENCES.

- (1) Comet Nucleus Sample Return,
Mission definition study - final report,
092/CC/332.87 MATRA ESPACE.
- (2) Rosetta/CNSR,
System definition study - final report,
MATRA (ESA CONTRACT : 8228/89/NL/SK).
- (3) Rosetta entry capsule,
Shape aerodynamics and aerothermodynamics assessment,
Fluid Gravity Engineering LTD TR23/90.
- (4) CNSR Rosetta - Sepcore concept,
Preliminary design study,
SEP DPPC, AEF 12167+AA.
- (5) AIAA-90-5208
Ceramic Matrix Composites, Key Materials for Future
Space Plane Technologies
A.Lacombe and C.Bonnet,

**SESSION
2.2.B**

**MATERIALS
V**

COMPOSITES

PRECEDING PAGE BLANK NOT FILMED

N92-23839

NOTCHED STRENGTH OF COMPOSITE MATERIALS

A. S. Herrmann¹⁾

German Aerospace Research Establishment (DLR)
Institute for Structural Mechanics
D - 3300 Braunschweig, W. Germany

Abstract:

The plane stress and displacement fields around an elliptical opening in an anisotropic plate with linear elastic material properties under arbitrary tensional forces and fiber direction are analytically determined by the method of complex stress functions. For this purpose a plate with infinite extension under uni-axial load is used as the mathematical model. Using a glass fiber reinforced composite with orthotropic material properties as an example it is shown that the data gathered from isotropic materials on the behavior of stress and displacement around elliptical and circular openings is not applicable to anisotropic materials. This is especially true if load and orthotropic principal directions (off-axis-load) do not coincide. For several particular cases the stress concentration factors which are decisive for constructural design are depicted in polar diagrams. Furthermore the location of the maximum stress is given for these examples as well which are - in contrast to isotropic materials - generally not on the tip of the opening.

Keywords: fiber reinforced epoxy, notches, tensile loading, off-axis loading.

1. INTRODUCTION

In the field of the design of lightweight structures anisotropic materials - e.g. fiber reinforced composites are more and more often used. These materials allow to design in respect to the optimal load distribution leading to the most weight efficient construction for the required purpose. Being able to satisfy the requirements for constructions out of these modern materials new criteria and guidelines for their dimension have to be established which take their anisotropic properties into consideration.

The fiber reinforced composites used with polymeric, metallic and ceramic matrix as well as the new self-reinforced polymers (Liquid crystal Polymers) show in general an anisotropic behavior. This behavior is called in the nomenclature of the physics of crystals as the orthorhombic anisotropy or orthotropy.

Stress concentration in such a material due to notches can barely be reduced by the effect of stress rearranging (macro-stiffening) due to its small elongation at rupture. This states the importance for the discussion of the stresses in anisotropic materials.

2. THEORETICAL SOLUTION FOR AN ANISOTROPIC PLATE BY THE METHOD OF COMPLEX STRESS FUNCTIONS AND THE CONFORMAL MAPPING

2.1 Hooke's Law for the two-dimensional orthotropic Stress State

In case of a two-dimensional orthotropic problem Hooke's Law in its general form can be rewritten in the principal coordinate system as follows

$$\begin{aligned}\epsilon_1 &= \sigma_1 S_{11} + \sigma_2 S_{12}, \\ \epsilon_2 &= \sigma_1 S_{12} + \sigma_2 S_{22}, \\ \gamma_{12} &= \tau_{21} = \tau_{12} S_{66},\end{aligned}\quad (1)$$

where $\sigma_1, \sigma_2, \tau_{12}$ are the stress components, $\epsilon_1, \epsilon_2, \gamma_{12}$ are the strains and $S_{11}, S_{12}, S_{22}, S_{66}$ are the compliances in the principal directions. The relations between the compliances, S_0 , and the constants of elasticity are

$$S_{11} = \frac{1}{E_{11}}, \quad S_{12} = -\frac{\nu_{12}}{E_{11}} = -\frac{\nu_{21}}{E_{22}}, \quad S_{22} = \frac{1}{E_{22}}, \quad S_{66} = \frac{1}{G_{12}}. \quad (2)$$

2.2 Equation for the orthotropic Plate and its Solution

The differential equation describing the stress state in an orthotropic plate can be obtained from Eq. (1) in consideration of the compatibility condition to

$$S_{11} \frac{\partial^4 F}{\partial x_2^4} + (2S_{12} + S_{66}) \frac{\partial^4 F}{\partial x_1^2 \partial x_2^2} + S_{22} \frac{\partial^4 F}{\partial x_1^4} = 0, \quad (3)$$

where F is the Airy Stress Function. The stresses result from the relations

$$\sigma_1 = \frac{\partial^2 F}{\partial x_2^2}, \quad \sigma_2 = \frac{\partial^2 F}{\partial x_1^2}, \quad \tau_{12} = \tau_{21} = -\frac{\partial^2 F}{\partial x_1 \partial x_2} \quad (4)$$

($x_1 = \perp$, $x_2 = \parallel$ to the fiber direction). It has to be pointed out that in contrast to the equation for an isotropic plate the equation for an orthotropic plate is influenced by the characteristic of the material.

If we use a complex representation of the Airy Stress Function

$$F = f(x_1 + \mu x_2) \quad (5)$$

the differential equation can easily be obtained in its characteristic form from Eq. (3)

$$\mu^4 + \frac{2S_{12} + S_{66}}{S_{11}} \mu^2 + \frac{S_{22}}{S_{11}} = 0, \quad (6)$$

1) Dedicated to Professor Dr.-Ing. H-W. Bergmann for his 65th birthday.

where the square roots depend on the elastic constants of the orthotropic material

$$\mu_{1,2,3,4} = \pm \sqrt{-\frac{2S_{12} + S_{66}}{2S_{11}}} \pm \sqrt{\left(\frac{2S_{12} + S_{66}}{2S_{11}}\right)^2 - \frac{S_{22}}{S_{11}}} \quad (7)$$

For the laminates, we want to discuss, these roots are in pairs conjugate complex and therefore known as the complex representation of the material characteristics. At best these roots can be complete imaginary but they can never be real [1]. In case of an isotropic material we get (with the double square root) $\mu = \pm i$ ($i = \sqrt{-1}$).

By denoting the roots

$$\mu_1 = \alpha_1 + i\beta_1, \quad \bar{\mu}_1 = \alpha_1 - i\beta_1, \quad \mu_2 = \alpha_2 + i\beta_2, \quad \bar{\mu}_2 = \alpha_2 - i\beta_2, \quad (8)$$

we can introduce the affine deformed coordinates in their complex form

$$z_k = x_1 + \alpha_k x_2 + i\beta_k x_2, \quad \bar{z}_k = x_1 + \alpha_k x_2 - i\beta_k x_2 \quad (k=1,2). \quad (9)$$

Goursat [2] states that a real biharmonic function, F , in a plane can be described by two analytic functions with the complex variable z_k

$$F = F_1(z_1) + \bar{F}_1(\bar{z}_1) + F_2(z_2) + \bar{F}_2(\bar{z}_2). \quad (10)$$

In the further approach we will use the more suitable derivatives of the functions F_1 and F_2 :

$$\Phi_1(z_1) = \frac{dF_1}{dz_1} = F_1'(z_1), \quad \Phi_2(z_2) = \frac{dF_2}{dz_2} = F_2'(z_2). \quad (11)$$

Under the restriction caused by the real part of the function F Eq. (4) leads to

$$\begin{aligned} \sigma_x &= 2 \operatorname{Re} [\mu_1^2 \Phi_1'(z_1) + \mu_2^2 \Phi_2'(z_2)], \\ \sigma_y &= 2 \operatorname{Re} [\Phi_1'(z_1) + \Phi_2'(z_2)], \\ \tau_{xy} &= -2 \operatorname{Re} [\mu_1 \Phi_1'(z_1) + \mu_2 \Phi_2'(z_2)]. \end{aligned} \quad (12)$$

By this method we reduced the original problem to the determination of two suitable potential functions $\Phi_1(z_1)$ and $\Phi_2(z_2)$, which have to satisfy the outer boundary conditions (load) and inner boundary conditions (at the opening edge).

For the comparison with a numerical solution e.g. finite element analysis or with experimental results it is recommendable to perform the calculation in a body orientated coordinate system (in this case in a cartesian x_1, x_2 -system). As we assume an analytic model with infinite extension, this conversion is not absolute necessary. Furthermore the axis of the elliptic opening are assumed to be parallel to the reference coordinate system. If the fiber orientated coordinate system (denoted as the x_1, x_2 -system) should be lying under an angle, ψ , to the reference system (Fig. 1) the transformation follows the equation

$$(x + iy)e^{i\psi} = x_1 + ix_2$$

respectively

$$x_1 = x \cos \psi - y \sin \psi, \quad x_2 = x \sin \psi + y \cos \psi. \quad (13)$$

By expressing the material characteristics in the reference system in its complex form $\bar{\mu}_k = \bar{\alpha}_k + i\bar{\beta}_k$ we can obtain out of

$$x + \bar{\mu}_k y = \lambda (x_1 + \mu_k x_2) \quad (\lambda \text{ distortion factor})$$

in consideration of Eq. (13) and elimination of λ the expression

$$\bar{\mu}_k = \frac{\mu_k \cos \psi - \sin \psi}{\cos \psi + \mu_k \sin \psi} \quad (k=1,2). \quad (14)$$

By using

$$\bar{z}_k = x + \bar{\mu}_k y = x + \bar{\alpha}_k x_1 + i\bar{\beta}_k x_2 \quad (15)$$

we obtain from Eq. (12) the stress components in the reference coordinate system

$$\begin{aligned} \sigma_x &= 2 \operatorname{Re} [\bar{\mu}_1^2 \Phi_1'(\bar{z}_1) + \bar{\mu}_2^2 \Phi_2'(\bar{z}_2)], \\ \sigma_y &= 2 \operatorname{Re} [\Phi_1'(\bar{z}_1) + \Phi_2'(\bar{z}_2)], \\ \tau_{xy} &= -2 \operatorname{Re} [\bar{\mu}_1 \Phi_1'(\bar{z}_1) + \bar{\mu}_2 \Phi_2'(\bar{z}_2)]. \end{aligned} \quad (16)$$

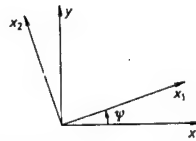


Figure 1: Coordinate systems

For given external forces X_n, Y_n acting on the boundary surfaces we can rewrite the boundary condition along the contour (0...s)

$$\frac{\partial F}{\partial x} = \int_0^s Y_n ds + c_1, \quad \frac{\partial F}{\partial y} = -\int_0^s X_n ds + c_2 \quad (17)$$

respectively

$$\begin{aligned} 2 \operatorname{Re} [\Phi_1(\bar{z}_1) + \Phi_2(\bar{z}_2)] &= \int_0^s Y_n ds + c_1, \\ 2 \operatorname{Re} [\bar{\mu}_1 \Phi_1(\bar{z}_1) + \bar{\mu}_2 \Phi_2(\bar{z}_2)] &= -\int_0^s X_n ds + c_2, \end{aligned} \quad (18)$$

where c_1 and c_2 are arbitrary (but irrelevant) constants. (They have no influence on the stress evaluation and indicate for the displacement only a additional rigid body movement, which remain indeterminated.)

To adjust the functions $\Phi_1(\bar{z}_1)$ and $\Phi_2(\bar{z}_2)$, which have to behave regular in the infinity these functions are being used in the form of series. The coefficients of the series can be defined by comparison of the coefficients for the functional values at their boundary $\Phi_1 = \Phi_1^0, \Phi_2 = \Phi_2^0$. This definition is with $z = |z|e^{i\theta}$ in particular simple for the unit circle with the contour $|z|=1$. Based on the circular shaped opening every individual boundary problem can be dealt with by using the affine transformation, as the potential functions, Φ_k , do not change its characteristics. References to this and other solution methods can be found by Muskhelishvili [3] as well as by Kantorowitsch and Krylov [4].

In the case of an elliptic opening the integrals at the contour Eq. (17) (where $s = 2\pi$) are elliptic functions in dependence of the (a so called) elliptic parameter, Θ , and have a period of 2π . These functions can be represented in Fourier series, hence the boundary conditions Eq. (18) can be laid down in the form

$$\begin{aligned} \int_0^1 Y_n ds + c_1 &= a_0 + \sum_{n=1}^{\infty} (a_n e^{i n \theta} + \bar{a}_n e^{-i n \theta}) \\ - \int_0^1 X_n ds + c_2 &= b_0 + \sum_{n=1}^{\infty} (b_n e^{i n \theta} + \bar{b}_n e^{-i n \theta}) \end{aligned} \quad (19)$$

(where a_m, b_m are complex coefficients).

We assume that the exterior of the z -plane with an elliptic opening (original plane) is represented on the outer contour of the unit circle in the ζ -plane by the function $z=z(\zeta)$ (Fig. 2).

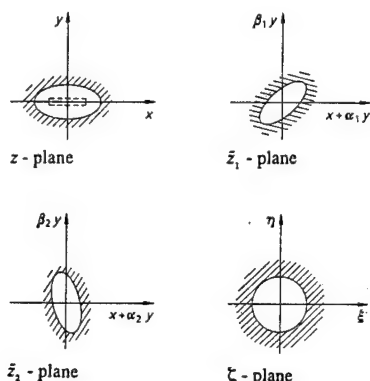


Figure 2: Conformal mapping

Both stress functions, $\Phi_1(\bar{z}_1)$ and $\Phi_2(\bar{z}_2)$, are related to two different coordinate systems which emerge from the x, y -system in the original plane by the affine transformation $\bar{z}_k = x + \bar{\mu}_k y$ ($k=1, 2$). For this we have as the (modified) mapping function

$$\bar{z}_k = \frac{a - i\bar{\mu}_k b}{2} \bar{\zeta}_k + \frac{a + i\bar{\mu}_k b}{2} \frac{1}{\bar{\zeta}_k} \quad (k=1, 2), \quad (20)$$

where a and b are the major axis of the elliptic opening. (The difference in ζ is a formal one and only important for the back transformation.)

We want to express both potential functions, $\Phi_1(\bar{z}_1)$, in the ζ -plane by series in analogy to Lekhnitskii [5]

$$\Phi_1(\bar{z}_1(\bar{\zeta}_1)) = \sum_{n=1}^{\infty} A_n^{(1)} \bar{\zeta}_1^{-n}. \quad (21)$$

To calculate the complex coefficients, $A_n^{(1)}$, we substitute Eq. (21) into the boundary conditions (18)

$$A_n^{(k)} = \frac{\bar{\mu}_1 \bar{a}_n - \bar{b}_n}{\bar{\mu}_2 - \bar{\mu}_1} \quad (k=1, 2; \bar{\mu}_1 \neq \bar{\mu}_2). \quad (22)$$

By proceeding reciprocally we obtain for the potential functions, Φ_1 ,

$$\begin{aligned} \Phi_1(\bar{z}_1(\bar{\zeta}_1)) &= \sum_{n=1}^{\infty} \frac{\bar{\mu}_1 \bar{a}_n - \bar{b}_n}{\bar{\mu}_2 - \bar{\mu}_1} \bar{\zeta}_1^{-n}, \\ \Phi_2(\bar{z}_2(\bar{\zeta}_2)) &= \sum_{n=1}^{\infty} \frac{\bar{\mu}_1 \bar{a}_n - \bar{b}_n}{\bar{\mu}_2 - \bar{\mu}_1} \bar{\zeta}_2^{-n}, \end{aligned} \quad (23)$$

where \bar{a}_n, \bar{b}_n are the Fourier coefficients as given in the series form for the given forces acting on the edge of the elliptic opening:

$$\begin{aligned} X_n &= \sigma_n^0 \cos(n, x) + \tau_{xy}^0 \cos(n, y), \\ Y_n &= \sigma_n^0 \cos(n, y) + \tau_{xy}^0 \cos(n, x). \end{aligned} \quad (24)$$

In the case of an elliptic contour (major axis a , b) Eq. (25) is valid

$$\begin{aligned} \cos(n, x) &= \frac{dy}{ds} = \frac{b \cos \Theta}{\sqrt{a^2 \sin^2 \Theta + b^2 \cos^2 \Theta}}, \\ \cos(n, y) &= -\frac{dx}{ds} = \frac{a \cos \Theta}{\sqrt{a^2 \sin^2 \Theta + b^2 \cos^2 \Theta}}. \end{aligned} \quad (25)$$

3. STRESS FIELD NEAR THE ELLIPTIC OPENING IN AN ANISOTROPIC PLATE WITH INFINITE EXTENSION AND GENERAL FIBER ORIENTATION UNDER TENSIONAL LOADING

The stress state in the whole plate distorted due to an opening can be interpreted as a superposition of the undisturbed stresses in a plate and the distorted stresses in a plate with opening which has no influence on the stress state in a certain distant to the opening. In the actual case the plate with infinite extension, laying under the angle, φ , to the direction of the tensional loading, p , is splitted up into the undisturbed stress state I and the disturbed stress state II as shown in Fig. 3.

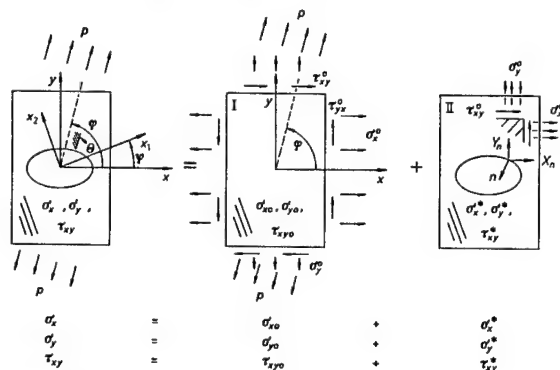


Figure 3: Split up of the plate problem

For state I the transformation into the reference coordinate system gives for the boundary stress values

$$\begin{aligned} \sigma_{x_0} &= p \cos^2 \varphi = \sigma_x^0, \\ \sigma_{y_0} &= p \sin^2 \varphi = \sigma_y^0, \\ \tau_{x_0 y_0} &= p \cos \varphi \sin \varphi = \tau_{xy}^0. \end{aligned} \quad (26)$$

For the Fourier coefficients we obtain by the use of Eq. (19)

$$\begin{aligned} \int_0^1 Y_n ds &= p(b \sin \varphi \cos \varphi \sin \Theta - a \sin^2 \varphi \cos \Theta) \\ &= a_0 + \sum_{n=1}^{\infty} (a_n e^{i n \theta} + \bar{a}_n e^{-i n \theta}), \\ - \int_0^1 X_n ds &= p(a \sin \varphi \cos \varphi \cos \Theta - b \cos^2 \varphi \sin \Theta) \\ &= b_0 + \sum_{n=1}^{\infty} (b_n e^{i n \theta} + \bar{b}_n e^{-i n \theta}) \end{aligned} \quad (27)$$

and comparison of the coefficients

$$\begin{aligned}\bar{a}_1 &= -\frac{P}{2} \sin \varphi (a \sin \varphi - ib \cos \varphi), \\ \bar{b}_1 &= +\frac{P}{2} \cos \varphi (a \sin \varphi - ib \cos \varphi), \\ a_0 &= b_0 = 0, \quad \bar{a}_m = \bar{b}_m = 0 \quad \text{for } m \geq 2.\end{aligned}\quad (28)$$

In order to obtain the unknown function, $\Phi_1(\bar{z}_1(\zeta_1))$, in the ζ -plane we substitute Eq. (28) into Eq. (23)

$$\begin{aligned}\Phi_1(\bar{z}_1(\zeta_1)) &= \frac{p(\bar{\mu}_2 \sin \varphi + \cos \varphi)(a \sin \varphi - ib \cos \varphi)}{2(\bar{\mu}_1 - \bar{\mu}_2)\zeta_1}, \\ \Phi_2(\bar{z}_2(\zeta_2)) &= \frac{p(\bar{\mu}_1 \sin \varphi + \cos \varphi)(a \sin \varphi - ib \cos \varphi)}{2(\bar{\mu}_1 - \bar{\mu}_2)\zeta_2}.\end{aligned}\quad (29)$$

By using the inverse mapping

$$\zeta_k = \frac{\bar{z}_k \pm \sqrt{\bar{z}_k^2 - a^2 - \bar{\mu}_k^2 b^2}}{a - i\bar{\mu}_k b} \quad (30)$$

the results can be transformed back into the \bar{z}_1 - resp. \bar{z}_2 -coordinates:

$$\begin{aligned}\Phi_1(\bar{z}_1) &= \frac{p(\bar{\mu}_2 \sin \varphi + \cos \varphi)(a \sin \varphi - ib \cos \varphi)(a - i\bar{\mu}_1 b)}{2(\bar{\mu}_1 - \bar{\mu}_2)(\bar{z}_1 \pm \sqrt{\bar{z}_1^2 - a^2 - \bar{\mu}_1^2 b^2})}, \\ \Phi_2(\bar{z}_2) &= \frac{p(\bar{\mu}_1 \sin \varphi + \cos \varphi)(a \sin \varphi - ib \cos \varphi)(a - i\bar{\mu}_2 b)}{2(\bar{\mu}_1 - \bar{\mu}_2)(\bar{z}_2 \pm \sqrt{\bar{z}_2^2 - a^2 - \bar{\mu}_2^2 b^2})}.\end{aligned}\quad (31)$$

Based on the derivatives of the potential functions Eq. (31) i.e.

$$\begin{aligned}\Phi_1'(\bar{z}_1) &= \frac{p(\bar{\mu}_2 \sin \varphi + \cos \varphi)(a \sin \varphi - ib \cos \varphi)U_1}{2(\bar{\mu}_1 - \bar{\mu}_2)(a + i\bar{\mu}_1 b)}, \\ \Phi_2'(\bar{z}_2) &= \frac{p(\bar{\mu}_1 \sin \varphi + \cos \varphi)(a \sin \varphi - ib \cos \varphi)U_2}{2(\bar{\mu}_1 - \bar{\mu}_2)(a + i\bar{\mu}_2 b)},\end{aligned}\quad (32)$$

which are simplified by the expression

$$U_k = 1 - \frac{\bar{z}_k}{\sqrt{\bar{z}_k^2 - a^2 - \bar{\mu}_k^2 b^2}} \quad (k=1,2), \quad (33)$$

we are able to determine the stress components in the cartesian coordinate system to

$$\begin{aligned}\sigma_x &= \sigma_{x0} + \sigma_x^* = p \left\{ \cos^2 \varphi + \operatorname{Re} \left[\frac{a \sin \varphi - ib \cos \varphi}{\bar{\mu}_1 - \bar{\mu}_2} \right. \right. \\ &\quad \times \left. \left. \left(-\bar{\mu}_1^2 \frac{\cos \varphi + \bar{\mu}_2 \sin \varphi}{a + \bar{\mu}_1 b} U_1 + \bar{\mu}_2^2 \frac{\cos \varphi + \bar{\mu}_1 \sin \varphi}{a + \bar{\mu}_2 b} U_2 \right) \right] \right\}, \\ \sigma_y &= \sigma_{y0} + \sigma_y^* = p \left\{ \sin^2 \varphi + \operatorname{Re} \left[\frac{a \sin \varphi - ib \cos \varphi}{\bar{\mu}_1 - \bar{\mu}_2} \right. \right. \\ &\quad \times \left. \left. \left(-\frac{\cos \varphi + \bar{\mu}_2 \sin \varphi}{a + \bar{\mu}_1 b} U_1 + \frac{\cos \varphi + \bar{\mu}_1 \sin \varphi}{a + \bar{\mu}_2 b} U_2 \right) \right] \right\}, \\ \tau_{xy} &= \tau_{xy0} + \tau_{xy}^* = p \left\{ \sin \varphi \cos \varphi + \operatorname{Re} \left[\frac{a \sin \varphi - ib \cos \varphi}{\bar{\mu}_1 - \bar{\mu}_2} \right. \right. \\ &\quad \times \left. \left. \left(-\bar{\mu}_1 \frac{\cos \varphi + \bar{\mu}_2 \sin \varphi}{a + \bar{\mu}_1 b} U_1 + \bar{\mu}_2 \frac{\cos \varphi + \bar{\mu}_1 \sin \varphi}{a + \bar{\mu}_2 b} U_2 \right) \right] \right\}.\end{aligned}\quad (34)$$

It has to be noticed that the roots $\sqrt{\bar{z}_k^2 - a^2 - \bar{\mu}_k^2 b^2}$ in the mapping function Eq. (30) can be positive as well as negative. In case that the z -plane can be regarded as being cut open between the two focus of the ellipse (Riemannsch's plane) (cp. Fig. 2), the relation is reversible inverse definite. Since the circumferential loading along the elliptic opening is significant for the failure (crack development) of notched components, we will give the expression for the tangential stress, σ_t , explicitly. After the transformation into a natural coordinate system (tangential and normal to the contour of the ellipse), i.e.

$$\begin{aligned}\sigma_t &= \sigma_x \cos^2(t, x) + \sigma_y \cos^2(t, y) + 2\tau_{xy} \cos(t, x) \cos(t, y), \\ \sigma_n &= \sigma_x \cos^2(n, x) + \sigma_y \cos^2(n, y) + 2\tau_{xy} \cos(n, x) \cos(n, y), \\ \tau_{tn} &= \sigma_x \cos(n, x) \cos(t, x) + \sigma_y \cos(n, y) \cos(t, y) \\ &\quad + 2\tau_{xy} [\cos(n, x) \cos(t, y) + \cos(n, y) \cos(t, x)]\end{aligned}\quad (35)$$

we obtain with Eq. (25) and $\cos(t, x) = -\cos(n, y)$, $\cos(t, y) = -\cos(n, x)$, for the unloaded elliptic opening contour $\sigma_n = \tau_{tn} = 0$ based on Eq. (34) in combination with Eq. (35)

$$\begin{aligned}\sigma_t(\Theta) &= p \left\{ 1 + \sin(2\varphi) + \operatorname{Re} \left\{ \frac{a \sin \varphi - ib \cos \varphi}{\bar{\mu}_1 - \bar{\mu}_2} \left[\frac{a^2 \sin^2 \Theta}{a^2 \sin^2 \Theta + b^2 \cos^2 \Theta} \right. \right. \right. \\ &\quad \times \left. \left. \left(-\bar{\mu}_1^2 \frac{\cos \varphi + \bar{\mu}_2 \sin \varphi}{a + \bar{\mu}_1 b} U_1 + \bar{\mu}_2^2 \frac{\cos \varphi + \bar{\mu}_1 \sin \varphi}{a + \bar{\mu}_2 b} U_2 \right) \right. \right. \\ &\quad + \frac{b^2 \cos^2 \Theta}{a^2 \sin^2 \Theta + b^2 \cos^2 \Theta} \left(-\frac{\cos \varphi + \bar{\mu}_2 \sin \varphi}{a + \bar{\mu}_1 b} U_1 + \frac{\cos \varphi + \bar{\mu}_1 \sin \varphi}{a + \bar{\mu}_2 b} U_2 \right) \\ &\quad + \frac{2ab \sin \Theta \cos \Theta}{a^2 \sin^2 \Theta + b^2 \cos^2 \Theta} \left(-\bar{\mu}_1 \frac{\cos \varphi + \bar{\mu}_2 \sin \varphi}{a + \bar{\mu}_1 b} U_1 + \bar{\mu}_2 \frac{\cos \varphi + \bar{\mu}_1 \sin \varphi}{a + \bar{\mu}_2 b} U_2 \right) \left. \right\} \Bigg| \Bigg|, \quad (36)\end{aligned}$$

where

$$U_k = 1 - \frac{\bar{z}_k}{\sqrt{\bar{z}_k^2 - a^2 - \bar{\mu}_k^2 b^2}},$$

and $\bar{z}_k = \bar{z}_k(\Theta) = a \cos \Theta + \bar{\mu}_k b \sin \Theta$ ($k=1,2$).

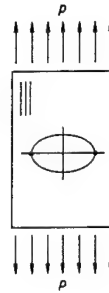


Figure 4: Orthotropic plate with elliptical opening under loading in fiber direction

In the special case that the fiber direction and the direction of the loading coincide ($\varphi = 90^\circ, \psi = 90^\circ$; cp. Fig. 4) we obtain for the points at the diametrical ends parallel to the tensile forces ($\Theta = 0$ resp. π) the simplified expression

$$\sigma_t = p \left(1 + \frac{a}{b} \frac{\beta_1 + \beta_2}{\beta_1 \beta_2} \right). \quad (37)$$

This expression yields for a circular opening ($a = b$) and an isotropic material ($\beta_1 = \beta_2 = 1$) in the well known stress concentration factor

$$\alpha_0 = \frac{\sigma}{p} = 3.0. \quad (38)$$

4. EVALUATION OF THE STRAIN - AND DISPLACEMENT FIELD IN NOTCHED ANISOTROPIC PLATES UNDER TENSION

In the dimensioning of polymeric fiber reinforced composites it is often more efficient to use a strain criteria instead of a stress criteria for the failure hypothesis. For this purpose we will give the strain and displacement values assigned for the calculated stress field.

Based on the reference coordinate system (x, y -system), Hooke's Law (1) in its orthotropic form has to be transformed accordingly which leads by the use of the transformation matrix (cp. Fig. 1)

$$[T] = \begin{bmatrix} \cos^2 \psi & \sin^2 \psi & \sin \psi \cos \psi \\ \sin^2 \psi & \cos^2 \psi & -\sin \psi \cos \psi \\ -2 \sin \psi \cos \psi & \sin \psi \cos \psi & \cos^2 \psi - \sin^2 \psi \end{bmatrix} \quad (39)$$

due to

$$\begin{bmatrix} \epsilon_x \\ \epsilon_y \\ \gamma_{xy}/2 \end{bmatrix} = [T] \begin{bmatrix} \epsilon_1 \\ \epsilon_2 \\ \gamma_{12}/2 \end{bmatrix}, \quad \begin{bmatrix} \sigma_x \\ \sigma_y \\ \tau_{xy}/2 \end{bmatrix} = [T] \begin{bmatrix} \sigma_1 \\ \sigma_2 \\ \tau_{12}/2 \end{bmatrix} \quad (40)$$

and in combination with the compliance tensor

$$\begin{bmatrix} \tilde{S}_{11} & \tilde{S}_{12} & \tilde{S}_{16} \\ \tilde{S}_{12} & \tilde{S}_{22} & \tilde{S}_{26} \\ \tilde{S}_{16} & \tilde{S}_{26} & \tilde{S}_{66} \end{bmatrix} = [T] \begin{bmatrix} S_{11} & S_{12} & 0 \\ S_{12} & S_{22} & 0 \\ 0 & 0 & S_{66} \end{bmatrix} [T]^{-1} \quad (41)$$

to the extended form

$$\begin{aligned} \epsilon_x &= \tilde{S}_{11} \sigma_x + \tilde{S}_{12} \sigma_y + \tilde{S}_{16} \tau_{xy}, \\ \epsilon_y &= \tilde{S}_{12} \sigma_x + \tilde{S}_{22} \sigma_y + \tilde{S}_{26} \tau_{xy}, \\ \gamma_{xy} &= \tilde{S}_{16} \sigma_x + \tilde{S}_{26} \sigma_y + \tilde{S}_{66} \tau_{xy}. \end{aligned} \quad (42)$$

(We relinquish of the presentation of the full transformation formula.)

The integration of the strains yields according to Eq. (34) with Φ_k and Eq. (31) in the displacements (except for the unimportant rigid body movement).

$$u(\bar{z}_1, \bar{z}_2) = \int \epsilon_x dx = 2 \operatorname{Re} \left[(\tilde{S}_{11} \bar{\mu}_1^2 + \tilde{S}_{12} - \tilde{S}_{16} \bar{\mu}_1) \Phi_1(\bar{z}_1) + (\tilde{S}_{11} \bar{\mu}_2^2 \bar{\mu}_1 - \tilde{S}_{16} \bar{\mu}_2) \Phi_2(\bar{z}_1) \right],$$

respectively

$$v(\bar{z}_1, \bar{z}_2) = \int \epsilon_y dy = 2 \operatorname{Re} \left[\left(\tilde{S}_{12} \bar{\mu}_1 + \frac{\tilde{S}_{22}}{\bar{\mu}_1} - \tilde{S}_{26} \right) \Phi_1(\bar{z}_1) + \left(\tilde{S}_{12} \bar{\mu}_2 + \frac{\tilde{S}_{22}}{\bar{\mu}_2} - \tilde{S}_{26} \right) \Phi_2(\bar{z}_1) \right]. \quad (43)$$

To be able to evaluate the deformation of the elliptical opening contour in case of an orthotropic material, and especially under off-axis loading, and therefore to be capable for a comparison with isotropic materials, the displacement components Eq. (42) can be expressed through Eq. (25) in the normal and tangential direction:

$$\begin{aligned} u_n(\Theta) &= \frac{1}{\sqrt{a^2 \sin^2 \Theta + b^2 \cos^2 \Theta}} [u(\bar{z}_1, \bar{z}_2) b \cos \Theta + v(\bar{z}_1, \bar{z}_2) a \sin \Theta], \\ u_t(\Theta) &= \frac{1}{\sqrt{a^2 \sin^2 \Theta + b^2 \cos^2 \Theta}} [-u(\bar{z}_1, \bar{z}_2) a \sin \Theta + v(\bar{z}_1, \bar{z}_2) b \cos \Theta], \end{aligned} \quad (44)$$

$$\text{with } \bar{z}_k = \bar{z}_k(\Theta) = a \cos \Theta + \bar{\mu}_k b \sin \Theta \quad (k=1,2).$$

5. DETERMINATION OF THE STRESS FIELD IN NOTCHED GLASFIBER REINFORCED EPOXY PLATES

We can calculate with the established equations the stress and displacement distributions in the complete field for arbitrary direction of the applied force, any material properties (compliances), S_{ij} , and for any diametrical ratios of the semiaxis, a/b , of the elliptical opening as well as the fiber orientation, indicated by the angle, φ .

For the evaluation of the stress increase a stress intensity factor, as defined for isotropic material, will be applied for the anisotropic material as well. The stress concentration factor, α_0 , characterizes the ratio between the maximum stress at the notch contour and the nominal stress of the cross section without a notch or crack. The stress concentration factor is independent of the magnitude of the applied load and therefore in particular qualified for the dimensioning of structural components.

Figure 5 and Fig. 6 show polar diagrams for the stress intensity factor in notched anisotropic plates under tension. The diagrams for elliptical openings are valid for plates with a large width in comparison to the existing notch radius. The notched induced stress distributions were calculated for the technical relevant GFR-materials with the given elastic constants. In the polar diagrams in Fig. 5 and Fig. 6 the stress intensity factor is shown normal to the notch contour which is also the zero position of the tangential stress, in relation to the parameter Θ of the ellipse: for tension outwards, for compression inwards. The load direction is indicated by the arrow (F) resp. by the angle, φ . The angle between the main orthotropic axis for the larger elastic modulus and the abscissa of the global coordinate system is represented by the letter ψ . For comparison; the fine line stands for the equivalent known stress distribution in isotropic materials.

The calculation indicates for a load acting parallel to the fiber direction (Fig. 5a) and a given elliptical opening with the dimensions e.g. $a = 20.0 \text{ mm}$ and $b = 12.5 \text{ mm}$ a stress intensity factor in the notch ground which is 1.73 times the value for isotropic materials. It has to be noticed that the maximum stress concentration factor is in addition to the notch geometric and load case affected by the elastic constants as well. Under such extreme conditions of E_1/E_2 , as in carbon fiber reinforced laminates (CFR), much larger stress concentration factors can exist.

The calculation shows for load acting perpendicular to the fiber direction (Fig. 5b) stress intensity factors in the notch ground of the same order as for isotropic materials. On the other hand the compressive stresses are near the notch tip larger than by isotropic materials so that for thin plates attention has to be paid to the danger of instability due to buckling. In multilayer laminates additional danger arises through delamination. In materials with a large ratio of E_1/E_2 the increase in compressive stress can become even larger than the increase in tensile stress.

Off-axis loading results in notched induced stress distributions as shown in Fig. 6. Conspicuous is in this connection that the stress maximum is not at the notch tip as in case of a loading in direction to the main axis of orthotropy but outside to the notch ground. If the load direction, φ , next to the fiber direction, ψ , is tilted against the main elliptic diameter as well, stress distributions occurs as depicted in Fig. 6b e.g. $\psi = 30^\circ$ and $\varphi = 40^\circ$.

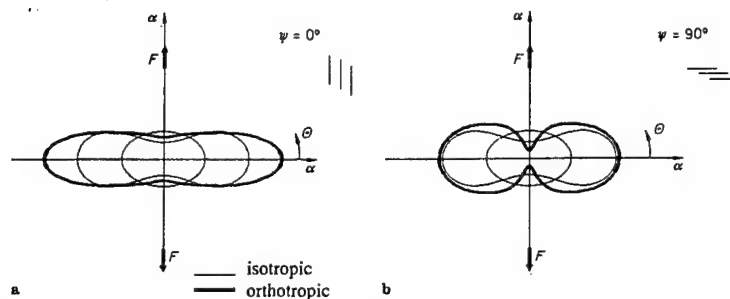


Figure 5a and b: Polar diagram of the stress concentration factor, α_G , under loading in the principal direction of the coordinate systems of the orthropy [6]. Characteristic values of elasticity: $E_1 = 39.5$ GPa, $G_1 = 3.54$ GPa; $E_2 = 12.16$ GPa, $\nu_{12} = 0.21$. Maximum stress intensity factor: a $\alpha_G = 7.28$ at $\Theta = 0^\circ$; b $\alpha_G = 4.48$ at $\Theta = 0^\circ$

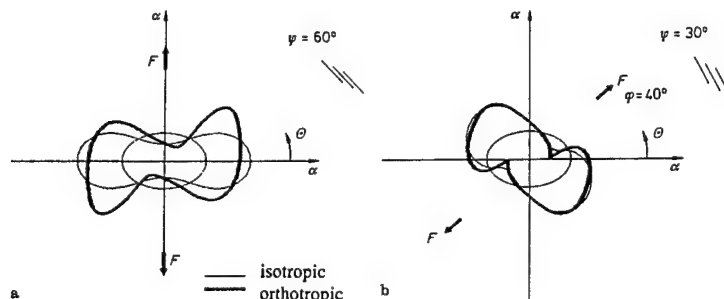


Figure 6a and b: Polar diagram of the stress concentration factor, α_G , under off-axis loading [6]. Same characteristic values of elasticity as in figure 5. Max. stress intensity factor: a $\alpha_G = 4.44$ at $\Theta = 22^\circ$; b $\alpha_G = 3.11$ at $\Theta = 142^\circ$

6. SUMMARY AND CONCLUSION

The investigation of notch induced stress problems is of major technical importance, as in the production of structural components openings e.g. drill-holes can rarely be avoided. In particular for anisotropic materials there are only a few informations available in literature about stress concentration behavior and therefore no guidelines for their dimensioning. In this paper the stress and strain fields near an elliptic opening in an orthotropic plate under tensional loading and arbitrary fiber orientation are calculated (for this purpose) using the complex stress functions. Since the tangential stress distribution on the contour of the opening is of major importance for the evaluation of a component failure, its knowledge is extremely important.

The results indicate that the stress concentration factor, α_G , in direction of the larger elastic modulus can become several times of the value for isotropic materials. Under extreme conditions E_1/E_2 , e.g. CFR-laminates, the increase in compressive stress at the place on the opening tip can become in total larger than the increase in tensional stress, whereby the probability of delamination and instability increases.

Attention has to be paid to the fact that in the case of off-axis loading the maximum increase in stress occurs outside the notch contour and neither in the direction of the applied load nor in the direction of either principal axis of orthotropy.

Anisotropic materials show next to the direction orientated elastic moduli a directional dependence in strength as well. Therefore, the location of the maximum stress increase in general does not determine the failure the composite structure.

7. REFERENCES

1. Lekhnitski, S. G.: *Theory of elasticity of an anisotropic elastic body*. San Francisco: Holden-Day 1963
2. Goursat, E.: *Sur l'equation $\Delta\Delta u = 0$* . Bull. Soc. Math. France 26 (1898) 236-237
3. Muskhelishvili, N. I.: *Einige Grundaufgaben zur mathematischen Elastizitätstheorie* München: C. Hanser 1971
4. Kantorowitsch, L. W.; Krylov, W. I.: *Näherungsmethoden der höheren Analysis*. Berlin: VEB Deutscher Verlag der Wissenschaften 1956
5. Lekhnitski, S. G.: *Plane static problem of the theory of elasticity of an anisotropic body*. J. Appl. Math. Mech. 1 (1937) 77-90
6. Herrmann, A. S.: *Experimentelle und theoretische Untersuchungen von Kerbspannungsproblemen anisotrop glasfaserverstärkter Epoxidharzscheiben*. Dissertation TU Clausthal 1989

N92-23840
84752

STRENGTH AND DEFORMATION BEHAVIOUR OF KEVLAR AND CARBON COMPOSITE SANDWICH STRUCTURES FOR SPACE APPLICATIONS

H. Bansemir, O. Haider

Messerschmitt-Bölkow-Blohm GmbH
P.O.Box 80 11 40
D-8000 Munich 80, Germany

ABSTRACT

For space applications composite structures are of main importance because of their low weight, their high stiffness and strength and their thermal deformation stability. For many years MBB has developed solar arrays for satellites such as Exosat, DFS Kopernikus, Intelsat V and VI, HS393, SCS1, and DFH3.

For the solar panels a sandwich structure with Kevlar fabrics or filament wound high modulus carbon composite face sheets with $0^\circ/90^\circ$ fiber orientation was chosen. For the core a light weight perforated aluminum honeycomb is usually used. The panels are mainly loaded by bending moments with sandwich wrinkling as the critical failure mode. As the face sheet thickness usually is very small and the honeycomb core is of low density, the wrinkling strength was studied with the help of four-point bending specimens.

In several test series with a high number of test samples the influence of the Young's moduli, the thicknesses of the face sheets and the core on the wrinkling stress was examined. The results showed, that the prefactor of the wrinkling formula has to be remarkably reduced in comparison to the theoretical value of 0.816.

Keywords: composite, sandwich, solar arrays, antennas, thermal stability

1. COMPOSITE SANDWICH STRUCTURES FOR SOLAR ARRAYS

Several solar arrays were developed by MBB in a period of twenty years (Figure A), such as OTS (Orbit Test Satellite), Intelsat V, Exosat, Intelsat VI, DFS Kopernikus (Deutscher Fernmeldesatellit), HS393, SCS1 (Super Bird), and DFH3 (Dong Fang Hong 3). The spectrum of designed solar arrays covers the range from research satellites such as Exosat (Figure B) to communication satellites such as Intelsat V and VI. Intelsat V is a typical three axes stabilized communication satellite transmitting from point to point with a capacity of 12000 phone calls (Figure C). The necessary power of such satellites is in the range of 500 to 3000 W [1]. Typical requirements on solar arrays are:

High stiffness in the folded position because of the vibrations during launch and in the deployed position because of the position control of the satellite in orbit.

High strength at the hold-down points because of vibrations and at the hinge connections of two panels because of the lock-down shock.

For these requirements and the aim of low structural weight and large areas of usable surfaces, sandwich structures with filament wound face sheets are manufactured. The skins of the sandwich are composites made of high modulus carbon fibers with an epoxy resin; the fiber orientation is $0^\circ/90^\circ$.

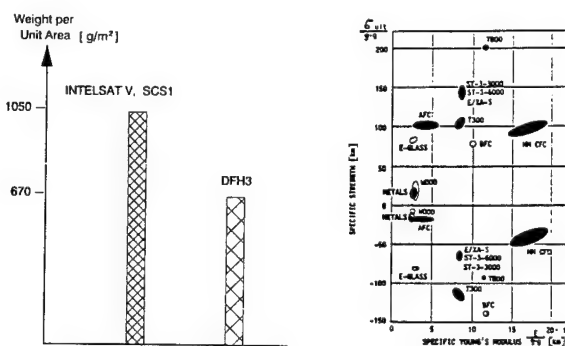


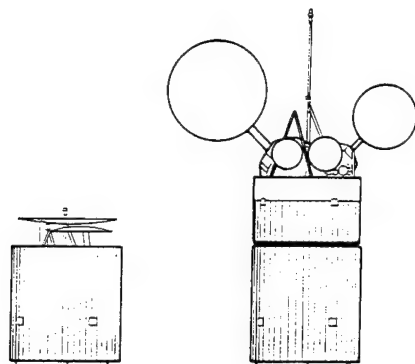
Figure 1a: Weight per Unit Area of different Solar Arrays

Figure 1b: Specific Strength versus Specific Young's Modulus of Various Materials (UD-Composites with 60% Fiber Volume Content)

In Figure 1a the typical mass per unit area of SCS1 and Intelsat V can be seen in relation to the sandwich structure of DFH3. Figure 1b shows the specific strength and stiffness of different fiber composite materials. In the present, extreme light-weight sandwich structures with an open net as face sheet are being developed by MBB in order to meet the requirements for the Chinese communication satellite DFH3.

Besides homogeneous sandwich areas, the panels have reinforced zones with edge profiles and strengthened corner parts, carrying the lock-down shock and eventual transfer orbit loads. A test sample of a corner part after wrinkling failure can be seen in Figure D. The inserts at the hold-down points are highly loaded by the launch vibrations. Composite doublers are used to increase the ultimate wrinkling stresses in critical areas. For the core a light perforated aluminum honeycomb with a specific weight of 16 kg/m^3 was used.

A sandwich structure with Kevlar 0°/90° fabric face sheets was used in the design of the cylindrical telescoping solar array Intelsat VI. The solar array development has combined the HS-376 deployable cylindrical technology (Hughes) with the light-weight Intelsat V and ULP (Ultra Light Panel) solar cell assembly and installation (MBB).



DIAMETER:	DIAMETER:
3.6 m (12 ft)	3.6 m (12 ft)
HEIGHT STOWED:	HEIGHT DEPLOYED:
5.3 m (17.5 ft)	11.7 m (39 ft)
	WEIGHT:
	1781 kg (3918 lb)

Figure 2: Intelsat VI, Undeployed and Deployed Configuration

The solar array consists of two cylindrical solar panels. During transfer orbit, the deployable solar panel, stowed over the fixed solar panel, provides power for the satellite. In synchronous orbit, the deployable solar panel telescopes to its normal (fully deployed) position. So power is provided by both solar arrays. The design of each panel section is a simple curved sandwich shell. Again, the basic core has a density of 16 kg/m^3 and a height of 13 mm.

The solar panel was designed to suffer no damage when exposed to environmental conditions. All materials should withstand temperature extremes of -168°C to $+177^\circ\text{C}$ while under no load condition. This condition proved to be severe especially regarding the stresses due to constraints.

In the test series with more than 150 specimens the Young's moduli of the Kevlar sandwich configurations were studied with the help of compression, shear and bending specimens in order to ensure the required eigenfrequencies. Several influences such as Young's moduli and thickness of the face sheets on the wrinkling strength were examined. The fractured samples can be seen in Figure E and F.

In more recent developments efforts were made in order to diminish the structural weight of the solar arrays by reducing the face skin weight. Therefore 'open net' filament wound face sheets were designed for quasiisotropic and orthotropic flat and cylindrical sandwich panels (Figure E). Open net structures were tested with the solar array Mark IV by sinus vibration and acoustic noise. The basic design proved to have enough strength and stiffness to meet the launch loads and frequency requirements.

2. SANDWICH DESIGNS FOR ANTENNA STRUCTURES

Several space antenna configurations were evaluated by MBB in the past ten years. An antenna system with polarization sensitive reflectors was studied in the near past [9]. The described reflector consists of two sandwich shells with a diameter of about 1100 mm. They are located one behind the other in order to get a compact design. The face sheets were made of quasiisotropic Kevlar 0°/90° fabrics. A Nomex core with a thickness of 7.4 mm was used. Several influences were studied for these sandwich configurations such as influence of honeycomb Young's modulus and coefficient of thermal expansion on the distortion of the reflector, and influence of humidity on the deflections of Kevlar structures.

The knowledge gained by designing and testing the Kevlar sandwich reflectors was used for the development of the PSR (Polarization Sensitive Reflector) and the substructure of the Chinese DFH3 satellite.

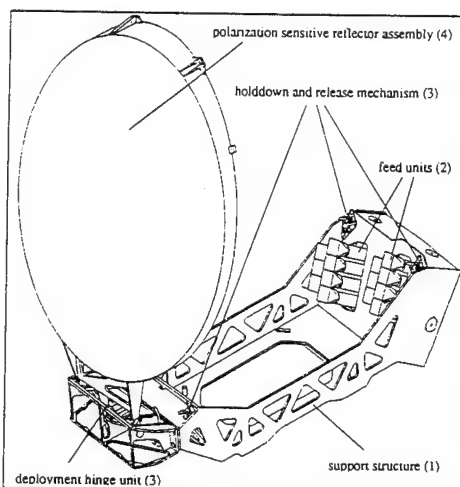


Figure 3: Polarization Sensitive Reflector System and Support Structure of DFH3

The deployable DFH3 antenna system exists of two sandwich reflector shells mounted behind each other and a stiff sandwich support substructure. The electrically transparent reflector shell consists of Kevlar quasiisotropic face skins and a Nomex honeycomb core with a height of 13 mm. The shells are connected to a carbon ring with four hold down elements. The laminate of the ring was tuned in such way, that its coefficient of thermal expansion (CTE) meets the CTE of the quasiisotropic face sheets including the effect of CTE of the core.

The support structure consists of double cantilever quasiisotropic carbon composite sandwich plates. The bottom sandwich plate with four brackets form the interface between spacecraft and antenna. Another four brackets, located at the upper area of the structure form the support of the antenna reflectors in the stowed configuration.

All sandwich plates consist of a quasiisotropic high modulus 0°/+60° face sheet lay up and a low density aluminum core. The plates are stiffened by unidirectional high modulus Thornel 75S straps in regions where high stiffness is needed to meet the frequency requirements.

The mechanical behaviour of the antenna system was tested and qualified. The main electrical performance specifications have been verified by test with the integrated antenna module in the 'Compact Antenna Test Range' (CATR) of MBB.

3. LOCAL STABILITY OF SANDWICH STRUCTURES

Local stability of sandwich structures having isotropic and orthotropic cores has been analyzed by many authors [3],[5],[6], and [7]. At MBB for space structures usually the approach of the Manual for Structural Stability Analysis [3] is used. The panels and antenna shells are generally loaded by compression, tension and bending moments. The possible failure modes include wrinkling and intercellular buckling. As the thicknesses of the composite face sheets are of low magnitude intercellular buckling often occurs. This buckling mode does not mean a failure but the stresses in the supported areas increase. The higher stresses may cause an earlier wrinkling failure. For the wrinkling analysis a beam on continuous elastic foundation is calculated. Antimetrical or symmetrical buckling modes may occur. The symmetrical modes lead to lower buckling stresses, when orthotropic honeycomb cores are used. In this case the theoretical buckling stress for a sandwich stripe can be calculated by the formula:

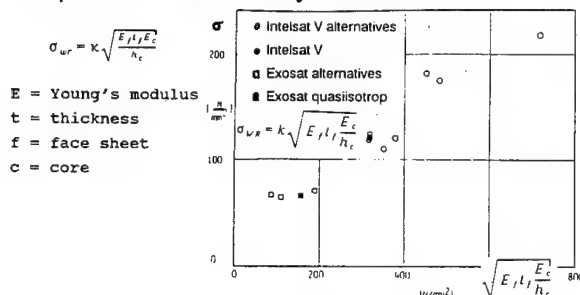


Figure 4: Test Results of Compression Loaded Sandwich Stripes

The relation between measured strength and theoretical parameters can be established for different test specimens. For tests with samples loaded in compression a relation is given in Figure 4.

For sandwich plates with thin composite face skins the formula should be modified. The local bending stiffness of the face sheets should be included. With the local bending stiffness

$$B = \frac{E_f t_f^3}{(1 - \nu_{xy} \nu_{yx}) 12}$$

we get:

$$\sigma_{vr} = k \frac{\sqrt{12}}{t_f} \sqrt{\frac{E_c B}{h_c}}$$

The theoretical prefactor of $\kappa = 0.816$ has to be reduced according to tests remarkably to $\kappa = 0.33$ to 0.41 . This value is in accordance with [3]. At MBB several tests were performed with compressive and bending specimens. The bending tests give higher stresses with lower scatter values than compressive tests. When the skins are subjected to biaxial compression, it is recommended that one uses according [3] the interaction formula

$$R_x^3 + R_y^3 = 1$$

$$R_i = \frac{[\text{Applied Compressive Loading in Subscript Direction}]}{[\text{Critical Compressive Loading (when acting alone) in Subscript Direction}]}$$

and the y-direction corresponds to the direction of maximum compression. For cases involving shearing stresses which are coplanar with the facings, it is recommended to calculate the principal stresses.

If the face sheets are isotropic the calculated stresses can be used in the above interaction formula. For $0^\circ/90^\circ$ layers the shear modulus is low and shear forces are not transferred by the sandwich panels.

For a general wrinkling theory, the equations given in [5], should be derived for anisotropic face sheets.

The influence of temperature was studied while designing the Kevlar sandwich of Intelsat VI using the resin system M10 and the adhesive Redux 312 UL.

4. SANDWICH BEHAVIOUR UNDER DYNAMIC LOAD

The dimensioning load cases for solar arrays are vibrations and acoustic noise during launch. The maximum loads usually occur at a frequency between 50 and 200 Hz. In order to investigate the influence of frequency on the wrinkling stress, double cantilever beams were loaded dynamically. Four samples of the Intelsat V and SCS1 type of face sheet and a core with 16 kg/m^3 were manufactured and tested (Figure 5 and 6). For comparison the light weight 'open net' face skin was used for another two double test beams.

The specimens were equipped with strain gauges and accelerometers and were fixed to a shaker (Figure 5 to 8). The strain gauges were applied at the area of maximum stresses near the doublers of the central reinforcements. The acceleration was performed at a frequency from 1 to 200 Hz. In Figure 5 to 8 the resonance frequencies of the two cantilever beams are shown together with the input accelerations. On the upper vertical axis the corresponding strains are shown. On the lower axis the critical damping calculated from the amplification factor is shown. For the SCS1 type sandwich the static mean value of $\epsilon_{wr} = 0.88 \text{ [mm/m]}$ was tested. Test specimens A and B had a maximum strain of about $\epsilon_{wr, dyn} = 0.7 \text{ [mm/m]}$ at a frequency of 108 Hz. Test specimen C had a maximum strain of $\epsilon_{wr, dyn} = 0.99 \text{ [mm/m]}$ at a frequency of 44.5 Hz. Test specimen C was equipped with some additional masses in order to reduce the resonance eigenfrequencies. The three SCS1 type specimens had a maximum damping of about 2.5 %.

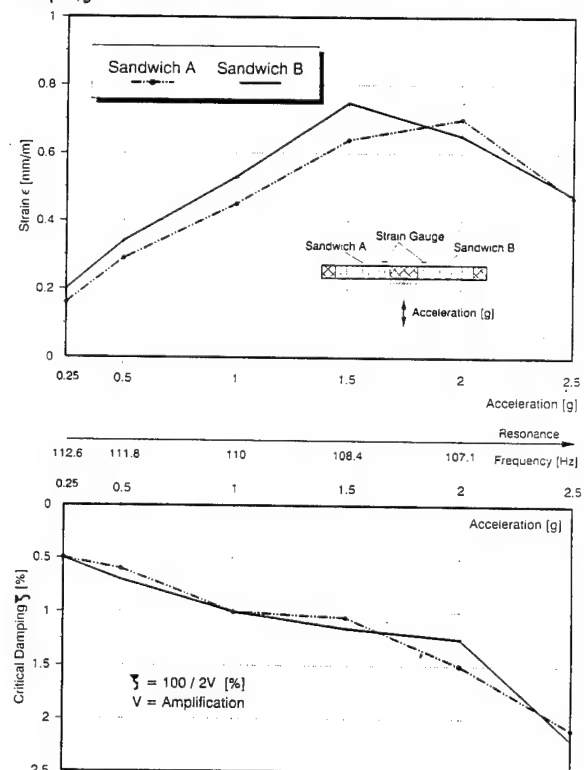


Figure 5: SCS1 Solar Array Sandwich Behaviour under Dynamic Load (Sample A, B)

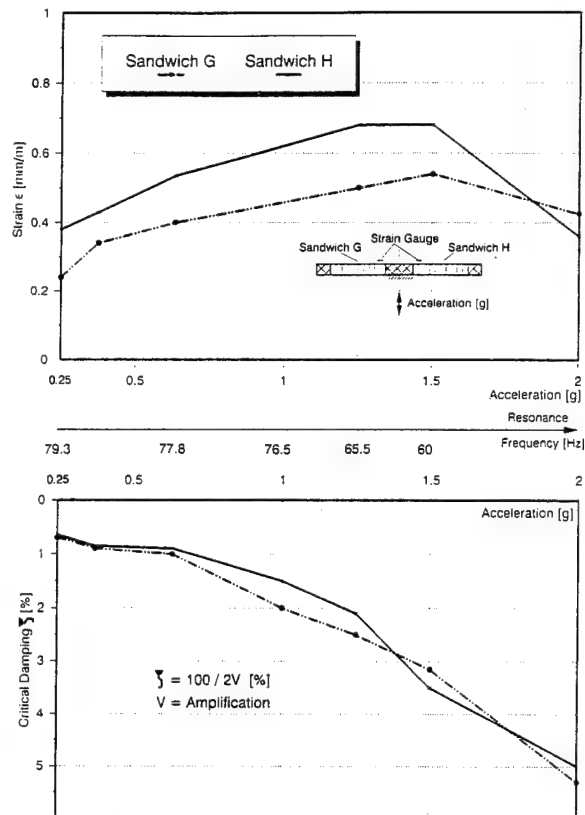
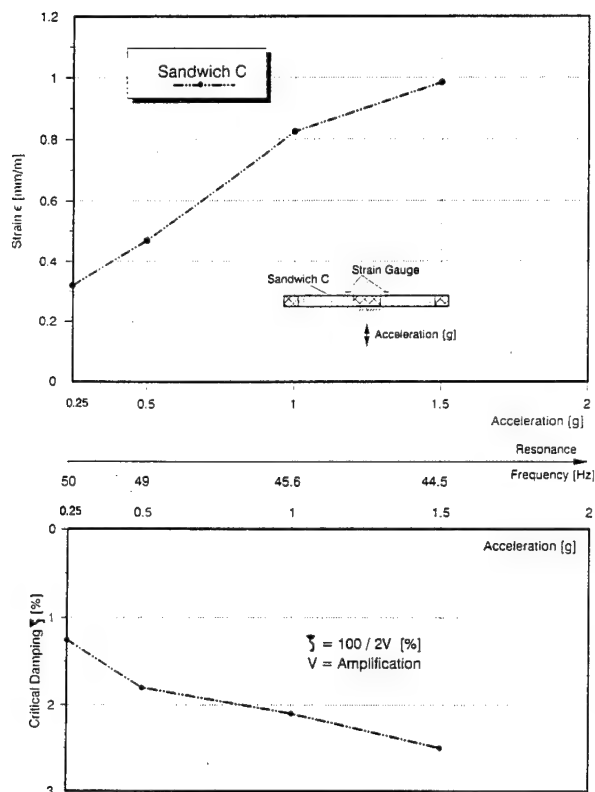


Figure 6: SCS1 Solar Array Sandwich Behaviour under Dynamic Load (Sample C)

Figure 8: DFH3 Solar Array Net Sandwich Behaviour under Dynamic Load (Sample G, H)

5. SUMMARY AND IMPROVEMENTS OF SANDWICH STRUCTURES

The objective of the paper was to show improvements gained in the last twenty years concerning the weight of sandwich solar array structures. The 'open net' structure is a reliable sandwich design which is used for the satellite DFH3.

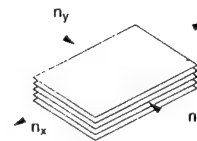
The analytical tools allow the design of highly stable antenna designs. Effects, such as thermal distortions due to core deformations, and deflections due to humidity, are studied with the help of analytical models and test samples. Sandwich structural improvements will be gained in the future due to the available analytical optimization procedures on 'Panel-' and 'System-' level (Figure 9).

Optimization of Composite Structures

Optimization of Composites on "Panel"-Level:

Variation of Layer-Thicknesses and Fiber-Angles in one Element.

Compliance of Strength-, Stiffness- and other Restrictions (e.g. Thermal Conductivity)



Optimization of Structures on System-Level:

Variation of Layer-Thicknesses and Fiber-Angles in every Element of the FE-Model

Compliance of Global Strength- and Stiffness Restrictions (Stress, Strain, Deflection, Eigenfrequencies)

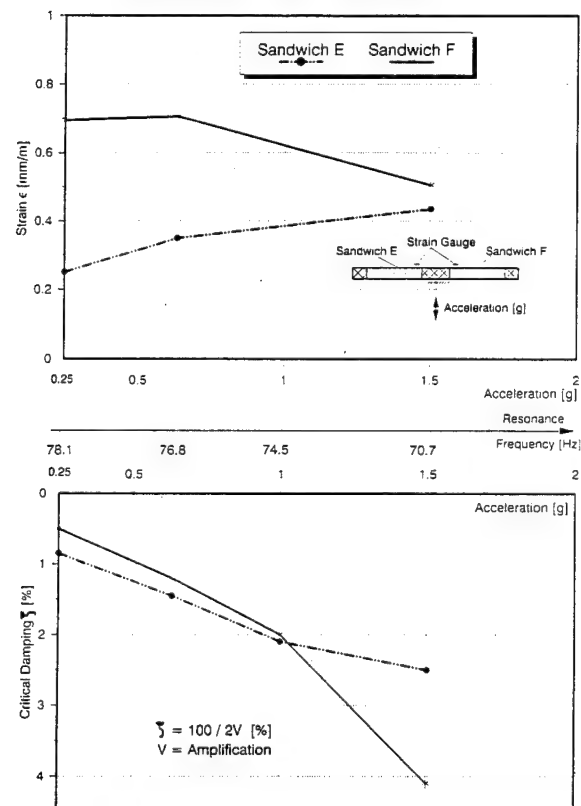
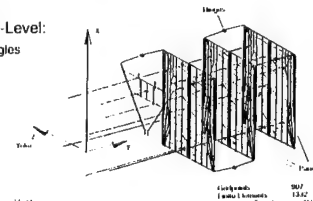


Figure 7: DFH3 Solar Array Net Sandwich Behaviour under Dynamic Load (Sample E, F)

Figure 9: Optimization of Composite Structures

7. REFERENCES

- [1] H. Bansemir W. Buchs Leichtbaustrukturen aus CFK für Satellitengeneratoren verschiedener Grösse Jahrestagung der DGLR, 1981 Vortrag Nr. 81-080
- [2] W. Weiss H. Rapp Kevlar and T300 Fabric Prepregs- Their Material Properties and Their Use in High Loaded Areas of Solar Array 35th IAF Congress, Lausanne, Switzerland October 7-13, 1984
- [3] R. E. Sullins Manual for Structural Analysis of Sandwich Plates and Shells G. W. Smith E. G. Spier NASA-Contractor Report NASA CR 1457 NASA, Washington D.C., December 1969
- [4] H. Brodersen D. Pfefferkorn G. LaRoche Intelsat VI Solar Array Design and Performance MBB Space Division, Munich, Germany 84-0728-CP
- [5] A. S. Benson J. Mayers General Instability and Face Wrinkling of Sandwich Plates- Unified Theory and Applications AIAA Paper Nr. 66-138, N.Y., January 1966
- [6] Goodier Hsu Nonsinusoidal Buckling Modes of Sandwich Plates Stanford University, 1953
- [7] H. Bansemir K. Pfeifer Local Stability of Sandwich Structures with Thin Fiber Reinforced Face Skins for Space Application Engineering with Composites SAMPE European Chapter Third Technology Conference London, 14th - 16th March 1983
- [8] W. Weiss K. Pfeifer R. Leitner Structural Analysis, Manufacturing and Test Evaluation of a Polarization Sensitive Reflector Composites Design for Space Applications ESTEC Workshop, Noordwijk, The Netherlands October, 15-18 MBB-Report No. UD-460/85 0
- [9] O. Haider K. Pfeifer Stress and Deformation Analysis and Tests of Composite Structures for Space Application 38th IAF Congress Brighton, GB October 10-17, 1987 MBB-Report No. UD 519-87 PUB
- [10] J. Bode Einfluss von Steifigkeit und Wärmeausdehnungskoeffizienten auf das Verformungsverhalten von flächigen (ebenen und gekrümmten) Faserverbundstrukturen Diplomarbeit an der Universität der Bundeswehr München, 1986
- [11] P. Scholz Steifigkeit und lokale Stabilität von Sandwichstrukturen Diplomarbeit an der Universität der Bundeswehr München, 1985
- [12] K. Pfeifer J. Bode Stress and Deformation Analysis of Thermally Loaded Light Weight Composite Structure 37th IAF Congress Innsbruck, Austria October 4-11, 1986 MBB-Report No: UD 489-86 0
- [13] H. Rapp New Computer Codes for the Structural Analysis of Composite Helicopter Structures Seventh European Rotorcraft Forum Glasgow, GB September 18-20, 1990 MBB-Report No: UD-0580-90-PUB
- [14] Qi Faren L. Laux M. Reindl N. Nathrath H. G. Schnell Mechanical Solar Array and Antenna for the Chinese DFH-3 Satellite System Global Satellite Communications Symposium Nanjing, China May 28-31, 1991

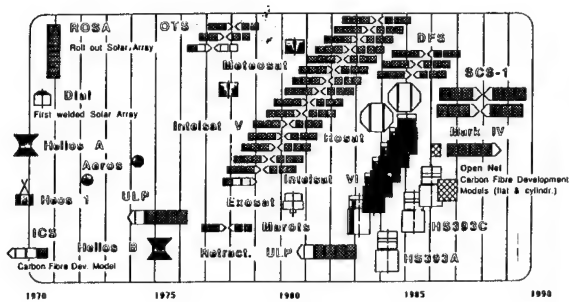


Figure A: MBB Solar Array Experience

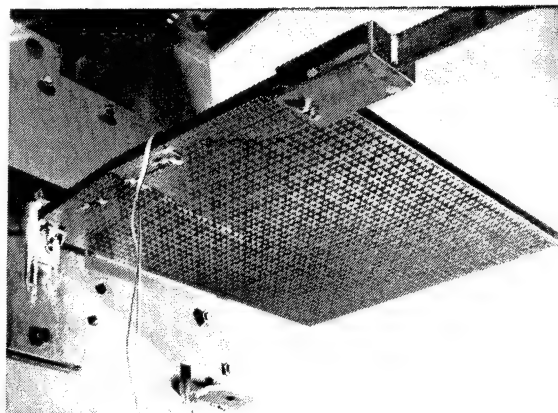


Figure D: Corner Structure Test Sample after Wrinkling Failure

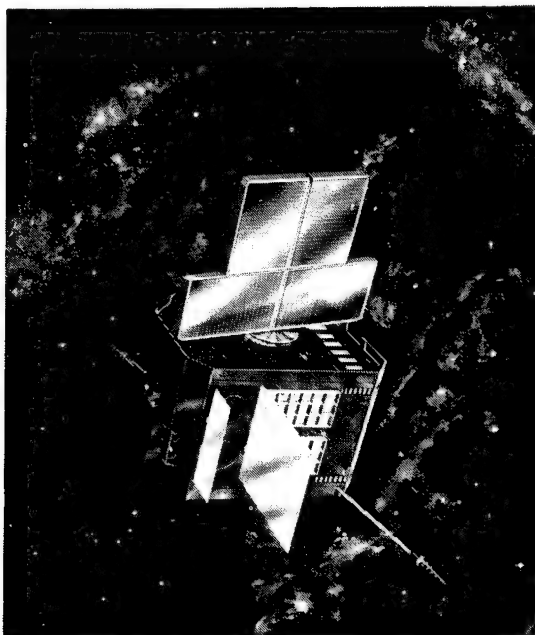


Figure B: Research Satellite EXOSAT with fixed Carbon Epoxy Sandwich Solar Array

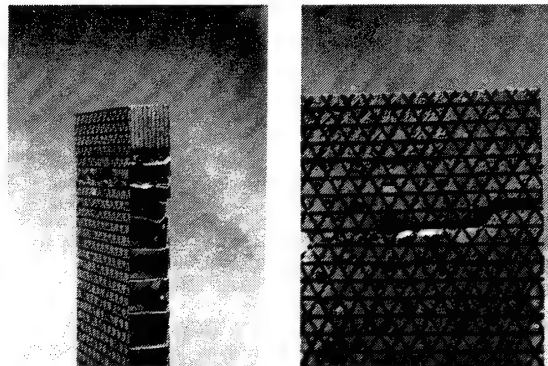


Figure E: Low Weight Quasiisotropic Net Sandwich Compression Specimen

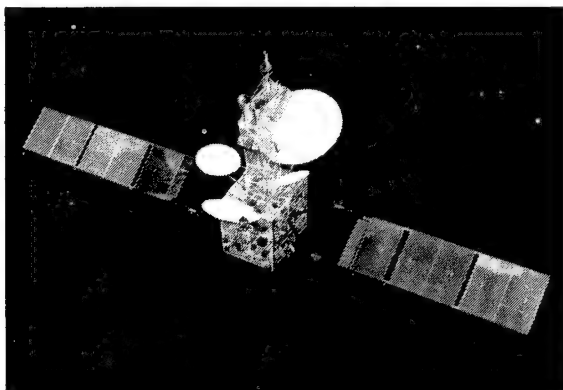


Figure C: Communication Satellite Intelsat V with Deployable Carbon Epoxy Sandwich Array

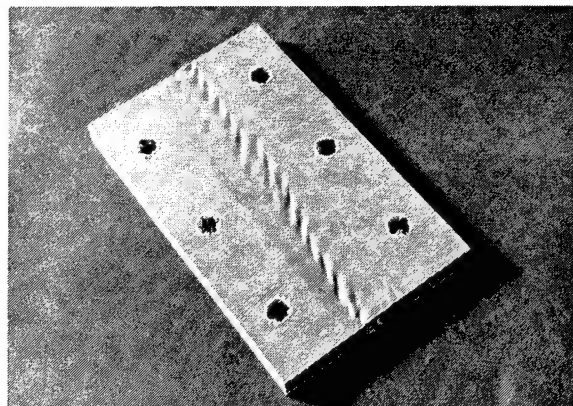


Figure F: Fractured Shear Sample

N92-23841

84733

MODELING OF HONEYCOMB CORE FOR SANDWICH CTE PREDICTION

L. Scolamiero

Alenia Spazio, Italy

ABSTRACT

The overall mechanical behavior of sandwich panels depends on and can be predicted from the mechanical properties of their constituents: fibers, resins, core, adhesives.

As far as the honeycomb core is concerned, its in-plane mechanical properties are difficult to define (it being expandable in nature), and are often neglected.

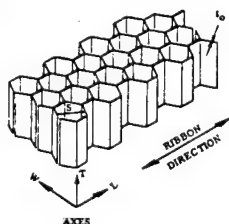
When performing thermoelastic analyses, in a context of high dimensional stability, this is not yet applicable.

Different sandwich CTE prediction methodologies are reviewed and discussed.

A new concept practical method, also based on core measured properties from material supplier data sheets is presented.

Keywords: Sandwich CTE, Honeycomb Core Modeling, Core cell distortions, Dimensional Stability

Nomenclature



a	cell hexagon side length
S	cell size
to	cell foil thickness
α	honeycomb degree of expansion
t	generic thickness - T direction
E	generic Young's modulus
i	relative to the i-th layer
LL	equivalent ribbon length L-direction
LW	equivalent ribbon length W-direction
LT	total ribbon length
EL	equivalent Young's modulus L-direction
EW	equivalent Young's modulus W-direction
ETm	measured compression modulus T-direction
ETc	computed compression modulus T-direction
CTE	coefficient of thermal expansion

1. INTRODUCTION

High dimensional stability is increasingly required for new generation reflector antennas.

Sandwich panel structures (typically CFRP skins bonded to an aluminum core) are widely used for their excellent stiffness to weight ratio and thermal dimensional stability.

For static and dynamic response computation the core in-plane elastic constants can often be neglected. In Fig. 1.1 the relative contribution of sandwich components for what concerns the in-plane panel stiffness, for two typical antenna sandwich configurations, is shown.

For thermo-elastic distortion analysis, on the contrary, the high aluminum core CTE makes a detailed material characterization unavoidable (see Fig. 1.2).

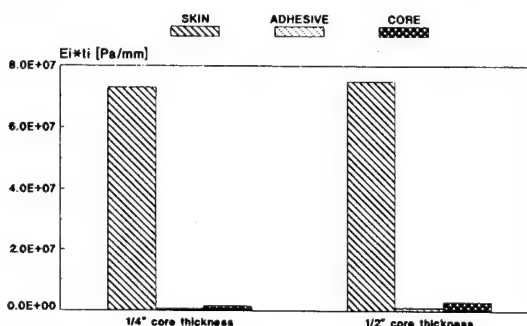


Fig. 1.1 Individual layer contribution to in-plane sandwich stiffness

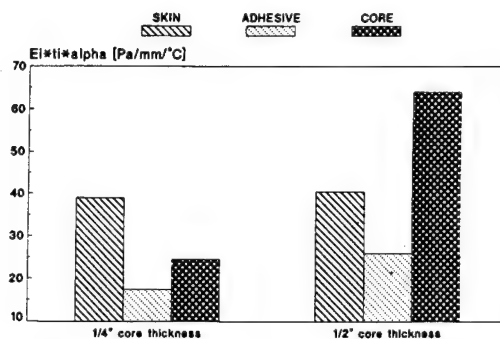


Fig. 1.2 Individual layer contribution to in-plane sandwich CTE

The core experimental characterization, particularly for what concerns the in-plane elastic moduli, is a cumbersome task. In fact, if the core layer is tested separately from the facings, the measured elastic moduli can be wrong (this will be clarified in para. 2.3). If it is tested when bonded to the facings, its very low contribution to overall stiffness will be hardly identified. Core modeling is usually approached by means of a more or less detailed analysis of its mechanical behavior at cell scale level (Refs. 1 to 5). FE models and analytical approaches are commonly adopted.

2. HONEYCOMB MODELING APPROACHES

The basic problem is the identification of the core equivalent homogeneous thermo-elastic properties to be introduced at sandwich level. Limiting the analysis to the bi-dimensional case, which is very appropriate for large plane panels, the in-plane core elastic moduli have to be identified. In the following paragraphs published techniques are reviewed.

2.1. Cell structure FE models

Core structure FE modeling (Refs. 2,3,4) proceeds through the identification and modeling of the minimum representative portion of the elementary core cell (see, from Ref. 3, fig. 2.1.1).

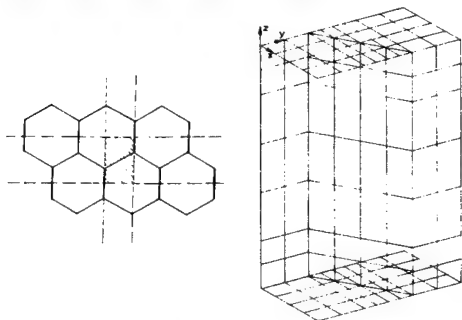


Fig. 2.1.1 Honeycomb core FE modeling (from Ref.3)

Different levels of model complexity may concern the skin to core adhesive schematization and the congruence conditions inside the cell. Also the buckling behavior of the thin cell walls can be accounted for in a more sophisticated analysis approach.

This technique, of course, does not have a great flexibility, in a design phase, for performing a parametric analysis on different core configurations.

FE models allow a better understanding of the core mechanics at cell scale level, and provide reference values for validating simpler prediction models.

2.2. Analytical models

This approach is based on considering the microstructure of the cells as built up by solid aluminum walls, placed according to the cell geometry (Refs. 1 to 4).

By further dividing the cell in sub-elementar zones and solving the elastic problem with adequate congruence conditions, the core stiffness matrices can be derived (see, from Ref. 3, Fig. 2.2.1).

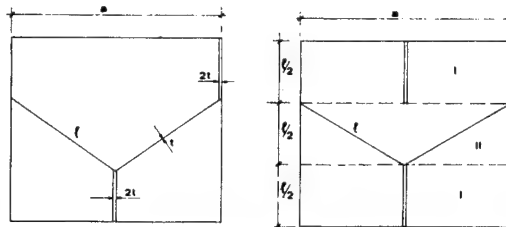


Fig. 2.2.1 Sub-elements identification for analytical method (from Ref.3)

Core, adhesive and skin stiffness matrices are then assembled according to classical lamination theory. The derived expressions are quite simple and easy to implement on a computer code.

2.3. Test simulation models

One option for computing core equivalent homogeneous elastic constants (Ref. 5), has been found by simulating real test a portion of core layer separated from the two facings (see, from Ref. 5, Fig. 2.3.1).

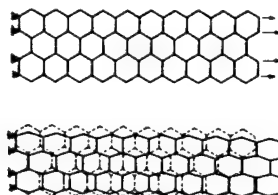


Fig. 2.3.1 Test simulation model (from Ref.5)

Particular care is suggested when modeling or testing the honeycomb in a free condition; in fact, different deformed shapes (and thus elastic properties) can be found with respect to the real case (i.e. bonded facings).

This because the very low bending stiffness of the cell walls is involved instead of their in-plane reaction capabilities.

To better clarify let us extrapolate to the case of cell hexagon vertices to be substituted by frictionless cylindrical hinges (Fig. 2.3.2).

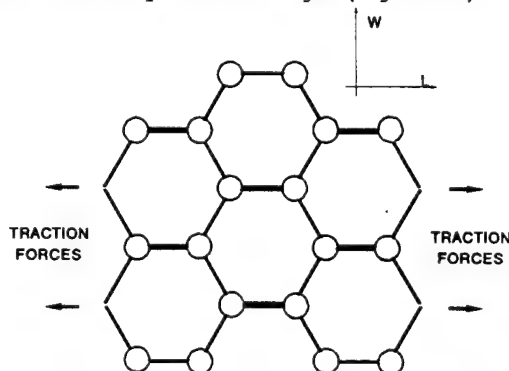


Fig. 2.3.2 Cylindrical hinges scheme

It would result in a completely labile honeycomb structure (zero in-plane stiffness), while its contribution, when bounded to facings, would remain practically unchanged.

3. EFFECTS OF CELL DISTORTIONS

Honeycomb core suppliers provide material data sheets (Ref. 6), which include compressive (stabilized) elastic moduli: ET_m . This value can be used to check the adequacy of considering the core as a solid aluminum structure. From the above assumption, in fact, the equivalent homogeneous compression modulus can be easily computed.

It will simply be determined by the core base material modulus (aluminum) scaled by the core effective mass density (w.r.t. solid aluminum). By plotting the ratio ET_c/ET_m in function of core foil thickness (Fig. 3.1) a clear tendency to overestimate the core stiffness is visible.

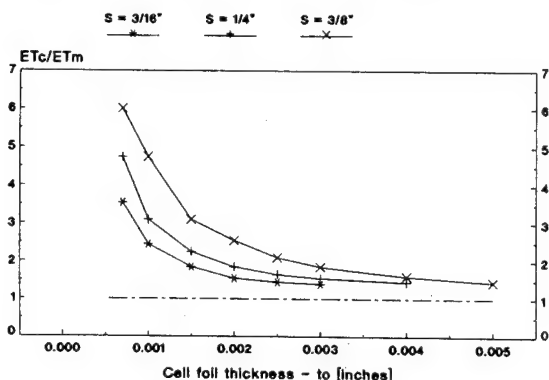


Fig. 3.1 Compression stiffness ratios for 5052 Hexcel Honeycomb Core Aero. Grade

The discrepancy can be explained by hypothesizing a reduced core reaction capability due to the buckled/deformed condition of the thin cell wall. This is clearly shown by the asymptotic tendency of the curves when increasing the wall thickness, and by the effect of the cell size (which stresses the phenomenon).

The primary cell distortion source can be found in the core manufacturing process, namely when expanding the hobe slice to reach the final hexagonal shape.

The above identified discrepancies should be also expected for the in-plane moduli computations (if the same mechanical assumptions are maintained). It must also be stressed that commonly utilized honeycomb cores, for antenna applications, fall in the foil thickness range between 0.0007 and 0.001 inches which, of course, is the most affected by the stiffness reduction effect.

4. PROPOSED CONCEPT

A new practical method for estimating the in-plane core stiffness properties (and thus overall sandwich CTE) is presented.

It is based on the knowledge of the real core compression modulus from the material supplier, plus a simplified mechanical schematization at cell level.

With reference to Fig. 4.1 let us define and compute an equivalent active ribbon length for both the L and W directions.

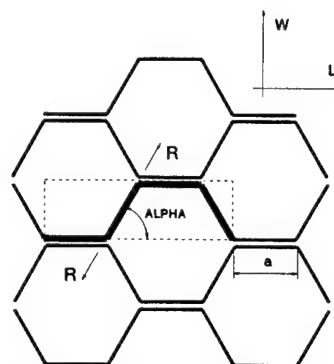


Fig. 4.1 Reference scheme for equivalent ribbon lengths computation

This can be done by simply assuming the cell walls only to react on their physical plane (bending deformations are excluded), and imposing congruence conditions on the boundaries.

The following expressions will result:

$$LL = 2a \cdot (1 + \cos^2 \alpha)$$

$$LW = 2a \cdot \sin^2 \alpha$$

$$LT = LL + LW$$

The total amount of sandwich in-plane stiffness capability is derived by the measured compression modulus (available from material data sheets), and shared between the L/W directions according to the LL/LW ratios, namely:

$$EL = ET_m \cdot LL / LT$$

$$EW = ET_m \cdot LW / LT$$

The core base material CTE is well known, thus the overall sandwich CTE can be computed by applying the weighting formula:

$$CTE_{overall} = \frac{\sum t_i \cdot E_i \cdot CTE_i}{\sum t_i \cdot E_i}$$

The above described method is easily applicable to any degree of core expansion (being it parametric with α), up to the over-expanded ox-core ($\alpha = 90^\circ$, i.e. rectangular cell).

A comparison between computed and measured values is shown in Fig. 4.2 for two different sandwich configurations.

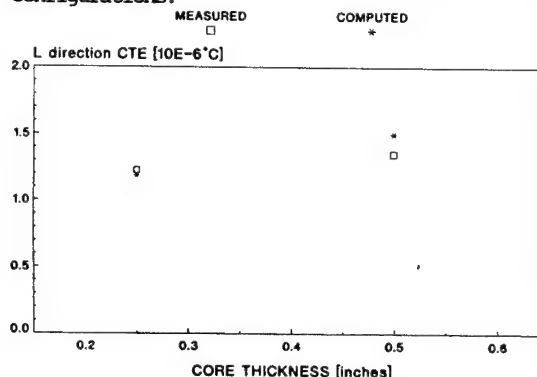


Fig. 4.2 Computed/measured CTE for different sandwich configurations

Namely 300*70 mm. samples, made from Pitch 75/934 skins, and 5052 aluminum core (for two different core thicknesses, foil thicknesses, cell sizes) have been tested.

The CTE differences along the L-W directions can play an important role when performing thermal distortion analyses.

In Fig. 4.3 the computed/measured comparison refers to a single sandwich sample (Gy70/69, 5052 aluminum core), tested along both the L and W directions.

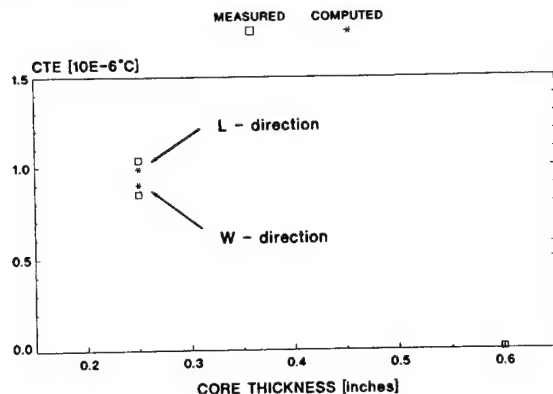


Fig. 4.3 Computed/measured CTE along two orthogonal directions

All above reported measurements refer to average values over the test temperature range.

Good agreement can be observed both for absolute CTE value predictions (different sandwich configurations), and in accounting for orthotropic behavior (different CTE along L-W directions).

The need for a higher degree of accuracy in evaluating sandwich CTE is a questionable matter.

In fact, when performing thermal distortion analyses, the scattering in composite material properties and practical difficulties in computing accurate temperature fields, are often unavoidable. Sophisticated CTE predictive models could lead to fictitious final analysis result accuracy.

5. CONCLUSIONS

The relevance of honeycomb thermo-elastic characterization for sandwich structure dimensional stability analyses is pointed out.

Different prediction methodologies are critically reviewed with particular reference to the mechanical behavior singularities of the honeycomb core layer as a self-standing structure.

Discrepancies between idealized properties and real behavior (especially for very low cell foil thickness configurations) have been investigated.

A new concept approach, based both on measured properties from material suppliers and simplified theoretical assumptions is described.

Good agreement with measured sandwich CTE values has resulted.

The adequacy of the proposed method accuracy, in the frame of thermo-elastic distortion analyses has also been established.

6. REFERENCES

1. Ko W.L. 1980, Elastic constants for superplastically formed/diffusion-bonded corrugated sandwich core, NASA TP 1562
2. Chamis C.C., Aiello R.A., Murthy P.L.N. 1986, Composite sandwich thermostructural behavior: computational simulation, NASA 0948, p. 370-381
3. Marchetti M., Morganti F. 1983, Prediction of thermal expansion coefficient of sandwiches using finite elements methods validated by experimental test results, Acta Astronautica Vol. 10, p. 409-427
4. Groth H. 1986, Thermal stability of sandwich reflectors, ESA SP-243, p. 133-139
5. Helwig G. 1986, Analysis of high precision composite sandwich antennas, ESA SP-261, p. 51-55
6. Hexcel Aerospace 1972, Mechanical properties of Hexcel honeycomb materials, TSB-120
7. MIL-STD-401B 1967, Sandwich constructions and core materials; general test methods

N92-23842

562-27

84734

INVESTIGATIONS OF THE DYNAMIC BEHAVIOUR OF COMPOUNDS UNDER PRELOADING

1) A. Geissler, W. Schmitt 2) H. Weber

1) Fraunhofer-Institut (ICT) D-7507 Pfinztal 1
2) Universität Karlsruhe (MVM) D-7500 Karlsruhe

Abstract

Polymers with characteristic dissipation properties are obtained by compounding them with additives. The mechanical behaviour under vibration conditions of these compounds are characterized by dynamic moduli, which depend on the static preload. The test results of an PU-Compound is presented in this paper. The obtained results enable to calculate the complex moduli of a special dynamic constitutive equation, which then enables to calculate stress and strain of dynamic deformations of structures under static preload.

Nonlinear, viscoelastic, compound

1 Description of the Problem and Aims

The dynamic behaviour of solid propellants is complex because of there viscoelastic response. When used as grains, geometrical and physical nonlinearities can be observed as a result of different static deformations.

For the deformation analysis of grains, mathematical procedures such as the Finite Element Method (FEM) become more and more important, because of the availability of more efficient and less expensive computers [1]. The essential advantage of this approach is the ability to calculate the deformation response of the complex structures used in realistic applications.

The precision of FEM-analyses depends on the constitutive equation which describes the response of the material.

This means that the nonlinear viscoelastic material behaviour must be investigated by creep-, relaxation- and forced vibration experiments.

This paper describes the investigations conducted on a PU-Compound to measure the influence of the static deformation on the dynamic material properties. Based on these results, a multiaxial constitutive equation was developed. Using this equation in connection with an FEM-program, the dynamic response of complex foam structures can be calculated.

2 Kinematic and Constitutive Equation

The loading condition of a grain can be described by a superposition of a larger static and a small harmonic strain. Because of the large static deformation, the Green tensor G is used to describe the kinematic situation of the supposed strains

$$G = G^m + G^o$$

with:

G^m = static deformation
 G^o = dynamic deformation

If this strain description is used in a nonlinear constitutive equation [3], the solution can be divided into static and dynamic components. The result is that the complex module of the dynamic part of the solution depend on the excitation frequency and the static deformation. The complex moduli of this dynamic solution can be calculated if the dependency on static deformation for the complex Young's - and shear modulus is known.

3 Complex Material Description

When a viscoelastic material such as a foam is deformed dynamically, one part of the deformation energy is stored and the other part is dissipated as heat. This material behaviour for a given prestrain and a exertation frequency f_0 can be described by a complex modulus:

$$E(\epsilon_{xx}, f_0) = E'(\epsilon_{xx}, f_0) + i E''(\epsilon_{xx}, f_0)$$

with an absolute value of

$$|E|(\epsilon_{xx}, f_0) = (E'(\epsilon_{xx}, f_0)^2 + E''(\epsilon_{xx}, f_0)^2)^{1/2}$$

where $E'(\epsilon_{xx}, f_0)$ is the storage modulus which describes the reversible material behaviour, and the irreversible behaviour is described by $E''(\epsilon_{xx}, f_0)$, the loss modulus.

The quotient of these values

$$\tan(d(\epsilon_{xx}, f_0)) = E''(\epsilon_{xx}, f_0) / E'(\epsilon_{xx}, f_0)$$

is an expression for the damping behaviour of the material. The dynamic behaviour of the investigated foam was characterized through these material properties. As /3/ shows, they are the basic parameters needed to obtain sufficient material description for dynamic analysis of nonlinear viscoelastic structures.

4 Results of the Vibration Experiments

The results of the vibration tests are illustrated in Figs. 1 to 4.

5 Application

When the dependence of the prestrain on the shear modulus $G(\epsilon_{xx}, f_0)$ and the elastic modulus $E(\epsilon_{xx}, f_0)$ is known, a nonlinear constitutive equation can be prepared /2/. The determined functions can then be used in a Finite Element code /3/ to calculate the dynamic deformation of solid propellant structures with realistic geometries.

6 References

/1/ Bathe, K. J.: Finite Elemente Methoden. Berlin: Springer 1986

/2/ Weber, H.; Geißler, A.; Kugler, H.-P.: Einsatz der experimentellen Mechanik in der statischen und dynamischen Prüfung unverstärkter Kunststoffe. In: Experimentelle Mechanik in Forschung und Praxis. Düsseldorf: VDI-Verlag, 1988. VDI-Berichte 679

/3/ Weber, H.; Geißler, E.: Safe Cushion Design for Sensitive Products. Vortrag, 6th IAPRI World Conference on Packaging '89, Hamburg 27. 29. Sept. 1989

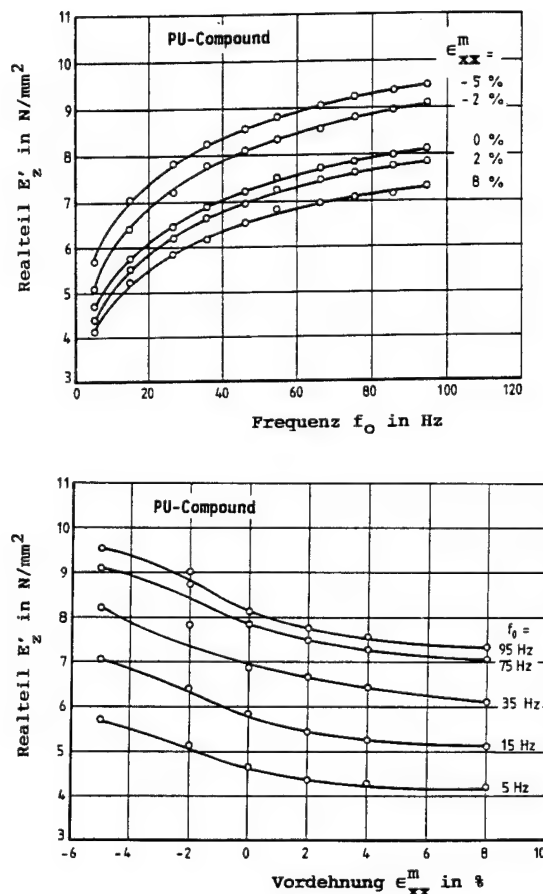


Figure 1: Real Part E' of the complex elastic modulus E of an PU-Compound in dependence of
a) the load frequency
b) the predeformation

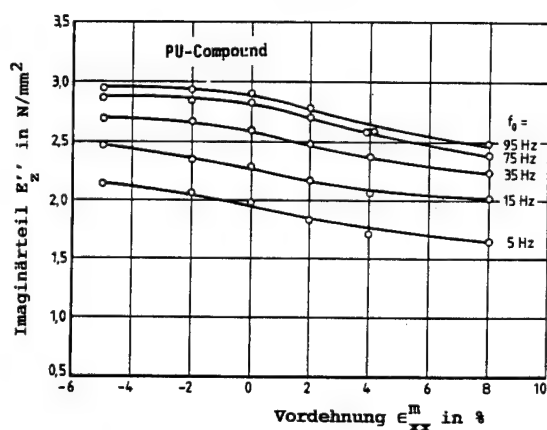
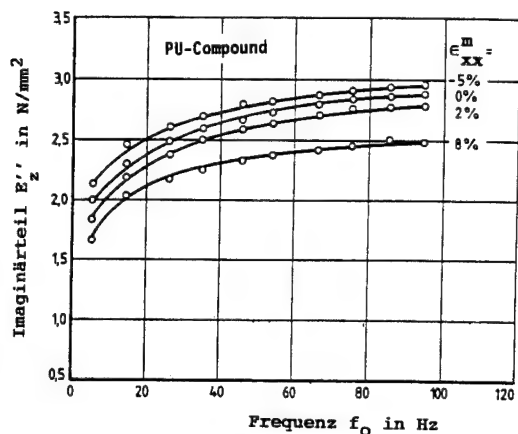


Figure 2: Imaginary Part E'' of the complex elastic modulus E of an PU-Compound in dependence of
a) the load frequency
b) the predeformation

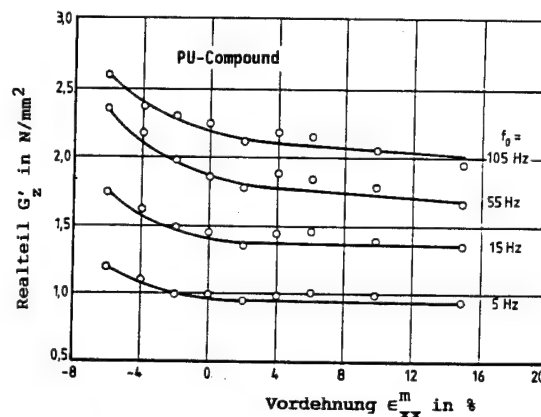
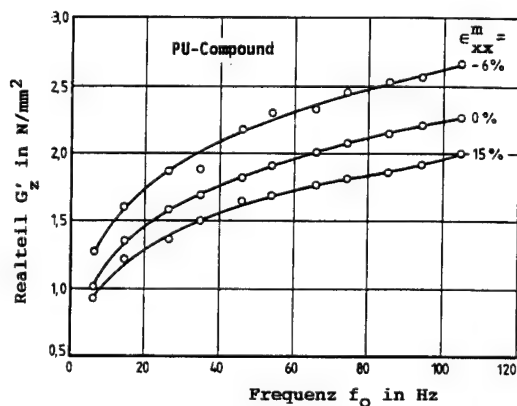


Figure 3: Real Part G' of the complex shear-modulus G^* of an PU-Compound in dependence of
a) the load frequency
b) the predeformation

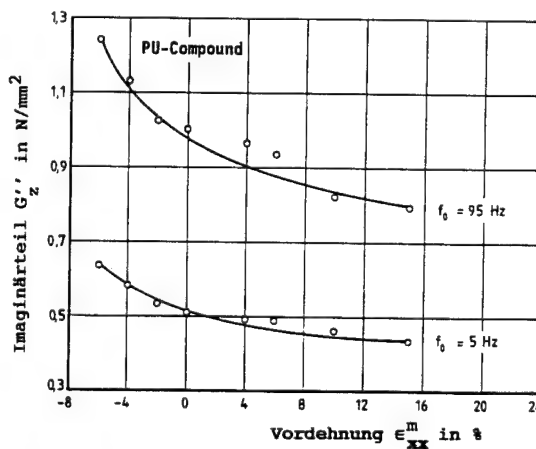
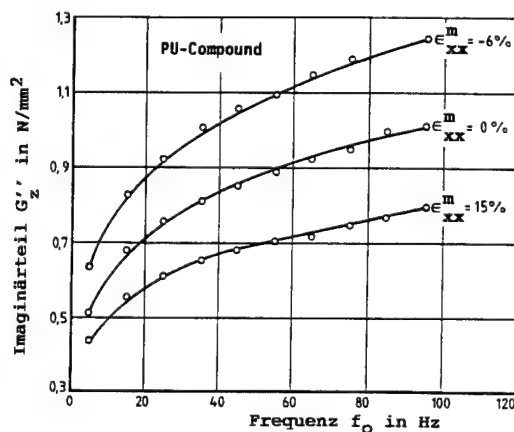


Figure 4: Imaginary Part G'' of the complex shear-modulus G of an PU-Compound in dependence of
a) the load frequency
b) the predeformation

**SESSION
2.3.B**

**ANALYSIS
V**

**FLUID/STRUCTURE
INTERACTION**

PRECEDING PAGE BLANK NOT FILMED

N92-23843

84755

ON THE ANALYSIS OF LIQUID FILLED FREE-FREE TANKS

Andreas Kreis

Michel Klein

Kreis Consultancies
Jarella
CH-7231 Pragg-Jenaz
Switzerland

ESA/ESTEC
Postbus 299
NL-2200 AG Noordwijk
The Netherlands

ABSTRACT

The general problem discussed in this paper is the analysis of free-free flexible tanks filled with an incompressible fluid. Gravity effects due to thrust forces are considered both for the fluid and the structure. A numerical analysis methodology is presented which uses the boundary element method for the fluid model and the finite element method for the structural model. For the analysis of free-free tank-fluid systems under gravity conditions it is essential to include the rigid degrees of freedom explicitly in the model in order to get a correct rigid mode behaviour. Besides numerical solutions two benchmark problems are presented which have been solved analytically by means of Fourier series expansions. Only two-dimensional problems are discussed in the paper. The generalisation to three dimensions is, however, straightforward.

Keywords: Fluid-structure interaction, FEM-BEM coupled analysis, free-free tanks, rigid modes

1. INTRODUCTION

The mass of the liquid propellant in modern launchers and spacecrafts represents a high percentage of the total mass and therefore the adequate modelling of these fluids is essential for the spacecraft dynamic behaviour. In this paper it is discussed how the fluid can efficiently be modelled with the boundary element method and how this model is coupled to the structural model obtained by the finite element method. Special emphasis is placed on the effects of gravity both on the fluid and the structure and on the correct rigid mode behaviour of the model under gravity conditions.

During launch, such systems are subjected to gravity and thrust forces, the latter being partly governed by the control system of the launcher. Due to these forces such systems are not free-free in the usual sense, since the forces acting on the system determine its motion. However, they are free-free in the sense that they are not fixed at any point to the inertial system. Here some general aspects of the mathematical model of such systems shall be introduced for a very basic model of a launcher, having in mind, that more complex models have similar characteristics. In Figure 1a, the flexible beam (mass m_1) corresponds to a launcher and the attached pendulum (mass m_2) represents the fluid propellant. T is the thrust force, which, for

reasons of simplicity, is assumed to be constant and to point always in the opposite direction of the acceleration of gravity g (no control system included). Such a system can be reduced to an equivalent system as shown in Figure 1b, where the vertical motion is suppressed in the point (hinge) where the thrust T is applied. l_r is the distance from the beam centre of gravity (cog) to the hinge. The acceleration of gravity g is replaced by an apparent acceleration $a = T/m$ with $m = m_1 + m_2$. Y_R and θ_R are the remaining rigid degrees of freedom of a two-dimensional problem which describe the motion of a rigid reference frame attached to the beam in its undisturbed position.

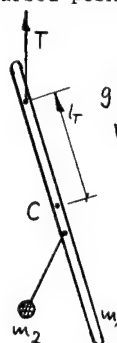


Figure 1a

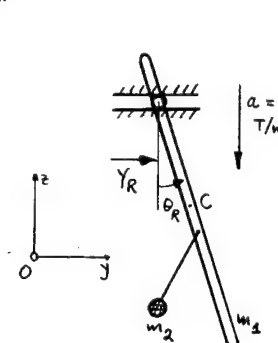


Figure 1b

Rigid modes:

Such systems obviously have a rigid mode with zero eigenfrequency corresponding to a rigid translation in y -direction. There is a second rigid mode which is related to rigid rotations about a horizontal axis. However, under gravity conditions this is only a 'pseudo' rigid mode or a so-called pendulum mode with an eigenfrequency larger than zero, if the thrust force (hinge) is applied above a critical location on the beam axis. The mode shape exhibits in this case comparably large rigid rotations of the beam, only small elastic deformations and significant oscillations of the attached pendulum (i.e. fluid sloshing). Such a mode is recovered in a real spacecraft model by explicitly introducing the rigid dof's (see sect. 3). If the hinge is located below a critical location the system obviously is unstable (negative eigenvalue) if no control system is active. If the hinge is located just at the critical location a true rigid mode with a zero eigenvalue is obtained for the pendulum mode. In this particular case the beam is rigidly rotated and the attached pendulum remains vertical (i.e. the fluid free surface remains horizontal).

Gravity effects of the structure:

Considering the flexible beam only, we have a simple model of a dry launcher (no propellant). If the governing equations are derived from Hamilton's principle, additional gravity terms must be included in the potential energy (see sect. 3). The first one is related to geometric stiffness effects. In the beam example this term takes the form

$$\frac{1}{2} m_s a \int_0^l (u')^2 ds \quad (1.1)$$

and is related to the vertical elevation of the beam cog due to the beam deflection u . Two additional terms stem from the vertical elevation of the beam cog due to the rigid rotation about a horizontal axis and have the following form

$$\frac{1}{2} m_s a l_r \theta_R^2 + m_s a \theta_R \frac{1}{l} \int_0^l u ds \quad (1.2)$$

In section 3 these terms are given in more general form.

Gravity effects of the fluid:

A direct consequence of gravity is the sloshing of the fluid free surface. In the beam model this is represented by oscillations of the attached pendulum and its gravity potential energy is proportional to its vertical elevation. For a fluid, the gravity potential energy is related to the vertical elevation of its cog in a disturbed position (see sect. 3).

In the following sections the methodologies are briefly outlined, which are used for the solution of general tank-fluid systems and which are implemented in the FAFE software developed by the authors of this paper. In sections 5 and 6 numerical solutions are compared against analytical solutions which are based on a Ritz analysis of rectangular boxes.

Some fundamental concepts related to fluid analysis are discussed in more detail in refs. 1 and 2. An introduction to the boundary element method used for the computation of the fluid mass matrix is given in ref. 3. The work presented in this paper is further discussed in refs. 4 and 5.

2. HAMILTON'S PRINCIPLE

Consider a free-free liquid filled tank as shown in Figure 2a which is subjected to a thrust force T in point B and the acceleration of gravity g . For reasons of simplicity T is assumed to be constant and to point always in the vertical direction. Point B where the thrust is applied may be chosen according the problem at hand. Here B is chosen such that the system is stable without an active control system. This tank-fluid system can be represented by an equivalent system, as shown in

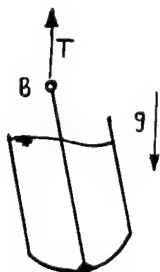


Figure 2a

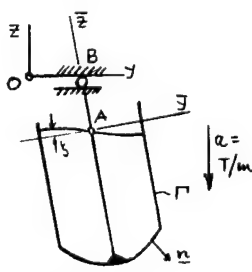


Figure 2b

Figure 2b. The tank is fixed in vertical direction at B to a reference frame $O\tilde{y}\tilde{z}$. This reference frame is accelerated in vertical direction by $a=g$, where a is the acceleration due to the thrust force ($a=T/m$, with m being the total mass). However, $O\tilde{y}\tilde{z}$ can be considered as an inertial coordinate system if the tank-fluid system is subjected to the apparent acceleration a .

Hamilton's principle is given by

$$\delta \int_{t_1}^{t_2} T - \Pi dt = 0 \quad (2.1)$$

The kinetic energy T and the potential energy Π consist of the respective energies of the structure (index s) and the fluid (index f) which are defined as follows

$$T_f = \frac{1}{2} \rho_f \int_{V_f} (\nabla \bar{\varphi})^2 dV \quad (2.2)$$

$$T_s = \frac{1}{2} \rho_s \int_{V_s} \dot{u}^2 dV \quad (2.3)$$

$$\Pi_f = \rho_f a \int_{V_f} z dV \quad (2.4)$$

$$\Pi_s = \Pi_{sd} + \rho_s a \int_{V_s} z dV \quad (2.5)$$

$\bar{\varphi}$ is the fluid velocity potential, \dot{u} the velocity in a structural point and ρ_f and ρ_s are the mass densities of the fluid and the structure. The potential energy of the structure consists of the elastic deformation energy Π_{sd} and the potential energy due to the apparent gravity acceleration a . The above energy terms shall be evaluated for small displacements of the structure and the fluid. Hence in order to get the energies correct up to second order terms the domain of integration in the kinetic energies are the volumes of the fluid and the structure respectively in the undisturbed position, whereas for the potential energies due to gravity the fluid and structural cog's must be evaluated for a disturbed configuration.

3. NUMERICAL SOLUTION METHODOLOGY

Hamilton's principle as stated in the previous section is the basis for the mathematical model of the coupled tank-fluid system. The structural mass and stiffness matrices will be computed in a standard way with the finite element method. The fluid mass matrix is obtained from the boundary element solution of the related potential problem. Additional stiffness matrices for the structure and the fluid which are related to the gravity potential will be derived below. A non-standard feature of the proposed methodology is the representation of the rigid motion of the system with the explicit rigid dof's Y_R and Θ_R .

Rigid dof's and the reference frame $A\tilde{y}\tilde{z}$:

The rigid dof's Y_R and Θ_R define the position of the rigid reference frame $A\tilde{y}\tilde{z}$. The elastic tank is assumed to be fixed to $A\tilde{y}\tilde{z}$ in some point and the structural deformation u and the fluid free surface elevation ζ shall be defined relative to $A\tilde{y}\tilde{z}$. As an example in Figure 2 the tank is clamped at the bottom point to $A\tilde{y}\tilde{z}$. A is the centre point of the fluid free surface in its undisturbed configuration.

Structural mass matrix:

Approximating the structural kinetic energy, eqn. (2.3), using the finite element method yields the mass matrix M_s with respect to the structural dof's u . Shall ϕ_R be the matrix of the rigid mode vectors with respect to the rigid dof's Y_R and θ_R and u_R be the vector consisting of the rigid dof's Y_R and θ_R . Then the equivalent mass matrix where the rigid dof's are explicitly included can be written in the following form

$$\begin{bmatrix} M_s & M_s \phi_R \\ \phi_R^T M_s & \phi_R^T M_s \phi_R \end{bmatrix} \begin{bmatrix} \ddot{u} \\ \ddot{u}_R \end{bmatrix} \quad (3.1)$$

Fluid mass matrix:

The fluid kinetic energy, eqn. (2.2), can be transformed to the following boundary integral

$$T_f = \frac{1}{2} \rho_f \int_{V_f} (\nabla \bar{\psi})^2 dV = \frac{1}{2} \rho_f \int_r \bar{\psi} \bar{\psi}_{,n} d\Gamma \quad (3.2)$$

The relation between $\bar{\psi}$ and $\bar{\psi}_{,n}$ on the fluid boundary is given for a two-dimensional problem by the following integral equation

$$\pi \bar{\psi}_0 + \int_r \bar{\psi}_{,n} \ln r d\Gamma = \int_r \bar{\psi} \frac{\partial \ln r}{\partial n} d\Gamma \quad (3.3)$$

$\bar{\psi}_0$ is the value of the fluid velocity potential in one point on the boundary (source node) and r is the distance from this specified point to all other points (influence nodes) on the fluid boundary. Discretization of the fluid boundary with boundary elements and subsequent evaluation of the above boundary integral equation for all source nodes yields

$$\begin{bmatrix} H_{11} & H_{12} \\ H_{21} & H_{22} \end{bmatrix} \begin{bmatrix} \bar{\psi}_1 \\ \bar{\psi}_2 \end{bmatrix} = \begin{bmatrix} G_{11} & G_{12} \\ G_{21} & G_{22} \end{bmatrix} \begin{bmatrix} \bar{\psi}_{1,n} \\ \bar{\psi}_{2,n} \end{bmatrix} \quad (3.4)$$

where for reasons to be explained, $\bar{\psi}_2$ shall denote the potential at an arbitrarily selected boundary node and $\bar{\psi}_1$ shall be the vector of the potentials at the remaining $N-1$ nodes. From the above equation the potential at the boundary nodes may be computed for given normal derivatives (i.e. for given fluid normal velocities) by inverting H . However, H is singular since in a Neumann problem the potential is determined only within an arbitrary constant. Thus H can only be inverted, if the potential is fixed to a certain value at one node, e.g. $\bar{\psi}_2 = 0$. Rearranging the sub-matrices in equation (3.4) yields

$$\begin{bmatrix} H_{11} & -G_{12} \\ H_{21} & -G_{22} \end{bmatrix} \begin{bmatrix} \bar{\psi}_1 \\ \bar{\psi}_{2,n} \end{bmatrix} = \begin{bmatrix} G_{11} & -H_{12} \\ G_{21} & -H_{22} \end{bmatrix} \begin{bmatrix} \bar{\psi}_{1,n} \\ \bar{\psi}_2 \end{bmatrix} \quad (3.5)$$

The left-hand side matrix is now regular. Shall F denote the product matrix of the inverted left-hand side matrix with the right-hand side matrix. Hence

$$\begin{bmatrix} \bar{\psi}_1 \\ \bar{\psi}_{2,n} \end{bmatrix} = \begin{bmatrix} F_{11} & F_{12} \\ F_{21} & F_{22} \end{bmatrix} \begin{bmatrix} \bar{\psi}_{1,n} \\ \bar{\psi}_2 \end{bmatrix} \quad (3.6)$$

Since $\bar{\psi}_2 = 0$, the above equation can be rewritten

$$\begin{bmatrix} \bar{\psi}_1 \\ \bar{\psi}_2 \end{bmatrix} = \begin{bmatrix} F_{11} & 0 \\ 0 & 0 \end{bmatrix} \begin{bmatrix} \bar{\psi}_{1,n} \\ \bar{\psi}_{2,n} \end{bmatrix} \quad (3.7)$$

The following equation which results from (3.6)

$$\bar{\psi}_{2,n} = [F_{21}] [\bar{\psi}_{1,n}] \quad (3.8)$$

is an additional constraint equation for the fluid normal displacements along the fluid boundary and is known as the incompressibility condition. This condition must be implemented in the final numerical model of the tank-fluid system by means of a Lagrange multiplier or a multi-point constraint equation.

The fluid mass matrix may now be defined based on the discretized fluid kinetic energy. Approximation of the fluid potential and its normal derivative by boundary elements with appropriate shape functions gives

$$\bar{\psi} = [b]^T [\bar{\psi}], \quad [B] = \int_r [b][b]^T d\Gamma \quad (3.9)$$

$$T_f = \frac{1}{2} \rho_f \int_r \bar{\psi} \bar{\psi}_{,n} d\Gamma = \frac{1}{2} \rho_f [\psi_{,n}]^T [B][F][\psi_{,n}] \quad (3.10)$$

Shall N relate the normal displacements u_n in the boundary nodes to the displacement components u in these nodes. Hence

$$[u_n] = [N][u] \quad (3.11)$$

$$T_f = \frac{1}{2} \rho_f [\dot{u}]^T [N]^T [B][F][N][\dot{u}] \quad (3.12)$$

The fluid mass matrix is thus defined by

$$[M_f] = \frac{1}{2} \rho_f [N]^T ([B][F] + [F]^T [B]^T) [N] \quad (3.13)$$

The rigid dof's Y_R and θ_R may be explicitly introduced in the fluid mass matrix as shown in equation (3.1) for the structural mass matrix.

Structural stiffness matrix:

The elastic stiffness matrix K_{se} of the structure and the geometric stiffness matrix K_{sg} due to body forces caused by the apparent acceleration of gravity may be derived from the structural potential energy using the finite element method. Since

$$[K_{se} + K_{sg}][\phi_R] = 0 \quad (3.14)$$

where ϕ_R again is the matrix of the rigid body mode vectors, these stiffness matrices do not contribute to the sub-matrices related to the rigid dof's Y_R and θ_R . The potential energy of the structure due to small rotations of the reference frame $A\bar{y}\bar{z}$ in the gravity field a is given by

$$\Pi_{sr} = \frac{1}{2} m_s a l_s \theta_R^2 + m_s a \theta_R u_y^c \quad (3.15)$$

where l_s is the distance from the structural cog to the hinge and where u_y^c denotes the displacement of the structural cog in y -direction and is defined by

$$u_y^c = \frac{1}{V_s} \int_{V_s} u_y dV \quad (3.16)$$

Hence, the structural stiffness matrix takes the following form, where A is defined by the second term of equation (3.15)

$$\begin{bmatrix} K_{se} + K_{sg} & 0 & A \\ 0 & 0 & 0 \\ A^T & 0 & m_s a l_s \end{bmatrix} \begin{bmatrix} u \\ Y_R \\ \theta_R \end{bmatrix} \quad (3.17)$$

Description of solution:

For reasons of limited space only a brief description of the further solution is given here. The relative fluid velocity potential and the plate displacements u are expanded in series in terms of the eigensolutions of the plate and the fluid. The expansion for the fluid velocity potential must fulfill the boundary condition $\psi_n = 0$ along the rigid sides. Equating the normal derivative of the potential along the flexible plate with the expansion of the plate ensures compatibility. Incompressibility of the fluid must be enforced. These series expansions, which are truncated after a finite number of terms, are inserted in the energy expressions of Hamilton's principle and the standard Ritz procedure yields the eigenvalue problem in the coefficients of the series expansions and the rigid dof's. Some results are presented in the next two sections and are compared with numerical results.

5. BENCHMARK I

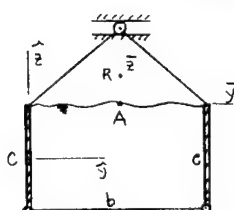


Figure 4a:

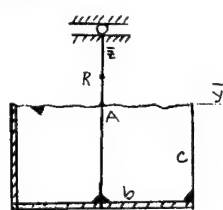


Figure 4b:

The example defined in Figure 4a was solved for the following data set:

box length in y- and z-direction:	1.0m, 0.5m
plate thickness:	0.05m
mass density of structure:	3000.0kg/m ³
Young's modulus of plate:	10 ¹⁰ N/m ²
mass density fluid:	1000.0kg/m ³
distance free surface-hinge:	1.0m
distance free surface-ref. point:	1.0m

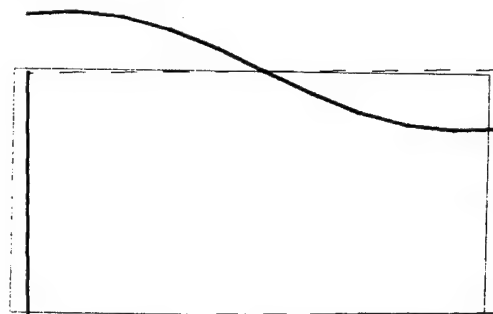
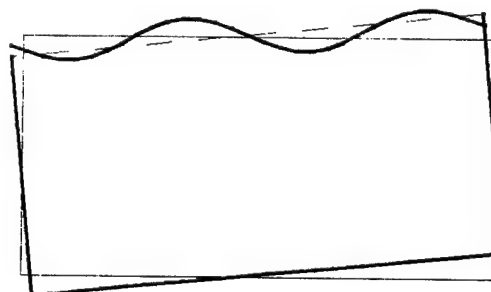
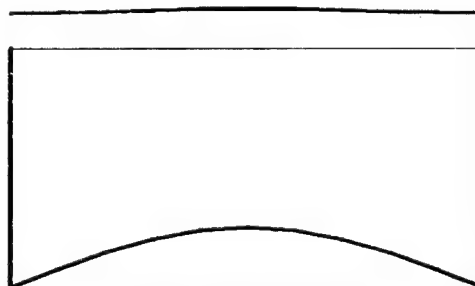
The plate thickness and mass density are identical for the rigid and flexible plates. The structural geometric stiffness terms are not included in the models below, because the primary objective of these benchmarks is to verify the numerical implementation of the proposed fluid modelling. The results of the Ritz analysis have been obtained by truncation of the series expansions after a finite number of terms. The number of terms have been determined such, that numerical convergence was reached for the lowest fluid and structural eigenfrequencies and mode shapes. For the numerical analysis with FABE2D/ASKA the following models have been used:

Mesh A: 10 by 5 elements
 Mesh B: 20 by 10 elements
 Mesh C: 40 by 20 elements

The results for the eigenfrequencies are as follows:

mode	Mesh A f[Hz]	Mesh B f[Hz]	Mesh C f[Hz]	Ritz f[Hz]
rigid	0.0	0.0	0.0	0.0
1, fluid	0.9959	0.9921	0.9912	0.9908
2, fluid	1.2635	1.2517	1.2484	1.2472
3, fluid	1.5771	1.5480	1.5395	1.5365
pendulum	1.7708	1.7638	1.7619	1.7612
4, fluid	1.8542	1.7921	1.7737	1.7671
1, plate	21.131	21.007	20.975	20.965
2, plate	130.53	128.18	127.56	127.34
3, plate	275.85	266.68	264.30	263.48

Some typical mode shapes are given in the following plots, where the initial position of the box is plotted together with the disturbed position. The respective results from the Ritz analysis and the FABE2D/ASKA analysis are identical.

Figure 5: First fluid mode, $f = 0.9908$ HzFigure 6: Pendulum mode, $f = 1.7612$ HzFigure 7: First plate mode, $f = 20.965$ Hz

A second set of results is given below for the identical example as above except that the hinge and the reference point were located slightly above the critical stability location, namely at

0.1927m below the free surface.

For this configuration the pendulum frequency is almost zero and the fluid free surface remains horizontal for small disturbances from the equilibrium position (Figure 8). The eigenfrequencies are

mode	Mesh A f[Hz]	Mesh B f[Hz]	Mesh C f[Hz]	Ritz f[Hz]
rigid	0.0	0.0	0.0	0.0
pendulum	0.0033	0.0033	0.0032	0.0047
1, fluid	1.0423	1.0380	1.0368	1.0364
2, fluid	1.2635	1.2517	1.2484	1.2472
3, fluid	1.5942	1.5619	1.5526	1.5493
4, fluid	1.8542	1.7921	1.7737	1.7671
1, plate	21.131	21.007	20.975	20.954
2, plate	130.53	128.18	127.56	127.34
3, plate	275.85	266.68	264.30	263.46

Figure 8: Pendulum mode, $f = 0.0047$ Hz

6. BENCHMARK II

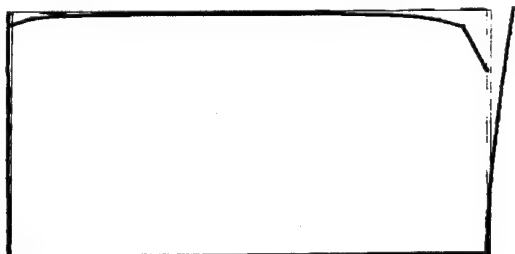
The second example as defined in Figure 4b was solved for the same data set as defined for the above example. Again the structural geometric stiffness terms are not included in the models. In addition to the 3 meshes defined above, a fourth one will be used, since this benchmark has worse convergence properties:

Mesh D: 80 by 40 elements

The results for the eigenfrequencies are as follows:

mode	Mesh B f[Hz]	Mesh C f[Hz]	Mesh D f[Hz]	Ritz f[Hz]
rigid	0.0	0.0	0.0	0.0
1, fluid	0.9922	0.9911	0.9908	0.9908
2, fluid	1.2516	1.2483	1.2474	1.2472
3, fluid	1.5480	1.5395	1.5372	1.5364
pendulum	1.7638	1.7618	1.7613	1.7611
4, fluid	1.7921	1.7737	1.7688	1.7671
1, plate	51.115	50.987	50.942	50.917
2, plate	284.45	282.58	282.00	281.73
3, plate	860.91	851.01	848.04	846.75

The first few fluid modes are identical in eigenfrequency and mode shape as the respective modes of benchmark I. The shape of the first plate mode is given in Figure 9.

Figure 9: First plate mode, $f = 50.917$ Hz

7. FABE SOFTWARE

The numerical solutions presented above, have been obtained with the FABE fluid analysis program, which currently is interfaced with the finite element analysis system ASKA. The analysis has been performed with a two-dimensional prototype of the three-dimensional version, which currently is under development and will have the following capabilities:

- Linear quadrangular and triangular boundary elements, which may be continuous or discontinuous.
- Single zone analysis (i.e. analysis of tanks of more or less concave shape)
- 6 explicit rigid degrees of freedom for correct rigid mode modelling
- Computation of fluid mass and stiffness matrices

For the near future an update is foreseen, which will include quadratic elements and possibly multi-zoning capabilities. It is also feasible, that for fluid analysis of tanks in a low-gravity environment, the additional fluid stiffness matrix due to capillary free surfaces can be included in FABE. However, in this case, it is necessary to determine in advance the equilibrium shape of the free surface.

8. CONCLUSIONS

Comparing the numerical results from the above benchmark examples with the respective results from the Ritz analysis indicates that the proposed numerical methodology for the analysis of free-free tank-fluid systems is correct. Although a conventional boundary element technique (boundary collocation) was used, which yields unsymmetrical system matrices, the resulting fluid mass and stiffness matrices are symmetrical since they are derived from Hamilton's principle. Symmetrical fluid matrices facilitate the dynamic analysis of the coupled system within a finite element analysis system. Further, it was shown, that for the correct rigid mode behaviour of such systems, it is advantageous, to include explicit rigid degrees of freedom in the model. This makes it also feasible to include an active control system in the model of free-free systems and to perform stability analyses.

REFERENCES

- /1/ N.N. Moiseyev, V.V. Rumyantsev, "Dynamic Stability of Bodies Containing Fluid", Springer, 1968.
- /2/ H.N. Abramson (ed.), "The Dynamic Behavior of Liquids in Moving Containers", NASA SP-106, 1966.
- /3/ C.A. Brebbia et al., "Boundary Element Techniques", Springer, 1984.
- /4/ A. Kreis, "FABE Tools and Benchmarks for the Analysis of Free-free Flexible Tanks; Part 1: Two-dimensional Benchmarks", Final report for ESTEC/YMD (M. Klein) by Kreis Consultancies, CH-7231 Pragg-Jenaz, April 1991.
- /5/ A. Kreis, "FABE Tools and Benchmarks for the Analysis of Free-free Flexible Tanks; Part 2: FABE2D Documentation", Final report for ESTEC/YMD (M. Klein) by Kreis Consultancies, CH-7231 Pragg-Jenaz, April 1991.

N92-23844

NUMERICAL INVESTIGATION OF FLUID-STRUCTURE-INTERACTION PROBLEMS WITH THE FINITE ELEMENT METHOD

H.-P. Flicke and W. Mohr

Industrieanlagen-Betriebsgesellschaft mbH
Department TFF
8012 Ottobrunn, FRG

ABSTRACT / RESUME

This contribution presents a procedure for the description and solution of fluid-structure-interaction (FSI) problems. In contrast to many other approaches a complete coupling of the fluid with the structure is obtained. The derived eigenvalue problem of the coupled system is solved with a modified subspace iteration method. The time integration is performed with the method of modal superposition. In two examples the influence of the fluid-structure-interaction on the eigenfrequencies of mechanical systems is shown.

Keywords: Fluid-Structure-Interaction, Subspace-Iteration-Method, Coupled Frequencies, Fluid Sloshing, Modal Superposition

1. INTRODUCTION

In a wide range of technical problems fluid-structure interaction (FSI) phenomena occur and must be considered in the design process of mechanical systems. Due to the additional mass and the dynamic forces of the acting fluid the loading of a wetted structure is more severe in the case of an excitation of the system. Furthermore the frequencies of the coupled system are changed in comparison to the frequencies of the fluid or the structure alone. Typical examples for FSI phenomena are: Fluid fuel rockets during the launching phase, tanks or dams under earthquake excitation, water towers excited by wind forces, and so on.

The numerical treatment of coupled fluid-structure-systems requires a high computer performance with respect to computational speed and central memory. Using the finite element method for the description of the motion of the fluid and the structure, the stiffness and mass matrices for both systems must be built up and stored. If for both systems a displacement method is used (Refs. 1-3), symmetrical system matrices are obtained. However, in this case every nodal point of the fluid has three degrees of freedom and large matrices are the consequence. Assuming, on

the other hand, an inviscid, irrotational, ideal fluid a velocity or displacement potential can be introduced for the description of the fluid which leads to a considerable reduction of the number of degrees of freedom (dof). Unfortunately, in this case the favourable properties of the system matrices (symmetric, banded) are destroyed by an additional coupling matrix (Refs. 4,5). To overcome these shortcomings Olson and Bathe (Ref. 6) used a velocity potential and additionally the pressure as the unknown functions for the fluid (see also Refs. 7, 8). But in this case a modal analysis is more difficult due to a supplementary matrix (no damping matrix) which is multiplied by the first time derivative of the unknown nodal variables.

In this contribution the motion of the fluid is described by a displacement potential. The submatrices of the fluid only have the dimension of n_f , if n_f denotes the number of nodal points of the fluid. The disadvantage (nonsymmetric) is abolished by multiplication of the system matrices by a transformation matrix which leads to a symmetric formulation of the coupled fluid-structure system (Ref. 9). The structure of the submatrices for the fluid and the solid is not changed by this operation. For this symmetric system equation the eigenfrequencies and associated mode shapes can be computed by means of a modified subspace iteration method.

2. DESIGNATIONS, ASSUMPTIONS AND BASIC EQUATIONS

The motion for both continua is described in an arbitrary coordinate system with the basis vectors a_i ($i=1,2,3$). For the formulation of the boundary and coupling conditions local coordinate systems are defined. In these coordinate systems the 3' or 3'' direction is normal to the boundary of the considered continuum. All quantities which are related to the fluid are marked by an "f", all quantities, which are related to the structure, are indicated with an "s" (Fig. 1).

In this first step only isotropic, linear elastic materials and small displacements and distortions are considered. The motion of the solid is described by the Lamè-Navier equations, in which the inertia terms are

introduced.

$$\rho_s \ddot{u}^i = \sigma_j^i |^j + f^j \quad \text{in } V_s \quad (2.1)$$

ρ_s : density of the structure

u^i : contravariant displacement component

σ_j^i : component of the mixed stress tensor

f^j : component of the load vector

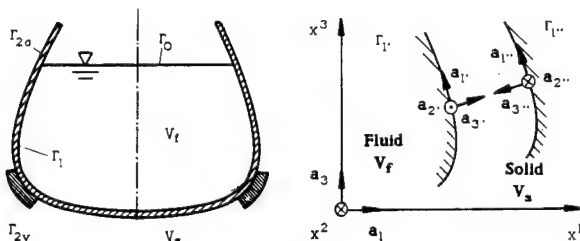


Fig. 1: Designations and coordinate systems

At the boundary Γ_2 (Fig. 1) of the structure either displacements or stresses must be prescribed as boundary conditions:

$$\sigma_{\alpha 3}^{i''} = \hat{\sigma}_{\alpha 3}^{i''} \quad \text{or} \quad u^{i''} = \hat{u}^{i''} \quad \text{at } \Gamma_2'' \quad (2.2)$$

The motion of the inviscid, irrotational ideal fluid with small density changes is described by the wave equation

$$\Phi |^i_1 - \frac{1}{c^2} \ddot{\Phi} = 0 \quad \text{in } V_f, \quad (2.3)$$

where Φ : displacement potential,

c : sound velocity of the fluid.

The boundary condition at the free fluid surface Γ_0 follows from the nonstationary Bernoulli equation by assuming small amplitudes:

$$\ddot{\Phi} + g \Phi |^{3'} = 0 \quad \text{at } \Gamma_0. \quad (2.4)$$

At the common boundary, denoted as Γ_1 (see Fig. 1), the coupling conditions between the fluid and the structure must be accomplished. The relationships between the two local coordinate systems, in which the coupling conditions are described, are also shown in Fig. 1. The coupling conditions are

a.) equal normal displacements of the fluid and the structure

$$\Phi |^{3'} + u^{3''} = 0, \quad (2.5)$$

b.) and equal normal stresses

$$\sigma_{\alpha 3}^{i''} + \rho_f \ddot{\Phi} = 0. \quad (2.6)$$

In consequence of the assumption of an inviscid fluid the tangential stress components are zero

$$\sigma_{\alpha \alpha}^{3''} = 0. \quad (2.7)$$

Using the method of weighted residuals (Refs. 5, 10) the equivalent variational problem is received from the basic equations, boundary and coupling conditions (Eqns. (2.1 - 2.7)).

$$\begin{aligned} & \int_{V_f} \left(\Phi |^i_1 \delta \dot{\Phi} |^i_1 + \frac{1}{c^2} \ddot{\Phi} \delta \dot{\Phi} \right) \rho_f dV_f + \int_{V_s} \left(\sigma_j^i \delta \varepsilon_j^i + \rho_s \ddot{u}^i \delta u_i \right) dV_s + \\ & \int_{\Gamma_0} \ddot{\Phi} \delta \dot{\Phi} \frac{\rho_f}{g} dA_{3'} - \int_{\Gamma_1} (\ddot{\Phi} \delta u^{3'} - u^{3'} \delta \ddot{\Phi}) \rho_f dA_{3'} + \\ & \int_{\Gamma_{2s}} \sigma_{\alpha 3}^{i''} \delta u^{i''} dA_{3''} = 0. \end{aligned} \quad (2.8)$$

3. FINITE-ELEMENT-FORMULATION

The variational problem (2.8) represents the basis for a further treatment with the finite element method. Using this discrete approach the variational problem yields to the coupled system equation (Ref. 10)

$$\begin{bmatrix} \mathbf{K}_f & \mathbf{F} \\ \mathbf{0} & \mathbf{K}_s \end{bmatrix} \begin{bmatrix} \mathbf{d}_f \\ \mathbf{d}_s \end{bmatrix} + \begin{bmatrix} \mathbf{M}_f & \mathbf{0} \\ -\mathbf{F}^T & \mathbf{M}_s \end{bmatrix} \begin{bmatrix} \dot{\mathbf{d}}_f \\ \dot{\mathbf{d}}_s \end{bmatrix} = \begin{bmatrix} \mathbf{0} \\ \mathbf{r}_s \end{bmatrix} \quad (3.1)$$

where

$$\mathbf{B}_s = \mathbf{L} \mathbf{H}, \quad \mathbf{B}_f = \nabla \mathbf{h},$$

$$\mathbf{K}_f = \int_{V_f} \mathbf{B}_f^T \mathbf{B}_f \rho_f dV_f,$$

$$\mathbf{M}_f = \int_{V_f} \mathbf{h} \mathbf{h}^T \frac{\rho_f}{c^2} dV_f + \int_{\Gamma_0} \mathbf{h}_\Gamma \mathbf{h}_\Gamma^T \frac{\rho_f}{g} dA_f,$$

$$\mathbf{K}_s = \int_{V_s} \mathbf{B}_s^T \mathbf{D} \mathbf{B}_s dV_s, \quad \mathbf{M}_s = \int_{V_s} \mathbf{H}^T \mathbf{H} \rho_s dV_s,$$

$$\mathbf{r}_s = - \int_{\Gamma_{2s}} \mathbf{H}_\Gamma^T \mathbf{N} \mathbf{H}_\Gamma^T \mathbf{p} dA, \quad \mathbf{F} = \int_{\Gamma_1} \mathbf{h}_\Gamma \mathbf{n}^T \mathbf{H}_\Gamma \rho_f dA,$$

and

\mathbf{D} : elasticity matrix for linear elastic materials,

\mathbf{L} : operator matrix,

\mathbf{u} : displacement vector of the structure,

\mathbf{n} : components of normal vectors on Γ_1 ,

\mathbf{N} : matrix with the direction vectors of the local coordinate systems at Γ_1 ,

\mathbf{H} : matrix of shape functions describing \mathbf{u} ,

\mathbf{h} : vector of shape functions describing Φ ,

\mathbf{p} : vector with the prescribed stresses at Γ_1 .

\mathbf{K}_f and \mathbf{M}_f are the stiffness and mass matrices of the fluid, and \mathbf{K}_s and \mathbf{M}_s denote the stiffness and mass matrices of the structure. The matrix \mathbf{F} is the coupling matrix which contains the interface conditions between the fluid and the structure. The vector \mathbf{r}_s is the load vector of the structure in case of prescribed stresses at Γ_2 .

4. SOLUTION OF THE COUPLED EIGENVALUE PROBLEM

For the computation of eigenvalues and eigenfrequencies of mechanical systems with the finite element method many procedures have been developed. These procedures use the special properties of the element matrices, such as the symmetric and banded structure and allow the computation of a small number of eigenvalues and eigenmodes (p -eigenvalues) even if the number of unknowns is high. After separating the time function the algebraic eigenvalue problem of the coupled system can be received from equation (3.1).

$$\text{With } \mathbf{d}_f = f(t) \tilde{\mathbf{d}}_f, \quad \mathbf{d}_s = f(t) \tilde{\mathbf{d}}_s \quad \text{or} \quad \mathbf{d} = f(t) \tilde{\mathbf{d}},$$

$$\text{and } \ddot{f}(t) = -\omega^2 f(t) \quad (4.1)$$

the following eigenvalue problem is obtained:

$$\left(\begin{bmatrix} \mathbf{K}_f & \mathbf{F} \\ \mathbf{0} & \mathbf{K}_s \end{bmatrix} - \omega_i^2 \begin{bmatrix} \mathbf{M}_f & \mathbf{0} \\ -\mathbf{F}^T & \mathbf{M}_s \end{bmatrix} \right) \begin{Bmatrix} \tilde{\mathbf{d}}_f \\ \tilde{\mathbf{d}}_s \end{Bmatrix}_i = \mathbf{0}, \quad (4.2)$$

or with the matrices \mathbf{K} and \mathbf{M} of the entire system

$$(\mathbf{K} - \omega_i^2 \mathbf{M}) \tilde{\mathbf{d}}_i = \mathbf{0}.$$

ω_i denotes the i -st eigenfrequency of the system and $\tilde{\mathbf{d}}_i$ is the appertaining eigenvector. In consequence of the fluid-structure coupling the system matrices \mathbf{K} and \mathbf{M} are nonsymmetric. Standard procedures of the finite element method require symmetric matrices for the solution of the eigenvalue problem. Therefore, to be able to apply these standard methods, the system matrices must be symmetrized. To receive symmetric matrices \mathbf{K}^* and \mathbf{M}^* the eigenvalue problem (4.2) is multiplied by a transformation matrix \mathbf{T} :

$$\mathbf{T}^* (\mathbf{K} - \omega_i^2 \mathbf{M}) \tilde{\mathbf{d}}_i = \mathbf{0}, \quad (4.3)$$

$$\mathbf{K}^* = \mathbf{T} \mathbf{K}, \quad \mathbf{M}^* = \mathbf{T} \mathbf{M}. \quad (4.4)$$

The symmetric conditions for the matrices \mathbf{K}^* and \mathbf{M}^* are:

$$\mathbf{K}^* = \mathbf{K}^{*T}, \quad \mathbf{M}^* = \mathbf{M}^{*T}. \quad (4.5)$$

For the unknown transformation matrix follows (Ref. 9):

$$\mathbf{T} = \begin{bmatrix} \mathbf{I} & -\mathbf{F} \mathbf{K}_s^{-1} \\ \mathbf{0} & \mathbf{M}_s \mathbf{K}_s^{-1} \end{bmatrix}. \quad (4.6)$$

By multiplication of the eigenvalue problem by this transformation matrix the following symmetric formulation is obtained:

$$\left(\begin{bmatrix} \mathbf{K}_f & \mathbf{0} \\ \mathbf{0} & \mathbf{M}_s \end{bmatrix} - \mathbf{D}_\omega \begin{bmatrix} \mathbf{M}_f + \mathbf{F} \mathbf{K}_s^{-1} \mathbf{F}^T & -\mathbf{F} \mathbf{K}_s^{-1} \mathbf{M}_s \\ -\mathbf{M}_s \mathbf{K}_s^{-1} \mathbf{F}^T & \mathbf{M}_s \mathbf{K}_s^{-1} \mathbf{M}_s \end{bmatrix} \right) \begin{Bmatrix} \mathbf{E}_f \\ \mathbf{E}_s \end{Bmatrix} = \mathbf{0}, \quad (4.7)$$

where \mathbf{E}_f and \mathbf{E}_s denote the matrices of the eigenvectors of the fluid and the structure. The dimension of these matrices is $(n_f \times p)$ and $(n_s \times p)$ respectively, where n_f is the number of unknowns of the fluid, n_s the number of unknowns of the structure and p the number of eigenvectors to be determined. The solution of this coupled eigenvalue problem is performed with a modified subspace iteration method (Ref. 10). The flowchart of this procedure is shown in Fig. 2.

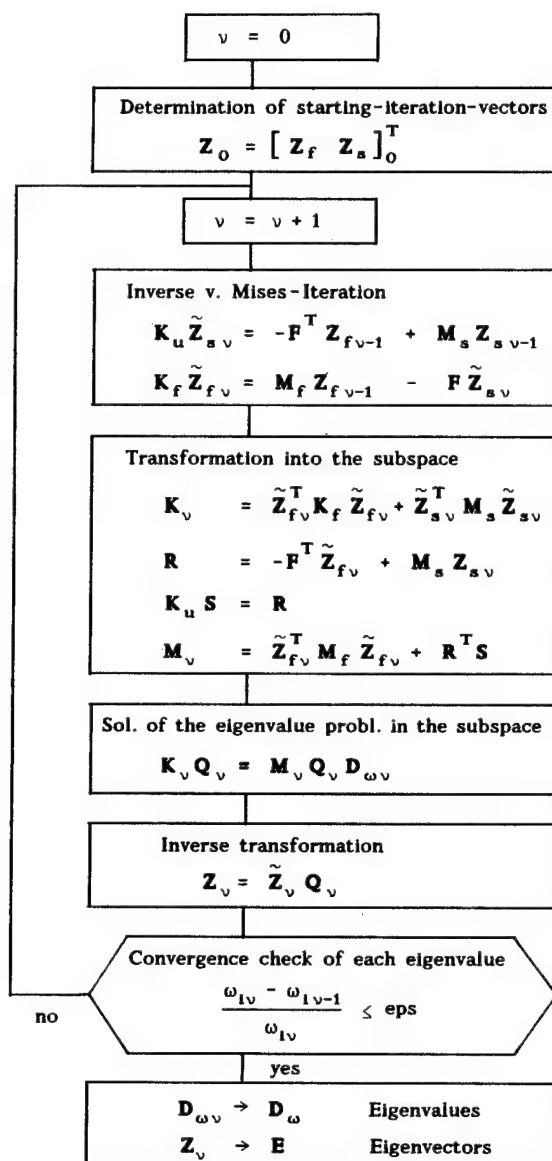


Fig. 2: Flowchart for the solution of the coupled eigenvalue problem

To avoid the computation of the inverse stiffness matrix \mathbf{K}_s^{-1} , two auxiliary matrices \mathbf{R} and \mathbf{S} are introduced. The advantage of the subspace iteration method (Ref. 11) is the solution of the reduced eigenvalue problem. That means that for the solution of the eigenvalue problem only p -iteration vectors are used. The eigenvalue problem is transformed into a subspace with the dimension $p \times p$, in which the solution is accomplished. This is a very efficient method with regard to computation time and memory requirement.

The data of the masses and spring constants for the two cases are given in table 1. The side-wall of the container is made of steel with $E = 206000 \text{ N/mm}^2$, $\nu = 0.3$ and $\rho = 7800 \text{ kg/m}^3$.

case	k_s [N/mm]	m_c [kg]	m_s [kg]	m_a [kg]	m_o [kg]
1	14	7.4	1.3	0.16	8.21
2	1900	7.4	4.9	1.50	11.35

where

k_s : spring-constant,

m_c : mass of the oscillating cylinder,

m_s : spring-mass,

m_a : mass to attach the spring at the oscillator,

m_o : whole oscillating mass = $m_c + \frac{1}{2} m_s + m_a$.

Table 1: Spring constants and masses of the two cases

The system is excited by a sudden strike onto the rigid bottom plate in vertical direction. Figure 5 shows the time history of the excitation (case 2), i.e. the measured acceleration at the bottom of the container. The measured response of the oscillator is given in Figure 6 and Figure 7.

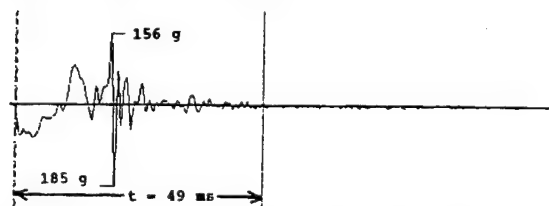


Fig. 5: Acceleration at the rigid bottom plate

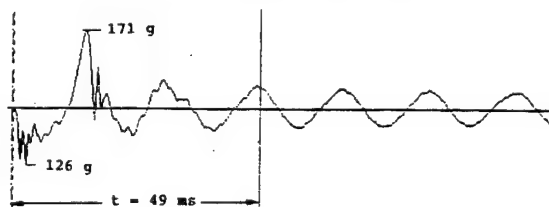


Fig. 6: Acceleration at the oscillator

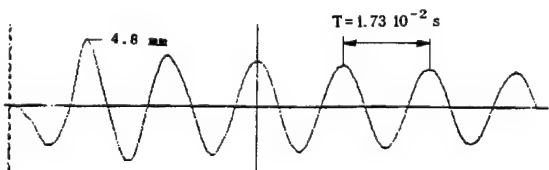


Fig. 7: Relative displacement bottom plate - oscillator

Figure 8 shows the discretization for the SOFLIN computation. Due to the axis-symmetric of this problem only the traces of the cylinder and the oscillating mass are discretized. The coupling of the fluid and the structure is accomplished with special coupling elements. These are located between the fluid and the

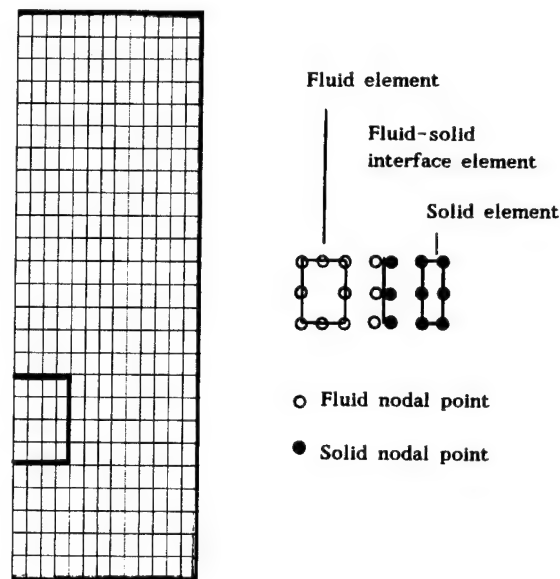


Fig. 8: Discretization of the system

structure and connect the degrees of freedom of the structure and the fluid at the common boundary Γ_1 . In table 2 the computed and measured frequencies are compared.

case	computed f_s [Hz]	with SOFLIN f_{sf} [Hz]	measured f_{sf} [Hz]
1	6.6	5.4	5.7
2	65.1	57.4	57.8

Table 2: Comparison between computed and measured frequencies

Table 2 shows a good agreement between the computed and measured frequencies f_{sf} . f_{sf} denotes the frequencies of the oscillator in water, while f_s are the frequencies without water (in air). Due to the effect of the added hydraulic masses the frequencies of the wetted oscillators are lower. In case 1 the difference between computation and experiment is larger than in case 2. An exactly orthogonal attachment of the coil spring (case 1) onto the bottom plate was not possible. Therefore, in this case the vertical vibration is superposed with small bending vibrations. This could be the reason for the larger deviation in case 1.

8. APPLICATION

At last for a more complex system, a water tower, the coupled frequencies are calculated. The structure consists of a slender shaft with a height $h = 35 \text{ m}$. At the top of the shaft a spherical water reservoir is attached. In this configuration the sphere is half filled with water. Figure 9 shows the geometry of the water tower.

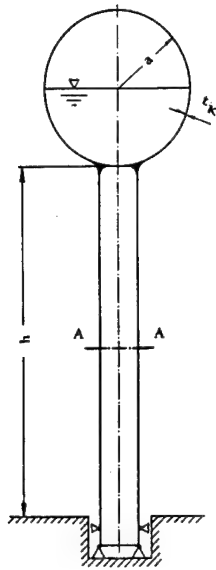


Fig. 9: Water tower

Due to the only partial filling of the sphere the dynamic boundary condition at the free surface must be taken into account. In the finite element computation this condition is described by special surface elements. Since the system is axis-symmetric also rotational symmetric finite elements can be used. For the computation of non-symmetric modes, the dependence of the state variables in circumferential direction is expressed in fourier-series

$$\mathbf{u} = \sum_{m=0}^{\infty} \begin{Bmatrix} m u_r(t, r, z) \cos(m\varphi) \\ m u_\varphi(t, r, z) \sin(m\varphi) \\ m u_z(t, r, z) \cos(m\varphi) \end{Bmatrix}, \quad (8.1)$$

$$\Phi = \sum_{m=0}^{\infty} m \Phi(t, r, z) \cos(m\varphi). \quad (8.2)$$

For the most important, first antisymmetric vibration mode, $m=1$, the first eigenfrequencies and ascending eigenvectors are calculated with SOFLIN. The following special cases are included in the general coupled eigenvalue problem (case 3)

$$(3): \begin{bmatrix} \mathbf{K}_f & \mathbf{F} \\ \mathbf{0} & \mathbf{K}_s \end{bmatrix} - \omega^2 \begin{bmatrix} \mathbf{M}_f & \mathbf{0} \\ -\mathbf{F}^T & \mathbf{M}_s \end{bmatrix} \begin{Bmatrix} \mathbf{e}_f \\ \mathbf{e}_s \end{Bmatrix} = \mathbf{0}. \quad (8.3)$$

(1): Empty tank, $\mathbf{d}_f = \ddot{\mathbf{d}}_f = \ddot{\mathbf{d}}_s = \mathbf{0}$:

$$(\mathbf{K}_s - \omega^2 \mathbf{M}_s) \mathbf{e}_{s1} = \mathbf{0}. \quad (8.4)$$

(2): Neglecting of the dynamic boundary condition at the free surface (no fluid sloshing), assuming an incompressible fluid: $\mathbf{M}_f = \mathbf{0}$.

$$[\mathbf{K}_s - \omega^2 (\mathbf{F}^T \mathbf{K}_f^{-1} \mathbf{F} + \mathbf{M}_s)] \mathbf{e}_{s1} = \mathbf{0}. \quad (8.5)$$

The term $\mathbf{F}^T \mathbf{K}_f^{-1} \mathbf{F}$ represents an additional mass term for the structure in consequence of the fluid.

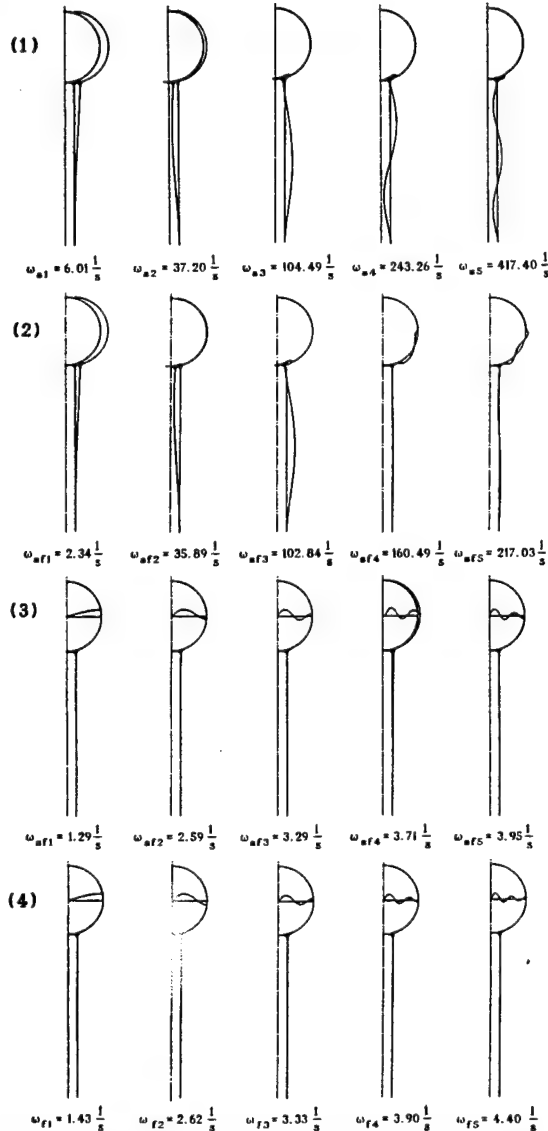
(4): Rigid tank, $\mathbf{d}_s = \ddot{\mathbf{d}}_s = \ddot{\mathbf{d}}_s = \mathbf{0}$:

$$(\mathbf{K}_f - \omega^2 \mathbf{M}_f) \mathbf{e}_{f1} = \mathbf{0}. \quad (8.6)$$

For these four cases the first ten calculated frequencies are given in table 3.

i	case 1 ω_{s1}	case 2 ω_{s1}	case 3 ω_{sf1}	case 4 ω_{f1}
1	6.0084	2.3378	1.2923	1.4257
2	37.1974	35.8948	2.5906	2.6216
3	104.4941	102.8356	3.2916	3.3287
4	243.2625	160.4913	3.7120	3.9017
5	417.3938	217.0253	3.9481	4.3987
6	454.0334	236.6883	4.4088	4.8446
7	575.8695	264.0267	4.8491	5.2534
8	596.3721	284.7402	5.2559	5.6340
9	625.5902	302.3349	5.6356	5.9928
10	647.5995	329.4111	5.9939	6.3345

Table 3: Computed eigenfrequencies in [1/s]

Fig. 10: Eigenforms of the system for mode $m=1$

Due to the additional fluid mass the frequencies in case 2 are lower than the frequencies of an empty tank (case 1). In case 3 the general coupled eigenvalue problem is solved, i.e. the fluid frequencies, the structural frequencies and some coupled frequencies are included. In Figure 10 the lowest five ascending eigenvectors for the four cases are presented. The first three coupled mode shapes (case 3) are primarily fluid eigenmodes. The frequencies decrease in comparison to the fluid frequencies of a rigid tank due to the elasticity of the structure. The fourth eigenmode is a coupled one, because it consists of the first structural mode shape and parts of the third and fourth fluid mode shapes. In case 2 the dynamic boundary condition at the free fluid surface is neglected. That means, that the sloshing modes of the fluid are suppressed, the fluid is not able to move relative to the surrounding structure. In this case the structure must accelerate the whole fluid, the computed frequencies are too small. In table 4 the first 3 structural frequencies, with and without neglecting the dynamic boundary condition at the free fluid surface, are compared:

$$\text{Error} = \frac{\omega_{1(3)} - \omega_{1(2)}}{\omega_{1(3)}} \cdot 100 \quad \text{in \%}$$

$\omega_{(1)}$ empty tank	$\omega_{(2)}$ without sloshing	$\omega_{(3)}$ with sloshing	error in %
6.008	2.338	3.712	37.02
37.197	35.895	36.153	0.71
104.494	102.836	102.846	0.01

Table 4: Comparison of the first structural frequencies

It can be observed, that for higher frequencies (in this example above 35 [1/s]) the dynamic boundary condition at the free fluid surface is negligible. For higher frequencies only a thin layer of the fluid in the vicinity of the free surface performs a relative motion to the structure. This shows, that for frequencies above 35 [1/s] only the reduced eigenvalue problem (case 2) must be solved. Only for lower structural frequencies (structural frequencies in the same order of magnitude as the first fluid frequencies) the whole coupled eigenvalue problem (case 3) must be solved. The solution of the reduced eigenvalue problem leads to a considerable reduction of computation time, because the eigenvalue problem only has the order of the number of degrees of freedom of the structure.

1. Fenves, G.; Vargas-Loli, L. M.: Nonlinear Dynamic Analysis of Fluid-Structure Systems. *Journal of Engineering Mechanics*, Vol. 114, No. 2 (1988), pp 219-240.
2. Wilson, E. L.; Khalvati, M.: Finite Elements for the Dynamic Analysis of Fluid-Solid Systems. *Intern. Journ. for Num. Methods in Eng.*, Vol. 19 (1983), pp. 1657-1668.
3. Hamdi, M. A.; Ousset, Y.; Vercherys, G.: A Displacement Method for the Analysis of Vibrations of Coupled Fluid-Structure Systems. *Intern. Journ. for Num. Methods in Eng.*, Vol. 13 (1978), pp. 139-150.
4. Everstine, G. C.: A Symmetric Potential Formulation for Fluid-Structure Interaction. *Journal of Sound and Vibration* (1981), 79 (1), pp. 157-160.
5. Schiffner, K.: Ein allgemeines Variationsproblem zur Beschreibung von Flüssigkeitsschwingungen in elastischen Strukturen. *ZAMM* 63, (1983), T 94 - T 96.
6. Olson, L. G.; Bathe, K.-J.: Analysis of Fluid-Structure Interaction. A Direct Symmetric Coupled Formulation Based on the Fluid Velocity Potential. *Computers & Structures*, Vol. 21, No. 1/2 (1985), pp. 21 - 32.
7. Combescure, A., et al: Fluid-Structure Interaction. A General Method Used in the Ceasemt Computer Programs. *Computer & Structures*, Vol. 12 (1980), pp. 471 - 474.
8. Antoniadis, I.; Kanarachos, A.: A Decoupling Procedure for the Modal Analysis of Structures in Contact with Incompressible Fluids. *Communications in Applied Numerical Methods*, Vol. 3 (1987), pp. 507-512.
9. Flicke, H.-P.; Schiffner, K.: Flüssigkeits-Festkörper-Interaktion von beliebigen rotationssymmetrischen Behälterformen. *ZAMM* 69, (1989) 5, T 417 - 420.
10. Flicke, H.-P.: Untersuchungen zur Fluid-Struktur-Interaktion rotationssymmetrischer Strukturen mit Hilfe der Methode der finiten Elemente. Dissertation, Universität - GH Siegen. VDI - Fortschritt - Berichte, Reihe 11, Nr. 144, VDI-Verlag, Düsseldorf 1991.
11. Bathe, K. J.: Finite-Elemente-Methoden. Springer-Verlag, Berlin Heidelberg New York Tokyo, 1986.
12. Böge, G.: MAKROS, Programmsystem für interaktives Pre- und Postprocessing mit FE - Makrostrukturen. Universität der Bundeswehr München, Neubiberg.

N92-23845

FLUID-STRUCTURE INTERACTION PROBLEMS : DEVELOPMENT OF SPECIAL PROCESSORS

M. KLEIN
Estec Noordwijk, The Netherlands

Y.M. LEFEVRE
Matra Espace, Toulouse, France

ABSTRACT

The dynamic analysis of liquid filled tanks has become an increasingly important topic as their mass may represent over half the total mass of some spacecrafts.

However, the analysis of such coupled systems is difficult because of the particular behaviour of fluids, especially when gravity effects are included. In this paper, a general method applicable to three-dimensional cases is presented, using fluid finite elements.

A general variational principle including gravity effects is established, from which a classical set of coupled equations is derived. Emphasis is put on the implementation of the formulation and its interface with a general FE code (NASTRAN) which is used to compute the structural matrices and to solve the system of equations. Test examples are shown which demonstrate the general usefulness of the procedure.

1. INTRODUCTION

The fluid-structure interaction is today a rather well-known problem and various techniques based on finite elements or boundary integrals have been developed to solve it. CNES for instance has built the ASTRAL code for its launch vehicle activities.

Commercial FE codes such as NASTRAN offer also some capability in this domain. But the implementation of these methods is not fully satisfactory because of restrictions which can be severe in some cases. The limitations may concern either the geometry of the tanks or the type of analysis. As an example the sloshing analysis for full 3D models including inner structures such as baffles, propulsion management device.. cannot be established without important simplifying assumptions.

For these reasons SEP and MATRA have developed on ESA contract a software which may be interfaced with large FE programs used as solvers. The program involves none of the limitations described above except for the linear behaviour of the system around its equilibrium position and assumptions about the fluid. Regarding this last point, the basic hypothesis is the nature of the fluid which is assumed to be incompressible and irrotational.

Compressibility effects can be considered negligible when low frequency - below 500 Hz - behaviour is analysed. The latter problem - the liquid is irrotational - deals rather with local boundary effects. It is clear that around sharp corners such as baffle edges turbulent flow is likely to occur. However, this kind of limitation is probably not critical when considering the purpose of this study.

2. THEORETICAL ANALYSIS

The theoretical analysis of the fluid structure interaction problem is based on the application of Hamilton's principle to the system (Ref. 1) :

$$\int_{t_0}^{t_1} \delta \left\{ T - V - \frac{1}{2} \iiint_{(D)} (\nabla \dot{\phi})^2 d\tau + \rho \iint_{(S)} \dot{\phi} (\vec{u} \cdot \vec{n}_e) d\sigma + \rho \iint_{(S)} \ddot{\phi} \eta d\sigma - \rho g P(u, \eta) \right\} dt = 0 \quad (1)$$

where the displacement potential ϕ has been selected as the fluid variable.

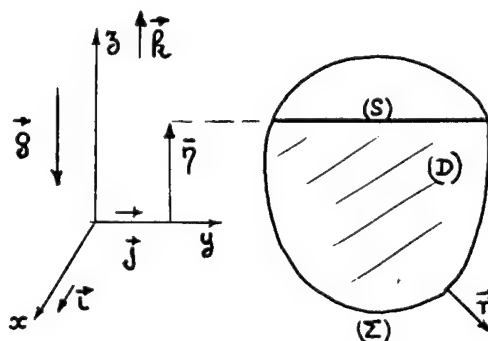


Figure 1 : Tank geometry

Definition of the variables :

u : displacement field of the structure
 η : displacement field of the free surface
 ϕ : displacement potential of the fluid.

Conjugate discretized variables :

q : generalized displacements of the structure
 $\bar{\eta}$: generalized displacements of the free surface
 f : displacement potential of the fluid.

Unit vectors : i, j, k .

In this expression, T is the kinetic energy of the structure, V its potential energy (including the effect of initial static loads if any). The next three terms represent the energy due to the dynamic pressure of the liquid. The last term is a complex function which describes the potential energy of the fluid in the gravity field :

$$P = \iint_{(S)} \eta^2 d\sigma + \iint_{(Z)} (\vec{u} \cdot \vec{h})(\vec{u} \cdot \vec{n}_e) d\sigma + \iint_{(S)} (\vec{z} \cdot \vec{\eta}) \sum (\vec{u} \cdot \vec{t}) \nabla \lambda (\vec{t} \wedge \vec{u}) \vec{n}_e d\sigma \quad (2)$$

The correct evaluation of this fluid potential energy is required in order to obtain accurate rigid body modes.

It is necessary to add to this principle an equation which states that the fluid volume is constant without gaps between the structure and the liquid :

$$\iint_{(S)+(Z)} (\vec{u} \cdot \vec{n}_e) d\sigma = 0 \quad (3)$$

Euler's equations of the principle are obtained by varying the independent variables u , and η . After discretization, these equations can be written in matrix form :

$$\begin{bmatrix} M & -D^T & 0 \\ D & N_1 & -B \\ 0 & -B^T & 0 \end{bmatrix} \begin{bmatrix} \ddot{q} \\ \ddot{f} \\ \ddot{\eta} \end{bmatrix} + \begin{bmatrix} K-S & 0 & 0 \\ 0 & 0 & 0 \\ 0 & 0 & C \end{bmatrix} \begin{bmatrix} q \\ f \\ \eta \end{bmatrix} = 0 \quad (4)$$

And the "constant volume" condition is :

$$i^T D q + i^T B \eta = 0 \quad (5)$$

where i is a unit vector.

The displacement potential of the fluid is not defined in a unique manner. Any function of time can be added to the potential which will still satisfy the principle. The mathematical consequence of this indetermination is the singularity of the fluid mass matrix N . It is possible to choose in the fluid domain a reference point where the potential is set to zero and thus eliminate the singularity. This operation is actually required so that the mass matrix N can be inverted. In practice it is sufficient to delete one d.o.f. from the matrices N , B and D . We write these matrices : N_1 , B_1 and D_1 .

It has been shown (Debongnie LTAS and Hamdi UTC) that the explicit incompressibility condition is required as a direct consequence of the removal of the N matrix singularity in order to preserve the initial nature of the problem.

The next step is the elimination of the fluid d.o.f.'s f , which is now possible since matrix N is non singular.

The final set of equations is :

$$\begin{bmatrix} M + D_1^T N_1^{-1} D_1 & D_1^T N_1^{-1} B_1 \\ B_1^T N_1^{-1} D_1 & B_1^T N_1^{-1} B_1 \end{bmatrix} \begin{bmatrix} \ddot{q} \\ \ddot{\eta} \end{bmatrix} + \begin{bmatrix} K-S & 0 \\ 0 & C \end{bmatrix} \begin{bmatrix} q \\ \eta \end{bmatrix} = 0 \quad (6)$$

$$i^T D_1 q + i^T B_1 \eta = 0. \quad (7)$$

It is also possible to derive the following expression for the dynamic pressure :

$$P = - N_1^{-1} (D_1 \ddot{q} + B_1 \ddot{\eta}) \quad (8)$$

If the potential is set to zero at a free surface d.o.f. It is important to notice that the formulation leads to a symmetric system of equations. It is therefore possible to use all the functional modules assigned to eigenvalue and eigenvector extraction which are available in the large FE codes.

3. PROGRAM ORGANIZATION

The computer program performs four major steps which are described in this section (Ref. 2).

The first module is the input file processor (IFP) which reads the input data deck, recognizes the headers and sorts the informations.

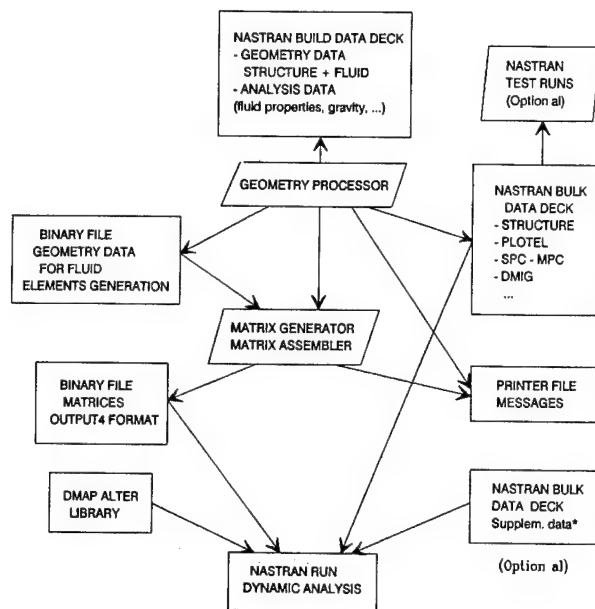
The second module, called the fluid geometry processor (FGP) is basically a NASTRAN card decoder which interprets the main geometry data.

The next module, the Boundary Fluid Processor (BFP) is dedicated to the analysis of the fluid regions. The purpose of this processor is to determine each distinct fluid region, defined by nodes and elements, as well as their boundaries, either walls or free surface.

In each fluid domain, matching between faces of different fluid elements is tested until the outer surface of the volume is determined. Then these unmatched faces are tested against the structural elements in order to detect the wetted walls. Remaining faces are usually free surface elements unless inappropriate meshing of the fluid volume has been performed.

The axial (Z) position of the grids of the free surface elements is checked before these nodes are classified as free surface grids. (The z axis is assumed to be parallel to the gravity field).

Further analysis of the "wetted" grids in order to assess whether the corresponding fluid node potential is uniquely defined. Grids which belong to multi-wetted walls, must be assigned different potential values according to the fluid configuration except for edge grids (figure 2). At last the module builds the data input for the fluid element subroutines.



* Definition of dynamic parameters :

- Eigen value extraction method
- dynamic excitation
- ...

The last module is the Matrix assembly and Calculation Processor (MCP). The various fluid and structural matrices are computed and assembled in this processor which also includes a bandwidth optimizer in order to decrease the storage space needed and CPU time for matrix inversion by NASTRAN (Ref. 3). In fact the connectivity of the fluid elements is not apparent in the final NASTRAN model even though the fluid mass matrix is inverted by one of the program subroutines.

4. PROGRAM OPERATION

The solution of the fluid interaction problem requires only two steps.

In phase 1, the user submits a data deck which contains the tank and fluid geometry as the input to the fluid software program. It is in practice a standard NASTRAN data deck with only some special features which are briefly described here.

The volume elements of each fluid region are identified through their property ID which references a special MFLUID card (one per region) which also contains added information about the position of the free surface (if need be) and fluid properties. When gravity effects are to be included, the information is delivered through a NASTRAN GRAV card.

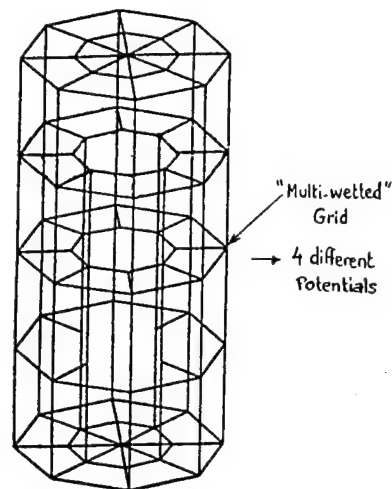


Figure 2 : Structure with inner walls
Definition of multipotential nodes

The main limitations in the FE model concern the elements which are recognized by the code. The tank structure may be modelled using any NASTRAN standard element, however only CTRIA3 and CQUAD4 elements are allowed wetted surfaces. Also the fluid domain has to be discretized with the following volume elements : CHEXA8, CPENTA and CTETRA.

It is worth noticing that any actual tank geometry can be described with these elements which are used on a standard basis by NASTRAN analysts.

The output of this phase is a number of binary files (NASTRAN OUTPUT4 format) containing the fluid and fluid/structure coupling matrices, and a modified data deck. All the data related to the fluid domain are deleted, except grid cards which may be referenced by the structure FE model. On the other hand new data are generated, essentially related to the matrices introduction procedure (partitioning vectors) and the free surface. In the same run a message file is created as well as special geometry data decks for checks and plotting purposes.

In phase 2, a modal extraction or dynamic response analysis may be directly performed using the data deck created in phase 1 and a specialized DMAP alter program for matrix introduction and operations.

It is clear that all the standard analyses - such as stress or acceleration calculations - can be run without restrictions.

5. TEST EXAMPLES

The accuracy of the determination of the sloshing modes has been checked on some simple examples where the theoretical solution is known (cubic or cylindrical reservoir). For instance the sloshing modes of a cubic tank with a free surface have been computed with only 8 fluid elements and yet the eigenvalues found at 1.98 Hz, 2.37 Hz and 2.93 Hz are very close to the theoretical eigen frequencies (Ref. 4).

Rigid body behaviour has also been checked. The strain energy of the rigid body modes is low and the rigid body mass matrix is fairly accurate (the error is of the order of 0.2 %).

The method has been tested in the case of the EUROSTAR tank developed by MATRA and SEP. This reservoir is composed of 3 parts : a cylinder and 2 hemispheres on each side. The bottom pole is fixed on the supporting structure, while the top pole is restrained only in the lateral directions (it is allowed to slide in the axial direction). The total mass of the structure when it is filled with liquid is approximately 340 kg.

The main sloshing modes are found at 1.73 Hz and the sloshing mass is 34 kg. These results are close to the values found by other means.

In the axial direction, the tank behaves like a single d.o.f. structure with a resonance at 59 Hz and a large modal mass (table 1, figure 3 and 4). The lateral behaviour is essentially governed by the position of the fixations (offset with respect to the poles). Again the modal mass of the first lateral mode at 68 Hz is a large fraction of the total mass.

The inertia I_z is very small as it should be. It is equal to the inertia of the structure, plus a limited amount of fluid due to the polygonal shape of the model. This example shows that reasonably good results can be obtained with a rather coarse model.

EUROSTAR MODEL
EIGENVALUES AND MODAL MASSES

MODAL MASS MATRICES : DIAGONAL TERMS							
UNITS : TIME = S LENGTH = M MASS = KG FORCE = N							
N°	FREQUENCY	T _X	T _Y	T _Z	R _X	R _Y	R _Z
1	1.73	11.54	34.24	0.00	0.82	0.28	0.00
2	1.73	33.91	11.45	0.00	0.28	0.82	0.00
3	2.08	0.00	0.00	0.03	0.00	0.00	0.00
4	2.10	0.00	0.00	0.00	0.00	0.00	0.00
5	2.11	0.00	0.00	0.00	0.00	0.00	0.00
6	2.36	0.00	0.00	0.00	0.00	0.00	0.00
7	58.62	0.00	0.00	335.73	0.00	0.00	0.00
8	68.20	268.83	24.64	0.00	0.04	0.45	0.00
9	68.21	24.63	268.75	0.00	0.46	0.04	0.00
10	115.66	0.00	0.00	0.00	0.00	0.00	0.68
11	141.19	0.00	0.00	0.00	0.00	0.00	0.00
12	141.19	0.00	0.00	0.00	0.00	0.00	0.00
MODAL MASS SUM		338.91	339.08	335.76	1.60	1.59	0.68
INERTIA MATRIX		342.48	342.64	341.24	8.98	8.98	0.68
PERCENTAGE		98.96	98.96	98.40	17.40	17.75	99.92

Table 1

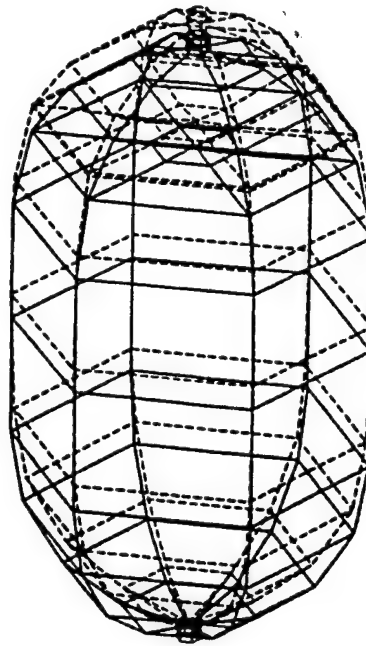


Figure 3 : EUROSTAR tank - Axial mode N = 59 Hz

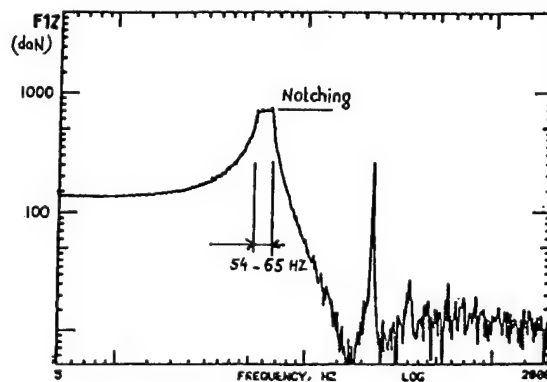


Figure 4 : EUROSTAR tank - Axial load at bottom pole measured during axial excitation test

6. CONCLUSION

The FE Software which has been developed and interfaced with MSC NASTRAN to solve fluid-interaction problems is general enough to be applicable to the analysis of most reservoirs. In a single analysis, sloshing and hydroelastic modes can be determined with good accuracy.

The tank geometry may be very complex, including several separate fluid regions, multi-wetted walls and free surface. The only potential limitations are inherent to the nature of the problem : coupling of the structural d.o.f's through the fluid may require rather large computer resources when important 3D models are developed.

Acknowledgements

This study was supported by ESA contract 6468/86/NL/PH.

References

1. M. BOUDET - Technical Note SEP TL+MM 7087/86
2. Final Report - Fluid Structure Interaction
TS/M 7804/89 JPF
3. SW SLOAN and M.F. RANDOLPH
Automatic element recording for finite element
analysis Int. J. for Numerical methods in eng.
Vol. 19, 1153-1181 (1983)
4. HN ABRAMSON (Ed). The dynamic behaviour of
liquids in moving storage containers Report N°
SP-106 NASA (1966).

N 92-23846

A SYMMETRIC COUPLING BETWEEN B.E.M AND F.E.M
FOR DYNAMICAL ANALYSIS OF SPACECRAFTA.OMRANI^{1,2}, M.A.HAMDI^{1,2}¹Université de Technologie de Compiègne -UTC,
DAVI Centre de recherche de Royallieu ; ²STRACO SA, Compiègne France

ABSTRACT

In modern spacecrafts a large percentage of the total mass consists of fluids. For satellites, this percentage can go up to 50%, and can be even higher for launcher elements (90% for Ariane V central body). To control the spacecraft behaviour the two following phenomena must be taken into account :

-Liquid sloshing for partially filled tanks.

-Hydroelastic modes.

To predict these phenomena, a convenient mathematical fluid modelling is required. In this study, we propose a new fluid modelling formulation based on coupled BEM - FEM technique in order to calculate sloshing modes.

Keywords: Boundary Element Method-BEM, Finite Element Method-FEM, Sloshing modes, Hydroelastic modes, variational formulation.

1. THE PROBLEM EQUATIONS

Let us consider a rigid container partially filled with a liquid (fig1). This liquid with a density ρ_f , is supposed inviscid and incompressible and is subjected to gravity acceleration g . Ω_f , Σ and Γ respectively denote the liquid domain, the wetted surface of the container and the free surface of the liquid in the equilibrium position. The liquid motion is supposed irrotational and small.

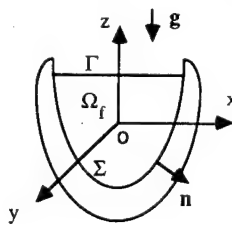


figure 1

For an harmonic motion of a pulsation ω , the potential displacement Ψ of the liquid satisfies the following eigenvalue problem:

$$\Delta \Psi = 0 \quad \text{in } \Omega_f \quad (1)$$

$$\frac{\partial \Psi}{\partial n} = 0 \quad \text{on } \Sigma \quad (2)$$

$$\frac{\partial \Psi}{\partial n} - \lambda \Psi = 0 \quad \text{on } \Gamma \quad (3)$$

(1) is Laplace's equation describing the incompressibility condition of the liquid.

(2) describes the fluid sliding on the wetted surface Σ .

(3) represents the waves equation on the free surface Γ , where:

$$\lambda = \frac{\omega^2}{g} \quad (4)$$

We can replace (3) by the following representation:

$$\left. \begin{aligned} \frac{\partial \Psi}{\partial n} &= \eta \\ \eta - \lambda \Psi &= 0 \end{aligned} \right\} \quad \text{on } \Gamma \quad (5)$$

where η is an auxiliary variable representing the elevation of the free surface above the plane Γ . η must satisfy:

$$\int_{\Gamma} \eta \, d\Gamma = 0 \quad (7)$$

This condition results from relation (1).

2. VARIATIONAL FORMULATION OF THE PROBLEM

2.1 Integral representation in the fluid domain

From Green's second identity and from boundary condition (2), point M in the fluid must satisfy :

$$\Psi(M) = \int_{\Gamma} \eta(Q) G(M,Q) \, d\Gamma(Q) - \int_{\Sigma} \Psi(Q) \frac{\partial G(M,Q)}{\partial n_Q} \, dS(Q) \quad (8)$$

where : $S = \partial\Omega_f = \Sigma \cup \Gamma$

$$G(M,Q) = \frac{1}{4\pi \|MQ\|} \quad \text{is the Green's function}$$

When M is a regular point on boundary S , the two following representations are satisfied:

$$\frac{1}{2} \Psi(M) = \int_{\Gamma} \eta(Q) G(M,Q) \, d\Gamma(Q) - v.p \int_{\Sigma} \Psi(Q) \frac{\partial G(M,Q)}{\partial n_Q} \, dS(Q) \quad (9)$$

$$\frac{1}{2} w(M) = v.p \int_{\Gamma} \eta(Q) \frac{\partial G(M,Q)}{\partial n_M} \, d\Gamma(Q) - p.f \int_{\Sigma} \Psi(Q) \frac{\partial^2 G(M,Q)}{\partial n_M \partial n_Q} \, dS(Q) \quad (10)$$

where:

$$w(M) = \frac{\partial \Psi(M)}{\partial n_M} = \begin{cases} 0 & \text{for } M \in \Sigma \\ \eta & \text{for } M \in \Gamma \end{cases} \quad (11)$$

(v.p) is Cauchy's principal value and (p.f) is Hadamard's finite part.

The solution of problem (1) -- (3) can be obtained using the collocation technique to solve the less singular equation (9), after taking into account of the equation (3). This gives:

$$\frac{1}{2} \Psi(M) + v.p \int_S \Psi(Q) \frac{\partial G(M,Q)}{\partial n_Q} dS(Q) = \lambda \int_{\Gamma} \Psi(Q) \frac{\partial G(M,Q)}{\partial n_Q} d\Gamma(Q) \quad (12)$$

The collocation method presents two main disadvantages:

- The first one is due to singularity of integrals.
- The second one is the non symmetrical final matrix.

2.2 Variational formulation of integral equations

To avoid these two disadvantages, the following variational equation is associated to equation (10) :

$$\mathbf{D}(\Psi, \Phi) - \mathbf{L}(\Phi) = 0 \quad \forall \Phi \in H^{1/2}(S) \quad (13)$$

where:

$$\mathbf{D}(\Psi, \Phi) = \int_{S \times S} \Psi(Q) \frac{\partial^2 G(M,Q)}{\partial n_M \partial n_Q} \Phi(M) dS(Q) dS(M) \quad (14)$$

$$\begin{aligned} \mathbf{L}(\Phi) &= \int_{S \times \Gamma} \eta(Q) \frac{\partial G(M,Q)}{\partial n_M} \Phi(M) d\Gamma(Q) dS(M) \\ &- \frac{1}{2} \int_{\Gamma} \eta(M) \Phi(M) d\Gamma(M) \end{aligned} \quad (15)$$

$\mathbf{D}(\Psi, \Phi)$ is a bilinear symmetric form and $\mathbf{L}(\Phi)$ is a linear form. As shown in (Ref. 1), $\mathbf{D}(\Psi, \Phi)$ is also given by:

$$\mathbf{D}(\Psi, \Phi) = - \int_{S \times S} (\mathbf{n}_M \wedge \nabla \Psi) \cdot (\mathbf{n}_Q \wedge \nabla \Phi) G(M,Q) dS(Q) dS(M) \quad (16)$$

This representation avoids the explicit evaluation of the finite part for the singular integral in equation (10).

For a known elevation of the free surface η , the potential Ψ makes the following functional stationary :

$$\mathbf{F}(\Psi) = \frac{1}{2} \mathbf{D}(\Psi, \Psi) - \mathbf{L}(\Psi) \quad (17)$$

In the same way, the following variational equation is associated to the equation (3),:

$$\mathbf{K}(\eta, \xi) - \omega^2 \mathbf{C}(\xi) = 0 \quad \forall \xi \in H^{1/2}(\Gamma) \quad (18)$$

where:

$$\mathbf{K}(\eta, \xi) = \rho_f g \int_{\Gamma} \eta(M) \xi(M) d\Gamma(M) \quad (19)$$

$$\mathbf{C}(\xi) = \rho_f \int_{\Gamma} \Psi(M) \xi(M) d\Gamma(M) \quad (20)$$

$\mathbf{K}(\eta, \xi)$ is a bilinear form and $\mathbf{C}(\xi)$ is a linear form.

The stationarity of the functional $\mathbf{F}(\Psi)$ eq. (16), allows to construct the application:

$$\eta \rightarrow \Psi = \mathbf{F}(\eta) \quad (21)$$

Green's identity allows to transform the linear form $\mathbf{C}(\xi)$ as:

$$\mathbf{K}(\eta, \xi) = \frac{1}{2} \rho_f \int_{\Gamma} \{ \mathbf{F}(\eta) \xi + \mathbf{F}(\xi) \eta \} d\Gamma \quad (22)$$

The solution (ω, η) of (1) -- (3) will be obtained by making the following functional stationary :

$$\mathbf{G}(\eta) = \mathbf{K}(\eta, \eta) - \omega^2 \mathbf{M}(\eta, \eta) \quad (23)$$

under condition:

$$\int_{\Gamma} \eta d\Gamma = 0 \quad (24)$$

$\mathbf{K}(\eta, \eta)$: is the potential energy caused by gravity field on the free surface Γ .

$\omega^2 \mathbf{M}(\eta, \eta)$: is the fluid kinetic energy.

3. DISCRETISATION

After discretisation of the boundary S by the finite element method and making the discrete form of the functional (17) stationary, the following algebraic system is obtained:

$$[\mathbf{D}] \{ \Psi /_S \} = [\mathbf{B} - 1/2 \mathbf{C}]^T \quad (25)$$

where:

$[\mathbf{D}]$: is the admittance operator given by discretisation of the bilinear form $\mathbf{D}(\Psi, \Psi)$. The $[\mathbf{D}]$ matrix is singular at first order.

$[\mathbf{B} - 1/2 \mathbf{C}]^T$: is the operator given by discretisation of the linear form $\mathbf{L}(\Psi)$.

After inverting $[\mathbf{D}]$ at the $(n - 1)$ order, the discrete form of application \mathbf{F} is obtained.

$$[\mathbf{F}] = [\mathbf{D}]^{-1} [\mathbf{B} - 1/2 \mathbf{C}]^T \quad (26)$$

The sloshing modes of the liquid are obtained by solving the following eigenvalue problem:

$$\left(\begin{bmatrix} \mathbf{K}_g & \mathbf{L} \\ \mathbf{L}^T & 0 \end{bmatrix} - \omega^2 \begin{bmatrix} \mathbf{M}_g & 0 \\ 0 & 0 \end{bmatrix} \right) \begin{Bmatrix} \eta \\ p \end{Bmatrix} = \{0\} \quad (27)$$

$[\mathbf{K}_g]$: is a stiffness matrix obtained by FEM discretisation of the bilinear symmetrical form $\mathbf{K}(\eta, \eta)$.

$[\mathbf{M}_g]$: is a mass matrix obtained by BEM discretisation of the bilinear symmetrical form $\mathbf{M}(\eta, \eta)$.

$$[\mathbf{M}_g] = 1/2 \{ [\mathbf{C}] [\mathbf{F}] + ([\mathbf{C}] [\mathbf{F}])^T \} \quad (28)$$

$[\mathbf{L}]$: is a vector describing the incompressibility condition equation (24)

p : is Lagrange's multiplier.

4. NUMERICAL RESULTS

Several geometrical container are investigated to calculate the sloshing modes, the simplest ones are the cube and the cylinder for which analytical solutions are known. The liquid is water with $\rho_f = 1000 \text{ kg/m}^3$ subjected to gravity $g = 10 \text{ m/s}^2$.

4.1 The cube example.

The discretisation of the boundary S is performed with quadrangular finite element.

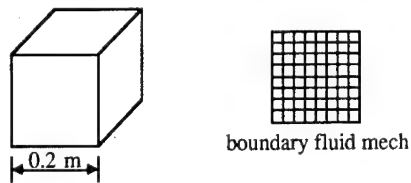
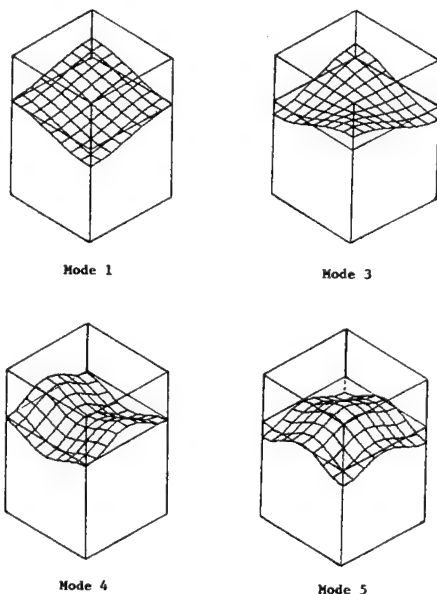


figure 2

Table 1: Numerical and analytical frequency .

Mode N°	Numerical Freq. (Hz)	Analytical Freq. (Hz)	%Error
1	1.97679	1.99098	0.71
2	1.97685	1.99098	0.71
3	2.3532	2.37179	0.78
4	2.8105	2.82093	0.36
5	2.8161	2.82093	0.17
6	2.9722	2.98278	0.35
7	2.9722	2.98278	0.35
8	3.3547	3.35469	0.00
9	3.4709	3.45494	-0.46
10	3.4709	3.45494	-0.46

MODESHAPES



4.2 The cylinder example.

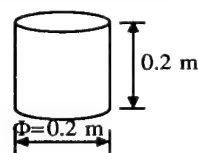
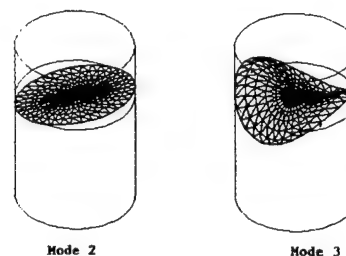


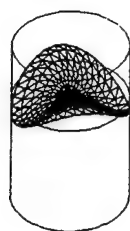
figure 3

Table 2: Numerical and analytical frequency .

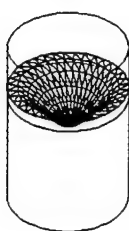
Mode N°	Numerical Freq. (Hz)	Analytical Freq. (Hz)	%Error
1	2.1651	2.1582	-0.32
2	2.1651	2.1582	-0.32
3	2.7922	2.7814	-0.38
4	2.7922	2.7814	-0.38
5	3.1159	3.1154	-0.02
6	3.2841	3.2621	-0.67
7	3.2841	3.2621	-0.67
8	3.7027	3.6700	-0.89
9	3.7027	3.6700	-0.89
10	3.7115	3.6748	-1.00

MODESHAPES





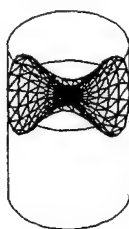
Mode 4



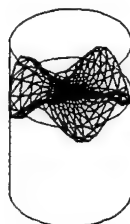
Mode 5



Mode 6



Mode 7



Mode 10

5. CONCLUSION

The variational formulation presented here avoids the discretisation of the fluid domain, and leads to symmetric fluid matrices. This can be solved by standard eigenvalue algorithms. Compared to FEM, this method has the main advantage of permitting an automatic condensation of the internal fluid degrees of Freedom.

This is performed by developing a prototype software which consists of a coupling between PATRAN for pre-post processing, ASKA for FEM structural computations and RAYON for BEM fluid modelling.

6. REFERENCES

1. M.A. HAMDI 1982, "Formulation variationnelle par équations intégrales pour le calcul de champs acoustiques proches et lointain" Thèse de Doctorat d'Etat U.T.C
2. A. OMRANI, M.A. HAMDI 1989, "Advances in Fluid Modeling using the Boundary Element Method Implementation of ASKA (WP1)" RFQ/3-6204/88/NL/PH - ESA Project
3. A. OMRANI, M.A. HAMDI 1990, "Advances in Fluid Modeling using the Boundary Element Method Implementation of ASKA (WP2)" Project RFQ/3-6204/88/NL/PH-ESA 90/03

**SESSION
2.4.B**

**DYNAMIC
IDENTIFICATION
I**

PRECEDING PAGE BLANK NOT FILMED

N 92-23847

84739

OPTIMAL EXCITER PLACEMENT AND FORCE VECTOR TUNING REQUIRED FOR EXPERIMENTAL MODAL ANALYSIS

Norbert Niedbal, Erhard Klusowski*

German Aerospace Research Establishment - DLR
Göttingen, Fed. Rep. of Germany

ABSTRACT

Experiences gained with present modal survey test techniques range from excellent results to unrealistic normal mode parameters. Present experimental modal analysis procedures suffer under the absence of a criterion for optimal exciter placement. In order to increase the reliability and robustness of modern identification methods, a technique for optimal exciter point selection was developed based on combinatorical optimization. Applying three force tuning procedures published in the past and a new method, reliable normal mode parameters of an analytical eleven-degree-of-freedom system and of a real structure could be determined, which verifies the performance of the proposed technique.

Keywords: structural dynamics, phase resonance, phase separation, normal mode parameters, optimal exciter points, optimal exciter forces.

1. INTRODUCTION

In order to improve the performance and efficiency of aerospace vehicles, the entire design has to be optimized. Reducing the structural masses while simultaneously increasing the payload and enlarging the dimensions are factors which add to the structural dynamic problems. Extensive finite-element investigations and modal survey tests provide the data base for analyzing and optimizing the dynamic behavior of such structures.

Therefore, modal survey testing plays an important role in the qualification procedure of these structures. In the past, most modal survey tests on large and complicated aerospace structures were performed mainly by means of the phase resonance method (sine dwell test). Excitation at the normal frequencies with an appropriated exciter configuration is the basic concept behind this test procedure (Refs. 1, 2). In this case, the structure under consideration will respond with only one real normal mode, thus presenting an opportunity to measure the real normal mode directly. However, the questions:

- How many exciters are necessary?
- Where to place the exciters?
- How to tune the exciter forces?

* Dr.-Ing. Norbert Niedbal, Dipl.-Ing. Erhard Klusowski: DLR - Dept. of Structural Dynamics

require a solution. Some force tuning procedures have been published which calculate the exciter force distribution by means of measured structural responses. But, in the absence of powerful microcomputers and optimal exciter point selection criteria, the application of these procedures within a modal survey test was difficult and time-consuming. Therefore, a computer-aided intuitive-iterative exciter force appropriation technique was applied (Refs. 3, 4). Powerful process computers now enable systematic selection of the optimal exciter points and calculation of appropriated exciter forces by means of measured response data. The *a priori* information necessary for these calculations can be gathered by means of various sweep-runs.

By solving the present shortcomings, a new computer-aided test management system can be realized which supports the test engineer. By employing the phase resonance method, the intuitive-iterative selection of excitation forces for the specific characteristics of the eigenmodes is supported and partially replaced by a systematic strategy. This should shorten the test duration while simultaneously retaining the high reliability and accuracy of the phase resonance method. Utilizing phase separation techniques, suitable excitation vectors are necessary as well, since only sufficiently excited eigenmodes can be calculated from complex structural response data by means of mathematical algorithms.

The new computer-aided test management system and the determination of optimal exciter points and exciter forces has been applied by simulating experimental modal analysis techniques on an analytical eleven-degree-of-freedom system and by performing a modal survey test on the real structure SIMOD. The results of all investigations and tests performed within this investigation document the necessity of optimal exciter placement and force vector tuning in order to obtain accurate and reliable normal mode parameters.

2. BASIC DYNAMIC EQUATIONS

Assuming a linear elastomechanical system with np physical-degrees-of-freedom (measurement points) and void of gyroscopic effects, the equilibrium of the inertial, stiffness, structural damping and external forces of a harmonically vibrating structure leads to the equations of motion

$$(-\omega^2 \mathbf{m} + j\mathbf{d} + \mathbf{k})\mathbf{u} = \mathbf{F} \quad (1)$$

The physical mass, damping and stiffness distributions are represented by the symmetric quadratic matrices \mathbf{m} , \mathbf{d} and

\mathbf{k} of order np . \mathbf{u} is the vector of the structural responses due to the external excitation vector \mathbf{F} , both of order np .

The complex structural response vector \mathbf{u} may be described by a series expansion of ng normal modes Φ_r of order np

$$\mathbf{u} = \Phi \mathbf{q} \quad (2)$$

Matrix Φ is the modal matrix. The ng normal modes in the frequency range of interest are equivalent to from one third to one tenth of np or even less. Column vector \mathbf{q} of the order ng comprises the generalized coordinates. Introducing Eq. (2) into Eq. (1) and premultiplying by Φ^T , Eq. (2) yields

$$(-\omega^2 \mathbf{M} + j\mathbf{D} + \mathbf{K})\mathbf{q} = \Phi^T \mathbf{F} \quad (3)$$

From a physical standpoint, the matrix transformation denotes a change from a force equation into an energy equation and a reduction of the physical-degrees-of-freedom from the order np to ng of the normal modes. According to Eq. (1), the matrices \mathbf{M} , \mathbf{D} and \mathbf{K} are called the generalized mass, generalized damping and generalized stiffness matrix, respectively. The orthogonality conditions of the normal modes require the diagonal generalized matrices \mathbf{M} and \mathbf{K} . On the other hand, real structures have physical damping distributions which may not be proportional to the physical mass and stiffness distributions. Therefore, the generalized damping matrix \mathbf{D} also has off-diagonal terms. Here, a structural damping law is assumed

$$\mathbf{D} = \Gamma \mathbf{K} \quad (4a)$$

which defines the global structural damping coefficient of the r -th normal mode in cases of proportional damping distribution as

$$\gamma_r = \frac{D_r}{K_r} \quad (4b)$$

and Eq. (3) reads

$$(-\omega^2 \mathbf{M} + \mathbf{K}(\mathbf{I} + j\Gamma))\mathbf{q} = \Phi^T \mathbf{F} \quad (5)$$

The measurement of the normal mode parameters, which control Eqs. (3) and (5), is accomplished by the modal survey test:

- normal circular frequencies ω_r ,
- normal modes Φ_r ,
- generalized masses M_r ,
- damping factors γ_r or the generalized damping matrix \mathbf{D} .

2.1 Phase Resonance Method

Considering real exciter forces with harmonic signals, the structure will also vibrate in a harmonic manner, but with a phase lag φ relative to the excitation which allows the separation of Eq. (3) into its real and imaginary parts:

$$(-\omega^2 \mathbf{M} \cos \varphi + \mathbf{K} \cos \varphi - \mathbf{D} \sin \varphi)\mathbf{q} = \Phi^T \mathbf{F} \quad (6a)$$

$$(-\omega^2 \mathbf{M} \sin \varphi + \mathbf{K} \sin \varphi + \mathbf{D} \cos \varphi)\mathbf{q} = 0 \quad (6b)$$

A phase shift of

- $\varphi = 90^\circ$ yields

$$-\mathbf{D} \mathbf{q} = \Phi^T \mathbf{F} \quad (7a)$$

$$(-\omega^2 \mathbf{M} + \mathbf{K})\mathbf{q} = 0 \quad (7b)$$

Eq. (7b) is satisfied if the excitation frequency is identical to the normal frequency and if the input energy of the

external excitation forces compensates for the structural damping energy, Eq. (7a). Eqs. (7a and b) define the phase resonance criterion. A proven tool to fulfill this objective is the indicator function (Ref. 3). More detailed information concerning the application of this phase resonance technique is given in Ref. 4.

All indicator function values determined in reference to the analytical investigations were calculated according to Breitbach (Ref. 3). As the modal survey test of the SIMOD structure was controlled by means of a small personal computer only, the indicator function values of the SIMOD structure were determined by means of

$$T = \frac{\sum_{i=1}^{np} |\text{im}(u_i)| (|\text{im}(u_i)| + |\text{re}(u_i)|)}{\sum_{i=1}^{np} (|\text{im}(u_i)| + |\text{re}(u_i)|)^2} \quad (8)$$

The T-function is defined in the region $0 \leq T \leq 1$ and reaches a value of 1 for the phase purity of a normal mode.

Four procedures were applied to determine the generalized mass values and damping factors while performing the modal survey test on the SIMOD structure. A detailed description of these methods is presented in Ref. 5.

2.2 Phase Separation Method

A broad spectrum of phase separation methods has been developed in the past in order to avoid the time-consuming force appropriation of the phase resonance method (sine dwell) and to reduce the required test effort and test period. The equations of motion are formulated in the phase separation methods such that only the damped or complex normal modes are identified, thus precluding a direct comparison and correlation with results of finite-element calculations. In order to eliminate this shortcoming, the complex normal modes have to be transformed into real normal modes (Refs. 6, 7).

All phase separation methods are similar in that they measure the complex responses and calculate the normal mode parameters by means of a numerical procedure. The method described in Ref. 7 was selected for this investigation. The complex response vector \mathbf{u} due to the excitation forces \mathbf{F} can be formulated by means of the normal mode parameters as follows:

$$\mathbf{u} = \sum_{r=1}^{ng} \frac{\Phi_r^N}{\lambda_r - \omega^2} \quad (9)$$

Normalization of the mode shapes Φ_r^N assumes that the input energy $\Phi^T \mathbf{F}$ divided by the generalized mass is equal to unity. λ_r represents the eigenvalues and ω is the circular frequency of the excitation. Eq. (9) yields in matrix notation

$$\mathbf{u} = \Phi^N \mathbf{S} \quad (10)$$

Taking a measurement on the left-hand side designated " α " and one on the right-hand side designated " β " of each normal frequency, Eq. (10) allows elimination of the unknown normal mode shapes

$$\mathbf{S}_\beta = \mathbf{S}_\alpha \cdot \mathbf{W} \quad (11)$$

Matrix \mathbf{W} contains the measured complex responses

$$\mathbf{W} = (\mathbf{u}_\alpha^T \mathbf{u}_\alpha)^{-1} \mathbf{u}_\alpha^T \mathbf{u}_\beta \quad (12)$$

The condition number of matrix W supplies information if ng normal modes were excited and included in Eq. (12). Here, close interaction with Asher's effective-degrees-of-freedom formulation (Ref. 8) can be noted. Eq. (11) allows formulation of the polynomial

$$P(\lambda) := ng - \sum_{s=1}^{ng} \sum_{r=1}^{ng} W_{rs} \frac{\lambda - (\omega_s^\beta)^2}{\lambda - (\omega_r^\alpha)^2} = 0 \quad (13)$$

The normal modes are determined by Eqs. (10). According to the normalization included in Eqs. (9), the generalized masses are calculated by

$$M_r = \Phi_r^T F_r \quad (14)$$

assuming renormalized normal modes, e.g. the largest deformation equal to 1.0.

3. DESCRIPTION OF THE TEST MODELS

3.1 Analytical Test Models

In order to check the performance of the proposed techniques, an analytical eleven-degree-of-freedom model was tuned to simulate a real structure's dynamic behavior. A sketch of this model is shown in Figure 1 and the physical mass and stiffness values are given in Table 1.

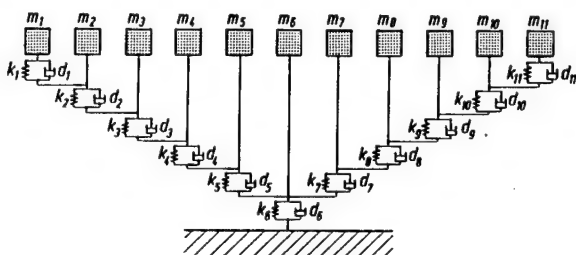


Fig. 1 Analytical Model with Eleven-Degrees-of-Freedom.

Nodal Point No.	Phys. Masses kg	Phys. Stiffnesses kg s ⁻²	Local Damping Factor		
			D1	D2	D3
1	1.0	2421.4	0.04	0.10	0.04
2	6.0	2989.4	0.04	0.04	0.05
3	1.0	3690.6	0.04	0.10	0.06
4	0.6	4556.3	0.04	0.04	0.07
5	1.0	5625.0	0.04	0.04	0.08
6	1.0	18000.0	0.04	0.10	0.09
7	1.0	5625.0	0.04	0.04	0.10
8	0.6	4556.3	0.04	0.04	0.11
9	1.0	3690.6	0.04	0.10	0.12
10	6.0	2989.4	0.04	0.04	0.13
11	1.0	2421.4	0.04	0.10	0.14

Table 1 Physical Masses, Stiffnesses and Structural Damping Factors of the Analytical Model.

As the damping distribution significantly influences dynamic behavior in modal survey testing, three structural damping distributions were taken into account to simulate

at least the fundamental effects. The physical damping values of the damping distributions D1, D2 and D3 are also presented in Table 1 and are pictured in Figure 2. The damping distribution D1 simulates damping proportional to the stiffness values. This decouples the dynamic Eq. (3) and sets up an ideal situation for modal survey testing. Damping distribution D2 counterfeits local damping concentrations, and distribution D3 has unsymmetric damping values compared to the symmetric stiffness distribution. Damping distribution D3 simulates the most difficult real structure situations and leads to complex normal modes when phase separation procedures are applied. Here, results of damping distributions D1 and D3 are presented only.

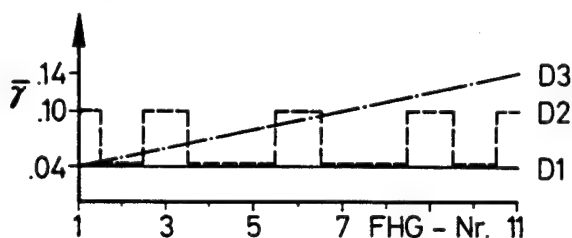


Fig. 2 Physical Damping Distributions D1, D2 and D3.

The appropriated normal frequencies, generalized masses and global structural damping factors are shown in Table 2. The normal frequencies show a frequency cluster of four normal modes in the frequency range between 7.7 cps and 9.3 cps. The real normal modes are illustrated in Figure 3; the deformation values are given in Table 3.

Mode No.	Normal Frequency Hz	Generalized Masses kg m ²	Global Damping Factor		
			D1	D2	D3
1	1.71	14.25	0.04	0.0618	0.09
2	1.82	13.85	0.04	0.0569	0.09
3	7.70	5.76	0.04	0.0675	0.09
4	8.18	3.00	0.04	0.0837	0.09
5	8.75	3.52	0.04	0.0877	0.09
6	9.26	5.64	0.04	0.0563	0.09
7	13.40	3.71	0.04	0.0661	0.09
8	14.62	3.86	0.04	0.0626	0.09
9	21.49	1.74	0.04	0.0683	0.09
10	22.13	1.87	0.04	0.0605	0.09
11	28.64	1.17	0.04	0.0687	0.09

Table 2 Normal Frequencies, Generalized Masses and Global Damping Factors of the Analytical Model.

1	-100	-100	-91	100	100	73	-4	-2	0	0	0
2	-95	-95	-3	-9	-25	-29	8	6	-1	1	0
3	-69	-66	83	-49	25	86	-100	-91	32	-29	2
4	-46	-40	100	-46	45	100	4	38	-100	100	-12
5	-27	-18	83	-28	43	67	85	100	33	-50	28
6	-10	0	35	0	19	0	43	0	34	0	-100
7	-27	18	83	28	43	-67	85	-100	33	50	28
8	-46	40	100	46	45	-100	4	-38	-100	-100	-12
9	-69	66	83	49	25	-86	-100	91	32	29	2
10	-95	95	-3	9	-25	29	8	6	-1	-1	0
11	-100	100	-91	-100	100	-73	-4	-2	0	0	0
1	2	3	4	5	6	7	8	9	10	11	

Table 3 Real Normal Modes of the Analytical Model.

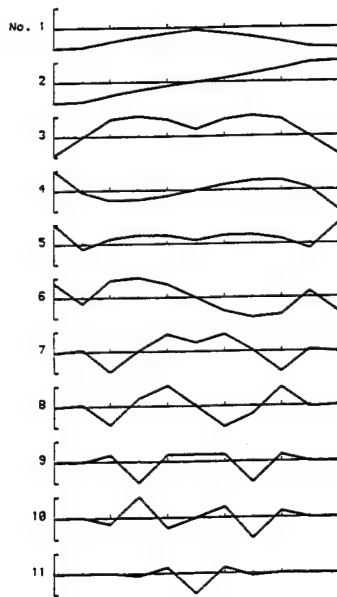


Fig. 3 Normal Modes of the Analytical Model.

Due to the proportionality of distribution D1, the generalized damping matrix is a unity matrix. The orthonormalized, generalized damping matrix of the physical damping distribution D3 is presented in Table 4 which shows significant damping coupling between neighboring normal modes. The maximum off-diagonal term is then equal to 37 between normal modes 5 and 6.

1	100										
2	-28	100									
3	0	-14	100								
4	7	0	37	100							
5	0	-6	0	-33	100						
6	-8	0	-5	0	-36	100					
7	0	-2	0	-8	0	17	100				
8	-2	0	6	0	4	0	-26	100			
9	0	0	0	0	0	1	0	8	100		
10	0	0	0	0	0	0	-4	0	25	0	100
11	0	2	0	2	-3	0	-5	0	9	100	
	1	2	3	4	5	6	7	8	9	10	11

Table 4 Orthonormalized Generalized Damping Matrix of Damping Distribution D3.

3.2 Real Test Model SIMOD

The overall dimensions of the SIMOD (Simple MODEL) structure are 1.10m (height), 1.05m (width) and 0.60m (depth). The total mass of the structure is about 206 kg. The material is aluminium and steel. Most panels are sandwich plates with aluminium sheets. The complete test structure clamped on a seismic block is shown in Figure 4.

To obtain modal densities similar to real satellite structures, the panels were equipped with a large number of rigid masses as shown in Figure 4. The "payload" mass of the SIMOD is equal to 129.3 kg; the total mass of the structure amounts to 71.7 kg leading to a mass ratio between payload and structure of 1.8:1.

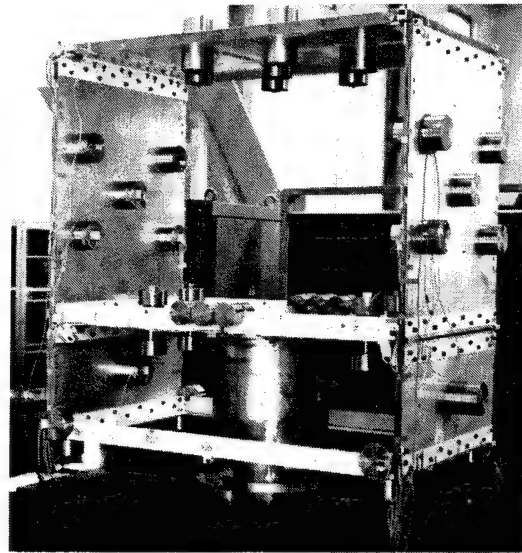


Fig. 4 SIMOD Test Structure.

4. ESTABLISHMENT OF AN A PRIORI DATA BASE

Computer-aided localization of the optimal exciter positions and calculation of exciter forces requires *a priori* information on the structural dynamic behavior of the structure. One possibility for collecting this data is to perform several sweep-runs and to store the structural deformations at the resonance or indicator function peaks (peak-picking method) as an approximation of the normal modes and normal frequencies. In order to create a reliable and adequate data base, the data set has to be condensed to the effective number of normal modes located in the frequency range of interest.

Some procedures have been published to determine the number of degrees-of-freedom and/or to correlate normal mode shapes. However, the original idea behind these procedures was not aimed at the establishment of a data base to realize a computer-aided test management system. The following criteria are taken into consideration:

- effective-degrees-of-freedom Ref. 8,
- orthogonality test,
- modal scale factor Ref. 9 and
- modal assurance criterion Ref. 10.

All criteria have to be assessed from an aerospace engineering point of view. Present and future complex spacecrafts are composed of many substructures, boxes, tanks, antennas etc., which may lead to many local normal modes in addition to some global normal modes. Due to the complexity of the structure and the limited number of deformation sensors, deformations of local modes are measured by one or two sensors only. All criteria presented above are global criteria taking into account all deformations simultaneously. Discrepancies for one or two deformations compared to the correlation of mode shape deformations for a hundred of measurement points will not result in a significant criterion value. Therefore, the relative deviation of all individual measurement stations

$$\varepsilon_{\text{rel}} = \frac{|\Phi_{is} - \Phi_{ir}|}{|\Phi_{is}| + |\Phi_{ir}|} \quad (15)$$

is calculated, where i represents a component of the s -th and r -th eigenvectors. For small normal mode components the absolute elevation ϵ_{abs} is regarded which means the numerator of Eq.(15) is taken into account only. If all normal mode components fulfill or violate a given value of ϵ , the two normal modes are defined as identical or different. By means of this difference criterion, all measured structural deformations are compared and the resulting independent displacement vectors with best indicator function values form the desired data base.

The performance of the proposed technique is documented with test results gathered on the real structure SIMOD. Nine exciter configurations have been selected to identify all normal modes in the frequency range up to 100 Hz. Based on this information, 129 peaks of the T-function have been localized, each of which indicates a normal mode. By means of the difference criterion, Eq.(15), all measured structural deformations have been analyzed and 21 independent deformation vectors have been identified. Table 5 presents the condensed listing of the identified normal modes. They are designated "SWP" (sweep) followed by two marks first indicating the number of the frequency sweep and secondly the number of the identified normal modes.

NO.	MODE	FREQUENCY	PRC	NC
1	SWP03-01	5.109	878	2
2	SWP01-02	5.530	805	0
3	SWP06-03	7.639	923	1
4	SWP01-04	9.748	929	2
5	SWP06-05	14.387	665	1
6	SWP09-06	16.918	800	4
7	SWP02-07	19.237	960	4
8	SWP09-08	34.420	920	3
9	SWP05-09	35.264	825	3
10	SWP08-10	56.984	789	6
11	SWP08-11	58.038	803	5
12	SWP07-12	62.677	918	3
13	SWP09-13	63.310	919	4
14	SWP01-14	71.955	839	3
15	SWP06-15	75.119	970	3
16	SWP05-16	77.016	949	4
17	SWP04-17	82.077	745	3
18	SWP05-18	85.030	906	5
19	SWP09-19	89.247	787	3
20	SWP03-20	95.362	835	4
21	SWP04-21	97.893	860	5

DISPLACEMENT VECTORS BEFORE CORRELATION : 129
DISPLACEMENT VECTORS AFTER CORRELATION : 21

Table 5 Condensed Data Set of Displacement Vectors of the SIMOD Structure Resulting from Sweep-Runs.

5. OPTIMAL EXCITER PLACEMENT

A literature study concerning exciter force tuning (Refs. 11-16). points at the influence of exciter placement and at the necessity of localizing optimal exciter points to guarantee reliable results from the force tuning procedures. Craig and Su (Ref. 17) stated in an investigation of multiple-shaker resonance testing: "... the combination (6, 8) produced very good second and third modes because each of these points is almost on a node line of one mode while it has large amplitude in the other mode". Salama, Rose and Garba presented a paper (Ref. 18) on the optimal placement of excitations and sensors to maximize the observed measurements by means of finite-element information. The task is solved by combinatorial optimization

based on kinetic and strain energy criteria. The method for optimal exciter placement proposed here is based on the formulation described in Refs. 14, 15. In order to excite only one normal mode, the input energy is tuned requiring

$$\tilde{\Phi}^T \mathbf{F}_r = \begin{Bmatrix} 0 \\ 0 \\ 1 \\ 0 \\ 0 \end{Bmatrix} \quad (16)$$

The necessity of tuning the exciter forces, even for phase separation test techniques, is neither generally accepted today nor taken into consideration in present modal survey testing. The literature study shows clearly that all publications concerning exciter force tuning focus exclusively on the problem of force appropriation with the sine-dwell method.

The basic idea behind the phase separation test technique is to avoid tuning of the exciter forces and to decompose the complex structural responses into normal mode parameters by means of numerical algorithms. As most arbitrary exciter configurations produce complex structural responses, phase separation test techniques are assumed to be much simpler and more efficient. However, it is essential not to produce complex structural responses only. The phase separation method (Refs. 4, 7) applied in this investigation - and possibly all phase separation procedures - requires the excitation of all normal modes of interest with amplitudes which allow correct measurements. Normal modes outside the frequency range of interest must not respond or the responses must be negligible compared to the structural responses of interest. This criterion is difficult to control and, therefore, remains uncontrolled in most of today's modal survey testing. The expansion of Anderson's method, Eq. (16), now offers an opportunity to control the input energy of the normal modes which leads to

$$\tilde{\Phi}^T \mathbf{F} = \begin{Bmatrix} 0 \\ 1 \\ 1 \\ 1 \\ 0 \end{Bmatrix} \quad (17)$$

As the formulation is identical to the one applied for phase resonance testing, Eq. (16), optimal exciter point localization is identical for both phase resonance and phase separation methods.

If, for example, five normal modes have to be taken into account, then the best combination of five observation/control points must be sought. Assuming, for example, $np = 50$ measurement points (and the same number of potential exciter points) and $ng = 5$ normal modes, the maximum number of combinations is equal to

$$\binom{np}{ng} = \frac{np!}{(np-ng)! ng!} = \frac{50!}{(50-5)! 5!} = 2.1 \cdot 10^6 \quad (18)$$

Here, the optimal combination of the ng excitation points is selected by combinatorial optimization applying the condition numbers of the $ng \times ng$ submatrices $\tilde{\Phi}^n$ as criterion.

5.1 Results of the Analytical Model

The isolation of normal modes 1 and 2 results in 55 exciter point combinations acc. to Eq. (18) which are presented in Table 6 combined with the appertaining condition numbers (multiplied by a factor of 1000). The optimal combination is given by the condition number 1.0 (no. 55) and

CONDITION NUMBERS

1	3	3	25	25	28	28	47	47	72	72	75	75	116	116	163	163	187	187	190	190	559	559	652
24	652	687	687	705	705	707	707	927	965	965	976	976	981	981	982	982	989	995	995	997	997	997	997
47	998	1000	1000	1000	1000	1000	1000	1000	1000	1000													

OPTIMAL EXCITER POINTS

1 2	10 11	1 2	9 10	2 3	9 11	1 3	8 9	3 4	8 10	2 4	8 11	1 4	4 5	7 8	3 5	7 9	2 5	7 10	1 5	7 11	5 6	6 7	4 6
	1	2	3	4	5	6	7	8	9	10	11	12	13	14	15	16	17	18	19	20	21	22	23
1 2	6 8	3 6	6 9	2 6	6 10	1 6	6 11	5 7	4 7	5 8	3 7	5 9	2 7	5 10	5 11	1 7	4 8	4 9	3 8	4 10	2 8	4 11	1 8
	24	25	26	27	28	29	30	31	32	33	34	35	36	37	38	39	40	41	42	43	44	45	46
1 2	3 9	2 9	3 10	1 9	3 11	2 10	2 11	1 10	1 11														
	47	48	49	50	51	52	53	54	55														

Table 6 Condition Numbers and Exciter Point Combinations of the Normal Modes 1 and 2.

CONDITION NUMBERS

1	576	576	587	587	607	607	610	610	631	631	636	636	641	641	654	671	671	677	677	687	687	691	691
24	711	711	721	721	723	723	724	724	761	761	781	781	787	787	885	907	910	910	921	921	927	927	928

OPTIMAL EXCITER POINTS

1	1	1	2	2	1	2	2	1	1	1	1	1	1	1	2	1	1	1	2	1	2	1	2
2	5	6	3	5	6	3	3	4	3	2	5	2	4	2	3	4	6	5	5	3	5	4	5
3	6	7	7	9	9	6	8	9	10	9	10	7	10	8	9	6	8	7	7	7	9	7	8
4	11	11	10	10	11	10	10	10	11	11	11	11	11	11	10	11	11	10	11	10	11	10	11
	1	2	3	4	5	6	7	8	9	10	11	12	13	14	15	16	17	18	19	20	21	22	23
1	3	2	3	1	3	2	1	2	1	2	1	2	1	2	1	1	1	1	1	1	1	1	1
2	3	4	3	6	5	4	4	4	3	3	4	3	5	3	3	5	3	4	3	5	4	5	4
3	8	9	6	9	8	7	8	8	9	9	9	8	9	7	9	7	8	9	7	9	7	8	8
4	10	11	11	11	10	11	10	11	10	11	10	11	10	11	11	11	11	11	11	11	11	11	11
	24	25	26	27	28	29	30	31	32	33	34	35	36	37	38	39	40	41	42	43	44	45	46

Table 7 Condition Numbers and Exciter Point Combinations of the Normal Modes 3-6.

the measurement points 1 and 11 are the appropriated points. As shown in Table 6, all exciter point combinations from 31-55 result in condition numbers larger than 0.92, which indicates acceptable exciter placement. All these exciter point combinations include one exciter point to the left and one to the right of the symmetry axis. The combinations from 21-30 give condition numbers from 0.71 to 0.56. Here, all combinations include measurement point no. 6 which is located in the nodal line of normal mode no. 2. The combinations from 1-20 show condition numbers smaller than 0.2, as both exciter points are located on either the left or the right side only. The examples demonstrate the performance of the proposed technique and correlate with experiences from modal testing.

For isolation of normal modes no. 3-6, the best exciter point combination has to be selected from 330 possible exciter point combinations. Table 7 gives the best 46 condition numbers and the pertaining exciter point combinations. The highest condition number is 0.928 and the optimal exciter points are the nodal points 1, 4, 8 and 11. The results of the four-normal-mode example demonstrate the complexity of optimal exciter point selection but still allow a physical interpretation.

Due to space limitations, detailed results on the real test model SIMOD are not presented here. The global results of the modal survey test will prove the proposed technique.

6. TUNING OF THE EXCITER FORCES

In order to assess the potential of published exciter force appropriation techniques, various proposals and methods have been analyzed (Refs. 11-16). All procedures aim at force appropriation for application of the sine-dwell test only. Some of the procedures are based on similar concepts and/or formulations thus allowing a condensed presentation.

6.1 Method of Traill-Nash, Asher and Ibáñez

One of the most original contributions concerning force appropriation is given in Refs. 11, 12. Exciting the structure at a normal circular frequency ω , with ng linear independent exciter forces \mathbf{F}_r , defines the complex response matrix \mathbf{u} . According to the phase resonance criterion, Eq. (7), the real parts \mathbf{u}' of the responses must vanish. This allows the formulation of ng linear, homogeneous equations with ng unknowns \mathbf{a} , as

$$\mathbf{u}' \mathbf{a}_r = 0 \quad (19)$$

Eq. (19) has a solution, since \mathbf{u}' is of the order $(ng - 1)$ which leads to the required force distribution

$$\mathbf{F}_r = \mathbf{a}_r^T \tilde{\mathbf{F}}_s \quad (20)$$

The solution of Eq. (19) requires a minimum of ng observation (measurement) points and Eq. (20) demands ng exciter vectors \mathbf{F}_i . Hereafter, this technique will be called Asher's method.

6.2 Method of Morosow/Ayre and Anderson

Another approach to shaker force appropriation based on the imaginary part of the structural responses was developed by Morosow and Ayre (Ref. 14) and by Anderson (Ref. 15). Both procedures are based directly on the modal force formulation (input energy). The determination of a force vector \mathbf{F} , over a set of modes is quantified by a finite value of 1.0 for the input energy of the target mode and by an input energy value of zero for every other mode in the set. This requirement can be expanded to define similar force vectors for the successive isolation of each mode in the group.

$$\tilde{\Phi}^{*T} \mathbf{F} = \mathbf{I} \quad (21)$$

A solution for Eq. (21) can be obtained by inversion

$$\mathbf{F} = (\tilde{\Phi}^{*T})^{-1} \quad (22)$$

Here, this procedure will be labelled Anderson's method.

6.3 Method of Hunt, Vold, Peterson and Williams

This method (Ref. 16) defines the norms for the real response and for the total response by

$$\|\mathbf{u}'\|^2 = \mathbf{u}'^T \mathbf{m} \mathbf{u}' \quad (23a)$$

$$\|\mathbf{u}' + j\mathbf{u}''\|^2 = \mathbf{u}'^T \mathbf{m} \mathbf{u}' + \mathbf{u}''^T \mathbf{m} \mathbf{u}'' \quad (23b)$$

to formulate a criterion. A force vector \mathbf{F} must be found such that the real response, Eq. (23a), is minimized compared to the total response, Eq. (23b). The indicator function formulation leads to the formulation

$$[\mathbf{H}'^T \mathbf{m} \mathbf{H}' - \lambda(\mathbf{H}'^T \mathbf{m} \mathbf{H}' + \mathbf{H}''^T \mathbf{m} \mathbf{H}'')] \mathbf{F} = 0 \quad (24)$$

Plotting the smallest eigenvalue versus the excitation frequency gives the multivariate mode indicator function and thus indicates the normal frequencies, a technique which is also proposed in Refs. 12, 13, 19. The ability to take all structural responses into account simultaneously is an important advantage of this force tuning procedure, which will be called Hunt's method.

6.4 Additional Method

Based on the literature study, three basic exciter force tuning procedures have been identified. Asher's method proposes exciter force appropriation by suppressing the real part of the structural responses. The method proposed by Morosow/Ayre and Anderson takes into consideration the imaginary parts of the structural responses only. Modal survey testing, applying the phase resonance method, demands consideration of both requirements. Thus, the following formulation has been developed

$$[\tilde{\Phi}^{*T}; \tilde{\Phi}^{*T}] \{\mathbf{F}\} = \begin{Bmatrix} 0 & 0 \\ 0 & 0 \\ 0 & 1 \\ 0 & 0 \\ 0 & 0 \end{Bmatrix} \quad (25)$$

Eq. (25) is a complex linear equation system which also leads to complex exciter forces. An analytical solution may

be achieved by adding the condition of a real exciter vector, but eigenvalue formulations (Refs. 12, 13, 16, 19) seem more promising. Therefore, taking into account Eq. (25) while minimizing the input energy of the real part components and establishing the input energy of the objective normal mode, the eigenvalue formulation

$$\min \Rightarrow \frac{\tilde{\Phi}'^T \mathbf{F}}{\tilde{\Phi}^{*T} \mathbf{F}} = \lambda \quad (26)$$

can be derived. However, Eq. (26) considers the structural responses of the excitation points only. In order to improve this formulation, a least square solution is applied and yields

$$(\tilde{\Phi}'^T \tilde{\Phi}' - \lambda \tilde{\Phi}^{*T} \tilde{\Phi}^*) \mathbf{F} = 0 \quad (27)$$

Comparing Eq. (27) to Eq. (24) from Hunt's method shows that both equations are based on similar formulations. However, Eq. (27) does not require physical mass values and represents a simpler formulation. In the comparison of selected force tuning procedures, the method given by Eq. (27) is called Niedbal's method.

7. COMPARISON OF MODAL SURVEY TEST RESULTS

7.1 Results Derived from the Analytical Model

As the normal modes are vectors, which precludes an efficient comparison, two criteria are applied in order to condense the test information. A proven tool for controlling the phase resonance criterion is given by the indicator function (Ref. 3). As the correct normal modes of the analytical model are known (designated by "a"), the averaged error of the "experimental" normal modes (designated by "e") can be used to control accuracy by

$$\varepsilon_r = \frac{1}{np} \sum_{i=1}^{np} |\Phi_{ir}^e - \Phi_{ir}^a| \quad (28)$$

7.2 Phase Resonance Method

The isolation of one normal mode in the neighborhood of three others is simulated in the frequency band from 7.7-9.3 Hz. Figures 5 and 6 depict the indicator function values and the mean error value of the four normal modes vs. the condition number of the exciter point deformations. The values equal to 23, 51, 74 and 100% of the optimal condition number are selected for comparison. The exciter point combinations are presented in Table 7.

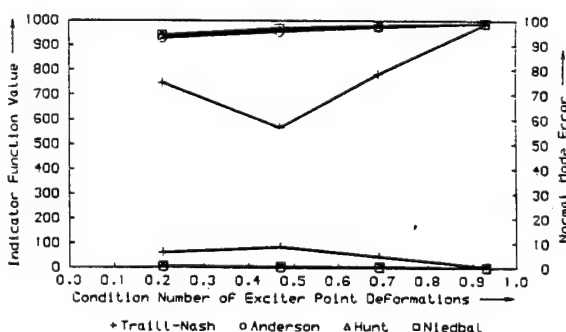


Fig. 5 Indicator Function Values and Normal Mode Errors of Normal Modes 3-6 (Damping Distribution D1).

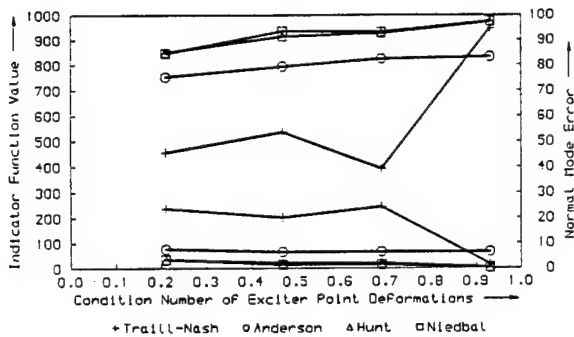


Fig. 6 Indicator Function Values and Normal Mode Errors of Normal Modes 3-6 (Damping Distribution D3).

Analyzing the results of the damping distributions D1 and D3, the Traill-Nash procedure fails if non-appropriated exciter point combinations are selected. Anderson's method provides considerably better values and the methods of Hunt and Niedbal are the most successful. The largest mean error value of the normal modes reaches 3.3% for Hunt and Niedbal's method simulating damping distribution D3 and an exciter point combination which produces a value equal to 23% of the optimal condition number only. Here, Anderson's method produces a mean error value of 7.6%. The indicator function determines values between 937 and 733 for Hunt's and Niedbal's methods and between 825 and 628 for Anderson's procedure, thus indicating larger mode shape errors.

7.3 Phase Separation Method

A first approximation of the exciter forces can be obtained from Eq. (7a). Assuming constant damping values, Eq. (7a) gives

$$\mathbf{F}_i = \sum_{r=1}^{n_g} \tilde{\Phi}_{ir} \quad (i = 1, 2, 3, \dots, np) \quad (29)$$

which supplies a moderate estimation of the exciter forces. Here, the number of exciter forces is equal to np . This exciter configuration will be denoted E1. The exciter forces resulting from Eq. (17) are designated E2.

The isolation of four normal modes within a frequency range of 1.6 Hz, including proportional as well as non-proportional damping, may be encountered in real test situations. The results of the isolation process of normal modes nos. 3 - 6 are presented in Tables 8 and 9 for the damping distributions D1 and D3.

Table 8 shows test results with damping distribution D1. Applying exciter configuration E1, the indicator function values denote excellent separation of the normal modes but the damping factors present errors of up to 55%. The orthonormalized generalized damping matrix, which is a unity matrix for damping distribution D1, presents off-diagonal values of up to 42%. The errors of the normal mode deformations (deformations larger than 0.1) reach 5.75%. By virtue of these normal mode errors, the generalized mass data show discrepancies of up to 3.8%. Applying the tuned exciter configuration E2, the phase separation method determines correct normal mode parameters. Complete phase purity is shown and a unity matrix is even determined for the generalized damping matrix.

EXCITER CONFIG. E1				EXCITER CONFIG. E2			
NORMAL FREQUENCIES				NORMAL FREQUENCIES			
7.70	8.18	8.75	9.26	7.70	8.18	8.75	9.26
DAMPING FACTORS				DAMPING FACTORS			
.031	.041	.053	.018	.040	.040	.040	.040
MODAL MATRIX				MODAL MATRIX			
-92	100	100	74	-91	100	100	73
-4	-9	-24	-27	-3	-9	-25	-29
82	-49	26	87	83	-49	25	86
100	-45	46	100	100	-46	45	100
83	-27	43	67	83	-28	43	67
34	0	18	0	35	0	19	0
82	27	42	-67	83	28	43	-67
99	45	43	-100	100	46	45	-100
82	48	24	-85	83	49	25	-86
-3	9	-24	29	-3	9	-25	29
-91	-100	98	-73	-91	-100	100	-73
GEN. MASSES				GEN. MASSES			
5.68	2.93	3.45	5.86	5.76	3.00	3.52	5.64
GEN. DAMPING MATRIX				GEN. DAMPING MATRIX			
100				100			
7	100			0	100		
14	34	100		0	0	100	
28	42	9	100	0	0	0	100

Table 8 Test Results for Normal Modes 3-6 with Physical Damping Distribution D1.

EXCITER CONFIG. E1				EXCITER CONFIG. E2			
NORMAL FREQUENCIES				NORMAL FREQUENCIES			
7.70	8.11	8.67	9.13	7.70	8.18	8.75	9.26
DAMPING FACTORS				DAMPING FACTORS			
.089	.313	.421	.325	.090	.090	.090	.091
MODAL MATRIX				MODAL MATRIX			
-89	82	75	100	-91	100	100	73
-5	-13	-16	-22	-3	-9	-25	-29
70	-60	-4	89	83	-49	25	86
89	-52	13	95	100	-46	45	100
74	-34	20	68	83	-28	43	67
32	-2	16	4	35	0	18	0
81	26	56	-48	83	28	43	-67
100	47	68	-78	100	46	45	-100
83	49	46	-68	83	49	25	-85
-2	10	-29	20	-3	9	-25	29
-92	-100	100	-48	-91	-100	100	-73
GEN. MASSES				GEN. MASSES			
5.02	2.71	2.20	4.06	5.75	3.00	3.53	5.64
GEN. DAMPING MATRIX				GEN. DAMPING MATRIX			
100				100			
26	100			36	100		
-4	-2	100		0	-33	100	
-2	-31	-35	100	-6	-1	-36	100

Table 9 Test Results for Normal Modes 3-6 with Physical Damping Distribution D3.

The results of damping distribution D3 are shown in Table 9. With the exciter configuration E1, the normal frequency of mode no. 6 is shifted by -1.4%. The damping factors show values up to 360% larger than the correct ones. The maximum difference between the corresponding off-diagonal elements of the orthonormalized generalized damping matrix is equal to 33. Exciting by means of exciter configuration E2, the normal frequencies are correct. Even the damping factors are much closer to the correct ones, the fourth damping value has a maximum error of 1.6%. The off-diagonal elements of the damping matrix differ by only one digit. Local mode shape errors resulting from exciter forces E1 reach values greater than 100%. On the other hand, the normal modes resulting from the tuned exciter forces E2 produce mode shape errors of less than 1%.

7.4 Results Derived from the Real Test Structure

Three modal survey tests were executed by applying:

1. The present approach of phase resonance method (sine-dwell),
(The results of this test are labelled "DWELL".)
2. the Sine Dwell test with Optimized Exciter Points and Forces and
(The normal mode parameters resulting from this test are called "DOEPF".)
3. the phase separation technique.
(The results of this test are designated "SEPAR".)

Based on the sweep-run information, Table 5, 21 normal modes were measured. The condensed data set created by the computer-aided test management system is given in Table 10 which corresponds to Table 5. Here, those normal modes with the best phase purity result from the DWELL (2 normal modes), DOEPF (12 normal modes) and SEPAR (7 normal modes) tests. The example demonstrates the feasibility of improving test management by means of computer-aided testing.

NO.	MODE	FREQUENCY	PRC	NC
1	DOEPF-01	5.292	982	2
2	DWELL-02	5.738	929	2
3	DOEPF-03	7.980	968	2
4	DOEPF-04	10.061	982	2
5	SEPAR-05	14.691	990	3
6	DOEPF-06	17.167	988	3
7	DOEPF-07	19.363	988	3
8	SEPAR-08	34.827	995	3
9	SEPAR-09	35.362	991	3
10	SEPAR-10	56.918	994	3
11	DOEPF-11	58.150	991	3
12	DWELL-12	63.296	978	3
13	SEPAR-13	63.913	979	3
14	DOEPF-14	72.156	956	3
15	DOEPF-15	75.816	981	3
16	DOEPF-16	78.033	972	3
17	SEPAR-17	83.116	968	3
18	DOEPF-18	86.147	972	3
19	DOEPF-19	89.781	987	3
20	SEPAR-20	95.794	968	3
21	DOEPF-21	97.138	980	3

DISPLACEMENT VECTORS BEFORE CORRELATION : 80
DISPLACEMENT VECTORS AFTER CORRELATION : 21

Table 10 Condensed Data Set of Normal Modes of the SIMOD Structure Resulting from SWEEP, DWELL, DOEPF and SEPAR Tests.

The normal frequencies of the DWELL, DOEPF and SEPAR tests resulted in excellent agreement. Only the normal modes nos. 9, 11 and 18-21 presented some discrepancies which were investigated by a linearity test. These normal frequencies showed variations of up to 1.75 cps depending on the vibration amplitudes, which may serve as a possible explanation.

All T-function values, Eq. (8), are larger than 900, which indicates good or even excellent isolation of the individual normal modes. While the DWELL method shows some smaller values, the DOEPF and SEPAR techniques reached values larger than 975.

The generalized mass values are depicted in Figure 7. Taking into account the total mass of the test structure (206 kg) and the normalization of the maximum deformation of normal modes to 1.0 m, the generalized mass values of normal modes nos. 2, 3 and 5 do not represent correct values for the test structure. The generalized masses no. 1-6 are influenced by the co-vibrating rigid body modes of the seismic block. All other values show excellent conformity when considering that generalized mass measurements are very sensitive. Most values lie within a $\pm 10\%$ tolerance range.

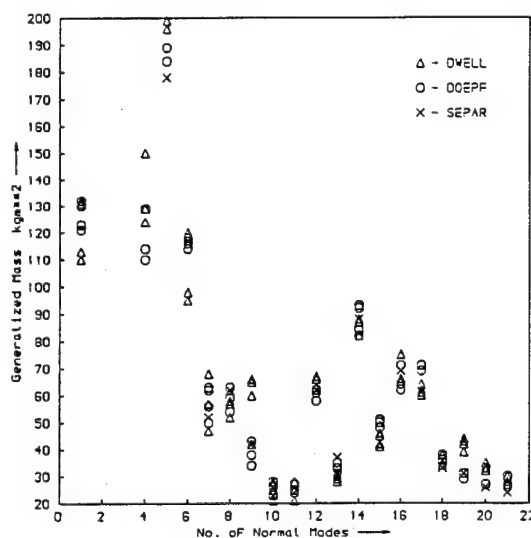


Fig. 7 Generalized Mass Values of the SIMOD Structure Resulting from the Tests DWELL, DOEPF and SEPAR.

The structural damping factors are shown in Figure 8. Most values show excellent conformity and acceptable tolerance ranges. The damping factors of normal modes nos. 1-3 indicate co-vibration of the rigid body modes of the seismic block, as these factors show much higher damping values due to the rubber suspension of the seismic block. Taking into account the results of the analytical test model and comparing with experiences gained from other test structures (Ref. 20), the proposed optimal exciter placement and exciter force tuning is proved.

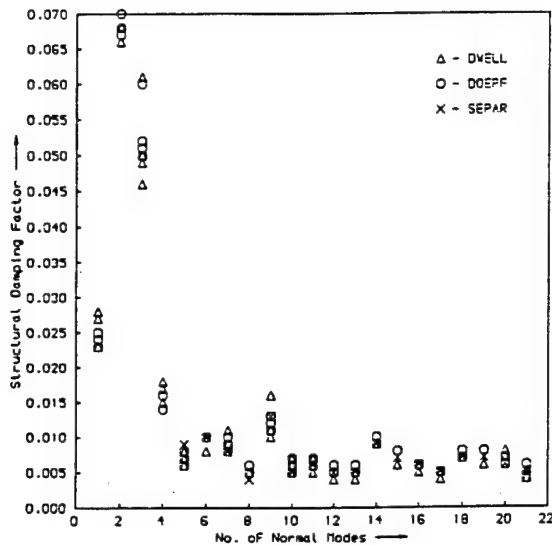


Fig. 8 Structural Damping Factors of the SIMOD Structure Resulting from the Tests DWELL, DOEPF and SEPAR.

The normal mode shape deformations are not presented here. A global comparison of the normal mode shapes resulting from the individual tests is used to indicate the performance of the test techniques applied. To enable a global comparison of the normal modes, the value of

$$\varepsilon = \frac{2 \sum_{i=1}^{np} |\Phi_{i1} - \Phi_{i2}|}{\sum_{i=1}^{np} (|\Phi_{i1}| + |\Phi_{i2}|)} \quad (31)$$

is used for comparison. The error criteria $\varepsilon_1 - \varepsilon_3$ multiplied by 100 are defined as follows:

- ε_1 - comparison of DWELL and DOEPF normal modes,
- ε_2 - comparison of DOEPF and SEPAR normal modes and
- ε_3 - comparison of SEPAR and DWELL normal modes,

which are presented in Table II. As an adequate seismic block was not available, the rigid body modes of the seismic block significantly influenced the normal modes of the test structure up to 10.0 Hz. For this reason, the phase separation method could not be applied in this frequency range. With the exception of normal mode no. 9 and with limitations on normal modes nos. 20 and 21, most error values are within a 4% tolerance range, which may be purely attributable to measurement accuracy. Normal mode no. 9 shows much larger discrepancies. The non-linearity test showed close interaction of both normal modes nos. 8 and 9. However, phase separation methods do not take into account the non-linearity effects which could provide a possible explanation. Larger non-linearity influences were also determined for modes nos. 20 and 21.

no. of normal mode	ε_1	ε_2	ε_3
1	0.6		
2	4.1		
3	3.5		
4	2.2		
5	0.8	3.1	2.7
6	0.6	0.8	1.1
7	2.2	2.7	3.9
8	0.4	2.0	1.9
9	11.9	25.6	9.5
10	3.1	0.7	2.7
11	1.8	1.6	3.3
12	2.1	1.8	2.5
13	2.6	1.7	2.1
14	3.5	3.4	5.5
15	1.8	2.9	3.4
16	1.9	3.7	4.6
17	3.0	0.9	3.3
18	2.1	4.0	3.1
19	4.2	3.4	2.6
20	10.9	4.4	14.1
21	4.2	6.7	9.3

Table II Global Error Values of the Normal Modes Measured with the Test Methods DWELL, DOEPF and SEPAR.

8. CONCLUSION

In order to overcome some shortcomings of present experimental modal analysis techniques, this investigation attacks the task of localizing optimal exciter points and determining adequate exciter forces by applying the phase resonance (sine-dwell test) as well as the phase separation test technique.

The optimal exciter point combinations were selected by combinatorial optimization applying the condition number of the exciter point deformation matrix as a criterion. Based on a literature study, three procedures for exciter force appropriation were selected for application of the phase resonance method and tested in combination with a new method developed in this investigation. As exciter force tuning is not regarded in present phase separation test techniques, an expansion of Morosow's/ Anderson's method is proposed as a solution.

Tests were performed on an eleven-degree-of-freedom system and on the real structure SIMOD. The test results on the incomplete analytical model show the feasibility of calculating the appropriated exciter forces required for phase resonance as well as phase separation applications. The complete test concept was tested on the real structure SIMOD. The computer-aided test management system, ranging from sweep-run analysis to normal mode shape correlation of individual test results, functioned successfully. Most normal mode parameters measured by means of the classical approach and the improved test techniques showed excellent conformity, which verifies the proposed techniques. At the same time it documents that the phase separation technique determines accurate and reliable normal mode parameters only if optimal exciter points are selected and suitable exciter forces are applied.

The concept of computer-aided test management may help to reduce the test periods and to improve the accuracy and reliability of the test data required for combining and updating finite-element models (Ref. 21). The technique of optimal observation point selection can even be applied during test preparations to determine the optimal meas-

urement stations based on results from finite-element calculations. Moreover, the selection of optimal observation points and tuning of the exciter forces may even be of interest for control purposes.

9. ACKNOWLEDGEMENT

This work was supported by the European Space Agency/European Space Research and Technology Centre in Noordwijk, The Netherlands. The interest and support of the contract monitors, Dr. Stavrinidis and Mr. Brunner, are gratefully acknowledged.

10. REFERENCES

1. Kennedy C C & Pancu C D 1947, Use of Vectors in Vibration Measurement and Analysis, *Journ. Aeron. Sci.*, 14, 603-625.
2. Lewis R C & Wrisley D L 1950, A System for the Excitation of Pure Modes of Complex Structures, *Journ. Aeron. Sci.*, 17, 705-722.
3. Breitbach E 1974, *Neuere Entwicklungen auf dem Gebiet des Standschwingungsversuchs an Luft- und Raumfahrtkonstruktionen*, VDI-Bericht 221, 33-40.
4. Niedbal N & Hüners H 1982, Modal Survey Testing for System Identification and Dynamic Qualification of Spacecraft Structures, *ESA Journal*, 6.
5. Niedbal N & Klusowski E 1989, Die Ermittlung der generalisierten Masse und des globalen Dämpfungsbeiwertes im Standschwingungsversuch, *Z. Flugwiss. Weltraumforsch.*, 13, 91-100.
6. Niedbal N 1984, Analytical Determination of Real Normal Modes from Measured Complex Responses, *AIAA Dynamics Specialists' Conference*, Palm Springs, Calif., USA, Paper No. 84-0995.
7. Niedbal N 1986, Advances in Ground Vibration Testing Using a Combination of Phase Resonance and Phase Separation Methods, *Proc. 11th Int'l. Seminar on Modal Analysis*, Leuven, Belgium, Sept. 22-25, 1-4.
8. Asher G W 1967, A Note on the Effective Degrees of Freedom of a Vibrating Structure, *AIAA Journ.*, 5, 822-825.
9. Ibrahim S R 1978, Modal Confidence Factor in Vibration Testing, *Journal of Spacecraft and Rockets (AIAA)*, 15, 5, 313-316.
10. Allemang R J & Brown D L 1982, A Correlation Coefficient for Modal Vector Analysis, *Proc. of the 1st Int'l. Modal Analysis Conf.*, Orlando, Florida, USA, 110-116.
11. Traill-Nash R W 1958, On the Excitation of Pure Natural Modes in Aircraft Resonance Testing, *Journal of the Aero/Space Sciences*, Dec., 775.
12. Asher G F 1958, A Method of Normal Mode Excitation Utilizing Admittance Measurements, *Proc. National Specialists' Meeting on Dynamics and Aeroelasticity*, Fort Worth, Texas, USA, Nov. 6-7.
13. Ibáñez P 1976, Force Appropriation by Extended Asher's Method, *Aerospace Engineering and Manufacturing Meeting*, San Diego, Calif., USA, Nov. 29-Dec. 2.
14. Morosow G & Ayre R S 1978, *Force Apportioning for Modal Vibration Testing Using Incomplete Excitation*, 48, Part 1.
15. Anderson J E 1981, Another Look at Sine-Dwell Mode Testing, *J. Guidance*, 5, 4, 358-365.
16. Hunt D, Vold H, Peterson E & Williams R 1984, Optimal Selection of Excitation Methods for Enhanced Modal Testing, *AIAA Dynamic Specialists' Conference*, Palm Springs, Calif., USA, Paper No. 84-1068.
17. Craig jr R R & Su Y-W T 1974, On Multiple-Shaker Resonance Testing, *AIAA Journal*, 12, 7, July.
18. Salama M, Rose T & Garba J 1987, Optimal Placement of Excitations and Sensors for Verification of Large Dynamical Systems, *AIAA Dynamic Specialists' Conference*, AIAA Paper 97-0782.
19. Angélini J J & Darras B 1973, *Détermination des modes propres de l'avion RF8 à partir d'un essai de vibration en sol avec excitation non appropriée*, ONERA NT 1/1984 RY, Août.
20. Chen J C 1984, Evaluation of Modal Testing Methods, *AIAA Dynamic Specialists' Conference*, Palm Springs, Calif., USA, ASD Paper No. 84-1071.
21. Niedbal N, Klusowski E & Lubert W 1988, Updating a Finite-Element Model by Means of Normal Mode Parameters, *Proc. 13th Int'l. Modal Analysis Seminar*, Leuven, Belgium, Sept. 19-23, Part 1, 1-15.

N92-23848

MATCHING FINITE ELEMENT MODELS TO MODAL DATA

COGAN S., Research Eng., LALLEMENT G., Professor

Laboratoire de Mécanique Appliquée, Associé au CNRS
UFRST, 25030 BESANCON CEDEX, FRANCE

ABSTRACT

This article presents the recent developments proposed by the LMA in the domain of parametric updating of finite element models.

The emphasis is placed on the preliminary step of localizing the dominant error zones prior to their correction. Two techniques for matching finite element models to modal data are presented, both of which exploit the identified real eigensolutions.

The first procedure is based on the minimization of the distances between the eigensolutions introduced as output quantities and while the second is based on the minimization of a mixed residual formed from the inputs and outputs. The advantages and disadvantages of these formulations are discussed.

Keywords : Parametric identification ; Updating finite element models ; Localization of the dominant errors.

1. INTRODUCTION

The general problem considered here is the parametric updating of finite elements models used in structural dynamics. It is assumed that the structures are linear elastodynamic and that their mathematical models are "simple" in the sense that they are governed by state matrices which are strictly diagonalizable. The case of non self-adjoint or "non simple" structures can be treated with analogous although more complicated methods.

The methods of parametric updating which have been developed at the LMA exploit data which are stationary with respect to time, either eigensolutions or frequency responses. It is sought to correct the state matrices, M^a ; $K^a \in R^{C,C}$ both symmetric and positive definite, representing the initial finite element estimation of the mass and stiffness matrices, respectively, using the measured dynamic behavior of the real physical structure. The parametric identification problem is reduced to a linear or non-linear parametric optimization problem with constraints.

Two formulations of the local parametric updating problem have presently been retained and will be evoked here. They are based on the exploitation of both the eigensolutions calculated using the finite element model M^a ; K^a and the identified eigensolutions of the conservative structure associated to the physical structure (Transformation of complex eigensolutions into the

real eigensolutions of the associated conservative structure). These two formulations have the following points in common :

- the minimization of the chosen cost function respects the topology, the connectivity, the discretization and the physical signification of the initial finite element estimation
- the following active variables x can be taken into account during the minimization : the physical parameters of the elementary sub-domains or the global (or homogenized) parameters of the sub-domains representing complicated zones
- the active variables are selected in such a way as to represent, in an independent manner, all the types of potential and kinetic energies participating in the observed frequency band
- these active variables are then processed in such a manner as to localize the sub-group of parameters responsible for the distances between the model and structure
- the parametric correction (minimization of the cost function) is then performed with the sub-group of variables selected during the localization
- the minimization of the cost function, eventually with constraints on the parameters, proceeds by successive iterations until convergence is reached
- the totality of the procedure described above can be iterated in a global manner in order to compensate for the influence of local linearizations (case of minimization of the outputs) or the influence of the incomplete basis of representation (case of the mixed minimization of the inputs and outputs).

2. PARAMETRIC CORRECTION BY MINIMIZATION OF THE DISTANCES BETWEEN THE EIGENSOLUTIONS INTRODUCED AS OUTPUT QUANTITIES (OUTPUT RESIDUAL)

2.1 Formulation

This method consists of an iterative minimization of a residual vector $r(x)$ formed from the distances between the real calculated and measured eigensolutions which are considered as output quantities.

The procedure consists in an iterative minimization of the scalar function $J(x)$:

$$J(x) = {}^T r(x) P_r r(x) + {}^T (x-x^*) P_x (x-x^*), \quad (1)$$

under the inequality constraints : $x_L \leq x \leq x_U$.

The localization and parametric correction are performed using the following data :

* $K^{(a)}(x)$; $M^{(a)}(x) \in R^{C,C}$, initial estimation for finite element mass and stiffness matrices

* $Y_1^{(a)}(x) = [\dots y_v^{(a)}(x) \dots] \in R^{C,M}$;

$\Lambda_1^{(a)}(x) = \text{diag} (\lambda_v^{(a)}(x)) \in R^{M,M}$, respectively

modal and spectral matrices such that :

$K^{(a)} Y_1^{(a)} = M^{(a)} Y_1^{(a)} \Lambda_1^{(a)}$; $Y_1^{(a)} M^{(a)} Y_1^{(a)} = I_N$

* $K_i^{(a)}(x)$; $M_i^{(a)}(x) \in R^{C,C}$, mass and stiffness matrices of the i^{th} sub-domain, $i = 1(1) \dots$

* $Z^{(m)} = [\dots z_v^{(m)} \dots] \in R^{C,M}$; $\Lambda^{(m)} = \text{diag} (\lambda_v^{(m)}) \in R^{M,M}$, $v = 1(1)M$, respectively sub-modal (normalized) and spectral matrices identified from the structure. The vector $z_v^{(m)} \in R^{C,1}$ is a sub-

vector of $y_v^{(m)} \in R^{C,1}$, solution of :

$$[K^{(m)} - \lambda_v^{(m)} M^{(m)}] y_v^{(m)} = 0, \quad v = 1(1)M$$

$K^{(m)}$; $M^{(m)} \in R^{C,C}$ are the unknown matrices to be identified. It is assumed that the modal identification technique yields eigenvectors $y_v^{(m)}$ (and consequently $z_v^{(m)}$) which are normalized by :

$$Y_v^{(m)} M^{(m)} Y_v^{(m)} = 1, \quad v = 1(1)M.$$

* $r = \begin{bmatrix} r_1 & r_2 \end{bmatrix}$, $r \in R^{(C+1)M,1}$

$$r_1 = \begin{bmatrix} \dots & r_{1v} & \dots \end{bmatrix} \in R^{C,M,1} ;$$

$$r_2 = \begin{bmatrix} \dots & r_{2v} & \dots \end{bmatrix} \in R^{M,1}$$

$$r_{1v} = 2 \frac{z_v^{(m)} - z_v^{(a)}(x)}{\|z_v^{(m)}\| + \|z_v^{(a)}(x)\|} \in R^{C,1} \quad v = 1(1)M$$

$$r_{2v} = 2 \frac{\lambda_v^{(m)} - \lambda_v^{(a)}(x)}{\lambda_v^{(m)} + \lambda_v^{(a)}(x)} \quad v = 1(1)M$$

* P_r ; P_x , diagonal, positive definite weighting matrices

* x^0 , initial estimation of $x = {}^T(\dots p_i^0 \dots) \in R^{n,1}$

The resolution of $J(x)$ by the Newton (or Gauss-Newton) method does not allow the convergence to be obtained in a single calculation step. The calculation thus proceeds in an iterative fashion with an updating of the sensitivity matrix S and the Hessian matrix V at each iteration. If a Gauss-Newton type approach is used ($V = 0$) and $P_x = 0$, eq. (1) is thus equivalent for over-determined systems $[(C+1)M > n]$ to the minimisation of :

$$\|\varepsilon\|_2^2 = {}^T \varepsilon \varepsilon, \quad \text{with } \varepsilon \text{ defined by :}$$

$$\varepsilon = P_r^{1/2} [r(x^0) - S(x^0) x] \quad (2)$$

2.2 Accounting for generalized mass errors

According to the definition of the residual vector r , the use of the identified sub-eigenvectors implies that these be normed in a coherent way with respect to the calculated sub-eigenvectors. In other words, the procedure requires the knowledge of the generalized masses of the structure. Now it is known that their identification is delicate and their values strongly affected by the presence of non-linearities (even weak ones) in stiffness or damping. Two remedies are proposed :

* at the experimental level, to perform complementary tests in order to refine their identification (micro-sweeping in frequency ; introduction of additional masses or feedback loops) [1] ;

* in terms of the localization and adjustment, to coarsely adjust the identified generalized masses with respect to the calculated generalized masses, then to introduce correction terms to the generalized masses as supplementary unknowns. The principle of this technique now is developed. Let :

$y_v^{(m)} \in R^{C,1}$, structure eigenvector with correct norm : $Y_v^{(m)} M^{(m)} Y_v^{(m)} = 1$, $v = 1(1)M$.

$\tilde{y}_v^{(m)} = \beta_v y_v^{(m)} \in R^{C,1}$, structure eigenvector with error in norm. β_v designates the norm error. Let

$\beta_v = (1 - \alpha_v)^{-1}$. The identified sub-eigenvectors containing only the c observed dof satisfy :

$$(1 - \alpha_v) \tilde{z}_v^{(m)} = z_v^{(m)} \quad \text{with : } \tilde{z}_v^{(m)} ; z_v^{(m)} \in R^{C,1}.$$

This can be rewritten :

$$\tilde{z}_v^{(m)} - z_v^{(a)} = S'_{zv} x + \alpha_v \tilde{z}_v^{(m)},$$

where : $S'_{zv} \in R^{C,n}$ is the Jacobian matrix of first derivative of the sub-eigenvector $z_v^{(a)}$; $x \in R^{n,1}$; $x = (\dots \Delta k_i/k_i \dots ; \dots \Delta m_i/m_i \dots)$

Introducing the normalization :

$$\frac{1}{h_v} (\tilde{z}_v^{(m)} - z_v^{(a)}) = \frac{1}{h_v} S'_{zv} x + \alpha_v \frac{1}{h_v} \tilde{z}_v^{(m)}, \quad \text{noted :}$$

$$\Delta \hat{z}_v = S_{zv} x + \alpha_v \hat{z}_v^{(m)}, \quad v = 1(1)M \quad (3)$$

With norm errors, the sensitivity of the eigenvalues remains unchanged and is written after normalisation :

$$\frac{1}{l_v} (\lambda_v^{(m)} - \lambda_v^{(a)}) = \Delta \lambda_v = \frac{1}{l_v} S'_{\lambda v} x$$

$$\text{where : } l_v = \frac{\Delta}{2} (\lambda_v^{(m)} + \lambda_v^{(a)})$$

$$\frac{\Delta \lambda'_v}{l_v} = \Delta \lambda_v = S_{\lambda v} x \quad v = 1(1)M \quad (4)$$

Equations (3) and (4) are regrouped in the following system :

$$\begin{bmatrix} \Delta \lambda_v \\ \Delta z_v \end{bmatrix} = \begin{bmatrix} \Delta \lambda \\ \Delta z \end{bmatrix} = \begin{bmatrix} S_{\lambda}^{(m)} & S_{\lambda}^{(k)} \\ S_z^{(m)} & S_z^{(k)} \end{bmatrix} \begin{bmatrix} x^{(m)} \\ x^{(k)} \\ \alpha_v \\ \alpha_v \end{bmatrix} \quad (5)$$

This system is to be solved with respect to : $x = ({}^T x^{(m)} ; {}^T x^{(k)})$ and $\alpha = (\dots \alpha_v \dots)$, $v = 1(1)M$ after introduction of the weighting matrix $P_r^{1/2}$.

2.3 Definition of the sub-domains

Here, the sub-domains of parametric correction are defined to be coherent with the effective modelization errors. The equation (5) has the general form :

$$Ax = b \quad A \in R^{m,n} \quad (6)$$

The problem consists in defining the columns A_i , $i = 1(1)n$ of the matrix A (and thus the corresponding components x_i of the vector x) coherent with the effective modelling errors. We propose the following method :

- Division of the structure in a overabundant number of sub-domains and selection of the correction parameters x_i in the interior of each of these sub-domains. Let N ($N \gg n$) be the initial total number of parameters x_i , $i = 1(1)N$, thus defined
- Calculate the columns A_i , $i = 1(1)N$ associated to each of these parameters
- Resolution with respect to x'_{ijk} of a series of least squares problems :

$$\min_{x'_{ijk} \dots} J(x'_{ijk} \dots) = \|\epsilon'_{ijk} \dots\|^2, \quad (7)$$

where : $\epsilon'_{ijk} \dots = \|b^{-1}\| [b - A'_{ijk} \dots x'_{ijk} \dots]$

In this series of problems the matrix column $A'_{ijk} \dots$ is formed by grouping the columns A_i , A_j , A_k, \dots

- Analysis of the evolution of the efficiency indicator $(1 - \|\epsilon'_{ijk} \dots\| \times 100)$. The variation as a function of the parameters $ijk \dots$ of the slope of this efficiency indicator give information on the regrouping of sub-domains which can be made and the dominant error regions.

2.4 Localization of the dominant errors

2.4.1 Preliminary test for localization of $Ax = b$.

The localization of the dominant modelling errors in the estimation M^b ; K^b is reduced to selecting in (6) among the columns of A those which are the closest to the direction defined by b . The global quality of this localization depends on the projection of the vector b in the sub-space whose basis vectors are the columns of A .

The first useful operation consists thus in evaluating the rank of the matrix A and that of the augmented matrix $\hat{A} = [A; b]$. If the ranks of these 2 matrices are the same, then the necessary condition for the localization is satisfied. If $R(\hat{A}) > R(A)$, a perfect localization will be impossible.

2.4.2 Localization by the sub-space method [2,3].

Starting with the matrix $A \in R^{m,n}$, the sub-matrix A_p formed of p ($p \ll n$) columns of A is extracted which allow the best representation, in the least squares sense, of the "distance vector" b of the initial problem : $Ax = b$. The procedure progresses in successive steps of p selected columns, $p = 1, 2, \dots, d$.

For $p = d$, the best sub-space of dimension d is sought in the space of the parameters $x \in R^{n,1}$ which best reduces, in the least square sense, the error vector ϵ_d of the over determined problem :

$$\epsilon_d = \frac{1}{\|b\|} [b - A_d x_d], \text{ hence : } x_d = A_d^+ b \text{ where :}$$

$A_d \in R^{m,d}$ is a sub-matrix of A formed by d columns ($d \ll m$)

$A_d^+ \in R^{d,m}$ is the Moore-Penrose pseudo inverse of A_d

$x_d \in R^{d,1}$ is the sub-vector of x associated with the d columns of A_d

The norm $\|\epsilon_d\|$ is a non-increasing function of d . Its evolution as a function of d and the variations in the slope of $\|\epsilon_d\|$ as a function of d are exploited in order to select the columns of the matrix A which are the most efficient for representing the vector b . In practice :

- Before localization, the following operations are performed : α) a regrouping (or elimination for the considered iteration) of the columns of A having small norms ; β) a regrouping of columns which are quasi-linearly dependent if and only if they correspond to adjacent sub-domains.
- The localization starts with a search for the best combination of $d = 1, 2$ to 3 columns (3 as a practical example) among the possible combinations of the columns of A . Retaining these 3 columns, the best fourth column among those remaining is selected, and so on, with the objective of limiting the number of combinations.
- The evolution of $\|\epsilon_d\|$ depends on the definition of the sub-domain partitioning and the parameterization chosen in these domains. Several localizations are performed associated with different definitions, then comparisons and intersections between the localized parameters are made.
- The quality of the localization in the sense of selecting the smallest number of poorly modeled parameters in the finite element model conditions the quality of the ulterior parametric adjustment. The selection of the equations forming the lines of A is thus considered to be very important.

2.5 Automatic pairing

The "distance" between the structure and its finite element model is evaluated by calculating the difference between homologous eigenvalues and eigenvectors. The evaluation of this distance makes sense only if the eigensolutions have been paired, (association of an identified eigenmode with its homologous F.E mode in eigenshape and in sign).

The mode pairing is performed automatically from a calculation of the projection of the identified modes $z_i^{(m)} \in R^{c,1}$, $v = 1(1)M$, on the modal sub-basis $Z_j^{(a)} \in R^{c,n}$ of the modes calculated by finite elements. The vector $z_v^{(m)}$ is projected on the basis of adjacent modes. In order to do this, a half bandwidth b_v associated to $z_v^{(m)}$ is defined.

In practice, two modes are considered to be matched if, for the projection column h_v , the following two conditions are satisfied :

- the maximum element must have an absolute value superior to 0.7
- the ratio between the maximum element and the next largest must be greater than 2.0

If these 2 conditions are not satisfied, the mode v under consideration is not taken into account in the parametric correction at the respective iteration. If the eigenmodes respectively calculated and measured are not in the same order, then the vectors of $Z_i^{(a)}$ are rearranged.

2.6 Optimal selection of the pickup dof vis à vis the conditioning of the sensitivity matrix [4]

This proposition can be considered as one of the techniques of test preparation in view of a parametric correction. The sensitivity matrix $S \in R^{(c+1)n,n}$ has the general form :

$$S = \begin{bmatrix} S_\lambda \\ S_z \end{bmatrix}$$

It is assumed in what follows to be written in adimensional form. In a deterministic approach, the 2 sub-matrices of S are considered to have the same relative importance. A weighting coefficient is thus introduced for the equations relative to S_z in such a way as to obtain matrices S_z and S_λ with the same norms.

In a stochastic approach, the weightings defined by P_λ ; P_z will then be introduced. The optimal pickup mesh is defined by one of the following two procedures.

2.6.1 Best orthogonality of S . S_z is rewritten in the form :

$$^T S_z = [^T s_1 ; ^T s_2 ; \dots ; ^T s_i ; \dots ; ^T s_R] , S_z \in R^{M \times n}$$

where : $s_i \in R^{M \times n}$ is the sensitivity matrix of the i^{th} dof; R corresponds to the number of pickup dof possible after having eliminated from among the C model dof : the inaccessible dof ; the rotational dof ; the dof having small displacements for the M identified modes... The procedure consists in selecting one by one the dof in such a way as to obtain a matrix $^T S S$ which tends toward a diagonal matrix.

- Choice of the first dof. Starting with the R potential dof, R matrices $S_i^1 = W_i^T [^T s_i | ^T S] \in R^{2M \times n}$ $i = 1(1)R$, are constructed, where W_i allows an identical norm to be obtained in the sensitivity blocks for the eigenvalues and eigenvectors. The dof i which best diagonalizes $^T S_i^1 S_i^1$ is retained.
- Choice of the second dof. The $R-1$ matrices $S_j^2 = W_j^T [^T s_j | ^T S_i^1 | ^T S] \in R^{3M \times n}$, $j = 1(1)R$ are constructed where W_j allows as before, to obtain the same norms in the sensitivity blocks for the eigenvalues and eigenvectors. The dof j is selected which best diagonalizes $^T S_j^2 S_j^2$.
- By proceeding in this way, step by step, a local minimum of the diagonality is obtained for a given number c of pickups. The global minimum is obtained by evaluating the diagonalities of the C_c^c combinations. This number is, in general, too large to envisage such a procedure. Thus a sub-optimum of the optimum pickup mesh is obtained.
- The number c which is selected corresponds to one of the first local minima of $\delta(S)$ as a function of the selected pickups.

2.6.2 Best conditioning for S . This method consists in selecting one by one the dof leading to the best possible condition number $R(S)$ of S with a maximal rank. From a numerical point of view, the following procedure is employed. Let σ_i be the i^{th} singular value of S

and : $r_i = \Delta \sigma_i / \sigma_i$. The condition number $R(S)$ of S is then defined to be equal to the number of quantities r_i superior to a given tolerance T .

Having chosen the M possible dof, a matrix S is constructed by a technique analogous to the preceding one (cf 2.6.1). Starting with S , the dof are selected one by one as to simultaneously obtain the maximum rank and the minimum condition number for the normalized sensitivity matrix. This normalization is performed by normalizing each column of S to 1. The optimal number c is that which yields a maximum rank with a minimum of dof and a minimum condition number.

2.7 Remarks concerning the weighting between the blocks of the sensitivity matrix S

An order of magnitude of the diagonal elements of these matrices is given by : $P_h = (\text{diag } \sigma_{ijh}^2)$, where σ_{ijh}^2 designates the uncertainty (standard deviation) for the quantity associated with the matrix P_h .

These weighting problems are very delicate and cannot be solved efficiently and correctly except in an approach based on the minimum variance estimators. These problems have only been superficially confronted and should be studied more thoroughly in future research [cf H.G. Natke [5-6] and M.I. Friswell [7]].

3. PARAMETRIC CORRECTION BY MINIMIZATION OF A MIXED RESIDUAL FORMED FROM THE INPUTS AND OUTPUTS

3.1 Formulation

In opposition to the previous formulation (cf 2), this approach :

- * does not impose any matching between the calculated and measured eigensolutions
- * allows the exploitation of the non-normalized measured eigenvectors.
- * does not depend on any linearization of the eigensolution distances with respect to the parameters
- * requires the expansion of the unobserved sub-eigenvectors.

The cost function has the following form :

$$\text{Min}_x J = \sum_{i=1}^3 \epsilon_i P_i \epsilon_i + ^T (x-x^*) P_4 (x-x^*) \quad (9)$$

submitted to the inequality constraints on the correction parameters :

$$x_L \leq x \leq x_U$$

and where : $\epsilon_i = A_i x - b_i \quad i = 1(1)3$
 $P_j, j=1(1)4$, weighting matrices, $P_j > 0$.

The unknown matrices $K^{(m)}$; $M^{(m)} \in R^{C,C}$ are written :

$$K^{(m)} = \sum_i k_i K_i^{(a)} ; M^{(m)} = \sum_j m_j M_j^{(a)}$$

where $K_i^{(a)}$; $M_j^{(a)}$ are the matrices associated with the i^{th} and j^{th} domain to be updated; k_i, m_j optimal values of the correction parameters, hence:

$$x = ^T (\dots \Delta k_i / k_i ; \dots ; \Delta m_j / m_j ; \dots)$$

The matrices A_i ; $b_i, i = 1(1)3$ are constructed from the following relations.

3.1.1 Equations relative to the eigenvalues. The model sought must satisfy, for each one of the M measured eigenvectors, the dynamic stiffness relation :

$$Z_v y_v^{(m)} = f_v(p) \quad , \quad v = 1(1)M$$

where : $Z_v = (K^a - \lambda_v^{(m)} M^a) f_v(p) = (\lambda_v^{(m)} \Delta M - \Delta K) y_v^{(m)}$.

Premultiplying by $^T y_u^{(a)}$, $u = 1(1)2 M$ leads to :

$$d_{uv} \Delta \lambda_{uv} = ^T y_u^{(a)} [\Delta K - \lambda_v^{(m)} \Delta M] y_v^{(m)}, v = 1(1) M \quad (10)$$

with : $\Delta \lambda_{uv} = \lambda_v^{(m)} - \lambda_u^{(a)}$; $d_{uv} = ^T e_u d_v$, is the u^{th} component of the linear combination vector defined by : $y_v^{(m)} = Y_1^{(a)} d_v$ where $Y_1^{(a)} \in R^{C,N}$ is the modal sub-basis formed by the N first eigenvectors of $M^{(a)}$; $K^{(a)}$.

Assuming a linear parameterization of ΔM ; ΔK :

$$\Delta M = M^{(a)} - M^{(a)} = - \sum_j m_j^{(0)} x_j M_j^{(a)} ,$$

$$\Delta K = K^{(a)} - K^{(a)} = - \sum_i k_i^{(0)} x_i K_i^{(a)} .$$

The equations (10) are regrouped in the form :
 $A_i x = b_i, A_i \in R_{1,i}^{a,n} \quad (11)$

The number a_i is defined by the condition :

$$d_{uv} \geq 0,5 \text{ and in practice : } M \leq a_i \leq 2M.$$

3.1.2 Orthonormality equations. They are defined by:

$$^T y_u^{(m)} [M^{(a)} + \Delta M] y_v^{(m)} = n_v \delta_{uv} .$$

$$^T y_u^{(m)} [K^{(a)} + \Delta K] y_v^{(m)} = \lambda_v n_v \delta_{uv} .$$

where : $u, v = 1(1)M$ and regrouped in the form :
 $A_2 x = b_2$, $A_2 \in \mathbb{R}^{a2, n}$ (12)

where : $a_2 = \begin{cases} M(M+1) & \text{if } n_v \text{ is correctly identified} \\ M(M-1) & \text{if } n_v \text{ is not identified} \end{cases}$

3.1.3 Dynamic flexibility relations. They have the form :

$$y_v^{(m)} = [K^{(a)} - \lambda_v^{(m)} M^{(a)}]^{-1} [\lambda_v^{(m)} \Delta M - \Delta K] y_v^{(m)} \quad v=1(1)M \quad (13)$$

and are regrouped in the form : $A_3 x = b_3$ where $A_3 \in \mathbb{R}^{a3, n}$ with : $cM \leq a_3 \leq CM$.

The difficulties related to the numerical conditioning of the matrix : $[K^{(a)} - \lambda_v^{(m)} M^{(a)}]$ are avoided by the introduction of shifts in the eigenvalues of the model $M^{(a)}$; $K^{(a)}$.

3.1.4 The totality of equations form the linear non homogeneous system : $Ax = b$ (14)

which is successively exploited for the localization of the dominant errors followed by the parametric correction.

3.2 Expansion of the unobserved sub-eigenvectors. Formulation in C space and 2C space

The relations (10) to (13) involve the eigenvector $y_v^{(m)} \in \mathbb{R}^{C, 1}$, $v = 1(1)M$. This implies the expansion of the unobserved sub-eigenvectors. An important number of recent studies have examined this problem in relation to model correction (see for example [8,9,10]).

3.2.1 Exploitation of the modal sub-bases of the estimated finite element model in C-space

a) Principle. Let $y_v^{(m)} \in \mathbb{R}^{C, 1}$, $v = 1(1)M$, be the v^{th} eigenvector of the conservative structure associated to the real structure. In practice, only the sub-vector $z_v^{(m)} \in \mathbb{R}^{C, 1}$ of $y_v^{(m)}$ corresponding to the measured dof is known. In order to expand (extrapolate) $y_v^{(m)}$ from $z_v^{(m)}$, one technique consists in using as a Ritz basis the modal basis of the finite element estimation :

$$y_v^{(m)} = Y_1^{(a)} c_v, \quad v = 1(1)M \quad (15)$$

where : $y_v^{(m)} \in \mathbb{R}^{C, 1}$; $Y_1^{(a)} \in \mathbb{R}^{C, N}$, $C \gg N$.

The linear combination vector c_v is evaluated using only the observed dof $z_v^{(m)}$:

$$z_v^{(m)} = Z^{(a)} c_v \text{ where : } z_v^{(m)} \in \mathbb{R}^{C, 1} ; Z^{(a)} \in \mathbb{R}^{C, N} \quad (16)$$

The solution of (16) in the least squares sense leads to (normal solution) :

$$c_v = Z^{+(a)} z_v^{(m)}, \quad Z^{+(a)} = [Z^{(a)} Z^{(a)}]^{-1} Z^{(a)} \quad (17)$$

This classical extrapolation technique, analogous to a method of spatial filtering [11], has been applied at the LMA to problems of parametric correction of finite element models since 1976 [12].

b) Evaluation of this expansion procedure. The following commentaries can be made with respect to this procedure :

* the representation basis $Y_1^{(a)}$ satisfies the geometrical and kinematical boundary conditions of the structure

* the quality of the expansion (extrapolation) will be as good as the eigenvectors of the finite element model are close to the real structure. This remark leads naturally to an iterative expansion procedure.

* the basis of representation $Y_1^{(a)}$ is :

- immediately available
- easier to use than a spline function polynomial basis and is a priori of better quality

* according to S. Cogan [13], a segmentation of the basis $Z^{(a)}$ into independent bases defined either a priori from natural physical substructures, or from and in function of the "discontinuities" of the observed displacements in the subvector $z_v^{(m)}$, allows, by increasing efficiently and in a logical manner the dimension of the Ritz basis, the representation of the effects of significant localized errors of the initial estimation.

3.2.2 Exploitation of the modal sub-bases of the finite element estimations. Formulation in 2C-space. The idea consists in applying the preceding extrapolation (cf 3.2.1) in the 2C state space defined by : $x = \begin{bmatrix} T y \\ T' y' \end{bmatrix}$:

* from a mathematical point of view, this space constitutes the natural space of second order differential systems.

* from a physical point of view, such a formulation should have a tendency to moderate the amplitude of the components of the basis vectors corresponding to distant modes.

It can be shown that, in the case of real modes considered here, the formulation in 2C leads to the same results as the extrapolation in C.

3.2.3 Exploitation of the modal bases of the finite element estimation. Formulation in C-space with the unobserved dof taken into account. This formulation is similar to the one developed in paragraph 3.2.1. Here it is sought to :

a) Define a linear combination vector whose component values are independent (case a) or quasi-independent (case b) of the dimension of the representation basis

b) Take into account in an indirect manner the relations with respect to the unobserved dof

Case_a) Limiting case : observation of the C dof of the structure

The following notations are used :
 $Y^{(a)} \in \mathbb{R}^{C, C}$, complete basis : $Y^{(a)} = [Y_1^{(a)} | Y_2^{(a)}]$

where $Y_1^{(a)} \in \mathbb{R}^{C, N}$. Having available the sub-basis $Y_1^{(a)}$, the eigenvector of the structure is represented by :

$$y_v^{(m)} = Y_1^{(a)} d_v + \varepsilon_v \quad v = 1(1)M \quad (18)$$

where ε_v belongs to the column space of $Y_2^{(a)}$. The linear combination vector d_v can be expressed :

$$d_v = Y_1^{(a)+} y_v^{(m)} \quad (19)$$

where $Y_1^{(a)+}$ is a pseudo-inverse of $Y_1^{(a)}$ for which the following conditions are satisfied :

$$\alpha) Y_1^{(a)+} Y_1^{(a)} = I_N \quad (20)$$

$$\beta) Y_1^{(a)+} \varepsilon_v = 0 \quad (21)$$

$\gamma)$ components $d_{jv} = \Delta^T e_j d_v$, $j = 1(1)N$, of the vector

d_v depend on the vectors $y_{v1}^{(a)} = \Delta^T e_v Y_1^{(a)}$ and $y_v^{(m)}$.

A pseudo-inverse satisfying these three conditions is :

$$Y_1^{(a)+} = Y_1^{(a)} M^{(a)} \quad (22)$$

Case_b) Practical case : $N \leq c \ll C$

The partitioning into observed (index c) and unobserved (index i) dof is defined as follows :

$$y_v^{(m)} = \begin{bmatrix} y_{cv}^{(m)} \\ y_{iv}^{(m)} \end{bmatrix} ; \quad Y_1^{(a)} = \begin{bmatrix} Y_{c1}^{(a)} \\ Y_{i1}^{(a)} \end{bmatrix} \quad \text{where : } Y_{c1}^{(a)} \in \mathbb{R}^{C, N} \\ Y_{c1}^{(a)} = Z^{(a)} \quad (cf \text{ para } 3.2.1)$$

$$Y_1^{(a)+} = \Delta \begin{bmatrix} Y_{c1}^{(a)+} & Y_{i1}^{(a)+} \end{bmatrix} = \begin{bmatrix} Y_{c1}^{(a)+} & Y_{i1}^{(a)+} \end{bmatrix} \begin{bmatrix} M_1 \\ M_2 \end{bmatrix} \quad (23)$$

Equation (18) leads to the relations :

$$y_{cv}^{(m)} = Y_{c1}^{(a)+} d_v + \epsilon_{cv}, \quad (24)$$

$$y_{iv}^{(m)} = Y_{i1}^{(a)+} d_v + \epsilon_{iv}. \quad (25)$$

Equation (19) gives :

$$d_v = Y_{c1}^{(a)+} y_{cv}^{(m)} + Y_{i1}^{(a)+} y_{iv}^{(m)}, \quad (26)$$

while taking into account (25) :

$$d_v = Y_{c1}^{(a)+} y_{cv}^{(m)} + Y_{i1}^{(a)+} [Y_{i1} d_v + \epsilon_{iv}]. \quad (27)$$

Expressing $Y_{i1}^{(a)+}$ as a function of $Y_{c1}^{(a)+}$ using (20) and accounting for (21) yields :

$$Y_{c1}^{(a)+} Y_{c1} + Y_{i1}^{(a)+} Y_{i1} = I_N,$$

$$Y_{i1}^{(a)+} \epsilon_{iv} = -Y_{ic}^{(a)+} \epsilon_{cv}.$$

The relation (27) then becomes :

$$Y_{c1}^{(a)+} Y_{c1}^{(a)+} d_v = Y_{c1}^{(a)+} [y_{cv}^{(m)} - \epsilon_{cv}], \quad (28)$$

to be solved in an iterative fashion with respect to the unknowns d_v and ϵ_{cv} . The expression (28) of the linear combination vector d_v obtained by taking into account the constraint equations (25) relative to the sub-vector $y_{iv}^{(m)}$ of unobserved dof can be compared to (17) corresponding to the solution of (16) or (24) with constraints and in the habitual least squares sense :

$$Y_{c1}^{(a)+} Y_{c1}^{(a)+} c_v = Y_{c1}^{(a)+} y_{cv}^{(m)} \quad (Z^{(a)} = Y_{c1}^{(a)+})$$

Remarks :

a) In the particular case $M^{(a)} = I_c$, the following relations are obtained :

$$Y_{c1}^{(a)+} = Y_{c1}^{(a)+}; \quad Y_{i1}^{(a)+} = Y_{i1}^{(a)+}$$

If the distribution of mass is nearly uniform, these relations are also nearly satisfied.

b) In the majority of the particular numerical cases treated :

- * the vector d_v was very close to the vector c_v ,
- * the quality of the expansion of the vector $y_v^{(m)}$ obtained from the vector d_v was also very close to the quality of the expansion obtained from the vector c_v , $v = 1(1)M$.

Taking into account the numerical costs in evaluating $Y_1^{(a)+}$ from (23), such a procedure seems to be of questionable efficiency.

3.3 Sensitivity of the different types of equations to truncations in the Ritz basis

The general tendencies of the influence of the unmeasured sub-eigenvector expansion errors on the different types of parametric correction equations have been developed in [14].

To summarize these results, the insensitivity I with respect to the truncation errors due to the exploitation of the sub-basis $Y_1^{(a)+}$ of representation can schematically be established as follows :

I (dynamic stiffness relations) $\ll I$ (flexibility relations) $< I$ (relations relative to the off diagonal elements of the orthonormality relations, with $I(1/K) < I(1/M) < I$ (relations relative to the diagonal elements of the orthonormality relations $< I$ (relations relative to the eigenvalues).

3.4 Optimal selection of pickup dof vis a vis the expansion [4]

It is assumed that this selection of pickup dof is made before the observation of the dynamic behavior of the structure. The vectors $z_v^{(m)}$, $v = 1(1)M$ thus cannot be used to define this choice. The problem of determining an optimal pickup mesh is reduced to the search for the maximum rank and minimum condition number of the matrix $Z^{(a)} \in R^{c,N}$. The method for constructing $Z^{(a)}$ is analogous to that described in paragraph 2.6.2.

The matrix $Z^{(a)}$ thus constructed is, by virtue of the chosen construction procedure, a sub-optimal matrix. The search for the strictly optimal conditioning requires the testing of c_r^{cop} combinations, that is to say, a number of combinations which is generally unacceptable. The sub-optimal matrix $Z^{(a)} \in R^{c,N}$ thus constructed leads to a significant improvement in the quality of the expansion and an improved robustness with respect to the uncertainties in $z_v^{(m)}$.

3.5 Definition of the sub-domains and localization of the dominant errors

It has been shown in paragraph 3.1 that the different relations exploited in this method can be rewritten in a form analogous to that exploited in the first correction method based on the outputs. The methods of sub-domain selection and localization developed previously thus remain strictly applicable (cf 2.3 and 2.4).

3.6 Iterative expansion of the eigenvectors [15]

The quality of the expansion conditions the quality of the localization and parametric correction. This quality improves as the projection basis approaches the eigenbasis of the structure, hence the following iterative procedure.

First iteration : it proceeds as defined in (3.2) and (3.4). A fairly crude localization is performed and the localized parameters are corrected. Let ΔK^1 ; ΔM^1 be the obtained correction. The eigensolutions of the problem are then evaluated :

$$[(K^{(a)} + \Delta K^1) - \lambda_v^{(1)} (M^{(a)} + \Delta M^1)] y_v^{(1)} = 0, \quad v = 1(1)M,$$

giving the modal matrix $Y^{(1)}$.

At the k^{th} iteration : the expansion is performed from :

$$y^{(k)} = Y^{(k-1)} d^{(k)}, \quad \text{where :}$$

$$d_v^{(k)} = [Z^{(a(k-1))}]^+ z_v^{(m)}, \quad v = 1(1)M.$$

These iterations are performed in view of improving the quality of the Ritz basis. The localization and adjustment are performed at each iteration in terms of the $M^{(a)}$; $K^{(a)}$ initial estimation.

Needless to say, the procedures presented above for optimal pickup selection and iterative expansion can be applied more generally to other parametric updating techniques requiring the expansion of the measured eigenvectors.

4. RECOMMENDATIONS AND LIMITATIONS OF THE METHODS

4.1 General conclusions concerning the methods proposed by the AML

Based on the experience to date, the following general remarks can be made relative to parametric updating techniques for finite element models :

- * acceptable and sometimes excellent results have been obtained in numerically simulated test cases even in the presence of simulated data errors
- * relatively little experience has been acquired in real industrial test cases and caution must be shown in extrapolating the results of simulated test cases.

4.1.1 The methods based on a minimization of a residual formed from the distances between the eigensolutions (output residual : cf 2). They are the only methods which are :

- * applicable when an insufficient number c of pickup dof are available to perform an expansion of the unobserved sub-eigenvectors
- * fairly robust vis-a-vis the incertainties in the observed data
- * directly minimize the distances between the fundamental quantities (eigenvalues and eigenvectors) and are the most general in terms of future applications of the updated model.

On the other hand :

- * they can lead to the situation where only a small number of equations are available, thus the necessity of having efficient methods for localizing dominant errors if the parametric correction of minimal norm is to be avoided ;
- * they are not well adapted to the case of large non-affine distances between the model and structure. They are based on a linearization of the model-structure distance, which can be dangerous for the localization techniques based on the matrix of first derivatives ;
- * the fact that they require mode matching and the taking into account of the generalized masses as supplementary unknowns are not in themselves serious flaws. However, they imply serious complications the case of multiple or quasi-multiple eigenvalues and this can become unacceptable on a practical level ;
- * the numerical evaluation of the first derivatives of the eigensolutions is costly. However, it should not be forgotten that this sensitivity matrix is fundamental for a very large number of other technical applications (Examples : structural modifications ; structural optimization).

4.1.2 The methods based on the minimization of a mixed residual formed from the inputs and outputs (cf 3) :

- * all require, either preliminarily or simultaneously with the parametric updating, the expansion of the unobserved dof. This remark implicitly excludes those strategies based on the condensation of the finite element model on the observed dof. Taking into account the duality and the identities of the formulations between the linear condensation transformation and the expansion, it is considered, and this remains to be proven, that no differences exist in the :

- observability of the modelization errors,
- quality of the updated models,

obtained by the two procedures of expansion and condensation ;

- * have been classified according to their sensitivity to expansion errors (cf. 3.3). Taking into account the usual orders of magnitude of the incertainties in the identified eigenvalues and sub-eigenvectors and in the absence of new strategies (which remain to be defined) :

- the exploitation of the dynamic stiffness relations is, at present, not advised
- the dynamic flexibility relations are much less sensitive to noise than the associated stiffness relations
- the bilinear forms and the quadratic forms are to be recommended

- * the quality of the parametric updating depends essentially on the quality of the eigenvector expansion. This quality is related to the choice of the Ritz basis which underlines the extreme importance given to the choice of the pickup dof.

4.2 Problems related to the presence of multiple or quasi-multiple eigenvalues

In the presence of multiple or quasi-multiple eigenvalues in the finite element model and for the corresponding eigensolutions :

- * the relations relative to the evaluation of the first derivatives of the eigensolutions (cf. 2.2) cannot be applied (inexact formulations and (or) non convergent series expansions) ;
- * the pairing between measured and calculated eigensolutions becomes meaningless.

Formulation 2 is thus inapplicable or incorrect for neighboring eigenmodes. The formulation 3 however remains entirely applicable. In order to avoid the intrinsic difficulties in the formulation 2.1, several complementary remedies have been proposed and will be evoked in the following paragraph :

- a) Separation of the multiple and quasi-multiple eigenvalues by the introduction of selective "numerical" modifications simultaneously in the finite element model and in the structure [16-17]
- b) Exploitation of the sensitivity relative to the sums and products of multiple or quasi-multiple eigenvalues
- c) Presently under study, a development based on the work of I.U Ojalvo [18] relative to the direct sensitivity problem and allowing the inverse sensitivity problem to be treated by the introduction of the notion of generalized diadics.

4.3 Conclusions. Points common to all the methods. Essential recommendations

4.3.1 It would be unrealistic to consider that there exists (or will exist) one method of model correction for linear elastodynamics. Depending on the particularities of the case under consideration, namely :

- * the value of the model-structure distance ; local or global corrections ; spectral density ; number of observation points, etc... and depending on the final objective envisaged ;
- * forced responses ; optimization using a reliable updated model ; coupled analysis...

One method will be better adapted than another. In a general manner, it will always be relatively inexpensive (with respect to the cost of the initial modelization and the tests) to apply several correction strategies in parallel and to compare the convergences.

4.3.2 Regardless of the chosen formulation :

- based on the estimated finite element model,
- in relation to the chosen parametric correction formulation,

The following questions must be answered :

- a) Preparation of tests with the objective of parametric correction. This point remains to be studied more thoroughly.

- b) Choice of the weighting between the different components of the cost functions. They must be defined as a function of :
 - * the variances in the observed data,
 - * the initial relative importance of the different components,
 - * the future applications of the corrected model.
- c) Choice of the parameterization of the sub-domains which respects the following aspects :
 - * independent representation of the different types of kinetic and potential energies participating, by sub-domain, in the considered frequency band (exploitation of modal energy maps). This poses the problem where by these constraints may eventually be poorly adapted to the types of finite elements which are currently available
 - * "intelligent" parameterization of the joints and the singularities
- d) Choice of the sub-domain divisions. This problem is not trivial and it conditions the quality of the parametric correction. The current strategy of the LMA is the following :
 - * division into small sub-domains and parameterization
 - * combinatory analysis of the contribution to the model-structure distance, that is to say, search for possible regroupings of the sub-domains
- e) Localization of the dominant errors

Acknowledgements : This article regroups the principle idea developed by the LMA, Besançon under the ESTEC Contract n°8219/89. We gratefully acknowledge the support of this organization and in particular Mr S. STAVRINIDIS, E. FISSETTE and O. BRUNNER.

5. REFERENCES

1. ZHANG Q., LALLEMENT G., FILLOD R. 1985, Modal identification of self-adjoint and non self-adjoint structures by additional masses techniques, 10th Conf. on Mechanical Vibration, Cincinnati OH, ASME Paper 85-DET 109,
2. FILLOD R., LALLEMENT G., PIRANDA J. 1986, Parametric correction of regular non dissipative finite elements models, 11th Int. Modal Analysis Seminar, Leuven
3. LALLEMENT G. 1988, Localization techniques, Proc. Workshop on Structural Safety evaluation based on System Identification approaches, June 29-July 1, Lambrecht, FGR, In Vieweg Int. Sci. Book Series, Braunschweig, pp. 213-233
4. ANDRIAMBOLOLONA H. 1990, Identifications modale et paramétrique, Thèse de Doctorat, Université de Franche-Comté, UFRST, Laboratoire de Mécanique Appliquée, Besançon
5. NATKE H.G. 1983, Einführung in Theorie und Modal - analyse- Identifikations-schwingungs -fähiger elasto-mechanischer Systeme. Friedr. Vieweg & Sohn, Braunschweig, Wiesbaden
6. NATKE H.G. 1987, Survey on the identification of mechanical systems, Proc. 2nd Workshop on Road-Vehicle systems and related mathematics, Torino
7. FRISWELL M.I. 1989, The adjustment of structural parameters using a minimum variance estimator, Mech. Syst. and Signal Processing, 3(2), 143-155,
8. O CALLAHAN J.C., AVITABILE P.A., RIEME R. 1989, System equivalent reduction expansion process (Serep), 7th International modal analysis conference, Las Vegas, Nevada,
9. GYSIN H. 1990, Comparison of expansion methods for FE modeling error localization, 8th International modal Analysis Conference, Kissimmee, Florida, p. 195-204,
10. PLACIDI F., POGGI F., D'AMBROGIO 1990, Expansion of measured modes to include finite element degrees of freedom, 15th International Seminar on Modal Analysis, UK Leuven, p.939-953,
11. VOLD H. 1986, Spatial filtering of experimental modes shapes, 11th International seminar on Modal Analysis, UK Leuven,
12. BUGEAT L.P., FILLOD R., LALLEMENT G., PIRANDA J. 1976, Ajustement du comportement dynamique d'un modèle discret conservatif, Contrat CNES n°76/3002, Rapport Final
13. COGAN S. 1990, Thèse de Doctorat, Université de Franche-Comté, UFRST, LMA Besançon
14. LALLEMENT G., COGAN S. 1991, Final Report Contrat ESTEC 8219/89, Noordwijk, The Netherlands
15. LALLEMENT G., ANDRIAMBOLOLONA H. 1990, Localization of errors in computational models using dynamic test data, Proceedings of the European Conference on Structural Dynamics, Eurodyn'90, Bochum, Germany
16. ZHANG Q. 1987, Identification modale et paramétrique de structures mécaniques auto-adjointes et non auto-adjointes, Thèse Doctorat Es Sciences Physiques, Université de Franche-Comté, UFRST, LMA, Besançon,
17. LALLEMENT G., ZHANG Q. 1988, Analysis of some difficulties encountered in the problem of parametric correction of finite element models, Proceedings of the 13th Int. Seminar on Modal Analysis, Leuven, Belgique, Part 1-16, 20 p.
18. OJALVO I.U. 1987, Modal sensitivity for structural systems with repeated frequencies, Nasa Rept. N 87-18868/6 GAR,

N92-238497

84761

COMPARISON OF MULTI-POINT MODAL TEST METHODS

KIMON ALEXIOU

JAN R. WRIGHT

CASA - SPACE DIVISION
MADRID - SPAINUNIVERSITY OF MANCHESTER
MANCHESTER - U.K.

ABSTRACT

In multi-point modal testing the appropriated force distributions for identifying and isolating pure modes of vibration may be determined by Iterative or Direct methods. A number of these methods which are based on the classical Phase Resonance criterion and operate on measured receptance matrix data have been investigated and compared using a simulated model.

Of the methods which operate on square matrix data a suggested variation on Asher's method was found useful for estimating the effective number of modes (and hence exciters needed) in the frequency range of interest. The Traill-Nash method provided the clearest estimate of appropriated forces but was more sensitive to noise. Of the methods which operate on rectangular matrices the Extended Asher method was not considered suitable. The Multivariate Mode Indicator Function method was the most promising but suffered from conditioning problems if too many exciters were used. An iterative method operating on updates of measured modal matrix data performed well and if improved could automate the modal tuning process.

KEYWORDS

Modal Testing, Phase Resonance, Normal Mode, Multi-Point Excitation, Force Appropriation

NOMENCLATURE

$A(\omega)$	real part of receptance matrix
$B(\omega)$	imaginary part of receptance matrix
e	number of exciters
f	force vector
j, k, l	integer counters
m	number of transducers
n	number of actual modes
n^*	number of effective modes
z	complex response vector
z_k	kth element of z
$\alpha, \beta, \lambda, \mu$	eigenvalues
ω	radian frequency
$ A(\omega) $	determinant of matrix $[A(\omega)]$
$[A(\omega)]^T$	transpose of matrix $[A(\omega)]$
ENDOF	Effective Number of Degrees of Freedom

1. INTRODUCTION

Modal testing has over the recent years been carried out using methods belonging to either of two different schools of approach, namely Phase Resonance and Phase Separation. The former approach aims to isolate and measure each normal mode on the structure by exciting it at its undamped natural frequency with a corresponding appropriated vector of exciter forces. The latter approach involves excitation over the whole frequency range containing the target modes (using either single or multiple exciters) and aims to extract the modal parameters of the modes from measured data using detailed multi degree of freedom (MDOF) curve fitting algorithms. Both approaches have inherent advantages and disadvantages to the extent that complementary use of methods from both approaches is not unusual.

Recently there has been a renewed interest in the traditional Phase Resonance methods, especially in the Aerospace industry, due to the methods' ability to identify and isolate closely spaced or coincident modes. The extraction of real normal modes is a further benefit of these methods since normal model parameters are directly comparable with analytical predictions. Effectively the methods aim to force a physical response on the structure composed of a single normal mode only by exciting this mode and suppressing all the rest. A "pure" mode response is defined when its phasing is coherent throughout the structure and in quadrature with the (monophase) sinusoidal excitation (Phase Resonance Criterion) (Ref.1). Forcing of the structure is at the natural frequency of the mode and via a number of exciters whose forces have been appropriated accordingly for that mode. A number of Direct and Iterative methods have been proposed over the years to derive these appropriated force vectors.

Iterative methods are those in which the excitation frequency and an initial force vector are progressively adjusted (with varying degrees of automation) (Refs. 2-4) until some predefined modal purity criterion is satisfied. Direct methods are those which operate on measured complex receptance function matrices and (without curvefitting) obtain natural frequencies and appropriated force distributions for the modes in the frequency range of interest. Receptance matrices are measured at discrete steps covering

the frequency range and relate a number of exciter and response locations. Of the methods which operate on square inertance matrices Asher's method (Ref.5), which owes much to Traill-Nash (Ref.6), involves a determinant solution approach and the Traill-Nash (Ref.7) and Modified Asher (Ref.8) methods involve an eigenvalue solution approach. The Extended Asher (Ref.9) and Multivariate Mode Indicator Function (MMIF) (Ref.10) methods also involve eigensolutions but can operate on rectangular (more response than excitation locations) inertance matrices. Clearly the latter two methods offer the advantage of more global structural monitoring and definition.

The central problem of all the methods is the definition of the number, locations/directions and amplitude of exciter forces needed to force the structure. The choice of the number of exciters, when related to the effective number of modes, can affect the conditioning of the receptance matrices and therefore the performance of the methods.

A number of Direct and Iterative methods were thoroughly investigated by Alexiou (Ref.11). Methods were expressed in a common mathematical formulation and were studied on their ability to identify and isolate closely spaced modes by defining the correct set of exciter forces under ideal and non-ideal conditions (noisy data, non-proportionally damped structures). Methods were evaluated on both simulated MDOF and measured data from realistic structures. In this paper some of the findings from the simulated data study are presented; results from using data from a real structure will be presented in a later paper.

2. PRELIMINARY THEORETICAL CONSIDERATIONS

Consider a structure whose complex response \underline{z} defined at m transducer locations is given by

$$\underline{z} = [A(\omega) + i B(\omega)] \underline{f} \quad (1)$$

where \underline{f} is the monophasic exciter force vector defined at e locations and $[A(\omega) + i B(\omega)]$ is the receptance transfer matrix at frequency ω . Each term in the matrix involves a series summation of contributions from all the modes of the structure, the expressions differing according to whether the damping is proportional or not. Although theoretically infinite the number of modes in the summation n is in practice finite. All the methods considered in the present paper operate on the inertance matrix as frequency ω changes and seek a force vector \underline{f} which when applied harmonically at the j^{th} undamped natural frequency ω_j ($j = 1, 2, \dots, n$) will excite the corresponding j^{th} undamped or "pure" mode. A "pure" mode is excited when response and excitation are in quadrature or when the real part of the response vector is zero, i.e. from (Eq.1)

$$[A(\omega)] \underline{f} = 0 \quad (2)$$

In order to solve Eq.2 for \underline{f} , the behaviour of the $[A(\omega)]$ matrix as frequency changes needs to be known and this depends on the relative values of m and e . For a square $[A(\omega)]$ matrix ($m=e$) a non-trivial solution of (Eq.2) is only possible when its determinant is zero, i.e.

$$|A(\omega)| = 0 \quad (3)$$

The variation of $|A(\omega)|$ with frequency depends upon the values of m (or e) and n . If the excitation and measurement locations are equal and coincident then for an n degree of freedom struc-

ture it can be shown theoretically that the determinant $|A(\omega)|$ vanishes at the natural frequencies of the n modes only, if and only if $m = e = n$. In this case phase quadrature is guaranteed at the measured m locations but not necessarily elsewhere on a continuous structure. If $m \neq n$ then the frequencies at which $|A(\omega)|$ vanishes are not necessarily natural frequencies. Overall examination of the conditioning of both the $[A(\omega)]$ and $[B(\omega)]$ matrices dictates that it is important to select a number of exciters equal to the number of modes n . Since however n is large the use of such a number of exciters should be impractical. Instead use is made of the number of modes actually effective in the immediate frequency range of interest (ENDOF), n^* and a number of exciters equal to n^* is used.

Asher's (Ref.5) method operates on the determinant of the real part $[A(\omega)]$ (Eq.2) whereas other methods (Ref.11) of the same category ($m=e$) operate on eigenformulations involving the real and imaginary parts $[A(\omega)]$ and $[B(\omega)]$ of the complex receptance matrix i.e. (dropping the frequency (ω) symbols),

$$\begin{aligned} A \underline{f} &= \lambda \underline{f} && \text{Modified Asher} & (4) \\ A \underline{f} &= \mu B \underline{f} && \text{Traill-Nash} & (5) \end{aligned}$$

When $m > e$ then the alternative eigenformulations are expressed by

$$\begin{aligned} A^T A \underline{f} &= \alpha \underline{f} && \text{Extended Asher} & (6) \\ A^T A \underline{f} &= \beta (A^T A + B^T B) \underline{f} && \text{MMIF (no weighting)} & (7) \end{aligned}$$

It can be shown that for the eigenformulations of Eqs. 4 and 5 modal frequencies correspond to frequencies where eigenvalues vanish whereas from Eqs. 6 and 7 natural frequencies correspond to local minima of the eigenvalues. In both cases the corresponding eigenvectors (interpolated) at each resonant frequency yield the appropriated force distributions. When $m > e$ then in practice the real part of the response can only be minimized in some way as defined by the following cost functions which correspond to Eqs. 6 and 7 above.

$$\sum_{k=1}^m [Re(z_k)]^2 \quad \text{Extended Asher} \quad (8)$$

$$\sum_{k=1}^m [Re(z_k)]^2 / \sum_{k=1}^m |z_k|^2 \quad \text{MMIF} \quad (9)$$

It should be noted that the original EA formulation in Ref.9 was incorrect; Ref.11 shows the correct analysis.

One of the main problems of the methods investigated (and generally all methods) is that the effective number of modes n^* is not known at the onset of the test. All that is known is that in the small frequency range of interest n^* is significantly smaller than n and also that n^* exciters (appropriately located) would be needed to excite all n^* modes. In practice the value of n^* is not easily deductible by observing some preliminary measurements from the structure e.g. frf's, indicator functions etc. However practical experience has shown that n^* is rarely larger than 5. From Eq.2, at each resonance ω_j , the rank of the $[A(\omega)]$ matrix is reduced by a number equal to the multiplicity of modes at ω_j ; the rank of the $[B(\omega)]$ matrix is not affected. If $e = n^*$ then $[A(\omega)]$ would be rank n^* away from ω_j and rank $(n^* - \gamma)$ at ω_j , where γ is the number of coincident modes at ω_j . If $e > n^*$ then both $[A(\omega)]$ and $[B(\omega)]$ would be singular at all resonant and non-resonant frequencies.

Clearly the choice of the number of exciters e will affect the conditioning of both the $[A(\omega)]$ and $[B(\omega)]$ matrices by virtue of the relation between e and n^* . Consequently, the performance of the methods based on the eigensolutions of Eq. 4 to 7 will also be severely affected.

3. MATHEMATICAL MODEL

In order to compare the methods, a 6-DOF "wing/engine" mathematical model was constructed; the wing could bend and twist and the engine could sway and yaw with reference to the wing. The natural frequencies of the model were at 57.4, 68.17, 70.72, 109.9, 165.7 and 410.3 Hz. A fairly high level of damping (5% critical) was used in the model to cause the second and third modes to interfere more. Figure 1 shows the shape of the wing second mode. Receptance matrices were evaluated for 8 ($m = 8$) transducer locations (5, 6, 9, 10, 11, 12, 13, 14) and 5 ($e = 5$) exciter locations (5, 9, 13, 10, 14) at discrete frequencies over the frequency range of interest. A receptance function corrupted by noise is plotted in Figure 2 which shows that a single input at the wing tip in the out of plane direction could not adequately separate the two close modes; a multi-point excitation would be needed.

The methods were studied by operating on subsets of the (8 x 5) receptance matrix in the 50 to 80 Hz frequency range. Square and rectangular subsets corresponding to different numbers of exciters (1 to 5) were employed; the effective number of degrees of freedom n^* in the 50-80 Hz range being essentially three. Different combinations of response and excitation locations were tried to simulate choices of accelerometer and exciter locations in practice. A full description of results is given in Ref.11 and a summary is presented here.

4. INVESTIGATION OF DIRECT METHODS

4.1. Equal Numbers of Response and Excitation Locations

The variation with frequency of the determinant $|A(\omega)|$ and the eigenvalues λ and μ for Eqs. 3 to 5 is shown in Figures 3 to 5 for a selection of coincident measurement/excitation locations and values of m . Note that the numbering on the eigenvalue plots is simply the ordering produced by the QR eigenvalue algorithm.

For a twin exciter combination 9, 13 in Figure 3 there are two zero crossings which indicate two modes. However the behaviour of the curves around 65 Hz shows the influence of an extra mode because they nearly cross again and μ does not increase monotonically.

The variation of the λ eigenvalues in Figure 3 is rather difficult to trace near the first zero crossing where the eigenvalues come close together. This variation is needed for selection of eigenvalue (and corresponding eigenvector) elements to fit and interpolate in order to identify natural frequencies and corresponding appropriated force vectors.

It is apparent from the above results that $n^* > 2$ at least for modes 2 and 3. Figure 4 shows results for the 3 exciter combination 9, 13, 10 for noise corrupted data. There are three zero crossings close to the undamped natural frequencies and the eigenvalues behave sensibly, crossing only once in this region. Note that a poor exciter combination 13, 14, 9 produced two crossings on-

ly, proving that a good exciter location choice is necessary to determine n^* . Noise has a small effect on $|A(\omega)|$ and λ but a significant effect on μ away from resonance.

Some results for the MA method with the four exciter combination 9, 13, 10, 14 are presented in Fig. 5 for noise-free data. An additional small eigenvalue is seen but there are still only three crossings. The determinant variation (not shown) is similar to that for $e = 3$ but the numerical values are smaller. The μ eigenvalue behaviour is also similar except for an additional large eigenvalue.

For a five exciter combination 9, 13, 10, 14, 5 the noise-free results are sensible and when noise is included the determinant crosses the frequency axis many times and so indicates near singularity of the $[A(\omega)]$ over the frequency region. Thus n^* must be less than 5 and this is confirmed by the λ eigenvalue behaviour which shows the additional eigenvalue root as being essentially zero over the entire region, the remaining roots behaving sensibly; such results would indicate that fewer exciters ought to be used. The results of the μ eigenvalue with noise were very poor due to the near singularity of the $[B(\omega)]$ matrix.

4.2. Unequal Numbers of Exciter and Response Locations.

The Extended Asher, Eq. 6 (both the determinant and eigenvalue implementations) and the Multivariate Mode Indicator Function, Eq.7, methods were studied. Receptance matrix data were used for the same eight transducer ($m = 8$) locations and five exciter locations ($e = 1$ to 5) as before. Note therefore that the exciter locations were always coincident with transducers.

Figure 6 shows clear dips at frequencies corresponding to modes 1 and 3 for an exciter combination at locations 9 and 13. The MMIF eigenvalues give the clearest indication of the second mode by the double dip in the primary MMIF and the dip in the secondary MMIF. However mode 2 would not be excited very well because the primary MMIF only dips to around 0.2. It is arguable that the Extended Asher determinant is easier to interpret than the corresponding eigenvalues α .

Figure 7 shows clear dips at all three natural frequencies for the three exciter combination 9, 13 and 10 since n^* has been reached for mode 2. The eigenvalues α are difficult to interpret because of the tracking problem, the dynamic range of the eigenvalues and the obscuring of the dip by extra small eigenvalues associated with using $e > n^*$, as seen around mode 1. Random noise had a small effect, especially for the primary MMIF around each resonance where $\beta < 0.2$. Effects on the secondary and tertiary MMIF were slightly higher.

Results for a four exciter combination at locations 9, 13, 10 and 14 (not shown) are similar for those for three exciters. The undisturbed behaviour of the fourth MMIF as frequency changes shows that more exciters are being used than are really necessary. The α eigenvalues become still more difficult to interpret (much more so than the modified approach to Asher's method).

Figure 8 shows results for a five exciter combination at locations 9, 13, 10, 14 and 5 for the MMIF method with noise corrupted data. The noise free behaviour is much the same as before but the addition of noise corrupts the picture signi-

ificantly, especially for the secondary and tertiary MMIF values. It is most likely that this is due to the near singularity of both the $[A(\omega)]^T[A(\omega)]$ and $[B(\omega)]^T[B(\omega)]$ matrices.

When the MMIF analysis was performed on data with non-coincident transducer and exciter locations (Refs.11,12) then, depending upon the measurement and excitation directions, peculiar behaviour of the MMIF eigenvalues is sometimes seen, including spurious dips or even absence of a dip where a phase resonant excitation is impossible for the data set used.

Therefore it is sensible to include accelerometers at all excitation locations and to ensure that all important structural motions are measured. The choice of exciter positions is not straight forward.

The problem of matrix ill-conditioning when $e > n^*$ may be overcome by a singular value decomposition approach as proposed recently by Wright and Juang (Ref.13). Alternatively the MA eigenvalues show how many exciters are necessary.

4.3. Determination of Appropriated Force Distributions

Once a suitable accelerometer exciter set was selected then the natural frequencies could be obtained from the zero crossings of the λ or μ or from the minima of α or β . Due to the influence of noise the eigenvalues were curve fitted with a simple polynomial in the resonance region and zero crossings or minima found from the fitted curve. Frequency results agreed well with the theoretical undamped natural frequencies.

Once the natural frequencies were identified the appropriated force distributions were obtained simply by recovering (at the natural frequency concerned) the eigenvector corresponding to the fitted eigenvalue. Curve fitting and interpolation avoids re-measuring at the natural frequencies. However it is important that the variation of the normalized eigenvector elements in this region is fairly smooth and passes through the desired values at the crossing frequency; this depends on the correct choice and hence "tracking" of eigenvalues.

Figure 9 shows normalised eigenvectors for the 3 exciter configurations considered earlier for all but Asher's method since solution of Eq.2 for f is difficult and very sensitive to measuring precisely at each natural frequency Ref.11. It was shown in Refs. 8 and 11 that the Modified Asher eigenvector varied in a discontinuous manner if the eigenvalues were assumed to cross each other near resonance but continuously when they were assumed not to cross (i.e. eigenvalues apparently discontinuous). This behaviour makes the Modified Asher method difficult to use for force distributions, especially for $e > n^*$ as seen in Figure 9. Indeed, whereas all the methods show fairly smooth eigenvector variation for $e = n^*$ (i.e. modes 2 and 3) only the Traill-Nash eigenvectors vary smoothly for $e > n^*$ (i.e. mode 1). However all methods yielded similar force distributions.

Figure 10 shows a "pure" mode 3 response that was obtained when the appropriated force vector was "applied" to the model. Off-quadrature errors were less than 2.5° , the largest error occurring at locations of low response. Corresponding Indicator Functions were of the order of 0.96 to 0.99.

5. ITERATIVE APPROXIMATE METHOD

An iterative method proposed by Morosow and Ayre (Ref.14) and Anderson (Ref.15) was also investigated using data from the 6-DOF wing-engine model. The main assumption of the method is that of proportional damping although the present study concluded that for low damping with a low degree of non-proportionality the method still worked adequately.

Effectively the method operates on a group of closely spaced modes, one of which is classified as the target while the rest are the "contaminating" modes. Initially the target mode is defined. The rest of the group modes are selected by virtue of the proximity of their frequencies to the target mode frequency or by virtue of their contaminating effect on the target mode. A number of exciters not exceeding the number of modes in the group is used and an iterative procedure is initiated. In the first cycle of the iteration each mode is excited at (or close to) its natural frequency using an initial estimate of its appropriated force vector. Once measurements for all modes in the group are obtained an initial estimate of the mode shape matrix is derived from the imaginary parts of the response vectors. The forcing matrix for the next iteration cycle is obtained from the inverse of the transpose of the subset of the mode shape matrix defined at the exciter locations. This inverse yields the physical forces required to produce generalised forces only in each mode of interest. Iterations are continued until the applied physical force vector, for each mode, has converged to the respective appropriated vector required to isolate the mode. Convergence is monitored by checking modal purity on the response via the Indicator Function, phase errors and diagonality of the generalised force matrix. The advantage of the method is that provided the correct number of exciters is used then it can automatically converge on tuning all the modes in the group.

The first 3 modes of the model were selected in a target group, exciters were selected at locations 9, 13, 10 and responses were measured at locations 5, 6, 9, 10, 11, 12, 13 and 14. The variation of the Indicator Function with iteration cycle is shown in Figure 11 from which it is clear that reasonable convergence was achieved after 5 or 6 iterations for all modes. The Indicator functions shown in Figure 12 correspond to a proportionally damped model and converged much more rapidly reaching values in the range of 0.99-1.00; proportionality in damping was achieved by reconstructing the damping matrix so that each of its elements was proportional to the respective elements of the mass matrix. Finally the effects of including only the two close modes 2 and 3 in the target group and using exciters at locations 9 and 13 are shown in Figure 13. Mode 3 converges to a value that is perhaps acceptable whereas mode 2 is not adequately isolated. Such poor results can indicate too small a target group and/or inappropriate choice of exciter locations.

It may be that this approach could be used to "fine tune" force distributions obtained from direct methods.

6. CONCLUSION

A number of methods has been investigated for identifying and isolating pure modes of vibration using appropriated multi-point excitation. The performance of the methods was evaluated on simulated data. It was found that the methods, can

successfully identify and isolate a number of closely spaced modes and that use of a combination of methods may be appropriate, each having different strengths.

REFERENCES

1. Gladwell G.M.L. and Bishop R.E.D. An investigation into the Theory of Resonance Testing. Aeronautical Research Council 22/381/0.1596 A.1 Report, September, 1960.
2. Taylor G.A. and Gaukroger D.R. and Skingle C.W. Mama - A Semi-Automatic Technique for Exciting the Principal Modes of vibration of Complex Structures. RAE TR 67211, M.O.T., Farnborough Hants, August, 1967 and H.M.S.O. RM No. 3590, 1969.
3. Breitbach E. A Semi-Automatic Modal Survey Test Technique for Complex Aircraft and Spacecraft Structures. Proceedings of the 3rd Esro Testing Symposium, Frascati, Italy 22-26, Oct. 22-26 1973, Esro SP-99, p. 519-528.
4. Coupry G. Nouvelle Method D'Identification Des Modes D'Une Structure. Recherche Aerospaciale, No. 5 September-October 1989, p. 347-352.
5. Asher G.W. A Method of Normal Mode Excitation Utilizing Admittance Measurements. Proceedings of the National Specialists Meeting on Dynamics and Aeroelasticity, Fort Worth, Journal of Aeronautical Sciences, Volume 6, November 1958, pp. 67-76 AIAA Journal Volume 20, No. 9, p. 1310, 1982.
6. Traill-Nash R.W. On the Excitation of Pure Natural Modes in Aircraft Resonance Testing. Journal of Aero. Sc. volume 125, No. 12, p. 775-782, December 1958 and ARL, Australia Report 254, 1957.
7. Traill-Nash R.W. Some Theoretical Aspects of Resonance Testing and Proposals for A Technique Combining Experiment and Computation. Department of Supply, Australian DSS, Aeronautical Research Labs. Report ARL/SM 280, Melbourne, April, 1961.
8. Alexiou K. and Wright J.R. Determination of Force Distribution in Multi-Point Resonance Testing Using Various Direct Methods. Proc. 2nd International Symposium on Aeroelasticity and Structural Dynamics, Aachen. April 1985, pp. 553-564.
9. Ibañez P. and Blakely K.D. Automatic Force Appropriation - A Review and Suggested Improvements. Proc. 2nd IMAC. 1984.
10. Williams R. Crowley J. and Vold H. The Multivariate Mode Indicator Function in Modal analysis. Proc. 4th IMAC. 1986.
11. Alexiou K. Comparison of Multi-Point Vibration Test Methods. Ph.D. Dissertation, University of London, June 1990.
12. Nash M. Use of the Multivariate Mode Indicator Function for Normal Mode Determination. Proceedings 6th IMAC, 1998.
13. Juang J.N. and Wright J.R. A Multi-Point Force Appropriation Method Based upon a Singular Value Decomposition approach. Proceedings 7th IMAC, Las Vegas, 1989.
14. Morosow G. and Ayre R.S. Force Apportioning for Modal Vibration Testing Using Incomplete Excitation. Sound and Vibration Bulletin, Vol. 48, Part 1, pp. 39-48, 1978.
15. Anderson J.E. Another Look at Sine-Dwell Modal Testing. AIAA Report 81-0530.

FIGURES

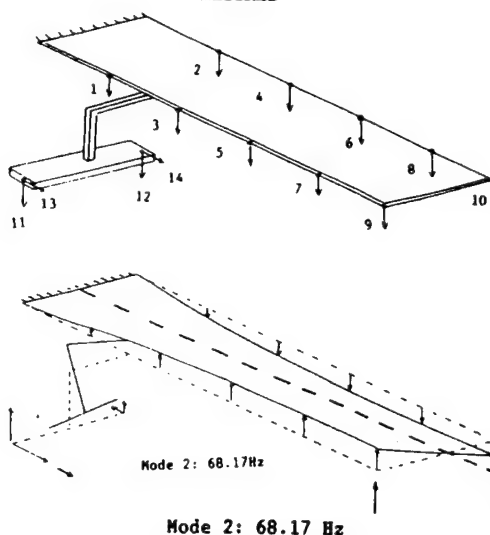


FIGURE 1 SIX-DOF Model: undeformed shape and mode shape of second normal mode.

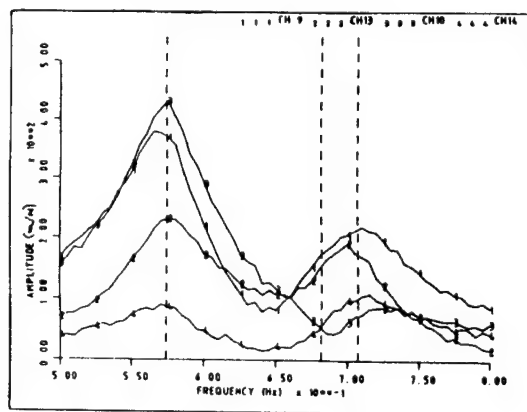


FIGURE 2 SIX-DOF Model: Sample transfer function (with noise) excitation at location 9, response at locations 9, 13, 10, 14.

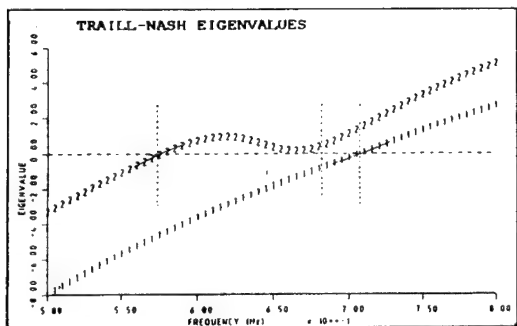
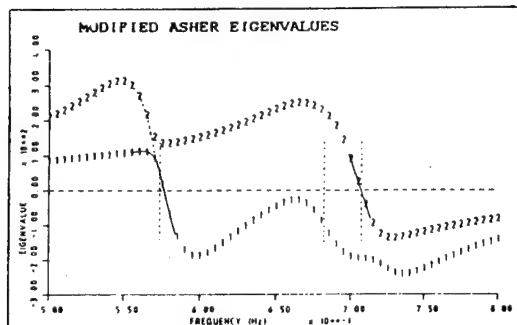
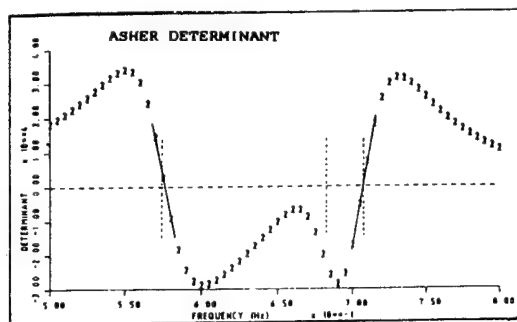


FIGURE 3 SIX-DOF Model: Variation of determinant/eigenvalues for A/MA/TN methods - excitation/response at locations 9,13 ($\epsilon=2$).

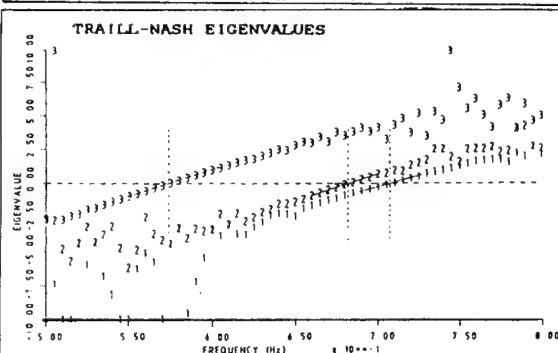
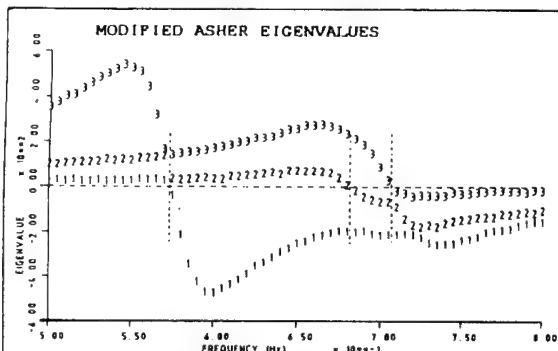
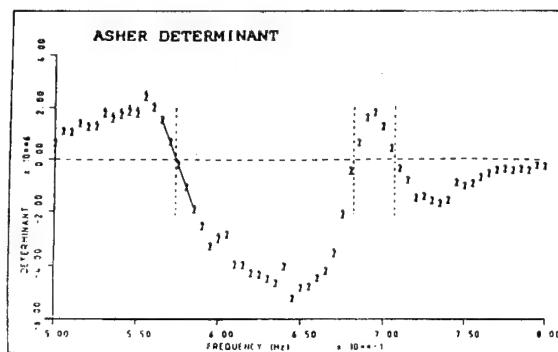


FIGURE 4 SIX-DOF Model (with noise): Variation of determinant/eigenvalues for A/MA/TN methods - excitation/response at locations 9, 13, 10 ($\epsilon=3$).

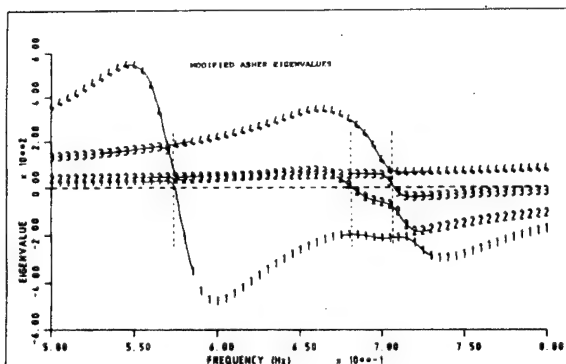


FIGURE 5 SIX-DOF Model: Variation of eigenvalues for MA method - excitation/response at locations 9, 13, 10, 14 ($\epsilon=4$).

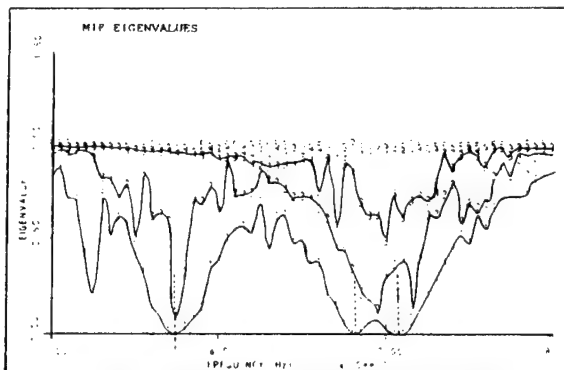


FIGURE 8 SIX-DOF Model (with noise): Variation of eigenvalues for MIF method - excitation at locations 9, 13, 10, 14, 5 ($\epsilon=5$), response at locations 5, 6, 9, 10, 11, 12, 13, 14 ($\epsilon=8$).

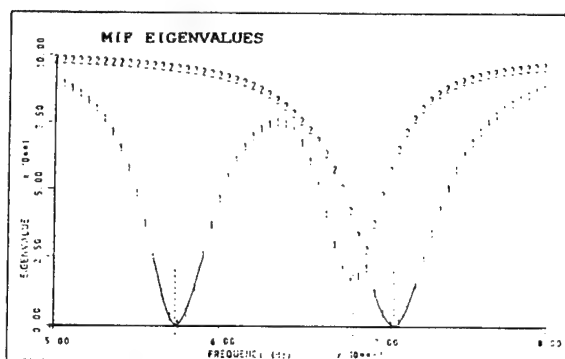
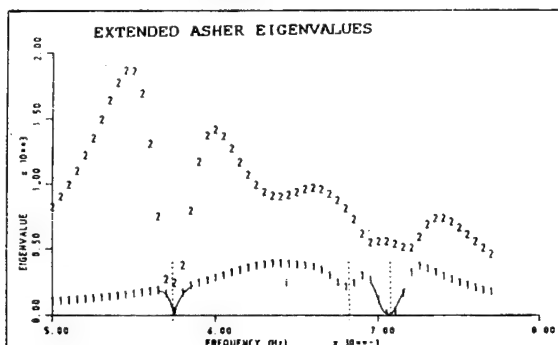
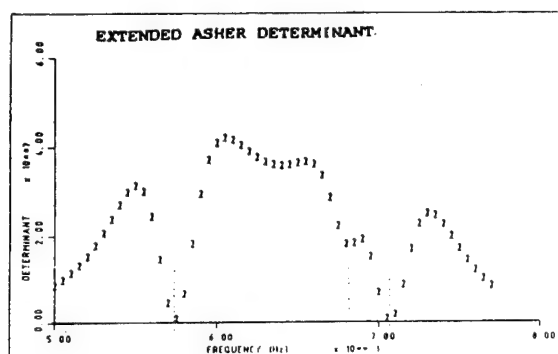


FIGURE 6 SIX-DOF Model: Variation of determinant/eigenvalues for EA/MIF methods - excitation at locations 9, 13 ($\epsilon=2$), response at locations 5, 6, 9, 10, 11, 12, 13, 14 ($m=8$).

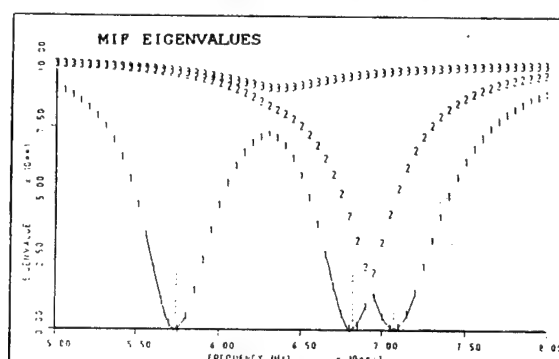
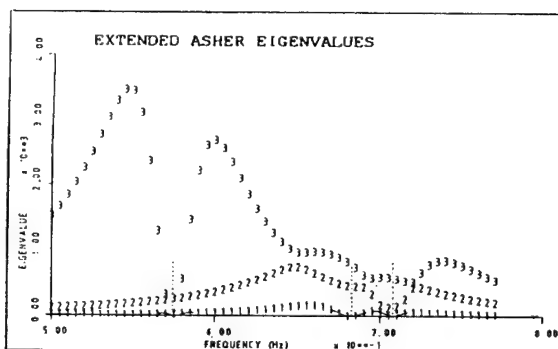
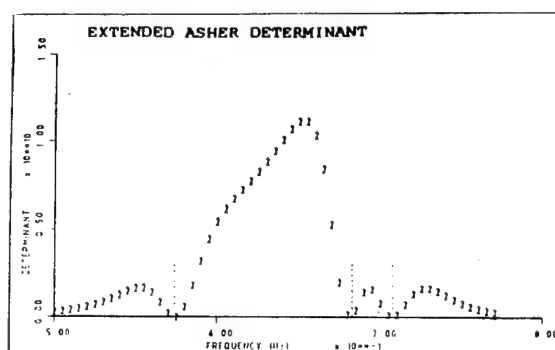


FIGURE 7 SIX-DOF Model: Variation of determinant/eigenvalues for EA/MIF methods - excitation at locations 9, 13, 10 ($\epsilon=3$), response at locations 5, 6, 9, 10, 11, 12, 13, 14 ($m=8$).

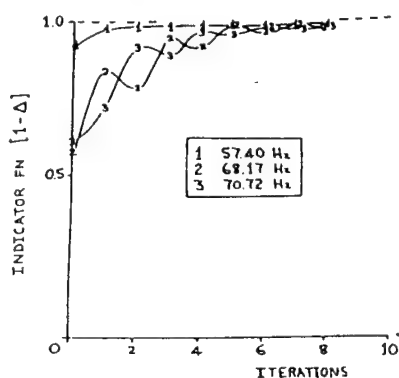


FIGURE 11 SIX-DOF Model: Variation of Indicator function with iteration number - Morosov and Ayre method, 3 mode target group - excitation at locations 9, 13, 10 ($\epsilon=3$), response at locations 5, 6, 9, 10, 11, 12, 13, 14 ($m=8$).

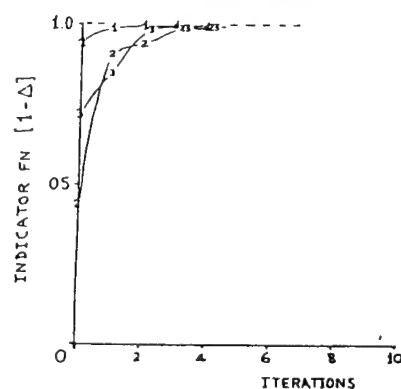


FIGURE 12 SIX-DOF Model (proportional damping): Variation of Indicator function with number - Morosov and Ayre method, 3 mode target group - excitation at locations 9, 13, 10 ($\epsilon=3$), response locations 5, 6, 9, 10, 11, 12, 13, 14 ($m=8$).

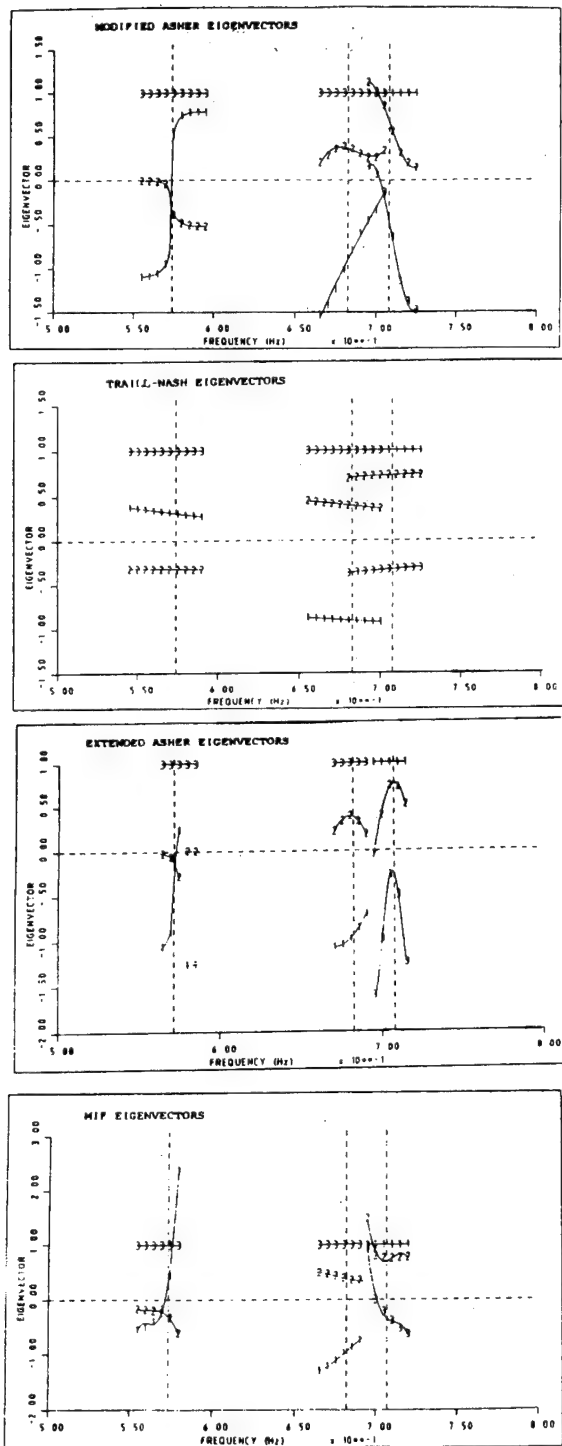


FIGURE 9 SIX-DOF Model: Variation of eigenvector elements for NA/TN/EA/MIF methods - excitation at locations 9,10 (e=3) response at locations 5, 6, 9, 10, 11, 12, 13, 14 (m=8).

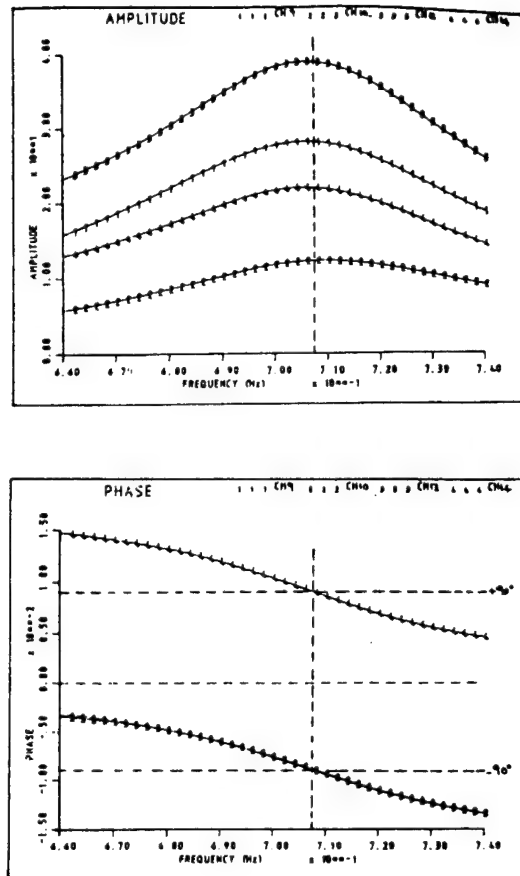


FIGURE 10 SIX-DOF Model: Transfer functions from appropriated 3 force distribution, mode 3 - excitation/response at locations 9, 13, 10, (e=m=3).

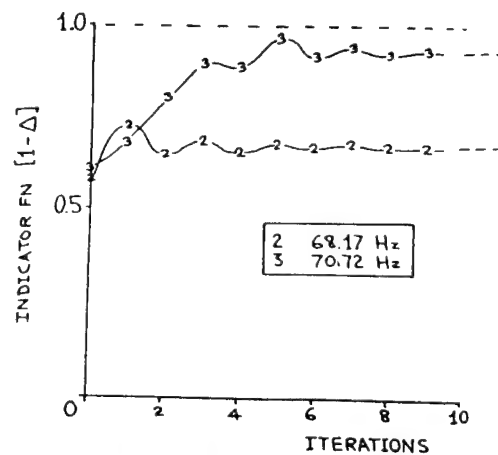


FIGURE 13 SIX-DOF Model: Variation of Indicator function with iteration number - Morosov and Ayre method, 2 mode target group - excitation at locations 9, 13 (e=2), response at locations 5, 6, 9, 10, 11, 12, 13, 14 (m=8).

N92-238509
84762

DESIGN PARAMETER UPDATE OF DYNAMIC MATHEMATICAL MODELS IN PRESENCE OF TEST NOISE AND MODE PAIRING PROBLEMS

B. Caesar¹, L. Eckert¹, A. Hoppe²

¹ Dornier GmbH, Friedrichshafen, FRG

² University of Stuttgart, FRG

ABSTRACT

An update procedure is described, which improves design parameters towards the correct ones so that the eigenfrequencies and mode shapes of a mathematical model converge to the measured ones. Design parameter can be any input parameter of a Finite Element- (FE-) model. The objective is to minimize the weighted differences of measured and analysed eigenfrequencies and mode shapes with minimum changes of the design parameters. Any type of finite element may be used in the FE-model. The in general nonlinear functions of the eigenfrequencies and modes w.r.t. the design parameters are linearized based on FE-sensitivity analyses. The new mode shapes are calculated as a linear combination of the initial ones.

The procedure is able to update erroneous design parameters in the presence of noisy test data. The test data may be incomplete. No condensation to the test degrees of freedom or expansion of the test to the analysis data is necessary.

The procedure requires the calculation of eigenfrequency and mode shape differences. This calculation is possible only, if test and analysis modes can be paired. In case of crossing eigenfrequency sequences between test and analysis and mode coupling pairing criteria as the Model Assurance Criterion (MAC) fail and lead to significant convergence problems. The paper shows how to treat such pairing problems.

Numerical examples using noisy and incomplete test data demonstrate the successful application of the update procedure.

Keywords: Model Update, Structural Dynamics, Test Data, Noise, Mode Pairing.

NOMENCLATURE

J	objective function
J^f, J^a, J^a	terms of objective function
ω_k	k-th circular eigenfrequency [rad/s]
f_k	k-th eigenfrequency [Hz]

p_l	l-th design parameter
a_l	l-th correction parameter
a	vector, containing the correction parameters $a_l, l=1, L$
c_l	l-th correction factor ($c_l=1+a_l$)
w_l^a	weighting factor for l-th parameter
w_k^f, w_k^a	weighting factor for k-th eigenfrequency, eigenvector
W^f, W^a, W^a	weighting factors for different terms in objective function
Φ	modal matrix, containing eigenvectors as columns
Φ_k	k-th eigenvector
Φ_{ik}	i-th component of k-th eigenvector
$\Phi_{\max, k}$	maximum component of k-th eigenvector
$\ \phi\ $	euclidian norm of vector ϕ

Indices:

Subscripts:

$i=1, I$	index for measured degree of freedom
$k=1, K$	index for mode
$l=1, L$	index for design parameter

Superscripts:

i	initial analysis
u	updated model
m	measured

1. UPDATE OBJECTIVES

The update procedure described in this paper shall improve design parameters of dynamic mathematical models towards the correct ones. Satisfying this major objective results in a mathematical model that

- reproduces the measured data, namely eigenfrequencies, mode shapes and if available generalized masses and total mass,
- improves additionally the not measured properties (effective masses, not measured eigenfrequencies, modes shapes and generalized masses, local stiffnesses and mass distributions),
- can be used as a submodel for coupled analyses and
- can be used for static and control analyses.

The reference data, eigenfrequencies and mode shapes, are gained from tests.

The update procedure shall run

- in presence of random errors on the test data (noisy test data),
- with incomplete test data, i.e.
 - with a number of measurement pick-ups much smaller than the number of degrees of freedom of the mathematical model and
 - with an incomplete number of measured mode shapes.

The procedure shall converge fast and stable and shall support the process of error localization and error source detection.

2. THEORY

The theory of the update procedure is described in detail in Ref. 1.

2.1 Principal Ideas

The update procedure gives a frame in which different programme packages, in general FE programmes, can be run. Actually the procedure is coupled with PERMAS and ASKA.

Any input parameter may be selected as update variable e.g. material properties (density, modulus of elasticity, ...), geometrical input data (thickness, cross sectional area, moment of inertia, ...) or even nodal point coordinates. A set of such physical variables called design parameters has to be selected by the user.

The l -th updated design parameter p_l^u is described as a function of the l -th correction parameter a_l and the initial design parameter p_l^i by:

$$p_l^u(a_l) = (1+a_l) \cdot p_l^i \quad (1)$$

Iteratively the design parameters are improved minimizing the differences between measured and analysed eigenfrequencies and mode shapes.

The procedure works with a selected number of degrees of freedom (dofs) of the analysis which can be correlated with test dofs (pick-ups). Thus no condensation of the analysis model to the test (e.g. by Guyan reduction) or expansion of the test dofs to the complete analysis model is required.

2.2 Objective Function

The objective function minimizes the weighted differences of eigenfrequencies and mode shapes from analysis and test with minimum changes of the design parameters. So, the objective function (Eq. 2) consists of three terms:

$$\text{minimize } J(a) = J^f(a) + J^\phi(a) + J^a(a) \quad (2)$$

with

$$J(a) = W^f \sum_{k=1}^K w_k^f \left[\frac{f_k^u(a) - f_k^m}{f_k^m} \right]^2 + W^\phi \sum_{k=1}^K w_k^\phi \sum_{i=1}^I w_i^\phi \left[\frac{\phi_{ik}^u(a) - \phi_{ik}^m}{\phi_{\max,k}^m} \right]^2 + W^a \sum_{l=1}^L w_l^a a_l^2 \quad (3)$$

and

$a = \{a_1, a_2, \dots, a_l, \dots, a_L\}^T$: vector of correction parameters

$W^f, W^\phi, W^a, w_k^f, w_k^\phi, w_l^a$: weighting factors
 f_k : k -th eigenfrequency

ϕ_{ik} : i -th component of k -th eigenvector
 superscript m : measured, superscript u : updated analysis and superscript i : initial analysis.

The updated eigenfrequencies and eigenvectors are approximated by a first Taylor's series expansion based on sensitivities of eigenfrequencies and eigenvectors.

$$f_k^u(a) = f_k^i + \sum_{l=1}^L \frac{\partial f_k(a_l)}{\partial a_l} \cdot a_l \quad (4)$$

$$\phi_k^u(a) = \phi_k^i + \sum_{l=1}^L \frac{\partial \phi_k(a_l)}{\partial a_l} \cdot a_l \quad (5)$$

The analysis eigenvector sensitivities are assumed to be a linear combination of the M lowest eigenvectors of the initial model (superscript i)

$$\frac{\partial \phi_k(a_l)}{\partial a_l} = \sum_{m=1}^M d_{mk}(a_l) \cdot \phi_m^i \quad (6)$$

2.3 Minimization with Constraints

The objective function Eq. 2 is minimized by a routine described in Ref. 3 solving nonlinear constrained optimization problems. The constraints may be general functions of the correction parameters a_l

$$g_j(a) \leq 0 \quad (7)$$

or

$$a_l^{LB} \leq a_l \leq a_l^{UB} \quad (8)$$

superscript LB: lower bound
 superscript UB: upper bound

so, that changes of the design parameters can be limited between upper and lower bounds.

2.4 Scaling of Measured Eigenvectors

The eigenvectors of analysis and test have to be paired to calculate the difference of the eigenvector components in Eq. 2. Prior to this difference calculation the eigenvectors are scaled either

- to generalized masses equal to 1

or

- to the length of the analytical vector using the Modal Scale Factor MSF with

$$\phi_k^{m*} = \text{MSF} \cdot \phi_k^m \quad (9)$$

The MSF is defined by

$$\text{MSF}(\varphi_i^u/\varphi_j^m) = \frac{\varphi_i^{uT} \varphi_j^m}{\varphi_j^{mT} \varphi_j^m} \quad (10)$$

The Modal Scale Factor is taken if the accuracy of the measured generalized mass is insufficient.

2.5 Mode Pairing

The measured and analytical mode shapes are paired on the basis of maximum values of the Modal Assurance Criterion (MAC) (see Ref. 2).

$$\text{MAC}(\varphi_i^m, \varphi_j^u) = \frac{(\varphi_i^{mT} \varphi_j^u)^2}{(\varphi_i^{mT} \varphi_i^m) (\varphi_j^{uT} \varphi_j^u)} \quad (11)$$

3. NUMERICAL EXAMPLES

Three different numerical examples are discussed in the following:

- The problem of mode pairing by maximum MAC-values is described with a two degree of freedom spring-mass system (2-DOF-System).
- A small scale beam model, due to its shape called FORK, will demonstrate the robustness of the update method w.r.t. noise on test data (random errors).
- Finally a hardware test case is presented with update results of a 2 m by 5 m frame structure.

3.1 The Pairing Problem

Design Parameter Update with the objective to minimize the weighted differences of measured and analytical eigenfrequencies and mode shapes requires paired eigenfrequencies and mode shapes to calculate these differences.

Good correlation between two mode shapes, one measured and one analysed, should be a sufficient criterion for pairing. So,

commonly the Modal Assurance Criterion MAC is used as a measure for correlation. Modes are paired according to the maximum MAC-value.

A simple example of a two degree of freedom spring-mass system shall demonstrate that mode pairing by maximum MAC-values is not sufficient and can be the reason for convergence problems.

Fig. 1 shows the change of the eigenvalues ω_1 and ω_2 of the spring-mass system w.r.t. changes of the stiffness k_2 . The influence of k_2 at the starting point ($k_2 = 0.4$) is mainly on ω_1 and switches over to ω_2 in the range of $0.8 < k_2 < 1.2$. We have a coupling or crossing point of the two modes in this range. In addition Fig. 1 shows an extreme sensitivity of the effective masses of both modes in the range of $0.8 < k_2 < 1.2$ indicating significant coupling w.r.t. the forced response behaviour, too. So, such an area is sensitive and of major interest for the prediction of the dynamic behaviour of the system.

Finally let us check the behaviour of the MAC-values (Fig. 2) according to stiffness changes of k_2 . The maximum MAC-value at the starting point indicates very good correlation between analysis mode 2 and test mode 1 (φ_2/φ_1^m) together with no correlation between analysis mode 1 and test mode 2 (φ_1/φ_2^m). At the crossing-point of

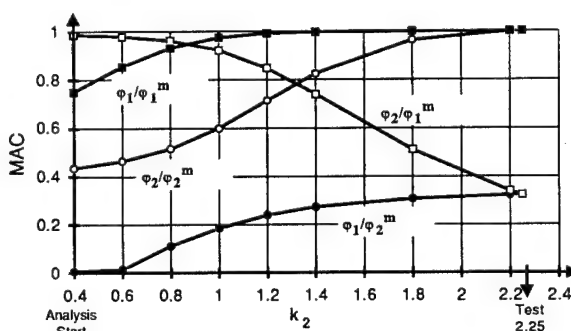


Figure 2: MAC-Value Evolution w.r.t. Stiffness Change

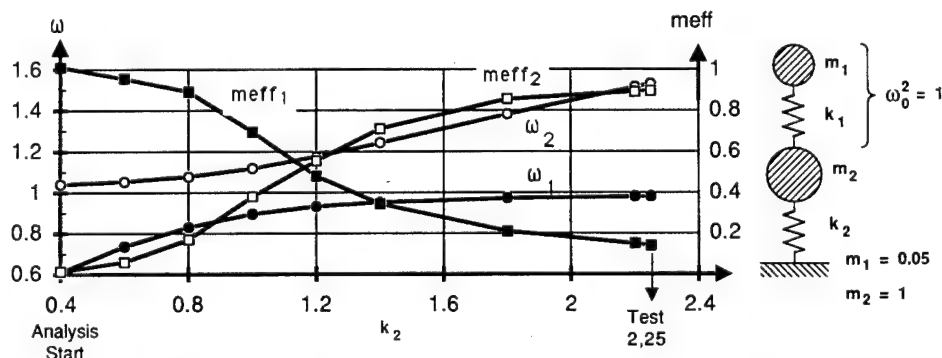


Figure 1: Eigenvalue and Effective Mass Change w.r.t. Stiffness Change

the two MAC-curves (ϕ_2/ϕ_1^m) and (ϕ_1/ϕ_1^m) the system changes. From that point on the maximum MAC-value indicates pairing of analysis mode 1 with test mode 1 and analysis mode 2 with test mode 2.

An update of the spring stiffness from the starting point $k_2 = 0.4$ to $k_2 = 0.6$ based on maximum MAC-value pairing would cause that the terms of the objective function change in the following way:

- increase of the eigenvalue difference $\omega_2^u - \omega_1^m$ (MAC-value 0.98),
- decrease of the eigenvalue difference $\omega_1^u - \omega_2^m$ (MAC-value 0.0),
- increase of the eigenvector difference $\phi_2^u - \phi_1^m$, acc. to decrease of MAC,
- decrease of the eigenvector difference $\phi_1^u - \phi_2^m$, acc. to increase of MAC.

This means, only two terms (out of four) of the objective function would decrease and an improvement of the design parameter k_2 from its starting point may not be possible due to an increase of the objective function. Leaving out the eigenfrequency and mode shape pair with the very poor MAC-value would even make worse the situation. The only term, that decreases with an improvement of k_2 would be thrown out.

As an alternative to the MAC-value one could check the linear combination between test and analysis mode shapes by

$$\min \epsilon = \phi_t - \phi_a B \quad (12)$$

with

$$B = [\phi_a^T \phi_a]^{-1} \cdot [\phi_a^T \phi_t] \quad (13)$$

Our actual experience is, that the B-matrix coefficients give similar results as the MAC-matrix and do not solve the problem.

Both, the MAC-matrix as well as the B-matrix, show significant coupling between the two mode pairs.

Recommendation:

- The maximum MAC-value shall be taken for mode pairing in general.
- An exception from this rule becomes valid, if the ascending eigenfrequency sequence of paired modes is disturbed, e.g. analysis mode i is paired with test mode j and vice versa (see Fig. 4 of the FORK-example).
- In the exception case
 - a) both pairs may be omitted in the first update steps until an undisturbed ascending sequence of mode pairs is reached or

- b) the undisturbed ascending sequence of mode pairs may be used in contradiction to the maximum B_{ij} or MAC_{ij} values if these values indicate modal coupling between two mode pairs (no experiences are available with this method).

Method a) is not applicable in case of the two dof spring-mass system omitting all available modes. In case of many modes and mode pairs this method has shown convincing results.

3.2 The FORK Test Case

The FORK model is shown in Fig. 3. It is a simple two dimensional beam model with 27 dofs. Tab. 1 and 2 give the model input data for stiffness and mass for both the analysis and the test model. The simulated test data, the eigenfrequencies and mode shapes, are disturbed by random errors (noise).

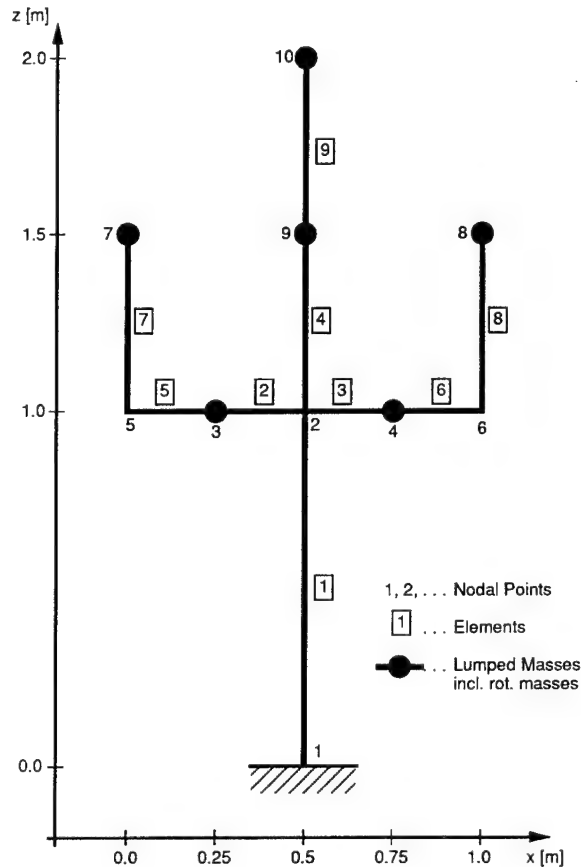


Figure 3: FORK-Geometry

3.2.1 Definition of Noise

The test inaccuracies in the measured eigenfrequencies and eigenvectors shall be of random nature. For this noisy test data a

Table 1: FORK. Beam Element Data

Element No.	Initial Analysis Model FORK			Test Model FORKP		
	Density	Area	Moment of Inertia	Density	Area	Moment of Inertia
	ρ 10^5 kg/m^3	A 10^{-4} m^2	I 10^{-6} m^4	ρ 10^5 kg/m^3	A 10^{-4} m^2	I 10^{-6} m^4
1	0.5384	7.4283	369.52	like	9.2854	369.52
2	1.0510	5.7103	5.2872	Initial	5.7103	5.2872
3	1.4010	6.8524	7.1377	Model	6.8524	7.1377
4	1.0770	9.2854	527.88		9.2854	527.88
5	1.0510	5.7103	5.2872		5.7103	5.2872
6	1.4010	4.5682	6.6090		4.5682	6.6090
7	5.0450	0.1487	1.9457		0.1487	2.5943
8	10.0900	0.1487	2.8198		0.19827	3.7598
9	0.0000	0.08566	0.46396		0.08566	0.71378

Modulus of Elasticity: $E = 7 \cdot 10^{10} \text{ N/m}^2$

Table 2: FORK. Mass Data

Nodal Point No.	Initial Analysis Model FORK		Test Model FORKP	
	Mass	Rotational Mass	Mass	Rotational Mass
	m kg	θ kgm ²	m kg	θ kgm ²
1	0.0	0.0	0.0	0.0
2	0.0	0.0	0.0	0.0
3	180.0	42.0	180.0	42.0
4	165.0	42.0	165.0	42.0
5	0.0	0.0	0.0	0.0
6	0.0	0.0	0.0	0.0
7	14.0	1.8	20.0	3.0
8	39.0	4.2	30.0	4.2
9	360.0	37.5	400.0	37.5
10	12.0	1.0	15.0	1.0

medium noise level of
maximum 1 % on the eigenfrequencies
and
maximum 10 % of the maximum component of
an eigenvector on each vector component
is assumed.
So, small components of the eigenvector may
have large errors well above 10 %.

The measured generalized mass is assumed to
be not reliable enough to be used for updat-
ing at all.

3.2.2 Results of the FORK Test Case

Initial Modal Data

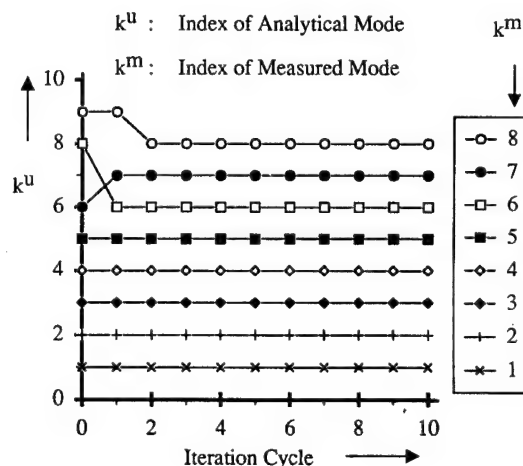
Tab. 3 gives a correlation between the mea-
sured eigenfrequencies of the test model
and the initial eigenfrequencies of the
analysis model prior to updating. The mode
shape correlation based on maximum MAC-
values figures out poor to bad correlation
from mode 4 to 7 within the first eight mode
shapes, although the eigenfrequency differ-
ences are less than 12 % (see Tab. 4).
The MAC-values indicate a sequence crossing
of the measured modes 6, 7 and 8 to the
analysis modes. Analysis mode shape 7 can
not be correlated to any of the eight mea-
sured modes.

Update Results

W.r.t. the experiences on convergence prob-
lems gained from other test cases and on
the pairing problems described in chapter
3.1, the update process was started leaving
out test mode 6, 7 and 8. At the end of
iteration 2 the correlation sequence appear-
ed undisturbed and all eight measured modes
could be used for further updating (see
Fig. 4).

Fig. 5 and 6 show the fast convergence of
the MAC-values and the frequency differen-
ces, indicating the fast convergence of the
analysis mode shapes and eigenfrequencies
towards the test values.

In Fig. 7 one can see the evolution of the
correction factors of the design param-
eters. Based on this results one could have
stopped the update process at the end of
iteration 5 having reached already perfect
MAC-values close to 1 and eigenfrequency
differences well below 1 %. Only some de-
sign parameters have not reached final but
already satisfying values (see Tab. 5).

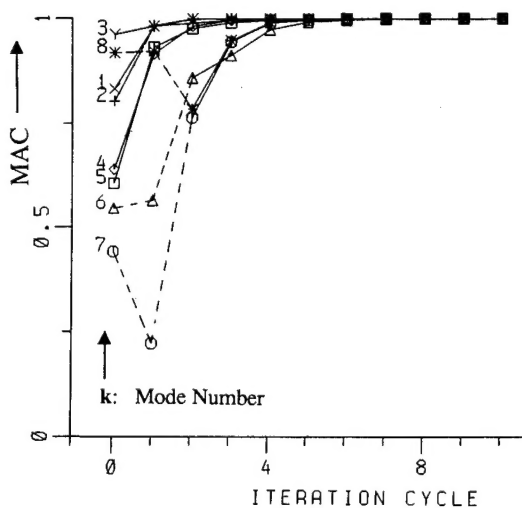
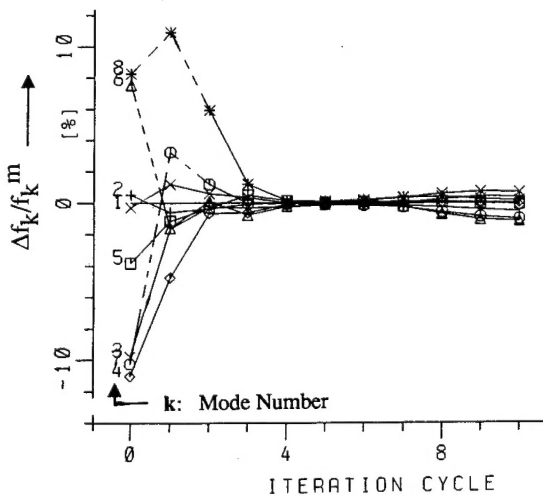
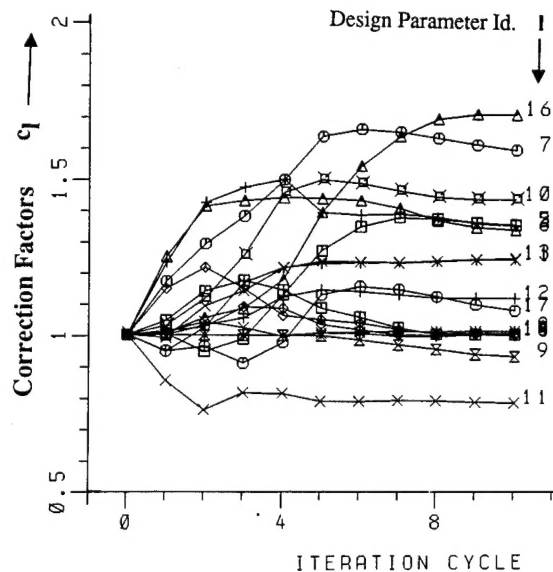
**Figure 4:** FORK.

Mode Pairing by Maximum MAC-Value

Table 3: FORK. Correlation of Test and Analysis Model

TEST MODEL			INITIAL MODEL			UPDATED MODEL		
k^m	f_k^m	f_k^m	k^i	f_k^i	MAC	k^u	f_k^u	MAC
	1)	2)			1), 2)			1), 2)
-	[Hz]	[Hz]	-	[Hz]	-	-	[Hz]	-
1	21.40	21.19	1	21.13	0.834	1	21.34	1.000
2	24.33	24.18	2	24.30	0.803	2	24.27	1.000
3	32.06	32.22	3	29.07	0.963	3	32.05	1.000
4	37.31	37.17	4	33.07	0.638	4	37.19	1.000
5	38.23	38.15	5	36.68	0.605	5	38.13	1.000
6	42.70	43.12	8	46.37	0.546	6	42.62	1.000
7	43.82	44.19	6	39.66	0.442	7	43.75	1.000
8	47.57	47.39	9	51.30	0.919	8	47.47	1.000
9	50.77	50.93	7	44.83	0.577	9	50.69	0.999
10	52.34	52.07	10	60.11	0.911	10	52.18	1.000
11	118.26	117.49	11	108.04	0.647	11	118.06	0.999
12	122.30	122.40	13	124.42	0.722	12	122.10	0.999

1) with respect to unnoisy modal test data
 2) with respect to noisy modal test data

**Figure 5:** FORK. Evolution of MAC-Values**Figure 6:** FORK. Evolution of Eigenfrequency Differences**Figure 7:** FORK. Correction Factor EvolutionConclusions from FORK Update

The update procedure works with incomplete, noisy test data, improves the physical design parameter towards the correct ones and with that improves also not measured properties as the eigenfrequencies and mode shapes number 9 to 12. Stiffness and mass errors can be located.

The FORK example is based on consistent updating. This means, the error can exactly be described by changes of the FE-model.

The algorithm is stable and converges rapidly.

Table 4: FORK. Deviations of Eigenfrequencies and Mode Shapes

INITIAL MODEL						UPDATED MODEL				
k^m	k^i	$\Delta f^i/f_k^m$	MAC	$\ \Delta \varphi^i\ /\ \varphi_k^m\ $	$\Delta f^i/f_k^m$	k^u	$\Delta f^u/f_k^m$	MAC	$\ \Delta \varphi^u\ /\ \varphi_k^m\ $	$\Delta f^u/f_k^m$
		1)	1)	1)	2)		1)	1)	1)	2)
-	-	[%]	-	[%]	[%]	-	[%]	-	[%]	[%]
1	1	-1.29	0.834	41.65	-0.30	1	-0.299	1.000	0.24	0.704
2	2	-0.14	0.803	47.02	0.50	2	-0.240	1.000	0.14	0.389
3	3	-9.34	0.963	29.98	-9.78	3	-0.047	1.000	0.80	-0.528
4	4	-11.37	0.638	62.05	-11.03	4	-0.340	1.000	0.52	0.043
5	5	-4.04	0.605	64.04	-3.85	5	-0.248	1.000	0.41	-0.057
6	8	8.59	0.546	81.14	7.55	6	-0.186	1.000	0.47	-1.141
7	6	-9.49	0.442	74.71	-10.26	7	-0.147	1.000	0.41	-0.996
8	9	7.85	0.919	64.76	8.26	8	-0.216	1.000	0.74	0.168
9	7	-11.70	0.577	67.31	-11.98	9	-0.157	0.999	3.32	-0.468
10	10	14.84	0.911	43.49	15.45	10	-0.304	1.000	1.65	0.225
11	11	-8.642	0.647	72.580	-8.042	11	-0.168	0.999	3.43	0.487
12	13	1.731	0.722	53.160	1.643	12	-0.158	0.999	3.59	-0.244

1) with respect to unnoisy modal test data

2) with respect to noisy modal test data

Table 5: FORK. Correction Factors (True Values and from Update). Deviations from True Values

Type of Design Parameter			Correction Factors				Deviations from True Correction Factors		
			INITIAL MODEL	True Value	UPDATE 10 Iterations	UPDATE 5 Iterations	INITIAL MODEL	UPDATE 10 Iterations	UPDATE 5 Iterations
l	p_l	element no./ node no.	c_l^i	c_l^{true}	c_l^u	c_l^u	$\Delta c_l^i/c_l^{true}$	$\Delta c_l^u/c_l^{true}$	$\Delta c_l^u/c_l^{true}$
-	-	-	-	100 %	-	-	%	%	%
1	A	1	1.00	1.250000	1.24700	1.237	-20.00	-0.24	-1.04
2	A	8	1.00	1.333334	1.35513	1.394	-25.00	1.63	4.55
3	I	2	1.00	1.000000	1.00528	1.008	0.00	0.53	0.80
4	I	3	1.00	1.000000	1.00563	1.036	0.00	0.56	3.60
5	I	7	1.00	1.333334	1.35825	1.272	-25.00	1.87	-4.60
6	I	8	1.00	1.333334	1.34237	1.439	-25.00	0.68	7.92
7	I	9	1.00	1.538500	1.59736	1.637	-35.00	3.83	6.40
8	p	1	1.00	1.000000	1.01891	1.008	0.00	1.89	0.80
9	p	8	1.00	1.000000	0.93800	1.000	0.00	-6.20	0.00
10	m	7	1.00	1.428600	1.43855	1.498	-30.00	0.70	4.86
11	m	8	1.00	0.769200	0.79032	0.791	30.01	2.75	2.83
12	m	9	1.00	1.111111	1.12286	1.147	-10.00	1.06	3.23
13	m	10	1.00	1.250000	1.25167	1.230	-20.00	0.13	-1.60
14	θ	3	1.00	1.000000	1.01100	1.051	0.00	1.10	5.10
15	θ	4	1.00	1.000000	1.00786	1.088	0.00	0.79	8.80
16	θ	7	1.00	1.666667	1.70995	1.394	-40.00	2.60	-16.36
17	θ	10	1.00	1.000000	1.08432	1.130	0.00	8.43	13.00

3.3 Update of the SPACE FRAME

The SPACE FRAME is a 2 m by 5 m truss structure with a mass of 90 kg, similar to a light weight frame structure which is planned to be used in future orbital space stations (see Fig. 8). The test as well as the FE-model data are based on Ref. 4.

The structure consists of 117 beams, 6 plates and 48 structural nodes, connecting the beams and plates. The FE-model consists of 146 nodes, 117 times 2 beam elements, 6 times 4 plate elements and 48 concentrated masses and has 146 times 6 dofs. The beams have been assumed to be incorrect. Three

types of beams exist,

- beams in x,y-plane
 - beams parallel to the z-axis and
 - diagonal beams
- with 4 design parameters each, namely
- cross-sectional area A,
 - moments of inertia I_x , I_y
 - St. Venant torsion constant J and
 - density ρ .

This results in 48 design parameters to be updated. No detailed information about design and test of the structure to support the update process are available to the authors.

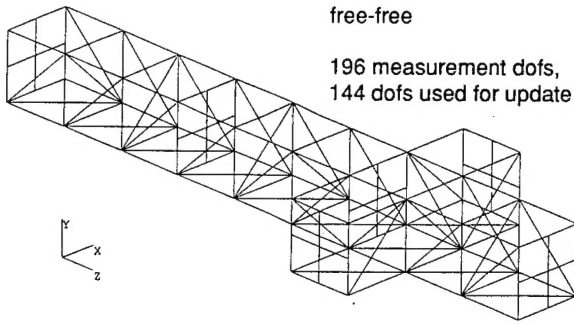


Figure 8: SPACE FRAME. FE-Model

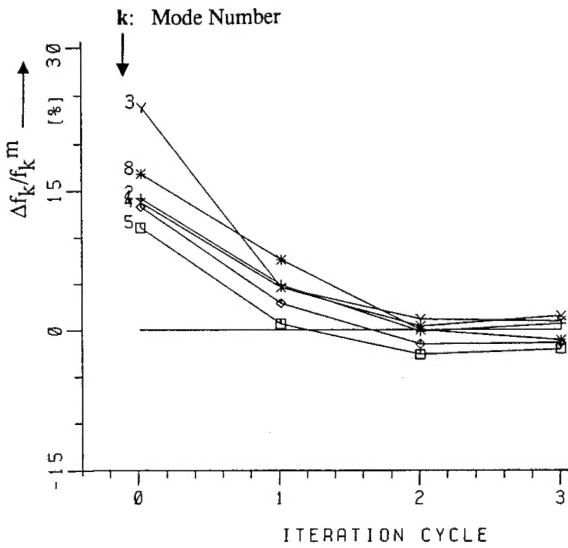


Figure 9: SPACE FRAME. Evolution of Eigenfrequency Differences

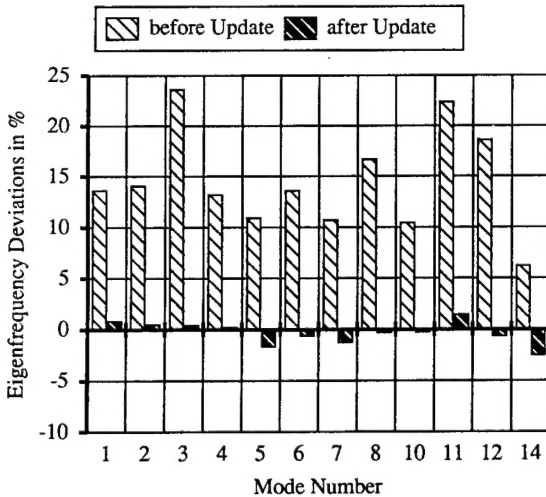


Figure 10: SPACE FRAME. Eigenfrequency Deviations for Update with 12 Measured Modes

Table 7: SPACE FRAME. Update with 12 Measured Modes (4 Iterations)

TEST		INITIAL MODEL				UPDATED MODEL			
k^m	f_k^m [Hz]	k^i	f_k^i [Hz]	$\Delta f^i/f_k^m$ [%]	MAC	k^u	f_k^u [Hz]	$\Delta f^u/f_k^m$ [%]	MAC
1	25.40	1	28.89	13.71	0.919	1	25.63	0.90	0.954
2	27.94	2	31.89	14.15	0.918	2	28.10	0.57	0.951
3	37.88	3	46.85	23.69	0.994	3	38.07	0.52	0.991
4	52.57	4	59.54	13.26	0.985	4	52.72	0.29	0.970
5	55.28	5	61.37	11.01	0.977	5	54.30	-1.77	0.971
6	61.67	6	70.10	13.66	0.982	6	61.23	-0.72	0.975
7	75.91	7	84.12	10.82	0.952	7	74.87	-1.37	0.983
8	86.73	8	101.24	16.74	0.963	8	86.38	-0.40	0.992
10	97.09	9	107.33	10.55	0.723	9	96.75	-0.35	0.944
11	100.69	13	123.29	22.45	0.984	11	102.19	1.50	0.984
12	101.73	12	120.73	18.68	0.963	10	100.97	-0.75	0.968
14	109.72	10	116.66	6.32	0.754	12	106.85	-2.62	0.776

Table 6: SPACE FRAME. Update with 6 Measured Modes (3 Iterations)

TEST		INITIAL MODEL				UPDATED MODEL			
k^m	f_k^m [Hz]	k^i	f_k^i [Hz]	$\Delta f^i/f_k^m$ [%]	MAC	k^u	f_k^u [Hz]	$\Delta f^u/f_k^m$ [%]	MAC
1	25.40	1	28.89	13.71	0.919	1	25.79	1.51	0.982
2	27.94	2	31.89	14.15	0.918	2	28.13	0.69	0.976
3	37.88	3	46.85	23.69	0.994	3	38.24	0.95	0.992
4	52.57	4	59.54	13.26	0.985	4	51.85	-1.36	0.981
5	55.28	5	61.37	11.01	0.977	5	54.15	-2.05	0.979
8	86.73	8	101.24	16.74	0.963	8	85.79	-1.08	0.987
6*	61.67	6	70.10	13.66	0.982	6	56.30	-8.72	0.986
7*	75.91	7	84.12	10.82	0.952	7	74.47	-1.90	0.974
10*	97.09	9	107.33	10.55	0.723	9	93.66	-3.53	0.896
11*	100.69	13	123.29	22.45	0.984	11	97.76	-2.91	0.986
12*	101.73	12	120.73	18.68	0.963	10	97.86	-3.80	0.962
14*	109.72	10	116.66	6.32	0.754	12	110.01	0.26	0.814

*) not measured

Update Results Using 6 Test Modes

One update run has been performed using only 6 out of 12 available test modes. The test modes 1 to 5 and 8 have been selected. This selection and restriction is based on the idea that the updating should be successful also in the case of incomplete measurements. If the changes of the design parameters are physically meaningful also the residual eigenfrequencies and modes should be improved and approximated to the measured ones.

Tab. 6 shows the test eigenfrequencies, the corresponding initial and updated ones. Within three iterations the analytical eigenfrequencies could be significantly improved. The frequency differences (Fig. 9) are reduced from maximum values of 23.7 % to values below 2.1 % and the MAC-values are better than 0.976 for those modes participating in the update process. For the residual modes one finds a significant improvement, too. Only test mode 6, a local mode, shows still a frequency difference of 8.72 %, all other differences are less or equal to 3.8 %.

Update Results Using 12 Test Modes

Tab. 7 shows the measured eigenfrequencies as well as the correlated analysis eigenfrequencies of the initial and updated model using 12 test modes. Test modes 9 and 13 could not be correlated to any analysis mode.

After 4 iterations the update process is stopped. All MAC-values have reached values greater than 0.95 except for test mode 14. Most frequency differences are below 1 % with a maximum of 2.6 % for test mode 14 (updated analysis mode 12) - see Fig. 10.

Some Remarks to the SPACE FRAME Update

Only the cross-sectional areas and the densities of the beams are modified significantly by the updating. The cross-sectional areas are reduced indicating errors in the longitudinal stiffnesses. This seems to be caused by an erroneous respectively to rough description of the structural nodes and their connections to the beams. The reduction of the cross-sectional areas of the beams is compensated by an increase of the densities to keep the total mass within limits. Both the areas and densities of simple Aluminium tubes should be well known, so that the conclusion of erroneous stiffnesses in the connections between the tubes and the structural nodes has a high probability. So, the SPACE FRAME is an example for inconsistent updating, for which the updated FE-model is able to describe the real structure only with substitute stiffness and mass parameters.

Test mode 9 could not be correlated with any analysis mode before and after update. It has not been used for updating and is assumed to be a noise mode (see also Ref. 4).

The SPACE FRAME could be updated successfully. This was possible without any design or test information except the FE-input data deck and the test results. The update method has given good indications of the error sources.

4. CONCLUSION

The theory of an update procedure has been described and application results published. The numerical results of the update applications have demonstrated

- convergence of erroneous design parameters towards correct ones,
- very good convergence of eigenfrequencies and mode shapes towards correct ones,
- improvement of not measured properties,
- and robustness in presence of noise on simulated test data and under real hardware test conditions.

Convergence problems due to wrong mode pairing have been explained, circumvented and solved.

Due to the fact that erroneous design parameters can be corrected by the procedure and the updated FE-models still consist of standard finite elements (not macro elements), such update models can be used for static, dynamic response and coupled analysis as well as control analyses.

Updating has been successful using measured eigenfrequencies and mode shapes, only. So, the test is not requested to deliver generalized masses, effective masses or participation factors, properties which are hard to be measured with high accuracy and standard effort.

Errors could be localized and even error sources could be detected. The latter has been possible in the FORK example including only analysis errors. The SPACE FRAME update has given good indications on the possible error sources with a final proof to be outstanding.

Acknowledgements

Part of this work has been founded by the European Space Agency with Mr. E. Fissette and Mr. O. Brunner as responsible contract officers. The finite element model input data deck and the test results of the SPACE FRAME have kindly been delivered by the company of LMS, Leuven.

5. REFERENCES

1. Eckert, L., Caesar, B., April 1991, Model Updating Under Incomplete and Noisy Test Data, Proceedings of 9th IMAC, Florence, Editor: Union College, Schenectady, NY.
2. Allemang, R.J., Brown, D.L., Nov. 1982, A Correlation Coefficient for Modal Vector Analysis, Proceedings of 1st IMAC, Orlando, Editor: Union College, Schenectady, NY.
3. Vanderplaats, G.N., August 1973, CONMIN - A FORTRAN Program for Constraint Function Minimization, User Manual, Ames Research Center, Moffet Field, Cal..
4. LMS, September 1990, Large Scale Modal Testing of a Space Frame Structure, from Pretest Analysis to FEA Model Validation, LMS International Application Notes Nr. 1.